

Lecture Notes in Mechanical Engineering

Dipak Kumar Mandal
Chanan Singh Syan *Editors*

CAD/CAM, Robotics and Factories of the Future

Proceedings of the 28th International
Conference on CARs & FoF 2016

 Springer

Lecture Notes in Mechanical Engineering

About this Series

Lecture Notes in Mechanical Engineering (LNME) publishes the latest developments in Mechanical Engineering—quickly, informally and with high quality. Original research reported in proceedings and post-proceedings represents the core of LNME. Also considered for publication are monographs, contributed volumes and lecture notes of exceptionally high quality and interest. Volumes published in LNME embrace all aspects, subfields and new challenges of mechanical engineering. Topics in the series include:

- Engineering Design
- Machinery and Machine Elements
- Mechanical Structures and Stress Analysis
- Automotive Engineering
- Engine Technology
- Aerospace Technology and Astronautics
- Nanotechnology and Microengineering
- Control, Robotics, Mechatronics
- MEMS
- Theoretical and Applied Mechanics
- Dynamical Systems, Control
- Fluid Mechanics
- Engineering Thermodynamics, Heat and Mass Transfer
- Manufacturing
- Precision Engineering, Instrumentation, Measurement
- Materials Engineering
- Tribology and Surface Technology

More information about this series at <http://www.springer.com/series/11236>

Dipak Kumar Mandal · Chanan Singh Syan
Editors

CAD/CAM, Robotics and Factories of the Future

Proceedings of the 28th International
Conference on CARs & FoF 2016

 Springer

Editors

Dipak Kumar Mandal
Department of Mechanical Engineering
College of Engineering and Management
Kolaghat, West Bengal
India

Chanan Singh Syan
Department of Mechanical
and Manufacturing Engineering
The University of the West Indies
St. Augustine
Trinidad and Tobago

ISSN 2195-4356 ISSN 2195-4364 (electronic)
Lecture Notes in Mechanical Engineering
ISBN 978-81-322-2738-0 ISBN 978-81-322-2740-3 (eBook)
DOI 10.1007/978-81-322-2740-3

Library of Congress Control Number: 2015959937

© Springer India 2016

This work is subject to copyright. All rights are reserved by the Publisher, whether the whole or part of the material is concerned, specifically the rights of translation, reprinting, reuse of illustrations, recitation, broadcasting, reproduction on microfilms or in any other physical way, and transmission or information storage and retrieval, electronic adaptation, computer software, or by similar or dissimilar methodology now known or hereafter developed.

The use of general descriptive names, registered names, trademarks, service marks, etc. in this publication does not imply, even in the absence of a specific statement, that such names are exempt from the relevant protective laws and regulations and therefore free for general use.

The publisher, the authors and the editors are safe to assume that the advice and information in this book are believed to be true and accurate at the date of publication. Neither the publisher nor the authors or the editors give a warranty, express or implied, with respect to the material contained herein or for any errors or omissions that may have been made.

Printed on acid-free paper

This Springer imprint is published by SpringerNature
The registered company is Springer (India) Pvt. Ltd.

Preface

We have great pleasure in announcing the 28th International Conference on CAD/CAM, Robotics and Factories of the Future, hosted by the International Society for Productivity Enhancement and College of Engineering and Management, Kolaghat, West Bengal, India. The conference is also supported and sponsored by Robotics Society of India, AMM, BRNS, IEI, DST, MTAB and TEQIP-II.

The conference includes plenary lectures in key areas of the conference which are followed by parallel sessions. The plenary lectures are delivered by the eminent personalities invited to introduce the theme of the conference. Each parallel session starts with an invited talk on specific topic followed by contributed papers. Papers are invited from industry, academic institutions, R&D organisations and professional engineers. Through Easychair 120 full papers were submitted, which were reviewed by experts from the review committee of CARS & FOF 2016, composed of 35 members from over 30 institutions/organisations from 12 countries. Finally, 93 full papers, authored by over 130 researchers from 70 institutions/organisations from five countries, were selected for presentation at the conference and for publication as chapters in this volume. Among them, 81 papers were registered for oral presentation as well as publication in the proceedings. This conference specially focuses on the positive changes made in the field of robotics, CAD/CAM and the future predication of emerging factories. Some of the important topics that are discussed in the conference are product development and sustainability, modelling and simulation, automation, robotics and handling systems, supply chain management and logistics, advanced manufacturing processes, human aspects in engineering activities, emerging scenarios in engineering education and training.

CARS & FOF 2016 includes nine keynotes from prominent researchers and practitioners from around the world: Prof. M. Rahman, Professor of Manufacturing Engineering, National University, Singapore; Dr. Brian Prasad, Technical Director, Knowledge Solutions, Irvine, CA, USA; Prof. Ashitava Ghosal, Professor of Mechanical Engineering, IISc, Bangalore; Dr. Ashish Dutta, IIT Kanpur; Dr. D.N. Badodkar (OS), BARC, Trombay, Mumbai; Dr. Prabir K. Pal, DRHR, BARC,

Mumbai, India; Dr. Subir Kumar Saha, IIT Delhi; Dr. Debanik Roy, BARC, DAE, Mumbai, India; Dr. Pradeep Kumar, VSSC, Thiruvananthapuram.

Acknowledgements

The editors thank Robotics Society of India, AMM, MTAB, BRNS, IEI, DST and TEQIP-II for their support of this event. Organising an event such as this would not have been possible without the help of many colleagues. We are grateful to the members of the Organising Committee, the International Scientific Committee, our sponsors and all those colleagues who have helped in the review of many abstracts and consequently full papers. This has required meticulous attention to detail and strict adherence to very tight deadlines. The organisers also recognise the support provided by our sponsors. Their continued support over the course of the planning period and also during the event itself is very much appreciated. We are also indebted to all the contributors to the conference, particularly the researchers and practitioners.

Finally, we would like to thank Springer, especially Swati Meherishi, Senior Editor, Applied Sciences and Engineering and Aparajita Singh, Editorial Assistant, Physical Sciences, for the wonderful support extended in the publication of these proceedings for the CARS & FOF 2016 International Conference.

Dipak Kumar Mandal
Chanan Singh Syan

Contents

Design and Development of a Low Cost Automation Injection Molding Machine of 250 g Capacity Using Microcontroller	1
Soumya Kanti Manna, Saibal Kumar Pradhan and Dipak Kumar Mandal	
Design, Development and Testing of a Three Component Lathe Tool Dynamometer Using Resistance Strain Gauges	13
Rahul Jain, J.K. Rathore and V.K. Gorana	
Study of Laser Transmission Welding Process Using a Volumetric Heat Source Model and Experimental Analysis	23
Bappa Acherjee, Arunanshu S. Kuar, Souren Mitra and Dipten Misra	
Comparison of Grinding Performance Under Different Eco-Friendly Environment.	33
D. Dewanjee, P. Kundu, B. Sikder, D. Biswas, Bijoy Mandal and Santanu Das	
Design of a Maintenance Optimisation Approach for Offshore Oil and Gas Production Systems	43
Chanan S. Syan and Geeta G. Ramsoobag	
Investigating the Feasibility of BCI-Based Social Media Interaction.	51
Chanan S. Syan and Randy E.S. Harnarinesingh	
Virtual Experiments for Integrated Teaching and Learning of Robot Mechanics Using RoboAnalyzer.	59
Ratan Sadanand, Ravi Prakash Joshi, Rajeevlochana G. Chittawadigi and Subir Kumar Saha	
Fuzzy Based Object Shape Recognition Using Translation, Rotation and Scale Invariant Parameters—An Automatic Approach.	69
Jeet Banerjee, Soma Banerji, Ranjit Ray and Sankar Nath Shome	

Need of Agriculture Hand Tool Design Using Quality and Ergonomics Principles	77
R. Jain, M.L. Meena and G.S. Dangayach	
Inverse Dynamics and Feet-Terrain Collision Model for Optimal Distribution of the Contact Forces During Crab Motion of a Hexapod Robot	85
Abhijit Mahapatra, Shibendu Shekhar Roy and Dilip Kumar Pratihar	
Sensing Human Pulse Bit Using Ionic Polymer Metal Composite (IPMC).	97
Debabrata Chatterjee and Adrish Bhaumik	
Order Reduction of Interval SISO Systems Using Least Square Methods with a Linear Shift ‘a’ Obtained by Harmonic Mean	103
K. Kiran Kumar and G.V.K.R. Sastry	
Identifying and Updating the Kinematics of KUKA-iiwaR800 in CAD for Accurate Simulation	115
Abdullah Aamir Hayat, Arun Dayal Udai and Subir Kumar Saha	
Parametric Optimization of Link Lengths of a SCARA Robot for Deburring of Circular Paths	127
P.V.S. Subhashini, N.V.S. Raju and G. Venkata Rao	
Integrating Artificial Intelligence and Simulation for Controlling Steady Flow of Fixtures.	137
Fentahun Moges Kasie, Glen Bright and Anthony Walker	
Predictions of Hip and Knee Power Consumptions of Patients Having Different Body Heights and Masses During Normal Walking	149
Abhishek Rudra Pal, Ankit Omprakash Mundada and Dilip Kumar Pratihar	
CFX, Static Structural Analysis of Tractor Exhaust System Based on FEA.	159
Faraz Ahmad, Ashwani Kumar, Karuna Kanwar and P.P. Patil	
FEA Simulation Based Thermo-mechanical Analysis of Tractor Exhaust Manifold	173
Faraz Ahmad, Vipul Tomer, Ashwani Kumar and P.P. Patil	
Stress Analysis of a Circuit Breaker Switchgear Mechanism by Using Multi Body Dynamics	183
J. Anjaneyulu, G. Krishna Mohana Rao and G. Venkata Rao	

Integration of Fuzzy Logic with Response Surface Methodology for Predicting the Effect of Process Parameters on Build Time and Model Material Volume in FDM Process. 195
 Manu Srivastava, Sachin Maheshwari, T.K. Kundra, Ramkrishna Yashaswi and Sandeep Rathee

A Study on State of the Art Technology of Laminated Object Manufacturing (LOM) 207
 Bewketu Gizachew Mekonnen, Glen Bright and Anthony Walker

Design Analysis and Manufacturing of Device for Rehabilitation of Hand Fingers Based on Illusionary Movements by Tendon Vibrations. 217
 Bonny Bernard and Preethika Immaculate Britto

Experimental Investigation of Process Parameters for Build Time Estimation in FDM Process Using RSM Technique. 229
 Manu Srivastava, Sachin Maheshwari, T.K. Kundra, Sandeep Rathee and Ramkrishna Yashaswi

Analysis of Prismatic Springs of Non-circular Coil Shape Using Finite Element Method 243
 Arkadeep Narayan Chaudhury, Arnab Ghosh, Krishnendu Banerjee, Abhijit Mondal and Debasis Datta

TiC, W₂C Reinforced Ti-W MMC Coating Developed on Ti-6Al-4V Substrate Through Laser Cladding 253
 Parth Gattani, Adil Azeem and Partha Saha

Motion Programming of SCORBOT ER-4u Using Fusion of Robot Kinematics and Inertial Sensor 263
 Abhishek Jha, Shital S. Chiddarwar and Veer Alakshendra

Trajectory Tracking Control of Three-Wheeled Omnidirectional Mobile Robot: Adaptive Sliding Mode Approach 275
 Veer Alakshendra, Shital S. Chiddarwar and Abhishek Jha

Point Mass Models for Dynamic Balancing of Industrial Manipulators Using Genetic Algorithm 287
 Devi Singh Kumani and Himanshu Chaudhary

Application of the Attractive Ellipsoid Methodology to Robust Control Design of a Class of Switched Systems 299
 V. Azhmyakov and J.H. Carvajal Rojas

A Three Finger Tendon Driven Robotic Hand Design and Its Kinematics Model 313
 I.A. Sainul, Sankha Deb and A.K. Deb

An Intelligent Methodology for Assembly Tools Selection and Assembly Sequence Optimisation	323
Atul Mishra and Sankha Deb	
Alignment Based Inspection Framework for Additive Manufactured Parts	335
Vimal Kumar Pathak and Amit Kumar Singh	
An Investigation on Slab Milling Operation to Find Out Optimum Cutting Parameters	345
Spandan Guha, Tapas Banerjee, Asish Bandyopadhyay and Santanu Das	
Recognition of Force Closed Point Grasp for 2D Object	357
Abhijit Das and Sankha Deb	
Developing a GUI for Optimization of Acoustic Enclosure of a Compressor Chamber	367
T. Ramamohan Rao and S. Kirthana	
A Pilot Study of Sustainable Machining Process Design in Indian Process Industry	379
Sumit Gupta, G.S. Dangayach, Amit Kumar Singh and P.N. Rao	
Sagittal Position Analysis of Gait Cycle for a Five Link Biped Robot	387
Ramanpreet Singh, Himanshu Chaudhary and Amit Kumar Singh	
A Note on Mechanical Feasibility Predicate for Robotic Assembly Sequence Generation	397
M.V.A. Raju Bahubalendruni, Bibhuti Bhusan Biswal, Manish Kumar and B.B.V.L. Deepak	
Weld Seam Tracking and Simulation of 3-Axis Robotic Arm for Performing Welding Operation in CAD Environment	405
B.B.V.L. Deepak, C.A. Rao and B.M.V.A. Raju	
A Comparative Performance Analysis of Discrete Wavelet Transforms for Denoising of Medical Images	417
Yogesh S. Bahendwar and G.R. Sinha	
Deterministic Model for RF Hot Spots Location and Probability Within Empty Rectangular Structures	425
Ricardo Rodriguez and Winston G. Lewis	
Heat Stress in the Workplace: A Case Study of a Cement Manufacturing Facility in Trinidad	435
Winston G. Lewis and Ricardo Rodriguez	

Modeling and Simulation of a Near Omni-Directional Hexapod Robot 445
 D. Mahata, Ranjit Ray and Sankar Nath Shome

Optimization of Vibration of Collecting Plates of Electrostatic Precipitator Through FEA 455
 Harshal Shinde, Akshata Sangle, Sumit Shendkar, Omkar Kulkarni, Ninad Kulkarni, G.M. Kakandikar and V.M. Nandedkar

Full Aperture Optical Polishing Process: Overview and Challenges 461
 Raj Kumar Pal, Harry Garg and Vinod Karar

Stability Analysis of Haptic Virtual Environment Systems for Active Interactions in Surgical Robot Simulators 471
 Rishika Khandelwal and Asokan Thondiyath

Synchronized Optimization of Injection Moulding Parameters for Higher Acceptance of Polypropylene Products 481
 Bikash Bepari, Tanumoy Kolay, Kamal Nayan and Subham Mishra

Use of Visual Analytics and Durometer in Risk Reduction of Foot Problems in Diabetes. 491
 Vinaytosh Mishra, Anubha Rautela, B. Manjunatha, Cherian Samuel, S.K. Sharma and A. Mishra

On the Complexities in Machining Titanium Alloys 499
 Paramjit Singh, Harish Pungotra and Nirmal S. Kalsi

Modeling, Analysis and Trajectory Planning of a 5 Degree of Freedom Robotic Arm for a Transmission Line Crossing Robot 509
 C.M. Shruthi, A.P. Sudheer and M.L. Joy

Design and Modelling of Dual Faceplate Centrifugal Casting Equipment for Manufacturing of Turbine Bearing 523
 Saamil Desai, Saurin Sheth and Purvi Chauhan

Design and Control of Tendon Driven Robotic Hand for Prosthesis Applications 535
 Roshan Kumar Hota, Arvind Ahirwar and Cheruvu Shiv Kumar

Stabilization of Posture of Humanoid Using PID Controller in Gazebo Simulator Using Robot Operating System (ROS) 543
 V. Madhu Babu, G.V.V. Surya Kiran, S.K. Sameer, Roshan Kumar Hota and Cheruvu Shiv Kumar

Robotic Picking of Cylindrical Fuel Pellets from a Boat Using 3D Range Sensor. 553
 Rahul Jain, Abhishek Jaju, Namita Singh, Sanjeev Sharma and Prabir K. Pal

Swachh-Bharat Bot: A Sweeping Robot	563
Swapnil Jogonal and Kamal Sharma	
Force Sensitive Robotic Gripper	569
Meher Tabassum and D.D. Ray	
Electron Beam Melting of Steel Plates: Temperature Measurement Using Thermocouples and Prediction Through Finite Element Analysis	579
Debasish Das, Dilip Kumar Pratihar and Gour Gopal Roy	
Design and Analysis Towards Successful Development of a Tele-Operated Mobile Robot for Underground Coal Mines	589
Dip N. Ray, Riddhi Das, Bijo Sebastian, Biplob Roy and Somajyoti Majumder	
Design-of-Experiments (DOE) to Compute the Effect of Chromium Abrasives in Kerosene Oil as Dielectric of EDM of OHNS Die Steel . . .	603
Kamal Sabharwal and Paramjit Singh	
CFD Modeling for Slurry Flow Through Bends and Straight Pipe Line	615
Arvind Kumar	
Role and Significance of Visualisation in Product Design at Prototyping Stage	625
Sawankumar Naik and Ravi Terkar	
Positional Analysis of a DC Brushed Encoder Motor Using Ziegler-Nichols Algorithm	637
Priyam Anilkumar Parikh, Saurin Sheth and Trupal Patel	
A Hybrid Approach to Motion Planning for Stepping over and Obstacle Avoidance in Humanoids	651
H. Prasanth and A.P. Sudheer	
Web Based Simulation and Remote Triggered Laboratory for Robots	665
A.T. Navaraja, Neha Jain, Debashree Sengupta and C.S. Kumar	
Modular Robotic Assistance in Cluttered Environments: A Broad-Spectrum of Industrial Applications	679
Satwinder Singh, Akshit Kaplish and Ekta Singla	
A Benchmarking Model for Indian Service Industries	689
Bhupender Singh, Sandeep Grover and Vikram Singh	
Optimal Design of a Production System	697
P.K. Arora, Abid Haleem, M.K. Singh, Harish Kumar and D.P. Singh	

Modelling and Analysis of a Novel Ancillary Braking System for All Terrain Vehicle	705
Amitansu Pattanaik and Nirbhay Jain	
Nonlinear Tracking Control of Parallel Manipulator Dynamics with Intelligent Gain Tuning Scheme	715
K.V. Varalakshmi and J. Srinivas	
Study of Joining Different Types of Polymers by Friction Stir Welding	731
Nitin Panaskar and Ravi Terkar	
Single Point Incremental Forming Using Flexible Die	741
D. Panjwani, P.K. Jain, M.K. Samal, J.J. Roy, D. Roy and P. Tandon	
Hilbert Curve Based Toolpath for FDM Process.	751
Saquib Shaikh, Narendra Kumar, Prashant K. Jain and Puneet Tandon	
Development of Edge Processing and Drawing Algorithms for a 6 Axis Industrial Robot.	761
G. Kalaiarasan, A. Tony Thomas, C. Kirubha and B. Saravanan	
Experimental Investigation and Fuzzy Modelling of Flatness and Surface Roughness for WCB Material Using Face Milling Operation	769
Saurin Sheth and P.M. George	
A Retrospective Investigation of Different Uncertainty of Measurement Estimation Approaches.	779
Harish Kumar, P.K. Arora, Girija Moona, D.P. Singh, Jasveer Singh and Anil Kumar	
Design of Automatic Fuel Filling System Using a Mechatronics Approach	785
Saurin Sheth, Kavita H. Patel and Harsh Patel	
A Framework for Evaluation of Environmental Sustainability in Pharmaceutical Industry	797
Geo Raju, Harpreet Singh, Prabir Sarkar and Ekta Singla	
Aero-Structure Interaction for Mechanical Integration of HP Compressor Blades in a Gas Engine Rotor.	807
N. Vinayaka, Nilotpal Banerjee, B.S. Ajay Kumar and Kumar K. Gowda	
Appraisalment of Mass Customization Capability Level Using Multi-grade Fuzzy Approach	821
Jayant K. Purohit, M.L. Mittal, Milind Kumar Sharma and Sameer Mittal	

**Analysis of Solar Ejector—Jet Refrigeration System
Using Eco-Friendly Material R1234yf 831**
Gaurav and Raj Kumar

**Numerical Investigation of Thermo hydraulics Performance
in Elliptical Twisted Duct Heat Exchanger 839**
Su vanjan Bhattacharyya, Himadri Chattopadhyay, Tarun Kanti Pal
and Anirban Roy

**Erratum to: TiC, W₂C Reinforced Ti-W MMC Coating Developed
on Ti-6Al-4V Substrate Through Laser Cladding E1**
Parth Gattani, Barun Haldar, Adil Azeem and Partha Saha

Author Index 851

About the Conference

The International Society for Productivity Enhancement (ISPE) was founded in 1984 in the USA with the goal to accelerate and augment the international exchange of ideas and scientific knowledge in the field of technological applications. The primary aim of ISPE is to integrate technologies, strategies and resources to enhance productivity, competitiveness, and thereby, improve the quality and standard of life. ISPE has been promoting research and education by organising conferences, training workshops and seminars and various other professional activities. Among others, the primary aim of ISPE is to unite, on a common platform, policy makers, researchers, people from academia, engineers and users of CAD/CAM, robotics and automation, advanced technologies and factories and systems research and development.

International institutions globally have been hosting the CARs & FoF conference since its formation in 1984. Middlesex University organised the 27th CARs & FoF in 2014. The 28th CARs & FoF 2016 Conference is hosted by College of Engineering and Management, Kolaghat, from 6 to 8 January 2016. The College of Engineering and Management, Kolaghat is situated in the integrated complex of the Kolaghat Thermal Power Station of the West Bengal Power Development Corporation Limited, a premier power generation company in India. The college has a close institute–industry partnership with the power station. Established in 1998, it is one of the premier private engineering colleges in the state of West Bengal. The college has received a INR 100 million assistance from the World Bank.

About the Editors

Dr. Dipak Kumar Mandal completed his Master's Degree in Heat Power Engineering from Bengal Engineering and Science University, Shibpur, West Bengal in the year 1999. He obtained his Ph.D. in the year of 2010 from the same university. He is currently Associate Professor and Head of Mechanical Engineering Department at the College of Engineering and Management, Kolaghat, West Bengal. He has worked at the Kolaghat Thermal Power Plant. His research fields are computational fluid dynamics and bio-fluid dynamics. He has published several papers in international journals and conference proceedings. He has authored one book and is a regular reviewer for several journals.

Prof. Dr. Chanan Singh Syan graduated from the University of Bradford, UK in 1983 with a B.Eng. (Hons) in Mechanical Engineering. In 1988 he obtained a doctorate from the University of Hull, UK in Artificial Intelligence in Design for Manufacture. He has over 15 years of industrial experience and over 28 years of academic experience. Presently, he is Head of Production Engineering and Management Office (postgraduate office), Leader of Graduate Programmes and Professor at the University of the West Indies. His research specialisations include brain-computer interface (BCI), manufacturing, design and manufacture, and asset management. He is heading the BCI and Robotics and Automation research groups.

Design and Development of a Low Cost Automation Injection Molding Machine of 250 g Capacity Using Microcontroller

Soumya Kanti Manna, Saibal Kumar Pradhan
and Dipak Kumar Mandal

Abstract This article will describe an innovative way of implementing the automation of an injection molding machine using microcontroller which in turn will reduce total automation cost to only a few thousands rupees. In the piston side, toggle mechanism is used instead of direct drive to get extra mechanical advantage and safety features. The whole design is being simplified by cutting out some features which in turn reduce the total cost of the system without affecting its effectiveness. The system can be operated in two modes. In primary mode, the operator can easily operate through on-board keypad by entering only time sequences with the help of the manual. In the second one, it can be remotely controlled through a PC based application software.

Keywords Automation · Microcontroller · Hybrid control · GUI · PC based control · Predefined control

1 Introduction

Now a day's plastic is an essential material in our daily life. That's why polymer industry has been grown up day by day. There are a few pioneers in the manufacturing industry which manufacture automation injection molding machine like Wilson, Ferro Milacron, Magnum industries etc. Existing injection molding machines are costly as they use PLC based system for automation. Thus it is difficult for the SSI (Small Scale Industry) and MSI (Micro Scale Industry) unit to install those machines for production. Also in case of manually controlled machine the production rate is very low and labor cost is very high. It is known to everybody that the production rate and control architecture of an injection molding machine

S.K. Manna (✉) · S.K. Pradhan · D.K. Mandal
College of Engineering & Management, Kolaghat, India
e-mail: soumyakanti.mid@gmail.com

© Springer India 2016
D.K. Mandal and C.S. Syan (eds.), *CAD/CAM, Robotics and Factories of the Future*, Lecture Notes in Mechanical Engineering,
DOI 10.1007/978-81-322-2740-3_1

depend on the hardware specification of machine. The control of an injection-molding process would be differentiating into three categories such as all-phase control, phase-dependent control, and cycle to cycle control. Each manufacturer producing injection molding machine has its proprietary control technique, which generally depends on system specifications and hardware components of controllers and instrumentation. Those control methods are solely dedicated to a specific brand of machines and cannot be used by others. Besides, control codes are usually implemented with special software toolkits owned by different companies. It is very much needed to apply a general control strategy to all types of injection molding machines so that maintenance and innovations will be an easy task for engineers. Different computer aided technology and designing software like ROBOTMASTER (case study, ROBOTMASTER) is used for tool movement in 6 axes without using G code. Cox (Hadzistevic et al. 2010) is a new tool which has opened a new direction of numerical simulation of injection molding and mold design in plastic industry. Researchers are finding new way to resolve the problems in CAD-CAM modeling (Bohatier et al. 1988). Cheng et al. (2002) have used the java technology for the automation technique. But it requires sophisticated programming technology as well as highly advanced processor to implement. People are very much concerned about the kind of automation tool or technique being used for getting better performance criteria. Frank et al. (2014) have used model-driven engineering (MDE) of Manufacturing Automation Software Projects (MASP). But complexity in this technique is higher and implementation is getting tougher. Also it is much more oriented to proprietary hardware components. Becker et al. (2013), have used software tool for cooling in automation injection molding machine as it is one of the main criteria in designing. Network based distributed control is also used for injection molding machine (Abraham and Muthamizhselvi 2013). Also there is a disadvantage of in terms of its speed of communication and no of devices connected through it. Flex Ray based network (Komathi et al. 2014) is used to control a series of injection molding machine through a PC based controller. To maintain the productivity and quality of the output, operator has to stand beside the machine. So this kind of network based control will make those systems a standalone system and product quality will be much better. Ahmed 2007 have discussed hydroelectric model of injection molding machine. Developed CAD model and a small prototype are shown below in Fig. 1.

2 Embedded System

People generally use standard techniques for controlling injection molding machine such as G code and M code or part programming where operator should also be a technical person for prominent control. The rate of production and the production quality solely depend on the performance criteria of the operator. Here in the machine, the controlling portion is very much simplified by adding some extra features to the system. In the generalized standard machine, nothing is predefined

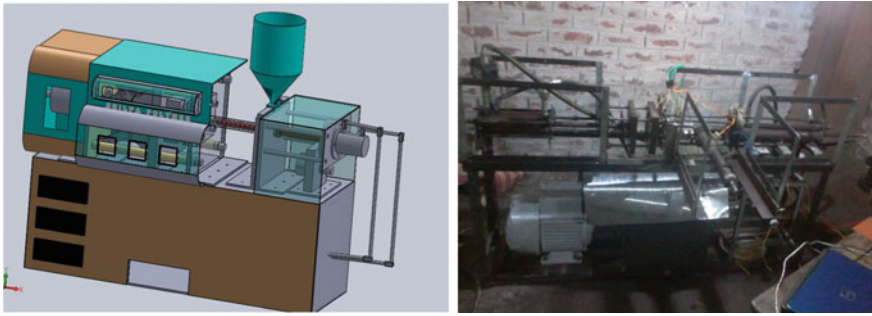


Fig. 1 CAD model and prototype developed at our workshop

like the path of the tool or hydraulic drive, screw or speed of those as well as the time of molding. So operator has put the command through keypad for defining those phenomena's to run the system. But here that complicity has been removed. Basically some of the criteria which are quite unchangeable for a system are hereby fixed to avoid extra hurdles regarding the control action. As a result, it will become a cost effective and user-friendly system.

- (i) Generally the speed of a particular hydraulic or AC motor is limited to a certain range. In the other way, the speed of the hydraulic drive for running the piston as well as the screw can be fixed up to a certain limit.
- (ii) The length between the starting position and the mold position from both ends can be fixed for a particular system. That means the time needs to travel for piston as well as the screw to travel from its starting position to the mold position can be fixed.

There are few things only depend upon the production rate and production quality of the machine

- (i) The stop time in the molding position is changeable. It depends upon the raw material as well as the quality of the final product.
- (ii) The production rate is also one of the main criteria for a particular injection molding machine. It depends upon the size of the mold and the no of runs. The size of mold is totally depends upon the mold maker and the people using them for their production. If the user makes the mold having a huge no of slots, therefore production rate is also higher after each shot. Also the machine can be controlled by entering value through keypad before initialization.

Ultimately if predefined phenomena can be fixed, the no of shots per minute or production rate can be determined. User can easily enter molding time as well as the no strokes to run the machine through the keypad. User can easily get the help from manual which defines required time for each material and its quality. This will make the machine operated as per the required no of times.

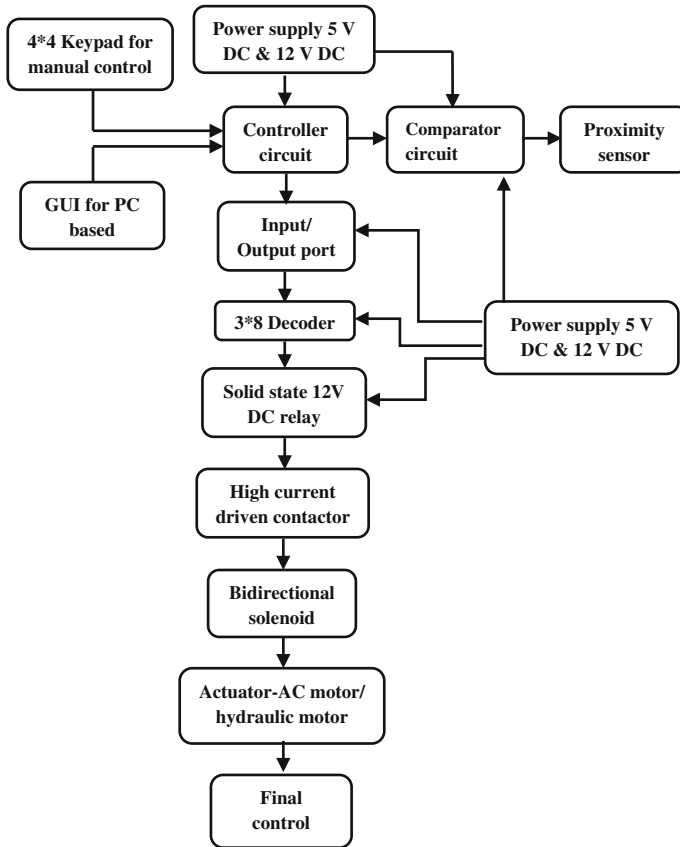


Fig. 2 Block diagram of the controlling circuit

Here a two way control has been used for the control of the system. The machine can be controlled by software module as well as hardware. In manual control, there is a keypad through which all the functions can be operated because any kinds of commands can be transmitted to the system. Also a GUI is there through which the same function can be transmitted from PC. A feedback loop is there for monitoring whether it is following the particular path or not. Proximity sensor is used at the end position to detect the end position as well as to continue the motion for the required no of times.

Though the feedback sensor is sensing the instantaneous position all the time, it also has some safety scheme to avoid accidents. If any actuator moves beyond the particular range of motion, the end limit switch automatically activate and cut down power supply. Also there is a mechanical barrier at the end of every joint end so that actuator cannot move further. Block diagram of the whole circuit is shown in Fig. 2.

3 Interfacing of Driver Circuit with Microcontroller for PC Based Control

As per design, a Graphical User Interface (Fig. 3) is used to send particular command related to a particular motion control which totally depends upon the material, thickness of the product, product quality and the no of strokes. First of all, signals and inputs come to the PC through Controller. PC activates those relays which are required for that particular motion. It sends the command bits in a package through serial communication. When it receives the command bit serially from PC, it activates those particular port pins of the controller.

The interfacing circuit between microcontroller and other components is shown in Fig. 4. Eight SPDT relays are interfaced with I/O ports of the microcontroller followed by a driver transistor. Driving current from microcontroller port is not high enough to make the relay on. Therefore to supply high current, power transistor is needed for amplifying the signal. Those relays are used to operate hydroelectric motor or any electromagnetic contact. Command will be sent to the microcontroller pin to activate relay. A diode is used in the circuit to prevent back EMF from damaging driving transistor when the relay releases. A LED will indicate on stage of relay (Fig. 4).

In GUI portal, first of all, user has to configure serial communication. Actually USB communication is very much complicated and difficult to implement in case of sending commands for a PC based automation technique. So there is another easy way to convert any command from USB to RS232 protocol though readymade software. Basically any command can be easily sent through serial communication only by converting it into ASCII code. There is an IC MAX232 at

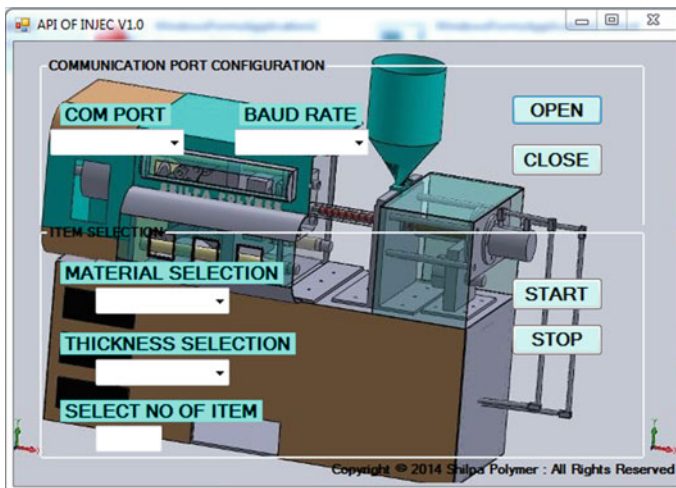


Fig. 3 GUI for PC based control

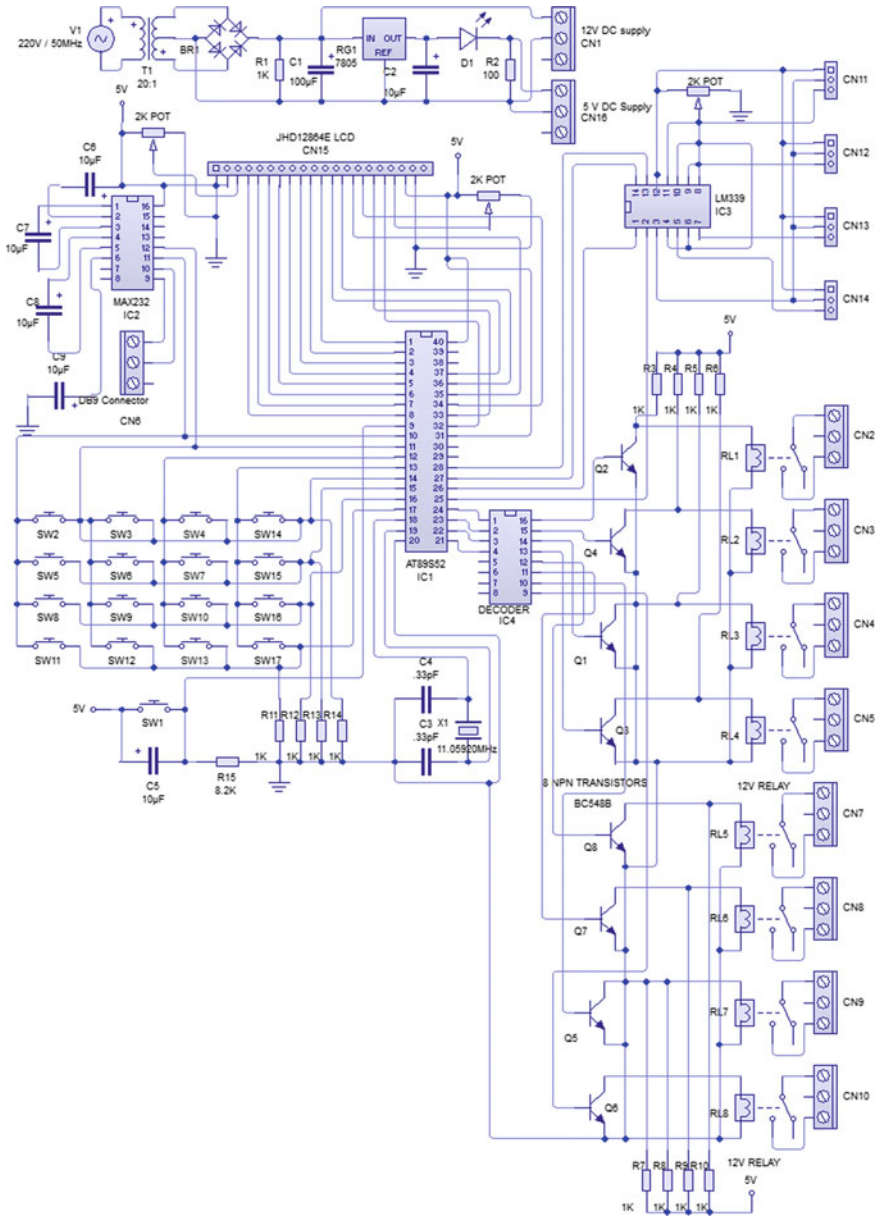


Fig. 4 Schematic diagram of controlling circuit

the receiving end for receiving command. As shown in the figure, one dedicated 7805 is connected to microcontroller for 5 V DC power supply. A serial IC MAX232 is connected to the microcontroller to convert the RS232's signals to TTL

voltage levels that will be compatible to 8051's Txd and Rxd pins. In RS232 communication, logic 1 is represented by -3 to -25 V, while a logic 0 bit is $+3$ to $+25$ V, making -3 to $+3$ undefined. In serial communication the packet data always in ASCII character. In the command frame, the original data is surrounded by a single start bit, whereas the stop bit will includes one or two bits. The start bit is always a 0 (low) and the stop bit(s) is 1 (high). It receives those ASCII code via serially. First of all, COM port will be selected as well as baud rate for setting up serial communication. COM port is being selected from device manager. Actually microcontroller can communicate with several other devices via several standard speeds. Generally it is in the multiplication factor of 4800 bps. Internally it can be decided by setting up a few register of the controller in software mode. Also we need to see whether microcontroller is compatible with the particular speed. When microcontroller receives particular command from PC, it activates particular port pins. Those port pins are being connected to solid-state relay for driving the output. Actually before sending activation signal to relay, first of all it should be amplified from $+5$ to $+12$ V by using the NPN transistor. Microcontroller has the logical output logic 1 or 0 which is equivalent to $+5$ or 0 V DC level. Therefore for driving the relay circuit, it should be amplified first. Here total 8 no of relays are being operated through microcontroller using 3:8 decoder. Using decoder, all the relays can be easily controlled using less no of port pins of microcontroller. The line current of 12 V DC solid-state relays is around 7.5 a, 240 V AC. But when system is running at full automatic condition, it will consume a huge current near to 15 A which may create a loading effect on the internal circuit. Therefore optocoupler is required create an isolation between input and output circuit. This is not also sufficient to reduce the loading effect especially when 2 HP AC motor is used to drive the hydraulic cylinder or screw. Actually pressure is created for driving those hydraulic cylinders is near about 10 N which create an extra load on the driving relay. So sometimes it will trip down. The only solution is contactor which is also another kind of electromagnetic relay having high current driving facility. Contactor is used to supply coil voltage which is very small near about 12 or 24 V DC. Line voltage near about 440 V AC with a current rating up to 1000 A can be easily driven at the output. Ultimately final control element such as solenoid valve or motor is connected to the contactor output for production (Fig. 5).

4 Manual Control

We generally use Keyboards and LCDs for manual control operation. First key press and keyboard detection mechanisms have been discussed. At the lowest level, keyboards are oriented in a matrix of rows and columns. We are able to access a switch in the array of rows and columns by scanning port pins; therefore a keypad containing 4×4 matrix of keys is connected to a 8 pin port of microcontroller.

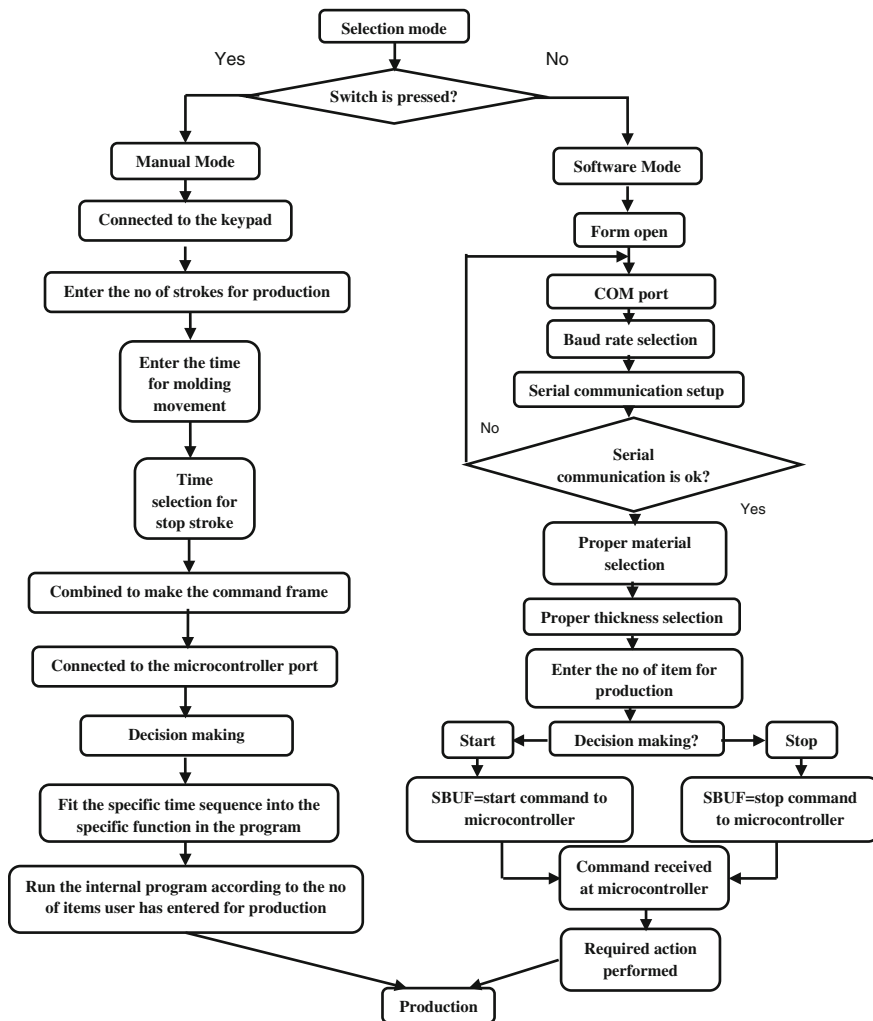


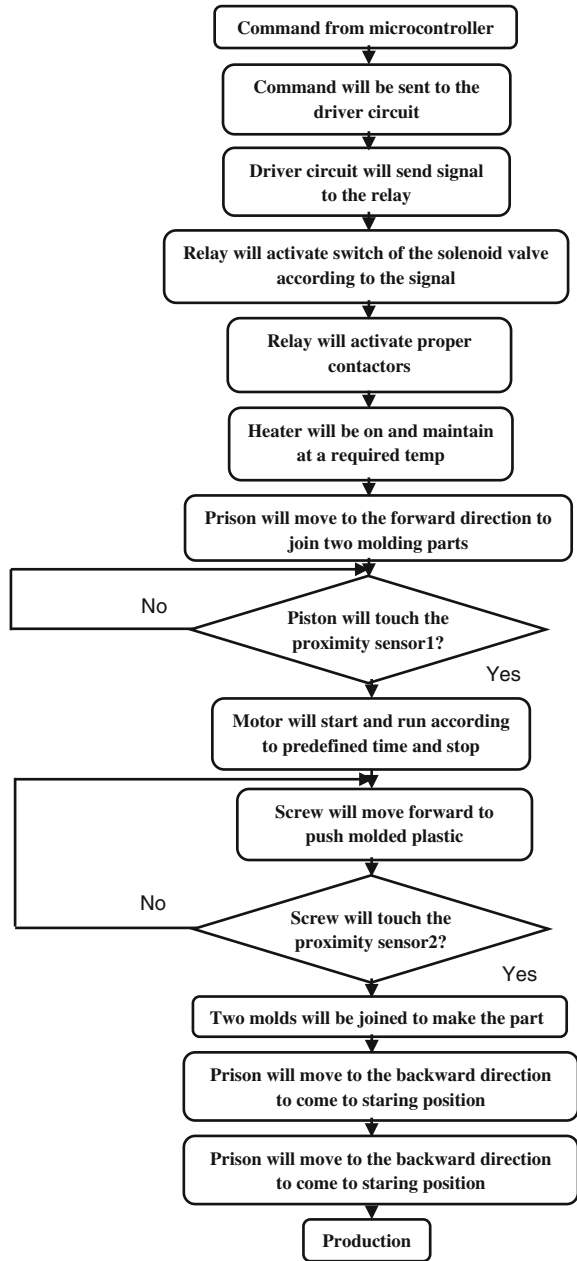
Fig. 5 Flowchart about the total function operated in the machine

When a key is pressed, it will make a contact with a particular row and column. Figure 4 shows the configuration of a 4×4 matrix connected to a single port. The rows of the keypad matrix are connected to a port considered as the output one and the columns are connected to another port considered as the input one. If no key has been pressed, the input port will show 1 s for all columns after scanning because they are all connected to high (Vcc). If all the rows are connected to ground and a key is pressed, the pressed switch connected to the column will receive 0 since the key pressed provides the path to ground. There is an infinite loop through which

microcontroller used to scan the keyboard continuously to detect and identify which of the key in the keypad has been pressed. To detect a pressed key, microcontroller connects all rows to ground by providing 0 to the output port and then it reads input port through the columns. If the data read after scanning the columns is $D3 - DO = 1111$, it indicates that no key has been pressed and the same process continues until a key press is detected. If one of the column bits shows a zero after scanning, this determines the occurrence of a key press. For an example, if we find the column port $D3 - DO = 1101$, that means a key in the D1 column has been pressed. Starting with the top row, the microcontroller will connect DO to ground by providing a low to row DO only; then it reads the input port. If we get all 1 s in the column port pins, it means no key is activated in that particular row and the process is repeated to the next row. It generally grounds the next row until the last, scans the input column port, and checks whether any zero is getting or not. This iterative process continues thoroughly until the row of the press key is identified. To determine if any key is pressed, the column port pins are scanned in an infinite loop until one of them has got a 0 on it. After detection of a key press, the microcontroller needs to wait 20 ms for the bouncing period and then it scans those columns again. Basically it mainly serves two important functions: first of all, it ensures about genuine key press detection and the same function can be occurred due to a spike noise, therefore the result can be erroneous one and (b) it prevents multiple key press. If the key is still pressed after the 20 ms delay, it determines the row it belongs to; otherwise, it goes back again into that infinite loop to detect a genuine key press. After finding the row where the key press belongs to, it sets the starting address of the look-up table that stores ASCII value of that scan codes for that row and goes to the next stage to identify the key.

There is an infinite loop always running inside the microcontroller for uninterrupted production. Actually as per discussion before, there are two things need to enter through the keypad. One is no of strokes and another is molding time. Those values will be returned to the sub function of the main program. Each time main function is running for the no of required times, those functions containing the time sequence will be called and the machine will run accordingly. All the other functions regarding relay and contactor are described in the PC based automation technique. The only difference is that in PC based automation user doesn't have to go to the system. By controlling the PC, the user can control all the operations. In manual control, user has to select few things therefore the machine will be running automatically and give the production. Here also all kinds of precautions are being taken care off for all safety features. Proximity sensor as well as limit switch is there for notifying the end position to establish positioned based control as well as end position. All the controlling actions are same for both PC based and manual control. The flow chart of hybrid control is shown in Fig. 6.

Fig. 6 Flow chart of hybrid control



5 Conclusion

The developed machine can be operated in fully automatic and semi-automatic modes. NXP microcontroller is being used for automation and controlling movement of each component starting from motor, solenoid valve, piston, screw and mold. A GUI has been developed in Microsoft Visual Studio platform where all the motions are being loaded in predefined manner. People can operate the machine from the keypad as well as the application based interface through PC. Ultimately the process of operation is getting easier because earlier different numeric codes are needed to move any component. But here user has to put only the time sequences as per given manual. As a result a non-technical person can easily handle those machines. It will create a user-friendly and low cost operation.

6 Discussion

There are many advancements have been taken place in the field of embedded system. A lot of products are being developed using microcontroller because of low cost and high speed operation. Microcontroller is a very small device with enormous facility. The automation of the whole machine is being implemented using the same technology. The main aim of using this technology is not to implement high accuracy or precision. If the PLC based automation technology is being replaced by microcontroller, the automation cost will be reduced to a huge amount. Actually the basic motivation of using this technology is to make the system affordable by small scale and medium scale industry owner. The machine is under full working condition. Using proper feedback sensor, the standard accuracy can be achieved. It is being further improved to get it fit for batch commercial production.

References

- Abraham, M., & Muthamizhselvi, M. (2013). Design and Implementation of can bus for distributed injection molding machine based on arm controller. *International Journal of Computer Applications*, 0975–8887.
- Ahmed, S. F. (2007). A new approach in Industrial automation application “Embedded system design for Injection Molding Machine”. In *IEEE Multitopic Conference*. Lahore, Pakistan.
- Becker, J. M. J., Hansen, H. N., Houten, F., & Tosello, G. (2013). Performance evaluation of a software engineering tool for automated design of cooling systems in injection molding. *Proceedings of Forty Sixth CIRP Conference on Manufacturing Systems*, 7, 270–275.
- Bohatier, C., Cagnasso, F., Dubois, B., & Thomas, M. C. (1988). Knowledge base of components and connections for a CAD/CAM system. In *5th International Symposium on Robotics in Construction*. Tokyo, Japan.

- CAD/CAM based robot programming for milling & trimming by using robots in case study, Robotmaster. <http://www.robotmaster.com/assets/data/pdf/success/armatecSurvivabilityOttoBockHealthcare.pdf>.
- Cheng, C. C., Lee, W. C., Liu, T. K., Tseng, Y. T., & Zhao, Y. J. (2002). Flexible process control for injection molding machines using java technology. In *American Control Conference*. Anchorage, AK.
- Frank, T., Heuser, B. V., Legat, C., & Schütz, D. (2014). Model-driven engineering of manufacturing automation software projects—A SysML-based approach. *Mechatronics*, *24*, 883–897.
- Hadzistevic, M., Hodolic, J., Matin, I., Tadic, B., & Vukelic, D. (2010). Development of CAD/CAE system for mold design. *Journal of Production Engineering*, *13*(1).
- Komathi, C., Saranya, M., Saranya, R., & Sreenidhi, R. (2014). Flexray rooted distributed intelligent governing of injection press. In *5th IRF International Conference*, Chennai, India.

Design, Development and Testing of a Three Component Lathe Tool Dynamometer Using Resistance Strain Gauges

Rahul Jain, J.K. Rathore and V.K. Gorana

Abstract In this paper, a lathe tool dynamometer that can evaluate fixed cutting forces by using level of resistance stress gauges has been designed and developed. These stress gauges insured to the cylindrical bar. The alignment of the cylindrical bar and stress gauge places has been identified to increase sensitivity and reduce cross-sensitivity. The designed dynamometer is capable of computing the forces acting on the workpiece in turning operation using any data acquisition system. The sensing system measures the deflection in stress gauges, and these signals are modified into other quantity and computed in the form of forces on the display system as well as on PC also. Tests finished at different machining factors revealed that the dynamometer could be utilized continually to evaluate cutting forces.

Keywords Cutting forces • Dynamometer • Resistance strain gauge • Turning

1 Introduction

The metal cutting process (Jain and Chitale 2010) defined as removing a layer of metal from the blank to get a product of quantified shape and size with identified precision and surface finish. The cutting process was carried out on metal cutting machine tools with the help of metal cutting tools.

R. Jain (✉)

Department of Mechanical Engineering, Malaviya National
Institute of Technology Jaipur, JLN Marg, Malaviya Nagar, Jaipur
Rajsathan, India
e-mail: rjmahesh207@gmail.com

J.K. Rathore

Industrial Engineering, Tata Steel Processing and Distribution Limited,
Jamshedpur, Jharkhand, India

V.K. Gorana

Department of Mechanical Engineering, University College of Engineering,
RTU, Akelgarh, Kota, Rajsathan, India

© Springer India 2016

D.K. Mandal and C.S. Syan (eds.), *CAD/CAM, Robotics and Factories of the Future*, Lecture Notes in Mechanical Engineering,
DOI 10.1007/978-81-322-2740-3_2

The rise in responsiveness vis-à-vis the requirement to optimize manufacturing process (Milfelner et al. 2005) efficacy has directed to an excessive deal of investigation directed at machine tool condition monitoring. One of the primary difficulties that live in testing metal-forming force reductions was a great spread in the measures (Astakhov and Shvets 2001) of the physical pressure force(s). One of the unique purposes in manufacturing is the smart machining arrangement (Kuljanic and Sortino 2005), so for designing of such intelligent system for lathe tool dynamometer for turning process this literature have studied in which these process of machining included like turning (Panzera et al. 2012; Totis and Sortino 2011; Yaldiz et al. 2007), orthogonal cutting (Kim and Kim 1997), drilling (Korkut 2003), grinding (Korkut 2003), milling (Korkut 2003; Seker et al. 2002) and shaping (Seker et al. 2004; Yaldiz and Unsacar 2006) was the major investigation area of the researcher. Various type of assemblies like octagonal rings assembly with strain gauge (Korkut 2003; Yaldiz and Unsacar 2006; Yaldiz et al. 2007), Kistler dynamometer (Kim and Kim 1997), load cells on the tool post (Seker et al. 2002; 2004), piezoelectric force ring integrated into a commercial tool shank6 and square cross-section bar with strain gauge (Panzera et al. 2012) has used by several researchers for their research work but there is no such literature found for design and develop a cylindrical bar assembly for mounting using resistance strain gauge.

2 Literature Review

Machining of metal comprises driving of cutting tool from end to end the excess material of the workpiece and the process factors in tool cutting (Astakhov and Shvets 2001). This information provides the chance for a fast determination of the cutting speed resultant to the highest possible produced area of workpiece before the selected wear restrict obtained, reducing with straight line movement (Seker et al. 2002) allows us to assess the impact of tool life and surface area roughness of the workpiece.

2.1 *Cutting Force Measurement*

Research on the contrivance of flaw development was first carried away by French scientist Tresca, as far back as 1873. However, fundamental theories have been developed only during the past three or four decades. The compression of the chip, however, was recognized correctly by Tresca. Tresca wrote that the material of workpiece started to flow over the tool face in an upward direction, shearing along an oblique plane as the planner tool advances. Many other earlier scientists were interested in the problem of the shearing of metals undercut; among them were Thime in 1877, Hauser in 1892 and others. However, they did not arrive at any significant conclusion. After so many years, Merchant (1945) and others had

developed the fundamentals in the field of metal cutting. Merchant (1945) castoff an intellectual thought of chip formation, for which an exact geometry might be reserved as the base for various readings of the mechanism of metal cutting. That was for the cutting forces created in the development of steel cutting have a continuous effect on the heat creation, and therefore tool wear, worth formed area and precision of the workpiece. Outstanding and innovative device arrangements/cutting configurations of metal cutting procedures and roughly unidentified issues and pressures, risk in cutting force computations failed in producing accurate results. Subsequently, the investigational statistic of the reducing causes changes out to be inevitable. On behalf of this objective, various dynamometers have been designed. In these dynamometers, cutting force measurement is mostly depending on flexible deformation (Korkut 2003; Panzera et al. 2012; Yaldiz and Unsacar 2006; Yaldiz et al. 2007) of the components. Determination of cutting force(s) depending on three key philosophies:

- (1) Measurement of flexible deflection of a body exposed to the cutting force.
- (2) Measurement of flexible deformation, i.e. stress caused by the force.
- (3) Measurement of stress designed in a method by the force.

The kind of the transducer relies on how that deflection, stress or strain recognized and quantified. Literature shows that there was no research work found on cutting force measurement by using under category measurement of the flexible deformation of the cylindrical bar using resistance strain gauge. So in this paper we will discuss the design and fabrication of this type of dynamometer assembly for turning process. Each functional module discussed in detail, materials and method used, strain gauge classification, and testing discussed in more information.

3 Design and Building of a Resistance Strain Gauge Based Dynamometer for Lathe

3.1 Fundamental Design Requirement for Dynamometer

For reliably exact and consistent measurement, the resulting rations which were considered in previous literatures (Korkut 2003; Panzera et al. 2012; Yaldiz and Unsacar 2006; Yaldiz et al. 2007) in design and creation of tool dynamometers are as:

- Sensitivity: The dynamometer should be reasonably delicate for flawlessness measurement.
- Hardness: The dynamometer need to be quite firm to hold up against the causes without resulting in much deflection which may impact the machining situation.
- Cross understanding the dynamometer should be totally exempt from combination understanding such that one force (say P_z) does not impact statistic of the other forces (say P_y and P_x).

- Steadiness in contradiction moisture and heat range.
- Rapid time reaction.

A high-frequency reaction such that the observations were not suffering from vibrations within a rationally great variety of regularity consistency, i.e. the dynamometer should perform desirably over an longer timeframe.

3.2 Design Standards and Material of Dynamometer

Sensitivity, hardness, flexibility, precision, relaxed correction, budget and stability in the cutting environment carried in the account for developing the dynamometer. Dimensions, shape and subject material of dynamometer were deliberated to be useful aspects on powerful qualities of the dynamometer. A dynamometer mainly involves of a major cylindrical section. The hardness, high natural regularity, deterioration level of resistance and great temperature conductivity aspects were reserved into deliberation while choosing the cylindrical materials. Also, deformation within the fill should comply with that of stress gauges (Tlusty and Andrews 1983).

In this study, AISI 4140 metal, which satisfies above requirements, was chosen as the cylindrical content. The qualities of this content are given in Table 1.

3.3 Determination of Measurements of the Cylindrical Bar

Probably the simplest method measuring unidirectional force is to use some bar in tension and compression. For maximum sensitivity strain gauge may be arranged as shown and connected to form a Wheatstone bridge. It is clear that gauges 1 and 4 will measure axial strain while the circumferential strain caused by origins effect will be measured by gauges 2 and 3. The strain in the gauges will be,

$$e_1 = e_4 = \frac{F}{AE}$$

$$e_2 = e_3 = -\frac{\nu F}{AE}$$

where, F is the axial force, A is the cross-sectional area, E is the Young modulus of elasticity and ν is the Poisson's ratio. Subscripts 1, 2, 3, 4 refer to the gauges.

By using the concepts of design for maximum force and strain as used in the previous studies (Korkut 2003; Yaldiz and Unsacar 2006; Yaldiz et al. 2007) the dimension of the cylindrical bar has been determined. So below Fig. 1 shows the

Table 1 Properties of AISI 4140 steel

Strength	Elasticity	Poisson ratio	Hardness
550–900 N/mm ²	210000 N/mm ²	0.3	217 HB

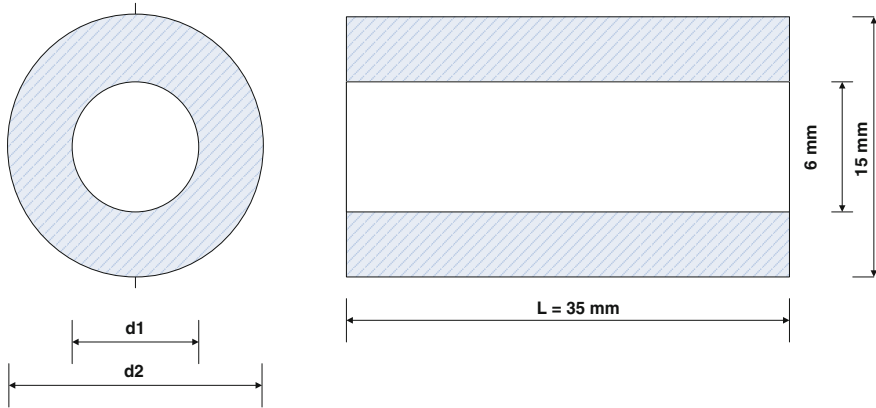


Fig. 1 Cylindrical bar with dimensions

designed specifications for the cylindrical hollow bar with inner and outer diameter of 6 and 15 mm along with length of 35 mm.

4 Materials and Method

A lathe tool dynamometer was a multi-component dynamometer that castoff to evaluate forces in the employment of the machine tool. Trial forecasts of these causes can be cross-checked and verified experimentally using these machine tool dynamometers. With a progression of technology, machine tool dynamometers have progressively used for precise statistic of forces and optimization of the machining process. These multi-component forces are approximated as an individual element force in individually coordinate, based on the organize system used. The forces through machining are reliant on the depth of cut, feed rate, cutting speed, device content and geometry, the content of the workpiece. Other aspects such as the use of lubrication/chilling during machining also impact machining considerably. The graphic interpretation of the cutting force measurement prearrangement presented in Fig. 2.

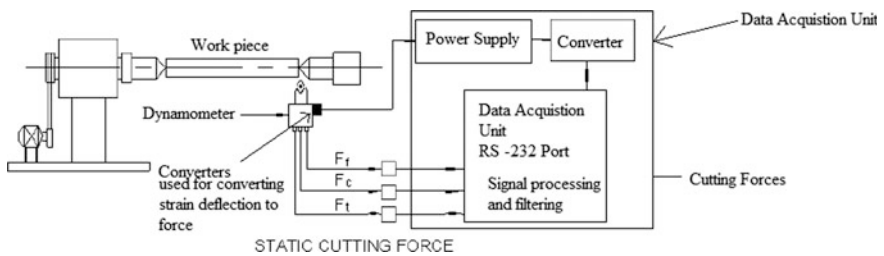


Fig. 2 Schematic diagram of measurement system

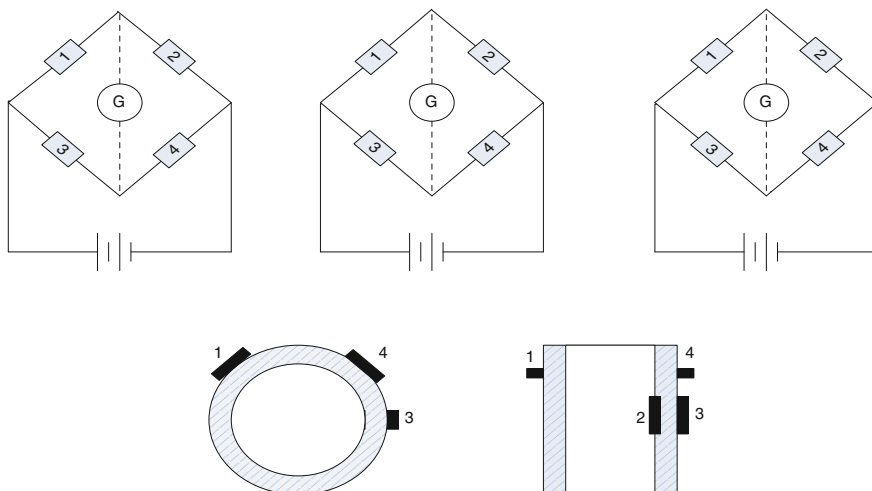


Fig. 3 Manufactured cylindrical dynamometer bar and there placing in Wheatstone bridge

4.1 Dynamometer

The designed and developed dynamometer is accomplished of computing main cutting force (F_c), feed force (F_f) and radial or thrust force (F_t). Figure 3 provides the Wheatstone bridge acquaintances for F_c , F_t , and F_f forces.

4.2 Data Acquisition

Real-time data of the cutting force information is instantly read and deposited in an arrangement in the course of metal cutting. As the yield of Wheatstone bridge circuits is minute due to the high rigidity needs of the dynamometer. The analogue dynamometer elevated by stress gauge feedback segments (Microcontroller AT89C52) are then transformed to digital signals and taken by RS-232 information acquisition card set up in MS-Windows based PC.

4.3 Estimating Various Parameters Related to Strain Gauges

After the considerations of various studies about parameters and application of the different type of strain gauges and principles. Wheatstone bridge for measuring forces that strain gauge to be used (to posted on bar) have following characteristics:

- **Input Voltage:** For excitation of the strain gauges minimum voltage required usually according to the TML standards 10–20 V is necessary.
- **Resistance of Strain Gauges:** Resistance of the strain according to the machining required is 350 Ω .
- **Gauge Factor:** For the resistance type strain gauge of 350 Ω the gauge factor is $2.13 \pm 1 \%$.
- **Bridge:** The full bridge operation can be used. By using gauges as entirely four supports of the Wheatstone bridge, is a rational addition of the half bridge and can be used to additional rise the sensitivity of a computing scheme.

With this arrangement of gauges, bridge output will be insensitive to any loading other than F. We are of course assuming that gauges symmetrically placed. Suppose a bending load causes additional strain in gauge 1, gauge 4 will then have an equal, and opposite strain. The effect will cancel out in the bridge since gauges 1, and 4 are a different arms. In the actual practice, however, they never cancel out completely, and the degree of accuracy be subject to the characteristics of the strain gauges, and the mounting technique is used.

5 Calibrations

5.1 Stationary Correction of the Dynamometer

In order to choose the flexible deformation of cylindrical bar and subsequently the outcome volts less than fixed load, the dynamometer was adjusted. The correction done in three ways for F_f , F_t , F_c and the outcome of millivolt be an average of volts to each route. The plenty up to 2000 N by 50 N durations were used and the stress principles documented for collectively load. Thus, correction graphs were acquired to turn the outcome numbers into cutting force values. Figure 4a, b and c displays the calibration curves produced by using Minitab 16 for feed force, thrust force, and main cutting force correspondingly.

To be able to confirm the reliability, the dimensions were recurring for three intervals and close values were acquired as seen in Fig. 4a, b, and c. The impact of loading in one path on another force elements also analysed, and minimal variations were noticed. These results were little sufficient to disregard. The dynamometer was run non-productive for 10–20 moments before each calibration assessments as it was prepared for measure the reliability in force.

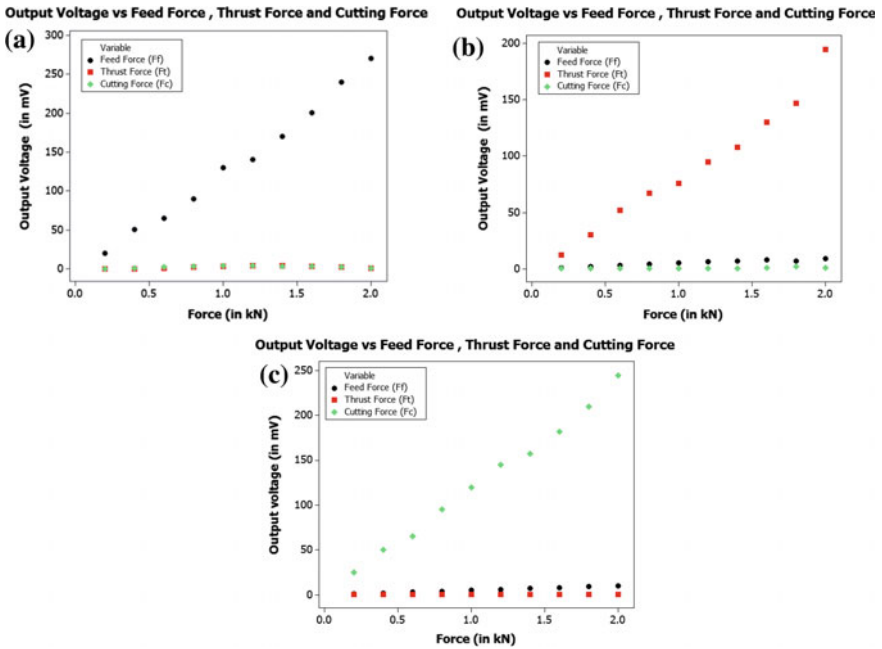


Fig. 4 Correction curve and cross-sensitivity for a feed force F_f , b thrust force F_t , cutting force F_c

6 Conclusion

In this paper, lathe tool dynamometer setup for turning has been produced and exhibited. It was developed and along with complete information procurement settlement made up. The dynamometer can cover three vertical force elements at the same time during turning, and the calculated mathematical principles can store on the PC by information procurement settlement. This dynamometer was developed to evaluate up to 3500 N extreme force with the comprehending of the application is ± 5 N. The setup can assume as consistent as the lesser value can be ignored. In machining processes, satisfactory outcomes were gained for force extents. The acquired results of machining assessments performed at different cutting factors show that the setup can be used effectively to evaluate at a various range of forces. Although this configuration was developed mainly for turning, it can be used for milling, drilling, etc.

References

- Astakhov, V. P., & Shvets, S. V. (2001). A novel approach to operating force evaluation in high strain rate metal-deforming technological processes. *Journal of Materials Processing Technology*, 117(1–2), 226–237.
- Jain, K. C., & Chitale, A. K. (2010). *Textbook of Production Engineering*. New delhi: PHI publishers.
- Kim, J. D., & Kim, D. S. (1997). Development of a combined-type tool piezo-film accelerometer for an ultra-precision lathe. *Journal of Materials Processing Technology*, 71(3), 360–366.
- Korkut, I. (2003). A dynamometer design and its construction for milling operation. *Materials and Design*, 24(8), 631–637.
- Kuljanic, E., & Sortino, M. (2005). TWEM, a method based on cutting forces—monitoring tool wear in face milling. *International Journal of Machine Tools and Manufacturing*, 45(1), 29–34.
- Merchant, M. E. (1945). Mechanics of the metal cutting process: I Orthogonal cutting and a type 2 chip. *Journal of Applied Physics*, 16(5), 267–275.
- Milfelner, M., Cus, F., & Balic, J. (2005). An overview of data acquisition system for cutting force measuring and optimization in milling. *Journal of Materials Processing Technology*, 164–165, 1281–1288.
- Panzer, T. H., Souza, P. R., Carlos, J., Rubio, C., Abrao, A. M., & Mansur, T. R. (2012). Development of a three-component dynamometer to measure turning force. *The International Journal of Advanced Manufacturing Technology*, 62(9–12), 913–922.
- Seker, U., Kurt, A., & Ciftci, I. (2002). Design and construction of a dynamometer for measurement of cutting forces during machining with linear motion. *Materials and Design*, 23(4), 355–360.
- Seker, U., Kurt, A., & Ciftci, I. (2004). The effect of feed rate on the cutting forces when machining with linear motion. *Journal of Materials Processing Technology*, 146(3), 403–407.
- Thrusty, J., & Andrews, G. C. (1983). A critical review of sensors for unmanned machining. *CIRP Annals - Manufacturing Technology*, 32(2), 563–572.
- Totis, G., & Sortino, M. (2011). Development of a modular dynamometer for triaxial cutting force measurement in turning. *International Journal of Machine Tools and Manufacturing*, 51(1), 34–42.
- Yaldiz, S., & Unsacar, F. (2006). A dynamometer design for measurement the cutting forces on turning. *Measurement*, 39(1), 80–89.
- Yaldiz, S., Unsacar, F., Saglam, H., & Isik, H. (2007). Design, development and testing of a four-component milling dynamometer for the measurement of cutting force and torque. *Mechanical Systems and Signal Processing*, 21(3), 1499–1511.

Study of Laser Transmission Welding Process Using a Volumetric Heat Source Model and Experimental Analysis

Bappa Acherjee, Arunanshu S. Kuar, Souren Mitra and Dipten Misra

Abstract In this paper, the laser transmission welding of polycarbonate is studied via numerical modeling and experimental investigation. A 3-dimensional transient heat transfer model is developed and experimentally validated. The developed model is able to predict the transient temperature field and weld pool size. It is found from the sensitivity analysis of boundary conditions that the effect of heat conduction is predominant on temperature field distribution during laser transmission welding. Temperature results from the numerical model and the experimentally measured of weld strength results are used as responses for parametric analysis. It is seen that the peak temperature reaches when the laser power is maximum and welding speed and beam diameter are at minimum values. However, the maximum welding strength is obtained when the laser power and beam diameter are at maximum values and welding speed is minimum. It is further noticed that, the maximum value of welding strength corresponds to the peak temperature of 595 °C, which is just above the decomposition temperature of the parent material.

Keywords Laser transmission welding · Finite element model · Welding strength · Temperature field · Experimental investigation

List of Symbols

I_a	Laser intensity
K	Absorption coefficient of the absorbing material
P	Laser power

B. Acherjee (✉)

Production Engineering Department, Birla Institute of Technology,
Mesra, Deoghar Campus, Deoghar 814142, India
e-mail: bappa.rana@gmail.com

A.S. Kuar · S. Mitra

Production Engineering Department, Jadavpur University,
Kolkata 700032, India

D. Misra

School of Laser Science & Engineering, Jadavpur University,
Kolkata 700032, India

© Springer India 2016

D.K. Mandal and C.S. Syan (eds.), *CAD/CAM, Robotics and Factories of the Future*, Lecture Notes in Mechanical Engineering,
DOI 10.1007/978-81-322-2740-3_3

T	Temperature
T_t	Transmissivity of the transparent polymer part
R_a	Reflectivity of the absorbing material
c	Specific heat
h	Convective heat transfer coefficient
h_r	Combined heat transfer coefficient
k	Thermal conductivity
r	$\sqrt{(x_s^2 + y_s^2)}$, where x_s and y_s are the Cartesian coordinates of that point
r_0	Laser beam radius (radius of Gauss function curve)
t	Time
q_v	Rate of internal heat generation
z_a	Depth (m) within the absorbing materials
σ	Stefan Boltzmann constant ($5.67 \times 10^{-8} \text{ W/m}^2 \text{ K}^4$)
ε	Emissivity
ρ	Radius of is the material density
∇	Gradient operator
CNC	Computer numeric controlled
FEM	Finite element model

1 Introduction

The application of laser as a light source has been started long before in early 1960s. The light source later converted into a viable industrial tool for a number of applications by the end of the twentieth century. Laser can be used to weld plastics in two different ways: either by targeting the laser-absorbing plastics by a laser beam to irradiate the mating surfaces and welding by fusion, or by projecting the laser beam on a overlapping transparent plastic and irradiate the joining interfere by using a laser-absorbing plastic at bottom. This latter process, coined as laser transmission welding (LTW), is proving to be very attractive as clean, precise, and flexible joining process for plastic surfaces, even of dissimilar plastics (Acherjee et al. 2011).

The top part of the plastic is transparent to the infrared laser. The bottom part is either transparent or opaque to the infrared laser. For the case of transparent bottom part, a layer of infrared absorbing dye coating is used as laser absorbing medium. Laser transmission welding can be applied to thin as well as thick plastic materials. Laser sources of 0.8–1.1 μm wavelength are used for the laser transmission welding process, as plastics have a high transmittance at this wavelength range.

Several research works have been carried out by the researchers working in the field of laser transmission welding process to study the thermal aspects of this welding process by process simulation. Kennish et al. (2002) developed an analytical model of LTW which is capable of predicting the process capabilities and

weld characteristics. The model can simulate the temperature profile in and around the weld zone. Becker and Potente (2002) developed a finite element model to investigate the heating phenomena during LTW of polypropylene. Russek et al. (2005) developed an analytical heat transfer model of LTW and validate the model using experimental data. Ilie et al. (2005) studied the scattering effect of laser beam in a semi-transparent reinforced/filled plastic part on LTW via physical modeling. Mayboudi et al. (2005) presented a 2-d thermal model by considering nylon 6 as work material to investigate the heat transfer phenomena during LTW. Van de Ven and Erdman (2007) developed a 2-d thermal model by considering polyvinyl chloride as work material to study the heating and cooling phase of LTW process. Mayboudi et al. (2007a) presented a 3-d transient finite element model of LTW for polyamide 6. In another work, Mayboudi et al. (2007b) presented a 3-d transient thermal model of LTW by considering a moving heat source. Coelho et al. (2008) investigated the influence of laser beam spot in high speed laser lap welding of thermoplastic films. Taha et al. (2009) simulated mathematically the LTW process to study the temperature distribution in and around the welding zone and the weld bead profile. Acherjee et al. (2010) developed a transient finite element model of laser transmission plastic-to-metal welding by considering a moving laser beam. In a further investigation by Acherjee et al. (2012), the effect of carbon black on the temperature field during LTW is studied by numerical simulation. Mingareev et al. (2012) carried out the experimental investigation with a Tm-fiber laser on the laser butt-welding and transmission welding of different polymers.

In this paper, laser transmission welding process is studied through numerical and experimental analyses. A 3-d transient thermal model is developed using finite element method. The results obtained from the developed model, for different welding conditions, are compared to the experimental results and a reasonable agreement is observed. Experimental investigation is also carried out to study the effect of process parameters on the responses. Effort is also made to correlate the evolution of temperature at weld zone with the welding strength.

2 Development of the Model

The contour welding variant of laser transmission welding with lap joint configuration is used in this investigation. Polycarbonate plaques of dimensions of 80 mm × 35 mm × 4 mm are used as work materials. The top part of the assembly is natural polycarbonate and the bottom part is the opaque polycarbonate, containing carbon black pigment in polymer matrix. The isometric view of the sample that is used for the present study is shown in Fig. 1. The technical details of the finite element model and the experimental validation of the developed model are presented earlier (Acherjee et al. 2012), thus, the physical aspects of the finite element modeling are summarized in brief.

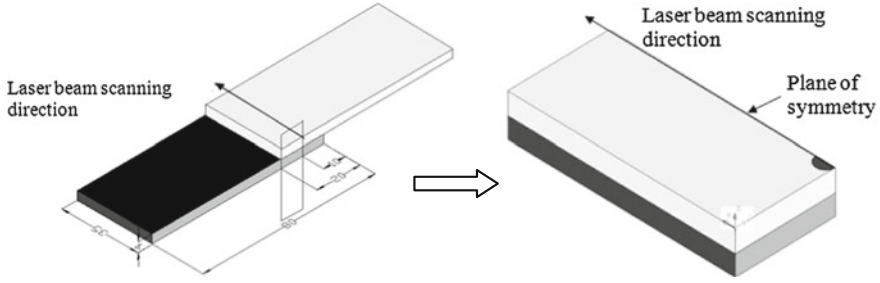


Fig. 1 Schematic of the sample with symmetry boundary conditions (dimensions are in mm)

A 3-d heat conduction equation is used as governing equation to describe the heat transfer during the laser transmission welding process. The model is developed as a heat conduction based model using the following equation:

$$\rho \cdot c \frac{\partial T}{\partial t} = \nabla \cdot (k \nabla T) + q_v \quad (1)$$

where, q_v is the volumetric heat generation within the bulk of the material at the weld zone and the neighboring zone. A Gaussian laser heat flux is modeled and the rate of internal heat generation is determined at irradiated zone in both the plastic parts using the equation given below:

$$q(x, y, z, t) = \begin{cases} 0 & ; \text{for laser transparent plastic} \\ (1 - R_a) K I_a \exp(-K z_a) & ; \text{for laser absorbing plastic} \end{cases} \quad (2)$$

where, I_a is the intensity of laser beam (W/m^2) reaching to the interface after transmitting through the top transparent plastic. The term I_a , can be expressed as:

$$I_a = \frac{T_t P}{\pi r_0^2} \exp\left(-\frac{r^2}{r_0^2}\right) \quad (3)$$

The heat loss from the exterior surfaces of the materials to the surrounding is considered by using a combined convection-radiation boundary condition using equation given below:

$$-k(T) \nabla T \vec{n} = h_r (T_s - T_0) \quad (4)$$

where,

$$h_r = h + \varepsilon \sigma (T_s + T_0)(T_s^2 + T_0^2) \quad (5)$$

A look up table is generated to store the temperature dependent values of h_r and those are used as materials properties data. The heat transfer coefficient of

convective heat transfer, h , is considered as $5 \text{ W/m}^2 \text{ K}$ (Mayboudi et al. 2005). Emissivity value is used as 0.95 for both the polycarbonate parts (Mitchell 2000). This parametrically developed model is built using APDL (ANSYS® Parametric Design Language) scripting language. The entire model is meshed using SOLID 70, a 3-d thermal brick element. The simulation work is performed on a computer having 2.66 GHz Core™ 2 Duo processor and 3.0 GB of RAM. Material properties like density, thermal conductivity and specific heat of polycarbonate are used for modeling and those are taken for different temperature range as these properties vary with temperature. More detailing about the finite element modeling and the realization of moving heat source are presented elsewhere (Acherjee et al. 2012).

3 Experimental Validation

A continuous wave diode laser system is used for experimental work. The laser system has 30 W maximum optical power and the laser wavelength is 809.40 nm. The laser radiation is delivered from the main unit to the workstation using an SMA 905 connector, which is a multi-mode, single core fiber optic transport cable of 800 μm diameter. The output power of the laser system is calibrated using a Gentec-EO SOLO-2 laser power and energy meter of 1 mW resolution.

The workpieces are moved via a CNC X–Y table. The table is connected with the motion system, which is controlled by a computer. A laser based Micro-Epsilon opto NCDT 1300-50 displacement sensor is used to cross-check the accuracy of the travelling speed of CNC X–Y table carrying a quite heavy hydraulic clamp pressure system. These trials give acceptable results except initial acceleration (jerk) before reaching to uniform velocity.

The weld seam widths are measured by using a measuring microscope (Olympus STM 6). This optical measuring microscope can precisely perform the three axis measurements of parts up to 0.1 μm precision levels. Inbuilt LED illuminator is used for reflected coaxial illumination during measurements.

Experiments are conducted under different parametric conditions and the weld width responses obtained from the developed FE model are compared with the experimentally measured results. Figure 2 shows the comparison of results that are obtained by laser transmission contour welding of polycarbonates via experiments and FE modeling. The glass transition temperature of polycarbonate is about 145–150 °C, so it softens gradually above this point. At glass transition temperature the amorphous polymers face a reversible transition from a solid state into a molten or rubber-like state. However, to obtain an acceptable weld, the welding condition is set to reach at least the melting zone of the polycarbonate which is 250 °C. Above this temperature the molten polycarbonate starts to flow, which enhances the quality of bonding. However, the temperature at interface is to be kept below than the decomposition temperature of the polycarbonate which is 500 °C. The region in the contours plot temperature above 250 °C represents the weld zone. The red region at the modeled weld interface denotes fusion zone where temperature exceeds 250 °C.

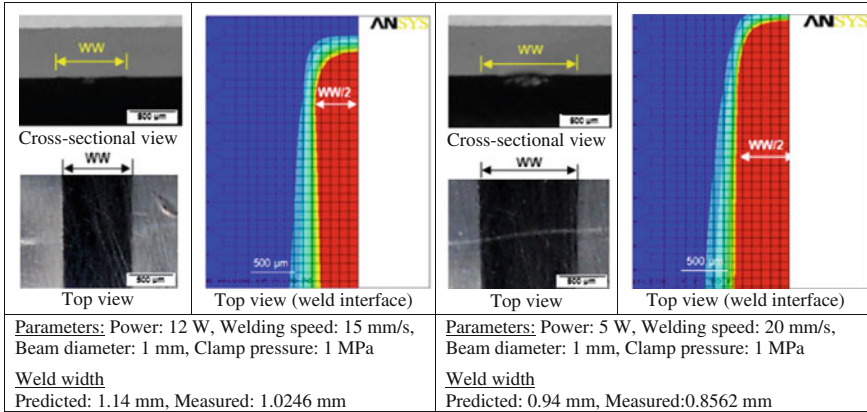


Fig. 2 Comparison of weld width results obtained from FE model and experimental measurements

A reasonable consistency is observed between the predicted and measured weld widths. The marginal difference between the predicted and measured widths is because of the assumptions made in the simulations, such as uniform material properties, constant optical properties of the materials, perfect Gaussian distribution of the laser beam intensity at weld interface, and the perfect contact between mating parts.

4 Results of Numerical Analyses

Figure 3a, b shows the transient temperature distribution during laser transmission welding of polycarbonates for laser power = 5 W, welding speed = 20 mm/s, and beam diameter of 1.5 mm. It is seen from this figure that the temperature attains to a peak of 340 °C (peak temperature) during heating phase at the irradiation zone, and is gradually transferred to neighboring zone by the thermal conduction. It is observed that the peak temperature occurs within the laser-absorbing plastic, which signifies the volumetric absorption phenomenon of the laser beam within an absorbing medium. It is also observed that the isotherms are dense in the front side of the moving laser beam than that in the trailing side.

Figure 3c shows the sectional view of temperature field distribution at X-Z plane. The region in the contours plot comprising temperature more than 250 °C, shows the depth of penetration in both the polycarbonate parts (DT and DA) from weld interface. From Fig. 3c, the half width (WW/2) of the weld can also be estimated.

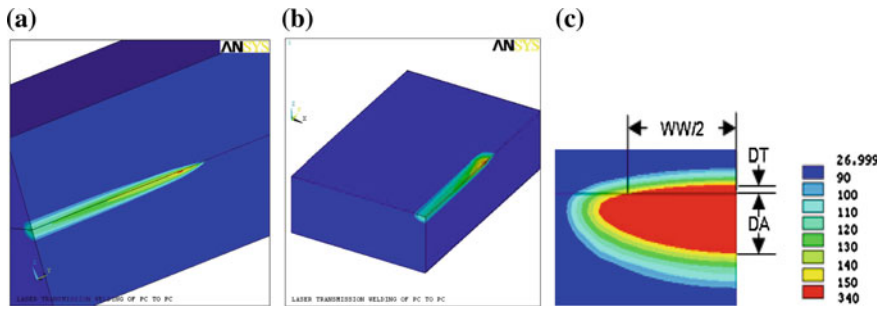


Fig. 3 Temperature distributions **a** at the symmetry plane (Y–Z plane), **b** at the weld interface (X–Y plane), and **c** at X–Z plane (where, *WW* weld width, *DA* depth of penetration in absorbing part, *DT* depth of penetration in transparent part)

5 Experimental Investigation and Parametric Analysis

Central composite design of response surface methodology is employed for the design of the experimental matrix. Laser power, welding speed, and beam diameter are the process parameters considered in this investigation. For entire experimental work, clamping pressure is kept constant at 1 MPa. Opaque polycarbonate part contains 0.1 % carbon black pigment by weight. Table 1 presents the parameters selected for experimental work along with their levels, units and symbols. The responses of interest are peak temperature at weld zone and welding strength. The peak temperature is determined from the developed numerical model, whereas, welding strength is determined experimentally, using an Instron universal testing machine. The variation of welding strength with peak temperature at weld zone is also the subject of interest in this work.

Figure 4a, b are cube plots, which show the values of peak temperature and weld strength at the corner points of the selected design space. This plot is useful to study the interaction effect of three factors at the same time. It is seen from these figures that maximum value of peak temperature is attained when the laser power is maximum and welding speed and beam diameter are at minimum values. This condition maximizes the power density and interaction time, thus increases the heat input. However, the maximum welding strength is achieved at different level of parameter setting. The maximum welding strength is obtained when the laser power and beam diameter are at maximum values and welding speed is minimum. The

Table 1 Welding parameters and their levels

Parameters	Units	Limits		
		-1	0	+1
A: Laser power	W	12	15	18
B: Welding speed	mm/s	7	10	13
C: Beam diameter	mm	1.25	1.50	1.75

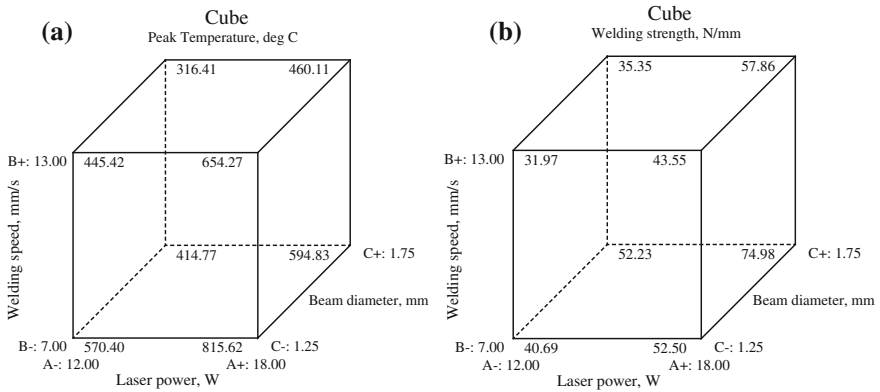
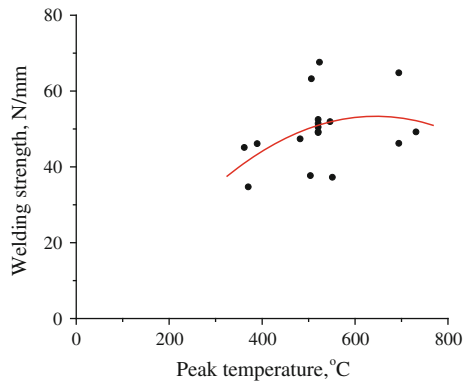


Fig. 4 Cube plot showing the effects of parameters on **a** peak temperature, and **b** welding strength, within the selected design space

maximum value of welding strength corresponds to the peak temperature of 595 °C, which is just above the decomposition temperature of the parent material. This implies that a small amount of overheating may improve the joint strength. This may cause partial decomposition at the middle of the weld seam, where the material is subjected to maximum heat. However, at the same time, due to melting of more base material at weld zone, the dimension of weld pool increases, which increase the weld strength. Figure 5 shows the relationship between the peak temperature and welding strength. It is seen that the data points are scattered over a wide zone, and do not show a perfect trend. This implies that the welding strength not only depends on peak temperature but also on temperature distribution in weld zone and the weld pool dimensions. A trend line is drawn on Fig. 5, which shows that the welding strength increases up to a peak temperature about 600 °C, and thereafter

Fig. 5 Scatter plot for peak temperature versus welding strength



decreases. The results show that weld strength is restricted at very high power density, which causes material decomposition and a very low power density which results in lack of fusion.

6 Conclusion

In this paper numerical and experimental approaches are used to study the laser transmission welding process. Polycarbonate is used as work material. A 3-d thermal model based on volumetric heat generation code is developed and experimentally validated. The developed model can predict the temperature at 3-d space and also weld pool dimensions. The temperature results (peak temperature at weld zone) from numerical simulation along with the experiential results of welding strength are used for parametric investigation. It is found that the peak temperature and weld strength increase with laser power and beam diameter, whereas, decrease with an increase in welding speed. It is also observed that the maximum value of welding strength corresponds to the peak temperature of 595 °C, which is just above the decomposition temperature of the parent material. This implies that a small amount of overheating may improve the joint strength, because of the melting of more base material at weld zone, which results in larger weld area to resist the shear load. It is further noticed from the trend line drawn based on experimental data that the welding strength increases up to a peak temperature about 600 °C, and thereafter it starts decreasing.

References

- Acherjee, B., Kuar, A. S., Mitra, S., & Misra, D. (2010). Finite element simulation of laser transmission welding of dissimilar materials between polyvinylidene fluoride and titanium. *International Journal of Engineering, Science and Technology*, 2(4), 176–186.
- Acherjee, B., Kuar, A. S., Mitra, S., & Misra, D. (2011). Laser transmission welding: A novel technique in plastic joining. In *Welding: Process, Quality and Applications* (pp. 365–387). New York: Nova Science Publishers, Inc.
- Acherjee, B., Kuar, A. S., Mitra, S., & Misra, D. (2012). Effect of carbon black on temperature field and weld profile during laser transmission welding of polymers: A FEM study. *Optics & Laser Technology*, 44(3), 514–521.
- Becker, F., & Potente, H. (2002). A step towards understanding the heating phase of laser transmission welding in polymers. *Polymer Engineering & Science*, 42(2), 365–374.
- Coelho, J. M. P., Abreu, M. A., & Rodrigues, F. C. (2008). Modeling the spot shape influence on high-speed transmission lap welding of thermoplastic films. *Optics and Laser in engineering*, 46, 55–61.
- Ilie, M., Kneip, J. C., Mattei, S., & Nichici, A. (2005). Effects of laser beam scattering on through-transmission welding of polymers. In *24th International Congress on Applications of Lasers and Electro-Optics*. Miami, USA.
- Kennish, Y. C., Shercliff, H. R., & McGrath, G. C. (2002). Heat flow model for laser welding of polymers. In *Annual Technical Conference 2002*. San Francisco, CA, USA.

- Mayboudi, L. S., Birk, A. M., Zak, G., & Bates, P. J. (2005). A 2-D thermal model for laser transmission welding of thermoplastics. In *24th International Congress on Applications of Lasers and Electro-Optics*. Miami, USA.
- Mayboudi, L. S., Birk, A. M., Zak, G., & Bates, P. J. (2007a). Laser transmission welding of a lap-joint: Thermal imaging observations and three-dimensional finite element modeling. *Journal of Heat Transfer*, *129*, 1177–1186.
- Mayboudi, L. S., Birk, A. M., Zak, G., & Bates, P. J. (2007b). A 3-D Thermal model of laser transmission contour welding for a lap Joint. In *Annual Technical Conference 2007*. Cincinnati, USA.
- Mingareev, I., Weirauch, F., Olowinsky, A., Shah, L., Kadwani, P., & Richardson, M. (2012). Welding of polymers using a 2 μm thulium fiber laser. *Optics & Laser Technology*, *44*, 2095–2099.
- Mitchell, M. (2000). *Design and microfabrication of a molded polycarbonate continuous flow polymerase chain reaction device*. Master thesis, Louisiana State University.
- Russek, U. A., Aden, M., & Pöhler, J. (2005). Laser beam welding of thermoplastics experiments, thermal modelling and predictions. In *3rd International WLT—Conference on Lasers in Manufacturing* (pp. 85–89). Munich, Germany.
- Taha, Z. A., Roy, G. G., Hajim, K. I., & Manna, I. (2009). Mathematical modeling of laser-assisted transmission lap welding of polymers. *Scripta Materialia*, *60*, 663–666.
- Van de Ven, J. D., & Erdman, A. G. (2007). Laser transmission welding of thermoplastics—Part I: Temperature and pressure modeling. *Journal of Manufacturing Science and Engineering*, *129*, 849–858.

Comparison of Grinding Performance Under Different Eco-Friendly Environment

D. Dewanjee, P. Kundu, B. Sikder, D. Biswas, Bijoy Mandal and Santanu Das

Abstract High heat generation at the grinding zone may cause several grinding difficulties. To control these thermal problems, generally, grinding fluid is applied; however, it increases the chance of environmental pollution. In the present work, an attempt is made to control grinding zone temperature by using eco-friendly environment, such as compressed air and ice cooled compressed air. Grinding experiments are conducted on low alloy steel specimens using alumina wheel under dry, compressed air and ice cooled compressed air environment. From experimental results, it is found that tangential force and normal force reduce more under ice cooled compressed air. With the use of ice cooled compressed air, wheel loading is the least of all other conditions tested, and large quantity of shear type chips are observed indicating good grindability. Hence, it may be recommended to use ice cooled compressed air as an eco-friendly grinding fluid to control grinding zone temperature.

Keywords Surface grinding · Grinding fluid · Compressed air · Eco-friendly manufacturing · Green manufacturing · Clean technology · Grindability

D. Dewanjee · P. Kundu · B. Sikder · D. Biswas · B. Mandal · S. Das (✉)
Department of Mechanical Engineering, Kalyani Government Engineering College,
Kalyani 741235, West Bengal, India
e-mail: sdas.me@gmail.com

D. Dewanjee
e-mail: dewanjee.007@gmail.com

P. Kundu
e-mail: prkshkundu00@gmail.com

B. Sikder
e-mail: bablu.kgec@gmail.com

D. Biswas
e-mail: debashis_bagula@rediffmail.com

B. Mandal
e-mail: bijoymandal@gmail.com

1 Introduction

Grinding is a well known manufacturing process, which is generally characterized by high specific energy consumption, large grinding forces, low material removal rate, and high heat generation at grinding zone. Higher grinding zone temperature is source of several grinding defects, such as surface burn, surface and subsurface cracks, intense wheel loading and induction of tensile residual stresses. To control this thermal problem, generally, large quantity of grinding fluid is applied using different fluid delivery techniques. It was reported that (Catai et al. 2006; Mandal et al. 2010, 2011a; Wu et al. 2009) most of the grinding fluid was wasted due to formation of stiff air layer around a rotating grinding wheel. However, fluid flow through grinding zone is controlled by several other factors, such as flow rate, fluid velocity, position and type of the fluid delivery nozzle and wheel porosity (Malkin 1990). Several research works was conducted to develop grinding fluid delivery techniques for controlling grinding zone temperature. Some of these are conventional flood cooling, Z-Z method of cooling, compound nozzle cooling, fluid delivery using pneumatic barrier, mist cooling, jet cooling, etc. (Ebbrell et al. 2000; Mahata et al. 2014; Mandal et al. 2013, 2014; Irani et al. 2005).

Kundu and Das (2001) employed a painted wheel and a scraper board fitted just above the fluid nozzle for penetrating the stiff air layer covering the wheel. Low wheel wear rate and improved grinding ratio were observed by them with the painted wheel. Sharmacharya et al. (1998) and Das et al. (2000) observed the favourable effect of deeper penetration of grinding fluid with the use of rexine-pasted wheel and selection of appropriate fluid jet velocity. Catai et al. (2006) reportedly optimized application of cutting fluid through grinding zone for reducing thermal problems by providing an aerodynamic deflector that could eliminate stiff air layer formation around the grinding wheel.

Mandal et al. (2010, 2011a), Wu et al. (2009) experimented on the distribution of air layer pressure. Mandal et al. (2011a) observed rexine-pasted wheel to result in remarkable suppression of air layer surrounding the wheel periphery. A special fluid delivery system introduced by Banerjee et al. (2007), a pneumatic barrier employed first by Mandal et al. (2011b, 2012), and high velocity coolant jet (Ramesh et al. 2004) were observed to be beneficial to control grinding temperature effectively. On the other hand, Choi et al. (2001) reported usefulness of applying compressed air and a coolant in grinding with a cBN wheel, and Nguyen and Zhang (2003) employed cold air and oil mist for effectively reducing grinding temperature and its subsequent effects. Das et al. (2015) used grease as lubricant for reducing grinding zone temperature.

Due to issues related to environment, synthetic oil is not encouraged to use as the grinding fluid. It can be harmful to the operator, and can be considered an environmental hazard. Paul and Chattopadhyay (1995, 1996) applied eco-friendly liquid nitrogen through a specially designed nozzle to observe substantial benefit in surface grinding different steels. Application of compressed cold air was investigated in cylindrical grinding by Choi et al. (2002) using alumina and cBN wheels.

In the present work, grinding performance of low alloy steel is studied under the environment of dry, compressed air and ice cooled compressed air. Here, instead of commonly used cutting fluid, compressed air and ice cooled compressed air are used to control grinding zone temperature making minimal environment pollution indicating a step toward green manufacturing.

2 Experimental Procedure

The experimental investigation is performed using horizontal surface grinding machine (make: Maneklal & Sons, India) with alumina grinding wheel (A46/54 K5 V8). Details of experimental conditions are mentioned in Table 1.

Wheel surface velocity is maintained at 30 m/s for all the experiments. Experiments are carried out in dry, compressed air and ice cooled compressed air environment. An air compressor is used to provide compressed air at 20 kPa pressure through nozzle having 4 mm inside diameter. Due to adiabatic expansion of compressed air at the nozzle exit, there is cooling effect. In this experimental condition, nozzle exit temperature of 20 °C is measured while the ambient temperature of 34 °C is noted. The pneumatic nozzle is placed 10 mm above the work

Table 1 Conditions of experiment

Machine tool	Surface grinding machine
	Make: Maneklal and Sons, India
	Main motor power: 1.5 kW
	Spindle speed: 2900 rpm
Grinding wheel	Disc type alumina wheel
	Make: Carborandum Universal Limited, India
	Specification: AA 46/54 K5 V8
	Size: Ø 200 mm × 13 mm × Ø 31.75 mm
Grinding environment	(1) Dry
	(2) Compressed air discharged through 4 mm diameter nozzle at 20 kPa pressure at 30 °C exit temperature
	(3) Ice cooled compressed air discharged through 4 mm nozzle at 20 kPa pressure at 10 °C exit temperature
Dressing condition	Vertical single point 0.5 carat diamond dresser
	Dressing depth: 30 µm
	Dressing feed: 0.36 m/min
Grinding parameters	Grinding velocity: 30 m/s
	Table feed: 4.5 m/min
	Depth of cut: 20 and 30 µm
Workpiece	Low alloy steel (0.17 % C, 0.21 % Si, 0.63 % Mn, 0.001 % Ni, 0.002 % Cr and rest Fe)
	Size: 118 mm × 60.7 mm × 6.7 mm

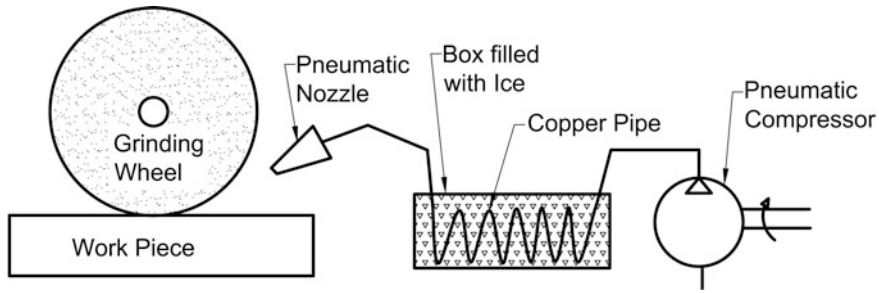


Fig. 1 Ice cooling setup

surface and the radial gap between pneumatic nozzle and the grinding wheel is maintained 10 mm. It is expected that supply of compressed air to grinding zone would extract some amount of grinding heat generated, thereby would become beneficial compared to that of dry grinding.

For obtaining ice cooled compressed air, a condenser made of copper coil is kept in an ice filled insulated box (Fig. 1). One end of the condenser is connected with pneumatic compressor for inflow of compressed air, and other end is connected with pneumatic nozzle for delivering cold compressed air. At this experimental condition, the nozzle exit temperature is measured as 10 °C while ambient temperature is measured as 34 °C.

Grinding experiments are conducted on low alloy steel using 20 and 30 μm infeed under each environment. Grinding forces are measured up to 20 grinding passes using strain gauge type dynamometer having resolution of 1 N. Grinding chips are collected after 19th grinding pass in all grinding condition tested here, and are observed under Mitutoyo make tool maker's microscope.

3 Results and Discussion

Variation of tangential (F_t) and normal (F_n) grinding forces obtained in grinding of low alloy steel specimens at 20 and 30 μm infeed under dry, compressed air and ice cooled compressed air environment are measured up to 20 grinding passes using dynamometer. Grinding forces is plotted in Figs. 2 and 3 respectively. It is observed that on the whole, both F_n and F_t forces are lower in grinding with compressed air cooling in comparison with dry grinding with 20 μm infeed (Fig. 2). However, at Initial few grinding passes, grinding forces are comparable both in dry grinding and grinding with compressed air cooling. It indicates that initially grits of grinding wheel retains its sharpness both in dry and compressed air condition. After 14 grinding passes, grinding forces are higher in dry grinding with comparison of grinding with compressed air cooling. With the increase in grinding passes, heat generation at grinding zone and wheel loading is more which increases grinding

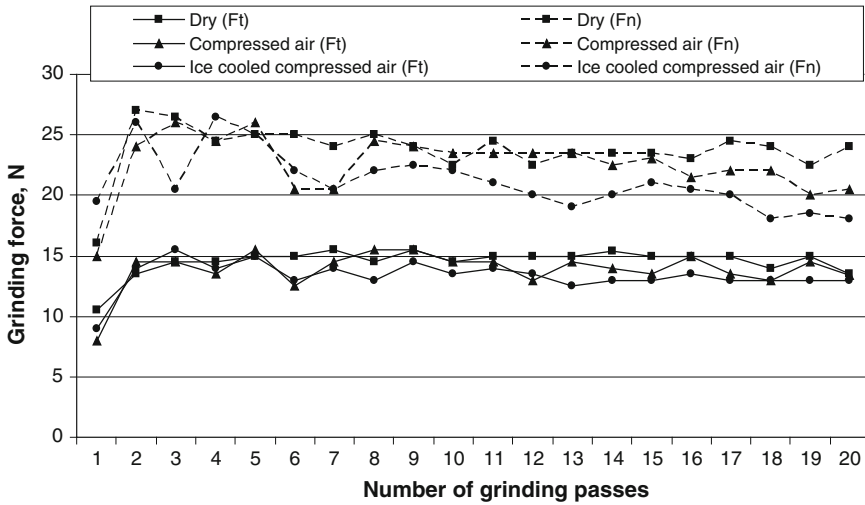


Fig. 2 Variation of normal and tangential grinding force under different environment at 20 μm infeed

forces in dry condition. Application of compressed air reduces thermal effects in grinding zone; hence, less grinding forces and wheelloading is observed with compared to dry grinding.

It is measured that temperature of ice cool compressed air is 10 °C, hence, more control of grinding zone temperature is achieved during grinding with ice cooled compressed air than the other two conditions. It is noticed from Fig. 2 that over all grinding forces are less in grinding with ice cooled compressed air than dry and compressed air grinding. Wheel loading is also observed low in ice cooled compressed air grinding than the other two grinding conditions.

Similar effects of grinding forces are also observed in Fig. 3 during grinding with 30 μm infeed. Here, on the whole both the grinding forces (Ft and Fn) are less in grinding with compressed air than dry grinding, and further grinding forces are significantly less in grinding with ice cooled compressed air than dry and compressed air grinding. It is observed that after 20 grinding passes, wheel loading is quite less in ice cooled compressed air condition than dry and only compressed air grinding. These indicate that better control of grinding zone temperature is achieved using ice cooled compressed air than other two.

Grinding chips are collected during 19th grinding pass and images are shown in Figs. 4 and 5. It is observed from Fig. 4 that most of the grinding chips are hollow spherical under dry grinding at 20 μm infeed. Hollow spherical chips generate due to exothermic reaction of highly heated grinding chips with atmospheric oxygen. This indicates high heat generation in grinding zone at dry grinding. Hollow spherical chips along with few shear type chips are observed in Fig. 4 under grinding with compressed air condition. In ice cooled compressed air grinding condition, most of the chips are shear type chips and few chips are hollow spherical

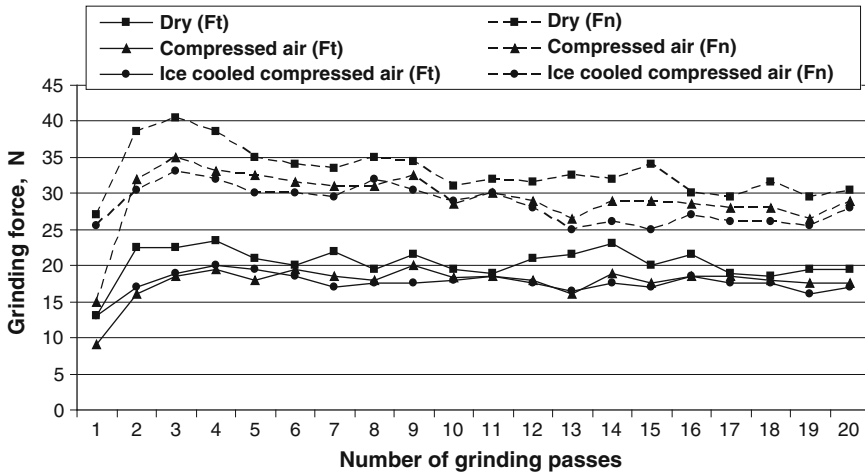


Fig. 3 Variation of normal and tangential grinding force under different environment at 30 μm infeed

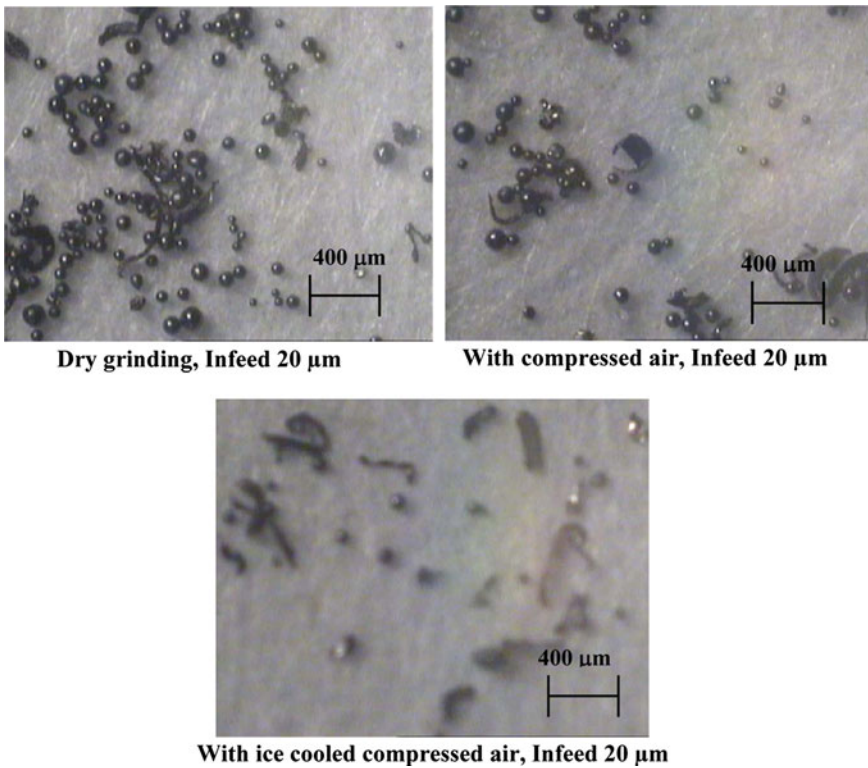


Fig. 4 Images of grinding chips observed under different environment at 20 μm infeed

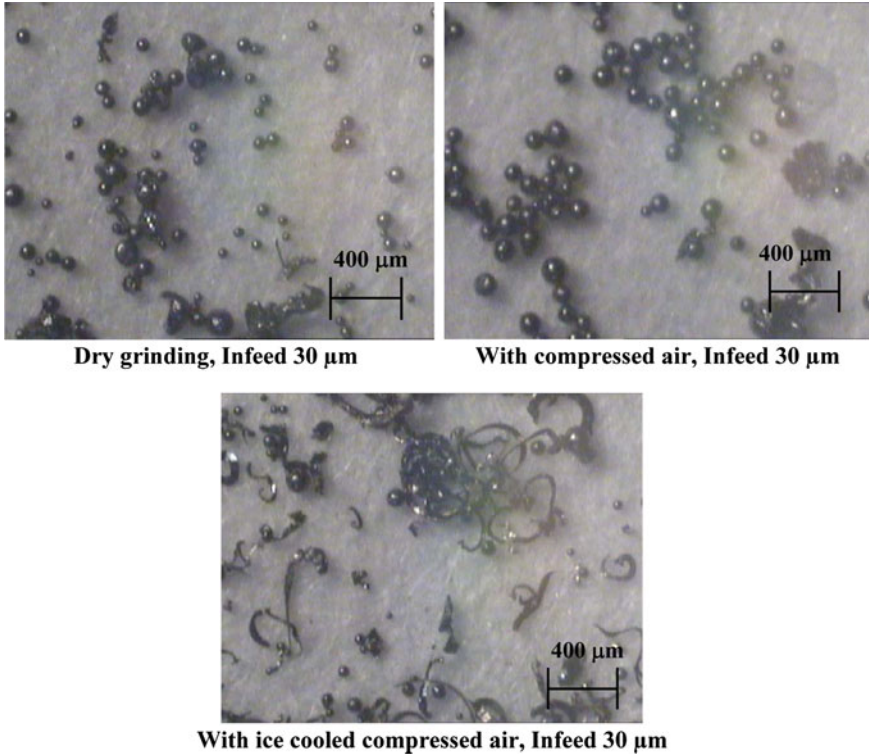


Fig. 5 Images of grinding chips observed under different environment at 30 μm infeed

type. This indicates better control of grinding zone temperature is achieved using ice cooled compressed air in grinding than only compressed air grinding.

Similar observations of chip formation are found under grinding with 30 μm infeed, as depicted in Fig. 5. In 30 μm infeed grinding, heat generation in grinding zone is higher than 20 μm infeed grinding naturally, hence, most of the grinding chips form are hollow spherical type under dry and compressed air cooling. In grinding with ice cooled compressed air, few hollow spherical chips, shear type chips and few blocky fragmented type chips are observed, indicating reduction of grinding zone temperature than other two conditions.

4 Conclusion

From the above experimental observation, following conclusions may be drawn.

1. It is observed experimentally that both normal and tangential grinding forces are low in grinding with compressed air than dry grinding. With the application of

ice cooled compressed air in grinding, normal and tangential grinding forces are found to be remarkably low compared to dry and compressed air-cooled grinding condition. Possible reason is better control of grinding zone temperature in ice cooled compressed air condition than the other two.

2. Wheelloading is also observed to be substantially low in ice cooled compressed air grinding than dry and compressed air grinding, and maximum wheel loading is observed in dry grinding naturally.
3. Most of the grinding chips are of hollow spherical type formed under dry and compressed air grinding at higher depth of cut (30 μm), however, few hollow spherical, shear type chips and few blocky fragmented type chips are observed in ice cooled compressed air condition. This also supports that better control of grinding zone temperature is achieved in ice cooled compressed air grinding indicating better grindability. Therefore, this eco-friendly grinding may find application in manufacturing industry.

References

- Banerjee, S., Ghosal, S., & Dutta, T. (2007). Development of simple technique for improving the efficacy of fluid flow through the grinding zone. *Journal of Materials Processing Technology*, *197*, 206–213.
- Catai, R. E., Bianchi, E. C., Zilio, F. M., Valarelli, I. D. D., De, M. C., Alves, S., et al. (2006). Global analysis of aerodynamics deflectors efficiency in the grinding process. *The Brazilian Society of Mechanical Science & Engineering*, *28*(2), 140–145.
- Choi, H. Z., Lee, S. W., & Jeong, H. D. (2001). A comparison of the cooling effects of compressed cold air and coolant for cylindrical grinding with a CBN wheel. *Journal of Materials Processing Technology*, *111*, 265–268.
- Choi, H. Z., Lee, S. W., & Jeong, H. D. (2002). The cooling effects of compressed cold air in cylindrical grinding with alumina and CBN wheels. *Journal of Materials Processing Technology*, *127*, 155–158.
- Das, M., Mandal, B., & Das, S. (2015). An experimental investigation on grindability of titanium grade 1 under different environmental conditions. *Manufacturing Technology Today*, *14*(2), 3–10.
- Das, S., Sharma, A. O., Singh, S. S., & Nahate, S. V. (2000). Improving grinding performance through effective application of grinding fluid. *Proceedings of the International Conference on Manufacturing (ICME)*, Dhaka, Bangladesh (pp. 231–239).
- Ebbrell, S., Woolley, N. H., Tridimas, Y. D., Allanson, D. R., & Rowe, W. B. (2000). The effects of cutting fluid application methods on the grinding process. *International Journal of Machine Tools and Manufacture*, *40*, 209–223.
- Irani, R. A., Bauer, R. J., & Warkentin, A. (2005). A review of cutting fluid application in the grinding process. *International Journal of Machine Tools & Manufacture*, *45*, 1696–1705.
- Kundu, P. K., & Das, S. (2001). On grinding wheel performance in dry and wet condition. In *Proceedings of the International Conference on Mechanical Engineering (ICME)*, Dhaka, Bangladesh (pp. 19–24).
- Mahata, S., Mandal, B., Mistri, J., & Das, S. (2014). Effect of fluid concentration using a multi-nozzle on grinding performance. *International Journal of Abrasive Technology*, *6*(4), 257–268.

- Malkin, S. (1990). *Grinding technology: Theory and application of machining with abrasives*. UK: Ellis Harwood Publication.
- Mandal, B., Biswas, D., Sarkar, A., Das, S., & Banerjee, S. (2013). Improving grindability of Inconel 600 using alumina wheel through pneumatic barrier assisted fluid application. *Advanced Materials Research*, 622–623, 394–398.
- Mandal, B., Das, G. C., Das, S., & Banerjee, S. (2014). Improving grinding fluid delivery using pneumatic barrier and compound nozzle. *Production Engineering Research and Development*, 8, 187–193.
- Mandal, B., Majumder, S., Das, S., & Banerjee, S. (2010). Predictive modeling and investigation on the formation of stiff air-layer around the grinding wheel. *Advanced Materials Research, Advances in Materials and Processing Technologies*, 83–86, 654–659.
- Mandal, B., Majumder, S., Das, S., & Banerjee, S. (2011a). Formation of a significantly less stiff air-layer around a grinding wheel pasted with rexine leather. *International Journal of Precision Technology*, 2(1), 12–20.
- Mandal, B., Singh, R., Das, S., & Banerjee, S. (2011b). Studying the performance of pneumatic barrier for controlling air flow around a grinding wheel. *International Journal of Machine Tools and Manufacture*, 51(9), 670–676.
- Mandal, B., Singh, R., Das, S., & Banerjee, S. (2012). Development of a grinding fluid delivery technique and its performance evaluation. *Materials and Manufacturing Processes*, 27(4), 436–442.
- Nguyen, T., & Zhang, L. C. (2003). An assessment of the applicability of cold air and oil mist in surface grinding. *Journal of Materials Processing Technology*, 140, 224–230.
- Paul, S., & Chattopadhyay, A. B. (1995). The effect of cryogenic cooling on grinding forces. *International Journal of Machine Tools and Manufacture*, 35(1), 109–117.
- Paul, S., & Chattopadhyay, A. B. (1996). A study of effects of cryo-cooling in grinding. *International Journal of Machine Tools and Manufacture*, 36(1), 63–72.
- Ramesh, K., Huang, H., & Yin, L. (2004). Analytical and experimental investigation of coolant velocity in high speed grinding. *International Journal of Machine Tools and Manufacture*, 44, 1069–1076.
- Sharmacharya, R. S., George, M. N., & Das, S. (1998). On grinding wheel performance through minor wheel modification. In *Proceedings of the 18th All India Manufacturing Technology Design and Research Conference (AIMTDR)*, Kharagpur, India (pp. 156–161).
- Wu, H., Morgan, M. N., & Lin, B. (2009). Investigation of the grinding wheel air boundary layer flow. *Advanced Materials Research, Advances in Abrasive Technology*, 76–78(XII), 113–118.

Design of a Maintenance Optimisation Approach for Offshore Oil and Gas Production Systems

Chanan S. Syan and Geeta G. Ramsoobag

Abstract The expediency of production in the Offshore Oil and Gas Industry is dependent upon high asset integrity levels as a result of well organised maintenance practices. There arises a need for a structured approach to maintenance optimisation for such a complex system. This paper outlines a process for designing an approach for maintenance optimisation of an Offshore Oil and Gas Production System. A detailed literature research on maintenance optimisation is performed to highlight the key tools, techniques and strategies applicable to this industry. In addition, further research was conducted on past optimisation frameworks in the area. The findings highlighted several key stages which were used to design the proposed framework however some stages were modified to accommodate specific elements relating to the industry of interest. This would serve to guide users on achieving effective optimisation for a range of assets. Although the initial stages have been tested future work will attempt to validate the complete framework with a practical case and perhaps extend it to include multi-criteria optimisation techniques.

Keywords Maintenance optimisation · Preventative maintenance · Risk based maintenance

1 Introduction

With current oil prices at around US\$50 a barrel, the Oil and Gas industry needs to reduce its operating costs to remain competitive (Meenagh 2015). A significant portion of these operating costs are maintenance related. World Offshore Maintenance Modifications and Operations Market Forecast 2014–2018 reports a total cost of US\$112 billion in maintenance, modifications and operations for the

C.S. Syan (✉) · G.G. Ramsoobag
Department of Mechanical and Manufacturing Engineering, The University
of the West Indies, St. Augustine, Trinidad
e-mail: chanan.syan@sta.uwi.edu

global Oil and Gas industry (PR Newswire 2014). The complex nature of assets, remote location for operations and harsh environmental conditions magnifies the risks associated with equipment failure. This industry must ensure high levels of uninterrupted production to meet its demands and thus remain profitable. Implementation of effective asset management through optimised maintenance practices is one avenue to aid in maximising return on investment and provides a strategic function for creating a competitive advantage. Maintenance must be performed in a timely manner accounting for high production levels at low costs. Thus, there arises a requirement for an approach which guides researchers on performing maintenance optimisation for this industry.

Although past literature research has revealed many generic approaches to optimisation, due to the variation in complexity of various systems tailoring is often required before success becomes a reality (Waeyenbergh and Pintelon 2002). A case which requires an industry-specific approach involves Oil and Gas offshore production. This should serve to holistically achieve maintenance optimisation by targeting the particular maintenance practices associated with this industry. Hence the following research questions for this paper are formulated:

- (1) What maintenance optimisation approaches, techniques and strategies are most applicable to an Offshore Oil and Gas Production setting?
- (2) How can these approaches, techniques and strategies be utilised effectively to achieve maintenance optimisation for an Offshore Oil and Gas Production System?

2 Review of Maintenance Optimisation Approaches

The literature research process encompassed a review of 136 papers in total. This facilitated both the familiarisation with tools and techniques applicable to maintenance optimisation and framework development.

Publications consisting of several approaches have been proposed and some applied to achieve maintenance optimisation. The findings of eleven review papers illustrated certain general classifications which are compiled and illustrated in Fig. 1. Dekker (1996) has segmented these approaches as either Qualitative including Reliability Centred Maintenance (RCM) and Total Productive Maintenance (TPM) or Quantitative which are data driven rather than expert based. Jardine and Tsang (2013) further classified Quantitative approaches as either Deterministic or Stochastic. The classification has shown that a myriad of factors such as maintenance strategy, replacement or inspection decisions and multi-component or single component cases also affects the optimisation approach that could be employed (Van Horenbeek et al. 2010 and Vasili et al. 2011). A further twenty-two papers were reviewed which have targeted optimisation efforts to the Oil and Gas Industry to allow for further investigation into the most relevant techniques and strategies. Applications to numerous aspects of this

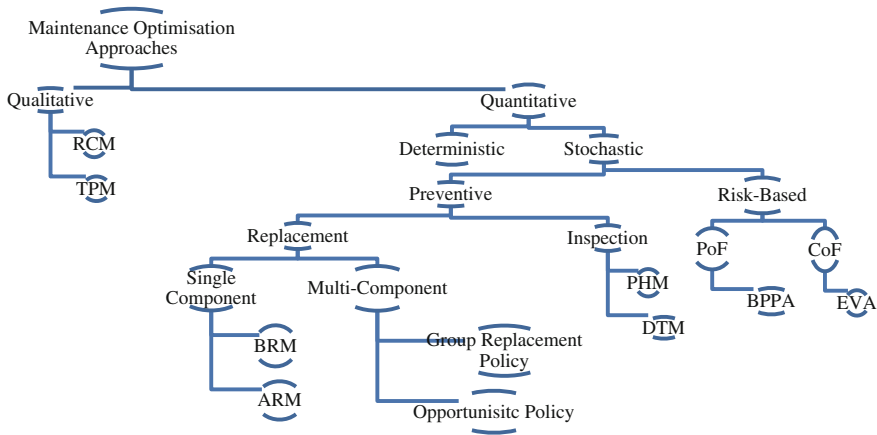


Fig. 1 The classification of maintenance optimisation approaches

industry including static assets such as pipelines and pressure vessels (Dawotola et al. 2011) and rotating assets such as pumping systems, certain topside process components and fuel systems (Gowid et al. 2014) were noticed. Increasing use of maintenance strategies such as Condition Based Maintenance (CBM) (Telford et al. 2011) for rotating elements and Risk Based Inspections (RBI) for static assets highlighted a need for techniques in optimisation with the capability to handle variances.

Eighty-six papers were studied which have effectively utilised tools and techniques to treat with varying maintenance strategies. The page limit of the current paper prohibits the display of the complete list of reviewed papers however Table 1 shows extracts of how the publications were reviewed highlighting categories such as year, maintenance strategy, application, optimisation criteria and techniques used for each.. Authors such as Thodi (2011) and Topalis et al. (2012) attempted to optimise the risk criterion which was evaluated to an equivalent cost in terms of Probability of Failure (PoF) and Consequences of Failure (CoF). Techniques such as Bayesian Prior-Posterior Analysis (BPPA), Fault Tress Aanalysis (FTA) and Rate Models were shown as effective in modelling the Pof while Economic Value Analysis (EVA) was the most popular means of analysing CoF. In addition several authors such as Tian and Liao (2011) and Wang et al. (2010) optimised CBM inspections using techniques such as Proportional Hazards Modelling (PHM) and Delay Time Modelling (DTM), both of which proved successful. Since cost was the most popular optimisation criterion the research also focused on certain papers which have attempted Availability optimisation as this is another important criterion in the industry of interest (Chan and Asgarpour 2006). Jardine and Tsang (2013) have detailed the concept of Age and Block Replacement Models (ARM and BRM) for optimising Preventive Replacements.

Also reviewed were techniques utilised for assessment of maintenance strategies. Analytical Hierarchy Process (AHP) is a flexible, multi-criteria decision making

tool which has been utilised significantly in this context (Ahmadi et al. 2010). Authors such as Rashidpour (2013) have applied AHP to aid in maintenance strategy selection. Andrawus (2008) has expounded on a combined Reliability Centred Maintenance (RCM) and Asset Life-Cycle Analysis (ALCA) approach to maintenance strategy selection to assess the economic viability of a particular strategy. The above research findings provide a comprehensive basis of tools and techniques to facilitate the maintenance optimisation process. However, to be able to effectively achieve results a structured approach must be formulated which directs users on applying such tools and techniques. As a result, the following section details further review of past frameworks utilised to achieve optimisation and explains the design of one such framework targeted towards the Oil and Gas industry.

3 Optimisation Framework Review

The work done in this publication follows the definition of a framework as “*a guideline, procedure or step by step process used to plan or decide for something*” (Ahmad et al. 2011). A framework which provides a guideline for planning decisions to achieve maintenance optimisation would prove tremendously beneficial. (Tam and Price 2006). Asset intensive industries such as Oil and Gas require such a framework to ensure proper operations and high levels of continuous production. Although numerous frameworks have been proposed in the past success is often non-materialistic due to the lack of specificity. To fully realise optimisation benefits technical factors and clear system details must be incorporated into the framework. A total of seventeen further publications were analysed to gain an understanding of the key stages which must be included in such a framework. A limitation encountered in many past approaches is the apparent disconnect between maintenance targets and organisational objectives (Vasili et al. 2011). As a result, a promising framework should provide allowance for maintenance performance targets to directly relate to the company objectives. Mishra et al. (2006) discusses the concept of World Class Maintenance, which emphasises the need for integration between corporate strategy and maintenance management. Parida and Chattopadhyay (2007) comment on the challenge experienced when combining these company goals and maintenance objectives through top-down or bottom-up approaches. The authors have indicated an increase in subjectivity when using a bottom up approach. Marquez et al. (2009) developed a Maintenance Management framework which utilises a Balanced Scorecard (BSC) technique to establish the system key performance indicators allowing for alignment with the organisational strategic objectives.

Offshore Oil and Gas production systems are amongst the most complex, multi-dimensional systems. Maintenance performance targets realised should be represented in terms of different sub-level performance evaluations. A publication by Gowid et al. (2014) has looked at performance evaluation through system

Table 1 Publications showing techniques utilised based on maintenance strategy and optimisation criteria

Author/year	Maintenance strategy	Criteria optimised	Application	Technique(s) used
Thodi (2011)	Replacement	Risk (cost)	Offshore process components (pipelines)	BPPA, EVA
Topalis et al. (2012)	Inspections	Risk (cost)	Atmospheric storage tanks	EVA, modified failure frequency
Jardine and Tsang (2013)	PM replacements	Cost and availability	Bearing replacement age	ARM/BRM
Tian and Liao (2011)	CBM inspections	Cost and reliability	Shear pump bearings of food processing plant	PHM and EXAKT software
Jardine et al. (2001)	CBM oil analysis	Cost	Haul truck wheel motors	PHM and EXAKT software
Wang et al. (2010)	CBM inspections	Cost	Numerical example	DTM
Andrawus (2008)	CBM inspections	Cost	Offshore wind turbine components	DTM
Chan and Asgarpour (2006)	Preventative maintenance	Availability	Numerical example	Markov model
Sachdeva et al. (2008)	PM replacements	Cost, availability life cycle costs	Paper production system (forming dryer units)	Genetic algorithms and monte-carlo optimisation
Dawotola et al. (2011)	Inspections	Risk (cost)	Petroleum pipelines	AHP

Availability assessment. The analysis has evaluated system parameters methodically throughout different levels of asset systems. Furthermore, Seifeddine (2003) presented a maintenance program which has targeted risk evaluation through the product of failure consequences and probability of failure categorising risk as low, medium and high and treatment is assigned accordingly. Seratella et al. (2007) outline a combined Risk and Reliability approach to optimisation for offshore in-service ships. These authors have noted benefits projected from RBI analyses and thus sought to combine Risk and Reliability. The integrated approach addressed safety and environmental concerns, increased integrity and facilitates optimisation of both strategy types. The analysed papers have shown variations in the number of stages utilised to achieve the end objective however, several similar key principles which should be included in the framework were noted. These principles alongside additional steps which would guide optimisation in the industry of interest were studied and developed into a logical framework shown in Fig. 2.

Stage 1 seeks to develop a link between maintenance and business level objectives. Consider an offshore production case in which business objectives include high uninterrupted production levels to ensure customer satisfaction. This objective can be translated to a maintenance target such as percentage availability. The segmentation of the overall system into various levels and identification of

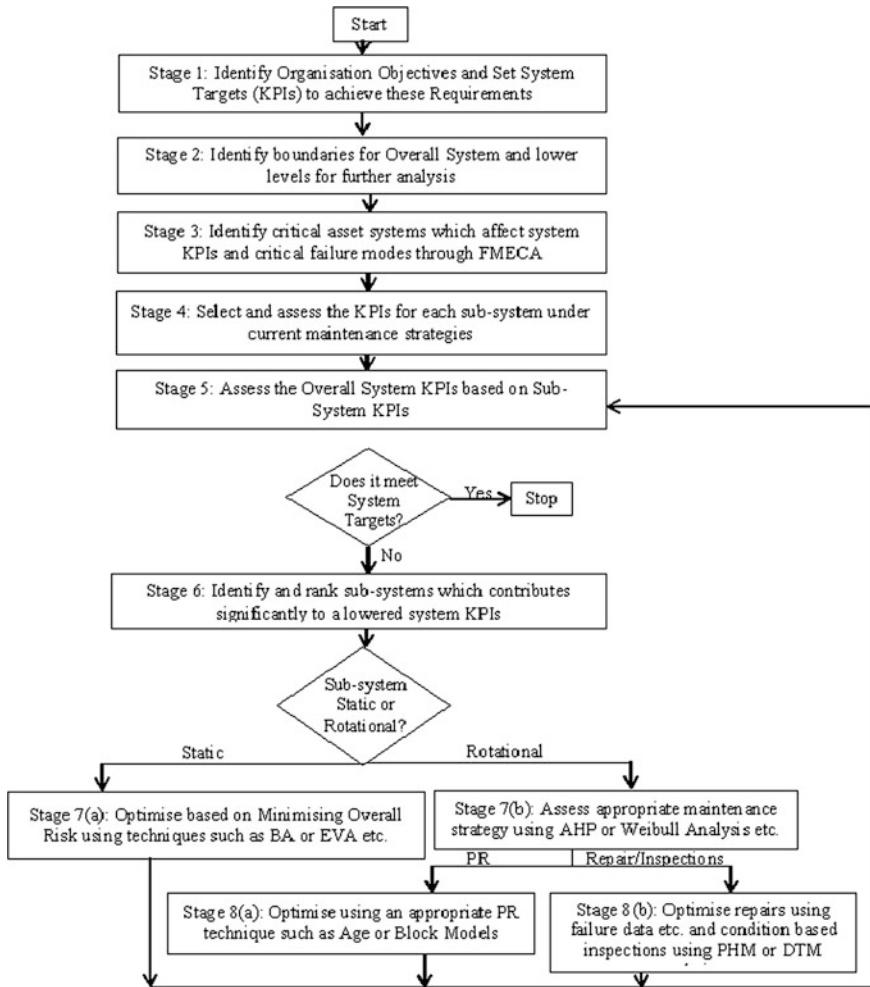


Fig. 2 Designed approach for maintenance optimisation in the oil and gas industry

boundaries allows for performance evaluations to be assessed in such a manner that the overall system is shown as a function of lower sub level systems. Further analysis then follows to allow for critical assets and failure modes to be determined and the system KPI assessed. The outcome of step 5 would identify assets or systems for which maintenance optimisation efforts would greatly impact the overall system.

The final stages of the framework categorise static and rotational assets and in this manner allows for simple application of the relevant tools and techniques for optimisation. If a static asset is selected which after evaluation impacts the performance criteria significantly risk methods can be implemented to optimise the

inspection interval. On the contrary, if the asset is rotational an appropriate maintenance strategy must first be validated and the appropriate optimisation technique employed. In this manner the tools and techniques outlined above can simply be fitted at the appropriate stage and implemented to achieve results. The first five steps in Fig. 1 have been tested for an offshore gas production system using a qualitative FMECA for asset criticality analysis and a hybrid Markov and Reliability theory approach for determining system Availability. OREDA (2002) handbook was the main data source.

4 Conclusion and Future Recommendations

In conclusion, an approach which acts as a tool for maintenance optimisation is designed for the Offshore Oil and Gas Industry. It allows for practitioners and academics in the field to further attempt optimisation for such an industry taking into consideration the complexities in asset size and varying maintenance strategies. Furthermore, although the first few steps of the framework have been tested continued validation is required through complete application to a practical case. The framework can be extended to include multi-criteria optimisation techniques and thus present a wider range of achievable targets for the organisation.

References

- Ahmad, R., Kamaruddin, S., Azid, I., & Almanar, I. (2011). Maintenance management decision model for preventive maintenance strategy on production equipment. *Journal of Industrial Engineering International*, 7(13), 22–34.
- Ahmadi, A., Gupta, S., Karim, R., & Kumar, U. (2010). Selection of maintenance strategy for aircraft systems using multi-criteria decision making methodologies. *International Journal of Reliability, Quality and Safety Engineering*, 17(3), 223–243.
- Andrawus, J. A. (2008). *Maintenance optimisation for wind turbines*. PhD dissertation, The Robert Gordon University.
- Chan, G. K. & Asgarpoor, S. (2006). Optimum maintenance policy with markov processes. *Electric Power Systems Research*, 76(6), 452–456.
- Dawotola, A. W., van Gelder, P. H. A. J. M., Vrijling, J. K., Mustaffa, Z., & Trafalis, T. B. (2011). Data-driven risk based maintenance optimization of petroleum pipelines subject to corrosion. In *The Twenty-first International Offshore and Polar Engineering Conference*.
- Dekker, R. (1996). Applications of maintenance optimization models: a review and analysis. *Reliability Engineering and System Safety*, 51(3), 229–240.
- Gowid, S., Dixon, R., & Ghani, S. (2014). Optimization of reliability and maintenance of liquefaction system on FLNG terminals using markov modelling. *International Journal of Quality and Reliability Management*, 31(3), 293–310.
- Jardine, A. K., & Tsang, A. H. (2013). *Maintenance, replacement, and reliability: Theory and applications*. CRC press.

- Jardine, A. K. S., Banjevic, D., Wiseman, M., Buck, S., & Joseph, T. (2001). Optimizing a mine haul truck wheel motors' condition monitoring program use of proportional hazards modelling. *Journal of quality in Maintenance Engineering*, 7(4), 286–302.
- Marquez, A., Crespo, P. Moreu, de Leon, J. F., Gomez Fernandez, C., Marquez, P., & Lopez Campos, M. (2009). The maintenance management framework a practical view to maintenance management. *Journal of Quality in Maintenance Engineering*, 15(2), 167–178.
- Meenagh, B. (2015). How oil and gas companies can optimize technology performance and costs during oil price volatility. United Arab Emirates RSS Feed, January 21.
- Mishra, P. R., Anand, G., & Kodali, R. (2006). Development of a framework for world-class maintenance systems. *Journal of Advanced Manufacturing Systems*, 5(2), 141–165.
- OREDA Participants. (2002). OREDA, SINTEF Industrial Management.
- Parida, A., & Chattopadhyay, G. (2007). Development of a multi-criteria hierarchical framework for maintenance performance measurement. *Journal of Quality in Maintenance Engineering*, 13(3), 241–258.
- PRNewswire (2014). World offshore maintenance, modifications and operations market forecast 2014–2018. Retrieved April 24, 2015, from <http://www.prnewswire.com/news-releases/world-offshore-maintenance-modifications-operations-market-forecast-2014-2018-239079061.html>.
- Rashidpour, K. (2013). *Using improved AHP method in maintenance approach selection*. Master's Thesis, Malardalen University, Sweden.
- Sachdeva, A., Kumar, D., & Kumar, P. (2008). Planning and optimising the maintenance of paper production systems in a paper plant. *Computers and Industrial Engineering*, 55(4), 817–829.
- Serratella, C. M., Wang, G., & Conachey, R. (2007). Risk-based strategies for the next generation of maintenance and inspection programs. In *International Symposium on Maritime, Safety, Security and Environmental Protection (SSE)*, Athens, Greece (pp. 20–21).
- Seifeddine, S. (2003). Effective maintenance program development/optimization. In *12th International Process Plant Reliability Conference, Houston, Texas*.
- Tam, A. S. B., & Price, J. W. H. (2006). Optimisation framework for asset maintenance investment. *Monash Business Review*, 2(3), 1–10.
- Telford, S., Mazhar, M. I., & Howard, I. (2011). Condition based maintenance (CBM) in the oil and gas industry: an overview of methods and techniques. In *Proceedings of the 2011 International Conference on Industrial Engineering and Operations Management, Kuala Lumpur, Malaysia*.
- Thodi, P. (2011). *Risk based integrity modeling for the optimal maintenance strategies of offshore process components*. Ph.D. Memorial University of Newfoundland (Canada), Ann Arbor.
- Tian, Z., & Liao, H. (2011). Condition-based maintenance optimisation for multi-component systems using proportional hazards model. *Reliability Engineering and System Safety*, 96(5), 581–589.
- Topalis, P., Korneliussen, G., Hermanrud, J., & Steo, V. (2012). Risk based inspection methodology and software applied to atmospheric storage tanks. *Journal of Physics: Conference Series*, 364(1).
- Van Horenbeek, A., Pintelon, L., & Muchiri, P. (2010). Maintenance optimization models and criteria. *International Journal of System Assurance Engineering and Management*, 1(3), 189–200.
- Vasili, M., Hong, T. S., Ismail, N., & Vasili, M. (2011). Maintenance optimization models: A review and analysis. In *Proceedings of the 2011 International Conference on Industrial Engineering and Operations Management Kuala Lumpur, Malaysia, January 22–24*.
- Waeyenbergh, G., & Pintelon, L. (2002). A framework for maintenance concept development. *International Journal of Production Economics*, 77, 299–313.
- Wang, W., Hussin, B., & Jefferis, T. (2010). A case study of condition based maintenance modelling based upon the oil analysis data of marine diesel engines using stochastic filtering. *International Journal of Production Economics*, 136(1), 84–92.

Investigating the Feasibility of BCI-Based Social Media Interaction

Chanan S. Syan and Randy E.S. Harnarinesingh

Abstract Brain-computer Interfaces (BCIs) use the inherent brain activity of subjects in order to communicate with external devices. BCIs have been utilised by disabled users to navigate and interact with their environments using a host of application platforms such as mouse cursor controllers, virtual keyboards and mobile wheelchairs. These platform highlight the wide assistive potential of BCIs. These applications however are restricted to the subjects local environment and do not readily present an opportunity to communicate over long distances or allow messaging to multiple recipients. Social media platforms allow long distance communication over the internet and messaging to multiple recipients which can be leveraged for BCI-based communication. However, the integration of BCIs with social media platforms for communication is limited. This paper investigates the integration of a BCI with Twitter for the communication of public posts and private messages. An online P300-based BCI was developed which allowed for communication to Twitter. Three subjects participated in a programme of experimentation using the developed BCI. The BCI yielded an average classification accuracy of 86 % for the identification of user messages. All user messages however were successfully communication to Twitter. This paper therefore highlighted social media as a viable communication platform which can further improve the assistive value of BCIs. Possible areas of future study include the investigation of other classification methodologies and the integration of the BCI with further social media platforms such as Facebook and LinkedIN.

Keywords BCI · Feasibility · Brain activity

C.S. Syan (✉) · R.E.S. Harnarinesingh
Department of Mechanical and Manufacturing Engineering,
The University of the West Indies, St. Augustine, Trinidad and Tobago
e-mail: chanan.syan@sta.uwi.edu

© Springer India 2016
D.K. Mandal and C.S. Syan (eds.), *CAD/CAM, Robotics and Factories of the Future*, Lecture Notes in Mechanical Engineering,
DOI 10.1007/978-81-322-2740-3_6

1 Introduction

There are various disorders that can limit human function. These range from sensorimotor impairment due to cerebrovascular accidents (CVA) commonly known as strokes (Coffey et al. 1994) to a complete loss of neuromuscular function due to degenerative diseases such as Amyotrophic Lateral Sclerosis (ALS) (Lonergan et al. 2014). Individuals in the late stages of ALS suffer from complete paralysis and are said to be in a Completely Locked-in State (CLIS). Patients in the CLIS stage suffer a loss of autonomy and require assistance in performing daily activities. Brain-Computer Interfaces (BCIs) however can be used to enhance the autonomy of CLIS patients and similarly disabled individuals.

A Brain-Computer Interface (BCI) permits subjects to send commands to devices using brain waves (Itturate et al. 2009). BCI subjects therefore perform mental or physical tasks that represent intended actions. For example, users can focus on directional stimuli on a computer monitor in order to navigate a mobile robot. BCI therefore record brain activity and identify the resulting modification of brain waves that signify the users intended command.

The typical BCI application platforms however are restricted to the local environment of the BCI user and do not readily present an opportunity to communicate over long distances or allow messaging to multiple recipients. Social media platforms such as Facebook, Twitter and LinkedIn however allow long distance communication over the internet and messaging to multiple recipients (Davenport et al. 2014; Ellison et al. 2007; Skeels and Grudin 2009) which can be leveraged for BCI-based communication. However, the integration of BCIs with social media platforms for communication is limited.

This projects investigates the integration of a BCI with the social media platform Twitter. The BCI utilises the P300 neurophysiological protocol. The P300 component is a positive deflection in the subject's Electroencephalogram (EEG) with a latency of 300–400 ms following the presentation of a deviant, rare or target stimuli (Andrews et al. 2008). Visual, auditory or somatosensory stimulation can evoke the P300 wave. However, this study uses the visual P300.

2 BCI Experimental Program

The details of the experimental study used to investigate the integration of a P300-based BCI with Twitter is included in this section.

2.1 *Subject Details*

Three subjects S1, S2 and S3 each participated in this work. The programme of experimentation consisted of 1 training session and 1 testing session. All subjects

provided informed consent for experimentation and the experiments were conducted under approval of the University of the West Indies Ethics Committee. Subjects S1 and S3 were male and subject S2 was female. All of the subjects were naïve to BCI experimentation and had normal or corrected-to-normal vision.

2.2 Data Recording

The g.tec g.MOBILAB was utilised to collect subject EEG at 8 locations of the 10/20 electrode placement guide at its sampling frequency of 256 Hz. Subject head circumferences were measured. These measurements were used to select the most suitable EEG 10/20 cap sizes according to manufacturer data sheets. The CZ positions of the 10/20 subject caps were positioned using the Nasion to Inion anatomical landmarks. The 8 EEG sites used for data collection were P7, P3, P4, P8, FZ, CZ, PZ and OZ. This 8-channel EEG channel set was shown to perform well for P300-based BCI experimentation in Hoffmann et al. (2008). The reference was taken at the left mastoid and ground was taken at the Inion.

2.3 Presentation Paradigm

The Stimulus Presentation Paradigms (SPPs) employed for experimentation were programmed as Graphical User Interfaces (GUIs) in MATLAB. However, the data collection was performed in Simulink for the g.MOBILAB kit. Subjects were comfortably seated at a distance of 75 cm from a 22-in. computer monitor. The lighting used in the experiments was kept constant.

Training Trials

The training trials were utilised to collect features to train classifiers to recognise subject-specific P300 brain responses. The GUI used for training sessions is given in Fig. 1. The default P300 Speller matrix consists of 36 alphanumerical elements (Davenport et al. 2014). However, the Speller matrix required modification in order to allow for Twitter communication. In this regard, the numerical '0' was replaced by a "Post to Twitter" command. Subjects were therefore instructed to use the alphabetical 'O' in place of the numerical '0' if needed.

The colour of target characters was changed to red for a period of 2 s. The users were asked to keep a mental count of the target characters flash frequency in the following flashing pattern. Each matrix command was highlighted in black for a time period of 100 ms. This was followed by a 75 ms Inter-Stimulus Interval (ISI) in which no character was flashed. The sequence of command presentation was randomised as to avoid expectation potentials. The trial therefore comprised of



Fig. 1 Graphical user interface for training trials

the flashing of all 36 matrix commands. Each character was flashed once as the target and was repeated for 5 trials. This generated a total of 36 5-trial segments.

Testing Trials

The classifiers were employed for online subject trials using the GUI in Fig. 2. The subject selected commands on their own cognition in these online trials. In these trials, the BCI had no previous knowledge of user command thereby providing a basis for the unbiased assessment of classifier accuracy.

Five trials of online presentation were used for Subjects S1, S2 and S3. The classified commands were displayed in a GUI dialog box at the top of the MATLAB screen.

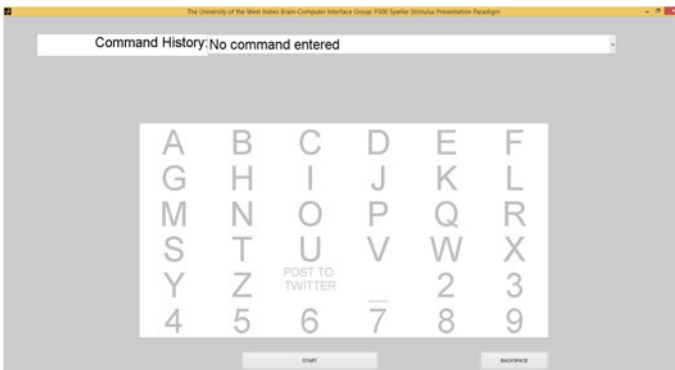


Fig. 2 Stimulus presentation paradigm GUI for testing sessions

2.4 Signal Analysis and Pattern Classification

The user EEGs were collected without pre-processing for the offline trials. N-fold Cross-Validation (NFCV) was employed to locate optimal pre-processing and feature extraction variables for Fishers Linear Discriminant Analysis (FLDA) classifiers for S1–S3. This variable search procedure is further described.

Forward-reverse signal filtering was applied to each channel using digital Butterworth filters whose order is determined using the procedure below. These filters possessed 3 dB cut-off frequencies at 1 and 12 Hz. The 500 ms temporal periods following stimulus presentation were down-sampled by a factor of K thereby generating temporal features relating to each channel. The temporal feature sets were then concatenated for all 8 channels. This method produced a spatiotemporal feature vector for every post-stimulus time segment. This procedure was used for the determination of pre-processing and feature extraction variables.

3 Results

The determined pre-processing and feature extraction variables for all participating subjects are presented in Table 1.

The words communicated to Twitter for each subject are presented in Table 2. Subjects S1 and S3 chose to communicate two public posts to Twitter. Subject S2 sent one direct message using the developed BCI.

The two successful posts made by Subject S3 are shown in Fig. 3 as a representative result.

The online classifier accuracies obtained for command identification are shown in Table 3.

Table 1 Pre-processing and feature extraction variables

Subject	K	n
S1	20	2
S2	18	1
S3	12	3

Table 2 Details of Twitter communication for subjects S1–S3

Subject	First communication	Type	Second communication	Type
S1	HOUSTON WON	Post	HELP 911	Post
S2	HI RAJ	Direct message		
S3	BCI IS WORKING	Post	HOPE	Post

Fig. 3 Public posts to Twitter made by subject S3

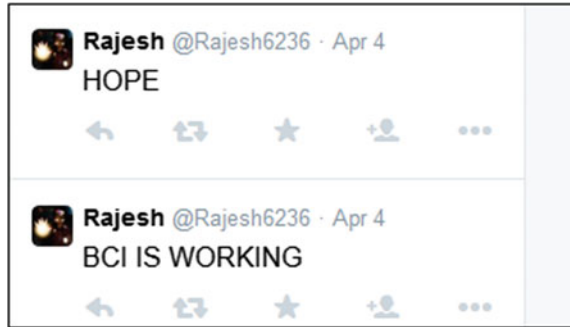


Table 3 Classifier accuracies for all subjects

Subject	Type of communication	Number of letters correctly communicated	Number of misclassified letters	Total number of letters attempted	Percentage classification accuracy (%)
S1	Post	11	5	16	68.75
	Post	8	2	10	80
S2	Direct message	6	0	6	100
S3	Post	14	0	18	100
	Post	4	0	4	100
Total		43	7	50	86

4 Discussion

The mean classifier accuracy for all subjects was 86 %. Subject S1 attained online classification accuracies of 68.75 and 80 % respectively for his two public posts. Subjects S2 and S3 however attained 100 % accuracy for their Twitter posts and messages. The difference in classification accuracies across subjects can be due to multiple circumstances. First, Subject S1 could have experienced more mental fatigue during his BCI usage. This is known to degrade classification accuracy for BCIs. Second, the electrode impedances for subject S1 could have been greater than S2 and S3. This would manifest itself as a lower Signal-to-Noise Ratio (SNR) which also can result in decreased classification accuracy. Finally, the relatively low classification accuracy for Subject S1 could be due to insufficient BCI training. It was observed that the classification accuracy for Subject S1 increased from the first to the second communication. This increase in classification accuracy suggests that S1 became better trained at using the BCI.

All subjects however were able to successfully communicate public posts and private messages to the Twitter platform. There are however other social media platform that could be exploited to achieve long distance communication. An area

of further study could be the investigation of BCI-based Facebook and LinkedIn communication. Another possible further area of study is the investigation of other classification methodologies. This paper utilised the FLDA classifier. However, other classifiers such as Bayesian Linear Discriminant Analysis (BLDA) have been shown to outperform the FLDA classifier for P300-based BCIs (Hoffmann et al. 2008; Syan et al. 2014). Post hoc of the dataset acquired in this paper could.

5 Conclusion

This paper reports on the feasibility of online BCI-based Twitter communication. Three subjects successfully utilised the developed BCI to communicate both public posts and private messages to Twitter. Further work can investigate the integration of the BCI with other social media platforms such as Facebook and LinkedIn. In addition, the developed BCI yielded an average classification accuracy of 86 %. It is possible to improve this classification accuracy by utilising other classification methodologies such as BLDA. There is therefore ample room for future study on BCI-based social media integration.

References

- Andrews, S., Palaniappan, R., Teoh, A., & Kiong, L. C. (2008). Enhancing P300 component by spectral power ratio principal components for a single trial brain-computer interface. *American Journal of Applied Science*, 5(6), 639–644.
- Coffey, C., Cummings, J. L., Lovell, M. R., & Pearlson G. D. (1994). *The American Psychiatric Press textbook of geriatric neuropsychiatry*. American Psychiatric Association.
- Davenport, S. W., Bergman, S. M., Bergman, J. Z., & Fearington, M. E. (2014). Twitter versus Facebook: Exploring the role of narcissism in the motives and usage of different social media platforms. *Computers in Human Behavior*, 32, 212–220.
- Ellison, N. B., Steinfield, C., & Lampe, C. (2007). The benefits of Facebook “Friends:” Social capital and college students’ use of online social network sites. *Journal of Computer-Mediated Communication*, 12(4), 1143–1168.
- Hoffmann, U., Vesin, J. M., Ebrahimi, T., & Diserens, K. (2008). An efficient P300-based brain-computer interface for disabled subjects. *Journal of Neuroscience Methods*, 167(1), 115–125.
- Iturrate, I., Antelis, J., Kubler, A., & Minguez, J. (2009). A non-invasive brain-actuated wheelchair based on a P300 neurophysiological protocol and automated navigation. *IEEE Transactions on Robotics*, 25(3), 617–627.
- Lonegan, R., Mistumoto, H., & Murray, B. (2014). Amyotrophic lateral sclerosis. In *Neuromuscular Disorders in Clinical Practice* (pp. 395–423). Springer.
- Skeels, M. M., & Grudin, J. (2009). When social networks cross boundaries: a case study of workplace use of Facebook and LinkedIn. In *Proceedings of the ACM 2009 International Conference on Supporting Group Work* (pp. 95–104). ACM Press.
- Syan, C. S., Hamarinesingh, R. E. S., & Beharry, R. (2014). Investigating the feasibility of a BCI-driven robot-based writing agent for handicapped individuals. In *Proceeding of 27th International Conference on CAD/CAM, Robotics and Factories of the Future* (pp. 1–10). IOP Press.

Virtual Experiments for Integrated Teaching and Learning of Robot Mechanics Using RoboAnalyzer

Ratan Sadanand, Ravi Prakash Joshi, Rajeevlochana G. Chittawadigi and Subir Kumar Saha

Abstract Increasing number of universities are offering robotics courses at undergraduate and graduate level. Introductory courses on robot mechanics involve topics from matrix multiplication, coordinate transformations and multivariate equations. Often, the physical meaning of concepts in kinematics and dynamics are lost behind the complicated mathematics involved in them. Hence, it may be the case that some fundamental concepts in robot mechanics may not be very intuitive to teach or learn. In order to appreciate the same, robotics teaching/learning software can be integrated into the curriculum. In this paper, the use of RoboAnalyzer, a 3D model based software for teaching and learning a course in robot mechanics is discussed. An integrated coursework that involves virtual experiments and projects in robot mechanics using RoboAnalyzer is also proposed in the paper. The foreseen advantages of using RoboAnalyzer in classroom and laboratory sessions are also discussed.

Keywords Robotics · Education · Kinematics · Simulation

R. Sadanand (✉) · R.P. Joshi · S.K. Saha
Department of Mechanical Engineering, Indian Institute
of Technology Delhi, New Delhi 110016, India
e-mail: ratan.sadan@gmail.com

R.P. Joshi
e-mail: ravi2008joshi@gmail.com

S.K. Saha
e-mail: saha@mech.iitd.ac.in

R.G. Chittawadigi
Department of Mechanical Engineering, School of Engineering, Amrita Vishwa
Vidyapeetham University, Bengaluru 560035, India
e-mail: rg_chittawadigi@blr.amrita.edu

1 Introduction

With the prevalent use of robots in industry, manufacturing, military, space exploration, medical applications, etc., fundamental and advanced courses on robot mechanics are being offered at undergraduate and graduate level. Majority of the introductory textbooks and courses on robot mechanics and control, focus on serial-chain manipulators. A holistic approach towards teaching robot mechanics is to explain the concepts using an actual serial or parallel robot manipulator. However, not all engineering departments in Indian universities have access to a real industrial robot. One approach towards tackling this issue in robotics education in India is to use a teaching-learning software in a robot mechanics course. The primary design philosophy behind such a software must be such that it would facilitate the instructors and students to learn and teach robot mechanics intuitively. There exists full-fledged software to allow dynamic simulation, path planning, real-time control, etc. of robot manipulators. However, majority of them do not cater towards intuitive learning of the concepts in robot mechanics. For a comprehensive learning, a robotics teaching software must complement the theoretical material prescribed in the syllabus; simultaneously, it must also provide students and teachers with the capability of simulating robots in a virtual environment. Implementing virtual experiments with such software in curriculum would overcome the limitation of not having an actual robot, to a great extent.

Software that aid robotics education have been reported in literature. The commonly used ones are Robotics Toolbox for MATLAB (Corke 1996), V-REP (Freese et al. 2010), RoKiSim (2015), Webots (Michel 2004; Guylot et al. 2011), ARTE (2015), etc. RoboAnalyzer (Rajeevlochana and Saha 2011) is another attempt at a 3D model based virtual learning and experimentation platform for mechanics of serial-chain robots. It has been developed since 2009. The core design philosophy behind RoboAnalyzer is to have a virtual learning environment that would aid in teaching and learning the geometry, kinematics and dynamics of serial-chain robots. Concepts like Denavit-Hartenberg (DH) parameters (Denavit and Hartenberg 1955), homogeneous transformation matrices (HTMs), etc. can be explained lucidly using features in RoboAnalyzer. While there are provisions for kinematic and dynamic simulations, RoboAnalyzer emphasizes on explaining the concepts in a more elegant manner and is primarily meant as a robotics education tool. The main graphical-user-interface (GUI) of RoboAnalyzer is shown in Fig. 1. A brief comparison of relevant features of different robotics teaching/learning software is given in Table 1.

This paper discusses how RoboAnalyzer can be effectively used for teaching and learning, in a course of robot mechanics. An overview of RoboAnalyzer and its functionalities are discussed in Sect. 2. Section 3 gives an overview of the different problems faced while teaching and learning robot mechanics, and how RoboAnalyzer is designed to tackle majority of them. This highlights the features of RoboAnalyzer that makes it a good fit for robotics education at a fundamental level. Section 4 details how virtual experiments can be conducted using RoboAnalyzer for

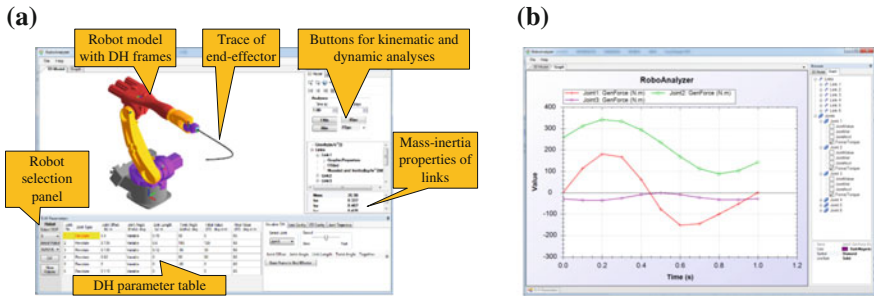


Fig. 1 RoboAnalyzer user interface. **a** Main user interface. **b** Graph plotting module

Table 1 Comparison of features of different robotics teaching/learning software

Features	Software				
	Robotics toolbox	V-REP	RoKiSim	ARTE	RoboAnalyzer
Schematic skeleton models	Readymade models available	Readymade models available	Not available	Readymade models available	Readymade models available. Can be modified using GUI
CAD models of industrial robots	Models can be imported in STL format	Available	Available	Available	Available
Visualization of coordinate frames	By writing code	Frames must be configured	All frames available	Not available	All frames by default
Animation of homogeneous transformations	By writing code	By writing code	Not available	By writing code	Available for all DH parameters using GUI
Animation of robot motion	Animation of kinematics and dynamics by writing code or using a teach pendant interface for jogging	Animation of kinematics and dynamics by writing code	Jogging of robot using teach pendant interface and readymade motions	Animation of kinematics and dynamics by writing code or using a teach pendant interface for jogging	Animation of kinematics and dynamics using GUI or using a teach pendant interface for jogging
Display of end-effector trace	Available	Available	Available	Available	Available
Plots	Using MATLAB plots	Dedicated plots	Not available	Using MATLAB plots	Dedicated plots
			Not available		

(continued)

Table 1 (continued)

Features	Software				
	Robotics toolbox	V-REP	RoKiSim	ARTE	RoboAnalyzer
Specify joint trajectory models	Only quintic polynomial model	By writing code		Multiple trajectory models available	Multiple trajectory models available
Multiple solutions for inverse kinematics	Calculation and visualization of different solutions	Not displayed in simulation	Calculation and visualization of different solutions	Available	Calculation and visualization, including animation between solutions
Coding prerequisites required	Knowledge of MATLAB	Knowledge of API (application programming interface)	None	Knowledge of MATLAB	None
Display of transformation data	Upon command	Using scope/graph	On screen	Upon command	On screen

a course in robot mechanics, and incorporating them into coursework. The implementation of the same at IIT Delhi is also discussed. The conclusions are discussed in Sect. 5.

2 Overview of RoboAnalyzer

RoboAnalyzer is a 3D model based robotics learning software developed as a Windows desktop application. The main aim here is to provide students and teachers with a platform to learn concepts in robot mechanics. RoboAnalyzer is modular in nature—each functionality like kinematics, visualization, etc. have been developed as a separate module and integrated together. A brief description of the main modules and the features are described below in Table 2.

3 Issues in Teaching and Learning Robot Mechanics

The task of teaching robot mechanics to beginner level engineering students is not an easy task—nor is learning the concepts. The relevant problems in teaching and learning robotics, along with the solution strategy employed by RoboAnalyzer in tackling them are mentioned below.

Table 2 Main modules and features of RoboAnalyzer software

RoboAnalyzer module	Features
3D model viewer	Displays the 3D model of robot, DH coordinate frames and trace of end-effector
DH parameter visualization	Animate and visualize the DH parameters of the robot and the associated transformations between the DH coordinate frames
Kinematics	Forward and inverse kinematics (Bahuguna et al. 2013) of different serial-chain robots, calculation of homogenous transformation matrices, selection of joint trajectories, etc.
Dynamics	Inverse dynamics of different serial chain robots; free and forced forward dynamic simulation
Virtual robots module (VRM)	Joint level and Cartesian level motion of more than 17 industrial robot models using a teach pendant like interface (Sadanand et al. 2013)
Graph plotting module	Relevant plots for kinematic and dynamic simulations of serial-chain robots
Add-in for other software	Integration of VRM with MS Excel, MATLAB, and robotics toolbox in MATLAB (Sadanand et al. 2015)

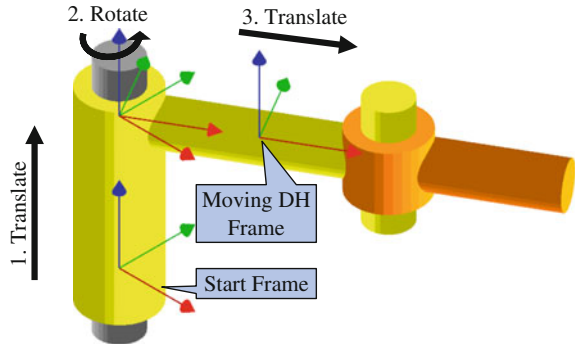
3.1 Limited Access to an Actual Robot

Not all engineering schools have the facility of a real industrial robot. Even in those schools which do possess a serial robot, beginner students of robotics can avail only a limited access due to constraints like prior training and programming experience required to operate the robot, robot being engaged for other research purposes, etc. In such a case, a virtual environment in which the robot motion can be simulated can be of key importance. RoboAnalyzer presents the user with an array of serial-chain robot models in a 3D environment that can be selected and modified by the user. This would let the user perform the kinematic and dynamic simulations offline and compare the results with the actual robot. For more realistic simulations of joint-level and Cartesian-level motions, the VRM of the RoboAnalyzer can be used.

3.2 Difficulty to Understand the DH Parameters and Coordinate Transformations

Each of the four DH parameter corresponding to a robot joint has an associated coordinate transformation, which has a corresponding 4×4 HTM. However, the 3D transformations are not easy to visualize from a book and are difficult to explain using conventional teaching medium. The DH parameter visualization feature will allow the students to see and understand the coordinate transformations associated

Fig. 2 Visualizing DH parameters in RoboAnalyzer



with a particular DH parameter. This feature is shown below in Fig. 2. The ‘Start Frame’ is transformed into the ‘Moving DH Frame’ until it coincides with the next DH frame.

3.3 Visualizing Simulations

Although conventional teaching aids can be used for visualizing planar robots, motion of robots in 3D space is difficult to understand without the help of a simulation software. Some robot manufacturers supply proprietary software for robot simulations and offline programming, but these are often available for a higher cost. RoboAnalyzer and its modules help in understanding the robot motion using animations. Users are also provided with the capability to specify the motion trajectories. The virtual robots can be programmed and simulated from MATLAB environment using the VRM visualization addin for MATLAB, as shown in Fig. 3.

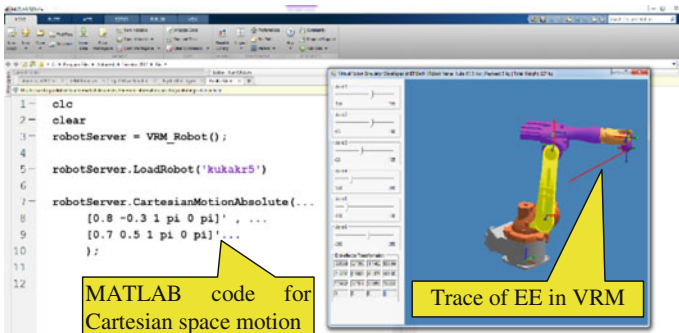


Fig. 3 Offline simulation using VRM addin for MATLAB

3.4 Advanced Calculations and Programming

As the number of degrees-of-freedom of the serial-chain robot increases, the computations involved in the kinematic and dynamic analyses may become complicated. Performing the same computations in MATLAB or other programming environment will require the user to create a program from scratch, which may be tedious. Although this maybe preferred for advanced research, it is not recommended for classroom education as it consumes a lot of time, which can otherwise be utilized for learning the concepts. RoboAnalyzer, with its readymade module can help solve a variety of analyses in robot mechanics, thus facilitating the students in problem solving, verification and basic offline motion simulation.

4 Structured Curriculum in Robotics with Practical and Simulation Sessions

A comprehensive learning experience is achieved when the theory taught in classroom is absorbed by the students at a conceptual level and is put into practice using a device or an experiment. However, as mentioned previously in Sect. 3, the lack of access to a robot or associated hardware can limit the practical learning experience in robot mechanics. RoboAnalyzer offers a possible solution in this scenario. The different modules of it can be used to perform virtual experiments using different kinds of robot models.

4.1 Virtual Experiments for an Introductory Coursework in Robotics

The authors have developed a list of virtual experiments using RoboAnalyzer. Due to the space constraints, only an overview of the experiments is listed in Table 3. Detailed report can be found in Sadanand and Saha (2015). The virtual experiments have been designed such that they can be completed as a part of a semester long course in robot mechanics. They have been structured to augment the classroom lectures. The different modules of RoboAnalyzer software can be used to complete the subtasks in the experiments, which cover different topics in robot mechanics. About 11 practical experiments have been proposed, which can be done on a weekly basis over a semester. Following this, a week or two may be utilized for conducting presentations based on the course material that has been already taught or for project presentations (as shown in Table 4). The course instructors familiar with the theory of robot mechanics can acquaint themselves with the RoboAnalyzer software using a user manual. Following this, the mentioned virtual experiments can be utilized in the coursework.

Table 3 Virtual experiments using RoboAnalyzer

Week	Laboratory assignments	Topics	Theoretical prerequisites in Saha (2014)
1	RoboAnalyzer: introduction and features	Usage of RoboAnalyzer	Appendix C
2	Virtual models of industrial robots	Industrial robots	Chapter 2, Appendix C
3	Coordinate frames and transformations in robot mechanics	Robot geometry, DH Parameters	Chapter 5, Appendix A
4	Forward kinematics of serial-chain robots	Robot kinematics	Chapter 6
5	Inverse kinematics of serial-chain robots	Robot kinematics	Chapter 6
6	Kinematics of MTAB mini robot	Robot kinematics	Chapter 6
7	Workspace analysis of a 6 axis robot	Workspace analysis	Chapter 6
8	Inverse and forward dynamics of robots	Robot dynamics	Chapter 8
9	Generating robot joint trajectories	Trajectory planning	Chapter 12
10	Application: using a virtual robot model to write a welding profile	Cartesian motion of industrial robots	Chapter 2, 12
11	Application: using a joystick to control a virtual robot model	Industrial robots	Chapter 13

Table 4 List of suggested projects using RoboAnalyzer

S. no.	Course project	Duration	Time required
1	DH parameters of an industrial robot: visualization and identification	2 weeks	15 h
2	Kinematic analysis of MTAB Aristo robot	3 weeks	20 h

4.2 Implementation at IIT Delhi

At IIT Delhi, the above virtual experiments were employed for learning robot mechanics using practical coursework and put into practice in the course ‘Mechanics of Robots (MEL-739)’. In the course, RoboAnalyzer was used for virtual experimentation along with other computational tools like MATLAB and RecurDyn. The weekly practical experiments in the course were coherent with the classroom coursework, and the theory developed in class is applied in laboratory sessions using RoboAnalyzer. This ensured that students get an opportunity to use the knowledge acquired in classroom to analyze and design serial-chain robots. An introductory textbook in robot mechanics (Saha 2014) integrates RoboAnalyzer in the explanatory problems as well as end-of-chapter exercises.

Table 5 RoboAnalyzer: user feedback results (sample size = 35)

Query/feature	Average rating (out of 5)
Student can use it independently after first use	4.38 ± 0.92
Student can learn at their own pace	4.24 ± 0.74
Helps student learn new concepts in robotics	4.20 ± 0.81
Helps better understanding of known concepts	4.09 ± 0.87
Robot simulations are realistic	4.32 ± 0.88
DH parameters can be clearly visualized	4.38 ± 0.88
3D animation makes the software more effective	4.35 ± 0.69

Apart from this, RoboAnalyzer can be used to solve problems in any fundamental textbook in robot mechanics. Thus, RoboAnalyzer coupled with a textbook, can serve as an inclusive package for teaching and learning robot mechanics. It was also observed that various difficulties mentioned in Sect. 3 could be overcome with the use of RoboAnalyzer, during the coursework. These virtual experiments were also used in a robotics workshop for beginner level students in robotics and favorable feedback was received. The salient points of the user feedback are listed in Table 5, where the average rating consists of mean and standard deviation.

The use of RoboAnalyzer for different robotics based courses was discussed in the workshop on Teaching Trends in Robotics (Saha 2012). The possible advantages derived from using a software like RoboAnalyzer is that, quick analyses can be performed, which would allow the students to easily progress through the course material. While RoboAnalyzer can definitely aid in class assignments, it is not meant as a tool to spoon-feed the students; rather it helps them to understand the concepts at a fundamental level. Having stated the above advantages, it should be noted that simulation/visualization software is no replacement for an actual robot for learning robotics. A possible way to address this limitation is to develop robust and low cost serial-robots that are tailor-made for educational purposes.

5 Conclusions

In this paper the use of RoboAnalyzer for robotics education and its possible integration in robotics courses for enhanced teaching and learning experience are discussed. The possible problems encountered in teaching and learning robotics at a beginner level are discussed and the use of RoboAnalyzer to solve most of them in an innovative manner is explained. A comprehensive course on robot mechanics can be achieved by integrating educational aids in the curriculum. RoboAnalyzer can serve as an effective 3D model based robotics learning software by allowing virtual experimentation and analysis. Supplementing the course syllabus with RoboAnalyzer will help the students to apply and verify the theoretical knowledge on robot mechanics to practical problems. A sample list of experiments using

RoboAnalyzer is also provided for the benefit of teachers of robot mechanics courses. RoboAnalyzer can be accessed from <http://www.roboanalyzer.com> and is freely available for educational use. It is getting evolved by incorporation of new modules and interfacing with other computational platforms.

References

- ARTE—A Robotics Toolbox for Education. Retrieved April, 2015 from http://arvc.umh.es/arte/index_en.html.
- Bahuguna, J., Chittawadigi, R. G., & Saha, S. K. (2013). Teaching and Learning of Robot Kinematics Using RoboAnalyzer Software. In *Proceedings of the Advances in Robotics: 1st International Conference on Advances in Robotics*, Pune, India.
- Corke, P. (1996). A robotics toolbox for MATLAB. *IEEE Robotics and Automation Magazine*, 3, 24–32 (March 1996).
- Denavit, J., & Hartenberg, R. S. (1955). A kinematic notation for lower pair mechanisms based on matrices. *ASME Journal of Applied Mechanisms*, 22(2), 215–221.
- Freese, M., Singh, S., Ozaki, F., & Matsuhira, N. (2010). Virtual robot experimentation platform (V-REP): a versatile 3d robot simulator. *Simulation, Modeling, and Programming for Autonomous Robots* (pp. 51–62). Berlin Heidelberg: Springer.
- Guyot, L., Heiniger, N., Michel, O., & Rohrer, F. (2011). Teaching robotics with an open curriculum based on the e-puck robot, simulations and competitions. In *Proceedings of the 2nd International Conference on Robotics in Education*, Vienna.
- Michel, O. (2004). Webots: professional mobile robot simulation. *International Journal of Advanced Robotic Systems*, 1(1), 39–42.
- Rajeevlochana, C. G., & Saha, S. K. (2011). RoboAnalyzer: 3D model based robotic learning software. In *Proceedings of the International Conference on Multi Body Dynamics*, (pp. 3–13) Vijayawada, India.
- RoKiSim. Retrieved April, 2015 from <http://www.parallemic.org/RoKiSim.html>.
- Sadanand, R., Chittawadigi, R. G., & Saha, S. K., 2013. Virtual Robot Simulation in RoboAnalyzer. *Proceedings of the 1st International and 16th National Conference on Machines and Mechanisms*, Roorkee, India.
- Sadanand, R., Joshi, R. P., Chittawadigi, R. G., & Saha, S. K. (2015). Virtual robots module: an effective visualization tool for robotics toolbox. In *Proceedings of 2nd International Conference on Advances in Robotics*, BITS-Goa.
- Sadanand, R., & Saha, S. K. (2015). Suggested practical assignments using RoboAnalyzer software. Retrieved May, 2015 from <http://www.roboanalyzer.com/virtual-experiments.html>.
- Saha, S. K. (2012). Proceedings of trends in teaching robotics for UG/PG students. Retrieved December, 2012 from <http://www.roboanalyzer.com/workshop.html>.
- Saha, S. K. (2014). *Introduction to Robotics* (2nd ed.). New Delhi: McGraw-Hill Higher Education.

Fuzzy Based Object Shape Recognition Using Translation, Rotation and Scale Invariant Parameters—An Automatic Approach

Jeet Banerjee, Soma Banerji, Ranjit Ray and Sankar Nath Shome

Abstract In this paper, an unsupervised (e.g. autonomous) shape recognition is performed in a structured environment with the help of rotation, translation and scale invariant parameters and fuzzy logic. In a practical scenario, it is undoubtedly difficult to apply a sharp cut-off for defining a particular object shape using an object parameter in crisp parameter based object recognition. To overcome this difficulty, we have proposed to use a well-known concept of fuzzy logic. Applying object's shape parameters as fuzzy logic inputs, it was observed that oval-shaped, triangular, rectangular, pentagonal and hexagonal objects are autonomously perceived with an overall recognition rate of 91.45 %. The proposed scheme has also been compared with two existing algorithms, presents better results. The detailed description of the results is provided towards the end of this paper.

Keywords Average moment invariant · Condensibility · Ratio of long span to short span · Shape recognition

1 Introduction

One of the common requirements in industrial automation is recognizing a particular shape before handle it for further specific manufacturing process autonomously. In this regard, machine vision is the most popular means for automatic

J. Banerjee
School of Mechatronics, CSIR-CMERI, Durgapur 713209, India
e-mail: jeet.iitkgp89@gmail.com

S. Banerji · R. Ray (✉) · S.N. Shome
Robotics and Automation Laboratory, CSIR-CMERI, Durgapur 713209, India
e-mail: ranjitray@cmeri.res.in

S. Banerji
e-mail: soma.banerjee87@gmail.com

S.N. Shome
e-mail: snshome@cmeri.res.in

recognition of an object shape. The prime object of this work is online recognition of object shapes based on machine vision approach using translation, rotation and scale invariant parameters. So far, a number of researches are available in this field. In general, objects are distinguished based on properties of images like texture and color (Smith et al. 2004). However, shape of an object is a dominant property which helps in near accurate object recognition (Moomivand et al. 2011). Based on the dominant properties of shapes, researchers have proposed different parameters to describe a varied class of shapes, and also have introduced numerous approaches to solve the recognition problem. Ku et al. (2010) used width to height ratio (WTHR), base to abdomen ratio (BTAR) and shape boundary test (SBT) for distinguishing different object shapes. Belongie et al. (2010) introduced shape context (description of entire boundary points of a shape with respect to single edge point) to recognize the object shapes via matching with database images. Shape recognition of an object through sensing the surrounding edges using tactile sensors was proposed by Amit Konar et al. (Singh et al. 2012). Shape recognition based on condensibility and shape-signature identification has been described by Banerjee et al. (2012, 2013). Chang et al. (2002) have proposed a two stage scene analysis using combined fuzzy logic based technique, where the scene is classified using fuzzy classification rules first, and then the classified results has refined using K-means nearest neighbor algorithm. Similarly, works related to automatic object recognition using image morphology based techniques have also been carried out in (Shih et al. 1988a, b). A plenty of research are going on the application of fuzzy logic in image enhancement, filtering, image classification and edge detection (Tyan et al. 1993; Nedeljkovic 2008; Mathur et al. 2008).

In the present work, object shape recognition is performed using rotation, translation and scale invariant parameters, e.g. condensibility (C), ratio of long span to short span ($RLSTSS$) and average moment invariant (AMI) combined with fuzzy logic technique (Chang et al. 2002). Standard shapes like oval (**OV**), triangle (**TR**), rectangle (**RT**), pentagon (**PT**) and hexagon (**HX**) are used for object shape understanding purpose.

The rest of the paper is organized as follows. Proposed method is presented in Sect. 2. Consequent simulation results and comparison are discussed in Sect. 3. Section 4 concludes the manuscript with a few inferences and remarks on the proposed scheme and future scope.

2 Proposed Method

The proposed scheme is basically meant for automatic fuzzy based shape recognition of oval, triangle, rectangle, pentagon and hexagon shaped objects. Here, in this algorithm, three well-known object parameters, e.g. condensibility (C), ratio of long span to short span ($RLSTSS$) and average moment invariant (AMI) have been used, and calculated a range of those parameters from 100 different sizes of each OV, TR, RT, PT and HX. Furthermore, the ranges of parameters are used to select

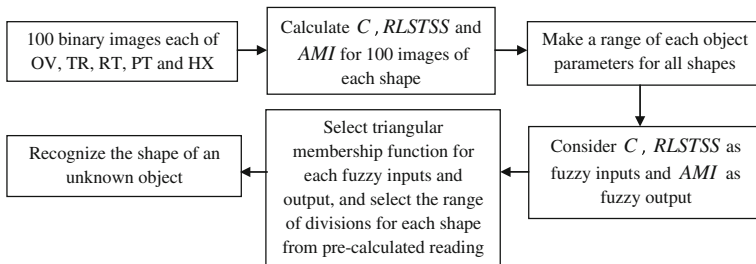


Fig. 1 Flow diagram of the proposed method

the boundary of fuzzy membership functions, while considering C , $RLSTSS$ as fuzzy input parameters and AMI as output parameter. Hence, the proposed fuzzy based system is ready for automated recognition of the shape of an unknown object. Algorithm for the proposed scheme is depicted in Fig. 1.

2.1 Calculation of Object Parameters

As mentioned earlier, in this proposed approach, automatic object shape identification is performed using rotation, translation and scale invariant parameters, i.e. C , $RLSTSS$ and AMI . These parameters are calculated as shown below in the Eqs. (1), (2) and (5), respectively.

$$C = \frac{4\pi \times \text{Area}}{\text{Perimeter}^2} \tag{1}$$

$$RLSTSS = \frac{\text{Length of major axis of the ellipse, just covers a shape}}{\text{Length of major axis of the ellipse, just covers a shape}} \tag{2}$$

AMI calculation: Two dimensional moment of an image $f(x, y)$ is given by

$$M_{pq} = \sum_{x=1}^{N-1} \sum_{y=1}^{N-1} x^p y^q f(x, y) \tag{3}$$

The central moment of the order $(p + q)$ can be represented as

$$\mu_{pq} = \sum_{x=1}^{N-1} \sum_{y=1}^{N-1} (x - \bar{x})^p (y - \bar{y})^q f(x, y), \text{ where } \bar{x} = \frac{M_{10}}{M_{00}}, \bar{y} = \frac{M_{01}}{M_{00}} \tag{4}$$

A set of seven 2-D moment invariants (ϕ_i) that are insensitive to translation, scale change, mirroring and rotation are defined in Gonzalez et al. (2009). Hence, average moment invariant (*AMI*) can be expressed as

$$\phi_{avg} = \frac{1}{7} \sum_{i=1}^7 \phi_i \quad (5)$$

From the Eqs. (1), (2) and (5), *C*, *RLSTSS* and *AMI* are calculated for each shape of 100 different sizes. This gives an idea about the ranges of three parameters for OV, TR, RT, PT and HX for all possible circumstances. Image resolution of 744×557 is used to prepare the database images with different shape patterns.

2.2 Fuzzy Logic Design

In this proposed technique, *C* and *RLSTSS* are considered as fuzzy input parameters and *AMI* as output. Each inputs and output are divided into five divisions (for five different shapes) according to pre-calculated range for each shape, and triangular membership functions are drawn for each division. Decision about the shape of an unknown object is evaluated through fuzzy rule base (based on how much close the unknown object's parameters with respect to the means on intersected standard shapes) applied on the membership functions of output parameter, *AMI*. In the proposed scheme, centroid method is used for defuzzification. Figure 2 depicts fuzzified *C*, *RLSTSS* and *AMI*.

2.3 Decision Making

As a final step, the shape of an unknown object need to be recognized for a particular value of *C* and *RLSTSS*. Corresponding to the specific input parameters, possible fuzzy rules are fired. The minimum fuzzy membership value is extracted from each of the fired fuzzy rules. Each of these membership values are used for defuzzification, where they provide a corresponding area in the output membership function *AMI*. As a next step, the equivalent centroid position is obtained by moment-area method. In this proposed approach, the similarity between an unknown object's shape and predefined standard shapes is expressed in a percentage form.

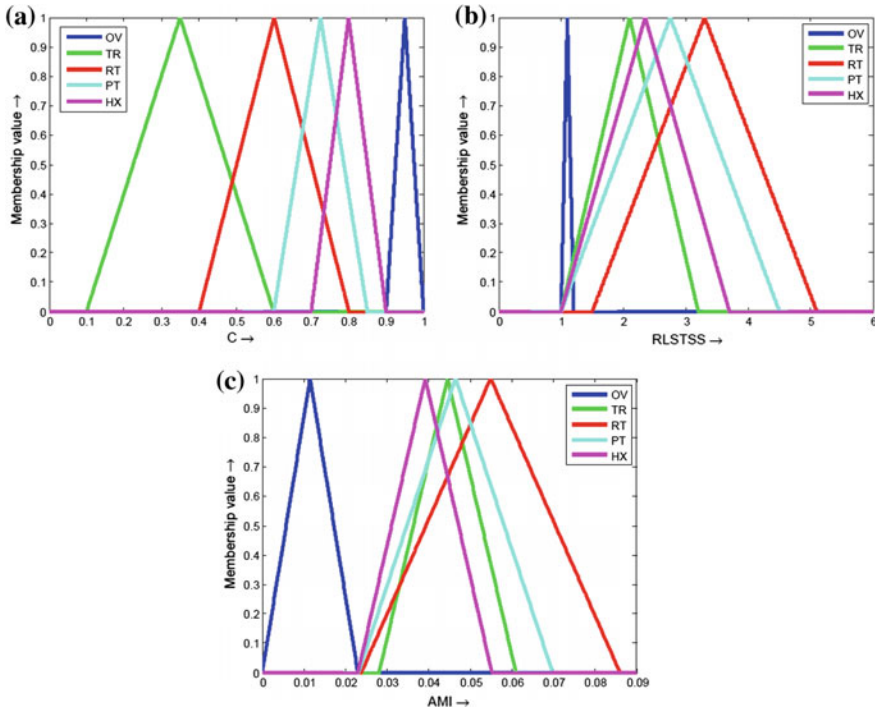


Fig. 2 Fuzzification of a C , b $RLSTSS$ and c AMI

3 Simulation Results, Comparison and Discussion

A set of 100 different forms each of OV, TR, RT, PT and HX are taken for generating the range of C , $RLSTSS$ and AMI . Furthermore, these values are used for determining the range of triangular membership functions of fuzzy inputs and output variables. A set of 10 different sizes (from a database of 100 images) of triangular shaped object is depicted in Fig. 3. The corresponding values of C , $RLSTSS$ and AMI are tabulated in Table 1. The proposed fuzzy logic-based shape recognition technique has been tested on more than 500 images. A few sample test results are given in Table 2. From Table 2, it is clear that similarity measure (in %) of unknown objects with standard OV, TR, RT, PT and HX using proposed method



Fig. 3 A set of 10 triangles of different sizes from a database of 100 images for calculating C , $RLSTSS$ and AMI

Table 1 Shape parameters for triangular shape

	TR1	TR2	TR3	TR4	TR5	TR6	TR7	TR8	TR9	TR10
<i>C</i>	0.558	0.559	0.507	0.520	0.560	0.554	0.547	0.370	0.573	0.533
<i>RLSTSS</i>	1.016	1.157	1.536	1.429	1.279	1.085	1.086	3.119	1.011	1.678
<i>AMI</i>	0.028	0.028	0.031	0.030	0.029	0.028	0.028	0.061	0.028	0.033

Table 2 Shape similarity (in %) for unknown inputs of the proposed method

<i>C</i>	<i>RLSTSS</i>	Similarity measure
0.903	1.1	OV = 99.13, TR = 0, RT = 0, PT = 0, HX = 0
0.709	1.938	OV = 0, TR = 54.711, RT = 90.675, PT = 76.231, HX = 20.0
0.836	1.057	OV = 0, TR = 80.851, RT = 56.591, PT = 78.372, HX = 86.250
0.370	3.1190	OV = 0, TR = 99.088, RT = 66.237, PT = 91.220, HX = 67.500
0.790	1.0890	OV = 0, TR = 94.224, RT = 69.774, PT = 95.931, HX = 60.625

Table 3 Shape recognition accuracy (in %) of the proposed method

OV: 98.18	TR: 85.45	RT: 97.27	PT: 94.54	HX: 81.81
-----------	-----------	-----------	-----------	-----------

Table 4 Comparison results: overall shape recognition rate (in %)

Fonseca et al. (2000)	Moomivand et al. (2011)	Proposed
84.52	90.86	91.45

is satisfactory. Shape-wise recognition accuracy of the proposed technique is tabulated in Table 3. Moreover, the proposed method is compared with two existing methods as mentioned in Table 4. From Table 4, it is cleared that proposed scheme shows better results in shape identification as compared to existing techniques.

4 Conclusion

In this paper, we have reported a fuzzy logic based automatic shape recognition technique. From the different shapes recognized using the proposed method, it is observed that the shape recognition is performed to a 91.45 % certainty which is better compare to existing techniques. Shape recognition accuracy towards triangular and hexagonal shaped objects need to be improved. Proposed approach can be extended towards the recognition of real-world objects, treated as a future work.

References

- Banerjee, J., Ray, R., & Shome, S. N. (2012). A novel approach for freeman chain coding with prior modification using cubic interpolation. In *IEEE International Conference on Computational Intelligence & Computing Research (ICIC)* (pp. 1–4).
- Banerjee, J., Ray, R., Vadali, S. R. K., Layek, R. K., & Shome, S. N. (2013). Shape recognition based on shape-signature identification and condensibility: Application to underwater imagery. In *National Conference on Computer Vision, Pattern Recognition, Image Processing and Graphics (NCVPRIPG)* (1–4).
- Belongie, S., Malik, J., & Puzicha, J. (2010). Shape matching and object recognition using shape contexts. *IEEE Transactions on Pattern Analysis and Machine Intelligence*, 24(4), 509–522.
- Chang, J. Y., & Cho, C. W. (2002). Scene analysis system using a combined fuzzy logic-based technique. *Journal of the Chinese Institute of Engineers*, 25(3), 297–307.
- Fonseca, M. J., & Jorge, J. A. (2000). Using fuzzy logic to recognize geometric shapes interactively. *FUZZ-IEEE*, 1, 291–296.
- Gonzalez, R. C., Woods, R. E., & Eddins, S. L. (2009). *Digital image processing using MATLAB* (2nd ed.). Pearson Education.
- Ku, Z. K., Ng, C. F., & Khor, S. W. (2010). Shape based recognition and classification for common objects- an application for video scene analysis. In *2nd International Conference on Computer Engineering and Technology (ICCET)* (vol. 3, pp. 13–16).
- Mathur, S., & Ahlawat, A. (2008). *Application of fuzzy logic on image edge detection* (pp. 24–28). Institute of Information Theories and Applications.
- Moomivand, E., & Abolfazli, E. (2011). A modified structural method for shape recognition. *IEEE Symposium on Industrial Electronics and Applications (ISIEA)*, 1, 332–336.
- Nedeljkovic, I. (2008). Image classification based on fuzzy logic. *The International Archives of the Photogrammetry, Remote Sensing and Spatial Information Sciences*, 34, 24–28.
- Shih, F. Y., & Mitchell, O. R. (1998a). Automated fast recognition and location of arbitrarily shaped objects by image morphology. In *Conference on Computer Vision and Pattern Recognition (CVPR)* (pp. 774–779).
- Shih, F. Y., & Mitchell, O. R. (1998b). Industrial parts recognition and inspection by image morphology. In *IEEE International Conference on Robotics and Automation* (pp. 1764–1766).
- Singh, G., Jati, A., Khasnobish A., Bhattacharyya, S., Konar, A., Tibarewala, D. N., et al. (2012). Object shape recognition from tactile images using regional descriptors. In *Fourth World Congress on Nature and Biologically Inspired Computing (NaBIC)* (pp. 53–38).
- Smith, D., & Lu, G. (2004). Review of shape representation and description techniques. *Journal of the Pattern Recognition Society*, 37, 1–19.
- Tyan, C., & Wang, P. P. (1993). Image processing-enhancement, filtering and edge detection using the fuzzy logic approach. *FUZZ-IEEE*, 600–605.

Need of Agriculture Hand Tool Design Using Quality and Ergonomics Principles

Rahul Jain, M.L. Meena and G.S. Dangayach

Abstract Ergonomics contributes as a whole to formulate strategies and support the objectives of different functions for field work. To develop hand tools for farmers, needs and requirements of farmers must be brought to attention. By engaging the QFD (Quality Function Deployment) technique, the requirements are methodically checked with the product features, which can benefit to advance the quality of implements. Microscopic literature found in agriculture that is using QFD for designing the hand tools. In this study, the practice of QFD for developing the hand tools in the agriculture and various areas other than agriculture by using concepts of ergonomics principles were investigated. The findings of these works of literature will use for preparing a framework or strategy for designing the hand tools used by farmers in the agricultural sector of India.

Keywords Agriculture · Ergonomics · Hand tools · QFD · Quality

1 Introduction

The discipline of ergonomics plus the field of quality have a history as two distinct restraints. In a quicker contrast, numerous connections become visible, yet many changes distinguished. Mutually areas are comparatively new and mostly of a

R. Jain (✉) · M.L. Meena · G.S. Dangayach
Mechanical Engineering Department, Malaviya National Institute of Technology,
Jaipur, India
e-mail: rjmahesh207@gmail.com

M.L. Meena
e-mail: mlmeena.mech@mnit.ac.in

G.S. Dangayach
e-mail: gsdangayach.mech@mnit.ac.in

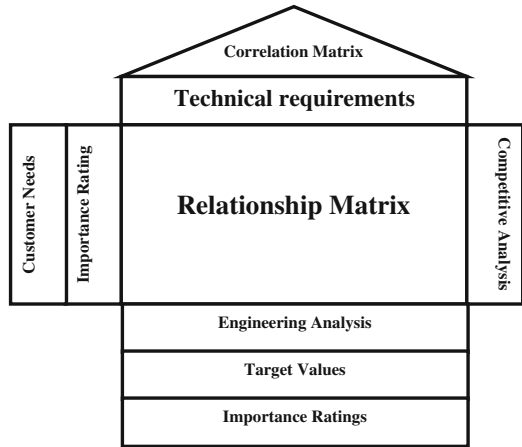
virtual environment. The dominating paradigms have undergone changes in recent years. Subsequently ergonomics and operational setting issues were frequently at the center of the conflict for bargaining between unions and organization, usually alleged before belief that ergonomic improvements are expensive, and the benefits was uncertain. Ergonomics recognized by comprehensive information in various places such as technological innovation, structure, sociology and thinking of the ergonomist extremely able of determining the customer needs extensively. Experience and knowledge in using quality techniques would probably further increase the proficiency of the ergonomist.

The basic aim of the Quality plus ergonomics is to fulfill the requirements of the user. A creation built by adapting the ergonomics and quality concepts gives a high-quality ergonomic product that can quickly deal with high-end human capabilities and boundaries. In this area of product development (Marsot and Claudon 2004; Marsot 2005; Nagamachi 1995, 2002) various methods like QFD (Keith and Derek 1994; Haapalainen et al. 2000; Leppanen et al. 2000; Marsot 2005; Tsai et al. 2008) and Kansei Engineering (Chen et al. 2015; Hartono 2012; Huang et al. 2011; Ishihara 1997; Nagamachi 1995, 2002) have been used mainly by researchers for developing the new product design, and also concluded QFD and Kansei Engineering as the best approach for simplifying and finding the best target characteristics for design. These both methods have friendly and systematically approach and could be having compatibility with ergonomics principles for giving advantageous results. The QFD was a famous and a methodical approach that centered on the impression of adjusting knowledge to users. Kansei Engineering was a technique to transfer a user's unclear appearance of product into detailed plan (Nagamachi 1995; Ishihara et al. 1997). Kansei Engineering and QFD give good results for manufacturing, and the only QFD is suitable for almost all areas. So QFD is a right approach for broad applicability and better outcomes.

QFD is basic approach to improving the quality of product by using the inter-relation matrix (HOQ) which uses these methods during implementation (Shown in Fig. 1):

- User's requirements (What's)
- Design Parameters (How's)
- Correlations between What's and How's
- Importance rating of user requirements
- Correlation between design parameters
- Competitive analysis for user needs
- Engineering analysis for design needs
- Target value for identification of importance of design parameters and technical difficulties
- Importance ratings

Fig. 1 House of quality (HOQ)



2 Literature Review

The literature contains readings displaying a strong association between, on the first hand, poor working conditions and, on the other, effects on human performance from the various awkward postures. This study analyses the works matching the different fields of ergonomics plus quality in different areas, comprising working conditions with awkward position in the long hour of working. To improve the conditions of work and to reduce the fatigue during the work in the agriculture field, this is crucial to find the relationships between the ergonomics and various quality and productivity factors. This analysis will be done by examining the different works of literature from agriculture as well as other sectors (Haapalainen et al. 2000; Meena and Dangayach 2012; Meena et al. 2013, 2014a, 2014b; Jain et al. (in press)).

Table 1 shows the tools improved by using the various quality and ergonomics principles.

Table 1 Investigation studies on various tools

Reference	Tool for investigation	Tool of application
Bergquist and Abeyssekera (1996)	Safety shoes	QFD
Ishihara et al. (1997)	Shoes	Kansei Engineering
Leppanen et al. (2000)	Pruning tool	QFD
Haapalainen et al. (2000)	Hand tool	QFD
Marsot (2005)	Knife	QFD
Tsai et al. (2008)	Mobile assisting devices	QFD
Kuijt-Evers et al. (2009)	Hand tool	QFD
Chen et al. (2015)	Home delivery	Kansei Engineering

From Table 1, it can be said that QFD has benefited subsequently from the late nineties through the perseverance of building the improvement product procedure more efficient. The American Supplier Institute describes QFD as follows: A system that converts customer needs into the company's requirements in every step of the growth procedure viz. marketing, growth, manufacturing and sales and services. QFD used as a means of new items creating and to alter current items.

In the application domain, a significant similarity between ergonomics and quality is found in the place of product style. However, quality inadequacies in production are in many cases due to the short style of work, office buildings, and atmosphere. Regardless of this, quality hardly deals with these aspects; neither does it apply such ergonomic knowledge, except certain factors of inspiration and other issues in the place of the psychosocial environment.

Table 2 summarizes the various user requirements considered by the researchers for finding the what's in HOQ (House of quality). These user needs have been developed by using the user opinions and literature available for the research in the same field.

Table 2 shows the various types of user characteristics used by the different researchers for which user give some numerical values that indicate the importance of those user requirements. So this will help to prioritize the various user needs (What's in the HOQ). To identify the design parameters (How's in the HOQ), a brief literature survey of the tool investigated. Haapalainen et al. (2000) identified following ten characteristics after discussing with the professionals for pruning hand tool: Material selection, Force output, Grip span, Operating instructions, Environmental resistance, Stiff, Good locking mechanism, Shapenable, Suitable length and Balanced tool. After applying all the steps of QFD for investigation of pruning hand tool, Haapalainen et al. (2000) concluded the three design parameters: Material selection, Force output and Grip span as desirable needs. Figure 2 shows the various pruning tool used in the study of Haapalainen et al. (2000). In this study (Haapalainen et al. 2000) five type of pruning tool has been evaluated in which results suggested that success of pair B is high due to the higher technical details assessed in the QFD process.

Table 2 User requirements for need assessment

Reference	User requirements
Bergquist and Abeysekera (1996)	Mobility, thermal comfort, good appearance, ease to use, fit weight, durability, adjustability, anti-slip, and protection from work hazards
Haapalainen et al. (2000)	Handle characteristics and properties, material selection, durability, fit, easy to carry, maintenance, comfort, functional, good exposure to weather, weight
Marsot (2005)	Handle characteristics and properties, ease of recycling, and Color
Tasi et al. (2008)	Usability, comfort, safety, expandable, maintenance, and price
Kuijt-Evers et al. (2009)	Fit, functionality, handle characteristics and properties, professional look

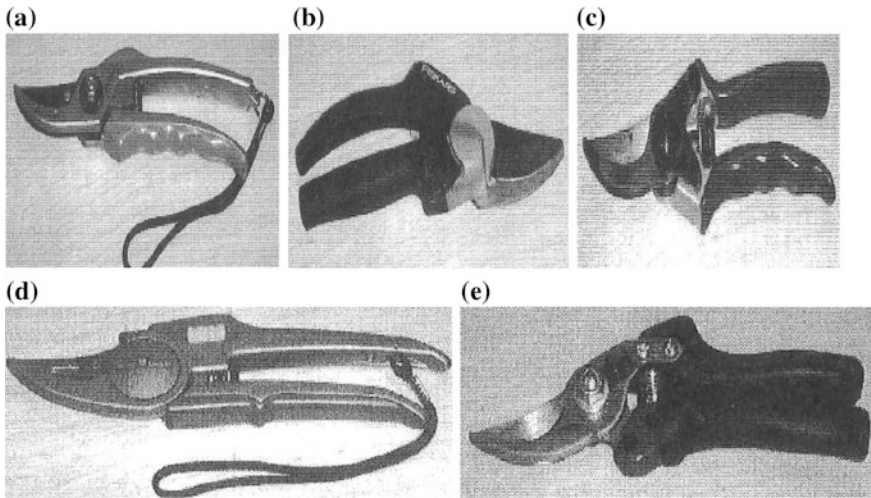


Fig. 2 Pruning tools used in Haapalainen et al. (2000). **a** Pruning shear pair A: Gardena 343. **b** Pruning shear pair B: Fiskars 9654 Pro. **c** Pruning shear pair C: Felco 11. **d** Pruning shear pair D: Wolf RR26. **e** Pruning shear pair E: Sandvik P2-20

3 Framework Development

Several techniques used for service rely on a cooperation between the developer and the customer. Concentrating on the customer, i.e. the individual, is what these techniques do have in typical.

According to these two studies (Marsot and Claudon 2004; Marsot 2005), current approaches for classifying the user requirements are sufficient. However, it needs more evaluation for this purpose; it needs a comprehensive implementation of the QFD (Haapalainen et al. 2000).

By using the QFD technique, the customer needs are planned out and incorporated into the complete procedure. The QFD technique would, therefore, be an appropriate supplement to ergonomic techniques where the aim is to recognize the individual needs and specifications. Figure 3 shows the framework to utilized for the ergonomically development of agriculture hand tools. This framework developed from the past study experienced by the various researchers (Haapalainen et al. 2000; Marsot and Claudon 2004; Marsot 2005). They used QFD tool and concluded the success of the hand tool design by using the concepts of QFD in their research.

After reading the various literature and field survey below framework will be developed for the development of hand tool that is showing the necessary steps to follow during development.

Step 1 Hand Tool design: First selection of hand tool for design has been done from the various field surveys and literature.

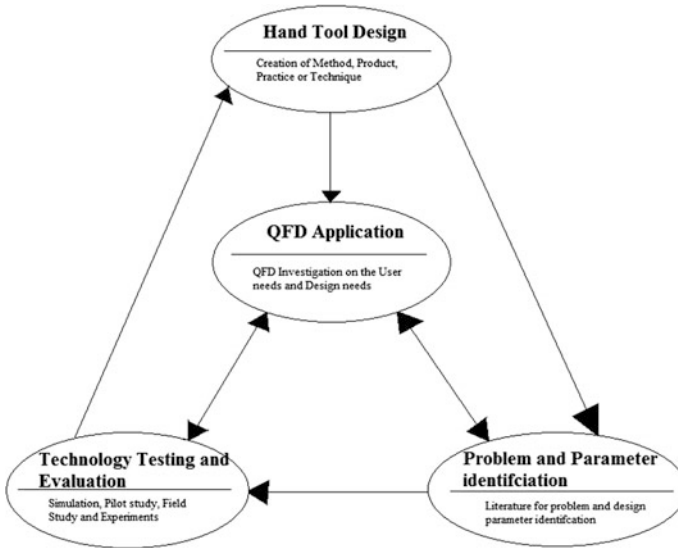


Fig. 3 Framework for hand tool design

- Step 2 Problem and parameter identification: In this step main area of problem and their shortcomings from the previous research has been imported. These literatures also provide some solutions and their impact on the various parameter like force, torque etc. for the same problem. User and academicians also give proper input for the problem solution which is also taken place during the first step.
- Step 3 QFD Application: Applying the QFD approach for identified user and design requirements. Steps 1 and 2 also give us customer needs and technical requirements which are essential requirements for QFD process as shown in Fig. 1.
- Step 4 Technology Testing and Evaluation: Target values and importance ratings form the QFD gives us a strategy for design the hand tool. The newly designed tool used further for pilot/field test. Results from the pilot/field test will be utilized for the development of the standards for the hand tool design that will be implemented for further real-time applications.

4 Discussion and Conclusion

The QFD research gives some useful details on what item qualities are essential when it comes to achieving the requirements of the user. The QFD technique is useful since it encourages a methodical way of considering where all the customer

requirements put on all the item features. Further, the item features are in comparison to recognize qualities with an inverse connection.

It was felt that there is no such study has been found which has used such quality concepts for the agriculture tool development. For better investigation of Indian agriculture hand tools like the sickle (Darati), long and short handled hoes (Khurpi), spade (Phora), plough. There is need of investigation of the quality of working life of the agriculture farmers for finding the factors that will increase the comfort and discomfort in using the hand tools.

References

- Bergquist, K., & Abeyssekera, J. (1996). Quality function deployment (QFD)—a means for developing usable products. *International Journal of Industrial Ergonomics*, 18(4), 269–275.
- Chen, M., Hsu, C., Chang, K., & Chou, M. (2015). Applying Kansei Engineering to design logistics services—a case of home delivery service. *International Journal of Industrial Ergonomics*, 48, 46–59.
- Haapalainen, M., Kivisto-Rahnastom, J., & Mattila, M. (2000). Ergonomic design of non-powered hand tools: an application of quality function deployment (QFD). *Occupational Ergonomics*, 2(3), 179–189.
- Hartono, M. (2012). Incorporating service quality tools into Kansei Engineering in services: a case study of Indonesian tourists. *Procedia Economics & Finance*, 4, 201–212.
- Huang, M. S., Tsai, H. C., & Huang, T. H. (2011). Applying Kansei engineering to industrial machinery trade show booth design. *International Journal of Industrial Ergonomics*, 41(1), 72–78.
- Ishihara, S., Ishihara, K., Nagamachi, M., & Matsubara, Y. (1997). An analysis of Kansei structure on shoes using self-organizing neural networks. *International Journal of Industrial Ergonomics*, 19(2), 93–104.
- Jain, R., Gupta S., Meena, M. L., & Dangayach, G. S. (in press) Optimization of labour productivity using work measurement techniques. *International Journal of Productivity and Quality Management*.
- Keith, N., & Derek, F. (1994). Customer-driven designs through QFD. *World Class Design to Manufacture*, 1(6), 12–19.
- Kuijt-Evers, L. F. M., Morel, K. P. N., Eikelenberg, N. L. W., & Vink, P. (2009). Application of the QFD as a design approach to ensure comfort in using hand tools: can the design team complete the house of quality appropriately? *Applied Ergonomics*, 40(3), 519–526.
- Leppanen, M., Mattila, M., & Kivisto-Rahnastom, J. (2000). Designing the ergonomic properties of pruning shears using quality function deployment (QFD). *Proceedings of the Human Factors and Ergonomics Society Annual Meeting*, 44(22), 647–650.
- Marsot, J. (2005). QFD: a methodological tool for integration of ergonomics at the design stage. *Applied Ergonomics*, 36(2), 185–192.
- Marsot, J., & Claudon, L. (2004). Design and ergonomics methods for integrating ergonomics at hand tool design stage. *International Journal of Occupational Safety and Ergonomics*, 10(1), 13–23.
- Meena, M. L., & Dangayach, G. S. (2012). Analysis of employee satisfaction in banking sector. *International Journal of Humanities and Applied Sciences*, 1(2), 78–81.
- Meena, M. L., Dangayach, G. S., & Bhardwaj, A. (2013). Measuring anthropometric data for designing hand tools in handicraft industries. *International Journal of Process Management and Benchmarking*, 3(3), 334–351.

- Meena, M. L., Dangayach, G. S., & Bhardwaj, A. (2014a). Measuring quality of work life among workers in handicraft industries in Jaipur. *International Journal of Industrial and Systems Engineering*, 17(3), 376–390.
- Meena, M. L., Dangayach, G. S., & Bhardwaj, A. (2014b). Investigating ergonomic issues among workers in hand block textile printing industries. *International Journal Business and Systems Research*, 8(4), 392–401.
- Nagamachi, M. (1995). Kansei engineering: a new ergonomic consumer-oriented technology for product development. *International Journal of Industrial Ergonomics*, 15(1), 3–11.
- Nagamachi, M. (2002). Kansei engineering as a powerful consumer-oriented technology for product development. *Applied Ergonomics*, 33(3), 289–294.
- Tsai, K., Yeh, C., Lo, H., Li, C., Cheng, C., & Chang, G. (2008). Application of quality function deployment in design of mobile assistive devices. *Journal of Medical and Biological Engineering*, 28(2), 87–93.

Inverse Dynamics and Feet-Terrain Collision Model for Optimal Distribution of the Contact Forces During Crab Motion of a Hexapod Robot

Abhijit Mahapatra, Shibendu Shekhar Roy
and Dilip Kumar Pratihar

Abstract The present study deals with the kinematics, dynamics and feet-ground contact modeling of a hexapedal robotic system. Feet-ground interaction generates contact forces, which play a very important role for locomotion on varying terrains. In this study, the constrained inverse dynamical model is formulated as a coupled dynamics problem using Newton-Euler approach with implicit constraints in Cartesian coordinates. The contact force distribution in the feet during interaction with the terrain is considered to be a constrained optimization problem. For a more realistic locomotion analysis, impact of feet-tip with the terrain is considered, which is assumed to be governed by a compliant normal contact force model. The paper also investigates the optimal feet forces' distributions under body forces, total power consumption etc. without any external disturbance during the robot's locomotion with wave-crab gait (duty factor = $\frac{1}{2}$).

Keywords Hexapod robot · Inverse dynamics · Wave-Crab gait · Feet-Terrain interaction · Impact force · Power consumption

A. Mahapatra
Virtual Prototyping & Immersive Visualization Lab, CSIR-Central Mechanical
Engineering Research Institute, Durgapur 713209, India

A. Mahapatra · S.S. Roy (✉)
Department of Mechanical Engineering, National Institute of Technology,
Durgapur 713209, India
e-mail: ssroy99@yahoo.com

D.K. Pratihar
Department of Mechanical Engineering, Indian Institute of Technology,
Kharagpur 721302, India

© Springer India 2016
D.K. Mandal and C.S. Syan (eds.), *CAD/CAM, Robotics and Factories
of the Future*, Lecture Notes in Mechanical Engineering,
DOI 10.1007/978-81-322-2740-3_10

1 Introduction

The generation of contact forces due to interaction of the feet-tip with the terrain is a complex phenomenon. They are highly nonlinear, their solution is always expensive in terms of time and resources. Several attempts were made by various investigators to develop contact models for legged robots. But, the models were simplified and did not analyze the actual contact under each foot. Moreover, the effect of momentary impulse (impact) with the terrain was ignored. For a realistic situation, the effect of such impulse has to be taken into account in the models during the robot's locomotion. The force-deformation equation is augmented with damping term in the models to reflect dissipation in the contact area. This leads to effective modelling of the contact area as a spring damper system. A few researchers (Gilardi and Sharf 2002; Brach 2007) studied explicitly the normal contact force models which are functions of local indentation along normal and its rate. Some other researchers (Goldsmith 2001; Marhefka and Orin 1999) modeled the contact as linear spring-damper with one spring. The force contact model is simple with discontinuity at the initial time of impact due to the form of the damping term and sticking effect at the time of separation, holding the objects together. A few others (Bibalan and Featherstone 2009) studied the contact phenomenon with linear spring-damper considering two springs which is a bit improved model, since the contact force is continuous. But, the contact phenomenon can be best described with a non-linear spring damper model like the one developed by Hunt and Crossley (1975). The model is generally called the compliant normal contact force model (Marhefka and Orin 1999; Lankarani and Nikravesh 1990; Ding et al. 2013). It has some added advantages over other models described above because it can handle impacts, no stick phenomena, evolution of the contact forces continuously with time etc. For oblique impact between the feet-tip and terrain both normal and tangential components of contact forces exist; the tangential force being the dry friction force which opposes the tangential relative velocity and is termed as sliding or slip. The effects of dry friction on changes in velocity during impact can be obtained from Amontons-Coulomb law of sliding friction (Johnson 1985).

The development of such contact model algorithm is mainly based on minimization of energy consumption or minimization of the variance of foot forces or minimization of the variance of joint torques. So far, the optimization methods implemented by various researchers to obtain the feet forces and study the dynamics of the legged robots include linear programming (Kerr and Roth 1986; Cheng and Orin 1990), quadratic programming (Kar et al. 2001; Erden and Leblebicioglu 2007), pseudo inverse (Roy and Pratihar 2011) or additional constraint equation to create a determinate set (Kumar and Waldron 1988).

Legged robots has to move along straight forward path or transverse (crab motion) or take turns or ascend and descend slopes, and others as per demand of situation during the course of locomotion. The present study concentrates on inverse dynamic analysis with feet-terrain contact modeling and energy efficiency

analysis for generating crab motions of a hexapod robot only (Kumar and Waldron 1988; Zhang and Song 1990). It is to be noted that the effect of impulsive collision at the start of support phase on energy efficiency and optimal distribution of contact forces for a coupled dynamical hexapedal robotic system has not been reported till date. An attempt has been made in the present study to address the issue. The impact based contact model implemented by MSC.ADAMS is used here, which is the Hunt-Crossley model with some modifications to calculate the compliant normal impact force. Further, it is assumed that tangential compliance of the leg tip and the terrain is negligible in the contact region (a case of no slip condition).

The paper has six sections. The preceding Sect. 2 describes the CAD model of the hexapod robot and the mathematical formulation of the inverse dynamic model. Section 3 describes the foot-terrain interaction mechanics model for a deformable foot (hard) versus hard (little deformation) terrain. Section 4 describes the optimization methodology (i.e. least square method) with the imposition of a naturalistic objective function i.e. minimization of the sum of squares of joint torques to subsequently minimize power consumption for determination of optimal foot-force distribution and joint torques. In Sect. 5, the simulated results are discussed followed by a conclusion in Sect. 6.

2 Dynamic Modeling of the Robotic System

A realistic CAD model (refer to Fig. 1) is built in CATIA V5 with specific dimensions. The essential robot model parameters are listed in Table 1. The main body-parts of the robot are made of aluminum (density: 2740 kg/m^3). The total mass of the robot without payload is estimated to be equal to 2.456 kg. Each of the legs has three motorized revolute joints with angular variables, $\theta_{i1}-\beta_{i2}-\beta_{i3}$ corresponding to local axes configuration Z-Y-Y respectively as shown in Fig. 1. Therefore, the hexapod robot can be considered as robotic system having twenty

Fig. 1 CAD model of a realistic hexapod robot

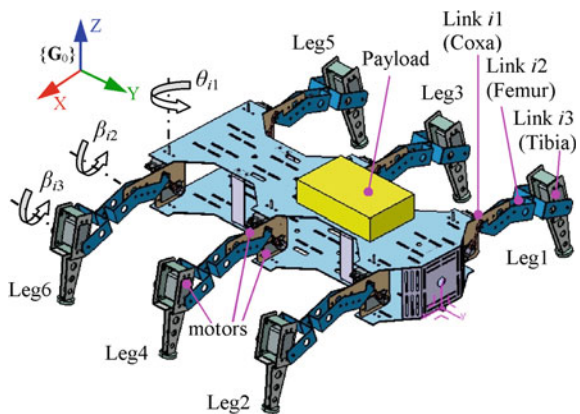


Table 1 System parameters of the robot

Robot model		Values				Locomotion			Foot-ground	
Parameters		TB	PL	Link $i1$	Link $i2$	Link $i3$	Parameters	Values	Parameters	Values
$(i = 1-6)$		0.650	4.244	0.150	0.041	0.110	DF	0.5	e	2.2
Mass (kg)		0.01665	0.009	7.1E-5	2.0 E-5	9.80E-5	Hm_{i1}	0.015 m	K	1.0e+5 N/m
Mass moment of inertia (kg-m ²)	I_{xx}	0.00252	0.003	10.8E-5	8.7 E-5	8.70E-5	Δh	0.002 m	C_{max}	10 N-s/m
	I_{yy}	0.01690	0.011	5.7E-5	10.0 E-5	2.08E-5	s_0	0.030 m	p	0.01 mm
	I_{zz}	0.495	0.150	0.085	0.120	0.100	$x_{P_0}^G$	0.005 m/s	μ_i	0.3
Length (m)										

Joint offsets: $d_{i1} = 0.008$ m, $d_{i2} = 0.018$ m; $d_{i3} = 0.02$ m; DF = Duty factor; Hm_{i1} is the maximum terrain height (on the path of swing); Δh is the swing height over and above the maximum terrain height. s_0 is the stroke of trunk body; $x_{P_0}^G$ is the maximum translational velocity of the trunk body along x; TB Trunk Body; PL Payload

four degrees of freedom (DOF), out of which six DOF corresponds to the trunk body and eighteen DOF to the legs. The system has been generalized by using orientation vector of *Bryant angles* (Hahn 2003), $\boldsymbol{\eta}_G = [\alpha_G \beta_G \theta_G]^T$ with respect to global fixed frame \mathbf{G}_0 having origin at O. The working frame of reference \mathbf{G} called the dynamic global reference is also chosen whose origin also coincides with the origin O. All the bodies in the system are assumed to be rigid.

Inverse kinematic analysis of the robotic system is carried out for a proposed three-dimensional (3D) trunk body motion, swing leg trajectory planning of the feet-tip as well as gait planning with crab motion in varying terrain to calculate the angular displacement of the various joints ($i = 1-6, j = 1-3$). The locomotion parameters are also listed in Table 1. Evaluation of the joint angles with respect to time leads to the determination of the kinematic motion parameters like velocity, acceleration, aggregate center of mass etc. The parameters are subsequently transformed from reference frame \mathbf{G} to frame \mathbf{G}_0 .

In the present problem, the objective is to determine the optimal distribution of feet-forces that must act on the system to produce a specified motion in the robot. The implicit constrained dynamic equation of the robotic system is given by the expression:

$$\mathbf{M}(\mathbf{p}^{G_0}) \cdot \dot{\mathbf{v}}^{G_0} = {}^c\mathbf{f} + \mathbf{f}(\mathbf{p}^{G_0}, \mathbf{v}^{G_0}) + \mathbf{q}_{GC}(\mathbf{p}^{G_0}, \mathbf{v}^{G_0}) \in \mathbb{R}^{114} \quad (1)$$

where $\mathbf{M}(\mathbf{p}^{G_0}) \in \mathbb{R}^{114,114}$ is the combined mass matrix of the robotic system; $\mathbf{v}^{G_0}, \dot{\mathbf{v}}^{G_0} \in \mathbb{R}^{24}$ are the velocity and acceleration vector of the system in cartesian space; ${}^c\mathbf{f} \in \mathbb{R}^{114}$ being the vector of constant reaction forces and torques of the joints associated with system coordinates; $\mathbf{f}(\mathbf{p}^{G_0}, \mathbf{v}^{G_0}) \in \mathbb{R}^{114}$ is the vector of both known and unknown applied forces and torques; $\mathbf{q}_{GC}(\mathbf{p}^{G_0}, \mathbf{v}^{G_0}) \in \mathbb{R}^{114}$ is the vector of centrifugal forces and gyroscopic terms.

The implicit constraint dynamic Eq. (1) is expressed in over complete cartesian coordinates (\mathbf{p}^{G_0}) are transformed by kinematic transformation to the joint space (Bennani and Giri 1996) in terms of generalized coordinates (\mathbf{q}) where $\mathbf{q} \in [(\mathbf{r}_{P_0O}^{G_0})^T, (\boldsymbol{\eta}_0)^T, \theta_{11}, \beta_{12}, \beta_{13}, \theta_{21}, \beta_{22}, \beta_{23}, \theta_{31}, \beta_{32}, \beta_{33}, \theta_{41}, \beta_{42}, \beta_{43}, \theta_{51}, \beta_{52}, \beta_{53}, \theta_{61}, \beta_{62}, \beta_{63}]^T \in \mathbb{R}^{24}$. Hence, the transformation of the dynamic model in the joint space is realized by considering the following relation:

$$\mathbf{D}(\mathbf{q})\dot{\mathbf{u}} + \mathbf{C}(\mathbf{q}, \dot{\mathbf{q}}) = \boldsymbol{\tau} \in \mathbb{R}^{24} \quad (2)$$

where $\mathbf{D}(\mathbf{q})$ is the coupled mass and inertia matrix of the robotic system in terms of generalized coordinates, $\boldsymbol{\tau}$ vector of ground reaction forces and coupled joint torques. Also,

$$\mathbf{D}(\mathbf{q}) = \mathbf{J}^T \mathbf{M}(\mathbf{p}^{G_0}) \mathbf{J} \in \mathbb{R}^{24 \times 24} \quad (3)$$

$$\mathbf{C}(\mathbf{q}, \dot{\mathbf{q}}) = \mathbf{J}^T \mathbf{M}(\mathbf{p}^{G_0}) \dot{\mathbf{J}} \mathbf{u} \in \mathbb{R}^{24} \quad (4)$$

$$\boldsymbol{\tau} = \mathbf{J}^T [\mathbf{f}(\mathbf{p}^{G_0}, \mathbf{v}^{G_0}) + \mathbf{q}_{GC}(\mathbf{p}^{G_0}, \mathbf{v}^{G_0})] \in \mathbb{R}^{24} \quad (5)$$

where $\mathbf{u}, \dot{\mathbf{u}} \in \mathbb{R}^{24}$ are the velocity and acceleration vector of the system in joint space; $\mathbf{J} \in \mathbb{R}^{114,24}$ is the jacobian matrix of the system in terms of generalized coordinates (\mathbf{q}) related to ground reaction forces and coupled joint torques. Twenty four number of equations are obtained in terms of ground reaction forces and coupled joint torques by substituting the necessary input values in (2).

3 Optimization Criteria for Optimal Distribution of Joint Torques

The solution to the problem is to be obtained by optimization corresponding to minimization of the sum of the squares of joint torques. It is considered as the objective function and is expressed by,

$$\text{Minimize } (\mathbf{M}^T \hat{\mathbf{H}} \mathbf{M} / 2) \quad (6)$$

subject to (a) inequality and (b) equality constraints. $\hat{\mathbf{H}}$ is the positive definite weight matrix. \mathbf{M} is the overall vector of joint torques denoted by $[\mathbf{M}_1 \mathbf{M}_2 \mathbf{M}_3 \mathbf{M}_4 \mathbf{M}_5 \mathbf{M}_6]^T$ where \mathbf{M}_i is the vector of actuator torques of leg i denoted by $[M_{i1} M_{i2} M_{i3}]^T$, $i = 1-6$. For details of the constraints refer (Mahapatra et al. 2015).

4 Feet-Terrain Interaction Modeling

To simplify the dynamic analysis, it is assumed that both the foot and terrain are rigid except for an infinitesimally small deformable region that surrounds the initial contact point. The contact point is assumed to be governed by a visco-elastic model. For oblique impact between the feet-tip and terrain, the impact force ${}^m\mathbf{F}_i$ (refer Fig. 2) with respect to \mathbf{G} is composed of two components both in normal and tangential direction, i.e., (i) compliant normal impact force ${}^m\mathbf{F}_{iz}$ and (ii) compliant horizontal impact force (resultant) ${}^m\mathbf{F}_{iy}$. In the present problem, the impact-based compliant normal contact force model implemented by MSC.ADAMS is used, which is the nothing but the Hunt-Crossley model with some modifications. The compliant normal impact force ${}^m\mathbf{F}_{iz}$ for a deformable foot (hard) and hard (little deformation) terrain is governed by a impact function that depends mainly on the foot's deformation, its velocity, contact stiffness, damping etc. Further, it is assumed that tangential compliance of the leg tip and the terrain is negligible in the contact region, which is a case of no slip condition.

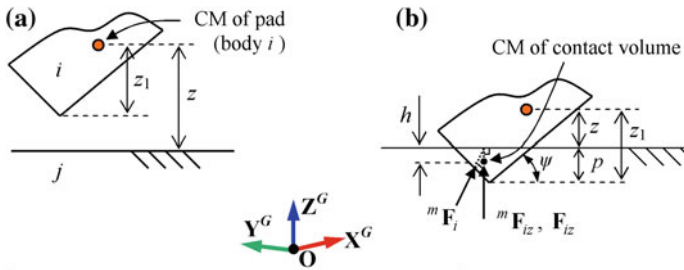


Fig. 2 Foot-terrain model **a** before impact, **b** after impact (h is the center of mass of the pad in contact with the ground; F_{iz} is the normal foot reaction force)

Normal impact force,

$${}^m\mathbf{F}_{iz} = \begin{cases} 0 & z > z_1 \\ K(z_1 - z)^e - C_{\max} \cdot \dot{z} \cdot STEP(z, z_1 - p, 1, z_1, 0) & z \leq z_1 \end{cases} \quad (7)$$

and

$$STEP(z, z_1 - p, 1, z_1, 0) \equiv (1 - \bar{a} \cdot \Delta_z^2(3 - 2\Delta_z)) \quad (8)$$

where $\bar{a} = 1 - 0 = 1$; $\Delta_z = (z - z_1 + p)/p$; z is the distance function, z_1 is the trigger distance; \dot{z} is the derivative of z to impact, e is the force exponent (mostly material property, $e > 1$ for non-linear spring); K is contact stiffness which is based on both material properties (Young's Modulus and Poisson's Ratio) and geometrical properties (radius of curvature); C_{\max} is the maximum damping; p is the boundary penetration at which full damping is applied (reasonable, $p < z_1$).

It can be seen that when $z \leq z_1$, the impact function activates, i.e., when the distance between the two objects is smaller than the free length of z (refer to Fig. 2). Subsequently, the force becomes non-zero and consists of two parts: an exponential spring force and a damping force that follows a step function as mentioned above. It should be noted that both forces are strictly positive since the calculated normal force oppose the compression that occurs during penetration.

5 Case Study: Robot's Locomotion on Flat Terrain with Wave-Crab Gait (DF = 1/2)

A case study is carried out to simulate the walking robot with wave-crab gait (DF = 1/2) on a flat terrain in order to determine the efficacy of the model. The kinematic analysis of the hexapod robot is carried out followed by dynamic analysis. The robot moves in transverse direction from left to right with a positive crab

angle (θ_c) of 80° . The translational velocity components of the trunk body with respect to global frame G are assumed to follow the relationship:

$$\dot{\mathbf{r}}_{P_0O}^G = (\dot{x}_{P_0O}^G, \dot{y}_{P_0O}^G \cdot \cot \theta_c, 0)^T \quad (9)$$

At time $t = 0$, the position and orientation of P_0 with respect to global frame G are given by $\mathbf{p}_0^G = \{0, 0.45, 0.15, 0, 0, 0\}^T$. All the initial velocity, acceleration components (both translational and angular) are zero. The initial geometrical configuration of the robot corresponds to $\boldsymbol{\eta}_G = (0, 0, 0)^T$, $\theta_{i1} = \pm(90^\circ - \theta_c)$, $\beta_{i2} = \pm 16^\circ$, $\beta_{i3} = \pm 69^\circ$ (for $i = 1-6$). In addition to the above, other relevant locomotion parameters are obtained from the Table 1.

The simulations are run for three duty cycles $n = 3$, and time step $h = 0.1$ s in a commercially available compiler MATLAB. The relevant motion parameters of the trunk body and leg tip obtained from kinematic analysis are provided as inputs to the inverse dynamic analysis code. The optimization problem formulation is based on quadratic programming (interior-point-convex quadprog algorithm) corresponding to the objective function, minimization of the sum of the squares of the joint torques. The torque limits of the motors are ± 6 nm. The computed results of the optimal force distribution are shown in Fig. 3 over three gait cycles with total cycle time 12.4 s. The normal feet-force component F_{iz} of all the six legs of the hexapod are plotted against time at an interval of $h = 0.1$ s, as shown in Fig. 3. Since in a wave-crab tripod gait the DF is equal to $1/2$, the support and swing phase times are kept equal for all the legs following a sequence: (1) legs 1-4-5 in support phase, legs 2-3-6 in swing phase; (2) legs 2-3-6 in support phase, legs 1-4-5 in swing phase (refer to Fig. 1 for the leg numbering sequence).

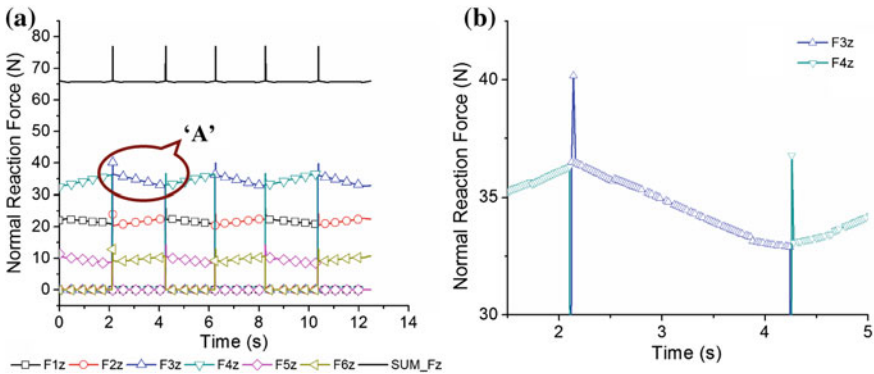


Fig. 3 Feet-force distribution in the legs with respect to frame G_0 **a** normal reaction forces, **b** close view of 'A' showing normal impact forces (spikes) for leg 3 and 4 during feet-terrain interaction

From observations of the feet forces, as shown in the graph in Fig. 3a, the normal force patterns on the legs 1-2, 3-4 and 5-6 form a wave like pattern. Moreover, the normal forces in legs 1-3-5 have a descending trend while those in legs 2-4-6 have an ascending trend. It happens so, due to the transverse motion of the trunk body from left to right. In other words, as the trunk body moves along the transverse direction, the entire center of gravity of the hexapod also moves in that direction. Hence, during support phase the feet forces on the legs 1-3-5 (odd numbered legs) will decrease, while those on the legs 2-4-6 (even numbered legs) will increase with time till the start of swing phase. When the legs are lifted during swing phase, the forces on leg tips are zero and denoted by straight line. Again, from a close view of the graph as shown in Fig. 3b, one can infer that when the leg tip collides with the terrain (start of support phase), a momentary impulsive force is generated. Another observation is that the summation of all the foot forces along z-direction with respect to G_0 balances the weight of the hexapod (65.7 N) at any instant of time (Fig. 3a).

Figure 4 shows that for leg 1, the joint torques of joints 2 and 3 in support phase take significant values, while in swing phase are close to zero. Also, the joint torque values of joint 1 of leg 1 are very small since the crab angle (with respect to joint 1) is constant and theoretically it has zero angular velocity. It is also observed that the joint 2 experiences maximum torque at any instant of time. Further, the effect of the impulsive force can be well observed in the joints of the legs as well as the total power consumption of the robot. There is momentary change (increase or decrease) in the value of joint torques and power consumption. The variation of instantaneous power (P_{in}) consumption throughout a locomotive cycle of the hexapod is as shown in Fig. 5. The highest peak arises at the time, when the swing and support legs change stance.

Fig. 4 Distribution of joint torques in leg 1

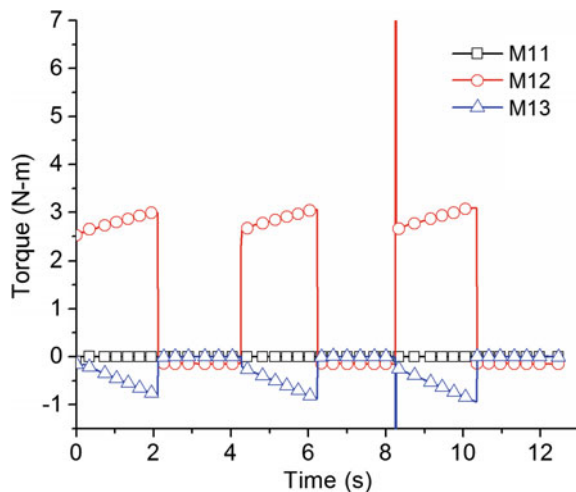
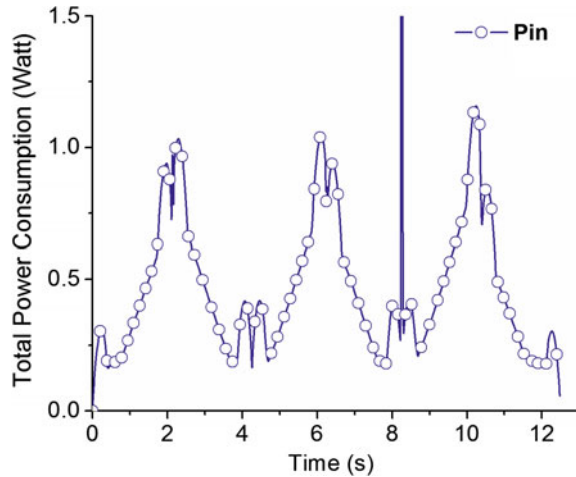


Fig. 5 Variation of total power consumption by the joints of all the legs



6 Conclusion

More realistic foot-terrain interaction mechanics are taken into account in the inverse dynamic model of the coupled robotic system for locomotion on flat terrain with wave-crab gait. The effect of impact force at the time of leg strike on the ground is established without any slippage or sliding of the feet-tip with respect to terrain. Optimal feet-force distributions in the legs, corresponding to minimization of the sum of the squares of joint torque are computed using quadratic programming. Momentary peak is observed in the force versus time plot, which depicts the impulsive collision at the instant leg tip strikes the ground. Significant changes in the torque and overall power consumption are also observed during collision. Future study in the area will focus on the effect of both impact and slip on energy efficiency with different gait patterns and walking speeds. The real time implementation of the model in robot control will also be addressed in the future scope of work.

References

- Bennani, M., & Giri, F. (1996). Dynamic modelling of a four-legged robot. *Journal of Intelligent and Robotic Systems*, 17(4), 419–428.
- Bibalan, P. T., & Featherstone, R. (2009). A study of soft contact models in simulink. In *Proceedings of the Australasian Conference on Robotics and Automation (ACRA)*. December 2–4, 2009, Sydney, Australia.
- Brach, R. (2007). Mechanical impact dynamics: rigid body collisions. Brach Engineering, LLC.
- Cheng, F. T., & Orin, D. E. (1990). Efficient algorithm for optimal force distribution the Compact-dual LP method. *IEEE Transactions on Robotics and Automation*, 6(2), 178–187.

- Ding, L., Gao, H., Deng, Z., Song, J., Liu, Y., Liu, G., & Iagnemma, K. (2013). Foot–terrain interaction mechanics for legged robots: Modeling and experimental validation. *International Journal of Robotics Research*, 32(13), 1585–1606.
- Erden, M. S., & Leblebicioglu, K. (2007). Torque distribution in a six-legged robot. *IEEE Transactions on Robotics*, 23(1), 179–186.
- Gilardi, G., & Sharf, I. (2002). Literature survey of contact dynamics modelling. *Mechanism and Machine Theory*, 37(10), 1213–1239.
- Goldsmith, W. (2001). *Impact: The theory and physical behaviour of colliding solids*. Courier Dover Publications.
- Hahn, H. (2003). *Rigid body dynamics of mechanisms 2* (1st ed.). Berlin: Springer.
- Hunt, K. H., & Crossley, F. R. E. (1975). Coefficient of restitution interpreted as damping in vibroimpact. *ASME Journal of Applied Mechanics*, 42(2), 440–445.
- Johnson, K. L. (1985). *Contact mechanics*. Cambridge University Press. ISBN: 978-0521347969.
- Kar, D. C., Issac, K. K., & Jayarajan, K. (2001). Minimum energy force distribution for a walking robot. *Journal of Robotic Systems*, 18(2), 47–54.
- Kerr, J., & Roth, B. (1986). Analysis of multifingered hands. *International Journal of Robotics Research*, 4(4), 3–17.
- Kumar, V., & Waldron, K. J. (1988). Gait analysis for walking machines for omnidirectional locomotion on uneven terrain. In A. Morecki, G. bianchi & K. Kectzior (Eds.), *Proceedings of 7th CISM-IFTOMM Symposium on Theory and Practice of Robots and Manipulators, Udine, Italy* (pp. 37–62).
- Lankarani, H. M., & Nikravesh, P. E. (1990). A contact force model with hysteresis damping for impact analysis of multibody systems. *Journal of Mechanical Design*, 112(3), 369–376.
- Mahapatra, A., Bhavanibhatla, K., Roy, S. S., & Pratihari, D. K. (2015). Energy-efficient inverse dynamic model of a hexapod robot. In *Proceedings of International Conference on Robotics, Automation, Control and Embedded Systems, (RACE2015), Chennai, India*.
- Marhefka, D. W., & Orin, D. E. (1999). A compliant contact model with nonlinear damping for simulation of robotic systems. *IEEE Transactions on Systems, Man and Cybernetics, Part A*, 29(6), 566–572.
- Roy, S. S., & Pratihari, D. K. (2011). Dynamic modeling and energy consumption analysis of crab walking of a six-legged robot. In *IEEE Conference on Technologies for Practical Robot Applications (TePRA)* (pp. 82–87).
- Zhang, C. D., & Song, S. M. (1990). Stability analysis of wave-crab gaits of a quadruped. *Journal of Robotic Systems*, 7(2), 243–276.

Sensing Human Pulse Bit Using Ionic Polymer Metal Composite (IPMC)

Debabrata Chatterjee and Adrish Bhaumik

Abstract In this work, we have developed a wrist band using Nafion based ionic polymer-metal composites (IPMC) for sensing the rhythm of human pulse bits. Each pulse bit produces dynamic deformation of IPMC band, and signals (voltage) are generated due to endo-ionic mobility inside the IPMC strip wrapped around the wrist. This work introduces the concept of a novel pulse bits rhythm sensing device. We show proof-of-principle of the mechano-electrical functions of the device, namely IPMC film prepared by surface platinization of the ionic-polymer film.

1 Introduction

Development of smart material using ionic polymer-metal composites (IPMCs) is a demanding area of research (Shahinpoor and Shahinpoor 2001; de Gennes et al. 2003; Punning et al. 2007; Carpi and Smela 2009; Pugal et al. 2010; Bhandari et al. 2012; Kim et al. 2012; Tiwari and Kim 2013). The IPMCs are now recognized to have potential applications in developing bio-mimetic sensors, actuators, transducers, and artificial muscles. The IPMCs offer several advantages such as bio-compatibility, low power consumption and miniaturization. IPMCs consist of a ion exchange electroactive polymer membrane and thin conductive metal electrodes chemically deposited on both sides of the membrane. Although many ion-exchanged polymers have been studied, NafionTM, a fluorocarbon polymer with linear backbone (Fig. 1) with no cross linking and attached with fixed ionic groups ($-\text{SO}_3^-$ for cation exchange), has been shown to be a viable material (Shahinpoor and Shahinpoor 2001). The noble metals such as gold or platinum can be electrode materials to improve surface conductivity.

D. Chatterjee (✉) · A. Bhaumik
Chemistry & Biomimetics Group, Central Mechanical Engineering
Research Institute, Durgapur 713209, India
e-mail: dchat57@hotmail.com

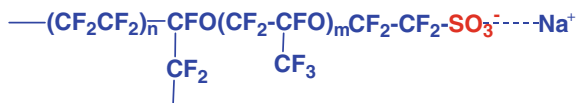


Fig. 1 Pictorial representation of fluorocarbon polymer with linear backbone

We have been engaged in developing IPMC based actuators and sensors (Chatterjee 2009; Chatterjee et al. 2013). Very recently we have reported results of the actuation and sensing studies of a five-fingered miniaturized robotic hand fabricated by using IPMC (Chatterjee et al. 2013). We have shown that under low applied voltages (2.5 V) the IPMC actuator demonstrates big bending deformations (Chatterjee et al. 2013) because of the passage of hydrated ions in the ionic polymer membranes under externally applied voltage. We had shown further that the IPMC based robotic hand exhibited mechanoelectric behaviours under the imposed stresses due to the endo-ionic mobility. Dynamic deformation of such ionic polymers produces dynamic electric fields across their electrodes, and the signals are generated when the fingers are bent and released for a short period (Pugal et al. 2010). In the present work we report exploring the possibility of using IPMC strip as a wrist band for sensing and monitoring the rhythm of human pulse bits.

2 Experimental

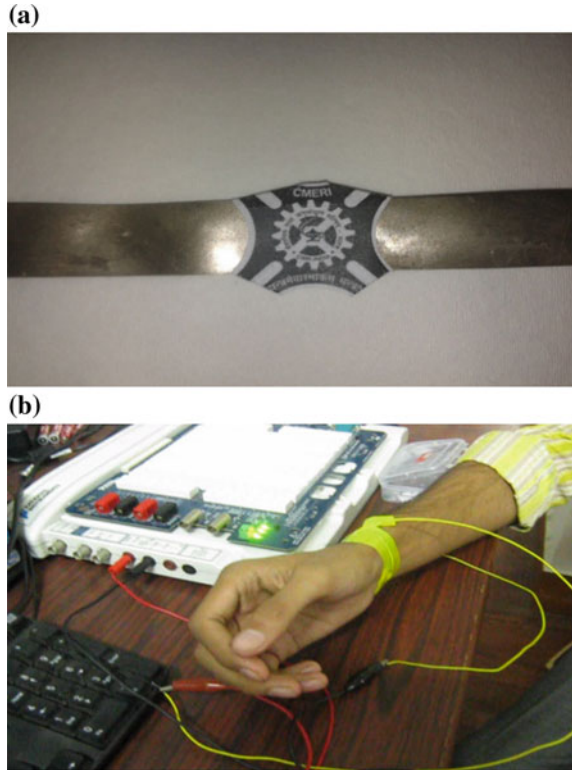
2.1 Fabrication of IPMC Sensor

Fabrication of IPMC strip was achieved by following the previously reported procedure (Chatterjee 2009; Chatterjee et al. 2013). A piece of Nafion¹¹⁷ pretreated polymer strip (6" × 1") was immersed in a solution of [Pt(H₂O)₄] (ClO₄)₂ (0.02 M) at room temperature for 24 h to allow [Pt(H₂O)₄]²⁺ to diffuse through the ion-exchange process, and then washed several times with multi-distilled water. In order to metalize platinum particles on the inner layer surface of the polymer, platinum salt soaked Nafion pieces was then placed into NaBH₄ solution (0.2 g in 200 ml Water) at 70 °C for 3 h.

2.2 Sensing Studies Using IPMC Strip

The length of the IPMC wrist-band was such a size so that the wrist is just covered appropriate dimension of the IPMC wrist-band used in the present experiment was 12.5 × 5 × 0.2 mm. Flexible connecting wires were used to establish the connection of IPMC sensor during online recording of voltage signals. The wires were connected to IPMC platinum electrodes on either side as shown in an illustrative

Fig. 2 **a** IPMC sensor strip and **b** schematic representation of experimental set up



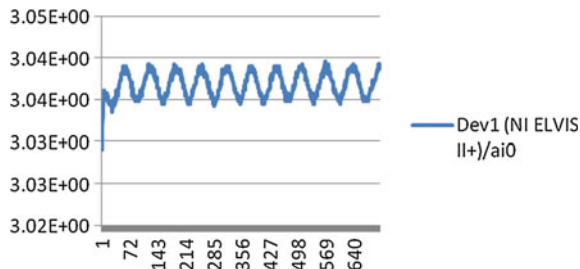
schematic of the experimental setup (Fig. 2). Surface morphology of the IPMC strip was characterized by AFM studies.

The IPMC sensor strip was wrapped around the wrist of a 22 years old healthy male human being who showed systolic and diastolic blood pressure, 79 and 121, respectively (recorded by standard blood pressure measuring machine). The output voltage signals generated by the IPMC sensor strip wrapped around the wrist was acquired via a data acquisition board—NI Educational Laboratory Virtual Instrumentation Suite (NI ELVIS—II) during the experiments. NI ELVIS II (National Instruments Corporation, USA) combines hardware and software into one complete laboratory suite. It is used to sense very low voltage in this experiment. A PC based data acquisition program (LabView) was used to record and process the data.

3 Results and Discussion

Very recently we have reported fabrication of a five-fingered miniaturized robotic hand using IPMC (Chatterjee et al. 2013). This IPMC based robotic mini-hand demonstrated large bending deformations under low applied voltages (2.5 V) due to

Fig. 3 Output signals of the IPMC wrist-band sensor tied over wrist (as shown in Fig. 2)



the migration of hydrated ions in the ionic polymer membranes. Noteworthy here that the IPMC based robotic hand also revealed mechanoelectric behaviour under imposed stresses due to the endo-ionic mobility. Dynamic deformation of such IPMC produces dynamic electric fields across their electrodes, and the signals are generated when the fingers are bent and released for a short period (Pugal et al. 2010; Chatterjee et al. 2013).

Above observation, specially the mechano-electrical response as reported earlier (Chatterjee et al. 2013) for the IPMC made robotic hand prompted us to undertake the present study exploring the possibility of sensing and monitoring the rhythm of human pulse bits. The dynamic sensing response (voltage signal) of the IPMC strip (2 cm wide, 15 cm long and 0.2 mm thick) wrapped around the wrist due to a dynamic stresses imposed by the pulse bits is shown in Fig. 3. The rhythmic features as shown in Fig. 3 is attributed to the endo-ionic mobility in the IPMC strip due to the impact of stresses caused by the pulse bits. The features and periodicity of the sensing signals (Fig. 3) are found to be quite regular in nature. This could be related to the rhythms of the pulse bits characteristics of a 22 years old healthy male human being who showed systolic and diastolic blood pressure, 79 and 121, respectively (recorded by standard blood pressure measuring machine).

Every pulse bit causes continuous mechanical stress of the IPMC sensor due to contraction and relaxation of the pulsating vein of the wrist which results in the generation of dynamic signal (voltage) at regular interval of time due to endo-ionic mobility (Pugal et al. 2010) as shown in Fig. 3.

4 Conclusion

In conclusion, results of our studies show that IPMC strip could be able to sense the human pulse bits as well as the pulse bit rhythms. The results of the above studies explore the possibility using IPMC sensor as a surface mounted sensor/device on human body for cardiac diagnosis. Studies pertinent to this issue are in progress.

Acknowledgments This work was carried out under the financial support from CSIR, New Delhi (Project No. ESC 0203). DC is thankful to Dr. P. Pal Roy, Director, of this institute for his encouragement to this work.

References

- Bhandari, B., Lee, G.-Y., & Ahn, S.-H. (2012). A review on IPMC material as actuators and sensors: fabrications, characteristics and applications. *International Journal of Precision Engineering and Manufacturing*, *13*, 141–163.
- Carpi, F., Smela, E. (2009). *Biomedical applications of electroactive polymer actuators* (pp. 568–78). New York: Wiley.
- Chatterjee, D. (2009). Use of $[\text{Pt}^{\text{II}}(\text{H}_2\text{O})_4]^{2+}$ complex towards development of ionic-polymer-metal-composite actuators. *Indian Journal of Chemistry*, *48A*, 1201–1203.
- Chatterjee, D., Hanumaiah, N., Bahramzadeh, Y., & Shahinpoor, M. (2013). Actuation and sensing studies of a miniaturized five fingered robotic hand made with ion polymeric metal composite (IPMC). *Advanced Materials Research*, *740*, 492–495.
- de Gennes, P. G., Okumura, K., Shahinpoor, M., Kim, K. J. (2003). Mechanoelectric effects in ionic gels. *Europhysics Letters*, *50*, 513–518.
- Kim, K. J., Tan, X., Choi, H. R., Pugal, D. (2012). *Biomimetic Robotic Artificial Muscles*, World Scientific Publishing Company.
- Pugal, D., Jung, K., Aabloo, A., & Kim, K. (2010). Ionic polymer–metal composite mechano-electrical transduction: review and perspectives. *Polymer International*, *59*, 279–289.
- Punning, A., Kruusmaa, M., & Aabloo, A. (2007). A self-sensing ion conducting polymer metal composite (IPMC) actuator. *Sensors and Actuators A*, *136*, 656–664.
- Shahinpoor, M., & Shahinpoor, M. (2001). Ionic polymer–metal composites: I. *Fundamental, Smart Material and Structure*, *10*, 819–833.
- Tiwari, R., & Kim, K. J. (2013). IPMC as a mechanoelectric energy harvester: tailored properties. *Smart Materials and Structures*, *22*, 015017.

Order Reduction of Interval SISO Systems Using Least Square Methods with a Linear Shift ‘a’ Obtained by Harmonic Mean

K. Kiran Kumar and G.V.K.R. Sastry

Abstract The least squares and time moment method has been extended for high order interval systems reduction. Systems with poles of magnitude less than unity can arise numerical problems. An approach is suggested to renew the technique more robust. Thus the denominator and numerator of the reduced interval model obtained by Least square methods and Time moment technique respectively.

Keywords Control system · Controller design · Least squares · Interval system · Kharitonov’s theorem · Order reduction

1 Introduction

In general a high order control system often contains less important poles that have a little effect on the system response. To reduce the effort of design and analysis it is desirable to find a lower order approximating system. This approximation in the sense that the responses of the two systems are similar according to some prescribed criterion. Model reduction consists of replacing the original system with one of a much smaller dimension called as reduced model. The reduced model must be an accurate representation of the original one for the analysis performed. Shoji et al. (1985) came out with a suggestion of applying least squares moment matching technique for an unchanging linear time invariant systems. In a short time, this method was polished by Lucas and Beat (1990) in improving the dynamic response by including Markov parameters. On applying this technique to systems having

K. Kiran Kumar (✉) · G.V.K.R.Sastry
EE Department, A.U.C.E. (A), A.U., Visakhapatnam, India
e-mail: kirankalyana1@gmail.com; kirankalyana1@yahoo.co.in

G.V.K.R.Sastry
e-mail: profsastrygvkr@yahoo.com

dominant poles of smallest magnitude may cause an increase in the magnitudes of consecutive time moments and makes tedious to solve reduced denominator. To triumph over this difficulty, the degree of stability increased with the use of linear shift $s \rightarrow (s + a)$ and therefore reducing the sensitivity of the technique. On doing so, all the dominant poles are shifted to the region of one. The paper here presents the key idea of applying this technique for order reduction of linear time interval systems containing poles of magnitude less than one. It is shown that this generalization is straightforward to apply for order reduction of Interval systems to illustrate its benefits. The least square and generalized reduction procedure has no limitation of using time moments and Markov parameters which guarantees the stability and accuracy of the reduced model.

To show the superiority of the method it's being applied to typical numerical examples and compared with some of the existing methods in the literature.

2 Proposed Procedure

Considering the transfer function of an nth order interval system be denoted as

$$H(s) = \frac{[a_0^-, a_0^+] + [a_1^-, a_1^+]s + \cdots + [a_{n-1}^-, a_{n-1}^+]s^{n-1}}{[b_0^-, b_0^+] + [b_1^-, b_1^+]s + \cdots + [b_n^-, b_n^+]s^n} \quad (1)$$

Here $[a_i^-, a_i^+]$ represents numerator interval coefficients for $i = 0$ to $n - 1$ and $[b_i^-, b_i^+]$ represents the denominator interval coefficients for $i = 0$ to n . Let us assume $\delta(s)$ is a real polynomial of order 'n' structured as

$$\delta(s) = \delta_0 + \delta_1 s + \cdots \delta_n s^n \dots \quad (2)$$

The parameters of the above polynomial lie within the given ranges of

$$\delta_0 \in [x_0, y_0], \delta_1 \in [x_1, y_1], \dots, \delta_n \in [x_n, y_n].$$

The $K_1(s)$, $K_2(s)$, $K_3(s)$ and $K_4(s)$ shown below are the four fixed polynomials derived from Kharitonov's theorem

$$K_1(s) = x_0 + x_1 s + y_2 s^2 + y_3 s^3 + \cdots$$

$$K_2(s) = x_0 + y_1 s + y_2 s^2 + x_3 s^3 + \cdots$$

$$K_3(s) = y_0 + x_1 s + x_2 s^2 + y_3 s^3 + \cdots$$

$$K_4(s) = y_0 + y_1 s + x_2 s^2 + x_3 s^3 + \cdots$$

The numerator and the denominator polynomials are obtained from the above equations individually and represent the four transfer functions with fixed coefficients. This can be generalized as follows. The generalized nth order system transfer function with fixed coefficients are described as

$$G_p(s) = \frac{A_{p0} + A_{p1}s + A_{p2}s^2 + \dots + A_{pn-1}s^{n-1}}{B_{p0} + B_{p1}s + B_{p2}s^2 + \dots + B_{pn}s^n} \tag{3}$$

Here $p = 1, 2, 3, 4$ and $n =$ order of the high order system. Substitute the $G_p(s)$ by $G_p(s + a)$. By using harmonic mean the value of ‘a’ can be determined as

$$\frac{1}{a_p} = \sum_{i=1}^n \left[\frac{1}{|K_{pi}|} \right] / n \quad p = 1, 2, 3, 4. \tag{4}$$

where K_{pi} are the real parts of poles of $G_p(s)$. By expanding $G_p(s + a)$ about $s = 0$, the shifted time moments c_{pi} are found by

$$G_p(s + a) = \sum_{i=0}^{\infty} c_{pi}s^i \quad p = 1, 2, 3, 4. \tag{5}$$

Similarly, by expanding $G_p(s + a)$ about $s = \infty$, then the shifted Markov parameters m_{pj} are obtained by:

$$G_p(s + a) = \sum_{j=1}^{\infty} m_{pj}s^{-j} \quad P = 1, 2, 3, 4.$$

Let the corresponding shifted rth order reduced model is defined as

$$R_{pr}(s + a) = \frac{d_{p0} + d_{p1}s + d_{p2}s^2 + \dots + d_{pr-1}s^{r-1}}{e_{p0} + e_{p1}s + e_{p2}s^2 + \dots + s^r} \tag{6}$$

where $p = 1, 2, 3, 4$ and $r < n$, n is a positive integer.

The above mentioned Eqs. (5) and (6) are equated to preserve the time moments of the original system $G_p(s + a)$, subsequently set of equations are as follows

$$\begin{bmatrix} c_{pr} & c_{pr-1} & \dots & c_{p1} \\ c_{pr+1} & c_{pr} & \dots & c_{p2} \\ \dots & \dots & \dots & \\ \dots & \dots & \dots & \\ c_{p2r-1} & c_{p2r-2} & & c_{pr} \end{bmatrix} \times \begin{bmatrix} e_{p0} \\ e_{p1} \\ \cdot \\ \cdot \\ e_{pr-1} \end{bmatrix} = \begin{bmatrix} -c_{p0} \\ -c_{p1} \\ \cdot \\ \cdot \\ -c_{pr-1} \end{bmatrix} \tag{7}$$

Equation (7) can also be written as $H e = c$, in matrix vector form. The successive parameters of matrix vector ‘e’ of the shifted reduced denominator estimated by least squares technique.

$$e = (H^T H)^{-1} H^T c \tag{8}$$

If the reduced shifted denominator obtained by the coefficients of vector ‘e’ do not make up a stable polynomial then it is suggested to add another row as shown below to the equation set mentioned in Eq. (7) and ensure the matching of the next time moment of the original shifted system.

$$[c_{p2r}c_{p2r-1} \dots c_{pr+1}] \text{ and } [-c_{pr}] \tag{9}$$

Repeat the above procedure till we achieve a satisfactory and stable shifted reduced denominator and ensure the matching of time moments of the shifted original system. In order to improve the initial transient approximation of a system response, incorporate Markov parameters in the least square method, as follows:

$$\left. \begin{aligned} d_{p0} &= e_{p0}c_{p0} \\ d_{p1} &= e_{p1}c_{p0} + e_{p0}c_{p1} \\ d_{p2} &= e_{p2}c_{p0} + e_{p1}c_{p1} + e_{p0}c_{p2} \\ &\quad \cdot \quad \cdot \quad \cdot \quad \cdot \\ &\quad \cdot \quad \cdot \quad \cdot \quad \cdot \\ &\quad \cdot \quad \cdot \quad \cdot \quad \cdot \\ d_{pr-1} &= e_{pr-1}c_{p0} + \dots + e_{p0}c_{pr-1} \\ 0 &= e_{pr-1}c_{p1} + \dots + e_{p0}c_{pr} \\ 0 &= e_{pr-1}c_{p2} + \dots + e_{p0}c_{pr+1} \\ &\quad \cdot \quad \cdot \quad \cdot \quad \cdot \\ &\quad \cdot \quad \cdot \quad \cdot \quad \cdot \\ 0 &= e_{pr-1}c_{pt} + \dots + e_{p0}c_{pr+t-1} \end{aligned} \right\} \tag{10}$$

and

$$\left. \begin{aligned} d_{pr-1} &= m_{p1} \\ d_{pr-2} &= m_{p1}e_{pr-1} + m_{p2} \\ &\quad \cdot \quad \cdot \quad \cdot \quad \cdot \\ &\quad \cdot \quad \cdot \quad \cdot \quad \cdot \\ d_{pt} &= m_{p1}e_{pt+1} + m_{p2}e_{pt+2} + \dots + m_{pr-t} \end{aligned} \right\} \tag{11}$$

where the c_{pj} are the time moment coefficients and m_{pk} are the Markov parameters of the system, such that $j = (0,1, \dots, r + t)$ and $k = (1, 2, \dots, r - t)$ where $t = 0 \leq t \leq r$ respectively. By equating Eqs. (10) and (11), we can eliminate $d_{pr-1}, d_{pr-2}, d_{pr-3}, \dots, d_{pt}$ and this gives the coefficients of the reduced shifted denominator in its matrix form as

$$\begin{aligned}
 & \begin{bmatrix} c_{pr+t-1} & c_{pr+t-2} & \dots & \dots & \dots & \dots & c_{pt} \\
 c_{pr+t-2} & c_{pr+t-3} & \dots & \dots & \dots & c_{pt} & c_{pt-1} \\
 \cdot & \cdot & \dots & \dots & \dots & \cdot & \cdot \\
 c_{pr-1} & c_{pr-2} & \dots & \dots & \dots & c_{p1} & c_{p0} \\
 c_{pr-2} & c_{pr-3} & \dots & \dots & \dots & c_{p0} & -m_{p1} \\
 c_{pr-3} & c_{pr-4} & \dots & \dots & c_{p0} & -m_{p1} & -m_{p2} \\
 \cdot & \cdot & \dots & \dots & \cdot & \cdot & \cdot \\
 \cdot & \cdot & \dots & \dots & \cdot & \cdot & \cdot \\
 \cdot & \cdot & \dots & \dots & \cdot & \cdot & \cdot \\
 c_{pt} & c_{pt-1} & \dots & c_{p0} & -m_{p1} & \dots & -m_{pr-t-1} \end{bmatrix} \times \begin{bmatrix} e_{p0} \\
 e_{p1} \\
 \cdot \\
 \cdot \\
 \cdot \\
 \cdot \\
 \cdot \\
 e_{pr-1} \end{bmatrix} \\
 & = \begin{bmatrix} 0 \\
 0 \\
 \cdot \\
 m_{p1} \\
 m_{p2} \\
 m_{p3} \\
 m_{p4} \\
 \cdot \\
 \cdot \\
 m_{pr-t} \end{bmatrix} \tag{12}
 \end{aligned}$$

The above equation can be written as $H e = m$ in matrix vector form and ‘e’ can be estimated by

$$e = (H^T H)^{-1} H^T m \tag{13}$$

If the reduced shifted denominator obtained by the coefficients of vector ‘e’ do not make up a stable polynomial then it is suggested to add another row as shown below to the equation set mentioned in Eq. (13) and ensure the matching of the next shifted Markov parameter of the original shifted system in Least Squares equivalent. Now apply the inverse shift $s \rightarrow (s-a)$ to the obtained shifted lower order denominator polynomial, from vector ‘e’. Thus rth order reduced model obtained as

$$D_{pr}(s) = E_{p0} + E_{p1}s + E_{p2}s^2 + \dots + s^r$$

where $p = 1, 2, 3, 4$ and $r = 1, 2, 3 \dots n - 1$. Later, using equation

$$C_{pi} = \frac{1}{B_{p0}} \left[A_{pi} - \sum_{j=1}^i B_{pj} C_{pi-j} \right] \tag{14}$$

$i > 0$ with $A_{pi} = 0$ for $i > n - 1$ and $p = 1, 2, 3, 4$.

Equating the exact number of time moments of $G_p(s)$ and $R_p(s)$, we can determine the reduced model numerator coefficients such that

$$N_{pr}(s) = D_{p0} + D_{p1}s + D_{p2}s^2 + \cdots + D_{pr-1}s^{r-1}$$

where $p = 1, 2, 3, 4$ and $r = 1, 2, 3 \dots n - 1$.

Then the corresponding r th order reduced models with fixed coefficients are defined as $R_{pr}(s) = \frac{N_{pr}(s)}{D_{pr}(s)}$

$$R_{pr}(s) = \frac{D_{p0} + D_{p1}s + D_{p2}s^2 + \cdots + D_{pr-1}s^{r-1}}{E_{p0} + E_{p1}s + E_{p2}s^2 + \cdots + s^r}$$

where $p = 1, 2, 3, 4$ and $r = 1, 2, 3 \dots n - 1$.

The reduced Interval model is determined by considering the lowest and highest values of the coefficients of reduced interval models with fixed coefficients.

$$R_r(s) = \frac{[D_{p0min}, D_{p0max}] + [D_{p1min}, D_{p1max}]s + \cdots + [D_{pr-1min}, D_{pr-1max}]s^{r-1}}{[E_{p0min}, E_{p0max}] + [E_{p1min}, E_{p1max}]s + \cdots + [1, 1]s^r}$$

To match the steady state step responses of lower boundary and upper boundary of original system and reduced model separately they are multiplied with their individual gain parameter considering $s = 0$.

3 Comparison with Other Existing Methods

Example 1 Now let us use an Original stable eighth Order Interval System with transfer function given by Bandyopadhyay et al. (1994)

$$G(s) = \frac{[35, 36]s^7 + [1086, 1087]s^6 + [13285, 13286]s^5 + [82402, 82403]s^4 + [278376, 278377]s^3 + [511812, 511813]s^2 + [482964, 482965]s + [194480, 194481]}{[1, 2]s^8 + [33, 34]s^7 + [437, 438]s^6 + [3017, 3018]s^5 + [11870, 11871]s^4 + [27470, 27471]s^3 + [37492, 37493]s^2 + [28880]s + [9600, 9601]s} \quad (\text{Original stable})$$

The 2nd order reduced interval model determined by the proposed method using six time moments to the denominator and two time moments to the numerator with values of $a_1 = 1.900661$, $a_2 = 1.961999$, $a_3 = 1.661691$ and $a_4 = 1.636508$ are as follows:

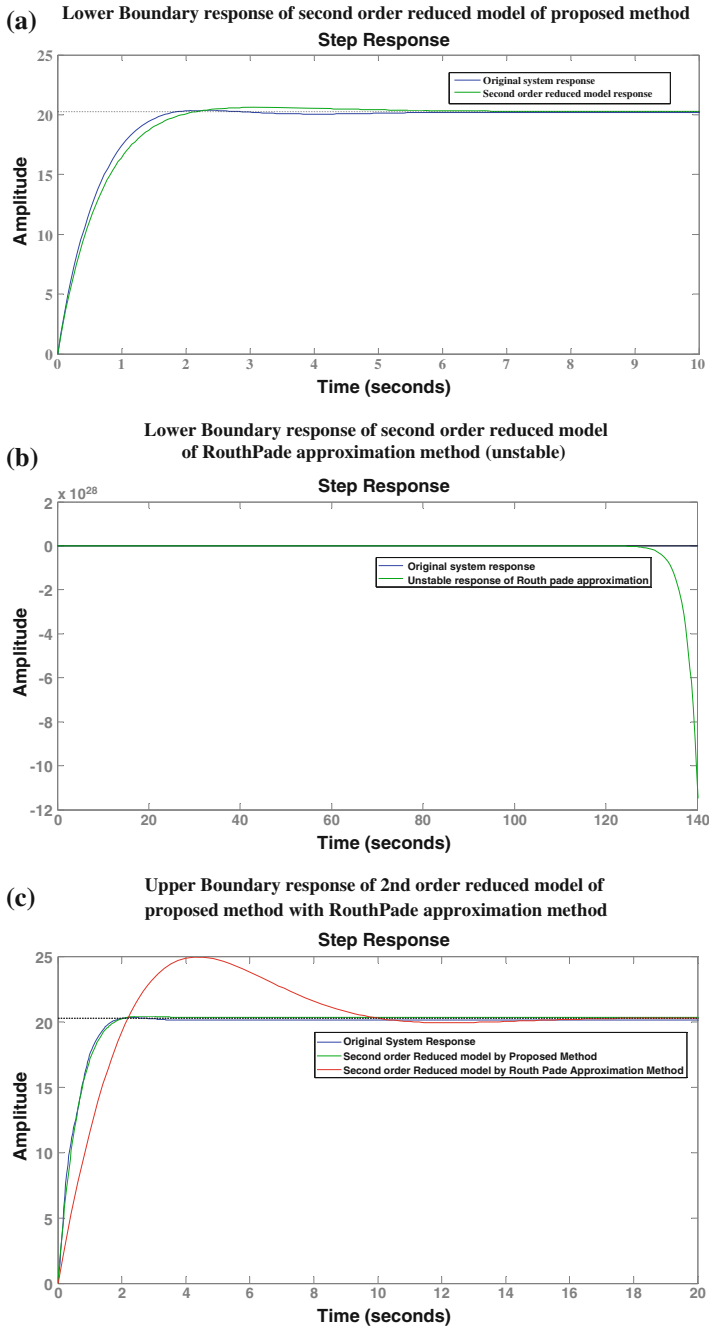


Fig. 1 Example 1 a-c Comparison of step responses

$$R(s) = \frac{[30.810692, 30.92124]s + [20.873516, 570379608]}{[1, 1]s^2 + [2.063887, 3.007266]s + [1.0300367, 2.832676]} \quad (\text{stable})$$

The 2nd order reduced interval model determined by the Routh–Pade approximation method of Bandyopadhyay et al. (1994) is given by:

$$R_{2B}(s) = \frac{[-26180619.28, 1522933.981]s + [622597.2952, 622665.3527]}{[-244232.7878, 112616.9868]s^2 + [-109949.9392, 75328.80773]s + [2998.7544, 30736.0996]} \quad (\text{Unstable})$$

Figure 1a–c shows the superiority of the proposed method over Routh–Pade approximation method by generating stable reduced interval models for a stable Original interval system. Table 1 represents the time domain specifications of the proposed reduced model which approximates the original interval system. Table 2 denotes the (I), (J) values are less when compared to Bandyopadhyay method with that original system.

Table 1 Time domain specifications of original and reduced interval models

Transfer function	Lower boundary			Upper boundary		
	T_d	T_r	T_s	T_d	T_r	T_s
Original system	0.399	1.13	7.1	0.364	1.11	5.01
Proposed model	0.442	1.3	7.1	0.418	1.12	5.01
Bandopadhyay model	Unstable	Unstable	Unstable	0.856	1.83	17.1

where T_d delay time; T_r rise time; T_s settling time

Table 2 Comparison of I, J values of proposed method with Bandyopadhyay (Bandyopadhyay et al. 1994)

Transfer function	Proposed method relative I.S.E value		Routh–Pade approximation method relative I.S.E value	
	I	J	I	J
Lower boundary	0.007545	0.013385	Unstable	Unstable
Upper boundary	0.047177	0.004076	0.364622	1.006422

where I relative integral square error of impulse; J relative integral square error of step

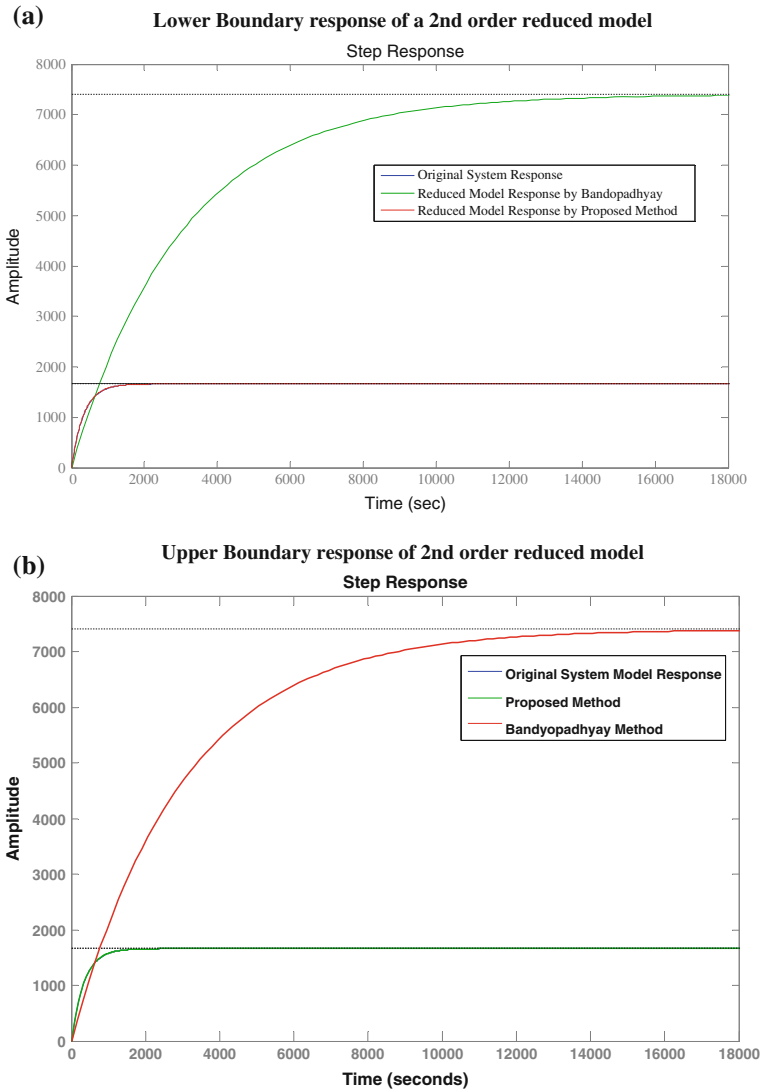


Fig. 2 Example 2 a–b Comparison of step responses

Example 2 Now let us use an Original stable fourth Order Interval System with transfer function given by Bandyopadhyay et al. (1997)

$$G(s) = \frac{[54, 74]s + [90, 166]}{[1, 1]s^4 + [2.8, 4.6]s^3 + [50.4, 80.8]s^2 + [30.1, 33.9]s + [0.1, 0.1]}$$

Table 3 Time domain specifications of original and reduced interval models

Transfer function	Lower boundary			Upper boundary		
	T _d	T _r	T _s	T _d	T _r	T _s
Original system	210	703	2370	232	753	2100
Proposed model	210	703	2370	232	753	2100
Bandyopadhyay model	232	771	1600	2030	6860	16,000

where T_d delay time; T_r rise time; T_s settling time

Table 4 Comparison of I, J values of proposed method with Bandyopadhyay (Bandyopadhyay et al. 1997)

Transfer function	Proposed method relative I.S.E value		γ-δ method of Bandyopadhyay relative I.S. E value	
	I	J	I	J
Lower boundary	0.000877	0.000024	0.288876	0.285268
Upper boundary	0.000805	0.000116	1.432940	160.579712

where I relative integral square error of impulse; J relative integral square error of step

The 2nd order reduced interval model obtain by the proposed method using four time moments to the denominator and two time moments to the numerator with a₁ = 0.0134351, a₂ = 0.011856, a₃ = 0.013087 and a₄ = 0.011881 is as follows:

$$R(s) = \frac{[0.6018899, 1.259805]s + [1.140512, 3.537981]}{[1, 1]s^2 + [0.383357, 0.711652]s + [0.001274, 0.001267]}$$

The 2nd order reduced interval model determined by the γ-δ method of Bandyopadhyay et al. (1997) is given by

$$R_{2B}(s) = \frac{[0.98912, 3.7103]s + [0.5269, 1.8628]}{[1, 1]s^2 + [0.33.8, 0.7577]s + [0.00097579, 0.000251727]}$$

Figure 2a, b displays the lead of the proposed method over γ-δ method. Table 3 represents the time domain specifications of the proposed reduced model which approximates the original interval system. Table 4 denotes the (I), (J) values are less when compared to Bandyopadhyay method with that original system.

4 Conclusions

In this paper, a new approach being suggested for the reduction of higher order interval systems using least squares moment matching technique with a linear shift ‘a’ obtained by harmonic mean. The reduction procedure involves the reduction of

high order interval denominator polynomial by least square and generalized least square method while the reduction of high order interval numerator polynomial by time moment technique. This way of approach has no limitations in using the number of time moments and Markov parameters therefore assure stability and accuracy in the reduced model. Typical numerical examples from the literature are considered to show the superiority of the method over the other existing methods in computational wise and results wise. It is observed from the results that the Time domain specifications of the reduced model obtained by the proposed method matches good with time domain specifications of the original system when compared with other existing methods. It is also observed that Relative I.S.E Value of step (J) and impulse (I) obtained by the Proposed method is less than Relative I.S.E Value of step (J) and impulse (I) obtained by other methods.

References

- Bandyopadhyay, B., Ismail, O., & Upadhye, A. (1997). γ - δ Routh approximation for interval systems. *IEEE Transactions on Automatic Control*, 42(8), 1127–1130.
- Bandyopadhyay, B., Ismail, O., & Gorez, R. (1994). Routh-Pade approximation for interval systems. *IEEE Transactions on Automatic Control*, 39(12), 2454–2456.
- Lucas, T. N., & Beat, I. F. (1990). Model reduction by least squares moment matching. *Electronics Letters*, 26, 1213–1215.
- Shoji, F. F., Abe, K., & Takeda, H. (1985). Model reduction for a class of linear dynamic systems. *Journal of the Franklin Institute*, 319, 549–558.

Identifying and Updating the Kinematics of KUKA-iiwaR800 in CAD for Accurate Simulation

Abdullah Aamir Hayat, Arun Dayal Udai and Subir Kumar Saha

Abstract Kinematics and dynamics of the robot are affected by the addition of the link in the form of end-effector in the robots. An approach is presented for updating the CAD model kinematics as per customized installed robot KUKA-iiwaR800 with its gripper. KUKA-iiwaR800 is a light weight manipulator with seven degrees of freedom (DOF) which is popular in robotics research nowadays. We present a method to match the kinematic data of the installed robot with the CAD model in SimMechanics (SM) and in-house developed software RoboAnalyzer (RA). The CAD assembly of the customized robot was done in Autodesk Inventor and then imported to the Matlab environment for simulation. The validation of CAD model kinematics is done by matching the forward kinematics results from the installed robot using the log data of joint angles. After kinematic validation the model is updated in RA software with the kinematics of actual robot and the dynamic parameters as in SM. Again cycloidal trajectories were used to validate the kinematic model in RA with SM. Inverse and forward dynamics of the robot was carried out in RA using the mass and inertial properties listed in the paper.

Keywords CAD assembly · Kinematics · Simulation · RoboAnalyzer · Seven DOF robot

A.A. Hayat (✉) · A.D. Udai · S.K. Saha
Department of Mechanical Engineering, Indian Institute of Technology Delhi,
New Delhi 110016, India
e-mail: aamir7hayat@gmail.com; aamir_hayat@rediffmail.com

A.D. Udai
e-mail: arun_udai@mech.iitd.ac.in

S.K. Saha
e-mail: saha@mech.iitd.ac.in

1 Introduction

The development of the accurate kinematic model is necessary for the design of accurate motion controller with better performance (Khalil and Dombre 2002). The kinematic and dynamic model is subjected to change with the additional linkages being attached. Updating the customized robot model which is installed, in simulation environment is vital to study the behavior of the robot kinematics accurately. In this paper we focused on robot kinematics with identifying and updating the kinematic model accordingly.

In recent years, a large research interest is on new generation robots with seven degrees of freedom (DOF) intended for safer physical human robot interaction (HRC). Seven DOF such as KUKA-iiwaR800 robot are actively used as they imitate the kinematics of human hand. The identification of the kinematic model of the KUKA-iiwaR800 was done using method presented in Hayat et al. (2013). In this paper KUKA-iiwaR800 CAD parts were assembled as per the installed robot with its customized gripper in Autodesk Inventor and then exported to MATLAB SimMechanics (SM) as model for further analysis. Then kinematic behavior of the robot in simulation with actual installed robot is verified in this paper. Then the model is incorporated in RoboAnalyzer (RoboAnalyzer 2014) and is validated using the SM results.

Virtual simulation and augmented reality are active field of research, and attempts are made to exactly match the behavior of real application in simulated environment (Bugalia et al. 2015). It is vital that the robot programmers be able to visualize and analyze the behavior of the robots in different circumstances with the accurate robot model. Advantage of MATLAB based tool in simulating the robotic manipulate is discussed in (SIMULINK User's Guide 2014). Robotic simulation in the software packages like Simulink, SimMechanics (2014) allows to test robot kinematics and dynamics offline, i.e., before the experimentation on the robot. In (Shaoqiang et al. 2008), modeling of inverted pendulum using SM is presented. In this paper, the simulation of robot was also done in RoboAnalyzer of KUKA-iiwaR800 where it is easier to analyze and visualize.

This paper is divided into five sections. Section 2 explains the modeling of the robot with customized add-ons which is the gripper attached with real robots. Identifying the robot kinematics model and then importing the CAD assembly in the Simulink environment is also discussed. Section 3 presents the comparison of the kinematics of the CAD assembly and the identified model. Section 4 discussed the dynamic behavior of the customized CAD model followed by the conclusion in Sect. 5.

2 Modeling of Robot

The kinematic model of the robot is most widely presented using Denavit-Hartenberg (DH) convention (Denavit and Hartenberg 1955). The set of four parameters relates the transformation between two successive Frames (say i to $i + 1$) by b_i , θ_i , a_i and α_i , explained in (Saha 2014). The KUKA-iiwaR800 robot installed at PAR lab IIT Delhi is shown in Fig. 1a, b. The robot is having a gripper attached to the flange of the robot. The tool calibration was done with an edge point on the gripper and then the circle point method was used to identify the DH parameters (Hayat et al. 2013) by actuating one joint axis at a time and locking the others. Table 1 shows the identified DH parameters of the installed robot.

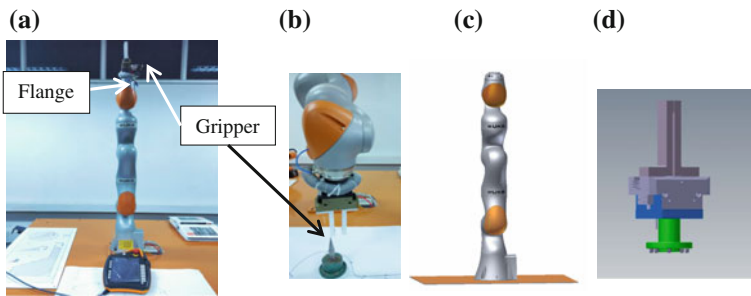


Fig. 1 Installed and CAD model of the robot with its custom designed gripper. **a** Installed KUKAiiwaR800 robot. **b** Gripper and point taken for calibration. **c** CAD model of the robot till flange. **d** Schunk gripper with custom designed finger

Table 1 Identified kinematic parameters

Link	Joint offset b (mm)		JV θ (Degrees)		Link length a (mm)		TA (Degrees)
	IR	CAD	IR	CM	IR	CAD	
1	340.01	340	θ_1	θ_1	0	0	$\pi/2$
2	0	0	θ_2	$-\theta_2$	0	0	$\pi/2$
3	399.98	400	θ_3	θ_3	0	0	$-\pi/2$
4	0.002	0	θ_4	$-\theta_4$	0	0	$\pi/2$
5	400.02	400	θ_5	θ_5	0	0	$\pi/2$
6	0	0	θ_6	$-\theta_6$	0	0	$-\pi/2$
7	126 + GO = 236	238	θ_7	θ_7	0 + GL = 15	15	0

JV Joint variable, TA Twist angle, IR Installed robot, GO Gripper offset, GL Gripper length, CM Corresponding values taken in analytical model

2.1 Identifying CAD Model Kinematics

The stereolithographic (.stl) file of the robot was taken from <http://www.kuka-labs.com/en/downloads/>. The CAD part was then imported in the Autodesk Inventor platform. This model of the robot when after defining the joint constraints in the Autodesk Inventor does not account for the gripper attached as in case of real robot. The additional part drawing of the SHUNK gripper model (SCHUNK-0371102 PGN-plus 100-1) with fingers was then attached to the CAD model for accurate modeling. The DH parameter identification process was then carried in the Autodesk environment considering the same end-effector (EE) point as was done experimentally. The identified value is depicted in Table 1. There is good match in the DH parameters between the CAD model and the installed robot with the gripper. The assembly of the gripper to the CAD model and then identifying the parameters resulted in accurate kinematic model. Note that the angular values of even joints are with minus sign in order to match the forward kinematic values, since robot follows different convention to consider the positive direction of rotation.

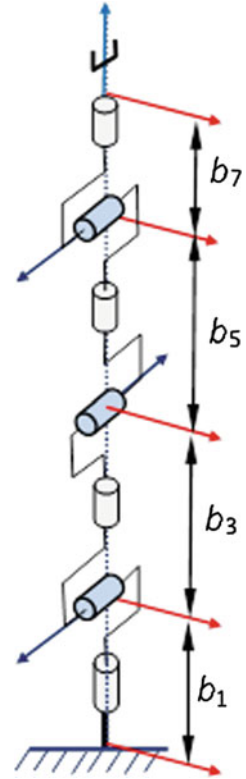
2.2 Importing CAD Assembly

The CAD of the robot with gripper was translated to SM format from Autodesk Inventor using SM Link Inventor Plug-in. The plug-in will get attached to the Autodesk inventor in the Add-ins menu and then the model was exported as SimMechanics first generation file. This CAD translator of SimMechanics (http://www.mathworks.com/products/simmechanics/download_cad.html) for further analysis. This creates the STL files and the XML files which is readable by SM. The XML file was then called in MATLAB environment by `mech_import('filename.xml')` command. The block diagram in Fig. 3 shows the brief procedure of CAD translation to SM. This results in forming the SimMechanics blocks as shown in Fig. 4. Figure 4a shows the imported model with joint input trajectory. Table 2 lists the mass and inertia parameters of the robot which is utilized by the SM model. The gripper which is attached to the flange is replaced by the welded joint in Fig. 4b as there is no relative motion between them and can be considered as the last link of the robot. Note that the dynamic properties of the link, i.e., inertia, mass moments and masses in RA were assigned the values in Table 2. The user can change these parameters as per the exact value known or can simulate the dynamic performance by varying them (Fig. 2).

Table 2 Mass and inertia properties of each link in CAD model

Link #	1	2	3	4	5	6	7
b	0.34	0	0.4	0	0.4	0	0.236
a	0	0	0	0	0	0	0
α	90	-90	-90	90	90	-90	90
m	3.4525	3.4821	4.05623	3.4822	2.1633	2.3466	3.129
r_x	0	-0.03441	-0.02	0	0	0.000001	0.0000237
r_y	0.06949	0	-0.089	-0.034412	0.14	0.000485	-0.0002707
r_z	-0.03423	0.06733	-0.02906	0.067329	-0.02137	0.002115	0.063866
I_{xx}	0.02183	0.02076	0.03204	0.02178	0.01287	0.006509	0.01464
I_{yy}	0.007703	0.02179	0.00972	0.02075	0.005708	0.006259	0.01465
I_{zz}	0.02083	0.00779	0.03042	0.007785	0.01112	0.004527	0.002872
I_{xy}	-1.1785E-08	-4.1482E-08	-1.6251E-08	8.3438E-08	4.6669E-08	2.6398E-08	0.0005912
I_{yz}	-0.003887	-4.7255E-08	0.006227	-0.003625	-0.003946	0.00031891	1.35593E-05
I_{zz}	-8.01381E-09	-0.003626	4.9393E-08	5.6097E-08	6.2225E-08	7.07101E-09	-2.55604E-06

Fig. 2 Kinematic model of KUKAiiwaR800



3 Kinematic Simulation and Validation

The accurate kinematic model is vital to match the numerical values of position from the robot with the analytical model. The position of the end effector is given by the successive multiplication of the transformation matrix as

$$\mathbf{T} = \prod_{i=1}^n \mathbf{T}_i \quad (1)$$

The Jacobian matrix is calculated from the above transformations as a function of joint angle positions as given in Eq. 2.

The i th column of the Jacobian matrix is given in Eq. 2. For KUKA-iiwaR800 $i = 7$, since there are seven revolute joints. The accurate model will result in accurate Jacobian of the robotic model, which is very useful in Dynamic analysis as well. The Jacobian of the robot also gives a notion of manipulability index (MI) of the robot (Yoshikawa 1985) as in Eq. 3.



Fig. 3 Translating CAD model to SimMechanics

$$\mathbf{j}_i \equiv \begin{bmatrix} \mathbf{e}_i \\ \mathbf{e}_i \times \mathbf{a}_{ie} \end{bmatrix}, \text{ if Joint } i \text{ is revolute} \quad (2)$$

where \mathbf{e}_i is the joint axis direction along z-axis given by the third column of the transformation matrix \mathbf{T}_i , and \mathbf{a}_{ie} is the vector joining i th joint with the end-effector obtained by the fourth column of the transformation matrix obtained by subtracting \mathbf{T}_{EE} and \mathbf{T}_i .

$$MI = \sqrt{\det(\mathbf{J}(\boldsymbol{\theta}_i)\mathbf{J}^T(\boldsymbol{\theta}_i))} \quad (3)$$

The identified kinematic model is verified using the sensor reading from the robot and also from the analytical model forward kinematics. The cycloidal trajectory (Saha 2014) as in Eq. (4) was implemented in Simulink as shown in Fig. 3c is used for actuating each joint axis with corresponding joint velocity $\dot{\theta}$ and acceleration $\ddot{\theta}$ obtained by successive differentiation. The trajectory traced by the point on the end-effector obtained by sensor and from the forward kinematic model utilizing the identified DH is shown in Fig. 4a.

$$\theta = \theta(0) + \frac{\theta(T) - \theta(0)}{T} \left[t - \frac{T}{2\pi} \sin\left(\frac{2\pi}{T}t\right) \right] \quad (4)$$

The plots of the trajectory in Fig. 5a were in close match with each other. This shows the correctness of the kinematic model. The CAD model and the analytical expression for kinematics are in close match. The root mean square (RMS) error for the trajectory obtained from sensor data and analytical model is 0.638 mm. The manipulability (Yoshikawa 1985) index plot is shown in Fig. 5b which shows that when the robot was at fully stretched position as in Fig. 1a the manipulability was least, i.e., equivalent to zero. The variation of manipulability as shown in Fig. 5b is corresponding to the trajectory shown in Fig. 5a. Note that the normalized value of the manipulability is plotted, i.e., the variation is between 0 meaning least manipulable and 1 is for maximum manipulable. In the next section the dynamics of the model in Simulink is discussed with the mass and inertial parameters taken as default from the CAD. In future the CAD model dynamics will be made similar to the real dynamic model using dynamic identification techniques.

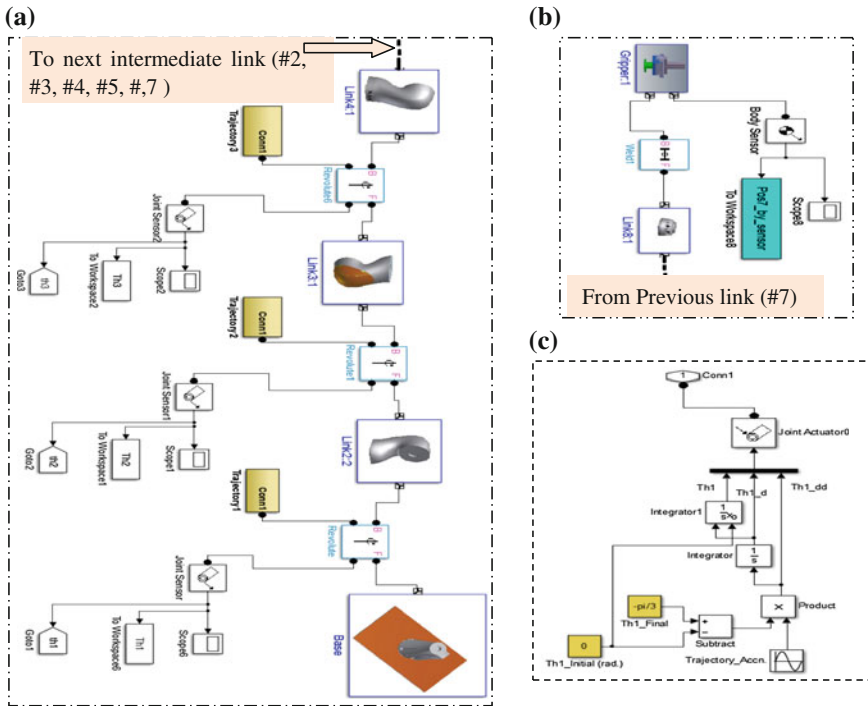


Fig. 4 SimMechanics model of the robot with cycloidal trajectory. **a** SM model of KUKAIiwaR800 robot. **b** Last link (#8) with gripper. **c** Cycloidal trajectory as in Eq. (4) input to joints in the trajectory block of Fig. 4a

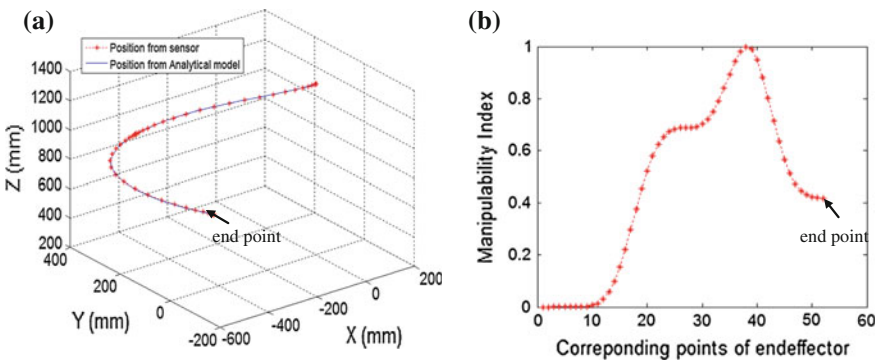


Fig. 5 Validating the gripper position with the identified model by actuating each joint with cycloidal trajectory. **a** Trajectory plot of the point on the gripper of the robot. **b** Manipulability Index plot of the points on the trajectory

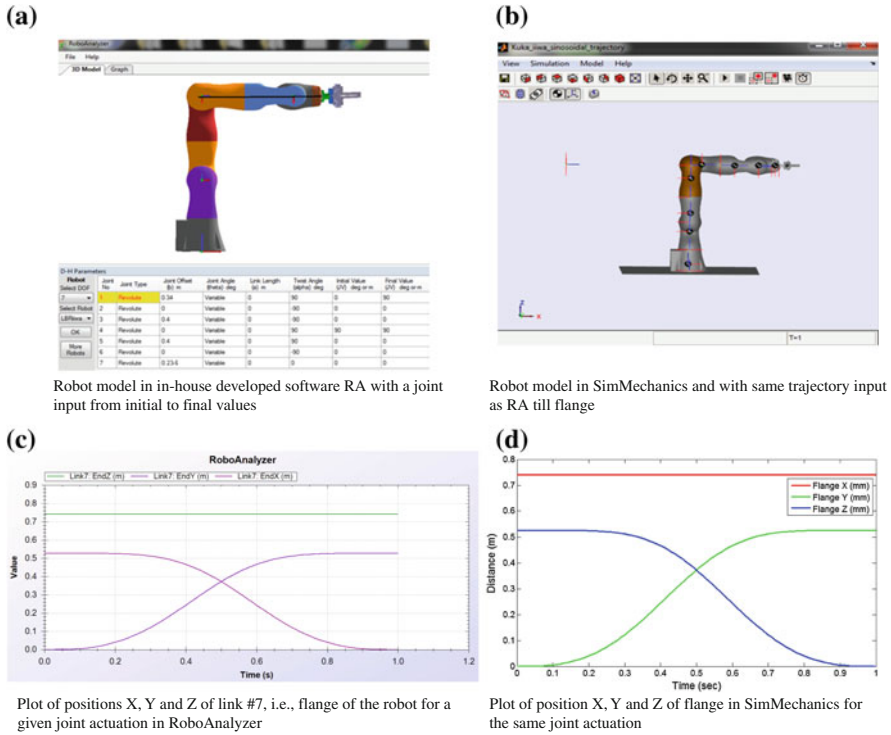
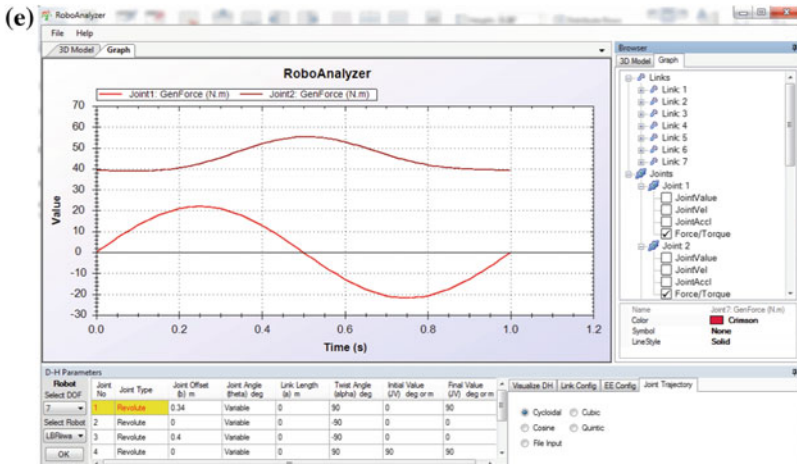


Fig. 6 Here **a, b** are robot model in RA and SimMechanics, **c, d** are the plots for the trajectory components for a given joint actuation, **e** is the inverse dynamics results showing torque coming on Joint 1,2 and the forward dynamics result for free fall under gravity with joint variation in (**f, g**)

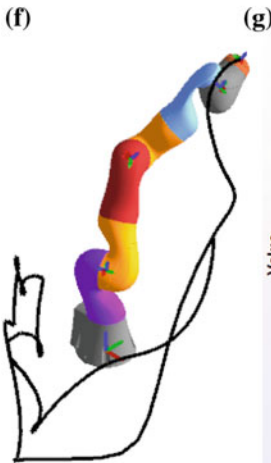
The 7-DOF robot KUKA-iiwaR800 was added in the RoboAnalyzer (Bugalia et al. 2015), a freeware software for 3D model based robotics learning as shown in the Fig. 6a. The DH parameters are listed in the tabular form in the Fig. 6a till the flange only. The end-effector trajectory components X, Y and Z were plotted in Fig. 6c, d which exactly matches in both the environment, by actuating joint 1 only.

4 Dynamic Simulation Results Using RA

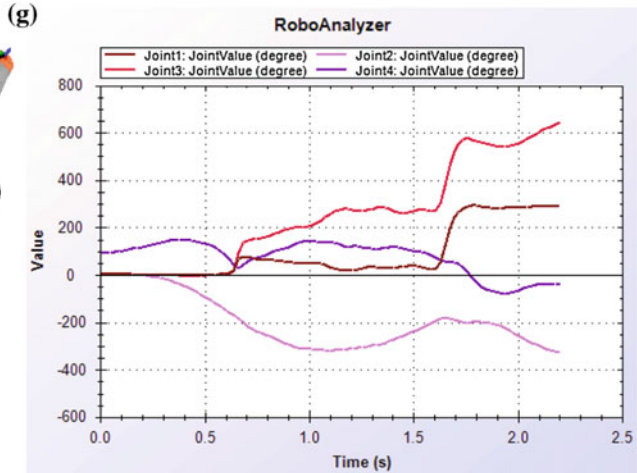
Dynamic simulation was done only in RA with the mass and inertia values listed in Table 2 about links center of mass. These data are saved inside the RA for the simulation purpose. The inverse dynamics was performed by actuating joint 1 from 0 to 90 degrees only using the cycloidal trajectory given in Eq. (4). The torque variation is shown for the first two joints for this trajectory in Fig. 6e. Using the



Inverse dynamics carried out for the trajectory given in Figure 6(c), i.e., moving Joint 1 from 0 to 90 degrees in 1 second with the cycloidal profile. Torque at joint 1 and 2 is plotted above.



Free fall of the robot under gravity for 2.2 seconds. Forward kinematics under free fall was used in RA.



Torque plot for the given cycloidal trajectory for Joint 5, 6, and 7 using SimMechanics (SM).

Fig. 6 (continued)

forward kinematics module of RA interesting simulation of free fall of the robot under the action of gravity is shown in Fig. 6f where the trail of the end-effector is depicted. The joint variation corresponding to the free fall is shown in Fig. 6g. In RA user can change the dynamics parameters as per requirement and analyze the system dynamics and sensitivity towards the dynamic parameters.

5 Conclusions

Simulating the robot with its accurate model in programming environment like SimMechanics or Autodesk Inventor gives an edge in predicting the accurate robot behavior. Simulation with this model in SimMechanics is advantageous in later building the control laws, sending accurate signals for better performance, etc. Also RoboAnalyzer helps in understanding the physics and visualizing the robot manipulation in better way. Present works reported on updating the kinematics of the CAD model in Autodesk Inventor and then exporting in SimMechanics for further kinematic analysis and validation with the forward kinematic applied on the joint sensor data obtained from the installed robot. The position of the robot with the sensor data and the identified model were in close match with each other with an RMS error of 0.638 mm. The kinematic results were also validated with the imported model of Kuka-iiwaR800 in RoboAnalyzer using cycloidal trajectory input to one of the joint. The outcome of this study is the accurate model of KUKA-iiwaR800 in RA and the method to have it in SM which the end-user can utilize directly to study the forward kinematics and dynamics of the 7-DOF robot. Hence, the kinematic results given by RA will replicate with that of the actual installed robot. The present platform will be utilized in near future to identify the dynamic model of the robot in CAD with optimized trajectory input which is easier in simulated environment.

Acknowledgments The financial support to the first two authors is from the sponsored project entitled “Adaptive Force Control of an Industrial Robot (KUKA KR6) Equipped with Force/Torque Sensor” by BRNS/BARC Mumbai under the setting up of “Programme for Autonomous Robotics Lab” at IIT Delhi is sincerely acknowledged. We also thank Mr. Zubair with helping in CAD model and Rajeevlochana, Rata Sadanand O.M. with RoboAnalyzer.

References

- Bugalia, N., Sen, A., Kalra, P., & Kumar, S. (2015). Immersive environment for robotic tele-operation. In *Proceedings of Advances in Robotics*, pp. 1–6.
- Hayat, A. A., Rajeevlochana, C. G., Udai, A. D. & Saha, S. K. (2013). Identification of Denavit-Hartenberg parameters of an industrial robot. In *Advances in Robotics, International Conference of Robotics Society of India, (AiR 2013), R & DE (Engrs.)* (pp. 1–6), Pune, 4–6th July, 2013.
- Khalil, W., & Dombre, E. (2002). *Modeling, Identification and Control of Robots*. London: Hermes Penton.
- RoboAnalyzer. (2014). *3D model based robotics learning software*. <http://www.roboanalyzer.com>.
- SIMULINK User’s Guide. (2014). The Mathworks, Inc.
- The MathWorks Inc. (2014). *SimMechanics User’s Guide* March, 2014.
- Denavit, J., & Hartenberg, R. S. (1955). A kinematic notation for lower-pair mechanisms based on matrices. *Transactions of the ASME, Journal of Applied Mechanics*, 23, 215–221.
- Saha, S. K. (2014). *Introduction to Robotics*. Tata McGraw Hill: 2nd ed.

- Shaoqiang, Y., Liu, Z., & Xingshan, L. (2008). Modeling and simulation of robot based on Matlab/SimMechanics. In *27th Chinese Control Conference*, IEEE.
- KUKA-iiwaR800 Step file. <http://www.kuka-labs.com/en/downloads/>.
- SimMechanics CAD Translator. http://www.mathworks.com/products/simmechanics/download_cad.html.
- Yoshikawa, T. (1985). Manipulability of robotic mechanisms. *The International Journal of Robotics Research*, 4(2), 3–9.

Parametric Optimization of Link Lengths of a SCARA Robot for Deburring of Circular Paths

P.V.S. Subhashini, N.V.S. Raju and G. Venkata Rao

Abstract SCARA (Selective Compliant articulated robot arm) is a special manipulator used for high speed applications. SCARA is a 4-DOF manipulator with 3 revolute and 1 prismatic joint. It is well known that deburring is burr removal process after machining or casting processes. Circular components are very common in engineering applications. This paper aims at optimizing the power of the first two link lengths of a SCARA manipulator used for deburring of circular path. A circular path for deburring of 0.06 m diameter is considered and it is assumed that to complete one cycle of circular path it takes 10 s of time and the analysis is carried out in 12 steps in this time. The range of link lengths are provided as input along with distance between base of a SCARA robot and position of the deburring component as 0.35 m. Kinematic and dynamic equations of a SCARA robot are used to calculate the objective function for minimizing power. 12 steps are used to complete one cycle and to obtain the power at 12 steps and also there by obtain minimum power required in that operation for the combination of link lengths. A MATLAB program is generated which computes power at each set of link length combination which when plotted for all combinations yields information on the optimized set of link lengths.

Keywords SCARA · Deburring · Optimization · Power · MATLAB

Nomenclature

- a_x Linear acceleration in x-axis (m/s^2)
- a_y Linear acceleration in y-axis (m/s^2)
- b_1 Width of the link1 (m)
- b_2 Width of the link2 (m)
- c_1 $\text{Cos}(\theta_1)$

P.V.S. Subhashini (✉) · G. Venkata Rao
VCE, Hyderabad, Telangana, India
e-mail: Siva726@yahoo.co.in

N.V.S. Raju
JNTU, Jagithyala, Telangana, India

c_{12}	$\text{Cos}(\theta_1 + \theta_2)$
d	Diameter of the component (m)
l_1	Length of link1 (m)
l_2	Length of link2 (m)
m_1	Mass of the link1 (kg)
m_2	Mass of the link2 (kg)
m_3	Mass of the link3 (kg)
P_1	Power of joint1 (watt)
P_2	Power of joint2 (watt)
p_x	Linear displacement in x-axis (m)
P_y	Linear displacement in y-axis (m)
S_1	$\text{Sin}(\theta_1)$
S_{12}	$\text{Sin}(\theta_1 + \theta_2)$
T_1	Torque of joint1 (N-m)
T_2	Torque of joint2 (N-m)
v_x	Linear velocity in x-axis (m/s)
v_y	Linear velocity in y-axis (m/s)
θ_1	Angular displacement of joint1 (rad)
θ_2	Angular displacement of joint2 (rad)
$\dot{\theta}_1$	Angular velocity of joint1 (rad/s)
$\dot{\theta}_2$	Angular velocity of joint2 (rad/s)
$\ddot{\theta}_1$	Angular acceleration of joint1 (rad/s ²)
$\ddot{\theta}_2$	Angular acceleration of joint2 (rad/s ²)

1 Introduction

SCARA is a well known manipulator for electronic assemblies. SCARA manipulator with 4-DOF i.e. 3 revolute and 1 prismatic joint is presented in Fig. 1. As SCARA is a well established manipulator kinematic and dynamic equations are used in MATALAB analyses. Robotic deburring is being carried out presently on large gears, castings and forgings. However no detailed investigations appears to have been carried out and reported in open literature regarding deburring of components, which are small and used widely in many assembly situations like I.C engines and also in small machinery.

In the area of SCARA robot kinematics and dynamics, some of the investigations carried out earlier are given below.

Rehiara (2011) formulated and solved the kinematics problem for an Adept Three robot arm. Graphical solution in a virtual instrumentation (VI) of Lab view is implemented for simulating and calculating the robot kinematics and inverse kinematics.

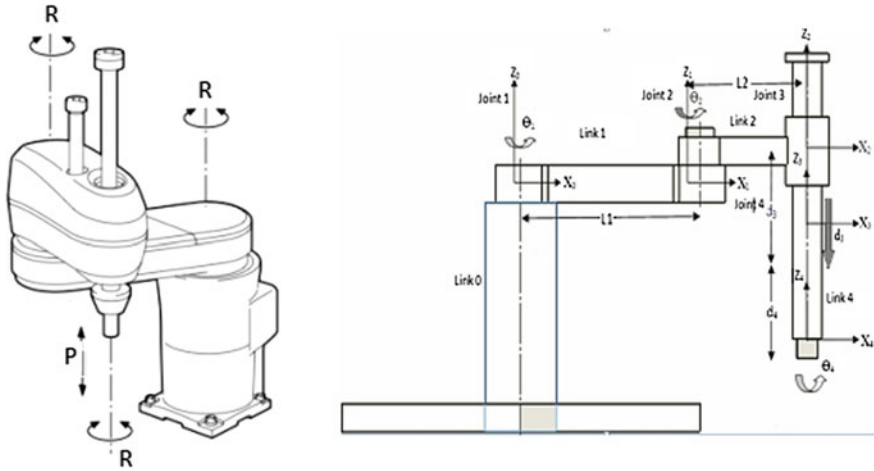


Fig. 1 Anatomy of SCARA manipulator

Fang et al. (2013) proposed SCARA robot kinematics and inverse kinematics in MATLAB environment using Robotics tool box.

Das et al. (2005) presented a complete mathematical model including servo actuator dynamics. The Equations of motions are derived using Lagrangian mechanics. Robot is instructed to achieve pick and place operations of three different size cylindrical objects through assigned holes. Both simulation and experimental responses of robot match reasonably good by considering highly nonlinear characteristics of the robot arm.

Alshamasin et al. (2009) developed a complete mathematical model of SCARA robot including servomotor dynamics and also presented dynamic simulation. Kinematic equations for DC servomotor which drives each robot joint also presented. A SCARA robot was modelled to achieve drilling operation using solid dynamic software. The performance of robot-actuator system was analyzed with solid dynamic simulation and checked with MATLAB/Simulink.

Padhy (1992) presented kinematics and dynamics of a SCARA robot and also discussed the changes on torques of different links using a computer code. It is observed that the torque is independent of the angular position, which makes the robot highly compliant.

Elaiikh et al. (2013) presented a procedure for assessing the vibration analysis of SCARA robots. The simulation studies were performed by the MATLAB software. Modal and dynamic analysis was performed and proposed that in design of the SCARA robot the resonant and excitation frequencies are not close to each other.

Tao et al. (2006) investigated on residual vibrations of SCARA robots used in wafer handling applications. Developed a mathematical model suitable for residual vibration and verified it with experimental results and also presented the trajectories of the robot arm developed by the model.

In the present work optimization of the link lengths for a specific circular deburring path on a component with a specified placement position from the robot base is carried out so as to obtain the minimum power needed for the deburring operation among all the link length sets. This methodology can then be extended to other sizes of the path and placement positions.

The rest of the paper is organized as (i) Summary of mathematical equations used in the analyses (ii) Problem formulation (iii) Results and discussions and (iv) Conclusions.

2 Summary of Mathematical Equations Used in the Analyses

SCARA is a special robotic manipulator with developed kinematic and dynamic equations. The following are the kinematic and dynamic equations available in literature used for the analysis in MATLAB.

$$\theta_2 = \cos^{-1} \left(\frac{p_x^2 + p_y^2 - l_1^2 - l_2^2}{2l_1^2 l_2^2} \right) \quad (1)$$

$$\theta_1 = \tan^{-1} \left(\frac{(l_1 + l_2 c_2) p_y - l_2 s_2 p_x}{(l_1 + l_2 c_2) p_x - l_2 s_2 p_y} \right) \quad (2)$$

$$\dot{\theta}_1 = \left[\frac{(v_x c_{12}) + (v_y s_{12})}{l_1 s_2} \right] \quad (3)$$

$$\dot{\theta}_2 = \left[\frac{(-v_y(l_1 s_1 + l_2 s_{12})) - (v_x(l_1 c_1 + l_2 c_{12}))}{l_1 l_2 s_2} \right] \quad (4)$$

$$\ddot{\theta}_1 = \frac{[a_x + (a_y * \frac{s_{12}}{c_{12}})] - [\dot{\theta}_1^2(l_1 c_1 + l_2 c_{12})] - [2l_2 \dot{\theta}_2^2 c_{12}] - [l_2 c_{12} \dot{\theta}_2^2] - [(\dot{\theta}_1^2(-l_1 s_1 - l_2 s_{12})) + (2l_2 s_{12} \dot{\theta}_1 \dot{\theta}_2) - (l_2 s_{12} \dot{\theta}_2^2)] * \frac{s_{12}}{c_{12}}}{-l_1 s_{12} - l_2 s_{12} + (l_1 c_1 + l_2 c_{12}) \left(\frac{s_{12}}{c_{12}} \right)} \quad (5)$$

$$\ddot{\theta}_2 = \frac{[[\dot{\theta}_1(-l_1 s_1 - l_2 s_{12})] - a_x] + [\dot{\theta}_1^2(-l_1 c_1 - l_2 c_{12})] - (2l_2 c_{12} \dot{\theta}_1 \dot{\theta}_2) - (l_2 c_{12} \dot{\theta}_1 \dot{\theta}_2)}{l_2 s_{12}} \quad (6)$$

$$\begin{aligned} T_1 = & \left\{ \left[\left(\frac{m_1}{3} + m_2 + m_3 \right) l_1^2 \right] + [(\ddot{m}_2 + 2m_3) l_1 l_2 c_2] + \left[\frac{m_2}{3} + m_3 \right] l_2^2 \right\} \dot{\theta}_1 \\ & - \left\{ \left[\left(\frac{m_2}{2} + m_3 \right) l_1 l_2 c_2 \right] + \left[\left(\frac{m_2}{3} + m_3 \right) l_2^2 \dot{\theta}_2^2 \right] \right\} + b_1 \dot{\theta}_1 \\ & - l_1 l_2 s_2 \left[(m_2 + 2m_3) (\dot{\theta}_1 \dot{\theta}_2) - \left(\frac{m_2}{2} + m_3 \right) \dot{\theta}_2^2 \right] \end{aligned} \quad (7)$$

$$T_2 = -\left\{ \left[\left(\frac{m_2}{2} + m_3 \right) (l_1 l_2 c_2) \right] + \left[\left(\frac{m_2}{3} + m_2 \right) (l_2^2) \right] \right\} \ddot{\theta}_1 + \left[\left(\frac{m_2}{3} + m_3 \right) l_2^2 \ddot{\theta}_2 \right] + \left[\left(\frac{m_2}{2} + m_3 \right) l_1 l_2 s_2 \dot{\theta}_1^2 \right] + b_2 \dot{\theta}_2 \quad (8)$$

$$P_1 = T_1 * \dot{\theta}_1 \quad (9)$$

$$P_2 = T_2 * \dot{\theta}_2 \quad (10)$$

3 Problem Formulation

The following assumptions are used for optimizing the link lengths for minimizing power at two joints of SCARA robot. As the burrs are very minor on the component it is assumed that the forces acting on the end-effector are negligible.

3.1 Data Used in the Analyses Is as Follows

The diameter of the circular path is 0.06 m,
 Position of the deburring component is 0.35 m from centre of SCARA robot base.
 Time required to complete one cycle is 10 s,
 Steps taken to complete one cycle is 12 steps,

The Objective function to minimize power subjected to constraints

$$0.350 \leq l_1 \leq 0.400$$

$$0.100 \leq l_2 \leq 0.150$$

$$l_1 + l_2 = 0.500$$

3.2 The Steps Adopted in the Analyses Are as Follows

For the completion of one cycle of circular path, the path is divided into 12 steps as shown in Fig. 2 which represents the top view of SCARA robot. The path is divided into 12 steps are shown as points P_0, P_1 so on to P_{12} . Each step represents 30° . Power is computed at each and every step i.e. for 12 steps and also for the link lengths ranging as mentioned in constraints.

From the given constraints of $l_1 + l_2 = 0.500$ at each and every point of P_0, P_1 , so on up to P_{12} , 51 set of data will be generated as shown in Table 2 for every 0.001 m increase in link length.

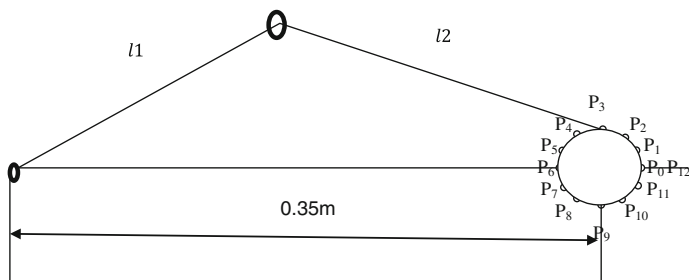


Fig. 2 Top view of a SCARA robot

Table 1 Input data used for analyses

S. no	Time	P_x	P_y	V_x	V_y	a_x	a_y
0	0.00	0.380	0.000	-0.005	0.018	-0.010	-0.006
1	0.83	0.376	0.015	-0.013	0.013	-0.006	-0.010
2	1.67	0.365	0.026	-0.018	0.005	0.000	-0.012
3	2.50	0.350	0.030	-0.018	-0.005	0.006	-0.010
4	3.33	0.335	0.026	-0.013	-0.013	0.010	-0.006
5	4.17	0.324	0.015	-0.005	-0.018	0.012	0.000
6	5.00	0.320	0.000	0.005	-0.018	0.010	0.006
7	5.83	0.324	-0.015	0.013	-0.013	0.006	0.010
8	6.67	0.335	-0.026	0.018	-0.005	0.000	0.012
9	7.50	0.350	-0.030	0.018	0.005	-0.006	0.010
10	8.33	0.365	-0.026	0.013	0.013	-0.010	0.006
11	9.17	0.376	-0.015	0.005	0.018	-0.006	-0.022
12	10.00	0.380	0.000	0.000	0.000	0.000	0.000

In order to decide the motor torque required, it is necessary to find the maximum power generated among the 12 points and also minimum power for each of these 51 variants required among the given constraints of increase of 0.001 m in link length.

$$m_1 = 1.499 \text{ kg} \quad m_2 = 1.001 \text{ kg} \quad m_3 = 0.462 \text{ kg} \quad b_1 = 0.022 \text{ m} \quad b_2 = 0.022 \text{ m}$$

Table 1 presents the input data used for computing power data at two joints.

As there are 12 steps in the circular path and 51 variants at every step the power equations generated are 12 in number. Power equation (objective function) generated from MATLAB is too large (around 8 pages of MS-word), and therefore only part of data is presented in Fig. 3 for joint1 and joint2 respectively (Table 2).

```
(a)
-----Solution of two link robotic arm-----
-----Number of equations obtained-----
The power equation of joint1 is: -(0.5*(0.0195*sin(atan((0.38*L2*(1.0 - (0.25*(L1^2 + L2^2 - 0.144
The power equation of joint1 is: {0.5*(1.0 - (4.0*L1^2*L2^2*((0.25*(L1^2 + L2^2 - 0.1415865339941
The power equation of joint1 is: -(0.5*(0.02*cos(atan((0.02598*L1 - (0.01299*(L1^2 + L2^2 - 0.133
The power equation of joint1 is: -(0.5*(0.019*cos(atan((2.0*L1*L2*(1.0 - (0.25*(L1^2 + L2^2 - 0.1
The power equation of joint1 is: -(0.5*(1.0 - (4.0*L1^2*L2^2*((0.25*(L1^2 + L2^2 - 0.112899960400
The power equation of joint1 is: -(0.5*(0.005*cos(atan((0.015*L1 - (0.0075*(L1^2 + L2^2 - 0.10521
The power equation of joint1 is: -(0.5*(0.005*cos(atan((0.32*L2*(1.0 - (0.25*(L1^2 + L2^2 - 0.102
The power equation of joint1 is: -(0.5*(1.0 - (4.0*L1^2*L2^2*((0.25*(L1^2 + L2^2 - 0.105213466594
The power equation of joint1 is: -(0.5*(1.0 - (4.0*L1^2*L2^2*((0.25*(L1^2 + L2^2 - 0.112899960400
The power equation of joint1 is: -(0.5*(1.0 - (4.0*L1^2*L2^2*((0.25*(L1^2 + L2^2 - 0.1234)^2)/(L1
The power equation of joint1 is: -(0.5*(0.014*cos(atan((2.0*L1*L2*(1.0 - (0.25*(L1^2 + L2^2 - 0.1
The power equation of joint1 is: (0.5*(0.005*cos(atan((2.0*L1*L2*(1.0 - (0.25*(L1^2 + L2^2 - 0.14
The power equation of joint1 is: 0
The final power equation of joint2 is: (0.5*(0.005*cos(atan((2.0*L1*L2*(1.0 - (0.25*(L1^2 + L2^2 -

(b)
-----Solution of two link robotic arm-----
-----Number of equations obtained-----
The power equation of joint2 is: (0.5*(1.0 - (4.0*L1^2*L2^2*((0.25*(L1^2 + L2^2 - 0.144
The power equation of joint2 is: (0.5*(1.0 - (4.0*L1^2*L2^2*((0.25*(L1^2 + L2^2 - 0.141
The power equation of joint2 is: (0.5*(1.0 - (4.0*L1^2*L2^2*((0.25*(L1^2 + L2^2 - 0.133
The power equation of joint2 is: -(0.5*(1.0 - (4.0*L1^2*L2^2*((0.25*(L1^2 + L2^2 - 0.12
The power equation of joint2 is: -(0.5*(1.0 - (4.0*L1^2*L2^2*((0.25*(L1^2 + L2^2 - 0.11
The power equation of joint2 is: (0.5*(1.0 - (4.0*L1^2*L2^2*((0.25*(L1^2 + L2^2 - 0.105
The power equation of joint2 is: (0.5*(1.0 - (4.0*L1^2*L2^2*((0.25*(L1^2 + L2^2 - 0.102
The power equation of joint2 is: (0.5*(1.0 - (4.0*L1^2*L2^2*((0.25*(L1^2 + L2^2 - 0.105
The power equation of joint2 is: (0.5*(1.0 - (4.0*L1^2*L2^2*((0.25*(L1^2 + L2^2 - 0.112
The power equation of joint2 is: -(0.5*(1.0 - (4.0*L1^2*L2^2*((0.25*(L1^2 + L2^2 - 0.1
The power equation of joint2 is: -(0.5*(1.0 - (4.0*L1^2*L2^2*((0.25*(L1^2 + L2^2 - 0.13
The power equation of joint2 is: (0.5*(1.0 - (4.0*L1^2*L2^2*((0.25*(L1^2 + L2^2 - 0.141
The power equation of joint2 is: 0
The final power equation of joint2 is: (0.5*(1.0 - (4.0*L1^2*L2^2*((0.25*(L1^2 + L2^2 -
```

Fig. 3 a Generation of equations in MATLAB for joint1. b Generation of equations in MATLAB for joint2

4 Results and Discussions

For the given constraint $l1 + l2 = 0.50$ in the work space, the number of combinations obtained for the given constraints are 51. Every combination of link lengths has to complete one cycle which consists of 12 steps. So in order to decide the torque of a motor of joint1 or joint2 it is necessary to choose maximum power from the 12 steps. From the 51 combinations it is necessary to choose minimum power in order to get the best combination of link1 and link2.

Figure 4 represents the power of joint1 with respect different combinations of link lengths. Here it is observed that for $l_1 = 0.35$ m and $l_2 = 0.15$ m is the best configuration for minimum power. Similarly Fig. 5 represents the power of joint2 with respect different combinations of link lengths and this is also yielding the same combination.

Table 2 Data for link length combination

S. no	l_1	l_2	S. no	l_1	l_2	S. no	l_1	l_2	S. no	l_1	l_2
1	0.4	0.1	14	0.387	0.113	27	0.374	0.126	40	0.361	0.139
2	0.399	0.101	15	0.386	0.114	28	0.373	0.127	41	0.36	0.14
3	0.398	0.102	16	0.385	0.115	29	0.372	0.128	42	0.359	0.141
4	0.397	0.103	17	0.384	0.116	30	0.371	0.129	43	0.358	0.142
5	0.396	0.104	18	0.383	0.117	31	0.37	0.13	44	0.357	0.143
6	0.395	0.105	19	0.382	0.118	32	0.369	0.131	45	0.356	0.144
7	0.394	0.106	20	0.381	0.119	33	0.368	0.132	46	0.355	0.145
8	0.393	0.107	21	0.38	0.12	34	0.367	0.133	47	0.354	0.146
9	0.392	0.108	22	0.379	0.121	35	0.366	0.134	48	0.353	0.147
10	0.391	0.109	23	0.378	0.122	36	0.365	0.135	49	0.352	0.148
11	0.39	0.11	24	0.377	0.123	37	0.364	0.136	50	0.351	0.149
12	0.389	0.111	25	0.376	0.124	38	0.363	0.137	51	0.35	0.15
13	0.388	0.112	26	0.375	0.125	39	0.362	0.138			

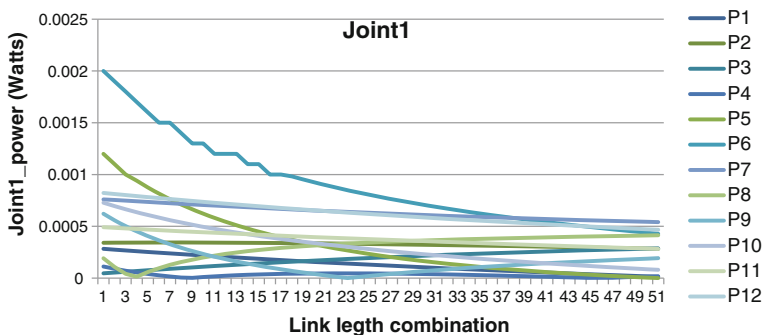


Fig. 4 Joint1 power at 12 steps

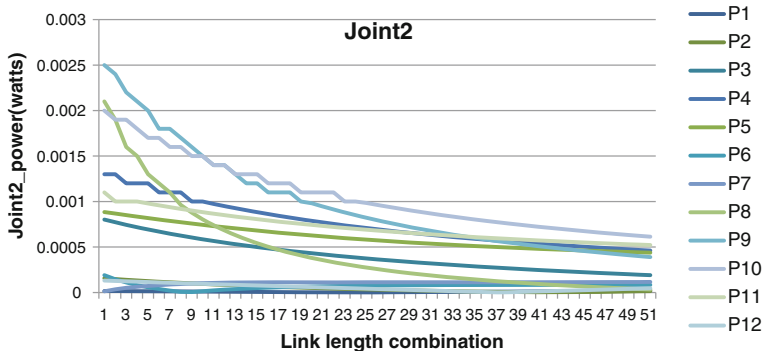


Fig. 5 Joint2 power at 12 steps

5 Conclusions

In the present work it is assumed that the deburring path of circular shaped is positioned at 0.35 m from the base of the SCARA robot, and the diameter of the component is 0.06 m. The Power needed at joint1 and joint2 are computed for different combinations of link lengths for the given constraints. The best configurations of link lengths for minimizing power are obtained for this configuration is 0.35 m for link1 and 0.15 m for link2. It is observed that the link lengths (i.e. Joint1 and Joint2) of a SCARA robot are optimized for minimizing power. The paper presented a method for best configuration of SCARA robot for minimizing power within the workspace constraints. Similar analyses can be repeated for other sizes of robotic circular paths and placement of the component to optimize the power. If a range of products with different diameters are to be deburred, such analyses are carried out for each and every component and minimum power needed to deburr all components in the range. The procedure will enable robotic designers to choose link lengths where customization is needed.

References

- Alshamasin, M. S., Ionescu, F., & Al-Kasasbeh, R. T. (2009). Kinematic modeling and simulation of a SCARA robot by using solid dynamics and Verification by Matlab/Simulink. *European Journal of Scientific Research*, 37(3), 388–405.
- Das, M. T., & Dülger, L. C. (2005). Mathematical modelling, simulation and experimental verification of a SCARA robot. *Simulation Modelling Practice and Theory*, 257–271.
- Elaikh, T. E. H., H. J. Abed, K. M., Swadi, S. M., & Kadhim K. M. (2013). Vibration and kinematic analysis of SCARA robot structure. *Diyala Journal of Engineering Sciences*, 6(3), 127–143.
- Fang, J., & Li, W. (2013). Four degrees of freedom SCARA robot kinematics modelling and simulation analysis. *International Journal of Computer, Consumer and Control*, 2(4), 20–27.
- Padhy, S. K. (1992). On the dynamics of SCARA. *Robotics and Autonomous Systems*, 10(1), 71–78.
- Rehiara, A. (2011). *Kinematics of adept three robot arm*. InTech, <http://www.intechopen.com/books/robot-arms/kinematics-of-adeptThree-robot-arm> (pp. 21–38).
- Tao, W. M., Zhang, M. J., MA, O., & Yun, X. P. (2006). Residual vibration analysis and suppression for SCARA robots in semiconductor manufacturing. *International Journal of Intelligent Control and Systems*, 11(2), 97–105.

Integrating Artificial Intelligence and Simulation for Controlling Steady Flow of Fixtures

Fentahun Moges Kasie, Glen Bright and Anthony Walker

Abstract Fixtures are one of the major problematic components in a manufacturing system because of their complicated design and management requirements. Fixture planning and management problems were not well addressed in the past publications as compared with the attention paid to the design issues. This paper is designed to address this problem using a decision-based fixture assignment and control method. A decision support framework is proposed to determine a steady state flow of fixtures for part orders planned in a specific production period. This framework integrates artificial intelligence technologies, simulations models and database management techniques in order to accommodate flexibility in a dynamic manufacturing situation. The artificial intelligence reveals how case-based and rule-based reasoning techniques work in synergy. The simulation models include discrete event and visual interactive approaches. A decision logic diagram is presented so as to depict the conditions and corresponding decision alternatives.

Keywords Fixture · Decision support system · Artificial intelligence · Simulation · Framework

1 Introduction

Factories of the future are expected to consider several factors so as to compete in a dynamic global market. The fundamental requirements are flexibility, responsiveness, quality of products and efficient resource utilization. Among various activities involved in manufacturing processes, fixtures are one of the major problematic components. Fixtures are required to hold, support and locate work-pieces for a specific manufacturing operation. They directly affect the product quality,

F.M. Kasie (✉) · G. Bright · A. Walker
School of Mechanical Engineering, University of KwaZulu-Natal, Durban,
South Africa
e-mail: fentahunmk@gmail.com; 214584670@stu.ukzn.ac.za

productivity and cost of products (Kumar and Paulraj 2014; Ostojic et al. 2011). The past research results revealed that the cost of fixture design and manufacture contributes to 15–20 % of the total cost of manufacturing (Consalter and Boehs 2004; Ostojic et al. 2011). This cost rises more if they are not well managed and utilized. Fixture planning and organization requires the right decisions to be made by firms so as to reduce operational costs, increase productivity and enhance on-time delivery. Although the issues of fixture manufacture and planning are one of the complex problems, fixture management problems were not adequately researched in the past. Manufacturing firms yet use inconvenient decision making approaches in order to control the flow of fixtures within a system. This causes them unstable flow of fixtures and lower utilization of the available resources. This paper addresses this problem by proposing a theoretical framework which serves as a platform to develop the right decision support systems (DSS). This framework is proposed using the latest literature in DSS.

The remainder of this paper is organized as follows: Sect. 2 describe the importance of the study area. Section 3 briefly presents the roles of artificial intelligence, simulation and their synergy. In Sect. 4, the decision support framework with its implementation steps is discussed. Finally, conclusions and suggestion for future research are forwarded in Sect. 5.

2 Study Area Description

A DSS framework is proposed in this paper by combining artificial intelligence (AI), discrete event and visual interactive simulation (DEVIS), and database management (DBM) methods. DSS is an interactive computer-based systems, which utilizes the required data, models, documents, knowledge and communication technologies to support people who are required to solve complex problems, can be developed through adaptive process of learning and evolutions so as to accommodate changes in dynamic environments at present and in the future (Power 2004a; Keen 1980). DSS has been defined in various contexts following its evolutionary development stages (Power 2004b). The DSS framework in this paper is proposed based on the ideas of this generic definition and it mainly focuses on database/document-based systems, AI and simulation modeling. The database provides the required facts concerning the existing situation. Discrete event simulation (DES) models help to study the performance scenarios of different fixture assignment decisions. The visual interactive capabilities of simulation models are required to visualize blocked and starved work centers because of the unbalanced flow of fixtures within a manufacturing system. The AI component incorporates rule-based reasoning (RBR) and cased-based reasoning (CBR) approaches that provide explanations and machine learning capabilities to the proposed assignment decisions.

The past publications were largely concerned on modular fixture design concepts using computer-aided fixture design (CAFD) facilities. A wide range of techniques

were devised to make designs more flexible and modular so as to accommodate various part types (e.g. see Wang et al. (2010) and Boyle et al. (2011)). However, research in fixture planning and management to enhance the utilization of such fixtures and all the available resources, was not well addressed. This is because part planning is considered as a major issue but fixture management is underestimated. This misunderstanding causes low resource utilization and poor performance (Özbayrak and Bell 2003; Rahimifard and Newman 1997). In Rahimifard and Newman (1997), a simulation based multi-flow scheduling system was presented namely work-piece dominated, tool dominated and fixture dominated planning strategies. The fixture dominated planning strategies were two types: (1) fixture cluster-based job allocation which clusters jobs into similar fixture requirements to assign specialized fixtures, and (2) fixture availability-based job allocation which assigns jobs into the available modular fixtures.

This paper presents a novel DSS framework which combines AI, DEVIS and DBM for on-demand fixture manufacture, storage and supply. Combining AI, DEVIS and DBM is popular in several manufacturing operations at shop floor level, however it has not adequately been addressed in fixture and tool management problems as mentioned above. This paper aims at filling this gap and introducing this approach during fixture assignment decisions. The proposed theoretical DSS framework provides a platform for empirical research in the future. Using this framework, fixtures can be planned in parallel to any feasible part flow plans. This avoids the unnecessary congestion of fixtures and production downtime by ensuring the steady state flow of fixtures in advance in a particular production period. It also is used to validate and test alternative plans prior to the final implementation by utilizing DEVIS models.

3 Artificial Intelligence and Simulation

Embedding AI into a DSS enhances the quality of decision outputs (Turban and Watkins 1986). RBR is a deductive reasoning approach, which uses the existing domain knowledge largely from expert systems in the form of rules to infer about a new situation, while CBR is an inductive reasoning approach, which draws inferences based on experiences learned from the previously encountered cases (Chi and Kiang 1991; Prentzas and Hatzilygeroudis 2007). RBR and CBR are two extreme approaches, having their own merits and demerits. Many real-life problems occur between these ends. Combining RBR and CBR are popular strategies to be benefited from their synergic effects in reality (Chi and Kiang 1991; Prentzas and Hatzilygeroudis 2007; Aamodt and Plaza 1994; Kolodner 1992). According to Aamodt and Plaza (1994), a general CBR cycle is presented by four processes named retrieve, reuse, revise and retain (Fig. 1).

Retrieve is searching of the most similar historical case that matches to a new case by developing predefined similarity measures. If the retrieved case directly matches to the new problem, it reuses the retrieved case as a solution. If the critical

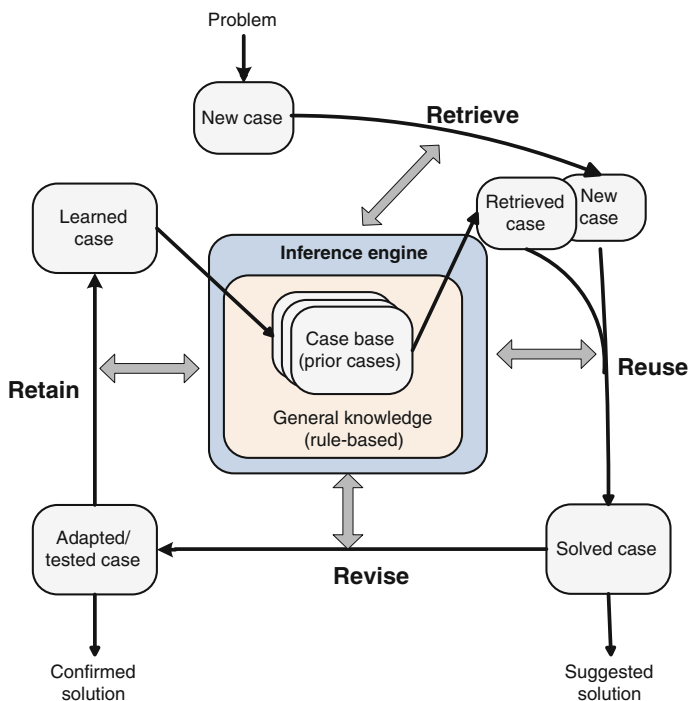


Fig. 1 CBR cycle integrated with RBR adapted from Aamodt and Plaza (1994)

features of the retrieved case do not match to the new case, it undergoes a revision so as to adapt to the new problem. The adaptation rules can be applied from the general knowledge domain. The adapted solution is tested and verified using techniques like simulation. Finally, the confirmed solution is retained with its corresponding problem as the learned case for future reuse and adaptation. This cycle continues to improve the CBR using a retrieve-adapt-learn process.

Simulation involves the imitation of descriptive computer models of a complex system and exercising those models to predict the operational performances of the underlying system being investigated (Smith 2003). It is widely accepted in decision making because of its computational power, cost reduction, addressing the complex systems with no productivity-paradoxes, visual interactive capabilities for identifying bottlenecks and flexibility in dynamic situations (Jahangirian et al. 2010; AlDurgham and Barghash 2008; Ali and Seifoddini 2006).

A combination of AI and simulation models are essential to develop intelligent simulation models for planning and control of production systems (Rahimifard and Newman 1997). Designing a simulation alone DSS may not usually be practical because it is time-consuming and results in significant delays due to the users intervention to compare the candidates actions and interpret simulated results (Pehrsson et al. 2013; Rogers and Gorden 1993). Integrating simulation with an AI is required so as to address these challenges (Chan and Chan 2004). An integrated

approach makes the DSS more flexible and knowledgeable to emulate human expertise that helps decision makers in understanding, expressing and structuring their problems (O’Keefe and Roach 1987; Angehrn and Lüthi 1990; Mahdavi et al. 2010; Conteh and Forjionne 2005).

4 Theoretical Framework

The conceptual framework indicated in Fig. 2 is proposed by assuming the manufacturing environment is dynamic and deterministic in a specific production period. Assuming m products are scheduled to be produced in this short production period, the framework aims at determining n -bounded stable flow of fixtures using a decision-based part order to fixture assignment. This framework consists of four major components named simulation model, database/document base, artificial intelligence and user interface. The database/document base component

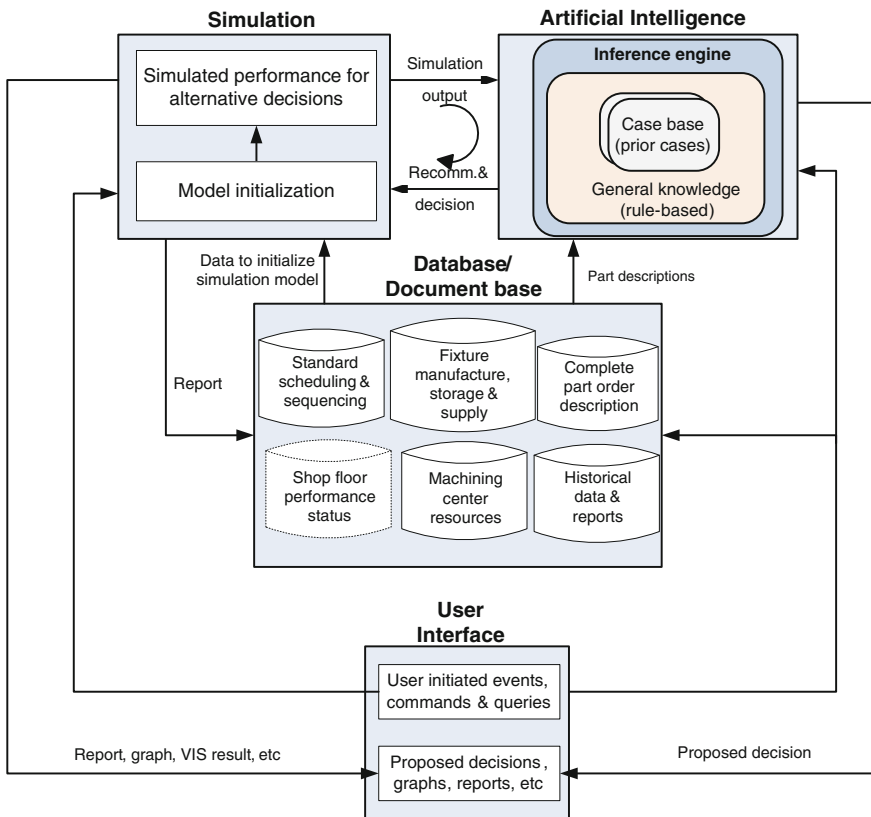


Fig. 2 Theoretical framework

incorporates all the facts that are required to simulate and run the system. It specifically includes part descriptions (e.g. geometric features and process plan sets); the resources required at shop floor level (operators, available machines, work centers, fixture, tools, jigs, buffers, material handling equipment, AS/R, etc.); and the operational parametric specifications such as the capacities and working principles of machines, materials handling equipment, etc.

The simulation component receives the required information from the database and the recommended decisions from the AI component. It performs ‘what-if’ analysis for alternative fixture assignment decisions. The AI component retrieves the most similar historical case of fixture assignment decision that fits at most with a new part order. The inference engine utilizes both cases and rules so as to recommend the right decision with sufficient explanations to the users and decision-based control systems that are anticipated to take the necessary measures. The user interface is the one which communicates the user and DSS. The users interact with the DSS and receive recommendations with their corresponding explanations from the AI subsystem.

This framework can be adapted to the research problem using the decision logic indicated in Fig. 3. Consider a planner is in charge to assign fixtures to different part orders. The part orders are arriving with different geometric features and process requirements. The planner wants to determine a steady state flow of fixtures for his production plan in a specific and short production period, which avoids blocking and starving within a manufacturing system. The best approach to solve such a complex problem is referring to the past experiences of similar part orders i.e. remembering the fixtures that were assigned to the most similar part orders. Remembering the historical decisions is really a difficult solution approach to the planner in a complex manufacturing situation. Nevertheless, this complex problem can be solved using the combination of AI technologies and simulation modeling. All the historical cases can be retrieved and reused or adapted to the new situation by applying CBR technique, and these activities can be directed by developing different rules using RBR approach.

The simulation models are used to confirm the validity of the decisions made by this hybrid AI approach. In Fig. 3, the new case represents a part order arrival with a complete description of geometric features and process requirements. The planner is required to assign the right fixture to a new part order with help of the recommendation from DSS. The special tool in AI, the inference engine evaluates all the past assignment decisions in the case base and retrieves the most similar prior case using a similarity function. The similarity metrics consists of all the parametric features of the new part order, which can identify the best historical decision in order to match to the new problem. The rules and procedures for implementing this framework are briefly described as follows:

1. Database preparation

- Determine the feature vectors of part orders that characterize their similarities for fixture assignment;

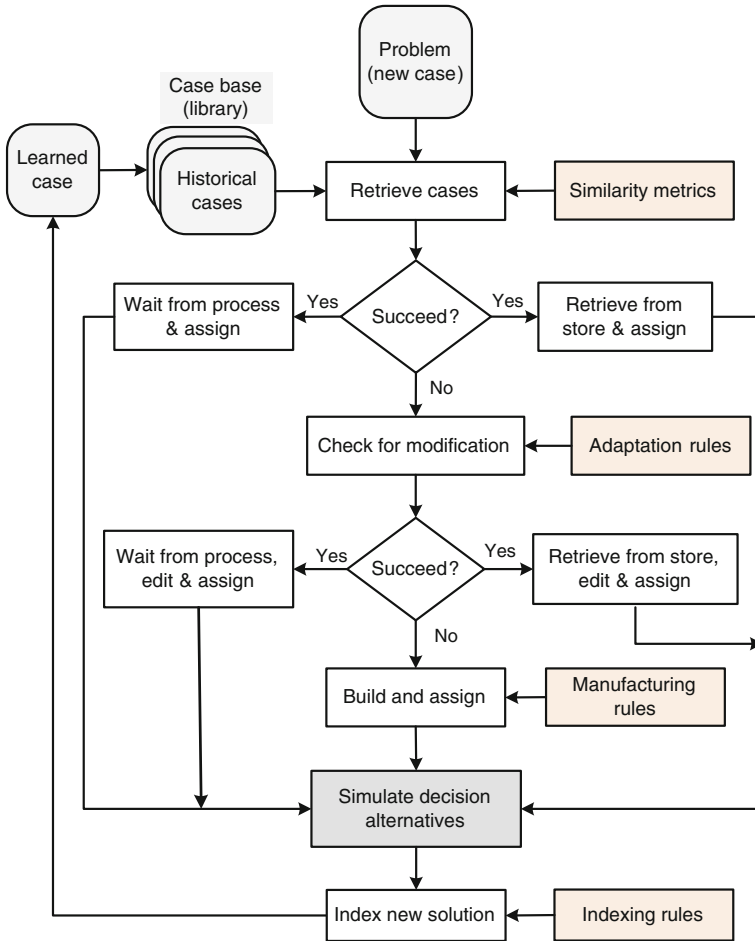


Fig. 3 Decision logic and flowchart for problem statement

- Prepare the database for the part orders based on their feature vectors (Table 1);
- Prepare database for fixtures availability; and
- Prepare database for all the required resources mentioned above to run the system.

2. Initializing

- Initialize the system program by assigning a limited number of fixtures for the first part orders the can serve as references or prepare training samples in the case base.
- Initialize the DEVIS models.

Table 1 Incidence matrix of feature vectors

	W_1	W_2	...	W_n
	F_1	F_2	...	F_n
P_1	a_{11}	a_{12}	...	a_{1n}
P_2	a_{21}	a_{22}	...	a_{2n}
\vdots	\vdots	\vdots	...	\vdots
P_m	a_{m1}	a_{m2}	...	a_{mn}

where

m is the total number of part order in the feasible part schedule
 n is the total number of feature vectors

$P_1 \dots P_m$ are m finite part-orders

$F_1 \dots F_n$ are n finite feature vectors

a_{ij} is the (standardized) value of feature vector F_j ($j = 1 \dots n$) for each part-order P_i ($i = 1 \dots m$)

$w_1 \dots w_m$ are normalized weights assigned to feature vectors

3. Running the system

- A problem (new case) = a part-order arrival with its feature vectors from the database.
- When the new part order arrives, retrieve the prior cases from the case base and compare them with the new case using the nearest neighbor similarity functions (commonly Euclidean distance d_e). The d_e between two n -dimensional vectors, for any two part-orders k and l is given by the equation:

$$d_e = \sqrt{\sum_{j=1}^n w_j^2 (a_{lj} - a_{kj})^2}$$

- Sort the d_e values and select the historical case with minimum d_e value.
- When $d_e \approx 0$, re-use the selected case and check the availability of the required fixture in a store (database).
 - If it is available, retrieve and assign (fixture assignment decision-I).
 - If it not available, wait from the process and assign (fixture assignment decision-II).
- When d_e is a bit larger, check for adaptation. This adaption maybe either permanent or temporary modification based on the utilization history of the fixture. The d_e value for adaptation (e.g. reconfiguration) must be decided ahead from experience.
- If modification is succeeded, check the availability of the required fixture in a store.
 - If it is available, retrieve, edit and assign (fixture assignment decision-III).
 - If it not available, wait from the process, edit and assign (fixture assignment decision-IV).

- If modification is impossible, the selected case is not applied.
 - Manufacture a new fixture and assign (fixture assignment decision-V).
4. Validating and testing
 - Simulate all the decision alternatives using DEVIS method to test and validate the performance of each assignment decision.
 5. Indexing
 - Provide an identification label to every accepted assignment decision with its corresponding problem for the immediate future retrieval, reuse and adaptation. Every new solution must be retained as the learned cases and stored in the case library as new historical cases.

5 Conclusions and Suggestions for Future Research

The proposed framework reveals how the integrated components DSS such as AI, DEVIS and DBM technologies work together so as to perform decision-based fixture assignment to part orders. Five alternative subsets of fixture assignment decisions are clearly illustrated. The end result of these subsets of decision is ensuring stable n -bounded flow of fixtures in parallel to any feasible part plans. The required knowledge to implement this framework is identifying the feature vectors which are needed to determine the similarity between the new case and prior cases. This knowledge can effectively be represented by developing a standard program/software in any modern programming languages. Object-oriented programming, knowledge and data structuring, and graphical user interfacing skills are essential to develop and make practical this DSS framework. The performance of this decision-based assignment can easily be validated and tested using the available commercial simulation software packages. According to this framework, RBR and CBR are not usually incompatible each other, users are able to emerge synergistic capabilities in order to solve such complicated problems. The framework proposed in this paper is so flexible that it can easily be adapted to any decision-based assignments like control of jigs, tools, pallets, etc. It can serve as a platform for academicians and practitioners who are interested to carry out research in decision-based control and assignment of any flowing items in a firm.

In the future, a practical DSS will be developed using the proposed theoretical framework and realistic results will be presented. Currently, the authors are working on the development of a real DSS using C++ programming language and FlexSim simulation software package. The entire real system including test results will be presented in the near future. When this DSS framework is developed as a full package, users without having complex analytical skills can efficiently run it with help of AI technologies, which is the major benefit of this framework over the simulation alone DSS. Recently, commercial simulation software packages are

available incorporating powerful 3D visual interactive simulation graphics and appropriate environments for developing intelligent algorithms. The machine learning and pattern recognition capabilities in AI will provide a superior power to recognize document-oriented and non-numeric information. This will be a good opportunity for the future manufacturers in order to utilize a large portion of their unstructured document/text-oriented information. More complex problems will easily be solved by integrating the best combinations simulation, AI and database management technologies in the next generation manufacturing systems.

References

- Aamodt, A., & Plaza, E. (1994). Case-based reasoning: foundational issues, methodological variations, and system approaches. *AI Communications*, 7(1), 39–59.
- Aldurgham, M. M., & Barghash, M. A. (2008). A generalised framework for simulation-based decision support for manufacturing. *Production Planning and Control: The Management of Operations*, 19(5), 518–534.
- Ali, S. A., & Seifoddini, H. (2006). Simulation intelligence and modelling for manufacturing uncertainties. In L. F. Perrone, F. P. Wieland, J. Liu, B. G. Lawson, D. M. Nicol, & R. M. Fujimoto, (Eds.), *Winter Simulation Conference* (pp. 1920–1928).
- Angehrn, A. A., & Lüthi, H. J. (1990). Intelligent decision support systems: a visual interactive approach. *Interfaces*, 20(6), 17–28.
- Boyle, I., Rong, Y., & Brown, D. C. (2011). A review and analysis of current computer-aided fixture design approaches. *Robotics and Computer-Integrated Manufacturing*, 27, 1–12.
- Chan, F. T. S., & Chan, H. K. (2004). A comprehensive survey and future trend of simulation study on FMS scheduling. *Journal of Intelligent Manufacturing*, 15(1), 87–102.
- Chi, R. T. H., & Kiang, M. Y. (1991). An integrated approach of rule-based and case-based reasoning for decision support. In *Proceedings of the 19th annual conference on Computer Science* (pp. 255–267).
- Consalter, L. A., & Boehs, L. (2004). An approach to fixture systems management in machining processes. *Journal of the Brazilian Society of Mechanical Sciences and Engineering XXVI*, 2, 145–152.
- Conteh, N. W., & Forgionne, G. (2005). A just-in-time approach to intelligent decision support systems. *Journal of Decision Systems*, 14(2), 39–54.
- Jahangirian, M., Eldabi, T., Naseer, A., Stergioulas, L. K., & Young, T. (2010). Simulation in manufacturing and business: a review. *European Journal of Operational Research*, 203, 1–33.
- Keen, P. G. W. (1980). Adaptive design for decision support systems. *Database, Sloan School of Management Review*, 12(1–2), 15–25.
- Kolodner, J. L. (1992). An introduction to case-based reasoning. *Artificial Intelligence Review*, 6, 3–34.
- Kumar, K. S., & Paulraj, G. (2014). Analysis and optimization of fixture under dynamic machining condition with chip removal effect. *Journal of Intelligent Manufacturing*, 25(1), 85–98.
- Mahdavi, I., Shirazi, B., & Solimanpur, M. (2010). Development of a simulation-based decision support system for controlling stochastic flexible job shop manufacturing systems. *Simulation Modelling Practice and Theory*, 18, 768–786.
- O’keefe, R. M., & Roach, J. W. (1987). Artificial intelligence approaches to simulation. *The Journal of the Operational Research Society*, 38(8), 713–722.
- Ostojic, G., Stankovski, S., Vukelic, D., Lazarevic, M., Hodolic, J., Tadic, B., & Odrli, S. (2011). Implementation of automatic identification technology in a process of fixture assembly/disassembly. *Strojniški vestnik – Journal of Mechanical Engineering*, 57(11), 819–825.

- Özbayrak, M., & Bell, R. (2003). A knowledge-based decision support system for the management of parts and tools in FMS. *Decision Support Systems*, 35, 487–515.
- Pehrsson, L., Amos, H. C., Ng, A. H. L., & Stockton, D. (2013). Industrial cost modeling and multi-objective optimisation for decision support in production systems development. *Computers & Industrial Engineering*, 66, 1036–1048.
- Power, D. J. (2004a). Specifying an expanded framework for classifying and describing decision support systems. *Communications of the Association for Information Systems*, 13, 158–166.
- Power, D. J. (2004b). Decision Support Systems: From the past to the future. *Proceedings of the Americas Conference on Information Systems*, (pp. 2025–2031).
- Prentzas, J., & Hatzilygeroudis, I. (2007). Categorizing approaches combining rule-based and case-based reasoning. *Expert Systems*, 24(2), 97–122.
- Rahimifard, S., & Newman, S. T. (1997). Simultaneous scheduling of workpieces, fixtures and cutting tools within flexible machining cells. *International Journal of Production Research*, 35 (9), 2379–2396.
- Rogers, P., & Gorden, R. J. (1993). Simulation for real-time decision making in manufacturing systems. *Winter simulation conference* (pp. 866–874).
- Smith, J. S. (2003). Survey on the use of simulation for manufacturing system design and operation. *Journal of Manufacturing Systems*, 22(2), 157–171.
- Turban, E., & Watkins, P. R. (1986). Integrating expert systems and decision support systems. *MIS Quarterly*, 10(2), 121–136.
- Wang, H., Rong, Y., Li, H., & Shaun, P. (2010). Computer aided fixture design: recent research and trends. *Computer-Aided Design*, 42, 1085–1094.

Predictions of Hip and Knee Power Consumptions of Patients Having Different Body Heights and Masses During Normal Walking

Abhishek Rudra Pal, Ankit Omprakash Mundada
and Dilip Kumar Pratihar

Abstract A range of body heights is assumed for human-beings and the corresponding body masses are calculated based on body mass index (BMI). Masses, moments of inertia, lengths and centers of masses of all body limbs are computed. Inverse kinematics is conducted to find out the required joint angles to achieve a suitable gait cycle. Based on these angles, forward kinematics and inverse dynamics are carried out in order to determine torques and subsequently, power consumptions at knee and hip joints for flexion/extension. By taking body heights and masses as inputs and power consumptions at knee and hip joints as the outputs, multilayer feed-forward neural network architecture is developed. The neural network is trained using back-propagation algorithm. After the training, an input-output relationship between body heights, body masses and power consumption at knee and hip joints, is established. From this data bank, it is possible to predict the required power consumptions at knee and hip joints for a variety of patients of different body heights and masses, on-line.

Keywords Hip and knee power consumptions · On-line predictions · Multilayer feed-forward neural network · Back-propagation algorithm

1 Introduction

To design a suitable orthotic device, which will suit to various patients of different body heights and masses, it is essential to have prior information of gait cycle and joint torque or power consumption data. Variable damping was applied at the knee

A.R. Pal

Advanced Technology Development Center, Indian Institute of Technology Kharagpur,
Kharagpur 721302, West Bengal, India

A.O. Mundada · D.K. Pratihar (✉)

Department of Mechanical Engineering, Indian Institute of Technology Kharagpur,
Kharagpur 721302, West Bengal, India
e-mail: dkpra@mech.iitkgp.ernet.in

© Springer India 2016

D.K. Mandal and C.S. Syan (eds.), *CAD/CAM, Robotics and Factories of the Future*, Lecture Notes in Mechanical Engineering,
DOI 10.1007/978-81-322-2740-3_16

149

joint of a novel orthotic device designed by Nikitzuk et al. (2010). The brakes of these devices were filled with electro-rheological fluid, whose viscosity could be altered by changing the electric field. This resulted in a wide range of torques. But, this device was not tested in patients during walking under practical circumstances. Moreover, this device was heavy, as the power source was over-designed due to the lack of information on power consumptions or torque requirements for the patients of various body heights and masses. A plenty of valuable studies on gait cycle analysis had been reported (Dollar and Herr 2008), and in several other work. Artificial neural network was widely used along with inverse dynamics to predict the joint torque from EMG signal and kinematic angle data (Wang and Buchman 2002). A study of predicting lower extremity joint torque, from ground reaction force and related parameters derived from ground reaction force, in case of counter-movement and squat jumping had been reported by Liu et al. (2009). But, only a few attempts were made, where by solving inverse kinematics, the appropriate values of angles had been found for different sizes of the patients. In the present study, a range of body height along with body mass is considered. Then, individual body segment or limb's length, location of center of mass and moment of inertia are calculated. Inverse kinematics problem is solved using these data to find out a set of suitable joint angles. By using Lagrangian energy approach, inverse dynamics problem is solved to find out power consumption. By feeding these data in a neural network, an input-output model has been established. Inputs are body height and body mass, and the outputs are power consumptions at knee and hip joints. This model is developed to predict the values of maximum power consumption required by a patient of any height and mass to complete a normal gait cycle, within the pre-assumed range of body height and mass.

2 Mathematical Modeling

The necessary parameters for kinematics and dynamic analysis, as for example, the data related to masses, lengths and centers of mass locations of body limbs are taken from Plagenhoef et al. (1983), Drillis and Contini (1966). Radii of gyration data are taken from Paolo (1996). The values of all the parameters are obtained by averaging the corresponding parameters' values of male and female, where average mass, height and age of men are 73 kg, 1730.1 mm and 23.8 years, respectively, and that for women are 61.99 kg, 1730.5 mm and 19.0 years, respectively. These parameters' values are shown in Table 1.

In the present study, head, arms and trunk are considered to be one link, called as HAT (refer to Fig. 1) for simplicity. For calculating the moment of inertia of a particular segment, the following expression is used (Drillis and Contini 1966).

Table 1 Limbs' masses, lengths, centers of masses and radii of gyration of human lower extremity

Limbs	Mass (% total body weight)	Mean length (% total body height)	Center of mass location from proximal end (% segment length)	Radius of gyration in sagittal point (% segment length)
Head	8.23	10.75	55.00	34.60
Trunk	45.92	29.50	59.95	36.45
Upper arm	3.08	17.25	44.70	28.15
Lower arm	1.72	15.85	43.20	26.85
Hand	0.58	5.75	46.80	57.95
Thigh	11.13	24.05	43.05	34.90
Shank	5.05	25.20	42.65	26.30
Foot	1.38	15.20	50.00	27.80

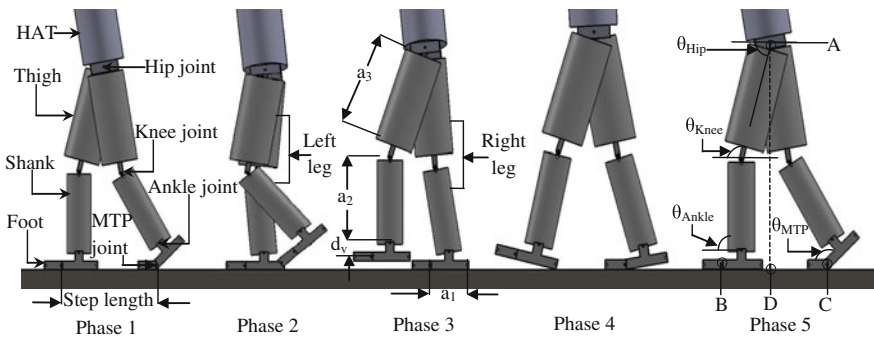


Fig. 1 Phases in normal half-gait cycle

$$I = M \times \bar{m} \times (l \times \bar{r}^2) \tag{1}$$

where M is total body mass, l is segment length, \bar{m} and \bar{r} are the relative mass and radius of gyration of a limb.

In Fig. 1, a solid-works model of human lower extremity along with HAT has been shown for half of a gait cycle during normal walking. The gait cycle has been divided into four phases. Phase 1 indicates loading response for right leg and pre-swing for left leg. In phase 2, initiation of middle stance for right leg and initial swing for left leg are started. Phase 3 starts with the ends of mid-stance for right leg and mid-swing for left leg. Finally, terminal stance of right leg and terminal swing of left leg are occurred in phase 4. Then, motion reversal is taken place in phase 5. The lengths of foot, shank, and thigh for both the legs are denoted by a_1 , a_2 and a_3 , respectively. The vertical distance between ankle and MTP (metatarsophalangeal articulation) joint is shown by d_v .

For inverse kinematics formulation, MTP joint angle (θ_{MTP}), ankle joint angle (θ_{Ankle}), knee joint angle (θ_{Knee}) and hip joint angle (θ_{Hip}) are indicated by $\theta_1, \theta_2, \theta_3$ and θ_4 , respectively, for the left leg and by $\theta_5, \theta_6, \theta_7$ and θ_8 , respectively, for the right leg. BC (refer to Fig. 1) represents step length (Murray et al. 1964). Step length is assumed to vary from $(0.414 \times (\text{body height} / 2))$ to $(0.614 \times (\text{body height} / 2))$ with an increment of 0.1 (Dutton 2012).

Now, from kinematic analysis, the expressions for displacement along the horizontal (x) and vertical directions (y) for both the right and left legs (as each leg consist of three limbs: thigh, shank and foot) are given as follows:

$$\left. \begin{aligned} x &= a_1 c_1 - d_v s_1 + a_2 c_{12} + a_3 c_{123} \\ y &= a_1 s_1 + d_v c_1 + a_2 s_{12} + a_3 s_{123} \end{aligned} \right\} \quad (2)$$

Here, $c_1 = \cos \theta_1$, $s_1 = \sin \theta_1$, $c_{12} = \cos(\theta_1 + \theta_2)$, $s_{12} = \sin(\theta_1 + \theta_2)$, $c_{123} = \cos(\theta_1 + \theta_2 + \theta_3)$, $s_{123} = \sin(\theta_1 + \theta_2 + \theta_3)$. From Eq. (2), the expressions for x and y can be transformed to $x = K_1 c_1 - K_2 s_1$, $y = K_1 s_1 + K_2 c_1$.

Where $K_1 = a_1 + a_2 c_2 + a_3 c_2 c_3 - a_3 s_2 s_3$ and $K_2 = d_v + a_2 s_2 + a_3 s_2 c_3 + a_3 c_2 s_3$.

Now, x and y can further be written as follows: by $x = r \cos(\lambda + \theta_1)$, $y = r \sin(\lambda + \theta_1)$. where $r = \sqrt{K_1^2 + K_2^2}$, $\gamma = \tan^{-1} \left(\frac{K_2}{K_1} \right)$.

Finally, the expression of θ_1 can be determined as follows:

$$\theta_1 = \tan^{-1} \frac{y}{x} - \gamma \quad (3)$$

Now, squaring and adding the expressions for x and y from Eq. (2), the following expression for θ_2 can be obtained.

$$\theta_2 = \cos^{-1} \frac{T}{R} + \lambda, \quad (4)$$

where $T = \frac{(x^2 + y^2 - a_1^2 - d_v^2 - a_2^2 - a_3^2 - 2a_2 a_3 c_3)}{2}$ and $\lambda = \tan^{-1} \frac{(d_v a_2 - a_1 a_3 s_3 + d_v a_3 c_3)}{(a_1 a_2 + a_1 a_3 c_3 + d_v a_3 s_3)}$.

For the phase when motion reversal starts (that is phase 5), the foot is in contact with ground. In this phase, left foot remains flat or neutral, which indicates that MTP joint (θ_1) and ankle joint (θ_2) become equal to 0° and 90° , respectively. In this phase, 15° to 20° (with an increment of 1°) of knee flexion (θ_3) is assumed (Shultz et al. 2009). From Eq. (2), BD and DA can be determined, which are the displacements along x and y-directions, where MTP joint of left foot is considered to be the starting point. Now, DC can be calculated by subtracting BD from BC. Now, the front foot of right leg also touches ground and remains neutral. For the right leg, the displacements in horizontal and vertical directions are denoted by DC and DA, respectively. These two displacements are already obtained as discussed above. Now, the expression of MTP joint angle (θ_5) and ankle joint angle (θ_6) for right leg can be obtained by using the Eqs. (2)–(4), as a function of knee flexion angle of right leg (θ_7). Flexion angle for right leg can be assumed to vary from 35° to 40°

(with an increment of 1°) (Loudon et al. 2008). During normal walking, it is assumed that the pelvis (for present study HAT) is moving forward with an angle of 10° with respect to the ground. This pelvis angle is the sum of MTP, ankle, knee and hip joints angles. Now, after calculating the value of MTP and ankle joint angle as function of knee flexion angle, which is assumed to vary within a range, the value of hip angle (θ_8) can be obtained by subtracting sum of MTP, ankle and knee joints angles from the pelvis joint angle. Now, depending on the variations of length of thigh, shank and foot of different patients, different sets of MTP, ankle, knee and hip joints' angles can be found out, by the procedure mentioned above. For the phase 4, knee flexion angle (θ_3) for left leg is assumed to be equal to 5° (as thigh and shank cannot be collinear for normal human being). MTP and ankle joint angle (θ_1 and θ_2) are also set to be equal to 0° and 90° in phase 4. Now, hip joint angle (θ_4) can be found by subtracting the sum of MTP, ankle and knee joints' angles ($\theta_1 + \theta_2 + \theta_3$) from the already assumed pelvis angle in phase 5 (that is, 10°). Similarly, for right leg, the different joint angles (θ_5, θ_6 and θ_8) can be determined by assuming a range of right leg knee flexion angle (θ_7) from 12° to 17° (with an increment of 0.1°). For phase 2, a flexion of 20° knee joint angle for the leg in swing phase (left leg) and an extension of 25° hip joint angle are considered. The MTP joint and ankle joint angles' for the left leg remain neutral and for the right leg, a dorsiflexion of 5° from neutral is occurred. The knee and hip joints' angles of the right leg (the leg in stance phase) extend about 5°. Then, in phase 3, an extension of 20° of knee joint angle and 10° of hip joint angle is occurred for the leg in swing phase. MTP and ankle joints' angles become neutral for the leg in swing phase. For the leg in stance phase, ankle joint flexes to 10°. Hip and knee joints' extensions of 10° and 25°, respectively, are taken place. Loading response (Phase 1) is the same, as in phase 5, except the legs are interchanged.

It is assumed that during double support phase, both the legs experience ground reaction forces, which are so exerted that the total load is equally distributed between the two legs. Inverse dynamics problem is solved to obtain the expressions of torque and power consumption by using a total number of 12 degrees of freedom, which are as follows: hip, knee, ankle, MTP joints' flexion/extension and hip's abduction/adduction (4° abduction and adduction are assumed) for both the legs. Torque is determined by taking into account the half of mass of the HAT system for the purpose of analysis in double support phase.

Torque for i th joint is expressed using Eq. (5), as given below.

$$\tau_i = \frac{d}{dt} \left(\frac{\partial L}{\partial \dot{\theta}_i} \right) - \frac{\partial L}{\partial \theta_i}, \tag{5}$$

where $L = \sum_{i=1}^n (K_i - P_i)$, $K_i = \frac{1}{2} m_i v_i^2 + \frac{1}{2} I_i \omega_i^2$, $P_i = m_i g y_i$, $v_i = \sqrt{(\dot{x}_i^2 + \dot{y}_i^2)}$, m_i is the mass of i th link and g is the acceleration due to gravity. I_i indicates the moment of inertia (kg mm^2) of i th link, \dot{x}_i and \dot{y}_i are linear velocities of center of mass of i th link along horizontal and vertical directions, respectively. ω_i is the angular velocity (rad/s) of i th link. Linear displacements of the center of mass of i th

link along the horizontal (x_i) and vertical (y_i) directions can be calculated by using D-H parameters' rules. To consider the heat loss of motor, an extra term is added to obtain the expression for actual power consumption (P_{ci}) for i th link, as given by Eq. (6). Akima cubic spline derived by Fried and Zietz (1973) forms the basis for variation of time and different parameters of joint, such as angular displacement θ_i and angular velocity $\dot{\theta}_i$.

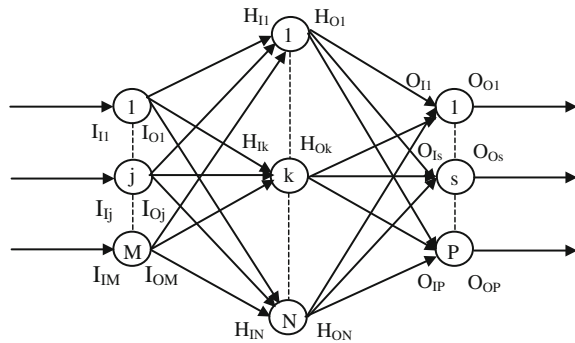
$$P_{ci} = \tau_i \dot{\theta}_i + \int_0^t C \tau_i^2 dt \quad (6)$$

where energy loss due to heat emission is denoted by the integral term in Eq. (6). Here, the value of C is taken from Nishii et al. (1998), which (dependent on the properties of motor) is assumed to be equal to 0.025.

3 Input-Output Modeling by Back-Propagation Neural Network

Human always tries to maintain a gait cycle, in which minimum power is consumed by each joint of lower or upper extremity. To establish the input-output relationship, a range of patients of various body heights and masses is taken. Body heights of the patients vary from 4 feet 10 in. (1473.2 mm) to 6 feet 5 in. (1955.8 mm) with an increment of 1 inch (25.4 mm). Body mass (kg) is calculated by multiplying the body mass index (BMI) with the square of body height (mm). BMI varies from 19 to 29 with an increment of 0.1. So, the total number of training scenarios (or number of patients) is calculated to be equal to 2020 (this number is obtained by $((1955.8 - 1473.2)/25.4 + 1) \times ((29 - 19)/0.1 + 1)$). For each scenario, the total number of sets of angles or gait cycles is calculated to be equal to 648 (obtained by $((20 - 15)/1 + 1) \times ((40 - 35)/1 + 1) \times ((17 - 12)/1 + 1)$). So, each patient is tested against 648 number of gait cycles. Each gait cycle is defined for 8 s with an increment of 0.04 s (duration of each of 4 phases for each of two legs is taken as 1 s). Then, the maximum power consumption value is calculated from these 201 time-steps' $((8 - 0)/0.04 + 1)$ values. So, only a single value of power consumption is obtained from each gait cycle. Now, among these gait cycles, that with the minimum power consumption values at knee and hip joints is selected. Therefore, two outputs of the developed neural network system are taken to be power consumptions at knee and hip joints corresponding to the two inputs, which are body height and body mass. Now, a multilayer feed-forward neural network model (refer to Fig. 2) is developed with these sets of inputs and outputs. The architecture of the multilayer feed-forward neural network involves one hidden layer along with the one input and output layers, each consists of two neurons. The Levenberg-Marquardt algorithm, developed by Levenberg (1944), Marquardt (1963) is used, for training the network. It is assumed that a linear transfer function is used in input layer. The network is trained in order to

Fig. 2 Multi-layer feed-forward neural network



get the minimum mean squared error between the predicted and target outputs. It is to be noted that power consumptions at the knee and hip joints are considered as the outputs of the network. Here, the expression for mean squared error (MSE) in prediction for t_s number of training scenario and n_p number of output neurons can be expressed as $MSE = \frac{1}{t_s n_p} \sum_{l=1}^{t_s} \sum_{k=1}^{n_p} (T_{olk} - O_{olk})^2$, where T_{olk} and O_{olk} are the corresponding target and predicted outputs, respectively, for l th training scenario and k th output neuron.

In Fig. 2, I_{Ij} and I_{Oj} indicate the input and output of j th input neuron. H_{Hk} and H_{Ok} denote the input and output of k th hidden neuron and O_{Is} and O_{Os} indicate the inputs and outputs of s th output neuron.

4 Results and Discussion

In order to get the minimum MSE, the network is trained for four different cases by taking 2020×2 input and output data. Each of the cases is trained for 2000 number of iterations with a pair of transfer functions by taking 11 hidden neurons (selected at random). For the first case, both the hidden and output layers are assumed to have log-sigmoid transfer function. Log-sigmoid transfer function for the hidden layer and tan-sigmoid transfer function for the output layer are considered in the second case. Tan-sigmoid for hidden layer and log-sigmoid function for output layer are taken in the third case. Finally, tan-sigmoid functions are considered for both the hidden and output layers, in the fourth case. The minimum value of MSE is obtained for the case, where both the hidden and output layers are considered to have tan-sigmoid transfer function. The value of MSE is found to be 0.13121. Now, to find the optimum number of hidden neurons in order to get minimum MSE, the neural network is trained for several times by taking different number of hidden neurons. The number of hidden neurons is varied from 2 to 20. The MSE values corresponding to different numbers of hidden neurons of the network are shown in Fig. 3.

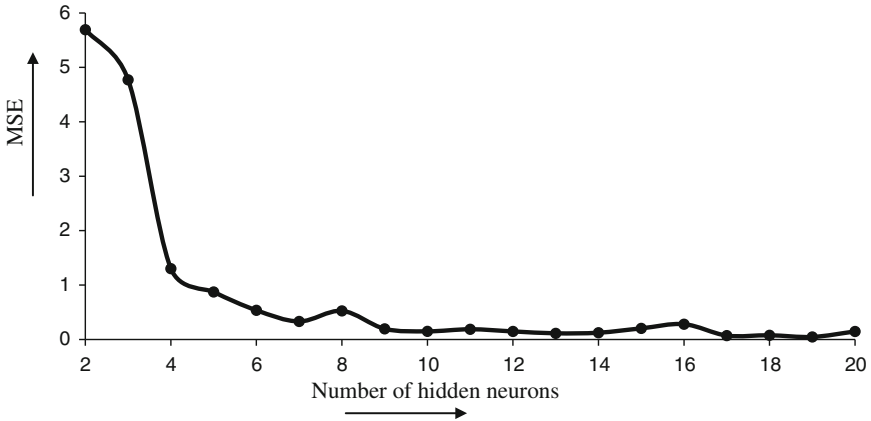


Fig. 3 Plot of MSE versus number of hidden neurons

The minimum value of MSE (that is, 0.045923) is obtained for 19 hidden neurons. Now, in order to determine the deviation of predicted output from the target output, average absolute percentage error in prediction is calculated by using the expression as follows: $APE = \frac{1}{t_s n_p} \sum_{l=1}^{t_s} \sum_{k=1}^{n_p} \left| \frac{T_{olk} - O_{olk}}{T_{olk}} \right| \times 100 \%$. The symbols carry the meaning as stated above. The APE and MSE values for the test cases are found to be equal to 0.252933 % and 0.049855, respectively. Therefore, the neural network has predicted the outputs within a reasonable accuracy limit. Moreover, once trained, the network is able to make the predictions within a fraction of second.

5 Conclusion

A reasonably good prediction has been obtained by the developed neural network. So, it can be concluded that to design an orthotic device for a patient of certain body height and mass, the required values of maximum power consumption at knee and hip joints can be predetermined. The power source of orthotic device can now be designed or ordered, which helps to reduce the overall cost and time. Thus, this input-output modeling not only helps to design a cost effective orthotic device but also can predict the necessary gait cycle, with which a human can walk with the less consumption of power at knee and hip joints.

References

- Dollar, A. M., & Herr, H. (2008). Lower extremity exoskeletons and active orthoses: Challenges and state-of-the-art. *IEEE Transactions on Robotics*, 24(1), 144–158.
- Drillis, R., & Contini, R. (1966). *Body segment parameters*. New York, New York: Office of Vocational Rehabilitation. Report No.: No. 1166-03.
- Dutton, M. (2012). *Physical therapist assistive exam review guide, J B review*. David D. Cella Publication (pp. 521–523).
- Fried, J., & Zietz, S. (1973). Curve fitting by spline and Akima methods: Possibility of interpolation error and its Suppression. *Physics in Medicine & Biology*, 18(4), 550–558.
- Levenberg, K. (1944). A method for the solution of certain non-linear problems in least squares. *Quarterly of Applied Mathematics*, 2, 164–168.
- Liu, Y., Shih, S. M., Tian, S. L., Zhong, Y. Z., & Li, L. (2009). Lower extremity joint torque predicted by using artificial neural network during vertical jump. *Journal of Biomechanics*, 42(7), 906–911.
- Loudon, J., Swift, M., & Bell, S. (2008). *The clinical orthopedic assessment guide* (2nd ed., pp. 395–408). Kansas: Human Kinetics.
- Marquardt, D. (1963). An algorithm for least-squares estimation of nonlinear parameters. *SIAM Journal on Applied Mathematics*, 11(2), 431–441.
- Murray, M. P., Drought, A. B., & Kory, R. C. (1964). Walking patterns of normal men. *Journal of Bone & Joint Surgery*, 46A, 335–360.
- Nikitczuk, J., Weinberg, B., Canavan, P. K., & Mavroidis, C. (2010). Active knee rehabilitation orthotic device with variable damping characteristics implemented via an electrorheological fluid. *IEEE Transactions on Neural Systems and Rehabilitation Engineering*, 15(6), 952–960.
- Nishii, J., Ogawa, K., & Suzuki, R. (1998). The optimal gait pattern in hexapods based on energetic efficiency. In *Proceedings of 3rd International Symposium on Artificial life and Robotics*, Japan, JA.
- Plagenhoef, S., Evans, F. G., & Abdelnour, T. (1983). Anatomical data for analyzing human motion. *Research Quarterly for Exercise and Sport*, 54, 169–178.
- Paolo, d L. (1996). Adjustments to Zatsiorsky-Seluyanov's segment inertia parameters. *Journal of Biomechanics*, 29(9), 1223–1230.
- Shultz, S., Houglum, P., & Perrin, D. (2009). *Examination of musculoskeletal injuries* (2nd ed., pp. 55–60). North Carolina: Human Kinetics.
- Wang, L., & Buchman, T. S. (2002). Prediction of joint moments using a neural network model of muscle activations from EMG signals. *IEEE Transactions on Neural Systems and Rehabilitation Engineering*, 10(1), 30–37.

CFX, Static Structural Analysis of Tractor Exhaust System Based on FEA

Faraz Ahmad, Ashwani Kumar, Karuna Kanwar and P.P. Patil

Abstract The main objective of this research work is to design and static analysis of exhaust manifold of Tractor. Exhaust manifold is subjected to high gas temperature and pressure. Present study deal with the behavior of exhaust manifold material under applied high gas temperature and pressure. The Solid Modeling of exhaust manifold has been done using Pro-E. ANSYS 14.5 has been used for analysis. The simulation parameter is exhaust gas temperature and pressure. A maximum exhaust gas temperature of 800 °C and pressure of 2 bars was applied to the exhaust manifold. Numerical simulation results were used to calculate the deformation, strain and stress induced in the exhaust system due to applied temperature and pressure. Present research work can effectively solve the problem of design optimization for different materials. The simulation results were validated with experimental results available in literature.

Keywords FEA · CFX · Structural analysis · Total deformation · Exhaust manifold · Stress · Strain

1 Introduction

Kumar et al. (2014) have studied the thermo-mechanical and modal analysis of 321-Austenitic Stainless steel exhaust manifold. The main objective was to find the total deformation, stresses and modal frequency. The parameter used for the simulation is exhaust gas temperature. A maximum exhaust gas temperature of 800 °C which is applied to the full body of exhaust manifold for thermal analysis. Solid modeling of exhaust manifold was done using Solid Edge software. FEA simulation was performed using Ansys 14.5. Gopaal et al. (2014) stated that the exhaust manifold is subjected to pressure waves. Exhaust gas increase and decrease the temperatures of manifold during

F. Ahmad (✉) · A. Kumar · K. Kanwar · P.P. Patil
Department of Mechanical Engineering, Graphic Era University,
Dehradun 248002, India
e-mail: faraz4433@gmail.com

engine operation. Due to this pressure waves and sudden change in temperature thermal fatigue failure occurs. The major factors in the failure of the exhaust manifold are thermal and mechanical loading. To reduce fatigue failure exhaust gases should be vented out smoothly from the piston chambers to the exhaust manifold.

David Rathnaraj (2004) has investigated that the automotive engine operates under severe thermo-mechanical loading condition and temperature increases up to 800 °C from ambient temperature and large thermal stress is induced. These thermal stresses are the main reason of thermal fatigue. ABAQUS software is used to complete this study. In this research study the main focus was application of constitutive equation to the thermo-mechanical condition of a model based on isothermal data. Using the proposed model, the thermal stress analysis and life prediction of exhaust manifold was completed. The material used for analysis is 429EM stainless steel. Tractor is important agricultural machinery used in planting, transporting, retaining and harvesting operations in India. Very few cases of failure analysis of agricultural vehicles have been reported till date Mahesh and Sonekar (2011). In 2004 Deger et al. (2004) have investigated the fluid flow and the heat transfer through the exhaust manifold, using CFD analysis. Exhaust manifolds are subjected to thermal stress that's why it is sensitive and prone to crack damage. Cast alloys material was used for analysis at high operational temperatures. The exhaust manifold surfaces attached to the engine have a fixed temperature of 150 °C (internal) and 30 °C (external) was assumed to be the ambient temperature around assembly. Heat transfer coefficient is 5 w/m² K. In exhaust system the components nearer to the engine require high oxidation resistance, because the temperature varies from 100 to 660 °C.

2 Establishment of CAD Model

The modeling of exhaust manifold consists of more than 30 parts. The assembly of exhaust consists of exhaust inlet, exhaust pipe and outlet etc. Solid Edge and Pro-E were used as modeling tools suited for complex geometry. Numerical simulation based Finite Element Analysis (FEA) have powerful analysis features and its results are reliable for product performance measurements. It is used for the thermal, structural, magnetic effect analysis. The 3 D CAD model of exhaust is shown as Fig. 1. Figure 2 shows the discretized mesh FEA model exhaust. Meshing is coarse and fine depends upon geometry. Tetrahedron and hexahedral elements were used for meshing. The total no of Nodes is 27,398 and elements are 13,798. Wall thickness of exhaust manifold is 2 mm and the internal diameter is 46 mm.

3 Materials Mechanical Properties

Austenitic Stainless steel-321 is stabilized steel consisting of carbon, nickel and titanium. This titanium addition prevents carbide precipitation at high temperature 427–816 °C and improves the elevated temperature properties of the alloy.

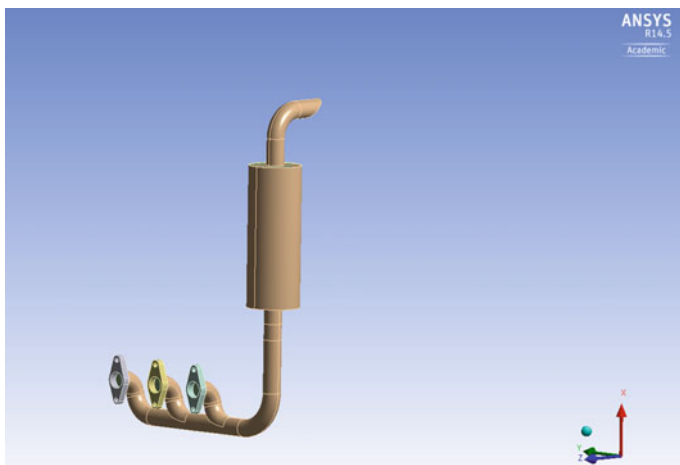


Fig. 1 3-D model of the exhaust manifold

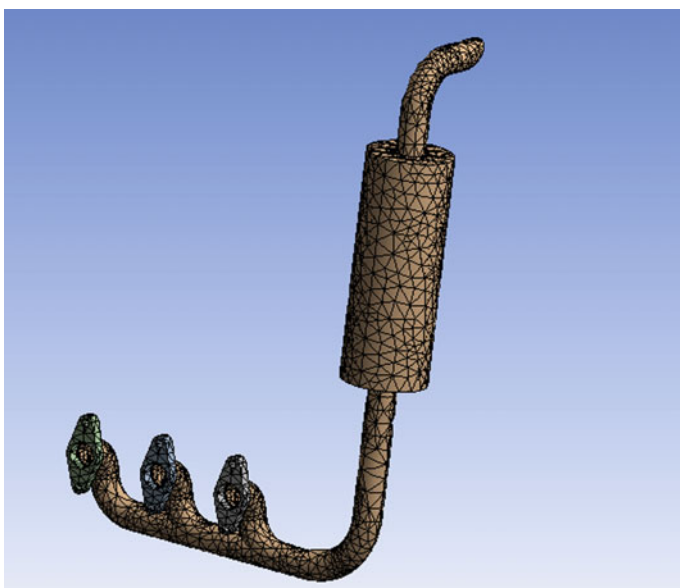


Fig. 2 3-D mesh model of the exhaust pipe

Austenitic Stainless steel-321 provides excellent resistance to oxidation, corrosion and possesses good creep strength at higher temperature (Kumar et al. 2014). Its mechanical properties are as following:

Density: 9.01 g/cc, Hardness (Rockwell B): 80, Ultimate Tensile Strength: 621 MPa, Yield Tensile Strength: 276 MPa, Modulus of Elasticity: 193 GPa, Poisson's Ratio: 0.24, Shear Modulus: 78 GPa, Thermal Conductivity: 22 W/m k @ Temperature 500 °C, Specific heat: 500 J kg⁻¹ K⁻¹, Maximum service temperature: 870 °C and Melting Point: (1371–1399) °C.

Exhaust gas have following properties:

Density: 0.345 kg m⁻³, Specific Heat Capacity: 1.141 J kg⁻¹ K⁻¹, Dynamic viscosity: 0.424 Pa, Thermal conductivity: 0.0681 W m⁻¹ K⁻¹.

Finite Element Analysis (FEA) is a numerical approximation technique based on meshing phenomena. Meshing is discretization of big domain in small elements. In present research work we have used CFX and static structural module of Ansys 14.5. CFX module work like CFD module in which boundary condition are applied on the 3-D model to calculate the result. Boundary conditions are applied to simulate the real operating conditions.

4 FEA Results and Discussion

The maximum temperature of exhaust increases up to 800 °C during the operating time and the pressure varies 1.5–2 bar Gopaal et al. (2014). So in present research work for CFX analysis a temperature of 800 °C and pressure of 2 bars is applied on each inlet of the cylinder after that the result of CFX analysis is import to the static structural module of Ansys 14.5 to check the behavior of material under the applied temperature and pressure condition (Figs. 3 and 4).

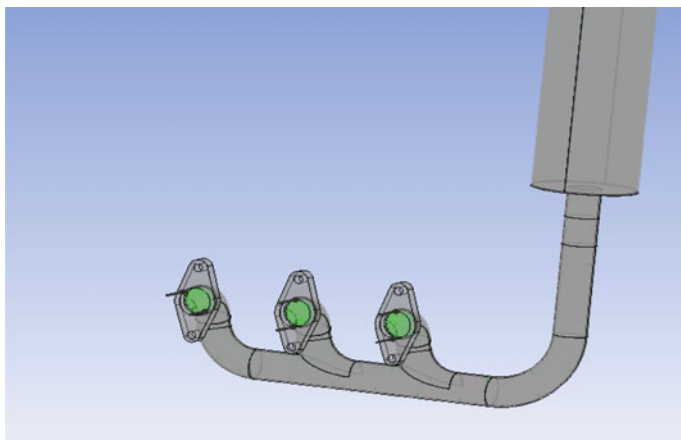


Fig. 3 Inlet boundary conditions for CFX

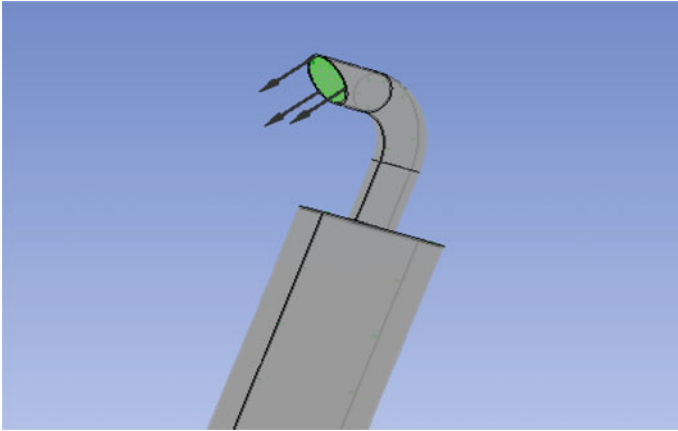


Fig. 4 Outlet boundary conditions for CFX

4.1 FEA Results: CFX Pressure Effect

In CFX analysis calculated temperature and pressure is imported to Ansys 14.5 for structural analysis. In FEA environment to apply the real operating conditions exhaust inlet to cylinder is fixed using fixed constraint (Figs. 5, 6, 9, 10, 11 and 12).

Figure 7 shows the total deformation which is maximum at outlet point (red hues) which shows that the chances of failure are maximum at outlet and Fig. 8 shows the maximum principal stress variation.

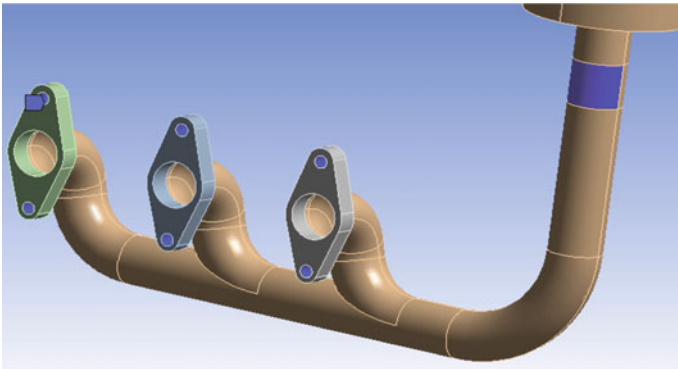


Fig. 5 Fixed constraint boundary conditions applied

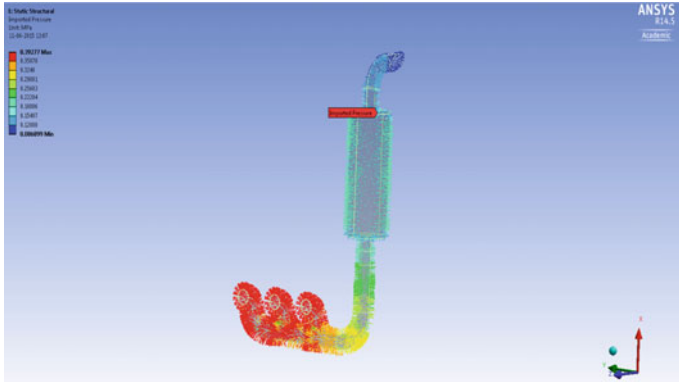


Fig. 6 Imported pressure from CFX results

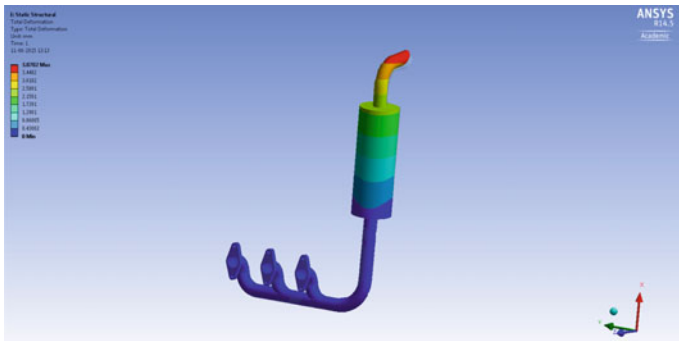


Fig. 7 Total deformation

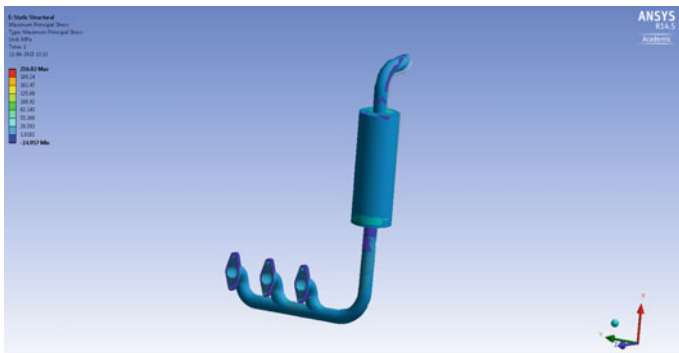


Fig. 8 Maximum principal stress

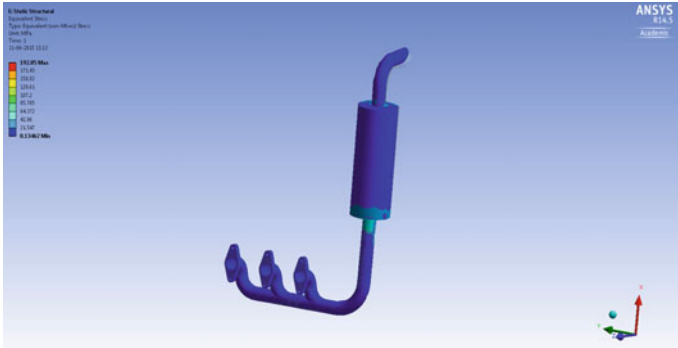


Fig. 9 Equivalent (von-mises) stress

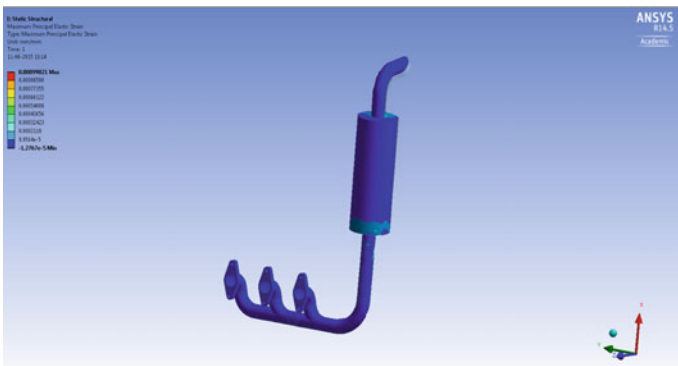


Fig. 10 Principal elastic strain

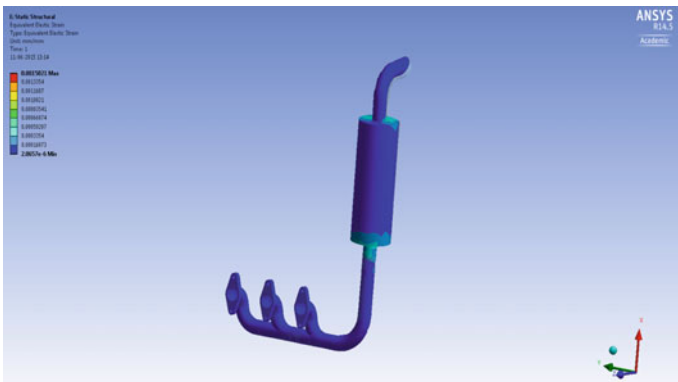


Fig. 11 Equivalent elastic strain

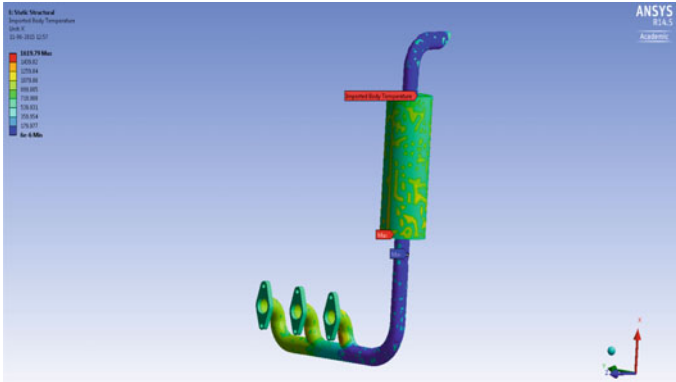


Fig. 12 Imported temperature from the CFX result

4.2 FEA Result: CFX Temperature Effect

See Figs. 13, 14, 15, 16, 17 and 18.

4.3 FEA Result: CFX Pressure and Temperature Combined Effect

In this section combined effect of temperature and pressure was studied (Figs. 19, 20, 21 and 22.)

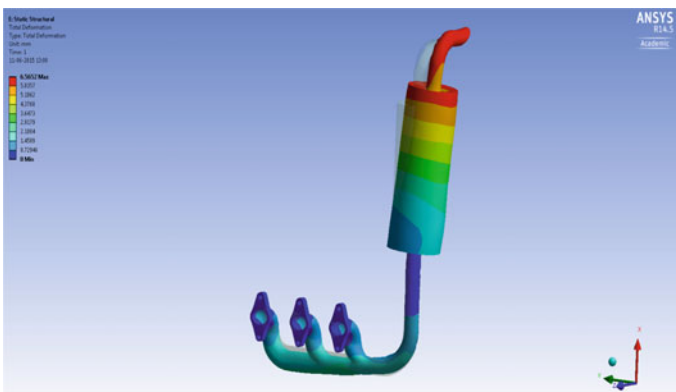


Fig. 13 Total deformation

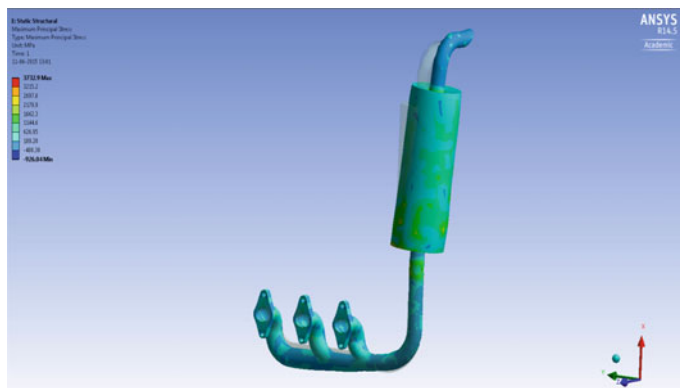


Fig. 14 Maximum principal stress

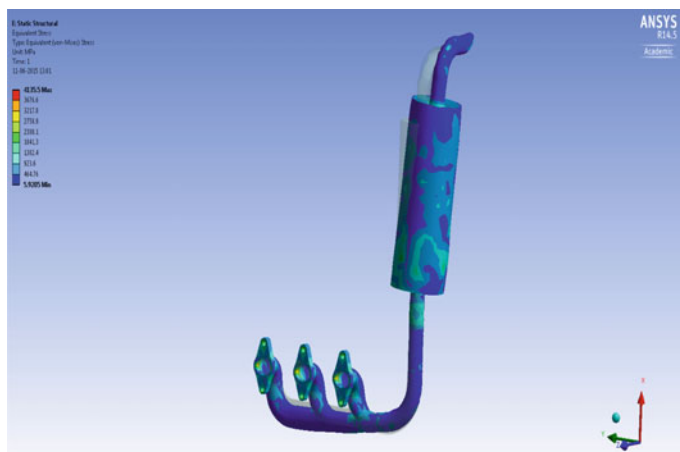


Fig. 15 Equivalent (von-mises) stress

The deformation is maximum at inlet point (red hues) which shows that the chances of failure is maximum at inlet because it is subjected to high temperature and high oxidation. Principal stress variation in exhaust manifold is uniform (blue and green hues) which shows that there is less chances of stress, so design is accurate. The Von-Mises stresses are in normal range.

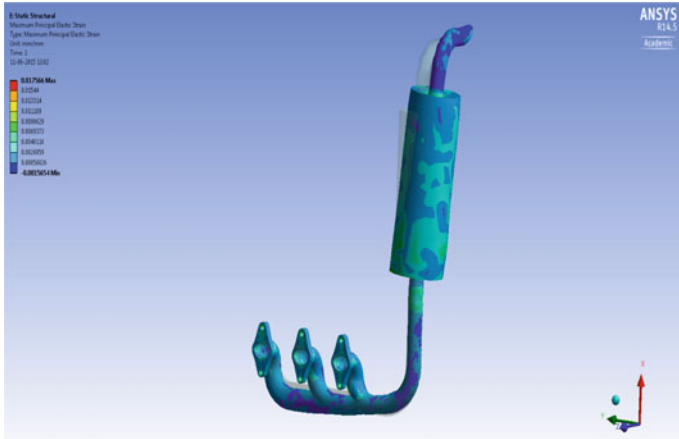


Fig. 16 Maximum principal strain

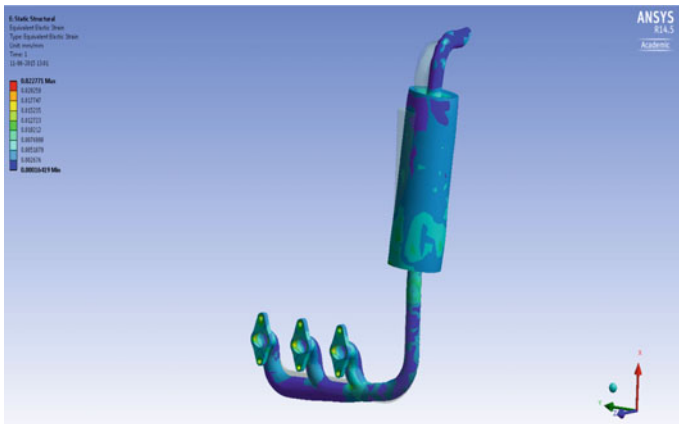


Fig. 17 Equivalent elastic strain

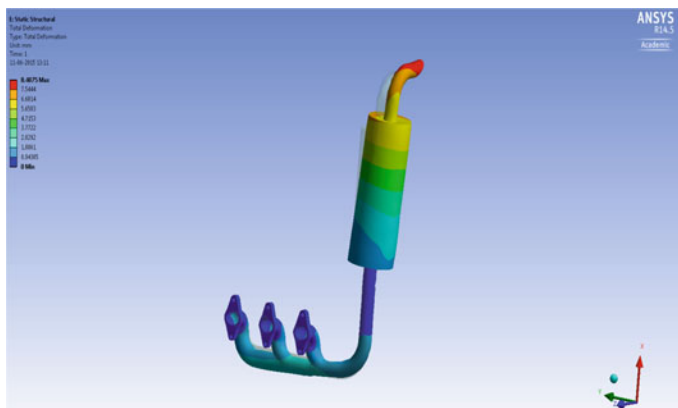


Fig. 18 Total deformation

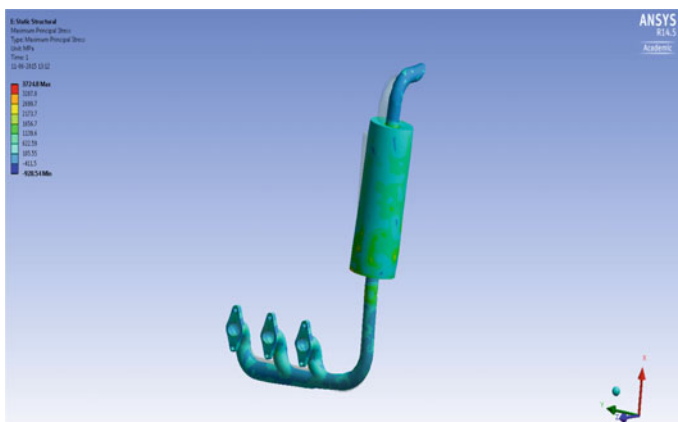


Fig. 19 Maximum principal stress

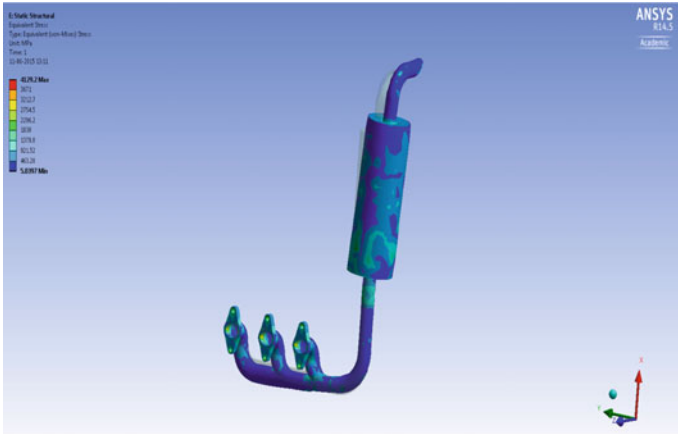


Fig. 20 Equivalent (von-mises) stress

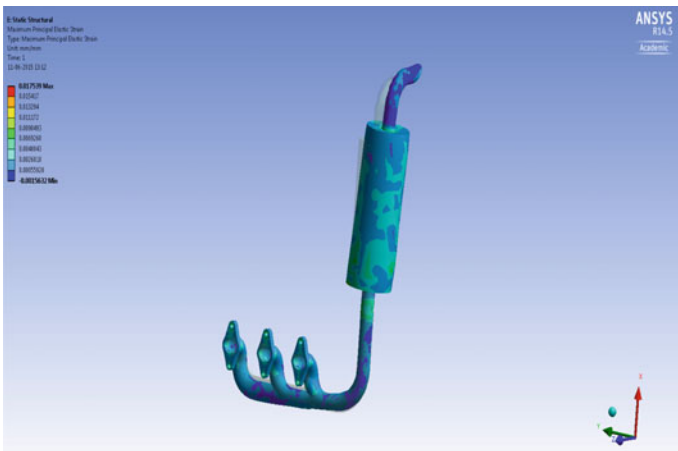


Fig. 21 Maximum principal strain

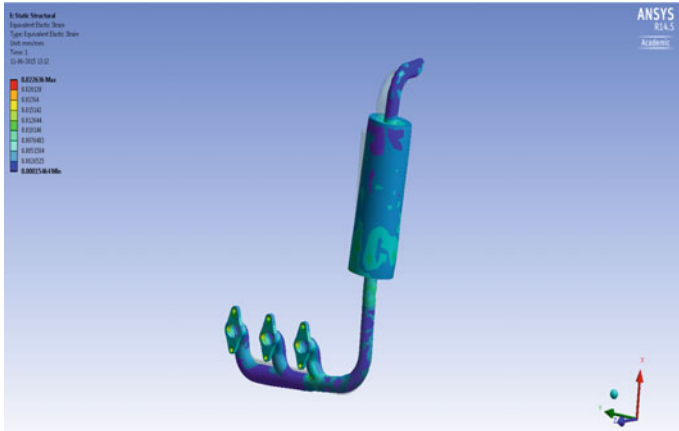


Fig. 22 Equivalent elastic strain

5 Conclusion

From the Figures and Table 1 it is observed that in temperature and pressure, temperature is the main technical index for exhaust manifold failure. The maximum deformation and stress concentration was found due to imported CFX temperature. In Austenitic Stainless steel-321 exhaust Manifold, titanium addition prevents carbide precipitation at high temperature which reduces environmental damages and can maintain its properties at higher temperature. The exhaust manifold design is safe. The results of this study show that the thermal stresses which are produced during the operations for 321-Austenitic Stainless steel Exhaust Manifold are in the safe region. The 321-Austenitic Stainless steel Exhaust Manifold can maintain its properties at higher temperature (800 °C). Pro-E software has a powerful function of solid modeling and Ansys has powerful analysis capabilities. They are suited for FEA analysis for parts with complex shape.

Table 1 Comparison of FEA results

FEA result condition	Max. total deformation (mm)	Max. principal stress (MPa)	Max. equivalent (von-misses) stress (MPa)	Max. principal elastic strain (mm/mm)	Max. equivalent elastic strain (mm/mm)
Pressure effect	1.47	93.631	73.655	0.00043014	0.0005338
Temperature effect	7.21	3699.2	5771.3	0.018964	0.030685
Combined temperature and pressure effect	7.55	3701.3	5777.1	0.018995	0.030715

References

- David Rathnaraj, J. (2004). Thermo-mechanical fatigue analysis of stainless steel exhaust manifolds, IRACST—engineering science and technology. *An International Journal (ESTIJ)*, 2, 265–267.
- Deger, Y., Simperl, B., & Jimenez, L. P. (2004). Coupled CFD-FE-analysis for the exhaust manifold of a diesel engine. In *ABAQUS Users' Conference*.
- Gopaal, Kumara Varma, M. M. M., Suresh Kumar, L. (2014). Exhaust manifold design—FEA approach. *International Journal of Engineering Trends and Technology (IJETT)*, 17(10).
- Kumar, A., Kumar, A., Dwivedi, A., & Patil, P. P. (2014). Thermo-mechanical analysis of 321-austenitic stainless steel exhaust manifolds of a diesel engine based on FEA. In *Proceedings of International Conference on Advances in Communication, Networking and Computing, CNC* (pp. 251–256). ISBN-978-81-910691-7-8. (ACEEE, Elsevier).
- Sonekar, M. M. (2011). Fracture analysis of exhaust manifold stud of mahindra tractor through finite element method (fem)—a past review. *International Journal of Engineering and Technology*, 3(2), 131–135.

FEA Simulation Based Thermo-mechanical Analysis of Tractor Exhaust Manifold

Faraz Ahmad, Vipul Tomer, Ashwani Kumar and P.P. Patil

Abstract The main objective of this research work is thermo-mechanical analysis of tractor exhaust manifold. Present study analysed the response of exhaust manifold under higher temperature. Thermal effect was considered to evaluate the FEA simulation results. Free vibration based modal analysis was performed to find the fundamental frequencies. The solid model of exhaust manifold was designed using Pro-E. Finite element analysis was performed using Ansys 14.5. The parameter used for the FEA simulation is constant exhaust gas temperature of 800 °C which was applied to the exhaust manifold. The natural frequency and vibration mode of the exhaust manifold was obtained in modal analysis and vibration characteristics of exhaust manifold was analysed. The analysis show that the natural frequency of vibration varies from 53.2 to 466.68 Hz.

Keywords Modal analysis · Total deformation · Exhaust manifold · FEA · Tractor

1 Introduction

There are significant research works (ANSYS 2011; David Rathnaraj 2004; Deger et al. 2004; Gopaal et al. 2014; Kumar et al. 2014; Mavropoulos 2011; Sonekar 2011) proposing, for exhaust manifold designs, new geometries, materials and manufacturing techniques, and this evolution has undergone with a continuous improvement over the past decades and required thorough examination of the smallest details. The exhaust system of a vehicle is subjected to thermo-mechanical fatigue. Exhaust manifolds are sensitive and prone to crack damage. The new

F. Ahmad (✉) · V. Tomer · A. Kumar · P.P. Patil
Department of Mechanical Engineering, Graphic Era University,
Dehradun 248002, India
e-mail: faraz4433@gmail.com

material like cast alloys are also subjected to high deformation at relatively high operational temperatures. The methodology for analyzing the Exhaust Manifold is a uniformly distributed temperature of 800 °C is applied to the 321-Austenitic Stainless steel exhaust manifold for the transient thermal Analysis. The thermal deformations and stresses (Figs. 6, 7 and 8) are calculated for one complete working cycle of 1 s. For vibration analysis the first 05 order vibration mode (Fig. 11) of exhaust manifold is obtain. The natural frequency of vibration varies from 53.2 to 466.68 Hz.

In present research work FEA simulation method was used for the Thermal, Structural and Modal analysis of 321-Austenitic Stainless steel exhaust manifold. For thermal analysis a uniform temperature of 800 °C is applied and various results were calculated. The natural frequency and mode shape of the exhaust manifold was obtained using modal analysis. The main objective of the vibration analysis is to identify natural frequencies and vibration modes of the exhaust manifold.

2 Material Properties

Austenitic Stainless steel-321 is stabilized steel consisting of carbon, nickel and titanium. This titanium addition prevents carbide precipitation at high temperature (427–816 °C) and improves the elevated temperature properties of the alloy. Austenitic Stainless steel-321 provides excellent resistance to oxidation, corrosion and possesses good creep strength at higher temperature. Its mechanical properties are as following:

Density: 9.01 g/cc; Hardness, Rockwell B: 80; Ultimate Tensile Strength: 621 MPa; Yield Tensile Strength: 276 MPa; Modulus of Elasticity: 193 GPa; Poisson's Ratio: 0.24; Shear Modulus: 78 GPa; Thermal Conductivity: 22 W/m - k @ Temperature 500 °C; Specific heat: 500 J kg⁻¹ K⁻¹; Maximum service temperature: 870 °C; Melting Point: 1371–1399 °C.

3 FEA Simulation

In present research work for thermal analysis a constant temperature of 800 °C is applied on exhaust manifold (Figs. 1 and 2) for complete cycle of 1 s. The result of thermal analysis was imported for static structural analysis. Static structural analysis evaluates the deformation, strain and various stresses. Pro-E software was used for design the cad modal. FEA based Ansys 14.5 was used for the thermal, structural and modal analysis. For FEA the geometry is divided into elements. These elements are interconnected to each other at a point known as Node. Element size can be kept as per our requirements. Very small element size increases the calculation time. The total no of Nodes is 27,398 and elements are 13,798. Wall thickness of exhaust manifold is 2 mm and the internal diameter is 46 mm.

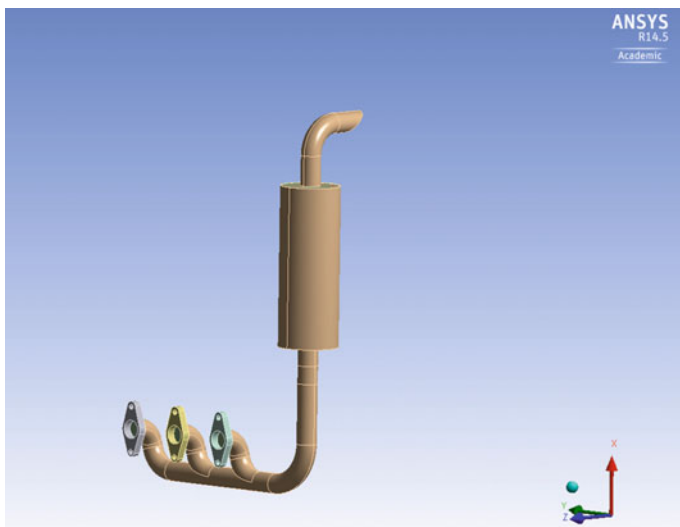


Fig. 1 CAD model of the exhaust manifold

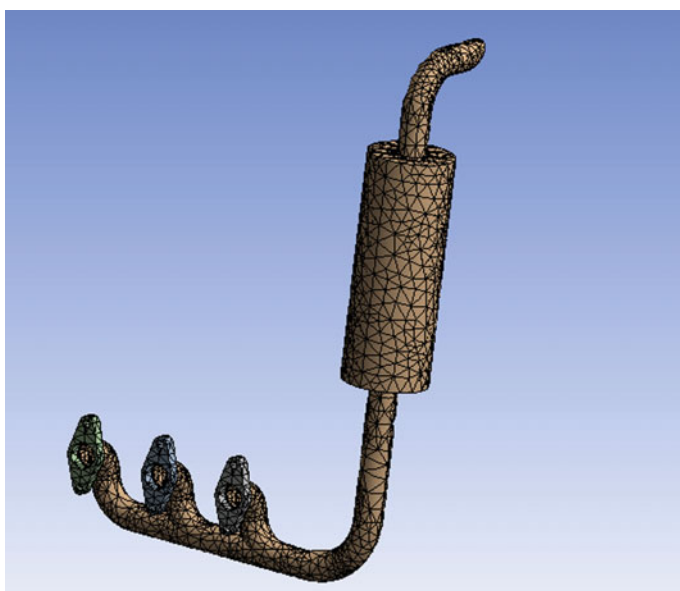


Fig. 2 Meshing of exhaust manifolds

4 Computation of Results

The Thermo-mechanical analysis of Austenitic Stainless steel-321 Exhaust Manifold is important from different prospective. First, the temperature distribution leads to thermal deformations and thermal stresses. Thermal deformation has an important role in Exhaust Manifold design. In this analysis the thermal stresses and maximum temperature distribution is calculated (Figs. 3 and 4) for one complete cycle of 1 s for Exhaust Manifold temperature to remain constant at 800 °C throughout a working cycle. To exhaust manifold a temperature of 800 °C is

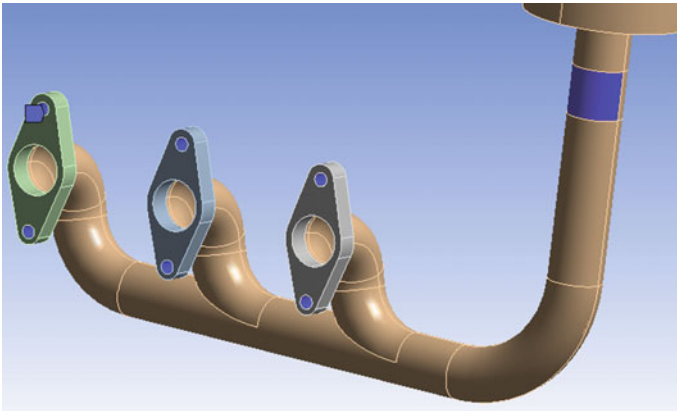


Fig. 3 Boundary conditions applied

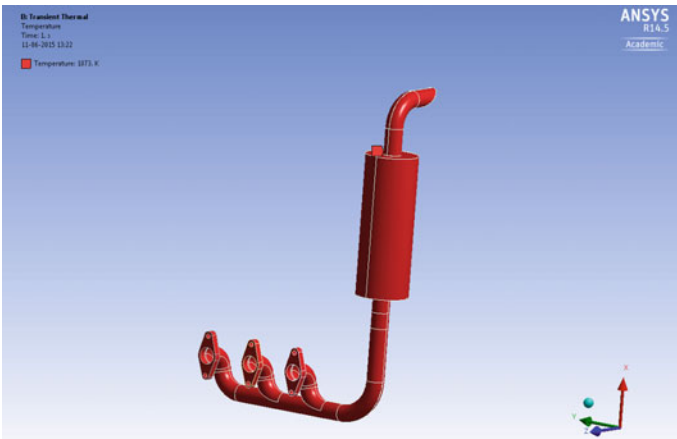


Fig. 4 Constant temperature applied

applied and thermal analysis result is obtained. During static structural analysis of exhaust manifold the thermal results of exhaust manifold was considered.

Figure 5 shows the maximum temperature variation in 1 s. The applied temperature is 800 °C which is increased by 51.3 °C in 1 s cycle. In all places the deformation (Fig. 6) is within prescribed limit showing the safe design conditions.

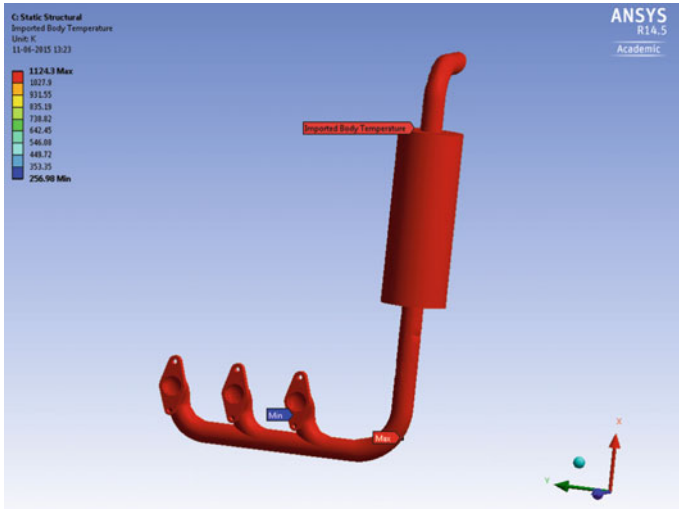


Fig. 5 Maximum temperature variations in 1 s

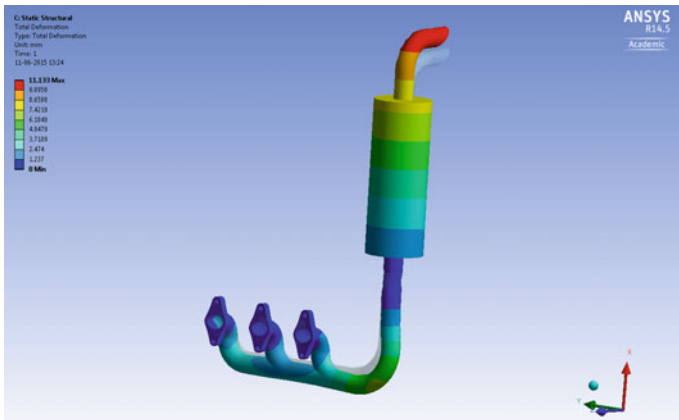


Fig. 6 Total deformation in exhaust manifold

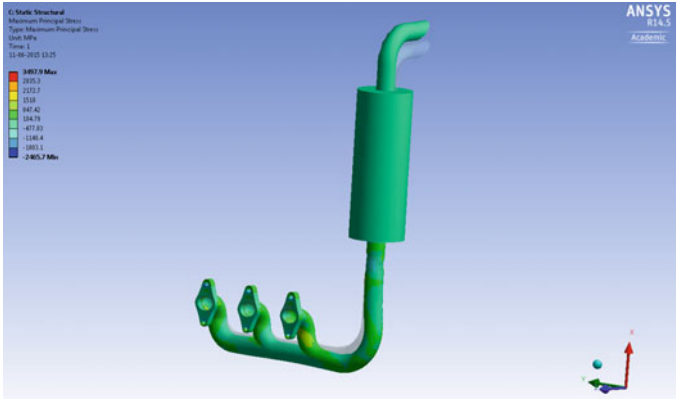


Fig. 7 Maximum principal stress

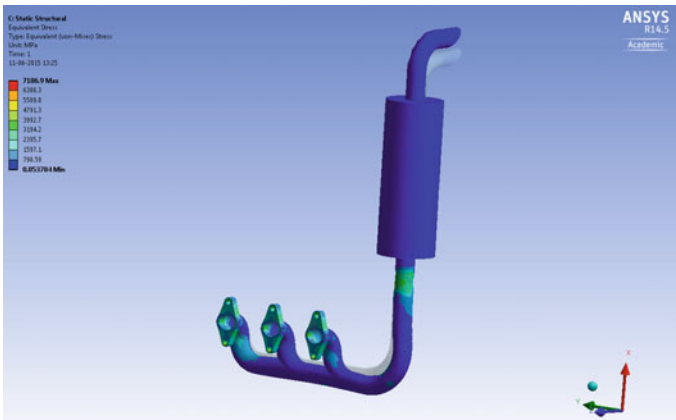


Fig. 8 Equivalent stress

4.1 Static Structural Analysis

In this analysis (Figs. 7, 8, 9 and 10) the temperature value obtain from the thermal analysis was imported for structural analysis.

5 Modal Analysis

In modal analysis the load is applied by program automatically, by applying the suitable boundary conditions. The fixed supported boundary condition and material properties was applied. The exhaust manifold of tractor is subjected to external

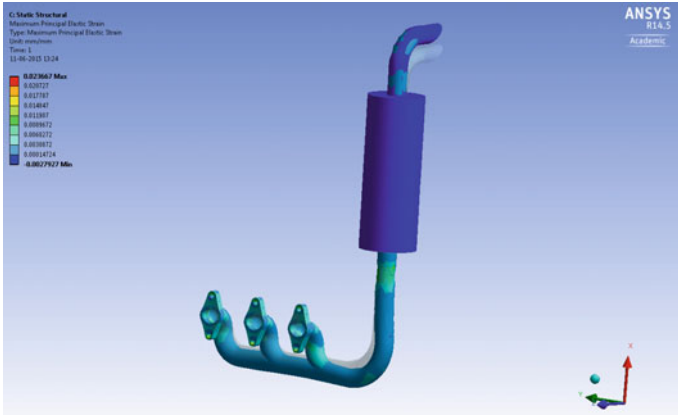


Fig. 9 Maximum principal elastic strain

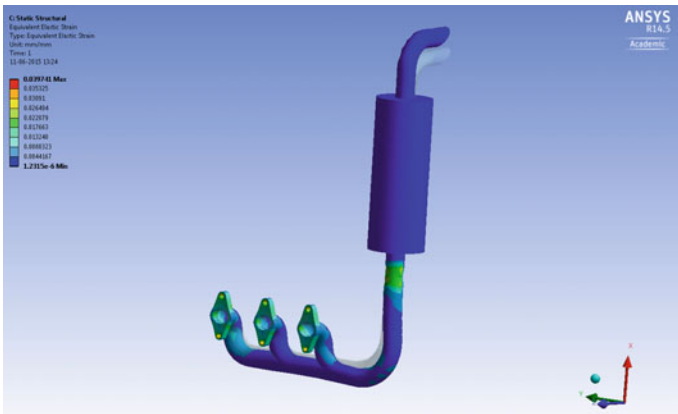


Fig. 10 Equivalent elastic strain

excitation. The reason for the fracture is matching of external excitation frequency to natural frequency of the exhaust manifold. The natural frequency of exhaust manifold vibration varies from 53.24 to 466.68 Hz. The modal frequency results are free vibration result if exhaust manifold is subjected to forced vibration the chances of fracture will be maximum. In order to prevent fracture during external loading the design should be modified so that the excitation frequency does not match, to the natural frequency. All five vibration mode of exhaust manifold is shows in Fig. 11, to find out the fracture location during the external loading condition. Figure 12 Natural frequency variations for exhaust manifold.

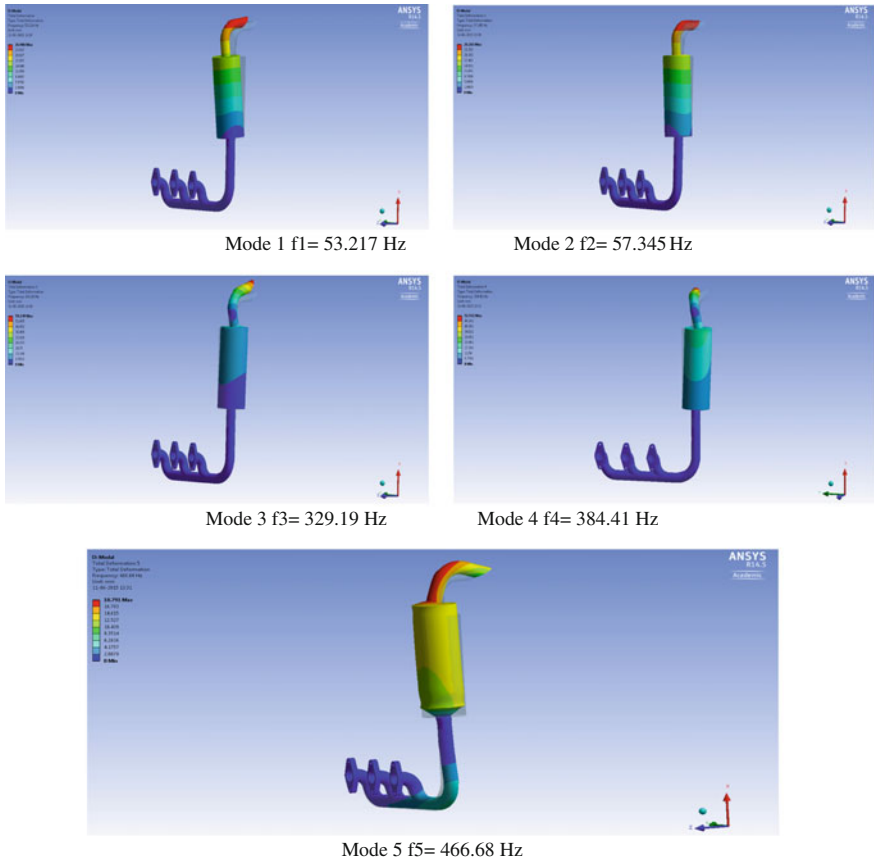


Fig. 11 Five mode shape and corresponding natural frequencies

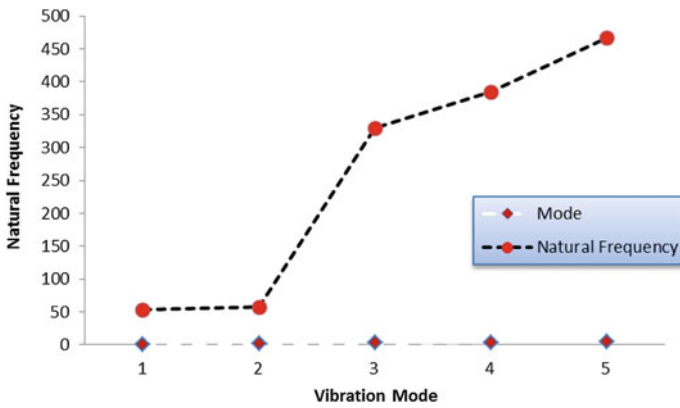


Fig. 12 Natural frequency variations for exhaust manifold

6 Conclusion

In Austenitic Stainless steel-321 Exhaust Manifold, titanium addition prevents carbide precipitation at high temperature which reduces environmental damages and can maintain its properties at that temperature. It is observed that thermo-mechanical fatigue is the main reason for exhaust manifold failure. In form of thermo mechanical fatigue an exhaust manifold is subjected to vibration and thermal stresses. The first 5 order natural frequency of the exhaust manifold and its vibration mode were obtained. The results of this study show that stresses which are produced during the operations for 321-Austenitic Stainless steel exhaust manifold are in the safe region. This study also provides the way for a developer to deal with thermal, structural analysis of different exhaust manifold of different materials.

References

- ANSYS. (2011). Structural analysis Guide, release 14.0.
- David Rathnaraj, J. (2004). Thermo-mechanical fatigue analysis of stainless steel exhaust manifolds. *IRACST-Engineering Science and Technology: An International Journal (ESTIJ)*, 2, 265–267.
- Deger, Y., Simperl, B., & Jimenez, L. P. (2004). Coupled CFD-FE-analysis for the exhaust manifold of a diesel engine. In *ABAQUS Users' Conference*.
- Gopaal, Kumara Varma M. M. M., & Suresh Kumar L. (2014). Exhaust manifold design–FEA approach. *International Journal of Engineering Trends and Technology (IJETT)* 17(10).
- Kumar, A., Kumar, A., Dwivedi, A., & Patil, P. P. (2014). Thermo-mechanical analysis of 321-austenitic stainless steel exhaust manifolds of a diesel engine based on FEA. In *Proceeding of the International Conference on Advances in Communication, Networking and Computing*, CNC, pp. 251–256, ISBN-978-81-910691-7-8. (ACEEE, Elsevier).
- Mavropoulos, G. C. (2011). Experimental study of the interactions between long and short-term unsteady heat transfer responses on the in cylinder and exhaust manifold diesel engine surfaces. *Journal of Applied Energy*, 88, 867–881.
- Sonekar, M. M. (2011). Fracture analysis of exhaust manifold stud of mahindra tractor through finite element method (fem)–a past review. *International Journal of Engineering and Technology*, 3(2), 131–135.

Stress Analysis of a Circuit Breaker Switchgear Mechanism by Using Multi Body Dynamics

J. Anjaneyulu, G. Krishna Mohana Rao and G. Venkata Rao

Abstract Although a large number of mechanisms like valve opening mechanism, satellite deployment mechanisms have been analyzed by earlier investigators, the fast acting switchgear spring operated mechanisms do not appear to have been investigated using flexible multi body dynamic analysis methodology. This paper presents the analysis of switchgear mechanism used for 69 kV-SF₆ circuit breaker. As time of operation of this mechanism is very short (0.07 s), the members of the mechanism are required to be considered as flexible for analyses. A scaled down 1:2 model of the switchgear mechanism to perform its open operation has been fabricated for the purpose of this analysis. The dynamic response of this spring operated switchgear mechanism during opening operation has been carried out by using equations of motion with the help of MATLAB. The stress analysis of this mechanism is carried out by using MBD analysis software (Adams). The results obtained by using the members of the mechanism as rigid in the theoretical equations method and the flexible multi body dynamic method in which the members are treated as flexible are compared and presented.

Keywords Circuit breaker · Flexible MBD · MATLAB · Stress analysis · Switchgear mechanism

J. Anjaneyulu (✉) · G.V. Rao
VCE, Hyderabad, Telangana, India
e-mail: anjaneyulu_jalleda@yahoo.co.in

G.V. Rao
e-mail: gvrao10@gmail.com

G. Krishna Mohana Rao
JNTU, Hyderabad, Telangana, India
e-mail: kmrgurram@gmail.com

1 Introduction

A circuit breaker is a device made to cut-off power supply automatically when there is overloading current to isolate a circuit, or city from becoming power less. The design considerations for a CB (Circuit Breaker) are heat insulation, conduction of heat and electricity, mechanical strength and so on. The important design criterion of this device is quick and timely disconnection and reconnection of conducting parts for protection and control. A sluggish response of circuit breaker mechanism causes damage to the equipment in electrical sub-station. For a gas insulated CB, the breaking time is important factor and is usually fixed in the range of a few milliseconds to prevent prolonged time of arcing which may cause overheat and melting of moving and fixed contact components. A medium voltage 69 kV-SF₆ gas insulated CB (Physical model shown in Fig. 1a) with its interrupter at top and at bottom, the spring type switchgear mechanism (SGM) is shown in Fig. 1b (Chen and Yih 2002) is chosen for a detailed investigation in this paper.

The equation of motion for general elastic mechanisms has been presented by Nagarajan and Turcic (Kang et al. 2006). They also developed equations (Nagarajan and Turcic 1992) by considering the combined displacements, velocities at the joints.

The equations for deformable bodies with large rotation and translational deformations are developed using scalars and matrices which are time invariant based on spatial coordinates and approximated displacement field by Shabana (1990). Chen and Hsu (2002) presented transmission efficiency of spring type switchgear mechanism and transmission efficiency is optimized with computer simulations. Chen and Yih (2002) studied the dynamic response of a spring—type operating mechanism for a 69 kV SF₆ CB in open operation and mentioned that for one degree of freedom resistant mechanical system motion subjected to forces

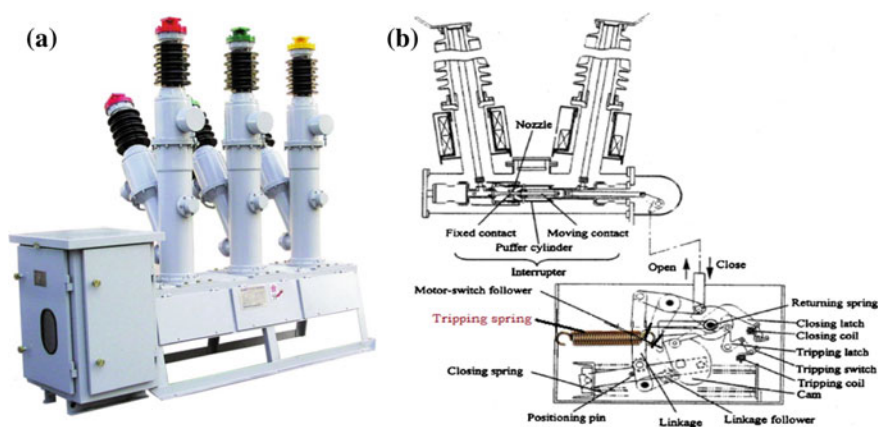


Fig. 1 69 kV SF₆ CB switchgear mechanism (a). Physical model (b). Construction details

externally can be indicated by nonlinear second order differential equation. The 4th order Runge-Kutta method is used in solution and results are compared with experimentation by Chen (2003a). For a spring type CB switchgear mechanism dynamic characteristics are analysed by Chen (2003b). A new type of switchgear has been presented by Kang et al. (2006) using electro magnetic force driving actuator (EMFA) developed and analyzed which is applicable to high voltage gas circuit breakers (HGCB). The theoretical and experimental methods are compared for a half scale fabricated model of switchgear mechanism by Anjaneyulu et al. (2015). This paper presents the theoretical equations method for dynamic response of the switchgear mechanism. The multi body dynamic analysis of the fabricated scaled down model of the switchgear mechanism is also presented. A comparative analysis of the results of both theoretical and MBD analyses are presented and the reasons for deviations in results are highlighted.

2 Analysis Based on Theoretical Equations

The switchgear mechanism’s vector loop diagram is shown in Fig. 2a. The open operation of the mechanism is caused by the action of release of the energized tripping spring that rotates T-link (i.e. *input link*) in the counter clockwise direction, then moving other links in the mechanism and ultimately to move the slider from the fixed contact so that the electrical circuit is open. The Lagrangian dynamic formulation is employed in this work to derive EOM (Equations of motion). A single DOF system with all its members rigid and neglecting friction and inertia, the EOM can be represented by nonlinear differential equations of second order. All the required parameters are taken using angular velocity, ω_6 of input T-link.

Therefore the equation of motion by using Lagrange equation can be expressed as (Nagarajan and Turcic 1992)

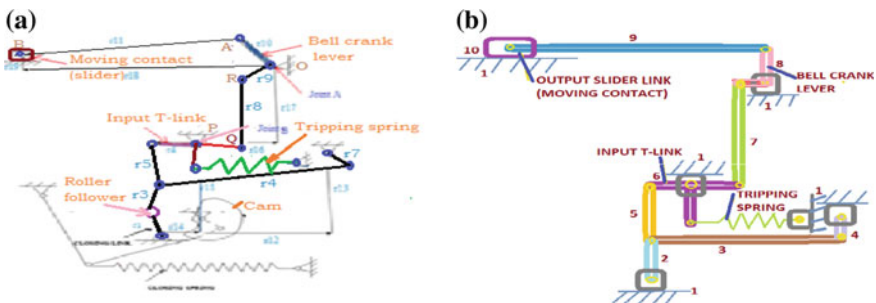


Fig. 2 a Vector loop diagram used for opening mode operation of SGM. b Model of the SGM used for opening mode of operation

$$\frac{d}{dt} \left(\frac{\partial L}{\partial \omega_6} \right) - \frac{\partial L}{\partial \theta_6} = T_{ext} \quad (1)$$

It can be brought into a compact form as (Nagarajan and Turcic 1992)

$$I(\theta)\ddot{\theta}(t) + C(\theta)\dot{\theta}^2(t) = M(\theta) \quad (2)$$

This equation is named as general EOM. Where θ is angular displacement of input link, $I(\theta)$ is generalized inertia moment, $C(\theta)$ is $(1/2)(d[I(\theta)]/d\theta)$ and $M(\theta)$ is generalized moment. Using number of links in mechanism is n , $I(\theta)$ and $M(\theta)$ are calculated from

$$I(\theta) = \sum_{i=1}^n [m_i (j_{gix}^2 + j_{giy}^2) + I_i j_{hi}^2] \quad (3)$$

$$M(\theta) = \sum_{i=1}^n [m_i (j_{gix} j_{gix}' + j_{giy} j_{giy}') + I_i j_{hi}^j h_i'] \quad (4)$$

where m_i is mass of link- i , I_i is mass moment of inertia for link- i , j_{hi} is kinematic coefficient for link- i with respect to input link- j . j_{gix} and j_{giy} are kinematic coefficients for centre of gravity of link- i in X and Y axes respectively with respect to input link- j . The symbol ($'$) indicates derivative of variable. For translating links, the coefficient is represented using j_{fi} , j_{gix} and j_{giy} are kinematic coefficients for centre of gravity for link- i in X and Y axes respectively with respect to input link- j and j_{gix}' , j_{giy}' are the derivatives of them. The Eq. (2) is then solved to find values of $M(\theta)$ using numerical methods by applying initial conditions and results obtained from positional analysis. A MATLAB program has been used to obtain the results and they are presented in Figs. 7a, 8a and 9a.

3 Analysis by Using Multi Body Dynamic Analysis Software Adams

A MBD system consists solid bodies or links which are connected by joints with constrained relative motion between the elements. The operation of mechanism with high speed requires that members of the mechanism have to be considered as flexible by including the elastic effects in them during rigid body motion of the members of mechanism. In rigid body motion analysis, nonlinear material, nonlinear deformations and large strain effects cannot be included in the models. The major advantages of MBD are its ability to yield deformation in the members and also the stresses developed in them during the operation of the mechanism.

Fig. 3 Fabricated half scale model of switchgear mechanism used for opening operation



Fig. 4 Switchgear mechanism developed in Adams software

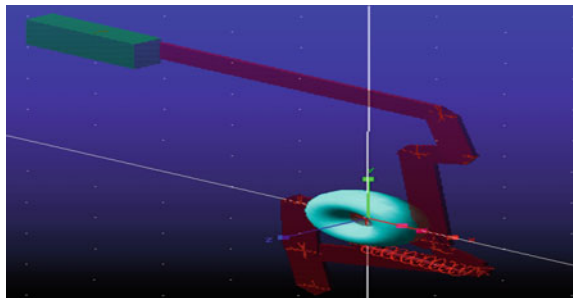
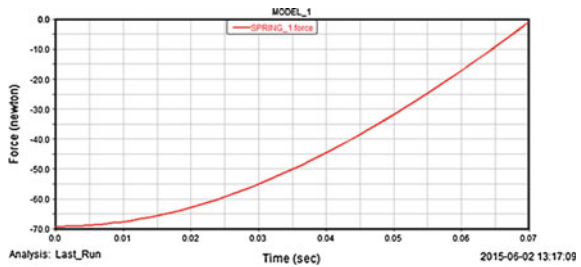


Fig. 5 Input spring force applied to T-link



The SGM with same dimensions used in a fabricated 1:2 scaled model of the switchgear mechanism (Fig. 3) is modelled in Adams software as shown in Fig. 4.

The motion simulation is performed for open operation of the switchgear mechanism by releasing the tripping spring which results in the spring force 69 N going to 2 N in 0.07 s as shown in Fig. 5. This spring action in the Adams model results the angular displacement of the T-link which is taken as input in the theoretical equations method as shown in Fig. 6. The results for the kinematic analysis obtained for slider displacement, velocity and acceleration are shown in Figs. 7b, 8b and 9b respectively.

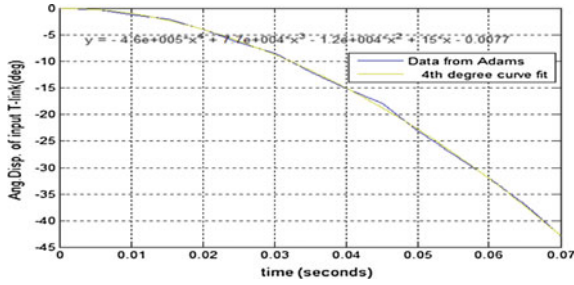


Fig. 6 Input T-link angular displacement curve from Adams fit into mathematical equation in MATLAB

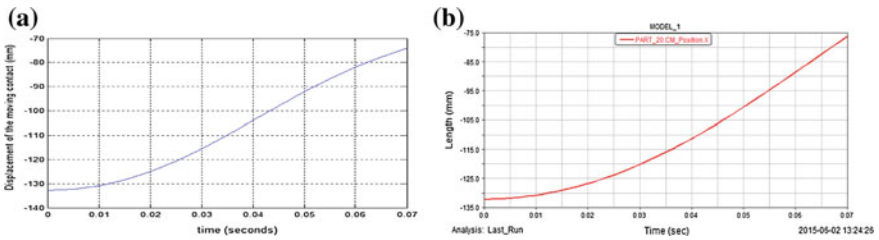


Fig. 7 Output link slider linear displacement. a From theoretical method. b From Adams

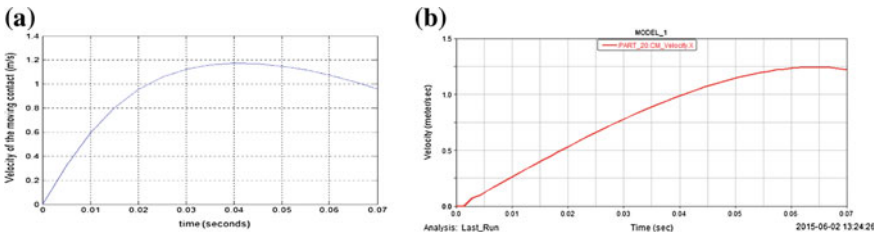


Fig. 8 Output link slider linear velocity. a From theoretical method. b From Adams

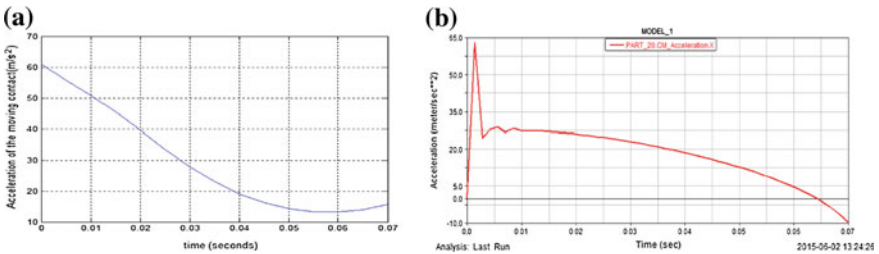


Fig. 9 Output link slider linear acceleration. a From theoretical method. b From Adams

4 Results and Discussion

The results from both theoretical and Adams methods are shown for the different parameters side by side for ease of comparison. The most important parameter, namely the displacement of the slider obtained from theoretical analysis and the corresponding Adams simulation are shown in Fig. 7a, b respectively with the first one shown as decreasing in the displacement while the second one showing the displacement as increasing towards the end of operation. The difference between the equation method and Adams may be due to (i) Slight difference between the initial angular displacement of the T-link given as input between the two approaches (ii) The numerical solution adopted in Adams and (iii) The approximation involved in the representation of the curve for the input to the T-link in the two methods The associated velocity and acceleration of the slider are given in Figs. 9 and 10 respectively. The initial transients observed in Fig. 10b from Adams are due to sudden application of spring force in the beginning of operation, wherein the friction at the contact between the slider and its constraining guide ways has to be overcome initially. Due to the same reason, the stress is more and also the link is subjected to oscillations at that period of initiation.

A summary of the results of important parameters is given in Table 1. The results show the maximum variation of 5 % in displacement, velocity and acceleration values. As the kinematic results show the similar trend in reasonable manner from both analyses, the mechanism is further analyzed for finding the deformations and Von-mises stresses (resultant stresses) by making the links flexible in MBD Adams software. The information of stresses developed in the links cannot be obtained directly by using theoretical method.

Fig. 10 Switchgear mechanism model with flexible links from Adams software

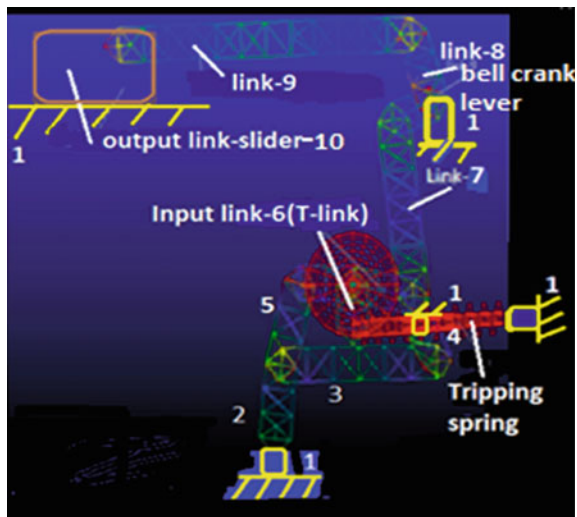
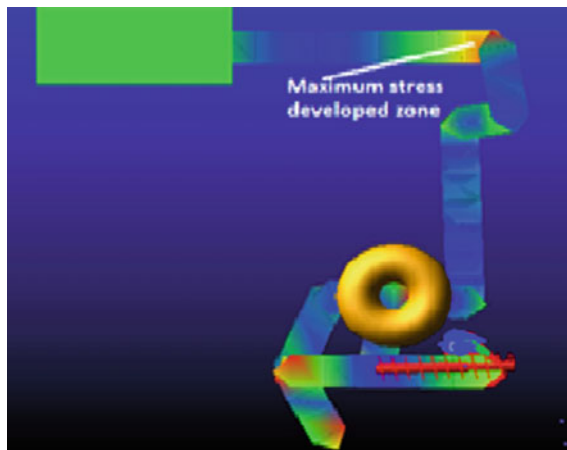


Table 1 Comparative results of kinematic characteristics by theoretical method and Adams software

Name of link	Name of kinematic parameter	Theoretical MATLAB output	Adams output	Remarks
Input T-link-6	Angular displacement (degree)	43	43	Same input
Output slider link-10	Linear displacement (mm)	58	55.5	4.3 % difference
	Maximum linear velocity (m/s)	1.19	1.25	5.0 % difference
	Maximum linear acceleration (m/s^2)	60.5	63.5	4.9 % difference

Fig. 11 Stresses developed in links at one instant during the operation of mechanism

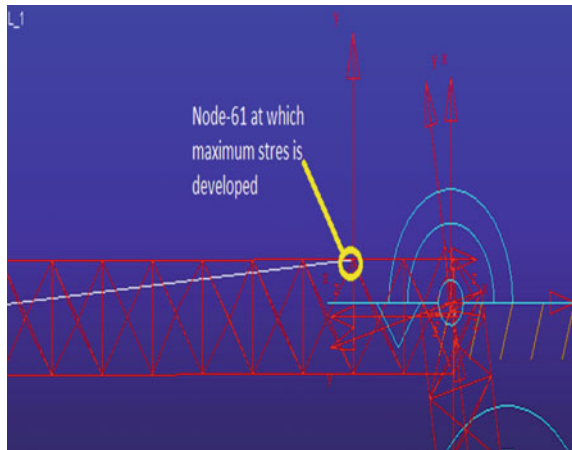


The mechanism with flexible links is shown in Fig. 10. The Von-mises stresses developed at one instant of operation in all the links is shown in Fig. 11. Table 2 lists the values of Von-mises stresses developed in descending order at ten nodes on link-9 during the operation of the mechanism. Figure 11 shows the node at which maximum stress is developed on link-9 and the stress variation at this node during the short term operation of the mechanism is shown in Fig. 13. The deformation at this node on link-9 in transverse direction to its length is shown in Fig. 13. The deformations and stress values obtained in link-9 are listed in Table 3. In physical switchgear mechanisms, usually the input T-link-6 (with disc attached), bell crank lever link-8 and slider link-10 are made heavier with high inertia, hence the possible links subjected to high stress and deformation during this opening operation mode of the switchgear mechanism are the links 7 and 9, therefore in this work, the deformations and stresses during the short term operation of the mechanism for those flexible links only are presented (Figs. 12 and 14).

Table 2 Von-mises stress values developed at ten nodes on link-9 during operation of mechanism

VON MISES hot spots for PART_9_ses date = 2015-06-02 13 30 56						
Model MODEL_1		Analysis Last_Run		Time 0.01 s		
Top 10 hot spots			Abs	Radius = 0.0 mm		
Hot spot	Stress	Node	Time	Location wrt LPRF (mm)		
	(fxtwton*mm ²)	1	(sec)	X	Y	Z
1	1.23693	61	0.0014	91.406	284.78	-1.5
2	1.23361	50	0.0014	91.406	284.78	1.5
3	1.22708	9	0.0014	-101.23	299.106	-0.0010200
4	1.22201	35	0.0014	-111.764	310.123	1.5
5	1.21442	35	0.0014	-101.23	284.836	1.5
6	1.2114	62	0.0014	-91.4583	284.836	-1.5
7	1.20572	45	0.0014	-91.4033	310.18	-1.5
8	1.20509	34	0.0014	-91.4583	310.18	1.5
9	1.3882	10	0.0014	-81.0435	298.11	-0.00471367
10	1.9837	45	0.0014	-111.764	310.123	-1.5

Fig. 12 Location of node-61 on link-9 at which maximum stress is developed



5 Conclusions

The dynamic response for a medium voltage spring operated 69 kV-SF₆ gas insulated circuit breaker switchgear mechanism scaled down fabricated model has been carried out by using Theoretical (vector loop and kinematic coefficients) method using MATLAB coding and by using MBD method with the help of Adams software. The kinematic results show the maximum variation of 5 %. It is evident from the MBD analysis that the links are subjected to the high stress value at the initial period during the short term operation of the mechanism. The force at the

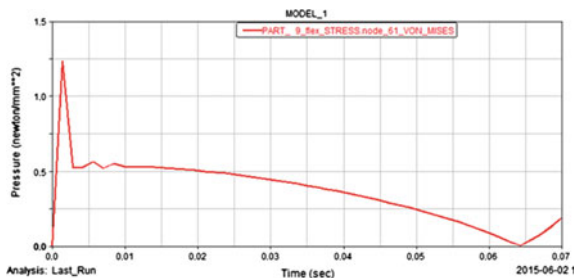


Fig. 13 Variation of Von-mises stress at node-61 during the operation of mechanism

Fig. 14 Variation of deformation in transverse direction on link-9

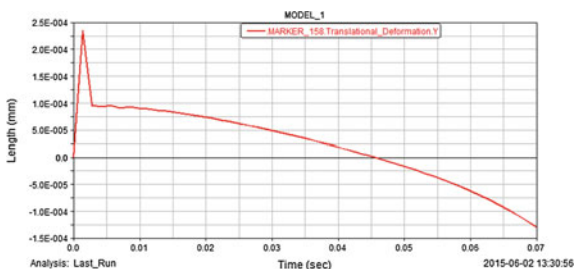


Table 3 Deformation and Von-mises stress in typical links from Adams

Name of link	Maximum deformation (mm)		Maximum Von misses stress (N/mm ²)
	In the direction of length of link	In the transverse direction to the length of link	
Llink-7	0.0019	2.5e-4	1.29
Link-9	0.0016	2.3e-4	1.23

joints of link-9 obtained by theoretical method is 55.6 N, which when divided by it’s cross sectional area yields the value of stress 0.73 N/mm². This value is obtained by not considering the flexibility of the link. Analysis by Adams software yields the stress value for the same member as 1.23 N/mm² which is about 1.7 times that of rigid body analysis. This is to be expected since in an impact like situation, stresses are double those in static case. Hence this work forms a basis for analyzing the stresses developed in members of high speed mechanisms e.g., switchgear, gunnery mechanisms in which the flexibility of members is essentially required to be considered due to their high speed operations.

References

- Anjaneyulu, J., et al. (2015). Theoretical and experimental dynamic analysis of high speed mechanism of a switchgear. *International Journal of Applied Engineering and Research*, 10(2), 5271–5283.
- Chen, F.C., & Hsu, M. H. (2002). On the transmission efficiency of a spring type operating mechanism for an SF6 gas insulated circuit breaker. *Proceedings of the Institution of Mechanical Engineers, Part C*, 215(2), 1239–1249.
- Chen, F. C., & Yih, T. (2002). On the dynamics of the spring-type operating mechanism for 69 KV SF6 gas insulated circuit breaker in open operation. *Journal of Computers and Structures*, 80, 1715–1723.
- Chen, F. C. (2003a). On the design of spring-actuated mechanism for 69KV SF6 gas insulated circuit breaker. *Journal of Mechanical Design, ASME*, 125, 840–845
- Chen, F. C. (2003b). Dynamic response of spring-type operating mechanism for 69 kV SF6 gas insulated circuit breaker. *Mechanism and Machine Theory*, 38, 119–134.
- Kang, J.-H., et al. (2006). Development and analysis of new type of Switchgear for high voltage gas circuit breaker. *IEEE, Proceedings of the 6th WSEAS/IASME International Conference on Electric Power Systems, High Voltages, Electric Machines*, Tenerife, Spain, December 16–18.
- Nagarajan, S., & Turcic, D. A. (1992a). Lagrangian formulation of the equations of motion for elastic mechanisms with mutual dependence between rigid body and elastic motions: part-I. *Journal of Dynamic Systems, Measurement, and Control*, 114(1), 126–130.
- Nagarajan, S., & Turcic, D. A. (1992b). Lagrangian formulation of the equations of motion for elastic mechanisms with mutual dependence between rigid body and elastic motions: part II. *Journal of Dynamic Systems, Measurement, and Control*, 114(1), 131–136.
- Shabana, A. A. (1990). Dynamics of flexible bodies using generalized Newton-Euler equations. *Journal of Dynamic Systems, Measurement, and Control*, 112(3), 496–503.

Integration of Fuzzy Logic with Response Surface Methodology for Predicting the Effect of Process Parameters on Build Time and Model Material Volume in FDM Process

Manu Srivastava, Sachin Maheshwari, T.K. Kundra,
Ramkrishna Yashaswi and Sandeep Rathee

Abstract Fused Deposition Modelling (FDM) is a promising additive manufacturing (AM) technique used for various prototyping requirements where relatively cheap yet robust models are required. To improve FDM process effectiveness, appropriate process parameters selection is required for high productivity and cost effectiveness. Build time (BT) and volume of Model material (MMV) required are important responses to measure cost effectiveness. In this work, response surface methodology (RSM) and fuzzy logic (FL) have been applied to reduce the build time and model material volume for experimentation. The process parameters namely contour width, air gap; raster angle and spatial orientation are considered. Also, build time and model material volume has been taken as responses for this study. Thirty experiments were conducted on AcrylobutadieneStyrene (ABS) P400 for conical primitives using full factorial central composite RSM design. The optimum process parameter conditions were obtained from FL. The results obtained provide useful information of the method to control responses and ensure minimal build time and model material volume for prototyping requirements. The assessment outcome

M. Srivastava (✉) · S. Maheshwari · S. Rathee
Division of Manufacturing Processes and Automation Engineering,
Netaji Subhas Institute of Technology, New Delhi, India
e-mail: manyash@gmail.com

S. Maheshwari
e-mail: ssaacchhiinn@gmail.com

S. Rathee
e-mail: rathee8@gmail.com

T.K. Kundra
Department of Mechanical Engineering, Indian Institute of Technology,
New Delhi, India
e-mail: tkkundra@gmail.com

R. Yashaswi
Computer Sciences Corporation Ltd., New Delhi, India
e-mail: ryashaswi@gmail.com

provided a scientific reference to obtain minimal values of build time and model material volume utilized, and it was found out that these correspond to a contour width of 0.654 mm, air gap of 0.0254 mm, raster angle of 0° and orientation (rotation about x-axis keeping z height minimum) of 30° .

Keywords Fused deposition modelling (FDM) · Fuzzy logic (FL) · Response surface methodology (RSM) · Build time (BT) · Model material volume (MMV)

1 Introduction

In recent years enormous development is witnessed in the field of additive manufacturing (AM) processes owing to the inherent advantages of this technology over conventional manufacturing processes (Thrimurthulu et al. 2004; Chua et al. 2005; Upcraft and Fletcher 2003; Levy et al. 2003; Pilipovic et al. 2009). Owing to this, lots of research is carried to develop appropriate methodologies in the field of optimizing AM processes (Levy et al. 2003; Gibson et al. 2010; Srivastava et al. 2014). There are a variety of commercially successful AM techniques available including Selective Laser Sintering (SLS), Stereolithography (SLA), Laminated Object Manufacturing (LOM), Fused Deposition Modelling (FDM), Electron Beam Melting (EBM), etc.

Lots of research work is carried in the past and present with an aim to reduce experimental work. Previously number of researchers used trial and error based approach which increased experimental times and corresponding costs. Later, number of statistical techniques based design of experiments (DOE) emerged. In the present times, these techniques are coupled with other evolutionary optimization techniques like fuzzy logic (FL) to further improve their effectiveness (Suresh and Baskar 2013). Arghavani et al. suggested that application of FL reduces experimental runs, test points, time and related costs (Arghavani et al. 2002). Tarng et al. presented FL as a novel and effective quality optimization technique with a consideration for multiple responses (Tarng et al. 2000). Karthikeyan et al. concluded that FL is effective for modelling drilling characteristics (Karthikeyan et al. 2002). However, application of these innovative techniques for response optimization in the field of additive manufacturing is relatively limited.

In this work, the experiments are designed using RSM. The models for build time and model material volume are developed, analyzed and verified using RSM only. Fuzzy logic model is developed to attempt multi response optimization. Remaining Sect. 2 introduces FDM process, RSM technique and FL briefly. Section 3 discusses methodology adopted, Sect. 4 outlines the results and Sect. 5 discusses conclusions and scope for future work.

2 Materials and Methods

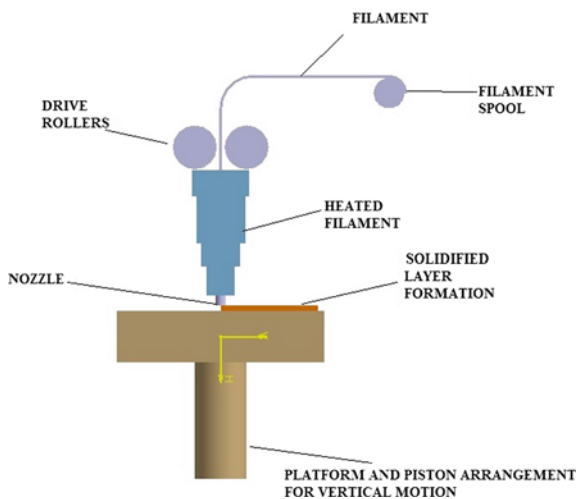
This section briefly describes FDM process, RSM technique and FL approach.

2.1 Fused Deposition Modelling

Fused deposition modelling (FDM) (Fig. 1) developed by S. Scott Crumb and marketed commercially by Stratasys, is one of the most promising and robust RP techniques owing to its ability to build prototypes of complex and intricate shapes with appreciably reasonable time requirements. FDM has distinct advantage in manufacturing industries owing to its ability to manufacture parts with complex shapes without any tooling requirement and human interface (Chouksey 2012). FDM works on an “additive” or “generative” principle by laying down material in layers. A plastic filament is uncoiled from a coil and this in turn supplies material to an extrusion nozzle. The nozzle is heated to melt the material and can be moved in both horizontal and vertical directions by a automated computational mechanism, directly controlled by a computer-aided manufacturing (CAM) software package. The model or part is produced by extrusion of thermoplastic material to form layers as the material hardens immediately after extrusion from the nozzle (Ahn et al. 2002; Sood 2011).

The material used in FDM prototype formation is ABS (Acrylonitrile butadiene styrene) plastic. Manufacturing of specimen is done by diffusion welding. This results in non uniform distribution of material as welding is non continuous. This non uniformity affects the strength of the specimen and results in anisotropy in FDM parts.

Fig. 1 Schematic diagram of fused deposition modelling (FDM)



Apart from ABS, FDM technology can be used on Polycarbonates, Polycaprolactone, Polyphenylsulphones and waxes. For providing support during manufacturing, water soluble material by Stratasys under the brand name Waterworks is generally used. This soluble material is quickly dissolved with metal agitators utilizing a solution of sodium hydroxide as solvent.

Typical applications include conceptual modelling, fit and form applications, models for further manufacturing process, investment casting, injection moulding, quick and cheap generation of models and no worry of exposure to toxic chemicals.

2.2 Response Surface Methodology (RSM)

RSM is quite useful and modern technique for the prediction and optimization of machining performances. It is a collection of statistical and mathematical techniques useful for developing, analyzing, validating and optimizing some performance measure or quality characteristic which is dependent on several input variables. The performance measure or quality characteristic is called the **response**. The input variables are called **factors**. Applying RSM consists of the finding an experimental strategy for exploring the space of the process parameters as also empirical statistical modelling to develop an approximated relationship between the responses and the factors. Also, with the help of RSM, optimization can be done for finding the values of the factors that produce desirable values of the response. Apart from RSM, Taguchi Technique can also be applied for the experiment design and model prediction. In our case, we have applied RSM mainly to obtain the effect of input parameters on responses even beyond their range used in the study. This is mainly important because FDM maxum offers a narrow range of input parameters.

2.3 Fuzzy Logic Analysis

Fuzzy logic is a mathematical theory of inexact reasoning which enables modelling of human reasoning process in linguistic terms (Ross 1995). This is quite suitable to define relationship between multiple system inputs and desirable responses. Fuzzy controllers and reasoning find applications in complex industrial applications where modelling is not possible even under numerous approximations. A fuzzy system is composed of a fuzzifier, membership functions, an interference engine, data base, rule base and defuzzifier. The flow chart of fuzzy logic controller coupled with RSM method used in this study is shown in Fig. 2 (Tzeng and Chen 2007). Figure 2 illustrates the incorporation of input from experiment designed using RSM for estimation of build time and model material volume in an FDM process into a fuzzy logic controller unit in order to obtain multi-objective optimization for attaining cost effectiveness.

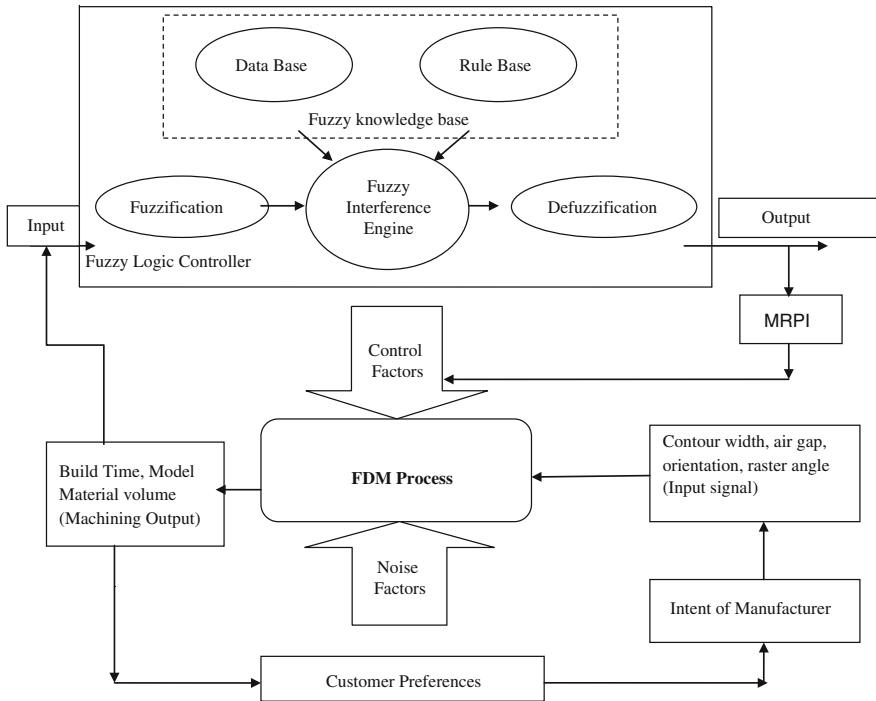


Fig. 2 Illustration of fuzzy logic controller coupled with RSM used for FDM process optimization

3 Experiments Conducted

The work methodology starts with experiment design using RSM. Individual responses are analyzed. Fuzzy model is developed. Finally the results obtained for individual responses are analyzed for multi response using FL.

Experiments were individually conducted to acknowledge significance of process parameters i.e., Contour width, orientation, raster angle and air gap on build time and model material volume of the ABS work piece on a FDM Maxum Modeler. A conical Primitive was taken of STL Size X = 20 mm, Y = 20 mm, Z = 69.999 mm. The arrangement to conduct the experiments use a face-centered CCD with four variables, having a total of 30 runs in three blocks (Stratasy 2014). The different factors and their levels are depicted in Table 1. The CAD drawing for conical primitive was made using Solidworks software and then it was converted into .stl format. This .stl was inputted to Insight 6.4 and the different experimental runs and corresponding responses are tabulated in Table 2.

Table 1 Input variables used in the experiments and their level

S. no.	Parameters	Units	Level 1	Level 2	Level 3
1	Contour width (A)	Millimeters	0.4290	0.5415	0.6540
2	Orientation (D)	Degrees	0	15	30
3	Raster angle (E)	Degrees	0	15	30
4	Air gap (F)	Millimeters	-0.0254	0	0.0254

Table 2 CCD and experimental results for four variables in uncoded units

Std	Run order	A: contour width (mm)	B: air gap (mm)	C: raster angle (°)	D: orientation (°)	Build time (h)	Model volume (cm ³)
18	1	0.654	0	15	15	1.15	7.688
20	2	0.5415	0.0254	15	15	1.133	7.253
7	3	0.429	0.0254	30	0	1.283	7.256
10	4	0.654	-0.0254	0	30	1.133	8.121
29	5	0.5415	0	15	15	1.167	7.664
16	6	0.654	0.0254	30	30	1.267	7.279
3	7	0.429	0.0254	0	0	1.1	7.241
15	8	0.429	0.0254	30	30	1.283	7.255
8	9	0.654	0.0254	30	0	1.267	7.282
23	10	0.5415	0	15	0	1.167	7.663
6	11	0.654	-0.0254	30	0	1.317	8.144
11	12	0.429	0.0254	0	30	1.1	7.241
12	13	0.654	0.0254	0	30	1.083	7.264
1	14	0.429	-0.0254	0	0	1.15	8.149
22	15	0.5415	0	30	15	1.3	7.682
9	16	0.429	-0.0254	0	30	1.15	8.149
19	17	0.5415	-0.0254	15	15	1.183	8.139
21	18	0.5415	0	0	15	1.1	7.666
13	19	0.429	-0.0254	30	30	1.35	8.172
2	20	0.654	-0.0254	0	0	1.133	8.121
26	21	0.5415	0	15	15	1.167	7.664
30	22	0.5415	0	15	15	1.167	7.664
24	23	0.5415	0	15	30	1.167	7.666
14	24	0.654	-0.0254	30	30	1.317	8.141
28	25	0.5415	0	15	15	1.167	7.664
5	26	0.429	-0.0254	30	0	1.35	8.171
25	27	0.5415	0	15	15	1.167	7.664
17	28	0.429	0	15	15	1.167	7.666
4	29	0.654	0.0254	0	0	1.083	7.266
27	30	0.5415	0	15	15	1.167	7.664

4 Results and Discussions

Responses are noted and the RSM model is analyzed. These responses are then inputted to the fuzzy logic unit for multi response optimization.

4.1 Calculation of Responses

The responses were measured using FDM control center after slicing, tessellation, support material generation time of the .stl file. This is done automatically on Insight software and the corresponding build time, model material volume and support material volume can be directly calculated.

4.2 Fuzzy Logic Unit (FLU) for Build Time and Model Material Volume Prediction

First the fuzzifier fuzzifies the input signal using membership functions. The interference engine then performs fuzzy reasoning to generate fuzzy values using a set of fuzzy rules. Finally a multi response performance index is generated using a defuzzifier (Tarnag et al. 2000). Figure 3 shows the structure of two input one output Fuzzy Logic unit.

Fuzzy rule base comprises of set of if-then control rules with two inputs a and band one output c, i.e.,

- Rule 1: if a is A_1 and b is B_1 , then c is C_1 else
- Rule 2: if a is A_2 and b is B_2 , then c is C_2 else
- Rule n: if a is A_n and b is B_n , then c is C_n .

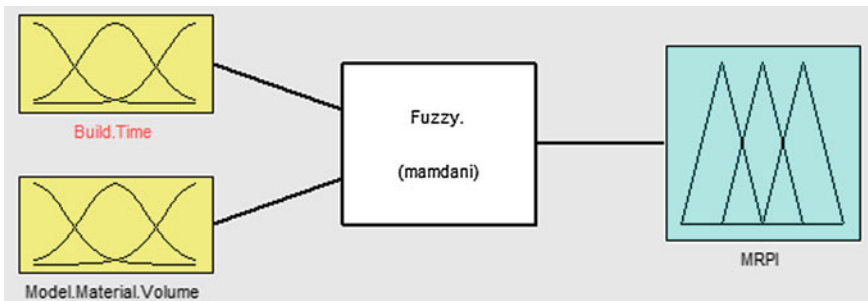


Fig. 3 Structure of two input one output fuzzy logic unit

Here A_i, B_i, C_i are fuzzy subsets defined by membership functions.

In this work, five fuzzy subsets are assigned to build time (Fig. 4) and three fuzzy subsets are assigned to model material volume (Fig. 5). Thus five sets are assigned to MRPI (Fig. 6). Various degrees of membership are calculated based on a, b and c. Fifteen fuzzy rules are assigned directly based on the fact that lower value of build time and model material volume would yield desirable result and hence better performance characteristic (Table 3).

The fuzzy reasoning tools are designed on the basis on understanding of the basic FDM technique and are summed up in Table 3. The total number of possible fuzzy rules used for this experimental controller is 15. After the two input variables are fuzzified, applying logic rules as stated in Table 3 along with Mamdani interference, fuzzy linguistic values and their membership function for MPRI is obtained. The fuzzy rules are designed in the form of if-then relationship and

Fig. 4 Membership functions for build material (3)

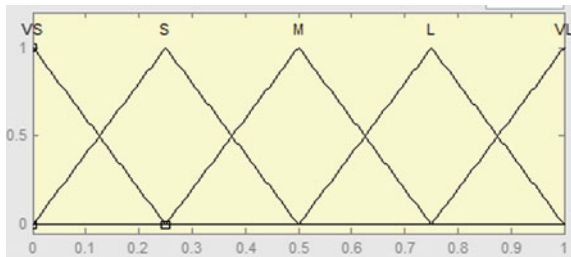


Fig. 5 Membership functions for model time (5)

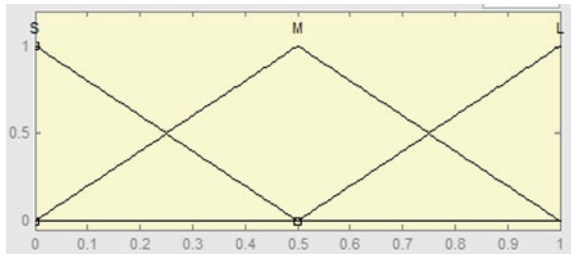


Fig. 6 Membership functions for MRPI

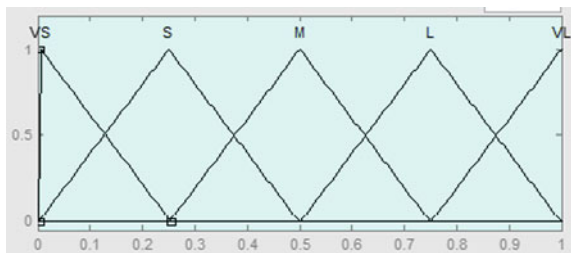


Table 3 Fuzzy rule base matrix

Build time model material	Very small (VS)	Small (S)	Medium (M)	Large (L)	Very large (VL)
Small (S)	VS	S	S	M	M
Medium (M)	S	S	M	M	L
Large (L)	M	M	M	L	VL

connect the input membership function to output membership function. These rules are listed below:

- Rule 1: If $BT_{normalized}$ is very small (VS) AND $MMV_{normalized}$ is small (S), then MRPI is very small (VS).
- Rule 2: If $BT_{normalized}$ is small (S) AND $MMV_{normalized}$ is small (S), then MRPI is small (S).
- Rule 3: If $BT_{normalized}$ is medium (M) AND $MMV_{normalized}$ is small (S), then MRPI is small (S).
- Rule 4: If $BT_{normalized}$ is large (L) AND $MMV_{normalized}$ is small (S), then MRPI is medium (M).
- Rule 5: If $BT_{normalized}$ is very large (VL) AND $MMV_{normalized}$ is small (S), then MRPI is medium (M).
- Rule 6: If $BT_{normalized}$ is very small (VS) AND $MMV_{normalized}$ is medium (M), then MRPI is small (S).
- Rule 7: If $BT_{normalized}$ is small (S) AND $MMV_{normalized}$ is medium (M), then MRPI is small (S).
- Rule 8: If $BT_{normalized}$ is medium (M) AND $MMV_{normalized}$ is medium (M), then MRPI is medium (M).
- Rule 9: If $BT_{normalized}$ is large (L) AND $MMV_{normalized}$ is medium (M), then MRPI is medium (M).
- Rule 10: If $BT_{normalized}$ is very large (VL) AND $MMV_{normalized}$ is medium (M), then MRPI is large (L).
- Rule 11: If $BT_{normalized}$ is very small (VS) AND $MMV_{normalized}$ is large (L), then MRPI is medium (M).
- Rule 12: If $BT_{normalized}$ is small (S) AND $MMV_{normalized}$ is large (L), then MRPI is medium (M).
- Rule 13: If $BT_{normalized}$ is medium (M) AND $MMV_{normalized}$ is large (L), then MRPI is medium (M).
- Rule 14: If $BT_{normalized}$ is large (L) AND $MMV_{normalized}$ is large (L) then MRPI is large (L).
- Rule 15: If $BT_{normalized}$ is very large (VL) AND $MMV_{normalized}$ is large (L) then MRPI is very large (VL).

Finally a defuzzification technique (centre of gravity method) transforms the fuzzy output to a non fuzzy value, called multi response performance index (MRPI). Larger MRPI value implies better performance characteristic. Table 4 shows MRPI values using experimental layout as obtained by RSM.

Table 4 Results of normalization and multiresponse performance index (MRPI)

Run order	Build time (BT) (h)	Normalized values of build time BT _{normalized} (Minimum)	Model volume (MMV) (cm ³)	Normalized values of model volume MMV _{normalized} (Minimum)	MRPI cost effectiveness
1	1.15	0.75	7.688	0.54	0.5272
2	1.133	0.81	7.253	0.99	0.7504
3	1.283	0.25	7.256	0.98	0.4857
4	1.133	0.81	8.121	0.05	0.5347
5	1.167	0.69	7.664	0.55	0.5347
6	1.267	0.31	7.279	0.96	0.4714
7	1.1	0.94	7.241	1.00	0.8295
8	1.283	0.25	7.255	0.98	0.4857
9	1.267	0.31	7.282	0.96	0.4714
10	1.167	0.69	7.663	0.55	0.5347
11	1.317	0.12	8.144	0.03	0.2202
12	1.1	0.94	7.241	1.00	0.8295
13	1.083	1.00	7.264	0.98	0.8990
14	1.15	0.75	8.149	0.02	0.5000
15	1.3	0.19	7.682	0.53	0.2720
16	1.15	0.75	8.149	0.02	0.5000
17	1.183	0.63	8.139	0.04	0.3790
18	1.1	0.94	7.666	0.54	0.6813
19	1.35	0.00	8.172	0.00	0.0885
20	1.133	0.81	8.121	0.05	0.5347
21	1.167	0.69	7.664	0.55	0.5347
22	1.167	0.69	7.664	0.55	0.5347
23	1.167	0.69	7.666	0.54	0.5286
24	1.317	0.12	8.141	0.03	0.2202
25	1.167	0.69	7.664	0.55	0.5347
26	1.35	0.00	8.171	0.00	0.0885
27	1.167	0.69	7.664	0.55	0.5347
28	1.167	0.69	7.666	0.54	0.5286
29	1.083	1.00	7.266	0.97	0.8898
30	1.167	0.69	7.664	0.55	0.5347

From the above work it is clear that highest value of MRPI of 0.8990 is obtained for run 13. This corresponds to contour width of 0.654 mm, air gap of 0.0254 mm, orientation angle of 30° and raster angle of 0°. The corresponding value of build time is 1.083 h and volume of model material used is 7.264 cm³.

5 Conclusion and Scope of Future Research

This paper presents application of FL with RSM for optimization of FDM process with multiple performance measures. Since FL performs a fuzzy reasoning of multiple responses therefore responses such as build time and model material volume can be simultaneously improved through this approach. Confirmatory tests have been conducted and results verified through modelling. Hence an efficient and effective approach for FDM process optimization has been proposed in this work.

This work can be further extended by verifying these results using other evolutionary multi objective optimization techniques. Also, the study can be conducted by considering many other responses including support volume, surface roughness, dimensional accuracy, etc.

References

- Ahn, S. H., Montero, M., Odell, D., Roundy, S., & Wright, P. K. (2002). Anisotropic material properties of fused deposition modelling ABS. *Rapid Prototyping Journal*, 8(4), 248–257.
- Arghavani, J., Derenne, M., & Marchand, L. (2002). Prediction of gasket leakage rate and sealing performance through fuzzy logic. *International Journal of Advanced Manufacturing Technology*, 20, 612–620.
- Chouksey, A. (2012). *Study of parametric optimization of fused deposition modelling process using response surface methodology*. Thesis, Mechanical Engineering Department, NITRourkela.
- Chua, C. K., Feng, C., Lee, C. W., & Ang, G. Q. (2005). Rapid investment casting: direct and indirect approaches via model maker II. *International Journal of Advanced Manufacturing Technology*, 25, 11–25.
- Gibson, I., Rosen, D. W., & Stucker, B. (2010). *Additive manufacturing technologies: Rapid prototyping to direct digital manufacturing*. New York: Springer.
- Karthikeyan, R., Jaiganesh, S., & Pai, B. C. (2002). Optimization of drilling characteristics for Al/SiCP composites using fuzzy/GA. *Metals and Materials*, 8(2), 163–168.
- Kumar, B. S., & Baskar, N. (2013). Integration of fuzzy logic with response surface methodology for thrust force and surface roughness modeling of drilling on titanium alloy. *International Journal of Advanced Manufacturing Technology*, 65, 1501–1514.
- Levy, G. N., Schindel, R., Kruth, J. P., & Leuven, K. U. (2003). Rapid manufacturing and rapid tooling with layer manufacturing (LM) technologies—State of the art and future perspectives. *CIRP annals-Manufacturing Technology*, 52(2), 589–609.
- Pilipovic, A., Raos, P., & Šercer, M. (2009). Experimental analysis of properties of materials for rapid prototyping. *International Journal of Advanced Manufacturing Technology*, 40, 15–105.
- Ross, T. J. (1995). *Fuzzy logic with engineering applications*. New York: McGraw-Hill Inc.
- Sood, A. K. (2011). *Study on parametric optimization of fused deposition modelling (FDM) process*. NIT Rourkela: Thesis Mechanical Engineering Department.
- Srivastava, M., Maheshwari, S., & Kundra, T. K. (2014). Virtual Modelling and simulation of functionally graded materials using FDM process. *Materials Today, Elsevier Proceedings*.
- Stratasys. (2014). StatEase, Design Expert, F.I.T. package, Editor.
- Tarnq, Y. S., Yang, W. H., & Juang, S. C. (2000). The use of fuzzy logic in the Taguchi method for the optimization of the submerged arc welding. *International Journal of Advanced Manufacturing Technology*, 16, 688–694.

- Thrimurthulu, K., Pandey, P. M., & Venkata, Reddy N. (2004). Optimum part deposition orientation in fused deposition modeling. *International Journal of Machine Tools and Manufacture*, 44, 585–594.
- Tzeng, Y.-F., & Chen, F.-C. (2007). Multi-objective optimisation of high-speed electrical discharge machining process using Taguchi fuzzy-based approach. *Materials and Design*, 28, 1159–1168.
- Upcraft, S., & Fletcher, R. (2003). The rapid prototyping technologies. *Rapid Prototyping Journal*, 23(4), 318–330.

A Study on State of the Art Technology of Laminated Object Manufacturing (LOM)

Bewketu Gizachew Mekonnen, Glen Bright and Anthony Walker

Abstract Laminated object manufacturing (LOM) process is one of rapid prototyping technology which is used to manufacture 3D dimensional solid object with sheet lamination process. The unique feature of this technology is its capacity to manufacture complicated geometrical parts with less cost of fabrication and operational time. Starting from 1980s, LOM process has been studied by many scholars and come up with promising outcomes. The main objective of this paper is to illustrate the overall idea and general working principle of LOM process and to review the existing technology on paper, composite and metals. In addition to this, current project of 3D metal printer with its extended future research has been discussed.

Keywords LOM · 3D · Rapid prototyping

1 Introduction

Laminated object manufacturing (LOM) is one of the additive rapid prototyping (RP) techniques which can print 3D solid objects from a digital model (Mueller and Kochan 1999; Yoo and Walczyk 2005; Kechagias 2007). The object is built by using an additive process in which different geometrical shape and size of materials are printed layer by layer. Mostly, LOM building mechanisms contain sequential cyclic stacking, bonding and cutting the material sheet layers to the desired geometrical shape. Stacking is performed via a roller to deliver a single adhesive-coated sheet material to platform. Then, the bonding process is performed to the layer below by heating and pressurizing with hot plate or hot laminating roller throughout the specified dimensions. Then carbon dioxide laser cuts portions of excess materials from each layer. After each cut is completed, the platform moves down by a

B.G. Mekonnen (✉) · G. Bright · A. Walker
University of KwaZulu-Natal, School of Mechanical Engineering, Durban, South Africa
e-mail: BewketuGizachew@stu.ukzn.ac.za; 214584669@stu.ukzn.ac.za

unit layer thickness and the next layer is stacked at the top. Following the above procedures, the hot roller or hot plate applies a pressure for bonding the new layer. This process is repeated until the desired part is completed (Chryssolouriset al. 2003; Klosterman et al. 1997; Falaleev and Nozhenko 2012; Spierings et al. 2013; Ghariblu and Abedi 2014).

Till this time, few researches are published on general review of additive manufacturing (AM) technologies, of which, Schindel et al. (2003) justified systematic input material and process oriented dependent classification of layer manufacturing. Chua et al. (1998) describe fundamental limitations for different technology of AM process as well compared their current and future perspectives.

Regarding laminated object manufacturing process, there is no reviewed literature material but different specific researches have been published in different journals. For instance, Klosterman et al. (1998a) addressed the application of Curved LOM for the fabrication of polymer matrix composites (PMCs). Also researchers investigated a styrene-acrylic latex binder manufactured with LOM process. Their work shows that the laminated product have a smooth surface, good toughness and homogeneous structure as well capacity to coil continuously by a roller (Cui et al. 2003). Moreover, Aravind et al. (2001) has justified an Octree-Based Algorithm for the Optimization of Extraneous Material Removal in Laminated Object Manufacturing. Chiu and Liao (2003) Laser Path Planning of Burnout Rule in LOM Process. On the other research, concept of rapid prototyping of metallic parts and moulds were proposed to reduce manufacturing cost and accuracy problem. In this research, near-net building of the layers and net-shaping methodologies were adopted in order to produce parts economically, accurately and rapidly (Karunakaran al. 2000). LOM Rapid prototyping of composite parts were produced for resin transfer modelling (RTM) to reduce product development cycle time and lower cost of developing composite parts (Tari et al. 1998). Kechagias et al. (2004) Process build-time estimator algorithm for laminated object manufacturing. In another study of laminated object manufacturing (LOM) process, a new approach of waste removal of LOM process which employs self-adhesive sheet with shielding papers were investigated. The main idea of this new process is to perform bond-then-cut at the same position; avoiding accumulated error resulted from reposition, and to de-cube the inner waste material (Liao et al. 2003). Zhang et al. (1999) Ceramic green tape extrusion for laminated object manufacturing. A thermal model for laminated object manufacturing (LOM) has been developed based on 3-dimensional transient heat conduction in a rectangular geometry LOM part. In this research, a mathematical model has been developed for heat distribution occurring overall parts of the body (Flach et al. 2014). Chiu et al. (2003, (Fig. 1), laser path planning of burnout rule for LOM process. The waste material removal process of laminated object manufacturing (LOM) is also studied by adaptive crosshatch approach to improve working efficiency and alleviate complicated decubing process involved (Liao and Chiu 2001). Dasa and Madra (2003) the binder removal studies were carried out in a LOM made body of alumina ceramics. Zak and Wang (2002) investigate the hot-roller method of thermoplastic adhesive bonding for metal laminations. This research justified that; a good bonding strength

can be obtained by supplying consistent heat and pressure. Strength of laminated object manufacturing (LOM) has been investigated experimentally by evaluating different variables. From this, process variables such as, Heater Temperature (HT), Platform Retract (PR), Heater Speed (HS), Laser Speed (LS), Feeder Speed (FS) and Platform Speed (PS) have minor effect and it was found that the tensile strength of a part produced by LOM depends mainly on the Layer thickness (Liao and Chiu 2006). Yoo and Walk (2005), an advanced cutting trajectory algorithm for laminated tooling. A numerical analysis of the thermo-mechanical behaviour of a laminate during the LOM process Models were developed to describe heat transfer and deformation phenomena. In this study, stress and heat transfer analyses of the LOM process have been carried out, and the effects of the process parameters on the resulting stress and temperature distributions have been investigated. From this research conclusion, large roller diameters are more favourable for good bonding and thickness of the laminate greatly affects the stress distribution of LOM process (Sonmez and Hahn 1986). Park et al. (2000) Characterization of the laminated object manufacturing (LOM) process.

The main purpose of this paper is to review metal and non-metal researches of LOM process and clarify future research perspectives. The overall content of this paper have four sections: Sect. 2, describe the development of LOM, Sect. 3: description of a 3D metal printer, Sect. 4: summary of the whole idea.

2 Basic Works in LOM Development

Laminated object manufacturing has shown much progress during the last 30 years. Like other fast prototyping technologies, there are many LOM researches conducted by different scholars and institutions. Klosterman et al. (1998b) fabricated composite laminated object products. In this research, particulate ceramic composite, ceramic matrix composites and polymer matrix composites were fabricated. Particulate ceramic composite was manufactured from silicon carbide (SiC) as the focus material. The ceramic tapes were laminated using heated roller at a temperature of (1808 °C) which is high enough to melt the binder. In this process a minimized shrinkage several near-net parts were produced but overall strength is not as high as that of commercially produced SiC (300–400 MPa). Ceramic matrix composites were produced using continuous fiber SiC/SiC as basic material. The part was developed by layup of separate, alternating layers of monolithic ceramic tapes and unidirectional preregs of continuous SiC fibres. In this system, SiC/SiC turbine engine seal was built as a sample. With regards to fabricating CMCs with LOM, the major result to report here is that, the entire process of fibre preform to a near-net-shape densified and part has been fully demonstrated. However, fibre damage at the interface was not solved. In polymer matrix composites, the LOM fabrication process was conducted using a continuous fiber glass and epoxy conducted using a continuous fiber glass and epoxy prepreg as the focus material. The lamination and cutting were automatically performed by the standard LOM process,

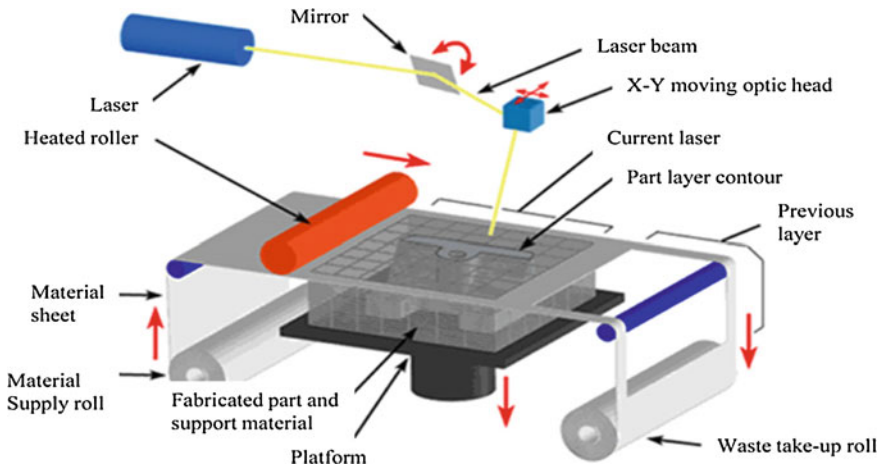


Fig. 1 Laminated object manufacturing (LOM) (Chiu et al. 2003)

as a result, PMC parts could not be fully consolidated and cured directly in the LOM process due to LOM heater droller was limited for full compaction and full cure. Consequently, the laminated part has shrinkage, warpage, and delamination during the post-processing.

Lamination of metallic material with LOM process faces many challenges. In post processing, the laser cutter induces high amount of thermal energy which reduces the efficiency of bonding between layers of the sheets. Additionally, LOM process conveyance mechanism is mostly used to transport sheets for bonding purpose. This mechanism could not fix at a proper position during conveying which causes misalignment of layers. To reduce this problem, another Bridge-LOM building process was investigated. In this research the manufacturing system is performed by the construction of bridge structure from the bonded layers to the outer frame of the work piece. This structure is used to fix the layers in a position to ensure the proper bonding and holding at a precise position. In this research, complicated geometry of large and small size hard materials including metallic and none metallic types having low costs and operational times were manufactured. Figure 2 shows Illustration of bridge-LOM equipment (Chiu et al. 2003). But its limitation was that; the strength and thermal analysis were not evaluated (Chiu et al. 2003).

Obikawa et al. (1999) investigated lamination of steels as raw materials. A laminated steel product is fabricated by repeating the two principal working processes of welding and heaping up thin sheet steels in a layer-by-layer fashion and cutting a cross-section of a 3D-CAD model out of the top sheet steel. The 3D CAD solid model changed to STL format data are sent to a system-controlling computer. Welding operation is conducted by induction heater using hot press and laser displacement meter is used to measure the height of the laminated work piece. The shape of 3D model was calculated on the reference plane and tool paths for

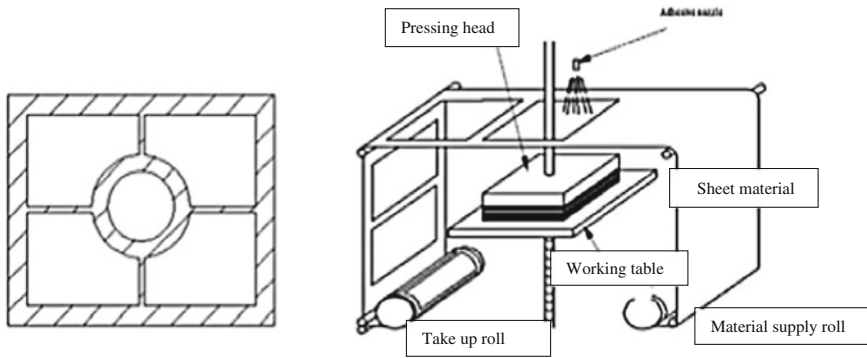


Fig. 2 Illustration of bridge-LOM equipment (Chiu et al. 2003)

cutting top sheet steels controlled by CAM installed in the computer. The cross-section of the model is cut out of using NC milling machine equipped with end-mill and a laminated product can be obtained by removing the unnecessary parts of the laminated work-piece. In this research, two mechanical components; laminated steel product of open wrench and miniature wheel were fabricated. The strength of the work-piece was evaluated by a peel and bending tests. In these experiments, a sheet steels coated with U-alloy 80 mm thick only one side of the sheet and a sheet steels, coated with U-alloy 40 mm thick on both sides were exposed to peel tests. Then the outcome of the experiment show that, metal bonding occurs between U-alloy coating layers at relatively low temperature. Metal bonding between the U-alloy and the steel or between steel and steel requires much higher welding temperature. Also from the 3 point bending tests, steel coated with U-alloy 40 mm thick on both sides had higher bulk strength. But here it should be noted that, as the layer is thickness is increased, temperature distribution is not uniform throughout the layer and lead to warping as well rough surface finish. Therefore extensive research is needed to solve the problem.

Himmer et al. (1999), conducted a research to produce injection molding tools on LOM process using aluminum alloy sheets as raw materials. The entire LOM process started by a 3D CAD modeling of the mold with the cooling channels. Then, this model is changed to a slice STL format data for laser cutting cooling channels parts and NC file format for milling excess materials. Bonding a flux coated aluminium alloy sheets were done using a press force and nitrogen gas, which serves as blocking oxidation on alloys. Following this procedure, the block was inserted in furnace for heat treatment purpose. In this LOM system, a complex cooling channels mold with high efficiency cooling system, better mechanical properties, optimized bonding strength and reduced cooling cycle time channels was manufactured. The main problem of this lamination process is that, the system is limited to work at low temperature and pressure levels. Therefore a significant investigation is needed for high pressure and thermal distribution through out the lamination processes.

Another LOM research lamination process was conducted using fully dense free form fabrication process (FDFP). In this method, a 3D functional parts fabricated using adaptive layering method for predefined sheets and slices were cut by a water cutter or laser cutter machine. In this research, the manufacturing process was conducted using a layer aligning and a multi-layer bonding approach for align layers accurately and position together and then, bond them together under pressure and heat. The fundamentals of the FDFP Process contain a combination of a thin layer cutting process, variable thickness layering and slicing in different orientations. In this method, like other lamination process, a CAD model is sliced into computer layers; the material sheet is then cut from the calculated value of computer layers. Then by adding the bonding materials between layers, the layers are aligned into a work holding system. After that using pressure and heat, layers are attached to form a 3D prototype from a fully dense material (Fig. 3). In this research special layer alignment mechanism was installed for total control of lamination process. The first is, for table could be raised and lowered, forming a stable, but traveling platform for the work piece to rest on. The second was an x and y positioning system that could reach any point above the work table and on its perimeter from two screw-driven actuators powered by stepper motors. The third was temporarily holding pieces together after they had been placed so they could be safely transferred to the heating and clamping process. Then a system of linear actuators move pins horizontally to each of the points, providing a stencil for the location of the layer to be remarked. The sliced layer and bonding material are then placed into the four-point stencil. Another actuator lowers the work table to proceed to the next layer, and the process is repeated. In the laminating system, a series of pins are used to touch the surface of the part and then be secured to prevent movement. Pins in uneven heights allow uniform pressure to the top and bottom parts. After locking pins, lifting mechanism lifts the bottom part and provides the required bonding force (Fig. 4). In addition, a heat source is used to melt the bonding materials and join the layers. From this research two mechanical components (hammer head and bike crank) were produced. The main advantage of this system, the cutting process is fast and ability to produce parts from any material. On the other hand the mechanical properties of the material produced with this system are not satisfied to STM standards. Therefore other researches focus on bonding properties and stress are needed (Glen et al. 2011).

Thomas et al. (2003) manufactured anew machine which is similar to other convectional LOM machine. This LOM machine equipped with a milling spindle which is used to cutting layers instead of lasers. The advantage of this machine is used to reduce building time, better accuracy and ability to metallic prototype model.

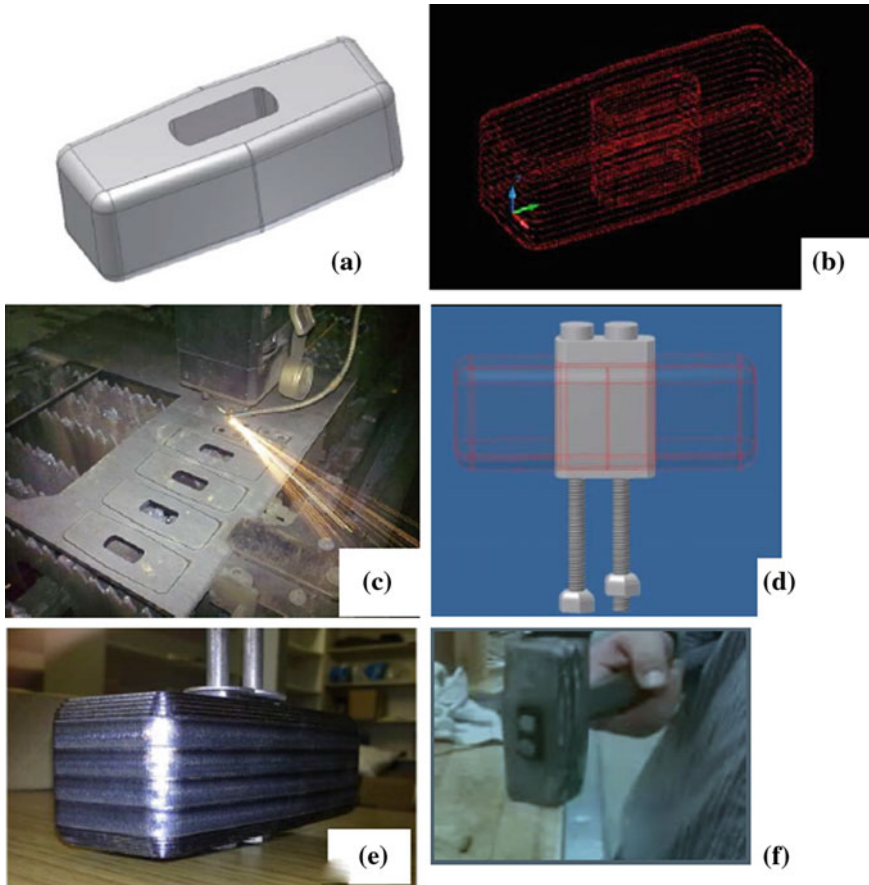


Fig. 3 General steps for the fully dense freeform fabrication (FDFF) method for a demolition hammer head: **a** 3D solid modelling **a** adaptive slicing **b** abrasive water jet cutting or laser cutting **c** alignment tooling design **d** bonding layers **(e)**, and final product test **(f)** (Glen et al. 2011)

3 3D Metal Printing Project

3D metal laminate printer was designed and built with medium size. The objective of this design was to print out mild steel or stainless into 3D functional small parts such as, nuts and small fixtures. This machine has 4 main components which are; placing of metal lamination, the heating system, the delivery and assembly station. The general lamination process starts with coated steel sheet layers are gradually added on a platform, then rectangular heater block apply pressure bonding purpose. The platform lowers by a depth equal to the sheet thickness of the first sheets and another sheet is advanced on top of the previously deposited layers. The procedure repeated until the parts building is finished. This machine prints out rough different

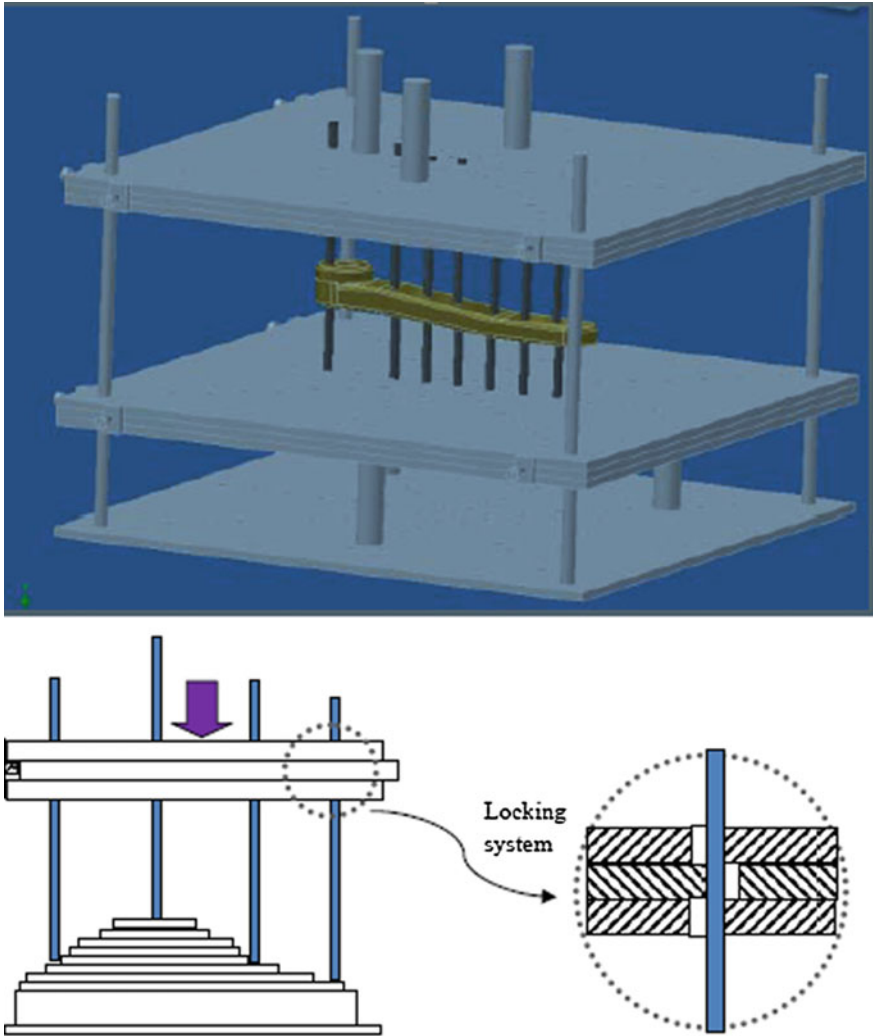


Fig. 4 Layer alignment and lamination for the fully dense freeform fabrication (Glen al. 2011)

geometrical profile models which can be applied in different applications (Fig. 5). From the experiment, it has seen a problem associated with poor edge accuracy and surface distortion due to non-uniform heat distribution through the surface of each laminate. To solve this problem the machine is redesigning again and extend the project to print 3D jigs and fixture models. The next research will be conducted to investigate defects which occur in the bonds and improve soldering distribution to get perfect joint through the use of modeling and process parameter optimization.

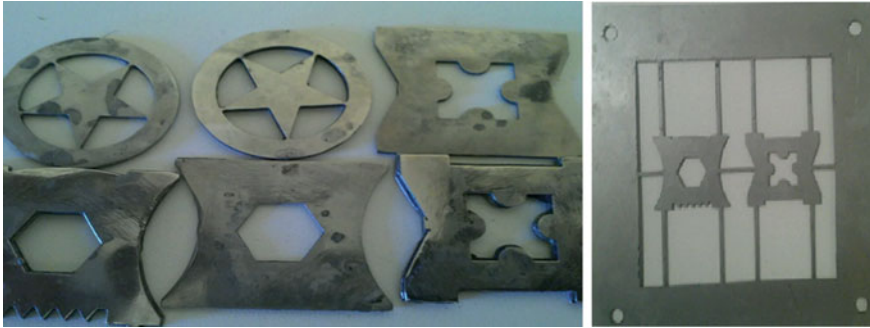


Fig. 5 3D printed models and bridge lamination sheet

4 Conclusions

Early development of metal 3D printer shows a good progress on the capacity of print a 3D object model profile. In this paper different LOM process were discussed. Lamination of paper, silicon carbide, different composite and metal Lamination was justified. Laminated object manufacturing is a good alternative approach to manufacture almost all geometry shape functional parts and it is useful to reduce cost and operation time. The mechanical properties of paper and composite lamination have shown a good result whereas lamination of metallic martial still needs further research.

References

- Aravind, K., Sridharan, & Joshi, S. (2001). An octree-based algorithm for the optimization of extraneous material removal in laminated object manufacturing, *Journal of Manufacturing Systems*, 19.
- Chiu, Y. Y., et al. (2003). Hou, automatic fabrication for bridged laminate object manufacturing (LOM) process. *Journal of Materials Processing Technology*, 140(1–3), 179–184.
- Chiu, Y. Y., & Liao, Y. S. (2003). Laser path planning of burn out rule for LOM process. *Rapid Prototyping Journal*, 9, 201–211.
- Chryssolouris, G., et al. (2003). An Experimental investigation of the tensile strength of parts produced by laminated object manufacturing (LOM) process. *CIRP Journal*, 171–180.
- Cui, X., et al. (2003). A study on green tapes for LOM with water-based, *Materials Letters*, 57.
- Dasa, A., et al. (2003). Binder removal studies in ceramic thick shapes made LOM. *Journal of the European Ceramic*, 23.
- Falaleev, A., & Nozhenko, O. (2012). Passive safety features of parts produced, Commission of motorization and energetics in agriculture, 12.
- Flach, L., Klostennan, D. A., & Chertoff, R. P. (2014). Thermal model for laminated object manufacturing (LOM).
- Ghariblu, H., & Abedi, S. (2014). A new layered manufacturing machine with cutting force analysis in tapered end milling. *Journal of Mechanical Science and Technology*, 28(8), 3087–3093.

- Glen Conner, T., et al. (2011). Layer alignment and lamination for the fully dense freeform fabrication.
- Himmer, T., Nakagawa, T., & Anzai, M. (1999). Lamination of metal sheets. *Computers in Industry*, 39.
- Karunakaran, K. P., et al. (2000). Rapid prototyping of metallic parts and moulds. *Journal of Materials Processing Technology*, 105.
- Kechagias, J. (2007). Investigation of LOM process quality using design of experiments approach, 14, 316–32.
- Kechagias, J., Stergios, M., & Stefanos, K. (2004). Process build-time estimator algorithm for laminated object manufacturing. *Rapid Prototyping Journal*, 10, 297–304.
- Klosterman, D., et al. (1997). Development and verification of a thermal model for a noble automated composite process: Laminated object manufacturing (LOM).
- Klosterman, A., et al. (1998a). Curved layer LOM of ceramics and composites.
- Klosterman, D., et al. (1998b). Interfacial characteristics of composite, *Composites Part A*.
- Liao, Y. S. & Chiu Y. Y. (2001). Adaptive crosshatch approaches for the laminated object manufacturing processing. *International Journal of Production Research*, 39, 3479–3490.
- Liao, Y. S., Li, H. C., & Chiu Y. Y. (2006). Study of laminated object manufacturing with separately applied heating and pressing. *International Journal of Advanced Manufacturing Technology*.
- Liao, Y. S., Chiu, L. C., & Chiu, Y. Y. (2003). A new approach of online waste removal process for laminated object manufacturing (LOM). *Journal of Materials Processing Technology*, 140, 136–140.
- Mueller, B., & Kochan, D. (1999). Laminated-object-manufacturing for rapid tooling and patternmaking in foundry industry. *Computers in Industry*, 39, 47–53.
- Obikawa, T., Yoshino, M., & Hinozuka, J. (1999). Sheet steel lamination for rapid manufacturing. *Journal of Materials Processing*.
- Park, J., Tari, M. J., & Hahn, H. T. (2000). Characterization of the laminated object manufacturing (LOM) process.
- Schindel, R., Levy, G. N., & Krutch, J. P. (2003). Rapid manufacturing and rapid tooling with layer manufacturing (LM) technologies, state of the art and future perspectives. *CIRP Annals-Manufacturing Technology*, 52(2), 589–609.
- Sonmez, F. O., & Hahn, H. T. (1986). Thermo mechanical analysis of the laminated object manufacturing (LOM) process. *Rapid Prototyping Journal*.
- Spierings, A. B., Starr, T. L., & Wegener, K. (2013). Fatigue performance of additive manufactured. *Rapid Prototyping Journal*, 19.
- Tari, J. M., et al. (1998). Rapid-prototyping of composite parts using resin transfer modelling and laminated-object Applied Science and Manufacturing. *Composites-Part-A*, 29.
- Thomas, et al. (2003) Recent developments in metal laminated tooling. *Rapid Prototyping*, 466–473.
- Yoo, S., & Walczyk, D. (2005). An advanced cutting trajectory algorithm. *Rapid Prototyping Journal*, 11/4.
- Zak, G., & Wang, W. X. (2002). Adhesive Bonding of Sheet for Laminated Metal Tooling. In *Proceedings of Solid Freeform Fabrication*.
- Zhang, Y., et al. (1999). Ceramic green tape extrusion for laminated object manufacturing. *Materials Letters*, 40.

Design Analysis and Manufacturing of Device for Rehabilitation of Hand Fingers Based on Illusionary Movements by Tendon Vibrations

Bonny Bernard and Preethika Immaculate Britto

Abstract This project is done in the field of rehabilitation of upper limb paresis on post stroke hemiplegic patients, and it aims at replacing the traditional rehabilitation methods with a more automated approach, currently concerning mainly on the rehabilitation of upper limbs of hands. The device applies linear mechanical vibrations on the tendons of the fingers at a particular frequency so as to result in the patient getting illusionary movements. The frequency of vibrations to generate illusions varies from person to person and so there should be a mechanism by which the user can change the frequency to suit him/her. Besides giving the vibrations, the project also focuses on developing a mechanism so that the patients can physically see the limbs moving in accordance with the vibrations perceived by them. This will speed up the treatment process.

Keywords Stroke rehabilitation · Tendon vibration · Paresis · Shape memory alloy actuators

1 Introduction

Paresis is a condition typified by a weakness of voluntary movement, or partial loss of voluntary movement or by impaired movement. Neurologists use the term paresis to describe weakness, and plegia to describe paralysis in which all voluntary movement is lost.

B. Bernard (✉)

Mechatronics School of Mechanical and Building Sciences,
VIT University, Vellore, India
e-mail: bonny.bernard@gmail.com

P.I. Britto

Biomedical Engineering, School of Biosciences and Technology,
VIT University, Vellore, India
e-mail: preethikabritto@vit.ac.in

© Springer India 2016

D.K. Mandal and C.S. Syan (eds.), *CAD/CAM, Robotics and Factories of the Future*, Lecture Notes in Mechanical Engineering,
DOI 10.1007/978-81-322-2740-3_22

217

Stroke, also known as cerebrovascular accident (CVA) can usually result in the patient being diagnosed with paresis; or complete paralysis in extreme cases (Gay et al. 2007). Signs and symptoms of a stroke may include an inability to move or feel on one side of the body (Hemiplegia), loss of sensory functions like touch etc.

Stroke rehabilitation is the process by which those with disabling strokes undergo treatment to help them return to normal life as much as possible by regaining and relearning the skills of everyday living.

Evidence exists that even mental practice of a movement has positive effects on motor function recovery in chronic stroke patients and improves motor performance in healthy subjects almost as successfully as physical practice (Hendricks et al. 2002).

Mirror therapy is one of the current sensorimotor rehabilitation methods building upon the previous concept, additionally providing visual feedback of the movement. To create the illusion that the impaired hand is moving, the stroke patient moves the healthy hand in front of a vertical parasagittal mirror, while the impaired hand is hidden behind the mirror. Through activation of various regions in the affected brain hemisphere, cortical reorganization takes place. A study by Dohle et al. (2009) showed that, in a group of patients with distal plegia at the beginning of the therapy, those receiving mirror therapy regained more distal function than the patients of the control group receiving equivalent therapy but without mirror, thus seeing the affected limb. Furthermore, mirror therapy improved recovery of surface sensibility across all patients.

Another way to induce such illusory movements is offered by tendon vibration, discovered in the early 1970s. These studies conclude that, by vibrating a muscle tendon of a static limb in the range of 50–100 Hz, a proprioceptive illusion of a movement corresponding to the limb is generated.

Rehabilitation therapy assisted by tendon stimulation is a relatively new therapeutic concept for stroke patients and only a few studies have been published so far.

There are many ways to stimulate tendon in physical therapy for pain reduction and improvement of muscle functions. Common forms of tendon stimulation methods include Electronic (Galvanic/Faradic) muscle stimulation, Therapeutic ultrasound frequency and applying mechanical vibrations. While Electronic muscle stimulation has been proven to produce illusions of motion, ultrasound therapy has not (Robertson et al. 2015). Also, experimental results revealed that tendon electrical stimulation elicited a similar illusion of motion to the kinesthetic illusion but with less accuracy and efficiency (Kajimoto 2013). Moreover, electrical stimulation would be challenging, because electrodes placed over the muscle (which contains muscle spindles) would inevitably stimulate muscle efferent nerves, resulting in undesirable motion. Hence providing mechanical vibrations to the tendons remains to be the most efficient and easy way to produce illusory motion.

Devices that use tendon vibrations have been designed until recently for major muscle groups such as biceps, knee joints etc. (Domenik 2012). Also these devices obtained little or no feedback from the patient. Rinderknecht et al. (2013) was

successful in combining tendon vibrations with virtual reality. This addition of virtual reality setup would be a great advantage over the existing device as the patient would be able to get a sense of physical feedback of the illusion that he/she is experiencing. And also addition of virtual reality would enable the patients who are still not ready to move their joints because of injuries from accidents.

Even though virtual reality combined with tendon vibrations is a novel idea, the concept still has a setback because of it still being virtual. The patient still gets the idea that the hand that he/she sees in the monitor is not the real one and this knowledge can hinder with the recovery process.

This project aims at replacing virtual reality setup completely with a mecha-tronics device which will not only apply vibrations at the tendons to produce illusions, but also aim at physically moving the joints in the manner in which the illusions are perceived. Here the design, analysis and implementation of the device is considered without the manufacture of the actuators to move the fingers. The electronic circuits for actuators of both the vibrating mechanism and the movement of fingers are designed and implemented.

2 Design and Modelling

2.1 Design Equations

Cam Design

Constant acceleration type cam is chosen for the model. This is so as to limit any sudden jerks in the motion. The general equations of the motion of the cam are shown below:

Here, a is linear acceleration of the follower (cm/s^2), v is linear velocity of the follower (cm/s), h is total displacement of the follower (cm), y is displacement at any point (cm), β is angular displacement of cam for displacement h (radians), θ is angular displacement of cam for displacement y (radians), t is time for cam to rotate through θ (s), T is time for cam to rotate through β (s)

For cam angle θ to $\beta/2$,

$$\text{Displacement } y_1 = 2 h(\theta/\beta)^2$$

$$\text{Velocity } v_1 = [4 h(\theta/\beta)]/T$$

$$\text{Acceleration } a_1 = 4 h/T^2$$

For cam angle $\beta/2$ to β

$$\text{Displacement } y_2 = h - 2 h(1 - \theta/\beta)^2$$

$$\text{Velocity } v_2 = [4 h(1 - \theta/\beta)]/T$$

$$\text{Acceleration } a_2 = -4 h/T^2$$

Substituting the values $h = 1$, $\beta = 180^\circ$

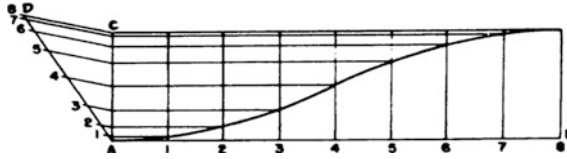
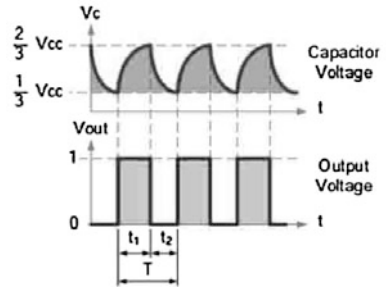


Fig. 1 Construction diagram for constant acceleration. Linear versus angular displacement

Fig. 2 Output waveforms of an astable multivibrator using 555 timer IC



$$\begin{aligned}
 y_1 &= \theta/90 \text{ cm} \\
 v_1 &= \theta * 0.0592 \text{ cm/s} \\
 a_1 &= 10.666 \text{ cm/s}^2 \\
 y_2 &= -\theta/90 \text{ cm/s} \\
 v_2 &= -\theta * 0.0592 \\
 a_2 &= 10.666 \text{ cm/s}^2
 \end{aligned}$$

The values of linear displacement for each value of angular displacement are noted and plotted on a displacement curve to obtain the cam profile. Construction of the displacement diagram is shown in Fig. 1.

The cams are constructed accordingly (Fig. 2).

Circuit Design

The standard equations of the 555 timer PWM generating circuits are

$$\begin{aligned}
 t_1 &= 0.693(R_1 + R_2) \\
 t_2 &= 0.693R_2 * C
 \end{aligned}$$

Fixing Capacitor C at a standard value, C = 220 μF.

The lower limit for the frequency is 60 Hz. Since we are using a 100 rpm DC motor, the duty cycle calculation is straight forward. We need a duty cycle of 0.6 to get 60 rpm on the DC motor.

So $t_1 = 0.6$ and $t_2 = 0.4$ for 60 rpm

From the equations, $R_1 = 1.049 \text{ k}\Omega$, $R_2 = 2.62 \text{ k}\Omega$

The upper limit for the frequency is 80 Hz.

So $t_1 = 0.8$ and $t_2 = 0.2$ for 80 rpm

Again, from the equations, we obtain, $R_1 = 3.936 \text{ k}\Omega$, $R_2 = 1.3118 \text{ k}\Omega$

2.2 Device Modelling

A 3D model of the device was created in Solidworks 2012. The perspective view of the 3D model of the complete device is shown in Fig. 3a.

It includes

1. Hand support with base
2. Five DC motors
3. Three motor holders
4. Five cams
5. Five vibrating shafts with heads.

The hand support rests on its base with the motor holders underneath them. The motor holders fix the motors in place and also supports the hand support. There are five DC motors which rotate individual cams so as to move the vibrating shafts in translational manner.

Hand support part of the device model is shown in Fig. 3a. The patient is asked to keep his hand over the hand support with his palm covering the dome and place it in such a manner that the tendon in each finger aligns with the holes in the dome. The holes are made according to the dimensions of the fingers obtained from Chelette et al. (2014). As shown on the top view, the thumb will be on the left side of the model and little finger on the right most slot. Straight slots are provided on the base so that the motor holders can be accurately placed under the hand support (Fig. 4).

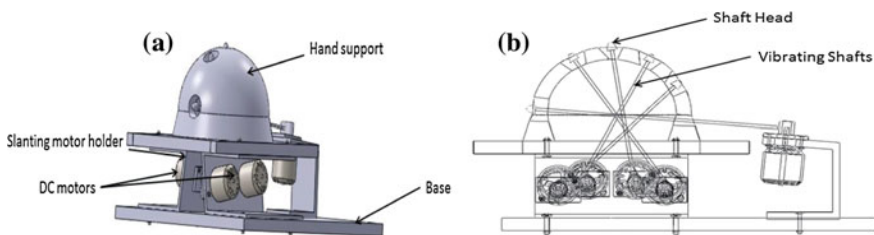


Fig. 3 a Perspective view of the device. b Transparent view

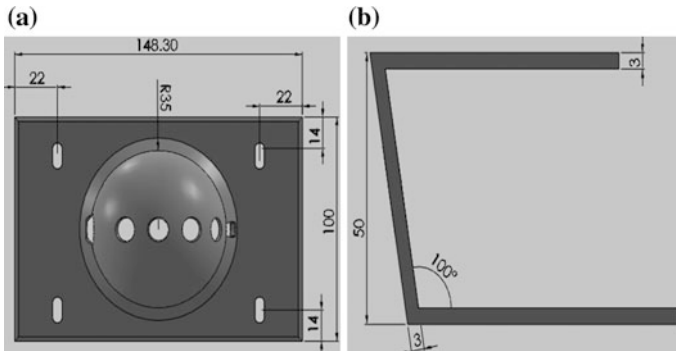


Fig. 4 Front views of the **a** hand support part and **b** slanting motor holder part

The slanting motor holder houses the hand support part above it. Dimensions of this part were decided so that it will fit under the Hand support part and the shafts can be aligned with the holes in the hand support. Straight slots were cut on the holders and also holes were drilled to insert the motors into the holders.

3 Simulation and Analysis on the 3D Model

Analysis of model was done for determining the following:

- (a) Whether the device is working as intended when the forces are applied.
- (b) The torque required to overcome the spring force and also the weight of the parts which are moved by the cam.
- (c) Are the displacement, velocity and acceleration of the shaft head in the required range?

3.1 *Implementing Solidworks Stress Analysis on Parts of the 3D Model*

Solidworks Stress Analysis is done on parts of the model where the weight of the hand would be applied. The results of this analysis are shown in Fig. 5. The deformations occurred in the model during the analysis is negligible and so the design and material selection is found to be correct.

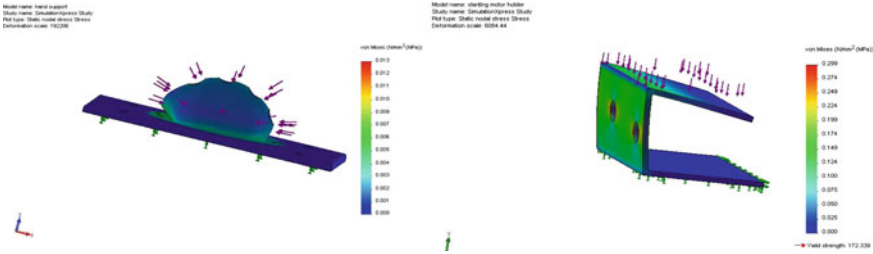


Fig. 5 Solidworks stress analysis on hand support and slanting motor holder parts

3.2 Determining the Torque of the Motor by Trial and Error

Motion analysis on the moving parts of the device was done as shown in Fig. 6. Here, the spring constant of the spring (not shown) is decreased from 1 kgcm to a value which gives the desired displacement of the shaft head.

The displacement of the shaft end with respect to time was plotted as shown above in Fig. 6. Parameters were selected as: Motor torque: 1.2 kgcm, RPM: 60, Spring constant: 1 kgcm. The motor torque is rated at 1.2 kgcm, which is not enough to overcome the spring force as shown in the plot.

In Fig. 7 displacement of shaft end with respect to time with parameters changed as: Motor torque: 1.2 kgcm, RPM: 60, Spring constant: 0.1 kgcm.

Here the shaft was shown to move in the desired manner with 1 cm displacement. As seen above, the spring constant should not exceed 0.1 kgcm for the motor to be able to move the vibrating shaft in the desired manner (Fig. 8).

Velocity and acceleration of the shaft head is also plotted in the similar manner. As designed, acceleration is found to be uniform.

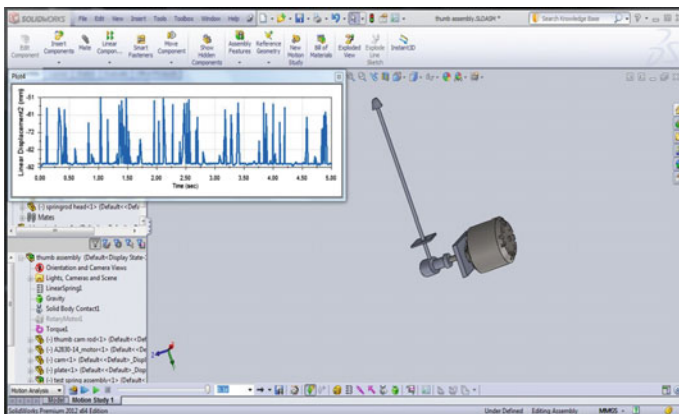


Fig. 6 Motion analysis, displacement of shaft end versus time

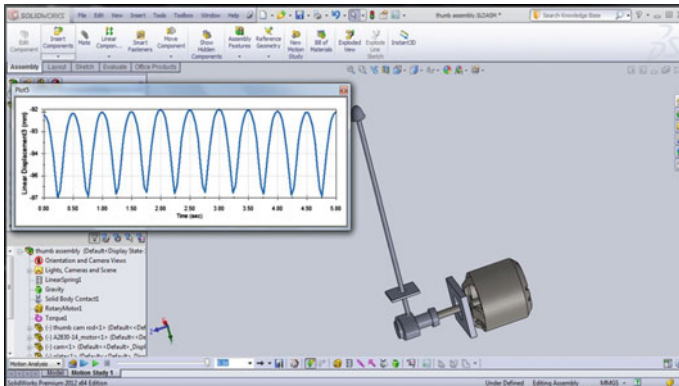


Fig. 7 Motion analysis 2, displacement of shaft end versus time

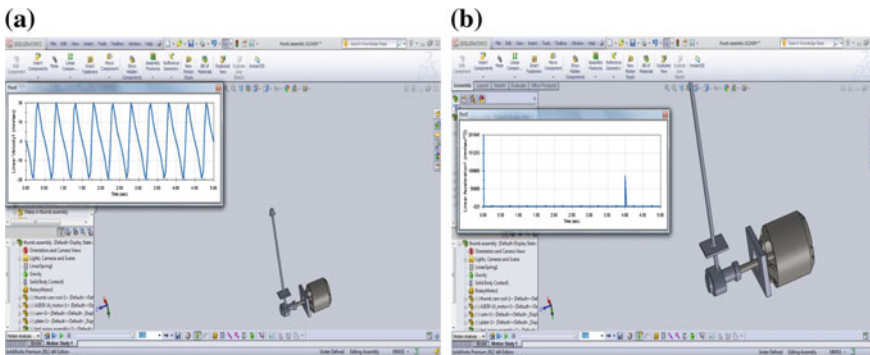


Fig. 8 Motion analysis, a velocity of shaft end versus time and b acceleration versus time

3.3 Simulation of Actuator Control Circuits Using Proteus 8

The circuit for generating PWM signal and controlling the motors are designed in Proteus 8 Professional and simulated.

As shown in Fig. 9, an Astable multivibrator is designed using 555 timer IC. The values of capacitors and resistors are chosen so as to limit the frequency of the PWM signal between 50 to 100 Hz. This PWM signal is then used to driver a motor driver IC L293D. A single L293D IC can drive two DC motors. So 3 such ICs are used to control 5 DC motors. The DC motors used are rated at 100 rpm so that the duty ratio of the PWM signal directly reflects the rotational speed of the motors.

There are two SMA wires acting as actuators. The wires are placed on the fingers as shown in Fig. 10b using rings so that the fingers move according to the

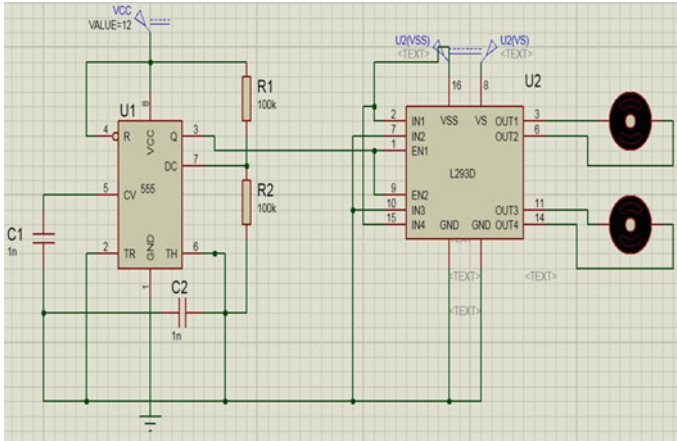
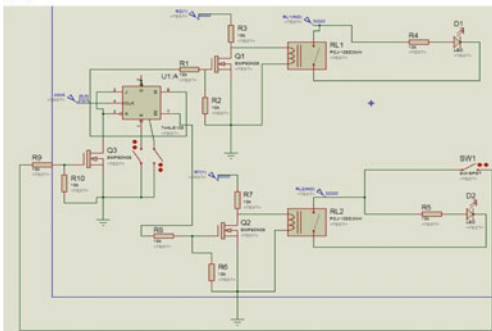


Fig. 9 555 PWM generator and L293D motor controller interfacing with DC motor

(a)



(b)

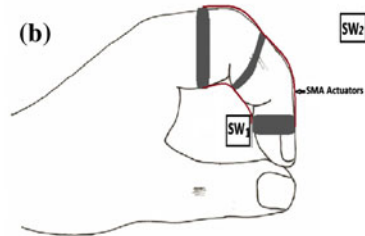


Fig. 10 a Simulation of SMA control circuit in Proteu. b Schematic showing placement of SMA actuators and switches for index finger of the left hand (thermal and electrical protection sheaths and circuits are not shown)

movement of the wires. One actuator is for flexing the fingers and the other one is for extending them. The JK flip flop here acts as a Toggle flip flop which is used to switch between the two SMA actuators. The Power MOSFETS Q1 and Q2 are provided to drive the relays and the relays are provided for isolating the SMA actuators from the flip flop. Switch SW1 is actuated when the SMA has reached its end point. When SW1 is turned on, the flip flop toggles and the other SMA actuator starts working. This process runs in a loop.

4 Hardware Implementation

4.1 Circuit Construction

The device has two different circuits made on PCB as shown in Fig. 11.

4.2 Device Construction

The hand support part and the cams were constructed by 3D printing. The material used was PLA. Slanting motor holder and the vibrating shaft holders were made using sheet metal (GI steel) (Fig. 12).

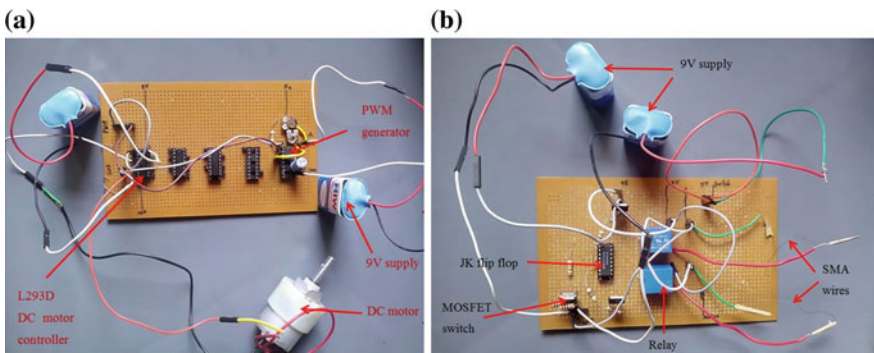


Fig. 11 a DC motor control circuit. b SMA actuator control circuit with only one actuator connected for simplicity

Fig. 12 Constructed device



5 Results

The actuators were found to be working in the desired speed of 60–100 Hz which is required to induce the illusions. The maximum displacement of the vibrating shafts were also at desired levels of 1 mm.

SMA actuators need to be calibrated for its speed and also the force with which they move should be found out. This project has focussed on the design and analysis of the mechanical components and also on designing the circuits for the actuators. Future work should focus on implementing the actuators for moving fingers with rings attached to them as shown in Fig. 11b.

The Shape memory alloy wires used in the circuit were of very small diameter (0.17 mm) and so the force that they could exert were not enough to overcome the weight of the fingers. Any increase in the diameter demanded an increase in the power supply also. Also, there were issues with accurately heating the SMA wires without affecting the delicate electronics components. More work is to be done to avoid the heat getting diverted from the SMA actuators towards the circuit components. One suggestion is to use a secondary high resistance heating device to heat up the SMA instead of supplying current to it directly. This will increase the efficiency of the actuators, allow using thicker wires and also avoid the circuits getting damaged.

Acknowledgments I would like to express my profound gratitude to my Research Guide Prof Preethika Immaculate Britto, CBMR, VIT University, without whose support and guidance I could not have completed this project. I would also like to thank my department guide Prof. T C Kanish, Mechatronics Department, SMBS, VIT University for his inspiration and assistance throughout the course of this project. Last but not least I thank all the faculties and my friends in mechatronics department at VIT University for their help and inspiration.

References

- Chelette et al. (IEEE Haptics Symposium 2014). Effects of low frequency continuous muscle vibration on learning and transfer of a knee joint positioning task.
- Dohle, C., Pullen, J., Nakaten, A., Kust, J., Rietz, C., & Karbe, H. (2009). Mirror therapy promotes recovery from severe hemiparesis: a randomized controlled trial. *Neurorehabil Neural Repair*, 23(3), 17–209.
- Domenik (IEEE 2012). Device for a novel hand and wrist rehabilitation strategy for stroke patients based on illusory movements induced by tendon vibration.
- Gay, A., Parratte, S., Salazard, B., Guinard, D., Pham, T., Legré, R., & Roll, J. P. (2007). Proprioceptive feedback enhancement induced by vibratory stimulation in complex regional pain syndrome type I: An open comparative pilot study in 11 patients. *Joint Bone Spine*, 74, 461–466.
- Hendricks, H. T., van Limbeek, J., Geurts, A. C., & Zwarts, M. J. (2002). Motor recovery after stroke: a systematic review of the literature. *Archives of Physical Medicine and Rehabilitation*, 83(11), 1629–1637.
- Kajimoto (IEEE World Haptic Conference 2013). Illusion of Motion Induced by Tendon Electrical Stimulation.

Moon, C. H. Cam design book, manual for engineers and draftsmen.

Rinderknecht et al. (IEEE World Haptic Conference 2013). Combined Tendon Vibration and Virtual Reality for Post-Stroke Hand Rehabilitation.

Robertson, V. J., & Baker, K. G. (2015). A review of therapeutic ultrasound: effectiveness studies. *Physical Therapy, 81*.

Experimental Investigation of Process Parameters for Build Time Estimation in FDM Process Using RSM Technique

Manu Srivastava, Sachin Maheshwari, T.K. Kundra, Sandeep Rathee and Ramkrishna Yashaswi

Abstract Effectiveness of any additive manufacturing process can be considerably enhanced by estimating optimal values of Build Time. Effect of contour width, raster width, raster angle, slice height, orientation and air gap on the BT requirements for the seven basic constructive solid geometry primitives is studied. Derivation, evaluation and validation of models is accomplished analytically and graphically using response surface methodology technique to deduce the effect of above parameters on the Build Time estimation for Fortus 250 mc modeler. This work establishes basic design principles for: (1) Estimation of Build Time estimation in given volume; (2) Different spatial orientations were evaluated for overall build-time optimization for Fused Deposition Modelling process using Fortus 250 mc modeler.

Keywords Build time · Contour width · Raster width · Air gap · Orientation · Layout optimization · Fused deposition modeling · Response surface methodology

M. Srivastava (✉) · S. Rathee
TRF, MPAE Division, NSIT, New Delhi, India
e-mail: manyash@gmail.com

S. Rathee
e-mail: rathee8@gmail.com

S. Maheshwari
MPAE Division, NSIT, New Delhi, India
e-mail: bssaacchhiinn@gmail.com

T.K. Kundra
MED, IIT Delhi, New Delhi, India
e-mail: tkkundra@gmail.com

R. Yashaswi
CSC, Noida, India
e-mail: ryashaswi@csc.com

1 Introduction

LM is an emerging engineering trend and is a feasible solution to the various design and production issues in conventional manufacturing. This technology paves way for pollution free green manufacturing and most of the manufacturing activities can be accomplished in office environment. LM offers drastic reduction in manufacturing times, freedom from jigs and fixtures, no restriction on the intricacy of the components, pollution and noise free environment, reduced supervision times and numerous other advancements over the conventional manufacturing processes (Thrimurthulu et al. 2004). LM processes need to be qualitatively and quantitatively optimized to get the best out of the given LM technique. For qualitative improvements, one needs to take care of properties like surface roughness (staircase effect), dimensional tolerance, flexural strength, tensile strength, compressive strength, torsional strength, etc. To achieve quantitative improvement the key aspects of optimization mainly include build time, support volume, model volume and production cost. In order to arrive at the best possible components for our case studies, we rounded upon the seven basic primitives used in constructive solid geometry which include: Sphere, Cylinder, Cube, Prism, Pyramid, Cuboid and Cone. It can be safely assumed that all the rest of the components can be arrived at by applying Boolean operations on these primitives (Srivastava et al. 2014a, b; 2015).

This paper proposes a novel method of optimization and evaluation of build-time for different feasible orientations at the design stage itself by virtue of model estimation using RSM and its corresponding validation. These build-time estimates combined with support material, model material and production cost estimations can easily enable the overall quantitative optimization of the given FDM process.

2 Literature Review

The driving force in today's competitive global market is growth in competition. New and innovative technologies are being developed to fabricate products. LM is one such technique whose success is based on achieving cost and quality optimization. One of the critical criterion is selection of best build orientation which effects parameters like build time, cost, surface finish etc. (Zhu 2013). Another crucial issue is selection of optimal combination of process parameters to arrive at the minimal build time. The aim of the study is to determine the optimum parameter settings and spatial orientation for minimizing build-time in FDM process.

Espalin et al. investigated build process variation for FDM in making contours and rasters using variable layer thicknesses and road widths and evaluated its effect on surface roughness, production times and mechanical properties. They used this to develop a unique FDM process which enabled multiple material deposition (F.G.M.) (Espalin et al. 2014). Vilalpando et al. proposed a method to create reconfigurable

internal structure to balance mechanical properties, material usage and build time (Vilalpando and Urbanic 2011). Stratasys the patent owner for FDM technology has itself launched a smoothing station which gives the RP people strength of FDM parts along with desirable surface smoothness which may probably result in the variations (increase) in the process times (Stratasys 2014a). Sheriff El-Gizawy et al. characterized mechanical properties & internal structure for polyetherimide (ULTEM 9085) with FDM using classical lamination theory (El-Gizawy et al. 2011). Panda et al. considered the effect of crucial process parameters on tensile, flexural and impact strength using central composite design and empirical model development. After validation using ANOVA theoretical parameter settings to simultaneously affect all three response optimization are suggested (Panda et al. 2009). Jacobs gave some basic guidelines for best orientation for part build which are still followed (Jacobs 1994). Bablani et al. quantified types of surface inaccuracies including process planning error due to component slicing and process error accounting for undesired material polymerization (Bablani and Bagchi 1995). Choi et al. proposed modeling and optimization for virtual reality system of RP processes by building mathematical model for BT estimation in SLS systems (Choi and Samavedam 2002). Zhe presented relationships between the build orientation and the maximum stress, maximum strain, and young's modulus for SLS, FDM and Objet (SLA), decision criteria for selecting the best orientation of the minimum strain and maximum external load through case studies (Zhe 2010). Mishra et al. have also reviewed the build orientations for different RP processes (Mishra and Thirumavalavan 2014).

Build-time is one of the critical responses in the quantitative optimization of the LM processes. A number of researchers have carried work in improving the effectiveness and efficiency of FDM processes. A lot of work has been done in the direction of qualitative improvements. However, from detailed literature review it can be concluded that there are research gaps in the quantitative aspect of FDM process optimization. In this study, models are derived, analyzed, evaluated and validated graphically and analytically using RSM for BT of FDM process.

3 Build Time (BT)

BT is a critical factor for optimization of any LM technique. It is the time that a part spends on a machine during its creation assuming zero bottlenecks. Though build-time is frequently used measure of process time/process speed, yet these two terms are not the same. Process time give an indication of the overall product completion time. Several factors need attention for the process time evaluation. These mainly include: model preparation/file generation, system preparation, part build time, post build operations/post processing operations (Stratasys 2014b). The main constituents of these four components of process time are detailed below:

Input collection/file preparation includes CAD model preparation, STL file preparation and the interfacing time.

System preparation time covers time includes model orientation, supports generation, layer thickness selection, applying build style, machine preparation loading/Swapping materials as well as time for machine warm up.

Build time includes the in-process time involving actual physical 3D model creation assuming zero bottlenecks.

Post build/post processing includes post build idle, part drainage/cooling off time, chamber cooling time, cleaning, post curing time, support material removal time, excess material removal time, finishing times.

File and system preparation time as also the post build time depends on the technological capability of the given machine as well as the individual operator expertise. This study therefore focuses on the estimation of the build-time only because this can be directly estimated as a function of process parameters (Stratasys 2014b; Yim and Rosen 2012).

Build time can be understood as:

$$T_B = F(x,y) \quad (1)$$

where T_B is the build time, x denotes fixed parameters which include part height, material volume, configuration, shape, part foot area, part surface area and y denotes variable parameters which include orientation, contour width, part fill style, support style, raster angle, raster width, no. of contours, slice height, air gap.

Though we have focused on achieving minimum build-time yet it should always be kept in mind that an inferior part can never compete with its superior counterpart even if the latter takes twice as much time. Therefore build-time should always be considered as one of the options and should always be weighed against other design objectives (Stratasys 2014b).

4 Experimental Design

The details of Modeler, Fixed parameters and Process parameters selected for this experimentation are given in Tables 1, 2 and 3 respectively. Table 4 gives the details of the CSG primitives used for case studies. Typical standard primitives are: cone, cylinder, sphere, cube, cuboid, prism and pyramid. This case study is based on the assumption that establishing design rules for these simple CSG primitives can be easily extended to complicated objects since they can be derived from basic

Table 1 Technical specifications of Fortus 250 mc modeller

Build envelope	10 × 10 × 12 in.
Layer thickness	0.007, 0.010 and 0.013 in.
Model material	ABS P430
Support material	ABS SR30
Powered by	Insightv9.0
Support structures	Soluble

Table 2 Parameters fixed during entire experimentation

S. no.	Parameter	Comments
1	Interior part style	Solid (normal)
2	Surface style	Normal
3	Support style	Sparse
4	Model material	ABS P430
5	Support material	ABS SR30
6	Part fill style	One contour/rasters
7	Part X shrink factor	1.007
8	Part Y shrink factor	1.007
9	Contour to raster air gap	0
10	Support style	Sparse
11	Support self-supporting angle	50
12	Contour base oversize	1.27
13	Contour base layers	8
14	Invert material	Yes
15	Support tip	T16

Table 3 Process parameters and their levels

S. no.	Parameters	Level 1	Level 2	Level 3
1	Slice height (mm)	0.1778	0.254	0.3302
2	Contour width (mm)	0.4	0.48	0.56
3	Air gap (mm)	-0.1	0.4	0.9
4	Raster width (mm)	0.4	0.48	0.56
5	Raster angle (degrees)	0	15	30
6	Orientation (degrees)	0	15	30

Table 4 Details (name and stl size) of CSG primitives used

Primitive number	Primitive name	Stl size (length × width × height) mm
1	Cylinder	20 × 69.999 × 20
2	Cone	20 × 20 × 69.999
3	Cube	10 × 10 × 10
4	Sphere	62.014 × 62.014 × 62.014
5	Cuboid	20 × 69.999 × 20
6	Pyramid	39.999 × 39.078 × 69.999
7	Prism	64 × 55.425 × 48.009

primitives. These primitives are studied at different spatial orientation based on scheme of experimentation illustrated in Table 5. The design methodology adopted is RSM. The 86 run Central Composite design (CCD) experimentation table with 6 process parameters and single response (BT) for C1PS1 (rotation of cylinder about x-axis keeping minimum z-height) is given in Table 6. BT is noted using FDM control center/FDM control panel with the help of Insightv9.1 software.

Table 5 Scheme of experimentation

Primitive		Spatial rotation about				
S. no.	Type	X-axis (θ_x)	Y-axis (θ_y)	Z-axis (θ_z)	X with min Z (θ_{xz})	Y with min Z (θ_{yz})
1	Cylinder	C1PS3	C1PS4	C1PS5	C1PS1	C1PS2
2	Cone	C2PS1	C2PS2	C2PS3	C2PS4	C2PS5
3	Cube	C3PS1	C3PS2	C3PS3	C3PS4	C3PS5
4	Sphere	C4PS1	C4PS2	C4PS3	C4PS4	C4PS5
5	Cuboid	C5PS1	C5PS2	C5PS3	C5PS4	C5PS5
6	Pyramid	C6PS1	C6PS2	C6PS3	C6PS4	C6PS5
7	Prism	C7PS3	C7PS4	C7PS5	C7PS1	C7PS2

Note CnPSm implies the evaluations for nth component at mth spatial orientation (1–5)

Table 6 Experimental results for C1PS1 based on CCD and experimental results for six variables in uncoded units using RSM

Std	Run	Factor 1 A: SH (mm)	Factor 2 B: CW (mm)	Factor 3 C: AG (mm)	Factor 4 D: RW (mm)	Factor 5 E: RA (Degrees)	Factor 6 F: O (Degrees)	Response1 BT (H)
13	1	0.1778	0.4	0.9	0.56	0	0	0.933
27	2	0.1778	0.56	-0.1	0.56	30	0	1.883
72	3	0.254	0.48	0.4	0.56	15	15	1.3
30	4	0.3302	0.4	0.9	0.56	30	0	0.517
60	5	0.3302	0.56	-0.1	0.56	30	30	1.617
53	6	0.1778	0.4	0.9	0.4	30	30	2.533
28	7	0.3302	0.56	-0.1	0.56	30	0	0.867
9	8	0.1778	0.4	-0.1	0.56	0	0	1.7
11	9	0.1778	0.56	-0.1	0.56	0	0	1.683
61	10	0.1778	0.4	0.9	0.56	30	30	2.483
39	11	0.1778	0.56	0.9	0.4	0	30	2.533
45	12	0.1778	0.4	0.9	0.56	0	30	2.483
38	13	0.3302	0.4	0.9	0.4	0	30	1.3
84	14	0.254	0.48	0.4	0.48	15	15	1.333
52	15	0.3302	0.56	-0.1	0.4	30	30	1.95
82	16	0.254	0.48	0.4	0.48	15	15	1.333
19	17	0.1778	0.56	-0.1	0.4	30	0	2.617

(continued)

Table 6 (continued)

Std	Run	Factor 1 A: SH (mm)	Factor 2 B: CW (mm)	Factor 3 C: AG (mm)	Factor 4 D: RW (mm)	Factor 5 E: RA (Degrees)	Factor 6 F: O (Degrees)	Response1 BT (H)
69	18	0.254	0.48	-0.1	0.48	15	15	1.9
43	19	0.1778	0.56	-0.1	0.56	0	30	3.4
73	20	0.254	0.48	0.4	0.48	0	15	1.333
46	21	0.3302	0.4	0.9	0.56	0	30	1.267
5	22	0.1778	0.4	0.9	0.48	0	0	0.917
34	23	0.3302	0.4	-0.1	0.4	0	30	2.0167
20	24	0.3302	0.56	-0.1	0.4	30	0	1.2
48	25	0.3302	0.56	0.9	0.56	0	30	1.2
41	26	0.1778	0.4	-0.1	0.56	0	30	3.433
26	27	0.3302	0.4	-0.1	0.56	30	0	0.933
21	28	0.1778	0.4	0.9	0.4	30	0	1.05
1	29	0.1778	0.4	-0.1	0.4	0	0	2.367
32	30	0.3302	0.56	0.9	0.56	30	0	0.467
79	31	0.2540	0.48	0.4	0.48	15	15	1.333
37	32	0.1778	0.4	0.9	0.4	0	30	2.55
35	33	0.1778	0.56	-0.1	0.4	0	30	4.133
8	34	0.3302	0.56	0.9	0.4	0	0	0.45
36	35	0.3302	0.56	-0.1	0.4	0	30	1.933
76	36	0.2540	0.48	0.4	0.48	15	30	1.8
10	37	0.3302	0.4	-0.1	0.56	0	0	0.833
23	38	0.1778	0.56	0.9	0.4	30	0	1.033
33	39	0.1778	0.4	-0.1	0.4	0	30	4.167
14	40	0.3302	0.4	0.9	0.56	0	0	0.467
81	41	0.2540	0.48	0.4	0.48	15	15	1.333
7	42	0.1778	0.56	0.9	0.4	0	0	0.917
75	43	0.2540	0.48	0.4	0.48	15	0	0.767
71	44	0.2540	0.48	0.4	0.4	15	15	1.383
58	45	0.3302	0.4	-0.1	0.56	30	30	1.683
74	46	0.2540	0.48	0.4	0.48	30	15	1.35
44	47	0.3302	0.56	-0.1	0.56	0	30	1.6
47	48	0.1778	0.56	0.9	0.56	0	30	2.467
65	49	0.1778	0.48	0.4	0.48	15	15	2.033
17	50	0.1778	0.4	-0.1	0.4	30	0	2.65
2	51	0.3302	0.4	-0.1	0.4	0	0	1.12
42	52	0.3302	0.4	-0.1	0.56	0	30	1.683
51	53	0.1778	0.56	-0.1	0.4	30	30	4.15
3	54	0.1778	0.56	-0.1	0.4	0	0	2.333
56	55	0.3302	0.56	0.9	0.4	30	30	1.233
55	56	0.1778	0.56	0.9	0.4	30	30	2.517

(continued)

Table 6 (continued)

Std	Run	Factor 1 A: SH (mm)	Factor 2 B: CW (mm)	Factor 3 C: AG (mm)	Factor 4 D: RW (mm)	Factor 5 E: RA (Degrees)	Factor 6 F: O (Degrees)	Response1 BT (H)
59	57	0.1778	0.56	-0.1	0.56	30	30	3.4
12	58	0.3302	0.56	-0.1	0.56	0	0	0.783
66	59	0.3302	0.48	0.4	0.48	15	15	1.033
18	60	0.3302	0.4	-0.1	0.4	30	0	1.25
40	61	0.3302	0.56	0.9	0.4	0	30	1.233
68	62	0.2540	0.56	0.4	0.48	15	15	1.317
62	63	0.3302	0.4	0.9	0.56	30	30	1.267
24	64	0.3302	0.56	0.9	0.4	30	0	0.5
80	65	0.2540	0.48	0.4	0.48	15	15	1.333
54	66	0.3302	0.4	0.9	0.4	30	30	1.3
57	67	0.1778	0.4	-0.1	0.56	30	30	3.433
31	68	0.1778	0.56	0.9	0.56	30	0	0.983
6	69	0.3302	0.4	0.9	0.4	0	0	0.483
49	70	0.1778	0.4	-0.1	0.4	30	30	4.2
16	71	0.3302	0.56	0.9	0.56	0	0	0.417
86	72	0.2540	0.48	0.4	0.48	15	15	1.333
22	73	0.3302	0.4	0.9	0.4	30	0	0.55
64	74	0.3302	0.56	0.9	0.56	30	30	1.2
4	75	0.3302	0.56	-0.1	0.4	0	0	1.083
70	76	0.2540	0.48	0.9	0.48	15	15	1.167
83	77	0.2540	0.48	0.4	0.48	15	15	1.333
78	78	0.2540	0.48	0.4	0.48	15	15	1.333
77	79	0.2540	0.48	0.4	0.48	15	15	1.333
25	80	0.1778	0.4	-0.1	0.56	30	0	1.917
15	81	0.1778	0.56	0.9	0.56	0	0	0.867
63	82	0.1778	0.56	0.9	0.56	30	30	2.47
50	83	0.3302	0.4	-0.1	0.4	30	30	2.033
67	84	0.254	0.4	0.1	0.48	15	15	1.367
29	85	0.1778	0.4	0.9	0.56	30	0	0.983
85	86	0.254	0.48	0.4	0.48	15	15	1.333

5 Results

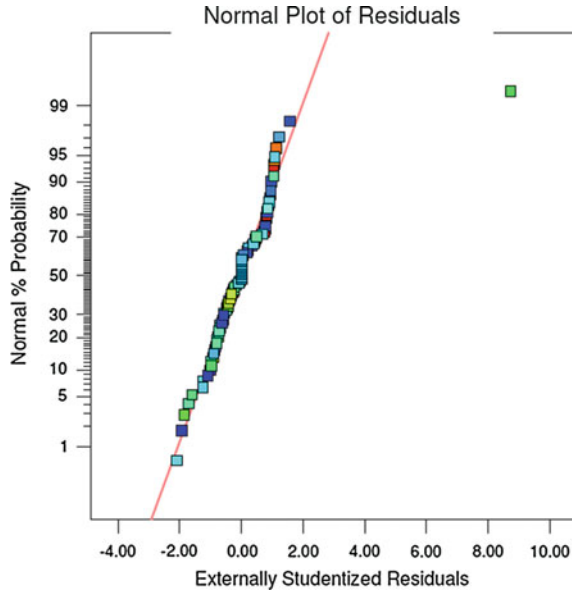
The model obtained using RSM for C1PS1 (cylinder with absolute rotation about x-axis keeping minimum z-height) is tabulated and discussed (Table 6).

RSM model details are tabulated in Table 7. The model was found to be significant with F value of 1959.30 and p-value < 0.0001. Figure 1 shows the normal probability plot of residuals for build time. It is evident that all the residuals are

Table 7 RSM model specifications for C1PS1

Model	Lambda	Model	Pure error	R-Sqrd	Adjus R-Sqrd
Power	1	Quadratic	0	0.9857	0.979

Fig. 1 Normal plot of residuals



clustered in the straight line implying that errors are normally distributed. Figure 2 shows the plot of actual vs predicted model values. Since the points are clustered around a straight line, the predicted value are in close adherence to the actual values. Normal plot of residuals and Predicted versus Actual graphs are attached below:

The Final model Equation for build-time in Terms of Actual Factors:

$$\begin{aligned}
 (\text{Build Time})_1 = & + 10.88518 - 26.32600 * SH - 4.73475 * AG - 5.11682 * RW - 1.93627E \\
 & - 003 * RA + 0.017724 * O + 2.47601 * SH * CW + 5.16732 * SH * AG \\
 & + 8.98643 * SH * RW + 3.66360E - 003 * SH * RA - 0.025098 * SH * O \\
 & - 0.065625 * CW * AG - 1.46973 * CW * RW + 8.22917E - 003 * CW \\
 & * RA + 6.92708E - 003 * CW * O + 3.63438 * AG * RW - 1.38750E \\
 & - 003 * AG * RA - 3.45833E - 004 * AG * O - 8.22917E - 003 * RW \\
 & * RA - 6.97917E - 003 * RW * O + 7.65278E - 005 * RA * O + 23.21960 \\
 & * SH^2 + 11.92550 * CW^2 + 0.93929 * AG^2 + 0.49582 * RW^2 + 8.10324E \\
 & - 006 * RA^2 - 1.40786E - 004 * O^2
 \end{aligned}
 \tag{2}$$

In this case SH, CW, AG, RW, RA, O, SH * CW, SH * AG, SH * O, AG * RW, AG * O, RW * O, RA * O, SH², AG², O² are significant Model terms. P-Values greater than 0.1000 for RSM models indicate the model terms are not significant.

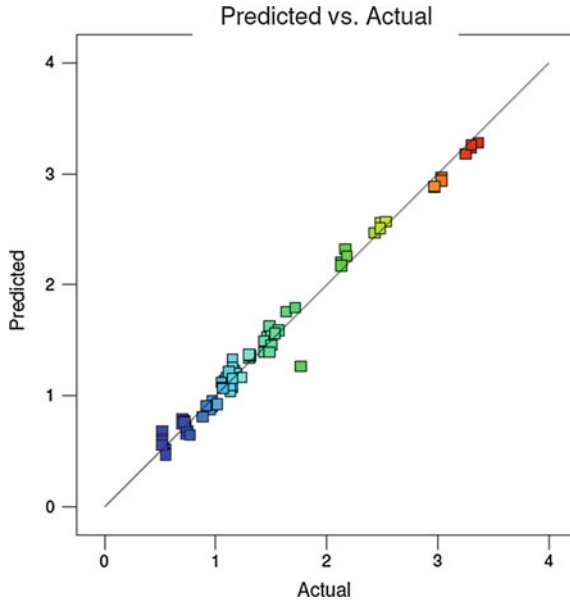


Fig. 2 Predicted versus actual

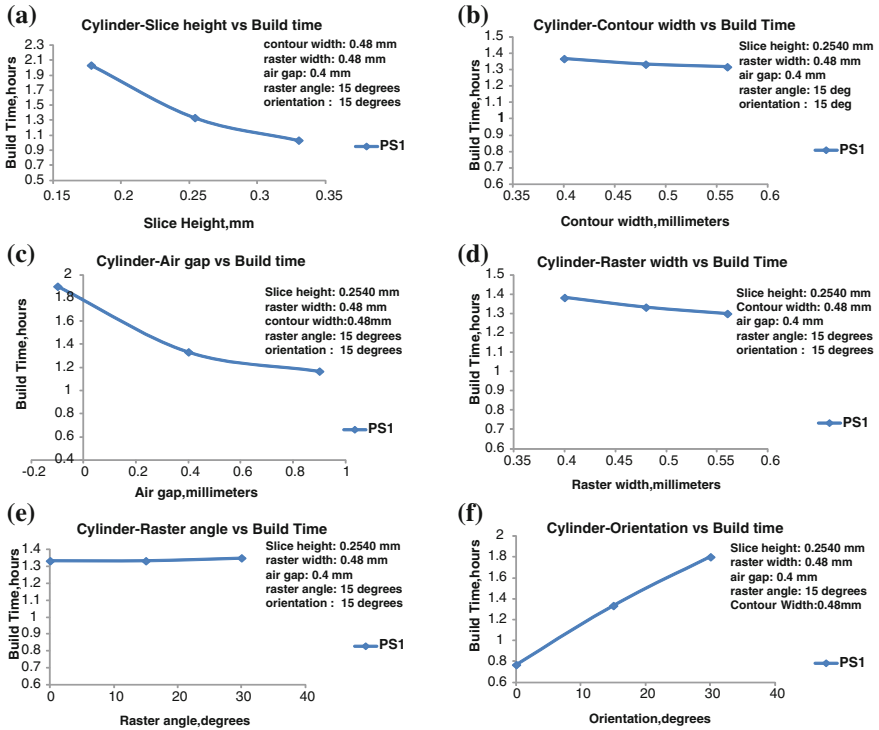


Fig. 3 a–f BT variation wrt the changes in SH, CW, AG, RW, RA and O respectively for the rotation of cylinder about X-axis keeping z height minimum (CIPSI)

Figure 3a–f shown below displays the BT variation with respect to changes in slice height, contour width, air gap, raster width raster angle and orientation respectively, for rotation of cylinder about x-axis keeping z height minimum. Similar to the model formation for CIPS1, models have been derived, analyzed and verified by experimentation and modeling for all primitives wrt to each process parameter as well as spatial orientation as per the scheme of experimentation. All of these cannot be included because of lack of space. The models and their graphs were thoroughly studied and compared to arrive upon the following outcomes:

1. Effect of each individual parameter on the build time for each primitive.
2. Best spatial Orientation for each primitive.

6 Conclusions

This study experimentally builds and evaluates the model for BT with respect to:

- (i) All six crucial process parameters and from the results the following can be safely concluded:
 1. B.T. invariably reduces with increase in slice height.
 2. B.T. invariably reduces with increase in air gap.
 3. B.T. depends slightly on the contour width as only minor reduction can be seen corresponding to increasing contour width.
 4. B.T. depends slightly on the raster width as only minor reduction can be seen corresponding to increasing raster width.
 5. B.T. increases with increase in raster angle in general though the increase is minor.
 6. B.T. invariably increases with increase in angle of rotation about any particular axis (orientation) though it remains constant for components which display rotational symmetry about any particular axis.
- (ii) Every feasible spatial orientation and from the results the following can be safely concluded:
 1. For cylindrical primitives, rotation about θ_{yz} gives the least value of build-time followed by rotations θ_z , θ_x & θ_y , θ_{xz} .
 2. For conical primitives, rotation about θ_z gives the least value of build-time followed by rotations θ_x & θ_y , θ_{yz} , θ_{xz} .
 3. For cubical primitives, θ_z gives the least value of build-time followed by rotations θ_x & θ_y & θ_{yz} & θ_{xz} .
 4. For spherical primitives, rotational symmetry is exhibited and B.T. corresponding to θ_x & θ_y & θ_{yz} & θ_{xz} & θ_z are equal.
 5. For cuboidal primitives, rotation about θ_z gives the least value of build-time followed by rotations θ_{yz} , θ_x & θ_y , θ_{xz}

6. For pyramidal primitives, rotation about θ_z gives the least value of build-time followed by rotations θ_x , θ_y , θ_{xz} , θ_{yz} .
7. For prismatic primitives, rotation about θ_z gives the least value of build-time followed by rotations θ_x & θ_y , θ_{xz} , θ_{yz} .

Corresponding to the above conclusions the issues of orientation for purpose of nesting can be solved. Moreover, since the modeling is done for all the primitives of constructive solid geometry the study can be thought of as universally applicable. Also, the study graphically and analytically explains the effect of all the crucial build parameters on the build-time estimations for a particular part.

The RSM models derived and the corresponding analysis can easily be used for many responses affecting the quantitative optimization of FDM process. Also, the effect of spatial orientation using the same design of experiment can be applied to evaluate various responses in order to accomplish qualitative FDM optimization.

References

- Bablani, M., & Bagchi, A. (1995). Quantification of errors in rapid prototyping processes, and determination of preferred orientation of parts. Clemson University: Product Realization Laboratory, Center for Advanced Manufacturing.
- Choi, S. H., & Samavedam, S. (2002). Modelling and optimization of rapid prototyping. *Computers in Industry, Elsevier*, 47, 39–43.
- El-Gizawy, S., Corl, S., & Graybill, B. (2011). Process-induced properties of fdm products. www.stratasys.com/fdmproducts.pdf.
- Espalin, D., Ramirez, J. A., Medina, F., & Wicker, R. (2014). Multimaterial, multitechnology FDM: Exploring build process variations rapid prototyping journal-emerald. *Insight*, 20(3), 236–244.
- Jacobs, P. F. (1994). Rapid prototyping and manufacturing: Fundamentals of stereolithography. Society of Manufacturing Engineers.
- Mishra, A. K., & Thirumavalavan, S. (2014). A study of part orientation in rapid prototyping. *Middle-East Journal of Scientific Research*, 20(9), 1197–1201.
- Panda, S. K., Padhee, S., Sood, A. K., & Mohapatra, S. S. (2009). Optimization of fused deposition modeling process parameters using bacterial for-aging technique. *Intelligent Information Management*, 1, 89–97.
- Srivastava, M., Maheshwari, S., & Kundra T. K. (2014a). (a). Virtual modelling and simulation of functionally graded materials using FDM process. In *Proceeding of the Materials Today*, Elsevier.
- Srivastava, M., Maheshwari, S., & Kundra, T. K. (2014b). (b). Experimental Evaluation of FDM Process for Support Material Optimization. In *International Conference on Advances in Design & Manufacturing*, NIT Trichy.
- Srivastava, M., Maheshwari, S., & Kundra, T. K. (2015). Optimization of build time and model volume for a FDM maxum modeler using response surface methodology. *International Journal for Technological Research in Engineering*.
- Stratasys. (2014a). Finishing touch smoothing station: Expanding possibilities. <http://www.stratasys.com/solutions/finishing-processes/smoothing-fdm-parts>.
- Stratasys. (2014b). Stratasys data sheets: The truth about speeds. www.stratasys.com.
- Thrimurthulu, K., Pandey, P. M., & Reddy, N. V. (2004). Optimum part deposition orientation in fused deposition modeling. *International Journal of Machine Tools and Manufacture*, 44, 585–594.

- Vilalpando, L., & Urbanic, J. (2011). Parametric internal matrix structure for components made by fused deposition modelling. In *4th International Conference on Changeable, Agile, Reconfigurable and Virtual Production (CARV2011)*.
- Yim, S., & Rosen, D. (2012). Build-time and cost models for additive manufacturing process selection. In *32nd International Design engineering technical conferences and Computers and Information in Engineering Conference*. ASME.
- Zhe, C. (2010). *Selection of Optimal Build Orientation with Minimum Strain and Maximum Strength in Rapid Prototyping*. The University of Hong Kong.
- Zhu, Z. (2013). Advances in sustainable and competitive manufacturing systems. In *23rd International Conference on Flexible Automation and Intelligent Manufacturing*. Springer.

Analysis of Prismatic Springs of Non-circular Coil Shape Using Finite Element Method

Arkadeep Narayan Chaudhury, Arnab Ghosh,
Krishnendu Banerjee, Abhijit Mondal and Debasis Datta

Abstract Common helical springs are of circular coil shape requiring equal space in all directions. But there are applications, such as firearms, where springs with non-circular coils are required. In this paper deflection and stress analysis of a spring with rectangular-semi circular coil is presented. Appropriate CAD model is developed in SolidWorks and Finite element analysis is performed in ANSYS Workbench environment. Results show that such springs undergo more deflection compared to a circular coil spring for same coil area, but with more stress developed. Deflections and von-Mises stresses are obtained for different aspect ratios of the said spring. The methodology presented may help the designer to select the right type of the non-circular coil spring for appropriate applications.

Keywords Prismatic springs of non-circular coil shape · CAD modeling · FEA

1 Introduction

The helical spring is one of the fundamental machine elements used in several industrial applications like brakes, vehicles suspensions, firearms etc. for absorbing energy and providing flexibility to the mechanical system. The known helical spring is presented as a cylindrical three dimensional curved beam, and characterized by its spiral shape.

For design and selection of springs, its deflection under axial load and maximum stresses induced are two major factors. Investigations in this area began early with Wahl (Ancher and Goodier 1958) who considered the wire of the spring as a curved round bar subjected to direct shear and torsion. Coupling between axial and torsional deformation was neglected and a correction factor was used to account for

A.N. Chaudhury · A. Ghosh · K. Banerjee · A. Mondal · D. Datta (✉)
Department of Mechanical Engineering, Indian Institute of Engineering Science
and Technology, Shibpur, Howrah 711103, West Bengal, India
e-mail: ddatta@mech.iiests.ac.in; ddatta.besus@gmail.com

the curvature of the spring. Ancher and Goodier (1958), Wahl (1944) used the boundary element method to apply the elasticity theorem for an approximate result. Nagaya (1987) solved equations governing the distribution of stresses in the spring and developed an analytical solution, applicable only for circular and rectangular cross section. Kamiya and Kita (1990) treated this problem also using boundary element method, but the analysis was limited to springs of small helix angle. Cook (1990) analyzed similar springs with small helix angle using Finite Element method. Haktanir (1994) solved similar problem by an analytical method to determinate the static stresses in the spring. Jiang and Henshall (2000) developed an FEM based approach to analyse the stress problem in a circular cross section helical spring by developing accurate boundary conditions. Fakhreddine et al. (2005) presented an efficient two-node finite element with six degrees of freedom per node, capable of modeling the total behavior of a helical spring.

In the approaches cited above all the analyses were done for prismatic springs with circular coil only. However springs of non-circular coil shape also have applications in practical cases when there is a limitation in space. Springs with cross-sections made of rectangle with semi-circular ends have usage in firearms. In this paper, an analysis has been done to obtain the analytical formulation for deflection and maximum stresses for the aforesaid spring. A basis for comparisons of the aforesaid springs with a standard cylindrical helical spring has been laid down.

2 Deflection Analysis of Prismatic Springs with Non-circular Coil Shape

Here analytical derivation to find deflection of a helical spring with constant pitch, wire diameter with above mentioned non-circular coil has been attempted. The result of this is compared with those obtained from FEA of a representative CAD model. Here the prismatic spring has a rectangular coil shape bounded by semi-circles on the smaller sides as shown in Fig. 1. Such springs are used in guns and rifles. The length of the straight portion of the coil is $2a$ with semicircular ends as shown in Fig. 1. It is observed that the profile has bi-axis symmetry and analysis of only one quarter of the coil would be sufficient.

Fig. 1 Schematic diagram of the non-circular coil showing its basic dimensions

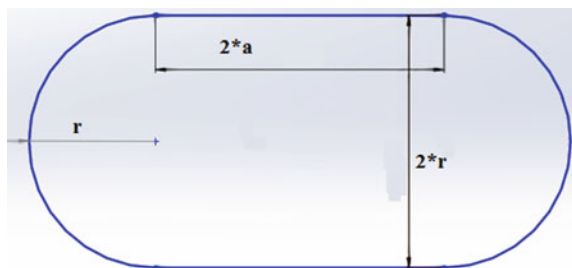
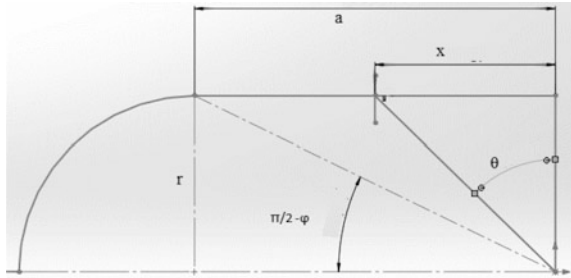


Fig. 2 Representative quarter section



The straight part of the spring, shown in Fig. 2, subtends an angle $\phi = \tan^{-1}(a/r)$ at the center of the coil. The force F , acting vertically at the centre, induces both bending and torsional moment on a section of the coil. Expressions of moments in the circular and straight parts are different and are shown separately. On a section of the spring at a distance x from the vertical centreline (Fig. 3), the moments induced by the force on the straight part are:

$$\begin{aligned} \text{Bending Moment } (M_x) &= F.r.\tan \theta \\ \text{Torsional moment } (T_x) &= F.r \end{aligned} \tag{1}$$

Again, from Fig. 3 it may be observed that,

$$p = \sqrt{a^2 + r^2 + 2ar \sin \theta} \tag{2}$$

where, θ is the angle as shown in Fig. 3. The value of ϕ may be obtained as:

$$\phi = \sin^{-1} \frac{r \cos \theta}{p} \tag{3}$$

The values of bending and torsional moments are obtained as,

$$\begin{aligned} \text{Bending moment } (M_\theta) &= F.p.\sin(\theta + \phi) \\ \text{Torsional moment } (T_\theta) &= F.p.\cos(\theta + \phi) \end{aligned} \tag{4}$$

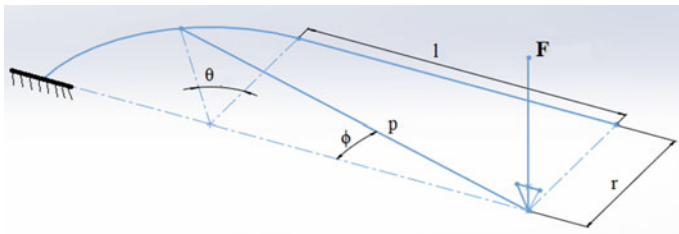


Fig. 3 Isometric view of the loaded quarter section

The total strain energy for the entire straight part of the quarter coil can be expressed as

$$U_{Straight\ Section} = \int_0^a \frac{M_x^2}{2EI} dx + \int_0^a \frac{T_x^2}{2GJ} dx \tag{5}$$

and the strain energy for the curved part of the quarter coil may be obtained as

$$U_{Curved\ Section} = \int_0^{\frac{\pi}{2}} \frac{M_\theta^2}{2EI} d\theta + \int_0^{\frac{\pi}{2}} \frac{T_\theta^2}{2GJ} d\theta \tag{6}$$

where in (5) and (6), $I = \frac{\pi d^4}{64}$ and $J = \frac{\pi d^4}{32}$, d being the wire diameter of the spring. Therefore, the total strain energy of the entire spring due to axial force F is $U_{Total} = 4 * N * (U_{Straight\ Section} + U_{Curved\ Section})$, N being the number of active coils. The axial deflection of the spring is then obtained by using Castigliano’s theorem as

$$\delta = \frac{\partial U_{Total}}{\partial F} \tag{7}$$

Integrations in Eqs. (5) and (6) have been performed using symbolic math tool of MATLAB. In Table 1 a comparison of the values of deflection of the rectangular-semicircular coil spring obtained analytically and through FEA is given. The spring material is taken as steel with Young’s modulus, E = 200 GPa and Poisson’s ratio, v = 0.25. The wire diameter is 3 mm and effective number coils is N = 7.5 for 8 complete turns with ground ends. The spring is under an axial load of 15 N. It is observed that the values are in close agreement validating the formulation. The dimensions of the spring viz. ‘a’ and ‘r’ are as shown in Fig. 1. FE Modelling of the spring is discussed in the next section.

It was also observed that with mesh refinement deflection values obtained through FEA approached the corresponding analytical values.

Table 1 Comparison of deflections under 15 N axial load obtained through FEA and analysis

#	‘a’ in mm	‘r’ in mm	Deflection (in mm) from analysis	Deflection (in mm) from FEA
1	13.26	13.26	10.47	10.39
2	14.30	12.87	10.75	11.40
3	15.53	12.42	11.17	11.75
4	17.02	11.91	11.56	11.96
5	18.66	11.32	12.23	12.45

3 CAD Modelling of the Spring and Assembly with Base Plates

Here steps of modelling of the spring in the SolidWorks CAD platform are discussed.

- Creation of the profile of the spring: For prismatic springs with non-circular coil shape the profile may be obtained by using the Boss-Extrude feature. Figure 1 may be used as the starting sketches for the spring in study.
- Obtaining the modified helix for the spring: The method used in this part may be visualized by the actual process of coiling a spring on an arbour. To start with, a direction of coiling the spring is required. A straight line is drawn on the face of the arbor and it is twisted about the axis of the spring. The twisting generates a surface which intersects the arbor along a continuous helical profile. The helix is selected for generating the spring and other geometries are kept hidden.
- Obtaining the spring coil: The wire diameter is selected and the helix is used as the path of sweep to obtain the continuous curve. This swept geometry is the required spring. The ends are cut along the mid plane of the wire for assembly with end plates on which the force is applied. This also represents the ground-end condition of the spring.

The model of the spring is shown in Fig. 4. There could be other methods of obtaining the model but this method had been chosen on comparative merit as it is more general in modelling any spring irrespective of coil shape.

Fig. 4 CAD model of the spring

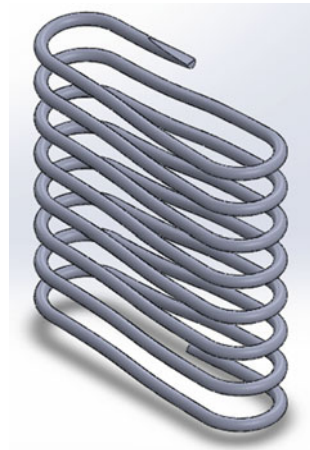
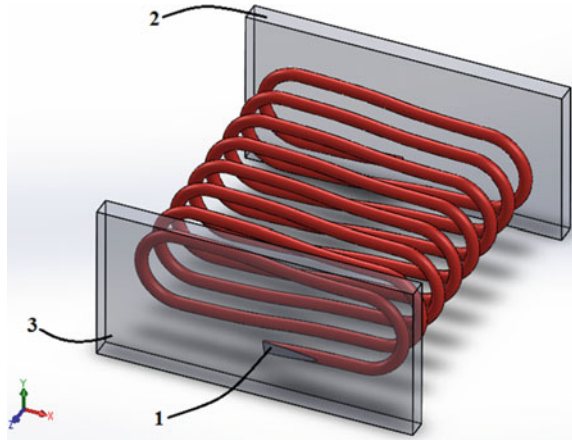


Fig. 5 Assembly of the spring



3.1 Assembly of the Spring with Base Plates

The spring has 6 degrees of freedom in space. The goal of the assembly is to restrict 5 degrees of freedom of the spring, leaving only one DOF along the axis of the spring. The digits included within curly braces in the discussion below are shown in Fig. 5.

1. The flat ground ends of the spring {1} are mated (using mating feature of SolidWorks) to remain co-planar with the flat surfaces of the end plates {2} and {3}. This restricts all degrees of freedom of the spring except, translation in the YZ plane and rotation about X axis.
2. The guide curve of the spring is fixed to remain parallel with the edges of the base plates {2, 3}.
3. The central axis of the spring is set to remain coincident with the central points of the end plates {2, 3} so that the spring cannot be moved around or detached from the plate.
4. The surfaces of the plates {2, 3} are made parallel so that rotations of the plates about X or Y axes are restricted.

4 FEA Analysis of the Spring Assembly Using ANSYS Workbench

FEA of the spring assembly was carried out by importing the assembled CAD part from SolidWorks (2014) environment to ANSYS Workbench Static Structural module (2012). After import of the assembly, meshing was done by 8 node brick element for the end plates and 4 node tetrahedral elements for the spring. The elements used may be inferior to those developed by Fakhreddine et al. (2005) or by

Choi et al. (1995), but their commercial availability and possibility of high h-refinement justifies their usage, particularly in the elastic regime. The force to be applied on the spring being axial, uniformly distributed pressure ($F/\text{area of the plate}$) was applied on the plates, instead of point loads, for better representation of the loading. As seen from Fig. 5, the backing plates have a thickness but the weights of the plates do not come into play as the gravity loading option was kept deactivated.

5 Comparison of Various Springs with a Common Cylindrical Spring

The motivation behind the study of prismatic springs with non-circular coil shape was to cater to design requirements where an elastic element is to be accommodated within a non-circular space. Such cases are found in firearms. These springs may have different aspect ratios while enclosing same coil area. But the deflection and stresses are expected to vary with variation in the aspect ratio. Here instead of using the aspect ratio, a parameter k is introduced that defines the ratio of the radius of the semi-circular end to the length of one straight edge of the coil. Thus in terms of Fig. 1, $r = k * a$. Again, the area enclosed by the coil is given as $A = \pi r^2 + 4ar$. Thus, for a particular area A and parameter k , corresponding r can be computed as $r = \sqrt{\frac{A}{\pi + 4/k}}$. In essence, r and a can easily be computed for the present spring for a given A and chosen k . In the present work A has been selected as 1256.64 mm^2 , corresponding to a circular coil of a diameter of 40 mm. Parameter k is varied from 0.4 to 2.0 in steps of 0.1. For each case axial deflection and maximum von-Mises stress are obtained and variations of them against k are plotted in the same graph as shown in Fig. 5. Other data used in the analysis are: $E = 200 \text{ GPa}$, $\nu = 0.25$, $d = 3 \text{ mm}$, $F = 15 \text{ N}$ and $N = 8$ with ground ends, the symbols being used in their meanings discussed previously.

The variations in Fig. 6 reveal that such springs undergo more axial deflection, i.e., absorb more energy, but at the cost of stress. With the methodology discussed and results given in Fig. 6, a designer may be able to decide on the right value of the parameter k for this type of non-circular coil spring in respect of his application.

The following table shows deflection and maximum von-Mises stress for a circular coil spring with coil diameter of 40 mm, i.e., having the same coil area of 1256.64 mm^2 . For same material, identical wire and number of coil this spring exhibits a smaller deflection of 8.88 mm but also experiencing lower stress value of 65.48 MPa approximately. Although it shows the general usefulness of a circular coil spring, but its space requirement in all directions is non-deniable. In this regard the rectangular-semi-circular coil shape tends to show advantage in specialised applications.

Load (N)	Deflection (mm)	Max von-Mises stress in MPa
15	8.88	65.48

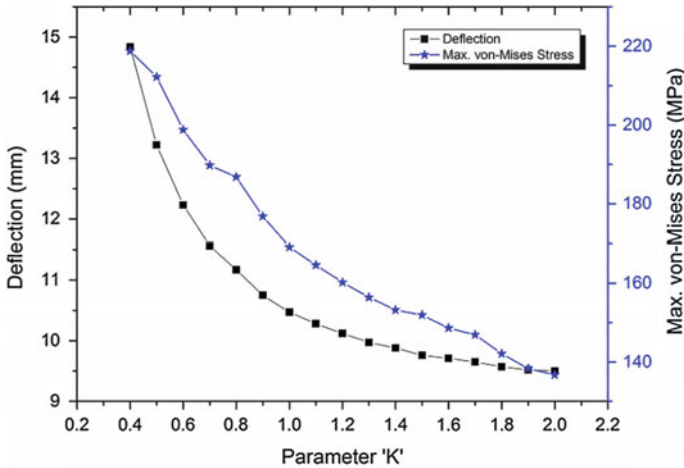


Fig. 6 Variation of axial deflection and maximum von-Mises Stress of the spring under 15 N load with variation of the parameter k

Therefore, the deflection and stress characteristics of the rectangular-semi circular coil springs may be summarised as:

1. For the same axial load, the deflection of the spring increases as the coil shape loses circularity.
2. Stress values of the spring are higher than that of the cylindrical spring and the value of maximum stress increases for lower values of k . This is attributed to the curvature effect of the spring. The higher value of k signifies approach towards a circular profile and thus the stress increasing effect due to curvature is less pronounced.

References

- Ancher, J., Jr. & Goodier, J. N., (1958a). Pitch and curvature corrections for helical springs. *Journal of Applied Mechanics*, 25, 466–470.
- Ancher, J., Jr. & Goodier, J. N. (1958b). Theory of pitch and curvature corrections for helical springs. *Journal of Applied Mechanics*, 25, 471–495.
- ANSYS Workbench 14.5. (2012). *Static structural module: ANSYS*. Canonsburg, PA, United States of America.
- Choi, J. K., & Lim, J. K. (1995). General curved beam elements based on the assumed strain fields. *Computers & Structures*, 55(3), 379–386.
- Computer Software. (2014). *Solidworks 2015, 64-bit*. Concord, MA: SolidWorks Corporation.
- Cook, R. D. (1990). Finite element analysis of closely-coiled springs. *Computers & Structures*, 34 (1), 179–180.
- Fakhreddine, D., et al. (2005). Finite element method for the stress analysis of isotropic cylindrical helical spring. *European Journal of Mechanics-A/Solids*, 24.6, 1068–1078.

- Haktanir, V. (1994). Analytical investigation of parameters affecting stiffness of helical springs of arbitrary shape under compression. In: *Proceeding of 6th International Machine Design and Production Conference, Ankara, September* (p. 473).
- Jiang, W. G., & Henshall, J. L. (2000). A novel finite element for helical springs. *Finite Elements Anal. Design*, 35, 363–377.
- Kamiya, N., & Kita, E. (1990). Boundary element method for quasi-harmonic differential equation with application to stress analysis and shape optimization of helical springs. *Computers & Structures*, 37(1), 81–86.
- Nagaya, N. (1987). Stresses in helical spring of arbitrary cross-section with consideration of end effects. *Journal of Vibration and Acoustics*, 109(3), 289–301.
- Wahl, A. M. (1944). *Mechanical springs*. Penton Publishing Company.

TiC, W₂C Reinforced Ti-W MMC Coating Developed on Ti-6Al-4V Substrate Through Laser Cladding

Parth Gattani, Barun Halder, Adil Azeem and Partha Saha

Abstract High specific strength, corrosion resistance and subzero to moderately elevated working temperature are the intrinsic properties of Ti-6Al-4V, which turn it one of the favourite aerospace engineering materials. Relatively soft and poor wear resistive properties restrict its further essential applications. In the present work, attempts were carried out to improve tribological properties of Ti-6Al-4V surface by developing hard and bulk clad layers for longer service life of that product. A pre-placed powder mixture of tungsten, graphite and titanium over the substrate, was irradiated by a fibre laser in argon shroud. The laser clad layers developed with in situ TiC and W₂C reinforced in Ti-W matrix that were confirmed by HR XRD phase analysis. Effects of laser scan speeds on coatings formation, microstructure, microhardness, and dry sliding wear performance were investigated. The microhardness of the coated surfaces was improved up to 700 HV_{0.05} on an average whereas microhardness value of the untreated Ti-6Al-4V substrate was 350 HV_{0.05}. The dry sliding wear performances of the hard coatings significantly improved.

Keywords Laser cladding · Ti-6Al-4V · Multi-component · Hard and bulk · Wear resistant coating

The original version of this chapter was revised: For detailed information please see Erratum. The Erratum to this chapter is available at [10.1007/978-81-322-2740-3_82](https://doi.org/10.1007/978-81-322-2740-3_82)

P. Gattani · B. Halder · A. Azeem · P. Saha
Department of ME, IIT Kharagpur, Kharagpur 721302, West Bengal, India

B. Halder (✉)
Department of ME, BIET, Suri, India
e-mail: b4barun@gmail.com

1 Introduction

Titanium is the ninth most abundant element in the earth and having a significant role in modern development. Among the different grades of titanium alloys, alpha titanium alloys experience no ductile-to-brittle transition temperature (Campbell 2008). At sub-zero temperature, these materials exhibit reasonably good mechanical properties including the capability to restrict dynamic failure in the structure. These characteristics are precious in aerospace and space shuttle applications that work at cryogenic temperature. The alpha-beta alloys include Ti-6Al-4V, which accounts for approximately 60 wt% of the titanium used in today's industries for its unique set of properties including good fabrication ability and strength. Some noteworthy characteristics (Matthew and Donachie 2000) of titanium and its alloys are:

- nonmagnetic and low heat conductivity,
- low to moderately elevated working temperature,
- forgeable by applying of standard techniques,
- castable (investment casting method is preferred),
- processable through PM technology,
- joinable (using fusion welding, brazing, diffusion bonding, etc.),
- inert to most organic chemical (bio-friendly with human tissues and bones),
- excellent corrosion resistance with high specific strength.

Titanium and its alloys are also useful in chemical, petrochemical applications, marine environment and biomaterials applications. Inferior wear and hardness properties of Ti-6Al-4V restrict further extensive exotic applications like light-weight vehicle parts fabrication.

Laser cladding (Gnanamuthu 1976) is one of the most efficient surface modification techniques. It is becoming an attractive process in coating industries due to process capabilities (Schutz and Glatzel 2009; Tian et al. 2011; Walker et al. 1985) like,

- the excellent bonding strength between clad layer and the substrate due to metallurgical bonding (alloying),
- generation of fine grain size due to rapid heating and cooling,
- significantly less heat affected zone (HAZ),
- adaptation to automation and ability to process a selective area,
- capability to process a wider varieties of materials,
- strengthening of coating-substrate system for the softer substrate material with a bulk coating (cladding) layer that is one of the promising characteristics to adopt laser cladding for surface modification of Ti alloys.

Laser cladding is also used in industries as 'additive manufacturing' and applied for the restoration of costly equipments like off-shore drill rig bit, hydraulic equipment, turbine blades, automobile equipments, die-punch, agricultural

equipment, tea processing equipment, electrical contacts, etc. Laser cladding on steel is almost standardised in hard facing industries. Other mostly useful engineering materials beyond steel like aluminium, titanium, magnesium and their alloys are difficult to laser process. Their extreme physical, thermal and chemical properties create enormous difficulties for developing laser cladding layers on these substrates. The very low thermal conductivity of Ti-6Al-4V (about $7 \text{ Wm}^{-1} \text{ K}^{-1}$) results (Ezugwua et al. 2005) in intense heating of surface while irradiating it during laser cladding process and that creates severe problems (Dahotre et al. 2007) like,

- evaporation of substrate material,
- thermal mismatch between the substrate and the pre-placed coating materials,
- narrow line energy working region etc.

Titanium is highly reactive with nitrogen, oxygen, carbon etc. and forms titanium nitride, titanium oxide, titanium carbide, etc. respectively. Tian et al. (2011), Schutz and Glatzel (2009) reported significant observations on laser nitriding to improve tribological properties of titanium-based work materials. Walker et al. (1985) developed TiC and TiN laser coating on Ti-6Al-4V with hardness value up to 1700 HV. Saleh et al. (2010) worked on carburizing the surface of Ti-6Al-4V by using pre-placed graphite powders in an argon environment. They found that the depth of alloyed zone was higher in pulsed laser compared to CW laser and observed an average hardness of 800 HV of the alloyed zone.

The recent trend is to develop multi-component/multi-phase coatings that are advantageous due to their high strain absorption capacity. Different types of phase boundaries in the microstructure increase the toughness of the coating by increasing capacity to dissipate strain energy (Holleck and Schutz 1988). Haldar et al. (2012) developed TiB, TiC, TiN reinforced Ni-Ti matrix coating on Ti-6Al-4V substrate by pre-placed laser cladding process. They used an intermediate layer of nickel coating to improve cladding ability and to use it as a coating matrix material.

In this present studies, experiments were carried out on a development of hard, bulk and wear resistive coating on Ti-6Al-4V substrate by developing titanium carbide and tungsten carbide reinforcements in Ti-W matrix clad layer. For the said purpose, pre-placed powder mixture of W, graphite and Ti were used on the Ti-6Al-4V substrates. A 2 kW Ytterbium multi-mode fiber laser was used to irradiate the samples. The developed coatings enriched with in situ reinforcements of TiC and W₂C in Ti-W matrix that result in improvement in tribological properties of Ti-6Al-4V surface.

2 Experimental Details

The powder mixture of Ti (50 vol.%), W (35 vol.%) and graphite (15 vol.%) were manually mixed for 4 h to get a homogeneous mixture of cladding powder materials. The powder materials were then mixed with 2 % polyvinyl alcohol

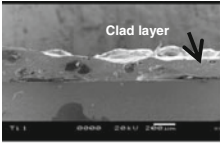
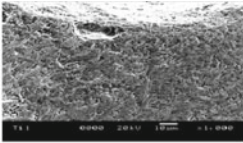
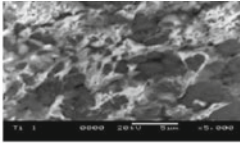
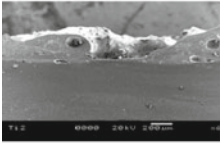
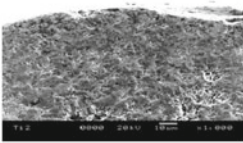
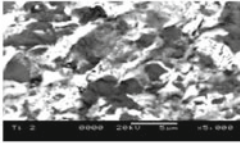
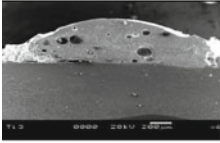
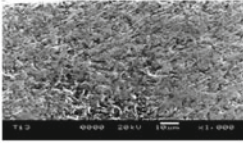
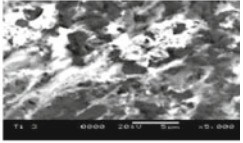
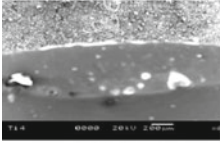
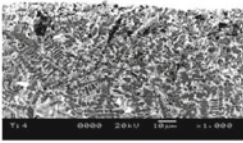
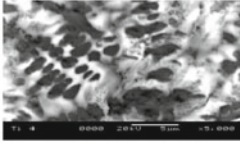
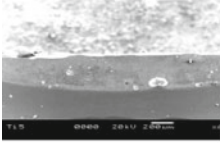
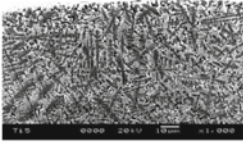
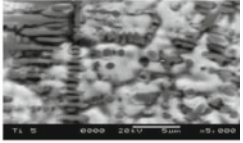
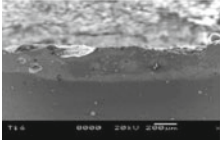
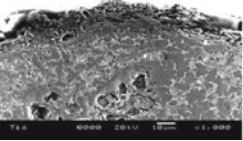
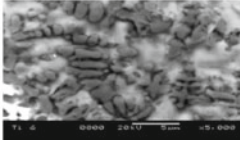
Table 1 Laser cladding process parameters

Fixed process parameters	Pre-placed powder thickness: 200 μm ; Sticking agent: 2 % PVA; Laser: CW energy supply, Beam size: 3 mm; Beam inclination angle: 12°; Power = 1.5 kW; Ar flow pressure: 1.5 bar		
Variable process parameters	Sample nos.	Scan speed (mm/min)	Observations
	1	3500	Improper melting
	2	3000	Improper melting
	3	2500	Track formed
	4	2000	Same as previous
	5	1800	Same as previous
	6	1600	Over melting

(PVA) solution and stirred to form a paste. The substrate was then polished with a SiC emery paper of grit size 600 meshes and cleaned with acetone. The semi-solid paste of powder materials was then placed on the substrates with the help of coater machine to obtain a uniform thickness of pre-placed powders. The thickness of pre-placed powder mixture applied on the substrate was 200 μm . The samples with the pre-placed powders were put into a muffle furnace for a period of about 10–15 min at a temperature of 150 °C for baking. Finally, the samples were irradiated with a Ytterbium Fibre Laser having wavelength 1.06 μm capable of delivering 2 kW maximum power in continuous mode with a spot diameter of 3 mm in argon shroud at a pressure of 1.5 bar. Sufficient time was allowed so as to cool the samples to room temperature before the subsequent operation. The parameters are shown in Table 1.

The clad tracks formed on the samples were cut by wire-EDM machine to get required shape, size and cross-section of the samples for various characterisations. To explore microstructure of the coating, the samples were sliced and hot-mounted by non-conductive phenolic resin. The hot-mounted samples were mirror polished, etched with Keller's reagent and prepared for SEM analysis. Microstructural analyses were carried out on the cross sections of all the samples using SEM (Model: Carl Zeiss Supra-40). Same specimens were used for microhardness measurement. Different samples of dimensions 10 \times 15 \times 10 mm³ were used for XRD (X-ray diffraction) analysis which was carried out by *X'PERT PRO, 3040/60, PANalytic* diffractometer with $\text{CuK}\alpha$ ($\lambda = 1.5418 \text{ \AA}$) radiation, so as to identify the various constituent compounds present inside the coating. Wear testing was performed using ball-on-disc type dry sliding wear and friction monitoring set up with WC ball of 5 mm diameter and working conditions of 5 N applied load, 5 mm track diameter, 10 min run time at 300 rpm.

Table 2 Clad geometries and their microstructures in various scan speeds

Sample no.: scan speed	Clad geometry	Microstructure in 1000X magnification	Microstructure in 5000X magnification
1:3500			
2:3000			
3:2500			
4:2000			
5:1800			
6:1600			

3 Result and Discussions

3.1 Microstructure Analysis

Clad geometries of different samples, treated with various scan speeds as process parameter (already listed in Table 1), and their corresponding microstructures are presented in Table 2.

The surfaces of the sample 1 and 2 were highly rough which might be due to improper melting. From the highly magnified (1000X and 5000X) view of the

coating, it can be said that laser sintering might be took place in case of sample 1, 2 and 3. As scan speed was decreased i.e. case of sample 4–6, the coating heights were decreased. It might be due to more explosive type in situ reactions taken place at higher energy input rate which result in either blowing away coating powders or evaporation loss or their combined effects. Inferior surface quality of sample 6 was an evidence of huge material loss.

4 XRD Analysis

Different phases present in the coating matrix were examined by XRD analysis. The XRD micrograph of samples 2 and 5 are shown in Figs. 1 and 2 respectively.

The XRD micrograph of sample 2 indicates the presence of TiC, W_3C , graphite and Ti_xW_{1-x} whereas sample 5 contains TiC, W_2C and Ti_xW_{1-x} in the coating. At a lower scan speed i.e. at a higher energy input rate (sample 5) the graphite was not present whereas W_2C was formed instead of W_3C . It might be due to in situ reactions with graphite and tungsten better taken-place at a higher energy input rate by a parametric control in the experiments.

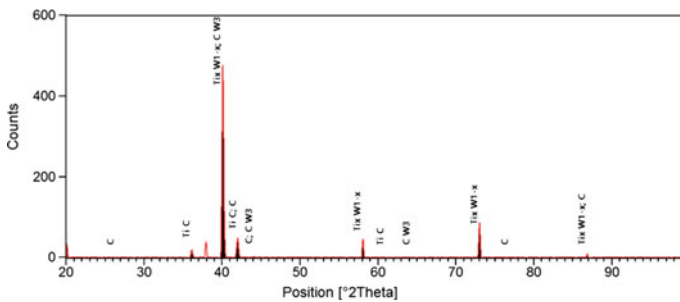


Fig. 1 XRD micrograph of sample 2 (at laser power of 1.5 kW and scan speed of 3000 mm/min)

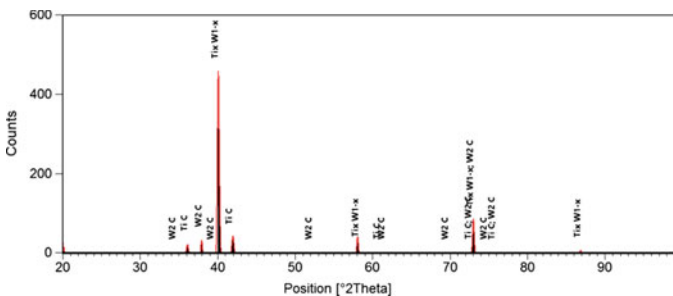


Fig. 2 XRD micrograph of sample 5 (at laser power of 1.5 kW and scan speed of 1800 mm/min)

5 EDS Analysis

The spots EDS were performed in different positions of a coating area. Results of the selected spots as in Fig. 3 are tabulated in Table 3.

From EDS result of sample (Fig. 3) it can be said that white portions (spectrum 1) are rich in tungsten, carbon and titanium whereas dark particles (spectrum 2) contain considerable amount of titanium and carbon. Gray parts (spectrum 3) are also rich in titanium and carbon. By considering the XRD analyses, it may be said that the phases, which are appearing as very light, may be tungsten carbide composition in Ti-W matrix. The phase, which is appearing as very dark, may be titanium carbide in Ti-W matrix. The gray phases may be a combination of both titanium carbide and tungsten carbide in Ti-W matrix.

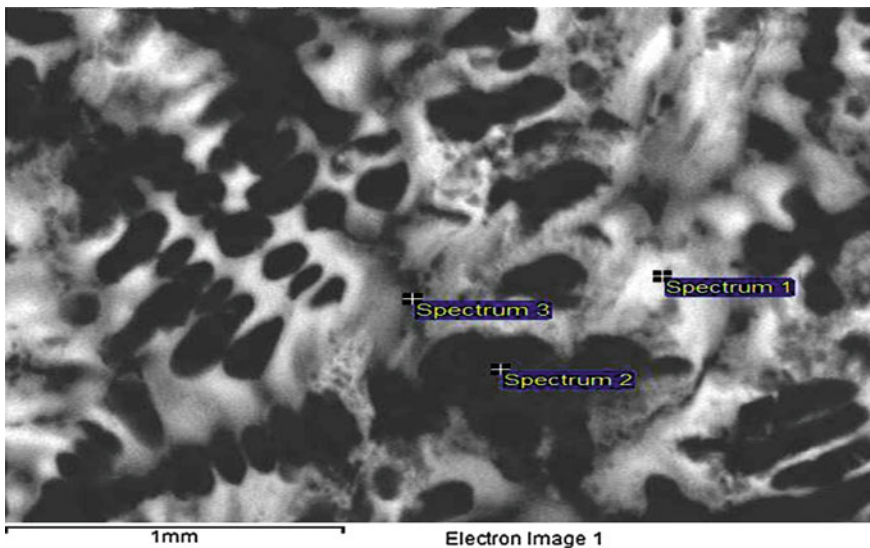
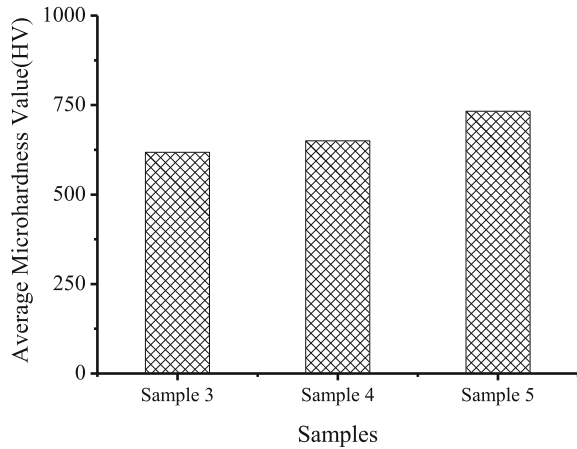


Fig. 3 Spot EDS done on the different spots as in spectrum 1, 2 and 3 in sample 3

Table 3 EDS elemental percentage in spectrum 1, 2 and 3

Element	Spectrum 1		Spectrum 2		Spectrum3	
	Weight %	Atomic %	Weight %	Atomic %	Weight %	Atomic%
Ti	44.19	39.22	67.89	42.06	63.61	47.89
C	14.47	51.22	22.85	56.45	15.42	46.29
W	41.34	9.56	9.26	1.50	19.48	3.82
Al					1.50	2.00

Fig. 4 Average micro-hardness values of different coating samples measured along transverse cross section



6 Micro-Hardness and Wear Performance

The polished cross-sections of cladding layers were examined for Vickers micro-hardness tests with an applied load of 50 g and dwell time of 10 s. A series of microhardness values, beginning from top and moving towards the substrate at successive distances of 30 μm on each of the three samples, were measured with repetitions. Huge variations in the microhardness values (600–1100 HV), which might be due to the non-uniform distribution of hard reinforcements in the matrix, were found. Average microhardness values on the different samples were shown in Fig. 4. As the scan speed was decreased, the microhardness increased. It might be due to better formation of tungsten carbide phases at higher energy input rate that is evident from XRD analyses in Figs. 1 and 2.

Fig. 5 Average co-efficient of friction values of different samples

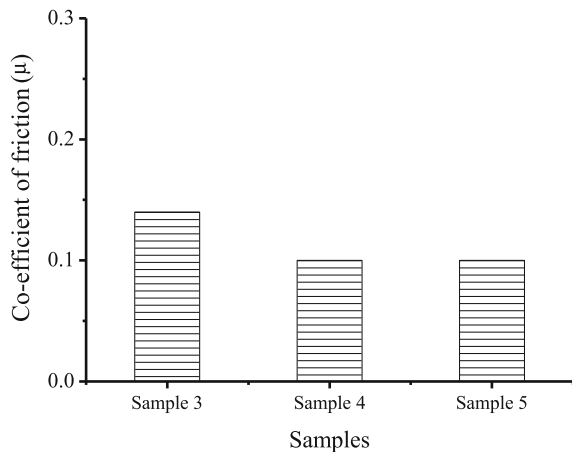


Fig. 6 Total wear depth in different samples after 10 min of wear testing

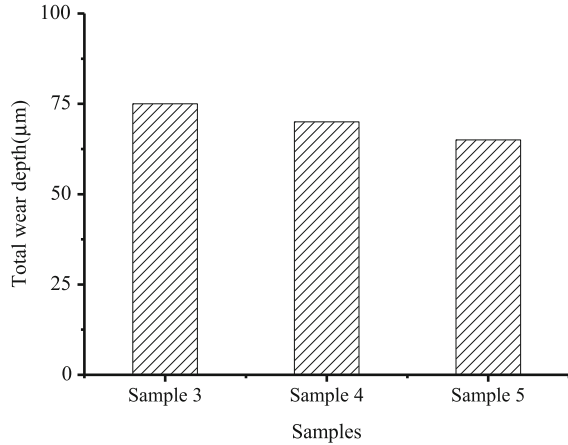
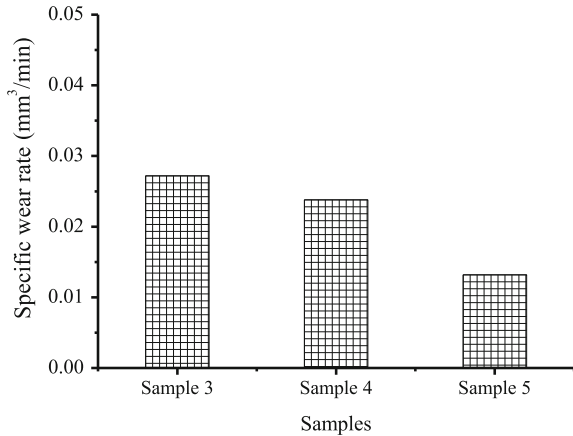


Fig. 7 Specific wear rate in different samples



Comparative wear performances of the clad layers are shown in Figs. 5, 6 and 7. The coefficients of friction of different samples found to vary from 0.04 to 0.18. The average values of coefficient of friction are shown in Fig. 5. Maximum wear depths after 10 min of sliding wear tests are shown in Fig. 6 and specific wear rates are presented in Fig. 7. The average value of the coefficient of friction decreased with increasing in heat input in the cladding process, and subsequently there was a decrease of wear rate. It might be due to better formation of TiC and W₂C reinforcement in the cladding matrix Ti-W.

7 Conclusions

Hard and wear resistive clad layers were developed in the present studies where the major observations were as follows:

- XRD analysis confirmed the presence of TiC and W₂C phases in the Ti-W matrix laser clad layer on Ti-6Al-4V substrate.
- The formation of various reinforcement phases and their distribution in the matrix can be controlled by scanning speed. For the given experimental parameters, a scanning speed in the range of 1800–2500 mm/min found suitable for cladding. The sample was made at laser scan speed 1800 mm/min (sample5) show higher hardness, lower coefficient of friction and better wear performance than the samples were made at laser scan speeds of 2000 mm/min (sample4) and 2500 mm/min (sample3). It might be due to better development of coating reinforcements in the lower scan speed of clad layer development.
- The average microhardness of the clad layer was 700 HV_{0.05} whereas that of as received bare Ti-6Al-4V substrate microhardness was 364 HV_{0.05}.
- Average value of the coefficient of friction of the clad layer for dry sliding was 0.12 whereas that of the as-received bare Ti-6Al-4V substrate was 0.35.

References

- Campbell, F. C. (2008). Titanium, in elements of metallurgy and engineering alloys. *ASM International, USA*, 19, 527.
- Dahotre, N. B., & Harimkar, S. P. (2007). *Laser fabrication and machining of materials*. USA: Springer.
- Ezugwu, E., Dasilva, R., Bonney, J., & Machado, A. (2005). Evaluation of the performance of CBN tools when turning Ti-6Al-4V alloy with high pressure coolant supplies. *International Journal of Machine Tools and Manufacturing*, 45(9), 1009–1014.
- Gnanamuthu, D. S. (1976). Cladding. US patent No. 3952180, pp. 219–121.
- Haldar, B., Agarwal, R., Saha, P., & Chattopadhyay, A. B. (2012). Laser cladding of in-situ TiB, TiC and TiN reinforced Ni-Ti MMC coating on Ti-6Al-4V for improving tribological performance. In *Proceeding of the 4th International and 25th AIMTDR, JU, Kolkata* (pp. 796). New Delhi: Excel India Publishers.
- Holleck, H., & Schutz, H. (1988). Preparation and behaviour of wear-resistant TiC/TiB₂, TiN/TiB₂ and TiC/TiN coatings with high amounts of phase boundaries. *Surface and Coating Technology*, 36(3–4), 707–714.
- Matthew, J., Donachie, Jr., 2000. Titanium: A Technical Guide. ASM International, USA.
- Saleh, A. F., Abboud, J. H., & Benyounis, K. Y. (2010). Surface carburizing of Ti-6Al-4V alloy by laser melting. *Optics and Lasers Engineering*, 48(3), 257–267.
- Schutz, A., & Glatzel, D. (2009). Partial laser and gas nitriding of Titanium components. *HTM Journal of Heat Treatment and Materials*, 64(5), 270–274.
- Tian, Y. S., Zhang, Q. Y., Qin, C. P., & Wang, D. Y. (2011). Effect of laser scanning speed on nitrided layers fabricated on Titanium alloy. *Surface Engineering*, 27(6), 424–427.
- Walker, A., Folkes, J., Steen, W. M., & West, D. R. F. (1985). Laser surface alloying of Titanium substrates with carbon and nitrogen. *Surface Engineering*, 1(1), 23–29.

Motion Programming of SCORBOT ER-4u Using Fusion of Robot Kinematics and Inertial Sensor

Abhishek Jha, Shital S. Chiddarwar and Veer Alakshendra

Abstract This paper addresses the framework of a novel approach for the real time robot motion control. The proposed approach amalgamates the kinematics of the human arm along with the Kinect based motion capture system and the inertial sensor to control the robot motion in a real time. The feasibility of the devised strategy is shown by the experimental results for hand path imitation problem. The performance of the approach is evaluated on the basis of geometrical similarity obtained during hand path imitation by the robot end effector in real time imitation scenario.

Keywords Kinect · Inertial sensor · Kinematics · Imitation · Motion control

1 Introduction

In recent years, the human motion controlled robotic systems have taken attention of research community and considerable amount of work have been done in this field. This observational learning approach provides an intuitive and natural way to teach robots and simplifies the complexities involved in the robot programming (Billard et al. 2008). The availability of low cost depth sensors like Microsoft Kinect has provided momentous advances in this domain. The capability of the Kinect sensor to track the human motion in real time has been substantially utilized for controlling the robot motion. A framework for the full human body pose imitation by a humanoid robot was proposed by Lie et al. (2015), where they utilized the skeletal tracking feature of the Kinect. For controlling the industrial robots, a method for teleoperation was given by Du and Zhang (2014). Their work was based on the wrist pose estimation from the depth image provided by the Kinect. Another

A. Jha (✉) · S.S. Chiddarwar · V. Alakshendra
Robotics & FMS Lab, Department of Mechanical Engineering,
Visvesvaraya National Institute of Technology, Nagpur, Nagpur, India
e-mail: abhishekdujjha@gmail.com

approach for object trajectory retrieval during a manipulation task using the Kinect based measurements was given by Vakanski et al. (2014), where they controlled the robot motion in offline manner. A human robot interaction framework for manufacturing operation using multiple Kinect sensors was proposed by Morato et al. (2014). So far, the existing works use the Kinect effectively for the human motion analysis for robot motion control. However, there are some challenges exists in this field. In most of the previous works, the main objective of the human motion analysis was to extract the human poses to use as input to the robotic systems. The Kinect provides 3D positional information during the human motion analysis and for extracting the orientation of the human body parts one has to rely on alternate approaches like image processing. This is one limitation of the Kinect based approach. The orientation extraction of human body parts can be achieved using the motion sensors. For analyzing the human motion, the kinematic features of the human body can be effectively used, as the human body possesses a well defined kinematic structure which can be used to describe the motion of the body parts in a more realistic manner. The kinematic features of the human body for Kinect based human motion analysis are not addressed in previous works. Also the previously developed approaches are more oriented towards humanoids, where similarity between the human body part and the robot structure exist, but for industrial robot with a limited flexibility, a more effective approach is needed.

The purpose of the presented work is to develop a framework addressing the above mentioned challenges. This work proposes a new approach for real time motion control of an industrial robot by using the natural motion of the human arm. The proposed approach integrates the kinematic features of the human arm along with the Kinect and the inertial sensor in order to control the robot motion. The frame work is tested on five degrees of freedom (DoF) industrial robot SCORBOT ER-4u for the real time hand path imitation problem. The proposed approach makes use of the task demonstration itself to control the robot motion hence it simplifies the complexities involved in robot programming. The main contribution of this work is the development of kinematics based architecture for position and orientation control of an industrial robot using the low cost sensors like Kinect and inertial sensor embedded in a Smartphone. The rest of this paper is organized as follows. Methodology of the developed approach is discussed in next section followed by experimentation, results and the last section briefly concludes the paper.

2 Methodology

The main intent of this work is to develop a self sufficient system for real time robot motion control by using the human arm motion. In order to accomplish this objective, the framework for integration of the human arm kinematics, Kinect and inertial sensor is proposed in this work. The proposed framework fuses the position and orientation data obtained from the two sensors in the kinematic model of the human arm to interpret its motion. The generated human arm configuration from the

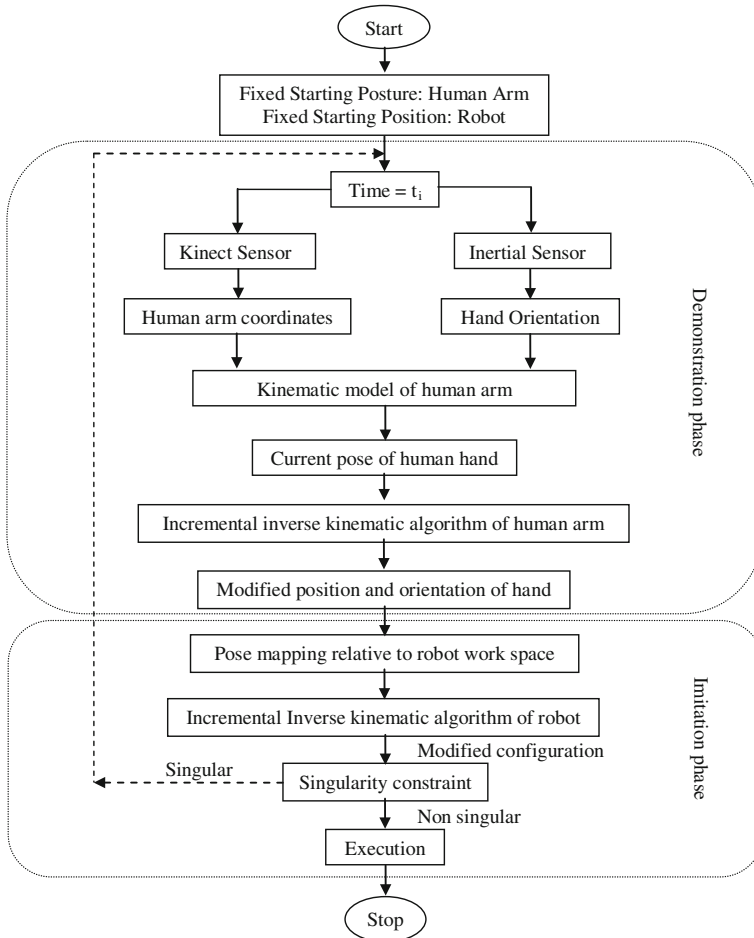


Fig. 1 Methodology for real time motion control of robot

motion analysis becomes the teaching parameter to control the robot motion in real time. The adopted methodology for hand path imitation problem is shown in Fig. 1. The methodology consist of two distinct phases namely demonstration and imitation phase as shown in the Fig. 1.

The main objective of the demonstration phase is to interpret the human arm motion during the task demonstration. In this work, the kinematic model of human arm is used to explicate the human arm motion in terms of its kinematic parameters. The considered model of human arm consists of seven DoF (Mihelj 2006) as shown in Fig. 2. The shoulder is modeled with 3 DoF, elbow with 1 DoF and the remaining 3 DoF are considered in wrist for defining the wrist rotation. The shoulder serves as the fixed base for defining the motion of the hand, which is considered as the end effector of the mechanism.

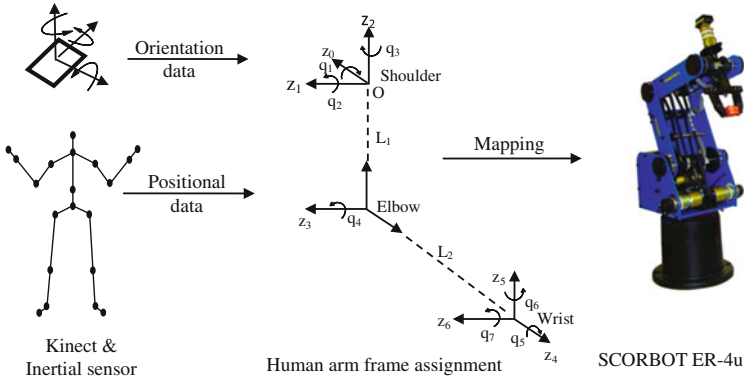


Fig. 2 Framework for human arm imitation

The position and the orientation of the hand is a function of seven joint variables associated with the human arm and is given by

$$P = f(q_1, q_2, q_3, q_4, q_5, q_6, q_7) \tag{1}$$

The forward kinematic equation of the human arm defines the position and orientation of the hand as given by Eq. (2)

$${}^0_7T = {}^0_1T_1 {}^1_2T_2 {}^2_3T_3 {}^3_4T_4 {}^4_5T_5 {}^5_6T_6 {}^6_7T_7 \tag{2}$$

where, 0_7T represent the 4×4 homogenous transformation matrix describing the position and orientation of the hand with respect to the shoulder base frame. Equation (2) can be represented in a six dimensional vector form as given by Eq. (3)

$${}^7_0T = [x_h \quad y_h \quad z_h \quad R_h \quad P_h \quad Y_h]^T \tag{3}$$

where, $(x_h \quad y_h \quad z_h)$ represents the position of the hand and $(R_h \quad P_h \quad Y_h)$ represents the orientation of the hand in terms of Roll, Pitch and Yaw angles relative to the shoulder base frame. During the task demonstration, the arm configuration changes with the hand movement and these changes are measured using the Kinect and the inertial sensor. In order to track the human arm movement, the skeletal tracking feature of the Kinect is used. The skeletal tracking feature provides 3D positions of the 20 joint locations of the human skeleton relative to its own reference frame in real time as shown in Fig. 2. Three joint locations of the right arm of the demonstrator namely shoulder, elbow and hand are tracked. Moreover, to correlate the human arm motion with a fixed base manipulator, the shoulder position obtained during motion tracking is constrained and kept fixed during the tracking. With fixed shoulder position, the obtained positions of elbow and hand are modified using the actual upper arm and forearm lengths of the demonstrator. Since, the forward kinematic Eq. (2) describes the position and orientation of the hand

relative to the shoulder base frame, it is transformed relative to the Kinect reference frame and can be given by Eq. (4)

$${}^k_7T = {}^k_0T_7^0T \quad (4)$$

where, k_0T represent the homogeneous transformation matrix which maps the position and orientation of the hand relative to the Kinect reference frame. The positional data obtained from arm motion tracking forms one part of the input data for the kinematic model of human arm. The orientation of the hand during the motion tracking is captured using an inertial sensor embedded in a Smartphone. The inertial sensor used in this work has 3 axes accelerometer and gyroscope which provides orientation in terms of Roll, Pitch and Yaw angles relative to its own reference system. To correlate the orientation data obtained from the inertial sensor with the kinematic model of the arm, it is transformed relative to the wrist frame and can be given by Eq. (5)

$$R_w = R_I R_{IS} \quad (5)$$

where, R_I is the rotation matrix which maps the orientation provided by the inertial sensor relative to the wrist frame. The orientation R_w is again transformed relative to the shoulder reference frame and can be given by Eq. (6)

$$O = R_{II} R_w \quad (6)$$

where, O defines the orientation of the hand obtained from the inertial sensor relative to the shoulder base frame. The orientation data obtained from Eq. (6) forms the second input data for the kinematic model of human arm as defined in Eq. (3).

One of the problems associated with the multi sensor data fusion is the operating frequency mismatch for the two sensors. In order to rectify this, the data of both sensors are fused at a common time frame. The time frame provided by the Kinect sensor is considered as the base for capturing the data from the inertial sensor. The time frame matching ensures that the position and the orientation data are captured at the same instant.

During task demonstration, the forward kinematic model of the human arm provides the hand position and orientation. To detect the change in the joint space configuration of the human arm, its inverse kinematic model is used. Since, the considered model of the human arm is redundant in nature; it is very difficult to get the analytical solution for real time application. Jacobian Pseudoinverse method is a popular iterative method for obtaining the inverse kinematic solution in such cases and is used in this work to detect change in joint space configuration of the human arm. The change in joint space configuration of the human arm as per Jacobian Pseudoinverse method can be given by Eq. (7)

$$\Delta q = J^{-1} \Delta P \quad (7)$$

where, Δq represents the incremental change in joint space configuration of the human arm for incremental change in pose ΔP . The term J^{-1} represents the human arm Jacobian matrix. Equation (7) provides the incremental change in the joint space configuration of the human arm and the new configuration can be given by Eq. (8)

$$q_{new} = q_{initial} + \Delta q \quad (8)$$

The kinematic model of the human arm discussed above generates the hand configurations during demonstration of the task. These generated configurations are mapped subsequently to the robot workspace for imitation by the robot. The objective of the imitation phase is to interpret the human hand configuration in the robot workspace for possible execution by the robot. This work uses a vertical articulated 5 DoF industrial robot SCORBOT ER-4u for imitation of the human arm motion. Due to different motion spaces and kinematic dissimilarities, the direct correlation between the two structures does not exist. Hence, the accuracy of the mapping strategy is critical for the extent of imitation achieved by the robot. In order to map the hand configuration into the robot workspace, it is transformed relative to the robot workspace and can be given by Eq. (9)

$$P_{RW} = {}^R_H T P_H \quad (9)$$

where, P_{RW} is the hand configuration defined in the robot workspace and ${}^R_H T$ is the transformation matrix which maps the hand pose P_H into the robot workspace.

Moreover to match the workspace limitations of the robot, the mapped positions are scaled and can be given by Eq. (10)

$$P_{RWS} = S P_{RW} \quad (10)$$

where, S represents the homogeneous scaling matrix which scales the mapped positions in the robot workspace. The mapped human arm configuration represents a six dimensional vector in the robot workspace and to interpret this vector in the robot joint space, the inverse kinematic model of the robot is applied. In this work, the incremental inverse kinematic model of the robot using Jacobian Pseudoinverse method is used to detect the change in the joint space configuration of the robot and can be given by Eq. (11)

$$d\theta = J_R^+ dP_{RWS} \quad (11)$$

where, J_R^+ represents the Pseudoinverse of the robot Jacobian matrix and dP_{RWS} represents the change in configuration of the robot. Equation (11) provides the relative changes in the initial joint space configuration of the robot and the next configuration can be given by Eq. (12)

$$\theta_{new} = \theta_{initial} + d\theta \quad (12)$$

The updated configuration of the robot is checked for singularity constraints, if obtained robot configuration is non singular and satisfies the joint limit constraints, the robot controller executes the obtained configuration otherwise the algorithm searches for next configuration.

The developed approach is tested for real time human hand path imitation problem and the experimentations carried out are reported next.

3 Experimentation

The experiments were carried out to assess the feasibility of the developed approach. The main objectives of the experiments were to identify the accuracy of the approach and extent of imitation achieved for real time hand path imitation problem. In the experiment, a Kinect based motion capture system was used to track the hand movement of the demonstrator. A Smartphone with embedded inertial sensor was fixed on the wrist of the demonstrator. The position and orientation data obtained from the two sensory systems were used in the kinematic model of the human arm to define the hand path traversed during the demonstration. The generated hand path parameters were mapped simultaneously to the robot workspace for real time imitation of the hand path. The experimental setup used in this work is shown in Fig. 3. During the experiments, the demonstrator moved his right hand gradually in front of the Kinect sensor such that the hand movement constitutes a geometric path. Four different paths were demonstrated to the robot and for each demonstration, the response of the robot was observed using path followed by the robot end effector.

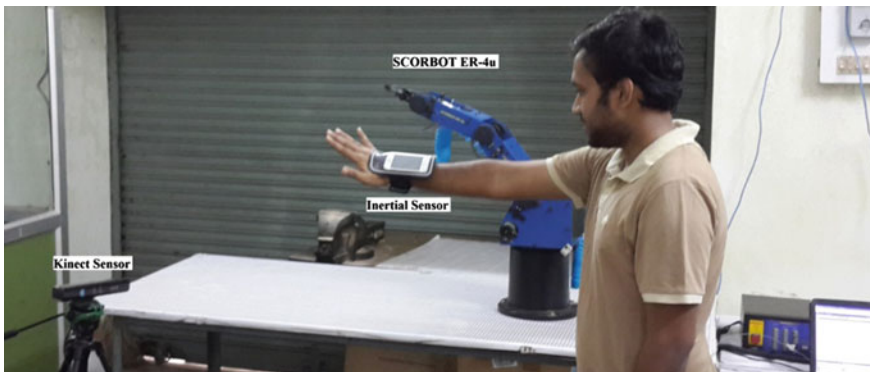


Fig. 3 Experimental setup used for human arm imitation

4 Results and Discussion

Figures 4, 5, 6 and 7 shows the different paths defined during experiment. Each Figure consists of 3 paths namely path defined by the demonstrator (demonstrated path), path mapped to the robot workspace (mapped path) and actual path followed by the robot end effector (imitated path). One circle (O) and arrow heads (\blacktriangleleft) are used on the paths to represent the starting point and the direction of motion respectively. The quantitative results of the experiments are shown in Table 1. It can be seen from Figs. 4, 5, 6 and 7 that for each demonstration, the robot end effector followed a path similar to the demonstrated path. During each experiment

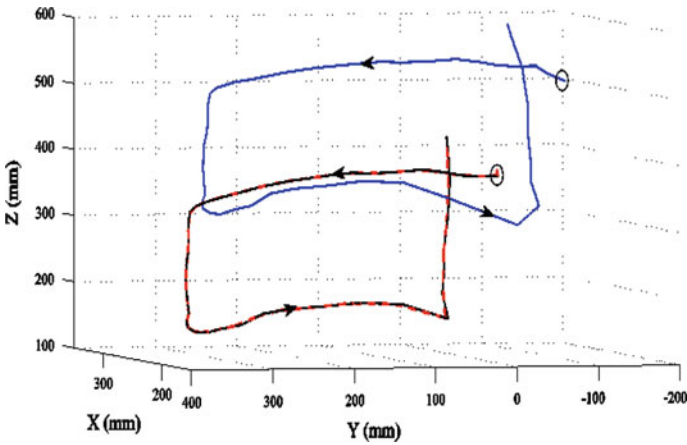


Fig. 4 Path demonstrated during experiment 1

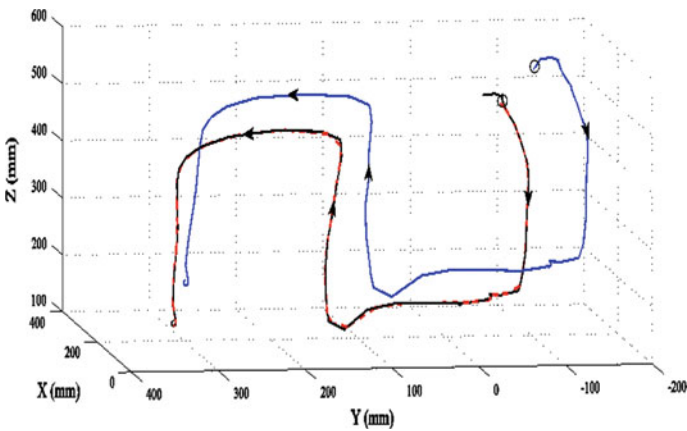


Fig. 5 Path demonstrated during experiment 2

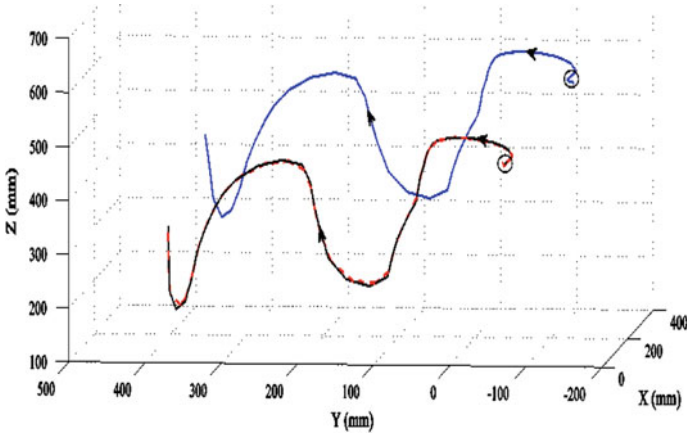


Fig. 6 Path demonstrated during experiment 3

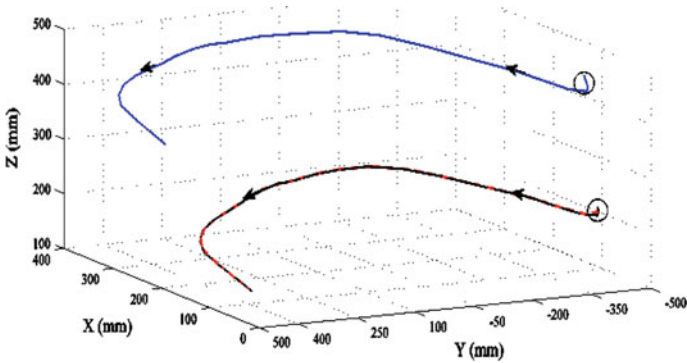


Fig. 7 Path demonstrated during experiment 4

Table 1 Quantitative results of the experiments

Expt. no.	Dissimilarity indices (d)			Mean position errors		
				Mapped path versus imitated path		
	Demonstrated and mapped path	Demonstrated and imitated path	Mapped and imitated path	P _x (mm)	P _y (mm)	P _z (mm)
1	0.0241	0.0257	0.0026	0.6923	1.1676	1.2651
2	0.0017	0.0021	0.0011	1.0475	1.6825	2.4596
3	0.0014	0.0022	0.0024	0.7309	3.0304	0.7473
4	0.0073	0.0074	0.0028	1.5279	0.8376	2.1123

the direction of motion of the robot end effector was same as that of the human hand. This directional control over the robot motion provided the geometrical similarity between the demonstrated and imitated paths. In order to quantify the geometrical similarity between the paths, Procrustes analysis has been used to compute the dissimilarity index (d) between the obtained paths. The Procrustes analysis is a statistical technique used for shape feature matching in the fields like CAD and image processing (Goodall 1991). The dissimilarity index d is a standardized dissimilarity measure to assess geometrical similarity between the target and the transformed shape.

It can be seen from Table 1 that the dissimilarity indices between the demonstrated and imitated paths are close to zero, which indicates the close geometrical similarity between the paths. The same phenomenon can be seen for the dissimilarity indices between the demonstrated and mapped, and the mapped and imitated paths. The close geometrical similarity between the three paths indicates the effectiveness of the mapping strategy. Since the motion spaces of the human hand and the robot end effector were different, the incremental inverse kinematic model based mapping provided notable directional and positional control over the robot motion. Even though the kinematic structure of the human arm and the robot were dissimilar, the robot end effector imitated the hand motion in different directions. Moreover to assess the accuracy of the mapping process, mean position errors between the mapped and imitated paths were estimated as listed in Table 1. These mean position errors indicate the deviation between the mapped path and the imitated path, however the deviation is not visible in the Figures due to selected scales of the Figures. The mean position errors obtained are 0.69–1.52 mm in x , 0.83–3.03 mm in y and 0.74–2.45 mm in z directions respectively. From the obtained values of positioning errors it can be inferred that the mapped path was closely reproduced by the robot end effector. It also justifies the adopted mapping strategy between the two workspaces and the incremental inverse kinematics model used for it. The positioning errors might be dependent on the speed of motion. However, this study is the future scope of this work.

5 Conclusions

This work presents a new framework for real time robot motion control through task demonstrations. The presented approach is based on the combination of human arm kinematics with the Kinect and inertial sensors and provides a simple and effective way for robot motion control. The obtained experimental results for different types of user defined path reveals that the method is reliable and efficient for controlling the robot motion. This approach reduces the complexities involved in robot programming hence it can be used effectively to teach robots. This approach can be implemented for industrial applications where path to be followed is known priori and which require continuous motion of the end effector like arc welding and spray painting.

References

- Billard, A., Calinon, S., Dillmann, R., & Schaal, S. (2008). Robot programming by demonstration. *Springer handbook of robotics* (pp. 1371–1394). Berlin Heidelberg: Springer.
- Du, G., & Zhang, P. (2014). Markerless human–robot interface for dual robot manipulators using Kinect sensor. *Robotics and Computer-Integrated Manufacturing*, 30(2), 150–159.
- Goodall, C. (1991). Procrustes methods in statistical analysis of shapes. *Journal of the Royal Statistical Society: Series B (Methodological)*, 53(2), 285–339.
- Lei, M., Song, M., Li, Z. N., & Chen, C. (2015). Whole-body humanoid robot imitation with pose similarity evaluation. *Signal Processing*, 108, 136–146.
- Mihelj, M. (2006). Human arm kinematics for robot based rehabilitation. *Robotica*, 24(03), 377–383.
- Morato, C., Kaipa, K. N., Zhao, B., & Gupta, S. K. (2014). Toward safe human robot collaboration by using multiple kinects based real-time human tracking. *Journal of Computing and Information Science in Engineering*, 14(1), 011006.
- Vakanski, A., Sharifi, F. J., & Mantegh, I. (2014). Robotic learning of manipulation tasks from visual perception using a kinect sensor. *International Journal of Machine Learning and Computing*, 4(2), 163–169.

Trajectory Tracking Control of Three-Wheeled Omnidirectional Mobile Robot: Adaptive Sliding Mode Approach

Veer Alakshendra, Shital S. Chiddarwar and Abhishek Jha

Abstract This paper proposes an adaptive and robust control for a three-wheeled omnidirectional mobile robot (TWOMR) in presence of disturbance due to friction and bounded uncertainties. Kinematic and dynamic modeling of TWOMR is done to obtain the equation of motion under the action of frictional forces. Controller is designed to track the desired path. First to make the system robust, Integral sliding mode controller (ISMC) is designed and then for estimation of design parameter and to reduce the chattering effect an adaptive integral sliding mode controller (AISMC) is built. Simulations are conducted to show the effectiveness of proposed controller for TWOMR.

Keywords Sliding mode control · Adaptive control · Omnidirectional wheel platform

1 Introduction

Omnidirectional wheel mobile robots are commonly used for applications like fork lifter, home purpose robot, omni wheel chair etc. Among various configurations like 2 wheel, 3 wheel and 4 wheel mobile robots, 3 wheel omnidirectional mobile robot is extensively used (Pin and Killough 1994). It consists of three omni wheels driven by separate motors. It has various advantages as compared to regular two or four wheel mobile robots, such as better maneuverability, ability to turn in confine spaces and ability to move in any direction. These aspects have increased the applicability of 3 wheel omnidirectional mobile robot. The kinematic and dynamic modeling of omnidirectional mobile is well presented in Tzafestas (2014) and Batlle and Barjau (2009). Earlier research work shows major use of PID controllers to

V. Alakshendra (✉) · S.S. Chiddarwar · A. Jha
Robotics and FMS Lab, Department of Mechanical Engineering, Visvesvaraya National
Institute of Technology, Nagpur 440010, India
e-mail: alakshendra.veer@gmail.com

control each motor. The major drawback with these types of controllers is that when the non linear effects in the dynamic environment are significant the robot is unable to track the desired trajectory. Hence, to make the system robust under such disturbances research proposed several non linear control methods like neural network techniques, fuzzy control, sliding mode control etc.

Sliding mode is extensively used for non linear control (Das and Mahanta 2014). It is a discontinuous control method to make the system robust. The desired system dynamics is maintained by defining a switching function which keeps the output states on the sliding surface. Besides having various advantages like insensitivity to disturbances and fast dynamic response, the control input and sliding function faces chattering effects due to employment of switching function. Apart from this, proper selection of switching gain is a major issue in the design process when the bounds of uncertainties are unknown. Higher selection of switching can lead to non smooth control input. Hence to eliminate the chattering effect and make the controller self tuned for unbounded uncertainties adaptive control methods are extensively used (Chen et al. 2013). Viet et al. (2012) proposed a sliding mode control law for an omnidirectional mobile manipulator but with bounded uncertainties. To track the desired trajectory in presence of unstructured uncertainties (Xu et al. 2009) employed neural network with sliding mode control approach.

The objective of this paper is to establish a robust and adaptive controller for a three wheel omnidirectional mobile robot to track the desired trajectory in presence of friction and unbounded uncertainties. The remaining content of this paper is organized in following manner. First kinematic and dynamic equations of TWOMR are derived. Next robust adaptive control law is derived and its stability is proved by Lyapunov stability criterion. The simulation results and conclusion are described in the subsequent sections.

2 Kinematic and Dynamic Modeling

A three wheel omnidirectional mobile robot (TWOMR) is shown in Fig. 1. It consists of three omnidirectional wheels installed at 120° from each other.

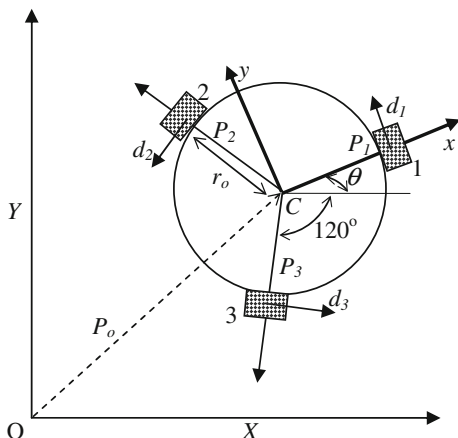
In Fig. 1 OXY is the fixed frame and Cxy denotes the moving frame of TWOMR. Rotation matrix

$$R(\theta) = \begin{bmatrix} \cos(\theta) & -\sin(\theta) \\ \sin(\theta) & \cos(\theta) \end{bmatrix} \text{ and the position vector } P_i \in \mathbb{R}^{2 \times 1} (i = 1, 2, 3) \text{ of}$$

each wheel relative to fixed frame. This position vector for each wheel is given as

$$\begin{aligned} P_1 = r_o \begin{bmatrix} 1 \\ 0 \end{bmatrix}, P_2 = R\left(\frac{2\pi}{3}\right) \begin{bmatrix} 1 \\ 0 \end{bmatrix} P_1 = \frac{r_o}{2} \begin{bmatrix} -1 \\ \sqrt{3} \end{bmatrix}, \\ P_3 = R\left(\frac{4\pi}{3}\right) \begin{bmatrix} 1 \\ 0 \end{bmatrix} P_1 = -\frac{r_o}{2} \begin{bmatrix} -1 \\ \sqrt{3} \end{bmatrix} \end{aligned} \quad (1)$$

Fig. 1 Schematic model of TWOMR



where r_o is the distance between center of geometry of TWOMR and center of wheels. The drive vectors $d_i(i = 1, 2, 3, 4) \in \mathbb{R}^{2 \times 1}$ relative to fixed frame denotes the drive direction of each wheel which can be written as

$$d_1 = \begin{bmatrix} 0 \\ 1 \end{bmatrix}, \quad d_2 = -\frac{1}{2} \begin{bmatrix} \sqrt{3} \\ 1 \end{bmatrix}, \quad d_3 = \frac{1}{2} \begin{bmatrix} \sqrt{3} \\ -1 \end{bmatrix} \tag{2}$$

$P_o = [x_o \quad y_o]^T$ is the position vector of geometric center relative to fixed frame. The sliding velocity of each wheel $v_i(i = 1, 2, 3)$ can be expressed in generalized form as

$$v_i = \dot{P}_o^T R(\theta) d_i + P_i^T \dot{R}^T(\theta) R(\theta) d_i \tag{3}$$

Substituting from Eqs. (1) and (2) to Eq. (3) yields

$$v_i = J \dot{q}_o \tag{4}$$

where, $J = \begin{bmatrix} -\sin(\theta) & \cos(\theta) & r_o \\ -\sin(\frac{\pi}{3} - \theta) & -\cos(\frac{\pi}{3} - \theta) & r_o \\ \sin(\frac{\pi}{3} + \theta) & -\cos(\frac{\pi}{3} + \theta) & r_o \end{bmatrix}$ is a Jacobian matrix and $q_o = [x_o \quad y_o \quad \theta]^T$ is the position vector of TWOMR. From Fig. 1, linear velocity v_o and angular velocity w_o of TWOMR is expressed as

$$v_o = \dot{x}_o \cos(\theta) + \dot{y}_o \sin(\theta) \tag{5}$$

$$w_o = \dot{\theta} \tag{6}$$

To drive the wheels, DC motors are attached at each wheel. Force F_i generated by i th wheel is given as

$$F_i = \alpha u_i - \beta v_i \tag{7}$$

where α and β are motor constants and $u_i (i = 1, 2, 3)$ is the voltage applied to each DC motor of the wheel.

The dynamic modelling of FWOMR is done using Newton’s second law of motion from which the linear and angular momentum balance equations are obtained as (Tzafestas 2014).

$$\sum_{i=1}^3 (F_i - f_{fi}) R(\theta) d_i = m \ddot{P}_o \tag{8}$$

$$r_o \sum_{i=1}^3 (F_i - f_{fi}) = I \ddot{\theta}_o \tag{9}$$

where m is the mass of TWOMR, I is the moment of inertia and $f_{fi} (i = 1, 2, 3)$ is the friction forces exerted at each wheel and the expression for its range of values is taken from Williams et al. (2002).

$$f_{fi} = \frac{2}{3\pi} mg \mu_{\max} \tan^{-1}(k v_i) \tag{10}$$

g is the acceleration due to gravity, μ_{\max} is the maximum value of coefficient of friction and k is a constant.

Using Eqs. (4), (7) and (10), dynamic Eqs. (8) and (9) can be written as

$$\hat{M} \ddot{q} + \hat{V} \dot{q}_o = u - u_f \tag{11}$$

where $\hat{M} = \frac{1}{\alpha} (J^{-1})^T \begin{bmatrix} m & 0 & 0 \\ 0 & m & 0 \\ 0 & 0 & I \end{bmatrix}$, $\hat{V} = \frac{1.5}{\alpha} (J^{-1})^T \begin{bmatrix} \beta & 0 & 0 \\ 0 & \beta & 0 \\ 0 & 0 & 2\beta r_o^2 \end{bmatrix}$, $u = [u_1 \quad u_2 \quad u_3]$

and

$$u_f = \frac{1}{\alpha} (J^{-1})^T \begin{bmatrix} -f_{f1} \sin(\theta) - f_{f2} \sin(\frac{\pi}{3} - \theta) + f_{f3} \sin(\frac{\pi}{3} + \theta) \\ f_{f1} \sin(\theta) - f_{f2} \cos(\frac{\pi}{3} - \theta) - f_{f3} \cos(\frac{\pi}{3} + \theta) \\ r_o(f_{f1} + f_{f2} + f_{f3}) \end{bmatrix}$$

Now let $z = [v_o \quad w_o]^T$. Then Eq. (11) can be further simplified as

$$\dot{z} = \hat{A}z + \hat{B}(u' - u'_f) \tag{12}$$

where $\hat{A} = -[(J^{-1})^T \hat{M} H]^{-1} \cdot [(J^{-1})^T \hat{V} H]$, $\hat{B} = [(J^{-1})^T \hat{M} H]^{-1}$, $u' = \alpha u$ and $u'_f = \alpha u_f$. $H = [\cos(\theta) \quad \sin(\theta) \quad 0; \quad 0 \quad 0 \quad 1]^{-1}$.

In presence of bounded matched uncertainties ζ Eq. (12) can be written as

$$\dot{z} = \hat{A}z + \hat{B}(u' - u'_f + \zeta) \quad (13)$$

3 Controller Design

To make the system robust sliding mode control knowledge is utilized to build the controller. The main aim of the controller is to follow the desired linear velocity v_d and desired and angular velocity w_d of TWOMR. To design the controller velocity error is defined as

$$e = z_d - z = \begin{bmatrix} e_1 \\ e_2 \end{bmatrix} = \begin{bmatrix} v_d - v_o \\ w_d - w_o \end{bmatrix} \quad (14)$$

The main challenge while using sliding mode control is the selection of sliding surface $\sigma_i (i = 1, 2) = [\sigma_1 \ \sigma_2]^T$. For simplicity sliding surface is defined based on error which is given as

$$\sigma = z_d - z + \rho \int_0^t (z_d - z) d\tau \quad (15)$$

Differentiating Eq. (15) we get

$$\dot{\sigma} = \dot{z}_d - \hat{A}z - \hat{B}(u + \zeta) + \rho(z_d - z) \quad (16)$$

To satisfy ideal sliding mode condition $\dot{\sigma} = 0$. Using Eq. (12) neglecting u'_f total control input is obtained as

$$u_{eq} = \hat{B}^{-1}[\dot{z}_d - \hat{A}z + \rho(z_d - z)] \quad (17)$$

u_{eq} brings the states on sliding surface but presence of uncertainties deviates the states and increases the error. Hence to keep the error zero a saturation function control input is added in Eq. (17). Therefore total control input is written as

$$u_T = \hat{B}^{-1}[\dot{z}_d - \hat{A}z + \rho(z_d - z) + G \text{sat}(\sigma)] \quad (18)$$

where ρ is the integral gain, G is the switching gain, and $sat(\sigma_i) = \begin{cases} sign(\sigma_i), & |\sigma_i| > \delta > 0 \\ \frac{\sigma_i}{\delta}, & |\sigma_i| \leq \delta \end{cases}$, δ is a small positive constant.

The major issue in the design of controller is the estimation of design parameters. Hence to tackle the problem an adaptive law is introduced to estimate the value of G . Let \hat{a}_ρ the estimates of G and $\lambda_i (i = 1, 2, 3)$ is a positive constant then adaptive law is defined as

$$\begin{aligned} \dot{\hat{a}}_\rho &= \begin{bmatrix} \dot{\hat{a}}_{\rho 1} & 0 & 0 \\ 0 & \dot{\hat{a}}_{\rho 2} & 0 \\ 0 & 0 & \dot{\hat{a}}_{\rho 3} \end{bmatrix} \\ &= \begin{bmatrix} \lambda_1 sign(\sigma_1) & 0 & 0 \\ 0 & \lambda_2 sign(\sigma_2) & 0 \\ 0 & 0 & \lambda_3 sign(\sigma_3) \end{bmatrix} \end{aligned} \tag{19}$$

Now using Eq. (19) in Eq. (18), modified adaptive integral sliding mode control law is obtained as

$$u_T = \hat{B}^{-1} [\dot{z}_d - \hat{A} z + \rho(z_d - z)] + \hat{B}^{-1} [\hat{a}_\rho sign(\sigma)] \tag{20}$$

Theorem *The states of dynamic system given by Eq. (11) can track the desired trajectory if proposed control law is used and control parameters are selected appropriately.*

Proof Let $\tilde{a}_\rho = \hat{a}_\rho - \bar{a}_\rho$ is the estimated error where \bar{a}_ρ is the nominal value of \hat{a}_ρ and Lyapunov function is selected as

$$V = \frac{1}{2} \sigma^2 + \frac{1}{2} \eta_1 \tilde{a}_{\rho 1}^2 + \frac{1}{2} \eta_2 \tilde{a}_{\rho 2}^2 + \frac{1}{2} \eta_3 \tilde{a}_{\rho 3}^2 \tag{21}$$

Differentiating Eq. (21) and using Eq. (16) yields

$$\dot{V} = \sigma[\dot{z}_d - \dot{z} + \rho(z_d - z)] + \eta_1 \tilde{a}_{\rho 1} \dot{\tilde{a}}_{\rho 1} + \eta_2 \tilde{a}_{\rho 2} \dot{\tilde{a}}_{\rho 2} + \eta_3 \tilde{a}_{\rho 3} \dot{\tilde{a}}_{\rho 3} \tag{22}$$

Substituting value of from Eq. (19) Lyapunov function can be further simplified as

$$\begin{aligned}
\dot{V} &= \sigma[\dot{z}_d - \dot{z} + \rho(z_d - z)] + \sum_{i=1}^3 \eta_i \tilde{a}_{\rho i} \lambda_i \text{sign}(\sigma_i) \\
&= \sigma[\dot{z}_d - \hat{A}z - \hat{B}\hat{B}^{-1}\{\dot{z}_d - \hat{A}z + \lambda \text{sign}(\sigma) + \rho(z_d - z)\} - \hat{B}\hat{B}^{-1}\xi + \rho(z_d - z)] \\
&\quad + \sum_{i=1}^4 \eta_i \tilde{a}_{\rho i} \lambda_i \text{sign}(\sigma_i) \\
&= \sigma[-\lambda \text{sign}(\sigma) - \xi] + \sum_{i=0}^3 \eta_i \tilde{a}_{\rho i} \lambda_i \text{sign}(\sigma_i) \\
&= -\sigma[\lambda \text{sign}(\sigma) + \xi] - \sum_{i=0}^3 \eta_i (\bar{a}_\rho - \hat{a}_\rho) \lambda_i \text{sign}(\sigma_i) \\
&\leq -|\sigma|(|\lambda||\sigma| - |\xi|) - \sum_{i=1}^3 |\eta_i| |\lambda_i| (|\bar{a}_\rho| - |\hat{a}_\rho|) |\sigma|
\end{aligned} \tag{23}$$

where $\eta < \frac{1}{\lambda}$. Therefore, it can be seen that by choosing proper value λ , derivative of Lyapunov function \dot{V} can be made zero or negative. Hence error e approaches zero asymptotically. To prove the efficacy of proposed controller simulation results are presented in next section.

4 Simulation Results

For the verification of proposed control law for TWOMR, simulations are carried on MATLAB/SIMULINK 2014. Parameter values are selected as $m = 9.5$ kg, $I = 0.17$ kgm², $r_0 = 0.17$ m, $\mu_{\max} = 0.26$, and $g = 9.8$ m/s². To generate a U-turn trajectory desired linear velocity and angular velocity is taken as

$$v_d = 0.05, \quad 0 < t \leq 50$$

and

$$w_d = \begin{cases} 0, & 0 < t < 10 \text{ and } 25 \leq t < 35 \\ 0.2, & 10 \leq t < 25 \text{ and } 35 \leq t < 50 \end{cases}$$

Figures 2 and 3 shows the tracking performance of linear and angular velocity of TWOMR and it can be seen that till 15 s both AISMC and ISMC provides an approximately same tracking capability in presence of friction. But between 15 and

Fig. 2 Linear velocity error

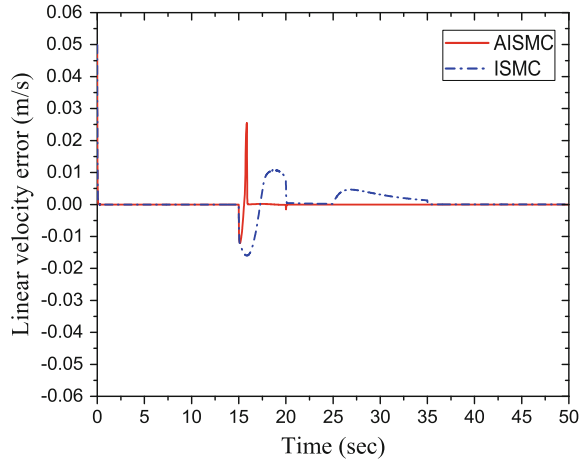
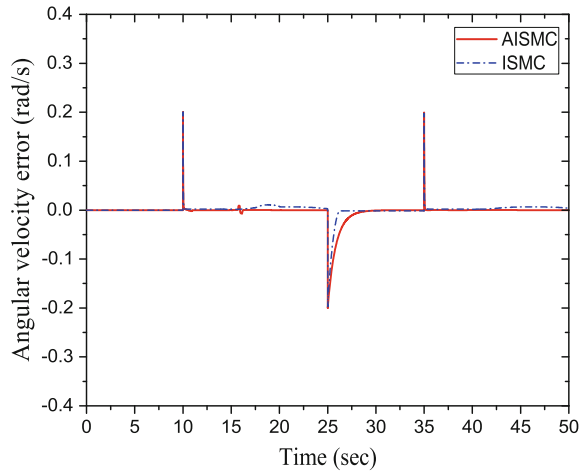


Fig. 3 Angular velocity error



25 s bounded uncertainty $\xi = 5 \cos(t)$ is fed in, which drops the efficacy of ISMC, whereas in case of AISMC there is a sudden increase in error for a fraction of second and robustness of the robot is maintained afterwards.

From Figs. 4 and 5 it is evident that the sliding mode condition is satisfied for AISMC and for ISMC sliding function does not converge to zero due to lack of knowledge of G value. The smooth control input voltage fed to all three wheels with no chattering is shown in Fig. 6. In presence of friction and uncertainty it is a

Fig. 4 Sliding surface 1

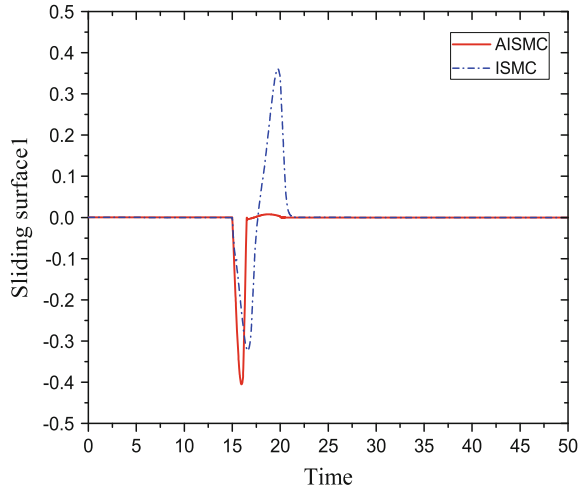
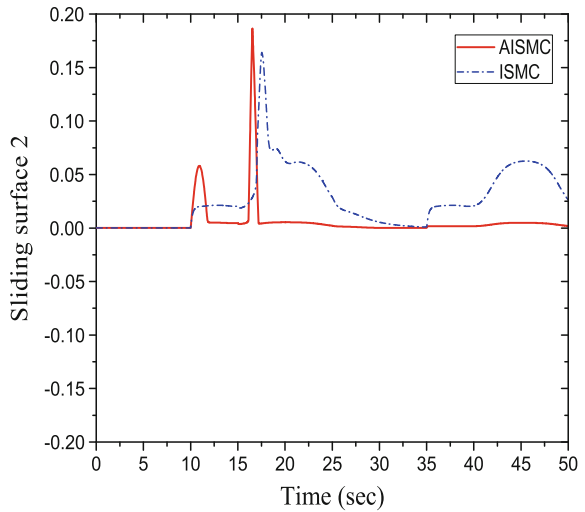


Fig. 5 Sliding surface 2



tedious job to select the correct value of design parameter G . Hence to tackle the problem, Fig. 7 shows the trend of \hat{a}_ρ with time which makes the controller adaptive. The generated trajectory obtained from desired linear and angular velocity is shown in Fig. 8 and it can be seen that by AISMC the robot successfully return to its starting point whereas by ISMC it deviates from its path due to lack of adaptation law.

Fig. 6 Control voltage applied at each wheel

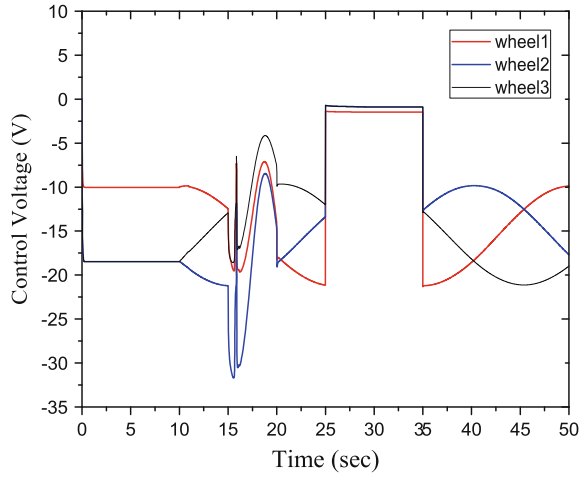
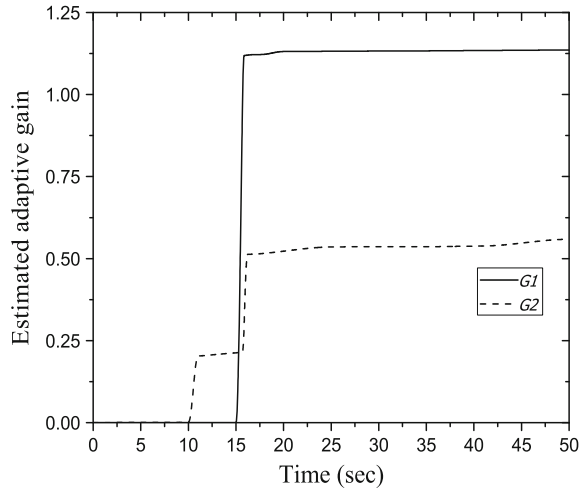


Fig. 7 Adaptive gain



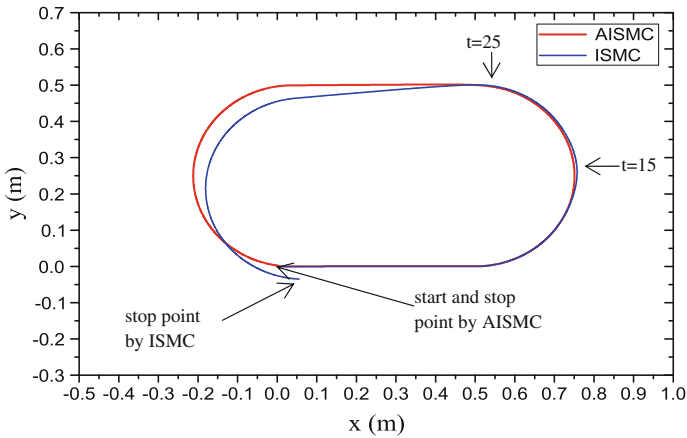


Fig. 8 Trajectory obtained by AISMC and ISMC

5 Conclusion

In this paper an adaptive robust controller is designed for a three wheel omnidirectional mobile robot to track a U-turn trajectory in presence of friction and unbounded uncertainties. Equation of motion is derived using Newton's second law. To make the system robust against uncertainties, chattering free and self tuned adaptive sliding mode control law is derived. The controller's stability is verified by Lyapunov stability theorem. There are some features of the proposed algorithm. Firstly, the tracking performance of both the controller bears similar properties when there is absence of external uncertainties. Secondly, when the uncertainties are introduced AISMC converges the error to zero faster and maintains its performance for the whole simulation time compared to ISMC. Finally, the control input obtained by AISMC is smooth and chattering free.

References

- Battle, J. A., & Barjau, A. (2009). Holonomy in mobile robots. *Robotics and Autonomous Systems*, 57, 433–440.
- Chen, N., Song, F., Li, G., Sun, X., & Ai, C. (2013). An adaptive sliding mode backstepping control for the mobile manipulator with nonholonomic constraints. *Communications in Nonlinear Science and Numerical Simulation*, 18, 2885–2899.
- Das, M., & Mahanta, C. (2014). Optimal second order sliding mode control for nonlinear uncertain systems. *ISA Transactions*, 53, 1191–1198.
- Pin, F. G., & Killough, S. M. (1994). New family of omnidirectional and holonomic wheeled platforms for mobile robots. *IEEE Transactions on Robotics and Automation*, 10, 480–489.
- Tzafestas, S. G. (2014). *Introduction to mobile robot control*. London: Elsevier.

- Viet, T. D., Doan, P. T., Hung, N., Kim, H. K., & Kim, S. B. (2012). Tracking control of a three-wheeled omnidirectional mobile manipulator system with disturbance and friction. *Journal of Mechanical Science and Technology*, *26*, 2197–2211.
- Williams, R. L., Carter, B. E., Gallina, P., & Rosati, G. (2002). Dynamic model with slip for wheeled omnidirectional robots. *IEEE Transactions on Robotics and Automation*, *18*, 285–293.
- Xu, D., Zhao, D., Yi, J., & Tan, X. (2009). Trajectory tracking control of omnidirectional wheeled mobile manipulators: Robust neural network-based sliding mode approach. *IEEE Transactions on Systems, Man, and Cybernetics. Part B Cybernetics*, *39*, 788–799.

Point Mass Models for Dynamic Balancing of Industrial Manipulators Using Genetic Algorithm

Devi Singh Kumani and Himanshu Chaudhary

Abstract The dynamic balancing of industrial manipulator is achieved in this paper by minimizing shaking moments and forces using octahedron and hexahedron point mass configuration with genetic algorithm (GA) as optimization tool. Comparison of seven/six point mass models in tetrahedron and hexahedron configurations respectively is also made. The minimization problem to minimize shaking moments and forces is formulated using seven and six equimomental point-masses in different configurations for each link such that positive values for all point masses and link's inertias are ensured. To calculate the shaking moments and forces equations of motion for manipulator expressed in terms of the equimomental point masses are used. The population based genetic algorithm (GA) is used as it gives more than one solutions close to the most optimal solution and the designer can choose the one best suited for the use. Methodology is applied to a six-dof PUMA robot. Shaking moments and forces at joints are minimized by redistribution of point masses optimally that reduces the inertia of link which reduces the shaking moments and smoothens out the shaking forces at the joints of robot. It also reduces the driving torques. The optimized value of shaking moments and forces at different joints of Puma robot using seven point octahedron and six point mass hexahedron models are nearly same and does not differ significantly.

Keywords Dynamic balancing · Genetic algorithm · Octahedron point mass model · Hexahedron point mass model · Shaking force and shaking moment · Driving torques

D.S. Kumani (✉)
Poornima College of Engineering, Jaipur, India
e-mail: profdevs@gmail.com

H. Chaudhary
Malaviya National Institute of Technology, Jaipur, India

1 Introduction

The shaking moment and shaking force at the base creates dynamic unbalance in the industrial manipulators and induces noise, wear and fatigue and are often undesired. A manipulator is called “Dynamically balanced”, if no shaking moments and shaking forces result at all. Balanced manipulators do not exert vibrations and can have both low cycle times and high accuracy. Therefore, there is a need to reduce the frame vibrations due to shaking moments and forces and we also have to reduce abnormal fluctuations in input torque to achieve smooth operation of the industrial manipulators. A good amount of mass and inertia is added to the system for complete balancing i.e. having no shaking moment and force at the frame of manipulator as per existing dynamic balancing principles as reported by Wijk van der et al. (2009), who compared various dynamic balancing principles and stated that the mass redistribution offers relatively less mass and additional inertia solution. Further, the shaking torques and forces at joints of a robot are to be considered for modeling of industrial manipulators. For simulation and control of the robot, we need to eliminate/reduce the shaking moments and forces from equation of motion as emphasized in the robotic literature Sciavico and Siciliano (1996) and Eberhard and Schienlen (2006). The various methods for complete balancing of shaking moments for planer linkages has been reviewed by Kochev (2000), most of these methods are based on addition of counter weights to moving linkages, attachment of rotating discs and mass redistribution (Papakostas et al. 1998) reported the dynamic design of dynamically balanced robotic manipulator having high speed and accelerations. Others Feng et al. (2000) and Seglo et al. (1998) have treated the mechanisms optimization problem with randomly generated population based solutions such as genetic algorithm.

In a manipulator, the shaking moments and forces are induced due to inertia of its moving links which depends on the mass distribution of the links (Sherwood and Hockey 1969). Thus to reduce the inertia induced shaking forces and moments, the masses of the links has to distributed optimally. This problem is resolved using dynamically equivalent system of point masses or equimoment system in parallelepiped configuration (Chaudhary and Shah 2007, 2008). The point-masses configurations proposed here satisfies the equimoment system conditions (Wenglarz et al. 1969).

The links of a manipulator are represented by the point masses using octahedron/hexahedron model with its CG coinciding with CG of link that ensures positive value for all point masses and offers practically implementable solutions. Then the equations of motion given in Chaudhary and Shah (2007) are used. An optimization problem is than formed to minimize the shaking forces and moments at joints of the industrial manipulator. The magnitude of point masses is obtained using genetic algorithm (GA). Objective function is to minimize the shaking moments and forces at the joints of the manipulator. It also reduces the driving torque. Than the results of seven/six point mass models are compared to find which point mass model offers better optimal solution.

2 Point—Mass Models

2.1 Seven Point—Mass Octahedron Model

To find optimal distribution of link masses, each rigid link is converted into dynamically equivalent system of point masses. A set of point masses in octahedron configuration as shown in Fig. 1 represents the rigid links. Body fixed frame $x_i y_i z_i$ is fixed to i th link at its CG and x_i, y_i, z_i are principal axes. Six masses lie at vertices of octahedron and seventh point mass lies at CG of the link. The point masses are rigidly fixed to the frame $x_i y_i z_i$. The two systems, the rigid link and the system of point masses in octahedron configuration, are dynamically equivalent, if (i) the sum of all point-masses equal the mass of link (ii) the CG of point masses coincides with the CG of rigid link, giving three conditions (iii) the moment of inertias and product of inertias for distributed point-masses is same as that of rigid link, giving six conditions. These conditions are known as equimomental conditions for i th link. The mass, m_i , mass center coordinates $(\bar{x}_i, \bar{y}_i, \bar{z}_i)$, the moment of inertia ($I_{ixx}, I_{iyy}, I_{izz}$) and the product of inertia ($I_{ixy}, I_{iyz}, I_{izx}$) are defined for i th link. The coordinates (x_{ij}, y_{ij}, z_{ij}) of point mass m_{ij} are defined for j th point mass of i th link.

For seven point mass model assuming equal point masses at equidistance on either side of axes x_i, y_i and z_i , we get

$$m_{i1} = m_{i4}, m_{i3} = m_{i5} \text{ and } m_{i6} = m_{i7} \tag{1}$$

$$x_{i1} = -x_{i4}, y_{i3} = -y_{i5} \text{ and } z_{i6} = -z_{i7} \tag{2}$$

The point mass m_{i2} is placed at CG of the link. Since the other point masses are placed on axes, their other coordinates are zeros. These assumptions lead product of inertias zeros and x_i, y_i and z_i become principal axes of the i th link. The mass center also is at the origin, i.e., $\bar{x}_i = \bar{y}_i = \bar{z}_i = 0$. This arrangement automatically satisfies the six equimomental conditions pertaining to location of center of mass and product of inertias, the remaining four conditions of total mass and inertia about three axes give:

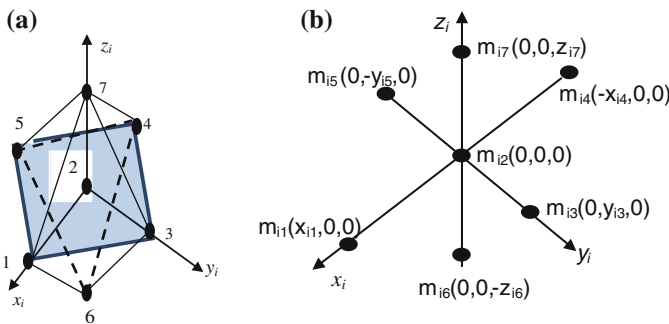


Fig. 1 Seven point-mass octahedron model. a Octahedron model. b Coordinates of point masses

$$m_i = 2m_{i1} + m_{i2} + 2m_{i3} + 2m_{i6} \tag{3}$$

$$I_{ixx} = 2m_{i3}y_{i3}^2 + 2m_{i6}z_{i6}^2 \tag{4}$$

$$I_{iyy} = 2m_{i1}x_{i1}^2 + 2m_{i6}z_{i6}^2 \tag{5}$$

$$I_{izz} = 2m_{i1}x_{i1}^2 + 2m_{i3}y_{i3}^2 \tag{6}$$

Equations (3)–(6) contain 7 unknowns, four point masses $m_{i1}, m_{i2}, m_{i3}, m_{i6}$, and three coordinates x_{i1}, y_{i3}, z_{i6} . Assuming $m_{i1} = m_{i3} = m_{i6} = \alpha m_i$, Eqs. (3)–(6) give:

$$m_{i2} = (1 - 6\alpha)m_i \tag{7}$$

$$x_{i1}^2 = (I_{iyy} + I_{izz} - I_{ixx})/4\alpha m_i \tag{8}$$

$$y_{i3}^2 = (I_{ixx} + I_{izz} - I_{iyy})/4\alpha m_i \tag{9}$$

$$z_{i6}^2 = (I_{ixx} + I_{iyy} - I_{izz})/4\alpha m_i \tag{10}$$

where, a constant α must satisfy $1 > (1 - 6\alpha) > 0$, i.e., $\alpha < 1/6$.

Since, the mass and inertias of rigid link are known, Eqs. (7)–(10) provides unknown parameters of the point mass system. It is dynamically equivalent to the rigid link and does not contain negative point masses.

2.2 Six Point—Mass Hexahedron Model

Similar to the seven point mass model in octahedron configuration, six point mass model is defined in hexahedron configuration as shown in Fig. 2.

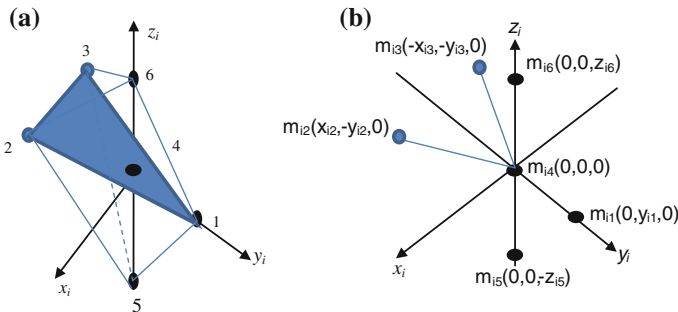


Fig. 2 Six point—mass hexahedron model. **a** Hexahedron model. **b** Coordinates of point-masses

For six point mass model the following relationships of point masses and their distances along axes x_i , y_i and z_i , are assumed to place CG of six point masses in hexahedron configuration at the CG of the link.

$$m_{i1} = 2m_{i2} = 2m_{i3} \text{ and } m_{i5} = m_{i6} \quad (11)$$

$$x_{i2} = -x_{i3}, y_{i1} = -y_{i2} = -y_{i3} \text{ and } z_{i5} = -z_{i6} \quad (12)$$

Since all other coordinates are zeros for point masses 1, 4, 5 and 6 as shown in Fig. 2 and the location of masses 2 and 3 being symmetric, the product of inertias become zeros. x_i , y_i and z_i are principal axes of the i th link and the mass center is at the origin, i.e., $\bar{x}_i = \bar{y}_i = \bar{z}_i = 0$. This arrangement automatically satisfies the six equimomental conditions pertaining to center of mass and product of inertias, the remaining four conditions of total mass and inertia about three axes gives:

$$m_i = 2m_{i1} + m_{i4} + 2m_{i5} \quad (13)$$

$$I_{ixx} = 2m_{i1}y_{i1}^2 + 2m_{i5}z_{i5}^2 \quad (14)$$

$$I_{iyy} = m_{i1}x_{i2}^2 + 2m_{i5}z_{i5}^2 \quad (15)$$

$$I_{izz} = m_{i1}x_{i2}^2 + 2m_{i1}y_{i1}^2 \quad (16)$$

Equations (3)–(6) contain 6 unknowns, three point masses m_{i1} , m_{i4} , m_{i5} , and three coordinates x_{i2} , y_{i1} , z_{i5} . Assuming $m_{i1} = 2m_{i5} = \alpha m_i$, Eqs. (3)–(6) gives:

$$m_{i4} = (1 - 3\alpha)m_i \quad (17)$$

$$x_{i2}^2 = (I_{iyy} + I_{izz} - I_{ixx})/2\alpha m_i \quad (18)$$

$$y_{i1}^2 = (I_{ixx} + I_{izz} - I_{iyy})/4\alpha m_i \quad (19)$$

$$z_{i5}^2 = (I_{ixx} + I_{iyy} - I_{izz})/2\alpha m_i \quad (20)$$

where, a constant α must satisfy, $1 > (1 - 3\alpha) > 0$, i.e., $\alpha < 1/3$.

Since, the mass and inertias of rigid link are known, Eqs. (17)–(20) provides unknown parameters of the point mass system. It is dynamically equivalent to the rigid link and does not contain negative point masses that being the problem with parallelepiped model in Chaudhary and Shah (2007).

3 Optimization Problem Formulation

3.1 Optimality Criteria

The objective function, used to minimize shaking forces and moments at joints of a manipulator of n moving links, based on the RMS values is as follows:

$$f(\mathbf{x}) = \sum_{i=1}^n w_{i1}f_i^c + w_{i2}n_i^c \quad (21)$$

where f_i^c and n_i^c are the RMS values of the constraint force, $f_i^c = |\mathbf{f}_i^c|$, and moment, $n_i^c = |\mathbf{n}_i^c|$, at the i th joint, respectively. We have taken weighing factors, w_{i1} and w_{i2} , as 1 so as to minimize the shaking force and the shaking moment both equally. The design variable vector \mathbf{x} is defined in the next sub section.

3.2 Decision Variables and Constraints

The point masses m_{i1}, \dots, m_{i7} for seven point mass model and m_{i1}, \dots, m_{i6} for six point mass model of each link are taken as the decision variables. The locations of the point-masses for each link are fixed in the link-fixed frame. For a manipulator having n moving links, the Vector of the decision variables, \mathbf{x} , is then defined as

$$\mathbf{x} \equiv [\mathbf{m}_1^T, \dots, \mathbf{m}_n^T]^T \quad (22)$$

where the 7-vector, \mathbf{m}_i for octahedron model and 6-vector, \mathbf{m}_i for hexahedron model is as follows:

$$\begin{aligned} \mathbf{m}_i &\equiv [m_{i1} \ m_{i2} \ m_{i3} \ m_{i4} \ m_{i5} \ m_{i6} \ m_{i7}]^T \\ \mathbf{m}_i &\equiv [m_{i1} \ m_{i2} \ m_{i3} \ m_{i4} \ m_{i5} \ m_{i6}]^T \end{aligned}$$

Then the optimization problem is formulated as follows:

$$\text{Minimize } f(\mathbf{x}) = \sum_{i=1}^n w_{i1}f_i^c + w_{i2}n_i^c \quad (23a)$$

Subject to

$$\begin{aligned} & - \sum_{j=1}^p m_{ij} + m_i \leq 0 \text{ for } i \\ & = 1, 2, 3, \dots, p \ (p = 7 \text{ for octa and } 6 \text{ for hexa model}) \end{aligned} \quad (23b)$$

$$-m_{ij} + \beta m_i \leq 0 \quad \text{for } j = 1, 3, \dots, 7 \text{ and } j \neq 2 \text{ for octa model} \quad (23c)$$

$$-m_{ij} + 2\beta m_i \leq 0 \quad \text{for } j = 2 \quad \text{for octa model} \quad (23d)$$

$$-m_{ij} + \beta m_i \leq 0 \quad \text{for } j = 2, 3, \dots, 6 \text{ and } j \neq 1, 4 \quad \text{for hexa model} \quad (23e)$$

$$-m_{ij} + 2\beta m_i \leq 0 \quad \text{for } j = 1, 4 \quad \text{for hexa model} \quad (23f)$$

where a constant β ensures minimum point mass and is a fraction of point mass to link mass, say $\beta = 0.0001$.

The inequality (23b) ensures that the minimum link mass is m_i . Constraints (23c), (23d), (23e), and (23f) are imposed to keep point masses more than zero. Constant β can be chosen to retain some +ve value for all point masses, however the higher value of this variable increases the shaking moment values.

4 Genetic Algorithm (GA) Technique

The optimization problem formulated using Eqs. (23a–23f), solves for each point mass using Genetic Algorithm, the total mass of each link, i.e. sum of point masses, is subjected to a lower limit equal to that of link mass and individual point masses are also subjected to lower limit equal to 0.0001–0.0002 times the mass of the link. The fitness/objective function is computed during the execution of the specified trajectory of the manipulator.

The GA calls for input information on decision/design variables (number of manipulator links multiplied by point masses per link), fitness/objective function and constraints (lower bound on sum of different point masses and individual point mass of each link). Further, it allows for variations in population size, number of generations, elite children count to be retained in next generation, crossover fraction, tolerance on function, and defining initial population (if required). We obtained number of feasible solutions. The feasible solutions reported here were obtained for hexahedron point mass model with population size of 7200, 20 generation counts, elite counts of 72 (1 % of population), 0.7 crossover fraction, 1e-90 tolerance function and defining point masses for unbalanced robot as initial population to preserve characteristics of links, particularly 5th and 6th links having very low inertia and mass values. The octahedron point mass model is solved with population of 7200 and 9000 with remaining parameters as that for hexahedron model. It is observed that the best result reported in Table 1 (objective function value of 822.3) is obtained with population size of 9000 and not 7200 as used for hexahedron model.

Table 1 RMS values of objective function for seven and six point models

S. no.	Model	Objective function value in different trials						Mean	Std. dev.	Best value
		1	2	3	4	5	6			
1	Seven Pt. octahedron	827.2	829.4	822.3	830.4	829.1	829.4	828.0	2.69	822.3
2	Six Pt. hexahedron	827.8	823.0	829.5	828.8	825.8	828.9	827.3	2.25	823.0

5 Application Illustration

The six-dof PUMA robot, the details of which are available in published literature, is considered to minimize shaking forces and moments using equations of motion given in Chaudhary and Shah (2007) and proposed methodology developed in Sects. 3 and 4. The Denavit–Hartenberg (DH) parameters, link’s masses, joint trajectory and inertias of the manipulator given in Saha (2014) are taken here for analysis and comparison purposes.

6 Results and Discussion

The results for RMS values for seven and six point models given in Table 1 demonstrates that the mean and the best value of objective function value for 6 trials of GA solution is nearly same for both models. The best value obtained for seven point model is with population of 9000 as against population of 7200 for six point model.

Table 2 gives the RMS values of shaking moment at different joints of PUMA robot for best value of objective function in both the cases. The shaking moments at joint 1, 2 and 3 is significantly reduced for both models vis-à-vis un-balanced robot.

Table 3 gives the RMS values of shaking force at joints 1–6. It demonstrates that the shaking force remains nearly the same in all three cases as it depends on the total mass of the linkages which comes out same, we have redistributed the mass through optimization, that changes the inertia of link and reduces the shaking moment at joints of robot.

Table 2 RMS values of shaking moment (N-m) at joints of seven and six point models

S. no.	Model	Shaking moment (N-m) at joints					
		1	2	3	4	5	6
1	Un-balanced Puma robot	73.659	76.173	14.704	5.447	0.105	0.076
2	Seven Pt. octahedron	5.376	23.782	4.178	4.680	0.112	0.076
	% reduction	92.7 %	68.8 %	71.6 %	14.1 %	~ Same	Same
3	Six Pt. hexahedron	5.102	26.813	2.663	4.132	0.112	0.076
	% reduction	93.1 %	64.8 %	81.9 %	24.1 %	~ Same	Same

Table 3 RMS values of shaking force (N) at joints of seven and six point models

S. no.	Model	Shaking force (N) at joints					
		1	2	3	4	5	6
1	Un-balanced Puma robot	367.98	264.79	110.22	24.14	13.80	3.45
2	Seven Pt. octahedron	367.92	264.71	110.13	24.13	13.80	3.45
3	Six Pt. hexahedron	367.92	264.71	110.13	24.12	13.80	3.45

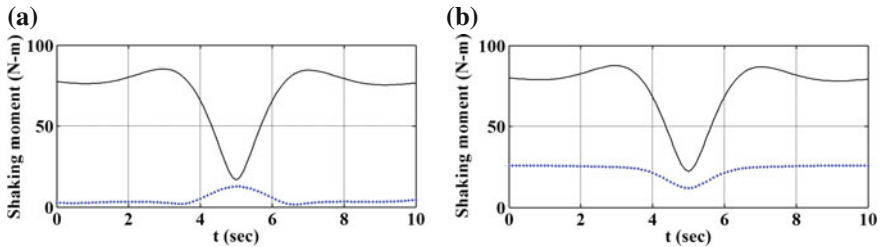


Fig. 3 Shaking moments of original (____) and optimally balanced PUMA (****) with 7 Point model. **a** Joint 1. **b** Joint 2

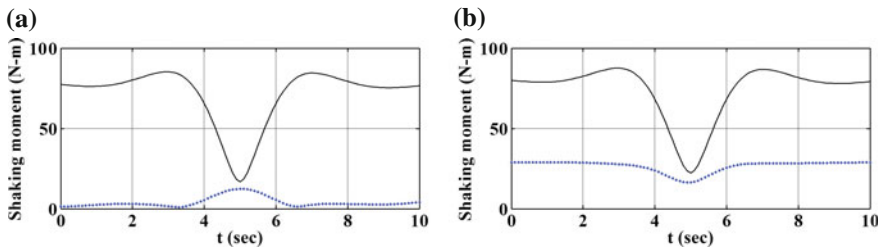


Fig. 4 Shaking moments of original (____) and optimally balanced PUMA (****) with 6 point model. **a** Joint 1. **b** Joint 2

However, the peak value of shaking force is reduced as demonstrated by Fig. 5. The Variation of shaking moments with respect to time for one complete cycle, for the original unbalanced and optimized manipulator for seven point and six point models are shown in Figs. 3 and 4 respectively. Shaking force variation for seven point and six point models is shown in Fig. 5. The objective function value for seven and six point models obtained using ‘fmincon’ is 810.64 and 817.33 respectively. ‘fmincon’ results are better than that of GA, GA results offer multiple solutions close to the optimal solution giving multiple choices and thus more helpful for link shape formation.

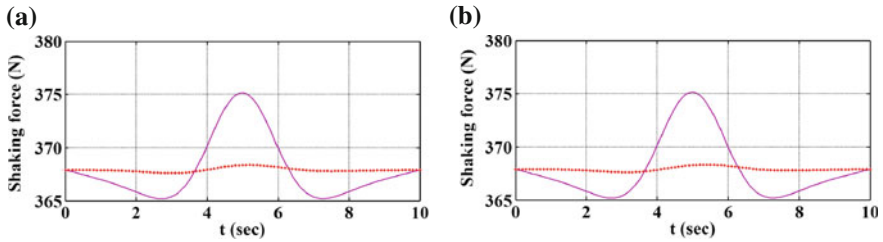


Fig. 5 Shaking force of original (—) and optimally balanced PUMA (****). **a** At joint 1 for seven point model. **b** At joint 1 for six point model

7 Conclusion

The mean objective function values for seven point octahedron and six point hexahedron models are 828 and 827.3 respectively. These are nearly same. Further, the best values of objective function for seven point octahedron and six point hexahedron models are 822.3 and 823.02 respectively. These are also not significantly different. Therefore, we conclude that seven point octahedron and six point hexahedron models offer same optimization results in case of GA solution. The one which is more convenient for manipulators link shape formation may be used.

References

- Chaudhary, H., & Saha, S. K. (2008). Balancing of Shaking forces and Shaking moments for planer mechanisms using the equipomental systems. *Mechanism and Machine Theory*, 43, 310–334.
- Chaudhary, H., & Saha, S. K. (2007). Minimization of constraint forces in industrial manipulators. *IEEE International Conference on Robotics and Automation*, 10–14
- Eberhard, P., & Schiehlen, W. (2006). Computational dynamics of multibody systems: History formalisms, and applications. *ASME Journal of Computational and Nonlinear Dynamics*, 1, 3–12.
- Feng, B., Morita, N., Torii, T., & Yoshida, S. (2000). Optimum balancing of shaking force and shaking moment for RSSR mechanism using genetic algorithm. *JSME International Journal Series C*, 43(3), 691–696
- Kochev, I. S. (2000). General theory of complete shaking moment balancing of planer linkages: A critical review. *Mechanism and Machine Theory*, 35, 1501–1514.
- Papakostas, K. D., Mouroutsos, S. G., & Porter, B. (1998). Genetic design of dynamically optimal robotic manipulators. *Proceedings of Institute of mechanical engineers Part-I, Journal of Systems & Control Engineering*, 212(6), 423–436.
- Saha, S. K. (2014). *Introduction to robotics* (2nd ed.). Mc Graw Hill (India) Pvt Ltd.
- Sciavico, L., & Siciliano, B. (1996). *Modeling and control of robot manipulators*. New York: McGraw-Hill.
- Segla, S., Kalker-Kalkman, C. M., & Schwab, A. L. (1998). Static balancing of a robot mechanism with the aid of genetic algorithm. *Mechanism and Machine Theory*, 33(1/2), 163–174.

- Sherwood, A. A., & Hockey, B. A. (1969). The optimization of mass distribution in mechanisms using dynamically similar systems. *Journal of Mechanisms*, 4, 243–260.
- Wenglarz, R. A., Forarasy, A. A., & Maunder, L. (1969). Simplified dynamic models. *Engineering*, 208, 194–195.
- Wijk van der, V., Herder, J. L., & Demeulenaere, B. (2009). Comparison of various dynamic balancing principles regarding additional mass and additional inertia. *Journal of Mechanisms and Robotics*, ASME, 11, 041006-1

Application of the Attractive Ellipsoid Methodology to Robust Control Design of a Class of Switched Systems

V. Azhmyakov and J.H. Carvajal Rojas

Abstract Our contribution is devoted to an application of the newly elaborated robust feedback-type control methodology to a class of industrial robotic systems. We consider a formal prototype of an automated Continuous Stirred Tank Reactor (CSTR) in the presence of bounded (operating) uncertainties and external disturbances. The nonlinear model of the CSTR has a switched nature and implies a sophisticated dynamical behaviour. Moreover, the resulting control design is supposed to be the defined only by the given system output. The robustness property of the closed-loop automated system is determined here in the sense of a “practical stability” concept and is based on the Attractive Ellipsoid (AE) approach. The implementable control design scheme we propose involves the Bilinear Matrix Inequalities (BMIs) techniques in combination with the Multiple Lyapunov functions analysis.

1 Introduction

Recently applications of the switched systems control methodology in modern robotics and industrial automation have attracted a lot of attention in the engineering community (see Martinoli et al. 2013; Shucker et al. 2007). The control design techniques based on the hybrid, switched and discrete event systems theory are nowadays a mature methodology for the theoretical and practical synthesis of several types of controllers for sophisticated robotic and automated processes (Antsaklis 2000; Azhmyakov et al. 2008, 2010, 2014, 2015; Barkhordari and Jahed-Motlagh 2009; Boskovic and Mehra 2000; Egerstedt et al. 2006; Kouhi et al. 2014; Liberzon 2003; Poznyak et al. 2011; Sajja et al. 2013; Shaikh and Caines 2007; Wicks et al. 1994). Recall that the general hybrid and switched dynamic

V. Azhmyakov (✉) · J.H. Carvajal Rojas
Faculty of Biomedical Engineering, Electronics and Mechatronics,
Antonio Nariño University, Neiva, Republic of Colombia
e-mail: vadim33tech@uan.edu.co

models constitute an adequate formal framework for numerous engineering applications and provide a computational basis for the corresponding prototyping and software developing. We refer to (Azhmyakov et al. 2015; Egerstedt et al. 2006; Liberzon 2003; Lunze and Lamnabhi-Lagarrigue 2009; Lygeros 2003) for some examples and additional facts. The areas of interest and technological applications here include (but not necessary restricted to) autonomous robotic systems in industrial electronics, aeronautic, automotive engineering, networked systems engineering, control of mechanical systems and process control.

In this paper we determine a “switched system” as a dynamic model that contains a set of continuous-time subsystems and an associated “switching mechanism” (supervisor). The last one involves the time-driven interconnections between the given subsystems (see e.g., Liberzon 2003; Lunze and Lamnabhi-Lagarrigue 2009). As a consequence the conventional system stability question for a general switched system becomes more difficult (see e.g., Branicky 1998; DeCarlo et al. 2000; Liberzon 2003; Poznyak et al. 2011; Sajja et al. 2013; Wicks et al. 1994) and reference therein for the corresponding theoretic details. The large number of existing results in automatic control literature concerning the Lyapunov-type stability of switched systems can be separated into two groups: the first one contains results that guarantee stability of a switched system under arbitrary switching rules. Meanwhile, the second group of results deals with the issue of design a suitable switching signal that involves the system stability (Liberzon 2003). Our paper studies a specific switched dynamic model in the presence of (practically inevitable) perturbations and uncertainties. Note that the control design problem under uncertainties and (external) disturbances problem constitutes a classic research area (see Dahleh and Pearson 1988; Doyle 1983; Duncan and Schweppe 1971; Poznyak et al. 2011, 2014). However, the corresponding robust control techniques are not sufficiently advanced to the nonlinear switched systems and to the existing engineering applications in the robotic and automated systems practice. In this paper we propose a new robust stabilization approach to a specific family of nonlinear switched systems with bounded uncertainties. We restrict consideration to a class of linear output-based feedback control strategies that stabilize in a “practical sense” the given system associated with a specific class of switching signals. We are specifically interested in application of the newly elaborated effective robust design algorithm called Attractive Ellipsoid method (see the Author’s work Azhmyakov et al. 2008; Poznyak et al. 2011, 2014; Davila and Poznyak 2011). This powerful method for a practical stability analysis and design is combined with a well-known Multiple Lyapunov functions approach (see e.g., Branicky 1998; Daafouz et al. 2002; Liberzon 2003) to switched dynamics and with the dwell-time scheme (Hespanha and Morse 1999; Zhai et al. 2001). From the numerical point of view the control synthesis problem is reduced to an auxiliary (relaxed) BMI-constrained optimization problem (see Azhmyakov 2011; Poznyak et al. 2011). Finally we apply the proposed control design approach to the automated Continuous Stirred Tank Reactor (Barkhordari and Jahed-Motlagh 2009) and establish the robustness of the dynamic behaviour of this industrial robotic system.

The remainder of our paper is organized as follows: Sect. 2 contains some necessary concepts and the general problem statement. Section 3 presents the Attractive Ellipsoid method in application to a class of switched system under consideration. In Sect. 3 we develop a “practically stable” control strategy that guarantees the robust dynamics of the resulting (closed-loop) automated system. In Sect. 4 we develop a consistent computational prototype of a feedback-type fully automated control system for the Continuous Stirred Tank Reactor. This Attractive Ellipsoid based control system we construct possesses the expected robustness properties and makes it possible an autonomous operation of the CSTR. Section 5 summarizes the paper.

2 Problem Formulation and Some Basic Facts

Consider a switched control system with an affine structure and the model of the system output

$$\begin{aligned} \dot{x}(t) &= f_{\sigma(t)}(x(t)) + B_{\sigma(t)}u(t) + v(t) \\ x(0) &= x_0, \quad \sigma(0) = \sigma_0 \\ y(t) &= C_{\sigma(t)}x(t) + \xi_y(t) \end{aligned} \quad (1)$$

where $x(t)$, $x_0 \in \mathbb{R}^n$, $t \in \mathbb{R}_+$, are the state vector and the initial state vector, respectively. The control input in (1) is denoted by $u(t) \in \mathbb{R}^m$. The vector $y(t) \in \mathbb{R}^q$ describes the system output; and $v(t)$, $\xi_y(t)$ are bounded disturbances associated of the variables $x(t)$ and $y(t)$, respectively. Moreover, $\{f_i(\cdot)\}$ with $i = 1, \dots, M \in \mathbb{N}$ is a family of so called quasi-Lipschitz functions $f_i: \mathbb{R}^n \rightarrow \mathbb{R}^n$ (see definition below). By $\{B_i, C_i\}$, where $B_i \in \mathbb{R}^{n \times m}$, $C_i \in \mathbb{R}^{q \times n}$, we denote a family of the given systems matrices. The time dependent switching mechanism in (1) is determined by the following piecewise-constant function

$$\sigma(t) \in \mathcal{I} = \{1, \dots, M\}, \sqcup \in \mathbb{R}_+$$

This function indicates the currently active subsystem given by the selected $f_{\sigma(t)}(\cdot)$, $B_{\sigma(t)}$ and $C_{\sigma(t)}$. We now recall the concept of a quasi-Lipschitz function (see Azhmyakov 2011; Poznyak et al. 2011, 2014):

$$\mathcal{C}(A, c_{1i}, c_{2i}) := \{f_i: \mathbb{R}^n \mapsto \mathbb{R}^n \mid \|f_i(x) - A_i x\|^2 \leq c_{1i} + c_{2i} \|x\|^2 \forall x \in \mathbb{R}^n\}$$

where $i = 1, \dots, M$, $A_i \in \mathbb{R}^{n \times n}$ are given suitable matrices, $c_{1i} > 0$ and $c_{2i} > 0$. We also introduce the following technical assumptions (A):

- $\|v(t)\|^2 \leq \bar{v}$, for a given bound $\bar{v} \in \mathbb{R}_+$,
- $\|\xi_y(t)\|^2 \leq \bar{\xi}_y$, for a given bound $\bar{\xi}_y \in \mathbb{R}_+$,

- the pairs (A_i, B_i) and (A_i, C_i) are controllable/observable, respectively, for every $i = 1, \dots, M$,
- the “Zeno behavior” (infinite switchings in a finite time) in (2) is assumed to be excluded.

The dynamic transitions between the given subsystems (initially enumerated by i) occurs at the given switching times t_k , where $k \in \mathbb{Z}$. Let us introduce some concepts concerning switched systems when the dwell-time approach is used. A constant $\tau_d > 0$, such that $t_k - t_{k-1} \geq \tau_d$ is called the “dwell-time”, because $\sigma(\cdot)$ dwells on each of its values for at least τ_d units of time.

Definition 1 (See Hespanha and Morse 1999; Zhai et al. 2001) For a switching signal $\sigma(\cdot)$ and any $T_2 > T_1 \geq 0$ define $N(T_1, T_2)$ as a switching number associated with $\sigma(t)$ over the time interval $[T_1, T_2)$. If

$$N(T_1, T_2) \leq N_0 + \frac{T_2 - T_1}{\tau_{av}}$$

holds for $N_0 \geq 1$, $\tau_{av} > 0$, then τ_{av} is called the “average dwell-time” and N_0 is the chatter bound.

Let us introduce the auxiliary variable

$$\tilde{\xi}_x(x(t), t) := f_{\sigma(t)}(x(t)) - A_{\sigma(t)}x(t) + v(t), \quad t \in \mathbb{R}_+$$

and rewrite (1) in a generic “quasi-linear” form

$$\begin{aligned} \dot{x}(t) &= A_{\sigma(t)}x(t) + B_{\sigma(t)}u(t) + \tilde{\xi}_x(x(t), t) \\ x(0) &= x_0, \quad \sigma(0) = \sigma_0 \\ y(t) &= C_{\sigma(t)}x(t) + \xi_y(t) \end{aligned} \quad (2)$$

A control system of the type (2) is usually associated with a set \mathcal{U} of feasible control functions $u(\cdot)$. In this article we deal with a class of linear control output feedback strategies (a class of linear state dependent control functions). Let us also note that the quasi-Lipschitz properties of functions $\{f_i(\cdot)\}$ and the bounded disturbances in (1) and (2) constitute an adequate modelling framework for the real uncertainties for the usual robot dynamics and an associated observer.

We next apply the conventional Luenberger observer (see e.g., Khalil 2002)

$$\dot{\hat{x}}(t) = A_{\sigma(t)}\hat{x}(t) + B_{\sigma(t)}u(t) + L_{\sigma(t)}(y(t) - C\hat{x}(t)), \quad (3)$$

where $L \in \mathbb{R}^{n \times q}$ is the matrix observer. Application of (3) to system (2) gives rise to the explicit structure of the control function we use

$$u(t) = -K_{\sigma(t)}\hat{x}(t) \quad (4)$$

A control of the type (4) is fully characterized by suitable gain matrices $K_i \in \mathbb{R}^{n \times n}$, $i = 1, \dots, M$. For the estimation error vector $e(t) := x(t) - \hat{x}(t)$ we obtain

$$\dot{e}(t) = (A_{\sigma(t)} - L_{\sigma(t)}C_{\sigma(t)})e(t) + (\zeta_x(t) - L_{\sigma(t)}\zeta_y(t)). \quad (5)$$

Relations (1)–(5) involve the resulting form of the closed-loop automated system under consideration

$$\dot{z}(t) = \tilde{A}_{\sigma(t)}z(t) + F_{\sigma(t)}\zeta(t), z(0) = (x_0^T, e_0^T)^T, \quad (6)$$

where $z(t) = [\hat{x}^T(t), e^T(t)]^T$, $\zeta(t) = [\zeta_x^T(t), \zeta_y^T(t)]^T$ and

$$\tilde{A}_{\sigma(t)} := \begin{bmatrix} A_{\sigma(t)} - B_{\sigma(t)}K_{\sigma(t)} & L_{\sigma(t)}C_{\sigma(t)} \\ 0 & A_{\sigma(t)} - L_{\sigma(t)}C_{\sigma(t)} \end{bmatrix},$$

$$F_{\sigma(t)} := \begin{bmatrix} 0 & L_{\sigma(t)} \\ I_n & -L_{\sigma(t)} \end{bmatrix}$$

Here $I_n \in \mathbb{R}^{n \times n}$ is a n -unit matrix.

Our aim is to design an output feedback control strategy (the gain matrices in (4)) and determine the corresponding observer matrices L_i such that each invariant asymptotically stable ellipsoid

$$\mathcal{E}(0, P) := \mathcal{E}(z, P) := \{z \in \mathbb{R}^n \mid (z)^T P(z) \leq 1\},$$

where P is a positive defined symmetric matrix, has a “minimal size”. Let us present the exact concept (see Blanchini and Miani 2008; Haddad and Chellaboina 2008; Khalil 2002, for more details and basic set-stability definitions).

Definition 2 An ellipsoid $\mathcal{E}(z, P)$ centered in $z \in \mathbb{R}^n$

$$\mathcal{E}(z, P) := \{z \in \mathbb{R}^n \mid (z - z)^T P(z - z) \leq 1\}$$

where $P \in \mathbb{R}^{n \times n}$, $P = P^T > 0$, is called the Attractive Ellipsoid for (6) if $\mathcal{E}(z, P)$ is a Lyapunov asymptotically stable invariant set.

Evidently a “minimal size” AE $\mathcal{E}(z, P)$ associated with the given dynamic system (6) means in fact the “practical stability” of this closed-loop controlled model. The concrete aim is to design an output feedback control and determine suitable controller and observer matrices $\{K_i, L_i\}$ such that each invariant asymptotically stable ellipsoid $\mathcal{E}(0, P_i)$ has a “minimal size”. This minimality requirement can be easily formalized by the following specific optimization problem:

$$\begin{aligned}
& \text{minimize } \text{tr}(P_i^{-1}) \\
& \text{subject to } P_i^T = P_i > 0 \\
& P_i \in \Gamma_1(z(\cdot)); K_i, L_i \in \Gamma_2(z(\cdot)) \quad i = 1, \dots, M
\end{aligned} \tag{7}$$

Here $\Gamma_1(z(\cdot))$ is a set of symmetric and positive definite $2n \times 2n$ -matrices P_i ($i = 1, \dots, M$) that guarantee the property from Definition 2. Moreover, $\Gamma_2(z(\cdot))$ denotes a subset of the space of K_i, L_i stabilizing matrices, the subsets mentioned above formally describe the admissible feedback K_i and observer L_i gains. The corresponding ellipsoidal matrices associated with every subsystem of a general switched system are determined by P_i . We assume that the basic optimization problem (7) has at least one optimal solution denoted by $\{\hat{P}_i, \hat{K}_i, \hat{L}_i\}$, where $i = 1, \dots, M$. This minimization problem formulated above guarantees the “minimal size” of the invariant ellipsoid $\mathcal{E}(0, P_i)$ in the state space of system (6). Note that the set $\Gamma_1 \otimes \Gamma_2$ in (7) is a set of general restrictions. Evidently, the main problem is to give a concrete constructive characterization of the given restrictions set $\Gamma_1 \otimes \Gamma_2$.

3 The Attractive Ellipsoid Method

In this section we develop a numerical approach to the main optimization problem (7). Let us define a piecewise continuous Lyapunov-like function

$$\mathbf{V}(t) = V_{\sigma(t)}(z(t)) = z^T(t)P_{\sigma(t)}z(t) \tag{8}$$

for the basic switched system (6). Assume that there exists a constant $\mu > 1$ such that

$$V_i(z) \leq \mu V_j(z), \quad \forall z \in \mathbb{R}^{2n}, \quad \forall i, j \in \mathcal{I} \tag{9}$$

This last property is fulfilled, for example, with

$$\mu = \sup_{r, l \in \mathcal{I}} \frac{\lambda_{\max}(P_r)}{\lambda_{\min}(P_l)},$$

where $\lambda_{\max}(P)$ ($\lambda_{\min}(P)$) denotes the largest (smallest) eigenvalue of the positive definite symmetric matrix P . Therefore in the switching times it is held

$$\mathbf{V}(t_k) \leq \mu \lim_{t \rightarrow t_k^-} V_{\sigma(t)}(z(t)) = \mu \mathbf{V}(t_k^-), \quad k \in \mathbb{Z} \tag{10}$$

Let $N(t_0, t)$ be the number of switchings of $\sigma(\cdot)$ in the open interval (t_0, t) , such that

$$0 \leq t_0 < t_1 \cdots < t_{N(t_0,t)} < t < t_{N(t_0,t)+1} = T$$

The “partial” Lyapunov-like functions $V_{\sigma(t)}(z)$ associated with subsystems of (6) determine a family of ellipsoids in the state space of the switched dynamic system under consideration. These ellipsoids have a non-empty intersection. It is evident that in the case of “minimal size” ellipsoids $\mathcal{E}(0, P_i)$ the intersection is also an invariant set of (6) that possesses the minimal property. From the fundamental results of (Poznyak et al. 2011, 2014) we deduce the following theoretic fact.

Theorem 1 *Assume that all subsystems in (6) satisfy the basic assumptions. Let $\mathbf{V}(t) = z^T(t)P_{\sigma(t)}z(t)$ be a piecewise continuous function, and there exists a constant $\mu > 1$ such that $V_i(z) \leq \mu V_j(z), \forall i, j \in \mathcal{I}$. Then for any positive constants γ_0 and $\gamma_1 = \alpha_{\min} \cdot \left(\frac{\mu-1}{\mu}\right), r = 2, 3, 4, \dots, (\alpha_{\min} := \min_i \alpha_i, \alpha_i$ there exists a finite constant $\tau_{av} = \frac{\log \mu}{\alpha_{\min} - \gamma_1}$ such that $\mathbf{V}(t)$ is a storage (Lyapunov-like) function associated with the switched system (6) such that*

$$\mathbf{V}(t) \leq \exp(\gamma_0 - \gamma_1(t - t_0))\mathbf{V}(t_0) + \frac{\beta}{\alpha_{\min}} \mu^r \left(\frac{1 - \left(\frac{1}{\mu^{r-1}}\right)^{N(t_0,t)}}{\mu^{r-1} - 1} \right)$$

with the decay rate γ_1 and for any average dwell-time $\tau_d \geq \tau_{av}$. Moreover,

$$\limsup_{t \rightarrow \infty} \mathbf{V}(t) \leq \frac{\beta}{\alpha_{\min}} \left(\frac{\mu^r}{\mu^{r-1} - 1} \right). \tag{11}$$

The formal proof of Theorem 1 can be found in (Poznyak et al. 2014). Note that the obtained inequality (11) corresponds to the adequate choice of decay rate $\gamma_1 = \frac{1}{2} \alpha_{\min}$. It is clear that there is a trade-off in the choice of the bound $\epsilon = \frac{\beta}{\alpha_{\min}} \left(\frac{\mu^r}{\mu^{r-1} - 1} \right)$ and the dwell-time τ_d . The next result is a useful consequence of Theorem 1.

Theorem 2 *Consider the following auxiliary optimization problem*

$$\begin{aligned} & \text{minimize } \sum_{i=1}^M \text{tr}(P_i^{-1}) + \mu \\ & \text{subject to} \\ & W_i(P_i, K_i, L_i, \alpha_i) \leq 0, \quad \forall i, j = \{1, \dots, M\} \\ & P_i \leq \mu P_j, \quad i \neq j \\ & P_i > 0, \alpha_i > 0, \mu > 1 \\ & \frac{\alpha_i}{\beta} P_i > Q_{presc} \end{aligned} \tag{12}$$

has an optimal solution $\hat{Y} := (\hat{P}_i, \hat{K}_i, \hat{L}_i, \hat{\alpha}_i, \hat{\mu}_i)_{i=1, \dots, M}$. Then the intersection the ellipsoids $\mathcal{E}(0, \hat{Q}_i)$ and $\hat{Q}_i = \frac{2}{\beta} \hat{P}_i$ generates a minimal size attractive set for the switched system (6).

We refer to Poznyak et al. (2014) for the necessary details.

The matrix constraints in problem (12) constitute the so called Bilinear Matrix Inequalities (BMIs). One can solve this constrained optimization problem by using some advanced computational tools from the modern mathematical programming. Let us mention here the PENBMI-MATLAB package that can be applied to (12).

It is necessary to stress that it is still difficult to get a closed solution of a BMI-constrained optimization problem of the type (11) and (12). In order to avoid this technical difficulty in an engineering computation, we use a suitable relaxations of the constraints in the initially given optimization problem (12). Using the celebrated A -matrix inequality (see Poznyak et al. 2014) we get

$$z^T(t)P_i F_i \zeta(t) + \zeta^T(t)F_i^T P_i z(t) \leq z^T(t)P_i \Lambda P_i z(t) + \zeta^T(t)F_i^T \Lambda^{-1} F_i \zeta(t).$$

Note that the required size minimization in (12) is “interpreted” as a trace minimization of P_i^{-1} . Nevertheless, minimization of $\text{tr}(P_i^{-1})$ is a hard non-linear optimization problem. Therefore, we consider an upper bound $P_i^{-1} \leq H_i$ and use the well-known Schur complement in order to get a set of “relaxed” LMI (Linear Matrix Inequality) constraints. Let us also note that (6) we consider the minimization of μ with the aim to reduce the dwell-time associated with the dynamic system under consideration.

Corollary 1 Assume that the relaxed optimization problem

$$\begin{aligned} & \text{minimize } \sum_{i=1}^M \text{tr}(H_i) + \epsilon^+ \\ & \text{subject to} \\ & \bar{W}_i(P_i, K_i, L_i, \alpha_i) \leq 0, \quad \forall i, j = \{1, \dots, M\} \\ & \Theta_{1i} > 0, \Theta_{2i} > 0, \Theta_{3i} > 0 \\ & 4\beta - \alpha_i \epsilon^+ \leq 0 \\ & P_i \leq \mu P_j, \quad i \neq j \\ & P_i > 0, H_i > 0, \alpha_i > 0, \epsilon^+ > 0 \\ & \frac{2}{\beta} P_i > Q_{presc} \end{aligned} \tag{13}$$

has an optimal solution $\hat{Y} := (\hat{P}_i, \hat{K}_i, \hat{L}_i, \hat{H}_i, \hat{\alpha}_i, \hat{\epsilon}_i^+)$. Then the ellipsoid $\mathcal{E}(0, Q_i)$ determined by $Q_i = \frac{1}{\epsilon^+} P_i$ is an attractive ellipsoid for the switched system (6).

The obtained relaxed optimization problem (13) provides a theoretic basis for the necessary numerical approach to the robust output feedback control for nonlinear systems under consideration. We next use (13) and determine a robust control design for an automated CSTR. Let us also note that the proposed control design methodology has a general nature and can be easily applied to various robotic and automated industrial controlled plants.

4 Robust Control of Automated Continuous Stirred Tank Reactor

In this section we study an example of the fully automated CSTR and demonstrate the applicability of the proposed robust control design method. The dynamic system under consideration constitute a controlled switched model. The implementation of the combined numerical method presented in the above sections was carried out, using the standard MATLAB packages and the Author's programs. The CSTR plant includes a constant volume tank, supervisor and two different source streams. The complete scheme of the process is depicted on Fig. 1.

The position of the valve is determined by a supervisor such that the generated switching signal is assumed to be arbitrary but determined at each time. The reactor is characterized by an exothermic-irreversible reaction $A \rightarrow B$ which is cooled by a stream with a constant flow rate and a variable temperature T_c . Assuming constant liquid volume, perfectly mixing and a first-order reaction in reactant A, the CSTR at each operating mode can be described by the following formal model

$$\begin{aligned} \frac{d}{dt} C_A(t) &= \frac{F_{q(t)}}{V} (C_{Aq(t)} - C_A(t)) - a_0 \exp\left(-\frac{E}{RT(t)}\right) C_A(t), \\ \frac{d}{dt} T(t) &= \frac{F_{q(t)}}{V} (T_{q(t)} - T(t)) - a_1 \exp\left(-\frac{E}{RT(t)}\right) C_A(t) \\ &\quad + a_2 (T_c(t) - T(t)). \end{aligned}$$

Fig. 1 The CSTR conceptual scheme

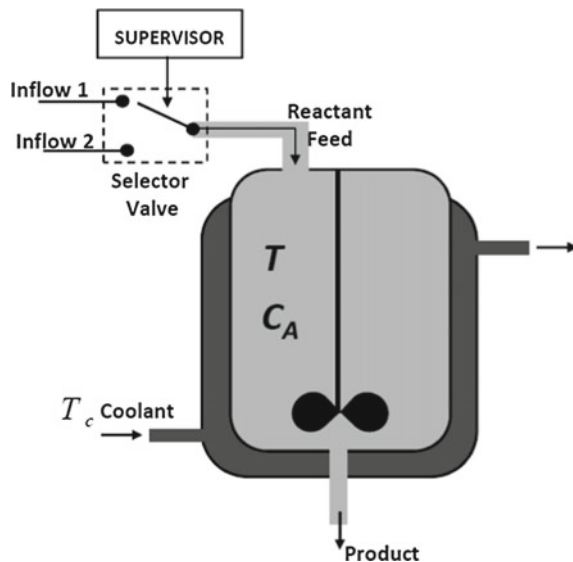


Table 1 Model parameters of CSTR

Symbol	Value	Meaning
a_0	7.2×10^{10}	Constant coefficient
a_1	-1.506×10^{13}	Constant coefficient
a_2	2.092	Constant coefficient
E/R	8750	$\frac{\text{Activation energy}}{\text{Gas constant}}$
V	100	Volume of the reactor
F_1	50	Feed flow rate 1
F_2	200	Feed flow rate 2
C_{A1}	1.5	Reactant A1 concentration
C_{A2}	0.75	Reactant A2 concentration
T_1	350	Inlet stream temperature 1
T_2	350	Inlet stream temperature 2

The corresponding parameter values are shown in Table 1 (see Barkhordari and Jahed-Motlagh 2009). The nominal operating conditions corresponding to an unstable equilibrium point are $T_c^* = 300$ K, $C_A^* = 0.5$ mol/L and $T^* = 350$ K for both reactor modes. We also suppose that the values of system states, T and C_A are available at each time.

The objective here is to regulate C_A and T over their nominal values by manipulating T_c under an arbitrary switching of the valve position. Note that only T can be measured variable. Let us select the state variables: $x := [C_A - C_A^*, T - T^*]$. The control input here is $u = T_c - T^*$. In order to rewrite the above original system in the form of (6) we put

$$\begin{aligned}
 f_{1i}(x) &= \frac{F_i}{V}(C_{Ai} - C_A^* - x_1) - a_0(x_1 + C_A^*) \exp\left(-\frac{E/R}{x_2 + T^*}\right) \\
 f_{2i}(x) &= \frac{F_i}{V}(T_i - T^* - x_2) - a_1(x_1 + C_A^*) \exp\left(-\frac{E/R}{x_2 + T^*}\right) \\
 &\quad + a_2(T_c^* - x_2 - T^*) \\
 A_i &= \begin{bmatrix} -\frac{F_i}{V} - a_0 C_e & -a_0 C_e C_A^* \frac{E/R}{(T^*)^2} \\ -a_1 C_e & -\frac{F_i}{V} - a_1 C_e C_A^* \frac{E/R}{(T^*)^2} - a_2 \end{bmatrix} \\
 B_i &= \begin{bmatrix} 0 \\ a_2 \end{bmatrix}, C_i = [0 \quad 1], C_e = \exp\left(-\frac{E/R}{T^*}\right)
 \end{aligned}$$

Let us now select

$$Q_{presc} = \begin{bmatrix} 10 & 0 & 0 & 0 \\ 0 & 25 & 0 & 0 \\ 0 & 0 & 250 & -250 \\ 0 & 0 & -250 & 500 \end{bmatrix}$$

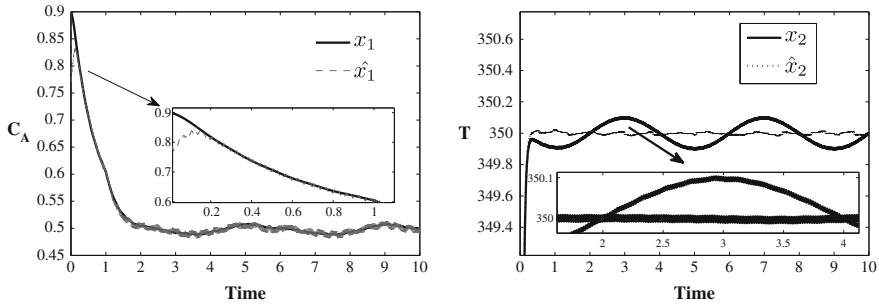


Fig. 2 Convergence behaviour of the estimated state variables

and solve the basic problem (11). Figure 2 shows the convergence of the real system state and estimated state variables (top figures): the convergence of C_A and T to the desired values.

Figure 3 includes the resulting attractive ellipsoids for the desired robust dynamics of the closed-loop system. The corresponding stabilizing input signal is depicted on Fig. 4.

The above graphics shows the dynamical behaviour of the given systems with the chosen initial condition

$$[C_A(t_0), T(t_0)] = [0.9, 340].$$

The gain matrices and the additional data are obtained as follows:

$$K_1 = [99.3088 \quad 11.7369],$$

$$K_2 = [99.6727 \quad 8.0830],$$

Fig. 3 The resulting attractive ellipsoid for the CSTR model

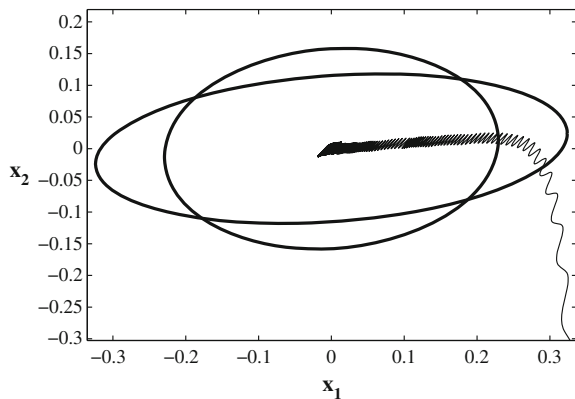
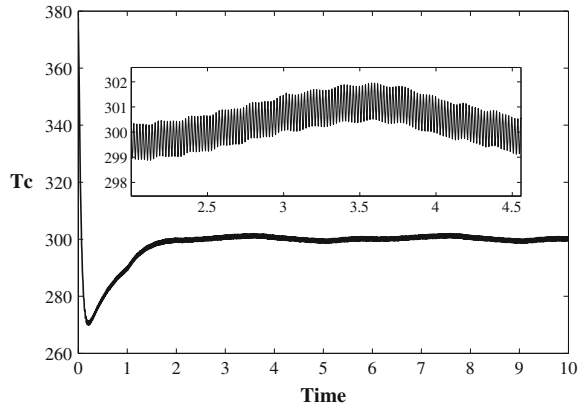


Fig. 4 Robust control input



and

$$L_1 = \begin{bmatrix} 191.3623 \\ 251.7547 \end{bmatrix}, L_2 = \begin{bmatrix} 200.4465 \\ 244.5836 \end{bmatrix}.$$

Moreover, we also obtain

$$P_1 = \begin{bmatrix} 5.106 & -2.880 & 0 & 0 \\ -2.880 & 38.447 & 0 & 0 \\ 0 & 0 & 522.798 & -309.919 \\ 0 & 0 & -309.919 & 409.301 \end{bmatrix},$$

$$P_2 = \begin{bmatrix} 9.832 & -1.195 & 0 & 0 \\ -1.195 & 20.648 & 0 & 0 \\ 0 & 0 & 444.401 & -260.797 \\ 0 & 0 & -260.797 & 377.356 \end{bmatrix},$$

and

$$\epsilon = 7.8, a_1 = 2.5023, a_2 = 3.0631.$$

5 Concluding Remarks

In this paper, we developed a robust control methodology for a wide class of nonlinear switched systems in the presence of bounded uncertainties. The control strategy we obtain constitutes a direct consequence of a specific extension of the invariant ellipsoid method (called Attractive Ellipsoid). The elaborated approach generates an observer based admissible linear feedback control law which

guarantees existence and a constructive characterization of a minimal size attractive ellipsoid for the closed-loop dynamic system. The computational results are carried out by considering a suitable dwell-time scheme for the admissible switching signal. We finally obtain an attractive ellipsoid with some minimal properties that can be interpreted (under the given Q_{prescr}) as a stability region of the closed-loop system.

The elaborated control design scheme is next applied to a formal abstraction of the fully automated Continuous Stirred Tank Reactor. The mathematical model of the CSTR extended by an adequate control scheme constitutes an important example of an industrial autonomous robotic system. The stability properties (in the practical sense) for the obtained closed-loop system realisation and the robust dynamics established in the computational model make it possible to implement the proposed control scheme in the real prototype of an industrial CSTR.

Finally note that the feedback-type control technology proposed in this paper can be easily applied to some alternative classes of industrial robots and automated processes and systems.

References

- Antsaklis, P. (2000). Special issue on hybrid systems: Theory and applications—a brief introduction to the theory and applications of hybrid systems. *Proceedings of IEEE*, 88, 879–887.
- Azhmyakov, V., Boltyanski, V., & Poznyak, A. (2008). Optimal control of impulsive hybrid systems. *Nonlinear Analysis: Hybrid Systems*, 2, 1089–1097.
- Azhmyakov, V., Galvan-Guerra, R., & Egerstedt, M. (2010). On the LQ-based optimization technique for impulsive hybrid control systems. In *Proceedings of the 2010 American Control Conference* (pp. 129–135), Baltimore, USA, 2010.
- Azhmyakov, V., Basin, M., & Reincke-Collon, C. (2014). Optimal LQ-type switched control design for a class of linear systems with piecewise constant inputs. In *Proceedings of the 19th IFAC World Congress* (pp. 6976–6981), Cape Town, South Africa.
- Azhmyakov, V. (2011). On the geometric aspects of the invariant ellipsoid method: Application to the robust control design. In *Proceedings of the 50th IEEE Conference on Decision and Control and European Control Conference* (pp. 1353–1358), Orlando, USA.
- Azhmyakov, V., Cabrera Martinez, J., & Poznyak, A. (2015). Optimization of a class of nonlinear switched systems with fixed-levels control inputs. In *Proceedings of the 2015 American Control Conference*, Chicago, USA, 2015.
- Barkhordari, Y. M., & Jahed-Motlagh, M. R. (2009). Stabilization of a CSTR with two arbitrarily switching modes using modal state feedback linearization. *Chemical Engineering Journal*, 155, 838–843.
- Blanchini, F., & Miani, S. (2008). *Set-theoretic methods in control*. Boston: Birkhäuser.
- Boskovic, J. D., & Mehra, R. K. (2000). Multi-mode switching in flight control. In *Proceedings of the 19th Digital Avionics Systems Conference* (Vol. 2, pp. 6F2/1–6F2/8).
- Branicky, M. S. (1998). Multiple Lyapunov functions and other analysis tools for switched and hybrid systems. *IEEE Transactions on Automatic Control*, 43, 475–482.
- Daafouz, J., Riedinger, P., & Lung, C. (2002). Stability analysis and control synthesis for switched systems: A switched Lyapunov function approach. *IEEE Transactions on Automatic Control*, 47, 1883–1887.

- Dahleh, M. A., & Pearson, J. B., Jr. (1988). Optimal rejection of persistent disturbances, robust stability and mixed sensitivity minimization. *IEEE Transactions on Automatic Control*, 33, 722–731.
- Davila, J., & Poznyak, A. (2011). Dynamic sliding mode control design using attracting ellipsoid method. *Automatica*, 47, 1467–1472.
- Doyle, J. C. (1983). Synthesis of robust controllers and filters. In *Proceedings of the 22nd Conference on Decision and Control* (Vol. 22, pp. 109–114).
- Duncan, G. J., & Schweppe, F. C. (1971). Control of linear dynamic systems with set constrained disturbances. *IEEE Transactions on Automatic Control*, 16, 411–423.
- DeCarlo, R. A., Branicky, M. S., Pettersen, S., & Lennartson, S. (2000). Perspectives and results on the stability and stabilizability of hybrid systems. *Proceedings of IEEE: Special Issue Hybrid Systems*, 88, 1069–1082.
- Egerstedt, M., Wardi, Y., & Axelsson, H. (2006). Transition-time optimization for switched-mode dynamical systems. *IEEE Transactions on Automatic Control*, 51, 110–115.
- Haddad, W., & Chellaboina, V. (2008). *Nonlinear Dynamics Systems and Control*. Princeton: Princeton University Press.
- Hespanha, J. P., Morse, A. S. (1999). Stability of switched systems with average dwell-time. In *Proceedings of the 38th IEEE Conference on Decision and Control* (pp. 2655–2660), Phoenix, USA.
- Khalil, H. (2002). *Nonlinear systems*. Upper Saddle River: Prentice Hall.
- Kouhi, Y., Bajcinca, N., Raisch, J., & Shorten, R. (2014). On the quadratic stability of switched linear systems associated with symmetric transfer function matrices. *Automatica*, 50, 2872–2879.
- Liberzon, D. (2003). *Switching in systems and control*. Boston: Birkhäuser.
- Lunze, J., & Lamnabhi-Lagarrigue, F. (2009). *Handbook of hybrid systems control: Theory, tools and applications*. New York: Cambridge University Press.
- Lygeros, J. (2003). *Lecture notes on hybrid systems*. Cambridge, UK: Cambridge University Press.
- Martinoli, A., Mondada, F., Mermoud, G., Correll, N., Egerstedt, M., Hsieh, A., et al. (Eds.). (2013). *Distributed autonomous robotic systems.*, Springer tracts in advanced robotics New York: Springer.
- Poznyak, A., Azhmyakov, V., & Mera, M. (2011). Practical output feedback stabilization for a class of continuous-time dynamic system under sample-data outputs. *International Journal of Control*, 84, 1408–1416.
- Poznyak, A., Polyakov, A., & Azhmyakov, V. (2014). *Attractive ellipsoid method in robust control*. New York: Birkhäuser.
- Sajja, S., Corless, M., Zeheb, E., & Shorten, R. (2013). Stability of a class of switched descriptor systems. In *Proceedings of the 2013 American Control Conference* (pp. 54–58), Washington DC, USA.
- Shaikh, M. S., & Caines, P. E. (2007). On the hybrid optimal control problem: Theory and algorithms. *IEEE Transactions on Automatic Control*, 52, 1587–1603.
- Shucker, B., Murphey, T., & Bennett, J. K. (2007). Switching rules for decentralized control with simple control laws. In *Proceedings of the 2007 American Control Conference* (pp. 1485–1492), New York, USA.
- Wicks, M. A., Peleties, P., & DeCarlo, R. A. (1994). Construction of piecewise Lyapunov functions for stabilizing switched systems. In *Proceedings of the 33rd Conference on Decision and Control* (pp. 3492–3497), Lake Buena Vista, USA.
- Zhai, G. S., Hu, B., Yasuda, K., & Michel, A. N. (2001). Disturbance attenuation properties of time-controlled switched systems. *Journal of the Franklin Institute*, 338, 765–779.

A Three Finger Tendon Driven Robotic Hand Design and Its Kinematics Model

I.A. Sainul, Sankha Deb and A.K. Deb

Abstract Anatomy of human hand is very complex in nature. The structure of human hand consists of number of joints, bones, muscles and tendons, which creates a wide range of movements. It is very difficult to design a robotic hand and incorporate all the features of a normal human hand. In this paper, the model of a three finger robotic hand has been proposed. To replace the muscles and tendons of real human hand, it is proposed to use tendon wire and place the actuator at the palm. The advantage of using tendon and placing actuator at remote location is that it actually reduces the size of the hand. Pulling the tendon wire produces flexor motion in the hand finger. Currently torsional spring is considered at the joint for the extension motion of the finger. The purpose of design of such a hand is to grasp different kinds of object shapes. The paper further presents a kinematics model of the three finger hand and a mapping function to map the joint space coordinates to tendon space coordinates. Finally the hand model is simulated to validate the kinematics equations.

Keywords Multi-finger hand • Robotic gripper • Tendon-driven mechanism • Kinematics model

I.A. Sainul
Advanced Technology Development Centre, IIT Kharagpur,
Kharagpur 721302, India
e-mail: sainul.uit@gmail.com

S. Deb (✉)
Mechanical Engineering Department, IIT Kharagpur,
Kharagpur 721302, India
e-mail: sankha.deb@mech.iitkgp.ernet.in

A.K. Deb
Electrical Engineering Department, IIT Kharagpur,
Kharagpur 721302, India
e-mail: alokkanti@ee.iitkgp.ernet.in

1 Introduction

The structure of a real human hand comprises of bones, muscles, tendons, joints, and nervous system. Anatomical study of human hand shows that it is a very complex system and hence challenging to model in practice. An et al. (1979) proposed an accurate human hand model by studying the human hand anatomical structure. However, from the perspective of robotics, we do not need an exact human hand model, but a working model that is simple and can be realized in actual hardware. Leijnse and Kalkar (1995) proposed a simple human hand model with some limitations. Valero-Cuevas et al. (2007) came up with finger extensor mechanism by simulating human musculo-skeletal structure. After years of research, the researchers around the world succeeded in coming up with a simple model which does not fully mimic the real one but to some extent exhibits the real hand functions. Shirafuji et al. (2014) developed a tendon driven anthropomorphic hand shown in Fig. 1a based on the finger model given by Leijnse and Kalkar. In their work, they derived a mathematical model based on Leijnse's simple model. In order to remove the limitations of Leijnse's model, they reconstructed the model by rearranging the mathematical equations and they validated the model on 3D printed prototype. Matei Ciocariie et al. (2014) developed a two finger under-actuated gripper shown in Fig. 1b. They designed the gripper by investigating the human hand motion for stable grasps of various object shapes. The gripper uses one motor to drive the active tendon, passive tendon wire and torsional spring to extend the finger, and a four bar mechanism for parallel grasps of small objects. Tetsuya Mouri et al. (2002) developed a multi-finger hand called Gifu hand shown in Fig. 1c. Gifu Hand 3 is an improved version of Gifu Hand 2 in terms of backlash transmission and fingertips mobility in space and with these modifications it has higher dexterity. A group of researchers from University of Bologna (Palli 2006) have simplified the complexity of the mechanical design and developed a prototype of tendon-based articulated hand shown in Fig. 1d. A four finger tendon driven robotic hand was developed by a group researchers in Jadavpur University (Pal 2003; Pal et al. 2008) as shown in Fig. 1e.

This paper presents our ongoing research work at IIT Kharagpur on designing and developing a tendon driven multi-finger robotic hand.

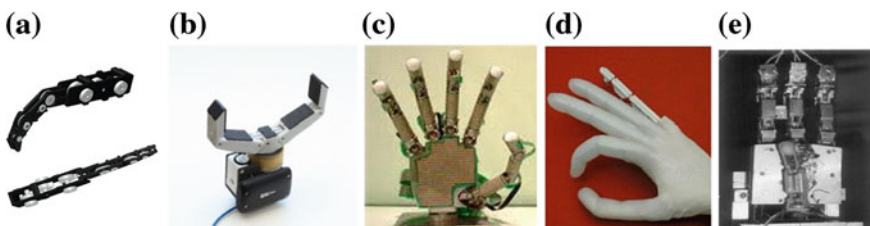


Fig. 1 a Robotic hand by Shirafuji et al. (2014) b velo gripper c Gifu 3 d UB hand e JU hand

2 Proposed Design of the Tendon Driven Robotic Hand

Figure 2 gives a comparison between the human hand finger anatomical structure and the proposed robotic finger design. With the exception of the thumb, human fingers are mainly controlled by five types of muscles. These are Flexor Digitorum Profundus (FDP), Flexor Digitorum Superficialis (FDS), Extensor Digitorum Communis (EC), Interosseous (IN) and Lumbrical (LU). All the fingers except thumb have three joints called the Metacarpophalangeal (MP) joint, the Proximal Interphalangeal (PIP) joint and the Distal Interphalangeal (DIP) joint. The PIP and DIP joints are collectively called IP joints (Shirafuji et al. 2014).

After analyzing the human hand finger anatomical structure, it is found that the EC, IN, and LU muscles collectively control the extensor motion, and FDS and FDP control the flexor motion. Five tendons originating from those five muscles run straight to the different phalanges as shown in Fig. 2a. The simplified finger model proposed by us has used only two tendons namely, Flexor Tendon and Extensor Tendon to execute the flexion and extension motions respectively. The Metacarpophalangeal (MP) joint and Distal Interphalangeal (DIP) joint have been considered to simplify the finger model as shown in Fig. 2b.

The mechanical structure of the proposed hand comprises of a palm and three identical fingers. Actuation mechanism is embedded into the knuckle and the motion is transferred to the finger via tendon driven mechanism. Instead of considering five fingers, the proposed design of the hand uses only three fingers in order to reduce the number of actuators, as otherwise increase in number of actuators will not only make the design bulky but the control scheme will also become more complex. A 3D CAD model of the proposed hand is shown in Fig. 3.

The mechanical design of each finger is made similar so that, the mathematical model of the hand is easier. Considering the finger model as shown in Fig. 4, each finger consists of three links namely, knuckle, middle phalange, and distal phalange. A pulley at each joint is used for joining the knuckle-middle phalange and the middle-distal phalange. The choice of the pulley radius is important because it decides the essential torque that needs to be generated at the joint. A tendon wire passes over the pulleys via some routing points inside the finger. This model considers routing point instead of using idle pulley which makes the model simple but may result in increase in friction force acting on tendon. The tendon path and actuation system are also shown.

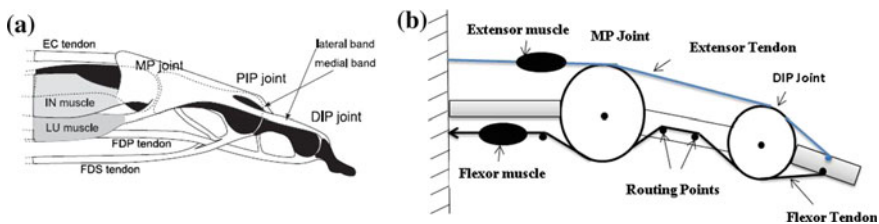


Fig. 2 a Human hand finger anatomical structure b simplified proposed robotic finger model

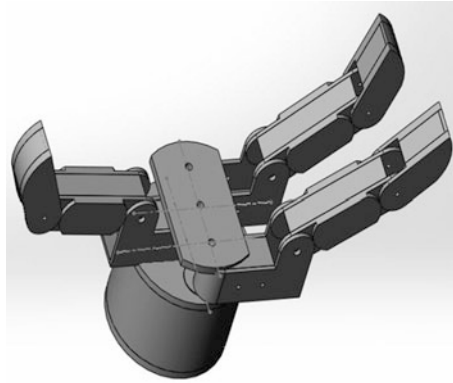


Fig. 3 CAD model of the proposed hand

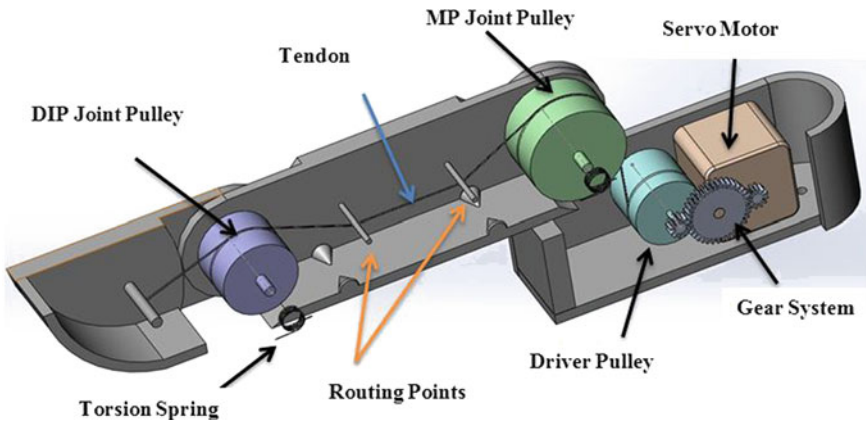


Fig. 4 Tendon and pulley arrangement

It is further proposed to place one servo motor and gear system within the palm for controlling the spread between the two fingers sideways. The fingers spread together as only one motor is proposed to be used.

3 Kinematic Model of the Proposed Hand

The hand has a total of 8DOF's that represent the joints. There are two types of finger configurations to describe the fingers with 2DOF's and 3DOF's and two separate kinematics models to describe the finger configuration. Tendons provide flexor and extensor motions for opening and closing the finger respectively. The

fingers can be spread sideways to reconfigure the finger position to have greater dexterity of the hand. Forward kinematics gives the finger-tip position and orientation in 3D Cartesian coordinate system based on finger joint angle displacement. Inverse kinematics gives the joint angle to reach a certain fingertip position with a certain orientation. A reference frame is attached to every joint to obtain the kinematics equation, joint denoted by J_{ij} , where i and j represent the finger number and joint number respectively.

3.1 Forward and Inverse Kinematics Solutions

Based on the finger model shown in Fig. 5 the forward kinematics equation is as follows:

$$x = \sin \theta_1(l_1 + l_2 \cos(\theta_2) + l_3 \cos(\theta_2 + \theta_3)) \tag{1}$$

$$y = l_2 \sin(\theta_2) + l_3 \sin(\theta_2 + \theta_3) \tag{2}$$

$$z = \cos \theta_1(l_1 + l_2 \cos(\theta_2) + l_3 \cos(\theta_2 + \theta_3)) \tag{3}$$

By using the forward kinematics Eqs. (1), (2), and (3), the inverse kinematics solution is as follows.

$$\theta_1 = \arctan 2(x, z) \tag{4}$$

$$\theta_3 = \arctan 2(s_3, c_3) \tag{5}$$

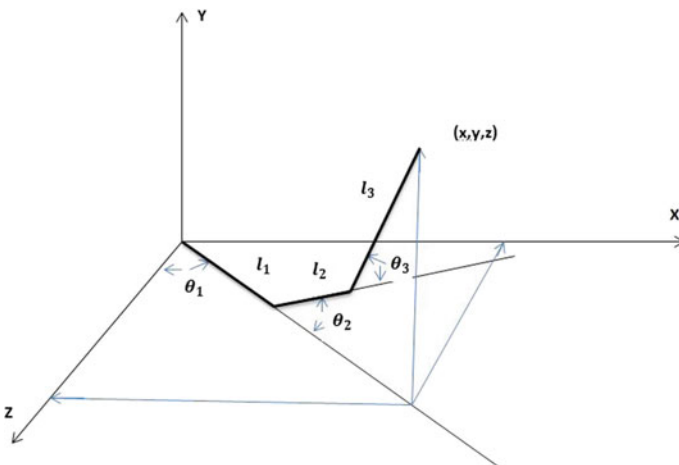


Fig. 5 Kinematics model of the finger

$$\theta_2 = \arctan 2 \left(\pm \sqrt{(x - l_1 \sin \theta_1)^2 + (z - l_1 \cos \theta_1)^2}, y \right) - \arctan 2(k_2, k_1) \quad (6)$$

where,

$$c_3 = \frac{(x - l_1 \sin \theta_1)^2 + y^2 + (z - l_1 \cos \theta_1)^2 - l_2^2 - l_3^2}{2l_1 l_2} \quad \text{and} \quad s_3 = \sqrt{1 - c_3^2}$$

$$k_1 = l_2 + l_3 c_3 \quad \text{and} \quad k_2 = l_3 s_3$$

3.2 Joint Space to Tendon Space Mapping

In this section a mapping function is formulated to calculate the required tendon displacement based on the joint displacement obtained by inverse kinematics. Pulleys with radii r_1 and r_2 where $r_1 > r_2$, and the tendon arrangement are shown in Fig. 6. Points P_0, P_1, P_2 , and P_3 are the routing points which guide the tendon wire. $\theta_{1 \max}, \theta_{2 \max}$ are the maximum joint angles for which the tendon keeps contact with the pulleys.

Maximum joint angle for which the tendon keeps contact with the pulley can be calculated from geometry as

$$\theta_{1 \max} = \varphi + \left[\pi - \arctan \left(\frac{b^2 - r_1^2}{r_1} \right) - \operatorname{atan} \left(\frac{d_1^2 - r_1^2}{r_1} \right) \right] \quad (7)$$

$$\theta_{2 \max} = \left[\pi - \arctan \left(\frac{d_3^2 - r_1^2}{r_1} \right) - \operatorname{atan} \left(\frac{d_4^2 - r_1^2}{r_1} \right) \right] \quad (8)$$

where, $\varphi = \arctan \left(\frac{t}{d_0} \right)$ and $b = \sqrt{t^2 + d_0^2}$

Total length of the tendon for finger open configuration is

$$L = \sqrt{b^2 - r_1^2} + r_1 \theta_{1 \max} + \sqrt{d_1^2 - r_1^2} + d_2 + \sqrt{d_3^2 - r_2^2} + r_2 \theta_{2 \max} + \sqrt{d_4^2 - r_2^2} \quad (9)$$

Now the tendon displacements for joint angle, θ_1 and θ_2 are as follows.

For $\theta_1 \leq \theta_{1 \max}$ and $\theta_2 \leq \theta_{2 \max}$, the tendon displacement is

$$dL = r_1 \theta_1 + r_2 \theta_2 \quad (10)$$

and for $\theta_1 > \theta_{1 \max}$ or $\theta_2 > \theta_{2 \max}$, tendon displacement is

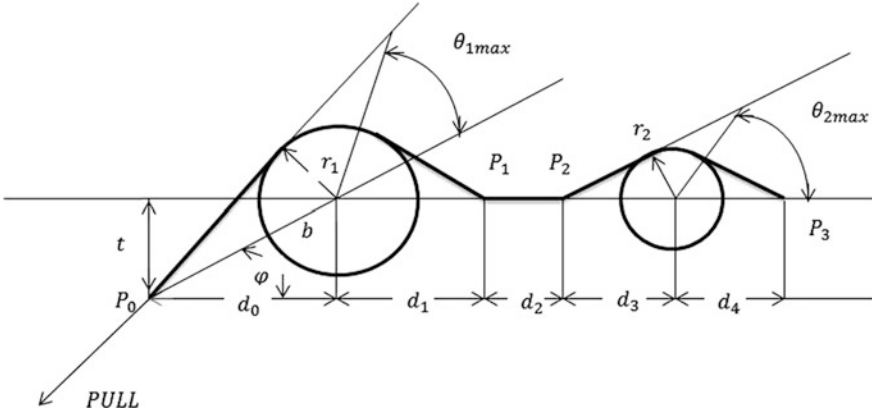


Fig. 6 Pulley and Tendon arrangement

$$\begin{aligned}
 dL = & r_1\theta_{1\max} + r_2\theta_{2\max} + (\sqrt{b^2 - r_1^2} + \sqrt{d_1^2 - r_1^2} \\
 & - \sqrt{(b + d_1 \cos \theta_1)^2 + (d_1 \sin \theta_1)^2}) + (\sqrt{d_3^2 - r_2^2} + \sqrt{d_4^2 - r_2^2} \\
 & - \sqrt{(d_3 + d_4 \cos \theta_2)^2 + (d_4 \sin \theta_2)^2})
 \end{aligned} \tag{11}$$

4 Illustrative Example: Results and Discussions

We have simulated the proposed three finger hand model in robotics simulation software Webots (Cyberbotics Ltd 2011). A CAD model of the proposed hand has been created with the dimensions given in Table 1. All the kinematics equations have been implemented on the simulation model. To validate the model, two objects have been considered: a cylindrical object with radius 40 mm and height 80 mm, and a sphere of radius 40 mm, and the fingertip positions in Cartesian coordinates were found out. Using the fingertip positions data, the inverse kinematics and tendon space mapping function give the tendon displacements. Results obtained by running the simulation are shown in Tables 2 and 3, and in Fig. 7.

Table 1 Dimensions of the finger

Parameter	l_1	l_2	l_3	r_1	r_2	d_0	d_1	d_2	d_3	d_4	t
Value (in mm)	40	60	40	9	7	9	20	20	20	20	20

Table 2 Results of Inverse kinematics and tendon space mapping function for spherical object

	(x, y, z) (in mm)	($\theta_1, \theta_2, \theta_3$) (in rad)	Tendon displacement (d) (in mm)
Fingertip 1	-40, 80, 0	0, 1.06544, 1.31812	20.4422
Fingertip 2	20, 80, -341	0.579882, 1.28341, 1.26196	21.7287
Fingertip 3	20, 80, 341	-0.579882, 1.28341, 1.26196	21.7287

Table 3 Results of Inverse kinematics and tendon space mapping function for cylindrical object

	(x, y, z) (in mm)	($\theta_1, \theta_2, \theta_3$) (in rad)	Tendon displacement (d) (in mm)
Fingertip 1	-40, 80, 0	0, 1.06544, 1.31812	20.4422
Fingertip 2	40, 80, -20	0, 1.06544, 1.31812	20.4422
Fingertip 3	40, 80, 20	0, 1.06544, 1.31812	20.4422

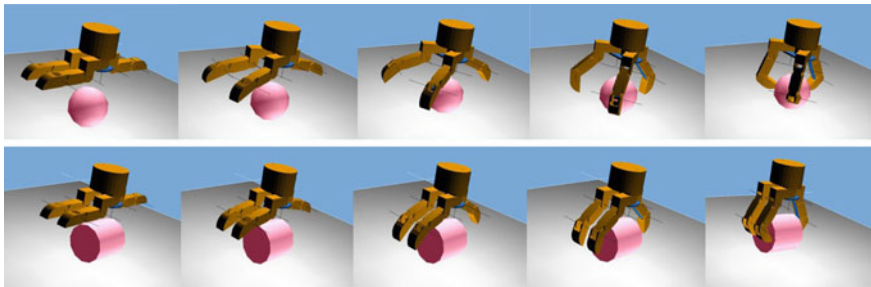


Fig. 7 Simulation results of the hand grasping spherical and cylindrical objects

5 Conclusions

In this paper, we proposed a three finger tendon driven robotic hand for handling different kinds of object shapes. The flexor motion in the hand finger is proposed to be accomplished by pulling the tendon wire and for the extension motion of the finger torsional spring is considered. The paper also presents a kinematic model of the hand and a mapping function to map the joint space coordinates to tendon space displacements. Finally the hand model is simulated to validate the kinematics equations for typical object shapes. Research work is in progress for optimizing the dimensions of the hand model and further to develop a working prototype of the proposed hand.

References

An, K., Chao, E., Cooney, W, I. I. I., & Linscheid, R. (1979). Normative model of human hand for biomechanical analysis. *Journal of Biomechanics*, 12(10), 775–788.
 Cyberbotics Ltd. (2011). Webots Reference Manual, <http://www.cyberbotics.com/reference/>.

- Ciocarlie, M., Hicks, F. M., Holmberg, R., Hawke, J., Schlicht, M., Gee, J., Stanford, S., & Bahadur, R. (2014). The Velo gripper: A versatile single-actuator design for enveloping, parallel and fingertip grasps. *The International Journal of Robotics Research*, 33, 753.
- Leijnse, J., & Kalker, J. (1995). A two-dimensional kinematic model of the lumbrical in the human finger. *Journal of Biomechanics*, 28(3), 237–249.
- Mouri, T., Kawasaki, H., Yoshikawa, K., Takai, J., & Ito, S. (2002). Anthropomorphic Robot Hand: Gifu Hand III, The ICCAS 2002, October 16–19, Muju Resort, Jeonbuk, Korea.
- Pal, S. (2003) *Design and Development of a Dexterous Instrumented Robot Gripper*. Doctoral Thesis, Department of Production Engineering, Jadavpur University.
- Pal, S., Chattopadhyay, S., & Deb, S. R. (2008). Design and development of a multi-degree of freedom dexterous instrumented Robot Gripper. *Sensors and Transducers Journal*, 87(1), 63–73.
- Palli, G. (2006). *Model and control of tendon actuated robots*. Doctoral Thesis, Department of Electronic Computer Science and Systems, University of Bologna.
- Shirafuji, S., Ikemoto, S., & Hosoda, K. (2014). Development of a tendon-driven robotic finger for an anthropomorphic robotic hand. *The International Journal of Robotics Research*, 33, 677.
- Valero-Cuevas, F., Yi, J., & Brown, D. (2007). The tendon network of the fingers performs anatomical computation at a macroscopic scale. *IEEE Transactions on Biomedical Engineering*, 54(6), 1161–1166.

An Intelligent Methodology for Assembly Tools Selection and Assembly Sequence Optimisation

Atul Mishra and Sankha Deb

Abstract In the present paper, an intelligent methodology has been used for assembly tool/gripper selection and determination of the optimal assembly sequence. Since it is well known that assembly sequence planning (ASP) is an NP-hard combinatorial optimization problem, in particular, with increase in number of components in the assembly, the computational complexity involved in searching for the optimal assembly sequence in such a large solution space also increases. Furthermore, assembly process planning, tool/gripper selection is also an important decision making task and becomes tedious and time consuming for an assembly with large number of components. Keeping the above in mind, in the present work, a knowledge based system has been developed for selection of assembly tools and grippers for performing the assembly, while a Genetic Algorithm (GA) based approach has been used to determine the feasible and optimal assembly sequences considering minimum number of tool changes and assembly direction changes.

Keywords Assembly sequence planning · Knowledge-based system · Tool selection · Optimisation · Genetic algorithm

1 Introduction

Assembly sequence planning is concerned with determination of sequence of assembly operations to assemble the components into the final product. It can not only improve the quality and efficiency of assembly, but can also reduce the product development cycle and cost (Yin et al. 2003). However, there are various constraints that can drive the choice of a feasible assembly sequence. Moreover, with increase in the number of components of which the product is made, the number of

A. Mishra · S. Deb (✉)

Mechanical Engineering Department, IIT Kharagpur, Kharagpur 721302, India
e-mail: sankha.deb@mech.iitkgp.ernet.in

A. Mishra
e-mail: atulmishra.chdi@gmail.com

feasible assembly sequences possible also increases considerably and the task of manually determining the optimal assembly plan becomes laborious and time consuming. To automate this task, numerous approaches have been discussed in the open literature. They include use of mathematical algorithms (Gottipolu and Ghosh 2003), graph theoretic approaches (Laperriere and ElMaraghy 1994), as well as with the advent of Artificial Intelligence (AI) techniques various approaches like expert system, fuzzy logic and evolutionary soft computing based optimization techniques (Rashid et al. 2011) which include GA (Chen et al. 2001) and swarm intelligence based approaches (Tseng et al. 2011; Youhui et al. 2012), etc. Zha et al. (1999) developed an expert system for concurrent product design and assembly planning including generation of assembly sequences as well as tool and gripper selection. Barnes et al. (2004) also proposed a knowledge based approach for selection of base part and generation of assembly sequence. Dong et al. (2007) used a knowledge based approach for generation of assembly sequences with the use of reasoning based on geometric and non-geometric knowledge about connection types. Hsu et al. (2011) also used a knowledge-based system with an embedded neural network engine to predict a near-optimal feasible assembly sequence in accordance with geometric constraints and precedence relations of the parts to be assembled represented using an APD tree. Li and Tian (2013) generated all the feasible sequences by using a knowledge-based petri net system. GA has been used by some researchers for assembly sequence optimisation. Chen et al. (2001) proposed an adaptive GA (where genetic-operator probabilities vary according to certain rules) for efficiently finding global-optimal or near-optimal assembly sequences. Choi et al. (2009) proposed the optimisation of assembly sequences using GA in which precedence preservative crossover and swap mutation have been used. Tseng et al. (2010) presented an integrated assembly and disassembly planning optimisation using GA approach where assembly precedence graph has been used to transform into a precedence matrix. In the present paper, an intelligent assembly process planning methodology based on GA has been developed to automatically generate feasible and optimal assembly sequences subject to various assembly precedence constraints based on minimization of number of orientation changes of the assembly and tool changes. Furthermore, a knowledge-based system has been also developed for automatic tool/gripper selection, which is used as input to the above GA program to calculate number of tool changes.

2 Proposed Methodology for Assembly Sequence Planning

2.1 Knowledge-Based System for Selection of Tools and Grippers

A knowledge-based system has been used to select the tools and grippers for performing the assembly. A database has been developed to store all the information about assembly tools and grippers available in the shop floor. It includes

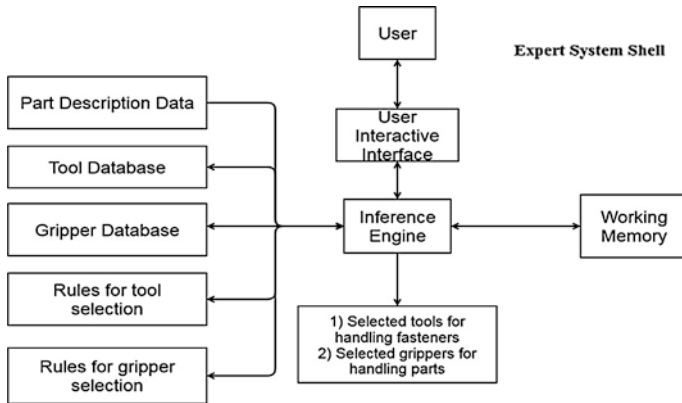


Fig. 1 Architecture of the developed knowledge-based system

```
(deftemplate MAIN::tool_available
  (slot assembly_type (type SYMBOL) (allowed-symbols manual robotic))
  (slot actuation_type (type SYMBOL) (allowed-symbols manual automatic))
  (slot number (type INTEGER)) (slot name (type SYMBOL))
  (slot type (type SYMBOL) (allowed-symbols slotted_screw_driver philips_screw_driver
    _press glue_gun))
  (slot size_1 (type NUMBER)) (slot size_2 (type NUMBER))
  (slot min_torque (type NUMBER) (default 0)) (slot max_torque (type NUMBER) (default 0))
  (slot max_load (type INTEGER) (default 0)) (slot cont_load (type INTEGER) (default 0))
  (deftemplate MAIN::tool_selected
    (slot assembly_type (type SYMBOL) (allowed-symbols manual robotic))
    (slot actuation_type (type SYMBOL) (allowed-symbols manual automatic))
    (slot number (type INTEGER)) (slot name (type SYMBOL))
    (slot type (type SYMBOL) (allowed-symbols slotted_screw_driver philips_screw_driver
      _press glue_gun)) (slot for_fastener (type SYMBOL))
    (slot size_1 (type NUMBER)) (slot size_2 (type NUMBER))
    (slot min_torque (type NUMBER) (default 0)) (slot max_torque (type NUMBER) (default 0))
    (slot max_load (type INTEGER) (default 0)) (slot cont_load (type INTEGER) (default 0))
    (slot fastening_time (type NUMBER))
```

Fig. 2 Templates for entering the available and selected tool data in databases

type of assembly (manual or robotic), actuation type (manual or automated, the type of assembly tool, sizes etc. in case of the assembly tool, and the gripper, name, shape handling capability, maximum opening, gripping force, actuation type, adaptability, number of fingers and type of tip, etc. in case of the gripper. Assembly tools include tools for manual and robotic assembly, actuation types of manual and automatic, slotted, and Phillips screwdrivers, Allen keys, open end wrenches, adjustable wrenches, etc. Figure 1 shows the architecture of the developed knowledge-based system implemented in CLIPS expert system shell. Figures 2 and 3 respectively show the templates for entering the data on available and selected tools in the databases and the tool data entered in the databases following the above templates.

As per availability of tools, a set of knowledge based rules are used to select the tools along with their fastening times based on the selected assembly method i.e. manual or robotic assembly and fastener’s characteristics viz. size, type and torque required. The fastening times are evaluated based on the part design features such as accessibility of assembly location, ease of operation of assembly tool, visibility of assembly location, ease of alignment and positioning during assembly, etc. (Design for assembly user guide 2009). Figure 4 shows an example of a knowledge-based rule for selection of tools. In the same way, a set of knowledge based rules are used to select the grippers for handling the components on the basis of part mass, its enveloping shape and size, and gripper’s shape handling capability, maximum opening, gripping force, etc. The user provides detailed information about the assembly which consists of part types (i.e. functional part or fastener), mass,

```

:fact_list 2
(defacts MAIN::tool_data
(tool_available (assembly_type manual)(actuation_type manual)(number 1)(name slotted_screw_driver1)(type slotted_screw_driver)(size_1 0.6)(size_2 0.4))
....
(tool_available (assembly_type manual)(actuation_type manual)(number 16)(name allen_key1)(type allen_key)(size_1 1.5))
....
(tool_available (assembly_type manual)(actuation_type manual)(number 41)(name open_end_wrench1)(type open_end_wrench)(size_1 6))
....
(tool_available (assembly_type manual)(actuation_type manual)(number 66)(name adjustable_wrench1)(type adjustable_wrench)(size_1 13))
....
(tool_available (assembly_type manual)(actuation_type automatic)(number 81)(name slotted_screw_driver1)(type slotted_screw_driver)(size_1 0.6)
(size_2 0.4)(min_torque 0.05)(max_torque 0.3))
.....)

```

Fig. 3 Tool data entered in the databases

```

(defrule MAIN::tool_selection_1
(or
(component (number 7a) (component_type fastener)(name 7c)(type screw) (specification 7s) (head_type $? slotted $?) (head_size_1 7f) (head_size_2 7h) (torque_required 7t)
(part_insertion_property added_and_secured(part_tool_reachability easy) (obstructed_access no) (restricted_vision no) (aligning_positioning difficult) (torsional_resistance no))
(component (number 7a) (component_type fastener)(name 7c)(type screw) (specification 7s) (head_type $? slotted $?) (head_size_1 7f) (head_size_2 7h) (torque_required 7t)
(part_insertion_property added_and_secured(part_tool_reachability easy) (obstructed_access no) (restricted_vision no) (aligning_positioning easy) (torsional_resistance yes))
....)
(or(tool_available (assembly_type 7a)(actuation_type 7a5)(number 7a) (name 7d) (type slotted_screw_driver) (size_1 7e)(size_2 7g))
and(tool_available (assembly_type 7a)(actuation_type 7a5)(number 7a) (name 7d) (type slotted_screw_driver)(size_1 7e)(size_2 7g)(min_torque 7m)(max_torque 7maxt))
(test (< 7t 7maxt))(test (> 7t 7mint)))(test (= 7f 7e))(test (= 7h 7g))
no
(assert(tool_selected(assembly_type 7a)(actuation_type 7a5)(number 7a) (name 7d) (type slotted_screw_driver)(for_fastener 7a)(size_1 7e)(size_2 7g)(fastening_time 8)))
)

```

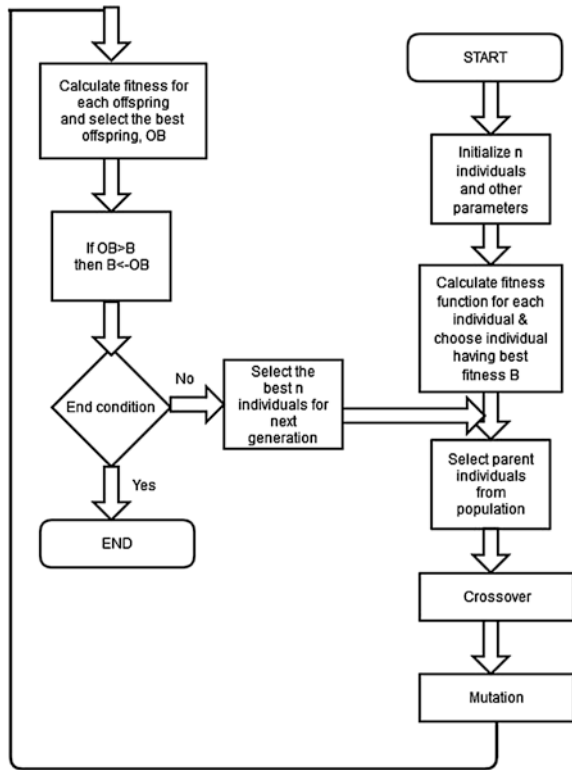
Fig. 4 A sample rule for selecting the assembly tools

material, enveloping shape, dimensions, their contacts with other parts and contact directions in case of functional parts and head size, torque required, thread numbers, fit size, repeat counts, joined components and the other parameters like hole type, presence of chamfer, alpha and beta symmetry in case of fasteners. The developed knowledge based expert system is then used for selection of tools and grippers to be used in performing the assembly. Next the developed GA based optimization approach discussed in the following section is used to determine a feasible and optimal assembly sequence by minimizing the number of tool changes as well as direction changes.

2.2 Genetic Algorithm Based Approach for Assembly Sequence Optimisation

A GA based optimisation approach has been used to determine the feasible and optimal assembly sequences and implemented using MATLAB. The very first step in GA is to generate the initial population which is generated randomly, but since there can be both feasible and infeasible solutions, the infeasible solutions are avoided using a precedence matrix (number of rows and columns equal to number of parts) which consists of the values 0 and 1 to indicate whether the part possess any precedence or not with other parts. The feasible initial population is evaluated using the fitness function which is composed of number of direction orientation changes and tool/gripper changes and feasibility of the sequence. Figure 5 shows the flowchart of the implemented GA.

Fig. 5 Flowchart of the implemented GA



Selection

Roulette wheel selection has been applied for selecting the solutions which go into the mating pool. The principle behind it is that first using the fitness function, all the solutions are evaluated, and then according to their fitness values the ranges are created. Random numbers (the number of random numbers is equal to the population size) are generated and then the range, in which they fall in, is found out. Those solutions are inserted into the mating pool on which crossover operation is performed.

Crossover

The partially matched crossover (PMX) has been used here. In PMX crossover, it builds an offspring by choosing a subsequence of a solution from one parent and preserving the order and positions of as many genes as possible from the other parent. A subsequence is selected by choosing two random points, which serve as boundaries for the swapping operations. But in ASP problem, no parts in the

assembly sequence can be repeated, which is taken care of by the above crossover operator.

Mutation

The swap mutation has been used here. In case of swap mutation, the genes are swapped randomly inside a solution.

Fitness Function

A fitness function has been built which comprises of mainly, number of orientation changes and tool/gripper changes. Solutions with lower fitness value possess high chance of survival as the objective of this work is to minimize the assembly time and cost, which are affected by the number of direction changes and number of tools/gripper changes. Hence the function is chosen so as to convert it into a maximization problem. The initial population (feasible population) is generated randomly. To avoid generating the infeasible population, after crossover and mutation the fitness function is also equipped with a feasibility index. During the solutions' evaluation, if they are found infeasible, a definite value (i.e. penalty) is deducted from the fitness function. Since, for the next generation, only the better solutions are picked up the algorithm gradually starts giving only feasible solutions. The Eq. (1) shows overall fitness function (FF) which has been used in the present work. Symbol w_x and w_y in the Eq. (1) are the weightages which are to be set by the user.

$$FF = 1 / (w_x * \text{number of direction changes} + w_y * \text{number of tools changes} - \text{penalty}) \quad (1)$$

3 Illustrative Example

A motor drive assembly (Design for assembly user guide 2009) with a total 12 parts has been considered as an illustrative example for showing the working of knowledge based expert system and the developed GA based optimization approach. Figure 6 shows the assembly with all its parts. The parts of the assembly have been classified according to whether they are functional parts or fasteners. There are 7 functional parts and 5 different fasteners (like screws, standoffs, and grommet) in the final assembly. The different fasteners include, there are motor screws of specification M5 and head type slotted with head sizes 0.6 and 0.4 mm, set screw of specification M1.5 and head type hexagonal slot with head size 1.5 mm, end plate screw slotted screws, Phillips cover screws, bolts (standoffs) and

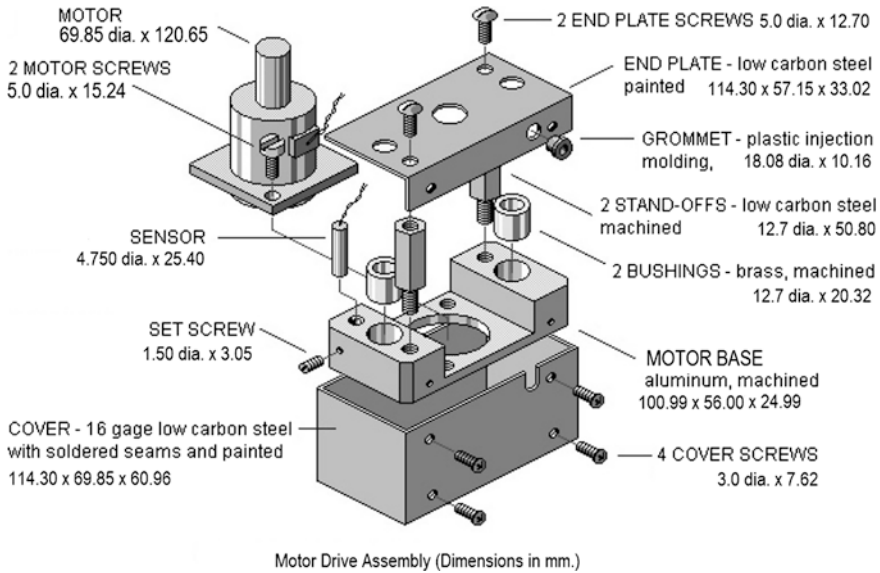


Fig. 6 A motor drive assembly (Design for assembly user guide 2009)

one grommet. All the data facts about the above components have been entered following the template format and loaded onto CLIPS environment. Next, the set of knowledge base rules for selection of assembly tools and grippers are loaded onto CLIPS and the program is executed. On execution of the program, the knowledge-based system automatically selects all the tools and grippers to be used in performing the assembly. For generating a feasible and optimal assembly sequence by using the GA based optimization approach, the user has to additionally input the directions in which the parts need to be assembled, the base component and the precedence matrix containing the information about precedence relationships among the parts shown in Table 1. These inputs are in addition to the tools and grippers information obtained from the output of the knowledge based system. Using the above input data, the developed GA program automatically generates a feasible and optimal assembly sequence.

4 Results and Discussions

The results of the developed knowledge based system and the GA program have been shown in the Tables 2 and 3 respectively. In Table 2, part numbers, their names, the assembly tool or gripper that has been selected automatically by the knowledge based system have been shown, along with the fastening time of

Table 1 Precedence matrix for motor drive assembly

	1	2	3	4	5	6	7	8	9	10	11	12
1	0	0	0	0	0	0	0	0	0	0	0	0
2	1	0	0	0	0	0	0	0	0	0	0	0
3	1	0	0	0	0	0	0	0	0	0	0	0
4	1	1	1	0	1	0	1	1	0	0	1	0
5	1	0	0	0	0	0	0	0	0	0	0	0
6	1	1	1	1	1	0	1	1	1	0	1	1
7	1	0	1	0	0	0	0	0	0	0	0	0
8	1	0	0	0	1	0	0	0	0	0	0	0
9	1	1	1	1	1	0	1	1	0	0	1	0
10	1	1	1	1	1	1	1	1	1	0	1	1
11	1	0	0	0	0	0	0	0	0	0	0	0
12	1	1	1	1	1	0	1	1	1	0	1	0
Assembly directions	-z	-z	-z	-z	-z	+z	-z	+x	-z	-y	-z	-z

Table 2 Summary of results of the knowledge based system showing selected grippers and assembly tools

Part no.	Part name	Tool/Gripper name	Fastening time (s)
1	Motor base	2-finger adaptive gripper, 2-finger parallel gripper, 3-finger adaptive gripper	–
2	Bushing_1	2-finger parallel gripper, 2-finger adaptive gripper, 3-finger adaptive gripper	–
3	Motor	2-finger adaptive gripper, 2-finger parallel gripper, 3-finger adaptive gripper	–
4	End plate	2-finger adaptive gripper, 2-finger parallel gripper, 3-finger adaptive gripper	–
5	Sensor	2-finger adaptive gripper, 2-finger parallel gripper, 3-finger adaptive gripper	–
6	Cover	2-finger adaptive gripper, 2-finger parallel gripper, 3-finger adaptive gripper	–
7	Motor screw_1	Slotted screw driver	12
8	Set screw	Allen key	5
9	End plate screw_1	Slotted screw driver	8
10	Cover screw_1	Philips screw driver	10.5
11	Stand off_1	Open end wrench adjustable wrench	–
12	grommet	Hammer	12

assembly fasteners. The system is capable of selecting more than one tool/gripper, if more than one tool/gripper is found suitable. Figure 7 shows the convergence graph of GA, showing the average and current fitness values. For the GA, in case there are multiple feasible assembly sequences with least number of direction changes and

Table 3 Summary of results of the GA program showing a feasible and optimal assembly sequence

GA crossover and mutation probabilities	0.90 and 0.05
Termination criteria used for GA	Number of predetermined iterations
Optimal assembly sequence	(1 2 3 7 11 5 8 4 9 12 6 10)
Number of orientation changes	4
Number of tool changes	9
Fitness function value	0.2222 (assuming $w_x = w_y = 0.5$)

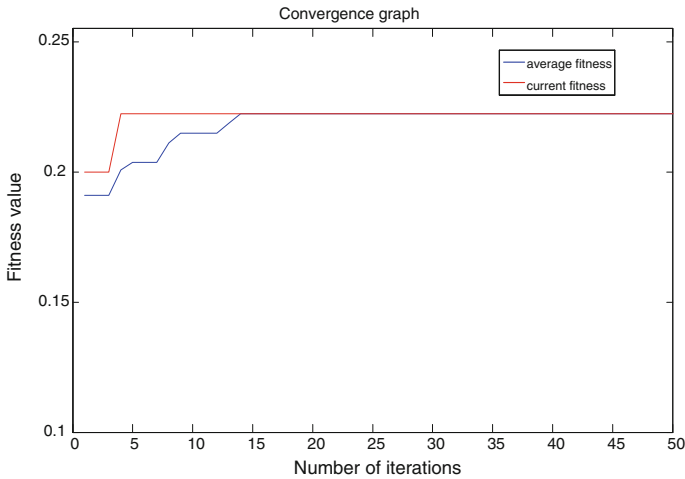


Fig. 7 Convergence Graph of GA

number of number of tool/gripper changes, the user can identify the optimal sequence by giving suitable weightages as per his needs. It has been found that GA takes on an average 2.5 s to determine the optimal solution.

5 Conclusions

In this paper, an intelligent methodology has been presented for assembly sequence planning and optimisation. A knowledge based expert system has been developed and implemented, which is capable of automatically selecting all the various tools/grippers needed for performing the assembly of a given product by considering the shop floor availability and capability of tools and grippers for handling functional parts and fasteners in the product. Further a GA based approach has been developed for assembly sequence optimisation and implemented using MATLAB. It takes as input the information on various tools/grippers from the output generated

by the knowledge-based system and additionally it also takes as input from the user the assembly directions of each part, the information about precedence relationships among them and information about the base component. It then automatically generates as output the feasible and optimal assembly sequences based on minimizing the number of orientation changes and tool changes. The proposed assembly process planning methodology can be integrated with a CAD based feature extraction module to minimize the user intervention and further reduce the time for generation of the assembly process plans.

References

- Barnes, C. J., Jared, G. E. M., & Swift, K. G. (2004). Decision support for sequence generation in an assembly oriented design environment. *Robotics and Computer-Integrated Manufacturing*, 20, 289–300.
- Chen, S., & Liu, Y. J. (2001). An adaptive genetic assembly sequence planner. *International Journal of Computer Integrated Manufacturing*, 14(5), 489–500.
- Choi, Y. K., Lee, D. M., & Cho, Y. B. (2009). An approach to multi-criteria assembly sequence planning using genetic algorithms. *International Journal of Advanced Manufacturing Technology*, 42, 180–188.
- Design for Assembly user guide. (2009). Version 9.4, Boothroyd Dewhurst Inc., Rhode Island, USA, 5, 37.
- Dong, T., Tong, R., Zhang, L., & Dong, J. (2007). A knowledge-based approach to assembly sequence planning. *International Journal of Advanced Manufacturing Technology*, 32, 1232–1244.
- Gottipolu, R. B., & Ghosh, K. (2003). A simplified and efficient representation for evaluation and selection of assembly sequences. *Computers in Industry*, 50, 251–264.
- Hsu, Y. Y., Tai, P.-H., Wang, M. W., & Chen, W. C. (2011). A knowledge-based engineering system for assembly sequence planning. *International Journal of Advanced Manufacturing Technology*, 55, 763–782.
- Laperriere, L., & ElMaraghy, H. A. (1994). Assembly sequences planning for simultaneous engineering applications. *International Journal of Advanced Manufacturing Technology*, 9, 231–244.
- Li, R., Tian, Y. (2013). Assembly sequence planning based on assembly knowledge database. In *Proceedings of the International Conference on Information Engineering and Applications* (Vol. 217, pp. 857–864).
- Rashid, M. F. F., Hutabarat, W., & Tiwari, A. (2011). A review on assembly sequence planning and assembly line balancing optimisation using soft computing approaches. *International Journal of Advanced Manufacturing Technology*, 59(1–4), 335–349.
- Tseng, Y. J., Kao, H. T., & Huang, F. Y. (2010). Integrated assembly and disassembly sequence planning using a GA approach. *International Journal of Production Research*, 48(20), 5991–6013.
- Tseng, Y. J., Kao, H. T., & Huang, F. Y. (2011). A green assembly sequence planning model with a closed-loop assembly and disassembly sequence planning using a particle swarm optimization method. *International Journal of Advanced Manufacturing Technology*, 57, 1183–1197.
- Yin, Z. P., Ding, H., & Li, H. X. (2003). A connector-based hierarchical approach to assembly sequence planning for mechanical assemblies. *Computer-Aided Design*, 35, 37–56.

- Youhui, L., Xinhua, L., Qi, L. (2012). Assembly sequence planning based on ant colony algorithm. In *Future Communication, Computing, Control and Management* (Vol. 141, pp. 397–404). Heidelberg: Springer.
- Zha, X. F., Lim, S. Y. E., & Fok, S. C. (1999). Development of expert system for concurrent product design and planning for assembly. *International Journal of Advanced Manufacturing Technology*, 15, 153–162.

Alignment Based Inspection Framework for Additive Manufactured Parts

Vimal Kumar Pathak and Amit Kumar Singh

Abstract Currently, Additive manufacturing (AM) processes do fabrication of parts having custom-made intricate profiles. It becomes an essential task to verify the accuracy of AM parts to meet customer's need and requirement. Effective measurement and quick inspection of geometric data, performed by implementing reverse engineering in coalition with additive manufacturing. This paper proposes a novel framework for measurement and verification of overall accuracy of the additive manufactured parts. Present method integrates additive manufacturing along with 3D scanner and reverse engineering hierarchy for its implementation. For effective inspection, suitable alignment technique for individual features and GD & T attributes reported. With its simplicity, speedy inspection and accurate results this method will be helpful for manufacturers to increase their competitiveness in global market.

Keywords AM · Accuracy · Alignment · GD&T · Inspection · Reverse engineering

1 Introduction

Lately, with the evolution of different technologies, custom-made parts with complex shapes and profile are becoming more and more common. Nevertheless, fabrication of such custom-made parts is still a challenge for traditional manufacturing processes. Additive manufacturing (AM) processes allow the fabrication of custom-made parts in very short time directly from CAD model. As defined by ASTM, process of joining materials to make objects from 3D model layer by layer, as opposed to subtractive manufacturing methodologies (ASTM 2010). In contrast to other traditional manufacturing process, additive manufacturing is more economical for custom-made parts or low volume fabrication (Ruffo et al. 2007). Since AM technique follows layered manufacturing, therefore it is capable to

V.K. Pathak (✉) · A.K. Singh
Malaviya National Institute of Technology, Jaipur, India
e-mail: vimalpthk@gmail.com

fabricate very complex and minute objects (Sachs et al. 1992). In addition, AM process works on adding material layer by layer from sliced computer model, there will be certain deviation in the manufactured part. So it becomes necessary to inspect AM parts to evaluate its quality in terms of dimensions and geometrical tolerances.

AM part deviation from actual computer model has mainly two reasons. Firstly, AM machine works on the STL file and not on the CAD model of the physical part. STL file is unstructured triangulated representation of nominal surface, produced by slicing operation. Secondly, due to slicing, “staircase” defect occurs in producing part layer-by-layer (Moroni et al. 2014). Due to all these reasons, the STL format does not represent the real profile or geometry of the actual product. Therefore, the part produced by AM process results in certain error or deviation due to slicing. Consequently, it is often necessary to take customers approval on actual product before producing in batches with AM.

In order to guarantee the dimensional accuracy of AM parts, speedy error comparison of manufactured parts and an original CAD model is often a toilsome yet significant quality control issue. Nowadays, 3D scanner and contactless inspection procedures are widely used for quality control of free form objects and complex parts (Savio et al. 2007). The correct use of reconstruction of models obtained by RE is imperative in order to ensure geometric and dimensional accuracy (Relvas et al. 2011). Slowly but surely these techniques are replacing traditional point wise contact measurement machines like CMM. Generally, for AM parts non-contact measurement instruments are more suitable as compared to contact measurement machines. It is remarkably advantageous to use a CAD model as a nominal component 3D model in the inspection operation, as not only it defines the geometric shape of the component but also provides information about component specification information, such as GD&T requirements. For better inspection results, apart from accuracy of contactless device, alignment technique of scanned data with CAD data is also a critical issue. This paper aims to address that the alignment techniques for a specific feature in a part plays a significant role in inspection process.

In this study, equipment and software used includes FDM type R3D2 additive manufacturing (AM) machine (see Fig. 1) and non-contact laser 3D scanner with RE software (COMET PLUS and INSPECT PLUS) (see Fig. 2). The proposed approach provide a means by which accuracy of fabricated AM parts inspected and analyzed quickly.

2 Methodology

Since the inspection, performance of any system depends largely on inspection planning strategy, so an optimum inspection framework is strongly required to achieve more accurate and faster results. Figure 3 shows the proposed flowchart of experimental procedure in this study. An AM part picked for case study and a blue

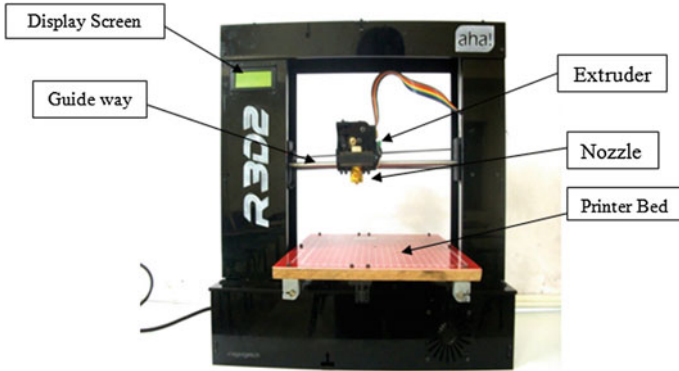


Fig. 1 R3D2 FDM based AM machine



Fig. 2 Steinbichler COMET L3D-blue light scanner

light L3D scanner chosen for scanning and inspection. The scanning device helps in retrieving the point cloud data that represents complete geometry of the AM part. Before inspection process, STL model of the scanned data needs proper alignment with the original CAD data. Since any mistake made in alignment may result in erroneous output. Therefore, this becomes an essential task to use correct alignment techniques during inspection. The aim of this paper is to develop a framework for quality control of complex parts by integrating 3D scanning, RE and AM technologies and emphasizing mainly on the feature based alignment of the parts during inspection. In this approach, one case study was selected (i.e. knuckle joint) and designed in PROE software.

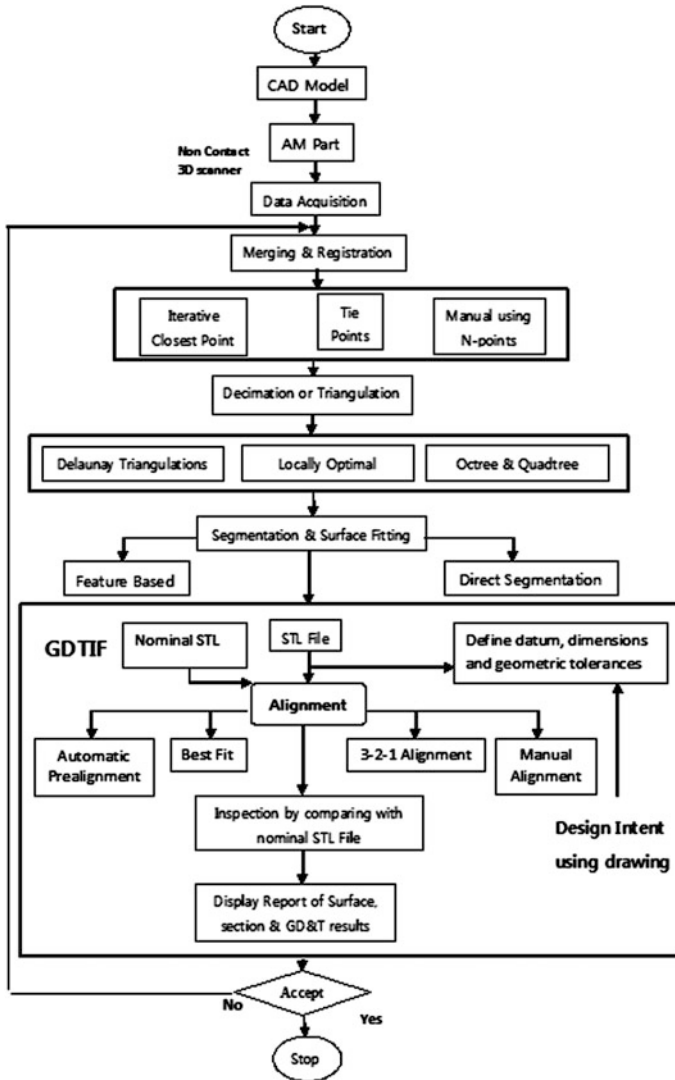


Fig. 3 Proposed framework of experimental procedure

After creation of part STL file, scanned STL file compared with nominal STL file for deviation determination. Before comparison, alignment of scan data model with actual model performed. In the inspection process, alignment operation is immensely important and plays a crucial part. Any error made in alignment operation prompt to an incorrect measurement, which results in erratic outcome of the inspection (Minetola 2012). The ‘alignment’ is an operation that brings the measured part into the coordinate system of a reference model (Gao et al. 2006). In a

reverse engineering environment, alignment techniques are available for end users to choose, such as best-fit alignment, automatic pre alignment, 3-2-1 alignment, and manual alignment etc. Availability of all these alignment techniques leads to confusion in the user to which one to select or reject. In this paper, each part of the case study aligned using all available techniques in framework. For various features (like hole, slot, planar etc.) in a part all alignment techniques were employed and reported in the form of GD&T attributes like circularity, cylindricity, flatness, parallelism etc. The report will provide deviation result of various GD&T attributes and make way for best alignment technique. With this, end users will have an option to choose specific alignment technique for individual feature and GD&T attributes and which in turn will lead to enhance the inspection process.

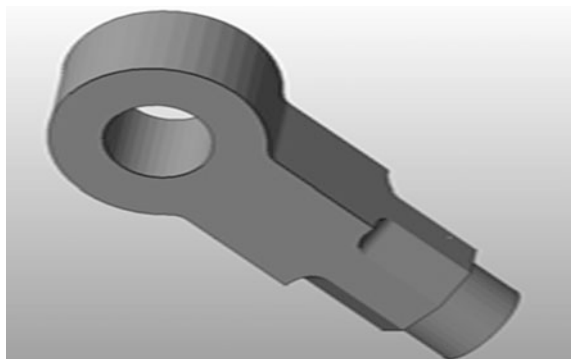
3 Case Study

In this study, knuckle joint middle part as shown in Fig. 4, selected as case study, which is designed using Creo parametric software. Part of the case study is solid and manufactured using Fused Deposition Modelling (FDM) type AM machine for scanning. Parts fabricated using a layer thickness 0.175 mm of ABS plastic. The part surface was neither finished nor polished after fabrication not to amend any deviation.

4 Non-Contact Digitization

The Steinbichler Comet L3D blue light scanner employed for non-contact optical scanning. The version used in this study for data capturing has resolution of 1 Mpx and 1170×880 pixels available. This is a portable scanner where the scanning head mounted over a tripod stand at the time of scanning. All dimensional sizes of the

Fig. 4 Case study part



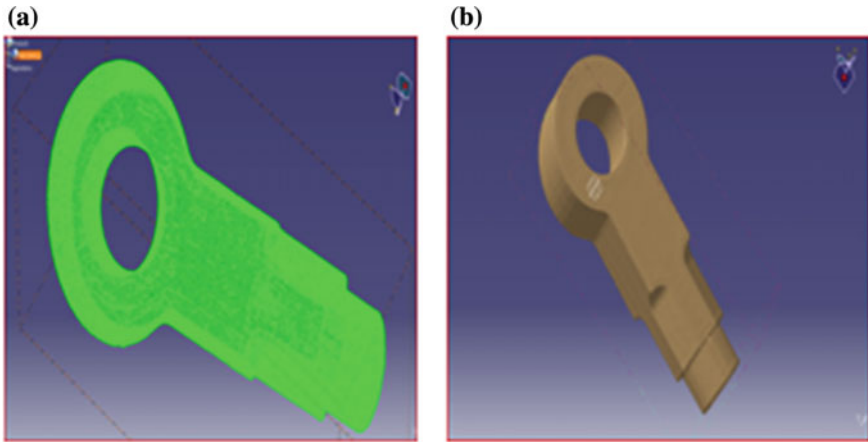


Fig. 5 a Point cloud and b solid model of scanned data

AM made test parts measured by: Blue light 3D scanner and RE (INSPECT PLUS) software. Pros and cons for each method evaluated at last. The experimental procedure for the proposed flowchart is as follows: (1) First, the test part models were prepared in Pro/E (Creo 2.0) software. (2) Several prototypes were then developed by using FDM type AM machine based on CAD design data available; (3) After that, AM prototypes were scanned and inspection is performed using various alignment techniques; (4) Reports of inspection are printed providing best alignment for various features. Now, imported point cloud data and solid model of scanned data shown in Fig. 5a. Using a RE software like COMET PLUS, whole development of the AM parts is performed and 3D model created after RE processes like merging, registration, decimation, segmentation and surface fitting. For this case study, merging and registration processes performed by N-point and tie-points technique. At last, solid model of one AM part after all RE steps depicted in Fig. 5b. Once complete model is built inspection is performed by using specific software module like INSPECT PLUS to analyze the dimensional deviation of AM prototypes. After the geometric comparison of measured part with CAD model, printed form of all the reports are available for further process. The inspection procedure for proposed framework begins with loading the CAD model and scanned model in software interface. After importing, various alignment performed on the two models. Different alignment techniques give different results for various features like hole, plane, parallel surface etc. Printed result will have the information of GD&T attributes for individual features that provide information about better alignment technique for respective features. Visual inspection performed to verify the difference in various alignment techniques by superimposing the scanned data and CAD model. Hence, there will be total twelve differently aligned files; each part will have four alignment files as per the proposed framework.

5 Results and Discussion

The differently-aligned scanned point clouds were compared to the nominal STL model by means of Steinbichler INSPECT plus software. For comparison, STL file is used as reference that’s why the result in deviation does not keep in mind the error introduced in slicing. The deviation shown is combination of FDM process parameters, scanning accuracy and error in alignment of parts. The average deviation of the scanned STL data from the actual STL data for twelve different aligned point clouds is given in Table 1.

Average deviation for various alignment techniques. In each row, the deviation is result of only alignment techniques; it has no connection with scanner accuracy, AM parameters or slicing operation. The average deviation is the distance between corresponding points in the scanned model and STL model. The least average deviation among the alignment techniques is shown by best fit technique. The manual technique have the next best average deviation, automatic pre alignment and 3-2-1 are 3rd and 4th respectively in terms of average surface distance. Colour GD&T deviation of the knuckle joint part is shown in Figs. 6 (best fit), 7 (automatic), 8 (manual), 9 (3-2-1 alignment). For circularity, cylindricity and flatness

Table 1 Comparison of differently aligned scan data

Technique	Ist part (mm)	2nd part (mm)	3rd part (mm)	Average deviation
Automatic	0.330	0.338	0.326	0.331
3-2-1	0.384	0.396	0.388	0.389
Manual	0.212	0.242	0.218	0.224
Best fit	0.132	0.142	0.124	0.133

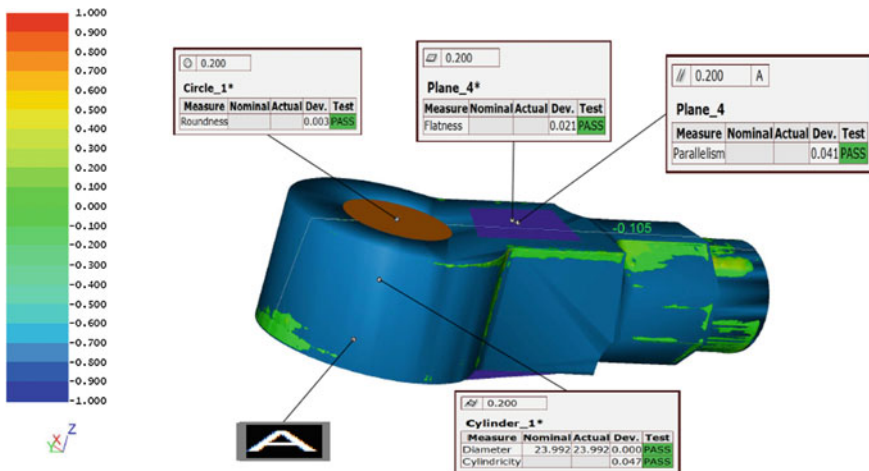


Fig. 6 GD&T inspection best fit alignment

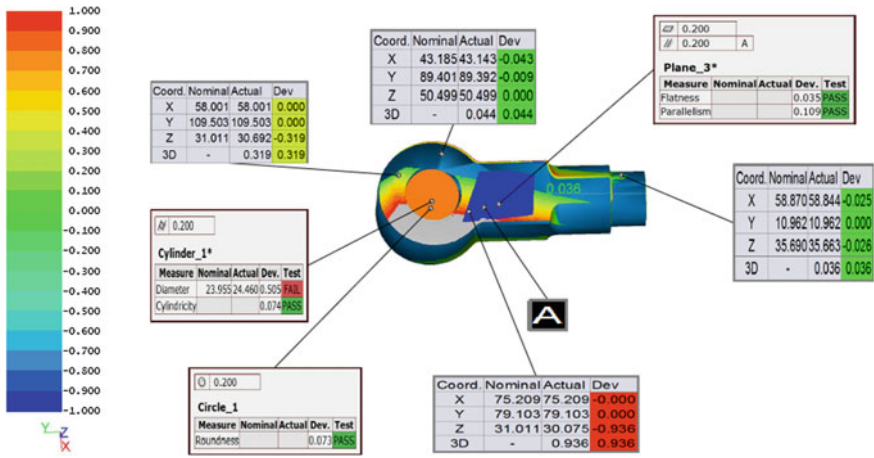


Fig. 7 GD&T inspection (automatic pre-alignment)

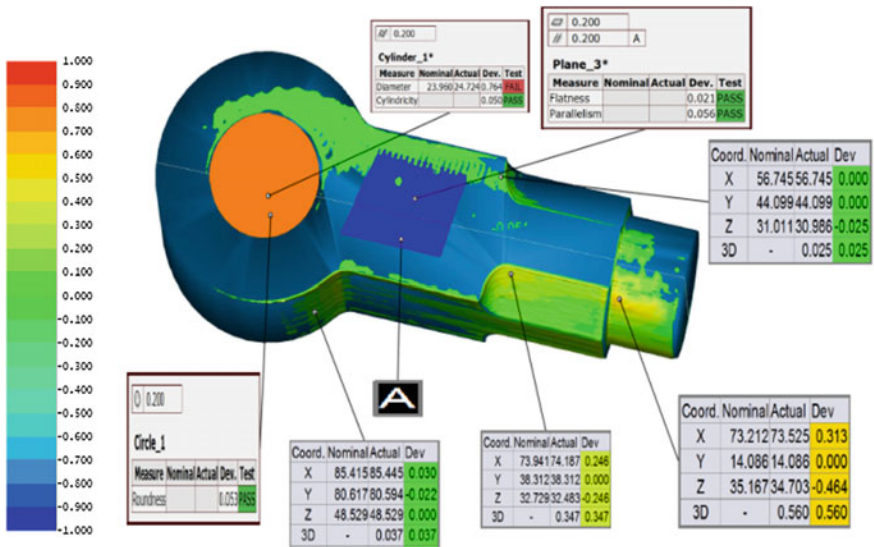


Fig. 8 GD&T inspection (manual alignment)

attributes evaluation, they do not require any datum for their definition. On the other hand, parallelism evaluation require datum for their definition as shown by A in the below figures.

For choosing optimum alignment of individual feature GD&T attributes are examined and evaluated. For part features like hole and planar surface, GD&T attributes like cylindricity, circularity, flatness and parallelism are employed to show the results of individual alignment techniques. Starting with hole feature, the

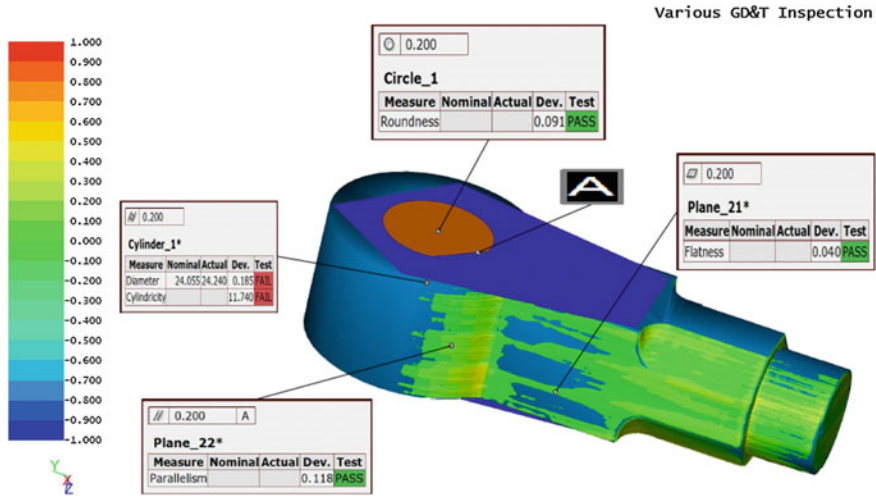


Fig. 9 GD&T inspection (3-2-1 alignment)

Table 2 GD&T report for different alignment

Feature	Automatic	3-2-1	Manual	Best fit
Circularity	0.073	0.091	0.053	0.003
Cylindricity	0.074	1.74	0.050	0.047
Flatness	0.005	0.040	0.021	0.021
Parallelism	0.109	0.118	0.056	0.041

circularity and cylindricity results for all the cases as shown in Table 2. The results revealed that best fit alignment has minimum deviation for circularity as well as cylindricity. In 3-2-1 alignment, circularity deviation is under acceptable level but when the measurement is taken along depth i.e. cylindricity gross error is coming. Also, for planar surface, flatness and parallelism attributes are used which is useful to define a complete surface. For these two characteristics also best fit alignment is giving less deviation as shown in Table 2. For flatness measurement, manual alignment is showing equally same result as best fit. Overall, 3-2-1 alignment is showing highest deviation for all the attributes and best fit is showing least deviation.

6 Conclusion

In product quality control, distinctive mechanical parts inspected by contact based CMM for a prolonged period. However, with the evolution of technology, contact based measurement systems replaced by non-contact instruments.

1. In this paper, a novel framework for alignment-based inspection for some GD&T features is proposed. Compared with contact-based inspection using CMM the proposed inspection system based on non-contact digitization technique can provide an efficient, automatic GD&T inspection solution not only for newly manufactured components with complex geometry, soft materials and a large size but also a free form surface inspection.
2. The proposed framework is useful for determination of geometric tolerances as well as dimensional tolerances. One of the key issues in the proposed approach is use of various alignment techniques in GD&T inspection framework (GDTIF) for the effective alignment of nominal CAD model and scanned model of the part, which will be helpful in fruitful inspection of the parts in a RE environment.
3. One decisive part of the proposed framework is GD&T inspection framework (GDTIF) which starts with loading two models in RE environment with defining datum, dimensional and geometrical tolerances on the nominal STL model. Four different alignment rules chosen for the most important alignment of the two models prior to inspection and in the end graphical reports displayed.
4. The average deviation results showed that for the case study (Table 1) reveals that average distance deviation is minimum for best fit and maximum for 3-2-1. Moreover, the other two techniques come between these two.

References

- ASTM F2792-10. (2010). Standard terminology for additive manufacturing technologies, ASTM International, West Conshohocken, PA, www.astm.org.
- Gao, J., Gindy, N., & Chen, X. (2006). An automated GD&T inspection system based on non-contact 3D digitization. *International Journal of Production Research*, 44(1), 117–134.
- Minetola, P. (2012). The importance of correct alignment in contactless inspection of additive manufactured parts. *International Journal of Precision Engineering and Manufacturing*, 13(2), 211–218.
- Moroni, G., Syam, W. P. & Petro, S. (2014). Towards early estimation of part accuracy in additive manufacturing. In *24th CIRP Design Conference* (Vol. 21, pp. 300–305).
- Relvas, C., Ramos, A., Completo, A., & Simoes, J. A. (2011). Accuracy control of complex surfaces in reverse engineering. *International Journal of Precision Engineering and Manufacturing*, 12(6), 1035–1040.
- Ruffo, M., Tuck, C., & Hague, R. (2007). Make or buy analysis for rapid manufacturing. *Rapid Prototyping Journal*, 13(1), 23–29.
- Sachs, E., Cima, M., Williams, P., Brancrazio, D., & Cornie, J. (1992). Three dimensional printing: rapid tooling and prototypes directly from a CAD model. *Journal of Manufacturing Science and Engineering*, 114(4), 481–488.
- Savio, E., De Chiffre, L., & Schmitt, R. (2007). Metrology of freeform shaped parts. *Annals of the CIRP*, 56(2), 810–835.

An Investigation on Slab Milling Operation to Find Out Optimum Cutting Parameters

Spandan Guha, Tapas Banerjee, Asish Bandyopadhyay
and Santanu Das

Abstract Milling is a widely used machining operation. For generating a flat wide surface, slab milling is usually employed in industry. In this experimental work, slab milling operation has been performed on low alloy steel to obtain appropriate cutting parameters in order to get low surface roughness, low vibration and high material removal rate. Taguchi method and composite desirability function of response surface methodology have been used to get required cutting parameters. It has been observed from Taguchi's methodology that surface roughness is affected mostly by variation of cutting velocity or speed; in case of material removal rate, effect of feed is quite high, and speed also has sufficient effect on it.

Keywords Slab milling · Low alloy steel · Taguchi method · Composite desirability · Optimisation

S. Guha

Department of Mechanical Engineering, Sikkim Manipal Institute of Technology,
Sikkim 737136, India
e-mail: spandan.guha@yahoo.com

T. Banerjee · A. Bandyopadhyay

Department of Mechanical Engineering, Jadavpur University, Kolkata 700032, India
e-mail: starcemintl@yahoo.com

A. Bandyopadhyay

e-mail: asish.banerjee@yahoo.com

S. Das (✉)

Department of Mechanical Engineering, Kalyani Government Engineering College,
Kalyani 741235, India
e-mail: sdas.me@gmail.com

© Springer India 2016

D.K. Mandal and C.S. Syan (eds.), *CAD/CAM, Robotics and Factories of the Future*, Lecture Notes in Mechanical Engineering,
DOI 10.1007/978-81-322-2740-3_33

1 Introduction

Milling is one of the widely used machining operations, and slab milling is used for flat surface machining. To achieve high productivity, it is tried to have high material removal rate (MRR). However, at high MRR, machine vibration may occur, and work-piece surface finish may be poor (Bhattacharya 2008; Chattopadhyay 2012). Vibration may be controlled by proper selection of machining parameters (Bhattacharya 2008). Many research works were done in the past to understand the effect of different process parameters on various aspects of milling operation theoretically and experimentally. Huang et al. (2012) analyzed milling force and acceleration component of vibration to identify occurrence of chatter, while Ko and Tan (2013) found that work-piece would vibrate differently under varying cutting velocities and feed rate, under the application of designed ultrasonic vibration. Huang et al. (2013) worked on vibration during dry machining of titanium alloy in moderate to high speed cutting conditions in down milling. Weinert et al. (2007) concluded through simulation that run out did not affect dynamic behaviour of milling process, but it had strong influence on the vibration trajectory of milling tool and on job surface quality. Chibane et al. (2013) tried to introduce a correlation between vibration and cutting conditions in an optimum situation using down milling of carbon/epoxy composites with a diamond insert. Depth of cut was found to influence feed and radial components of cutting force (Ignatov et al. 2008), and vertical component of cutting force affected surface roughness. Zhang and Li (2010–11) observed tool wear to be a predominant factor behind surface roughness during end milling of annealed Ti-6Al-4 V alloy. Goel et al. (2012) derived suitable parameters for slab milling under wet condition using Taguchi method on high and low alloy steels. Öktem et al. (2006) also used Taguchi's orthogonal array to obtain low surface roughness.

Niknam and Songmene (2013) used fitness mapping function and desirability index to find feed to have major influence on variation in burr size and surface roughness. Reddy and Rao (2006) made dry machining much effective and environment friendly by selecting proper parameters and cutter. Caliskan et al. (2013) saw interaction of coating type and depth of cut to affect surface roughness and not to have any effect on cutting forces. Jeyakumar et al. (2013) observed during machining of composites of aluminium that main cutting force component and tool wear rate were high at low cutting velocity. Shen et al. (2012) found finish of bottom of slot deteriorated but finish of vertical side wall was improved by the effect of ultrasonic vibration. Chen et al. (2012) performed end milling operation to obtain good surface finish by suppressing vibration.

In the present work, average surface roughness, volume of material removal and vibration along the axis of machining and perpendicular to the axis of machining was measured to find out the appropriate cutting parameters to optimize MRR, average surface roughness and vibration components.

Table 1 Experimental conditions

Milling conditions	5 HP Horizontal Milling Machine. Make: B.S. Machine Tools Corporation, Kolkata Type: Slab Milling (Helical)
Cutter	Material: HSS. Make: Addison Tool Manufacturer, Mumbai Size: $\phi 63.5$ mm \times 130 mm. No. of Teeth: 12. Helix Angle: 20°
Work piece	Material: Low Alloy Steel. Hardness: HRB 71. Size: 50 mm \times 50 mm \times 20 mm
Machining conditions	Composition: C- 0.3 %, Si- 0.13 %, Mn- 0.35 %, P- 0.08 %, S- 0.04 %, Fe- rest Speed, rpm [Cutting Velocity, m/min]: 42 [8], 73 [15], 134 [27], 235 [47], 410 [82] Feed, mm/min: 12, 21.5, 40, 72, 128. Environment: Dry Depth of cut, mm: 0.050, 0.10, 0.15, 0.20, 0.25

2 Materials and Methods of Experimentation

Milling operations were carried out on a horizontal milling machine by using an HSS milling cutter having a diameter of 63.5 mm. Machining parameters and details about tool and work-piece are given in Table 1. Design of experiment was made according to Taguchi's L_{25} Orthogonal Array. Speed, feed and depth of cut were varied five times from 42 to 410 rpm, 12 to 128 mm/min and 0.05 to 0.25 mm respectively. Cutting environment was dry and vibration was measured during milling operation. Vibration was measured in two directions, one along and the other perpendicular to the machining axis using Techtronix oscilloscope (Model No.-TDS 210). Surface roughness was measured after machining operation by utilizing portable stylus-type profilometer, Talysurf (Taylor Hobson, Surtronic 3+, UK). Stylus was placed on the machined surface along the direction of machining to measure roughness.

3 Results and Discussion

Responses obtained from slab milling of low alloy steel blocks are average surface roughness (R_a), vibration along the machining axis (X), vibration perpendicular to the machining axis (Y) and material removal rate (MRR) under each experimental run. Taguchi's L_{25} series was considered as the design of experiment. For the analysis of signal (mean) to noise (standard deviation) ratio, Taguchi's smaller the better concept was considered for surface roughness and vibration and Taguchi's larger the better concept was considered for material removal rate (Roy 2001; Taguchi 1987). Confidence level of 95 % has been used in this work. Signal to noise (S/N) ratio plots for surface roughness, vibration (Z), MRR and vibration

(X) are shown in Figs. 1, 2, 3 and 4 respectively. Figure 1 reveals the most effective parameter combine to minimize surface roughness to be 410 rpm speed, 21.5 mm/min feed and 0.05 mm depth of cut. As cutting velocity (or, speed) is the most effective parameter for surface roughness, generally it is required to maintain high to get low surface roughness. With high speed, if high depth of cut is given

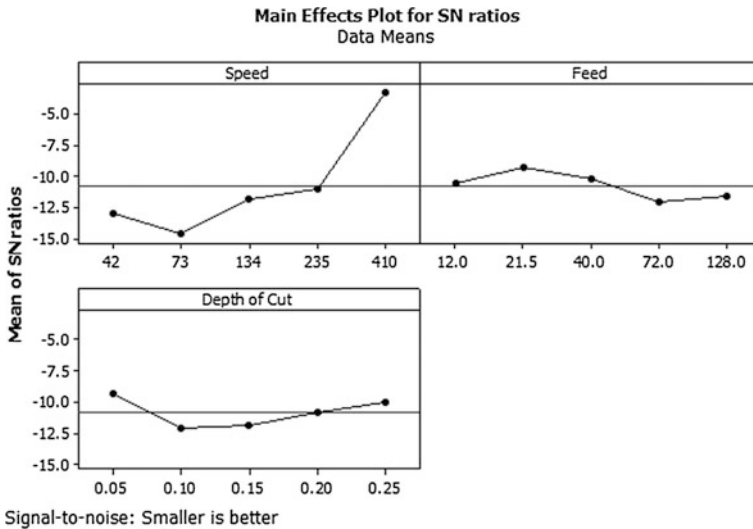


Fig. 1 S/N ratio plot for roughness

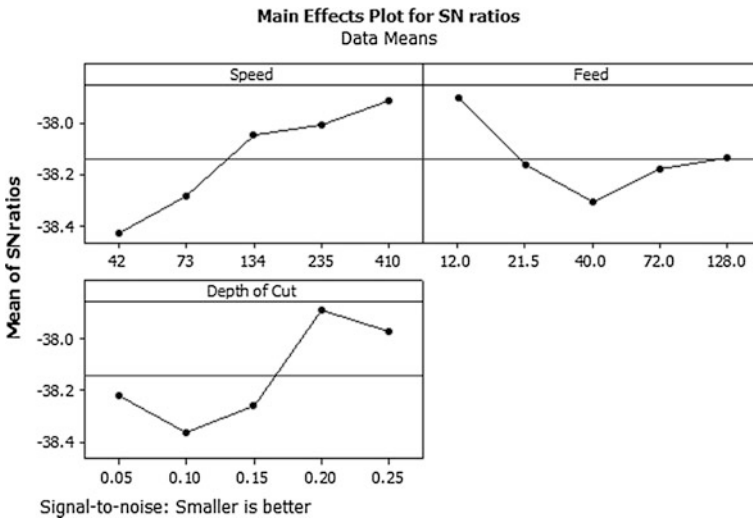


Fig. 2 S/N ratio plot for vibration (Z)

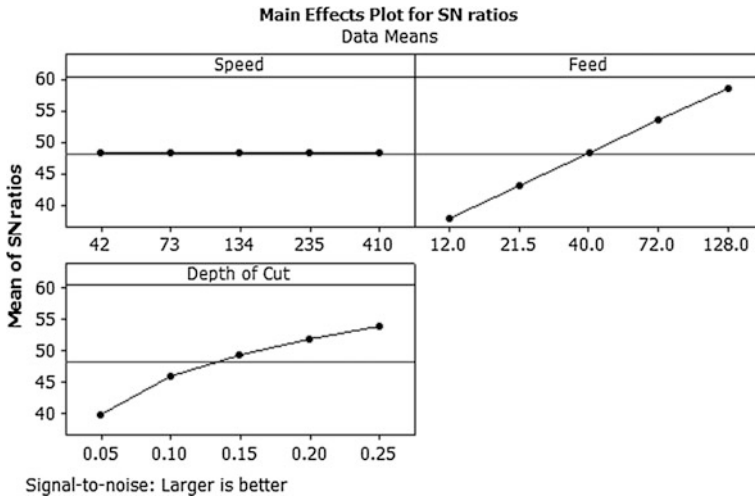


Fig. 3 S/N ratio plot for MRR

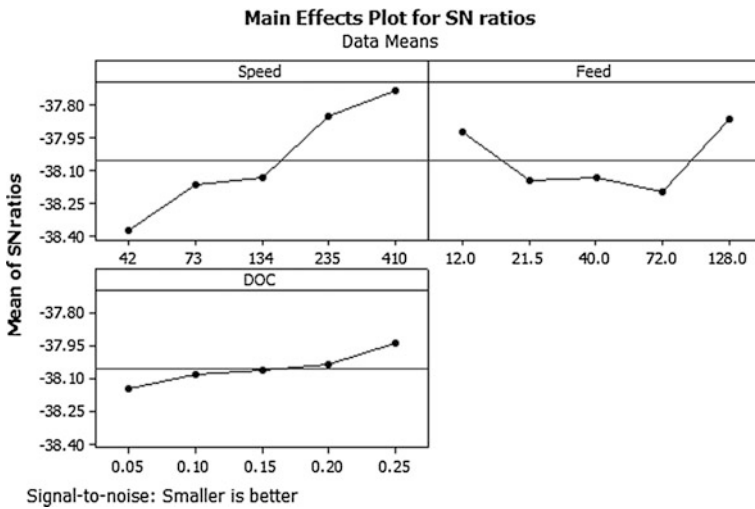


Fig. 4 S/N ratio plot for vibration (X)

then surface roughness becomes high. So, maintaining low depth of cut with medium feed value and high speed gives low surface roughness. From Fig. 2, it is clear that for the values of speed of 410 rpm, feed of 12 mm/min and depth of cut of 0.10 mm, vibration perpendicular to machining axis is quite high. For vibration perpendicular to the machining axis, speed, or cutting velocity, is found to be quite effective compared to the other two parameters, depth of cut and feed. So, high

speed with low depth of cut will generate less vibration, otherwise high depth of cut with high speed will generate high vibration as well as increased surface roughness.

Figure 3 shows the effect of various parameters on material removal rate and it is clear that for the value of feed of 128 mm/min, depth of cut of 0.25 mm and speed of 410 rpm, for material removal rate, effect of feed is maximum than speed and depth of cut. Higher values of these parameters are naturally expected to cause removal of more amount of material from the workpiece. From Fig. 4, it is clear that at 410 rpm speed, 128 mm/min feed and 0.25 mm depth of cut, vibration along the machining axis is minimum.

Response surface methodology (RSM) was also applied for prediction of surface roughness (R_a), MRR, vibration (X) and vibration (Z). The objective of generation of surface plot is to find out expected value of response corresponding to any of the two input parameters. Necessary programme can be run for developing response surface plots. Figures 5, 6 and 7 depict surface plot of surface roughness. These

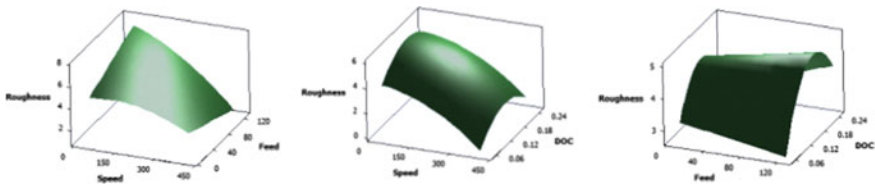


Fig. 5 Combined effects of parameters on surface roughness (At middle value with 226 rpm speed, 70 mm/min feed and 0.15 mm depth of cut)

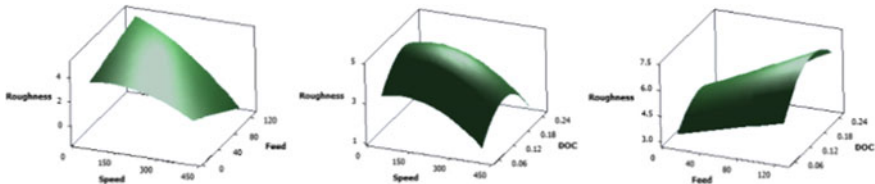


Fig. 6 Combined effects of parameters on surface roughness (At lowest value with 42 rpm speed, 12 mm/min feed and 0.05 mm depth of cut)

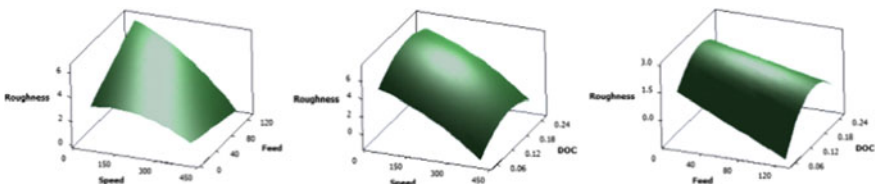


Fig. 7 Combination of parametric effects on surface roughness (At highest value with 410 rpm speed, 128 mm/min feed and 0.25 mm depth of cut)

suggest a significant fact that in all the three plots, interaction effect between speed and depth of cut and interaction effect between feed and depth of cut are significant as curvature of this surface plot is pronounced on surface roughness. With the variation of speed and depth of cut keeping feed constant and with the variation of feed and depth of cut keeping speed constant, sufficient amount of variation on surface roughness can be resulted. Figures 8, 9 and 10 show surface plots for material removal rate. These plots may be interpreted and utilized in the same manner as in case of surface roughness, but in this case, interaction effect between feed and depth of cut is found to be the most significant.

Interaction effects of different machining parameters on vibration (X) along machining axis are shown in Figs. 11, 12 and 13. It is clear from these figures that interaction effect between speed and feed is most effective on vibration as the curve is too pronounced. The interaction effect between feed and depth of cut is also very effective on it. Figures 14, 15 and 16 depict the interaction effect of different parameters on vibration (Y) perpendicular to the machining axis. For vibration

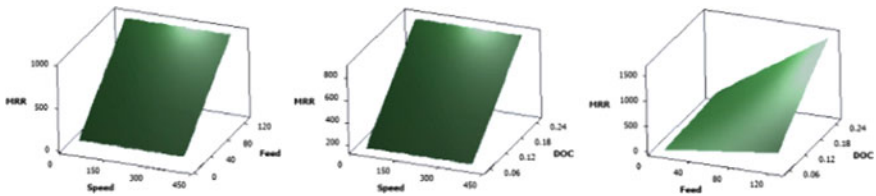


Fig. 8 Combined effects of parameters on MRR (At middle value)

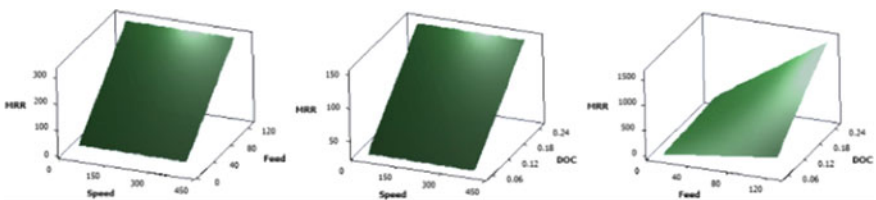


Fig. 9 Combined effects of parameters on MRR (At lowest value)

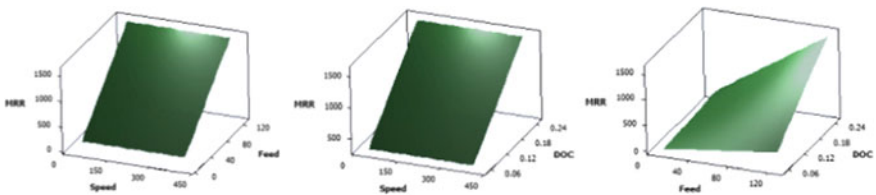


Fig. 10 Combined effects of parameters on MRR (At highest value)

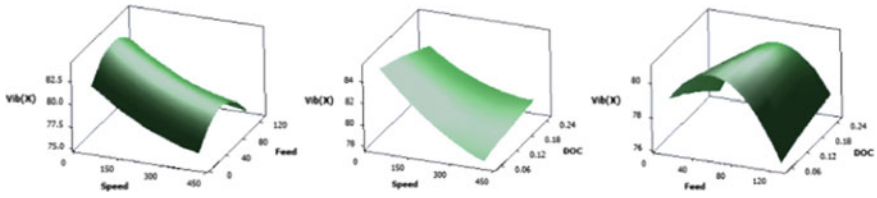


Fig. 11 Combined effects of parameters on vibration (X) (At middle value)

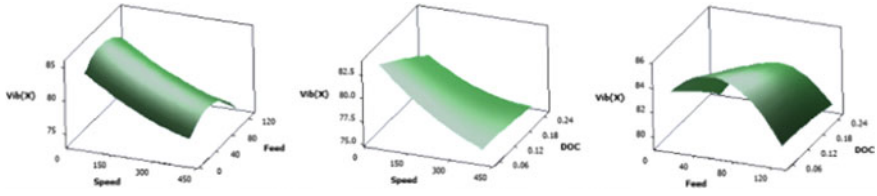


Fig. 12 Combined effects of parameters on vibration (X) (At lowest value)

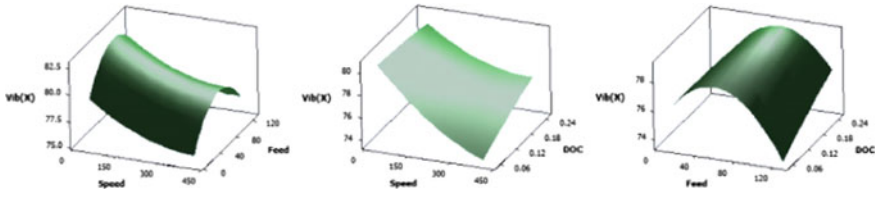


Fig. 13 Combined effects of parameters on vibration (X) (At highest value)

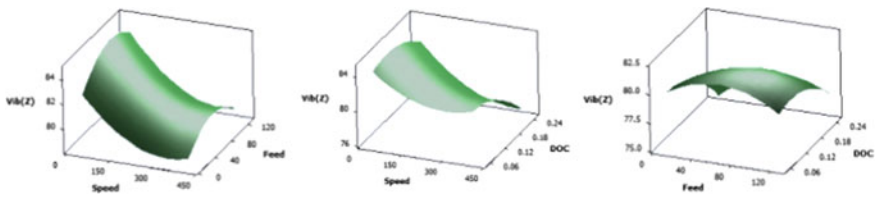


Fig. 14 Combined effects of parameters on vibration (Z) (At middle value)

(Z) perpendicular to the machining axis, interaction effect between all the three parameters with each other is seen to be quite effective.

Figure 17 depicts the process optimization by Desirability function. This function is one useful approach to optimize multiple responses by utilizing the simultaneous optimization technique. It is mainly based on the idea that the ‘quality’ of a

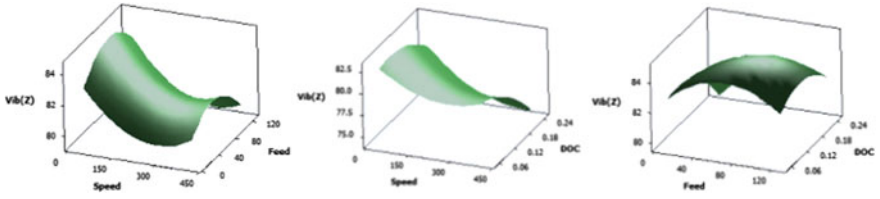


Fig. 15 Combined effects of parameters on vibration (Z) (At lowest value)

Fig. 16 Combined effects of parameters on vibration (Z) (At highest value)

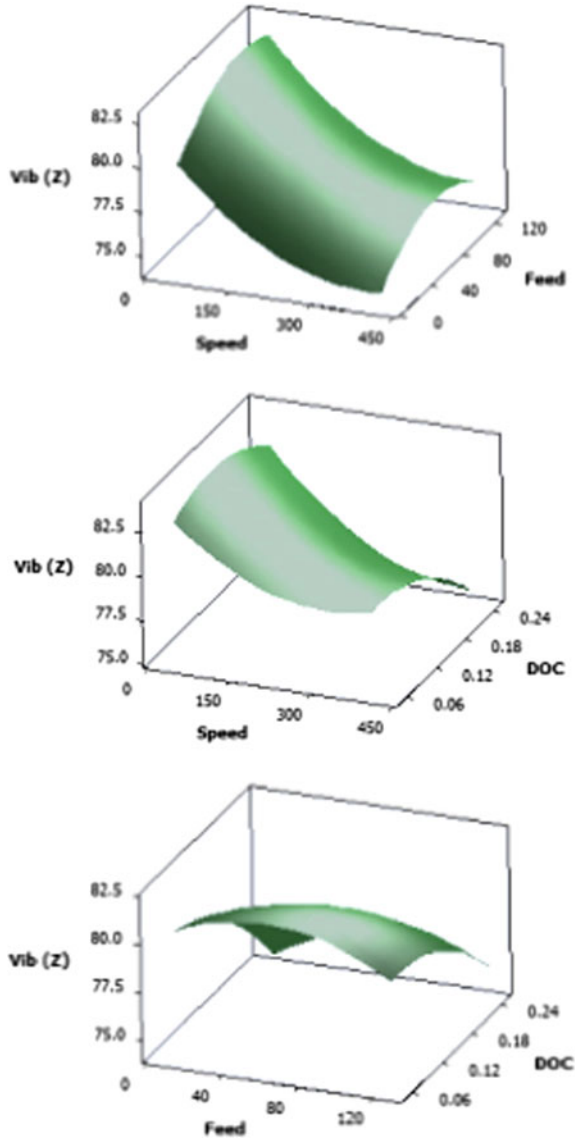
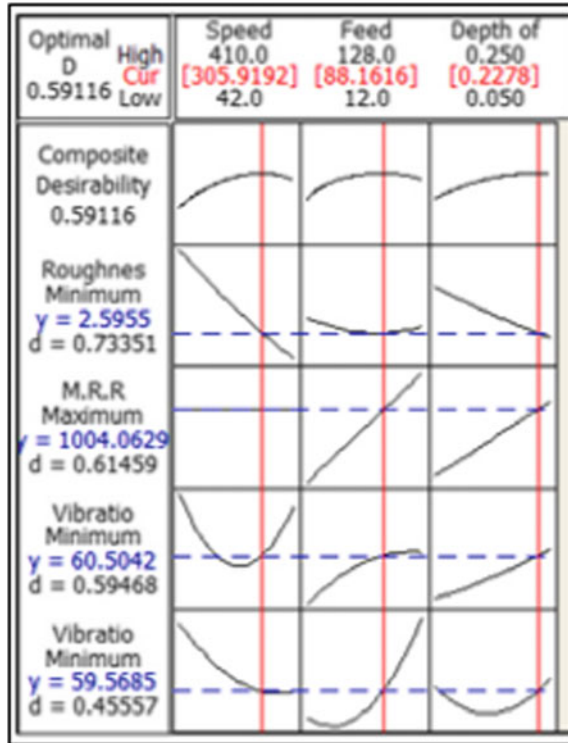


Fig. 17 Individual and composite desirability plot of process parameters



product or process that has multiple quality characteristics, with one of them outside some ‘desired’ limits, is completely unacceptable (Derringer and Suich 1980).

In this experimental work, there are four response variables, i.e. surface roughness, material removal rate, vibration (X) and vibration (Z). The predicted minimum value of surface roughness (R_a) is 2.6 μm , maximum value of material removal rate is 1004.1 mm^3/min , minimum value of vibration (X) is 60.5 db and vibration (Y) is 59.56 db along with individual desirability of 0.73, 0.61, 0.59 and 0.46 respectively (Fig. 17).

Individual desirability has its own factor setting for each response variable which most probably has a different factor setting. In fact, in a single experiment, it will have a single factor setting which is required to optimize all response variables. This problem is solved through composite desirability. The obtained value of composite desirability D is 0.59 to get a setting factor which optimizes all response variables taken all together. The factor setting is given by 305.92 rpm of speed (61 m/min of cutting velocity), 88.16 mm/min of feed and 0.23 mm of depth of cut.

4 Conclusion

From the present experimental work and analyses done, following conclusions may be drawn.

- Surface roughness is mostly influenced by cutting velocity or speed than feed and depth of cut.
- Cutting velocity is found to have larger influence on material removal rate than feed.
- For vibration in both the directions, cutting velocity or speed is found to be the more influencing parameter on the whole than feed or depth of cut. Within depth of cut and feed, depth of cut is found to have more effect on vibration along and perpendicular to machining axis than feed.

References

- Bhattacharyya, A. (2008). *Metal cutting, theory and practice*. Kolkata: New Central Book Agency.
- Calışkan, H., Kurbanoglu, C., Panjan, P., & Kramar, D. (2013). Investigation of the performance of carbide cutting tools with hard coatings in hard milling based on the RSM. *International Journal of Advanced Manufacturing Technology*, 66, 883–893.
- Chattopadhyay, A. B. (2012). *Machining and machine tools*. New Delhi: Willey-India.
- Chen, C. C., Liu, N. M., Chiang, K. T., & Chen, H. L. (2012). Experimental investigation of tool vibration and surface roughness in the precision end-milling process using SSA. *International Journal of Advanced Manufacturing Technology*, 63, 797–815.
- Chibane, H., Morandea, A., Serra, R., Bochou, A., & Leroy, R. (2013). Optimal milling conditions for carbon/epoxy composite material using DVA. *International Journal of Advanced Manufacturing Technology*, 68, 1111–1121.
- Derringer, G., & Suich, R. (1980). Simultaneous opt. of several response var. *Journal of Quality Technology*, 4, 214–219.
- Goel, P., Khan, Z. A., Siddique, A. N., Kamaruddin, S., & Gupta, R. K. (2012). Influence of slab milling process parameters in surface integrity of HSLA: A multi-performance characteristic optimisation. *International Journal of Advanced Manufacturing Technology*, 61, 859–871.
- Huang, P., Lie, J., Sun, J., & Ge, M. (2012). Milling force vibration analysis in high speed milling titanium alloy using variable pitch angle mill. *International Journal of Advanced Manufacturing Technology*, 58, 153–160.
- Huang, P., Li, J., Sun, J., & Zhou, J. (2013). Study of vibration reduction mechanism of variable pitch end mill and cutting performance in milling titanium alloy. *International Journal of Advanced Manufacturing Technology*, 67, 1385–1391.
- Ignatov, M. G., Parminov, A. E., & Prokof'ev, E. Yu. (2008). Influenced of the vertical cutting force on the surface precision and roughness in opposed milling. *Russian Engineering Research*, 28, 864–865.
- Jeyakumar, I., Marimuthu, K., & Ramachandran, T. (2013). Prediction of cutting force, tool wear and surface roughness of Al6061/SiC composites for end milling using RSM. *Journal of Mechanical Science and Technology*, 27, 2813–2822.
- Ko, J. H., & Tan, S. W. (2013). Chatter marks reduction in meso-scale milling through ultrasonic vibration assistance parallel to tooling's axis. *International Journal of Precision Engineering and Manufacturing*, 14, 17–22.

- Niknam, S. A., & Songmene, V. (2013). Simultaneous optimization of burrs size and surface finish when milling 6061-T6 aluminium alloy. *International Journal of Precision Engineering and Manufacturing*, 14, 1311–1320.
- Öktem, H., Erzurumlu, T., & Cöl, M. (2006). A study of the Taguchi optimization method for surface roughness in finish milling of mould surfaces. *International Journal of Advanced Manufacturing Technology*, 28, 694–700.
- Reddy, N. S. K., & Rao, P. V. (2006). Selection of an optimal parametric combination for achieving a better surface finish in dry milling using genetic algorithm. *International Journal of Advanced Manufacturing Technology*, 28, 463–473.
- Roy, R. K. (2001). *Design of Experiments Using the Taguchi's Approach*. John Willey & Sons.
- Shen, X. H., Zhang, J., Xing, D., & Zhao, Y. (2012). A study of surface roughness variation on ultrasonic vibration-assisted milling. *International Journal of Advanced Manufacturing Technology*, 58, 553–561.
- Taguchi, G. (1987). System of experimental design: Engineering methods to optimize quality and minimize cost. In *Proceedings UNIPUB/ Kraus International*, White Plains, NY.
- Weinert, K., Surmann, T., Enk, D., & Webber, O. (2007). The effect of runout on the milling tool vibration and surface quality. *Production Engineering—Research and Development*, 1, 265–270.
- Zhang, S., & Li, J. F. (2010–11). Tool wear criterion, tool life and surface roughness during high speed end milling Ti-6Al-4 V alloy. *Journal of Zhejiang University—Science A*, 8, 587–595.

Recognition of Force Closed Point Grasp for 2D Object

Abhijit Das and Sankha Deb

Abstract Robotic grasping of an object requires positioning the fingers of the robotic hand around the object in such a manner that the forces applied by the fingers on the object can create a force as well as moment equilibrium (Realeaux 1876) and keep the object stable within the grasp. Research on robotic grasping is relevant too (Tovar and Suarez 2014). Recognizing a grasp of an object by a robotic gripper requires a definition of the grasp. In this paper we have compared different definitions of robotic grasp proposed by different researchers and we have proposed our definition of grasp and an algorithmic approach to execute the definition. The results obtained show the promising prospect of the approach.

Keywords Robot · Grasping · Equilibrium · Stability · Optimization · Genetic algorithm

1 Introduction and Background

There are many approaches which defines a force closed point grasp. All these approaches define some criteria based on which a force closed grasp is defined. Algorithms are generated thereafter to implement the grasps and computer programs are written to execute the grasps in the real world.

Primarily grasping an object depends on the following factors:

1. Object geometry. The planar/spatial orientation of the grasping surfaces and their frictional coefficient.
2. Number of contacts to grasp the object.

A. Das (✉)
CMERI, Durgapur, India
e-mail: abhijit.random739@gmail.com

S. Deb
Department of Mechanical Engineering, IIT Kharagpur, Kharagpur, India
e-mail: sankha.deb@mech.iitkgp.ernet.in

3. Value and planar/spatial orientation of the grasping forces.
4. Equilibrium of the grasping forces.
5. Stability of the object.

The different approaches to solve the problem of grasping have been the following:

1. Analytical,
2. Empirical,
3. Graphical, and
4. Evolutionary.

Among them, empirical and graphical approaches are explained using analytical proof. Evolutionary techniques are not always based on rigorous analytical proof.

1.1 Frictionless Grasps on Four Edges

We shall present below some approaches developed by researchers to define force closed grasp.

Firstly we will explain the approach by Nguyen for planar force closed grasp. The algorithm proposed by Nguyen (1986) is graphically explained below (Fig. 1).

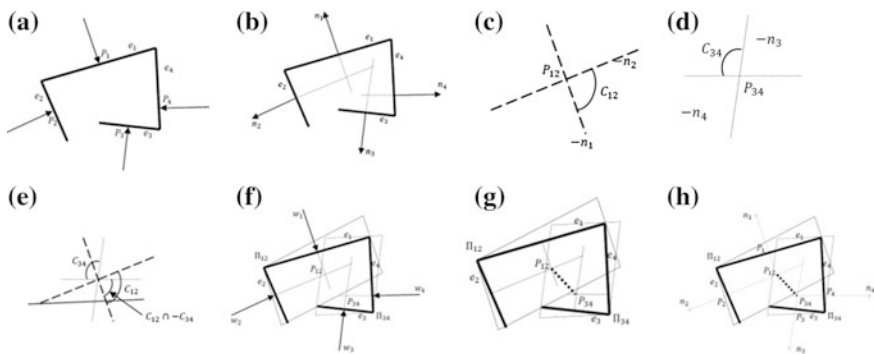


Fig. 1 It shows a four finger grasp and its synthesis. **a** A four finger force closure grasp. **b** Side-normals of the object. **c** Construction of sector C_{12} . **d** Construction of sector C_{34} . **e** Over-lapping of the sectors. **f** Pick any two points P_{12} and P_{34} . **g** check the line $P_{12}P_{34}$ passes through C . **h** Back-project from points P_{12} and P_{34} along the side-normals to find the grasping points P_1, P_2, P_3 and P_4

A force closure grasp between four edges e_1, \dots, e_4 can be constructed as follows:

1. Pair up two edges e_1, e_2 against e_3, e_4 such that the two sectors C_{12}, C_{34} are non null. By sector C_{12} we denote the smallest sector between the normals $-n_1, -n_2$. Similarly for sector C_{34} .
2. Check that the two sectors C_{12}, C_{34} counter-overlap, i.e. $C_{12} \cap -C_{34} \neq \emptyset$.
3. Find the parallelogram Π_{12} by intersecting the two infinite bands perpendicular to and containing the edges e_1 and e_2 . Parallelogram Π_{12} is the locus of the point P_{12} , where the lines of forces w_1 and w_2 intersect. Similarly we find the parallelogram Π_{34} which represents the locus of point P_{34} , where lines of forces w_3 and w_4 intersect.
4. Pick two points P_{12}, P_{34} respectively from the parallelograms Π_{12}, Π_{34} ; such that the direction of the line joining P_{12} and P_{34} is in the counter overlapping sector

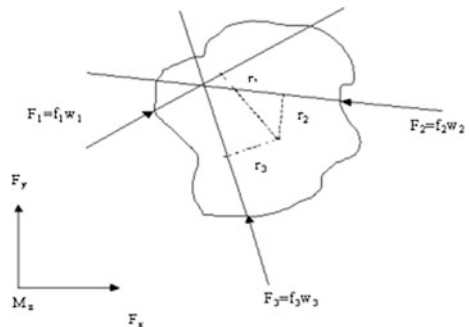
$$C = C_{12} \cap -C_{34}$$

5. From point P_{12} , back-project along the normal n_1 (resp. n_2), to find the grasp point P_1 , (resp. P_2), on edge e_1 (resp. e_2). Similarly we find the grasp points P_3 and P_4 , by back-projecting P_{34} respectively along the normals n_3, n_4 .
6. The four grasp points P_1, P_2, P_3, P_4 found as above form a force closure grasp $G (P_1, P_2, P_3, P_4)$ between the four edges.

Next we shall explain the approach by Mishra et al. (1987), Mishra and Silver (1989). His approach is rigorously mathematical, which can be graphically explained as below. Mishra’s approach is explained for a three finger case.

For a three finger robot gripper (Deb and Deb 2010) the relationship among the forces that can create an equilibrium grasp as well as counter the external disturbances can be obtained from the three contact forces F_1, F_2 and F_3 at points 1, 2 and 3 (Fig. 2) and their directions of application.

Fig. 2 Planar forces acting on a 2D object of arbitrary shape



A system of three wrenches, w_i , $i = 1, 2, 3$ corresponding to the set of three contact points is shown in Fig. 2.

- f_i intensity of the wrench at point i
- u_{ix} unit force direction vector along x direction
- u_{iy} unit force direction vector along y direction
- u_{iz} moment vector along z due to unit force vector u_i in the ‘ xy ’ plane
- $f_i w_i$ is the 2 dimensional wrench of the force applied.

For an equilibrium grasp, the sum of all contacting forces and moments acting on the object must be equal to zero as shown in Fig. 3.

The above equation in Fig. 3 can have non-trivial solution if one of the following conditions hold good.

1. The rank of the matrix A , i.e. $r(A) = 2$, or in other words, w_3 is linearly dependent on w_1 and, w_2 or
2. The intersection of the convex hull of w_1, w_2 and the linear hull of w_3 is non-empty as shown in Fig. 3a. i.e. $conv(w_1, w_2) \cap lin(w_3) \neq \emptyset$.
3. If we change the direction of F_3 then the origin of the force and moment space will lie in the interior of the convex hull of w_1, w_2 and w_3 as shown in Fig. 3b. $origin \in intconv(w_1, w_2, w_3)$.

All the three conditions required for a non trivial solution of grasping problems point to the fact that F_3 has to be linearly dependent on F_1 and F_2 . All the conditions satisfy Eq. 1 (Mishra and Silver 1989). Graphically the conditions can be explained as in Fig. 4a, b.

Empirical approaches were taken by Mirtich and Canny (1994), Chinellato et al. (2003), Baker et al. (1985), Ponce and Faverjon (1995) to practically implement a stable grasp using three finger grippers without considering the analytical aspect of a stable grasp. Researchers have focused their attention more on finding out various empirical quality measures for implementing a stable grasp, namely shared features, grasp assessment features and configuration assessment features given below.

- Shared features:
 - Grasping margin:

Contact point farther from the threshold region (λ) extremes the feature implies stable grasp. Stability is defined as $\frac{\lambda}{d_i} - 1$, where d_i is the distance of the contact point from the both the extremes of the contact region.

$$\begin{matrix} \begin{bmatrix} u_{1x} & u_{2x} & u_{3x} \\ u_{1y} & u_{2y} & u_{3y} \\ u_{1z} & u_{2z} & u_{3z} \end{bmatrix} \begin{bmatrix} f_1 \\ f_2 \\ f_3 \end{bmatrix} \\ AX \end{matrix} = \begin{bmatrix} 0 \\ 0 \\ 0 \end{bmatrix} \dots \dots \dots (1)$$

Fig. 3 Force equilibrium acting on a 2D object of arbitrary shape

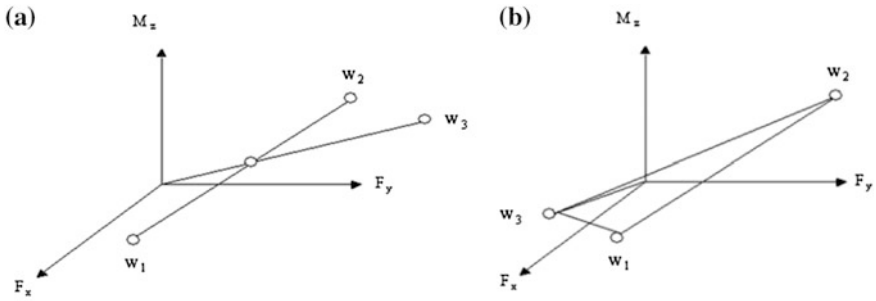


Fig. 4 **a** Non-empty intersection of the convex hull of w_1 and w_2 with the linear hull of w_3 . **b** Location of origin in the interior of the convex hull of w_1 , w_2 and w_3

$$Q_1 = \sum_i q_i; \quad \text{where } q_i = \begin{cases} 0 & \text{where, } d_i \geq \lambda \\ \frac{\lambda}{d_i} - 1 & \text{where, } d_i < \lambda \end{cases}$$

- Grasp Assessment features:

- Force arrangement:

The forces should ideally be aligned at 120° to each other. This gives the most stable grasp. Force arrangement is defined in the following way where $\varphi_1, \varphi_2, \varphi_3$ are included angles among the force directions.

$$Q_2 = \frac{\frac{\pi}{27}}{(\pi - \varphi_1)(\pi - \varphi_2)(\pi - \varphi_3)} - 1$$

- Configuration assessment features:

- Real focus deviation:

This feature measures the deviation of a grasp configuration from the ideal grasp. The measure is defined as follows: where, C_G is the focus of the ideal grasp, C_C is the focus of the real grasp, η is the maximum finger extension, μ is the coefficient of friction.

$$Q_3 = \frac{C_G - C_C}{\eta\mu/2}$$

2 Proposed Methodology

The above approaches have derived complex parameters to define a force closed grasp. In our approach of defining a grasp, we have used an evolutionary soft computing based algorithm namely, genetic algorithm along with parameters which are very elementary in nature. Intuitively when we human beings grasp an object,

1. We do not apply force on the surface of an object so that the object slips out of our hand.
2. We try to envelop the object shape with as much surface area as possible for a good grasp and also try to put our fingers as midway as possible on the surface of the object.
3. At the first instance we try to hold the object in such a manner that the object becomes immobile within the grasp.

The conditions 1 and 3 may appear to be similar, but mathematically speaking they are different. Here we define them in the context of our requirement as follows.

1. Force arrangement:

The directions of forces acting on the surfaces of the object are within the friction angle between the finger material and object material. If any of the grasps is found to violate the definition of force arrangement, that particular grasp is penalized statically.

$$\begin{cases} \tan \alpha \geq 0.3 & \text{unfit} \\ \tan \alpha < 0.3 & \text{fit} \end{cases} \quad \begin{cases} \alpha = \text{deviation of force dir. from surface normal} \\ 0.3 = \text{friction coeff. between the finger and object} \end{cases}$$

2. Grasping margin:

Ideal grasp points are assumed to be in the mid position of the sides assuming the object to be a 2D polygon. A grasp is dynamically penalized based on the extent of deviation of grasp point from the mid points of the sides.

$$\begin{cases} \frac{\Delta l}{l} \times \text{unfit} \\ \frac{\Delta l}{l} < \frac{1}{2} & \text{fit} \end{cases} \quad \begin{cases} \Delta l = \text{deviation of finger contact from mid point of side} \\ l = \text{length of the contacting side} \end{cases}$$

3. Real focus deviation:

The equilibrium grasp is ascertained by checking whether the origin of the wrench space is found inside the wrench triangle or outside. Each grasp is either penalized or not penalized based on this information.

$$\begin{cases} \text{origin} \in \text{int conv}(w_1, w_2, w_3) & \text{fit} \\ \text{otherwise} & \text{unfit} \end{cases}$$

The quantities *fit* and *unfit* have been assigned numerical values in the algorithm.

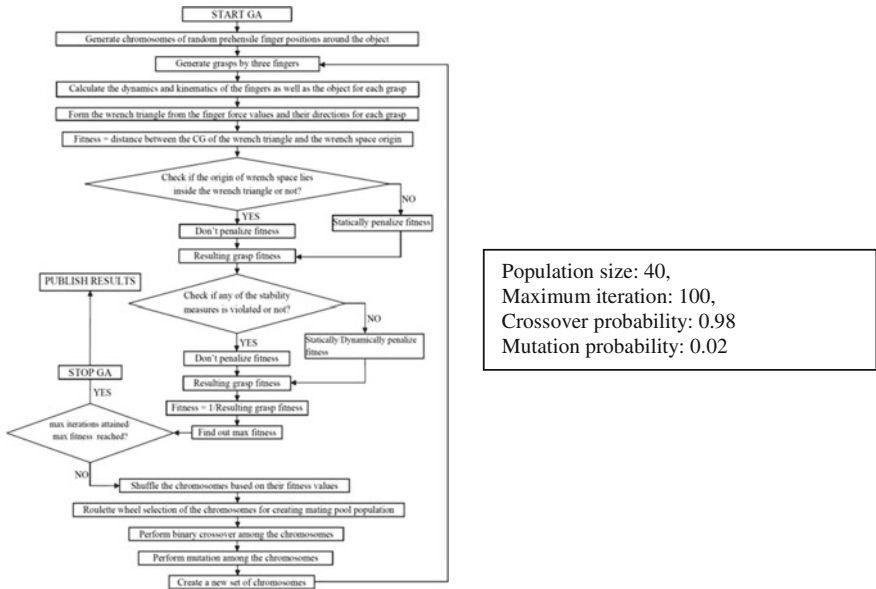


Fig. 5 Flow chart of the developed algorithm and parameters

These conditions henceforth will be called stability measures because these conditions will be responsible for guiding a random process of grasping to the understanding of the process and finding out a feasible grasp. These conditions will also provide a stable grasp. The corresponding follow chart of the proposed algorithm is shown in Fig. 5.

3 Results and Discussions

The goal of this algorithm is to check if the CG of the object after grasping coincides with the CG of the object before grasping or not. The closer the two points are located to each other, the better the grasp is supposed to be. We have experimented with different shapes, with different parameters of the genetic algorithm, obtained through experimentation. The results are given in Fig. 6.

In all the given instances, the algorithm has been found to give satisfactory results. Through evolution of the solutions by the genetic algorithm, it refines the gripping positions to ultimately come out with the optimum result. In all the cases, the same assumptions and genetic algorithm parameters have been used to arrive at the optimum result. Analysis of the genetic algorithm outputs shows that in all the cases it converges very quickly, but the algorithm was run for 100 generations to see if there is any further improvement. It was seen that the computing time increases with the number of sides. One more reason of larger computing time was

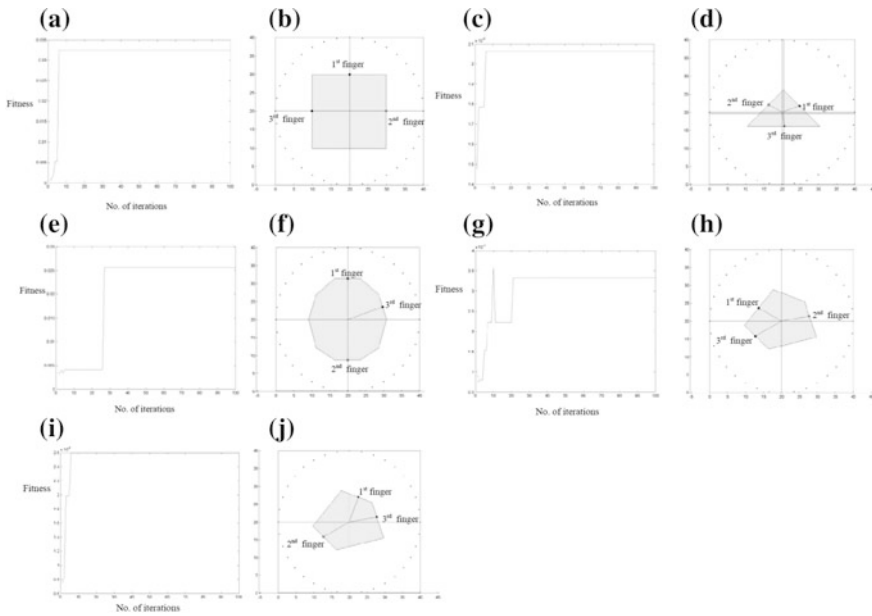


Fig. 6 a, c, e, g and i show the convergence of the genetic algorithm for 100 generations. b, d, f, h and j show the optimal grasping points on the boundary of the 2D objects after 100 generations

that the whole program runs on MATLAB platform in WINDOWS XP operating system. The computing time can be brought down if the whole code is translated in C language.

4 Conclusions

The problem of recognizing a grasp of an object by a robotic gripper requires a definition of the grasp. Most of the above previous approaches found in the literature review had derived complex parameters to define a force closed grasp. In this paper, we have compared different definitions of robotic grasp proposed by different researchers and we have proposed our definition of grasp, and to execute the definition we have used an algorithmic approach based on application of an evolutionary soft computing based algorithm GA along with parameters which are very elementary in nature. The algorithm is found to be a very robust one and can perform satisfactorily for many different types of 2D object shapes. But as most of the 2D shapes encountered in reality are rectangular, triangular or circular, so in that respect its performance is very much acceptable. The main drawback of this algorithm is that the shape vertices are to be input manually to the computer program. In future, it is proposed that an algorithm will be developed that will

approximate the shape of an object from its 2D image with minimum number of straight lines, and the shape vertices will be automatically generated from the approximated image. As the main aim of this work is to find out the prehensile positions of the fingers to grip the object, so the shape approximation will not degenerate the solution accuracy.

References

- Baker, B. S., Fortune, S., & Grosse, E. (1985). Stable prehension with three fingers. In *Proceedings of the 17th Annual Symposium on Theory of Computing*. Providence, RI (pp. 114–120).
- Chinellato, E. et. al. (2003). Ranking planar grasp configurations for a three finger hand. In *IEEE International Conference on Robotics and Automation*. Taipei, Taiwan (pp. 1133–1138).
- Deb, S. R., & Deb, S. (2010). *Robotics technology and flexible automation*. New Delhi: Tata McGraw Hill Education Private Limited, 2nd Edition.
- Mirtich, B., & Canny, J. (1994). Easily computable optimum grasp in 2D and 3D. In *Proceedings of the 1994 IEEE International Conference on Robotics and Automation*. San Diego, CA, May (pp. 739–747).
- Mishra, B., & Silver, N. (1989). Some discussion of static gripping and its stability. *IEEE Transactions on Systems, Man, and Cybernetics*, 19(4).
- Mishra, B., Schwartz, J. T., & Sharir, M. (1987). On the existence and synthesis of multifinger positive grips. *Algorithmica*, 542–558. Springer, New York Inc.
- Nguyen, V. D. (1986). *The synthesis of stable force-closure grasp*. Technical Report 905, MIT Artificial Intelligence Laboratory, Massachusetts Institute of Technology.
- Ponce, J., & Faverjon, B. (1995). On computing three finger force closure grasps of polygonal objects. *IEEE Transactions on Robotics and Automation*, 11(6), 868–881.
- Realeaux, F. (1876). *Kinematics of machinery*. London: Macmillan and Company.
- Tovar, N. A., & Suarez, R. (2014). Searching force-closure optimal grasps of articulated 2D objects with n links. In *19th IFAC World Congress*. Cape Town, South Africa (pp. 9334–9340). August 24–29, 2014.

Developing a GUI for Optimization of Acoustic Enclosure of a Compressor Chamber

T. Ramamohan Rao and S. Kirthana

Abstract Sound can be termed as NOISE when it is beyond the audible frequency. The source of most noise is mainly caused by stationary machines and transportation systems like automotive, aircraft, and trains etc. During the operation of a single compressor, noise is generated which is much above the Environmental Specification Standards. If in a place where more compressors mounted on one place for high pneumatic requirement the noise level is unbearable. Acoustic enclosures are a common solution for the noise reduction of air compressors chamber. The present work develops a user friendly Graphical User Interface (GUI) using MATLAB for designing of acoustic chamber and muffler for a series of compressors chamber. The GUI developed by using the experimental data and acoustic standards. User enters the input values for the Design of Acoustic Enclosure and Muffler in GUI. The program generates two most Cost effective Enclosure and Muffler Configurations satisfying the user requirement of Noise attenuation as output from the GUI.

Keywords Acoustic enclosure · Muffler design · Noise attenuation · GUI

Notation

- W Indicate width of the parallel baffle muffler
- L Indicate length of the muffler
- R_C Indicate cost of glass cloth,
- R_p Indicate cost of perforated plate
- R_w Indicate cost of mineral wool
- R_s Indicate cost of shell plate
- 2d Baffle thickness
- 2h Passes width

T.R. Rao (✉)
Vasavi College of Engineering, Hyderabad 500031, India
e-mail: trmrao@yahoo.com

S. Kirthana
Vidya Jyothi Institute of Technology, Hyderabad, India

c	Velocity of sound
S1	Total area
S2	Flow area
r	Radius of the muffler pile
S_m	Surface area of the hypothetical baffle
S	Surface area of the room
R	Room constant
α	Absorbton coefficient
$L_{P,t}$	Average sound pressure level at different points
$L_{P,i}$	Sound pressure level at insertion
f	Octave band frequency
Db	Decibels
IL	Insertion loss
TL	Transmission loss

1 Introduction

Reduction of noise levels is of greater importance as its prolonged exposure may lead to problems such as headache, increase in blood pressure, loss of concentration, stress, constriction of blood vessels and deterioration in work performance etc. It is advisable and better to consider noise control measures at the design stage itself rather than after the product is manufactured and installed.

Generally, Active and Passive methods of noise control are used to achieve required noise levels. Combined solutions seem to be the most appropriate key to cover the whole frequency range of frequencies (Tiseo et al. 2011).

Active noise control (ANC) is generally used for attenuation of low frequency noise sources. Resonant structures were introduced into the cavities of a honey-comb structure with large cells leading to a material with strong vibration attenuation in a low frequency region (Claeys et al. 2012, 2013; Lemoult et al. 2012). ANC requires expensive hardware software and control systems. It also requires large amounts of engineering time.

Methods of the passive noise control are practical and most effective at mid and high frequencies. When properly designed, a passive method using an acoustic resonator can effectively absorb acoustic energy from a targeted acoustic mode (Li and Viperman 2005, 2006; Lane et al. 2005). Industries use passive noise control for noise suppression by making use of barriers, enclosures made of acoustic material as it is cost effective.

Barriers are preferable when the source of noise is too big to fence it in a structure. Barriers are large wall like structures that break the sound waves from reaching the receiver. Enclosures are generally designed to solve two problems..., either to protect the target from the source or to hold the noise within it. Barrier

effectively works as an Enclosure when the source of noise permits the construction of barriers on all its sides.

The designing of acoustic enclosure and muffler become easier from this work. With this developed GUI the user has to specify the required suppression level of sound in the GUI, and then it will give the design parameters and its cost as the output. Two best design configurations it will provide for Noise attenuation.

2 Theory

A general model for the design of Acoustic Enclosure and Parallel Baffle Muffler considering the sound emitted by the compressor is developed by using the following theoretical approach (Lent 2013; Crocker 2007; Munjal et al. 2006).

2.1 Acoustic Enclosure

Performance of an acoustic enclosure is measured in terms of its insertion loss. Insertion Loss (IL) of the enclosure is always less than Transmission Loss (TL). Partial Enclosures turn out in low IL values for low-frequency sounds, which tend to propagate spherically, easily skirting around the openings. For practical purposes,

$$IL = TL - C, \quad C \equiv -10\log(\bar{\alpha}) \tag{1}$$

where $\bar{\alpha}$ is the overall absorption coefficient.

The values of C for different frequencies are determined by conducting experiments and are listed in Table 1.

Table 1 Values of constant C (Db) to account for enclosure internal acoustic conditions

Octave band center frequency (Hz)	Enclosure internal acoustic conditions			
	Live	Fairly live	Average	Dead
63	18	13	13	11
125	16	12	11	9
250	15	11	9	7
500	14	12	7	6
1000	12	12	5	5
2000	12	12	4	4
4000	12	12	3	3
8000	12	12	3	3

2.2 Parallel Baffle Muffler

Figure 1 shows the parallel baffle muffler with a rectangular duct lined on two sides. The length of the muffler (Z-direction) can be calculated based on the attenuation as specified by the user. It may be noted that the intermediate layer or baffle of thickness '2d' would be servicing both the passages, the left half of it associated with the left passage and the right half with the right passage. One of the important design parameter 'h', defined as

$$h \equiv \frac{\text{cross-section of the flow passage}}{\text{wetted (or lined) perimeter}} \tag{2}$$

For a duct of length 'l', Transmission loss is given by

$$TL = TL_h \times \frac{l}{h} \tag{3}$$

where TL_h is the specific TL of the lined duct of length 'l' equal to 'h'. Transmission loss curves for a parallel baffle muffler are as shown in Fig. 2 (In the X-axis of the graph, 'f' indicates frequency in Hz, 'C₀' is the velocity of sound in air).

3 Formulation for the Design of Acoustic Enclosure and Muffler

The Sound Pressure Level (SPL) at different points for different frequencies around the compressor is measured using Sound Level Meter. The experimental setup to measure the sound intensity at different points surrounded to the compressor setup is shown in Fig. 3.

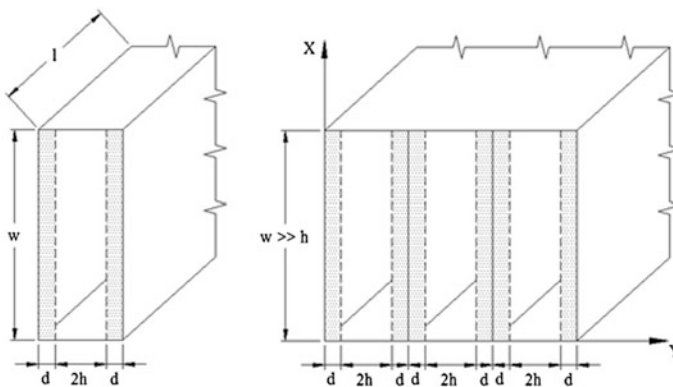


Fig. 1 Parallel baffle muffler with a rectangular duct lined on two sides

Fig. 2 Specific TL of a parallel baffle muffler for various d/h values

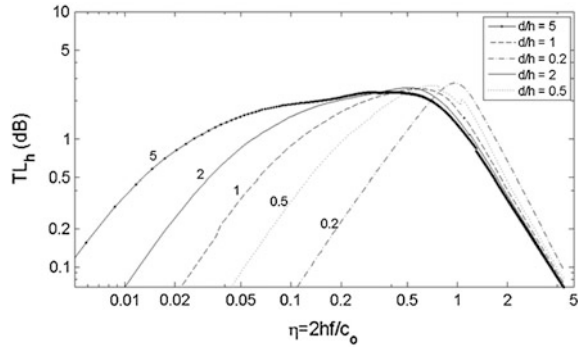


Fig. 3 The experimental setup



These values are stored in a text file. Average SPL at different points around the compressor is found. The formula for finding average SPL is:

$$L_{p,t} = 10 \log \left[\sum_{i=1}^n 10^{0.1 L_{p,i}} \right] \tag{4}$$

where $L_{p,i}$ indicates the SPL for different values of ‘i’.

3.1 Design of Acoustic Enclosure

The overall absorption coefficient for the selected machine condition is found out using the formula:

$$\bar{\alpha} = 10^{(-0.1 * C)} \tag{5}$$

The next important design parameter is to find out Room Constant (R) for the room in which source is located.

Table 2 Transmission loss for different materials

Material/frequency (Hz)	1.5 mm lead sheet	6 mm steel plate	1.6 mm galvanised steel sheet
63	22	25	9
125	28	27	14
250	32	35	21
500	33	41	27
1000	32	39	32
2000	32	39	37
4000	33	46	43
8000	36	46	42

$$R = \frac{S\bar{\alpha}}{1 - \bar{\alpha}} \tag{6}$$

where S indicates the surface area of the room in which the machine has been placed.

There are three materials considered for lining of the acoustic enclosure, namely lead, steel and galvanized steel sheet. The Transmission losses (TL) at different frequencies for these three materials are listed in Table 2.

Insertion loss for these three materials is calculated based on the machine condition selected. The formula for calculating the SPL at distance ‘d’ and code for calculating the average SPL at ‘d’ for various materials is as shown:

$$SPL_{(at\ 'd'\ distance)} = SPL_{(at\ source)} - IL + 10 \log \left[\frac{1}{S_m} + \frac{4}{R} \right] \tag{7}$$

where Sm is the Surface area of the hypothetical parallel piped surface.

Based on the SPL at ‘d’ distance for different materials opted, the selection of the Plate is designed taking cost consideration.

3.2 Design of Parallel Baffle Muffler

There are few important design parameters for the design of parallel baffle muffler.

The first step is to calculate the permissible SPL in each octave band inside the pipe (Lp1) based on the input distance of the Source from the measurement area outside the Muffler ‘R’, Permissible SPL, and diameter of pipe. The equation for calculating the permissible SPL inside the pipe is as follows:

$$Lp_1 = Lp_2 - 10 \log \left[\frac{Area\ of\ pipe}{4\pi r^2} \right] - 10 \log(8) \tag{8}$$

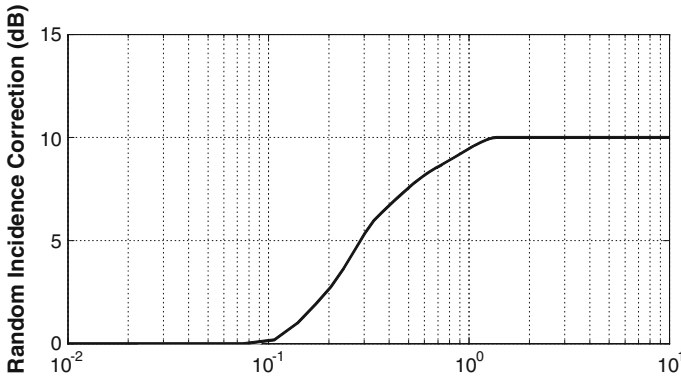


Fig. 4 Figure for finding transmission loss due to random coincidence

The next step involves calculation of transmission loss due to sudden expansion and contraction. For calculation purpose, loss due to sudden expansion and loss due to contraction are treated to be of same value.

$$TL(\text{exp or contr}) = 10 \log \frac{\left(\frac{S_1}{S_2} + 1\right)^2}{\frac{4S_1}{S_2}} \tag{9}$$

where S_1 is the total area and S_2 is the flow area.

Transmission loss due to random incidence can be calculated from the graph given in Fig. 4.

The X-axis of the graph ($\sqrt{S}\lambda$) is calculated using the following two formulas.

$$S = W \ 2h \ n_{\text{passes}}$$

$$\lambda = C/f$$

where, ‘C’ is velocity of sound in air, $C = 346$ m/s. ‘f’ indicate octave band frequency.

The total transmission loss can be obtained by summation of TL due to expansion, TL due to contraction and TL due to random incidence. The total insertion loss that has to be produced by the muffler is the difference of SPL emitted by the compressor and the Total transmission loss. Specific transmission loss can be calculated from the Fig. 2. Using Eq. 3, the dimensions for the length and height of the parallel baffle muffler can be calculated. Selection of the dimensions of the muffler is based on cost calculations. The effective cost of the muffler can be calculated based on the equation given below.

$$\text{Cost of the muffler} = 2n_{\text{passes}} W l (R_c + R_p + dR_w) + 4 W l R_s$$

where, n_{passes} indicate number of passes, W indicate Width of the parallel Baffle Muffler, l indicate length of the muffler, R_C indicate cost of glass cloth, R_p indicate cost of perforated plate, R_w indicate cost of mineral wool, R_s indicate cost of shell plate.

4 Problem Definition

The sound emitted by reciprocating compressor is much above the prescribed level because of the relative motion between moving parts. Even after using various methods for reducing the friction between moving parts, there is no reduction of the amount of decibel level emitted by the compressor. Hence, one of the ways of reduction of exposure of noise by the human operator is making use of Acoustic Enclosure. Current paper suggests a method for design of enclosure along with muffler taking cost and dimensional restrictions into consideration and gives two best possible configurations for the Enclosure and Muffler. If this enclosure can be realized and placed around the compressor, the noise level exposed to the human operator is under the prescribed level or as specified by the user.

4.1 *Developing GUI for the Design of Enclosure and Muffler*

The sound level emitted by the compressor is noted down taking different points around the compressor for various octave band frequencies and stored in a text file. A GUI was developed using MATLAB in which user specifications are entered for the design of Enclosure and Muffler. The GUI frontend window created for this work is as shown in Fig. 5.

MATLAB code is written by keeping the data given in Sects. 1 and 2 and correlated to the GUI created. After user enters all the values and opt the calculate button, a text file will be generated which will contain two best configurations for the enclosure and muffler taking cost and size into consideration as shown in Fig. 6.

5 Results and Discussions

A graph is plot between Octave Frequency Bands and corresponding SPL at distance 'd' for different materials considered for this work. The resulting graph is plotted as shown in Fig. 7.

The Fig. 7 indicates at 63 Hz frequency, steel attenuates more sound, and then followed by lead and then Galvanized steel. Arresting the sound at lower frequency

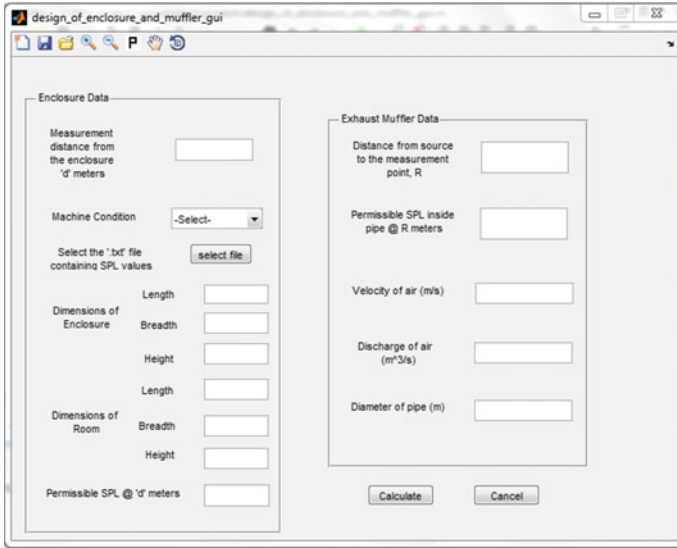


Fig. 5 GUI for the design of acoustic enclosure and muffler

The two most cost effective enclosure & muffler configurations:

```

Configuration 1:
-----
Passage Height, 2h: 0.100m
Baffle Thickness, 2d: 0.100m
Required Length, L: 0.091m
No. of passes, Np: 3.00
Width of the square muffler, W = 0.600m
Relative Cost of Muffler: Rs.417.2459
Relative Cost of Steel Enclosure: Rs.120243.1600
Total Cost: Rs.120660.4059

Configuration 2:
-----
Passage Height, 2h: 0.200m
Baffle Thickness, 2d: 0.200m
Required Length, L: 0.272m
No. of passes, Np: 2.00
Width of the square muffler, W = 0.800m
Relative Cost of Muffler: Rs.1137.9476
Relative Cost of Steel Enclosure: Rs.120243.1600
Total Cost: Rs.121381.1076
    
```

Fig. 6 The out file

is difficult than attenuating the sound at higher frequency. If Resultant SPL is taken into consideration at a distance, the Steel can be taken as the best choice for Acoustic Enclosure. If ease of construction is taken into consideration, Galvanized steel will be the best choice as thickness of galvanized steel (1.6 mm) is very much less than thickness of steel (6 mm).

A graph is plotted between length of the Muffler and cost incurred in building that particular muffler as shown in Fig. 8. It can be noted that the length of the

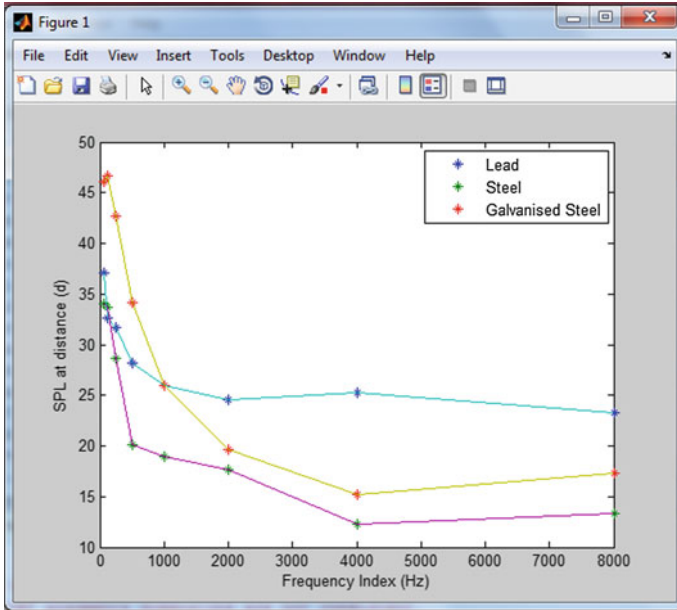


Fig. 7 SPL versus frequency plot

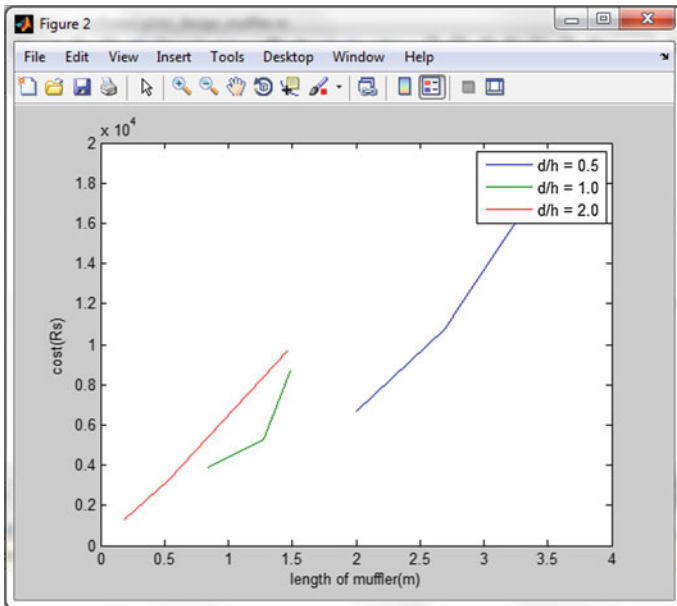


Fig. 8 Length versus cost plot

muffler increases, the cost of the muffler also increases. This is because of the quantity use of sound absorbing materials for increasing length.

From the parametric studies through this work have resulted the Attenuation of sound at lower frequency (larger wave length) is difficult than arresting the sound at higher frequency (smaller wave length). Increase in thickness of the absorbing material will increase the Transmission loss. Increase in diameter of pipe decreases the transmission loss of the pipe. And also Increase in length increases the cost of the muffler.

6 Conclusions

The constructive acoustic model proposed in most of the acoustic text books work well in predicting the insertion loss of noise in rooms. An analytical method for reduction of noise from compressor at a given distance as well as design of Enclosure and Parallel Baffle muffler has been outlined in this paper. The software developed and presented here should be adequate for most typical purposes. The present work has attempted to develop a user-friendly GUI for prediction and control of noise created by the compressors. Through the developed GUI the designer task can be easier and the lead time of design for acoustic chamber and muffler will be reduced.

References

- Claeys, C., Vergote, K., Sas, P., & Desmet, W. (2013). On the potential of tuned resonators to obtain low frequency vibrational stop bands in periodic panels. *Journal of Sound and Vibration*, 332(6), 1418–1436.
- Claeys, C., Vivolo, M., Sas, P., & Desmet, W. (2012). Study of honeycomb panels with local cell resonators to obtain low-frequency vibrational stopbands. In *1st International Conference on Composite Dynamics (DYNACOMP 2012)*.
- Crocker, M. J. (2007). *Handbook of noise and vibration control* (Chap. 56). New York: Wiley.
- Lane, S. A., Richard, R. E., & Kennedy, S. J. (2005). Fairing noise control using tube-shaped resonators. *Journal of Spacecraft and Rockets*, 42, 640–646.
- Lemoult, F., Kaina, N., Fink, M., & Lerosey, G. (2012). Wave propagation control at the deep subwavelength scale in metamaterials. *Nature Physics*, 9, 55–60.
- Lent, C. S. (2013). *Learning to program with MATLAB*. New York: Wiley.
- Li, D., & Vipperman, J. S. (2006). Noise control of mock-scale ChamberCore payload fairing using integrated acoustic resonators. *Journal of Spacecraft and Rockets*, 43, 877–882.
- Li, D., & Vipperman, J. S. (2005). On the noise transmission and control for a cylindrical Chamber Core composite structure. *Journal of Sound and Vibration*, 288, 235–254.
- Munjal, M. L., Galaitsis, A. G., & Ver, I. L. (2006). Passive silencers. In I. L. Ver & L. L. Beranek (Eds.), *Noise and vibration control engineering* (Chap. 9). New York: Wiley.
- Tiseo, B., Concilio, A., Gianvito, A., & Ameduri, S. (2011). Experimental characterization of hybrid noise control systems acting in acoustic duct. *Journal of Theoretical and Applied Mechanics*, 49(2), 313–326.

A Pilot Study of Sustainable Machining Process Design in Indian Process Industry

Sumit Gupta, G.S. Dangayach, Amit Kumar Singh and P.N. Rao

Abstract This paper aim to conduct a pilot study in India process industry for sustainable machining process design. A survey questionnaire was framed at five point likert type scale. Respondents were asked to five elements related to sustainable machining process design (SMPD) Fifty responses was collected from various process industries. Simple statistics mean, standard deviation, correlation and t test is applied for the analyse survey responses. It is evident that the Energy efficiency during the process, Vegetable based cutting fluid and machining process utilisation are more emphasised by the companies and the other factors like Waste minimization and cryogenic machining require more focused on it. One sample t test it is evident that Energy efficiency during the process (SMPD5) ($t = 6.194$) is the most important factor which is highly adopted by the process industry in practice.

Keywords Vegetable cutting fluid • Waste management • Energy efficiency

1 Introduction

The manufacturing process used to actually produce the product utilizes a large amount of resources and generates a large amount of emissions and waste that leads to environmental pollution in an enterprise. To reduce the environmental impacts of

S. Gupta (✉) · G.S. Dangayach · A.K. Singh
Department of Mechanical Engineering, Malaviya National Institute of Technology,
Jaipur 302017, India
e-mail: Sumitgupta2007@gmail.com

G.S. Dangayach
e-mail: Dangayach@gmail.com

A.K. Singh
e-mail: asmnitj@gmail.com

P.N. Rao
Department of Technology, University of Northern Iowa, Cedar Falls
IA 50614-0178, USA
e-mail: posinasetti@gmail.com

manufacturing processes we need to put more emphasis on the machining process design. The machining cost, environmental impact and operators' health concerns have driven researchers to find alternatives such as Minimum Quantity Lubrication (MQL) or equivalent dry cutting conditions that could satisfy the machining requirements without the use of cutting fluids. It is reported by Klocke and Eisenblatter that in Germany alone in 1994 it were estimated that 350,000 tonnes of cutting fluids were processed and subsequently disposed of.

It is also estimated that cutting fluids cost 7–17 % of the manufacturing cost of components when associated costs of monitoring, maintenance, health precautions and absenteeism are taken into account in the German automotive industry compared to the tool costs that are quoted as being 2–4 %. The cost of purchasing and disposing coolant is about one billion German Mark. The Objectives of this paper are to evaluate the sustainable machining processes in the process industry in India.

This research is based on the empirical investigation of sustainable machining process design in process Industry. In the process industry, it was observed that there was huge amount of machining waste was developed and the processes was exhausted. To overcome this problem the concept of sustainability was introduce. The objective of this research is to identify the various sustainable machining process design practice from the literature and empirically validated and suggested best practices for SMPD.

2 Literature Review

Machining process design is an important part of sustainable processes. If we talking about the sustainability then it is understood the we are focusing on the utilization resources and minimization of energy. In the literature there are lots of work has been done on the sustainable machining process by the various researchers (Belluco and De Chiffre 2002, 2004; Khan and Dhar 2006; Maleque et al. 2003; Gupta et al. 2015a, b).

2.1 *Vegetable Based Cutting Fluid (SMPDI)*

Vegetable based cutting fluids are more expensive compared to the conventional cutting fluids. In order to justify the use vegetable based cutting fluids it is necessary to include the life cycle costs of the use of cutting fluids. For this purpose it is necessary to establish the various costs that will be incurred during the total life cycle of the cutting fluid. Identify all the costs during the life cycle and develop a realistic cutting fluid cost model (Khan et al. 2006).

2.2 Utilization of Cryogenic Machining (SMPD2)

Cryogenic Machining provide individual machines or large-scale utilization. Specially designed tooling and tool holders make retrofitting existing machines easy, reduce downtime for implementation and eliminate the need to invest in new machines to take advantage of advanced cooling techniques (Maleque 2003). Cryogenic machining provides a better solution for marching of part faster as compare to others. Cryogenic machining increases the quality products, increases machining performance and the overall cost of the product (Yildiz and Nalbant 2008).

2.3 Machining Process Utilisation (SMPD3)

Machining process utilisation is one of the valuable factors for achieving sustainability. The utilisation of machining process for finishing of component is frequently overlooked by the management. The proper utilisation of machine leads to produce high standard products and decreases the low maintenance of machine (Konopka and Trybula 1996). The main role of machines is meant to work efficiently and effectively without interrupting the production process. The top management in the industry highly focus on the machine should be work in a proper manner without any shutdown (Khan and Dhar 2006). It is seen that in some many circumstances machines can be less productive due to improper preventive maintenance; in this case it is highly recommended that the machine should be checked at a proper time.

2.4 Waste Minimization (SMPD4)

Waste minimization usually beneficial for producer and customer with respect to costs minimization and environmental performance. For sustainability in manufacturing, waste minimization is a prominent factor (Gupta et al. 2015a). Different type of Wastes is associated with machining process which is directly affected to Environmental. Waste minimization during the process is very important due to increasingly stringent regulations on health and safety. The importance of manufacturing wastes on the product life cycle, emerging international standards on environmental performance, and a growing consumer preference for green products is highly recommended (Srinivasan and Sheng 1999).

2.5 Energy Efficiency During the Process (SMPD5)

In manufacturing industries, energy efficiency in machining processes is essential for effective response to competition and the desire for increasing product quality in the market. Energy efficiency provides the base for sustainable development. Energy efficiency in metal cutting processes depend on the machine tool, cutting tool, work piece and cutting process parameters such as feed rate, depth of cut, cutting speed and cutting tool geometry (Quintana and Ciurana 2011). However, determination of optimal cutting conditions is fairly complex process and over the years, a number of techniques of modelling and optimization have been developed. Many researchers working on in the field of reduction in the energy during machining process. It is an emerging field for the research.

3 Research Methodology

Based on literature the various factors of sustainable machining process design (SMPD) are identified as discussed in Sect. 2. This study is conducted in process industry. The survey questionnaire has been send to 250 industries for the response. The questionnaire was form on five Point Likert-type scales to collect the responses. Out of 250 sent questionnaire 50 valid and full filled questionnaires were received.

A reliability test was performed to examine the research findings have the ability to provide consistent results. The Cronbach's alpha was calculated to measure the internal consistency of the research instrument. A commonly used value for reliability in the literature is 0.70 (Nunnally 1978). The coefficients alpha for all the factors were calculated 0.78 which means that the reliability of factors up to the mark. For the pilot study, the instrument was improved and validated. The data has been tested on SPSS 17.0.

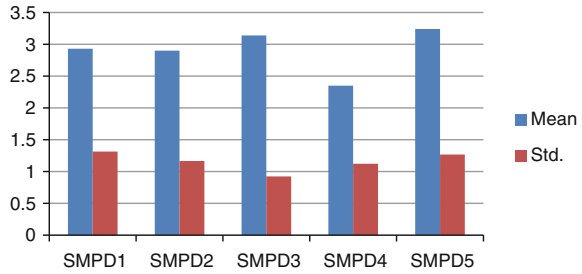
4 Data Collection and Analysis

The data was collected from the 50 process industries for pilot study. Table 1 and Figure 1 shows that most effective factor sustainable machining process design. In process industries Energy efficiency during the process (SMPD5) and machining

Table 1 Mean scores for SMPD factors

Factors	Mean	Std. deviation
SMPD1	2.93	1.314
SMPD2	2.90	1.165
SMPD3	3.14	0.923
SMPD4	2.35	1.122
SMPD5	3.24	1.268

Fig. 1 Mean score for SMPD factors



process utilisation (SMPD3), (Mean 3.24 and 3.14 respectively) is the main effective factors in SMPD. While Vegetable based cutting fluid (SMPD1), Utilization of cryogenic machining (SMPD2) and Waste minimization (SMPD4) are less in practice. It is evident to top management to put more emphasis on these factors to achieving sustainability.

Table 2 shows the correlation between five different factors sustainable machining process design. All are significantly correlated ($p \leq 0.05$) with other factors. The correlations show that the process industries in the survey are strongly emphasizing on these factors and strongly correlated.

Table 3 for one sample t test it is evident that Energy efficiency during the process (SMPD5) ($t = 6.194$) is the most important factor which is highly adopted by the process industry in practice.

Table 2 Correlation between SMPD factors

	SMPD1	SMPD2	SMPD3	SMPD4	SMPD5
SMPD1	1	–	–	–	–
SMPD2	0.344 ^b	1	–	–	–
SMPD3	0.378 ^b	0.352 ^b	1	–	–
SMPD4	0.232 ^b	0.316 ^b	0.125	1	–
SMPD5	0.548 ^b	0.398 ^b	0.245 ^b	0.518 ^b	1

^bCorrelation is significant at the 0.01 level (2-tailed)

Table 3 One sample t test for SMPD factors

	Test value = 3					
	t	df	Sig. (2-tailed)	Mean difference	95 % Confidence interval of the difference	
					Lower	Upper
SMPD1	1.787	50	0.082	-0.196	-0.44	0.04
SMPD2	2.867	50	0.003	-0.264	-0.43	-0.08
SMPD3	2.219	50	0.033	-0.176	-0.30	-0.09
SMPD4	5.936	50	0.225	-0.644	-0.93	-0.65
SMPD5	6.194	50	0.787	-0.020	-0.22	0.19

Sustainable machining process design is a prominent contract for achieving sustainability in manufacturing. All five factors are important for SMPD as literature suggested. Our results also suggest that the factors Vegetable based cutting fluid (SMPD1), Energy efficiency during the process (SMPD5) and machining process utilisation (SMPD3) are more adopted by the companies.

5 Conclusion

Sustainable machining process design (SMPD) is the important practice of sustainable manufacturing. The study is conducted in the Indian process industry through survey responses. Total 50 responses were chosen for pilot study. The five factors of SMPD were ranked by the respondents. The survey responses were analysed by SPSS 17. In this study, it is found that the energy efficiency, machining process utilisation and use of vegetable cutting fluid are highly rated by the respondent's means these elements are more in practice while on the other hand the waste minimization and cryogenic machining are less in practice.

This study is conducted only in process industry further the study may be carried out in automobile, machinery, electrical and electronics and other manufacturing industry.

References

- Belluco, W., & De Chiffre, L. (2002). Surface integrity and part accuracy in reaming and tapping stainless steel with new vegetable based cutting oils. *Tribology International*, 35(12), 865–870.
- Belluco, W., & De Chiffre, L. (2004). Performance evaluation of vegetable-based oils in drilling austenitic stainless steel. *Journal of Materials Processing Technology*, 148(2), 171–176.
- Gupta, S., Dangayach, G. S., & Singh, A. K. (2015a) Key determinants of sustainable product design and manufacturing. *Procedia CIRP*, 26, 99–102.
- Gupta, S., Dangayach, G. S., Singh, A. K., & Rao, P. N. (2015b) Analytic Hierarchy Process (AHP) Model for Evaluating Sustainable Manufacturing Practices in Indian Electrical Panel Industries. *Procedia-Social and Behavioral Sciences* 189, 208–216.
- Khan, M. M. A., & Dhar, N. R. (2006). Performance evaluation of minimum quantity lubrication by vegetable oil in terms of cutting force, cutting zone temperature, tool wear, job dimension and surface finish in turning AISI-1060 steel. *Journal of Zhejiang University: Science*, 7, 11.
- Konopka, J., & Trybula, W. (1996) Overall equipment effectiveness (OEE) and cost measurement semiconductor manufacturing. In *Nineteenth IEEE/CPMT Electronics Manufacturing Technology Symposium*, pp. 137–140.
- Maleque, M. A., Masjuki, H. H., & Supuan, S. M. (2003). Vegetable-based biodegradable lubricating oil additives. *Industrial lubrication and Tribology*, 55, 137–143.
- Nunnally, J. C. (1978). *Psychometric theory*. New York: McGraw-Hill.

- Quintana, G., & Ciurana, J. (2011). Chatter in machining processes: A review. *International Journal of Machine Tools & Manufacture*, 51, 363–376.
- Srinivasan, M., & Sheng, P. (1999). Feature-based process planning for environmentally conscious machining Part1: Micro planning. *Robotics and Computer Integrated Manufacturing*, 15.
- Yildiz, Y., & Nalbant, M. (2008). A review of cryogenic cooling in machining processes. *International Journal of Machine Tools and Manufacture*, 48(9), 947–964.

Sagittal Position Analysis of Gait Cycle for a Five Link Biped Robot

Ramanpreet Singh, Himanshu Chaudhary and Amit Kumar Singh

Abstract It is difficult to comprehend the humanoid walking trajectory due to large number of degrees of freedom during walking. This paper treats the trajectory planning for steady walking of planar 5 link biped robot on a leveled ground for single support phase and double support phase. To obtain smooth and continuous walking trajectory polynomial interpolation has been used for hip and swing limb, and polynomial coefficients are determined through constraint equations. A Double support phase (DSP) is generally neglected in gait synthesis at high walking speeds but for stable biped model with moderate walking speeds DSP must be considered. In this article geometric approach of inverse kinematic is used for generation of joint trajectories in single and double support phase. Effects of the proposed method (inverse kinematic for double support phase) are illustrated by computer simulations.

Keywords Sagittal gait · Biped robot · Synthesis · Inverse kinematics · Polynomial interpolation · Single support phase · Double support phase

1 Introduction

Biped robots are the class of walking machines that imitate the human locomotion (Tzafestas et al. 1996) when moving on rugged terrain, steep slopes, flat path with obstacles and industrial fields. It has always been mesmerizing for man to create mechanical system in his own image. Since 18th century (Chevallereau et al. 2009) the researchers has been working in this area which resulted in the creation of bipeds from Leonardo da Vinci humanoid robot to ASIMO, HONDA, SONY, iROBOT etc. Locomotion is an important aspect for bipeds and its trajectory planning would be required under different situations. Alternating repetition of same elementary

R. Singh (✉) · H. Chaudhary · A.K. Singh
Malviya National Institute of Technology, JLN Marg, Jaipur, India
e-mail: ramanpreet.gurudutta@hotmail.com

movement from one leg to another is walking. Biped is expected to walk on leveled ground, inclined, rough plane etc. Walking step is composed of two kinematically distinct phases: swing phase or single support phase (SSP) and double support phase (DSP) (Chevallereau et al. 2009). Most of the previous studies (Haghighi et al. 2011) considered walking pattern in SSP while DSP is usually neglected. DSP over wide range of walking speeds makes the biped walk stable.

Several studies focused on the five and/or seven link biped walking pattern for SSP and DSP. Walking trajectory generation is one of an important issue related to bipedal robots. The trajectory can be generated based on dynamic model (Arous and Boubaker 2012). It has observed that polynomial interpolations are used for foot trajectories. But under several constraints, polynomial order is too high and computation is difficult (Thant and Aye 2009). Alternatively, taking polynomial trajectory, its coefficients can be obtained by optimization methods under prescribed constraints. Cubic spline polynomial interpolation and cubic hermite polynomial interpolation (Haghighi and Nekoui 2011) are popularly used for foot and hip trajectory. Planar five link biped is decoupled into three sub-systems (Mu and Wu 2004 and Mu and Wu 2003). Cubic and quintic polynomials are used for foot coordinates and cubic polynomials for hip coordinates in SSP and DSP and inverse kinematics is used for determining the joint coordinates. Foot trajectories may be planned considering three phases starting step, steady walking and walking from start to steady (Lum et al. 1999) followed by inverse kinematics to obtain the joint trajectories. Among others, Vandermonde matrix interpolation method or third order spline may be used (Mousavi and Bagheri 2007) for generating smooth desired trajectory.

From the literature on sagittal five links bipedal robot it is observed that polynomial interpolation is mostly used for the determination of foot and hip trajectory. Method of mapping the foot and hip trajectory to joints trajectory is presented in complex form (Mu and Wu 2004). The objective of this paper is to propose a method for planar five links biped model to obtain the joint trajectories in DSP. Third order polynomial and fifth order polynomial are considered as the coordinates of swing limb. Constraints equations are developed in order to solve the swing limb trajectory. Third order polynomials in SSP and DSP are considered and constraint equations are developed for solving the hip trajectory. Biped joint profiles are obtained by using the inverse kinematics (geometric solution approach (Saha 2014)) for SSP and DSP, which is presented in elaborated form in this study.

This paper is organised as follows. Section 2 describes the gait cycle, constraint formulation for foot and hip in SSP and DSP, and trajectory generation method. Mapping of the foot cartesian coordinates to joint coordinates (complete joint trajectory) is given in Sect. 3. Section 4 discusses the numerical example of trajectory followed by bipedal robot for a complete gait cycle. Finally, conclusions are given in Sect. 5.

2 Trajectory Generation

2.1 Science of Walking

A five link planar biped model as shown in Fig. 1 is taken for sagittal position analysis. All the joints between the links are pinned joints and are actuated.

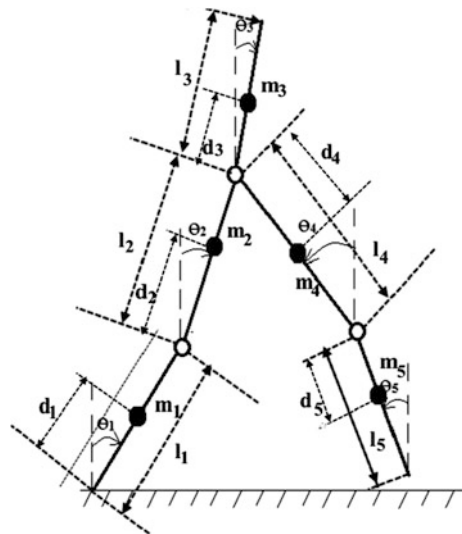
Each walking step is divided in two kinematically distinct phases SSP and DSP as shown in Fig. 2. SSP is the single support phase which begins with the movement of one limb (swing) in forward direction while another limb (stance) is pivoted on the ground and terminates with the tip of the swing limb touching the ground. DSP is the double support phase which begins when the heel of the swing limb strike the ground while stance limb being on the ground. In the subsequent step the support exchange takes place. Swing limb and hip trajectories are required for obtaining the biped joint profiles (Haghighi et al. 2011; Mu et al. 2004). These trajectories must satisfy configuration of the biped.

2.2 Foot Trajectory

For a planar five link biped robot, trajectory of swing limb during SSP can be generated using polynomial interpolation as:

$$\begin{aligned} x_a(t) &= a_0 + a_1t + a_2t^2 + a_3t^3 \\ y_a(t) &= b_0 + b_1t + b_2t^2 + b_3t^3 + b_4t^4 + b_5t^5 \quad \text{for } 0 \leq t \leq T_s \end{aligned} \tag{1}$$

Fig. 1 Five link biped



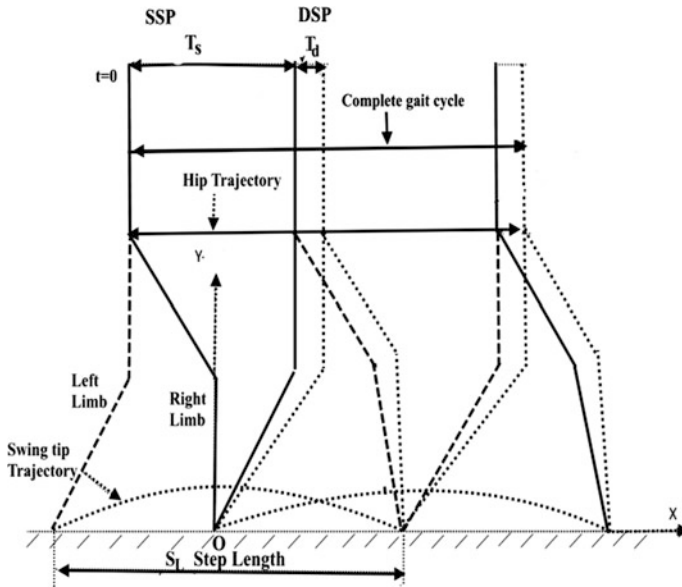


Fig. 2 Complete gait cycle

where $x_a(t)$ and $y_a(t)$ are coordinates of the tip of the swing limb at time t . The SSP will finish at $t = T_s$. Origin of coordinate frame is fixed at the tip of the supporting limb.

There is a total of ten unknown coefficients a_0, a_1, \dots, a_3 and b_0, b_1, \dots, b_5 . Therefore ten constraint equations are required to find them. In SSP, phase begins with lift off of the tip of swing limb and ends when it lands back on the ground. Mathematical constraint relations (Xiuping Mu and Qiong Wu 2004) are as follows:

Geometrical constraints:

$$y_a(0) = 0 \tag{2}$$

$$y_a(T_s) = 0 \tag{3}$$

Maximum clearance of swing limb from ground:

$$y_a(T_m) = H_m \tag{4}$$

$$\dot{y}_a(T_m) = 0 \tag{5}$$

$$x_a(T_m) = S_m \tag{6}$$

Minimizing impact effect:

$$\dot{y}_a(T_s) = 0 \quad (7)$$

$$\dot{x}_a(T_s) = 0 \quad (8)$$

Gait repeatability:

$$x_a(0) = -\frac{S_L}{2} \quad (9)$$

$$x_a(T_s) = \frac{S_L}{2} \quad (10)$$

$$\dot{x}_a(0) = 0 \quad (11)$$

$$\dot{y}_a(0) = 0 \quad (12)$$

where T_m is the time instant when tip of the swing limb reaches to maximum clearance from ground, H_m is the maximum clearance (y axis) of swing limb from ground, S_m is the location of maximum clearance (x axis) and S_L is the step length.

The above Eqs. (2)–(12) can be used for determining polynomial coefficients which are as follows:

$$a_0 = -0.36, a_1 = 0, a_2 = 6, a_3 = -6.667 \\ b_0 = 0, b_1 = 0, b_2 = 2.22, b_3 = -7.4074, b_4 = 6.1728, b_5 = 0$$

2.3 Hip Trajectory

Hip trajectory plays a significant role on biped stability. Hip trajectory is designed separately for SSP and DSP. A third order polynomial is used to define its x-coordinate while y-coordinate maintains constant. Thus trajectory of hip in SSP and DSP are as follows:

$$x_{hs}(t) = c_0 + c_1t + c_2t^2 + c_3t^3; \quad 0 \leq t \leq T_s \quad (13)$$

$$x_{hd}(t) = d_0 + d_1t + d_2t^2 + d_3t^3; \quad 0 \leq t \leq T_d \quad (14)$$

$$y_{hs}(t) = H_h; \quad 0 \leq t \leq T_s \quad (15)$$

$$y_{hd}(t) = H_h; \quad 0 \leq t \leq T_d \quad (16)$$

At time t , x_{hs} and x_{hd} denote x coordinates of hip during SSP and DSP, respectively, whereas y_{hs} and y_{hd} are y-coordinates. There are 8 unknown

polynomial coefficients c_0, c_1, c_2 and c_3 in Eq. (13) and d_0, d_1, d_2 and d_3 in Eq. (14). H_h is the height of hip which is kept constant for whole gait cycle. Mathematically, the constraints (Mu and Wu 2004) are presented as follows:

Gait repeatability (SSP and DSP):

$$x_{hs}(0) = -S_{so} \quad (17)$$

$$\dot{x}_{hs}(0) = V_{h1} \quad (18)$$

$$\dot{x}_{hd}(T_d) = V_{h1} \quad (19)$$

$$x_{hd}(T_d) = 0.5S_L - S_{so} \quad (20)$$

Gait continuity (SSP and DSP):

$$x_{hd}(0) = S_{d0} \quad (21)$$

$$x_{hs}(T_s) = S_{do} \quad (22)$$

$$\dot{x}_{hs}(T_s) = V_{h2} \quad (23)$$

$$\dot{x}_{hd}(0) = V_{h2} \quad (24)$$

where S_{so} and S_{do} represents position of the hip at the beginning of SSP and DSP respectively. The above Eqs. (17)–(24) can be used for determining unknown polynomial coefficients which are as follows:

$$\begin{aligned} c_0 &= -0.18, & c_1 &= 0.4, & c_2 &= 1.1667, & c_3 &= -1.3889 \\ d_0 &= 0.18, & d_1 &= 0.3, & d_2 &= 0.8, & d_3 &= -2.0 \end{aligned}$$

3 Joint Profile Generation

The joint angle profiles can be derived from designed trajectories of swing limb and hip using geometric solution approach of inverse kinematics.

3.1 Joint Trajectory in DSP

Simple geometric relations are desired for the SSP and DSP which are presented in Table 1.

Where all the notations are defined in Fig. 3 and similar diagram can be used for modeling in SSP. The above method is useful for generating the joint trajectory for steady walking on leveled ground.

Table 1 SSP and DSP geometric realtions

SSP (Haghighi H. R Elahi and Nekoui M.A)	DSP
<i>For Swing Leg</i>	<i>For Swing Leg</i>
$x_{coordinate} = x_{hs}$ $y_{coordinate} = y_{hs}$ $L_s^2 = x_{hs}^2 + y_{hs}^2$ $\gamma_1 = \tan^{-1} \frac{x_{hs}}{y_{hs}}$ $\beta_1 = \sin^{-1} \frac{l_2 \sin \alpha}{L_s}$ $\alpha_1 = \cos^{-1} \frac{-L_s^2 + l_1^2 + l_2^2}{2l_1 l_2}$ $\theta_2 = \gamma_1 - \beta_1$ $\theta_1 = \theta_2 + \pi - \alpha_1$ $\theta_3 = 0$	$x_{diffs} = x_{hd}$ $y_{diffs} = y_{hs}$ $L_{ds} = \sqrt{x_{diffs}^2 + y_{diffs}^2}$ $\gamma_{ds} = \tan^{-1} \frac{x_{hd}}{y_{hs}}$ $\beta_{ds} = \cos^{-1} \frac{L_s^2 + l_2^2 - l_1^2}{2L_{ds} l_2}$ $\alpha_{ds} = \cos^{-1} \frac{-L_{ds}^2 + l_1^2 + l_2^2}{2l_2 l_1}$ $\theta_{2d} = \gamma_{ds} - \beta_{ds}$ $\theta_{1d} = \theta_{2d} + (\pi - \alpha_{ds})$ $\theta_{3d} = 0$
<i>For Support Leg</i>	<i>For Support Leg</i>
$x_{diff} = x_a - x_{hs}$ $y_{diff} = y_{hs} - y_a$ $L_p^2 = x_{diff}^2 + y_{diff}^2$ $\gamma_2 = \tan^{-1} \frac{x_{diff}}{y_{diff}}$ $\beta_2 = \sin^{-1} \frac{l_5 \sin \alpha_2}{L_p}$ $\alpha_2 = \cos^{-1} \frac{-L_p^2 + l_4^2 + l_5^2}{2l_4 l_5}$ $\theta_4 = \gamma_2 + \beta_2$ $\theta_5 = \theta_4 - (\pi - \alpha_2)$	$x_{diffdsp} = 0.5S_L - x_{hd}$ $y_{diffdsp} = y_{hs}$ $L_{dsp} = \sqrt{x_{diffdsp}^2 + y_{diffdsp}^2}$ $\gamma_{dsp} = \tan^{-1} \frac{x_{diffdsp}}{y_{diffdsp}}$ $\beta_{dsp} = \cos^{-1} \frac{L_{dsp}^2 + l_4^2 - l_5^2}{2L_{dsp} l_4}$ $\alpha_{dsp} = \cos^{-1} \frac{-L_{dsp}^2 + l_4^2 + l_5^2}{2l_4 l_5}$ $\theta_{4d} = \gamma_{dsp} + \beta_{dsp}$ $\theta_{5d} = \theta_{4d} - (\pi - \alpha_{dsp})$

4 Numerical Example

A planar five link biped model is used here for sagittal position analysis. The values physical parameters (links) of biped are $l_1 = 0.332$, $l_2 = 0.302$, $l_3 = 0.486$, $l_4 = 0.302$, $l_5 = 0.332$, $d_1 = 0.189$, $d_2 = 0.236$, $d_3 = 0.282$, $d_4 = 0.236$, $d_5 = 0.189$. All dimensions are in meter. While other variables are $S_L = 0.72$, $T_s = 0.6$, $T_d = 0.1$, $H_m = 0.05$, $S_m = 0$, $T_m = 0.3$, $H_h = 0.575$, $S_{so} = 0.18$, $S_{do} = 0.18$. Several hip trajectories corresponding to V_{h1} and V_{h2} are obtained and two are shown in Fig. 4. From the series of values of V_{h1} and V_{h2} , those values are selected for which smooth hip trajectory is obtained in SSP and DSP. The smooth hip trajectory shown in Fig. 5 is obtained when $V_{h1} = 0.4$ and $V_{h2} = 0.3$. This smooth trajectory is selected for deriving the joint profiles.

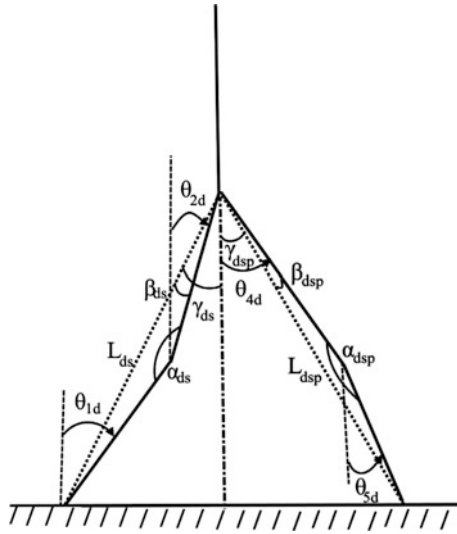


Fig. 3 Various definitions for five link biped in DSP

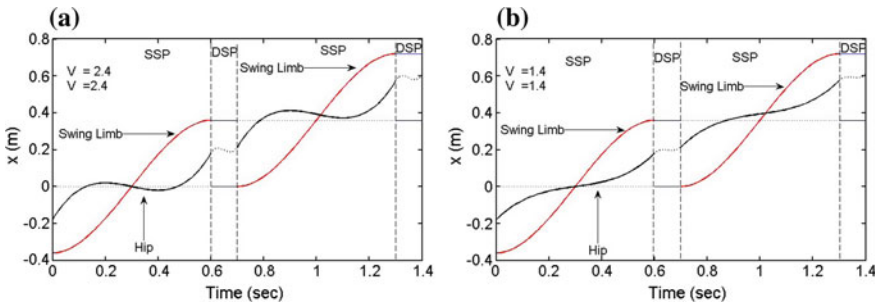
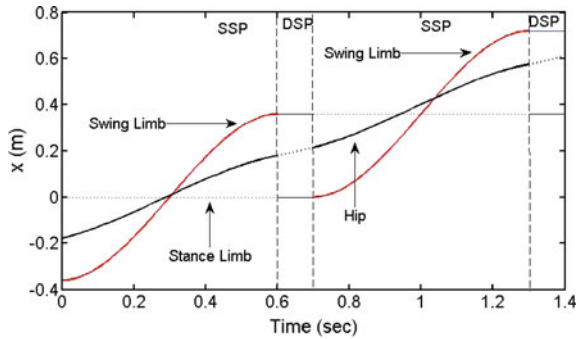


Fig. 4 x-displacement of hip and feet. a When $V_{h1} = V_{h2} = 2.4$ m/s. b When $V_{h1} = V_{h2} = 1.4$ m/s

Fig. 5 Hip and lower limb trajectories when $V_{h1} = 0.4$ and $V_{h2} = 0.3$ m/s



5 Discussion

The horizontal displacements of hip, swing limb tip and stance limb with respect to time is shown in Fig. 5. Figure 6 shows the path traced by the left and right limb for complete gait cycle. Joint profiles derived by inverse kinematics for all the joints are shown in Fig. 7. It is observed from Fig. 7 that trajectories are smooth and repeatable. Figure 8 shows the stick diagram of 5 link bipedal robot. It shows the

Fig. 6 Lower limb trajectories

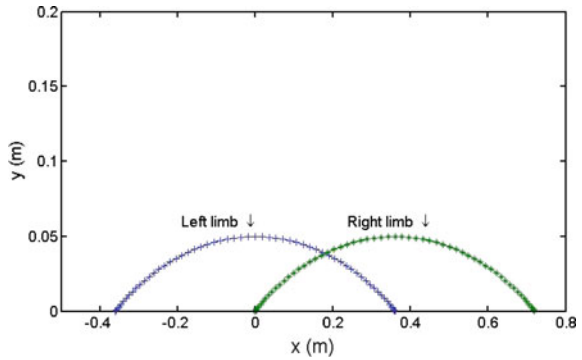


Fig. 7 Joint angle profiles

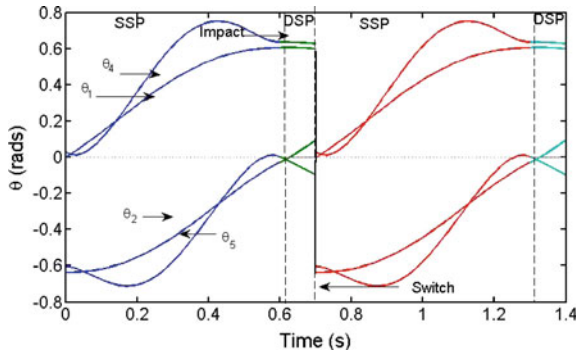
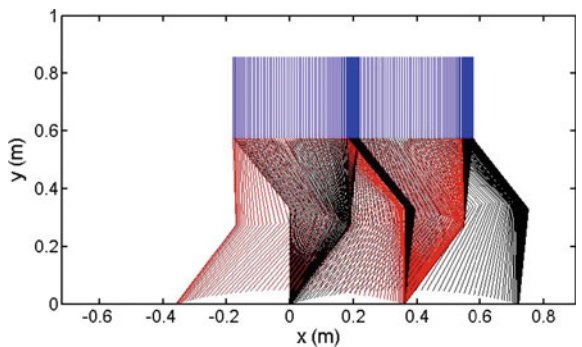


Fig. 8 Stick diagram



overall motion of biped for one complete gait cycle. Torso is represented by blue colour, red colour represents left limb and right limb is represented by black colour, it is observed that initial and final posture of biped are same.

6 Conclusion

This paper presents systematic geometrical method for determining joints angle profiles for a five link bipedal robot with attention being focused on DSP. As most of the previous works have focused on SSP and DSP is often neglected. This model includes both SSP and DSP but only DSP diagram is used to explain geometric relations. To demonstrate the effectiveness of this method computer simulation was carried out. It was found that gait pattern appears natural. This research provides a tool for generating walking patterns. This work can be extended to a 7 link model on different planes with stability check.

References

- Arous, Y., & Boubaker, O. (2012). A model for surface roughness in ultra precision hard turning. In *16th IEEE Mediterranean Electrotechnical Conference (MELECON)*, Yasmine Hammamet, Tunisia.
- Chevallereau, C., Bessonnet, G., Abba, G., & Aoustin, Y. (2009). *Bipedal Robots: Modeling Design and Walking Synthesis*. Great Britain and United States, ISTE Ltd. and Wiley, Inc.
- Haghighi, H. R. E., & Nekoui, M. A. (2011). Inverse kinematics for an 8 degrees of freedom biped robot based on cubic polynomial trajectory generation. In *2nd International Conference on Control, Instrumentation and Automation (ICCIA)*. Univeristy of Shiraz, Shiraz, Iran: IEEE.
- Lum, H. K., Zribi, M., & Soh, Y. C. (1999). Planning and control of a biped robot. *International Journal of Engineering Science*, 37, 1319–1349.
- Mousavi, N. P., & Bagheri, A. (2007). Mathematical simulation of a seven link biped robot on various surfaces and ZMP considerations. *Applied Mathematical Modelling*, 31, 18–37.
- Mu, X., & Wu, Q. (2003). Synthesis of a complete sagittal gait cycle for a five-link biped robot. *Robotica*, 21, 581–587.
- Mu, X., & Wu, X. (2004). Sagittal gait synthesis for a five link biped robot. In *Proceedings of the American Control Conference*, Boston, Massachusetts.
- Saha, S. K. (2014). Introduction to robotics. New Delhi: McGraw Hill Education (India) Private Limited.
- Thant, A. A., & Aye, K. K. (2009). Application of cubic spline interpolation to walking patterns of biped robot. *Proceedings of World Academy of Science: Engineering & Technolog*, 50.
- Tzafestas, S., Raibert, M., & Tzafestas, C. (1996). Robust sliding mode control applied to a 5-link biped robot. *Journal of Intelligent and Robotic Systems*, 15, 67–133.

A Note on Mechanical Feasibility Predicate for Robotic Assembly Sequence Generation

M.V.A. Raju Bahubalendruni, Bibhuti Bhusan Biswal,
Manish Kumar and B.B.V.L. Deepak

Abstract Assembly sequence generation at early stages of product design leads to minimal production time. In order to generate valid practically possible assembly sequence, several assembly predicates must be considered during the assembly sequence generation process. Mechanical feasibility predicate is one of the essential predicate, which ensures the geometric feasibility of physical connectors. In the current paper, representation of mechanical feasibility data is described for different types of connectors used in mechanical assemblies. The proposed representation method reduces the complexity of the assembly sequence generation problem compared to the traditional formulation. Method to extract the mechanical feasibility matrix is proposed and illustrated with an example through algorithms.

Keywords Mechanical feasibility · Assembly sequence generation · Assembly automation

1 Introduction

Assembly sequence generation methods aim toward producing single or multiple valid assembly sequences for a product by considering all the necessary assembly attributes of the product. Homem de Mello categorized four basic elements to define validity of an assembly sequence typically named as liaison predicate, geometric feasibility predicate, stability predicate and mechanical feasibility predicate (Homem de Mello and Sanderson 1988). Lots of research has been done to obtain necessary data to test assembly predicates. In order to test an assembly sequence for each assembly predicate; firstly the necessary data must be extracted from the

M.V.A.R. Bahubalendruni (✉) · B.B. Biswal · M. Kumar · B.B.V.L. Deepak
National Institute of Technology, Rourkela, India
e-mail: bahubalindruni@gmail.com

assembly model then the information will be used to test the assembly predicate. However extracting of assembly predicate information is a skillful and time consuming task. Recent advances in computer aided design (CAD) softwares reduce the efforts to represent assembly model and offers flexibility to retrieve assembly relation information (Bahubalendruni and Biswal 2015a, b).

Liaison predicate is the basic assembly predicate defined through graphical representation by Bourjault (Bourjault 1984). The matrix representation eases to store and retrieve the assembly contact information. Several researchers worked on extracting liaison matrix by performing contact analysis between the assembled parts (Vigano 2013). Geometrical feasibility predicate is used to find a collision free path for primary part during its assembly operation. In the initial days these data represented in graphical formats and later matrix mode of representation found helpful to automation (Bahubalendruni 2014). Interference matrices are the best to store the data, few researcher implemented algorithms to extract the data from CAD based products efficiently to reduce the computational time and human error (Mok and Pan 2001, 2005). More similar method to test economical geometric feasible direction was proposed by Bahubalendruni (2014a, b, c). Stability predicate ensures the stability of the assembled parts in a sub assembly with respect to their mating components. Smith proposed support matrix and stability matrix with two different categories of connections named as soft and hard (Smith 2001).

There exists lots of literature on liaison, geometric feasibility, stability matrix representation and CAD based extraction methods. Due to complex nature of mechanical feasibility data representation and most of researchers considered each physical connector as a primary part but this leads to high computational time. Hence a novel representation method to store the mechanical feasibility data and its extraction from CAD environment is proposed in detail.

2 Assumptions

In order to retrieve mechanical feasibility information from CAD based environment effectively, the below assumption are considered.

1. Nut, Bolt, Screw, Rivet and Pins are only considered as physical connectors to perform assembly operations.
2. All the hard connectors follow respective nomenclature and positioned next to the primary parts.
3. All the physical connectors are considered as secondary parts and the remaining are treated as primary parts while assembly subset generation.

4. Stability matrix is readily available to generate mechanical feasibility data.
5. Boundary box coordinates of the primary parts are available to test geometrical feasibility of physical connectors.

3 Mechanical Feasibility Representation

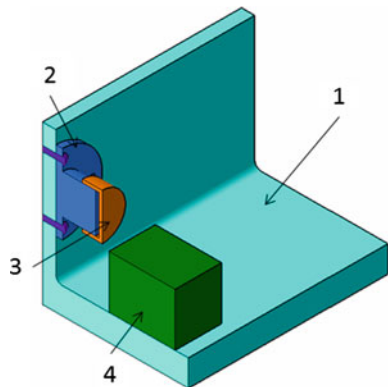
In order to represent mechanical feasibility of physical connectors, the number of physical connectors and the assembled primary parts information must be studied. From the assumption 4, the stability matrix element value “1” state that the part indicated in row is supported against gravity by part indicated in column; “2” denotes both the parts in row and column are connected by part features such as threading; “3” indicates that the parts in row and column together connected by set of external physical connectors stated in Assumption 1. An example assembly is considered to demonstrate the stability matrix in Fig. 1.

The stability matrix for the assembly shown in Fig. 1 is as follows

$$\begin{matrix} & \begin{matrix} 1 & 2 & 3 & 4 \end{matrix} \\ \begin{matrix} 1 \\ 2 \\ 3 \\ 4 \end{matrix} & \begin{bmatrix} 0 & 3 & 0 & 0 \\ 3 & 0 & 2 & 0 \\ 0 & 2 & 0 & 0 \\ 1 & 0 & 0 & 0 \end{bmatrix} \end{matrix}$$

Using the stability matrix, contact analysis will be done for both the parts represented in row and column where against all the physical connectors. The common connectors are grouped into one set. While placing set of connectors, any part in the existed assembly other than i and j can offer collision and hence, three dimensional matrix is required to store mechanical feasibility data. Mechanical feasibility matrix for the assembly shown in Fig. 1 is shown in Fig. 2.

Fig. 1 4 Part assembly to demonstrate assembly stability



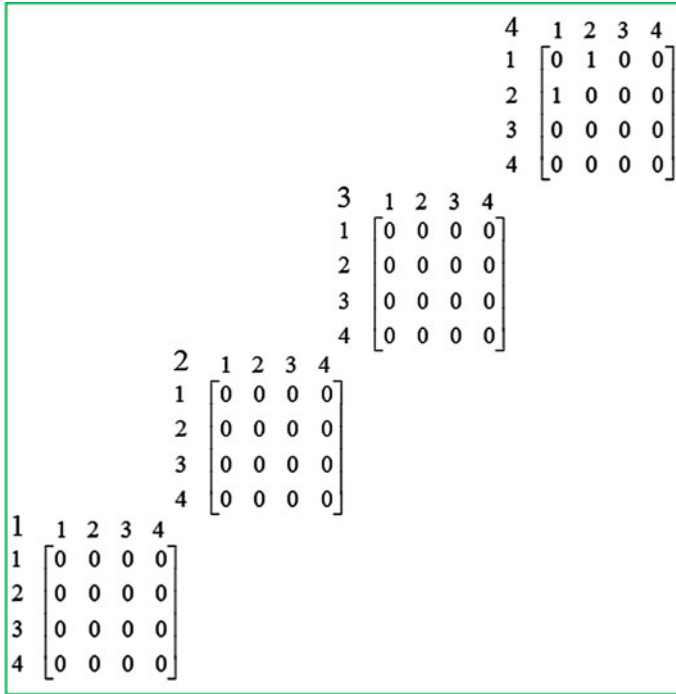


Fig. 2 Mechanical feasibility matrix for 4 parts assembly

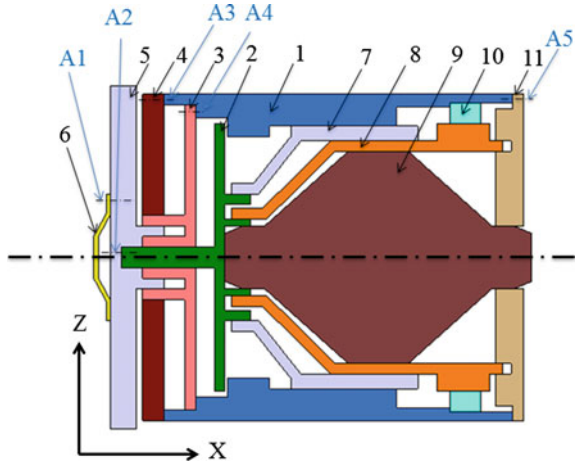
A pseudo code to generate mechanical feasibility matrix is presented here:

```

“n” is number of parts in the assembly; “p” is number of the connectors.
mfm (n,n,n) ← A null matrix of size (n-by-n-by-n)
for i = 1 to n
  for j= 1 to n
    if stb(i,j) = 3
      hide all primary parts other than part-i and part-j
      perform contact analysis for part-i against all connectors
      perform contact analysis for part-j against all connectors
      con(m)← store common connectors
      for k=1 to m
        unhide all primary parts and hide i and j
        for l = 1 to n
          dir= 1 to 6
          check geometrical feasibility of connector “k” existence of “part- l” along “dir”
          If not feasible
            mfm(i,j,l)= 1; l= l+1
          End If
        End for
      End For
    End If
  End for
End for
End for

```


Fig. 3 Assembly with 11 parts and 5 set of connectors



4 Case Study

An assembly with 11-parts (1–11) shown in Fig. 3 with 5 set of physical connectors (A1 to A5) from past bibliography is considered to implement the proposed method. Stability matrix for the assembly shown in Fig. 3 is as follows.

Stability matrix for the assembly shown in Fig. 3 is as follows.

	A	B	C	D	E	F	G	H	J	K	L
A	0	0	2	2	0	0	1	0	0	1	2
B	0	0	1	0	2	0	1	1	1	0	0
C	2	1	0	1	1	0	0	0	0	0	0
D	2	0	1	0	0	0	0	0	0	0	0
E	0	2	1	0	0	2	0	0	0	0	0
F	0	0	0	0	2	0	0	0	0	0	0
G	1	1	0	0	0	0	0	1	0	0	0
H	0	1	0	0	0	0	1	0	1	1	1
J	0	1	0	0	0	0	0	1	0	0	1
K	1	0	0	0	0	0	0	1	0	0	0
L	2	0	0	0	0	0	0	1	1	0	0

A macro using Visual Basic script has been written and run on a computer with (i7-3770 CPU @ 3.40 GHz, 4.00 GB RAM) configuration to test the computational performance. The proposed method is able to retrieve the mechanical feasibility matrix in 3 a seconds for the assembly shown in Fig. 3. The resulted mechanical feasibility matrix is shown in Fig. 4.

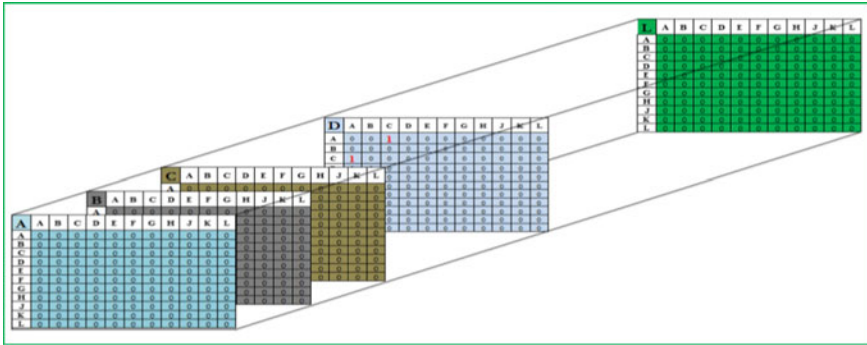


Fig. 4 Mechanical feasibility matrix for 11-part assembly

5 Validation

The assembly shown in Fig. 1 consists of 4 primary parts and 1 set of 4 connectors. The available algorithms will consider it as an eight parts assembly problem and the search space for the algorithm turns out to be factorial 8. Similarly, the assembly shown in Fig. 3 consists of 11 parts and 5 set of 6 connectors each. Even if an assembly designer takes each set of connector as one connector based on identical proposition in the assembly, the algorithm would consider this assembly sequence problem consisting of 16 parts and the search space is factorial 16. Through our method, we have significantly reduced the computational burden. Table 1 illustrates the effectiveness of the proposed method.

If connectors are also taken as primary parts as in traditional algorithm without considering mechanical feasibility, all the entities including connectors are taken to be primary parts. The part count gets increased and consequently the search space rises exponentially. We implemented the traditional method without considering mechanical feasibility and the proposed method by considering the mechanical feasibility. The above table establishes that considering mechanical feasibility predicate shortens the search space and the computational time is significantly reduced.

6 Conclusion

A new method to represent and store the mechanical feasibility data is proposed and an algorithm to retrieve the data from a 3D CAD product is clearly illustrated. This representation of mechanical feasible predicate is computational friendly where all the four assembly predicates are taken into consideration for assembly planning. The method is proven through a case study for its correctness and it also avoid possibility of human error. Compared to the previous works on retrieving geometric

Table 1 Evaluation of effectiveness of the MFM method

Figure number	Assembly	Method	No. of parts	No. of connectors	Search space	Solution count	Computational time in seconds
Figure 1	4 parts assembly	Traditional method without considering mechanical feasibility	8	0	8!	6	50
Figure 3	11 parts assembly		16	0	16!	1808	605
Figure 1	4 parts assembly	Proposed method with considering mechanical feasibility	4	4	4!	6	3
Figure 3	11 parts assembly		11	5	11!	1808	406

feasibility data considering each connector as a primary part, the proposed representation reduces the complexity of automated assembly sequence planning problem.

References

- Bahubalendruni, M. V. A., & Biswal, B. B. (2014a). Computer aid for automatic liaisons extraction from cad based robotic assembly. In *2014 IEEE 8th International Conference on Intelligent Systems and Control (ISCO)* IEEE. (pp. 42–45).
- Bahubalendruni, M. V. A., & Biswal, B. B. (2014b). An algorithm to test feasibility predicate for robotic assemblies. *Trends in Mechanical Engineering & Technology*, 4(2), 11–16.
- Bahubalendruni, M. R., & Biswal, B. B. (2015a). A review on assembly sequence generation and its automation. In *Proceedings of the Institution of Mechanical Engineers, Part C: Journal of Mechanical Engineering Science*, doi:[10.1177/0954406215584633](https://doi.org/10.1177/0954406215584633).
- Bahubalendruni, M. R., & Biswal, B. B. (2015b). An intelligent method to test feasibility predicate for robotic assembly sequence generation. In *Intelligent Computing, Communication and Devices* (pp. 277–283). India: Springer.
- Bahubalendruni, M. R., Biswal, B. B., & Vishal, U. (2014a). Assembly sequence generation and automation. In *International Conference on Design, Manufacturing and Mechatronics* (pp. 185–192). doi:[10.13140/2.1.2494.8488](https://doi.org/10.13140/2.1.2494.8488).
- Bahubalendruni, M. R., Biswal, B. B., & Khanolkar, G. (2014b). Computer aid to obtain assembly cut. sets from 3D CAD product. In *International Conference on Design, Manufacturing and Mechatronics* (pp. 161–167).
- Bourjault, A. (1984). Contribution à une approche méthodologique de l'assemblage automatisé: élaboration automatique des séquences opératoires. PhD Thesis, Université de Franche-Comte, France.
- Homem de Mello, L. S., & Sanderson, A. C. (1988). Automatic generation of mechanical assembly sequences (No. CMU-RI-TR-88-19). Carnegie-Mellon University Pittsburgh, PA Robotics Institute.
- Mok, S. M., Ong, K., & Wu, C. H. (2001). Automatic generation of assembly instructions using STEP. In *Robotics and Automation, 2001. Proceedings 2001 ICRA. IEEE International Conference on IEEE* (Vol. 1, pp. 313–318).
- Pan, C., Smith, S. S. F., & Smith, G. C. (2005). Determining interference between parts in CAD STEP files for automatic assembly planning. *Journal of Computing and Information Science in Engineering*, 5(1), 56–62.
- Smith, S. S. F., Smith, G. C., & Liao, X. (2001). Automatic stable assembly sequence generation and evaluation. *Journal of Manufacturing Systems*, 20(4), 225–235.
- Viganò, R., & Gómez, G. O. (2013). Automatic assembly sequence exploration without precedence definition. *International Journal on Interactive Design and Manufacturing (IJIDeM)*, 7(2), 79–89.

Weld Seam Tracking and Simulation of 3-Axis Robotic Arm for Performing Welding Operation in CAD Environment

B.B.V.L. Deepak, C.A. Rao and B.M.V.A. Raju

Abstract In this paper, a 3-axis robotic arm has been modelled using CAD tool for performing welding operations. For the developed robotic arm, forward and inverse kinematic analyses have been performed to move the weld torch in the desired trajectory. A new seam tracking methodology, named sewing technique has been introduced for the welded joints available in Computer Aided Design (CAD) environment. This methodology, gives the seam path by drawing a line through the adjacent centroids of curve fitted in the weld joint volume. Obtained geometric path and kinematic constraints are given as input to the modelled robot for performing welding operation followed by desired trajectory. Validation of the developed methodology has been done through simulation results while performing welding operations for different weld profiles.

Keywords CAD · Robotic arm · Forward and inverse kinematics · Weld seam tracking · Trajectory generation

1 Introduction

Most of the construction machinery parts are welded structures and arc welding technique is mainly used to produce such products. The welding process has been automated from the last few decades through the use of robots and 90 % or more of total weld lines are currently automated.

Bae et al. (2002) performed an extensive research work on automated welding robot applications and concluded that exact weld position and orientation of a work piece and its detailed surface geometry are necessary for the robot guidance. Among various sensors used for weld seam tracking, laser sensor technology gives accurate solutions. This technology is probably the most powerful form of sensory

B.B.V.L. Deepak (✉) · C.A. Rao · B.M.V.A. Raju
Department of Industrial Design, National Institute of Technology, Rourkela, India
e-mail: bbv@nitrkl.ac.in

feedback and it can provide 3D geometrical information of any arbitrary shaped work pieces in detail without requiring any contact with the work piece. A vision sensor is used in automatic welding to acquire image patterns of a three dimensional manner and two dimensional image patterns were tested using neural network (Yoo and Na 2003). Gao and Na (2005) performed a set of experiments to evolve weld position equations by estimating the centroid of the weld pool pictures. Ye et al. (2013) presented a passive vision-based robotic welding system, which can realize the seam tracking function for pulse-MAG welding.

Kim et al. (2003) obtained a relationship among the input welding process parameters and the output as the weld penetration. Using these relations, robotic welding process (arc welding) can be controlled in order to achieve desired weld quality. Fuzzy linear regression approach was employed by Xue et al. (2005) to determine the relationship between input as process parameters and output as weld quality in the robotic arc welding process. The input parameters are welding current, arc voltage, wire diameter, and torch speed and the weld quality they measured in terms weld bead width. Nagesh and Datta (2010) had come out with a set of empirical relations related to the process parameters and the bead shape. They considered the input parameters as the welding process variables and the output as the weld bead geometry in terms of bead front height and width and back height and width. Several number of experiments have been performed in order to establish a relationship among the robotic arc welding process variables (Dhas and Kumanan 2011). Later they implemented genetic algorithm and particle swarm optimization techniques to obtain optimal weld parameters. Katherasan et al. (2014) addressed a neural network based regression tool to predict weld bead geometry with respect to process parameters in flux cored arc welding process and then implemented particle swarm optimization to find optimal process parameters. The past research work concerned primarily on weld geometry/seam tracking or relation among very few process related parameters. But these involves more complications while performing welding operations. The proposed system is a simple seam tracker can be used for continuous and long seam welding. It can be controlled and monitored remotely without human operation, thereby reducing the risk of hazards. Since the welding operation can be monitored initially in the CAD environment, the produced weldments would be uniform, superior and the cycle time can be faster in comparison to the presently available systems.

2 Analytical Kinematic Models of 3-Axis Manipulator

In this investigation, a 3-axis manipulator has been considered for performing welding operation in virtual environment. 3-axis are correspond to base rotation, elbow rotation and wrist pitch as shown in Fig. 1. While the tool of the robot follows the seam path, the position (X, Y, and Z) of the weld torch will vary without varying the roll angle of the torch. Since the roll angle of the weld electrode will not influence the welding operation, the roll of the tool has not been considered

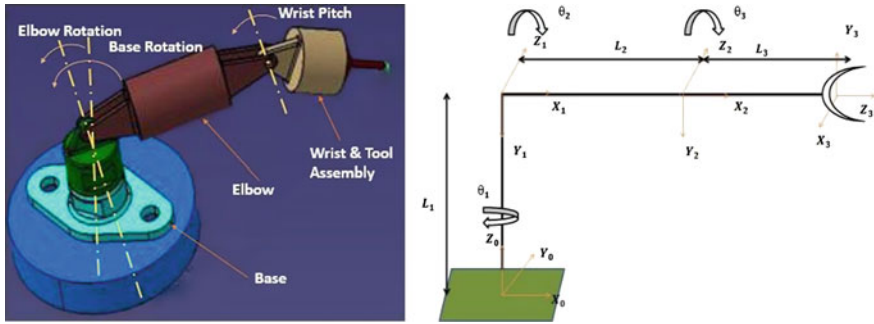


Fig. 1 CAD model of robot, its coordinate frames

throughout this analysis. It means the roll angle of the weld torch is fixed to a specific value.

In forward kinematic analysis, for given link lengths and joint angles, end-effector’s position and orientation with respect to base are to be calculated. Where as in the inverse kinematic analysis is, for given position and orientation of end-effector, joint parameters are to be obtained. A detailed explanation of forward and inverse kinematic models of a robotic manipulator is provided by Elias et al. (2012) and Parhi et al. (2013)

The developed 3-axis robot model, its coordinate frames and its work volume are shown in Figs. 1 and 2 and the specification of the manipulator is illustrated in Table 1.

2.1 Forward Kinematic Model

Forward kinematics generally refers to position analysis of the end-effector. So the forward kinematic analysis is equivalent to a determination of arm matrix by

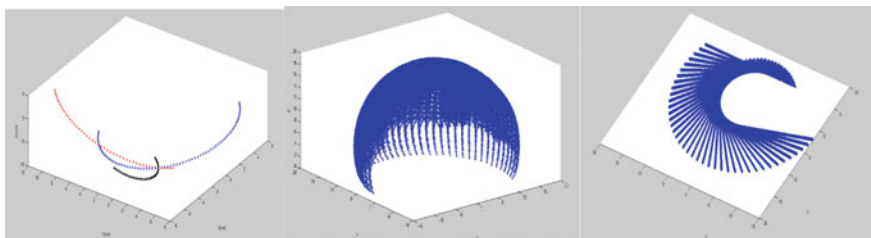


Fig. 2 Variation of end-effector position when all joint angles are varied uniformly and other joints are at fixed angle and its work volume (All dimensions are in cm.)

Table 1 Specification of the developed robot

Specification	Value	Units
Number of axes	3	
No. of links	3	
Lengths of link 1, link 2 and link 3	70, 100, 70	mm
Work envelope	Body rotation: 360	Degrees
	Elbow rotation: 180 to -180	
	Wrist rotation: 90, 270	

combining transformation matrices as represented in Eq. (1). The set of link coordinates assigned using DH convention is then transformed from coordinate frame (N_i) to (N_{i-1}). Using a homogeneous coordinate transformation matrix, the relation between adjacent links is given in Eq. (1).

$$\begin{aligned}
 T_i &= Rot(z, \theta_i) * Trans(0, 0, d_i) * Trans(a_i, 0, 0) * Rot(x, \alpha_i) \\
 &= \begin{bmatrix} C\theta_i & -S\theta_i C\alpha_i & S\theta_i S\alpha_i & a_i C\theta_i \\ S\theta_i & C\theta_i C\alpha_i & -C\theta_i S\alpha_i & a_i S\theta_i \\ 0 & S\alpha_i & C\alpha_i & d_i \\ 0 & 0 & 0 & 1 \end{bmatrix} \quad (1)
 \end{aligned}$$

Here $C_i = \cos(\theta_i)$, $S_i = \sin(\theta_i)$

On substituting the kinematic parameters illustrated in Table 1, individual transformation matrices T_0^1 to T_3^4 can be found and the global transformation matrix T_0^4 of the robot arm is found according to the Eq. (2).

$$T_{base}^{tool} = T_{base}^{wrist} * T_{wrist}^{tool}$$

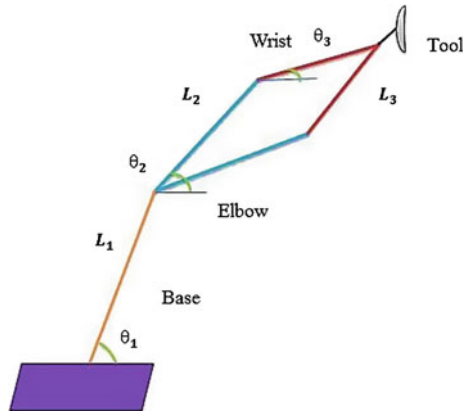
where $T_{base}^{wrist} = T_0^1 * T_1^2$

$$T_{base}^{wrist} = T_2^3 * T_3^4$$

$$T_{base}^{tool} = \begin{bmatrix} m_x & n_x & o_x & p_x \\ m_y & n_y & o_y & p_y \\ m_z & n_z & o_z & p_z \\ 0 & 0 & 0 & 1 \end{bmatrix} = \begin{bmatrix} R(\theta)_{3 \times 3} & P_{3 \times 1} \\ 0 & 1 \end{bmatrix} \quad (2)$$

where (p_x, p_y, p_z) represents the position and $R(\theta)_{3 \times 3}$ represents the rotation matrix of the end effector. From this transformation matrix, the position (translation) of end-effector with reference to base frame as a function of the joint angles is depicted in Fig. 3.

Fig. 3 Elbow and Wrist position for given end-effector position



Tool configuration is six-dimensional because arbitrary specified by three position co-ordinates (x, y, z) and orientation co-ordinates (yaw, pitch, roll).

$$X = \begin{Bmatrix} p_x \\ p_y \\ p_z \\ y \\ p \\ r \end{Bmatrix} = \begin{Bmatrix} c_1(a_2c_2 + a_3c_{23} - d_4s_{23}) \\ s_1(a_2c_2 + a_3c_{23} - d_4s_{23}) \\ d_1 - a_2s_2 - a_3s_{23} - d_4c_{23} \\ -[\exp(\theta_4)/\pi]c_1s_{23} \\ -[\exp(\theta_4)/\pi]s_1s_{23} \\ -[\exp(\theta_4)/\pi]c_{23} \end{Bmatrix} \tag{3}$$

Since the roll angle \$\theta_4\$ is fixed, tool orientation will change according to base rotation, elbow rotation and wrist pitch during its operation.

2.2 Inverse Kinematic Analysis

In a robotic arm, joint variables are the independent variables and will change with respect to the different reference frames. In this investigation, a simple analytical/geometrical approach method implemented to solve the inverse kinematic problem. For the considered 3-axis manipulator, Fig. 2 shows the elbow, wrist position for the same end effector position. Since the wrist angle (\$\theta_2\$) depends on elbow angle (\$\theta_3\$), there will be two wrist angles correspond to each angle as shown in the Fig. 2.

The base angle can be determined by Eq. (4)

$$\text{Base angle } \theta_1 = \arctan(P_Y/P_X). \tag{4}$$

After finding the base angle, the 3R problem can be converted into 2R planar problem. The two wrist angles ($\pm\theta_3$) can be found for the same tool position as follows:

The manipulator tip point global position is represented by Eqs. (5) and (6)

$$Y = l_2 \cos \theta_1 + l_3 \cos(\theta_2 + \theta_3) \quad (5)$$

$$Z = l_2 \sin \theta_1 + l_3 \sin(\theta_2 + \theta_3) \quad (6)$$

Therefore

$$Y^2 + Z^2 = l_2^2 + l_3^2 + 2l_2l_3 \cos_3$$

$$\cos_{\theta_3} = \frac{Y^2 + Z^2 - l_2^2 - l_3^2}{2l_2l_3} \Rightarrow \theta_3 = \cos^{-1} \left(\frac{Y^2 + Z^2 - l_2^2 - l_3^2}{2l_2l_3} \right) \quad (7)$$

To find θ_2 using atan2 function is represented by

$$\theta_2 = \pm \text{atan2} \sqrt{\frac{(l_2 + l_3)^2 - (Y^2 + Z^2)}{(Y^2 + Z^2) - (l_2 - l_3)^2}} \quad (8)$$

The \pm is because of the square root, which gives two solutions. These two solutions are called as elbow up and elbow down.

The joint angle θ_2 for elbow up position and for elbow down position is given by

$$\theta_2 = \text{atan2} \frac{Z}{Y} + \text{atan2} \left(\frac{l_3 \sin_3}{l_2 + l_3 \cos_3} \right) \quad (9)$$

$$\theta_2 = \text{atan2} \frac{Z}{Y} - \text{atan2} \left(\frac{l_3 \sin_3}{l_2 + l_3 \cos_3} \right) \quad (10)$$

Fixed Tool roll angle

$$\theta_4 = \pi * \ln \sqrt{(y^2 + p^2 + r^2)} \quad (11)$$

3 Sewing Technique for Obtaining Seam Path

From the existed CAD model, it is very easy to know the geometry where to be welded. In this approach, control points are considered along the length/periphery of the welding joint. The control points of opposite edges are connected by a curve and along the entire length we have to draw the curves. These curves representation is shown in Fig. 3. By joining the centroids of each curve we will get a path that

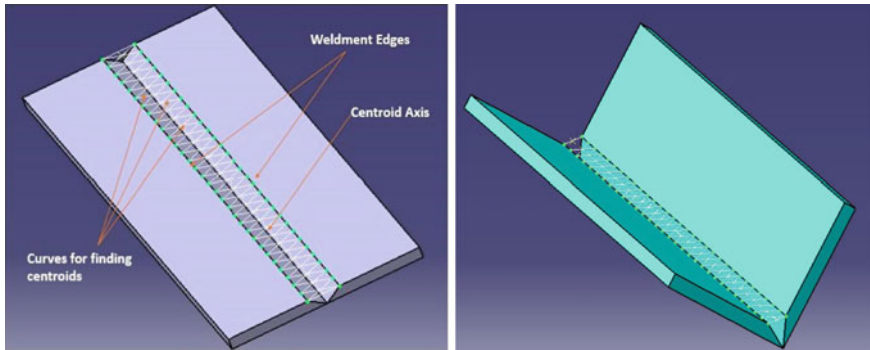


Fig. 4 Sewing technique to find seam path for plate and L-Joint

path is nothing but weld seam path. This technique is known as sewing technique and it can be modelled by generative shape design module in CATIA (Fig. 4).

By knowing weld seam coordinates it is very easy to obtain the joint angles of a robot using inverse kinematic model. Finally along the weld seam path and it will perform the welding operation. The key feature of this approach is that, the initial and end positions of the weld seams can be obtained easily. Because of this the robot can be controlled flexibly, during welding operation.

4 Simulation of Welding Operation

The obtained geometric path (seam path) and kinematic constraints will be given as input to the developed robotic arm for performing welding operation. The robot is known about the input parameters such as electrode consumption rate and weld torch speed prior to perform welding operation.

In this analysis the trajectory planning is performed according to the 3rd order cubic spline interpolation.

For the cubic spline trajectory

$$(t) = a1 * t^3 + a2 * t^2 + a3 * t + a4 \quad (12)$$

The constant values can be obtained while subjected to following boundary conditions:

- At $t = 0$, $a4 = \theta_0(\text{given})$ and $v_0 = a3/t$.
- At $t = 1$, $a1 + a2 + a3 + \theta_0 = \theta_f$
- $v_f = (3a1 * t^2 + 2a2 * t + a3)/t$.
- $a_f = (6a1 * t + 2a2)/t^2$

In experimental analysis, a program has been generated for inverse kinematic solution. This program is written in VB script. Robot welding operation is performed in virtual environment to validate developed methodology.

Class 1: Welding operation of butt joint

Importing Coordinate Data from CAD to Excel and Excel to MAT Lab

Weld seam coordinate data from sewing technique can be extracted to Excel. The program has been developed in VB script to extract the CATIA point coordinate data into Excel. The seam path obtained by the sewing technique for the considered butt joint is illustrated in Table 2.

For the point data imported in Excel, inverse kinematic solutions can be obtained using MATLAB program. The 3D plot of the end-effector trajectory for the generated weld seam is shown in Fig. 5.

Figure 6 shows the robot is performing welding task in virtual environment while following its kinematic constraints as discussed above. The considered weld joints thickness is 5 mm. and its length is 15 cm.

Class 2: Welding operation of L-joint

In the similar manner as discussed above, Fig. 7 shows the robot is performing welding task in virtual environment while following its kinematic constraints as discussed above. The considered weld joints thickness is 5 mm. and its length is 15 cm.

Table 2 Shows the point coordinate data of weld seam path

Co-ordinate	X	Y	Z	Co-ordinate	X	Y	Z
1	120	90	80	16	1.034483	105.5172	61.89655
2	112.069	91.03448	78.7931	17	-6.89655	106.5517	60.68966
3	104.1379	92.06897	77.58621	18	-14.8276	107.5862	59.48276
4	96.2069	93.10345	76.37931	19	-22.7586	108.6207	58.27586
5	88.27586	94.13793	75.17241	20	-30.6897	109.6552	57.06897
6	80.34483	95.17241	73.96552	21	-38.6207	110.6897	55.86207
7	72.41379	96.2069	72.75862	22	-46.5517	111.7241	54.65517
8	64.48276	97.24138	71.55172	23	-54.4828	112.7586	53.44828
9	56.55172	98.27586	70.34483	24	-62.4138	113.7931	52.24138
10	48.62069	99.31034	69.13793	25	-70.3448	114.8276	51.03448
11	40.68966	100.3448	67.93103	26	-78.2759	115.8621	49.82759
12	32.75862	101.3793	66.72414	27	-86.2069	116.8966	48.62069
13	24.82759	102.4138	65.51724	28	-94.1379	117.931	47.41379
14	16.89655	103.4483	64.31034	29	-102.069	118.9655	46.2069
15	8.965517	104.4828	63.10345	30	-110	120	45

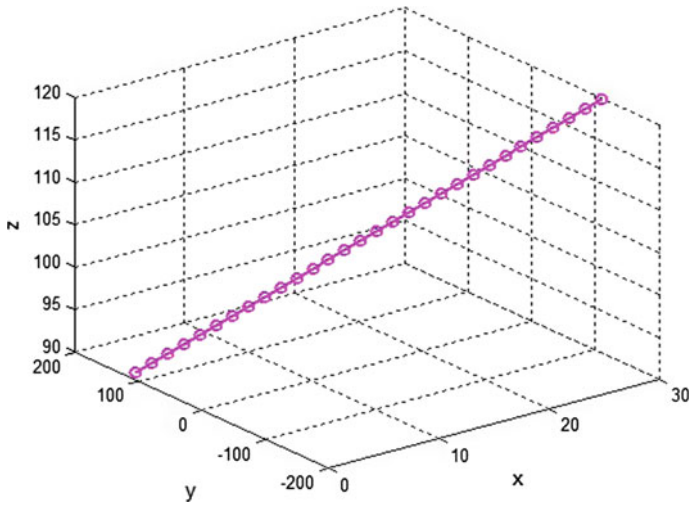


Fig. 5 3D plot for the weld seam coordinate data

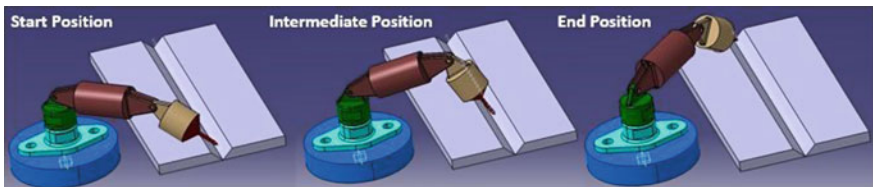


Fig. 6 Robot following seam path for performing welding operation of butt joint

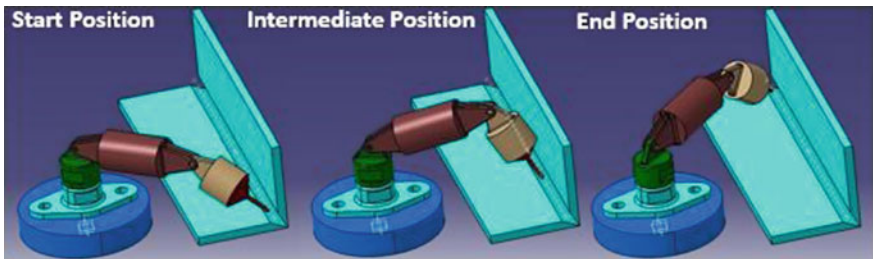


Fig. 7 Robot following seam path for performing welding operation of L-joint

4.1 Comparison with Previous Work

Some of the past research work as illustrated in Table 2 represents the various methodologies for performing seam tracking and welding operation. A detailed comparison has been provided in Table 3.

Table 3 Comparison with previous work

Past work	Method for weld seam Tracking	Seam Initial and Final Position detection	Robot Trajectory planning and Kinematic constraints
Bae et al. (2002)	Optical sensing system	✓	×
Yoo and Na (2003)	Laser sensing system	×	✓
Gao and Na (2005)	Passive vision system	×	×
Kiddee et al. (2014)	×	✓	×
Dahari and Tan (2011)	×	×	✓
Kumar et al. (2013)	CAD based	×	✓
Current study	CAD based	✓	✓

5 Conclusion

This investigation has been carried out to simulate the 3-axis robotic arm in CAD environment for performing welding operation while following the weld seam path and its kinematic constraints. A new seam tracking methodology, named sewing technique has been introduced for the welded joints available in Computer Aided Design (CAD) environment. Validation of the developed methodology has been done through simulation results while performing welding operations for different weld profiles. Still this work is in primary stage (simulation) and requires validation with real-time welding operation.

References

- Bae, K. Y., Lee, T. H., & Ahn, K. C. (2002). An optical sensing system for seam tracking and weld pool control in gas metal arc welding of steel pipe. *Journal of Materials Processing Technology*, 120(1), 458–465.
- Dahari, M., & Tan, J. D. (2011). Forward and inverse kinematics model for robotic welding process using KR-16KS KUKA robot. In *2011 4th International Conference on Modeling, Simulation and Applied Optimization (ICMSAO)* (pp. 1–6). IEEE.
- Dhas, J. E. R., & Kumanan, S. (2011). Optimization of parameters of submerged arc weld using non-conventional techniques. *Applied Soft Computing*, 11(8), 5198–5204.
- Elias, E., Parhi, B. B. V. L., Deepak, D. R., & Srinivas, J. (2013). Design & kinematic analysis of an articulated robotic manipulator. *International Journal of Mechanical and Industrial Engineering*, 3(1), 105–108.
- Gao, X. D., & Na, S. J. (2005). Detection of weld position and seam tracking based on Kalman filtering of weld pool images. *Journal of manufacturing systems*, 24(1), 1–12.

- Katherasan, D., Elias, J. V., Sathiya, P., & Haq, A. N. (2014). Simulation and parameter optimization of flux cored arc welding using artificial neural network and particle swarm optimization algorithm. *Journal of Intelligent Manufacturing*, 25(1), 67–76.
- Kiddee, P., Fang, Z., & Tan, M. (2014). Visual recognition of the initial and end points of lap joint for welding robots. In *2014 IEEE International Conference on Information and Automation (ICIA)* (pp. 513–518). IEEE.
- Kim, I. S., Son, J. S., Kim, I. G., Kim, J. Y., & Kim, O. S. (2003). A study on relationship between process variables and bead penetration for robotic CO₂ arc welding. *Journal of Materials Processing Technology*, 136(1), 139–145.
- Kumar, K. K., Srinath, A., Anvesh, G. J., Sai, R. P., & Suresh, M. (2013). Kinematic analysis and simulation of 6- DOF KUKAKr5 robot for welding application. *International Journal of Engineering Research and Applications*, 3(2), 820–827.
- Nagesh, D. S., & Datta, G. L. (2010). Genetic algorithm for optimization of welding variables for height to width ratio and application of ANN for prediction of bead geometry for TIG welding process. *Applied Soft Computing*, 10(3), 897–907.
- Parhi, D. R., Deepak, B. B. V. L., Nayak, D., & Amrit, A. (2012). Forward and Inverse Kinematic Models for an Articulated Robotic Manipulator. *International Journal of Artificial Intelligence and Computational Research*, 4(2), 103–109.
- Xue, Y., Kim, I. S., Son, J. S., Park, C. E., Kim, H. H., Sung, B. S., & Kang, B. Y. (2005). Fuzzy regression method for prediction and control the bead width in the robotic arc-welding process. *Journal of Materials Processing Technology*, 164, 1134–1139.
- Ye, Z., Fang, G., Chen, S., & Zou, J. J. (2013). Passive vision based seam tracking system for pulse-MAG welding. *The International Journal of Advanced Manufacturing Technology*, 67(9–12), 1987–1996.
- Yoo, W. S., & Na, S. J. (2003). Determination of 3-D weld seams in ship blocks using a laser vision sensor and a neural network. *Journal of manufacturing systems*, 22(4), 340–347.

A Comparative Performance Analysis of Discrete Wavelet Transforms for Denoising of Medical Images

Yogesh S. Bahendwar and G.R. Sinha

Abstract In general, during image acquisition and transmission, digital images are corrupted by noises due to various effect. The complex type of additive noises disturbs images, depending on the storage and capture devices. These medical imaging devices are not noise free. The medical images used for diagnosis are acquired from Magnetic Resonance Imaging (MRI), Computed Tomography (CT), and X-ray Instruments. Reduction of visual quality due to addition of noise complicates the treatment and diagnosis. Removal of additive noise in images can easily be possible using simple threshold methods. In this paper we proposed an algorithm for denoising using Discrete Wavelet Transform (DWT). Numerical results shows the performance (based on parameters like: PSNR, MSE, MAE) of algorithm using various wavelet transforms for different Medical Images corrupted by random noise.

Keywords Denoising · DWT · X-ray · CT · Image processing · Thresholding · Random noise · PSNR · MSE · MAE

1 Introduction

In diagnosis and treatment of patients, pathologist and practitioners are continuously relying on digital imaging. The images of different organs produced by several instruments are used during the analysis of various stages. In digital image processing, image denoising is a method aimed at the removal of noise, may corrupt an image during its acquisition and/or transmission while retaining its quality

Y.S. Bahendwar (✉)

Department of Electronics and Telecommunication, SSEC, Bhilai (C.G.) 490020, India
e-mail: bahendwar72@gmail.com

G.R. Sinha

SSGI, Bhilai (C.G) 490020, India
e-mail: ganeshsinha2003@gmail.com

© Springer India 2016

D.K. Mandal and C.S. Syan (eds.), *CAD/CAM, Robotics and Factories of the Future*, Lecture Notes in Mechanical Engineering,
DOI 10.1007/978-81-322-2740-3_40

417

(Agrawal and Bahendwar 2011). Medical images obtained from MRI, CT and X-Ray are the most commonly used tools for diagnosis. These images are usually affected by random noise that arises in the process of image acquisition. The noise in the image degrades the quality of image and most importantly obscures important information required for accurate diagnosis. In order to enhance and recover accurate details of image, removal of noise becomes essential in medical imaging applications.

X-ray, CT, MRI Positron Emission Tomography (PET), Ultra sound (US) and Single Photon Emission Computed Tomography (SPECT) and many more optical imaging methods are used in treatment of patients. Due to imperfect acquisition and transmission, the distortion of visual signal is the primary problem in medical imaging system. The various factors like time exposure, lighting, moment of patient, sensitivity of devices which are responsible for visual distortion, which may affect images in terms of contrast, distortion and artifacts introduced, blur and sensitivity. It is there for become necessary to use image enhancement techniques like histogram equalization, image smoothing, sharpening, contrast adjustment, edge and/or boundary enhancement and denoising to improve these quality parameters.

Having a good localization properties both in space and frequency, wavelets are much popular in medical image denoising and enhancement. The adaptive representation of signal is possible in wavelet packets. The survey of various image denoising technique is now presented. Lee et al. discussed about use of wavelets for medical image enhancement in (Tsai et al. 2003). Various filter like ratio, log ratio and angle image filter are compared by Zadeh et al. in enhancement of MR images (Peck et al. 1992). In (Archibald Gelb 2002), the author discussed about suppression of noise in MR images using Fourier spectral methods. Prager et al. used FIR filters along with wavelet decomposition, image edge enhancement and edge detection. Tsai and Lee (2004) manipulated transform coefficient using wavelet mapping functions. The mapping functions are selected in such a way that the coefficients with low frequency should not affect, as they prevent distortions. The coefficient with large absolute values comprises more information where as the high frequency coefficient gives edge information. Thus the coefficients be a part of any of these classes where heavily weighted with respect to other coefficient. Donoho (1995), discussed application of soft-thresholding in imaging denoising. In (Rissanen 2000) author introduced denoising using NDL based thresholding. In (Umadevi et al. 2011), author used hybrid model with wavelet and Independent Component Analysis(ICA) that uses ICA technique coupled with multiple denoising (MWD) for removing noise from X-ray images.

From the above review, it is observed that wavelet has provided a very good amount of contribution in denosing. But among these papers, it is found that some of the techniques are developed for only one dimensional signals and are not applied to two dimensional images.

1.1 Discrete Wavelet Transform (DWT)

The transform of a signal is just representation of the signal in another form without change in content or information contained in the signal. The Wavelet Transform that are developed to overcome the short comings of the Short Time Fourier Transform (STFT), provides the time frequency representation of signal, which can also be used to analyze non stationary signals. The Wavelet Transform uses multi resolution technique for analyzing different techniques with different resolutions, while STFT provides constant resolution at all frequencies (Kumar and Agnihotri 2010).

A wave is always periodic in nature and oscillates with the time. On the other hand wavelets are localized. Wavelets of finite energy are suitable to analyzed transient signals as they have their energy concentrated in time and space. Consequently, Fourier Transform and STFT use waves to analyze signals Fig. 1a Demonstration of wave and Fig. 1b a wavelet (Agrawal and Bahendwar 2011).

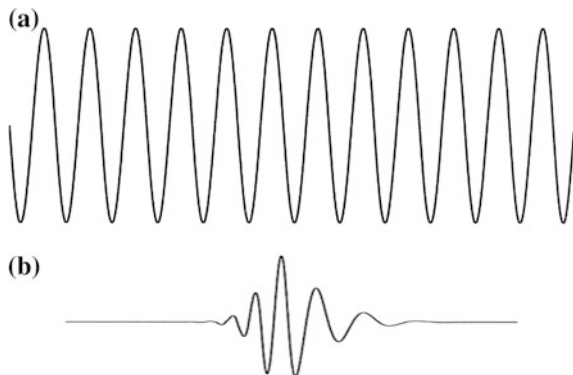
2 Image Denoising

Noise removal contained in images is an important issue of image processing. Denoising is a method to retain a signal that is corrupted by noise. The coefficients resulted from wavelet decomposition are modified to eliminate unwanted signal components. A wavelet Shrinkage method for denoising the image for implementation of wavelet thresholding has been verified. The algorithm (Agrawal and Bahendwar 2011) used consist of the following steps:

Algorithm: (Bahendwar and Sinha 2012)

- Choice of a wavelet with number of scales and levels for decomposition.
Calculation of the forward WT for image corrupted by noise.

Fig. 1 Demonstration of
(a) a wave and (b) a wavelet



- Shrinkage rule (Taswell 2000) is selected based on estimated thresholds and are applied to detail coefficients. This is accomplished by soft-thresholding (Eq. 2) and hard thresholding (Eq. 1).
- Inverse transform is applied to modified (threshold) coefficients.

2.1 Thresholding

It is a Technique used for denoising of signal and images. The method of applying thresholding is defined by Shrinkage rule (Yoon and Vaidyanathan 2004). The two main approaches are:

- I. **Hard Thresholding** (Prasad et al. 2008) eliminates the coefficients which are smaller than threshold (λ) and others are kept are unchanged. This is defined as:

$$\bar{C}_h(k) = \begin{cases} \text{sign } c(k)(|c(k)|) & \text{if } |c(k)| > \lambda \\ 0 & \text{if } |c(k)| \leq \lambda \end{cases} \quad (1)$$

Where λ is the threshold and coefficients which have value above it are only considered and coefficients below it are set to zero.

- II. **Soft-Thresholding** The soft threshold method deletes the coefficients under the threshold, but scales those that are left. The general soft shrinkage rule is defined by:

$$\bar{C}_s(k) = \begin{cases} \text{sign } c(k)(|c(k)| - \lambda) & \text{if } |c(k)| > \lambda \\ 0 & \text{if } |c(k)| \leq \lambda \end{cases} \quad (2)$$

- (a) **Global Threshold**

This method is proposed by Donoho (Eq. 4.3) has universal threshold (Ruikar and Doye 2011):

$$\lambda = \sigma\sqrt{2\log(N)} \quad (3)$$

Where σ^2 is the noise variance of the signal samples and N is the size of the coefficient arrays.

- (b) **Level Dependant Threshold**

It is achieved by Eq. (4). Noise standard deviation σ_k is estimated by using robust median estimator is the Highest sub band of WT.

$$\lambda k = \sigma k\sqrt{2\log(N)} \quad (4)$$

The scaled noise estimator is computed by:

$$\sigma k = \frac{MADk}{0.6745} = \frac{(\text{median}(|wi|))k}{0.6745} \quad (5)$$

MAD: median absolute deviation of the magnitude of all the coefficients at the finest decomposition scale.

ω_i : Coefficients for each given sub bands.

Threshold estimation is repeated separately for each sub band as the sub band exhibit different characteristics.

(c) **Optimal Threshold** (Agrawal and Bahendwar 2011)

In this the mean square error function that computes the error of the output to minimize the function is estimated. Minimum MSE act as a solution to the optimal threshold. A function of the threshold value which is minimized is defined in Eq. (6)

$$G(\lambda) = MSE(\lambda) = \frac{1}{N} ||y - y\lambda||^2 \quad (6)$$

If the output of the threshold algorithm y_λ with a threshold value λ and why as vector of the clean signal, then The remaining noise on this output equals $e_\lambda = y_\lambda - y$.

3 Performance Analysis

According to three error criteria i.e. MSE, MAE, and the PSNR, the experimental results are evaluated to find the measure of the wavelet filter performance.

4 Experimental Results

An additive noise with a uniform distribution is considered for the test, which is used to corrupt real Medical image.

The performance of various wavelet functions is assessed by adding artificial noise to the medical images.

Implementation of Algorithm The denoising algorithm is implemented through MATLAB, as it contains a wavelet toolbox and functions which makes convenient to do the DWT. A common way for denoising is to find a processed image which minimizes MSE, MAE and improves the value of the PSNR (Agrawal and Bahendwar 2011) (Figs. 2, 3 and 4).

The quantitative de-noising results of the MRI, CT and X-Ray images are obtained by using optimal thresholding and Compared for three different wavelet

Fig. 2 MRI image

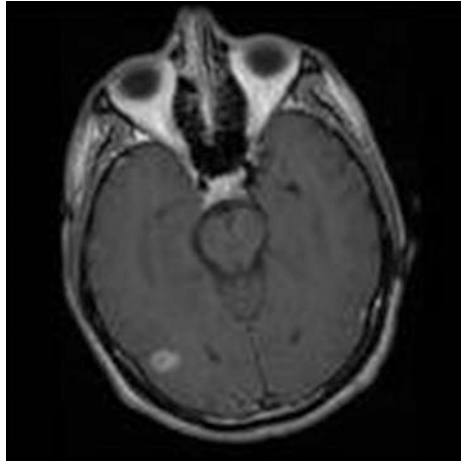


Fig. 3 CT image



Fig. 4 X-ray image

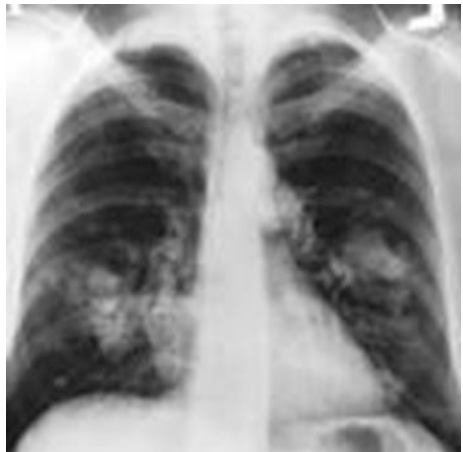


Table 1 Optimal thresholding

Wavelet	MRI image			CT image			X-ray image		
	MSE	MAE	PSNR (dB)	MSE	MAE	PSNR (dB)	MSE	MAE	PSNR (dB)
Haar	0.0089	0.0747	21.5544	0.0087	0.0739	20.8593	0.009	0.0746	20.8147
Sysm4	0.0084	0.0725	21.9326	0.0083	0.0721	20.4817	0.0087	0.0697	22.9286
bior1.3	0.0095	0.077	25.788	0.0093	0.0766	23.8995	0.0071	0.0677	21.244

Table 2 Global thresholding

Wavelet	MRI image			CT image			X-ray image		
	MSE	MAE	PSNR (dB)	MSE	MAE	PSNR (dB)	MSE	MAE	PSNR (dB)
Haar	0.0079	0.074	21.4544	0.0089	0.0539	20.6533	0.008	0.0646	20.7147
Sysm4	0.0086	0.0825	22.9326	0.0083	0.0621	21.6827	0.0077	0.0897	21.6286
bior1.3	0.009	0.076	21.4889	0.0093	0.0666	22.2995	0.0071	0.0677	21.244

Table 3 Level dependent thresholding

Wavelet	MRI image			CT image			X-ray image		
	MSE	MAE	PSNR (dB)	MSE	MAE	PSNR (dB)	MSE	MAE	PSNR (dB)
Haar	0.0088	0.0748	20.4544	0.0087	0.0739	20.8593	0.0083	0.0766	20.3147
Sysm4	0.008	0.0745	21.8326	0.0083	0.0721	21.4817	0.0087	0.0697	20.6206
bior1.3	0.0098	0.087	23.788	0.0093	0.0646	22.4995	0.0078	0.0877	20.814

functions, as shown in Tables 1a–c, 2a–c and 3a–c respectively. The performance of the wavelet function is analyzed and assessed with the error criteria like MSE, MAE, PSNR. Their numerical results are tabulated below.

Thus from the above tables, it is observed for the MRI and CT Images, *bior1.3* wavelet and *Optimal Thresholding* techniques gives the best denoised results for X-ray images *sym4* wavelet gives best results. It gives higher PSNR, lower MSE and MAE value.

5 Conclusion

The generalization of the DWT method for 2-D case is introduced in this paper. The proposed algorithm is implemented for the processing of noisy Medical images. In spite of the simplicity of the proposed algorithm experimental results proved that it produce prominently better results with reference to visual quality and mean square error values. We believe that the results are very encouraging for other forms of

denoising based on the simplicity of the proposed method, Compared to other wavelets for Medical images, the Bi-orthogonal wavelet (bior1.3) gave the better results. Optimal thresholding along with bior1.3 wavelet gives better denoised result.

References

- Agrawal, S., & Bahendwar, Yogesh. (2011). Denoising of MRI images using thresholding technique through wavelet transform. *International Journal of computer Applications in Engineering Science*, 1(3), 361–364.
- Archibald, R., & Gelb, A. (2002). Reducing the effects of noise in MRI reconstruction, July 2002, pp. 497–500.
- Bahendwar, Y., & Sinha, G. R. (2012). A modified algorithm for denoising MRI images of lungs using discrete wavelet transform (pp. 29–32). In *National Conference on Innovative Paradigms in Engineering & Technology (NCIPET-2012) Proceedings published by International Journal of Computer Applications® (IJCA)*.
- Donoho, D. L. (1995). De-noising by soft-thresholding. *IEEE Transactions on Information Theory*, 41(3), 613–627.
- Kumar, P., & Agnihotri, D., (2010). Biosignal denoising via wavelet thresholds. *IETE Journal of Research* 56(3), May–June 2010.
- Peck, D. J., Zadeh, H. S., Windham, J. P., & Yagle, A. E. (1992). A comparative analysis of several transformations for enhancement and segmentation of magnetic resonance image scene sequences. *IEEE Transactions on Medical Imaging*, 11(3), 302–318.
- Prasad, V. V. K. D. V., Siddaiah, P., & Prabhakara Rao, B. (2008). A new wavelet based method for denoising of biological signals. *IJCSNS International Journal of Computer Science and Network Security*, 8(1), January 2008.
- Rissanen, J. (2000). Mdl denoising. *IEEE Transactions on Information Theory*, 46(7), 2537–2543.
- Ruikar, S. D., & Doye, D. D. (1997). Wavelet based image denoising technique. In (*IJACSA International Journal of Advanced Computer Science and Applications*, 2(3), March 2011.
- Taswell, C. (2000) The what, how and why of wavelet shrinkage denoising. *Computing in Science and Engineering*, 12–19, May 2000.
- Tsai, D. Y., & Lee, Y. (2004). A method of medical image enhancement using wavelet-coefficient mapping functions. In *Proceedings of the IEEE International Conference Neural Networks and Signal Processing* (Vol. 2, pp. 1091–1094), Dec. 2004.
- Umadevi, N., & Geethalakshmi, S. N. (2011). Improved hybrid model for denoising poisson corrupted X ray images. *International Journal on Computer Science and Engineering (IJCSSE)*, 3(7), 2610–2619.
- Yoon, B.-J., & Vaidyanathan, P. P. (2004). Wavelet-based denoising by customized thresholding. Work supported in part by the ONR grant N00014-99-1-1002, USA.

Deterministic Model for RF Hot Spots Location and Probability Within Empty Rectangular Structures

Ricardo Rodriguez and Winston G. Lewis

Abstract This paper introduces a theoretical model for determining the number of hot spots (high intensity electric fields) and their locations within an enclosed empty rectangular space that acts as a waveguide for electromagnetic waves in the radio frequency range of the spectrum. The model combines ray and geometrical optics for wave direction and interference patterns after multiple reflections have taken place within the guide. The location of the hot zones and hot spots due to intersecting rays are determined using trigonometry and vector analysis. Once these locations are identified, the varying and non-varying patterns of the waves are contained in fixed triangular areas occurring on both sides of the waveguide. Within these fixed triangles (zones) lie the high probabilities of hot spots and dead spots for electromagnetic propagation, both of which have their importance in health and safety and communication. The probability of hot spots is calculated for each hot zone.

Keywords Electromagnetic waves · Hot spots · Waveguide · Rectangular structures · Health and safety

1 Introduction

Radiofrequency radiation (RF) is found in the electromagnetic spectrum and is used in medicine, manufacturing, RF heating, navigation and communication equipment. Frequencies in the range of about 27 MHz are used in manufacturing, induction

R. Rodriguez (✉) · W.G. Lewis
Department of Mechanical and Manufacturing Engineering,
The University of the West Indies, St. Augustine Campus,
St. Augustine, Trinidad and Tobago, West Indies
e-mail: ricardoj.rodriguez@yahoo.com

W.G. Lewis
e-mail: winston.lewis@sta.uwi.edu

heating, welding, sewing and sealing at industries across the world and has been found to be quite efficient, while radio broadcasting and wireless telecommunication operate at frequencies from about 80 MHz up to the microwave frequencies in the GHz range. Lower frequencies find use in electric arc furnaces and security systems in stores.

This energy is useful and if harnessed and managed optimally, may one day be the alternative fuel of the future powering generators, vehicles and domestic lighting in addition to its present uses. As a natural source of energy propagating undetected to the human senses in most instances, one may instinctively think that RF will not cause adverse effects on life forms since we have grown accustomed to but are not immune to its effects. Drawing such a conclusion may not be wise since there is compelling evidence to suggest that RF, in addition to causing thermal effects in humans, also produces non-thermal effects such as electric shocks, vomiting, nausea, and nerve-tingling sensations.

Wireless communication and navigation depend on RF propagation through the atmosphere (troposphere, stratosphere, tropopause) which may be an unreliable medium at times due to RF build-up, fading and communication loss. This fading and build-up of RF are as a result of reflections, diffraction and interference of waves as they collide with natural and man-made artefacts in their path. Upon reflection or diffraction from these obstacles, the path difference between two rays which meet later on may cause enhancement or diminution of the wave intensity at that interference point in comparison to if there were no obstacle and the waves were propagating freely. Improving the reliability of RF communication therefore is of importance and relies heavily on system design and RF modelling for performance prediction. Research continues apace to determine the loss in communication link from cell towers to receivers as the radiation is interrupted by obstacles in its path in order to facilitate quality service to customers. In some situations the transmission power may be increased above normal operating limits to facilitate drops in signal and even though the average spatial value of the radiation may be within the exposure limits, the peak intensity values may rise to even higher values causing increasing probability of adverse effects.

This field intensity enhancement of the wave and its location should be of primary concern as a potential health and safety threat especially for workers operating in and around high intensity RF fields, and any attempt at modelling to predict RF communication reliability in use, should also include the associated human factor risks.

Hazards from non-ionizing radiation have been neglected for some time until the end of the 60's when damage to eyes were observed from looking at solar eclipses, ultra violet exposure causing damage to skin tissue and exposure to infrared radiation found among steelworkers. After the 60's, greater use of microwaves and lasers prompted international bodies such as the International Commission on Radiological Protection (ICRP), to develop exposure limits and guidelines for occupational and public exposure to non-ionizing radiation, with recommendations for safe use and implementation procedures (Cember 1996).

The OSHA of the United States of America has instituted a maximum exposure level of 10 mWm^{-2} for frequencies of 10 MHz–100 GHz averaged over a 6 min period which has been set based on the thermal effects of the radiation and was believed to be the maximum heat that the homoeostatic thermo-regulating system of a healthy adult could sustain.

In addition, the threshold set for both thermal and non-thermal effects for harmful bio-effects gives the SAR (specific absorption rate) at 0.4 W/kg. Of special interest is the frequency region between 10 and 300 MHz where a standing man acts as a dipole for these frequencies and absorb maximum radiation and hence have the potential for maximum damage to tissue. Workers using RF within these frequencies such as those ISM bands (Industrial, Scientific and Medical) and those involved in industrial heating are at risk as well as persons within the vicinity of cell, television and radio broadcasting towers. So even though microwaves have frequencies outside 2000 MHz, they do have a bandwidth of 200 MHz which may be dangerous.

2 Ionizing Radiation

The hazards of ionizing radiation are immediate depending on the dose one is exposed to and the period of exposure. There is therefore a responsibility to the public for those in authority to ensure that there is a system in place to reduce exposure to RF since this has been found to cause cancer and genetic defects. Exactly what should the threshold exposure be for ionizing radiation? This is difficult since the tolerance depends on the individual. A zero-threshold model has been proposed and has been found to be too conservative given the ability of the body to repair damaged cells (Cember 1996). There is however an increased probability of contracting diseases based on the increase of dose and some threshold should be set for deterministic and stochastic probabilities. There are some persons who are hypersensitive and respond to even extremely low doses of the radiation while there are those who may not. In this regard, assigning a distribution susceptibility to a population may be met with a large degree of uncertainty.

According to Cember (1996), the ICRP the recommended dose limitation is based on three basic tenets which are: justification as decided on by the society, optimization where all exposures are to be kept as low as reasonably achievable and dose limitation where dose equivalent should not exceed some limit as prescribed by the relevant authorities.

Justification has been viewed as a societal decision and not a radiation one. This can only be true however if the society has information on the potential risks of the radiation hazard, the absence of which, only introduces confusion and ambiguity. The second tenet focuses on operational levels, where they should be kept very low but this can defeat the purpose of using the radiation for treatment and maintenance and manufacturing purposes. According to ICRP, the dose limit to a population is based on use and is the sum of several contributory doses.

3 Non-ionizing Radiation

This radiation has less energy than ionizing but is used in many applications in communications, navigation and manufacturing industries. To this end, a large range of frequencies is used to effect the benefits. The ICRP addresses ionizing radiation with less attention being paid to non-ionizing radiation despite public outcry that RF from Cell Towers is adversely affecting health. The probability of adverse effects due to exposure to low intensity RF will intuitively be believed to be low at worst, since there is no conclusive evidence that the radiation causes such. This should not discredit the complaints however since there may be hypersensitive persons just as in the case explained for the ionizing radiation.

As such, it is difficult to set a threshold for exposure to this radiation propagating in open space. There are guidelines from local authorities that restrict the use and intensity of RF in the community. As population size increases, there is a growing proliferation of humans living and working in close proximity to each other and to sources of this radiation. High rise buildings, schools, universities, homes all add to the complex nature of the propagation characteristics of this radiation.

RF from broadcasting and cellular towers radiates outwards in open space and dies out quickly with distance from the source. This may not be a health concern if the towers are far from civilization but they are not and these RF waves are now able to infiltrate our homes, offices, etc. and this is where the problem of exposure may lie. As RF waves of wavelength dimensions close to the dimensions of door-ways, window openings, tunnel entrances, air-condition ducts and confined spaces become incident on these man-made artefacts they tend to conserve and not disperse their energy as easily (Whitaker 2002). An RF wave of frequency 105 MHz as used in FM radio emanates from a source its wavelength can be calculated as; $\lambda = c/f$, $3 \times 10^8 / 1.05 \times 10^8$, which works out to be 2.9 m. This dimension is approximately equal to the width of some entrances. If this entrance is for an empty rectangular building of door entrance width equal to 1.45 m, then under certain conditions the building can operate as a TE₁₀ waveguide. Under the circumstances, the waves will travel down the guide in a zig-zag manner reflecting off of the walls and interfering with each other. The energy is contained within the confines of the boundary and points of higher than usual intensity (constructive interference) called hot spots and those of lower than usual intensity (destructive interference) dead spots will occur. An interference pattern is hence set up with varying high intensity and low intensity spots where they may be a potential health threat due to higher than usual exposure, or cause communication loss in wireless systems (Iskander et al. 2002). People working within these hot spots may be at risk to RF exposure and as such, need to know where these points are located to avoid contact with them.

4 A Deterministic Model for RF Location

Exactly where are these hot spots? Simple use of trigonometry, ray and geometric optics, and vector analysis may be helpful for this determination (Liang and Bertoni 1998). A deterministic model that gives the areas of highest probability (hot zones) for obtaining hot spots, and the location of these hot spots will be shown.

If we assume a confined empty rectangular space of entrance width ‘a’ = 1.75 m acting as a waveguide for vertically polarized waves entering the guide at an angle of incidence of 60°.

The cut-off frequency $f_{cmn} = c/2\{\sqrt{[(m/a)^2 + (n/b)^2]}\}$; $m = 1$ $n = 0$ for TE₁₀ mode which is 85.7 MHz for this guide dimension. For width ‘a’ = 1.75 m and angle of incidence 60°, then $f = fc/\sin 60$ which is equal to 98.9 MHz. If the antenna emits at 98.9 MHz, then since this frequency is higher than the cut-off, it should be able to propagate down the guide, air-condition duct for example, once excited. For the guide operating as a single mode operation, i.e., for the TE₁₀ mode only, waves with frequency 98.9 MHz that strike the entrance at 60° will propagate and fill up the spaces between the points $a = 0$ and $a = 1.75$ m. The reflections caused inside will set up triangular areas (hot zones) within which hot spots and dead spots can be found. The hot zones are all of same area and repeat periodically along the guide and give the probability of RF hot spot accumulation, where the waves interfere constructively.

5 Hot Zone Areas

The area of a hot zone is given by $a^2/4 \tan \theta$, where θ is the angle of incidence of the incoming waves to the xz (width and length of guide respectively) plane of the space and ‘a’ is the width of the space. As θ decreases, the zone area increases up to the guide length, otherwise the hot zone area within the guide begins to decrease. In this regard, the effective area of the hot zones found for a given width within the guide is therefore restricted by the length of the guide and defined for: $\theta < \tan^{-1} a/l$, where l is the length of the guide.

$$A = 1/2(a/2)l = a^2/4 \tan \theta = a^2/4 \cdot 1/2 = a^2/8$$

The maximum area A_0 of the hot zones for $a = 1.75$ m and length $l = 5.0$ m is therefore $1.75 \times 5.0/4 = 2.2$ m². The minimum angle for optimal area is $\tan^{-1} 1.75/5.0 = 19.20$. Larger angles of incidence will cause smaller triangles to form which will be subsets of the largest triangle. For example, propagation at 60° will have an area of $1.75^2/4 \tan 60 = 0.442$ m². Further for an angle close to 80°, then the area swept out will be $1.75^2/4 \tan 80 = 0.135$ m² which is small and as we get closer to 90° we see that the area reduces to zero. The probability therefore for interference of any kind becomes very remote and tends to zero as we move from

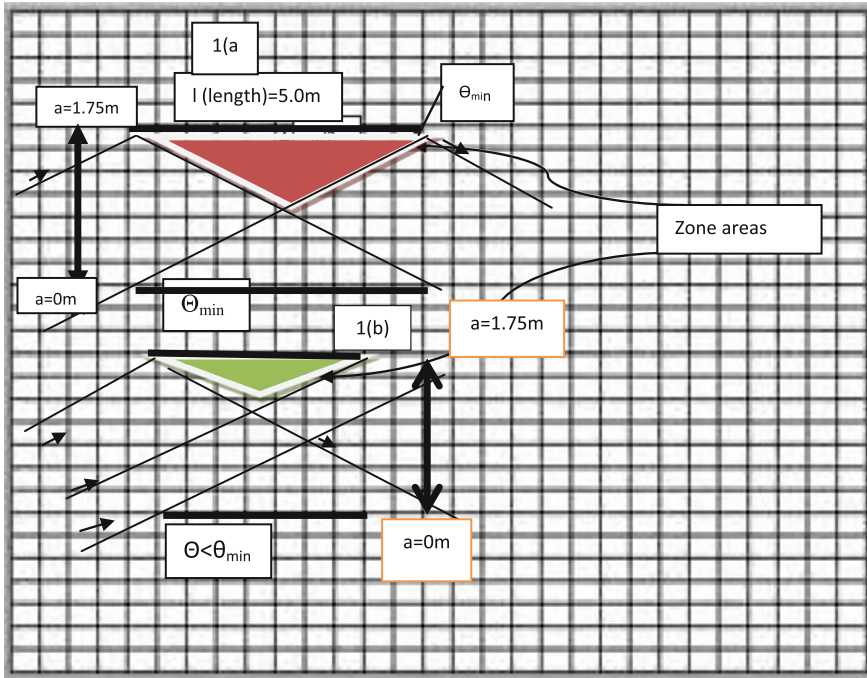


Fig. 1 Grid showing zone areas of high hot spot probability

low angles of incidence to large. As the angle of incidence increases also, for any one mode of operation, the frequency of waves allowed to propagate within the guide decreases.

Figure 1a shows the area swept out for the minimum angle of incidence causing the maximum zone area at top of figure, and Fig. 1b the area swept out for angle of incidence less than the minimum angle of incidence. For the second case, the ray at $a = 0$ goes outside the guide length. A smaller area is obtained. The reader may try to see what happens when the ray at $a = 0$ is greater than the minimum angle of incidence.

6 Hot Spot Location

The hot spot locations are identified by tracing any two rays from their origin at the entrance of the guide to their point of intersection and if the path difference Δ between them is a whole number of wavelengths, $n\lambda$, then we have constructive interference and a hot spot. First divide the guide space into a grid of equal squares as shown in Fig. 2. For the rays originating at P and R, P reflects at S and intersects R at Q. Using vector analysis then, vector r_3 is the resultant of vectors r_1 and r_2 ,

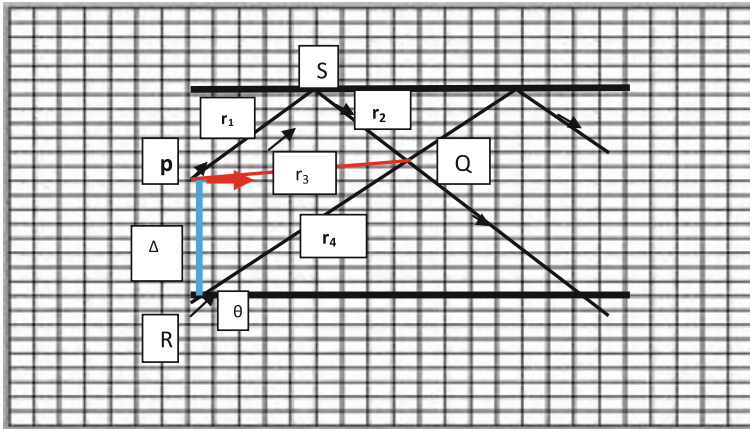


Fig. 2 Grid layout of guide showing vector analysis for hot spot location

Fig. 2. Note that $(r_4 - r_3)$ is the path difference Δ , which is the vector along the entrance width. Then, $r_3 = 8i + j$ and $r_4 = 8i + 9j$, so $r_4 - r_3 = 8j$. This $8j$ is equal to 8 units along the guide width and since $j =$ unit vector of magnitude equal to $1.75/14 = 0.125$ m, then the path difference $\Delta = 1$ m. This method of calculating Δ can be readily applied to any two waves of same frequency entering the guide. All we need to know is if the path difference between the waves at the guide entrance can be accommodated within the width and how many multiples of it. The number of multiples that can be accommodated is for $n\lambda = a$, $n\lambda < a$.

For $f = 98.5$ MHz which gives $\lambda = c/f = 3 \times 10^8 / 98.5 \times 10^6 = 3.1$ m, for angle of incidence of 60° , then is the point Q a hot spot for the two rays leaving any points from the guide entrance? We must now equate this to $n\lambda$, where $\lambda = 3.1$ m. As we see; $n = 1/3.1 < 1, 2, 3$ i.e., whole numbers so this is not a hot spot. If we allow for a higher frequency and hence larger area by making the angle of incidence smaller, then say for angle 30° , frequency = 171.4 MHz and $\lambda = 1.75$ m. This implies that $n = 1$ so we have a hot spot for the lower angle and wider area.

There is a potential hot spot then in the guide provided that the length is long enough to accommodate the zone area. We can therefore set up a table for the TE10 guide for different frequencies above the cut-off of 85.7 MHz and see what path differences and frequencies would lead to hot spots.

7 Analysis

This model sets the empty space scenario for arriving at the trivial solution using the guide entrance as the key variable which once known could be used to determine which wavelengths will interfere constructively leading to potential high risk RF hot spots. The probability of having x hot spots within a total possible n spots

for a number of propagating frequencies within a certain range can be achieved through a Binomial distribution for small values of n . Let x be the percent of hot spots that can be achieved within the guide for a given angle of incidence, in the TE10 mode, say, for a number of frequencies above the cut-off.

If, as calculated by the mode, there are a possible n spots (hot and dead), then the probability of finding fewer than n hot spots can be found by:

$$p(x) = P(X = x) = n!/x!(n - x)! [px (1 - p)]^{n - x}; \text{ for } x = 0.1.2...; \text{ and } 0 \text{ otherwise,}$$
 where p is the probability of a hot spot and $1 - p$ is the probability of not finding one, n is the number of trials.

The Poisson distribution can be used to determine the probability of the number of hot spots that can be obtained within a hot zone (triangular area) for larger n . Suppose that there are 9 hot spots calculated within a hot zone whose area is 0.442 m^2 . What is the probability of obtaining exactly 15 hot spots in the maximum area of 2.22 m^2 ? Nine hot spots calculated by the model for an area of 0.442 m^2 imply that for an area 5 times the size then there should be 45 hot spots.

Using the Poisson distribution then $P(X = 15) = e^{-45} 45^{15}/15! = 1.37 \times 10^{-7}$. This is very small, so let us see for a probability of obtaining exactly 30 and 40 hot spots. These work out to be 0.00426 and 0.0470 using the same Poisson equation. In this way therefore, the probability of obtaining a certain number of hot spots in a given area can be obtained once the model predicts the total number of them in any area. For a varying angle, which changes the area of the hot zone, the number of hot spots will change and the probability of obtaining this number can be calculated.

The argument presented so far is only for the TE10 mode and varying angles of incidence which could be extended to a multi-moded guide, also for varying angles of incidence. In this way, we can determine the probabilities of hot spots for all propagating waves within a guide operating as a single mode or multi-moded.

8 Discussion

The concept of hot spots is not restricted to this paper in that it finds current use in internet access where it has been defined as a physical location that offers internet access over a wireless local area network through the use of routers and internet service providers. Hot spots find importance in mines and tunnels where fading of RF occurs making it difficult to communicate via wireless mobile phones or internet. This could be dangerous since in the event of an accident, there is the need for fast and efficient communication in order to save lives or prevent a potential disastrous situation. Statistical models have been proposed to better understand the propagation characteristics (reflection, diffraction, refraction) of an enclosed environment and to quantify the delay spread in underground mine tunnels to allow engineers to produce low cost design for more efficient and high performing communication systems (Wang 2010).

There is again much impetus for determining RF hot spots to ensure smooth communication by using wireless mesh networking inside of buildings and mines.

These mines and, tunnels, in many instances behave as waveguides and different deterministic models have been tried using wireless mesh network to predict communication levels within them (IJCSNS 2008). Wireless mesh networking requires a series of fixed or mobile units such as routers, laptops and cell phones to propel the signal forward to a point of interest. Traditionally, networks relied on a small number of wired access points to connect users; these were called nodes. However with increasing need for communication in diminishing space due to high demand and population explosion, hundreds of mesh nodes will have to be deployed at various locations to share the network communication across a large area (IJCSNS 2008, pp. 12–15). Such a task could be onerous unless some level of prediction of natural hot spot location based on constructive interference can be modelled. In this regard the model proposed in this paper offers a theoretical approach at presumably, locating best points for mesh networking and can assist in complementing the mesh network approach through the reduction of repeater units by simply placing low cost antennas and adapters at the hot spots formed due to interference, within a confined space. With this advancement however, the author is concerned for the safety of users of this growing need for wireless communication in that there may be adverse health effects due to RF exposure for someone continually working in a radiation intense field. Factories (which are large confined spaces) of the future no doubt will find further use for wireless systems in their day to day operations. As such, future factories must be designed and constructed with dimensions that allow for efficient management of RF waste, usage and safety to workers. Storage of explosive chemicals at a hot spot can have a high probability of being engaged which could be disastrous in terms of life and limb as well as litigation suits.

9 Conclusion

We have to only know the width and height of the entrance to a rectangular empty confine space, the propagation characteristics to calculate the number of possible hot spots for each mode of operation. The TE₁₀ mode was used to develop the model but can also be applied to the multi-moded guide using the same principle. According to geometrical optics, a steady interference pattern is expected when waves from a coherent source interfere (amplitude and frequency the same or very close) which can be expected from a RF tower. Interference will also occur with varying frequencies coming within the band of a particular frequency but the pattern will not be steady but move through high and low intensities during the interference. Whether fixed pattern or not, the environment of a confined space within which RF transmission takes place is a hostile one and should be investigated further to intensify the search for RF hot spots. International guidelines on exposure limits do not adequately treat with setting limits on exposure within confined spaces. This is understood since confined spaces such as the one identified in this article, are not always empty but will have people, furniture and fittings inside.

Factories of the future will have to be jostling for space and will find their structures resembling a number of waveguides fitted one on top of the other as the factories take on a more vertical structure. Construction designs will therefore have to consider varying shapes of the buildings so as not allow RF build and RF hot spots from external sources to accumulate in unwanted locations within the structure. As the model shows, the hot spots are found in hot zones and determining the probability of finding hot spots within these hot zones may be more critical and useful than trying to pin-point exactly where the hot spots are located.

References

- Cember, H. (1996). *Introduction to health physics*. New York: McGraw Hill.
- Iskander, F., Magdy, F., & Zhengqing, Y. (2002). Propagation prediction models for wireless communication systems. *IEEE Transactions on Microwave Theory and Techniques*, 50(3), 2002.
- Liang, G., & Bertoni, H. L. (1998). Approach to 3-D ray tracing for propagation prediction in Cities. *IEEE Transactions on Antenna and Propagation*.
- Manani, M., Delisle, Y., Misson, M., Moutairou, M., Aniss, H. (2008). Wireless mesh networks performance assessment for confined areas deployment. Underground Communications Research Laboratory, UQAT, 450, 3rd avenue, Val d'Or, Qc, Canada, J9P 1S2, August 5, 2008.
- Wang, S. (2010). Radio wave attenuation character in the confined environments of rectangular mine tunnel. *Xi'an University of Science and Technology, China*, 4(2), 65.
- Whitaker, J. (2002). *The RF transmission systems handbook* (pp. 15–13). CRC Press LLC: 2000 N.W. Corporate Blvd., Boca Raton, Florida 33431.

Biography

Ricardo Rodriguez is currently pursuing a Ph.D. degree in Mechanical Engineering under the supervision of Professor Winston Lewis. His research focuses on the modelling of radiation intensity and location in confined spaces. Mr. Rodriguez holds a B.Sc. degree in Physics, M.Sc. in Engineering Management and M.Phil. in Mechanical Engineering from the University of the West Indies, and a certificate in Standards and Quality Assurance from the Indian Bureau of Standards. He was also awarded a special prize in the Bright Solutions Category Prime Minister's Award Function, 2004.

Winston G. Lewis is a Professor of Industrial Systems Engineering at the University of the West Indies. His research and development work is in the areas of Metallurgical and Industrial Engineering, Sheet Metal Forming, Manufacture of the Steelpan Musical Instrument, Applied Ergonomics and Workplace Design, Engineering Quality Management and Nano-technology. Professor Lewis is a Registered Professional Engineer and a Fellow of the Association of Professional Engineers of Trinidad and Tobago (APETT) and a Fellow of the American Society of Mechanical Engineers (ASME).

Heat Stress in the Workplace: A Case Study of a Cement Manufacturing Facility in Trinidad

Winston G. Lewis and Ricardo Rodriguez

Abstract Heat stress is a well-known occupational health disorder and since Trinidad is a tropical island in the Caribbean, there is a serious risk to heat stress illness occurring when workers operate in adverse thermal working environments. This paper aims at illustrating the prevalence of work-related heat stress within a cement manufacturing facility in Trinidad. Using the Threshold Limit Value (TLV) Standard, it was found that 10 out of 11 work stations exceeded the recommended time to perform the given task. The study of heat stress experienced by workers was linked to the subjective heat related symptoms as identified using a questionnaire. On average, kiln workers experienced a greater number of symptoms than mill workers with the most common symptoms to both groups being dehydration, fatigue and headaches. The study showed that symptoms increased with the age and body mass index (BMI) of the participants.

Keywords Work related heat–stress disorders • Heat stress • Heat strain

1 Introduction

Many indoor and outdoor occupations require employees to work in high temperature environments and in tropical countries such as Trinidad the problem of heat stress illness is thus increased. It is important to ensure that the Core Body Temperature (CBT) of workers in those conditions remain constant in order for the body to function efficiently (Parsons 2005). When the body gains heat, this heat

W.G. Lewis (✉) · R. Rodriguez
Department of Mechanical and Manufacturing Engineering,
The University of the West Indies, St. Augustine Campus,
St. Augustine, Trinidad and Tobago, West Indies
e-mail: winston.lewis@sta.uwi.edu

R. Rodriguez
e-mail: ricardoj.rodriguez@yahoo.com

must be continually dispersed to the surrounding. Factors that influences the rate of heat dissipation are; environmental parameters, metabolic rate and the clothing worn. These factors determine the overall heat load to which workers are exposed to (Bernard 2012). In extreme thermal conditions the body cannot dissipate enough heat causing the CBT to increase, this leads to heat strain on the body developing. Heat stress illnesses occur due to heat strain on the body, it is the body's way of responding to the intense thermal environment. Some heat illnesses are heat exhaustion, heat stroke and heat cramp (Adelakun et al. 1999). High levels of heat strain may lead to a complex range of heat related illnesses.

Heat stress illnesses can lead to the impairment of a person's physiology causing them to experience symptoms such as fatigue, headaches, nausea and dehydration. This affects the worker's performance causing a decrease in productivity, reduced physical performance, and an impairment of mental function leading to near misses, injuries or accidents.

Trinidad does not have specific laws or regulations governing heat exposure and resulting heat stress. In the absence of clearly prescribed standards, Threshold Limit Values (TLVs) for heat stress as outlined by the American Conference of Governmental Industrial Hygienists (ACGIH) should be followed (OSHA 1999). These TLVs can be used as a guideline for enforcing the legislation's general duty clause, which requires employers to take every precaution reasonable to protect workers' health and safety.

2 Literature Review

This study seeks to evaluate the levels of heat exposure and symptoms of heat-related disorders encountered by workers at a cement manufacturing facility in Trinidad. Although employees in many industrial manufacturing processes are at risk of suffering heat strain and heat-related illness, workers in a typical cement manufacturing plant may be particularly at risk due to the specific challenges of their work-environment. With the many demanding tasks combined with high working temperatures in a tropical country, the body may begin to accumulate heat from both the work-environment and metabolic load thereby increasing chances of heat related illness. At present there is a lack of studies seeking to evaluate heat stress in cement manufacturing facilities and no formal data focusing on heat related disorder in facilities in Trinidad.

Heat stress may pose significant problems for workers especially in a manufacturing facility. Workers may become disoriented, with impaired judgment, as heat stress increases. This increases the risk of injury as the ability to take protective measures is reduced due to impaired decision making (Glazer 2005). The body's inability to thermo-regulate and cool itself may result in heat related illnesses such as heat exhaustion or heat stroke. Such outcomes however are preventable by properly monitoring environmental and work conditions, applying the appropriate preventative measures, as well as training employees and supervisors on heat

exposure safety (Environmental Protection Agency 1993). However, with a lack of regulation and directed policy, it is difficult to implement these steps.

Occupational studies highlight the significant relationship between the environment, work rate metabolic load, and core body temperature. During work and activity, core body temperature remains relatively constant for a given metabolic rate even with an increase in environmental temperatures. This occurs until a threshold temperature is reached. At threshold temperature, core body temperature increases steeply in a highly non-linear fashion with increased ambient heat. As work rate increases, the amount of environmental heat a worker can tolerate decreases. Inversely, as environmental heat increases, work rate should be decreased for an exposed employee (Bernard et al. 1994).

Thermoregulation in humans is the ability to regulate a constant core body temperature of approximately 38 °C under varying environmental conditions. In the event that the core body temperature rises above 41 °C, severe disorders may occur, with a core body temperature over 43 °C resulting in death. The specific transfer mechanisms of heat include radiation, convection, conduction and evaporation. The effectiveness of heat transfer as well as the direction in which heat transfer occurs depend on environmental factors including temperature, humidity and radiant temperature as well as the metabolic rate of the subject. Other factors may also affect the heat gain and heat loss transfer such as the type of clothing worn.

Whenever activity is performed there is an accompanied increase in internal heat production and an increase in the core body temperature. The rate of increase of core body temperature is higher in hot environments. If due to environmental or other factors, the ability of heat to be transferred from the body is diminished, even low levels of activity may result in a rapid rise in the core body temperature. Initial response may include sweating and increased skin blood flow for increase heat loss. The increased skin perfusion associated with this blood flow causes an increase in skin temperature facilitating greater heat loss by evaporation. An equilibrium is thus reached with the increased lost to new heat gained, so that the core temperature stabilizes at a higher level (Hunt 2011).

3 Heat Illnesses

Cement manufacturing poses a great risk to workers contracting heat related illnesses such as heat stroke which carries with it accompanying symptoms that include: headaches, speech disability, dizziness, cramps, confusion and in extreme cases, coma. The high temperatures in the factory environment which may occur due to high heat exposure as well as physiological strain induced by increased metabolic loads and work duration, could lead to core hyperthermia which is an abnormally high CBT above 41 °C. This is a serious medical condition that requires urgent attention when it occurs since it could lead to death through organ failure if the body temperature passes the threshold temperature for normal functioning. Other heat-related conditions that can occur include heat fatigue, heat cramps, heat

syncope, heat rash, and heat exhaustion, all of which play a pivotal role in the health and well-being of the worker and whether he is capable of executing his duties efficiently which could lead to downtime and loss of earnings and profits to the organization (EPA 1993).

4 Heat Strain

Upon exposure to heat stress, the body is focused on maintaining the CBT within an acceptable range. The body's resultant response from heat stress is known as heat strain (DiCorleto et al. 2002). Factors and conditions including hydration status, fitness, age, acclimatization and gender can influence the levels of heat strain. Individuals react differently to heat (Hancock and Vasmatazidis 2003) hence it is important to distinguish the risk factors that can substantially raise the potential of a worker experiencing heat stress (Bernard 2012).

5 Methodology

The use of empirical methods to determine situations where excessive heat may cause harm due to heat stress is critical in ensuring the protection of workers in hot environments. Thermal stress or heat stress indices attempt to predict the effect of hot environments, by preventing core body temperature from exceeding 38 °C. Many indices have been developed in the 20th century that seek to evaluate heat stress in the workplace for specific industries.

Indices can be categorized into either rational or empirical subgroups, where rational indices are based on the principles of heat exchange and heat balance in assessing human physiological responses. Unlike rational indices, empirical indices are based on processed data from field experiments that were performed under different thermal environmental conditions. These indices describe heat stress limits in relation to environmental conditions, work rate and clothing parameters without relying on physiological conditions and measurements.

Common empirical indices include Oxford index, Effective temperature, Corrected effective temperature, Wet bulb temperature and Wet bulb globe temperature index. The accuracy of empirical and rational indices have been well studied and document all over the world with the WBGT being deemed as the most appropriate index for use in studies and evaluations in workplaces (Hartley and Waterhouse 2003).

Parsons (2005) have noted that the WBGT Index is the most common method for the assessment of occupational heat stress, due to its reliability, simplicity and robustness as well as the fact that it is appropriate for both outdoor and indoor analyses of exposure to extreme or moderate heat. Comparison between WBGT and other heat stress indices for many occupational settings have been investigated.

Bernard (2012) concluded that the WBGT is correlated with CBT rather than heart rate or sweat loss.

The WBGT provides a combined measure aimed at estimating the effect of temperature, humidity, and solar radiation on humans. The WBGT data collection instrument collects all three parameters simultaneously and calculates values that are used to estimate if a problem exists by determining whether measured values exceed reference values. WBGT values are used most commonly in conjunction with work rest schedules based on metabolic rates and clothing adjustment factors.

6 Data Collection and Analysis

Data for the thermal environmental exposures of workplaces in Trinidad is lacking. Information is needed to evaluate the symptoms experienced upon heat exposure that exceeds the threshold values. The prevalence of worker heat related disorder symptoms will also be investigated and assessed through a questionnaire.

7 Environmental Monitoring

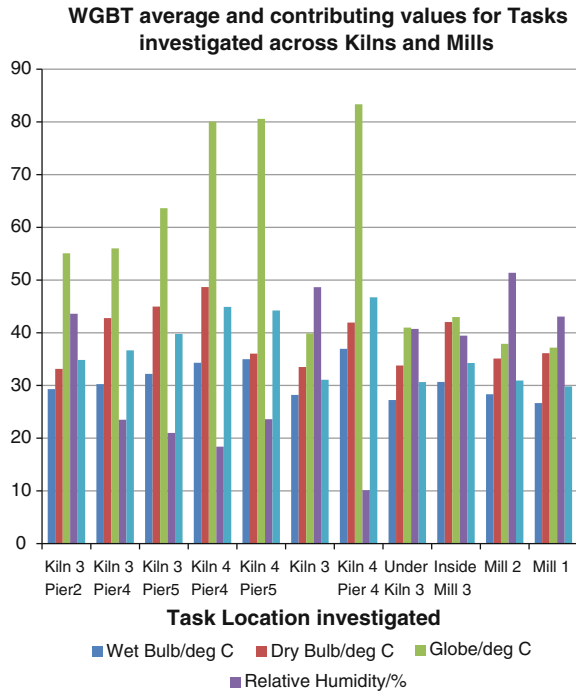
To assess the heat stress in the thermal environment the Wet Bulb Globe Temperature (WBGT) was found. This was used to evaluate the heat stress that workers are exposed to along the kilns and mills in accordance to the standards set out by ACGIH (2012). The types of jobs monitored at the kilns were; creep measurements along piers, greasing, hot kiln alignment and maintenance under the kiln. The types of jobs monitored at the mills were; inspection inside the mill, cleaning inside the mill and maintenance at the mill.

For each task, interviews were done with workers and observational assessment for existing work practices were recorded to assess the type of work load category the work performed is categorized as light, moderate, heavy or very heavy. It was determined that the tasks monitored for this study at the kilns varied from light to moderate whereas, the workload at the mills varied between light to heavy.

Analyzing the results seen with the increasing values of dry bulb, wet bulb and black globe temperature from pier 2 to pier 5, this directly relates the expected trends of the WBGT values to increase as well. The WBGT readings obtained can be seen in Fig. 1. These WBGT values were analyzed using the ACGIH Standards (ACGIH 2012). Using the work rest regimes for light work load determined from the ACGIH Standards, it can be seen that these values have exceeded the TVL value of 32.5 °C. Thus the work rest regime derived is 0/100 %, this means work 0 % and rest 100 %.

The TVL Standards take into account a recommended hourly rate, therefore workers are required to rest for the 60 min and work for 0 min. This value means that for light workloads, workers cannot tolerate the heat exposure and no work

Fig. 1 Shows the WBGT average and contributing values for tasks investigated across kilns and mills



should be performed. Since work is performed exceeding the recommended TLV Standard workers are exposed to heat stress, this would give rise to individuals experiencing heat related symptoms. All workers working or performing tasks should take precaution and control measures.

Even though work at these temperatures is not permitted according to the Standards set out by ACGIH, work must be performed. All workers performing tasks should take precautions and recommended control measures must be taken.

8 Characteristics of Participants

The data collected using a questionnaire was analyzed to obtain statistical trends regarding the prevalence of symptoms in relation to heat strain as well as underlying contributing factors and predispositions of the subjects. The administration of the questionnaires was conducted at all stations where the environmental heat stress survey was conducted.

The participants of the survey were characterized by age, BMI, activity levels conducted per week and years of employment. This is because the literature points to these characteristics as having an influence on the degree of heat strain

experienced by the individual. From the results it was found that the majority of workers both at the kilns and mills were in the 30–40 year age group (75 % of the mill workers were in this category, while 58.4 % of kiln worker were in this category). The second largest age group for both kiln and mill workers was the 20–30 year age group, with the 25 % remaining mill workers and 33.3 % of kiln workers falling in this group. The final 8.3 % of kiln workers fell in the 40–50 year age group. No mill worker age 40–50 participated in the survey. These results clearly indicate that most of the survey participants were middle aged. A total of 66.7 % of the kiln worker participants and 75 % of mill worker participants were employed for more than 5 years.

The participants were separated into categories of overweight and not overweight using BMI. Equal percentages of kiln worker participants were categorized into overweight and not overweight. The majority (75 %) of mill worker participants were found to be overweight. Participants were grouped into those that engaged in no physical activity per week and those engaging at least one activity per week. The majority of the participants of the survey engaged in no physical activity whatsoever (75 % of all kiln workers and 62.5 % of all mill workers). Since the majority of the participants are middle aged (30–40 yrs.) and engaged in no physical activity it was expected that many of the participant in the survey would have experienced some degree of heat strain and associated symptoms obtained. This is because the level of heat strain increases with age and lack of physical activity (Havenith et al. 1988).

From the data collected on kiln workers, the most affected participants experienced 29 % of possible symptoms and no worker experiences less than 5 % of total symptoms. By contrast, the most affected participants in the mill experience a total of 15 % less symptoms than the most affected individual working in the kiln. In addition, there is more than one mill worker exhibiting no sign or symptoms of heat strain. The data shows that the average percentage of total symptoms experienced in the kiln workers was 15 %, while the average percentage of total symptoms experienced by mill workers was 8 %. These trends suggest that kiln workers are more affected by heat stress and are at a greater risk for heat strain than workers in the mill. This is supported by the data obtained from the environmental monitoring, with WBGT values being all higher in the kilns than those recorded at the mills.

9 Discussion

The distribution of each heat strain symptom occurring in kiln and mill workers were examined for each symptom mentioned in the questionnaire and the frequency of participants reporting this symptom was noted. It was found that the three most common symptoms reported by participants both in the kiln and mills are; dehydration, fatigue and headaches. These symptoms occur in the same order. Studies done by Mei-Lien et al. (2003) found that the most prevalent symptom among steel workers were dehydration and fatigue.

In general, kiln workers experience a greater number of symptoms than mill workers. Specifically five symptoms: muscle cramps, weakness, low coordination, hot and dry skin and high body temperature are experienced by kiln workers but not by mill workers. Also, it was found that symptoms common to both groups are experienced to a greater degree by workers in the kiln. This again confirms the general trend outline previously that kiln workers are much more affected by heat stress and are at a greater risk for heat strain than workers in the mill.

A total of 11 symptoms included in the survey were not experienced by any of the participants either in Kiln or Mill. These symptoms were occurrence of red rash, fainting, nausea, dizziness, confusion, irrational behavior, loss of consciousness, seizures, unable to concentrate, difficulty in breathing and nervousness. This suggests that the heat stress experienced by workers at the mill are not as adverse as those experienced by the kiln workers.

10 Conclusions

Based on a comparison with the recommended ACGIH (2012) TLVs the workers at the cement manufacturing facility were monitored at the kilns and mills. It was found that using the TLV Standards that 7 out of 9 kiln studies and 1 out of 3 mill studies had a recommended work rest regime of 0/100 %. To ensure worker safety against environmental heat stress it is recommended that no work should be performed. It can also be noted that the WBGT obtained at the kiln exceeded those at the mills. The physiological response the body has towards heat stress in the work environment is termed heat strain. Individuals at the kilns and mills are exposed to a high likelihood of heat strain and an increased risk of heat illness. When investigating subjective heat related disorder symptoms via a questionnaire given to kiln and mill worker it was found that in general kiln workers experienced an average of 8 % more symptoms than those of mill workers and a total of 5 symptoms that were reported by kiln workers were not experienced by mill workers. The most common symptoms to both groups were dehydration, fatigue and headaches. The extent of symptoms varied among different participants depending on age, BMI and activity levels. It was found that the amount of symptoms increased with the age of the participants; BMI (≥ 25 for an overweight person) and person who perform no weekly activity. Workers that were above the TLV Standards indicate that a recommended Work Rest Regime should be implemented and general controls at the facility such as self-pacing, training programs, health surveillance, shielding of radiant heat sources, ventilation, PPE, acclimation programs must be implemented and maintained.

References

- ACGIH. (2012). *TLV's and BEI's*. Edited by The American Conference of Governmental Industrial Hygienists. Cincinnati: Siginure Publications.
- Adelakun, A., Schwartz, E., & Blais, L. (1999). Occupational heat exposure. *Applied Occupational and Environmental Hygiene*, 14(3), 153–154.
- Bernard, T. (2012). Occupational heat stress. *Occupational Ergonomics*, 737–764 (CRC Press).
- Bernard, T., Dukes-Dobos F., Ramsey, J. (1994). Evaluation and control of hot working environments. Part II-the Scientific bases Guide. *International Journal of Industrial Ergonomics*, 119–138.
- Chen, M.-L., Chen, C. J., Yeh, W. Y., Huang, J. W., & Mao, I. F. (2003). Heat stress evaluation and worker fatigue in a steel plant. *AIHA Journal number*, 64(3), 352-352.
- DiCorleto, R. D., Coles, G., Firth, I. (2002). Documentation of heat stress standard developed for use in the Australian environment. In *Tullamarine Institute of Occupation Hygienists*.
- Environmental Protection Agency (EPA). (1993). *A Guide to Heat Stress in Agriculture*. EPA: Washington DC.
- Glazer, J. (2005). Management of heatstroke and heat exhaustion. *American Family Physician*, 71 (11), 2133–2140.
- Hancock, P., & Vasmatazidis, I. (2003). Effects of heat stress on cognitive performance: the current state of knowledge. *International Journal of Hyperthermia*, 19(3), 355–372.
- Hartley, C., & Waterhouse, P. (2003). *Health and Safety: Hazardous Agents*, Institution of Occupational Safety and Health (IOSH) Services Limited.
- Havenith, G., Coenen, J. M. L., Kistemaker, & Kenney, L. (1988). Relevance of individual characteristics for human heat stress response is dependent on exercise intensity and climate type. *European Journal of Applied Physiology and Occupational Physiology*, 77(3), 231–241.
- Hunt, A., (2011). Heat strain, hydration status, and symptoms of heat illness in surface mine workers. Ph.D. thesis.
- OSHA. Heat Stress (1999). http://www.osha.gov/dts/osta/otm/otm_iii/otm_iii_4.html#2.
- Parsons, K. (2005). Ergonomics assessment of thermal environments. *Evaluation of Human Work* (3rd ed., pp. 643–661). Boca Raton: CRC Press.

Author Biography

Winston G. Lewis is a Professor of Industrial Systems Engineering at the University of the West Indies. His research and development work is in the areas of Metallurgical and Industrial Engineering, Sheet Metal Forming, Manufacture of the Steelpan Musical Instrument, Applied Ergonomics and Workplace Design, Engineering Quality Management and Nano-technology. Professor Lewis is a Registered Professional Engineer and a Fellow of the Association of Professional Engineers of Trinidad and Tobago (APETT) and a Fellow of the American Society of Mechanical Engineers (ASME).

Modeling and Simulation of a Near Omni-Directional Hexapod Robot

D. Mahata, Ranjit Ray and Sankar Nath Shome

Abstract The present paper describes design and modelling aspects of a near omni-directional legged-wheel robot. While discussing the importance of twin frame legged robots with wheels in mobile robotic research, the basic geometrical configuration of the system was presented. The kinematic and dynamic analysis of the system facilitated improved overall design of the robot. Results of virtual simulation of the movement of this hybrid legged wheel system are also presented. An experimental lab-scale prototype has been developed and simulation results are compared with the test results to ascertain the technical feasibility of geometric model with respect to the mobility on different terrains.

1 Introduction

Mobile robots have become popular with myriad potential applications e.g. inspection, welding, painting, material/tool handling and transportation in manufacturing and hostile hazardous environment. In real factory world terrains and environment are not always smooth or structured. Wheeled locomotion has higher reliability, superior stability and higher energy efficiency when moving on flat terrain (Dutta et al. 2007). Legged locomotion has the highest adaptability to rough terrain because the contact points with the ground where the feet support can be chosen efficiently and safely. The added advantages introduce certain problems in terms of dead weight, energy efficiency, and speed of movement, etc. In order to acquire the benefits of both wheel and legged robots, researchers are trying to hybridize legged locomotion with wheeled locomotion depending on specific requirements to make it terrain adaptive which is the prime objective of this work.

D. Mahata
School of Mechanical & Building Sciences, Vellore Institute of Technology,
Vellore, Tamilnadu, India

R. Ray (✉) · S.N. Shome
Robotics & Automation Lab, CSIR-CMERI, Durgapur 713209, India
e-mail: ranjitray@cmeri.res.in

Over the last decade a number of legged mobile robot prototypes were developed, from biped to quadruped and hexapod robots (Sakagami 2002; Fielding and Reg Dunlop 2004; Ma et al. 2005; Fujii et al. 2006). Robots are independently driven by legs having degree of freedom (dof) 12 for quadruped, 18 for hexapod. More number of dof means low power to weight ratio with more control complexity leading to less efficient system. In order to rationalize these problems, total number of dof has to be abridged with minimum hindrance in the degree of mobility. Most of the practical walking robots are having hexapod configuration for stable motion. Researchers throughout the world have developed a number of mechanisms e.g. hexapod with 3 dof (Gurocak and Peabody 1998), 6 dof (Ota et al. 2001), 8 dof (Tsumaki 1993), 9 dof (Fukudaa et al. 1995; Koyachi et al. 1990), 11 dof (Krishna et al. 1997) and 18 dof.

Design of hexapod robot faces several challenges such as stability, turning, coordination of the legs, and path planning. It involves design of mechanism along with generation of complex control algorithm. Also for any legged vehicle, selection of proper gait and its sequence is essential depending on environmental and physical constraints. The environmental constraints are terrain condition, presence of obstructions and physical constraints are dof, speed, smoothness of body motion, stability of the body, ease of control, and power requirement. Large number of moving links makes the system more complicated necessitating further investigation and experimentations. In the present work, a simple twin frame near omni-directional hexapod system with wheels mounted at the tip of the feet is designed.

The paper is organized as follows. The proposed system is described in Sect. 2 including system configuration, characteristics, kinematics. Section 3 provides simulation and experimental results. Finally, Sect. 4 summarizes a few conclusions emanating from this work.

2 Configuration of the System

The robot consists of two parallel platforms having a relative rotational motion as shown in Fig. 1. Each platform holds three legs (Top platform holds Leg 1-3-5 and bottom platform holds Leg 2-4-6) in triangular fashion. Six legs formed a star like configuration providing a wide support area. 2D pantograph type leg is considered because of its decoupled kinematic characteristic for horizontal and vertical motion. Rigidity is high as the actuators are placed on the main body. This configuration with 13 dof enables the robot to move in any direction like an omni-directional robot. But here during change of direction of movement the robot is not rotating as a whole. One platform remains fixed allowing other platform to rotate for aligning in the direction of movement. Thus the proposed system is termed as near omni-directional system instead of omni-directional system. Walking motion can be accomplished as: (i) Legs 1-3-5 will go to the home position; (ii) First half cycle: Legs 2-4-6 will lift off and go to the home position and simultaneously bottom

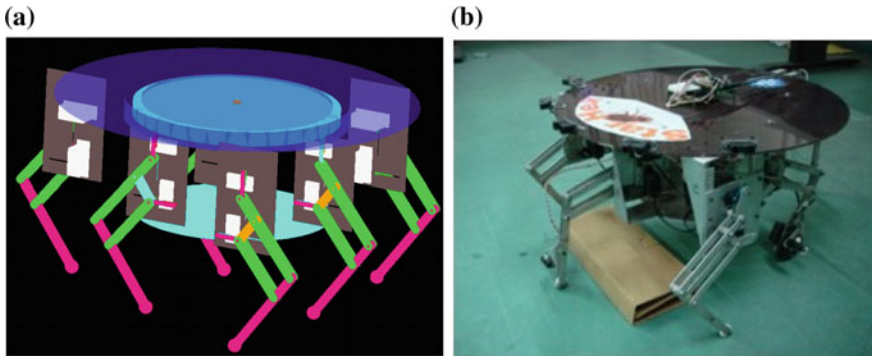


Fig. 1 a 3D model of the proposed hybrid system. b Prototype model

platform will rotate to the desired heading angle. At the same time Legs 1-3-5 which is on the ground will push the body in the forward direction until the full stroke; (iii) Second half cycle: Legs 1-3-5 will lift off and go to the home position and simultaneously top platform will rotate in the opposite direction depending on the desired heading angle. Besides that, two motorised wheels are mounted at the tip of Leg 1 and 3 for rolling motion on flat terrain where Leg 5 gives the support with the help of a roller.

The proposed hybrid system have the following performance characteristics:

- (a) It can navigate on flat terrain with high speed using wheels. If required it can also walk over rough terrain.
- (b) During walking, translational and rotational movements are decoupled in nature. Translation will be accomplished by the actuation of six legs, whereas rotational movement is carried out only by the central actuator within top and bottom plate.
- (c) The system does not have to change the gait pattern to move any direction. Only single gait pattern is sufficient for entire movement.
- (d) Because of pantograph configuration of the leg, length of the stride and lift has the flexibility to overcome the obstacles within its limit.
- (e) For the smooth relative rotational movement between top and bottom frames, top frame is sufficiently large enough compared to bottom.

The sizes of top and bottom platforms are largely dependent on the workspace of the each leg to avoid any obstruction for the continuous movement. System rigidity would decrease with increase of the top plate size. In transfer phase, the three legs which are mounted on the top plate are hanging away from the center support by the bottom plate. In the proposed system, smooth relative motion between two platforms is accomplished by means of thrust bearing. Based on design considerations the diameter of the top and bottom plates are found as 500 and 250 mm respectively.

Array of IR sensors is mounted at different levels to detect the obstacles. Five sensors are mounted on the top plate as shown in the Fig. 1b. One sensor is fitted just above the foot of the Leg 2 and another two sensors are mounted on wheels. These three sensors will guide the change of locomotion mode from wheeled to legged whereas array of five sensors is utilized for detection and avoidance of the obstacle. Thirteen Hitec motors (weighing 65 g each) are used as actuators. The controller resides on one PIC based microcontroller with capability of sensor interfacing and motor actuation according to locomotion requirement.

2.1 Kinematics of Legs

As shown in Fig. 2a, B_0 is the body frame about which top and bottom platform can rotate. Two frames for top and bottom platforms are B_t and B_b respectively. On each platform three more frames are attached at the hips of three legs. E is the earth-fixed frame. In order to increase the system stability, legs in front and rear direction are mounted on the platform in opposite direction as shown in Fig. 1. Each pantograph legs (as shown in Fig. 2b) have five moving links and translational motions in vertical and horizontal direction are imparted through slider-crank mechanism. In order to increase the area of support polygon, horizontal slots are placed away from the center line. The constant R is the magnification factor of pantograph legs, and is defined as

$$R = \frac{BC}{BA} \tag{1}$$

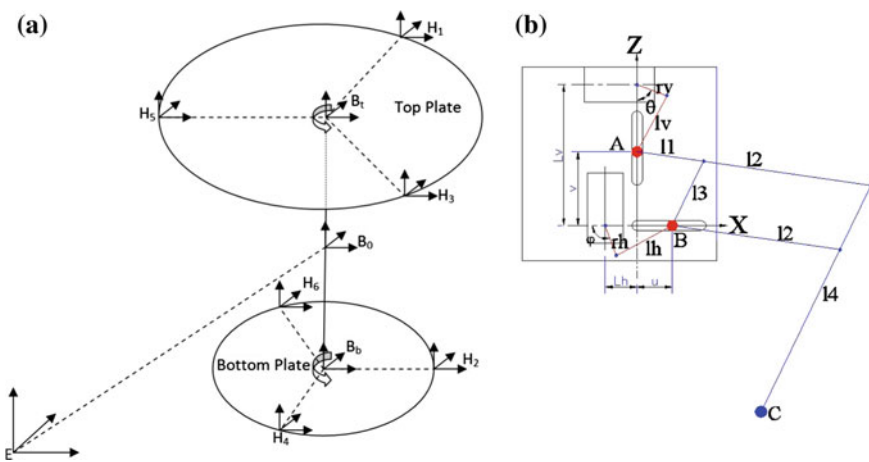


Fig. 2 a Schematic diagram of all the co-ordinate frames. b 2D Pantograph leg mechanism

The forward kinematics equation which relates the foot position $[X_{ff}^h \ Y_{ff}^h \ Z_{ff}^h]$ attach to the hip of Leg j with the displacements of the two actuators (θ_j, ϕ_j) can be defined as

$$P_{ff}^h = [X_{ff}^h \ Y_{ff}^h \ Z_{ff}^h] = \begin{bmatrix} (1+R)u_j \\ 0 \\ Rv_j \end{bmatrix} \tag{2}$$

where,

$$u_j = Lh - rh \cos \phi_j^h + lh \sqrt{1 - \left(\frac{rh}{lh}\right)^2 \sin^2 \phi_j^h},$$

$$v_j = Lv - rv \cos \theta_j^h - lv \sqrt{1 - \left(\frac{rv}{lv}\right)^2 \sin^2 \theta_j^h}.$$

And the inverse kinematics can be determined as

$$IP_{ff}^h = [\theta_{ff}^h \ \phi_{ff}^h] = \begin{bmatrix} 2 \tan^{-1} \sqrt{\frac{1-M}{1+M}} \\ 2 \tan^{-1} \sqrt{\frac{1-N}{1+N}} \end{bmatrix} \tag{3}$$

where,

$$M = \frac{\left(Lv - \frac{Z_{ff}^h}{R}\right)^2 + rv^2 - lv^2}{2\left(Lv - \frac{Z_{ff}^h}{R}\right)rv}, N = \frac{\left(Lh - \frac{X_{ff}^h}{R}\right)^2 + rh^2 - lh^2}{2\left(Lh - \frac{X_{ff}^h}{R}\right)rh}.$$

The geometrical parameters of each leg of the developed lab scale prototype with magnification factor is 2.516 are provided in Table 1.

2.2 Gait

The developed omni-directional robot can move in any direction but it first needs to align towards the direction by means of the central actuator for relative motion

Table 1 Geometrical dimensions of each leg

Links	Dimensions (mm)	Weight (g)	Links	Dimensions (mm)	Weight (g)
rv	18	6	lv	36	10
Lv	80	–	l1	38.2	10
l2	134	68	l3	41	14
l4	143	71	rh	18	6
lh	36	10	Lh	18	–

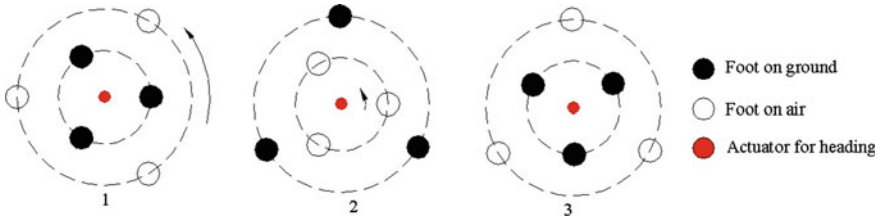


Fig. 3 Representation of wave gait with central rotation

between two plates and then moves in a straight path. The system can take spot rotation though it cannot execute curvilinear motion with high accuracy. It can follow any curve piecewise by adopting the most popular and simple wave gait with the central rotation. When three legs are on the ground, other three are reconfigured for the next turn. Simultaneously, it would change the heading as shown in Fig. 3.

3 Simulation and Results

Proposed model has been simulated over circular as well as a spline path as shown in Fig. 4. From the figures it is observed that the proposed system can move in any direction but piecewise.

The proposed system was also simulated using Adams software. Solid model was developed with specified leg parameters and diameters of top and bottom plates. Here stroke length and ground clearance is 120 and 90 mm respectively. Material of construction is considered as aluminium except the top and bottom plate and ball mounted twin plates which are made by acrylic plastic. Weight of each

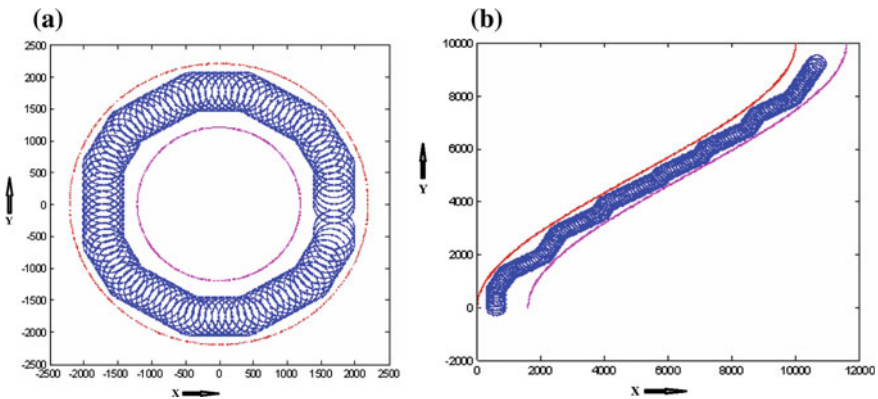


Fig. 4 Robot path over a circular path and b spline path

motor is 65 g. In the leg, two slots for sliding motion are layered with acrylic plastic to reduce friction force.

In order to select the motor, simulation has been carried out for a path as first go straight, then turned 30 and then go straight with full stride. Parameters for foot contact with ground are considered as follows: static co-efficient of friction = 0.3, dynamic co-efficient of friction = 0.1, damping co-efficient during landing = 10.0, allowable penetration depth = 5 mm. Figure 5 depicts the foot contact forces. Contact forces are dependent on the distribution of mass. It is clearly evident from the curve that due to the forward motion of body with respect to the support foot, contact forces for the supporting front legs are gradually increasing, whereas for rear legs, the effect is just opposite.

Simulation has also been carried out to find out the minimum frictional forces required for the turning action. It has been observed that system can turn efficiently if the friction co-efficient is below 0.11. Required motor torques has been computed from the simulation results and is shown in Fig. 6. Based on the average torque requirement of each joint, suitable actuator with maximum torque of 32 kg cm has been selected in our experimental prototype.

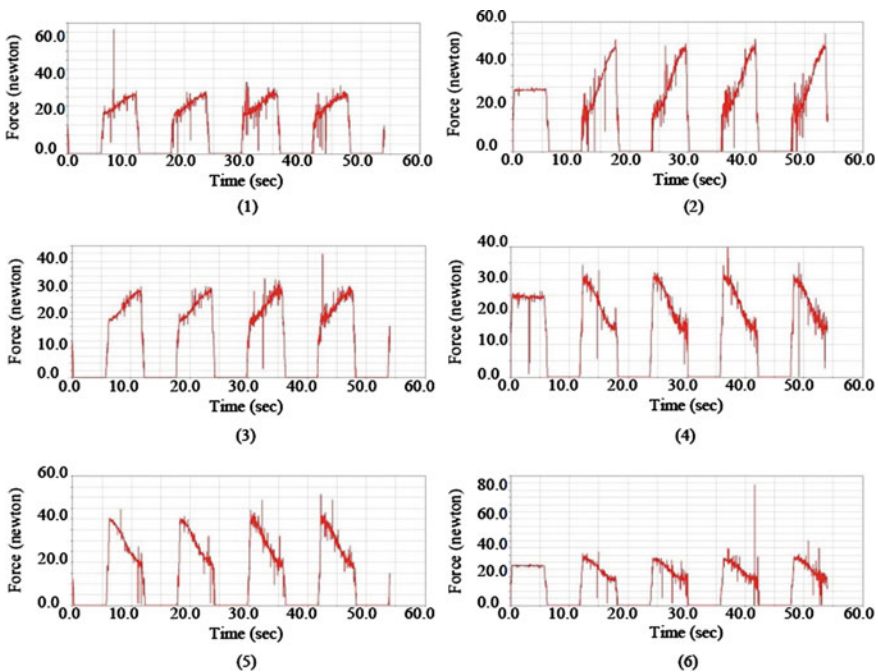


Fig. 5 Foot contact forces for legs 1–6 are shown in curve (1)–(6) respectively

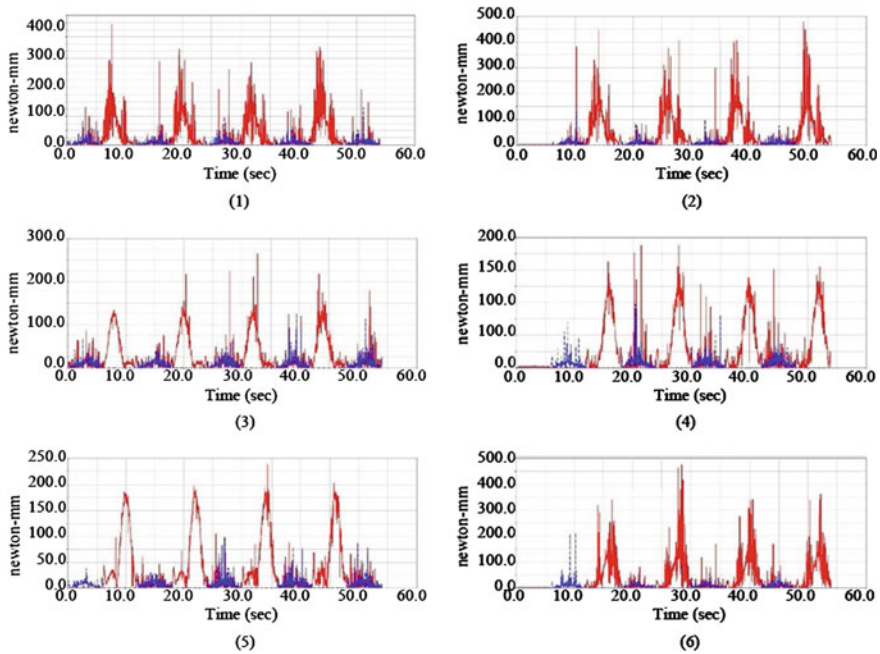


Fig. 6 Motor torques in legs 1–6 are shown in curve (1)–(6) respectively where *red lines* depict for horizontal and *blue* for vertical actuators

4 Conclusions and Future Work

An experimental prototype of a very simple hybrid legged-wheel system called near omni-directional hexapod has been developed. Legged system is a twin frame based hexapod where three wheels (two active, one castor) are fitted with three legs mounted on the bottom frame. The system can move near omni-directionally either by walking mode or wheel mode subject to terrain as well as environment condition. Wave gait pattern is adopted for translational motion during walking whereas turning motion is generated by a central motor attached within the two frames. Required work envelope has been evaluated for each leg which is the main parameters for fixing the dimensions of each frame. The developed prototype has been tested successfully in the laboratory. The system can be utilized for remote inspection of any hazardous environment.

References

- Dutta, S., Ray, R., & Banerji, D. (2007). Development of autonomous mobile robot with manipulator for manufacturing environment. *International Journal of Manufacturing Technology*, 38, 536–542.
- Fielding, M. R., & Reg Dunlop, G. (2004). Omnidirectional hexapod walking and efficient gaits using restrictedness. *International Journal of Robotics Research*, 23, 1105–1110.
- Fujii, S., Inoue, K., Takubo, T., & Arai, T. (2006). Climbing up onto steps for limb mechanism robot “asterisk”. In *Proceedings International Symposium on Automation and Robotics in Construction* (pp. 225–230).
- Fukudaa, T., Adachib, Y., Hoshinoc, H., Matsunagad, I., & Arai, F. (1995). An omni-directional six-legged walking robot. *Advanced Robotics*, 9(2), 177–191.
- Gurocak, H. B., & Peabody, J. (1998). Design of a robot that walks in any direction. *Journal of Robotic Systems*, 15(2), 75–83.
- Koyachi, N., Adachi, H., Nakamura, T., & Nakano, E. (1990). Terrain following control of self-contained semi-fixed gait hexapod walking robot. In *Proceedings IEEE/RSJ International Conference on Intelligent Robots and Systems* (pp. 309–314).
- Krishna, M., Bares, J. E., & Mutschler, E. (1997). Tethering system design for Dante II. In *Proceedings IEEE International Conference on Robotics and Automation* (pp. 1100–1105).
- Ma, S., Tomiyama, T., & Wada, H. (2005). Omnidirectional static walking of a quadruped robot. *IEEE Transaction of Robotics*, 21(2), 152–161.
- Ota, Y., Yoneda, K., Ito, F., Hirose, S., & Inagaki, Y. (2001). Design and control of 6-dof mechanism for twin-frame mobile robot. *Autonomous Robots*, 10(3), 297–316.
- Sakagami, Y., et al. (2002). The intelligent asimo: System overview and integration. In *Proceedings IEEE/RSJ International Conference on Intelligent Robots and Systems* (pp. 2478–2483).
- Tsumaki, T. (1993). Development of practical hexapod walking robot. *Proceedings JRSJ International Conference on Robotics and Mechatronics*, 93(4), 336–339.

Optimization of Vibration of Collecting Plates of Electrostatic Precipitator Through FEA

Harshal Shinde, Akshata Sangle, Sumit Shendkar, Omkar Kulkarni, Ninad Kulkarni, G.M. Kakandikar and V.M. Nandedkar

Abstract Electrostatic Precipitator is air pollution control equipment which separates the dust particles from flue gases. It is basically used for boiler applications. Dust is collected on collecting electrodes and gets separated by of excitation of collecting plates. The excitation is nothing but the vibrating collecting electrodes from its mean position by means of rapping system. Time is another major constraint for checking of such continuous improvements. So analysis and further actual measurement is more practical method. This paper presents FEA concept of modeling using CATIA V5 and analysis of collecting electrodes of ESP by Modal analysis for getting natural frequency and Harmonic analysis for getting acceleration of plates.

Keywords Discharge electrode · Rapping · Electrostatic precipitator (ESP) · Modal analysis · Harmonic analysis

1 Introduction

Electrostatic Precipitator is one of the most popular and frequently used devices to remove the ash particles coming from various industries. Since collecting electrode of ESP collects the dust particles, therefore it is very essential to remove the particle from the plate regularly. Continuous hammering helps this process. The efficiency of ESP depends on the time to time cleaning of collecting electrodes (Wanjari and Narkar 2014; More and Burande 2013; Barkanov 2001). Accelerations are primarily depends on hammering of the rapper and the direction of force and its effects on its geometrical portions of collecting plates. Sequential rapping's causes to

H. Shinde (✉) · A. Sangle · S. Shendkar · O. Kulkarni · N. Kulkarni · G.M. Kakandikar
Zeal College of Engineering and Research, Pune, India
e-mail: sanket312@gmail.com

V.M. Nandedkar
Shri Guru Gobind Singhji Institute of Engineering and Technology, Nanded, India

generate normal and tangential acceleration on plates and hence ultimately it would affect the efficiency of dust removal. Various research experiments were taken place by many researchers to guarantee effective dust removal of collecting electrodes. This physical experimental testing's were time consuming and money oriented. Due to current scenario it is required to produce fast and trustworthy process to calculate the vibration of ESP. CAE simulations are generally used for calculating the end effects. This paper depicts analytical methodology of calculating vibration of ESP through FEA.

2 Details of ESP System

A basic ESP has several rows of collecting plates (electrodes) are placed longitudinal and parallel and suspended between top and bottom hangers (Fig. 1). Top hanger is attached to side channel, which are pivoted by roof bolts. Anvil is situated on upper hangers against it rapper rod is locked or welded. Now above this plunger rod is provided which is governed by electromagnetic principle causing it to continuously hammer on collecting plates (electrodes) (More and Burande 2013). Due to continual hammering process collecting plates (electrode) starts getting vibrated. These sinusoidal processes of hammering causes to detach dust particles from plates. Figure 2 shows typical assembly of collecting electrodes and rapping system of ESP (Amero 1973).

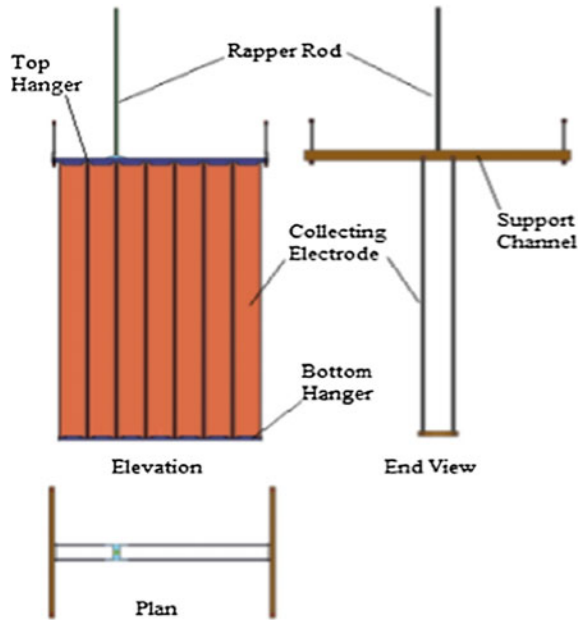
3 Analysis Methodologies

Following FEA methodologies are done for evaluation and calculation of vibration of collecting plates of ESP.

Fig. 1 Electrostatic precipitator



Fig. 2 Assembly of collecting electrodes of ESP



Modal analysis In the present study, a structure or a machine component is being designed and machined to evaluate the vibration natures (natural frequencies and mode shapes). Modal analysis is the initial step for more detailed, dynamic analysis, such as a transient dynamic analysis, a harmonic response analysis, or a spectrum analysis ([Course in FEM-ANSYS Classic](#)) (Fig. 3).

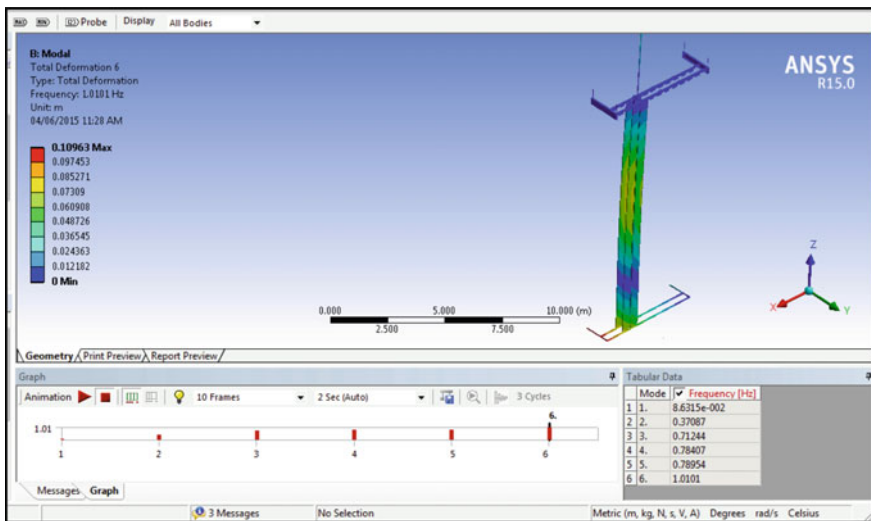


Fig. 3 FE modal analysis

Harmonic analysis Any sustained cyclic load when comes into action it will result in a sustained cyclic response in a structural system. This harmonic response analysis gives the ability to predict the sustained dynamic behavior of the structures, which enables to analyze whether or not the designs will satisfactorily overcome resonance, fatigue, and other harmful effects of forced vibrations ([Course in FEM–ANSYS Classic](#)). This type of analysis is basically carried out for getting acceleration at various points in system. We considered for three position viz. top, middle and bottom.

4 Load Calculations

In present paper, harmonic analysis is used to calculate plate’s natural vibrations when plunger impacts suspended rapper rod. To find the possible impact force and pulse width time of hammering process. The greatest hammering forces occurs when there would be metal to metal contact. The initial and final velocities possibly depends on structural inner rigidity. The acceleration is obtained from following equation ([Metz 2007](#)).

$$a = \frac{dv}{dt} = \frac{dv}{t_{pulse}} = \frac{V_{initial} - V_{final}}{t_{pulse}} = 2 \times \frac{\sqrt{2gh}}{t_{pulse}}$$

The force can be estimated from Newton’s 2nd law equation, $F = ma$ ([More and Burande 2013](#))
 Red inverse triangles show the boundary conditions ([Fig. 4](#)).

Fig. 4 Boundary conditions

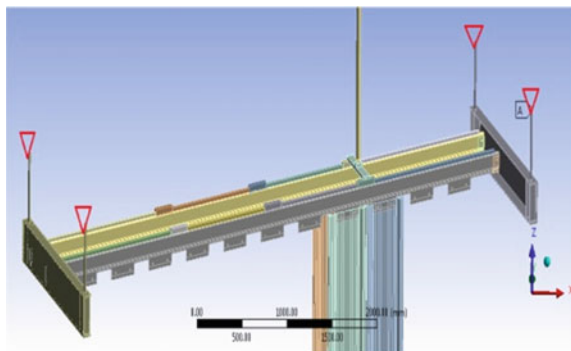


Table 1 Comparison of physical and actual results

Sr. no.	Acceleration at various position's	Physical result (m/s ²)		Actual result (m/s ²)	
		Y (g)	Z (g)	Y (g)	Z (g)
1	Top	55.4	45.9	24.22	46.99
2	Middle	47.9	33.5	75.88	75.30
3	Bottom	86	41.4	80.15	45.70

5 Result and Discussion

This discussion deals with the validation of actual and physical results by comparing the results magnitude along Y and Z directions. So the Table 1 shows the acceleration at various positions over the plates in respective direction. The physical results were carried out by actually attaching accelerometers to collecting plates and actual results were found out by FEA. Results such obtained are discussed.

6 Conclusion

Hence, we have concluded from this project that comparing actual results obtained from FEA approach with physical results shows that both results are marginally close with one another. There are various obstacles which occur during physical testing on site such as it requires skilled manpower, lot of time and mainly enormous capital is needed for testing. The calculations of vibrations of collecting plates more importantly depends upon hammering force and geometry of system. The results which were obtained by FEA validated with actual results firmly confirms that the FEA analysis is quite simple, cost and time saving process. From the above discussion it emphasis to use FEA method with respect to calculations of vibrations in design stage.

References

Amero, R. C. (1973). *Electrostatic precipitators. From Section 9 of Perry's chemical engineer's handbook* (5th ed.). New York: McGraw Hill

Barkanov, E. (2001). *Introduction to the finite element method*. Institute of Materials and Structures Faculty of Civil Engineering Riga Technical University.

Course in FEM-ANSYS Classic. *Analysis types-computational mechanics*. Esbjerg: AAU.

Metz, R. (February 2007). Impact and drop ICP force sensors, PCB. *Journal of Sound and Vibration*.

- More, P., Burande, D. H. (Jul–Aug, 2013). Vibration performance evaluation of collecting plates of electrostatic precipitators using FEA approach. *International Journal of Engineering Research and Applications (IJERA)*, 3(4), 442–446.
- Wanjari, P., & Narkar, K. M. (August, 2014). Design modification of rapping system to improve the dust collection efficiency of electrostatic precipitator. *International Journal of Innovative Research in Science, Engineering and Technology*, 3(8).

Full Aperture Optical Polishing Process: Overview and Challenges

Raj Kumar Pal, Harry Garg and Vinod Karar

Abstract The aim of advanced optical fabrication is to produce highly accurate optical surface with better reproducibility. It demands a good control and systematic understanding of the process and its parameters. Optical polishing process defines the final surface figure and finish of the component. Controlled amount of finishing forces and material removal rate are necessary for polishing of brittle materials. However, the conventional or full aperture polishing process still depends on the operator's skills to achieve the desired surface figure and finish. The process may be well optimized at individual manufacturing setups but there appears to be a little prediction about polishing outputs. Thus, it is essential to study the fundamental mechanisms of material removal during polishing in order to achieve the accurate prediction of process outputs. This paper reviews the work carried out in the area of full aperture optical polishing.

Keywords Brittle · Finishing · Lapping · Material removal · Optical · Polishing

Symbols

R_a	Average surface roughness
k	Preston's constant
P	Pressure
V	Relative velocity
E	Workpiece Young's modulus
ρ_w	Wafer density
N	Number of active abrasives
V_{rem}	Volume removed by single abrasive

R.K. Pal (✉)

Advanced Instrumentation Engineering,
Academy of Scientific and Innovative Research, Chennai, India
e-mail: rajkpal@gmail.com

R.K. Pal · H. Garg · V. Karar
Optical Devices and Systems, CSIR-Central Scientific Instruments Organisation,
Chandigarh, India

- n Number of effective abrasive particles
 δ_{aw} Penetration depth of single abrasive particle into the wafer-abrasive interface
 R_{aw} Radius of contact area of a single effective abrasive at wafer-pad asperity interface
 C Constant
 x Slurry concentration

1 Introduction

Fabrication of optical grade surfaces (surface figure $< 0.1 \mu\text{m}$ peak to valley, $R_a < 30 \text{ nm}$) have always been a challenge. Highly polished surfaces are demanded in optical systems where lasers are involved, as the optical surface has to either transmit or reflect high amount of energy. Rough surface may lead to scattering of light or deformation of surface due to absorption of energy because of surface defects (scratch and digs), which may even lead to failure of components. High precision surfaces are also required where the intensity of incoming light signal is quite low, for example telescope. Loss of signal, due to scattering of light from surface defects, cannot be afforded. Other applications, where highly polished optical surfaces are required, are head up display and helmet mounted display for avionics applications, surgical microscopes, optical navigation systems, etc.

The polishing process is basically a surface smoothing operation used to produce high quality surface (Liang et al. 1997; Chekina et al. 1998). It removes the sub-surface damage or surface scratches produced during the grinding process and to improve the final surface figure. Although the process is very precise and of high significance, there is not much research done in this process. It has been considered as an art more than science (Marinescu et al. 2007). Basically the polishing setup involves rotating a workpiece by giving linear strokes against a rotating polisher with abrasive slurry fed continuously at the interface (Fig. 1a). The center distance between workpiece and polisher and stroke length may be varied in order to achieve

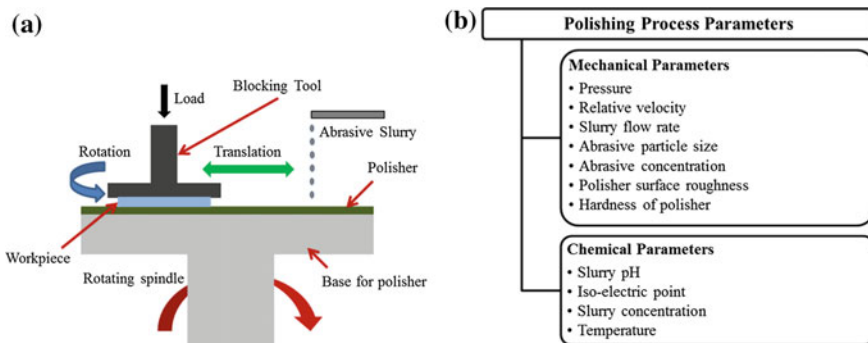


Fig. 1 a Schematic of polishing setup. b Polishing process parameters

variable relative motion. Polisher is a layer of viscoelastic material; optical pitch and polyurethane pads are commonly used polishers. But optical pitch is still preferred for high precision applications.

The chemical interactions between the slurry medium and workpiece surface prepare the surface for polishing (Lei and Luo 2004; Bozkaya and Müftü 2009). Apart from this, the workpiece-polisher interface also experiences the effects of contact and lubrication. The asperities on the polisher surface provide a seat for free abrasives and retain them during polishing. There is a three-body contact as abrasive particle gets confined between the polisher and workpiece surface, and a two body contact of the workpiece and polisher which are responsible for physical material removal (Chauhan et al. 1993; Marinescu et al. 2004). The pressure applied over the workpiece gets distributed non-uniformly over workpiece-polisher interface, which when combine with rotation of polisher, creates an interfacial dynamic friction which tends to remove the material (Suratwala et al. 2010, 2012). The polishing process has smaller material removal rate (MRR) when compared to lapping, so it is good for brittle materials. Being a free abrasive process, the fundamental mechanism of material removal during polishing is still not well understood (Xin et al. 2010; Kimura et al. 2012; Daniel Waechter and Fritz 2013). There are number of process parameters (Fig. 1b) which affect the polishing process outputs i.e. surface figure and surface finish.

A systematic understanding of process parameters is crucial for process to be more repeatable, less tedious and more economic. Various hypotheses have emerged over time to understand the process better and utilize it in the best possible way. This paper reviews these material removal hypotheses and the effects of various process parameters on polishing outputs such as surface quality and MRR in optical polishing process.

2 Workpiece-Polisher Interface (WPI)

Based on type of contact between workpiece and polisher surfaces, WPI has been modeled in three modes: contact mode, hydroplaning mode, and mixed mode (Fig. 2) (Lai 2001). In contact mode, direct surface contact of workpiece and polisher leads to higher friction coefficient generally high of the order of 0.1. In

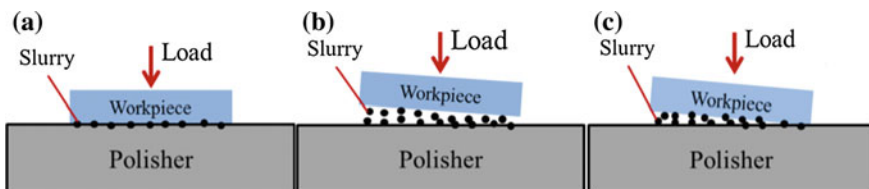


Fig. 2 Types of interfacial contact between workpiece and polisher: **a** contact mode, **b** hydroplaning mode, and **c** mixed mode

hydroplaning mode, as there is no direct contact between workpiece and polisher, friction coefficient is very small in the range of 0.001–0.01. Mixed mode is a transition from hydroplaning mode to contact mode. The friction coefficient is generally in the range of 0.01–0.1. Thus, it is the friction coefficient which characterizes the interfacial contact conditions. Modeling has been done by different researchers taking various contact conditions at the interface.

3 Material Removal and Effects of Process Parameters

The first fundamental model for material removal during glass polishing was proposed by Preston (1927) based on macro level material removal:

$$MRR = kPV \quad (1)$$

This equation has been used widely and further lot of research work was carried out using this equation as reference. But the Preston's equation is a very basic model for MRR considering only pressure and relative velocity. It was further modified by researchers. Brown et al. (1982) proposed a model based on Hertz theory which replaced Preston's constant by $(1/2E)$ as:

$$MRR = PV/2E \quad (2)$$

Cook et al. (1990) suggested that at molecular level, material removal is accomplished mainly through chemical actions. Material removal takes place as slurry particles react with glass surface and take out silica molecules. Xie and Bhushan (1996) informed that the surface roughness increased with increase in particle size and pad hardness during free abrasive polishing and normal contact pressure has little effect on surface roughness. Tseng and Wang (1997) developed a model on the basis of the analogy of polishing process to traveling indenters:

$$MRR = kP^{5/6}V^{1/2} \quad (3)$$

Zhang et al. (1999) proposed another model considering normal and shear stress acting at interface of abrasives and workpiece surfaces:

$$MRR = k\sqrt{PV} \quad (4)$$

Luo and Dornfeld (2001) proposed a model based on plastic contact at wafer-abrasive and pad-abrasive interfaces considering a normal distribution of particle size and a uniform pad roughness distribution:

$$MRR = \rho_w NV_{rem} \quad (5)$$

In the model, apart from pressure and relative velocity, they also took wafer, pad and abrasive properties into consideration for predicting MRR. Guanghai et al. (2001) developed a model for material removal during Chemical mechanical polishing (CMP), where the abrasive particles abrade the hydroxylated layer which was modeled as a perfectly plastic material and deformation profile of soft pad was modeled as bending of thin elastic beam. The two different regimes of material removal were explored based on relatively stiff pad and high abrasive concentration in which pad and wafer do not contact each other and entire load is transferred through abrasives, and second one in which soft pad and low abrasive concentration was considered. It was confirmed that most of the CMP operations follow the soft pad-low abrasive concentration model for material removal where MRR varies as $P^{9/8}V$ for spherical particles but as $P^{3/4}V$ for sharp particles.

Evans et al. (2003) discussed various mechanism of material removal during lapping and polishing processes. Four main material removal hypotheses were summarized: (a) *the abrasion hypothesis*, in which material removal is achieved by inducing very fine cracks on the glass surface; (b) *the flow hypothesis*, linking plastic material displacement with local material softening due to the frictional heating; (c) *the chemical hypothesis*, in which material removal is attributed to the formation and removal of a layer of gel; and (d) *the friction wear hypothesis*, developed in response to the lack of information provided by the chemical hypothesis regarding the influence exerted by the polishing medium.

Terrell and Higgs (2006) reviewed the studies of slurry hydrodynamics which gave significant insight into some of the phenomenon behind polishing hydrodynamics but the studies did not consider rotation of wafer, deflection of pad and wafer, etc. which made them concluded that the studies were insufficient to completely explain the dynamic behavior of slurry in CMP. Jeng and Huang (2005) suggested a CMP material removal model based on micro-contact mechanics also considering the effect of abrasive particles, which was ignored in other studies:

$$MRR = n\delta_{aw}R_{aw}V \quad (6)$$

Lin et al. (2009) developed a two-dimensional quasi static finite element contact model to study von Mises stress distribution on wafer surface and reported the similar results for relationship with MRR as Wang et al. (1997). Bozkaya and Müftü (2009) proposed a material removal model based on the contact mechanics of pad, abrasives and wafer. The model was developed by considering a contact regime at the pad-wafer interface. Lubrication effects were neglected and MRR was assumed to be linearly dependent on relative velocity. The model developed depicted non-linear relationship between MRR and pressure applied with exponent lying within 0.85–1.1. The model depicted a linear relationship of MRR with abrasive concentration when small, and tends to be stable after that until a critical concentration level after which MRR starts decreasing with further increase in abrasive concentration. Ludwig and Kuna (2012) studied the contact pressure distribution between pad and wafer in CMP process using an analytical approach based on plate theory to describe the behavior of the carrier.

Lin (2007) presented an analytical model based on elastic-plastic contact mechanics for predicting MRR during polishing:

$$MRR = CPV\lambda^2 \quad (7)$$

The model was based on abrasive wear theory and described as advancement to Preston's model revealed that the MRR is proportional to pressure and the workpiece-pad relative velocity and also proportional to the two-third power of volume concentration of slurry particle.

Wang et al. (2007) reported some controversial results that the material removal increased when the ceria particles concentration was decreased from 1 to 0.25 wt% during optical CMP which was explained to be a quantum phenomenon. Zhang et al. (2010) stated that MRR increased linearly with increase in abrasive concentration till 20 wt% and then became stable. Park et al. (2008) investigated the correlation between the spatial distribution of pad surface roughness and the material removal profile for CMP and reported that there is a higher MRR at the wafer center because of accumulation of ceria particles at the center which also increase the roughness of the pad. Lien and Guu (2008) used Taguchi technique and Analysis of Variance (ANOVA) to optimize the polishing process parameters for glass substrate reported that "surface finish is significantly affected by platen speed followed by applied pressure, speed and time."

Belkhir et al. (2009) observed that during polishing process friction coefficient increases initially for some time and then tends to be stable. They reported an inverse relationship of friction coefficient with velocity and concluded that pad properties are responsible for variation in friction coefficient. Kelm et al. (2012) investigated variation of friction coefficient in polishing process and presented a method to measure the friction coefficient using an offset tool which is based on measuring the effective electric power from the polishing tool. It was concluded that material removal in polishing process depends upon variation in friction coefficient between workpiece and polisher. Suratwala et al. (2010) investigated ceria pad polishing of fused silica glass and proposed a model for predicting material removal and surface figure as a function of kinematics, loading conditions and polishing time. It was indicated that pressure distribution over the workpiece is non-uniform and a complex parameter which is not well understood. Tian et al. (2013) investigated and optimized the CMP for glass substrate and reported that pad rotational speed, polishing head rotational speed and down force significantly affect surface roughness, surface figure and MRR. Recently Belkhir et al. (2014) conducted a study to understand the relationship between the polishing pressure, contact surface, and friction coefficient during the optical polishing, which was based on direct measurement of the mentioned parameters. It was reported that contact surface and pressure distribution affect the glass surface shape and frictional behavior which influences the material removal mode during the process.

Authors have carried out polishing experiments on BK7 optical glass using Taguchi's method taking abrasive slurry concentration, pressure and relative

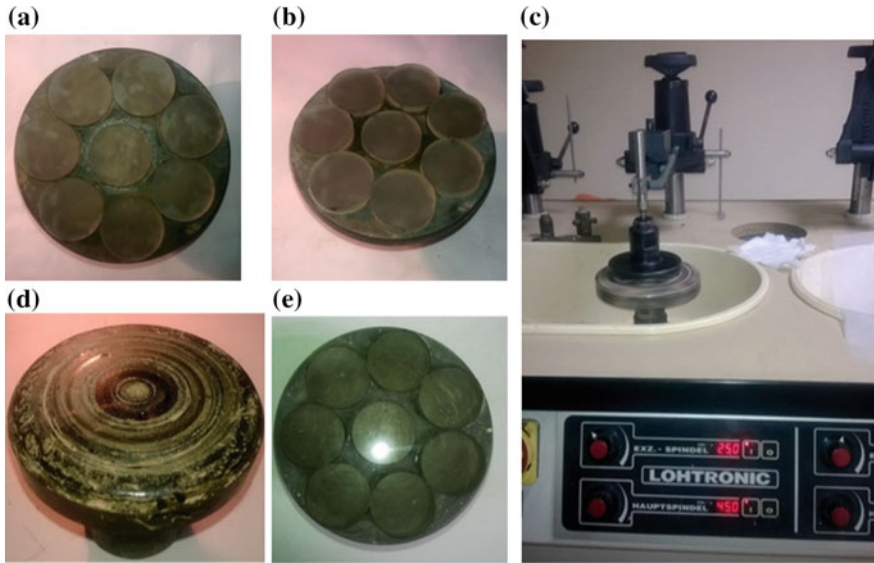


Fig. 3 a Workpiece before lapping process; b workpiece after lapping process; c full-aperture polishing machine; d pitch polisher used for polishing; e workpiece surface after 2 h of polishing

velocity as variable parameters (Fig. 3). It is observed that abrasive slurry concentration plays the most significant role in determining MRR and R_a . Pressure is observed to have little effect on R_a .

4 Discussion and Conclusion

Polishing process can produce precision optical surface for high end applications. However to make the process more repeatable and controlled, it is required to understand the material removal characteristics of the optical polishing process. The initial material removal models developed by researchers are similar to Preston’s model which took only applied pressure and relative velocity into formulation. The major limitation of Preston’s equation and its modified versions is that the parameters related to consumables (i.e. abrasive slurry and polisher) and workpiece are not explicitly defined in the equations. Thus, there was no information regarding control of these parameters. The model proposed by Brown was applicable for metals, not for glass. The models proposed by Cook and Xie and Bhushan were superior to Preston’s equation as they considered consumable parameters also. Other studies were performed based on finite element modeling of WPI and elastic and elastic-plastic nature of materials to understand the behavior of process parameters. Other researchers have proposed empirical models, but are limited to their individual machine setups and not valid for generalized polishing process.

The coefficient of friction at WPI is a complex parameter and is closely related to contact pressure and relative velocity. It requires further exploration to understand the role of friction and how it varies and affects polishing outputs. The distribution of abrasive particles over the interface of workpiece and polisher significantly affects pressure distribution, coefficient of friction, MRR, and thus surface quality. Till now, researchers are not able to properly incorporate this parameter properly in their formulations.

It can be concluded that the polishing process is a very critical step of optical fabrication process, time consuming, laborious and very important. It is not an established process; material removal mechanism is still a topic of research. There are number of process parameters which affect final output but their individual and mutual effect is not clear. Different researchers have optimized process parameters but are limited to their individual setups and applicable only in certain conditions. In this paper, authors have attempted to explain the full aperture optical polishing process and have highlighted the issues involved in understanding the material removal behavior of the process.

Acknowledgments The authors are thankful to Director, CSIR-Central Scientific Instruments Organisation, Chandigarh for providing the necessary resources and facilities for performing this study.

References

- Belkhir, N., Bouzid, D., et al. (2009). Determination of the friction coefficient during glass polishing. *Tribology Letters*, 33(1), 55–61.
- Belkhir, N., Aliouane, T., et al. (2014). Correlation between contact surface and friction during the optical glass polishing. *Applied Surface Science*, 288, 208–214.
- Bozkaya, D., & Müftü, S. (2009). A material removal model for CMP based on the contact mechanics of pad, abrasives, and wafer. *Journal of the Electrochemical Society*, 156(12), H890–H902.
- Brown, N. J., Baker, P. C., et al. (1982). Optical polishing of metals. In *Proceedings of Contemporary Methods of Optical Fabrication* (vol. 0306, pp. 42–57). San Diego: SPIE.
- Chauhan, R., Ahn, Y., et al. (1993). Role of indentation fracture in free abrasive machining of ceramics. *Wear*, 162–164, Part A(0), 246–257.
- Chekina, O. G., Keer, L. M., et al. (1998). Wear-contact problems and modeling of chemical mechanical polishing. *Journal of the Electrochemical Society*, 145(6), 2100–2106.
- Cook, L. M. (1990). Chemical processes in glass polishing. *Journal of Non-Crystalline Solids*, 120 (1–3), 152–171.
- Daniel Waechter, O. D., & Fritz, K. (2013). Analysis and modeling of tribology effects in conventional glass polishing. In *Proceedings of Optical Manufacturing and Testing X* (vol. 8838). California: SPIE.
- Evans, C. J., Paul, E., et al. (2003). Material removal mechanisms in lapping and polishing. *CIRP Annals—Manufacturing Technology*, 52(2), 611–633.
- Guanghui, F., Chandra, A., et al. (2001). A plasticity-based model of material removal in chemical-mechanical polishing (CMP). *IEEE Transactions on Semiconductor Manufacturing*, 14(4), 406–417.

- Jeng, Y.-R., & Huang, P.-Y. (2005). A material removal rate model considering interfacial micro-contact wear behavior for chemical mechanical polishing. *Journal of Tribology*, 127(1), 190–197.
- Kelm, A., Boerret, R., et al. (2012). Improving the polishing accuracy by determining the variance of the friction coefficient. *Journal of the European Optical Society Rapid Publication*, 7, 12049.
- Kimura, K., Suzuki, K., et al. (2012). Study on fine particle behavior in slurry flow between wafer and polishing pad as a material removal process in CMP. In *Proceedings of International Conference on Planarization/CMP Technology (ICPT 2012)* (pp. 1–6). Grenoble, France.
- Lai, J. Y. (2001). *Mechanics, mechanisms, and modeling of the chemical mechanical polishing process*. Ph.D. thesis, Massachusetts Institute of Technology.
- Lei, H., & Luo, J. (2004). CMP of hard disk substrate using a colloidal SiO₂ slurry: preliminary experimental investigation. *Wear*, 257(5–6), 461–470.
- Liang, H., Kaufman, F., et al. (1997). Wear phenomena in chemical mechanical polishing. *Wear*, 211(2), 271–279.
- Lien, C. H., & Guu, Y. H. (2008). Optimization of the polishing parameters for the glass substrate of STN-LCD. *Materials and Manufacturing Processes*, 23(8), 838–843.
- Lin, T. R. (2007). An analytical model of the material removal rate between elastic and elastic-plastic deformation for a polishing process. *The International Journal of Advanced Manufacturing Technology*, 32(7–8), 675–681.
- Lin, Y.-Y., Chen, D.-Y., et al. (2009). Simulations of a stress and contact model in a chemical mechanical polishing process. *Thin Solid Films*, 517(21), 6027–6033.
- Ludwig, C., & Kuna, M. (2012). An analytical approach to determine the pressure distribution during chemical mechanical polishing. *Journal of Electronic Materials*, 41(9), 2606–2612.
- Luo, J., & Dornfeld, D. A. (2001). Material removal mechanism in chemical mechanical polishing: theory and modeling. *IEEE Transactions on Semiconductor Manufacturing*, 14(2), 112–133.
- Marinescu, I. D., Rowe, W. B., et al. (2004). *Tribology of abrasive machining processes*. William Andrew: United States of America.
- Marinescu, I. D., Uhlmann, E. et al. (2007). *Handbook of lapping and polishing*. London: CRC Press/Taylor & Francis Group.
- Park, B., Lee, H., et al. (2008). Pad roughness variation and its effect on material removal profile in ceria-based CMP slurry. *Journal of Materials Processing Technology*, 203(1–3), 287–292.
- Preston, F. W. (1927). The theory and design of plate glass polishing machine. *Journal of the Society of Glass Technology*, 11(44), 214–256.
- Suratwala, T. I., Feit, M. D., et al. (2010). Toward deterministic material removal and surface figure during fused silica pad polishing. *Journal of the American Ceramic Society*, 93(5), 1326–1340.
- Suratwala, T., Steele, R., et al. (2012). Convergent pad polishing of amorphous silica. *International Journal of Applied Glass Science*, 3(1), 14–28.
- Terrell, E. J., & Fred Higgs, C. (2006). Hydrodynamics of slurry flow in chemical mechanical polishing: A review. *Journal of the Electrochemical Society*, 153(6), K15–K22.
- Tian, Y. B., Ang, Y. J., et al. (2013). Chemical mechanical polishing of glass disk substrates: preliminary experimental investigation. *Materials and Manufacturing Processes*, 28(4), 488–494.
- Tseng, W. T., & Wang, Y. L. (1997). Re-examination of pressure and speed dependences of removal rate during chemical-mechanical polishing processes. *Journal of the Electrochemical Society*, 144(2), L15–L17.
- Wang, D., Lee, J., et al. (1997). Von Mises Stress in chemical mechanical polishing processes. *Journal of the Electrochemical Society*, 144(3), 1121–1127.
- Wang, L., Zhang, K., et al. (2007). Ceria concentration effect on chemical mechanical polishing of optical glass. *Applied Surface Science*, 253(11), 4951–4954.
- Xie, Y., & Bhushan, B. (1996). Effects of particle size, polishing pad and contact pressure in free abrasive polishing. *Wear*, 200(1–2), 281–295.

- Xin, J., Cai, W., et al. (2010). A fundamental model proposed for material removal in chemical–mechanical polishing. *Wear*, 268(5–6), 837–844.
- Zhang, F., Busnaina, A. A., et al. (1999). Particle adhesion and removal in chemical mechanical polishing and post-cmp cleaning. *Journal of the Electrochemical Society*, 146(7), 2665–2669.
- Zhang, Z., Liu, W., et al. (2010). Effect of abrasive particle concentration on preliminary chemical mechanical polishing of glass substrate. *Microelectronic Engineering*, 87(11), 2168–2172.

Stability Analysis of Haptic Virtual Environment Systems for Active Interactions in Surgical Robot Simulators

Rishika Khandelwal and Asokan Thondiyath

Abstract A haptic interface is a link between a human operator and a virtual environment and conveys a kinesthetic sense of presence in the virtual environment to the operator. The combined system includes a virtual environment simulated in a digital computer, a human operator and a haptic display that are actual physical systems. Such interfaces are commonly used in tele-surgical simulators and other systems to get a better feel for the user. For this system, stability is a prime concern because it may be affected by three major factors that are communication delay, controller discretization, and active operator intervention. In this paper, the stability of these systems is analysed and a framework which allows operator to interact actively with the virtual environment is proposed for telesurgical applications using surgical robots. Study of the simultaneous effect of all three de-stabilizing factors are carried out via the proposed framework. The well-known Colgate's stability condition for a 1-user haptic system with a passive operator is reproduced and then extended to the case which allows each operator to behave actively. Another extension to Colgate's condition comes by allowing communication delays to exist in the system. Simulations confirm the validity of the proposed conditions for stability of sampled-data Haptic Virtual Environment (HVE) systems.

1 Introduction

Applications of haptic enabled interfaces can fall into two main categories: Teleoperation systems and Haptic Virtual Environment (HVE) systems. A teleoperation system comprises of a human operator interacting with a master robot, thus remotely controlling a slave robot to perform a task in a remote environment. Robot-assisted surgery is a typical case of teleoperation system where the surgeon

R. Khandelwal · A. Thondiyath (✉)
Robotics Laboratory, Department of Engineering Design,
Indian Institute of Technology Madras, Chennai 600 036, India
e-mail: asok@iitm.ac.in

directly controls surgical instruments (Parker 2010; Haidegger 2009; Lum Mitchell et al. 2009). Despite the advantages associated with robot-assisted surgery, the technique presents several disadvantages possibly preventing its assimilation into the operating room and its benefits from being universally enjoyed. One of the most significant shortcomings of robotic-assisted surgery is the absence of effective haptic feedback, or the surgeon’s sensation of tool-interaction forces. Haptic signals can be either kinesthetic, vector forces applied at points or on joints, or tactile, textures and distribution of forces. Haptic cues are an important component of surgery and can enable a surgeon to differentiate tissue, perceive the amount of force applied to tissue, and generally determine the contour and compliance of tissue. Many researchers agree that the addition of tactile sensation under proper conditions would be a valuable feature in master-slave robot-assisted surgery. Tactile feedback typically requires an array of sensors whereas kinesthetic feedback may require the careful placement of very few sensors. Recently, there have been significant advances in telesurgery research. Many researchers acknowledge the potential benefits of force feedback for robotic surgical tools. For instance, Ishii et al. (2010) recently developed a novel robotic forceps bending-manipulator. Research into the proper use and benefits of haptic feedback is necessary for the successful implementation of haptic feedback devices.

A single-user HVE system consists of a human operator and a virtual environment and a haptic interface that acts as a link between them and conveys a kinesthetic sense of presence in the virtual environment to the operator. This is widely used in virtual reality based simulators and computer games (Fotoohi et al. 2007; Glencross et al. 2007; Orozco et al. 2012; Goncharenko et al. 2004). The combined system is sampled-data system as it includes a virtual environment simulated in a digital computer and a human operator and a haptic interface that are actual physical systems. Figure 1 shows the basic flow diagram of a haptic system. Interaction between a human and the haptic interface is a bidirectional exchange of information; a human operator controls the movement of a slave system as well as receives information about the forces and movements of the slave system via haptic interface.

For an HVE system, stability is a prime concern because it may be jeopardized by the discrete-time simulation of the virtual environment due to its inherent

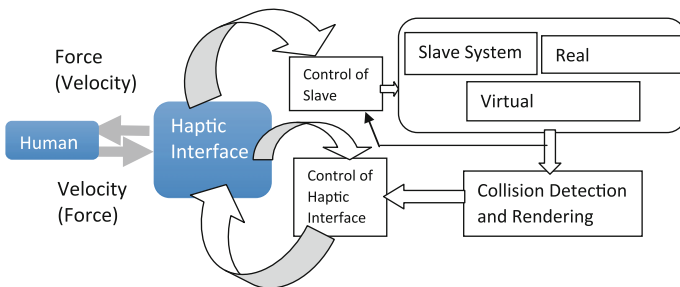


Fig. 1 Basic structure of a Haptic system

sampling effects. Stability of HVE systems was analysed by many researchers in the recent past (Minsky et al. 1990; Colgate and Schenkel 1997; Gil et al. 2004; Jazayeri and Tavakoli 2011). Minsky et al. (1990) were the first to study this problem. In the stability analysis of HVE systems, the entire system is assumed to be in continuous-time. While the human operator, the environment, and the robots operate in continuous-time, the controllers involved in teleoperation system are implemented via discrete-time components and we cannot neglect the discrete-time nature of the controller and the energy leaks caused by the Zero-Order-Hold (ZOH) (Hannaford and Ry 2002). The ZOH also accounts for half-sample delay (distinct from the communication channel delay) and has energy-instilling effects (Leung and Francis 1992). The stability analysis of delayed teleoperation systems is usually meant to passify the communication channel and assumes that the rest of the system is passive. In reality, however, passifying the communication channel alone does not guarantee the stability of the entire teleoperation system. Although the stability of sampled-data HVE systems have been studied extensively in the literature, the effect of active operator has been neglected. The assumption of operator passivity is not always valid and much depends on the task being performed by the operator. In this work we develop a framework using which stability can be investigated in the presence of both delay and active operator while considering the sampled-data nature of HVE systems. The developed framework should enable us to study the stability of HVE and enable us to study the simultaneous effects of all three destabilizing factors on the stability of system.

2 Modeling of HVE Syetm

A simplified, continuous-time model of a one degree-of-freedom (DOF) haptic device interacting with a discretely-simulated virtual wall was presented in Minsky et al. (1990). The robot (haptic interface) was modeled as a mass m and a damping b connected to the virtual wall by a virtual coupling (digital controller) modeled by a stiffness K as shown in Fig. 2.

It was shown via experiments that with the operator's mass m_h , damping b_h and stiffness k_h , and with a virtual damping B complementing the virtual stiffness K , the stability condition will become

$$B + b + b_h > \frac{(K + K_h) * T}{2} \quad (1)$$

There were many models proposed by researchers (Colgate and Schenkel 1997; Gil et al. 2004; Jazayeri and Tavakoli 2011; Hannaford and Ry 2002) to analyse the stability of HVE systems. However, passivity of the operator was simply a convenient assumption used in all of the above work for stability analysis of a system independent of the typically uncertain, time-varying and/or unknown dynamics of the operator. Given that the operator voluntarily manipulates the interface tool and

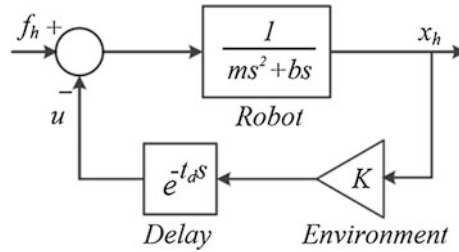


Fig. 2 A continuous model for a single-user HVE system (Minsky et al. 1990)

thereby has the capacity to inject energy into the virtual system, this assumption may not always be valid depending on the task. Active behavior of the operator in a haptic system has been reported in Dyck et al. (2013).

3 Modified Stability Model

In order to incorporate the operator interactions in the HVE model, a feedback layout is proposed as shown in Fig. 3. Operator applies a force input f_o to the haptic device. The velocity output from haptic display goes as input to the virtual environment which then calculates the reaction forces f_e and sends it back to the haptic device. In this layout or framework unlike the previous models in which some reference force input was taken, the operator applies the force which keeps on changing according to the velocity output obtained from haptic device. Also this framework accounts for communication delay caused due to various factors.

The block diagram of the above single-user HVE system is shown in Fig. 4, where $Z_h(s)$ is the unknown human operator model and $H(z)$ is the known discrete-time model of the environment (i.e., the digitally-implemented virtual coupling between the haptic interface and the virtual wall). The haptic interface is a rigid manipulator and is modeled as a mass m and damper b . The input and output of $H(z)$ pass through a sampler and a ZOH with a sampling period of T , respectively.

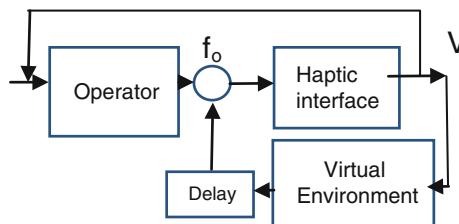


Fig. 3 Layout of feedback loop

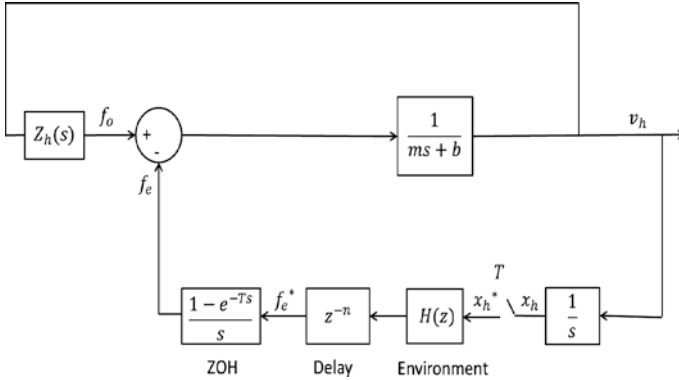


Fig. 4 Model of a 1-DOF HVE with active operator model

The closed-loop characteristic equation of the system can be given as

$$1 + H(z)G_T^*(s) = 0 \tag{2}$$

The relation between z and s parameter is given by $z = e^{sT}$ where T is the sampling time, hence the equation becomes

$$1 + H(e^{sT})G_T^*(s) = 0 \tag{3}$$

where

$$G_T^*(s) = \frac{1}{T} \sum_{n=-\infty}^{n=\infty} G(s + jn\omega_s) \tag{4}$$

3.1 Active Operator Without Time Delay

Eliminating the time delay, we get the transfer function as

$$G(s) = \frac{1 - e^{-Ts}}{s^2} \frac{1}{ms + b + Z_h(s)} \tag{5}$$

In previous related works (Hannaford and Ry 2002; Leung and Francis 1992; Artigas et al. 2008; Dyck et al. 2013) the impedance of the environment in the z domain has been approximated by considering the common implementation of virtual wall. The virtual wall composed of a virtual spring and virtual damper in parallel and then obtaining a velocity estimate via backward difference differentiation of position, giving the following transfer function within the wall as

$$H(z) = K + B \frac{z-1}{Tz} \quad (6)$$

where $K > 0$ is virtual stiffness, and $B > 0$ is virtual damping coefficient. The stability condition for this system can be obtained as

$$b - z_a > \frac{T}{2} \frac{1}{1 - \cos\omega T} \operatorname{Re} \left\{ (1 - e^{-j\omega T}) \left(K + B \frac{e^{j\omega T} - 1}{T e^{j\omega T}} \right) \right\} \quad (7)$$

The right-hand side is maximized at $\omega = \omega_N$ leading to the condition:

$$b - z_a > \frac{KT}{2} + B \quad (8)$$

It shows that, for a given fixed physical and virtual damping, sampling rate defines the achievable virtual stiffness. Further, the virtual damping is independent of the sampling rate.

3.2 Active Operator with Time Delay

In the case of a delayed HVE system in which the operator has shortage of passivity of z_a , again the approach is the same as for active operator without delay. In case of time delay the stability condition can be written as

$$b - z_a > \frac{T}{2} \frac{1}{1 - \cos\omega T} \operatorname{Re} \left\{ e^{-j\omega t_d} (1 - e^{-j\omega T}) \left(K + B \frac{e^{j\omega T} - 1}{T e^{j\omega T}} \right) \right\} \quad (9)$$

For the virtual wall and assuming that t_d a multiple of sampling time T this stability condition will reduce to the condition given below.

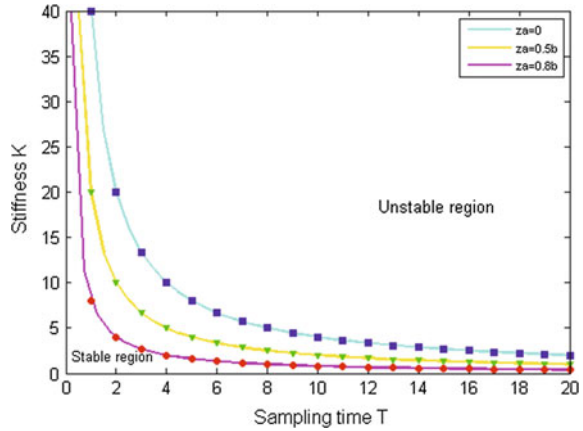
$$b - z_a + B > Kt_d + \frac{KT}{2} \quad (10)$$

The above stability conditions are simulated to find the best possible values of stiffness K to ensure stability of the HVE systems.

4 Simulation Studies

In order to test the stability conditions, the model of sampled-data, single-user HVE system was simulated in MATLAB/Simulink. To determine the stability of the system, the system outputs were monitored for boundedness at all times. If any

Fig. 5 Simulation data points and corresponding theoretical borderlines system without time delay



output goes unbounded, the system is unstable. During the simulations, the sampling time is increased by steps of 1 ms. For each sampling time, the stiffness K is changed to find the largest stiffness value for which the system remains stable.

4.1 Active Operator Without Time Delay

For non-delayed HVE systems each of the maximum stiffness values at a given sampling period are plotted in Fig. 5 for z_a of 0, 0.5b, and 0.8b. As evident from the figure these simulation data points are very close to the solid lines, which correspond to the theoretical borderline. Therefore, the simulations confirm the theoretical condition. Also, as expected from the equation, an increase in the shortage of passivity z_a will cause the stable region to shrink.

4.2 Active Operator with Time Delay

For the delayed single-user HVE system with $m = 0.15$, $b = 0.2$ and $B = 0$, the delay t_d is set to $10T$ and again simulations are conducted for the three cases involving shortages of passivity z_a of 0, 0.2b, and 0.5b. The results are shown in Fig. 6.

This time, there is a small difference between the simulation data points and the theoretical borderline, which corresponds to cases where condition is conservative for detecting the system instability. The conservatism of condition can be due to the fact that it is found as a sufficient condition for stability. Also, as before, any increase in the shortage of passivity z_a decreases the stability region as predicted by

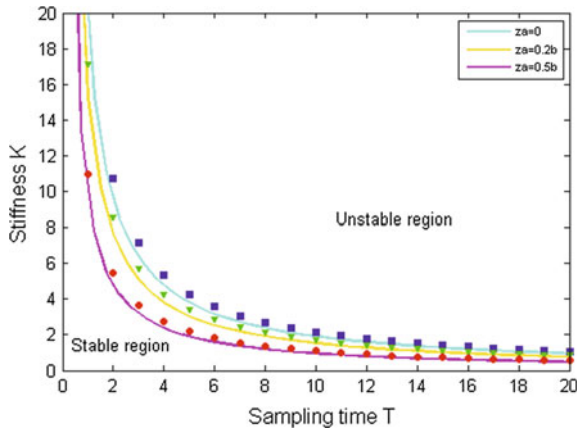


Fig. 6 Simulation data points and corresponding theoretical borderlines for system with time delay

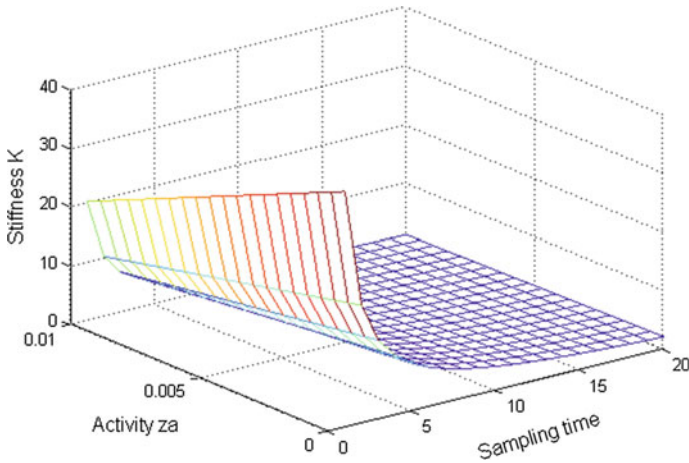


Fig. 7 Variation of K with Z_a and T

the theoretical condition. Figure 7 shows the variation of stiffness K as a function of sampling time and Z_a . The surface plotted in the figure shows the values of K to be taken for different values of activity and sampling time T to ensure the stability of system. This acts a guideline for the design of haptic system to ensure stable interaction.

5 Conclusions

The stability problem in the context of sampled data HVE systems is presented in this paper. A framework to study the stability of sampled-data HVE in the presence of three main de-stabilizing factors has been presented. The developed framework enables us to study the stability of HVE in the presence of active terminations (operator or environment). Necessary and sufficient condition for stability of HVE systems was derived in the presence and absence of time delay. The example of a virtual wall characterized by virtual stiffness and damping coefficients has been given and investigated in detail. It has been shown that the implementation of a stiff, passive virtual wall is aided by large physical damping and high sampling rate. The findings from this work can be used in the design of HVE systems which will ensure stability of interactions in the presence of time delay and active operator.

References

- Artigas, J., Preusche, C., Hirzinger, G., Borghesan, G., & Melchiorri, C. (2008). Bilateral energy transfer in delayed teleoperation on the time domain. In *Proceedings of IEEE International Conference on Robotics and Automation, Pasadena, CA, USA* (pp. 671–676).
- Colgate, J., & Schenkel, G. (1997). Passivity of a class of sampled data systems: Application to haptic interfaces. *Journal of Robotic Systems*, 14(1), 37–47.
- Dyck, M., Jazayeri, A., & Tavakoli, M. (2013). Is the human operator in a teleoperation system passive? In *Proceedings of IEEE World Haptics Conference, Daejeon, Korea* (pp. 683–688).
- Fotoohi, M., Sirouspour, S., & Capson, D. (2007). A multi-rate control approach to haptic interaction in multi-user virtual environments. In *Proceedings of IEEE International Conference on Robotics and Automation, Rome, Italy* (pp. 99–104).
- Gil, J., Avello, A., Rubio, A., & Florez, J. (2004). Stability analysis of a 1-DoF haptic interface using the Routh-Hurwitz criterion. *IEEE Transactions on Control Systems Technology*, 12(4), 583–588.
- Glencross, M., Jay, C., Feasel, J., Kohli, L., Whitton, M., & Hubbard, R. (2007). Effective cooperative haptic interaction over the internet. In *Proceedings of IEEE Virtual Reality Conference, Charlotte, NC, USA* (pp. 115–122).
- Goncharenko, I., Svinin, M., Matsumoto, S., Masui, Y., Kanou, Y., & Hosoe, S. (2004). Cooperative control with haptic visualization in shared virtual environments. In *Proceedings of International Conference on Information Visualization, London, UK* (pp. 533–538).
- Haidegger, T., et al. (2009). Force Sensing and Force Control for Surgical Robots. In *Proceedings of the 7th IFAC Symposium on Modelling and Control in Biomedical Systems* (pp. 413–418). Denmark: IFAC.
- Hannaford, B., & Ry, J. H. (2002). Time-domain passivity control of haptic interfaces. *IEEE Transactions on Robotics and Automation*, 18(1), 1–10.
- Ishii, C., et al. (2010). Robotic Forceps Manipulator with a Novel Bending Mechanism. *IEEE/ASME Transactions on Mechatronics*, 5(15), 671–684.
- Jazayeri, A., & Tavakoli, M. (2011). A passivity criterion for sampled data bilateral teleoperation systems. In *Proceedings of IEEE World Haptics Conference, Istanbul, Turkey* (pp. 487–492).
- Leung, G., & Francis, B. (1992). Bilateral control of teleoperators with time delay through a digital communication channel. In *Proceedings of the Thirtieth Annual Allerton Conference on Communication, Control and Computing, Urbana, IL, USA* (pp. 692–701).

- Lum Mitchell, J. H., et al. (2009). The RAVEN: design and validation of a telesurgical system. *The International Journal of Robotics Research*, 28, 1183–1197.
- Minsky, M. Ming, O.-Y., Steele, O., Brooks, Jr., F. P., & Behensky, M. (1990). Feeling and seeing: Issues in force display. In *Proceedings of the 1990 Symposium on Interactive 3D Graphics, New York, NY, USA* (pp. 235–241).
- Orozco, M., Silva, A. P. E., & El Saddik, J. (2012). The role of haptics in games. *Haptics Rendering and Application*, 2, 1221–1226.
- Parker, W. H. (2010). Laparoscopic and robotic myoelectomy. Retrieved April 25, 2011, from <http://www.fibroidsecondopinion.com/laparoscopic-myomectomy>.

Synchronized Optimization of Injection Moulding Parameters for Higher Acceptance of Polypropylene Products

Bikash Bepari, Tanumoy Kolay, Kamal Nayan and Subham Mishra

Abstract The present exploration focuses on synchronized optimization of injection moulding parameters to adjudge the suitability of the polypropylene products in view of higher acceptance. A full factorial experimental layout was framed for the moulding parameters like injection temperature, pressure and speed, all at three levels. Before launching into the market, polypropylene products need to qualify the strength test (ASTM-D638-03), density test (ASTM-D 792), and Vicat Softening Point test (ASTM-D 1525). Grey Relational Analysis (GRA) was adopted to convert the multiple objectives into a single objective. Specimens were prepared at all the parametric combinations through injection moulding in compliance with ASTM-D 638-03-TYPE-I. The above mentioned tests have been carried for every specimen and the responses were obtained. It has been observed that products manufactured at 200 °C Injection Temperature, 70 bar Injection Pressure and 80 rpm Injection speed are poised with higher level of suitability from acceptance point of view. Grey analysis reveals injection temperature is the most dictating factor followed by injection velocity and injection pressure.

Keywords Polypropylene · Injection moulding · Optimization · Grey relational analysis

1 Introduction

Plastic is the material to drive the expansion of revolutionary innovations to convene society's major challenge. Currently, 58 % of the materials encountered are comprised of polymer. Unambiguously it is evident that the usage of plastic is ubiquitous in everybody's life. Since the utilization of plastic products is increasing over the sphere, the production techniques are also escalating side-by-side. Injection

B. Bepari (✉) · T. Kolay · K. Nayan · S. Mishra
Haldia Institute of Technology, Haldia, West Bengal, India
e-mail: bikashbepari@gmail.com

moulding technology being one of the techniques in plastic product manufacturing converts raw plastics into its functional counterpart. Survey reveals that, utilization of polypropylene goods are more compared to the useable counterparts. Polypropylene is a linear polymer composed of repeating units of isopropene. The main attractive features of PP are excellent flex life, commendable surface hardness, enhanced corrosion resistance and form stability at higher temperature. Before introduction of a polypropylene product in the market, it must undergo a series of qualifying tests, out of which tests as per (ASTM-D638-03), (ASTM-D 792) and (ASTM-D 1525) are the three mandatory tests. However, parametric optimization during moulding of polypropylene keeping in view of three above mentioned tests is unavailable in the literature as far as the knowledge of the authors are concerned.

Doong et al. (2000) optimized for injection moulding of reinforced polycarbonate composites by considering filling time, melt temperature, mould temperature and ram speed. CAE flow simulation software was employed to simulate the injection moulding process and to predict the probable fiber orientation. Recyclability of High Density Polyethylene (HDPE) was studied by Siddiquee et al. (2010). Objectives were attained by measuring the tensile, compressive and flexural strength which acted as the qualifying criteria subjected to the parameters like melt temperature, holding pressure, injection time and holding time (Kamaruddin and Mehat 2011) adopted Taguchi L_9 orthogonal array as DOE to improve mechanical properties of materials made from recycled plastics. They considered melt temperature, packing pressure, injection time and packing time as the parameters. They showed products produced at 1:3 (recycle to virgin ratio) exhibited enhanced flexural Strength (Ozcelik 2011) investigated the combined effect of mold parameters along with weld-lines. He considered injection temperature, packing pressure and injection pressure as the parameters while the responses were tensile load, elongation at break and impact strength and revealed that the injection pressure was the most influential parameter compared to melt temperature. Based on the literature survey, the objectives are primarily aimed (a) to optimize the process parameters for injection molding of polypropylene for the three factors; namely, injection pressure, temperature and speed to qualify the products made at all possible parametric combination so as to ensure all the tests pertinent to ASTM as mentioned in the abstract and (b) to determine the relative importance of the parameters.

2 Machining and Measuring Tabs

The experiments were conducted at Central Institute of Plastics Engineering and Technology. Figure 1 depicts the machining tab for injection molding. Figure 2a–c depict the measuring tabs to determine tensile strength, Vicat Softening Point and density respectively.



Fig. 1 The injection moulding machine

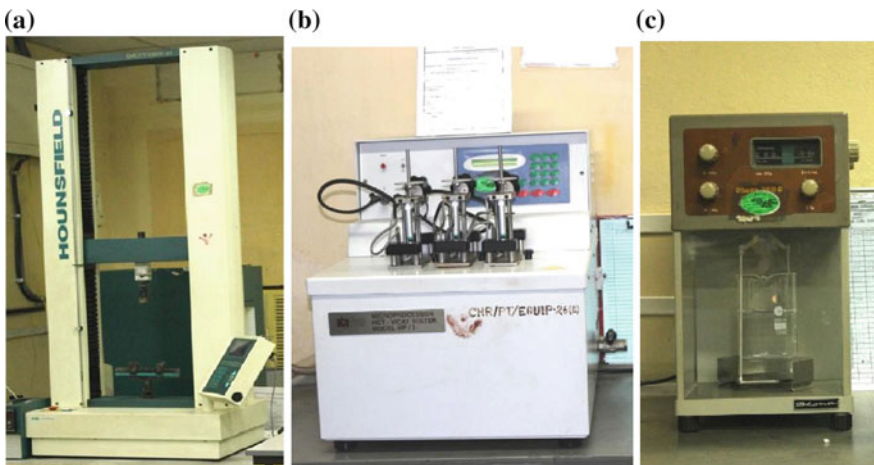


Fig. 2 The measuring tabs for different responses

3 Process Parameters and Responses

Injection pressure is the most important parameter during moulding of PP pertinent to dimensional accuracy when the mould temperature is held fixed (Rubin 1972). Higher injection pressure increases the density by increasing the compaction and to get rid of the shrinkage problem a higher holding time is essentially required. Moreover, higher pressure enhances rate of crystallinity. When higher tensile strength is expected from the molding upshots it is generally molded at moderately higher temperature and cooled gradually over a long period of time to avoid shrinkage and other imperfections. Higher temperature and pressure helps the molten material to propagate uniformly to the entire mold cavity instantaneously because of less viscosity. This phenomenon ultimately leads to fetch products with uniform density and higher abrasion resistive properties. It has been observed if the

Table 1 Notation of the parameters and their ranges during moulding

Parameter	Notation	Unit	Levels of factors		
			-1	0	+1
Injection temperature	IT	°C	190	200	210
Injection pressure	IP	Bar	50	60	70
Injection speed	IS	rpm	80	100	120

density is high then the quantum of mass for a considered volume is high and the porosity is less. Less porosity in other sense can be conferred as higher resistance to penetration and thus it increases the softening point. Therefore the authors found that temperature, pressure and speed of injection are the predominant parameters which have got significant importance on the objectives of the present experimental study. Table 1 shows the injection moulding parameters for the discrete range encapsulating their levels. The factors for the responses with regards to the present objective are higher tensile strength in yield, nominal density and higher VSP.

4 Grey Relational Analysis

Grey relational analysis (GRA) was introduced by Deng (1989), to judiciously approximate the relative suitability of a sequence based on grey relation grade. GRA has proven itself as a deft tool for multi objective optimization when it is subjected to inadequate information. The normalization of the original sequence is done in such a fashion so that the most preferred value reaches unity (White) and the least value becomes zero (Black). The intermediates are always lying in between them and therefore they are termed as grey entities.

In GRA, the discrete data is initially pre-processed through normalization to convert the original sequences into comparable sequence. Based on the orientation of the data sequence, different protocols for normalization were proposed by Fung and Kang (2005). When the target value is expected to be “the-higher-the-better”, then it is normalized through:

$$x_i^*(k) = \frac{x_i^o(k) - \min x_i^o(k)}{\max x_i^o(k) - \min x_i^o(k)} \tag{1}$$

For cost attributes the orientation is “The-least-the-better” and then this is normalized as follows:

$$x_i^*(k) = \frac{\max x_i^o(k) - x_i^o(k)}{\max x_i^o(k) - \min x_i^o(k)} \tag{2}$$

When the expectancy is a value which is nominal (generally a targeted value is prescribed) then the original sequence is normalized by the following equation:

$$x_i^*(k) = 1 - \frac{|x_i^o(k) - x_i^o|}{\max x_i^o(k) - x_i^o} \quad (3)$$

where, $i \in m$; $k \in n$. ‘ m ’ is the experimental layout number, ‘ n ’ is the number of factors. $x_i^o(k)$ indicates the original set of data, $x_i^*(k)$ is the normalized data set, $\max x_i^o(k)$ and $\min x_i^o(k)$ are the highest and lowest value of $x_i^o(k)$ respectively; x_i^o is the nominal value for $x_i^o(k)$.

The Grey Relational Coefficient (GRC) for k th factor for i th layout is stated by:

$$\xi_i(k) = \frac{\Delta_{\min} + \zeta \cdot \Delta_{\max}}{\Delta_{oi}(k) + \zeta \cdot \Delta_{\max}} \quad (4)$$

$$\begin{aligned} \Delta_{oi}(k) &= |x_o^*(k) - x_i^*(k)|, \\ \Delta_{\max} &= 1.00, \Delta_{\min} = 0.00, \end{aligned} \quad (5)$$

where, $\Delta_{oi}(k)$ refers to the degree of separation measured from unity(1) for the normalized sequence. ‘ ζ ’ is a identification coefficient for fine tuning to compress the data set and to make the whole data to skew towards unity. ‘ ζ ’ is having a range of $0 < \zeta < 1$ and the value is generally selected based on the discretion of the subjective requirement during experimentation (Abhang and Hameedullah 2011). For the present investigation the authors took this value as 0.5.

After determining the GRCs, generally average function is employed to determine the grey relational grade (GRG). The grey relational grade is the adjudging entity which reveals the goodness or badness of the layouts (Mathew and Rajendrakumar 2011). For weighted averaging the GRGs are obtained following the proposition by Lin and Ho (2003) which is expressed as:

$$\gamma_i = \sum_{k=1}^n w_k \xi_i(k) \quad (6)$$

where, $\sum_{k=1}^n w_k = 1$ and w_k denotes the weights of the factors based on which the judgment is conferred. The weights of the responses were determined by Grey Entropy Method proposed by Wen and Chang (1998).

5 Results and Discussion

The DOE was based on a 3^3 full factorial layout with ternary parameter levels and the corresponding measurands along with GRCs and GRGs have been shown in Table 2. While calculating the Grey Relational Grades the weights for yield strength, density and Vicat softening point were considered as 0.33332, 0.33329 and 0.33337 respectively.

Table 2 Experimental layout, response values and grey relational coefficients and grades

Experiment no.	Process parameters				Original sequence (responses)				GRG			GRG
	Injection temperature (°C)	Injection pressure (Bar)	Injection velocity (RPM)	Yield strength in tensile (MPa) average	Density (g/cc)	VSP (°C)	Yield strength in tensile (MPa) average	Density (g/cc)	VSP (°C)			
1	190	50	80	32.44	0.9043	154.00	0.666	0.467	0.533	0.555		
2	190	50	100	33.55	0.9045	154.20	0.957	0.429	0.615	0.667		
3	190	50	120	32.82	0.9042	153.70	0.743	0.488	0.444	0.559		
4	190	60	80	31.12	0.9042	153.80	0.489	0.488	0.471	0.483		
5	190	60	100	32.36	0.9041	154.00	0.651	0.512	0.533	0.566		
6	190	60	120	32.49	0.9043	153.50	0.675	0.467	0.400	0.514		
7	190	70	80	31.97	0.9042	153.40	0.590	0.488	0.381	0.486		
8	190	70	100	32.33	0.9044	153.60	0.646	0.447	0.421	0.505		
9	190	70	120	32.06	0.9042	153.90	0.603	0.488	0.500	0.530		
10	200	50	80	33.18	0.9036	153.50	0.835	0.677	0.400	0.637		
11	200	50	100	32.8	0.9052	154.70	0.739	0.333	1.000	0.691		
12	200	50	120	31.97	0.9041	153.70	0.590	0.512	0.444	0.515		
13	200	60	80	33.38	0.9051	154.20	0.897	0.344	0.615	0.619		
14	200	60	100	31.54	0.9032	153.80	0.534	0.913	0.471	0.639		
15	200	60	120	31.94	0.9043	153.10	0.586	0.467	0.333	0.462		
16	200	70	80	33.66	0.9034	153.40	1.000	0.778	0.381	0.720 ^a		
17	200	70	100	32.11	0.9043	153.50	0.611	0.467	0.400	0.492		
18	200	70	120	32.7	0.9042	153.60	0.717	0.488	0.421	0.542		
19	210	50	80	28.8	0.9043	153.40	0.333	0.467	0.381	0.394		

(continued)

Table 2 (continued)

Experiment no.	Process parameters			Original sequence (responses)				GRG		
	Injection temperature (°C)	Injection pressure (Bar)	Injection velocity (RPM)	Yield strength in tensile (MPa) average	Density (g/cc)	VSP (°C)	Yield strength in tensile (MPa) average	Density (g/cc)	VSP (°C)	GRG
20	210	50	100	32.91	0.9042	153.60	0.764	0.488	0.421	0.558
21	210	50	120	33.44	0.9041	153.80	0.917	0.512	0.471	0.633
22	210	60	80	32.34	0.9043	153.70	0.648	0.467	0.444	0.520
23	210	60	100	31.61	0.9042	154.00	0.542	0.488	0.533	0.521
24	210	60	120	32.21	0.9041	153.60	0.626	0.512	0.421	0.520
25	210	70	80	33.17	0.904	153.80	0.832	0.538	0.471	0.614
26	210	70	100	32.01	0.9041	154.10	0.596	0.512	0.571	0.560
27	210	70	120	31.4	0.9042	153.20	0.518	0.488	0.348	0.451

^aHighest value of GRG corresponds to optimal condition

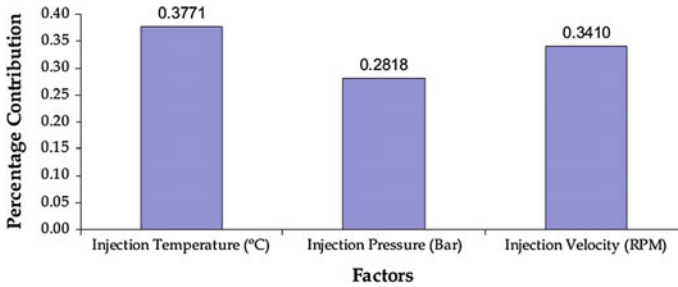


Fig. 3 Effect of injection parameters on multiple performance characteristics

After determining the GRGs, the Grey Response Analysis was accomplished. The Response Analysis considers the average of Grey Relational Grades for all the levels of all the process parameters and the difference in average GRGs for each parameter were determined to find out the importance of the parameters. This response analysis indicates that, for the present optimization problem; Injection temperature is the most influential parameter having a contribution of 37.71 % followed by Injection velocity and Injection pressure respectively having scores 34.10 and 28.18 % respectively. Figure 3 presents the graph for effect contribution of the control factors, which follows the descending order of feed rate, speed and depth of cut respectively. Furthermore it is evident that layout 16 fetches the highest GRG value which indicates parameter values as 200 °C Injection Temperature, 70 bar Injection Pressure and 80 rpm Injection velocity.

6 Conclusion

The present investigation was to find out a suitable combination of process parameters which would qualify polypropylene products pertinent to few mandatory tests as stated in ASTM guidelines. Owing to the previous survey of literature, experimentation and data interpretation the following conclusions are attained:

- Polypropylene products produced at 200 °C Injection Temperature, 70 bar Injection Pressure and 80 rpm Injection speed are having higher level of probability to qualify the tensile strength test, density test and VSP test concurrently.
- Injection temperature is the verbalizing parameter followed by injection velocity and injection pressure.
- The present investigation considers full factorial layout considering three levels for each parameters and thus the suitability among the discrete combinations were adjudged within the problem space. Hence it leads to quasi-optimal solution instead of optimal solution and to mitigate the same in the next attempt evolutionary soft computing techniques will be attempted in the pursuit of optimality.

References

- Abhang, L. B., & Hameedullah, M. (2011). Determination of optimum parameters for multi-performance characteristics in turning by using grey relational analysis. *International Journal of Advanced Manufacturing Technology* (published online).
- Chang, S., Hwang, J., & Doong, J. (2000). Optimization of the injection molding process of short glass fiber reinforced polycarbonate composites using grey relational analysis. *Journal of Materials Processing Technology*, 97, 186–193.
- Deng, J. L. (1989). Introduction to grey system. *Journal of Grey Systems*, 1(1), 1–24.
- Fung, H. C., & Kang, P. C. (2005). Multi-response optimization in friction properties of PBT composites using taguchi method and principal component analysis. *Journal of Materials Processing Technology*, 170, 602–610.
- Khan, Z. A., Kamaruddin, S., & Siddiquee, A. N. (2010). Feasibility study of use of recycled high density polyethylene and multi response optimization of injection molding parameters using combined gray relational and principal component analyses. *Materials and Design*, 31, 2925–2931.
- Lin, Z. C., & Ho, C. Y. (2003). Analysis and application of grey relation and ANOVA in chemical-mechanical polishing process parameters. *International Journal of Advanced Manufacturing Technology*, 21, 10–14.
- Mathew, M., & Rajendrakumar, P. K. (2011). Optimization of process parameters of boro-carburized low carbon steel for tensile strength by taguchi method with grey relational analysis. *Materials and Design*, 32, 3637–3644.
- Mehat, N. M., & Kamaruddin, S. (2011). Optimization of mechanical properties of recycled plastics products via optimal processing parameters using the Taguchi method. *Journal of Materials Processing Technology*, 211, 1989–1994.
- Ozcelik, B. (2011). Optimization of the injection parameters for mechanical properties of specimens with weld line of polypropylene using Taguchi method. *International Communications in Heat and Mass Transfer*, 38, 1067–1072.
- Rubin, I. (1972). *Injection molding theory and practice, SPE monographs*. Wiley.
- Wen, K. L., & Chang, T. C. (1998). The grey entropy and its application in weighting analysis. *Proceedings of IEEE International Conference on System, Man and Cybernetics*, 2, 1842–1844.

Use of Visual Analytics and Durometer in Risk Reduction of Foot Problems in Diabetes

Vinaytosh Mishra, Anubha Rautela, B. Manjunatha, Cherian Samuel, S.K. Sharma and A. Mishra

Abstract Foot Problems are a leading cause of hospitalization for patients having diabetes in India. Fifteen percent of all patients of diabetes develop foot ulcer during their life time. The cost of treatment increases significantly in people with diabetes and treatment may result in lower extremities amputations (LEAs). The Visual Analytics, Correction in Foot Care Hardness can help in early detection of people at risk of Foot Ulcer. The paper finds out the average hardness of male and female foot wears in Indian population. With help of visual analytics paper tries to find out the prevalence of people at risk of foot ulcer in diabetes. The paper also explores whether the risk of foot ulcer is significantly higher for a specific gender. The methods used for analysis is t-test and Chi-Square test.

Keywords Visual analytics · Risk management · Foot ulcer · Diabetes

1 Introduction

Diabetes has reached an epidemic proportion in the world and unfortunately the largest numbers of people suffering from diabetes live in India (Ramchandran 2011). With 62 million patients suffering from diabetes; India is one of the significant contributors (Mishra 2015) in this epidemic. The patients suffering from diabetes with foot complications spent 19,020 INR on an average in India (Bhansali 2013). Foot Problems are a leading cause of hospitalization for patients having diabetes mellitus. Foot Ulcers in diabetes precedes 85 % of non traumatic lower extremity amputation (LEAs) while 15 % develop foot ulcer during their lifetime (Nihal Thomas 2012).

V. Mishra (✉) · A. Rautela · B. Manjunatha · C. Samuel · S.K. Sharma
Indian Institute of Technology (BHU), Varanasi, India
e-mail: vinaytosh@gmail.com

A. Mishra
Diabetes Care Organization, New Delhi, India

2 Foot Ulcer

The person suffering from sensory neuropathy develop foot ulcer even in case of minor trauma. The neuropathy can be easily detected using Semmes-Weinstein monofilaments to determine whether patient is sensitive to the 10 g monofilament. The patients are asked to close their eye at time of application of the monofilament in various area of the foot with enough pressure to blend the nylon filament. The patients with loss of sensation are ten times more likely to develop a foot ulcer due course of the time (Ingrid Kruse 2006).

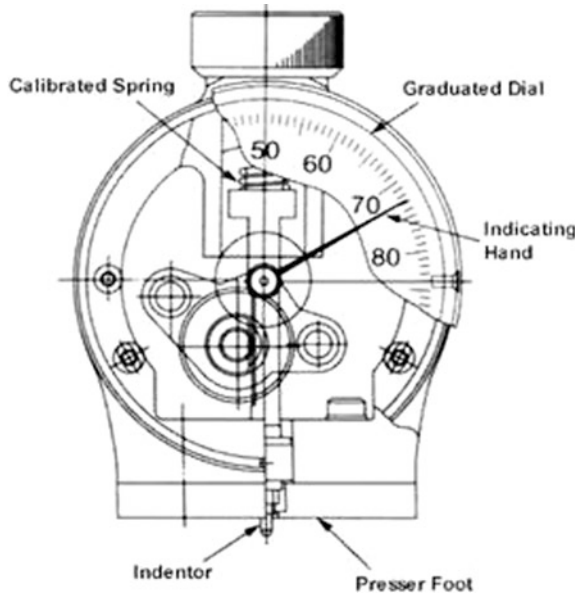
According to a study done, a diabetic foot ulcer has prevalence of 4.54 % in newly diagnosed diabetes patients. Neuropathic type of foot ulcer was found present in 46.06 % of patients (52.5 % in male and 38.88 % in female). Ischemic type of foot ulcer was present in 19.74 % of patients (22.5 % in male and in 16.66 % females). Neuroischaemic type of foot ulcer was present in 34.2 % of patients (25 % in males and 44.44 % in females). The research suggests that general awareness about the disease, early diagnosis and proper management will prevent this dreaded complication in case of diabetic foot (Sinharay 2012).

Another study confirms the high prevalence of foot ulcers among rural diabetes patients from Northern part of the India. The percentage of Foot Ulcer was found 14.30 % in diabetic patients. Out of 581 patients suffering from diabetes, 42.16 % belonged to rural areas whereas among the 97 cases with Diabetic Foot Ulcer 70.10 % belonged to rural areas (Shahi 2012).

3 Hardness of Footwear

Foot sole hardness is one of the main causes of foot ulcer in diabetes. The foot sole hardness is characterized by Shore level (Charanya 2004). The Shore Level can be measured by a device known as Durometer. Durometer is the international standard for measuring the hardness of most non metallic materials like rubber and plastic. The hardness of a material is its opposition to surface penetration (Durometer Made Easy). A Durometer comes with specifications like shape of Indenter, force should be applied and material to be tested. A Type-A Durometer with Conical Indentor with 35° included angle should be applied on soft rubber foot wear with 1.81 lb pressure, while a Conical Indentor with 31° should be applied on moderately hard rubber foot wear with similar pressure (Durometer Types and Specifications). The poor knowledge of instrument and measurement error can lead to wrong calculations of Shore Level. The following Fig. 1 depicts the important components of a Durometer.

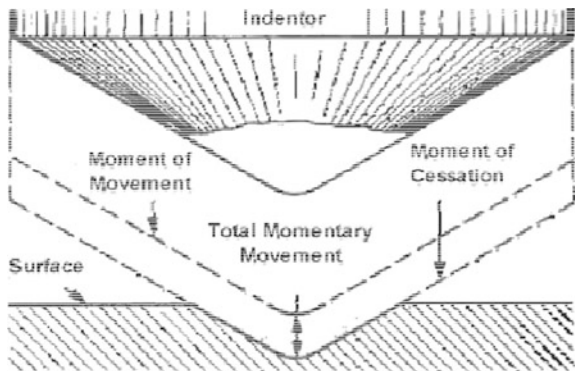
Fig. 1 Important components of a durometer (Durometer Types and Specifications 2015)



4 Durometer

The Shore Level testing depends on material characteristics, to overcome these barriers; a Durometer measures the relative movement of the indenter, rather than the depth of the indenter penetration. The movement of indenter is translated, either electrically, mechanically, or electro—mechanically to a scale. The values on scale indicate the shore value. It is recommended to take the readings within 1 s of the “moment of cessation” of the numerical increase of the indication. The digital scale is even better, because it further reduces measurement error. The Fig. 2 represents the momentary movement in conical indenter of a Durometer.

Fig. 2 Depiction of momentary movement in conical indenter (CCSI 2006)



A shore level between 8 and 15 is desirable for a person with diabetes. A shore value of less than eight is too soft and unlikely to give protection, whereas a value above 15 is too hard, leading to area of callosities due to the pressure (Nihal Thomas 2012).

5 Visual Analytics

Visual analytics (VA) is a field of information visualization that focuses on analytical reasoning facilitated by interactive visual interfaces. The heat maps created by software are easy to analyze and produce recommendation in terms of color coding.

Visual analytics helps us in understanding Big Complex Data with pictorial and interactive visualization (Thomas 2005). Visual Analytics is very useful technique in epidemiological investigations, which involves monitoring trends, detecting anomalies, and generating testable hypotheses. There is lack of studies on use of VA in bio surveillance. Experts suggest that uses of these techniques could lead to development of advance applications in surveillance. The recent developments in surveillance systems are pushing for constant innovations in data processing, synthesis, and communication (Thacker 1988).

Plantar pressure-measurement technology is being increasingly used by podiatric physicians and surgeons in both clinical practices (Bryant 2000). Plantar Pressure System can provide an economical and efficient method to measure static and dynamic plantar foot pressure distribution. The high resolution image of the pressure distribution across the planter surface can provide Visual Analytics about risk areas. A planter pressure can be measured using inked Harris Mat or using pressure appreciating sensors, but the earlier one is more economically viable solution (Nihal Thomas 2012). The inked mat is laid carefully face up on a white sheet of paper and patient is asked to walk over the mat to leave an impression of his foot on the paper. Then print pressure can be analyzed using the guidelines based on the study by Silvino et al. (1980). The inked paper can also be converted into a planter pressure heat map using image processing software. Figure 3 shows Harris Mat and Print Pattern for Respective Pressure Value. The Fig. 4 contains one of the heat map we found during out research.

VB Narayanmurthy and Indian Institute of Technology—Madras has developed a Portable Pedo Power Graph consisting of a glass plate mounted on wooden box and surrounded on longitudinal sides by light fixtures that illuminate it from its longitudinal thickness. Thin sheet covers the glass plate. When a person stand on the thin sheet, foot pressure images are formed at the contact surface of thin sheet and the glass plate by the scattering of light. Foot images have distribution of light intensities along the length and breadth of both feet. Distribution depends on foot sole hardness and pressure exerted by feet. Images are reflected through the mirror kept at an appropriate angle to the glass plate and captured by still digital camera. Images recorded as BMP files are analyzed to obtain the high frequency power and

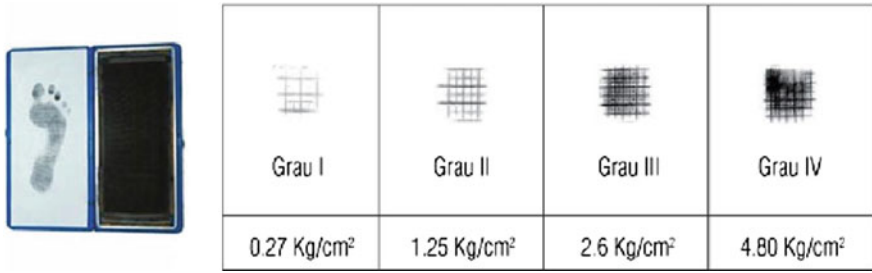
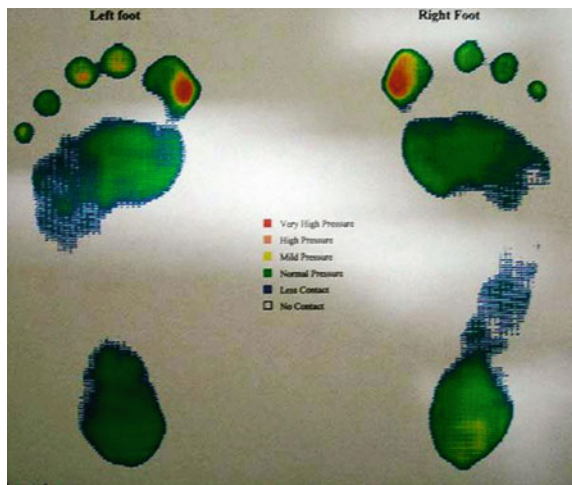


Fig. 3 Harris mat (*left*) print pattern for respective pressure value (*right*) (Nihal Thomas 2012; Silvino 1980)

Fig. 4 Visual analytic of planter pressure



the total power. Power ratio (PR) a new parameter is used in this device for screening of diabetic feet at risk.

The literature lacks the studies on use of durometer and planter pressure analysis as tools to access the risk of foot ulcer in the region (Eastern U.P and Bihar).

6 Research Objective

1. To evaluate the shore level in foot wear of Indian population. Is there a significant difference in average shore level between male and female population?
2. To find out which of the gender is more prone for developing foot ulcer in diabetes?

7 Methodology

The Shore values of 94 foot wear were tested using Durometer at 10 locations in Varanasi, India. Independent Sample t-test was used to find out whether there is a significant difference in average hardness of male and female shoes being sold in the region. Harris Mat and Visual Analytics of 102 patients were analyzed to find out their level of risk of foot ulcer. Based on the percentage of red colored region images were classified as high, medium and low risk. The chi-square was used to find out whether risk of Foot Ulcer is dependent on gender in diabetes.

The Karl Pearson’s chi-square tests was the method of choice for the study. It is one of the most popular statistical analysis for answering questions about the association or difference in case of categorical variables (Franke 2012). Chi-square is not a measure of degree of relationship or the form of relationship between two attributes but it is simply a technique of judging the significance of such association or relationship between two attributes (Kothari 2007).

8 Results and Discussion

H_0 = Average shore level for male and female is not different

H_A = Average shore level for male and female is different

The average shore level of footwear was found 21.24 for female while 20.27 for the male (Table 1). This indicates that shore level of shoes being used is higher than the permissible range of 8–15. The p-value for 95 % confidence interval was found to be 0.561; we failed to reject the Null Hypothesis. Hence we can conclude that there is no significant difference between hardness of foot wear between male and female population for the region of study.

The other study was performed on one hundred two patients at a diabetic clinic the heat map of the pressure point was analyzed to find out the risk level of diabetic patients.

H_0 = Risk of foot ulcer is independent of gender

H_A = Risk of foot ulcer is independent of gender

Table 1 Average shore level of footwear studied

	Sex	N	Mean	Std. deviation	Std. error mean
Shore_value	F	42	21.2381	7.54760	1.16462
	M	52	20.2692	8.55230	1.18599

Table 2 Contingency table for risk level among diabetes patients

	High	Medium	Low	Row total
Male	14	20	16	50
Female	19	12	21	52
Column total	33	32	37	102

A contingency table was created using the heat map of the participants in the study (Table 2). Chi-square value was found 2.918 which is significantly greater than expected Chi-Square value for $df = 2$ and Confidence Interval 95 %, which is 0.103.

9 Conclusion

Our study didn't find prevalence of foot ulcers amongst diabetics in female different from male population significantly. The finding doesn't concur with the finding of similar study done in Kolkata (Sinharay 2012). The study didn't find any significant difference between average shore levels of foot wears of male and female populations but it concludes that average shore level is higher than the recommended level. The reason behind high prevalence of diabetes foot ulcer may also be other risk variables like wear and tear of footwear, walking bare foot or not taking proper care of the foot. The simple tests like shore value and visual analytics of planter pressure can help us indentifying the risk of Diabetic Foot Ulcer early and can save foot of patients.

References

- Bhansali, A. (2013). Cost of diabetes care: Prevent diabetes or face catastrophe. *JAPI*, 61.
- Bryant A. R. (2000). Normal values of plantar pressure measurements determined using the EMED-SF system. *Journal of the American Podiatric Medical Association*, 295–299.
- CCSI. (2006). *Durometer Instrument Background*. Retrieved July 26, 2015, from CCSI Website: <http://www.ccsi-inc.com/>.
- Charanya, G. (2004). Effect of foot sole hardness, thickness and footwear on foot pressure distribution parameters in diabetic neuropathy. In *Proceedings of the Institution of Mechanical Engineers* (pp. 431–443).
- Durometer Made Easy. (n.d.). Retrieved July 26, 2015, from Paramount PDS: <http://www.paramountind.com/>.
- Durometer Types and Specifications. (n.d.). Retrieved July 26, 2015, from PTC Meterology: <http://www.ptc1.com/pdf/DurometerTechSheet.pdf>.
- Franke, T. M. (2012). The Chi-Square test often used and most often misinterpreted. *Americal Journal of Evaluation*, 33(3), 448–458.
- Ingrid Kruse, D. A. (2006). Evaluation and treatment of diabetic foot ulcers. *ADA: Clinical Diabetes*.
- Kothari, C. (2007). *Quantitative techniques*. New Delhi: USB Publishers Ltd.

- Mishra, V. (2015). Use of machine learning to predict the onset of diabetes. *International Journal of Recent advances in Mechanical Engineering (IJMECH)*, 4(2).
- Nihal Thomas, K. J. (2012). *A Practical Guide to Diabetes Mellitus*. New Delhi: Jaypee.
- Ramchandran A. (2011). *Burden of Type 2 Diabetes in India: Prevalence and Projection*. Micro Labs Ltd.
- Shahi, S. K. (2012). Prevalence of diabetic foot ulcer and associated risk factors in diabetic patients from north india. *The Journal of Diabetic Foot Complications*, 4(3 and 4), 83–91.
- Silvino, N. E. P. (1980). The harris and beath footprinting mat: diagnostic validity and clinical use. *Clinical Orthopaedics and Related Research*, 151, 265–269.
- Sinharay, K. P. U. (2012). Prevalence of diabetic foot ulcers in newly diagnosed diabetes mellitus patients. *Journal of Medical Association*, 608–11.
- Thacker, S. B. (1988). Public health surveillance in the United States. *Epidemiol Review*, 164–190.
- Thomas, J. J. (2005). *Illuminating the Path: The Research and Development Agenda for Visual Analytics: National Visualization and Analytics*.

On the Complexities in Machining Titanium Alloys

Paramjit Singh, Harish Pungotra and Nirmal S. Kalsi

Abstract Good corrosion resistance, high specific strength, superior high-temperature performance and good fatigue resistance makes titanium and its alloys excellent candidate for biomedical, automobile, marine and aerospace component manufacturers. However, higher machining cost due to excessive tool wear and low material removal rate restricts its share in current engineering market. High hardness and ability to retain it at extreme temperatures, strong chemical affinity, low modulus of elasticity and poor thermal conductivity are the main reasons for poor machinability of titanium alloys. In this paper, based on available literature, machining difficulties such as variable width and thickness of chips, thermal stresses, severe pressure on cutting tool, tool wear, springback effect and residual stress are reviewed and underlying mechanisms behind these difficulties are presented. At the end, potential research issues are highlighted.

Keywords Titanium alloys · Machining · Discontinuous chip · High temperature · Low Young's modulus · Chemical reactivity

1 Introduction

Commercial pure titanium exhibits α -phase (hexagonal close packed structure) at low temperatures. This α -phase transforms to β -phase (body centered cubic structure) at 882 ± 2 °C (Peters et al. 2003) but the transition is generally affected by presence of incorporated impurities, if any (Joshi 2006). These two different crystal structures attract many alloying elements such as aluminum, molybdenum,

P. Singh (✉)

Mechanical Engineering Department, Amritsar College of Engineering & Technology,
Amritsar 143001, India
e-mail: er.pannu266@gmail.com

H. Pungotra · N.S. Kalsi

Mechanical Engineering Department, Beant College of Engineering & Technology,
Gurdaspur 143521, India

© Springer India 2016

D.K. Mandal and C.S. Syan (eds.), *CAD/CAM, Robotics and Factories of the Future*, Lecture Notes in Mechanical Engineering,

DOI 10.1007/978-81-322-2740-3_49

manganese, vanadium etc. to act as phase stabilizers (Lütjering and Williams 2007). These alloying elements within size factor of fifteen percent (Fridlyander and Eskin 2006) attracted by an incomplete shell of electronic structure of titanium tends to form solid solution microstructures as α alloys, $\alpha + \beta$ alloys and β alloys (Veiga et al. 2012). Individual characteristics of α and β phases and their volumetric presence is the reason the titanium alloys shows a fascinated group of chemical and mechanical properties. These properties differentiate these alloys from other competitor metals and alloys. Mechanical properties like high fracture toughness and high specific strength are the primary attributes that makes titanium alloys a promising candidate for manufacturing of automobile (Veiga et al. 2012; Yamashita et al. 2002), airplane (Boyer 1996) and missile components (Gurrappa 2003). Low elastic modulus and good corrosion resistance makes these alloys equally suitable for manufacturing of biomedical and surgical components (Niinomi 2008).

Initial high extraction cost (Imam 2011) and high machining cost (Yang and Liu 1999; Pramanik and Littlefair 2015) of titanium and its alloys forces the manufacturers to use composite materials as a replacement to these alloys. Low volume specific heat, poor thermal conductivity, property of phase transition with temperature, high hardness and ability to retain it at higher temperatures, high strain hardening effect, high yield stress to tensile strength ratio, and high chemical reactivity of titanium alloys are enough to make the machining much complex when compared with steel, aluminum, etc. (Pramanik et al. 2013).

Recently some efforts are reported (Imam 2011) to develop titanium alloys using common low cost alloying elements (Mn, Fe, Cr, Sn, Si) for reducing the overall cost. Some publications (Pramanik and Littlefair 2015; Pramanik 2014) reported the efforts done by researchers to improve the machinability of titanium alloys. But there is no detailed document which describes the complexities in machining these alloys and the underlying reasons behind these complexities. The purpose of this paper is to discuss in detail about the inherent characteristics of titanium and its alloys which makes the machining process complex one.

2 Complexities Involved in Machining Titanium Alloys

Underlying complexities in machining titanium and its alloys due to its inherent thermal, mechanical and chemical characteristic are discussed in following sections.

2.1 *Discontinuous Chips with Variable Thickness*

Barry et al. (2001), Vyas and Shaw (1999), Obikawa and Usui (1996) noted two primary reasons behind chip formation (a) primary adiabatic shear band developed by localized shearing (b) crack initiation on the chip's outer surface. Critical cutting speed, depth of cut, chip load, machining environment etc. are the cutting parameters

which decides the type of chips produced in machining titanium alloys (Veiga et al. 2013). During machining of titanium alloys, at low critical cutting speed (Komanduri and Hou 2002, noted 9 m/min for Ti-6Al-4V alloy), thermal softening rate becomes more than strain hardening rate. At this speed adiabatic shear occurs in primary shear zone which results in discontinuous chips of varying thickness. Transformation from hexagonal close packed (α phase) to body centered cubic (β phase) with more slip systems during cutting process also favors adiabatic shear (Veiga et al. 2013). In one of his study on turning Ti-6Al-4V workpiece Sun et al. (2009) experimentally observed that segmentation of chip produces cyclic forces whose frequency also matches with frequency of chip segmentation. Another complicacy was noted in the process as the amplitude of cyclic forces varies linearly with increase in feed rate and depth of cut.

2.2 Thermal Stress

During cutting of titanium alloy workpiece the three main sources of rise in temperature are (a) primary shearing region where the workpiece is plastically deformed under the action of cutting tool (b) secondary shearing region where chip is rubbed on the rake face of cutting tool used (c) tertiary shearing region where flank face of cutting tool rubbed on newly machining surface. Shaw (1984) developed a model to relate machining temperature (T) with cutting conditions (cutting speed v , uncut chip thickness f) and properties of workpiece material (specific heat of workpiece material c , density ρ , thermal conductivity k , specific cutting energy u). The relation is given in Eq. (1):

$$\text{Machining temperature } (T) = u \sqrt{\frac{vf}{kpc}} \quad (1)$$

Combination of low thermal conductivity ($k = 18.67$ W/m °C at 1000 °C for Ti-6Al-4V which is about 25 % of steel) and low density for titanium alloys are responsible to generate very high and intense temperature (more than 500 °C) (Ginting and Nouari 2006) near the tool tip during machining these alloys. Low thermal conductivity value and its further decreasing trend up to 300 °C temperature during cutting process forces more than 80 % of heat generated into the body of cutting tool used (Abdel-Aal et al. 2009). Small elongation to break ratio with low thermal conductivity retains the heat conducted during cutting process for more time in titanium alloy workpiece (Ezugwu and Wang 1997). Ginting and Nouari (2006) noted that in machining titanium alloys, very high temperature is accumulated at the cutting edge of tool because chips are formed due to the action of cutting edge of tool only. This intense temperature produces a lot of thermal stress

at the cutting edge and catalyzes chemical reactions which reduces cutting tool life and deteriorates surface qualities (Abele and Frohlich 2008). High cutting edge temperature causes adiabatic shear by reducing strain hardening capacity of titanium alloys. Due to this adiabatic shear with of uncut chip thickness varies which results in pulsating forces and segmented chips. Extremely thin chip size with small tool-chip contact area (approx. half than that for steel turning) causes high compressive stress on cutting tool (Machado and Wallbank 1990). In addition to this, poor heat flow rate (thermal conductivity) of titanium alloys is responsible to collect massive temperature at contact area. Fitzsimmons and Sarin (2001) noted 1100 °C at the primary shearing zone during machining. Combined effect of elevated unit pressure and high temperature results in deterioration, dulling of cutting edge of tool and premature tool failure. Subramanian (1993) noted galling, chipping and pressure welding at contact areas.

2.3 Intense Mechanical Pressure on Tool

Wyen (2010) noted that cutting stress is strongly influenced by values of various parameters of cutting tool especially the rake angle used in machining titanium alloys. Titanium retains its hardness and strength at elevated temperatures generated due to the action of cutting tool during machining. Cutting tool itself influences high mechanical stress and thermal stress during cutting titanium alloys (Campbell 2006). Low plasticity of titanium alloys, generation of high thermal stress near the tool tip and segmentation of chips during machining involves gradual accumulation of wedge shaped material ahead of cutting tool. This wedge shaped material exerts high pressure on the cutting edge of tool. This intense pressure shows linear relation with cutting speed (Jawaid et al. 1999) and worn out the cutting edge of tool at faster rate.

2.4 Elastic Bouncing Effect

Friedrich and Kulkarni (2004) developed a model to relate elastic bouncing or springback (b_s) during milling with workpiece material properties (hardness H and Young's modulus of elasticity Y) and radius of cutting edge of milling cutter. The relation is given in Eq. (2):

$$\text{Springback } (b_s) = Zr_c \frac{H}{Y} \quad (2)$$

where Z is a constant. Comparatively high hardness (349 HV for Ti-6Al-4V) and low Young's modulus (113 GPa for Ti-6Al-4V) of titanium alloys are responsible for excessive elastic deflection under the action of force exerted by cutting tool during machining processes (Campbell 2006). As soon as the cutting edge of tool touches and exerts cutting force on surface of workpiece being cut, low Young's modulus makes the surface bounce away from the cutting edge. This causes rubbing of cutting edge against the surface of workpiece rather than performing real cutting action. Due to this excessive rubbing, friction comes into picture which deteriorates the surface quality and raises the interface temperature. Deep depth of cut is required to overcome the effect of bouncing and cut the titanium workpiece material. But deep depth of cut lowers the clearance angle on the flank face of tool which results in excessive chatter, machining vibrations more tool work interface friction.

2.5 *Microstructural Alterations and Residual Stresses*

Some studies (Che-Haron and Jawaid 2005; Che-Haron 2001) observed very thin plastically deformed layer of varying thickness under the surface of machined part. Other studies (Velásquez et al. 2010) observed directional change of grains parallel to cutting direction. Ibrahim et al. (2009) observed a very thin softening zone due to the effect of high temperature during cutting. All these microstructural changes during machining alter the characteristics of finished part (Sun and Guo 2008).

Complex aerospace structural parts having straight as well as variable curvature surfaces are generally manufactured from big castings of raw titanium alloy materials. Generally milling and turning processes are used to convert these heavy weight raw castings to final light weight thin components. Sometimes the weight of final machined components is even less than 1/50 times the weight of initial raw casting. Heavy weight castings are subjected to severe temperature gradient between surfaces during cooling time. These temperature differences setup the residual stresses in the castings. These residual stresses distort the components during cutting process and results in dimensional variability.

2.6 *Strong Chemical Affinity*

Titanium reacts chemically with almost all the available tool materials at elevated temperature (>500 °C) generated during cutting (Machado and Wallbank 1990). Strong chemical bonds are developed between the molecules at the contact zones (chip-tool interface and tool-worksurface interface) which obliterate the newly machined worksurface and cutting tool (Ezugwu and Wang 1997; Yang and Liu 1999). Titanium and its alloys shows strong affinity towards interstitial nitrogen

(N₂) and hydrogen (H₂) of heated removing layer which results in local hardening of workpiece. In addition, surrounding air molecules (preferably nitrogen and oxygen) easily diffused into the matrix of titanium workpiece surface at high temperature (above 600 °C) (He and Zhang 1985). Due to this chemical reaction, the cutting layer becomes harder. Combination of this local hardening and strain hardening effects poses difficulty in cutting.

Corrosive cutting environment strongly influences machining of titanium alloys. Titanium alloys are generally attacked and degraded by pitting corrosion. N₂ ion implantation (Schmidt 1998), CaCl₂ concentrations at the surface and high temperature effects are the main reasons behind pitting corrosion. In an experimental study, Gurrappa (2003) observed that rate of degradation of material from Ti-6Al-4V alloy depend upon the temperature during application and environment service nature (acidic, industrial and marine). High chemical reactivity and its increasing trend during machining titanium alloys demands cutting fluids with special characteristics like proper lubrication effect, high heat carrying capacity etc. and proper delivery systems (Shokrani et al. 2012). Su et al. (2006) observed that mixture of cold nitrogen gas and oil gives superior performance in machining titanium alloys.

2.7 Elevated Temperature Strength with Strain Hardening

Ability to maintain strength at elevated temperature generated in cutting is major hurdle to plastically deform the titanium alloy workpiece needed to remove the material in form of chip (Machado and Wallbank 1990). During cutting, much high power is needed to deform the workpiece plastically to form the chip. Enormous power involved and its consequent permanent deformation refers to work hardening of titanium alloys (Hosseini and Kishawy 2014). It is important to note that though diffused N₂ and H₂ molecules contributes in titanium work hardening rate but prime cause is plastic deformation during cutting (Yang and Liu 1999).

2.8 Poor Surface Quality and Machining Parameters

Another major hurdle in machining titanium alloys is poor surface qualities of machined part. High surface roughness of machined parts is influenced by process factors like formation of built up edge (Mantle and Aspinwall 2001), high temperature during machining (Ulutan and Ozel 2011; Calamaz et al. 2008) depth of cut (Ulutan and Özel 2012), cutting speed (Sun and Guo 2009; Che-Haron and Jawaid 2005), feed rate (Ginting and Nouari 2009) tool geometry and shape (Wang et al. 2005). In addition to mechanical and thermal cycling, titanium alloys shows microstructural alterations with temperature rise during machining. These are the main reasons behind above said process factors (Axinte and Dewes 2002).

3 Summary and Research Need

1. Intense mechanical pressure on cutting tool, variability in chip thickness and a lot of temperature in machining wears the cutting tool at much higher rate. These factors limit the machining speed and increases machining time. This results in more machining cost.
2. Special attention is needed during machining to consider the effect of residual stresses and elastic bouncing of titanium alloy workpiece.
3. Titanium alloys varies their thermal conductivity with rise in temperature during machining. This is big hurdle in stable machining.
4. Metallurgical alterations with the rise in temperature during machining results change in residual stresses and mechanical properties. This also contributes in unstable machining.
5. Titanium alloys exhibits work hardening property with temperature change during cutting. This alters built-up edge formation and chip formation mechanism with increase in shearing angle. Increased shearing angle put more pressure load on cutting tool and increases tool wear rate.
6. Low elastic modulus forces to provide extra machining error compensation and care during machining of slender workpiece.
7. Generation of cyclic forces and their amplitude variation, high chemically reactive environment and high hot hardness capability of titanium alloys during machining decides special cutting tool materials with extra characteristics (like resistance to chipping, good fatigue resistance, high toughness etc.)
8. High temperatures generated during machining, built up edge formation and wear of tool in cutting are the main causes which diminishes surface finish.

Being a major shareholder material in aeroengine and airplane body, titanium alloys' applications are directly influenced by their mechanical properties. Little work is reported on quantitative measure of influence of mechanical properties on machining response of titanium alloys. Further research is recommended in this direction. Mathematical models can be developed to establish the correlation between mechanical properties and optimized machining performance. Physical models should be developed to explain chip segmentation mechanism. Temperature issues in cutting titanium alloys explore comprehensive simulation and experimental studies. Optimum quantity of cutting fluid and its delivery methods during machining of titanium alloys is also research potential.

References

- Abdel-Aal, H. A., Nouari, M., & El Mansori, M. (2009). Influence of thermal conductivity on wear when machining titanium alloys. *Tribology International*, 42(2), 359–372.
- Abele, E., & Frohlich, B. (2008). High speed milling of titanium alloys. *Advances in Production Engineering and Management*, 3, 131–140.

- Axinte, D. A., & Dewes, R. (2002). Surface integrity of hot work tool steel after high speed milling experimental data and empirical models. *Journal of Materials Processing Technology*, 127, 325–335.
- Barry, J., Byrne, G., & Lennon, D. (2001). Observations on chip formation and acoustic emission in machining Ti–6Al–4V alloy. *International Journal of Machine Tools and Manufacture*, 41, 1055–1070.
- Boyer, R. R. (1996). An overview on the use of titanium in the aerospace industry. *Materials Science and Engineering A*, 213(1–2), 103–114.
- Calamaz, M., Coupard, D., & Girod, F. (2008). A new material model for 2D numerical simulation of serrated chip formation when machining titanium alloy Ti–6Al–4V. *International Journal of Machine Tools and Manufacture*, 48, 275–288.
- Campbell, F. C. (2006). *Manufacturing technology for aerospace structural materials* (1st ed.). Kidlington: Elsevier.
- Che-Haron, C. H., & Jawaid, A. (2005). The effect of machining on surface integrity of titanium alloy Ti–6%Al–4%V. *Journal of Materials Processing Technology*, 166, 188–192.
- Che-Haron, C. H. (2001). Tool life and surface integrity in turning titanium alloy. *Journal of Materials Processing Technology*, 118, 231–237.
- Ezugwu, E., & Wang, Z. (1997). Titanium alloys and their machinability—a review. *Journal of Materials Processing Technology*, 68(3), 262–274.
- Fitzsimmons, M., & Sarin, V. K. (2001). Development of CVD WC–CO coatings. *Surface & Coatings Technology*, 137(2), 158–163.
- Fridlyander, J. N., & Eskin, D. G. (2006). *Advances in metallic alloys, titanium alloys, Russian aircraft and aerospace applications*. : CRC Press.
- Friedrich, C. R., & Kulkarni, V. P. (2004). Effect of workpiece springback on micromilling forces. *Microsystem Technologies*, 10, 472–477.
- Ginting, A., & Nouari, M. (2006). Experimental and numerical studies on the performance of alloyed carbide tool in dry milling of aerospace material. *International Journal of Machine Tools and Manufacture*, 46, 758–768.
- Ginting, A., & Nouari, M. (2009). Surface integrity of dry machined titanium alloys. *International Journal of Machine Tools and Manufacture*, 49, 325–332.
- Gurrappa, I. (2003). Characterization of titanium alloy Ti–6Al–4V for chemical, marine and industrial applications. *Materials Characterization*, 51(2–3), 131–139.
- He, G., & Zhang, Y. Z. (1985). Experimental investigations of the surface integrity of broached titanium alloy. *CIRP Annals-Manufacturing Technology*, 34(1), 491–494.
- Hosseini, A., & Kishawy H. A. (2014). Cutting tool materials and tool wear. In J. P. Davim *Machining of titanium alloys* (pp. 31–56). Berlin: Springer.
- Ibrahim, G. A., Che-Haron, C. H., & Ghani, J. A. (2009). The effect of dry machining on surface integrity of titanium alloy Ti–6Al–4V. *Journal of Applied Sciences*, 9, 121–127.
- Imam, M. A. (2011). The 12th world conference on titanium presents research and applications of “wonder metal”. *The Journal of The Minerals, Metals and Materials Society*, 63(10), 16–23.
- Jawaid, A., Che-Haron, C. H., & Abdullah, A. (1999). Tool wear characteristics in turning of titanium alloy Ti–6246. *Journal of Material Processing Technology*, 92–93, 329–334.
- Joshi, V. A. (2006). *Titanium alloys: An atlas of structures and fracture features*. : CRC Press-Taylor & Francis.
- Komanduri, R., & Hou, Z. (2002). On thermoplastic shear instability in the machining of a titanium alloy (Ti–6Al–4 V). *Metallurgical and Materials Transactions A*, 33(9), 2995–3010.
- Lütjering, G., & Williams, J. C. (2007). *Titanium* (2nd ed.). Springer: Germany.
- Machado, A. R., & Wallbank, J. (1990). Machining of titanium and its alloys - a review. *Proceedings of Institution of Mechanical Engineers, Part B: Journal of Engineering Manufacture*, 204, 53–60.
- Mantle, A. L., & Aspinwall, D. K. (2001). Surface integrity of a high speed milled gamma titanium aluminide. *Journal of Materials Processing Technology*, 118, 143–150.
- Niinomi, M. (2008). Mechanical biocompatibilities of titanium alloys for biomedical applications. *Journal of the Mechanical Behavior of Biomedical Materials*, 1(1), 30–42.

- Obikawa, T., & Usui, E. (1996). Computational machining of titanium alloy: Finite element modeling and a few results. *Journal of Engineering for Industry*, 118(2), 208–215.
- Peters, M., Hempfenmacher, J., Kumpfert, J., & Leyens, C. (2003). Structure and properties of titanium and titanium alloys. In C. Leyens & M. Peters (Eds.) *Titanium and titanium alloys* (Vol. 1). Germany: Wiley.
- Pramanik, A., & Littlefair, G. (2015). Machining of titanium alloy (Ti-6Al-4V)-theory to application. *Machining Science and Technology: An International Journal*, 19(1), 1–49.
- Pramanik, A. (2014). Problems and solutions in machining of titanium alloys. *The International Journal of Advanced Manufacturing Technology*, 70(5–8), 919–928.
- Pramanik, A., Islam, M. N., Basak, A., & Littlefair, G. (2013). Machining and tool wear mechanisms during machining titanium alloys. *Advanced Materials Research*, 651, 338–343.
- Schmidt, H., Stechemesser, G., Witte, J., & Soltani-Farshi, M. (1998). Depth distributions and anodic polarization behaviour of ion implanted Ti-6Al-4V. *Corrosion Science*, 40(9), 1533–1545.
- Shaw, M. C. (1984). *Metal cutting principals*. Canada: Oxford University Press.
- Shokrani, A., Dhokia, V., & Newman, S. T. (2012). Environmentally conscious machining of difficult-to-machine materials with regard to cutting fluids. *International Journal of Machine Tools and Manufacture*, 57, 83–101.
- Su, Y., He, N., Li, L., & Li, X. L. (2006). An experimental investigation of effects of cooling/lubrication conditions on tool wear in high-speed end milling of Ti-6Al-4V. *Wear*, 261, 760–766.
- Subramanian, S. V., Ingle, S. S., & Kay, D. A. R. (1993). Design of coatings to minimize tool crater wear. *Surface & Coatings Technology*, 61, 293–299.
- Sun, J., & Guo, Y. B. (2008). A new multi-view approach to characterize 3D chip morphology and properties in end milling titanium Ti-6Al-4V. *International Journal of Machine Tools and Manufacture*, 48, 1486–1494.
- Sun, J., & Guo, Y. B. (2009). A comprehensive experimental study on surface integrity by end milling Ti-6Al-4V. *Journal of Materials Processing Technology*, 209, 4036–4042.
- Sun, S., Brandt, M., & Dargusch, M. (2009). Characteristics of cutting forces and chip formation in machining of titanium alloys. *International Journal of Machine Tools and Manufacture*, 49 (7), 561–568.
- Ulutan, D., & Ozel, T. (2011). Machining induced surface integrity in titanium and nickel alloys: A review. *International Journal of Machine Tools and Manufacture*, 51(3), 250–280.
- Ulutan, D., & Özel, T. (2012). Methodology to determine friction in orthogonal cutting with application to machining titanium and nickel based alloys. In *Proceedings of ASME 2012 International Manufacturing Science and Engineering Conference*. Notre Dame, June 4–8, 2012.
- Veiga, C., Davim, J. P., & Loureiro, A. J. R. (2012). Properties and applications of titanium alloys: A brief review. *Reviews on Advanced Materials Science*, 32, 133–148.
- Veiga, C., Davim, J. P., & Loureiro, A. J. R. (2013). Review of machinability of titanium alloys: The process perspective. *Reviews on Advanced Materials Science*, 34(2), 148–164.
- Velásquez, J. D. P., Tidu, A., Bolle, B., Chevrier, P., & Fundenberger, J. J. (2010). Sub-surface and surface analysis of high speed machined Ti-6Al-4V alloy. *Materials Science and Engineering: A*, 527, 2572–2578.
- Vyas, A., & Shaw, M. C. (1999). Mechanics of saw-tooth chip formation in metal cutting. *Journal of Manufacturing Science and Engineering*, 121(2), 163–172.
- Wang, Z. G., Rahman, M., & Wong, Y. S. (2005). Tool wear characteristics of binderless CBN tools used in high-speed milling of titanium alloys. *Wear*, 258, 752–758.
- Wyen, C.-F., & Wegener, K. (2010). Influence of cutting edge radius on cutting forces in machining titanium. *CIRP Annals—Manufacturing Technology*, 59(1), 93–96.
- Yamashita, Y., Takayama, I., Fujii, H., & Yamazaki, T. (2002). Applications and features of titanium for automotive industry. *Nippon Steel Technical Report*, 85, 11–14.
- Yang, X., & Liu, C. R. (1999). Machining titanium and its alloys. *Machining Science and Technology: An International Journal*, 3(1), 107–139.

Modeling, Analysis and Trajectory Planning of a 5 Degree of Freedom Robotic Arm for a Transmission Line Crossing Robot

C.M. Shruthi, A.P. Sudheer and M.L. Joy

Abstract Robots are used to provide help in unsafe, repetitive and dreary situations. This paper concentrates on a robotic arm which can be utilized for crossing of the dead wire structure to the jumper cable of an electrical transmission line. In order to achieve a good positional accuracy of the end-effector, the robotic arm is modeled and analyzed. Denavit-Hartenberg (DH) representation is used for the kinematic modeling and Lagrangian-Euler (LE) method for the dynamic modeling. Since the kinematic and dynamic modeling of robotic arm is highly nonlinear in nature, the optimum trajectory planning is a challenging issue in almost all obstacle avoidance problems. In trajectory planning, the desired trajectory needs to be followed for end-effector positioning. This paper presents kinematic modeling, dynamic modeling, workspace analysis and trajectory planning of a 5 Degree of freedom (DOF) robotic arm. The robotic arm is designed using SolidWorks 2014 software. The complete analysis of the proposed manipulator is simulated using MATLAB Software.

Keywords Degree of freedom · Kinematic and dynamic modeling · Workspace analysis · Trajectory planning

C.M. Shruthi (✉) · A.P. Sudheer · M.L. Joy
National Institute of Technology, Calicut, Kerala, India
e-mail: shrut.cm@gmail.com

A.P. Sudheer
e-mail: apsudheer@nitc.ac.in

M.L. Joy
e-mail: mlj@nitc.ac.in

1 Introduction

Robotic arms/manipulators have been drawing attention from researchers and industries for over three decades. A wide range of robotic arms are used in different areas including industrial applications. For any field of application either in research or industries the design and the mathematical modeling must be complying. Modeling of the robotic arm includes kinematic and dynamic analysis and so on. In kinematic modeling, direct and inverse kinematic equations are obtained, which gives the position and orientation of the end effector and joint variables respectively. The dynamic model represents the time-dependent aspects of a robot. It is concerned with the transient changes in the states of the parts in a robot. The dynamic modeling can also be described as the relation between the applied forces/torques and the resulting motion of an industrial manipulator. Likewise the space covered by the set of reachable points of the robotic arm need to be known during the modeling which comes under workspace analysis. The end-effector of the robotic arm is needed to be moved in a particular fashion to accomplish any specified task. The kinematic and dynamic modeling of the robotic arm oversee the move of posture with actuators exerting the desired torques. As no restrictions must be disregarded and no unmodelled behavior should be executed, it is important to devise planning algorithms that generate smooth trajectories.

Comprehensive study of an electrical line inspection robots has been carried out and a few existing working robots such as Expliner Robot (Debenest et al. 2008), Line Scout (Pouliot et al. 2015), Ti-EPRI (Phillips et al. 2013) and Legged Robot (Tsujimura et al. 2011) are studied in detail. Expliner Robot and Line Scout are found to be capable of crossing the dead wire structure and the obstacles. Other robots are capable of moving through straight line wire efficiently. Expliner robot is as shown in Fig. 1. The prototype is working by changing the position of its center of mass of the robot while moving. It is capable of avoiding the obstacles and crossing suspension type towers. Counter-weight makes the robot complicated and

Fig. 1 Expliner robot



Fig. 2 Line scout

heavy by weighing up to 90 kg. Line Scout is shown in the Fig. 2. Line Scout has arms and grippers, which offers grasping on both sides of the obstacle, allowing the wheels to disengage and flip down underneath the line prior to crossing to the other side. The operation is teleoperated from the ground and cannot cross tension type dead-end towers. It weighs 110 kg making the robot heavy with complicated crossing mechanism. From the literature gap, it is identified that the appropriate and efficient crossing mechanism is not available for both suspension and tension type transmission towers.

Many literature on robotics system design and analysis are available. Research papers closely related to the present work were reviewed thoroughly. A humanoid design of a 7-DOF dexterous robotic arm was proposed and the description on the design helps to understand the importance of the kinematic and dynamic modeling in system design (Yang et al. 2011). The kinematic modeling for a seven DOF robot was carried out. Its flexibility and ability of positioning were demonstrated using the software. The trajectory planning and dynamic analysis were not considered in both of the above work. The study on kinematic and dynamic modeling were carried out by Robo-Analyzer for various industrial robots and customizable lower DOF robots (Rajeevlochana and Saha 2011; Bahuguna et al. 2013). Tondu and team worked on a 7 DOF robot arm for picking up and placing the tele-operated task of a fragile object, highlighting both actuator sensitivity and its natural compliance. The detailed study on kinematic and dynamic analysis were explained. The trajectory planning was carried out for the velocity, acceleration and torque analysis. The kinodynamic motion planning algorithm was carried out and tested on the robot and the capability of generating time parameterized trajectories to pick up moving objects were obtained (Menon et al. 2014). Cycloidal trajectory was found as the optimal trajectory for the harvesting operation of the robotic arm, which gives minimum energy with smooth motion curve (Libin et al. 2009; Aljawi et al. 2004). Dynamic modeling and trajectory planning are limited for lower DOF robots and

joint trajectory performance of the robotic arm is not well addressed in any of the above research works.

This paper proposes the kinematic and dynamic modeling, workspace analysis and trajectory planning for a 5 DOF robotic arm of a transmission line robot. The objective is to select the actuator by finding the range of joint torque and to obtain the workspace of the robotic arm. Also, the trajectory planning is to accomplish a smooth motion of the manipulator using joint trajectory planning.

2 Modeling of the Robotic Arm

The CAD model of the robot made using Solid Works 2014 is given in Fig. 3. The robot has two arms with 5 DOF each, which helps in crossing the tower. The movement of the robot along the straight transmission line is illustrated with the help of Figs. 4 and 5. The robot first moves along the straight transmission line and reaches the tower's dead wire structure, then arm 1 will be unfolded to hold the straight transmission line and arm 2 will hold the jumper cable. Now the robot will be separated from the straight transmission line by disengaging the wheels (wheels at the upper part of the robot will help the robot to move along the transmission line), then the robot will be hanging from the junction using nylon string as shown in the Fig. 5c. Using the nylon string the robot will be going up and then get connected to the jumper cable with the help of a wheel mechanism. It then moves along the jumper cable till it reaches the other end of the dead wire structure. The same crossing mechanism takes place while crossing from jumper cable to the straight transmission line. This paper mainly concentrates on the modeling of

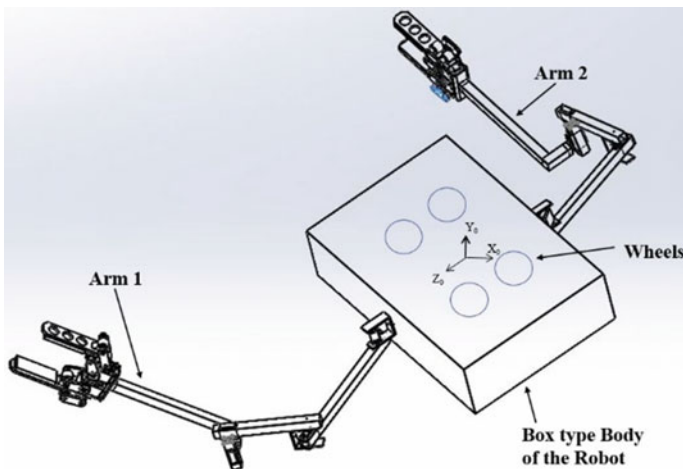


Fig. 3 CAD model of the robot

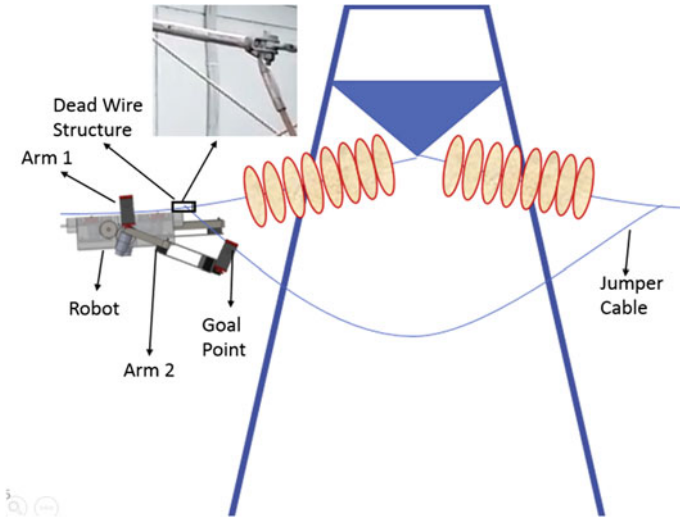


Fig. 4 Transmission line

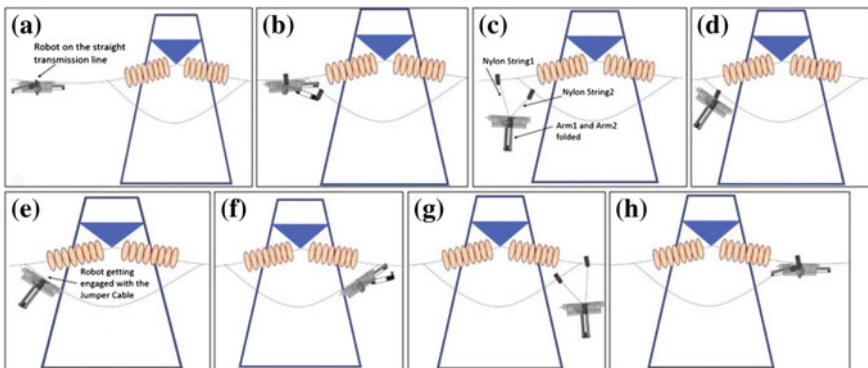


Fig. 5 Crossing of the transmission tower

5 DOF robotic arm. This robotic arm has five revolute joints hence 5 degree of freedom robotic arm. Forward and inverse kinematic modeling, dynamic modeling, workspace analysis and trajectory planning are done for the 5 DOF robot arm.

The arm lengths are finalized using virtual robotics experimentation platform's (V-REP) inbuilt inverse kinematics solver. Degrees of freedom are limited to five, based on which it is obtained as a feasible solution to the robot arm in various simulated positions in the V-REP software.

Table 1 Joint link parameters of 5 DOF arm

Link	a_i	α_i	d_i	θ_i
1	0	-90	0	θ_1
2	L_1	0	0	θ_2
3	L_2	0	0	θ_3
4	0	-90	d_1	θ_4-90
5	L_3	0	d_2	θ_5

2.1 Kinematic Modeling

Kinematics is the portrayal of movement without considering the force that causes it. The kinematic modeling of any robot system can be divided into two: forward kinematics and inverse kinematics. The relation between the joint variables, position and orientation of the end effector is kinematic model. Forward kinematics is characterized as the conversion of joint space to cartesian space whereas inverse kinematics is characterized as conversion from cartesian space to joint space. The goal of this section is to determine the analytical solution for both forward and inverse kinematics of a 5 DOF robotic arm. The position and orientation of the end effector are obtained with respect to the known reference frame from given joint link parameters. The standard Denavit-Hartenberg (DH) convention methodology is used for obtaining the joint link parameters.

The joint link parameters obtained from DH notation are tabulated in Table 1 and the coordinate frame representation is shown in the Fig. 6.

Based on the DH notation from Table 1, the transformation matrix is given in Eqs. (1) and (2).

$${}^0T_5 = \begin{bmatrix} n_x & o_x & a_x & p_x \\ n_y & o_y & a_y & p_y \\ n_z & o_z & a_z & p_z \\ 0 & 0 & 0 & 1 \end{bmatrix} \tag{1}$$

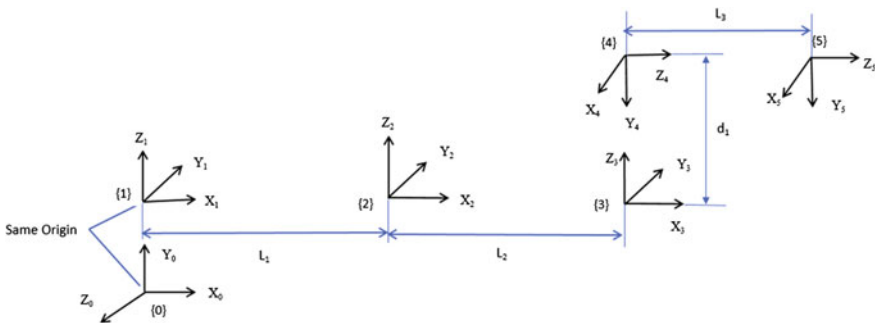


Fig. 6 5 DOF robotic arm frame assignment

$$\left. \begin{aligned}
 n_x &= S_1 S_5 + S_{234} C_1 C_5, \quad o_x = C_5 S_1 - S_{234} C_1 S_5, \quad a_x = C_{234} C_1 \\
 n_y &= S_{234} C_5 S_1 - C_1 S_5, \quad o_y = -C_1 C_5 - S_{234} S_1 S_5, \quad a_y = C_{234} S_1 \\
 n_z &= C_{234} C_5, \quad o_z = -C_{234} S_5, \quad a_z = -S_{234} \\
 p_x &= L_1 C_1 C_2 - d_1 S_1 + L_3 S_1 S_5 + L_3 S_{234} C_1 C_5 + d_2 C_{23} C_1 C_4 - d_2 S_{23} C_1 S_4 + L_2 C_1 C_2 C_3 - L_2 C_1 S_2 S_3 \\
 p_y &= d_1 C_1 + L_1 C_2 S_1 - L_3 C_1 S_5 - L_2 S_1 S_2 S_3 + L_3 S_{234} C_5 S_1 + d_2 C_{23} C_4 S_1 - d_2 S_{23} S_1 S_4 + L_2 C_2 C_3 S_1 \\
 p_z &= C_5 (L_3 C_{23} C_4 - L_3 S_{23} S_4) - L_1 S_2 - L_2 S_{23} - d_2 C_{23} S_4 - d_2 S_{23} C_4
 \end{aligned} \right\} \quad (2)$$

where, $\sin \theta_1 = S_1$, $\cos \theta_1 = C_1$, $\sin \theta_2 = S_2$, $\cos \theta_2 = C_2$, $\sin \theta_3 = S_3$, $\cos \theta_3 = C_3$, $\sin \theta_4 = S_4$, $\cos \theta_4 = C_4$, $\sin \theta_5 = S_5$, $\cos \theta_5 = C_5$, $\sin(\theta_2 + \theta_3) = \sin_{23}$, $\cos(\theta_2 + \theta_3) = C_{23}$, $\sin(\theta_2 + \theta_3 + \theta_4) = \sin_{234}$, $\cos(\theta_2 + \theta_3 + \theta_4) = C_{234}$, $L_1 = 0.3m$, $L_2 = 0.21m$, $L_3 = 0.345m$, $d_1 = 0.085m$, $d_2 = 0.05m$.

2.2 Inverse Kinematic Modeling

Inverse kinematics of the arm is done in order to attain the requisite pose for ascend and descend of the robot in various orientation. Taking specified position and orientation as the input of the end-effector, Joint variables like joint angles are achieved as output by inverse method. There are two methods to find the solution of an inverse problem, closed form solutions and numerical solutions. In the present work, inverse kinematic modeling is obtained by closed form method.

$$\theta_1 = A \tan 2(a_y, a_x) \quad (3)$$

$$\theta_5 = A \tan 2(-S_1 n_x + C_1 n_y, -S_1 o_x + C_1 o_y) \quad (4)$$

$$\theta_{234} = A \tan 2(-a_z, C_1 a_x + S_1 a_y) \quad (5)$$

$$\theta_2 = A \tan 2((\tan \theta_5 (C_1 n_x + S_1 n_y) + C_1 o_x + S_1 o_y), n_z \tan \theta_5 + o_z) \quad (6)$$

$$\theta_3 = A \tan 2(L_a, L_b)$$

$$\begin{aligned}
 L_a &= -C_1 S_2 p_x - S_1 S_2 p_y - C_2 p_z + 345 C_5 (C_1 C_2 a_x + C_2 S_1 a_y - S_2 a_z) \\
 &\quad - 50 (-S_2 C_1 a_x - S_2 S_1 a_y - C_2 a_z) \\
 L_b &= C_1 C_2 p_x + S_1 C_2 p_y - S_2 p_z - 300 - 345 C_5 (-S_2 C_1 a_x - S_2 S_1 a_y - C_2 a_z) \\
 &\quad - 50 (C_1 C_2 a_x + C_2 S_1 a_y - S_2 a_z)
 \end{aligned} \quad (7)$$

$$\theta_4 = \theta_{234} - \theta_2 - \theta_3 \quad (8)$$

2.3 Workspace of the Arm

Robot reachable workspace is the area where the end effectors can reach. It depends mainly on the degree of freedom, joint constraints and the arm link lengths. Workspace analysis for a 5 DOF robotic arm is carried out by using joint and link parameters. In this work the arm needs to stretch to the minimum distance of 0.9 m to reach the jumper cable of the line. The range of rotation of the each joint is considered based on the required poses of the end-effector to obtain the required motion through the transmission line.

2.4 Dynamic Modelling

Manipulator dynamics are the set of equations of motion (EOM) that describe the dynamic response of a manipulator. The dynamic modeling of the robotic arm is done by Lagrangian-Euler (LE) method. Dynamic model is developed using joint and link parameters. It is assumed that the links are rigid, no backlash and no effects on friction during the modeling. The resulting EOM are a set of second order coupled nonlinear differential equations consisting of inertia loading and coupling reaction forces between joints. One of the important objectives of dynamic analysis is the determination of joint torque for the selection of joint actuators. Dynamic model can also be used for the design of torque based controllers. The state space model of the dynamic equation for the manipulator can be written as

$$\tau = M(\theta)\ddot{\theta} + H(\theta, \dot{\theta}) + G(\theta) \quad (9)$$

where $M(\theta)$ is the effective inertia 5×5 matrix, $H(\theta, \dot{\theta})$ is the centrifugal and coriolis acceleration forces 5×5 matrix and $G(\theta)$ is the gravitational loading forces 5×1 matrix. $\theta, \dot{\theta}, \ddot{\theta}$ are the joint position, velocity and acceleration respectively.

The dynamic model based on LE formulation is obtained from a set of equations. For a 5 DOF robotic arm,

$$\tau_i = \sum_{j=1}^5 M_{ij}(\theta)\ddot{\theta}_j + \sum_{j=1, k=1}^5 h_{ijk}\dot{\theta}_j\dot{\theta}_k + G_i \quad \text{for } i = 1, 2, \dots, 5 \quad (10)$$

$$M_{ij} = \sum_{p=\max(i,j)}^5 Tr [d_{pi}I_p d_{pi}^T] \quad (11)$$

where M_{ij} is the coupling inertia between joint i and joint j and it's a 5×5 matrix.

$$h_{ijk} = \sum_{p=\max(i,j,k)}^5 Tr \left[\frac{\partial d_{pk}}{\partial \theta_p} I_p d_{pi}^T \right] \quad (12)$$

where h_{ijk} the Coriolis force coefficient is generated by the velocities of joint j and joint k and felt at joint i . $\sum_{j=1,k=1}^5 h_{ijk} \dot{\theta}_j \dot{\theta}_k$ is a 5×5 matrix.

$$G_i = - \sum_{p=i}^5 m_p g d_{pi}^p r \quad (13)$$

where coefficient G_i is the gravity loading force at joint i due to the links i to 5 and it's a 5×1 matrix. $\tau_1, \tau_2, \tau_3, \tau_4$ and τ_5 are obtained and the dynamic modeling is carried out using MATLAB.

2.5 Trajectory Planning

Trajectory planning is required to move the manipulator in the specified motion to accomplish a particular task. Trajectory is a path with specific qualities of motion like a path on which a time is specified in terms of positions, velocities and accelerations for each joint or end-effector of the manipulator. It is also moving from point A to point B while evading impact or collision over time. The smooth motion has the advantage of reducing vibration, wear and tear of the hardware system. In this case the goal point and the travel time are specified for the set of joint variable values and for the given goal point the set of joint variables are obtained from inverse kinematics. Joint position constraints and velocity constraints are the constraints used for acquiring the trajectory. Cycloidal motion curve can be described as

$$s(\tau) = \tau - \frac{1}{2\pi} \sin 2\pi\tau \quad (14)$$

Then its first and second derivatives can be expressed as

$$s'(\tau) = 1 - \cos 2\pi\tau \quad (15)$$

$$s''(\tau) = 2\pi \sin 2\pi\tau \quad (16)$$

where $\tau = \frac{t}{t_f - t_0} = \frac{t}{T}$, τ is normalized time; T is the operational time. $\theta_i(0)$ is initial joint angle and $\theta_i(f)$ is the final joint angle. $\theta_i(t)$, $\dot{\theta}_i(t)$ and $\ddot{\theta}_i(t)$ are the time history of joint angular position, joint angular velocity and joint angular acceleration respectively. For a smooth motion between the initial and goal points, the function. $\theta_i(t)$ and $\dot{\theta}_i(t)$ have to be smooth. This requirement imposes two constraints each on the joint position and velocity functions. The initial and final velocities are zero and it is taken as velocity constraints. The joint motion of the trajectory is obtained by considering the final time of 3 s. By considering these constraints the joint trajectory planning is computed using following Eqs. (17), (18) and (19).

$$\theta_i(t) = \theta_i(0) + (\theta_i(f) - \theta_i(0))s(\tau) \quad (17)$$

$$\dot{\theta}_i(t) = \frac{\theta_i(f) - \theta_i(0)}{T} s'(\tau) \quad (18)$$

$$\ddot{\theta}_i(t) = \frac{\theta_i(f) - \theta_i(0)}{T^2} s''(\tau) \quad (19)$$

3 Result and Discussion

3.1 Workspace Analysis

3D Workspace of the 5 DOF robotic arm is given in Fig. 7. The base joint of the arm is at (0, 0, 0) and this analysis showed that the end-effector is capable of reaching within the plotted work area. Based on the arm dimensions, the required position of the crossing point on the jumper wire can be achieved by the robot arm within the workspace.

3.2 Dynamic Modeling

Torque variations are plotted for a cycloidal trajectory for crossing to achieve the goal point as shown in Fig. 4 and the variations are shown in Fig. 8. It is clear from the Fig. 8 that the joint 1 requires high torque actuator compared to the other joints

Fig. 7 Workspace of the end-effector for the robotic arm

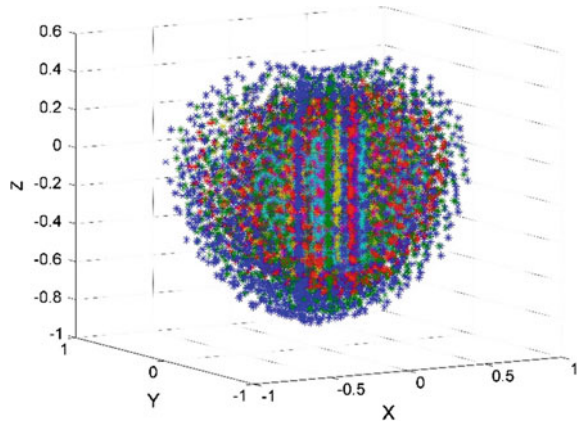
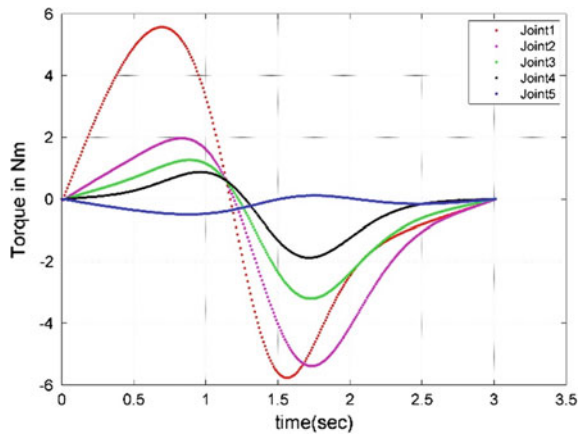


Fig. 8 Joint torque of 5 DOF robotic arm



since the weight and the inertial load carried by the previous links. The actual torque is calculated by giving a safety factor of 1.3 to the theoretical torque.

The motor with 1.5 Nm torque is feasible for the joint 1 which carries the load of the whole arm when in movement. Four servo motors (specification: High torque servo 17 kg cm torque, 6 V) and 1 encoder motor (specification: 131:1 Metal Gear motor 37Dx57L mm with 64 CPR Encoder) are mounted on arm. Energy calculation for the robotic arm is computed and the joint energy distribution of the same is shown in Fig. 9 which gives the range of energy required for the particular application of robotic arm. The joint energy on the joint 1 is higher compared to the other joints. The cycloidal trajectory gives the minimum and smooth energy graph as compared to cubic polynomial and blended spline.

Fig. 9 Joint energy of the 5 DOF robotic

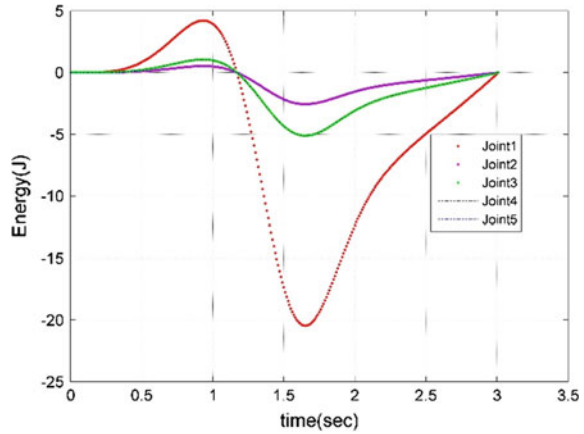
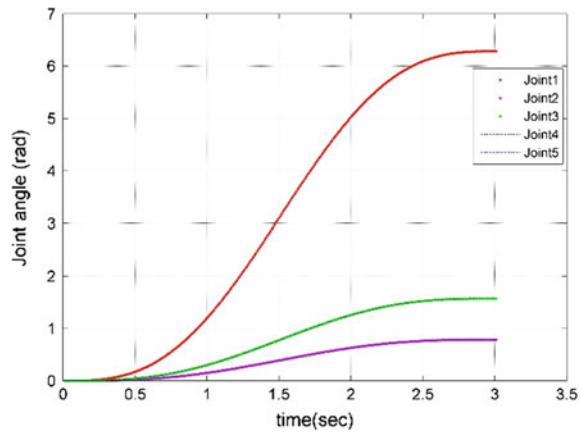


Fig. 10 Trajectory planning for the joint angle



3.3 Trajectory Planning

As shown in the Fig. 10, by giving the initial and final locations for all the joints as same, the smooth motion of the joint angle is obtained by using cycloidal trajectory. Also it is seen that the joint 1 has higher amount of torque, velocity distribution and acceleration distribution from the Figs. 8, 11 and 12 respectively, because joint 1 of the robotic arm has to carry the weight of rest of the links and inertial loads of every other link. Likewise it shows the joint 5 has less amount of torque, velocity and acceleration distribution because it need not carry the overall load of other joints. It is also seen that the acceleration curve is smooth, which shows that there will not be any jerk during the crossing operation.

Fig. 11 Results of joint velocity trajectory planning

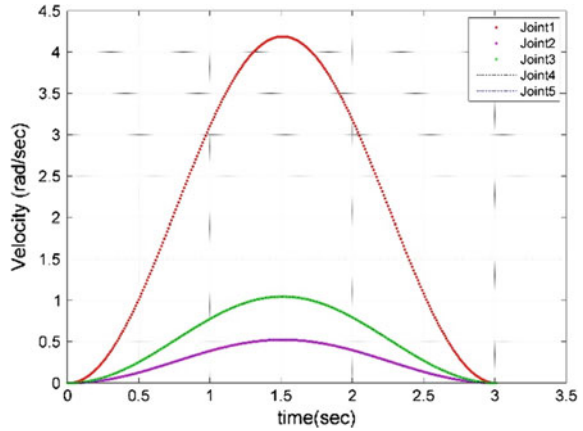
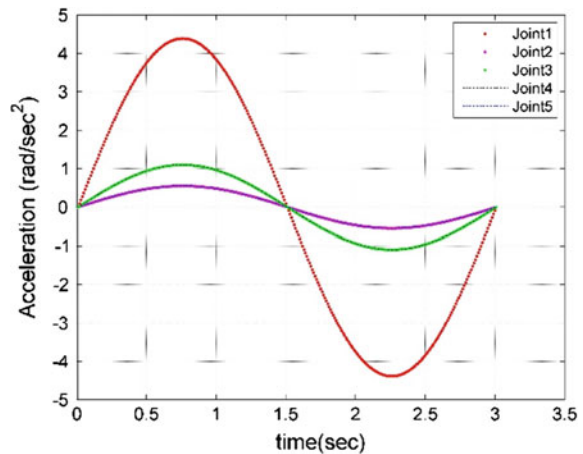


Fig. 12 Results of joint acceleration trajectory planning



4 Conclusion

This paper focuses on the robot with 2 arms of 5 DOF each, which aids in crossing operation from the dead wire structure to goal point of the jumper cable of a transmission line. The kinematic and dynamic modeling, trajectory planning and workspace analysis has been carried out on one of the 5 DOF robot arm. Joint torque and energy are computed during the cycloidal trajectory planning. This paper depicted the procedure for the selection of joint actuators of the 5 DOF robotic arm. The present paper proposed the modelling of arm for transmission line crossing application. This work presents the first phase in the development of the electrical line inspection robot. This work can be extended in several ways such as the fuzzy based optimum energy trajectory generation of crossing mechanism, conventional and unconventional design of controllers, fabrication and experimentation of arm for crossing applications.

References

- Aljawi, A. A. N., Diken, H., & Alshahrani, S. A. (2004). Selection of a trajectory function for minimum energy requirements of a spherical robot. *JKAU: Engineering Science*, 15(2), 99–110.
- Bahuguna, J., Chittawadigi, R. G., & Saha, S. K. (2013). Teaching and learning of robot kinematics using RoboAnalyzer software. In *Proceedings of Conference on Advances in Robotics* (pp. 1–6), ACM.
- Debenest, P., Guanieri, M., Takita, K., & Fukushima, E. (2008). Expliner-robot for inspection of transmission lines. In *Proceedings of the IEEE International Conference on Robotics and Automation* (pp. 3978–3984).
- Libin, Z., Yan, W., Qinghua, Y., Bao, G., Feng, G., & Yi, X. (2009). Kinematics and trajectory planning of a cucumber harvesting robot manipulator. *International Journal of Agricultural and Biological Engineering*, 2(1), 1–7.
- Menon, A., Benjamin, C., & Likhachev, M. (2014). Motion planning for smooth pickup of moving objects. In *IEEE International Conference on Robotics and Automation (ICRA 2014)* (pp. 453–460), *IEEE*.
- Phillips, A. (2013). EPRI's transmission assets inspecting robots enter next phase. *Magazine*, 22–30.
- Pouliot, N., Richard, P. L., & Montambault, S. (2015). LineScout technology opens the way to robotic inspection and maintenance of high-voltage power lines. *IEEE Power and Energy Technology Systems Journal*, 1–11.
- Rajeevlochana, C. G., & Saha, S. K. (2011). RoboAnalyzer: 3D model based robotic learning software. In *Proceedings of the International Conference on Multi Body Dynamics Vijayawada* (pp. 3–13), India.
- Tsujimura, T., & Yabuta, T. (2011). Control method of mobile legs to avoid aerial path obstacles. In *IEEE International Workshop on Intelligent Robots* (pp. 789–794).
- Yang, G., Mustafa, Lin Y. W., & Lim, W. B. (2011). Kinematic design of an anthropomorphic 7-DOF cable-driven robotic arm. *Frontiers of Mechanical Engineering*, 6(1), 45–60. Springer-Verlag, Berlin Heidelberg.

Design and Modelling of Dual Faceplate Centrifugal Casting Equipment for Manufacturing of Turbine Bearing

Saumil Desai, Saurin Sheth and Purvi Chauhan

Abstract Rise in the productivity can be achieved by automation or special purpose machine (SPM). The paper is focused on the design of a SPM for manufacturing of turbine bearing having with 3000 kg mass, 700 mm length and 1200 mm diameter. Centrifugal casting is the only process through which such dimensioned bearing is manufactured. As this machine is working on the concept of centrifugal forces the rotational speed plays a vital role, so provision is made to vary it from 10 to 350 rpm. According to length to diameter ratio, vertical machine is preferred, but the tendency of getting parabolic shape by material during rotating keeps us away from selecting this design. In the horizontal machine, there is a tendency that the molten metal might not match the synchronous speed i.e. rotational speed of mould, which keeps us away from selection. Hence dual faceplate centrifugal casting machine has been selected.

Keywords SPM · Turbine bearing · Design · Centrifugal casting · CAD

1 Introduction

Ultra-Mega Power Plants (UMPP) are working with high megawatt turbines, consisting of blades of around 40 m in length, and a rotor hub height of 60–100 m. Their weight may be around 200 tons. Therefore, the bearings used in turbines are

S. Desai (✉)

Institute of Technology, Nirma University, Ahmedabad, Gujarat, India
e-mail: saumil.desai@nirmauni.ac.in

S. Sheth

G. H. Patel College of Engineering & Technology, V. V. Nagar, Gujarat, India
e-mail: saurinsheth@gcet.ac.in

P. Chauhan

Birla Vishvakarma Mahavidhyalaya, V. V. Nagar, Gujarat, India
e-mail: pdchauhan@bvmengineering.ac.in

© Springer India 2016

D.K. Mandal and C.S. Syan (eds.), *CAD/CAM, Robotics and Factories of the Future*, Lecture Notes in Mechanical Engineering,

DOI 10.1007/978-81-322-2740-3_51

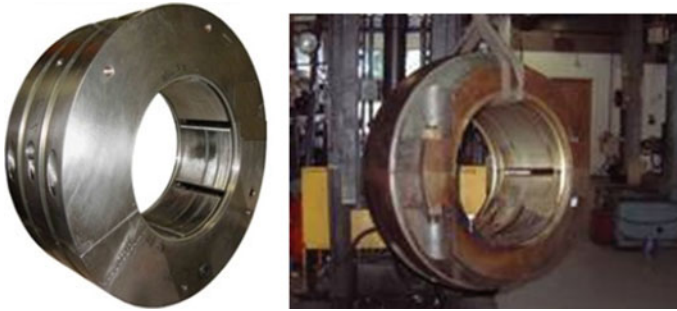


Fig. 1 Turbine bearings

very large, with bore diameters of between 100 and 700 mm, and even as much as 2 m in some instances. To produce such large sized product as shown in Fig. 1 (Desai 2012). Reliable manufacturing technique available is only the centrifugal casting because of its versatile effect of distribution of material in form of grains, directional solidification of grain and generating a cavity. In centrifugal casting, spinning a mould generates centrifugal force on molten metal to position the metal within a mould. As the molten metal solidifies from the outside to inside, a casting having directionally oriented grain structure with uniform distribution of grains is created. As a result of homogeneously dense grain structure the centrifugal process offers products with better physical properties than castings made using the static casting method. Unlike most other casting techniques, centrifugal casting is chiefly used to manufacture stock materials in standard sizes for further machining, rather than shaped parts tailored to a particular end-use. According to the orientation of mould axis, the centrifugal casting machine is classified as horizontal or vertical axis machine. Using dual faceplate centrifugal casting equipment, the bearing to be manufactured has length, 700 mm and diameter 1200 mm and the mould is oriented horizontally which resolves the problem of getting parabolic shape in vertical centrifugal casting machine. In conventional horizontal casting machine, due to long tubular shaped mould, the distribution of material might not take place uniformly throughout the length of mould which results in non-synchronous speed of molten metal because the process requires a diameter less compared to length of a job as per aspect ratio. So here a dual faceplate centrifugal casting has been selected for said purpose.

2 Literature Review

While designing a centrifugal casting machine, centrifugal force plays a key role which comes from rotational speed of mould. The rotational speed of shaft propelled the mould at required speed which results in positioning the molten metal

within the mold to create small sized cylindrical jobs under the effect of centrifugal force (Oyewole and Sunday 2011). The researchers suggested the alternate solutions for design of vertical centrifugal casting machine for piston production. They proposed solutions wherein design, less components are present because of compactness of structure but the problem was of high vibration of shaft. In another solution, they proposed a structure having low vibration and larger stability in the movement of flexible elements (Seabra et al. 2009). The selection and implementation of automation at various level helps to rise in the productivity. Here, the researchers have designed and developed an automatic back plug press fitting assembly for ball pen manufacturing as a special purpose machine. There is a significant rise in the productivity has been achieved (Gajjar and Sheth 2014a, b). A design has been carried out to perform an automatic locking arrangement of centrifugal casting machine using CAD and FEM (Kalne and Borkar 2014). A design of Special Purpose Equipment for Shell-Diaphragm Welding in Conveyor Pulley has been performed to reduce the setup time to hold pulley for welding and thus increase in productivity. Mechanical design of components have been carried out under various suitable design criteria to perform the operation very well (Gangadia et al. 2014).

3 Proposed Design

According to the requirement, the first thing is to hold the mould on faceplate. Then mould rotates at 10 rpm during pouring the molten metal inside the mold in the beginning and then speed will increase to 350 rpm. As shown in Figs. 2 and 3, 3-phase AC motor is used as prime mover which is connected to variable frequency drive for changing the mold rotational speed. The power is transmitted through

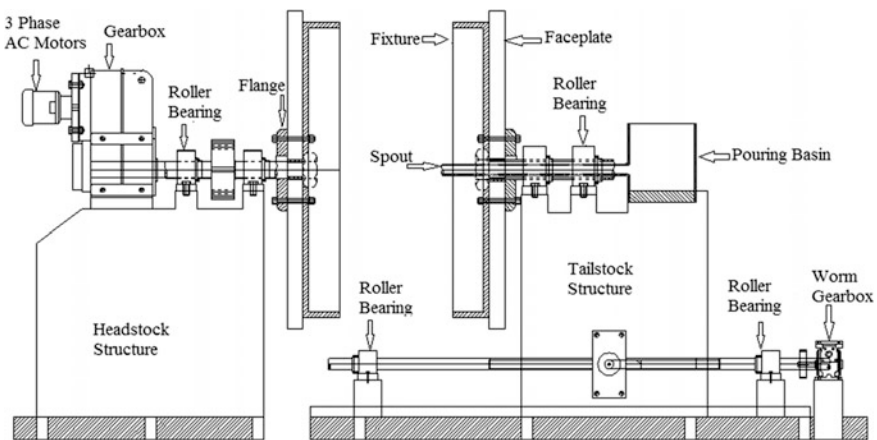


Fig. 2 Front view of proposed design (Desai and Sheth 2015)

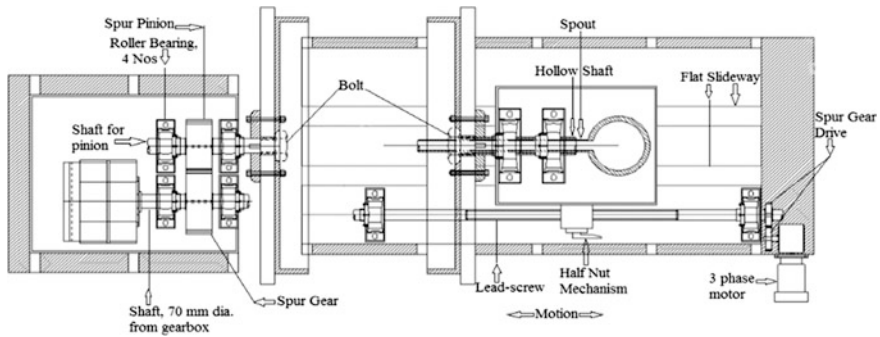


Fig. 3 Top view of proposed design

helical gear drive box. Still to increase the speed, a spur gear drive is used at output shaft. At a time of loading and unloading of job, a tail structure is required to move to and fro. For this, the leadscrew and half nut mechanism is used to move the structure as per operator's wish. A single stage reduction worm gear is used to rotate the leadscrew. The flat slideway is provided for to and fro motion of the tailstock structure (Desai and Sheth 2012, 2015).

4 Design and Selection of Components

4.1 Selection of Motor, Gearbox and Output Shaft

Motor is selected on the bases of torque required to rotate a mould. 3 phase synchronous flange mounted motor is selected as per IS 1231–1974. Assume center of gravity remains offset from 20 mm outside the central axis, Torque (T) required to rotate the object is 588.6 Nm and power required is 21.57 kW at 350 rpm. From the catalogue, a 3-phase AC motor is selected which is having input power of 22 kW and on that basis, a gearbox is selected which is having torque greater than 1.25 times the calculated output torque. So the gearbox model is F0920 which has output speed of 288 rpm and rated output torque of 707 Nm (Pbl.co.in 2011). Gearbox selected from elecon catalogue is a hollow output shaft gearbox. Size of the hole is 70 mm diameter. So, the size of shaft attached to the gearbox must have a 70 mm diameter, as per the availability. Output shaft is supported by two bearing blocks. At the mid span of the shaft between two bearing blocks, key is provided which can carry the gear as shown in Figs. 2 and 3. The length of the output shaft is decided by considering the dimension of the bearing blocks, thickness of pinion.

4.2 Design of Gear and Pinion

The required output speed is 350 rpm and the speed from the gearbox achieved is 288 rpm. So to increase the speed, there should be a gear and pinion. Direct Hardening Steel C40 and Case Hardening Steel 17Mn1Cr95 are selected for the material of gear and pinion respectively.

To achieve speed ratio of 1.21, the assumed teeth for gear and pinion is 31 and 25 m is module of gear. In relation with module, velocity of gear is 0.467 mm³/s.

For tooth profile of involute type having 20° pressure angle, tooth factor

$$y = 0.154 - \frac{0.912}{z} \tag{1}$$

Tangential load on gear tooth using Lewis’s equation,

$$W_T = \sigma_w \times b \times y \times \pi \times m \tag{2}$$

where σ_w = Working stress for the gear ($\sigma_{og} \times C_v$),

b = Width of the gear

Tangential load acting on gear,

$$W_T = \frac{P}{V} \times C_s \tag{3}$$

Comparing Eqs. (2) and (3),

$$\text{Module, } m = 12$$

Based on module, Pitch circle diameter, width and depth of tooth and clearance were found (Fig. 5). Free body diagram for shaft is shown in Fig. 4.

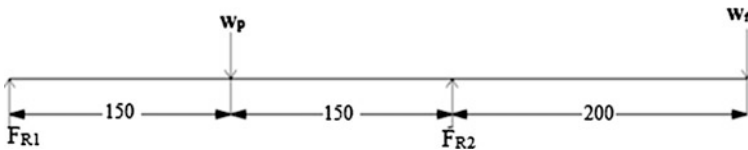


Fig. 4 Free body diagram for shaft, Φ90

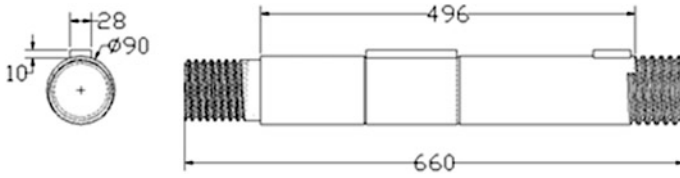


Fig. 5 Shaft, $\Phi 90$

4.3 Design of Shaft, $\Phi 90$

The output speed achieved by helical speed reducer gearbox is 288 rpm and required speed to rotate a mould is 350 rpm. A positive displacement drive is required to further increase the speed. Hence a spur gearing is used. For this, another shaft is required to design for mounting of pinion as shown in Fig. 5 (Desai 2012). The load acting by the pinion, W_p is 4577.15 N and load acting by faceplate, W_f is 23091.07 N considering weight of faceplate itself, fixture and half the weight of mould i.e. supported at two ends. The material for the shaft is taken as EN 8 which is medium carbon steel having yield stress = 465 MPa.

Using Equivalent torsional stress theory,

$$\frac{\pi}{16} \times \tau \times d^3 = \sqrt{(K_m \times M)^2 + (K_t \times T)^2} \tag{4}$$

Using Equivalent bending stress theory,

$$\frac{\pi}{32} \times \sigma_b \times d^3 = \frac{1}{2} [(K_m \times M) + T_e] \tag{5}$$

Using these stress theories, the maximum diameter obtained for the shaft is 90 mm (Figs. 6 and 7).

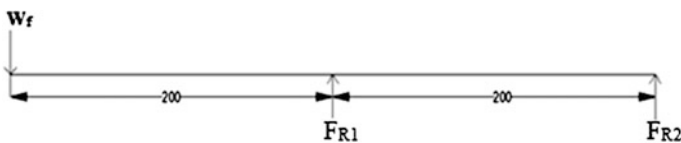


Fig. 6 Free body diagram for hollow shaft at tailstock

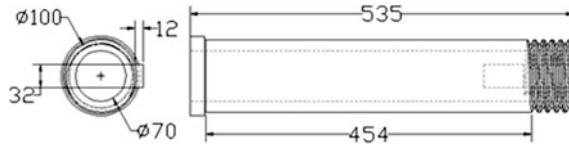


Fig. 7 Hollow shaft, Φ100

4.4 Hollow Shaft at Tailstock

Molten white metal is poured by the way of a suitable spout that passes through the rotating shaft. So hollow shaft is required at tailstock as shown in Fig. 7 (Desai 2012). The shaft material is EN8 which is medium carbon steel with yield stress of 465 MPa. Shaft length is decided by considering the dimensions of bearing blocks, faceplate along with mould and fixture and spacing between them. The ratio of inner diameter to outer diameter is 0.7.

Using Equivalent bending stress (5) and Equivalent torsional stress theory (4), outer diameter of shaft is 100 mm and inner diameter of shaft is 70 mm.

4.5 Bearing Selection for Shaft, Φ70

Due to the helical speed reducer there will be thrust load acting on a shaft. To absorb thrust load, Taper roller bearing is used which can absorb radial as well as thrust load. The arrangement of bearing shown in Fig. 8 is as simply supported beam and at mid span, spur gear is mounted. F_{R1} and F_{R2} are radial load acting on bearing 1, 2 respectively and F_R is the total load implied by spur gear mounted on shaft. Due to arrangement similar to simply supported beam, F_{R1} and F_{R2} are equal to half the F_R which is 4044.94 N. Axial load in taper roller bearing is calculated by following Eq. (6)

$$F_a = \frac{0.5 \times F_R}{K} \tag{6}$$

where K factor is geometry-specific coming from the relationship $K = 0.389 \cot \alpha$. α is half the included cup angle. Considering life of bearing equal to 30,000 h, Basic

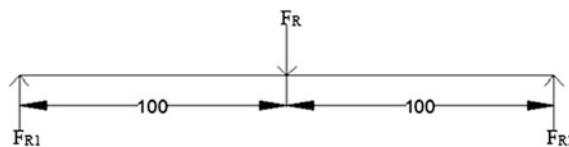


Fig. 8 Free body diagram for shaft, Φ70

Dynamic Load Rating, $C = 20.606$ kN. So, a taper roller bearing of designation 32014 X/Q and bearing unit of designation SYNT 70F are selected from SKF catalogue. So, a taper roller bearing of designation 32014 X/Q and bearing unit of designation SYNT 70F is selected from SKF catalogue (Skf.com 2012).

4.6 Bearing for Shaft, $\Phi 90$

As shown in Fig. 4, the bearing arrangement is such that the pinion is at the mid span of the shaft length covered by the bearing and at the end of shaft, faceplate along with fixture and mould is attached which is shown in figure. Considering life of 20,000 h. Basic Dynamic load rating, C is 388.077 kN. So, a taper roller bearing of designation 32318 J2 and bearing unit of designation 32317 BJ2 is selected from SKF catalogue.

4.7 Bearing for Hollow Shaft

As shown in Fig. 6, the faceplate along with mould is placed at the end of hollow shaft and the shaft is supported by two taper roller bearing blocks. The shaft will follow the rotational motion of shaft at headstock side only but there may be a chance of thrust load which may be transferred through faceplate at headstock side, rotating mould and faceplate at tailstock side to hollow shaft. So, taper roller bearing with bearing blocks are placed and the particular shaft will work as an overhung beam. By taking the reference of Fig. 6, F_{R1} and F_{R2} are radial load acting on front and rear bearing. The arrangement is such that maximum radial load is acting on front bearing which can be found as follows:

$$F_{R1} = \frac{(C+L)}{L} \times W_f \quad (7)$$

Axial load in taper roller bearing is computed by following equation:

$$F_a = \frac{0.5 \times F_{R1}}{K} \quad (8)$$

Considering a life of 20,000 h for bearing, basic dynamic load, C is 441.727 kN. So, a taper roller bearing of designation 32320 J2 and bearing unit of designation SYNT 100LTS is selected from SKF catalogue.

4.8 Leadscrew and Gearbox to Rotate Leadscrew

To load and unload the mould on faceplate, tailstock structure has to be moved. So, leadscrew with half nut mechanism is required to do this task. The engage-disengaging of nut with leadscrew will result into movement of tailstock structure. Initially, the assumed parameters of lead screw are as follows: (1) Pitch diameter, $d_p = 50$ mm (2) Minor diameter, $d_m = 47.5$ mm (3) Major diameter, $d_M = 52.5$ mm (4) Pitch, $t = 10$ mm. Whether these parameters are viable or not, Four criteria are required to check them. These are (1) Design of wear, (2) Design for strength using maximum stress theory, (3) Design for stiffness and (4) Design for buckling stability. The assumed parameters satisfy all criteria. Pulling force required for tailstock is 7806.69 N. Torque required to rotate the lead screw,

$$M_t = \frac{Q \times d_p (\cos\alpha \times \tan\lambda) + \mu}{2 \frac{\cos\alpha - \mu\tan\lambda}{\pi d_p}} \quad (9)$$

where Q is pulling force, $\alpha =$ half the included angle of the thread profile (14.5° in the case of acme threads), $\lambda = \tan^{-1} \frac{t}{\pi d_p} =$ helix angle of the thread = 3.64 , and $\mu =$ coefficient of friction, which generally lies between 0.1 and 0.15. $M_t = 45083.63$ N mm. The required speed to rotate the lead screw is 30 rpm and the motor input speed is 1500 rpm. Hence, worm gearbox is required to reduce the motor speed. Though the efficiency of worm gearing is low compared to other gearbox, large velocity ratio is possible through worm gearbox. Worm geared motor-SWM model overdriven reducer is selected from the Elecon worm gear catalogue for this application. The power required to rotate the lead-screw is 0.14 kW (Elecon.com 2012).

4.9 Design of Gear and Pinion for Lead Screw

Though the required speed reduction can be achieved by the worm gearbox in single stage, it is not a usual practice to assemble the lead-screw to the gearbox directly because of slenderness of shaft from gearbox. So, a gear and pinion pair is required which has speed ratio of 1:1. Cast iron grade 20 is selected for the material of gear and pinion respectively. Velocity of gear in terms of module is $0.0628 \text{ mm}^3/\text{s}$ and pressure angle is 20° for involute profile. Using Eqs. (1), (2) and (3), the module obtained is 3.

4.10 Halfnut

Half nut mechanism is used to engage or disengage lead-screw for moving tailstock on slideway. It comprises a pair of half nuts capable of moving in or out of mesh with lead screw. The two halves of the nut are connected in the cam slots in a circular disc by two pins. Closing the half nuts causes the tailstock to move a fixed distance for each revolution of lead screw. Length of nut (L) = 100 mm, number of thread in contact with nut = 10.

4.11 Bearing for Leadscrew

For lead-screw, the spherical roller bearing is selected to absorb thrust load. These bearings are self-aligning bearings. The self-aligning feature is achieved by grinding one of the races in the form of sphere. These bearings can normally tolerate angular misalignment in the order of $\pm 1.5^\circ$.

4.12 Integral Flat Slideway

The flat slide way is easy to manufacture and its geometrical parameter can be easily checked. The closed version of the flat slide way has poor lubricant retainment properties while the open has a tendency to accumulate the dirt. Generally, in heavy duty application, the flat slide ways are preferred. The material of the slide ways are cast iron and low alloy or low carbon steel.

5 Conclusion and Future Scope

For the given application, design calculations of various components are performed along with the selection of the components. The general arrangement drawing gives conceptual idea of a special purpose machine. Lead screw and half nut mechanism is provided to move the tailstock at the operator's will, to load and unload of job. A VFD unit is provided with the machine, which is helpful in varying the rotational speed of the mould. Figures 9 and 10 shows the assembly and exploded view of the designed special purpose machine. It can fulfil the specifications as designed machine has to manufacture the bearing with maximum specification as: Mass = 3000 kg, length = 700 mm and diameter = 1200 mm.

Selection of sensors, controller, actuators and step less drive gives versatility to the machine. Achieving the speed variation, as per the material property and dimensional changes, can be done by Pulse with Modulation (PWM). The use of hydraulic

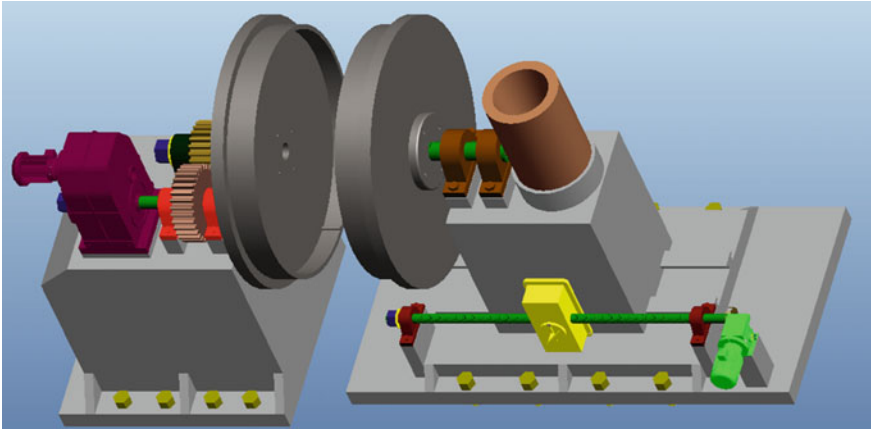


Fig. 9 Assembly of centrifugal casting equipment

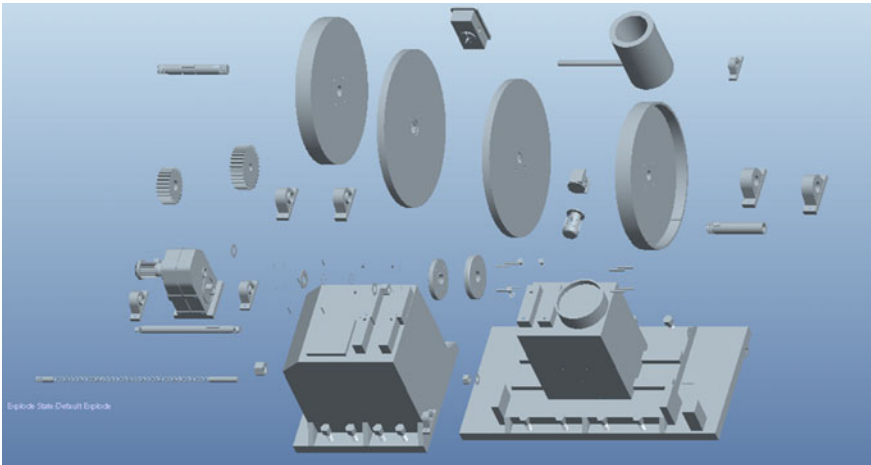


Fig. 10 Exploded view of assembly of centrifugal casting equipment

actuator justifies for small size and capacity of machine with PLC (Patel et al. 2015). The use of image processing (Sheth et al. 2010) in context of material type and temperature (Chauhan et al. 2011) may lead to the automation and GUI for the system.

Acknowledgments The authors wish to thank all the staff members of Amin Machinery Pvt. Ltd. A great thanks is extended to Mr. Vinay Makwana for his consistent and valuable support for providing all the information required regarding this Special Purpose Machine

References

- Chauhan, V., Sheth, S., Hindocha, B. R., Shah, R., Dudhat, P., & Jani, P. (2011). Design and development of a machine vision system for part color detection and sorting. In *Proceedings of Second International Conference on Signals, Systems & Automation (ICSSA)* (pp. 90–93). doi:[10.13140/2.1.1628.7526](https://doi.org/10.13140/2.1.1628.7526).
- Desai, S. H. (2012). *Design of centrifugal casting machine for manufacturing of turbine bearing*. M.E. Thesis, Birla Vishvakarma Mahavidhyalaya, Vallabh Vidhyanagar, Anand, Gujarat, India.
- Desai, S. H., & Sheth, S. M. (2012). Proposed design of centrifugal casting machine for manufacturing of turbine bearing. In *National Conference on Advances and Challenges in Engineering and Science (NCACES-2012)*. doi:[10.13140/RG.2.1.4529.2645](https://doi.org/10.13140/RG.2.1.4529.2645).
- Desai, S. H., & Sheth, S. M. (2015). Study and proposed design of centrifugal casting machine for manufacturing of turbine bearing. In *International Conference on Mechanical, Material, Industrial, Automotive, Aeronautical and Nano Technology (MIANT-2015)* (pp. 34–37). doi:[10.13140/RG.2.1.2503.0566](https://doi.org/10.13140/RG.2.1.2503.0566).
- elecon.com. 'Elecon Super Series in worm gear unit's catalogue', Web. 24 April 2012.
- Gajjar, B. R., & Sheth, S. (2014a). Design and automation in back plug press fitting process of ball pen assembly. *Applied Mechanics and Materials*, 592, 2596–2600.
- Gajjar, B. R., & Sheth, S. (2014b). Investigation of automation strategy and its effect on assembly cost: A case study on ball pen assembly line. *International Journal of Current Engineering and Technology, Special Issue-3*, 89–92.
- Gangadia, H., Sheth, S., & Chauhan, P. (2014). Design & modelling of special purpose equipment for shell-diaphragm welding in conveyor pulley. *Procedia Technology*, 14, 497–504.
- Kalne, P. M., & Borkar, N. B. (2014). Design for automated locking arrangement of centrifugal casting machine using CAD and FEM. *International Journal of Mechanical Engineering and Robotic Research*, 3(2), 498–504.
- Oyewole, A., & Sunday, A. M. (2011). Design and fabrication of a centrifugal casting machine. *International Journal of Engineering Science and Technology*, 3, 8204–8210.
- Patel, T., Sheth, S., & Patel, P. (2015). Design of semi-automatic hydraulic blanking machine using PLC. In *National Conference on Innovative & Emerging Technologies (NCIET-2015)* (pp. 410–412). doi:[10.13140/RG.2.1.4529.6803](https://doi.org/10.13140/RG.2.1.4529.6803).
- Pbl.co.in. 'Series F', Web. 15 November 2011.
- Seabra, E., Barbosa, J., & Puga, H. (2009). Design and development of a centrifugal casting machine for pistons production. In *XIII Congreso Internacional De Ingeniería De Proyectos* (pp. 1564–1571).
- Sheth, S., Kher, R., Shah, R., Dudhat, P., & Jani, P. (2010). Automatic sorting system using machine vision. *Multi-Disciplinary International Symposium on Control, Automation & Robotics*. doi:[10.13140/2.1.1432.1448](https://doi.org/10.13140/2.1.1432.1448).
- Skf.com. 'Tapered Roller Bearings, Single Row', Web. 21 February 2012.

Design and Control of Tendon Driven Robotic Hand for Prosthesis Applications

Roshan Kumar Hota, Arvind Ahirwar and Cheruvu Shiv Kumar

Abstract The paper reports the development of an underactuated tendon driven prosthetic hand. The cost of commercially available prosthetic hands is prohibitive for developing countries. There is need for indigenous low cost design and manufacturing. The computer model of the hand is prepared in SolidWorks™ and manufactured using 3D printing technology in ABS plastic material. Five servo motors are used to actuate the hand and the hand is controlled using a MATLAB® interface. The MATLAB interface shows the hand movements in simulation and the same motion is imparted to the robotic hand by actuating the motors.

Keywords Underactuated · Prosthetic hand · 3D printing

1 Introduction

Around 23,500 amputees get added to the population of India every year (Meanly 1995). They face problems from awkward cosmetic appearance to limited functional abilities. Robotic prosthesis have come a long way to alleviate some of these problems. Their cost, however, is still prohibitive for most individuals in a developing country like India. The notable commercially available prosthetic hands are: the Vincent Hand, iLimb Hand, iLimb Pulse, Bebionic hand (Belter et al. 2013), and Michelangelo hand. A review of these hands is done by Belter et al. (2013). The major focus of these hands is giving maximum functionality to the user while reducing the weight and operation complexity of the robotic hand. There are other secondary performance criteria increasing battery life, increasing grip force and having adequate flexion speed. All of these hands use linkage driven fingers. The linkage driven fingers are bulky and yield a fixed relation of the movement of different joints of the finger. Most of these hands have one actuator per finger.

R.K. Hota (✉) · A. Ahirwar · C.S. Kumar
Indian Institute of Technology, Kharagpur, India
e-mail: roshan1182.iitkgp@gmail.com

© Springer India 2016

D.K. Mandal and C.S. Syan (eds.), *CAD/CAM, Robotics and Factories of the Future*, Lecture Notes in Mechanical Engineering,
DOI 10.1007/978-81-322-2740-3_52

535

Circumduction of the thumb is manually set in iLimb as well as the Bebionic hand. They use DC motors with high gear reduction. Packaging is another challenge in making these hands.

Average human hand weighs around 400 g (Chandler et al. 1975). However, prosthetic should have even lesser weight because the prosthesis is worn over the soft tissues as opposed to the natural hand attached to the bones. Cosmetic appearance of the robotic hand is very important to be used as a prosthetic. Therefore the size of the fingers is chosen to be close to that of human hand. Prosthetic hands can be myoelectric devices, body powered devices or simple cosmetic devices.

Human hand is a miracle by nature. Mimicking abilities of a human hand in grasping and manipulation is a formidable challenge for researchers. Emulating the human hand in appearance as well as motion has been a long standing goal. Postural synergy is an important characteristic that researchers are trying to mimic. Postural synergy implies that human grasping poses happen in certain co-ordinated manner. Brown and Asada (2007), for example, have implemented the human hand postural synergies obtained by principal component analysis by mechanical means. Taking synergy into consideration reduces the control complexity as well as the number of actuators.

There are many challenges in developing the robotic prosthetics, important ones being compact design, ease of operation and less weight. Myoelectric devices are those operated by signals from the residual muscles of the amputees. Other kind of hands with electric actuators can be operated by a different interface that can be, for example, push buttons for doing grasping operations. We have tried to address these challenges in the hand that we have made.

2 Mechanical Design and Manufacture of the Robot Hand for Upper Limb Prosthesis

Open source design has been used for the prosthetic hand. The hand was chosen because it met our criteria for candidate prosthetic hand design viz: the hand should have five fingers, it should have an opposable thumb, it should have anthropomorphic dimensions. The hand has 17 degrees of freedom. The design is made in Solid Works® and manufactured using a 3D printer at the Direct Digital Manufacturing Lab, IIT Kharagpur. Each component of the hand is printed separately and then assembled using mechanical fasteners. The material used for the hand is ABS plastic, which is a very hard variety of plastic. Each finger in the hand is controlled by a single actuator, so there are five actuators in total. This is an underactuated design where we have lesser number of actuators than the degrees of freedom. This implies that the position of the three links in the finger is not independently controlled. The position is governed by contact with the target object. Figure 1 shows the Solid Works model of the robotic hand.

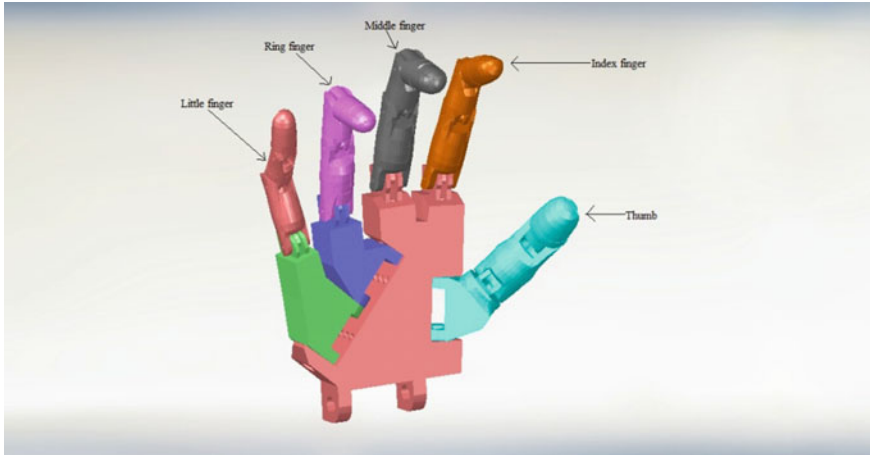


Fig. 1 Solid works model of the prosthetic hand

The dimensions are taken such that the hand is slightly bigger than an adult human hand. The actuators used are brushed DC motors from Dynamixel-AX 12A servos, these have integrated controller and are low-cost and low-weight servos. The transmission is done through cables (tendon). Tendon transmission is lighter than the linkage transmission and is closer to the muscle actuation used by nature. We have used the cables of a badminton racket as the tendon. Internal slots have been provided in the hand for the cable routing. Each finger has three phalanges, except the thumb that has two phalanges. In addition to that the little finger, ring finger and the thumb have an additional joint which is placed at the palm at an angle to other joints. These additional joints allow the hand to make an enveloping grasp. The position and orientation of the third joint of the thumb is very important. Thumb acts as the opposing finger which is very crucial for a grasp to happen. The orientation of the third joint allows the thumb to be opposable to index, middle and ring fingers. Two sets of tendons run through the finger: one for flexion and the other for extension. The flexion and extension motion of the finger is affected by opposite rotation of the motor. The flexion tendons run above the bolt used to fix the joint so that it can produce a flexion torque and the extension tendon runs below the joint bolt so that it can produce an extension torque. Both the flexor and extensor tendons are tied to the distal phalange of the finger. The tendons are routed internally through the palm and emerge at the wrist; they are then attached to different motors for each finger. A pair of tendon is tied to the motor shaft in such a way that one of them is extended and the other loosened for a particular rotation of the motor shaft.

The motors are arranged along the forearm in a line. The motors are facing in opposite directions so that tendons from the fingers are not all at the same place and interfering with each other. The 3D printed and assembled hand along with the motors is shown in the Fig. 2.

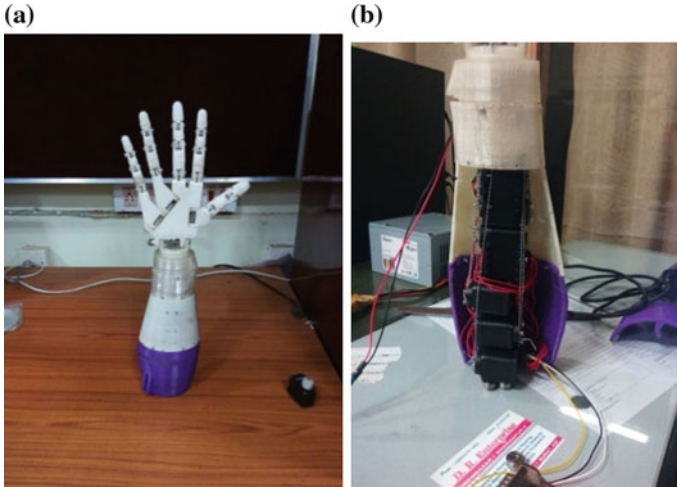


Fig. 2 **a** Robotic hand fully assembled. **b** View showing the motor arrangement in the forearm

Dynamixel AX-12A servos (shown in Fig. 2b) are high torque servos; they are placed in the region of the forearm. In the present work our goal is to test the functioning of the hand, so we have not focused on a compact actuation. In future design we would use actuators that will take up lesser space and can be placed in a smaller region so there is space to be attached to the hand of the amputee. The design of the hand chosen can nicely perform power grasp but is not very good at pinch grasps.

3 MATLAB Simulation and Hardware Control Interface

We have developed a MATLAB simulation and hardware control interface. Figure 4a shows the setup for control of the hand using MATLAB. The Dynamixel motors are controlled using a USB2dynamixel device. This converts message sent from a program in the computer to the USB port into a TTL signal that is used by the dynamixel motors. Dynamixel motors are high torque servo motors, they are networked to each other in a daisy chain fashion. Each dynamixel motor has a unique id by which it can be communicated. Dynamixel motor can be commanded by angle or by speed. Along with the command for the angular position or the angular speed the motor id information is also sent, the specified motor only executes the command for motion. The command for motion is sent using MATLAB. We have also developed a Graphical User Interface (GUI) in MATLAB for controlling the hand. Flow-chart for control of the prosthetic hand and the simulation is shown in Fig. 6. The GUI has the following features (snapshot of the GUI is shown in Fig. 3):

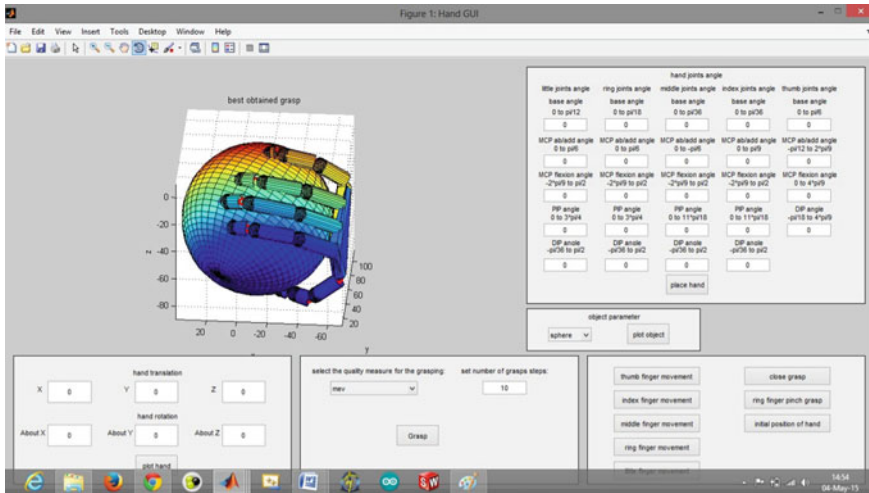


Fig. 3 Snapshot of the GUI created for controlling the hand

- a. On the left side there is a graphical representation of the hand.
- b. The right top panel lets us give the joint angles for individual joints. The resultant configuration is shown in the graphical representation.
- c. Right bottom panel gives options for different grasps. It provides the following buttons: thumb movement, index finger movement, middle finger movement, ring finger movement, closed fingers grasp, ring finger pinch grasp and initial position of the hand. Pressing these buttons makes the hand do the corresponding grasps in hardware.
- d. When the button for a particular grasp is pressed the information is sent to a MATLAB program that decides the combination of motors that has to be activated. The extent of motion of the motors for flexing the fingers has been determined by a trial method. The program conveys the message for movement along with the motor ids through the USB port. Figure 4b shows one such motion.
- e. For getting the motion in the hardware hand the command for angular motion of the finger joints are converted into angular motion of the actuating motor using an internal mathematical representation of the tendon transmission.
- f. The bottom middle panel lets us select a grasp quality measure that we want to apply for grasping the object. The grasp is computed using the SynGrasp toolbox in MATLAB.

The forward kinematics of the simulated hand (Fig. 3, left panel) is specified using the DH convention (Spong et al. 2006). A frame is attached to each phalange of the finger. When the user inputs the value of the angles in the GUI interface, the forward kinematics is calculated using the transformation matrices created with the help of the DH parameters and the same is plotted in the simulation. As an example,

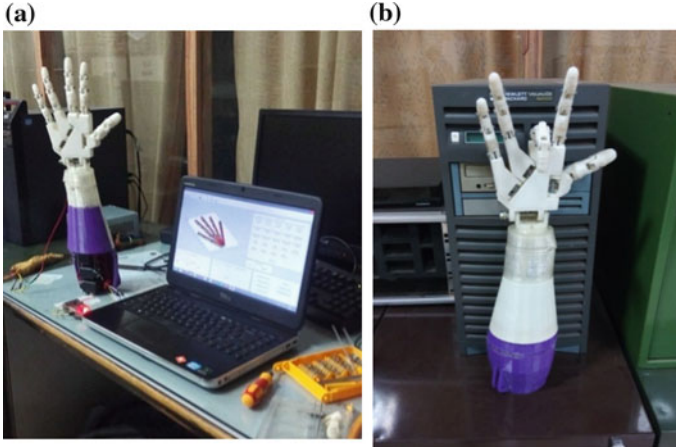


Fig. 4 **a** Setup of the hand for MATLAB control. **b** The action of the hand when the button for middle finger movement is pressed

we have shown below the transformation matrix corresponding to frames of two consecutive links in a manipulator specified by their DH parameters:

$$T_{i-1}^i = \begin{bmatrix} \cos \theta & -\cos \alpha \sin \theta & \sin \theta \sin \alpha & L_i \cos \theta \\ \sin \theta & \cos \alpha \cos \theta & -\sin \alpha \sin \theta & L_i \sin \theta \\ 0 & \sin \alpha & \cos \alpha & 1 \\ 0 & 0 & 0 & 1 \end{bmatrix} \quad (1)$$

where the DH parameters are as described below:

i Joint Number

T Homogeneous transformation matrix at a particular joint

θ Joint angle

α Link twist angle

L_i Length of the i th link

The hand manufactured satisfactorily performs power grasps, the finger-tip trajectories in flexion is shown in Fig. 5.

The diagram above shows the trajectory of the finger tips in the flexion motion. The trajectory has been calculated using a speed ratio of 2:1:1 between the proximal, middle and distal joints respectively. The trajectory in blue color shows the motion of the index finger tip in flexion, green- middle fingertip, black-ring fingertip, red-little fingertip (Fig. 6).

The diagram below shows the concurrent simulation and hardware control architecture that we have developed for the robotic hand. The user input is fed into the GUI which shows the result of the motion in simulation as well as affects the same motion in hardware.

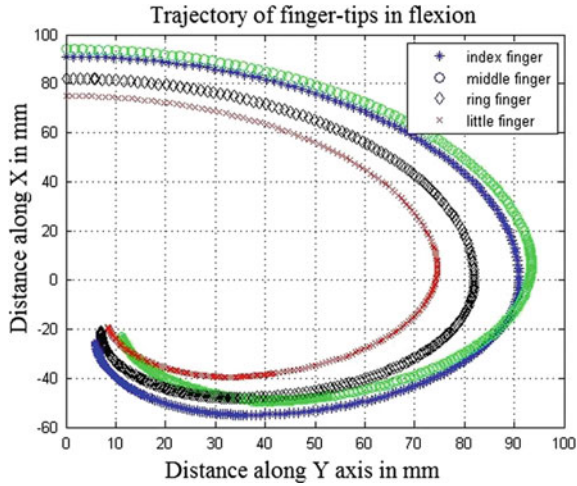


Fig. 5 Finger-tip trajectory in the flexion movement

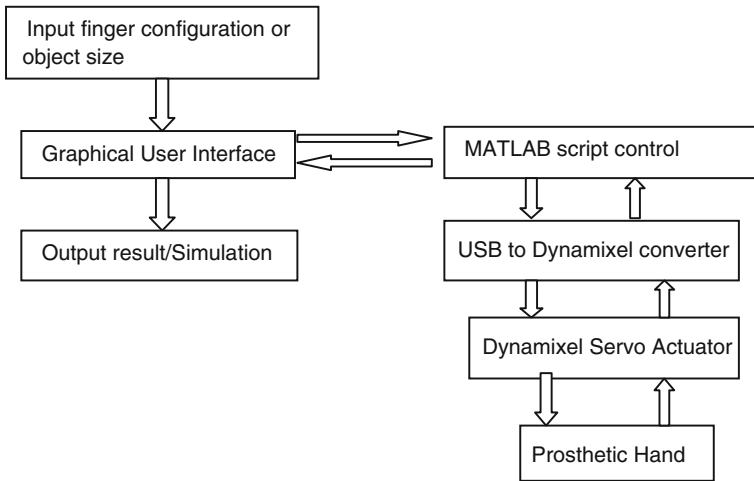


Fig. 6 Schematic for MATLAB interfaced control of the prosthetic hand

The grasp shown in Fig. 3 has been generated using the SynGrasp toolbox (Malvezzi et al. 2013) in MATLAB. SynGrasp is a tool which allows us to model robot as well as human hands. Coupling between joints in an underactuated scenario can be modeled, as is the case in our hand design also. Important grasp properties like manipulability analysis and grasp quality measures can be obtained from the toolbox. The hand kinematics is described using DH parameters. A grasp

is specified by contact type Grasp and Jacobian matrices. It can provide a simple graphical representation of the hand. Features like inter-finger synergy can be coded using MATLAB. Thus the GUI can be used for analysis of different hand designs.

4 Conclusion

The present work is a part of ongoing work towards development of a compact low-cost robotic hand as a prosthetic device. The initial design of the hand presented in this work illustrates the utility of 3D printing technology in prototype as well as final product development. The viability of various design decisions have been tested such as the use of tendon transmission and the position of the thumb. The MATLAB GUI interface developed is very useful in operating the hand in different modes. It provides an interface with the SynGrasp tool in MATLAB that allows analysis of the hand according to manipulability and different grasp quality measures. The MATLAB interface can also be adapted to interface the hand for online myoelectric signal. In the future the design of the hand will be made more compact.

References

- Belter, J. T., Segil, J. L., Dollar, A. M., & Weir, R. F. (2013). Mechanical design and performance specifications of anthropomorphic prosthetic hands: A review. *JRDD*, 50(5), 599–618.
- Brown, C. Y., & Asada, H. H. (2007). Inter-finger co-ordination and postural synergies in robot hands via mechanical implementation of principal component analysis. In *IEEE/RSJ International Conference on Intelligent Robots and Systems* (pp. 2877–2882).
- Chandler, R. F., Clauser, D. E., McConville, J. T., Reynolds, H. M. & Young, J. W. (1975). Investigation of inertial properties of the human hand. Washington (DC): U.S. Department of Transportation; Report No. DOT HS-801 430.
- Dynamixel AX 12A e-Manual. http://support.robotis.com/en/product/dynamixel/ax_series/dxl_ax_actuator.htm.
- Malvezzi, M., Gioioso, G., Salvietti, G., Prattichizzo, D. & Bicchi, A. (2013). SynGrasp: Analysis of human and robotic hands. In *Proceedings of the IEEE International Conference on Robotics and Automation* (pp. 1088–1093), May 2013.
- Meanly, S. (1995). Different Approaches and Considerations in Third World Prosthetics. *Prosthetics and Orthotics International*, 19(3), 176–180, December 1995.
- Spong, M., Hutchinson, S., & Vidyasagar, M. (2006). *Robot modeling and control*. New York: Wiley.

Stabilization of Posture of Humanoid Using PID Controller in Gazebo Simulator Using Robot Operating System (ROS)

V. Madhu Babu, G.V.V. Surya Kiran, S.K. Sameer,
Roshan Kumar Hota and Cheruvu Shiv Kumar

Abstract This paper presents an ongoing work for developing a simulation setup for testing gait algorithm for a humanoid robot. An open source simulator GAZEBO has been chosen for easy adoption by researchers. A model of humanoid robot has been built in Gazebo. A PID controller has been implemented using Ziegler Nichols tuning technique on the humanoid model for stabilizing the posture on the behalf of implementation of Reinforcement Learning based gait algorithm. The PID controller is written in Robot Operating System (ROS) and has been interfaced with the GAZEBO simulator.

Keywords PID controller · Robot operating system · Gazebo · Reinforcement learning · Zeigler-Nicholas PID tuning

1 Introduction

Humanoid robots (Anthropomorphic Robot) are different robots as compared to the industrial and service robots. A humanoid robot can be the design of a specific body part to even an imitation of the total human beings' mechanics (bio-mechanics) and should consist of similar Degrees of Freedom like human beings. Many researchers have built humanoid robots such as ASIMO (Hirai et al. 1998), TULIP, ATLAS, NAO, PETMAN etc. But these robots are now not a part of our society because they lack human like mobility. Human walking is periodic cycle of a stable phase (double standing phase) and with alternative unstable phases (single leg swing

V. Madhu Babu (✉)
RGUKT, R.K. Valley, Nuzvid, India
e-mail: accesstomadhu@gmail.com

G.V.V. Surya Kiran · S.K. Sameer
RGUKT, Nuzvid, India

R.K. Hota · C.S. Kumar
Indian Institute of Technology, Kharagpur, India

phase). In order to make the robot stable (not falling) we adopt the reinforcement learning process (Sutton and Barto 1998). With this reinforcement learning procedure the robot will have an optimal set of actions to make it stable while executing the gait (Hwang et al. 2013). The joint positions of gait were generated through Inverse Kinematics in Mat lab. These gait angles will make the model to access an instant dynamic posture while accessing the gait. For the successful application of the gait we need to stabilize that posture at the respective angle at that instant. But due to nonlinearities present in the linkage the link was not able to settle the desired position (Craig 2005). To solve this we decided to apply a PID controller to make the posture stable. In order to apply this PID controller we built a model of humanoid with 18 DOF was created in a simulator, GAZEBO. We adopt for Gazebo as our simulation tool and ROS as a platform to control the simulation.

Gazebo has the ability to accurately and efficiently simulate robots in complex indoor and outdoor environments. GAZEBO is a platform with robust physics engine, high quality graphics and convenient programmatic and graphical interfaces. To work with this a file in XML format with all physical parameters included and should be formatted as SDF or URDF. Gazebo facilitates good graphical visualization by importing the cad models and also it has the possibility to add up sensors by importing sensors.

To control this simulation (model) we adopt Robot Operating System (ROS) as programming platform. ROS is fixed frame work for building robot software. It is very hard for an individual to build complete robot software. For example in a laboratory someone might have an expert in computer vision, and could contribute a very good object detector. Somewhere else, someone is working on a drone which needs a object detector to stabilize on its own. ROS was designed for the people like above to collaborate and to work upon each other's work. Like the same by developing this PID controller in ROS, people who are in need of a controller which works with GAZEBO they can use this algorithm to develop their own robot. Along with all these ROS provides standard operating system facilities such as hardware abstraction, low level device control, implementation of commonly used functionalities, message passing between processes and package management. Best of all, GAZEBO and ROS both are free with a vibrant community.

A Proportional-Integral-Derivative controller (PID controller) is a control loop feedback mechanism (controller) is most commonly used in industrial applications. A PID controller will calculate an error value as the difference between reference value (set value) and the present value. The controller will minimize the error by adjusting the process through control variables such as joint effort, joint angle etc. The PID controller algorithm involves three separate constant parameters, and it also sometimes called as three-term control: the proportional, the integral and derivative values, denoted P, I, and D. This PID controller is time based controller. P depends on the present error, I on the accumulation of past errors, and D is a prediction of future errors, based on current rate of change. The weighted sum of these three actions is used to adjust the process via control elements; here in this case it is Joint Effort.

$$u(t) = K_p e(t) + K_i \int_0^t e(\tau) d\tau + K_d \frac{d}{dt} e(t) \quad (1)$$

General equation for PID control is, shown above where in that K_p is the Proportional gain, K_i is the Integral gain and K_d is the Derivative gain all the three are tuning parameters and the others, τ is time or instantaneous time (at present) and $e(t)$ is error that is the difference between the desired value and the present measured output.

Here the proposed algorithm of PID Controller development for our case:

```

previous_error = 0
integral = 0
start:
    error = reference_theata-current_joint_position
    integral = integral + error*dt
    derivative = (error - previous_error)/dt
    output = Kp*error + Ki*integral + Kd*derivative - non_linearity
    previous_error = error
    wait (dt)
    go to start

```

In this above algorithm the most difficult part is finding the PID constants K_p , K_i , K_d . We adopt the Ziegler-Nichols Method for PID tuning (www.engr.mun.ca/~nick/eng5951/Ziegler_Nichols.pdf).

2 Methodology Adopted

Ziegler-Nichols' method for tuning is heuristic method to tune the PID controller. Ziegler and Nichols proposed general rules for determining the values of proportional constant K_p and integral time T_i , and derivative time T_d based upon the transient characteristics of the given system (Ziegler and Nichols 1942; www.engr.mun.ca/~nick/eng5951/Ziegler_Nichols.pdf). There are two methods known as closed loop method and open loop method. In this paper Z-N' open loop method is described. The Ziegler-Nichols' open loop method is based on the process of step response (http://home.hit.no/~hansha/documents/control/theory/zn_open_loop_method.pdf). This step response is applied on uncontrolled process and there is no feedback taking (open loop). To apply this step response we calculated the transfer function of the model (We assumed each and every link of the model as an inverted pendulum and the effect of other links will be eliminated as error term while applying the PID controller).

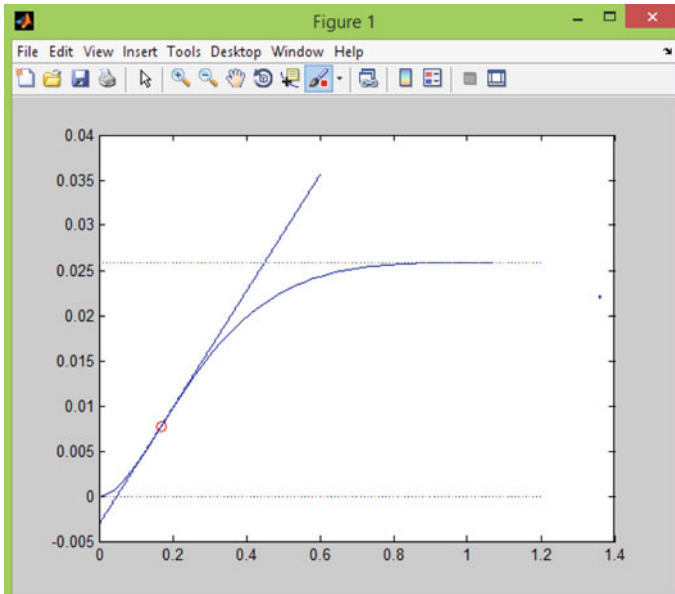


Fig. 1 S-Shaped curve with tangent at point of inflection

To get transfer function we need to get the equation of motion of a pendulum and then apply Laplace on both side and get the transfer function.

$$ml^2\ddot{\theta} + B\dot{\theta} + mgl\sin\theta = \tau \tag{2}$$

$$ml^2s^2\theta(s) + Bs\theta(s) + mgl\theta(s) = \tau(s) \tag{3}$$

$$G(s) = \frac{\theta(s)}{\tau(s)} = \frac{1}{s^2 + as + b} \tag{4}$$

where in Eqs. 2, 3, and 4 the m (0.32 kg) is mass of the link, B (0.234 N s/m) is the damping coefficient, l (0.259 m) is the length of the link and θ is the angle with respective to the vertical axis. For the large angle changes we considered $\sin \theta$ as 1 where both a, b are the constants equal to $\frac{B}{ml^2}, \frac{g}{l}$ respectively. After application of unit step response to the above transfer function, the output curve will be looking like S shaped as shown Fig. 1. This S shaped curve will be characterized into constants; those are delay time L , and time constant T . These constants will be known by drawing a tangent to the S shaped curve at the point of inflection. Then determine the determine the intersections of the line with time axis and the $f(t) = K$ (K is constant).

From the constants of L (dead time) and T constants, as per the Ziegler-Nichols rule based on step response plant the tuning constants will be

PID controller	$K_p = 1.2 \frac{T}{L}$	$T_i = 2L$	$T_d = 0.5L$
----------------	-------------------------	------------	--------------

Through the above Ziegler-Nichols formulations we calculated the constants K_p as 9.6, T_i as 100s, T_d as 25s. After calculation of K_p , T_i , T_d we can easily calculate K_i and K_d terms. The PID controller equation with T_i and T_d is show in 6.

$$C(s) = K_p + \frac{K_i}{s} + kds \tag{5}$$

$$= K_p \left(1 + \frac{1}{T_i s} + T_d s \right) \tag{6}$$

T_i : Reset Time = K_p/K_i and T_d : Rate time or Derivative time

PID controller is mainly applicable to linear systems but in reality many systems that we will deal with are nonlinear systems (Khalil 1996), many disturbances will be acting and those will make the system nonlinear. In order to apply PID first we have to convert any nonlinear system into a linear system (John 2005). This can be done by following the steps below

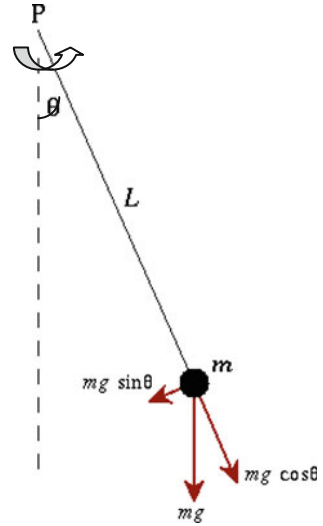
- (1) Compute a nonlinear model-based control law that will “cancel” the nonlinearities of the system to be controlled.
- (2) Reduce the system to a linear system that can be controlled with a simple linear servo law developed for the unit mass.

In the Fig. 2, the non-linearity present is due to weight of the link. Due to gravitational acceleration there will be force equal to weight of the body acting at the centroid of the link. Due to this force there will be torque generation at the joint that will tend to move the link downwards. To make the system linear we need to cancel that nonlinearity with adding the same opposite torque with reverse direction as the external one. So that nonlinear quantity and the applied one will cancel each other. Then the system is linear and it is ready for applying PID controller algorithm.

$$\tau = K_p e(t) + K_i \int_0^t e(\tau) d\tau + K_d \frac{d}{dt} e(t) - m.g. \frac{1}{2} \cdot \cos \theta \tag{7}$$

So the final equation becomes like the above where τ is the joint effort that we are going to apply, m is the mass of the link, g is the gravity (i.e. 9.81 m/s²), l is the length of the link and θ is the angle made by the link w.r.t ground.

Fig. 2 Pendulum physics



3 Experiment/Test Conducted

We had implemented the code for the above methodology with using ROS Services and Clients with GAZEBO messages. In the simulation model, it introduces the establishment of simulation environment and a humanoid robot. The GAZEBO world simulates the real world physics in real time. On humanoid robot, we used a 16 DOF humanoid model as our simulated robot as shown in Fig. 3.

The developed algorithm of PID for stabilizing given posture on the model with using ROS and gazebo will flow like below

```

Main
Initialize the clients for ROS clients
Initialize services from gazebo messages
Initialize the desired posture angles
Start:
Initialize the joint name to get the joint properties by calling service through client
Calculate the torque by the above proposed PID algorithm
Clear the previous joint effort on the joint
Apply the new calculated torque by calling the above services through clients.
Go to start

```

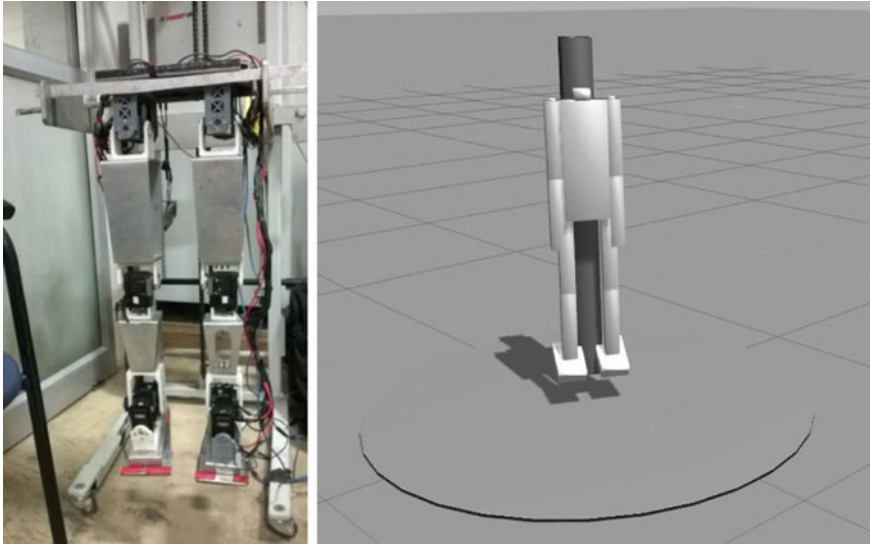


Fig. 3 Real time and GAZEBO models of Biped Robot

4 Results and Discussion

A PID Controller was developed by above algorithm with the described methodology and the tuning parameters were calculated using Ziegler-Nichols' method (Ziegler and Nichols 1942). While applying this controller, the model was showing a large over shoot in a small interval of time and then it is stabilizing at the commanded position as like shown in Fig. 4. This is not required because with this much jerk the model might fall. This happened because of high derivative constant K_d . However this Z-N approach is giving a very precise tuning constants K_p and K_i and after approximation of K_d the model accessing its commanded position with small vibrations (over shootings) that is present curve is much smoother than the previous shown in Fig. 5.

We say that we got values of constants from Z-N method but they were gotten for damping constant of 0.2 whereas we have to apply a damping constant of 5. This is because the masses of the links that we have used in our simulation are quite small and a torque applied to it produces a large motion in it. Thus by the time the next sensor input is received and action (torque) taken, the link has already moved by a considerable angle. A large damping helps to prevent this situation.

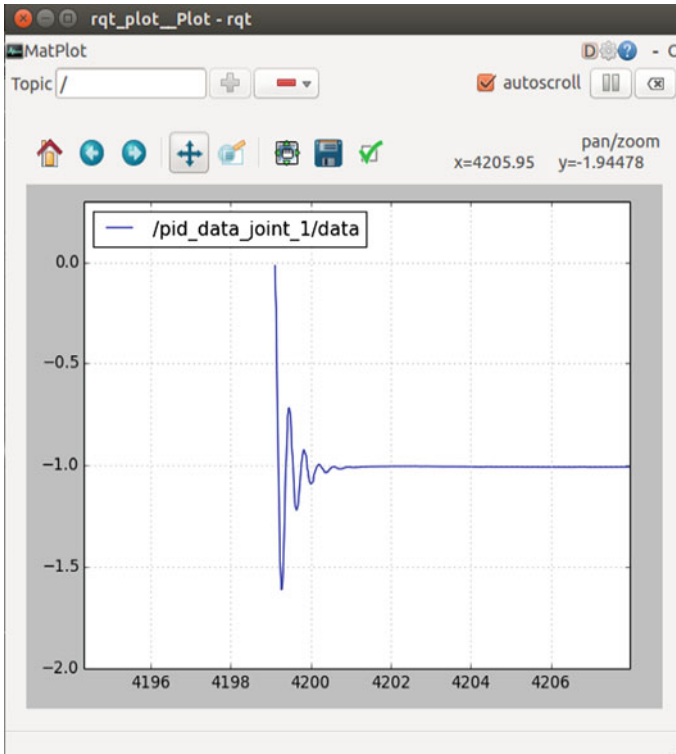


Fig. 4 Joint angle response with $K_d = 240$

5 Conclusion

In this paper the methodologies to calculate the tuning parameters and algorithm for PID controller is shown. In this paper the Z-N algorithm showing precise values of tuning parameters for the given transfer function using open-loop method. The calculated derivative constant term was approximated in order to make the system less vibratory while accessing the position. With this algorithm one can develop a PID controller for their model in Gazebo with ROS. Now we can apply this controller to the various joint (in the combination) of model in order to access a gait. Coming to the real time, the motors used for setup have their own PID controller as inbuilt. This PID controller, the above developed PID can be useful for one who wants to make his model simulate in GAZEBO.

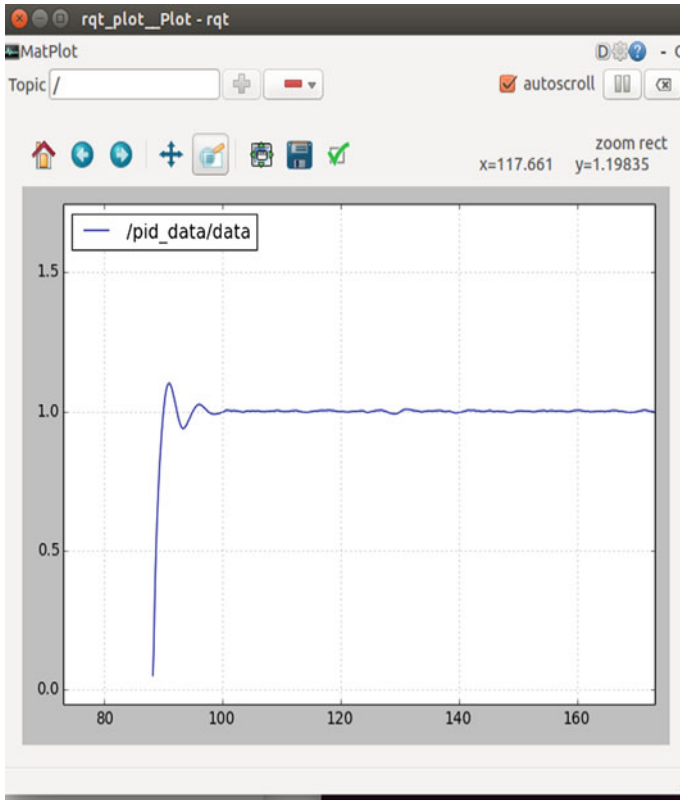


Fig. 5 Joint angle response with $K_d = 0.024$

6 Ongoing Work

After achieving posture stability, we will apply the Reinforcement Learning (Sutton and Barto 1998) in order to make the robot stable (not to fall) while executing the single leg swing phase (most unstable phase of human gait). We adopt for the Q learning process with look up table to make this out. For building the function $Q(s, a)$, for state space we are using the ZMP data of model and as an action space we are using array of angles which make the ZMP to move all over the foot polygon (Hwang et al. 2013). For getting ZMP (COP) data we fixed the pressure sensors below the model's foot by including pressure plugins in the simulator. We are following the Greedy policy as action policy to take care of stabilization of robot.

References

- Craig, J. J. (2005). *Introduction to robotics, mechanics and control* (3rd ed.). New Jersey: Prentice Hall.
- Haugen, F. Ziegler-Nichols' open loop method. Retrieved from http://home.hit.no/~hansha/documents/control/theory/zn_open_loop_method.pdf.
- Hirai, K., Hirose, M., & Takenaka, T. (1998). The development of honda humanoid robot. *IEEE International Conference on Robotics & Automation*, 2, 1321–1326.
- Hwang, K. S., Li, J. S., Jiang, W. C., & Wang, W. H. (2013). Gait balance of biped robot based on reinforcement learning. In *Proceedings of SICE Annual Conference SICE*, Japan, September 2013.
- Khalil, H. K. (1996). *Nonlinear systems* (2nd ed.). New York, NY: Macmillan Publishing Company.
- Sutton, R. S., & Barto, A. G. (1998). *Reinforcement learning: An introduction*. Cambridge, MA: MIT Press.
- Ziegler-Nichols' rules for tuning. Retrieved from www.engr.mun.ca/~nick/eng5951/Ziegler_Nichols.pdf.
- Ziegler, J. G., & Nichols, N. B. (1942). Optimum settings for automatic controllers. *Transactions on ASME*, 64, 759–768.

Robotic Picking of Cylindrical Fuel Pellets from a Boat Using 3D Range Sensor

Rahul Jain, Abhishek Jaju, Namita Singh, Sanjeev Sharma
and Prabir K. Pal

Abstract Fabrication of nuclear fuels comprises many intricate tasks that are difficult to automate. One such task is picking of cylindrical pellets from a container, called a boat. In the boat, pellets can be randomly oriented, touching and partly or wholly occluded. They have poor contrast with respect to each other and the boat. Hence, vision based techniques with either monocular or stereo camera configurations are not suitable for identification of pellet poses. This paper describes a novel technique in which 3D point cloud data is acquired by a 3D range sensor, and processed with optimized RANSAC (O-RANSAC) algorithm for estimating pellet poses for the robot to pick. First, cylinders are identified from point cloud data, and thereafter scores indicating the extent of matching is computed. We also present the improvement in processing time for O-RANSAC algorithm as compared to RANSAC. We demonstrate that O-RANSAC algorithm is robust even in presence of outliers and noise by testing in simulation with synthetic data. Proposed method was tested in an experimental setup consisting of an articulated robot, a 3D range sensor and dummy densely packed pellets in multilayer.

Keywords Bin picking · Robot · 3D point cloud · RANSAC

R. Jain · A. Jaju · N. Singh · S. Sharma (✉) · P.K. Pal
Division of Remote Handling and Robotic, Bhabha Atomic Research Centre,
Mumbai, India
e-mail: ssharma.drhr@gmail.com

R. Jain
e-mail: rahulj@barc.gov.in

A. Jaju
e-mail: ajaju@barc.gov.in

N. Singh
e-mail: namita@barc.gov.in

P.K. Pal
e-mail: pkpal@barc.gov.in

1 Introduction

Pose estimation of objects is an essential requirement for robotic bin picking applications. Until recently, poses were estimated by using cameras by processing 2D images. However, pose estimation by using camera images becomes challenging for densely packed featureless objects. Furthermore, occlusion along with ambiguous pose estimation for some views causes additional uncertainty in estimation of pose.

In order to overcome above challenges, sensors that can generate 3D point cloud with high resolution have been developed by the researchers, and are now commercially available. Thus, now main challenge is to develop robust algorithm for processing the 3D point cloud for estimating the poses accurately for reliable picking by robot. Furthermore, estimation shall be invariant to rigid body transformation, sensor noise and occlusion.

In this paper, we present a robotic bin-picking system that uses 3D point cloud data for detection of object poses. The system performs detection of 3D poses of cylindrical objects that are stacked in multiple layers in a part container, picks up the objects using an industrial robot, and place on rod trays for further processing. In order to achieve fast, reliable and accurate operation, imaging hardware that uses stereo cameras and structured light is used. Point cloud thus generated is processed by optimized RANSAC algorithm for faster pose estimation.

This paper is organized as follows. Related literature is briefly overviewed in Sect. 2. Robotic bin picking system is described in Sect. 3. Thereafter, in Sect. 4, we present pose estimation algorithm and its optimization. Experimental results and discussion are presented in Sect. 5. The paper is concluded in Section 6.

2 Related Work

Pose estimation methods can be generally classified as either segmentation or point clouds based. Segmentation based method generally fit the model to set of segmented points. Therefore, this method depends on the quality of segmentation which is affected by noise and outliers. In the second approach, data points are directly processed by using RANSAC, where a model is fit by using random sampling of minimum number of points.

In recent years, there has been considerable work on using 3D vision techniques for industrial bin picking problem (Pochyly et al. 2012). In order to detect multiple objects, key point detection along with RANSAC has been used (Hao-Yuan et al. 2014). A probabilistic approach for picking objects that do not fit into a shape primitive was proposed (Kensuke et al. 2013). Also, in order to get depth information, multi flash camera for estimating poses of objects was used (Ming-Yu et al. 2012). Further, pair features were used for detection of object poses for bin picking applications (Changhyun et al. 2012).

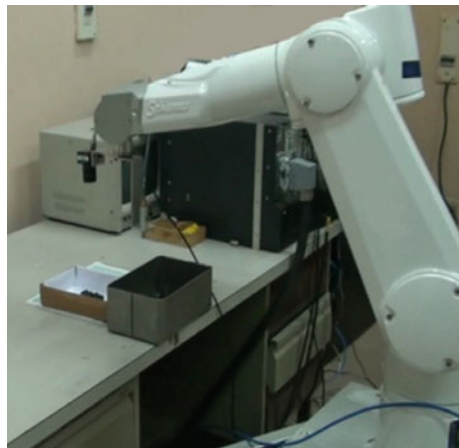
However, for our problem, pellets are feature less. Hence, techniques like key point or pair features are not suitable. Furthermore, probabilistic approach is not required as described objects fit into shape primitive. In the experimental setup, commercially available point cloud sensor is used instead of multi flash sensor as it provides robust high resolution depth data for accurate pose estimation.

3 Description of Bin Picking System

Figure 1 shows the setup of bin picking system. It uses a 6-axis industrial robot arm for picking the objects by using suction gripper. Here, pose estimation is performed by processing the 3D point cloud data generated by sensor mounted on robot arm.

In order to estimate 3d pose, it is essential to have depth data along with point location. Presently, many commercial sensors with such capability are available. However, for bin picking application with small objects it is desired to have sub millimeter resolution. In this paper, scanner from LMI Technologies with projection source and stereo scanning technology is used to acquire 3D point cloud data. This sensor is mounted on robot end effector for performing bin picking experiments. Figure 2 shows the 3D range sensor used for experimentation along with top and side view of a typical set of pellets arranged in multilayer. Here, distance of pellet from sensor is indicated by color. In this case, violet and green depict the nearest and farthest objects respectively from the sensor.

Fig. 1 Robotic system for picking randomly oriented texture less cylindrical objects in multiple layers



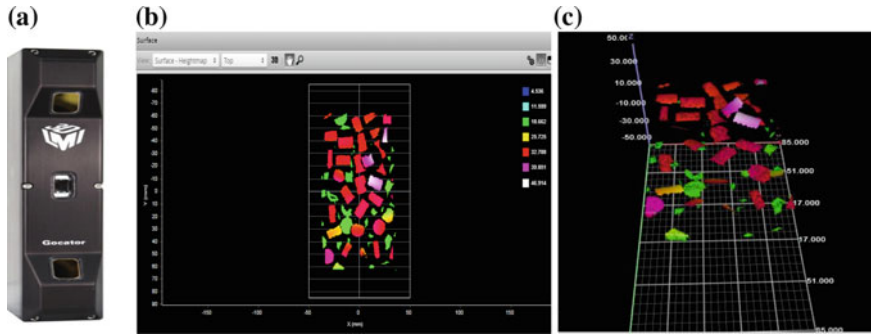


Fig. 2 **a** 3D point cloud sensor. **b** Top view of multilayer pellets displayed by sensor. **c** Side view of same pellet configuration violet color indicate pellet closer to sensor followed by red, yellow and green

4 Methodology for Pose Estimation

Point cloud generated by sensors needs to be processed for estimating the poses which is an essential requirement for a robust bin picking. In order to do this, these points are fitted into cylinder model. Among the various methods, RANSAC (Random Sample Consensus) algorithm (Martin and Robert 1981) is widely used for estimating model parameters from point clouds. Cylindrical pellet which is a small cylinder is described by a set of three parameters: axis orientation, a point on the axis and radius. Figure 3 shows the sequence of steps required for estimating the pose of cylinder from point cloud data.

4.1 Building Cylinder with Two Sample Points

In 3-dimensional space, a cylinder can be defined by orientation vector and radius. These parameters can be estimated from two points (p_1, p_2) from the cylindrical surface.

$$[p_1, p_2] \rightarrow [\bar{ax}, r] \tag{1}$$

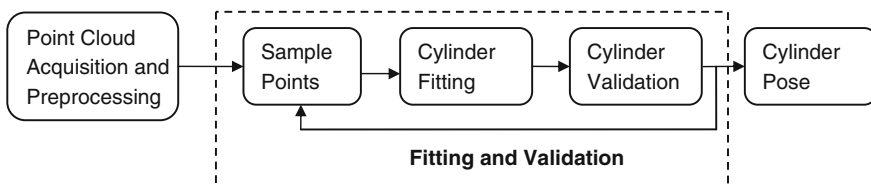


Fig. 3 Cylinder pose estimation for bin picking

One of the important steps in estimation of pose is computation of normal. For a point O on the surface, we can estimate normal as follows: find all the points inside a sphere of radius r centered at O , and then compute the least square plane fitting those points. The normal vector to fitting plane is our estimate of normal at O . After computation of normal, next step is finding the cross product of normal of two points. This gives the direction of cylinder axis (\vec{ax}). Once axis projection is known, the radius of the cylinder can be found as a distance from point to the axis.

4.2 RANSAC and O-RANSAC Algorithms

Input to the RANSAC and O-RANSAC algorithms are set of measurements, called point cloud. Proportion of these points will be consistent with a model with parameters from parameter space and are referred as inliers. Rests of the points are outliers. These algorithms also estimate the quality of estimated pose. The score is based on the number of points that lie within small band outside the cylinder. Out of these points only points whose normal do not deviate from the normal of shape are considered. Additionally, among the points that fulfill the previous two conditions, only those are considered that can constitute largest possible cylinder. Algorithm-1 outlines the steps of RANSAC algorithm for cylinder fitting.

Algorithm 1: RANSAC

1. Calculate the normal at the individual points in the cloud.
2. Pick 2 random points from the point cloud.
3. Use above points to fit a cylinder. If the radius is beyond the range, discard the cylinder. Calculate the score of the current cylinder, i.e., the no. of points that are consistent with the current cylinder. Call this as the score of that cylinder. Add this cylinder among the list of candidates.
4. Repeat 2 and 3 for the calculated number of iterations (using probability estimate).
5. Extract the best candidate which achieves the highest score.

In order to reduce the computational cost, O-RANSAC algorithm (Ruwen et al. 2007) is used. It is based on hierarchical structured sampling strategy which significantly reduces the sample size. Pseudo code for O-RANSAC algorithm for cylinder fitting is described in Algorithm 2.

Algorithm 2: O-RANSAC

1. Calculate the normal at the individual points in the cloud.
2. Subdivide 3d point cloud space into eight equal octants by using octree data structure.

3. Above cells are further partitioned into multiple levels using octree data structure thus creating a hierarchical data structure. Each node in the octree is referred as the cell. Initially the probability of a cell getting selected from each of the level is the same. This probability is then updated according to the scores obtained by the candidates chosen from a cell chosen from that level. The higher the score, the higher is the probability of a cell getting selected from that particular level (Ruwen et al. 2007).
4. Select 2 points from the selected cell to fit a cylinder. If this radius is more than the tolerance then discard the cylinder. Else, add this cylinder to the list of candidates.
5. Partition the point cloud into random subsets.
6. Calculate the score on the first subset instead of computing on the entire point cloud. Use induction (Ruwen et al. 2007) to extrapolate and get the score for the entire cloud. This is done to reduce the computations for score calculation.
7. Extract the best candidate which achieves the highest score among all and the points belonging to it.
8. Calculate probability that no undetected cylinder is larger than the current best candidate. If yes, extract the largest connected component for each candidate and recalculate size for each candidate. If no, then repeat 2 if max iterations have not been reached.
9. Extract the best candidate and the points belonging to it.

Described methods are iterative in nature. Therefore, these can produce a result only with certain probability. If $p(n)$ is probability of detecting the model in single pass from N points, and p_t is the desired probability of successful detection, then desired number of candidates (T) required to detect shape of size n can be given by following expression.

$$T \geq \ln(1 - p_t) / \ln(1 - p(n)) \quad (2)$$

Probability of detecting model $p(n)$ is more for O-RANSAC method.

5 Results and Discussion

In order to verify the accuracy of pose estimation, it is essential to measure the reference poses accurately. However, this is a complex task for densely packed pellets, as ensuring same orientation after measurement is complicated. Hence, initial verification is performed with synthetic data consisting of predefined pellet poses. Further, in order to test robustness of algorithm synthetic data is mixed with Gaussian noise.

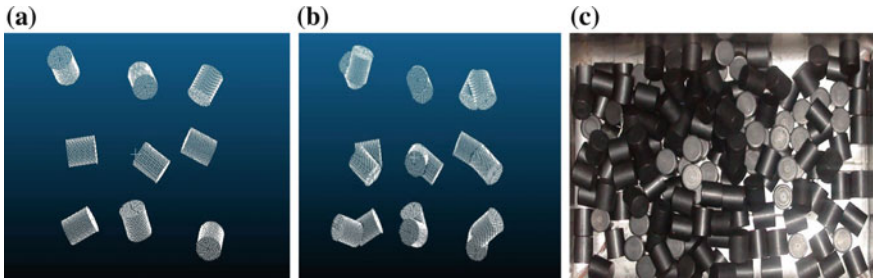


Fig. 4 **a** Single layer point cloud (synthetic data). **b** Multilayer point cloud (synthetic data). **c** Image from experimental setup

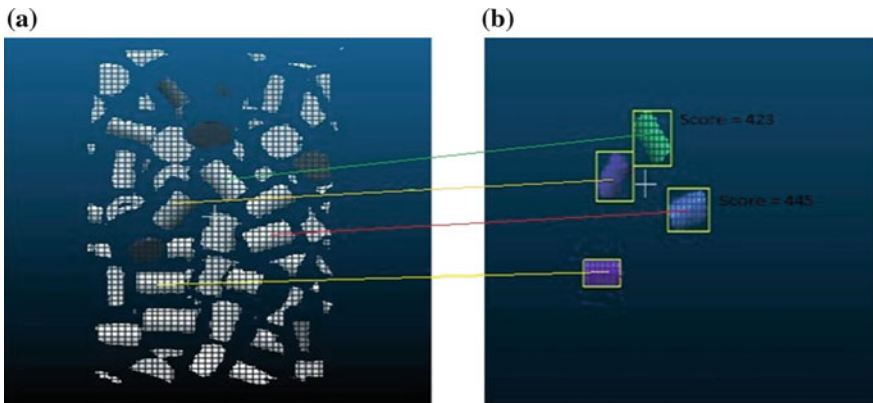


Fig. 5 **a** Sensor view of multilayer pellets. **b** Detection of pellets with score higher than threshold and pose estimation of cylinder from densely packed pellets in multiple layers

Figure 4 shows the point cloud data for single and multiple layers along with image of pellets from the experimental setup. In this paper, point clouds from multiple layers with different Gaussian noises are used for estimating the accuracy of poses. Figure 5 shows successful detection of pellets using O-RANSAC algorithm. In order to estimate the accuracy of radial and angular error, O-RANSAC algorithm, with different Gaussian noise, is applied on synthetic point cloud of multiple layers (Fig. 6). The results show reliable detection of cylindrical pellets even in the presence of outliers. Further use of localized sampling and revised score calculation strategy substantially improves the processing time (Fig. 7). Described algorithms are tested both in simulation and on experimental setup with variable sample length (14–18 mm) and fix radius. It is to be noted that performance of described algorithms is generally invariant to dimensional variance given the number of points in the point cloud remain same. However, time required for computation of connected components depends on the surface area of samples.

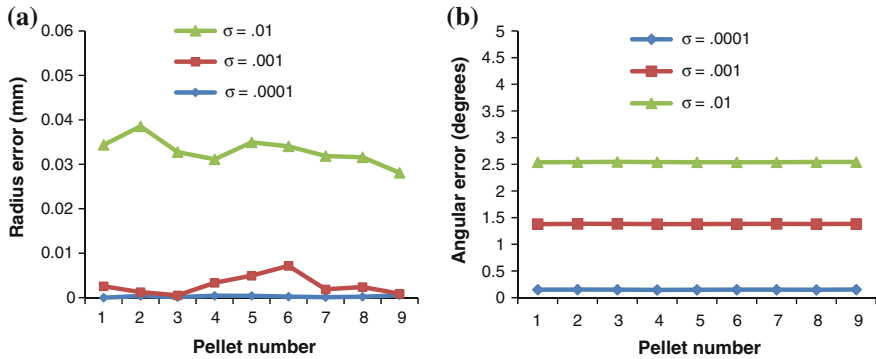


Fig. 6 Errors after estimation with O-RANSAC algorithm with synthetic data for multiple layers using different Gaussian noise. **a** Radius errors. **b** Angular errors

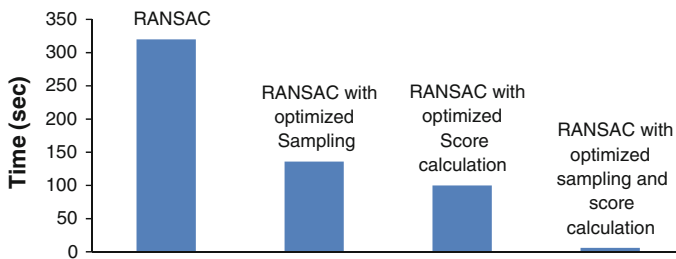


Fig. 7 Improvement of processing time with optimized sampling and score calculation using 18 cylinders from multilayer layer synthetic point cloud of Fig. 4. Nine cylinders of *top layer* along with few cylinders from lower layer were detected during 5 trials. Processing time presented here is average of time taken during these trials

6 Conclusion

In this paper pose estimation of cylinders from point cloud by using RANSAC and O-RANSAC algorithms has been presented. It is observed that RANSAC and O-RANSAC takes around 316 and 6 s respectively for processing of 1,00,000 points. Gaussian noises with different standard deviations are used for evaluating the accuracy of radius and orientation measurement. Simulation results with multiple layer pellets show that radial and angular error increases with increase in standard deviation of Gaussian noise. Maximum error of 0.04 mm in radius and 2.5° in angle is observed. Experimental results show success rate of around 80 %. Currently, we are investigating the robot and sensor calibration errors for more promising results. In addition, it is proposed to apply refitting on the estimated model for further improving the accuracy of robotic bin picking.

References

- Changhyun, C., et al. (2012). Voting based pose estimation for robotic assembly using a 3D sensor. In *IEEE International Conference on Robotic and Automation (ICRA)*, Minnesota, USA.
- Hao-Yuan, K., et al. (2014). 3D object detection and pose estimation from depth image for robotic bin picking. In *IEEE International Conference Automation Science and Engineering (CASE)*. Taipei, Taiwan, August 18–22.
- Kensuke, H., et al. (2013). Probabilistic approach for object bin-picking approximated by cylinders. In *IEEE International Conference on Robotic and Automation (ICRA)*, Karlsruhe, Germany, May 6–10.
- Ming-Yu, L., et al. (2012). Fast object localization and pose estimation in heavy clutter for robotic bin picking. *The International Journal of Robotic Research*, 31(8), 951–973.
- Martin, A., & Robert, C. B. (1981). Random sample consensus: A paradigm for model fitting with applications to image analysis and automated cartography. *Communications of the ACM*, 24(6), 381–395.
- Pochyly, A., et al. (2012). 3D vision systems for industrial bin-picking applications. In *15th International Symposium on Mechatronica*, Prague, December 5–7.
- Ruwen, S., et al. (2007). Efficient RANSAC for point cloud shape detection. *Computer Graphics Forum*, 26(2), 214–226.

Swachh-Bharat Bot: A Sweeping Robot

Swapnil Jugal and Kamal Sharma

Abstract The Swachh Bharat Mission was launched by the Government of India on 2nd October, 2014 aiming towards a clean and trash-free India. Many cities and places in India are suffering with trash and litter lying on the roads, railway platforms, etc. Generally, manual sweepers and laborers are deployed for collecting trash at such places. In this paper, we present a sweeper robot that is capable of sweeping trash. There are various such sweeping robots and machines available in the market, but they focus mainly on dust and small-sized trash. The sweeper robot presented here is designed mainly for sweeping large-sized trash like one-liter bottles (empty as well as filled), metallic-cans, etc. The design and fabrication of such a sweeping mechanism is discussed in this paper.

Keywords Swachh bharat mission · Swachh-Bharat bot · Sweeping machines · Sweeping robots

1 Introduction

There are several countries including India that are suffering from hygiene problems like trash lying at public places such as railway platforms, roads, etc. The laborers deployed by respective municipal corporations generally do the sweeping job. The laborers have their scheduled working hours and are not available 24×7 . Also the people involved in sweeping tasks work under unhygienic conditions and have a

S. Jugal (✉)
Hindustan Abhyantri, Mumbai, India
e-mail: swapnil.jugal@gmail.com

K. Sharma
Division of Remote Handling & Robotics, Bhabha Atomic Research Centre,
Mumbai, India
e-mail: ksharma@barc.gov.in

high risk of suffering from various diseases. Therefore the sweeping task is a perfect job to be done by a machine or a robot.

Hon'ble Prime Minister of India, Shri Narendra Modi, launched the Swachh Bharat Mission on 2nd October, 2014 and all the citizens of India took an oath to clean the trash at public places devoting at least two hours a week. The authors of this paper are also associated with the mission and went on railway platforms, roads and footpaths to sweep the trash lying there. It was observed that the trash lying there was containing large-sized items like plastic water bottles, metallic cans, pebbles, etc. There are various sweeping robots and machines available for automatic sweeping like (Patzold et al. 1984; Patzold et al. 1985; Haaga 1999; Jones et al. 2009) but these machines are built to sweep dust and small-sized trash like leaves, small wrappers, etc. The ones which collect large-sized trash, like (Voelkle 1892; Mott 1952; Weight 1887; Wendel Adolph and Worwa Richard 1971) are too expensive and very big in size. This paper presents a design that can collect large as well as small-sized trash over a flat, level surface and can help in promoting the Swachh Bharat Mission. We have named this design as Swachh-Bharat Bot. The design and fabrication of Swachh-Bharat Bot is discussed in the next section.

2 Swachh-Bharat Bot: Design and Fabrication

The authors of this paper went to various railway platforms and places that deploy automatic sweeping machines or robots. It was found that the available sweeping machines were assisted by a human operator who pushes the machine and the machine sweeps the platform just like a grass-cutting machine. These sweeping machines are based on the designs given in (Patzold et al. 1984; Patzold et al. 1985; Haaga 1999) in which the sweeping action is performed by a rotating brush. Also the sweeping robot (Jones et al. 2009) can autonomously sweep inside a room. But such machines or robots can sweep only dust and small-sized trash like leaves, small wrappers, etc. The machines that can sweep large-sized trash are based on the design as given in (Voelkle 1892; Mott 1952; Weight 1887; Wendel Adolph and Worwa Richard 1971). But these machines are very costly and huge in size. An operator generally rides on these machines to drive and sweep an area. Therefore we came up with a design that is smaller in size, cheaper in price, collects large as well as small-sized trash and is easy to be made autonomous. The design details are discussed below.

The Swachha-Bharat Bot (see Fig. 1) is a floor sweeping robot with an ability to sweep in the objects that lie in its line of action. It's a z-shaped robot when viewed from side. It consists of a four wheeled cart (1 in Fig. 2) and a sweeping mechanism. The cart has the provision for a removable bin for collection of objects that are swept in. Objects (trash) are transferred from floor to the bin through collecting pan (11 in Fig. 2). Collecting pan is always in contact with the floor. Sweeping mechanism is mounted on the front side of the robot. Two motors along with the battery are mounted on the rear side of the robot. Sweeping mechanism consists of

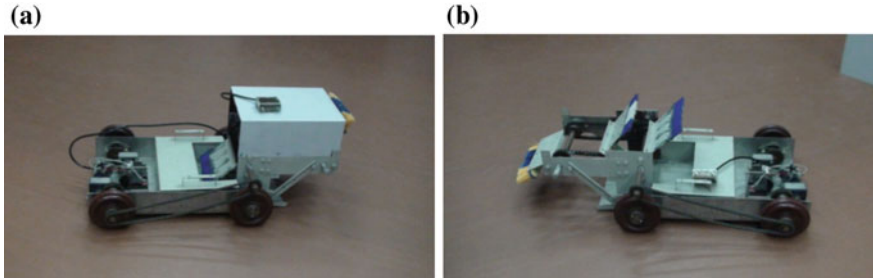
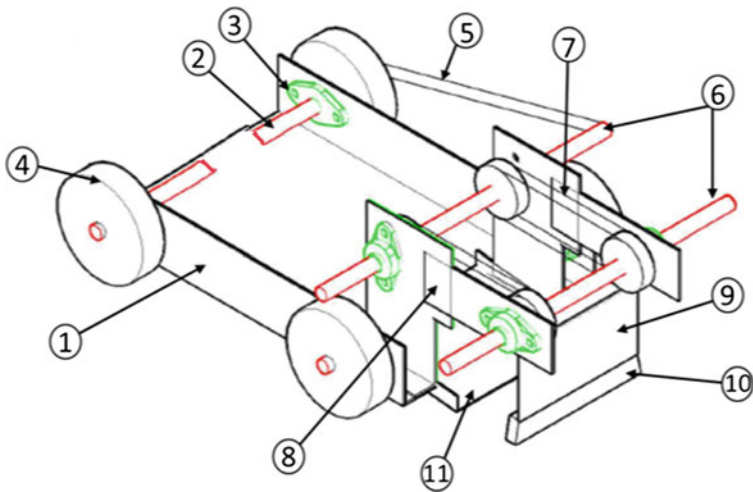


Fig. 1 a Swachh-Bharat Bot (side view). b Swachh-Bharat Bot (sweeping mechanism)



1	Chassis
2	Left Wheel Driving Shaft
3	Bearing
4	Wheel
5	Chain Drive that transmits motion from rear end wheel to Sweeping Mechanism Shaft

6	Sweeping Mechanism Shafts
7	Chain Drive between Sweeping Mechanism Shafts
8	Sweeping Mechanism Mounting Bracket
9	Brush-Mounting Plate
10	Brush
11	Collecting Pan

Fig. 2 Swachh-Bharat Bot (CAD model)

brushes (10 in Fig. 2), mounted on the brush-mounting plate (9 in Fig. 2), which revolve around the oblong path. The sweeping mechanism shaft (6 in Fig. 2) is interconnected with the left wheel driving shaft (2 in Fig. 2) through the chain drive (5 in Fig. 2). The left motor actuates the left wheel driving shaft which further actuates the sweeping mechanism leading to sweeping action of the brushes mounted on it. The setup can be driven manually too by pushing it forward. The motion of left rear wheel will be transmitted to the sweeping mechanism shaft through the chain drive.

The setup should be able to sweep the objects with size comparable to a one-liter mineral water bottle. With this assumption in mind, the collecting pan's width was decided. Accordingly then width of the chassis of the cart was finalized. The length of the cart is chalked out keeping in mind the provision for bin and the actuator mounting. The wheels to be mounted are decided on the standard wheels available in the market. A survey was done to check out the availability of brushes to be used and some of them were finalized. After deciding the brushes its mounting bracket was finalized. Accordingly the height of the sweeping mechanism and mounting bracket was fixed. The length of the sweeping mechanism was finalized with the span for which the brushes will be perpendicular to the floor while sweeping. The collecting bin is designed for easy removal and disposal of garbage from the robot. The provision for manual operation is also incorporated in the design. The total load (weight of the robot + load for sweeping action) was assumed to be 80 kgs.

The parameters were finalized and the CAD model was generated which is shown in Fig. 2. The mechanical structure was built according to this CAD model and minor modifications were incorporated to suit the flaws in manufacturability.

Two 12 V permanent magnet DC motors (0.1 hp and 25 rpm each) were mounted at the driving shaft (2 in Fig. 2). To run this setup, a 12 V, 18 Ah Battery was used. The electrical wiring line diagram is shown in Fig. 3. As shown in Fig. 3, two double-pole, double throw switches are provided in a wired, electrical remote. Each switch can rotate the respective motor, clockwise or anti-clockwise. Therefore, the four possible states (other than both switches off) can move the mechanism forward, backward, turn left or turn right, the turning being done by differential skid-steering.

The basic difference between the existing sweeping mechanisms and the Swachh-Bharat Bot is that the sweeping mechanism in existing machines is generally a rotating brush that is quite good for sweeping dirt and small-sized trash.

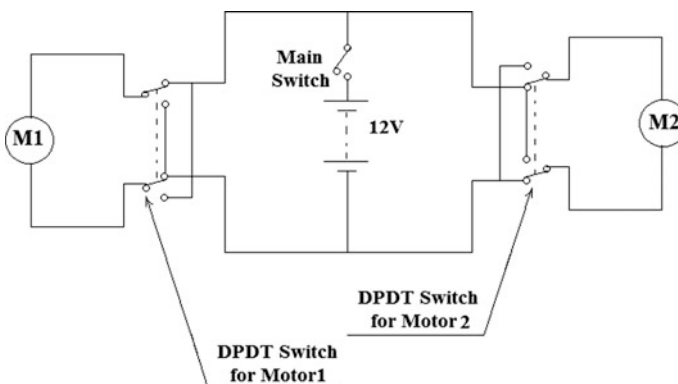


Fig. 3 Electrical wiring line diagram for Swachh-Bharat Bot

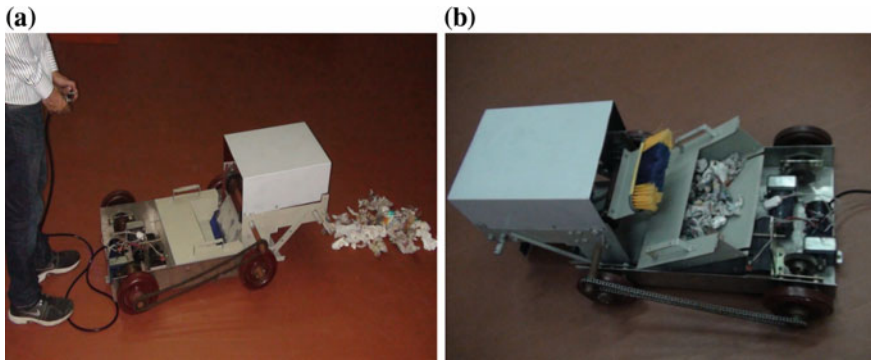


Fig. 4 a Swachh-Bharat Bot collecting trash. b Swachh-Bharat Bot with collected trash

The sweeping machines for large-sized trash deploy big rotating brushes and vacuum based sweepers. The Swachh-Bharat Bot, whereas, uses a chain-sprocket based platform over which the mounted brushes revolve rather than rotating. The brushes revolve around an oblong path while pushing trash inside the collecting pan. This allows for an increased duration of contact between the sweeping brushes and ground. Also it provides easy sweeping of comparatively larger objects. The trash slides down to the bin that can further be removed and the collected trash can be disposed off. This operation is similar to how a human performs sweeping while collecting the trash into a dust-pan.

In this fashion, the Swachh-Bharat Bot is capable of sweeping dust, small-sized trash (like pouches, wrappers, leaves, etc.) as well as large-sized (like empty or filled water bottles (up to 1 litre), metallic cans, pebbles, etc.). The sweeping action of the Swachh-Bharat Bot is shown in Fig. 4.

3 Conclusion and Future Work

The Swachh-Bharat Bot is developed to promote the Swachh-Bharat mission. It is designed to mimic the human action of sweeping. The important features are listed below:

1. The Swachh-Bharat Bot is capable of sweeping small-sized trash as well as large-sized trash.
2. The Sweeping brushes are removable and can be changed easily.
3. The size is quite small as compared to the other sweeping machines with similar sweeping capability.
4. The price is quite less (less than INR 50,000) as compared to the other sweeping machines with similar capabilities.
5. It can be operated manually also by pushing it over the sweeping area.

The Swachh-Bharat Bot is currently a sweeping machine rather than a robot. The future plans are to make it autonomous so that it can detect the trash on its own and collect it without human-guidance. Various sensors can be mounted as in (Mallik et al. 2014; Kuo et al. 2014) to make it autonomous.

Acknowledgment We would thank Dr. P.K. Pal and Dr. D.N. Badodkar for their invaluable guidance. We would like to thank Mr. Jagadish Kota, Mr. Peter Jacob and Mr. Mileswhar Dharne for providing help with the electrical setup of Swachh-Bharat Bot.

References

- Haaga, H. (1999). Sweeping machine. Patent No.: US 5896611 A, April 27, 1999.
- Jones, J. L., Mack, N. E., Nugent, D. M., & Sandin, P. E. (2009). Autonomous floor-cleaning robot. Patent No.: US 7571511 B2, August 11, 2009.
- Kuo, G.-H., Cheng, C.-Y., & Wu, C.-J. (2014). Design and implementation of a remote monitoring cleaning robot. In *Proceedings of International Automatic Control Conference (CACCS)*.
- Mallik, A., Raju, K. S., & Tanwar, P. K. (2014). Design of an elementary level surface sweeping and wiping robot for domestic use. In *Proceedings of International Conference on Devices, Circuits and Communications*.
- Mott C. W. (1952). Street sweeping machine. Patent No.: US 2614279 A, October 21, 1952.
- Patzold, D., Schreiber, A., & Tiwi, P. (1984). Floor-Sweeping machine. Patent No.: US 4484371 A, November 27, 1984.
- Patzold, D., Schreiber, A., & Tiwi, P. (1985). Floor-sweeping machine. Patent No.: US 4502173 A, March 5, 1985.
- Voelkle, A. (1892). Street Sweeping Machine. Patent No.: US 482663 A. September 13, 1892.
- Weight, T. (1887). Street sweeper. Patent No.: US 371722 A, October 18, 1887.
- Wendel Adolph, H., & Worwa Richard, G. (1971). Powered sweeping machine. Patent No.: US 3604051 A, September 14, 1971.

Force Sensitive Robotic Gripper

Meher Tabassum and D.D. Ray

Abstract Industrial robotic application of gripping unknown objects with two-finger gripper is a challenging task. A traditional grasp model does not fit the requirement of gripping unknown objects, as application of too much gripping force damages and deform the object; while small force results in slipping of the object. In this paper we propose the design, control and implementation of the two finger robotic gripper, its sensory and hardware interface and a programming solution to overcome the gripping problem. The approach adopted is to acquire force information acting on the object before and prevent the object's slip by increasing the gripping force even before the slip occurs.

Keywords Robotic gripper · Force sensor · Manipulators · Load cell

1 Introduction

Robotic research has evolved a lot, especially in the field of intelligent automation. To make a system intelligent enough with an aim to replace human control and inspection we need sensor integrated robotic systems. Augmentation of multiple sensory systems allows the robotic system to collect information and use them to perform a given operation in an intelligent way. The end-effector of any robotic system is mostly a gripper, which is used for grasping different objects and tools. The gripper employed should be intelligent enough to hold objects without damaging it or making it fall. For this gripper should have built-in sensors and offer a small compliance to adjust itself in performing a desired operation intelligently.

M. Tabassum (✉) · D.D. Ray
Division of Remote Handling and Robotics, Bhabha Atomic Research Centre,
Trombay, Mumbai 400085, India
e-mail: mehertab@gmail.com

D.D. Ray
e-mail: dray@barc.gov.in

Recent researches have concentrated in the development of intelligent and adaptive grippers. Human beings have a good grasping and manipulating ability with their hands. Various studies to explore this ability in humans to implement it in machines are being done. Nakazawa et al. (2001) has analysed the characteristics of human grasping forces. These characteristics are used to build a control model to determine the gripping forces for the robotic gripper, depending on the held object's acceleration. The movements caused by the acceleration are compensated by the optimum forces and a slip is prevented. Chen and Chong (2013) in his paper has presented a mechanical design to develop a force sensitive robotic gripper to handle delicate objects. Most industrial grippers (Robotiq 2015) are designed to grasp objects of different shapes, sizes and weights, using two or three fingers and they are a good fit for applications like pick-and-place. These adaptive grippers come with servo control of electric motors for the movement of the fingers using electric input from the robot controller. The state of art technology in modern robotic gripper research has boomed because of the availability of different kinds of sensors, like tactile, force, proximity etc. Kim (2007) has describes the development of 3-axis force sensor which is used in an intelligent gripper to grasp unknown objects by measuring the forces in the grasping direction as well as in the gravity direction to perform force control. Yoshihiro Ochiai et al. (1986) had built a force sensing gripper using a 2, 4 and 5 component beam type load cells. They indicated that more the number of sensors used in the finger make the gripper more effective and sensitive in holding brittle objects. Chan and Cheung (2001) describes the position and current control schemes for a novel two-finger gripper using variable reluctance actuator suitable for high precision gripping applications.

In this paper we propose the design, control and implementation of our two finger robotic gripper, giving the details of its sensory, hardware interface and a programming solution to overcome the gripping problem. The mechanical gripper used is a general purpose two finger gripper and we generate a controlled force for grasping using a pneumatic cylinder having a feedback from the force sensor attached in the gripper to hold the object without slip in real time. The two gripper fingers are made identical in size, shape and construction.

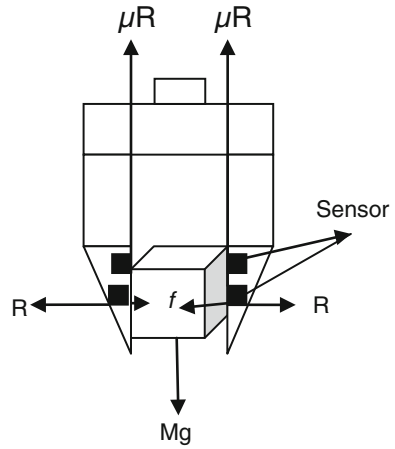
2 Implementation

When any gripper holds an object it can slip or fall due to two factors:

- (1) The force of gravity, and
- (2) The acceleration or vibration caused by robotic arm movement.

As shown in Fig. 1, to hold the object firmly the vertical force acting downward is to be balanced by frictional force $\mu\mathbf{R}$ acting opposite it, where μ is the coefficient of friction between the surface of the object and the gripper finger. The gripper when activated applies a force f on an object which results in a reaction \mathbf{R} . If $\Delta\mu$ is the acceptable deviation in the coefficient of friction then the new coefficient of

Fig. 1 Gripper holding an object of mass M



friction becomes $(\mu + \Delta\mu)$ and the new restraining force becomes $\mathbf{R}(\mu + \Delta\mu)$, which is in the direction opposite to the direction of anticipated slip. As we know that the gripper will always apply the force perpendicular to the surface of the object, the reaction \mathbf{R} will always be towards the outer surface of the fingers. Therefore, the force \mathbf{Mg} sensed as the component perpendicular to \mathbf{R} is responsible for the slipping. Since proposed gripper has identical two fingers and holds symmetry in structure, we will analyse only one finger. If we have $\mathbf{R}(\mu + \Delta\mu) > \mathbf{Mg}$, then the object will be gripped without slipping.

Different gripper orientations offers unsymmetrical load on the two fingers as shown in Fig. 2. The required reaction \mathbf{R} in these situations can be calculated on the basis of the force component in the direction of gravitational force when no other external forces are acting on the object shown in Fig. 2a. The most comfortable orientation is when an object is handled in horizontal position as in Fig. 2b, it requires minimum gripping force. It is advisable that the gripper should orient itself

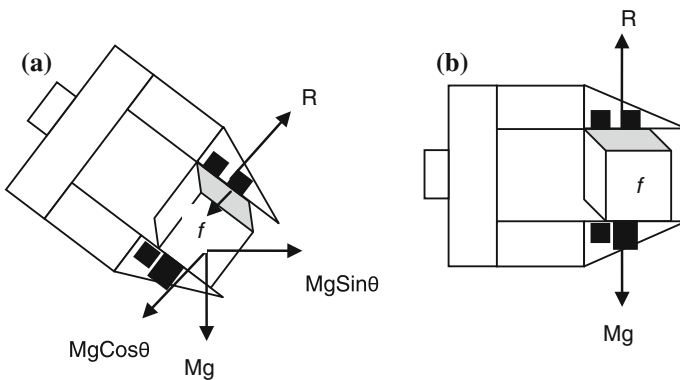


Fig. 2 Different orientations of the gripper

in this configuration applying minimum gripping force, thus reducing the stress on the object ($\mathbf{R} = \mathbf{0}$). The required orientation is computed with the joint angles of the robotic arm using the robot kinematics. The orientation is defined using roll, pitch and yaw of the robotic gripper with a reference point. If $(\mathbf{R}(\boldsymbol{\mu} + \Delta\boldsymbol{\mu}) < \mathbf{Mg})$, then the restraining force become less and the object is about to slip, the gripper orientation should be corrected for a quick recovery. In addition, the gripper should be rolled to support the object below its centre of gravity. Thus, to calculate the required gripping force, we need to know the gripper orientation (yaw, pitch, and roll) and the forces from four sensors. Each sensor gives an output, which tells the object's presence and the measured gripping force for holding. The outputs from these four sensors are then processed to determine the most favourable orientation and minimum force to grip the object without slip. The force f acting towards the finger is created by the pressing action of gripper as well as the mass of the object. The gripper maintains this force so that the magnitude of the force exceeds the maximum restraining force. The generated reaction helps in increasing the frictional force. To determine the slip direction, the four sensors are so mounted that the direction of the slip can be known. Any sensor when not in contact with the object will give an output indicating the object either loosely held or is slipping.

3 The Gripper Design

The proposed gripper is indigenously designed and developed. The design concept of the gripper is simple as seen in the Fig. 3. This gripper has two fingers, which can be used to hold objects of medium sizes of different materials or shape. Each gripper finger is mounted with two small load cells to measure the applied force as seen in Fig. 4. The selected load cell is an Entran-B1-125N. This load cell is strain gage based, very small and slender in size, and light in weight. It is embedded on the inner surface of fingers of the gripper to detect the gripping force. Any industrial robot equipped with this gripper can grip brittle objects, and detect the position and forces acting on it. The load cell embedded functions not only as a force sensor here but also as a tactile sensor in detecting the presence of the object held.

A schematic diagram of the robotic gripper control system is shown in the Fig. 5. It consists of a industrial computer and a sensor processing module from National Instrument TM. The sensor processing module consist of a rugged NI SCXI 1000, which is a 4-slot AC-powered chassis used for housing other SCXI modules, like 1520 and 1314. The NI SCXI-1520 is an 8-channel universal strain gage input module which measures signals from load cells. It offers programmable amplifier, filter and 0 to 10 V excitation source on each channel. The NI SCXI-1314 module is an 8 channel front mounting terminal block for the NI SCXI-1520 universal strain gauge input module. It has installed 350 Ohm quarter bridge resistors for each channel for their bridge completion. It also provides 11 terminals for all strain gauge channels, comprising of signal (+ and -) and power (+ and -) etc.

Fig. 3 Two finger gripper, with its control system

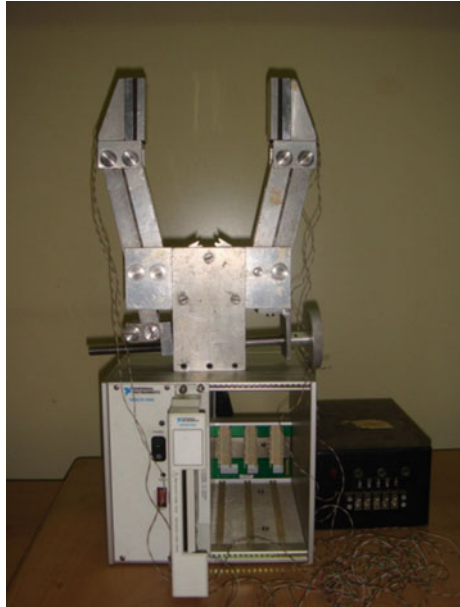


Fig. 4 Two small strain gauge force sensors are mounted on each finger



The opening and closing of the gripper is performed by a pneumatic cylinder. A control circuit for giving a direction sense for the two solenoids is commanded through the computer. The desired force for the gripper to hold an object is

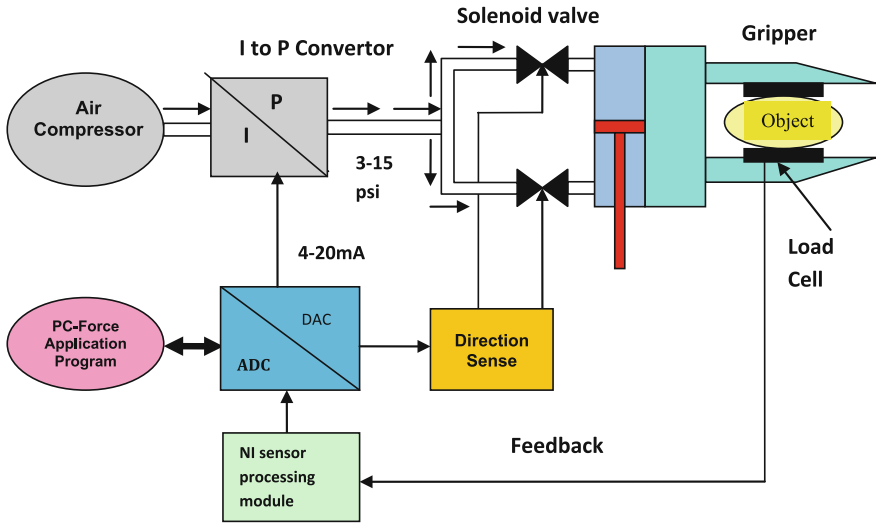
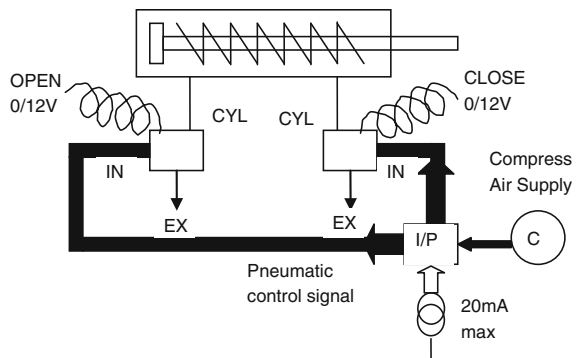


Fig. 5 Force sensitive robotic gripper system

Fig. 6 Pneumatic control signal to the actuator



computed using a proportional controller implemented in the computer. A current to pressure (I/P) transducer is used to convert the force calculated to pressure for pneumatic cylinder attached to the gripper. This conversion of current to pressure is performed by an independent system as shown in Fig. 6. The gripper system and its control modules are highly portable and can be installed in any manipulator. The user has an added advantage in assembling the force sensitive gripper in any orientation, best suited for his application of intelligent grasping. The gripper’s portability, it’s simple design structure and having desired output is all possible orientations becomes an added advantage in performing tasks like material handling and pick-n-place of objects without slip for a robot.

4 The Gripper Control System Hardware

As in any control paradigm, here also critical requirement is to establish the feedback and produce the corresponding desired actuation force. The feedback is obtained from a miniature load cell embedded on the inner side of the gripper fingers and the desired force generated using pneumatic cylinder as actuator. The details of these equipments used are given below:

A. Actuator

The gripper is opened and closed using a pneumatic cylinder as shown in Fig. 6. The input to the cylinder is compressed air which is received through a current to pressure converter (I/P). This I/P transducer in a closed loop operation allows accurate high-resolution pressure control, having a linear conversion of 4–20 mA analog input current to 3–15 psi pneumatic pressure. A graph of pressure variation corresponding to the sinusoidal current variation is plotted in Fig. 7.

B. Interface Card: Digital to Analog Card

The I/P converter is fed through a 12 bit D/A (digital to analog) card which is inserted into the computer’s PCI slot. A software library function of the card provided by the manufacturer, is used to generate the desired current in the range of 4–20 mA at the output.

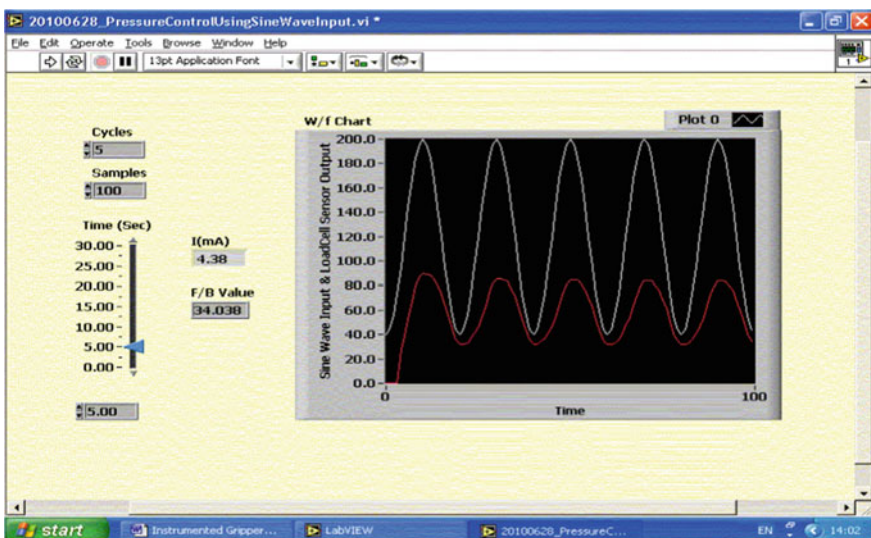


Fig. 7 Pressure control using sine wave input

C. Feedback from the Force Sensor

Sub miniature Entran™ strain gage load cells (ELFM-B1-125N) of high stability are used for the gripping force measurement. These sensors measures Tension/Compression in the range of 0–125 N. They have a small stainless steel body of diameter 9.5 mm. A Perspex acrylic plastic sheet is attached to the inner face of the two gripper fingers and these sensors are housed in it. The housing construction avoids damaging the delicate load cells and also guarantees that only orthogonal forces load the cells. Sheer forces result in giving false measurements. The Entran™ strain gage load cells comes with a calibrated in-line wired miniature amplifier modules, having an external null control screw and a compensated temperature range of 15–70 °C. The amplifiers has to be calibrated according to its own protocol, each having a non-linearity of 0.25 % FSO, a thermal sensitivity of 1 % per 50 °C and a hysteresis of 0.25 % FSO. The 1.5 m leads attached are Teflon insulated. The output from each load cell is 2 mV/V. A reasonably clean feedback signal was established using these load cell sensors embedded in each finger. Sensors were excited using National Instruments’ strain gage module and the data was obtained using NI-PC interfacing card as described in Sect. 3. An analog input configuration of load cell is shown in Fig. 8.

D. Force Measurement Program

The recording of the gripper finger forces was done with a software program. This program also provides software calibration functions for the load cells and displays

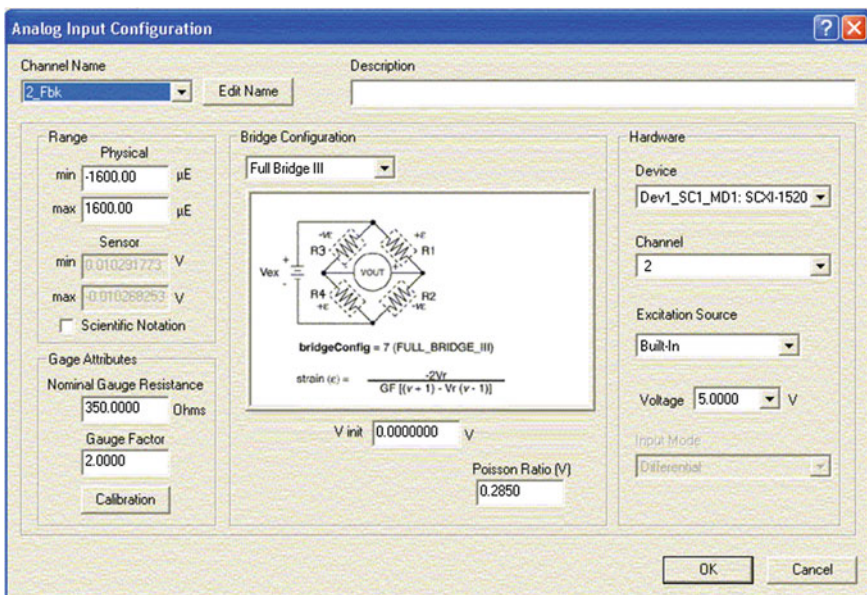


Fig. 8 Load cell configuration

a real-time graphical view of the data from each sensor. The algorithm used is a simple feedback loop. The gripping force is measured, if it is less than the maximum restraining force $R(\mu + \Delta\mu)$, the gripping force f is increased. The value of μ was taken as 0.61 for holding clean and dry surface objects. A proportional plus scheme with actuation control of one end of gripper (CLOSE) and release force for gripper (OPEN) from the other end of the pneumatic cylinder was successful implemented in software. The error between the commanded and actual value was limited within 10 %.

5 Conclusion

We have presented a design and control of a force sensitive gripper system with all its implementation details. A Test setup is shown in Fig. 9. Testing the gripper shows no slip of the object. The system works by acquiring the information from the load cells about the forces acting on the object in real-time. It relies on the sensitivity and linearity of the load cells. The four sensors in the gripper finger makes it ideal, effective and sensitive in holding brittle objects too. The gripper system is simple and can be employed in any manipulator with all its control. The current to pressure (I/P) converter has its own control loop which may affect the

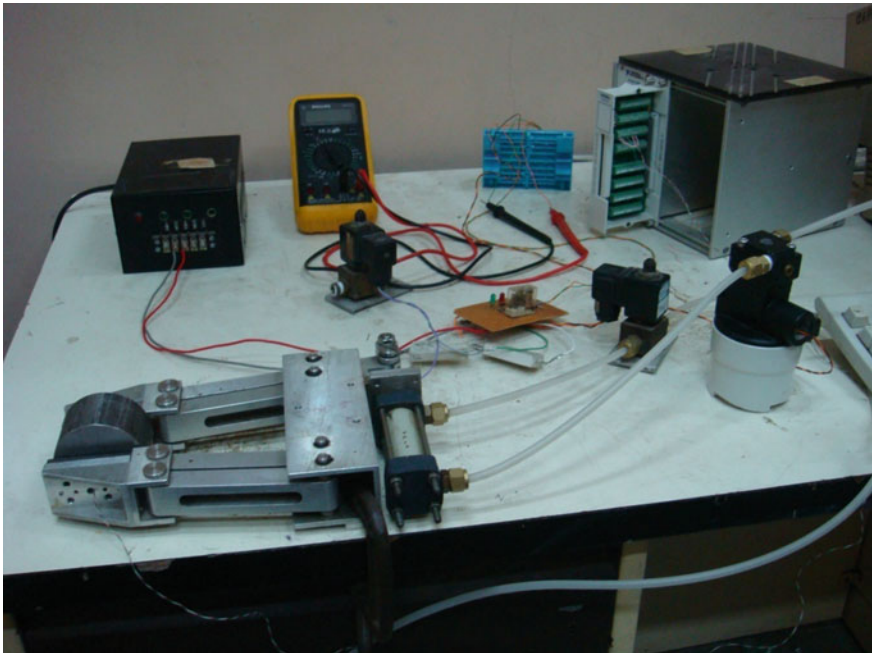


Fig. 9 Force sensitive gripper test setup

stability of the whole system. However, during initial testing no such problem was observed. A pressure amplifier for higher gripper capacity can be added for greater force requirement. The value of μ can be assumed considering the kind of object surfaces to be held. The gripper concept presented here does not need any special mechanical gripper design and can be implemented in any gripper.

Acknowledgments We extend our acknowledgements to Dr. Amar Banerji, Dr. Debanik Roy and Mr. Vijay Tike for the development and testing of the force sensitive gripper and thank our division technicians for the fabrication the various components for the test setup.

References

- Chan, K. K. C., & Cheung, N. C. (2001). Grasping of delicate objects by a novel two-finger variable reluctance gripper. In *The 36th IEEE Industry Applications Society Annual Meeting, IAS'2001*, October 2001, Chicago, USA.
- Chen, C.-H., & Chong, W. (2013). Force controlled robot gripper with flexible joint for delicate assembly task. In *13th International Conference on Control, Automation and Systems (ICCAS 2013)* (pp. 935–939), October 20–23, 2013, Gwangju, Korea.
- Kim, G.-S. (2007). Development of a three-axis gripper force sensor and the intelligent gripper using it. *Science Direct, Sensors and Actuators A*, 137, 213–222.
- Nakazawa, N., Il-hwan Kim, Inooka, H., & Ikeura, R. (2001). Force control of a robot gripper based on human grasping schemes. *Science Direct, Control Engineering Practice*, 9, 735–742.
- Ochiai, Y., Kameoka, K., Sugisako, T., & Ono, T. (1986). Application of a new beam type load cell to mechanical hand. In *Mechanical Problems in Measuring Force and Mass*, (Vol. 3, pp. 147–152) ITC Series No. 8.
- Robotiq, *How to Choose a Right End-Effector for your Applications*. <http://robotiq.com/wp-content/uploads/2015/06/How-to-Choose-the-Right-End-Effector-F.pdf?submissionGuid=e9cf220-d1e3-444c-9f69-e8d4ec716fff>.

Electron Beam Melting of Steel Plates: Temperature Measurement Using Thermocouples and Prediction Through Finite Element Analysis

Debasish Das, Dilip Kumar Pratihari and Gour Gopal Roy

Abstract The present study deals with electron beam melting of steel plates, where temperatures at four different locations situated away from the heat source have been measured using thermocouples. Finite element (FE) analysis is carried out to determine the temperature distributions during the heating and cooling of the plate. The results of this analysis have been validated through experiments carried out using thermo-couples. The micro-structures of the parent metal and fusion zone have also been studied.

Keywords Electron beam melting · Temperature distributions · FE simulations · Experiments using thermocouples

1 Introduction

The preference of high energy beam over conventional methods is observed in the field of die-less non-contact forming, heat treatment, drilling, welding, machining etc., as it offers a cutting-edge performance, such as narrow and deep beam, high cooling rate, resulting into minimized heat affected zone (HAZ) and residual stress. Among the various available high energy beams, the capacity and range of applications of electron beam are wider. Hence, it could be used for a wide range of different processes. Irrespective of the numerous differences in the above mentioned

D. Das

Indian Institute of Technology Kharagpur, Kharagpur, India

D.K. Pratihari (✉)

Department of Mechanical Engineering, Indian Institute of Technology Kharagpur, Kharagpur, India

e-mail: dkpra@mech.iitkgp.ernet.in

G.G. Roy

Department of Metallurgical and Materials Engineering, Indian Institute of Technology Kharagpur, Kharagpur, India

© Springer India 2016

D.K. Mandal and C.S. Syan (eds.), *CAD/CAM, Robotics and Factories of the Future*, Lecture Notes in Mechanical Engineering,

DOI 10.1007/978-81-322-2740-3_57

processes, it all go through a common heating process. Hence, this heating process inter-connects all the distinctly different processes, thereby forms a foundation or base for metal-beam interactions. Even though literature is available regarding these individual fields, no work is reported so far, which could unite and compare all these distinct processes under one scale.

Study of temperature distribution gives an insight into heat flow pattern, cooling rate, metallurgical changes etc., which help to understand the process. Literature related to it is available for the above mentioned distinct fields. The studies of temperature distribution, molten pool profile and cooling rate were carried out during electron beam heat treatment of SS304 samples by Cline and Anthony (1977), high energy beam drilling of copper by Wei and Ho (1990), electron beam butt welding of Inconel 706 plates by Ferro et al. (2005), electron beam melting for additive layer manufacturing (ALM) with 1.4404 (316L) stainless steel powder by Zähand Lutzmann (2010) etc. Similarly, finite element (FE) simulations were conducted to model and validate experiments for welding by Chang and Na (2001), Ferro et al. (2005), and Luo et al. (2010) and for ALM by Zäh and Lutzmann (2010). Numerical and analytical models for laser forming of thin plates were developed and compared by Shi et al. (2007).

The aim of the present work is to develop a common reference or base for both experiments and simulations, with respect to which, processes that appear different but have a common ground could be united and compared. Hence, in this work, temperature distributions are measured at different locations using K-type thermocouples. FE analysis is also carried out for this problem and its results are compared with that of real experiments.

2 Mathematical Formulation

The Fourier-Kirchoff Eq. (1) is the governing heat transfer equation (Chang and Na 2001) used in this study, as given below.

$$\rho C_p \frac{\partial T}{\partial t} = \frac{\partial}{\partial x} \left(k \frac{\partial T}{\partial x} \right) + \frac{\partial}{\partial y} \left(k \frac{\partial T}{\partial y} \right) + \frac{\partial}{\partial z} \left(k \frac{\partial T}{\partial z} \right) + Q, \quad (1)$$

where ρ is the density of the medium, C_p denotes the specific heat capacity, t represents time, k is the coefficient of thermal conductivity, x, y and z are the space coordinates, T is the temperature, and Q is the total heat input. Convection and radiation heat losses are calculated using Newton's law of cooling (refer to Eq. (2)) and Stefan-Boltzmann equation given in Eq. (3) (Chang and Na 2001):

$$q_c = h_f(T_{surface} - T_0), \quad (2)$$

$$q_r = \varepsilon\sigma(T^4 - T_0^4), \tag{3}$$

where T_0 denotes the ambient temperature, h_f represents the convection coefficient of value, ε and ρ indicates emissivity and Stefan-Boltzman constant respectively. Equation (4) represents the rotary solid characteristics (Ferro et al. 2005; Luo et al. 2010).

$$r^2 = y^2 + x^2, \tag{4}$$

In the conical region of the heat source, the beam radius was expressed as a linear function of depth, which linearly reduced, as the depth increased (Ferro et al. 2005; Luo et al. 2010). It is expressed in Eq. (5) as follows:

$$r_0(Z) = r_e - \frac{(r_e - r_i)(Z_e - Z)}{(Z_e - Z_i)}, \tag{5}$$

where r_e and r_i represent the largest and least cone radius, respectively; Z_e and Z_i are the heights corresponding to r_e and r_i , respectively. r_0 denotes the instantaneous beam radius at a depth of Z .

The total power input Q is calculated as follows (Luo et al. 2010):

$$Q = \eta VI \tag{6}$$

where η represents the overall efficiency; V and I denote the voltage and current, respectively. The total power input (Q) is sub-divided into Q_s (acting on the surface) and Q_v (acting into the volume), as given below. γ_s, γ_v are the coefficients depicting the ratio of power distribution between surface and volume, respectively (Luo et al. 2010).

$$Q_s = \gamma_s Q, \quad Q_v = \gamma_v Q \tag{7}$$

$$\text{and } \gamma_s + \gamma_v = 1 \tag{8}$$

$$\gamma_s \ll \gamma_v \tag{9}$$

From Eq. (9), it is evident that a very small portion of the flux is acting on the surface (Luo et al. 2010). Most of the volumetric heat flux is distributed over the conical region, as given in Eq. (10).

$$q_v(x, y, z) = \frac{9Q_v}{\pi r_e^2 h} e^{\left[\frac{-h^2}{(h-z)^2} \times \frac{3(x^2 + y^2)}{r_e^2} \right]} \tag{10}$$

where $0 \leq z \leq h$, h denotes the depth up to which the influence of heat source is prominent and also, can be represented as the difference between Z_e and Z_i .

In the present work, surface heat flux is neglected being small and only, conical heat flux is considered. ABAQUS 6.10 is used for simulations. Visual Studio 9 and Intel Fortran compiler 11.1 are used to write DFLUX code in order to provide heat source.

3 Experimental Procedure

Three replicates of the same sample, each of dimensions $34 \times 30 \times 10$ mm, are taken and drilled at a depth of 5 mm from the top surface at four different locations. Figure 1 shows the 2D representation of relative positioning of four thermocouples, while Fig. 2 shows the photograph of the thermocouples attached to the work-piece. Figure 3 displays a photograph of the work-piece without thermocouples attached to it, after it is heated. The K-type thermocouples are press-fitted for temperature measurement. The data acquisition system connected to the thermocouples record the temperature variations. For the given experiment, a beam having voltage of 60 kV and current of 40 mA (that is, Power = 2.4 kW) is allowed to fall at the centre of the job for 10 s in vacuum. After this heating cycle of 10 s, it is kept in the vacuum during the cooling cycle of around 2800 s (approx 45 min). Throughout the experiment, all the beam parameters are kept constant. Standard AISI Type SS 304 is used for this experiment, whose chemical compositions are given in Table 1, as obtained using X-ray fluorescence (XRF).

Fig. 1 2D representation of relative positioning of the thermocouples attached to the work-piece

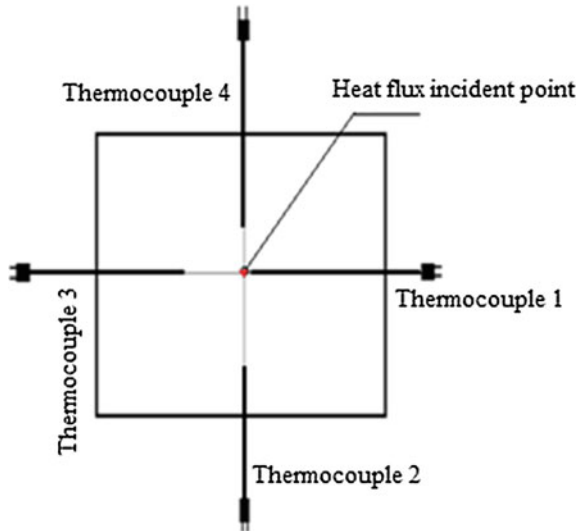


Fig. 2 Photograph of the thermocouples attached to the work-piece

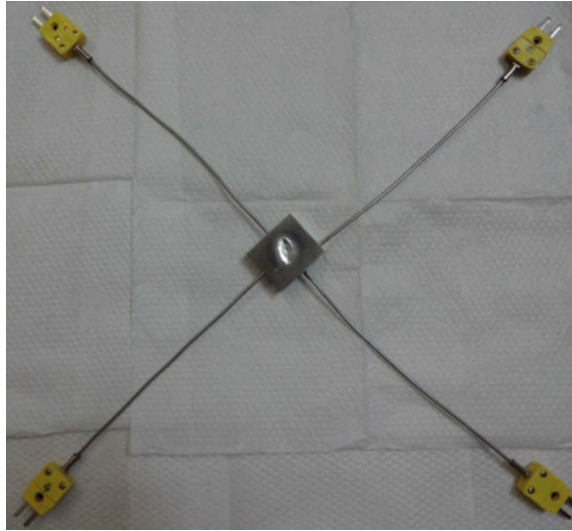
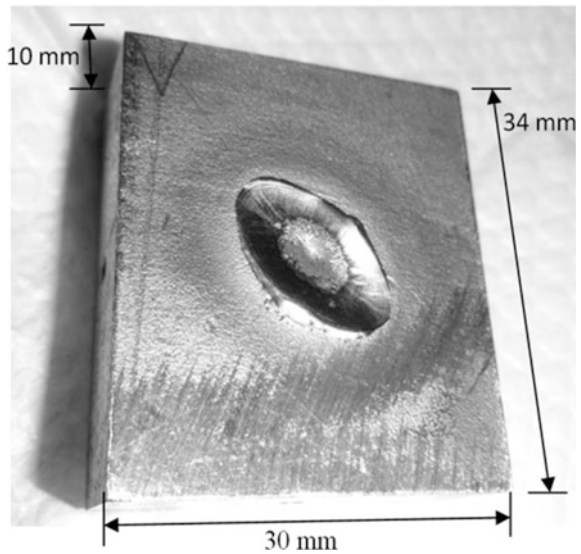


Fig. 3 Sample after electron beam heating



4 Finite Element (FE) Analysis

A rectangular plate of dimensions: $34 \times 30 \times 10$ mm is used for FE-based analysis. The constant material properties used in this study are summarized in Table 2 (Chang and Na 2001, <http://www.azom.com/properties.aspx?ArticleID=965>, 30 Dec 2014, 11.49 A.M). Rests of the temperature dependant properties are assumed

Table 1 Chemical compositions of the sample obtained through XRF

Fe	Cr	Ni	Mn	Cu	Si	Mo	Al	Co	
71.37 %	17.80 %	8.09 %	1.01 %	0.40 %	0.38 %	0.33 %	0.24 %	0.14 %	
V	W	P	Pb	Sn	As	Nb	S	Zn	Ta
0.06 %	0.04 %	0.04 %	0.02 %	0.02 %	0.02 %	0.02 %	0.02 %	0.01 %	0.01 %

Table 2 Temperature independent material properties (Chang and Na 2001, <http://www.azom.com/properties.aspx?ArticleID=965>, 30 Dec 2014, 11.49 A.M)

Density (Kg/m ³)	7900	Latent heat of fusion (kJ/kg)	247
Young's modulus (GPa)	193 GPa	Solidus temperatures (K)	1673
Poisson's ratio	0.277	Liquidus temperatures (K)	1773
Convective heat transfer coefficient (W/m ² K)	10	Emissivity	0.25

Table 3 Temperature dependant material properties (Chang and Na 2001)

Temperature (K)	Thermal conductivity (K)	Specific heat (Cp) (J/kg K)	Coefficient of thermal expansion $\times 10^{-6}$
300	13.74	372	14.20
400	15.69	402	15.20
500	17.505	426	16.30
600	19.67	452	17.20
700	21.4	501	17.90
800	23.206	550	18.50
900	24.904	571	19.00
1000	26.591	590	19.10
1100	28.321	602	19.30
1200	30.16	610	19.40
1300	32.41	623	19.60
1400	35.2	638	19.90
1500	37.581	650	20.20
1600	39.36	679	20.50
1673	40.39	696	20.70
1729	41.26	708	20.90
1800	42.32	725	21.10

to be isotropic and homogeneous, and are displayed in Table 3 (Chang and Na 2001). The total time is divided into heating time ($t_1 = 10$ s) and cooling time ($t_2 = 40$ s). The radius of the incident beam is found to be equal to 750 μm through trial and error method.

Fig. 4 Mesh distributions

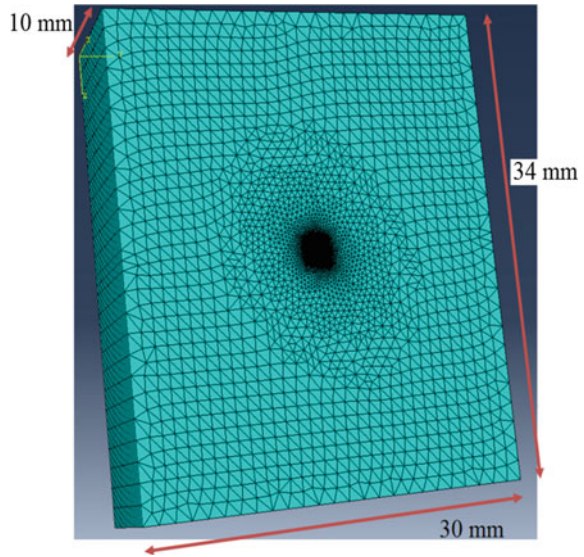
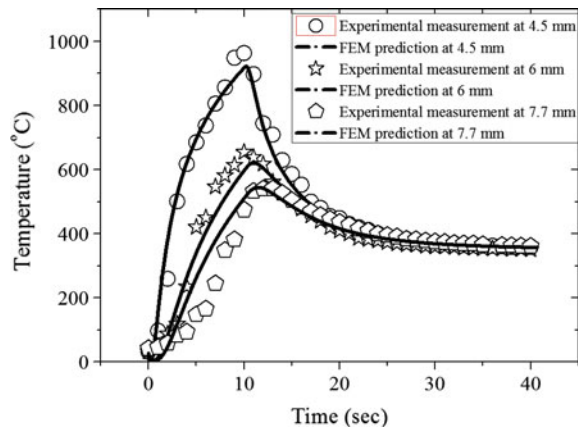


Fig. 5 Experiment versus FEM Time-Temperature distributions



The developed 3D FE model is having a total of 403,234 number of nodes, 772,850 number of linear wedge elements of type DC3D6 (6-node linear heat transfer triangular prism) with a static heat source. The minimum mesh size at the centre is 7 μ m and it increases radially outward to 1.28 mm at the edge. Neumann boundary conditions are assumed. The zone subjected to intense heat flux contains denser mesh, while the rest consists of coarse mesh, as shown in Fig. 4. The effects of conduction, convection and radiation are taken into account.

Fig. 6 Experiment versus FEM Distance-Temperature distributions

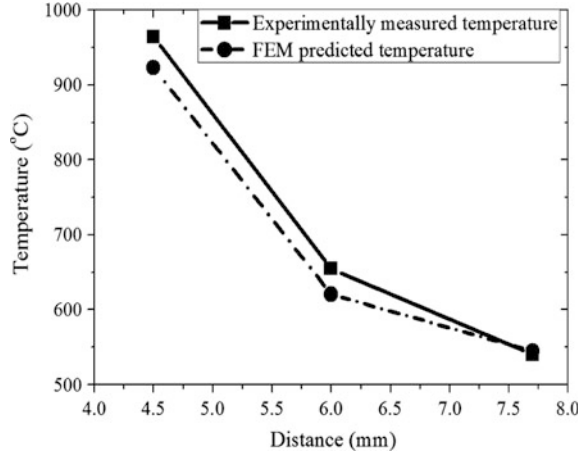
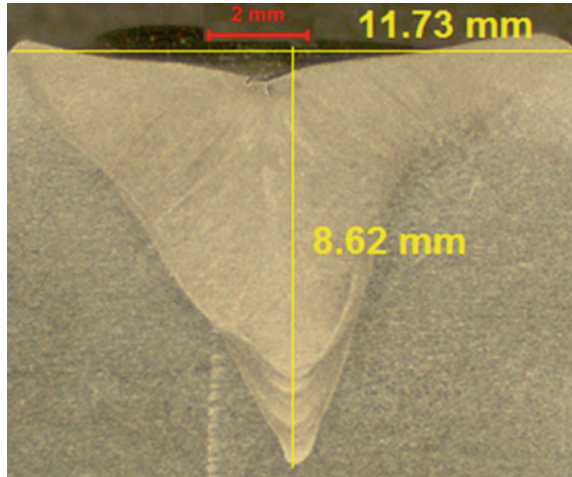


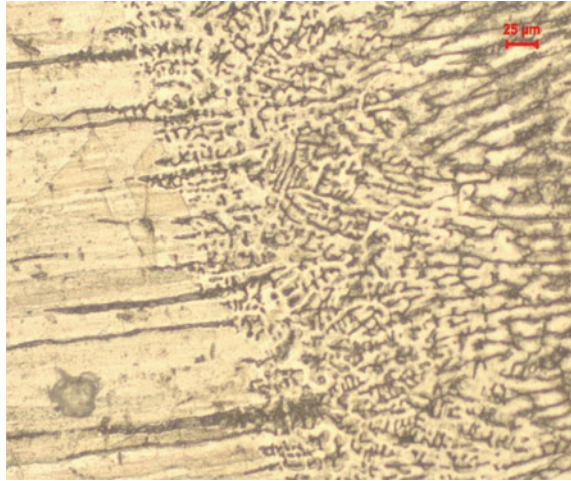
Fig. 7 Bead geometry of the spot heated sample



5 Results

The comparisons of time versus temperature at different locations between the experimental data and FE-predicted ones are displayed in Fig. 5. At the end of the heating cycle (10 s), maximum temperature is reached. During cooling cycle, initially, the temperature drops rapidly. After certain interval, a steady state condition is reached. Gaussian distribution profiles are obtained, which is in accordance with the literature survey. Figure 6 shows the variations of temperature with distance measured from the point of application of heat flux to that, where the temperature is either measured or predicted. The temperature is seen to gradually decrease, as the

Fig. 8 Interface between base metal and fusion zone at 20× magnifications



distance increases. This happens due to conduction, convection and radiation losses. The experimental and FEM predicted results are found to be very close. The maximum difference is around 5.162 % at 6 mm from the melt zone. It may be attributed to various factors, such as experimental errors, machine error, accuracy of the thermocouples, model assumptions etc. Figure 7 highlights the sample bead-geometry, as obtained during the experiments. Figure 8 shows the interface between base metal and fusion zone at 20× magnifications showing the microscopic views of the electron beam melting experiments. The difference in microstructure of parent material and fusion zone is clearly visible. Dendrite structures are found to occur in the fusion zone of the plate.

6 Conclusion and Scope for Future Work

For this study, the following conclusions have been drawn:

1. Electron beam melting experiment is done on AISI SS304 plates. The experimentally-measured and FE-predicted temperature distributions are seen to be very close.
2. Fast cooling during electron beam melting has allowed the growth of the fine dendrites inside the fusion zone.
3. Other heat source models (like double-ellipsoid) could also be applied in future to further improve the FE-predicted results.
4. Similar studies will be conducted in future on electron beam welding by the authors.

References

- Chang, W. S., & Na, S. J. (2001). Prediction of Laser-spot-weld shape by numerical analysis and neural network. *Metallurgical and Materials Transactions B*, 32(4), 723–731.
- Cline, H. E., & Anthony, T. R. (1977). Heat treating and melting material with a scanning laser or electron beam. *Journal of Applied Physics*, 48(9), 3895–3900.
- Ferro, P., Zambon, A., & Bonollo, F. (2005). Investigation of electron-beam welding in wrought Inconel 706—Experimental and numerical analysis. *Materials Science and Engineering*, 392(1–2), 95–105.
- <http://www.azom.com/properties.aspx?ArticleID=965>, December 30, 2014, 11.49 A.M.
- Luo, Y., You, G., Ye, H., & Liu, J. (2010). Simulation on welding thermal effect of AZ61 magnesium alloy based on three-dimensional modeling of vacuum electron beam welding heat source. *Vacuum*, 84(7), 890–895.
- Shi, Y., Shen, H., Yao, Z., & Hu, J. (2007). Temperature gradient mechanism in laser forming of thin plates. *Optics & Laser Technology*, 39(4), 858–863.
- Wei, P. S., & Ho, J. Y. (1990). Energy considerations in high-energy beam drilling. *International Journal of Heat and Mass Transfer*, 33(10), 2207–2217.
- Zäh, M. F., & Lutzmann, S. (2010). Modelling and simulation of electron beam melting. *Production Engineering. Research and Development*, 4(1), 15–23.

Design and Analysis Towards Successful Development of a Tele-Operated Mobile Robot for Underground Coal Mines

Dip N. Ray, Riddhi Das, Bijo Sebastian, Biplob Roy
and Somajyoti Majumder

Abstract The demand of coal is increasing day-by-day with the growth of civilization. In spite of enhancement of coal production, a huge amount of foreign currency has to be spent to import coal from outside to meet the demand-supply gap. The existing coal reserve cannot be extracted fully due to unavailability of proper technology in Indian coal mines. Suitable remote operation technology can be introduced either for extraction of coal from deeper seams or monitoring the mine environment for safety. A robotic system has been developed to remotely monitor the environment of a hazardous mine tunnel from the mine manager's desk before starting any extraction. The system is equipped with a set of navigational sensors (IR sensors, compass, laser range finder and camera) and operational sensors (CO, CO₂, CH₄, temperature and humidity sensor). The robot can be controlled either manually or autonomously based on the need. In both the cases, the data can be transferred to the over ground station for monitoring. Approximate mathematical modeling of the system has been performed and its working has been analysed through simulation in MSC ADAMS. Some of the critical components have been evaluated for stress-deflection behavior in static condition before manufacturing. The performance of the system has been demonstrated in laboratory successfully.

Keywords Field robot · Underground coal mine · Tele-robotics · Remote surveillance · Simulation

D.N. Ray (✉) · R. Das · B. Sebastian · S. Majumder
SR Lab, CSIR-CMERI, Durgapur 713209, West Bengal, India
e-mail: dnray@cmeri.res.in; dipnarayan.ray@gmail.com

S. Majumder
e-mail: sjm@cmeri.res.in

B. Roy
ADO Group, CSIR-CMERI, Durgapur 713209, West Bengal, India

1 Introduction

Coal is a vital source of energy in India and it supplies about half of the energy demand of the country. It is imperative to use renewable energy in a broader manner, but use of coal has still remained an old and dependable method. Planning Commission predicted that in the years 2031–32 coal will also be used to generate 47 % of the energy requirement of India (Sreenivas and Bhosale 2013). Every year India has to import large amount of coal from foreign countries in order to bridge the gap between demand and production. Most of the coal mines are underground and hence little difficult to extract coal. The non-availability of proper coal extraction methods is a major hindrance for coal industries in India. Workers have to enter narrow and constricted region with life risks. Mine gas is a serious threat, so it is necessary to develop technologies capable of extracting coal in a safe and secure manner. Robotic systems must be equipped with sensors which will collect data on a routinely basis and provide it to the mine manager remotely. A check must be done on the hazardous gas content, humidity and temperature before letting the workers enter the tunnel.

Only a few robotic technologies have been developed till now for conducting operations in mines. Mobile robots in mines are mainly used for three purposes: (a) coal extraction (b) mine mapping (c) surveillance and rescue operations. Tele-operated or automated Load-Haul-Dump trucks provide much more efficiency in the task of coal extraction than mobile robots. So only a single robot developed by Field Robotics Center, Carnegie Mellon University, USA has been found till date, which was able to extract coal without any human operator (Sahffer and Stentz 1992). Abandoned mines are hazardous to both surface life as well as mining operations in the neighbourhood. So mine mapping is an important task to overcome this threat and assist in future mining operations. Major research works have been reported in the domain of mine mapping. Groundhog by Carnegie Mellon University (Watzman 2002), Gemini by Sandia National Laboratories (Albuquerque 2011) is examples of such few robots. Sub-terranean robot (SR), developed by CSIR-CMERI, Durgapur is perhaps the first attempt in India towards the development of an experimental mobile robot for surveillance in the partially or fully flooded mine tunnels of Indian coal mines (Ray et al. 2009a, b; Maity et al. 2013). The robot has a caterpillar type, amphibian configuration which can operate both on dry land as well as water. Also it can either crawl on the bed or swim at the surface of any water-body. The system uses an underwater camera for locating a victim inside a mine tunnel (dry or water-logged) and SONAR for generating the map of the traversed path/tunnel.

Though several robots have been developed around the world, even robots are commercially available, still robots for monitoring the underground coal mine environments are not available. This is due to the fact that each and every mine is different from the others. Coal mines are different from copper mines or gold mines. Even each coal mine is different from the other due to different geological nature (such as types of soil, presence of rocks etc.) and position (location of surface water

bodies), gas content, depth under the ground, method of extraction etc. So the robots to be used for underground mines are also to be mine specific as well as application specific. Several guidelines set up by the Director General of Mine Safety (DGMS), Dhanbad have to be followed strictly (DGMS 2012).

As a result the Sub-terranean robot earlier developed by CSIR-CMERI, Durgapur for surveillance purpose cannot be used for the application of environment monitoring.

So, some of the major challenges for designing the present system are as follows:

- The operating voltage should be restricted to 32 V_{DC}.
- There should not be any spark while operating the system in underground tunnels. Spark suppression techniques need to be adopted in the electronic circuits/connections.
- All the electronics systems should be kept confined in metallic enclosures.
- No inflammable materials to be used in developing the body

The present paper represents the issues related to the design and analysis of the robotic system, where as the earlier work (Ray et al. 2015) focuses towards the development and lab-scale validation of the system. The analysis supported by the stress-strain-deflection evaluation and dynamic simulation has not been presented earlier. How the dynamic simulation has helped to revise the design is mentioned here. This paper is organized as follows: design, description and operation of the system follow this introduction; then the approximate mathematical modeling and simulation have been presented. Results, discussion and conclusion including the future scope of the work come thereafter.

2 Design of the Concept Model

The challenges mentioned above have been taken care of while designing the system. The design of a mobile robot largely depends upon the working environment and its application area. The information about the type of working environment plays the major role towards the selection of configuration (wheeled or track). A large number of literatures are available for deciding which configuration to adopt in different environments. With reference to the past experience, the wheeled model is preferred to track model for mobile robots operating in underground coal mines to avoid choking of coal flakes in between the track belt and pulleys (Ray et al. 2009a, b). Therefore wheeled configuration has been selected for smooth locomotion in underground coal mines. The grasshopper configuration adopted in case of All Terrain Mobile Robot (ATR) has also been adopted here for establishing stability of the mobile system (Maity et al. 2007). The 3D concept model of the system has been presented in Fig. 1a and all its associated mechanical components have been depicted in Fig. 1b.

The robot uses two graphite-brushed DC motors to supply driving power. The power of the DC motors was determined from earlier experience

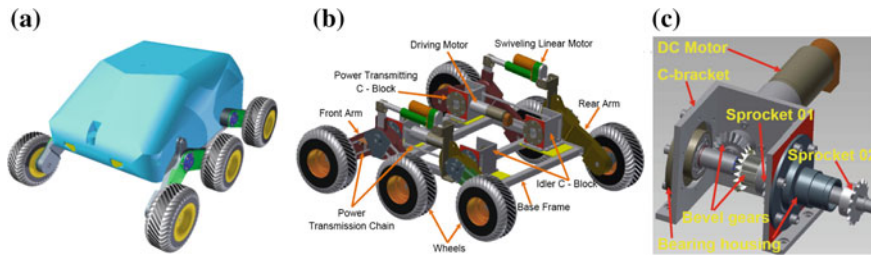


Fig. 1 **a** 3D concept model. **b** Mechanical chassis with drive and transmission system. **c** Integrated drive unit fitted with a DC motor

(CSIR—CMERI 2012). The power is transmitted to the wheel through a set of (Miter) bevel gears and chain—sprocket system. The (left and right) drive bracket (C-block) houses the driving motor, bevel gears and the sprocket as shown in Fig. 1c. Six-wheeled configuration has been employed for most stable movement over very rough terrains. The front two wheels are mounted on a single inverted Y-shaped rocker-bogie type bracket (Front arm) which also houses the transmission system for those two wheels. This front arm is actively compliant using a linear actuator to against shock. Attempt has also been made to use springs instead of linear actuators. The rear wheel is mounted on a smaller piece of bracket (rear arm). Rear arm is passively compliant. Power is also transmitted from the front to the rear through chain—sprocket mechanism so that all the three wheels on one side should rotate with same speed.

Power is another major issue in case of mobile robots operating in outdoor environments. This restricts the mission time for any operation. At present, a lot of advancements have taken place in the field of battery technology which has enhanced the power to volume ratio and thereby increased the mission time with reference to conventional lead acid batteries used earlier. Such a comparison has been presented in Fig. 2a and it reveals that the Li-Ion is most dense energy battery (160 W h/lcg) (CSIR—CMERI, Durgapur 2012). Li-Ion battery is used here.

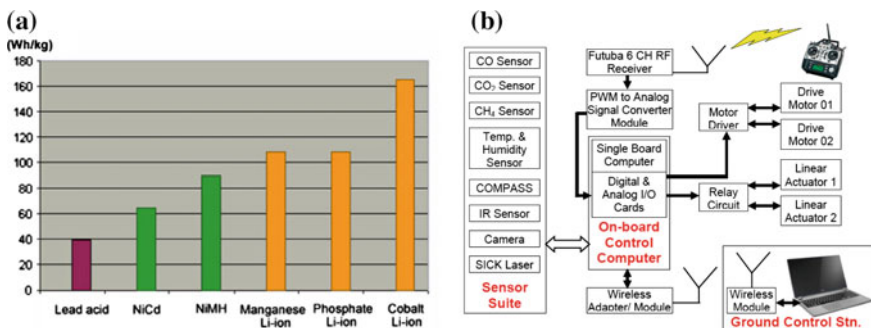


Fig. 2 **a** Comparison of energy densities of popular batteries. **b** Architecture of the mobile robot with option for remote controlling

The present robot is supposed to operate in gaseous mines for monitoring the underground environment. These mines sometimes contain CH_4 which often causes fire hazards. To satisfy the DGMS norms, as mentioned above, the whole unit is confined inside a metallic chamber with spark suppression plug-and-play electronic modules as shown below. The operating voltage has been limited to 24 V only.

The proposed system contains five major operational blocks; sensor suite, power block, control unit, signal/communication system and actuation block. Sensor suite contains different navigational sensors, such as (six nos.) IR sensors, Compass, SICK Laser, camera and operational sensors, such as CO sensor, CO_2 sensor, CH_4 sensor, Temperature and Humidity sensor. These sensors are powered with a separate 5 or 12 V supply and the output analog or digital signals are fed to the on-board Single Board Computer (SBC) for processing through a set of AD/DA cards. The power block includes a 24 V Li-Ion battery bank, 24–12 V and 5 V DC-DC converters, power distribution terminals for 24, 12 and 5 V for different equipments, actuators, instruments. The voltage and current readings of the batteries are displayed on two displays. The robot will be controlled by an on-board Single Board Computer (SBC) with cascaded support from microcontrollers. Due to limited number of analog and serial input terminals of the SBC, the output of six IR sensors and four gas sensors are separately processed through two microcontroller boards. The robot will use RF communication channel for communicating with its command station. Two different communication channels may be used for data/command and video streaming. The architecture of the system has been presented in Fig. 2b using schematic block diagram.

3 Operation of the System

Tele-operated Mobile Robot (TMR) is a remote controlled mobile robot along with limited autonomous mode. The robot uses wireless communication for communicating with the command control station. There are four different modes of operation, computer controlled, joystick based, voice command based and limited autonomous mode as shown in the Fig. 3a. The computer controlled mode can be activated from the remote command control station through an interactive GUI as shown in Fig. 3b. There are six different segments on the GUI such as graph windows, command response interface, laser data display, data logging segment, diagnostic window and camera display. The robot can also be operated using a 2.4 GHz joystick. The forward and reverse movements, left and right turns for the robot can be performed using this joystick. There is also a provision for pan-tilt operation of the camera mounted on the robot.

Alternate mode of operation for the mobile robot uses voice commands. There are a few specific voice commands by the user, such as ‘move forward’, ‘move backward’, ‘enable joystick’, ‘enable voice’, ‘system stop’, ‘turn left’, ‘turn right’ etc. For better voice recognition or change of operator new voice training needs to

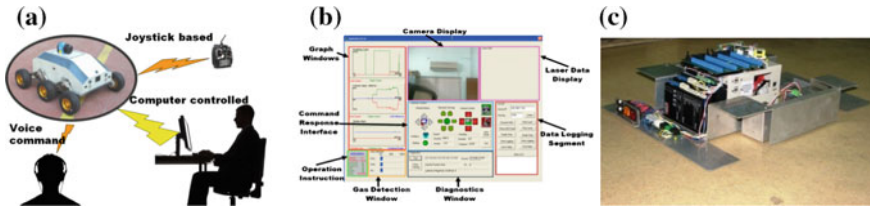


Fig. 3 a Modes of operation of the tele-operated mobile robot. b Interactive graphical user interface (GUI). c Plug-and-play electronics module

be performed. The performance of the voice command based system increases with the increase in training session.

The limited autonomous mode can be activated from the GUI and this mode uses the on-board navigation sensors for safe navigation. There are six obstacle (Infrared i.e. IR) sensors, two each at the front and rear, one on each side of the robot. The robot uses pre-defined instructions to move safely in a crowded environment. Some of the predefined instructions are; ‘take left turn when there is an obstacle on the right side (i.e. right IR is blocked)’, ‘take right turn when there is an obstacle on the left side (i.e. left IR is blocked)’, ‘make reverse movement when the front is fully blocked (both IRs are blocked)’. A compass module will assist the system for heading correction.

In case of all the modes, the operational as well as navigation data are transmitted to the command control station set up at the mine manager’s office halfway through wireless and halfway through wire. The robot operating inside the underground mine tunnels communicates with the underground station through wireless either directly or through repeaters in between. This underground station is then connected with the over ground station through wire passing through the mine escalator shaft. The over ground station is connected with the main server with which anyone can connect to receive the monitoring data.

4 Approximate Mathematical Modeling of the Robot

The kinematics and dynamics model of the system is very much important to control the robot in desired trajectory. The following assumptions have been made for simplified modeling (Caracciolo et al. 1999).

- The system is rigid and moving on a horizontal (x–y) plane only.
- The linear and angular velocities are relatively low.
- Tire deformation and effect of suspension is neglected.
- The wheels made contact with the ground at a single geometric point only.
- The weight of the system only contributes to the vertical load on wheels.
- Longitudinal wheel slippage is neglected.
- The mass of the system is distributed uniformly.

5 Kinematic Model

The vehicle is assumed to move on a two dimensional plane (x, y) with reference to a fixed frame (X, Y) as shown in Fig. 4. For ease of modeling the local frame is defined at the centre of mass (G) of the system at a distance a, b and c from front, middle and rear wheel respectively (Caracciolo et al. 1999). The generalized co-ordinates can be represented as $q = [X \ Y \ \theta]^T \in R^3$, where X, Y denote the position of centre of mass (G) and θ is the orientation of the local frame with respect to the inertial frame. $v = [v_x \ v_y]^T \in R^2$ is the velocity vector of centre of mass in local frame with v_x and v_y as the longitudinal and lateral velocity respectively of the vehicle. The kinematic equation of motion using rotation matrix can be represented as follows

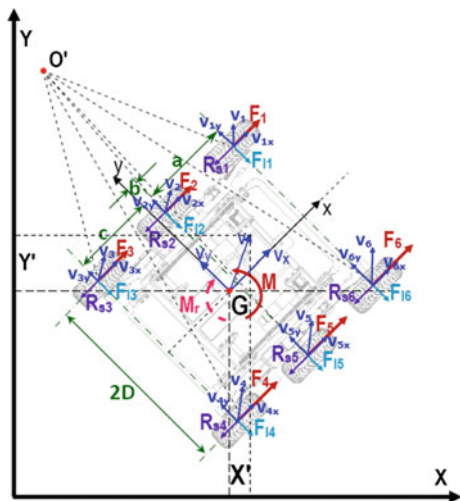
$$\dot{q} = \begin{bmatrix} \dot{X} \\ \dot{Y} \\ \dot{\theta} \end{bmatrix} = \begin{bmatrix} \cos \theta & -\sin \theta & 0 \\ \sin \theta & \cos \theta & 0 \\ 0 & 0 & 1 \end{bmatrix} \begin{bmatrix} v_x \\ v_y \\ \omega \end{bmatrix}$$

where $\dot{q} \in R^3$ denotes the generalized velocity vector and ω is the angular velocity of the vehicle.

Additional velocity constraints with reference to the inertial frame are required to be considered to complete the kinematic model of the system. The velocities of each contact point of the wheels with the ground can be visualized from Fig. 4 and they must satisfy (Pazderski et al. 2004a, b)

$$v_L \cong v_{1x} = v_{2x} = v_{3x}, v_R \cong v_{4x} = v_{5x} = v_{6x}, v_F \cong v_{1y} = v_{6y}, v_M \cong v_{2y} = v_{5y}, v_B \cong v_{3y} = v_{4y}$$

Fig. 4 Free body diagram and velocity relationship for kinematics and dynamic modeling of the robot (Pazderski et al. 2004b)



where v_L and v_R represent the longitudinal co-ordinates of left and right wheel velocities respectively; v_F , v_M and v_B are lateral co-ordinates of velocities of front, middle and rear (back) wheels respectively. For straight line motion, the lateral skidding is absent and so the lateral skidding velocity $v_{iy} = 0$ and angular velocity of the vehicle $\omega = 0$. The control inputs for the kinematic model without longitudinal slip are the angular velocities of left (ω_L) and right (ω_R) wheels and they are related with the longitudinal and angular velocity of the local frame as follows

$$v_x = \left(\frac{\omega_R + \omega_L}{2} \right) r, \omega = \left| \frac{\omega_R - \omega_L}{D} \right| r$$

where r and $2D$ represent the effective radius of the wheels and spacing between the left and right wheels as shown in Fig. 4. If the lateral slip is present, the velocity of lateral slip of the vehicle can be denoted (Watzman 2002) by $v_y + x_{ICR}\omega = 0$, where x_{ICR} is a co-ordinate of instantaneous centre of rotation (O') of the robot expressed along x -axis. This equation is not integrable and hence can be written in Pfaffian form as

$[-\sin \theta \quad \cos \theta \quad x_{ICR}] [\dot{X} \quad \dot{Y} \quad \dot{\theta}]^T = A(q)\dot{q} = 0$. As the generalized velocity \dot{q} is always in the null space of A , it can be written that $\dot{q} = S(q)\eta$, where $\eta \cong [v_x \quad \omega]^T \in R^2$ is a control input at kinematic level.

$S \in R^{3 \times 2}$ is the following matrix, $S(q) = \begin{bmatrix} \cos \theta & x_{ICR} \sin \theta \\ \sin \theta & -x_{ICR} \cos \theta \\ 0 & 1 \end{bmatrix}$ which satisfies

$$S^T(q)A^T(q) = 0.$$

6 Dynamic Modeling

The free body diagram of different forces acting on the vehicle has been shown in Fig. 4 (Pazderski et al. 2004b). Wheels develop tractive forces F_i for the movement of the system and subject to longitudinal resistive forces R_{Si} , for $i = 1, \dots, 6$. The wheel tractive force on each side needs to be equal so as to minimize the longitudinal slip that means $F_1 = F_2 = F_3$ and $F_4 = F_5 = F_6$. Lateral forces F_{li} act on the wheels as a result of the lateral skidding. The longitudinal resistive force and the lateral force can be denoted as $R_{si}(\dot{q}) \cong \mu_r N_i \text{sgn}(\dot{x}_i)$, $F_{li} \cong \mu N_i \text{sgn}(\dot{y}_i)$.

N_i is the vertical load on i -th wheel due to the weight of the vehicle. The load shared among the wheels can be calculated using Coulomb friction model. The rolling friction and the lateral co-efficient of friction are μ_r and μ respectively. A resistive moment M_r is acting around the centre of mass induced by the longitudinal resistive (R_{si}) and lateral (F_{li}) forces.

The equations of motion with reference to the local frame for a vehicle with mass m and inertia I about the centre of mass can be described as:

$$ma_x = 3F_1 + 3F_4 - \sum_{i=1}^6 R_{si}, ma_y = - \sum_{i=1}^6 F_{li} \text{ and } I\ddot{\theta} = 3D(F_1 - F_2) - M_r$$

The dynamic equation of the system can be obtained from Euler-Lagrange principle with Lagrange multipliers as follows

$M(q)\ddot{q} + R(\dot{q}) = B(Q)\tau + A^T(q)\lambda$, where $M \in R^{3 \times 3}$ is the diagonal, positive definite matrix represented as

$$M \begin{bmatrix} m & 0 & 0 \\ 0 & m & 0 \\ 0 & 0 & I \end{bmatrix} \text{ and } R(\dot{q}) \in R^3 \text{ is the vector of resultant reactive forces denoted}$$

as

$$R(\dot{q}) = \begin{bmatrix} R_s(\dot{q}) \cos \theta - F_l(\dot{q}) \sin \theta \\ R_s \sin \theta + F_l \cos \theta \\ M_r(\dot{q}) \end{bmatrix} \text{ and the input matrix } B \in R^{3 \times 2} \text{ is defined as}$$

$$B(q) = \frac{1}{r} \begin{bmatrix} \cos \theta & \cos \theta \\ \sin \theta & \sin \theta \\ -D & D \end{bmatrix}.$$

The term $\tau = [\tau_L \quad \tau_R]^T \in R^2$ represents the torques generated by the left and right side motor respectively and these contribute to the actuation forces (F_i) on the wheels. The reactive forces and torque are calculated as follows:

$$R_s(\dot{q}) = \sum_{i=1}^6 R_{si}(\dot{q}), F_l(\dot{q}) = \sum_{i=1}^6 F_{li}(\dot{q}) \text{ and}$$

$$M_r(\dot{q}) = a[F_{l1}(\dot{q}) + F_{l6}(\dot{q})] + b[F_{l2}(\dot{q}) + F_{l5}(\dot{q})] - c[F_{l3}(\dot{q}) + F_{l4}(\dot{q})]$$

For the purpose of simplification for controlling the robot, one can express the dynamic equation in terms of η and $\dot{\eta}$ as $\overline{M}\ddot{\eta} + \overline{C}\dot{\eta} + \overline{R} = \overline{B}\tau$, where $\overline{M} = S^TMS, \overline{C} = S^TMS, \overline{R} = S^TR$ and $\overline{B} = S^TB$.

7 Simulation and Analysis

Virtual simulation is an important and essential step for evaluation of the design models in order to reduce time and cost. The simulation of the robot was performed to analyze the functionality and expected capability. The model has been developed in details with real-time, easily available components in Autodesk Inventor 2014 and simultaneously the stress and deflection characteristics of the critical components in static condition have been evaluated with the integrated solver. The mass

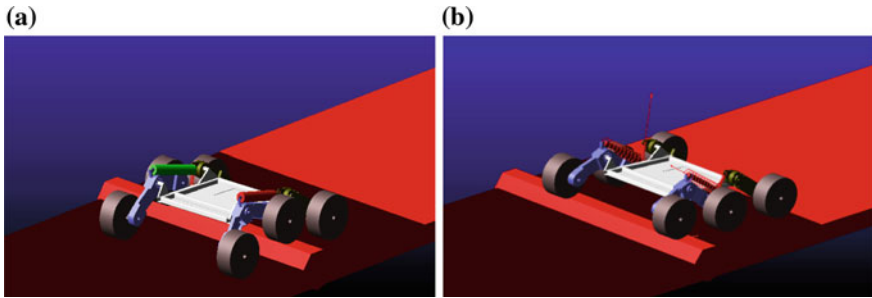


Fig. 5 Movement of the robot over the test track using **a** linear actuators, **b** springs

distributions, inertia properties, contact and friction forces between the wheel and ground were provided for performing the simulations. For successful simulation of the model, the robot parts were provided with optimal weights as expected for the real model assembly. The material properties have been selected closed to the actual material used for the development. The front arm and the drive bracket (C-block) can be identified as the most critical components. The different forces and moments acting at different locations of those components have been identified and used in the simulation. The overall mass of the prototype has been found around 60 kg and this load is assumed to act equally on all the six wheels (i.e. 100 N on each wheel). MSC ADAMS is the multi-body simulation software used to test the dynamic behaviour of the model. A test track was built with a bump. The system was made to traverse along the track alternately using springs and linear actuators.

The robot has a wheel diameter of 220 mm and wheel width of 90 mm. Initially linear actuators were used, but later two spring suspension systems have been mounted on either side as shown in Fig. 5. Both these actuators/springs are attached to an intermediate point on the chassis and providing damping to the motions of the front and rear arms. The spring stiffness coefficient and damping coefficient were taken to 2 and 0.05 N/mm. The coefficient of friction between the wheel and the road was taken to be 0.9. The final decision for selection of linear actuator or spring is based on the vertical motion (oscillation) of the centre of mass of the system when the robot travels along the test track as shown in Fig. 5a, b.

8 Results and Discussions

The design of the robotic system considering various limitations for underground coal mines have been carried out using prior knowledge, expertise and experience. The arm and wheel configuration is based up on the previous works for development of an all terrain mobile robot and sub-terranean robot for underground coal mines. The motor power, capacity of the battery, drive and transmission system,

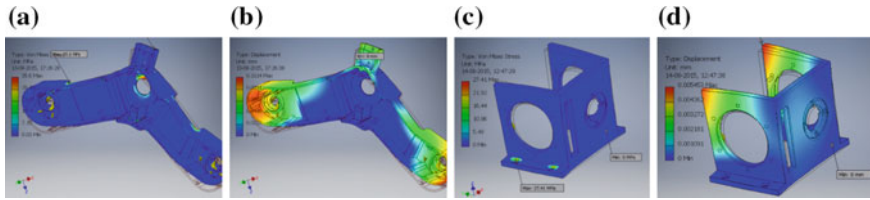


Fig. 6 Front arm—**a** Von Mises Stress. **b** Deflection; C-Bracket. **c** Von Mises Stress. **d** Deflection

communication and operation methodologies have been identified/developed based on the past experience. Two major issues were found critical during the design of the system. They are (1) optimized design of the front arm and drive bracket and (2) dynamic behavior of the system for use of linear actuators or springs.

The Von Mises stress and the deflection of the two critical components have been computed to check whether the design can withstand the load or not. It can be found from Fig. 6a, b that the maximum Von Mises stresses at the most critical points for the front arm and the drive bracket (C-block) are far less than the yield values of the corresponding materials. They are 35.6 and 27.41 MPa for the front arm and drive bracket respectively in comparison to the yield strength of the respective materials 275 MPa (Al 6061) and 207 MPa (Steel) respectively. The deflections are also negligible. Those are 0.11 and 0.005 mm for the front arm and drive bracket respectively. The deflections of both the components will be restricted to some extent as soon as the assemblies are completed. The Von Mises stress and the deflection for the front arm at the critical point have been shown in Fig. 6a, b respectively and the same for the drive bracket has been presented in Fig. 6c, d respectively.

The robot successfully overcame the bump of diameter 100 mm in both the cases using linear actuators or using the springs. From the analysis it can be inferred that the springs attached to the front arms experience more deformation than the rear arms. Graphs depicting the variations in the central markers were generated for both the cases as shown in the Fig. 7a, b. For the same simulation time of 3 s and same step size it can be seen that the system with spring (Fig. 7b) is undergoing more vibration than that of with the linear actuators. The maximum amplitude of vibration of the central marker was recorded to be 40 mm for both the cases. Based on this analysis, the design with linear actuators has been finalized and developed.

9 Conclusion

Design issues are one of the most important issues towards the successful development of any mechanical system. Presently different analysis and simulation tools help to evaluate the design with respect to sustainability, functionality and above all

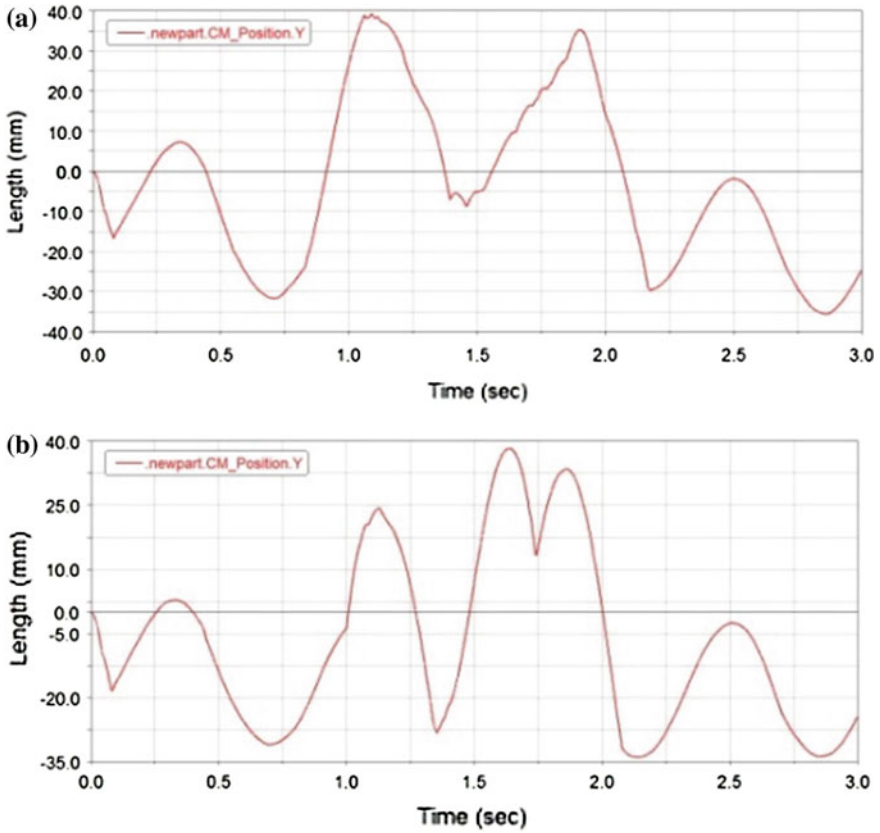


Fig. 7 Vertical oscillation of the centre of mass while moving over the test track using **a** linear actuators, **b** springs

optimization. Besides these, here another major challenge was to fulfill the DGMS norms and regulations for safe operation of the system in underground coal mines. Application of robotic technology for different applications in underground mines, especially the coal mines, is the demand of the day. The present system is a remote environment monitoring robot with a set of gas sensors and navigation sensors. The system is connected with the mine manager's office halfway through cable and halfway through wireless. The gas content of any tunnel can be assessed by the mine manager before starting extraction in that specific tunnel to avoid any mishap. The critical components of the mechanical design have been evaluated using integrated solver of Autodesk Inventor 2014 and the dynamic behaviour of the system is simulated in MSC ADAMS. The inferences from these analyses have been incorporated in the design and development has been done. Presently, clearance from the DGMS, Dhanbad is awaited for testing in underground coal mines filled up with hazardous gases. The integrated prototype developed is shown in Fig. 8a–d during various

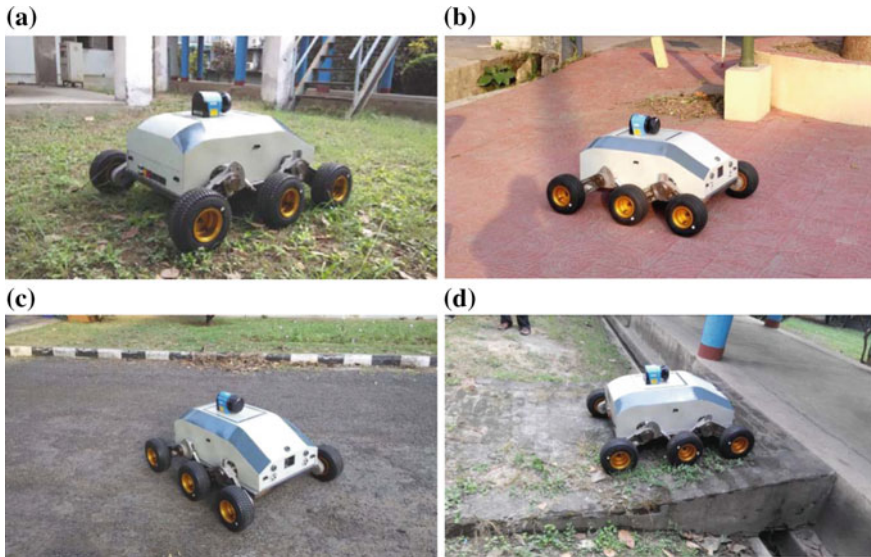


Fig. 8 Lab-scale testing of the robot on different kind of terrains **a** grassy land, **b** concrete pavement, **c** asphalt road, **d** inclined slope

lab-scale trials. The system has two major limitations presently. One is its large turning radius leading to higher power requirement and other is unsuitability of operation in water logged mine tunnels. Work is in progress to develop an amphibian model of the prototype which will have shorter turning radius.

Acknowledgments The present work is funded by Ministry of Coal, Govt. of India under coal S&T project head—MT 162. Authors are grateful to Ministry of Coal and CMPDI, Ranchi for their funding and support. Authors are also thankful to staffs and project assistants of SR Lab and other people who have directly or indirectly helped to develop this system.

References

- Albuquerque, N. M. (2011). Sandia Labs' Gemini-Scout robot likely to reach trapped miners ahead of rescuers. Sandia Labs News Releases. August 16, 2011.
- Caracciolo, L., De Luca, A., & Iannitti, S. (1999). Trajectory tracking control of a four-wheel differentially driven mobile robot. In *Proceedings of IEEE International Conference on Robotics and Automation* (vol. 4). Detroit, Michigan.
- CSIR—CMERI, Durgapur (2012). Completion report on Supra Institutional Project (SIP-24): Capability in mobile robot development for industrial, outdoor and hazardous applications.
- DGMS, Dhanbad, India (2012). Standard procedure for grant of equipment approval By DGMS. http://www.dgms.net/mse_proc.htm. January 20, 2012.
- Maity, A., Ray, D. N., Majumder, S., & Mistry, K. K. (2007). An all terrain mobile robot with passive compliance. In *Proceedings of Factory Automation, Robotics & Soft Computing, NIT, Warangal* (pp. 73–78).

- Maity, A., Majumder, S., & Ray, D. N. (2013). Amphibian subterranean robot for mine exploration. In *Proceedings of International Conference on Robotics, Biomimetics, Intelligent Computational Systems, Indonesia*.
- Pazderski, D., Kozlowski, K., & Lawniczak, M. (2004a). Practical stabilization of 4WD skid-steering mobile robot. In *Proceedings of 4th International Workshop on Robot Motion and Control, Puszczkovo, Poland*.
- Pazderski, D., Kozlowski, K., & Dixon, W. E. (2004b). Tracking and regulation control of a skid steering vehicle. In *Proceedings of American Nuclear Society Tenth International Topical Meeting on Robotics and Remote Systems, Gainesville, Florida*.
- Ray, D. N., Dalui, R., Maity, A., & Majumder, S. (2009a). Sub-terranean robot: A challenge for the Indian coal mines. *The Online Journal on Electronics and Electrical Engineering*, 2(2).
- Ray, D. N., Maity, A., & Majumder, S. (2009b). Comparison of performance of different traction systems for Terranean Robots. In *Proceedings of National Conference Machine and Mechanisms, NIT, Durgapur* (pp. 151–158).
- Ray, D. N., Maity, A., Majumder, S., Roy, B., & Karmakar, S. (2015). Design and development of a mobile robot for environment monitoring in underground coal mines. In *Proceedings of 2nd International Conference in Advances in Robotics (AiR), BITS Pilani, Goa*.
- Sahffer, G., & Stentz, A. (1992). A robotic system for underground coal mining. In *Proceedings of IEEE International Conference on Robotics and Automation, France* (pp. 633–638).
- Sreenivas, A., & Bhosale, K. (2013). *Black and dirty: the real challenges facing India's coal sector*. Pune, India: Prayas Energy Group.
- Watzman, A. (2002). Groundhog debut: Robot successfully maps portion of abandoned mine. *Carnegie Mellon Today*.

Design-of-Experiments (DOE) to Compute the Effect of Chromium Abrasives in Kerosene Oil as Dielectric of EDM of OHNS Die Steel

Kamal Sabharwal and Paramjit Singh

Abstract Experimentation is a valuable way to express casual claims in pragmatic manner at certain minimum confidence level. DOE popularly known as technique of metamodels is adopted as useful statistical experiments design method for process optimization. In the targeted research, authors used powerful DOE technique (Taguchi methodology) to compute the material removal rate performance of chromium abrasives suspended kerosene oil as dielectric during electro discharge machining of oil hardened non shrinking steel. Besides concentration of chromium abrasives in kerosene oil, other five input control variables namely electrode polarity, peak current, pulse on time, pulse of time and gap voltage are chosen for designing the experimental plan. Genichi Taguchi methodology' recommended mixed orthogonal array L_{18} with signal to noise ratio idea is used to optimize the output performance characteristic. Fisher's recommended F-test alongwith analysis of variance tool is used to identify the significant control variables and their contribution as process input.

Keywords Design of experiments · Taguchi · Abrasives mixed EDM · ANOVA · F-test

K. Sabharwal
Mechanical Engineering Department, Ramgarhia Institute of Engineering & Technology,
Phagwara 144402, Punjab, India

P. Singh (✉)
Mechanical Engineering Department, Amritsar College of Engineering & Technology,
Amritsar 143001, Punjab, India
e-mail: er.pannu266@gmail.com

1 Introduction

Efficient ‘designing the experiment’ and proper ‘analyzing the experiment’ are the two mutually intermingled tasks needed to draw important conclusions about the effects and causes of a process (Dean and Voss 1999). Simulation studies and shop floor experimentation involving large number of control variables finds exclusive use of DOE technique (Box et al. 2005). In 1930, Sir R.A. Fisher invented this multi-facet technique for the purpose to gain maximum output in his fields by varying crop varieties. In 1950, R.C. Bose makes further expansion in technique by adding combinatorial designs. Later in 1960s the concepts of signal to noise (S/N) ratio and orthogonal arrays (OA) purposed by Dr. Genichi Taguchi makes this technique as most reasonable tool for researchers (Taguchi 1986; Dehnad 1989; Montgomery 1997). Industrial engineers are the key user of this technique for modeling of production process.

Among all the feasible nonconventional machining process, electro discharge machining (EDM) is known for its precise cutting on conductive work materials. Anode and cathode heads of EDM, when connected to external potential source, produces tiny and heavily energized sparks in the inter-electrode narrow gap. The huge thermal energy of these intermittent sparks is responsible to melt and erode approaching workpiece and electrode surfaces. Despite having favorable pro like no chatter during machining, no vibrations, no mechanical stress etc. cons like high surface roughness with low material removal rate etc. are the major barriers to bring EDM in front production lines in industry. To remove these barriers, research investigations in the past mainly concentrated on the use of abrasive suspended fluid dielectrics (Kansal et al. 2005; Kumar and Singh 2010; Kolli and Kumar 2014), powder metallurgy processed electrodes (Simao et al. 2002; Beri et al. 2008; M'Saoubi et al. 2014; Gill and Kumar 2014), ultrasonic assistance in EDM (Huang et al. 2003; Zhang et al. 2006; Shabgard and Alenabi 2015).

This experimental work focused on the use of DOE (Genichi Taguchi approach) methodology to compute the MRR performance of chromium abrasive suspended kerosene oil as dielectric in blind hole sinking experimentation on OHNS die steel plate.

2 Materials and Equipment

OHNS die steel (O₂ group) plate of 40 mm thickness was the target workpiece to sink blind holes exactly of similar shape as that of tool electrode. Table 1 details OHNS material's chemical composition. Chromium abrasive powder and commercial kerosene oil were taken to prepare dielectric fluid for performing experiments. Electrolytic copper rod was taken as tool electrode.

A sinking OSCARMAX-S645 CNC electro discharge machine is used to perform blind holes of circular shape on OHNS plate. Up and down movement of

Table 1 Chemical constituents in OHNS die steel

Element	C	S	Mn	Cr	V	Mo	Ni	Iron
Weight (%)	0.82	0.18	0.52	0.49	0.19	0.13	0.05	Balance

Source Davis (1994)

9.5 mm diameter electrolytic copper rod electrode controlled by integrated servo control mechanism of machine during experiments. A special tank of mild steel sheet (3 mm thickness) made in welding section of workshop to mix chromium abrasives (100 μm grain size) and commercial kerosene oil. Utmost care was taken to supply abrasives suspended kerosene dielectric in the gap between OHNS workpiece surface and copper electrode during experimentation. An electrically operated small fluid pump placed in tank for continuous stirring of abrasives mixed kerosene dielectric. A 300 mm long pipe was fitted on the nozzle of pump. Ten small holes were drilled in this pipe to obtain uniform and continuous mixture of abrasives in kerosene oil. Mitutoyo make precision balance with digital display is used to note weight of OHNS plate before and after every cut.

3 Experimental Procedure

3.1 Design of Experiments

In a study, Ghoreishi and Atkinson (2002) noted that the material erosion rate and time elapsed in machining by EDM process is highly influenced by the product of energy transferred in single pulse and number of pulses per unit time. Proper selection of control variables and their variation range is important consideration in the process. In the targeted experimental work, total six control variables including tool electrode polarity, peak current, pulse on time, pulse off time, gap voltage and concentration of chromium abrasives in kerosene oil are taken as process inputs. Table 2 summarizes levels of control variables alongwith natural values of all variables at these levels.

Table 2 Design scheme used for control variables

Symbol	Control variable	Units	No. of levels	Level 1	Level 2	Level 3
A	Polarity	–	2	+ve	–ve	–
B	Peak current	A	3	4	8	12
C	Pulse on time	μs	3	90	150	200
D	Pulse off time	μs	3	30	45	60
E	Gap voltage	V	3	30	40	50
F	Chromium abrasives concentration in kerosene oil	g/l	3	0	5	10

A well structured experimental plan always contributes in analyzing entire variable space needed to optimize the process. Experimental design comprises a sequence of steps performed in a well defined fashion to study the relationship among input control variables, which affects process output. Genichi Taguchi's method made it possible to analyze entire variable space from the output of few experiments. In the targeted research work, Taguchi approach's recommended mixed level L_{18} orthogonal array is chosen to design the matrix which defines the variation of control variables at concerned levels.

3.2 Screening Formula

High material erosion rate is most essential characteristic to make EDM process feasible in production line of mechanical industry. Genichi Taguchi recommended 'larger-is-better' signal to noise ratio (S/N) quality measure is chosen to analyze and optimize process output in terms of MRR values. 'Larger is better' type S/N ratio quality measure used here is written in Eq. (1):

$$\{S/N\}ratio = -10\log \left[\frac{1}{Z} \sum_{j=1}^Z \left(\frac{1}{m_j^2} \right) \right] \quad (1)$$

where m_j denotes the observed MRR value and Z denotes total number of repetitions.

3.3 Analysis of Variance and F-Test

ANOVA, a statistical technique, works on the principle of breakdown of total variability of experimentally observed findings into definite components of variance to judge their impact in the process output. Interestingly, basic fundamental behind ANOVA technique is to evaluate residuals with variance value. ANOVA makes the use of p-values and standard F-test to assess % contribution of control variables and their significance in the process. To draw the significance of input variable, standard F-ratio value compares variable's effect variance with randomness (residual) variance (Logothetis 2004). In the targeted research work, ANOVA, p-values and F-test are used to analyze experimental findings for MRR characteristic. Following G. Taguchi method's standard procedure and by keeping degrees of freedom in picture, statistically obtained F-test values are compared with their counterparts taken from statisticians' tables (Pearson and Hartley 1972). Based upon this comparison, input control variables are categorized into significant and non significant variables. Standard statistical data analysis way based on S/N ratio data values is chosen in the present work. Main effects plot highlighting S/N data is made to view graphically the effects of control variables on MRR.

3.4 MRR Measurement

Integrated electronic timer of EDM machine is used to record the time elapsed in performing a particular experiment. Initial (before experiment) and final (after experiment) weights of OHNS plate are measured on precision balance used and the MRR values are calculated for corresponding experiment as per Eq. (2).

$$MRR \text{ (g/min)} = \frac{\text{Initial (before machining)weight (g)} - \text{final (after machining)weight (g)}}{\text{Time elapsed in machining (min)}} \tag{2}$$

4 Results and Discussion

Exactly, eighteen blind hole sinking experiments are performed on OHNS Die steel plate in chromium abrasives suspended kerosene oil as dielectric and the results are taken for MRR. It is important to mention here that these experiments were performed randomly to avoid the influence of miscellaneous unaccounted factors. Experimentally calculated MRR values, variation of natural and coded variables in form of designed matrix and S/N ratio values are shown in Table 3.

Table 3 Design layout: L₁₈ orthogonal array, signal to noise ratios and experimental results

Exp. run	Coded variables						Actual variable values						MRR (g/min)	S/N ratio (dB)
	A	B	C	D	E	F	A	B	C	D	E	F		
1	1	1	1	1	1	1	+ve	4	90	30	30	0	0.01957	-34.1703
2	1	1	2	2	2	2	+ve	4	150	45	40	5	0.01150	-38.7860
3	1	1	3	3	3	3	+ve	4	200	60	50	10	0.00934	-40.5902
4	1	2	1	1	2	2	+ve	8	90	30	40	5	0.11333	-18.9128
5	1	2	2	2	3	3	+ve	8	150	45	50	10	0.09511	-20.4355
6	1	2	3	3	1	1	+ve	8	200	60	30	0	0.08153	-21.7731
7	1	3	1	2	1	3	+ve	12	90	45	30	10	0.24818	-12.1048
8	1	3	2	3	2	1	+ve	12	150	60	40	0	0.19797	-14.0680
9	1	3	3	1	3	2	+ve	12	200	30	50	5	0.18274	-14.7632
10	2	1	1	3	3	2	-ve	4	90	60	50	5	0.00214	-53.4082
11	2	1	2	1	1	3	-ve	4	150	30	30	10	0.00181	-54.8415
12	2	1	3	2	2	1	-ve	4	200	45	40	0	0.00213	-53.4487
13	2	2	1	2	3	1	-ve	8	90	45	50	0	0.00539	-45.3718
14	2	2	2	3	1	2	-ve	8	150	60	30	5	0.00707	-43.0114
15	2	2	3	1	2	3	-ve	8	200	30	40	10	0.00601	-44.4202
16	2	3	1	3	2	3	-ve	12	90	60	40	10	0.00393	-48.1023
17	2	3	2	1	3	1	-ve	12	150	30	50	0	0.00621	-44.1385
18	2	3	3	2	1	2	-ve	12	200	45	30	5	0.00815	-41.7783

ANOVA and F-test statistical results are presented in Table 4.

Statistically calculated F-values in ANOVA table and same referred from “statisticians’ tables” significant effect of both tool electrode polarity and peak current is revealed for MRR characteristic of the process. F-value of electrode polarity is greater than F-values corresponding to other five variables involved. This observation shows that electrode polarity and peak current contributes 68.30 and 25.66 % in MRR of chromium suspended kerosene oil dielectric EDM process. Significant effect of both of these control variables is also observed from calculated P-values (0.000 and 0.005) which are less than 0.05 at ninety five confidence level. Other involved four control variables viz. pulse on time, pulse off time, gap voltage and chromium abrasive concentration in kerosene oil are moderately affecting MRR with a contribution of 0.05, 0.27, 0.34 and 0.24 % respectively. Moderate contribution of these variables is insignificant as the calculated F-values corresponding to all these variables are less than the F-value taken statisticians’ tables. Their insignificant effect is confirmed as P-values corresponding to all these variables are more than 0.05. It is important to mention here that all results including ANOVA and F-test statistics are confirmed at 95 % confidence level ($\alpha = 0.05$).

Graphic plots (main effects plot) of control variables using S/N ratio values are made with the help of Minitab 16 package and are shown in Fig. 1.

In inter-electrode gap, energy of discharge to erode material from worksurface is directly proportional to peak current supplied at the instant. This energy of discharge can be represented as per Eq. (3).

$$Z_d = \int_0^{t_0} D_v(t_0) C_p(t_0) dt \quad (3)$$

where Z_d : energy of discharge, D_v : discharge (gap) voltage, t_0 : pulse on time, C_p : peak current. Relationship given by Eq. (3) is appropriate in the targeted research work. Rising trend of MRR curve with levels 1-to-2-to-3 of peak current in main effects plot confirms the relation of Eq. (3). Each successful spark erodes small volume of material from OHNS plate in form of craters of indefinite shapes. This small amount of material melts immediately due to intense sparking temperature and washed away under the flowing pressure of chromium suspended kerosene oil. Total removed material per unit time is the measure of MRR. Sparks with more discharge energy at third level of peak current strongly hit OHNS surface plate and produces more deep and wide craters results higher MRR. Machining at +ve polarity condition erodes more material from OHNS steel as compare to -ve polarity condition. Heavy mass and high speed of +vely charged ions traveling in interelectrode gap produces more deep and wide craters on OHNS plate results more MRR. But in the reverse condition of polarity, -vely charged ions travels at low speed and hit OHNS plate with less striking momentum causing less MRR. Changing ‘on time per pulse’ from levels 1-to-2-to-3 shows insignificant effect towards MRR. Less amount of energy the pulses have at small ‘on time’ is probably insufficient to remove material from OHNS plate. On the other hand more ‘on time’ per pulse distributes pulse energy in expanded plasma channel. This results in lesser

Table 4 Analysis of variance and F-test for S/N data for MRR

Symbol	Source	DF	Seq SS	Adj SS	Adj MS	F-value	F-critical ^a	P-value	%age Contr.
A	Polarity	1	2518.54	2518.54	2518.54	79.62	5.99	0.000	68.30
B	Peak current	2	946.16	946.16	473.08	14.95	5.14	0.005	25.66
C	Pulse on time	2	1.93	1.93	0.96	0.03	5.14	0.970	0.05
D	Pulse off time	2	9.79	9.79	4.89	0.15	5.14	0.860	0.27
E	Gap voltage	2	12.43	12.43	6.22	0.20	5.14	0.827	0.34
F	Abrasive concentration	2	8.82	8.82	4.41	0.14	5.14	0.873	0.24
	Residual error	6	189.80	189.80	31.63				5.15
	Total	17	3687.46						

^aY-values are taken from statisticians' tables. Confidence level is 95 % ($F_{0.05,1,6} = 5.99$), ($F_{0.05,2,6} = 5.14$)

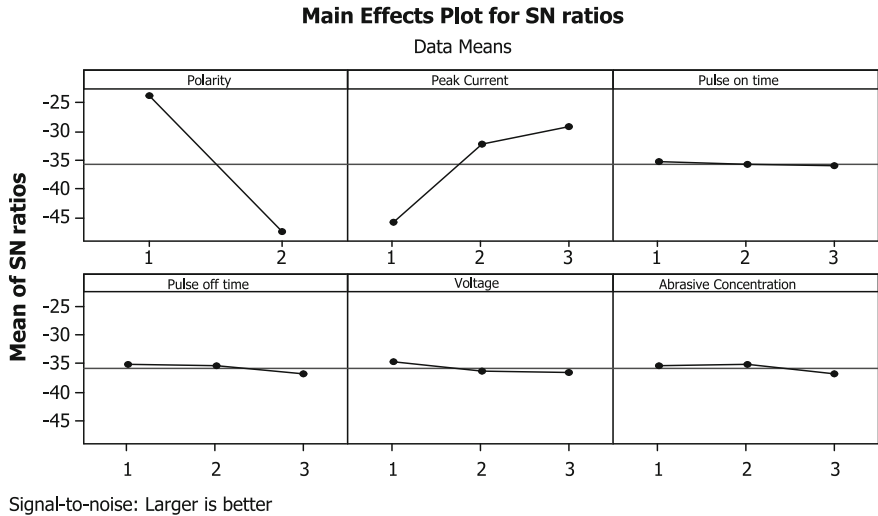


Fig. 1 Main effects plot for S/N ratio for MRR

energy density per pulse and net output is lesser MRR. Increased ‘off time’ from level 1-to-2-to-3 slightly lowers down MRR. More ‘off time’ means more the time no sparking between approaching surfaces of OHNS plate and copper tool electrode. No sparking means no erosion of OHNS material and hence reduced MRR. Changing gap potential from 30 to 40 and 40 to 50 has almost negligible influence on MRR. Addition of chromium abrasives in kerosene oil as dielectric is insignificant to change MRR of process. Chromium suspended kerosene dielectric gives slightly reduced MRR. This is probably due to the reason that chromium abrasives tiny particles increases the gap between OHNS steel surface and copper tool electrode during machining. In enlarged passage gap, discharge energy of pulse reduces which reduces its capability to eject more melted material from OHNS surface.

As per G. Taguchi method’s guidelines, larger is the S/N ratio—better is the overall process performance. Therefore levels of control variables with more S/N ratio represent optimized variable combination (Prassana et al. 2014). In this investigation, $A_1B_3C_1D_1E_1F_2$ (in Fig. 1) represents the optimum control combination for maximum process output i.e. MRR.

Calculated values of S/N ratio corresponding to each experimental run are taken to calculate average S/N ratio for each variable level. Each variable and associated levels gives a range of signal to noise ratio value. From this range ‘delta’ statistic values are taken using minimum and maximum S/N ratio values. These ‘delta’ statistic values are given in Table 5 and are used to compares the relative magnitude of variable effects. Larger is the delta statistic—larger is the variable affect on process output. Smallest ‘delta (Δ)’ statistic value (equal to 1.62 in Table 5) for pulse off time and largest the same for electrode polarity categorized them into the least influential control variable and the most influential control variable respectively.

Table 5 Response table for S/N data for MRR

Level	Polarity (A)	Peak current (B)	Pulse on time (C)	Pulse off time (D)	Gap voltage (E)	Abrasive concentration (F)	Mean (A + B + C + D + E + F)/6
1	-23.96	-45.87	-35.35	-35.21	-34.61	-35.50	-35.08
2	-47.61	-32.32	-35.88	-35.32	-36.29	-35.11	-37.09
3		-29.16	-36.13	-36.83	-36.45	-36.75	-29.22
Delta (Δ)	23.66	16.71	0.78	1.62	1.84	1.64	
Rank	1	2	6	5	3	4	

In Table 5, first level of tool polarity: A_1 , third level of peak current: B_3 , first level of pulse on time: C_1 , first level of pulse off time: D_1 , first level of gap voltage: E_1 and second level of chromium abrasive concentration: F_2 are having maximum S/N ratio. So, $A_1B_3C_1D_1E_1F_2$ represents optimized control variable combination for maximum process output i.e. MRR.

5 Conclusions

Taguchi's proposed DOE methodology is used to investigate and maximize the MRR performance of chromium abrasives in kerosene oil as dielectric in sinking EDM of OHNS die steel plate. Eighteen EDM experiments are performed and the obtained results are statistically analyzed to draw important conclusions as stated below:

- The DOE methodology helps in the present experimental work to find out the possible combinations of control variables at definite levels with an objective of optimization of MRR performance.
- 100 μm grain size chromium abrasives suspended commercial kerosene oil dielectric fluid is capable to machine OHNS (O_2 group) die steel in EDM process at both +ve and -ve tool polarity conditions.
- MRR of sinking EDM process is significantly affected by +ve/-ve tool polarity conditions.
- Peak current is significant variable affecting MRR of chromium suspended kerosene dielectric sinking EDM process.
- +ve tool polarity: A_1 , 12 A peak current: B_3 , 90 μs pulse on time: C_1 , 30 μs pulse off time: D_1 , 30 V gap voltage: E_1 and 5 g/l chromium abrasives concentration in kerosene oil: F_2 is the optimized combination of control variables for maximum MRR of chromium abrasives suspended dielectric EDM of OHNS die steel.
- Tool and Die, aerospace and automobile industries may take the benefits of these experimentally obtained results.

References

- Beri, N., Maheshwari, S., Sharma, C., & Kumar, A. (2008). Performance evaluation of powder metallurgy electrode in electrical discharge machining of AISI D2 steel using Taguchi method. *International Journal of Mechanical, Industrial and Aerospace Engineering*, 2, 167–171.
- Box, G. E., Hunter, W. G., & Hunter, J. S. (2005). *Statistics for experimenters* (2nd ed.). New York: Wiley.
- Davis, J. R. (1994). *ASM specialty handbook: Stainless steels*. ASM International: The materials Information Society.
- Dean, A. M., & Voss, D. (1999). *Design and analysis of experiments*. New York: Springer.

- Dehnad, K. (Ed.). (1989). *Quality control, robust design and the Taguchi method*. New York: Springer.
- Ghoreishi, M., & Atkinson, J. (2002). A comparative experimental study of machining characteristics in vibratory, rotary, and vibro-rotary electro-discharge machining. *Journal of Materials Processing Technology*, 120, 374–384.
- Gill, A. S., & Kumar, S. (2014). Surface alloying of H11 die steel by tungsten using EDM process. *International Journal of Advanced Manufacturing Technology*, 78, 1585–1593.
- Huang, H., Zhang, H., Zhou, L., & Zheng, H. Y. (2003). Ultrasonic vibration assisted electro-discharge machining of microholes in Nitinol. *Journal of Micromechanics and Microengineering*, 13(5), 693–701.
- Kansal, H. K., Singh, S., & Kumar, P. (2005). Parametric optimization of powder mixed electrical discharge machining by response surface methodology. *Journal of Materials Processing Technology*, 169, 427–436.
- Kolli, M., & Kumar, A. (2014). Effect of boron carbide powder mixed into dielectric fluid on machining of titanium alloy. *Procedia Materials Science*, 5, 1957–1965.
- Kumar, S., & Singh, R. (2010). Investigating surface properties of OHNS die steel after electrical discharge machining with manganese powder mixed in the dielectric. *International Journal of Advanced Manufacturing Technology*, 50, 625–633.
- Logothetis, N. (2004). *Managing for total quality: From deming to Taguchi & SPC*. Prentice-Hall of India.
- M'Saoubi, R., Czotschera, T., Andersson, O., & Meyer, D. (2014). Machinability of powder metallurgy steels using PcBN inserts. *Procedia CIRP*, 14, 83–88.
- Montgomery, D. C. (1997). *Design and analysis of experiments* (4th ed.). New York: Wiley.
- Pearson, E. S., & Hartley, H. O. (1972). Tables for statisticians. *Biometrika*, 2, 178.
- Prassana, J., Karunamoorthy, L., Raman, M. V., Prashanth, S., & Chordia, D. R. (2014). Optimization of process parameters of small hole dry drilling in Ti-6Al-4 V using and grey relational analysis. *Measurement*, 48, 346–354.
- Shabgard, M. R., & Alenabi, H. (2015). Ultrasonic assisted electrical discharge machining of Ti-6Al-4 V alloy. *Material and Manufacturing Processes*, 30(8), 991–1000.
- Simao, J., Aspinwall, D., El-Menshaw, F., & Meadows, K. (2002). Surface alloying using PM composite electrode materials when electrical discharge texturing hardened AISI D2. *Journal of Materials Processing Technology*, 127, 211–216.
- Taguchi, G. (1986). *Introduction to quality engineering*. Tokyo: Asian Productivity Organization.
- Zhang, Q. H., Du, R., Zhang, J. H., & Zhang, Q. B. (2006). An investigation of ultrasonic-assisted electrical discharge machining in gas. *International Journal of Machine Tools and Manufacture*, 46, 1582–1588.

CFD Modeling for Slurry Flow Through Bends and Straight Pipe Line

Arvind Kumar

Abstract In slurry pipeline, bends are important integral part and these are also prone to wear rapidly. The basic knowledge of the slurry flow through pipe and bends accomplish us to find the causes of wear in pipeline. In this study, computational fluid dynamics (CFD) calculations by using Eulerian–Eulerian model is employed to simulate the slurry flow in pipeline. Standard k-epsilon model is used to find turbulence in both liquid and solid phases. Volumetric concentrations of silica sand slurry were taken 3.9 % of 448 μm mono size silica sand particles. The flow velocity was 1.8 and 2.7 m/s, in the pipe line. The CFD results have been validated against experimental data for pressure drop and concentration distribution. It is observed that CFD modeling gives fairly good results for almost all the data considered in this study. The finding of the present study that pressure drop increases with flow velocity around bend and pressure values be maximum at outer surface and minimum at the inner surface across the pipe bend.

Keywords Pipe bend · Slurry flow · CFD · Eulerian model · Pressure drop · Concentration distribution

1 Introduction

The bends provide the flexibility for pipeline routing. The pressure drop in pipe and bends is very much depends upon the solid concentration, pipe line diameter, flow velocity, bend radius, bend angle, specific gravity of solid and also particle size

A. Kumar (✉)

Department of Mechanical Engineering, YMCAUST, Faridabad, India
e-mail: arvind_eem@yahoo.co.in

© Springer India 2016

D.K. Mandal and C.S. Syan (eds.), *CAD/CAM, Robotics and Factories of the Future*, Lecture Notes in Mechanical Engineering,
DOI 10.1007/978-81-322-2740-3_60

615

distribution (PSD) of the solid material. Literature review reflect few studies in CFD modeling of this area. Some studies for slurry flow which have concentrated on head loss (Toda et al. 1972; Kalyanraman et al. 1973) and studies solid particles distribution (Kazanskij and Hinsch 1974; Nasr-El-Din and Shook 1987; Ahmed et al. 1994). These studies reveals that there is redistribution of solid particles within the bend. Computational Fluid Dynamics (CFD) is the vast approach and it use of computers to solve different type of fluid flow problems. The basic advantage of CFD-based approach is that three dimensional multi phase flow problems under different range of flow conditions may be evaluated very fastly. Thinglas and Kaushal (2008) have performed 3D-CFD modeling for optimization of invert trap configuration and other study done by Kumar et al. (2008). In the present study, a developed turbulent flow with RNG k -turbulent model was used for simulation. For discretize the computational domain, an unstructured non-uniform grid was chosen an also a control volume finite difference method was used to solve the governing equations. The average of pressure gradients from the numerical solutions were compared with the experimental values in the literature for an average volumetric concentration of 3.9 % and the flow velocity varies 1.8–2.7 m/s. The simulation results were found to be in proper agreement with the experimental values.

2 Laboratory Setup of Experiment

The test loop of length 30 m with inside diameter 53 mm of pilot plant as shown in Fig. 1 is used in the study (the details of loop is given Kumar (2010)). Bend radius ratio of 5.6 is fitted in the test loop. Pressure drop is measured at different positions in upstream and downstream side of pipe bend in slurry pipeline.

3 Basic of Mathematical Modeling

In this study, silica sand slurry flow through pipeline and bends are simulate using granular-Eulerian model as described.

Eulerian two-phase model consider slurry flow consists of solid “s” and fluid “f” phases, which are separate to each other but they form interpenetrating continua, so that $\alpha_f + \alpha_s = 1.0$, where α_f and α_s are the volumetric concentrations of fluid and solid phase. The basic laws of the conservation of mass and momentum are satisfied

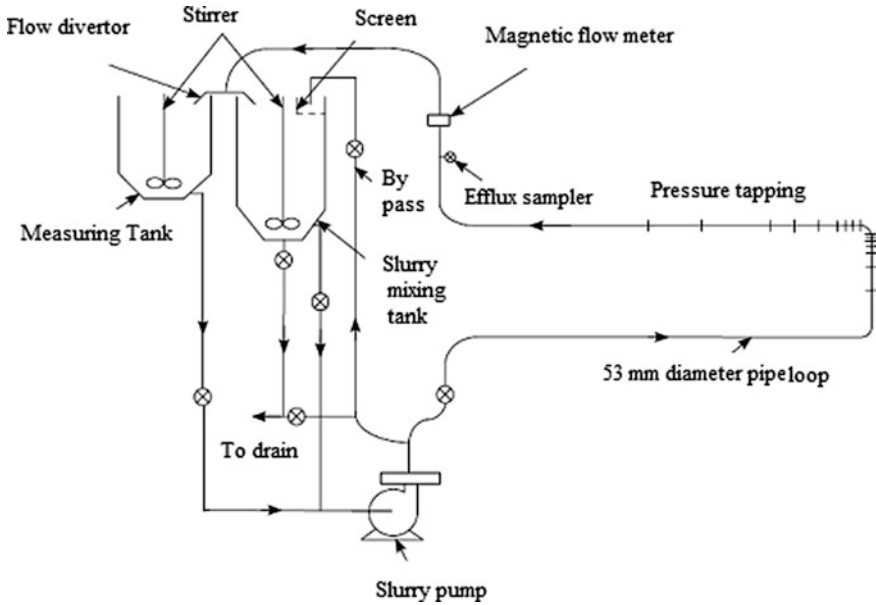


Fig. 1 Line diagram of test loop of pilot plant

by each phase individually. The coupling is achieved in solid and liquid phase by pressure and inter-phasing exchange coefficients.

The different forces acting on a single particle in the fluid:

1. The normal pressure force as a static pressure gradient, ∇P .
2. Solid pressure force or the inertial force because of particle interactions, ∇P_s .
3. Drag force because of the velocity differences between two phases, $K_{sf}(\vec{v}_s - \vec{v}_f)$, where, K_{sf} is the inter-phase drag coefficient, \vec{v}_s and \vec{v}_f are velocity of solid phase and fluid phase.
4. The viscous forces, $\nabla \cdot \bar{\bar{\tau}}_f$, where, $\bar{\bar{\tau}}_f$ is the stress tensor for fluid.
5. Body forces = $\rho \vec{g}$, where ρ is the mass density and g is gravitational acceleration.
6. Lift force, $C_L \alpha_s \rho_f (\vec{v}_f - \vec{v}_s) \times (\nabla \times \vec{v}_f) - C_{vm} \alpha_s \rho_f (\vec{v}_f \cdot \nabla \vec{v}_f - \vec{v}_s \cdot \nabla \vec{v}_s)$ where, C_L is the coefficient of lift force is taken as 0.5 in the present study.

4 Governing Equations for Multiphase Flow in Eulerian Model

4.1 Basic Continuity Equation

$$\nabla \cdot (\alpha_t \rho_t \vec{v}_t) = 0 \quad (1)$$

where, t is either s or f.

4.2 Basic Momentum Equations

For fluid phase:

$$\begin{aligned} \nabla \cdot (\alpha_f \rho_f \vec{v}_f \vec{v}_f) = & -\alpha_f \nabla P + \nabla \cdot \bar{\bar{\tau}}_f + \alpha_f \rho_f \vec{g} + K_{sf} (\vec{v}_s - \vec{v}_f) \\ & + C_{vm} \alpha_f \rho_f (\vec{v}_s \cdot \nabla \vec{v}_s - \vec{v}_f \cdot \nabla \vec{v}_f) + C_L \alpha_s \rho_f (\vec{v}_f - \vec{v}_s) \times (\nabla \times \vec{v}_f) \end{aligned} \quad (2)$$

For solid phase:

$$\begin{aligned} \nabla \cdot (\alpha_s \rho_s \vec{v}_s \vec{v}_s) = & -\alpha_s \nabla P - \nabla P_s + \nabla \cdot \bar{\bar{\tau}}_s + \alpha_s \rho_s \vec{g} + K_{fs} (\vec{v}_f - \vec{v}_s) \\ & + C_{vm} \alpha_s \rho_f (\vec{v}_f \cdot \nabla \vec{v}_f - \vec{v}_s \cdot \nabla \vec{v}_s) + C_L \alpha_s \rho_f (\vec{v}_s - \vec{v}_f) \times (\nabla \times \vec{v}_f) \end{aligned} \quad (3)$$

5 Criteria of Selection of Suitable Model

The selection of a suitable model in multiphase flow mainly depends on the volumetric concentration of solids. The sand slurry flow in practice is not a diluted flow, therefore the discrete phase model cannot be used to modeling the flow. In sand slurry flow Mixture model and Eulerian model can be used but Eulerian is appropriate model. In Eulerian model, granular version will be appropriate because it include friction and collisions between particles into account.

6 Numerical Solution for Simulation

The grid for the simulation of pipe bend just similar that the bend used in laboratory experiments has been develop with the help of GAMBIT software as shown in Fig. 2. A boundary layer, closely to the wall at 4–5 % of the diameter of the pipe and a growth factor of 1.2, was employed on the wall to improve the performance of the wall function to calculate the numerical solution economically. The hexagonal shape and Cooper type element have been used and flat velocity and volume fraction of liquid and solid phases were introduced at the inlet of pipe. It is insured a fully developed flow at upstream of bend inlet and also ensuring the development of similar flow characteristics to those developed in experimental set-up, i.e., $\vec{v}_m = \vec{v}_s = \vec{v}_f = V_f$, $\vec{U}_f = \alpha_f V_f$ where V_f is the mean flow velocity.

7 CFD Modeling Results

Variation in normalized pressure drop by simulation by two-phase modeling for silica sand slurry flow in pipeline at efflux concentration of 3.9 % and mean flow velocity of 1.8 m/s is shown in Fig. 3. The presentation of pressure drops are in the normalized form such as (Normalised pressure drop = $\Delta h / (v^2 / 2g)$), where, $\Delta h = \Delta p / \gamma$,

Fig. 2 Meshing of simulation geometry of pipe bend

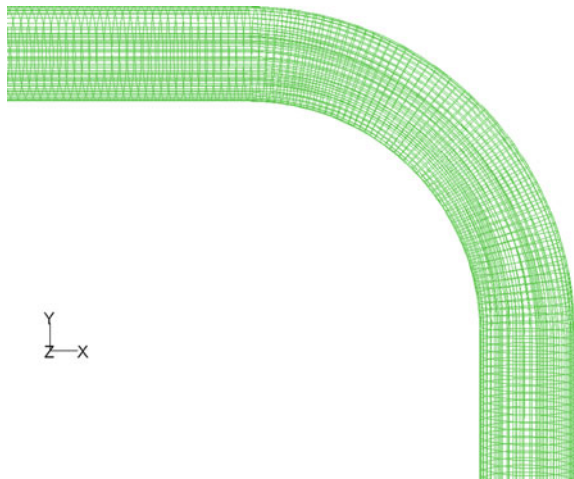




Fig. 3 Variation of Pressure drop at $C_{vf} = 3.9\%$ and $V_f = 1.8\text{ m/s}$

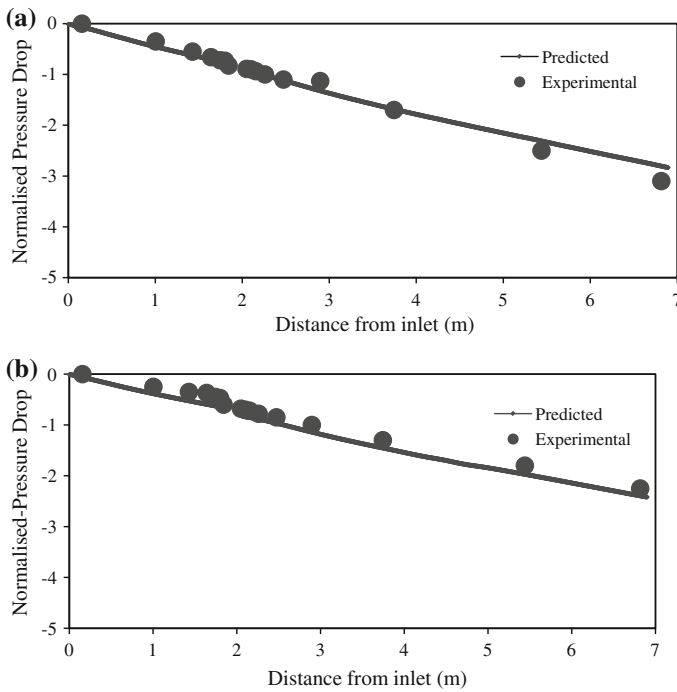


Fig. 4 Measured and predicted pressure drop for mono-sized silica sand slurry at $C_{vf} = 3.9\%$ **a** $V_f = 1.8\text{ m/s}$. **b** $V_f = 2.7\text{ m/s}$

Δp = pressure drop with reference to the inlet at a particular point, γ is the specific weight of the flowing fluid, v is the mean flow velocity and g is gravitational acceleration). The pressure gradually decreases towards flow direction, where the effect of pipe bend on flow is absent and while the flow reaches near pipe bend, the decrease in pressure rapidly in comparison to the horizontal pipeline. The change in

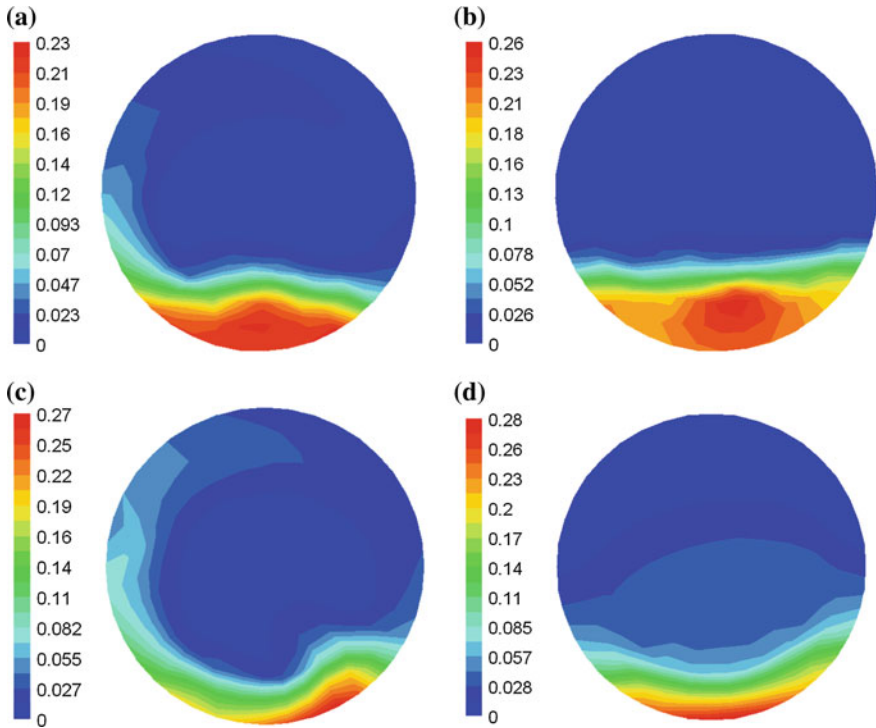


Fig. 5 **a** Concentration profile at $C_{vf} = 3.9\%$ and $V_f = 1.8$ m/s at bend exit. **b** Concentration profile at $C_{vf} = 3.9\%$ and $V_f = 1.8$ m/s at away from bend. **c** Concentration profile at $C_{vf} = 3.9\%$ and $V_f = 2.7$ m/s at bend exit. **d** Concentration profile at $C_{vf} = 3.9\%$ and $V_f = 2.7$ m/s at away from bend

pressure across the pipe bend cross-section, pressure at outer wall more than pressure on inner wall of the pipe bends.

In Fig. 4, comparison between practical values and simulate values of pressure drops shows the capability of CFD simulation to predict the pressure drop quite reliable. Regarding 3-dimensional concentration and velocity distributions, it is observed that the concentration and velocity distribution exhibit the turbulent flow pattern. In Figs. 5 and 6, it is observed that the concentration and velocity distribution become more homogeneous than the typical profile just downstream of pipe bend due to mixing of secondary flows generated in the pipe bend due to change in direction.

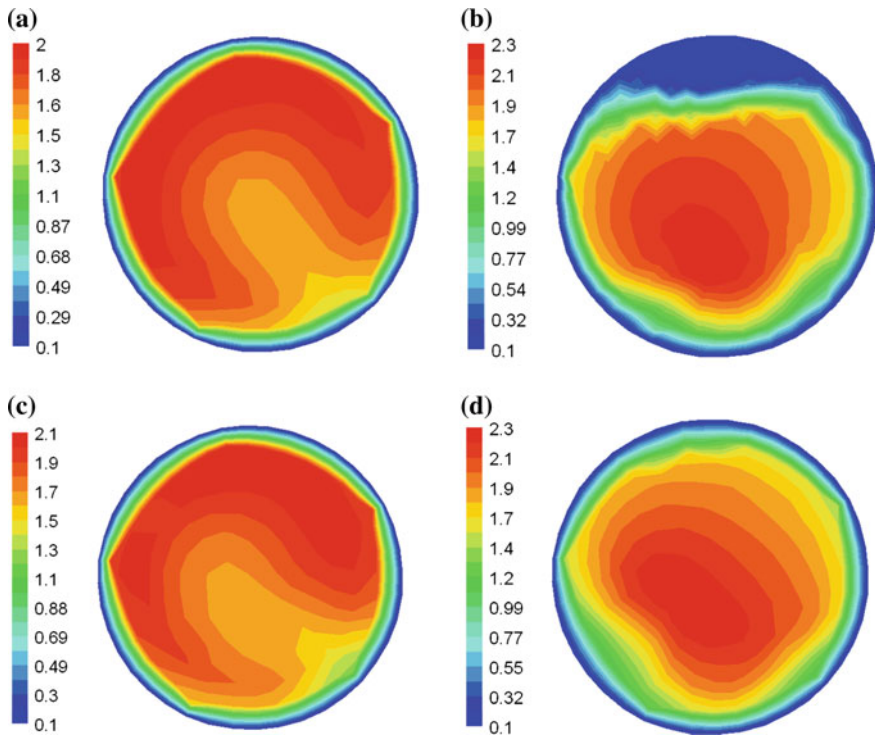


Fig. 6 **a** Velocity profile at $C_v = 3.9\%$ and $V_f = 1.8$ m/s at bend exit. **b** Velocity profile at $C_v = 3.9\%$ and $V_f = 1.8$ m/s at away from bend. **c** Velocity profile at $C_v = 3.9\%$ and $V_f = 2.7$ m/s at bend exit. **d** Velocity profile at $C_v = 3.9\%$ and $V_f = 2.7$ m/s at away from bend

8 Conclusions

There is quite good agreement in terms of trends and flow pattern between experimental and simulation results. These findings suggest that the Eulerian two-phase model is quite effective in the analysis and design of slurry pipeline. CFD modeling predicts quite accurate pressure drops (error of $\pm 10\%$) for the slurry flow of silica sand. Pressure intensity at outer wall in the bend is much higher than at inner wall because of secondary flow. Velocity and concentration profiles of silica sand slurry exhibit turbulent type of slurry flow. Concentration distribution and velocity profile of solids become more uniform in the downstream of pipeline because of secondary flows along the bend. The concentration distribution and velocity and pressure drop are not affected in the upstream of pipe line before bend due to turbulence developed by pipe bend.

References

- Ahmed, M., Singh, S. N., & Seshadri, V. (1994). Pressure drop in a long radius 90° horizontal bend for the flow of multi-sized heterogeneous slurries. *International Journal of Multiphase Flow*, 21, 329–334.
- Kalyanraman, K., Ghosh, D. P., & Rao, A. J. (1973). Characteristics of Sand Water Slurry in 90° Horizontal Pipe Bend. *IE (I) Journal-ME*, 54, 73–79.
- Kazanskij, B. H. & Hinsch, J. (1974). Influence of added fine particles on the flow structure and the pressure losses in sand-water mixture. In *Proceedings of Hydrotransport, BHRA Fluid Engineering, Colorado, USA* (vol. 3, Paper D2, pp. 11–21).
- Kumar, A. (2010). Experimental and CFD Modeling of Hydraulic and Pneumatic Conveying through Pipeline. Ph.D. Thesis. I.I.T. Delhi.
- Kumar, A., Kaushal, D. R., & Kumar, U. (2008). Bend pressure drop experiments compared with FLUENT. *Institution of Civil Engineers Journal of Engineering Computational Mechanics*, 161, 35–45.
- Nasr-El-Din, H., & Shook, C. A. (1987). Effects of 90° bend on slurry velocity and concentration distribution. *Journal of Pipelines*, 6, 239–252.
- Thinglas, T., & Kaushal, D. R. (2008). Comparison of two dimensional and three dimensional CFD modeling of invert trap configuration to be used in sewer solid management. *Particuology*, 6, 176–184.
- Toda, M., Kamori, N., Saito, S., & Maeda, S. (1972). Hydraulic conveying of solids through pipe bends. *Journal of Chemical Engineering of Japan*, 5(1), 4–13.

Role and Significance of Visualisation in Product Design at Prototyping Stage

Sawankumar Naik and Ravi Terkar

Abstract Before the arrival of Computer aided technologies in rapid prototyping, nature of industrial design demanded a methodology that remained virtually unaffected since origins of the profession. While being effective, this methodology favoured working practices whereby industrial designer was almost detached from overall New Product Development Process. In this paper, an attempt is made first to understand the Principles of Visualization and as to how the aesthetics of a product can be experimented without affecting the functionality of the product. The stages of the Conventional Designing process are discussed in detail with the help of case studies. The generation of a 3D-computer model, to make use of rapid prototyping, opens up a variety of benefits within the process of New Product Development. These benefits have been translated into reality by engineering and manufacturing disciplines to reduce time to market.

Keywords Product development · Modelling · Prototyping · Visualisation · Aesthetics · Functionality

1 Introduction

It is said, “A single picture is worth thousands of words”. It is used to describe what one wants to communicate. Nothing is truer, especially in the field of Industrial Product Design. Physically fabrication of a part without proper visualisation may lead to undesirable iterations. Central to industrial design creative work is modelling. Modelling is that activity whereby products are represented in a form other than in their final manufactured state. All design disciplines use different types of models. Initially a prototype was a handmade, mechanical model of a design.

S. Naik (✉) · R. Terkar
SVKM's NMIMS Mukesh Patel School of Technology Management and Engineering,
Mumbai, India
e-mail: naiks1@gmail.com

It gave both designers and users a hands-on feel of the product. This was a 3D physical model. This could be a non-functioning appearance model or a functional model to develop some technological feature, or a pre-production prototype, which is very close in appearance, construction and function to the manufactured item. As the Hardware and Software costs for Computer Aided Design continue to decrease, along with more designer friendly applications, a shift from the conventional methodology is becoming increasingly feasible (Choi and Chan 2003).

2 New Product Development Phase (NPD)

In order to minimize the Industrial design process the NPD phase, to achieve the target in the minimum time Concurrent Engineering is inevitable (Santos et al. 2005). Development of product involves having a good idea of human need, transformation of the ideas, designs, materials and information (data) into products aimed at satisfying the need (Oduola et al. 2014). The success of rapid prototyping in New Product Development therefore relies on the adoption of 3D computer modelling as a standard form of modelling in the design phase (Jirathearanat et al. 2000). This means that the industrial designers must adopt CAD systems as primary modelling tools as explained in this paper. The speed and flexibility of Rapid Prototyping technologies decreases the overall time to complete the new product with a significant role for industrial designer to incorporate the guiding principles (Lopez and Wright 2002).

A physical prototype is created by thin layer-by-layer fabrication generated from a Computer Aided Design. Virtual Prototype alternatively, provides a digital model for testing a property of the product or characteristics of the fabrication process involved (Choi and Cheung 2005). It allows for flexibility to improve quality in development cycle through computer support (Zheng et al. 2006).

In recent years, there has been pressing demand for multi-material objects to facilitate advanced product development (Choi and Cai 2014). In the modern form of additive manufacturing process, three dimensional computer designs are transformed into products from thin layers of materials. The free form fabrication provides designers and engineers the capability to literally print out their ideas in three dimensions, pushing the borders of manufacturability (Achillas et al. 2014). These ideas are not elusive and emerge from meeting the customer requirements in terms of function and appearance.

The appearance is most important for the Consumer goods and the Fashion goods such as jewellery, costumes, etc. However, for internal working parts such as gears, Carburetors appearance is insignificant. All other products lie within these extremes. The conventional way was to think about meeting the functional requirements and then applying the aesthetics (Campbell et al. 2002). But now the functional scope has become more or less accepted. Hence to distinguish the product from the market, the product must be first made appealing causing the customer to want to own it. Appearance of a product is SUBJECTIVE. It depends on

person to person. It cannot be MEASURED. When somebody likes a particular product it may be for different reasons. Nobody is wrong; all are right in their own way. Some people may like strict geometric shapes; others may prefer curved shapes. Thus it is difficult to draw Exact Rules. However, an attempt may be made to identify the common characteristics of the beautiful objects. One may first start by thinking about the compliment of beauty i.e. for a product to be beautiful it must not be ugly at least. It must not be made haphazardly, carelessly or defective. In other words, product must be given complete attention it deserves and care should be taken from the first to the last stage, at every stage, with the effect on end result in view. Just not being ugly, won't help. As per Kano's Model "not being ugly", is just a Hygiene need. Its presence doesn't matter much. But its absence does. One must remember that between the ugly and the beautiful lies the neutral and the uninteresting. To satisfy the customer, some extra features must be added.

Before starting of we must take care of what makes up the appearance. They are the following factors:

- (1) FORM—pertains to the basic shape of the object.
- (2) STRUCTURE—refers to the relative arrangement of various elements in the final product.
- (3) MATERIAL—plastics nowadays, are fast replacing other materials because of light in weight; any desired colour may be obtained and a variety of properties can be modified by changing the composition.
- (4) DIMENSION—means the object should look proportionate as seen in the figures to follow.
- (5) SURFACE—is responsible for reflectivity, texture, etc.

2.1 Geometric Forms

Most industrial products are built up of a number of elements of relatively simple geometric form as shown in Fig. 1. This is because of firstly ease of machining by conventional mass production methods. Also the eyes are inclined to perceive the horizontal and the vertical lines as the main visual directions. The projection planes are thus parallel to each other or at right angles as they are Easier to sketch. The

Fig. 1 Standard geometric forms

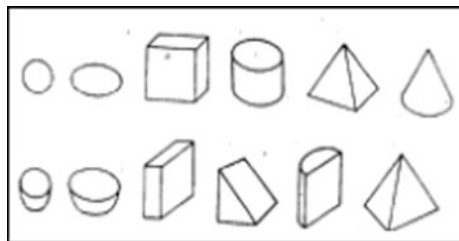
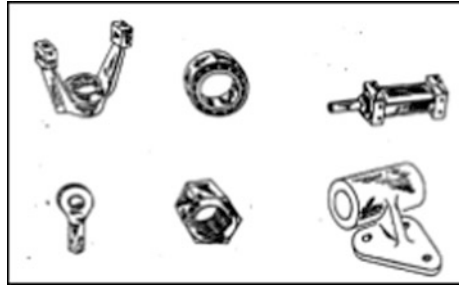


Fig. 2 Standard machine parts of various geometric forms



basic shapes are Cube, Cylinder, Sphere, Pyramid and Cone. In the components shown in Fig. 2, the geometric forms can be easily recognized.

2.2 *Unity and Order*

The first important need is that the product must appear as a finished complete unit. The separate elements must belong together in a logical and harmonic way. There must be no elements that stand out as if they don't belong or arouse questions or surprise. Any disturbance mars the appearance, especially if the product looks as if something is missing. Figure 3 depicts an object showing unity and order in its features.

2.3 *Physical Properties*

The form may be used to emphasize certain physical properties, which may be expected from a product.

Fig. 3 An aesthetic product characterized by unity and order

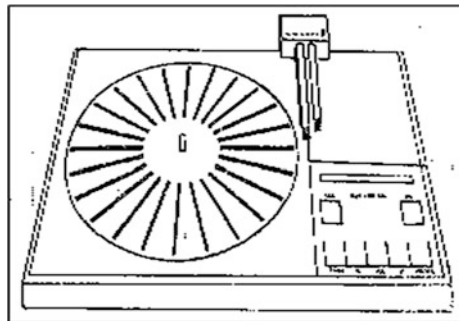
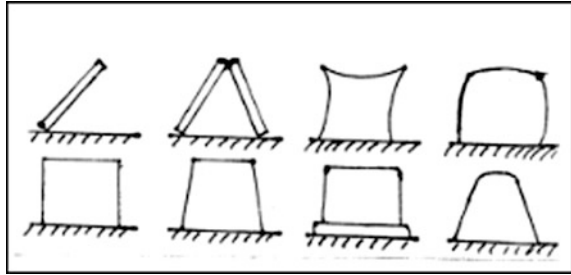


Fig. 4 Effect of curvature and linearity of object on projection of stability



2.4 Weight & Stability

As can be observed from Fig. 4, Object with curves arching outwards seem heavy as compared to those with curves arching inwards. In case of Sloping lines, a single line expresses instability, while two lines leaning towards each other express a high degree of stability.

2.5 Visual Balance

As can be seen in Fig. 5, a symmetry is present if the object is exactly same about an imaginary central line. If it cannot be symmetric in all of its components, the designer may make it Asymmetric attempting to stabilize the weight or the area about the central line. If no symmetry is possible then though visually imbalance the prominent lines should give a different rhythm.

2.6 Internal Design

After designing the looks one must go for the ergonomic aspects. The best example is the arrangement of controls in a Car. The Safety of the driver in emergency too has to be considered. In case of a car, it may be in the form of: Firstly, a Seat belt & Secondly, an Air bag.

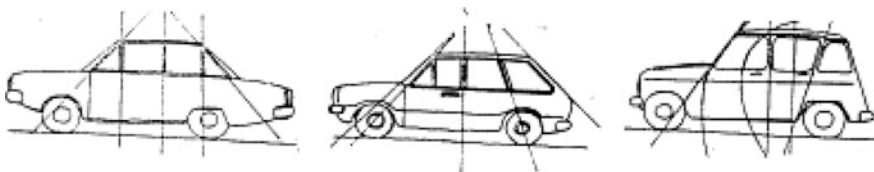
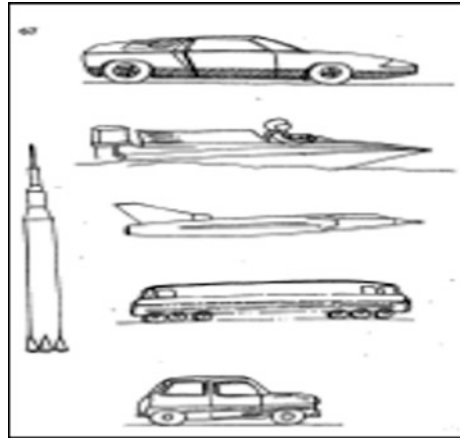


Fig. 5 Symmetry, asymmetry and visually imbalanced vehicle design

Fig. 6 Effect of angular merger on dramatization of movement of object



2.7 Movement

Like other properties, movement too can be emphasized by using sloping lines. Two lines meeting at a point give associations with an arrow; provided that the angle between them is not too great. This principle can be used to dramatize SPEED in case of fast moving bodies used for transportation, travelling, or space research such as Car, Boat, Aeroplane, and Rocket. One may note from Fig. 6; given that “the speedier the object, the lesser is the angle of the arrow and more pointed its external body seems to be”. The figure shows the objects emphasizing speed.

3 Scanning Technology for Virtual Product Realization

When a profile is difficult to be generated on computer model the scanning technology proves to be a great boon. For instance, a one time well crafted handmade sculpture can be directly scanned for generation of the computer model. This model can then be used for further analysis or reproducing the precision. The Fig. 7 shows the laser scanning system of a crafted car prototype. Here the profile of the car is first scanned into a wire mesh model. Later through the analysis software the model can be scaled and properties can be changed for virtual testing before fabrication of the prototype.

As shown in the figure, the laser scanner is away from the object at a certain distance called the Stand-off distance, so that the entire object can be covered. The Scanner moves parallel to the object recording a line at a time and thus it generates a virtual image in the computer’s memory. The surface is generated as per the variation in its distance from the plane of motion of the laser Scanner. This reduces the complexity of programming. Any physical model can be thus transferred on the

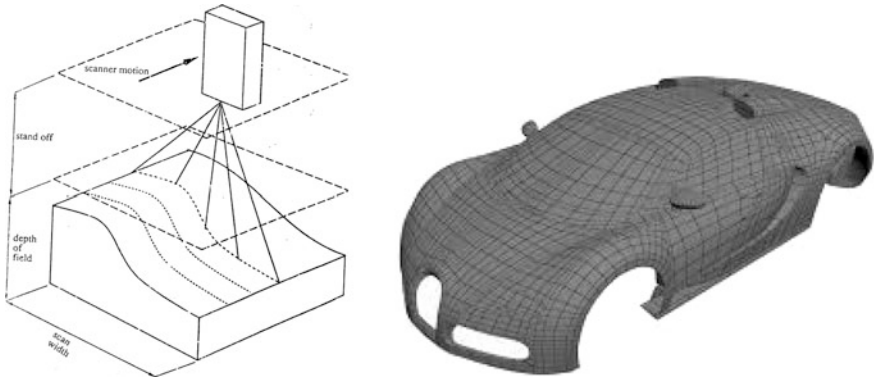


Fig. 7 Laser scanning system

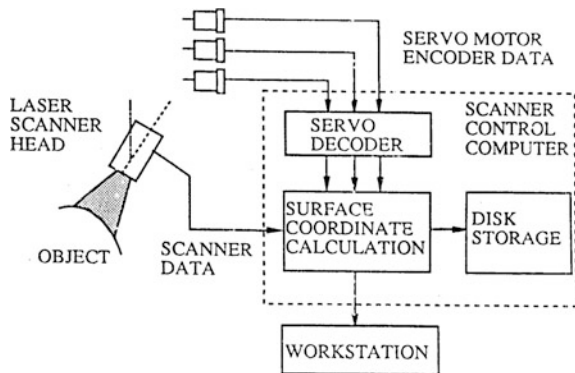
computer and experimented upon virtually. The technology is useful in customized products like jewellery (Siu and Dilnot 2001). Also objects in nature can be scanned to precision and their Computer Model generated with this technology.

4 Advancement

The most recent advancement is the ability to directly physically create the model without the intervention of the Programmer. Besides the CAD representation of the object, the data format for feeding the essential information to the Rapid Prototyping machine on material properties and geometric characteristics, needs to be established (Chiu and Tan 2000).

The Fig. 8 shows the connection of the Laser scanner to the CNC Machine Tool. The benefits obtained are that the Time consumption is reduced drastically and high degree of accuracy.

Fig. 8 Laser scanner interfacing with machine tool



Thus, with Technology there is no limitation to transfer our ideas to reality. However, there is no substitute for human intelligence. So, some skills and understanding of the basic principles of aesthetics is essential.

Case study 1 Visualization and testing of CAD models in a synthetic environment before they are physically fabricated is fast becoming an effective way of reducing product development cycle time (Deviprasad and Kesavadas 2003)

1. Sketch (2D): Sketching is an activity whereby the concept is expressed and developed for evaluation till it is adequate enough for further complex considerations. It's the skill central to the design process for projection of three-dimensional relationships using a two dimensional medium (Fig. 9). The ability to sketch is a vital skill for industrial designer to create drafts of the ideas for meeting the design requirements.
2. Sketch Model (3D): Whilst undertaking design activity it is often necessary to translate drawings into more representative 3Dformat. Materials such a card and foam (Fig. 10) can be quickly manipulated to give approximations of form that enable the designer to understand more fully the complex relationships between components, cavities, interfaces and form. This first stage of 3D physical modeling is generally undertaken during the early primitive stages (Fig. 11).

Fig. 9 2D sketching of ideas



Fig. 10 3D model of product

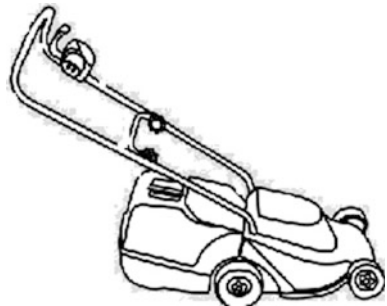
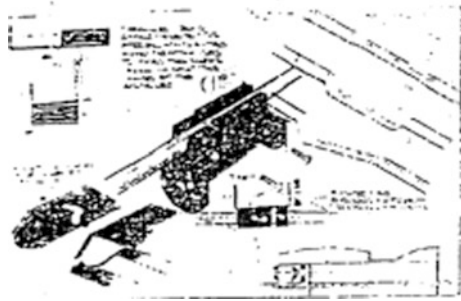


Fig. 11 Development drawing



3. Development drawing (2D): There is rarely a clear-cut demarcation between a Sketch and Development Drawing, but at some stage in the design process there is a need to establish greater control and accuracy of representation. Instead of continuing with a predominantly freehand, monochromatic technique as typified by Sketching; Development Drawings make use of drawing equipment and color (Fig. 3). The added realism afforded by Development Drawings facilitates an enhanced appreciation of product attributes, and continues to be employed until more formal 'Renderings' are produced.
4. Rendering (2D): Having generated ideas using highly interactive 2D Sketching and 3Dsketching and 3Dsketch Modelling, and refines these via Development Drawings, more formal Rendering is produced to communicate the design to a client or senior management team. Renderings depict the major features of a product proposal as accurately as possible (Fig. 12). This requires considerable skill in the generation of perspective drawings and application of colour. As many designers operate to tight time scales, the media and techniques developed for the production of renderings facilitate rapid yet effective results.
5. Appearance Model (3D): Appearance models are exact visual representations of the proposed product. Such models are made using materials like plastic sheets, wood (Fibreboard) and painted to give the precise surface finish. Metals may be preferred for the structural components. The purpose is to get the visual impression of the final proposed result. The result is a visual impression of the final proposal representing the form and finish (Fig. 13). As Appearance Models are essentially hand made, they are notoriously expensive. Appearance Model are used for assessing the ergonomics of the product. To test the performance of

Fig. 12 Rendering



Fig. 13 Appearance of product



the product it is imperative that the relative motion of the surfaces which is not taken into consideration for the Appearance Model.

6. **Appearance Prototype (3D):** The integration of the industrial design solution into a working prototype amounts to the highest level of 3D modelling in the NPD process. Fit and function can be assessed, along with accurate ergonomic evaluation (Fig. 14). Unlike the Appearance Model, the Appearance Prototype requires representative wall thickness to create the internal cavities for components. The production of these simulates components (typically representing injection mouldings) necessitates their fabrication from a combination of vacuum formings and bonded sheet material. The appearance Prototype is also necessary to confirm the accuracy of the engineering drawings that are required to produce the production tooling. With the transfer of information through so many media there is always a possibility of human error affecting the integrity of the processes. Unfortunately such errors tend not to appear until the tooling has been commissioned, at which stage modifications may be difficult and expensive or even impossible. In Industrial Design at Prototyping Stage, the key challenge lies in integrating an appearance model and a working prototype (Evans and Ian Campbell 2003).

Case study 2: The case study research has identified that the processes carried out computer based techniques and rapid prototyping are significantly related to the conventional process already described. Not rejecting the most useful aspect of the conventional route, changes are inevitable, and the following methodology draws on the case study findings. Here, in this we will briefly see how a “Water timer

Fig. 14 Appearance prototype



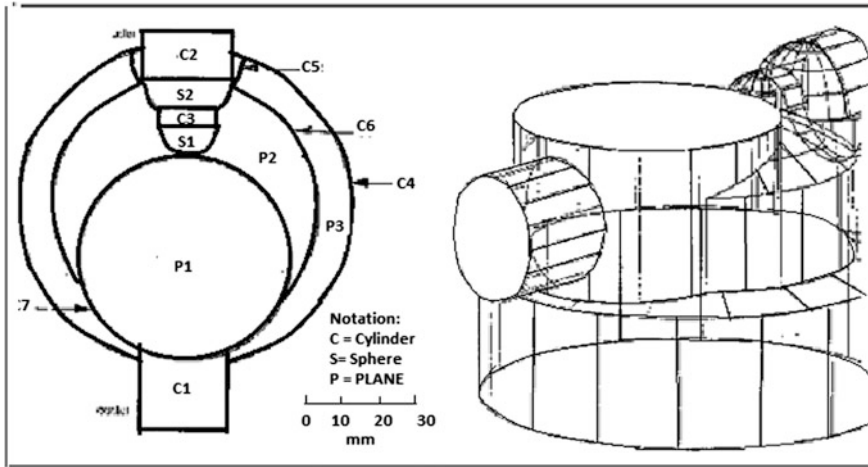


Fig. 15 2Dimensional and 3Dimensional model of water timer housing

housing” is designed using the computer systems. First, a 2Dimensional sketch is produced on a Computer and then using the various functions available it is converted to a 3Dimensional Model using the software package as shown below as shown in Fig. 15.

The last step is to apply Hidden line removal algorithm, depending on the direction of viewing to convert it into a Solid Model.

The Software packages can now manipulate the object on the screen. It can be viewed from different directions. Interference checking can be done. Most importantly, there is reduction in cost and we deal with Virtual Prototypes.

5 Conclusion

The working relationships of the various designers and engineers is a critical factor in the success of product development. The models used for product development play a large part in this relationship. Rapid prototyping has changed the approach to design modeling by increasing the concurrency employed. All rapid prototyping technologies rely on 3D computer models to generate the physical models which have the capability for use in further engineering development and production tooling. The practice of industrial design involves the integration of engineering elements of new product development with a visual form. While having a general engineering capability, the specialty of the Industrial Designer is predominantly visual. One of the most common forms of model is the Engineering Drawing in which all aspects of a product (form, finishes, construction details etc.) can be represented in 2D. The techniques of presentation, unique to the industrial designer, rely on 2D visualisation and 3D models, the nature of which has remained largely

unchanged since the beginnings of the profession. In the paper the principles in visualizing the product were considered to understand the factors making up the appearance and its role in good aesthetics emphasized. Irrespective of the Conventional Methodology or the use of Computer based techniques, the principles form the base for the design process.

References

- Achillas, C., Aidonis, D., Iakovou, E., Thymianidis, M., & Tzetzis, D. (2014). A methodological framework for the inclusion of modern additive manufacturing into the production portfolio of a focused factory. *Journal of Manufacturing Systems*, 37, 328–339.
- Campbell, R. I., Martorelli, M., & Lee, H. S. (2002). Surface roughness visualisation for rapid prototyping models. *Computer-Aided Design*, 34(10), 717–725.
- Chiu, W. K., & Tan, S. T. (2000). Multiple material objects: From CAD representation to data format for rapid prototyping. *Computer-Aided Design*, 32(12), 707–717.
- Choi, S. H., & Cai, Y. (2014). A virtual prototyping system with reconfigurable actuators for multi-material layered manufacturing. *Computers in Industry*, 65(1), 37–49.
- Choi, S. H., & Chan, A. M. M. (2003). A layer-based virtual prototyping system for product development. *Computers in Industry*, 51(3), 237–256.
- Choi, S. H., & Cheung, H. H. (2005). A multi-material virtual prototyping system. *Computer-Aided Design*, 37(1), 123–136.
- Deviprasad, T., & Kesavadas, T. (2003). Virtual prototyping of assembly components using process modeling. *Journal of Manufacturing Systems*, 22(1), 16–27.
- Evans, M. A., & Ian Campbell, R. (2003). A comparative evaluation of industrial design models produced using rapid prototyping and workshop-based fabrication techniques. *Rapid Prototyping Journal*, 9(5), 344–351.
- Jiratharanat, S., Vazquez, V., Rodríguez, C. A., Altan, T. (2000). Virtual processing—application of rapid prototyping for visualization of metal forming processes. *Journal of Materials Processing Technology*, 98(1), 116–124. Retrieved January 15, 2000.
- Lopez, S. M., & Wright, Paul K. (2002). The role of rapid prototyping in the product development process: A case study on the ergonomic factors of handheld video games. *Rapid Prototyping Journal*, 8(2), 116–125.
- Oduola, O. M., Omole, F. O., Akinluwade, K. J., & Adetunji, A. R. (2014). A comparative study of product development process using computer numerical control and rapid prototyping methods. *British Journal of Applied Science and Technology*, 4, 4291–4303.
- Santos, D. M. C., Pertence, A. E. M., Campos, H. B., & Cetlin, P. R. (2005). The development of 3D models through rapid prototyping concepts'. *Journal of Materials Processing Technology*, 169(1), 1–4.
- Siu, N. W. C., Dilnot, C. (2001). The challenge of the codification of tacit knowledge in designing and making : A case study of CAD systems in the Hong Kong jewellery industry. *Automation in Construction* (Vol. 10, pp. 701–714). China: Elsevier Science Publications.
- Zheng, X., Sun, G., & Wang, S. (2006). *An approach of virtual prototyping modelling in collaborative product design, computer supported co-operative work in design II* (pp. 493–503). Berlin Heidelberg: Springer.

Positional Analysis of a DC Brushed Encoder Motor Using Ziegler-Nichols Algorithm

Priyam Anilkumar Parikh, Saurin Sheth and Trupal Patel

Abstract In the present era, use of Automated Guided vehicles (AGV) has emerged for automation in material handling applications. AGVs are equipped with DC brushed/brushless motors with encoders. The encoders help AGV to move accurately on the track as encoders keep on monitoring the actual shaft position of DC motor. This is called a positional analysis of DC motor. The analysis will be helpful in track following as well as to prevent collision (Between two AGVs or between object and AGV). In the first phase of paper, the details of AGV, Interfacing of Arduino with DC encoder motor and Interfacing of Arduino with MATLAB are shown. In the second phase, the transfer function of the system, type of the system, order of the system, steady state and transient analysis are shown. In the final phase of the paper, system's response with P, PI and PID controllers are shown with the help of Ziegler-Nicholas (Z-N algorithm) algorithm (Real time and simulation both) with respect to step input.

Keywords AGV · Arduino · DC motor with encoder · SIMULINK · MATLAB data acquisition · Z-N algorithm · P, PD and PID controller

List of Symbols

S	Laplace operator
ω_n	Natural frequency of oscillations
K	Gain of the system
K _m	Motor size constant
K _b	Back emf constant

P.A. Parikh (✉)
SAL College of Engineering, Ahmedabad, Gujarat, India
e-mail: myrobo56@gmail.com

S. Sheth
G. H. Patel College of Engineering and Technology, Vallabh Vidhyanagar, Gujarat, India
e-mail: saurinsheth@gcet.ac.in

T. Patel
Vishwakarma Government Engineering College, Ahmedabad, Gujarat, India
e-mail: trupalpatel394@gmail.com

J	Inertia of the motor
ξ	Damping ratio
ω_d	Damped angular velocity
K_p	Positional error constant
K_v	Velocity error constant
K_a	Acceleration error constant
e_{ss}	Steady state error
G(s)	Transfer function
Z-N method	Ziegler Nichols method
T-L	Tyreus-Luyben method
C(t)	Time domain output response
T_d	Delay time
T_r	Rising time
T_p	Pick time
M_p	Overshot in %
T_s	Settling time
Ku	Ultimate gain
Pu	Ultimate time
Ti	Integrated time
Td	Differentiated time

1 Introduction

The present research work demonstrates the methodology of doing a real time positional analysis of a DC motor with Encoder. The Errors in control systems may be attributed to many factors (Ian 2004). Changes in the reference input will cause unavoidable errors during transient periods, and also cause steady state errors (Ahmed 2013). Any physical control system inherently suffers from steady state error in response to certain types of inputs (Bashir 2005). Whether a given system will exhibit steady state error for a given input depends on the type of the open loop transfer function of the system (Aung 2007). Various applications are there where controlling of DC motors are required. The present work is focused on AGV, which is required to stop at certain distances frequently and accurately. AGV has to stop for loading/unloading/detecting any product in context of material handling. The Positional analysis of DC brushed encoder motor becomes essential to achieve the above mentioned phenomena.

The AGV, as shown in Fig. 1 detects RFID number of the product and sends it to the server. The AGV travels on a straight black track as shown in Fig. 2. A Line sensor (Infrared sensor) array is used to detect and to follow the black track (Parikh et al. 2013). AGV follows only black track, which is detected by IR sensor array (Parikh et al. 2014). The analysis is carried out just by considering the self-weight

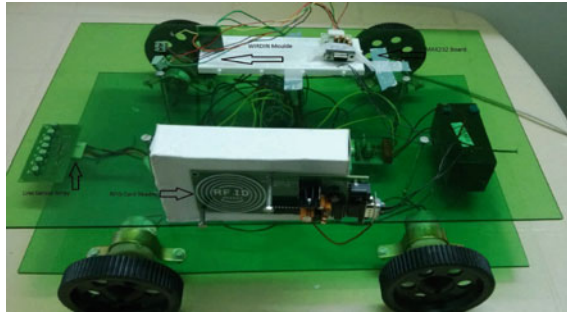


Fig. 1 Prototype of AGV

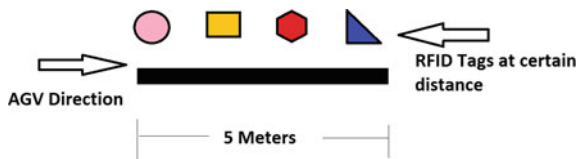


Fig. 2 Path to be followed by AGV

of AGV and accordingly the control system is designed. The present system is having 5 different products with different RFID numbers. For example, product 1 is at 200 mm from the beginning then to make AGV stop at exact 200 mm, encoder values are to be calculated according to the diameter of the wheel. Encoder keeps on monitoring the shaft position. Encoder feeds the shaft position to the Arduino board. Arduino tries to solve the error, which is based on the algorithm as well as type of the controller and gives the manipulated output to the motor via motor driver. That manipulated signal is a pulse width modulated signal. As far as error solving is concerned, P, PD and PID controllers are used. Kp, Ki and Kd parameters are chosen according to Ziegler-Nichols algorithm (Bashir 2005). The specifications of the AGV are shown in Table 1.

Table 1 AGV Specifications

Sr. no.	Parameters	Values
1	LXBXH	35 cm × 25 cm × 15 cm
2	Mass of AGV	3.2 kg
3	No. of motors	4
4	Type of motors	DC brushed with Encoder
5	Motor specification	6 V, 120 rpm, 3.6 kg cm at 2.2 A
7	Wheel diameter	10 cm
8	Path to be followed	Straight dark line (5 m)
9	Path followed by	IR sensor array and Arduino controller
10	Motor gear ratio	47:1

2 Block Diagram of the System with the Problem Description

The block diagram of the overall system is shown in Fig. 3. Step input is given to the system as 6 V DC. Encoder's highest count values are 65,535 (www.pololu.com 25th June 2015). Any set point can be fed into the system (depends upon the application). Error signal generated from the summation of the set point and feedback signal is given to the Arduino microcontroller. Arduino manipulates the signal and gives to the motor via motor driver, because motor driver gives PWM signals (Parikh et al. 2013). The connections for experimental positional analysis technique are shown in Fig. 4. Feedback signal produced by Encoder is compared with the set point. Error signal is solved by Arduino using various controllers (P, PI or PID) and control algorithm (Z-N algorithm). Finally the signal solved by Arduino, is given to DC motor of AGV.

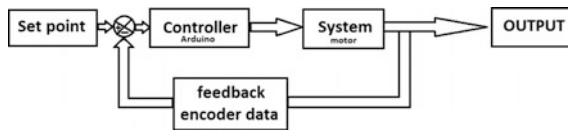
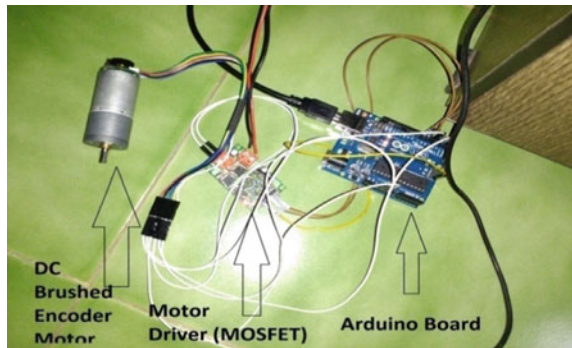


Fig. 3 Block diagram of the system

Fig. 4 Interfacing motor with Arduino Board



3 Hardware Description

It is well mentioned in the introduction part that, Arduino board is used as a microcontroller. MOSFET drive is used as a motor driver and DC encoder motor is used as a plant.

3.1 Arduino Board

Arduino is an open-source physical computing platform based on a simple microcontroller board. It can be used to develop interactive objects. Taking inputs from a variety of switches or sensors, controlling of variety of lights, motors, and other physical outputs can be achieved. It has 14 digital I/O and 6 Analog I/O. It works on +5 V DC, 10 bit analog to digital converter and 14 kb ROM (www.arduino.cc, 4th July 2015).

3.2 DC Encoder Motor

The DC motor used in this application is a brushed DC motor with 47:1 metal gear box. It is equipped with 48 CPR quadrature encoders on the motor shaft. It provides 2249 counts per revolution of the gear box's output shaft. These motors are intended for use at 6 V. In general, these kinds of motors can run at voltages above and below this nominal voltage, so they should comfortably operate in the 3–9 V range, though they can begin rotating at voltages as low as 1 V. Higher voltages could start negatively affecting the life of the motor. Key specifications of motor at 6 V: 120 rpm and 80 mA free-run, 50 oz-in (3.6 kg cm) and 2.2 A stall current (www.pololu.com, 28th June 2015). A two-channel Hall Effect encoder is used to sense the rotation of a magnetic disk on a rear protrusion of the motor shaft. The quadrature encoder provides a resolution of 48 counts per revolution of the motor shaft when counting both edges of both channels. To compute the counts per revolution of the gearbox output, multiply the gear ratio by 48. The motor/encoder has six color-coded, 11" (28 cm) leads terminated by a 1 × 6 female header with a 0.1" pitch, as shown in the Table 2 (www.pololu.com, 28th June 2015).

Table 2 Encoder connections

Sr. no.	Wire color	Function
1	Red	Motor power
2	Black	Motor power
3	Green	Encoder ground
4	Blue	Encoder Vcc (3–20 V)
5	Yellow	Encoder A OUTPUT
6	White	Encoder B OUTPUT

4 System Information with and Without Control Approach

Figure 5 shows the simulated block diagram of the system and Table 3 gives the information about all physical parameter of the DC brushed encoder motor (Brian 2008). Equation 1 shows the type of the system and Eq. 2 shows the order of the system (Aung 2007). From below two equations, it could be observed that, the present system is a second order system and type of the system is zero (as $j = 0$ in Eq. 2) (Parikhet al. 2014a, b; Ian 2004).

$$G(s)H(s) = (K (1 + T_1s) (1 + T_2s) \dots) / (1 + T_a s)(1 + T_b s) \tag{1}$$

$$G(s)H(s) = (K(1 + T_1s)(1 + T_2s) \dots) / s^j(1 + T_a s)(1 + T_b s) \tag{2}$$

$$G(s) = K_a / (0.5s + 13) * (0.003s + 0.1) \tag{3}$$

$$1 + K_a * G(s) * H(s) = 0; \tag{4}$$

K_a (motor torque constant can be found from Routh’s criteria and Eq. 4, which is a characteristic equation for stability) (Ian 2004).

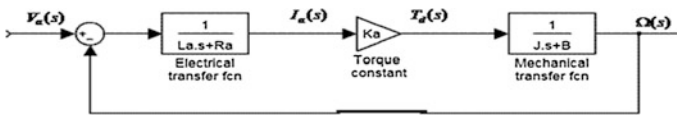


Fig. 5 Block diagram for simulation (Ian 2004)

Table 3 Physical parameters of motor

Sr. no.	Physical parameter	Symbol	Quantity
1	Motor Inductance	L_a	0.5 Henry
2	Armature Resistance	R_a	2 Ω
3	Motor inertia	J	0.03 kg m ²
4	Torque Constant	K_a	0.01 N m/A
5	Type of the system	Equation 2	Type zero
6	Order of the system	Equation 1	Second order
7	Type of feedback	–	Unity

4.1 Steady State Analysis

Equation 5 is applicable for under damped system ($\xi < 1$). The time domain response is calculated based on Eq. 5 (Brian 2008). Now it is important to know the steady state parameters (K_p , K_v , K_a and e_{ss}) of the system (Parikh et al. 2014a, b).

$$C(t) = \left(\left(\frac{w_n}{(1-x)^{0.5}} \right) * e^{-\xi * \omega_n * t} \right) * \sin(\omega_d * t) \tag{5}$$

$$K_p = \lim_{s \rightarrow 0} (s - > 0) [G(s) * H(s)] \tag{6}$$

$$K_v = \lim_{s \rightarrow 0} (s - > 0) [s * G(s) * H(s)] \tag{7}$$

$$K_a = \lim_{s \rightarrow 0} (s - > 0) [s^2 * G(s) * H(s)] \tag{8}$$

$$E_{ss} = 6 / (1 + K_p) \tag{9}$$

4.2 Transient Analysis of the System

It becomes essential to find transient parameters of the system. Every system opposes an oscillatory behavior (damping). This tendency controls the closed loop poles of the system (Parikh et al. 2014a, b). The closed loop poles decide the response of the system. Equations 10–14 belong to the transient parameters of the system (Table 4). Table 3 shows all the steady state and transient parameters values for this particular system (Brian 2008).

$$T_d = (1 + 0.7\xi) / \omega_n \tag{10}$$

$$T_r = \pi - \beta / \omega_d \tag{11}$$

$$T_p = \pi / \omega_d \tag{12}$$

$$Mp \text{ in } \% = 100 * e^{-(\xi * \pi) (1 - \xi^2)^{0.5}} \tag{13}$$

$$T_s = (4 * \xi) / \omega \tag{14}$$

Table 4 Routh’s criteria

S^2	0.015	$0.2 + K_p$
S^1	0.11	0
S^0	$0.2 + K_p$	-

4.3 MATLAB Simulation for Without Controller, P, PI and PID Controllers

Figures 6 and 7 shows the simulated block diagram and simulated response respectively.

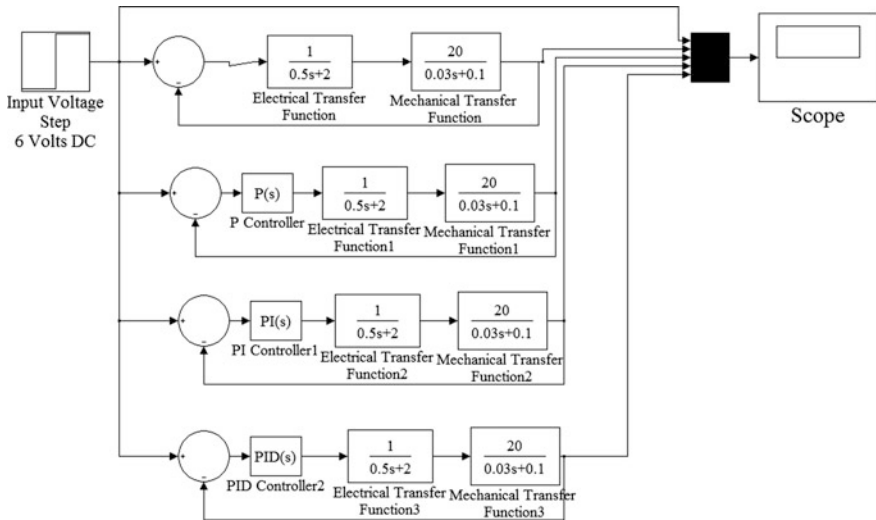


Fig. 6 MATLAB Simulation block diagram of uncompensated system, P, PI and PID controllers

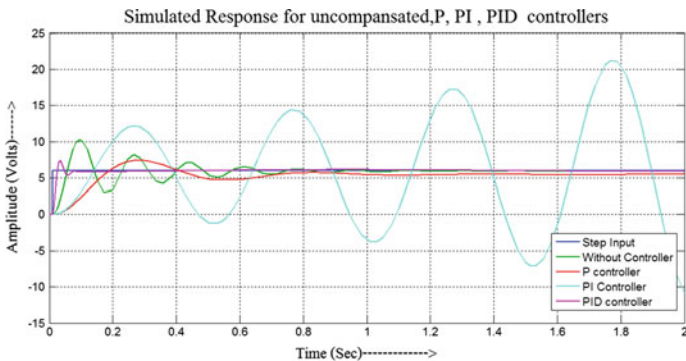


Fig. 7 MATLAB Simulated response of uncompensated system, P, PI and PID controller

4.4 Ziegler-Nichols Algorithm for P, PD and PID Controller

It can be observed from Figs. 7 and 8, that system without any controller is oscillatory and bit slow. It is necessary to design a compensator to make system stable and fast (Bashir 2005). Ziegler and Nichols published in 1942 a paper where they described two methods for tuning the parameters of P-, PI- and PID controllers (Thomas 2004). These two methods are the Ziegler-Nichols’ closed loop method, and the Ziegler-Nichols’ open loop method (Parikh et al. 2014a, b). Among these two methods, the closed-loop method is the most useful, and it is applied in the present work. Table 5 shows the Z-N tuning chart for K_p , k_i and k_d . Equation 16 shows the transfer function of the plant (Bashir 2005). Equation 17 shows the overall transfer function of the system. Equation 18 shows the characteristic equation of the system (Brian 2008).

$$C(S) = K_p + (1/T_i) * (1/s) + T_d * s \tag{15}$$

$$G(s) = K_p / (0.015s^2 + 0.11s + 0.2) \tag{16}$$

$$T.F = K_p / (0.015s^2 + 0.11s + 0.2 + K_p) \tag{17}$$

$$C.C. Eq = (0.015s^2 + 0.11s + 0.2 + K_p) \tag{18}$$

Routh’s criteria are shown in Table 4 (Brian 2008).

$K_p > -0.2$, taking Even equation from the above Table 4 (Parikh et al. 2014a, b),

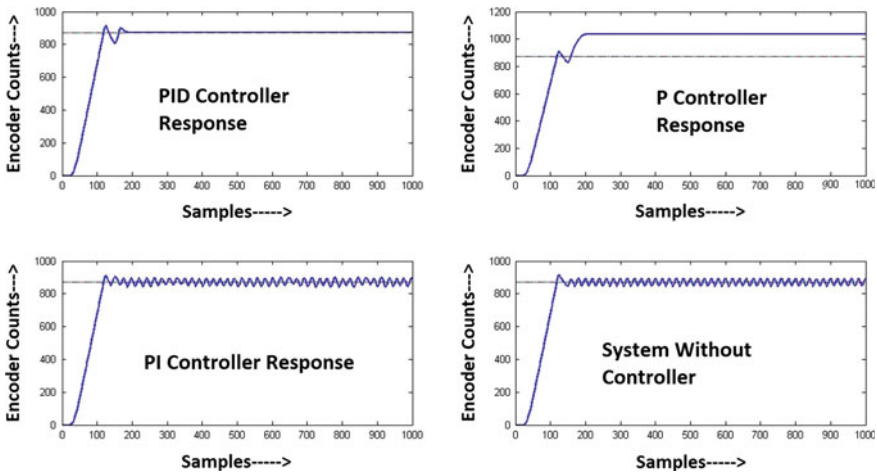


Fig. 8 Final practical results for P, PI and PID controllers

Table 5 Ziegler Nicholas tuning chart

Controller	K _p	T _i (s)	T _d (s)
P	K _u /2	–	–
PI	K _u /2.2	P _u /1.2	–
PID	K _u /1.7	P _u /2	P _u /8

Table 6 Values of K_p, K_i and K_d based on controllers

Sr. No	K _p	K _i	K _d
P	0.1	–	–
PI	0.1	1	–
PID	0.12	1.66	0.15

$$\text{C.C. Eq} = (0.015s^2 + 0.11s + 0.2 + K_p), (K_u = \text{ultimate gain} = 0.2) \quad (19)$$

$$0.015s^2 = 0.4, s = jw, w = 5.16 \text{ rad/s},$$

$$\omega = 2*\pi/P_u, P_u (\text{ultimate time}) = 1.21 \text{ s (Brian 2008)}.$$

Main aim of this work is to reduce steady state error, less settling time, less overshoot and less velocity gain. A proportional–integral–derivative controller (PID controller) is a generic feedback controller (Thomas 2004). It can be used whenever a mean position has to be achieved but the controls of the system do not react instantaneously and accurately. The PID algorithm, takes in account the following three things are to be taken in account- the existing error, the time the system has stayed away from the mean position and the possibility of overshooting the mean position. Using these three quantities, the system is controlled better, allowing it to reach the mean position faster and without over shooting it. Table 6 shows values of K_p, K_i and K_d according to the Z-N algorithm.

4.5 Applying Z-N Algorithm to Without Controller, P Controller, PI and PID Controller

See Fig. 8.

5 Results and Discussion

Referring Table 7, Figs. 6, 7 and 8 following things are observed:

- (1) Overshoot in P controller is lesser but system becomes slower with higher steady state error. It clearly shows that AGV with P controller consumes more time to get settled.

Table 7 Steady state and transient values for without controller, P, PI and PID controller

Sr. no.	Parameters	Without controller theoretical	Without controller practical	Theoretical values P	Practical value P	Theoretical PI	Practical value PI	Theoretical PID	Practical value PID
1	Kp	100	100	100	100	100	100	100	100
2	Kv	0	0	0	0	0	0	0	0
3	Ka	0	0	0	0	0	0	0	0
4	Ess	0.8 V	40 counts	0.65 V	30 counts	NaN	22 counts	0.2 V	12 counts
5	Mp	73 %	61 %	36.6 %	30.2 %	NaN	25.3 %	24.6 %	19 %
6	Ts	1.05 s	1.12 s	0.95 s	1 s	NaN	0.25 s	0.22 s	0.22 s
7	Tp	0.09 s	0.09 s	0.06 s	0.06 s	NaN	0.04 s	0.0257 s	0.03 s
8	Tr	0.03 s	0.03 s	0.111 s	0.12 s	NaN	0.014 Sec	0.010 s	0.010 s
9	Td	0.01	0.01 s	0.01 s	0.01 s	NaN	0.01 s	0.005 s	0.01 s

- (2) AGV with PI controller becomes unstable. It will not be able to stop itself at the exact location. PI controller is not suitable according to the simulated results.
- (3) AGV with PID controller works well in all criteria. System becomes fast with less steady state error and negligible overshoot for PID controller. Z-N Algorithm and PID controller suits well as far as simulated results are concerned.
- (4) Referring actual results as per Fig. 8, AGV works well for PID and P controller, but becomes oscillatory for PI controller.
- (5) The error between simulated and actual response is due to misalignments of motors and wheels, voltage fluctuations in step input, viscous friction, wheel mounting, motors inductance and internal resistance.
- (6) Delay time is almost same for all controllers.
- (7) Positional gain is 100 for all the controllers since this system is a type zero system.
- (8) Velocity and acceleration gain are zero since this system is a type zero system.
- (9) It is a under damped system ($\xi < 1$)
- (10) Steady state error is higher for P and PI controller.
- (11) Steady state error is lesser for PID controller.
- (12) PID and PI controller have given lesser overshooting compared to P controller.

6 Conclusion and Future Scope

The present research paper elaborates the interfacing technique between Arduino and DC encoder motor, simulation of the system in SIMULINK, real time data Acquisition in MATLAB. Moreover it demonstrates the use of Ziegler-Nicholas algorithm for P, PI and PID controller for real time applications. It can be concluded that:

- Z-N algorithm for PID controller works well for a positional analysis of a DC brushed motor with Encoder.
- PID controller gives less steady state error, overshoot and settling time.
- After applying PID controller from Z-N algorithm, AGV stops itself within 220 ms as shown in Table 7 after the destination comes.
- Steady state error is only 12 counts of encoder values, which is similar to 2.5 mm according to the wheel diameter.
- The analysis can be extended for velocity and acceleration of DC encoder motor.

In future the same approach may be adopted for positional analysis of AGV. The approach may be evaluated in context of constant velocity of AGV, achieving constant RPM of a servo Motor in CNC machines and automatic stir up bending mechanism (Virani et al. 2013), color based sorting system automation (Sheth et al. 2010), motor of a conveyor belt, back plug press fitting assembly (Gajjar and Sheth 2014a, b), checking parallelism of a railway track (Tamboli et al. 2015). The methodology will be very useful in electro hydraulic circuits used for retrofitting of machine tools (Patel et al. 2015).

References

- Ahmed, A. M., & Ayman, A. A. (2013). Mechatronic design of a mobile robot system. *International Journal of Intelligent Systems and Applications, Modern Education and Computer Science Press*.
- Aung, W. P. (2007). Analysis on modeling and simulink of DC motor and its driving system used for wheeled mobile robot. *World Academy of Science, Engineering and Technology*, 32, 299–306.
- Bashir, M., & Nouri, Y. (2005). Modeling and control of mobile robot. In *Proceeding of the First International Conference on Modeling, Simulation and Applied Optimization, Sharjah, U.A.E.*
- Brian. R. (2008). Design of PID controller using Z-N tuning.
- Gajjar, B. R., & Sheth, S. (2014a). Design and automation in back plug press fitting process of ball pen assembly. *Applied Mechanics and Materials*, 592, 2596–2600.
- Gajjar, B. R., & Sheth, S. (2014). Investigation of automation strategy and its effect on assembly cost: A case study on ball pen assembly line. *International Journal of Current Engineering and Technology*, Special Issue-3, 89–92.
- Ian, C. (2004). Control system design. Lecture on 14, Feb-2004.
- Parikh. P. A, Joshi. K. D., & Sheth, S. (2013). Color guided vehicle—an intelligent material handling mechatronic system. In *Proceedings of the 1st International and 16th National Conference on Machines and Mechanisms (iNaCoMM2013)* (pp. 628–635). India: IIT Roorkee.
- Parikh, P., Shah, H., & Sheth, S. (2014). A mechatronics design of a line tracker robot using Ziegler Nichols control technique for P, PI and PID controllers. In *International Mechanical Engineering Congress (IMEC-2014)*. Retrieved June 13–15, 2014. doi:10.13140/RG.2.1.4107.4722.
- Parikh, P., Shah, H., & Sheth, S. (2014). Development of a multi-channel wireless data acquisition system for swarm robots—a mechatronic approach using Arduino UNO and MAT Lab. *International Journal of Engineering Development and Research (IJEDR)*, 2(1), 717–725. Retrieved from <http://www.ijedr.org/papers/IJEDR1401130.pdf>. ISSN:2321–9939.
- Patel, T., Sheth, S., & Patel, P. (2015). Design of semi-automatic hydraulic blanking machine using PLC. In *National Conference on Innovative & Emerging Technologies (NCIET- 2015)* (pp. 410–412). doi:10.13140/RG.2.1.4529.6803.
- Sheth, S., Kher, R., Shah, R., Dudhat, P., & Jani, P. (2010). Automatic sorting system using machine vision. *Multi-Disciplinary International Symposium on Control, Automation & Robotics*,. doi:10.13140/2.1.1432.1448.
- Tomas, B. (2004). *Ziegler Nicholas Method*. Houghton: Michigan Technological University.

- Tamboli, K., Sheth, S., Shah, V., Modi, V., Gandhi, C., & Amin, N. (2015). Design and development of a mechatronic system for the measurement of railway tracks. In *Proceeding of the International conference CCEED under IEEE* (pp. 264–269).
- Virani, M., Vekariya, J., Sheth, S., & Tamboli, K. (2013). Design and development of automatic stirrup bending mechanism. In *Proceedings of the 1st International and 16th National Conference on Machines and Mechanisms (iNaCoMM2013)* (pp. 598–606). India: IIT Roorkee.

A Hybrid Approach to Motion Planning for Stepping over and Obstacle Avoidance in Humanoids

Hari Prasanth and A.P. Sudheer

Abstract Obstacle avoidance and path planning of biped are challenging issues addressed by researchers across the globe. Tackling with obstacles in mobile robots generally involves obstacle avoidance by choosing via points away from the obstacle. In addition to this, legged robots particularly humanoids, have the potential to step over or step up on obstacles to cross them. This approach can be more effective in case of certain category of obstacles which are not stretched along the lateral direction and there by not hindering the stance foot placement. This necessitates a separate study of these category of obstacles to tap the full potential of humanoids to step over them where ever possible and thereby reducing the necessity of a path modification. The approach involves per-determining the optimum step length of the robot by energy optimization and dynamic analysis, followed by the selection of best trajectory for stepping over obstacles that are fitted into basic 3-D shapes for easiness of real time computation. A fuzzy based trajectory planning for these basic shapes are studied in detail and the intelligent fuzzy based planner selects the best trajectory, after cross checking the stability of the choice.

Keywords Dynamic analysis · Fuzzy · Gait · Motion planning · Energy optimization · Stepping over

1 Introduction

The two widely used locomotion methods in mobile robots are legged locomotion and wheeled locomotion. While legged locomotion evolved out through bio-inspiration from terrestrial organisms, wheeled locomotion is an artificial cre-

H. Prasanth (✉) · A.P. Sudheer
National Institute of Technology Calicut, Kozhikode, Kerala, India
e-mail: harip.research@gmail.com

A.P. Sudheer
e-mail: apsudheer@nitc.ac.in

ativity. Though legged robots such as humanoids are familiar to us, the necessity of using multi-DOF expensive legged locomotion often requires justification even among roboticists. Though a single phrase answer to this is its effectiveness in unknown terrains, this often demands more clarity.

Both legged and wheeled robots are stronger in their own domains. One of the main reason why wheeled robots are more preferred is due to its simpler construction requirements and much lesser use of actuators for performing similar simpler tasks. Also, the greater computational complexity associated with the control of legged robots favors the latter. Even though there are all terrain wheeled vehicles, catering to the needs of maneuvering in difficult terrains, when it comes to intermittent environments similar to stepping stones or ditches, legged robot serves the purpose better. Another domain where legged robot finds its application is its ability to adapt to the situation and modify the gait to continue locomotion, even after losing some of its legs. Dogs and spiders, for example, perform gait modification to continue locomotion with reduced number of legs. Thus, a legged robot is more effective in an unknown terrain, while a wheeled robot is better in a flat and continuous environment. One of the keys to the development of legged robots therefore lies in their ability to cater with unknown or intermittent environments and this paper attempts to contribute to a solution for such challenges.

Various global path planning techniques (Qiu Bo et al. 2010) were introduced by researchers across the globe. (Kulkarni et al. 2006) developed a PRM and reinforcement learning for global path planning in a static environment. (Khatib 1986) developed an artificial potential field approach for obstacle avoidance in manipulators, where the field has a strong repelling force in the vicinity of the obstacle and an attracting force towards the target, resulting in a net potential field at each location which ultimately contributes to the decision making. Here, the obstacles are represented using combination of primitives, where a geometry base of some fundamental shapes are chosen and represented using analytical equations.

The position of the stance foot is critical in stepping over an obstacle and this requires a proper planning of the step lengths of the previous few steps. (Sabourin et al. 2008) developed a fuzzy Q learning approach to address the issue, dealing with global path planning and foot step placement in dynamic environments. Most of the global path planning approaches resides on 2-D obstacle maps such as visibility graphs and Voronoi diagrams (Leena and Saju 2014), often neglecting the height of the obstacle and approximating the contours to polygonal blocks or by locating the obstacles in square grids in the map (Ahmed and Deb 2011) (Sedighi et al. 2004). This renders the algorithm ineffective in utilizing the potential of legged robots to step up and step over obstacles. If the obstacles are feasible with in the swing foot trajectory, constrained by the maximum possible step height and step length, an intelligent selection of these parameters can help in stepping over obstacles effectively rather than changing the path of the robot to avoid obstacles. (Kim and Noh 2007) used a 2.5 Dimensional map to represent a smart home environment and considered the height of the obstacle, which enabled them to utilize the stepping on and stepping over strategies to cross obstacles. (Ayaz et al. 2009) developed a hybrid approach that chooses between stepping over and

circumventing based on a 2.5 D map that takes into account, a 2-D map of the top view of the obstacle cluttered environment and the height of the obstacle. Obstacles are classified into three categories based on the variation of height. Nevertheless, the approach doesn't incorporate the geometric shape of the obstacle and considered objects of only cuboidal shape. A mere consideration of just the height of the obstacle and not the geometric shape of it in 3 Dimension, particularly in the case of obstacles that are not stretched laterally, restricts the algorithm from reaping the benefits of stepping over capabilities of humanoids to its maximum extend. This paper attempts to contribute to a solution to this defect by classifying the obstacles based on their shapes into basic geometric shapes and then studying each of them closely.

Determining the normal distance from each point of the surface of the obstacle to determine a swing foot trajectory free of collisions, for stepping over is computationally demanding, if not impossible. The proposed method assumes an algorithm that fits the obstacle into one of the basic 3D geometries listed in Table 2. The research also assumes sufficient visual-odometric data to be available from sensors that helps in generating the 3-D map required for the research. Then, the idea is to develop walking primitives for stepping over based on the category of obstacle. Selection of optimum swing foot trajectory for these basic 3D geometries are studied closely. Hybrid Fuzzy inference systems developed for these geometries decides whether to go ahead with a path modification or to a change in the swing foot trajectory when an obstacle is detected. If the output from the engine favors a change in ankle trajectory, then the engine specific to the geometry evaluates the parameters required for the modified trajectory (step length and/or step height) based on the geometric parameters of the obstacle. Effectiveness of the method is verified for various obstacles by simulating in MATLAB. Walking primitives and categorization of obstacles helps in significantly reducing the computational complexity and at the same time enables us to closely study each geometry separately to come up with the best strategy to determine the ankle trajectory for that category. This paper also discusses an energy minimization approach to determine the optimum step length during normal walking.

2 Motion Planning

Motion planning is performed to describe the time sequence of motion of joints and links of the robot. It generally involves the position, velocity and acceleration associated with the planned motion. There are numerous approaches to trajectory generation in bipedal locomotion. Most of these approaches reside on a simplified approximated dynamic model of the biped so as to reduce the computational complexity. One such approach is the inverted pendulum method (IPM) which is utilized here for the study.

2.1 Stance Leg Trajectory Generation

The dynamics of an inverted pendulum nearly approximates the dynamics of the stance leg of a biped. Thus, an inverted pendulum is used to model the bipedal walking with the stance foot representing the hinged base of the pendulum and the mass of the robot, being assumed to concentrate at the hip, is represented by the bob of the pendulum. It is also assumed that the height of the hip remains constant. These constraints when applied (as boundary conditions) to the equations of motion of the inverted pendulum helps us to determine the joint space trajectory planning for the stance leg. This model, though out of numerous assumptions gives an appropriate trajectory of the hip.

2.2 Swing Leg Trajectory Generation

Park and Kim (1998) presents a Gravity compensated approach to determine the natural dynamics of swing leg, but the method gives little freedom for researchers to control the swing foot trajectory of the robot and hence the method in its pristine form is unsuitable for obstacle avoidance. Another approach is to define the ankle trajectory of the robot, which along with the trajectory of the hip obtained through IPM will give sufficient constrains to determine the joint space trajectory of the swing leg. Selection of swing foot trajectory depends on various parameters including a smooth profile, computational simplicity and aesthetic resemblance to human walking. One of the most widely accepted choice is the cycloidal trajectory. Cycloidal trajectory being a superposition of linear and trigonometric functions has continuous first and second derivatives, which ensures a smooth trajectory with a gradual increase and decrease in speed.

Despite having this advantage, a cycloidal trajectory offers very less flexibility. Unlike a cosine curve, where we have the freedom to choose both the step height and step length simultaneously, a cycloidal curve only offers the freedom to choose one out of the two parameters. This renders the cycloidal curve less favorable when dealing with the stepping over strategy. However, the plot of velocity and acceleration profiles of both curves as illustrated in Fig. 1 indicates that a cycloidal profile is free of jerk and has a constant acceleration profile. Because of this reason, we would like to have a modified cycloidal curve with a flexibility to choose both the variables simultaneously when required. This is represented by Eqs. 1 and 2.

$$X = \frac{L_s}{2\pi} \left[\frac{2\pi t}{T} - \sin\left(\frac{2\pi t}{T}\right) \right] - \frac{L_s}{2} \quad (1)$$

$$Z = \frac{H_f}{2} \left[1 - \cos\left(\frac{2\pi t}{T}\right) \right] \quad (2)$$

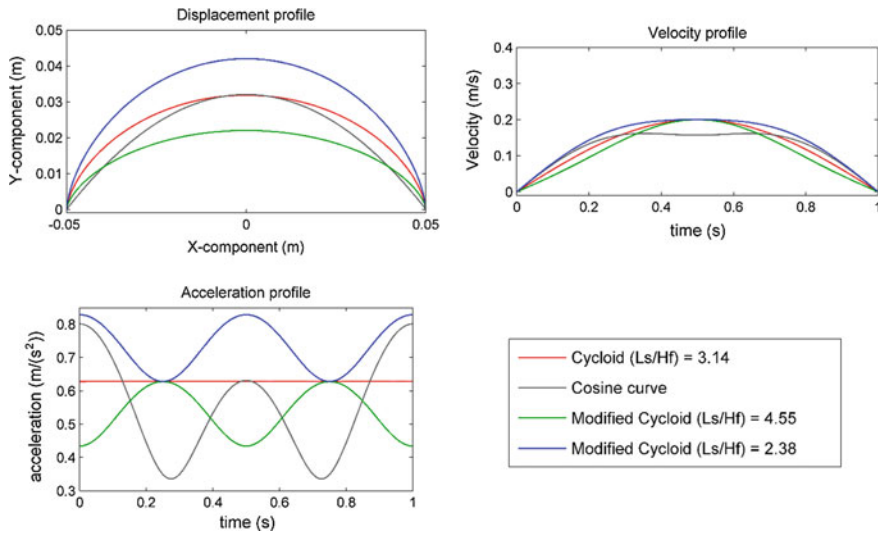


Fig. 1 Displacement, velocity and acceleration profiles for cycloid, modified cycloid and cosine curves

It can be observed from Fig. 1 that when the ratio L_s/H_f approaches π , the modified cycloidal profile tends close to a cycloidal profile and maintains a constant acceleration curve. Thus, for the steps in normal walking conditions where there are no obstacles to be crossed, the optimum ratio L_s/H_f is preserved. It is to be noted that higher the deviation of L_s/H_f from π , higher will be the change in acceleration and hence jerk.

Once the swing foot trajectory is identified, we can evaluate the swing leg trajectory, which when coupled with the stance leg trajectory gives the joint space trajectory of the biped for completing one step. The variation of θ and $\dot{\theta}$ for one step under normal walking conditions are as shown in Fig. 4.

3 Optimum Step Length

The criteria for determining the optimum step length varies depending on the walking algorithm that governs the bipedal locomotion of the robot. For normal walking, which is in the case where there is no obstacle in the near vicinity of the path, the walking should take place with minimum energy consumption. Thus, we need to determine the optimum value of step length that corresponds to a minimum energy per unit distance covered. This is evaluated by performing the kinematic modelling and dynamic analysis which are then used to determine the torque equations followed by estimation of power consumed and energy spend, as explained in the following sections.

3.1 Kinematic Modelling

A 12 DOF biped robot is used for the study, with the dimensional parameters taken from Poppy Robot. The kinematic modelling of the biped is done using standard Denavit Harternberg(DH) method and is illustrated in Fig. 2. The corresponding DH parameters are tabulated as shown in Table 1. The kinematic modelling was

Fig. 2 DH model representing the 12 DOF Biped

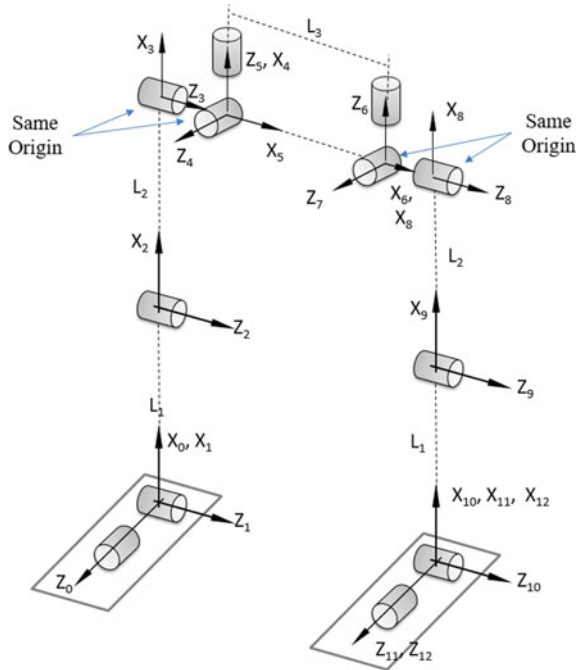


Table 1 DH parameters

Link	θ	d	a	α
1	θ_1	0	0	90^0
2	θ_2	0	L_1	0^0
3	θ_3	0	L_2	0^0
4	θ_4	0	0	-90^0
5	$\theta_5 - 90^0$	0	0	-90^0
6	θ_6	0	L_3	0^0
7	θ_7	0	0	90^0
8	$\theta_8 + 90^0$	0	0	90^0
9	θ_9	0	$-L_2$	0^0
10	θ_{10}	0	$-L_1$	0^0
11	θ_{11}	0	0	90^0
12	θ_{12}	0	0	0^0

verified by using MATLAB and the mathematical model thus obtained is represented using a ball stick model as shown in Figs. 5 and 6.

3.2 Dynamic Analysis

Dynamic analysis is performed to determine the equations of motion of the biped using Lagrange-Euler formulation method. Since, all the joints are revolute joints, the equations of motion given by Eq. 3 represents the torque equation of the biped.

$$\tau_i = \sum_{j=1}^n M_{ij}(q) \ddot{q}_{ij} + \sum_{j=1}^n \sum_{k=1}^n h_{ijk} \dot{q}_j \dot{q}_k + G_i \tag{3}$$

Where q_i represents the displacement of i th joint, M represents the inertia matrix, h represents the Coriolis and centrifugal force coefficients and G represents the gravity generated moment. The torque variation of each joint for one step is obtained as shown in Fig. 4.

3.3 Power Consumed and Optimum Step Length

Power consumed and hence energy are obtained by determining $\tau_i \cdot \dot{\theta}_i$ where τ_i is obtained from Eq. 3 and $\dot{\theta}_i$ is generated as already discussed in Sects. 2.1 and 2.2 and illustrated in Fig. 4. The power consumed for each joint is obtained from $\tau_i \cdot \dot{\theta}_i$ and is plotted against time as shown in Fig. 4. Energy consumed per unit distance covered by the biped is computed from $\tau_i \cdot \dot{\theta}_i$ for various step lengths and is plotted to determine the optimum step length as shown in Fig. 3. It is to be noted from the plot that a nearly flat bottom of the curve represents a region of optimum step length (in this case, ranging from 0.5 to 0.175). The step length obtained by this method

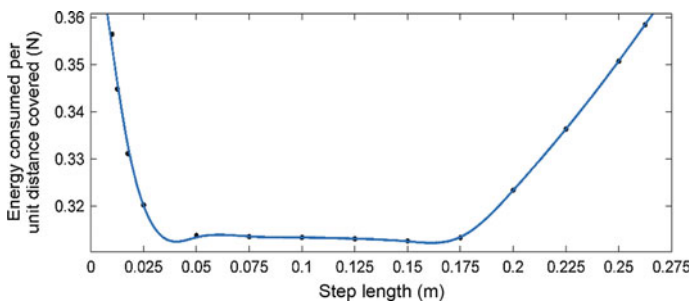


Fig. 3 Choosing optimum step length

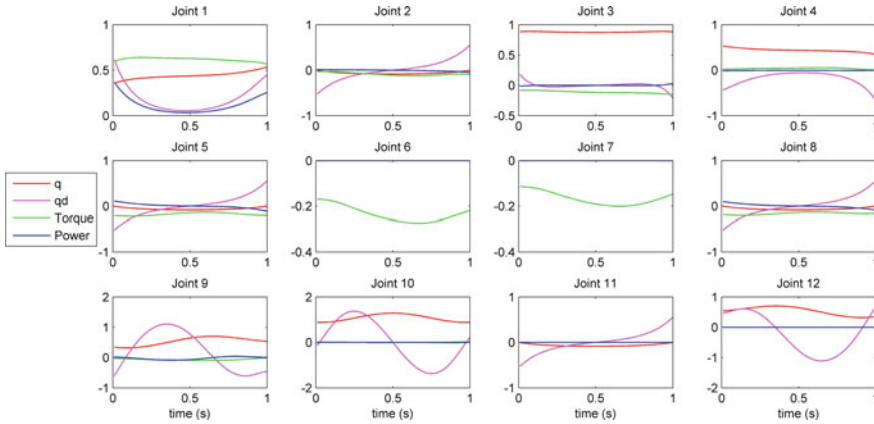


Fig. 4 Plot showing variation of joint space trajectory, torque and power with respect to time

ensures that minimum energy is utilized during normal walking, for the type of swing foot trajectory chosen.

4 Obstacle

A humanoid serving in an unknown environment often have to deal with various types of obstacles. Obstacles such as stairs and door steps are generally observed in an indoor environment. Researchers have addressed the stepping up or stepping over strategies for obstacle avoidance in these type of obstacles. When we analyze the nature of these obstacles, one could identify that these obstacles are generally stretched along the lateral direction. This renders the stepping over strategy less effective as only obstacles of much less cross section can be stepped over. It can't utilize the convex space formed between the swing foot trajectory and the floor as illustrated in Fig. 5. This is because of the requirement that for a successful stepping over, the stance foot should be placed just before the obstacle and the swing foot

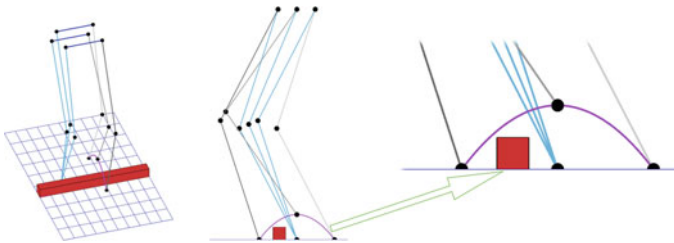


Fig. 5 Crossing a laterally stretched obstacle (cuboidal obstacle)

Table 2 Classification of obstacles

	Spheroid	Hemi-Spheroid	Cone	Cylinder (Vertical axis)	Cylinder (Horizontal axis in lateral direction)	Cuboid (Not stretched laterally)
Obstacle parameters	R, H	R, H	R, H	R, H	R, H	B, H
Feasibility of lateral shift	Yes	Yes	Yes	Yes	No	No

after it (in the sagittal plane). This means that only the obstacles with size less than half of the step length only can be stepped over (see Fig. 5).

However, in the case of obstacles that are not stretched along the lateral direction, we don't have such a restriction for the stance leg in the sagittal plane (see Fig. 5). This means that obstacles of much larger cross section now fits underneath the swing leg trajectory and hence increases the effectiveness of stepping over strategy for this category of obstacles. This is particularly applicable to obstacles with an axis of revolution such as cone, cylinder, spheroid, hemi-spheroid and even to other types of obstacles that doesn't restrict the placement of stance foot.

The various category of Basic 3D shapes considered are as mentioned in Table 2. The geometric parameters of the obstacle are also listed out along with the feasibility of a lateral shift, which is addressed in the next section.

4.1 Lateral Shift in Path Planning for Obstacles with an Axis of Revolution

During local motion planning, researchers generally consider their cross sectional view in sagittal plane for gait planning. However, in the case of obstacles with an axis of revolution, the obstacle parameters in the cross section varies. For e.g., the cross section of the cylinder/cone/spheroid is the largest when taken through the

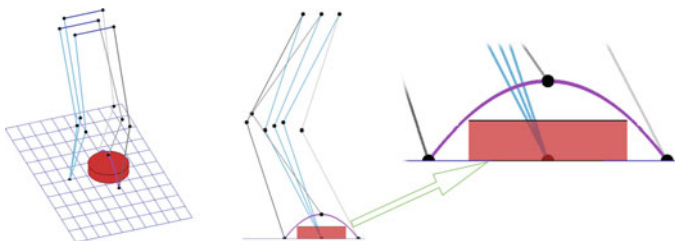
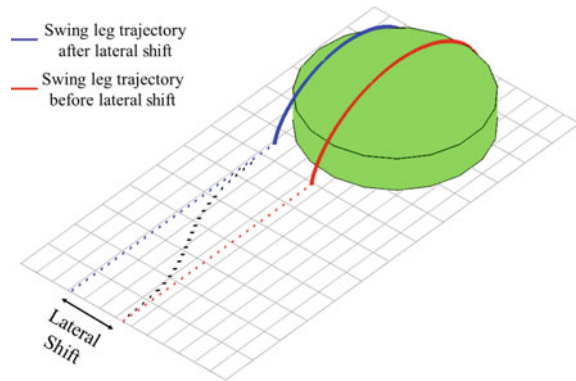


Fig. 6 Crossing an obstacle that is not blocking the stance foot placement (*cylindrical* obstacle)

Fig. 7 Crossing cylinder with a lateral shift in path planning



center and decreases when moved away from it. This necessitates the need for a closer look from the transverse plane. Even in the case of obstacles where stepping over strategy is not achievable at the largest cross section, a lateral shift in the path planning by an optimum amount can lead to a feasible stepping over at a slightly smaller cross section. This is illustrated in the Fig. 7. This method also facilitates the robot to select the parameters of ankle trajectory optimally, even when the robot is not approaching the obstacle through its largest cross section.

4.2 Fuzzy Inference System

A two input two output fuzzy inference system is developed that takes two geometric parameters defining the cross section of the obstacle as input and step length and step height as output. The two geometric parameters chosen depends on the geometric shape of the obstacle and is listed out in Table 2 for each category. Five degrees of fuzziness are chosen for both the input and output variables, with triangular membership functions. The triangular membership functions for input variables are taken to be uniformly distributed within the range, with the five degrees of fuzziness as VS (very small), S (small), M (Medium), L (large) and VL (very large). The five degrees of fuzziness for the output variable 'step length' are VS (very small), OS (optimum small), OM (optimum medium), OL (optimum large) and VL (very large). The triangular membership functions for output variable 'step length' is in agreement with the optimum step length range discussed in Sect. 3 and hence OS to OL ranges from 0.05 to 0.175. Mamdani's fuzzy inference method is followed and centroid method is used for defuzzification.

Fig. 8 Two input two output rule base

Height \ Width	VS	S	M	L	VL
VS	S / OS	S / OS	M / OM	L / OL	VL / VL
S	S / OS	S / OS	M / OM	L / OL	VL / VL
M	M / OM	M / OM	M / OM	L / OL	VL / VL
L	L / OL	L / OL	L / OL	L / OL	VL / VL
VL	VL / VL	VL / VL	VL / VL	VL / VL	VL / VL

Rule Base

The rule base or the knowledge base illustrated in Fig. 8 is designed by incorporating the discussions carried out in Sect. 2.2 regarding the optimum L_s/H_f ratio. For example, take the case of an obstacle whose input parameters, height and width takes the respective degrees (values) as L and M. The rule base in this case suggests the best combination of output parameters, step height and step length respectively as L and OL and not as L and OM, which is according to the optimum L_s/H_f ratio discussed earlier.

Along with this notion which is adopted throughout the rule base, the region highlighted in blue color is designed considering the discussions carried out in Sects. 3 and 3.3 regarding optimum step length and energy optimization per unit distance covered. This region of the rule base ensures that when the obstacle parameters are very small (VS), the step length chosen is within the optimum region for minimum energy consumption per unit distance covered. However, this principle is not applied to other parts of the rule base (see the last row and last column of the rule base in particular). This is because, in this case, prior consideration is given to stepping over the obstacle at the expense of energy optimization, which otherwise would have resulted in opting for path modification and circumventing the obstacle rather than stepping over it, which in turn would have resulted in much higher energy consumption. Please note that the lower triangle represents the output variable step length and upper triangle represents step height. An illustration of the rule base for varying size of conical obstacles is shown in Fig. 9.

Hybrid Control

From the previous discussions, it is evident that when the size of the obstacle is small enough, we only need to modify the swing foot trajectory, whereas when the size of the obstacle is large, we need to modify the path of the robot to cross the

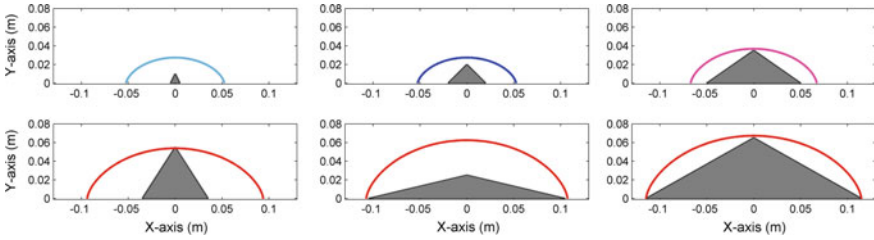


Fig. 9 Illustration of rule base

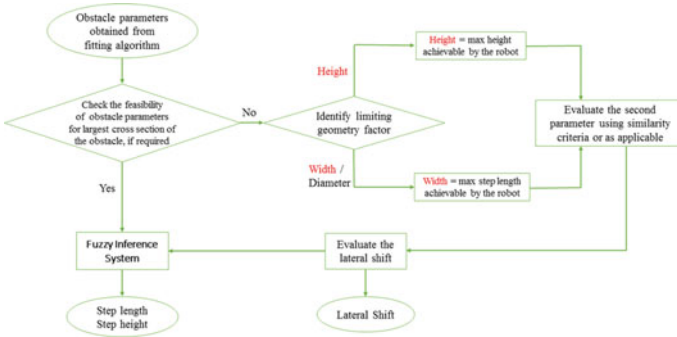


Fig. 10 Flowchart showing the hybrid planning algorithm

obstacle. And obstacles that lie in between these two extreme cases often requires a combination of both swing foot trajectory modification and path modification for an optimum control. This situation necessitates the requirement of a decision making system capable of taking online decision as to whether or not to modify the path, based on geometric parameters of the obstacle ahead. The Fuzzy Inference System coupled with the algorithm that incorporates lateral shift in path planning enables us to achieve this. The flow chart illustrating the algorithm for hybrid planning is as shown in Fig. 10.

5 Conclusion and Future Scope

Walking patterns for stepping over various kind of obstacles are studied in detail and a hybrid model of Fuzzy inference system is developed that permits an energy efficient stepping over strategy. The hybrid system decides the step length, step height and lateral shift required for the motion planning and path panning of the robot. The research also utilizes the advantage of certain category of obstacles and increase the effectiveness of stepping over such obstacles. The paper also discussed

an approach of optimum step length determination by minimizing the energy consumed per unit distance covered.

For taller obstacles, the rule base discussed here favors a larger step length than what is just necessary to step over the obstacle. This is done to minimize the energy requirements and maintain the optimum L_s/H_f ratio so as to avoid jerk. However, in a cluttered environment, closely packed with obstacles where enough space may not be available between obstacles, a trade-off between minimum energy consumption and effective obstacle avoidance should be met depending on the density of obstacle. In tightly packed spaces, a three input two output fuzzy inference system can be developed that takes into account, the density of obstacles in the immediate vicinity as the third input. And with aid from the third input, the rule base can be modified such that the L_s/H_f ratio now moves away from the optimum when more effective obstacle avoidance is demanded. In the case of dynamic environments where enough time/distance is not available to plan the step lengths of the next few steps that are necessary for a comfortable stepping over, introducing the capability to make a wise choice of skewness and kurtosis (Seungsuk et al. 2007) at such highly demanding situations, can to a great extent, enhance the effectiveness of stepping over strategy in such environments.

References

- Ahmed, F., & Deb, K. (2011). Multi-objective path planning using spline representation. In *Proceedings of the IEEE international conference on robotics and biomimetics (IEEE-ROBIO 2011)* (pp. 1047–1052). Piscataway: IEEE.
- Ayaz, Y., Konno, A., Munawar, K., Tsujita, T., & Uchiyama, M. (2009). Planning footsteps in obstacle cluttered environments. In *IEEE/ASME International Conference on Advanced Intelligent Mechatronics* (pp. 156–161).
- Khatib, O. (1986). Real-time obstacle avoidance for manipulators and mobile robots. *The International Journal of Robotics Research*, 5(1), 90–98.
- Kim, Y. T., & Noh, S. H. (2007). Humanoid navigation strategy using fuzzy motion planner in a uneven smart home environment. In *ISIS 2007 Proceedings of the 8th Symposium on Advanced Intelligent Systems* (pp. 597–601).
- Kulkarni, P., Goswami, D., Guha, P., & Dutta, A. (2006). Path planning for a statically stable biped robot using PRM and reinforcement learning. *Journal of Intelligent and Robotic Systems (Springer)*, 47(3), 197–214.
- Leena, N., & Saju, K. K. (2014) A survey on path planning techniques for autonomous mobile robots. In *IOSR Journal of Mechanical and Civil Engineering (IOSR-JMCE)* (International Conference on Advances in Engineering and Technology—2014 (ICAET-2014)) (pp. 76–79).
- Park, J. H., & Kim, K. D. (1998). Biped robot walking using gravity-compensated inverted pendulum mode and computed torque control. In *Proceedings of IEEE International Conference on Robotics and Automation* (pp. 3528–3533).
- Bo, Z. Q., Rong, H. B., Hao, P. S., & Shu, P. Q. (2010). Complex motion planning for humanoid robot: A review. *Information Technology Journal*, 9, 1270–1277 (Asian Network for Scientific Information, 308-Lasani Town Sargodha Rd Faisalabad 38090 Pakistan).
- Sabourin, C., Madani, K., Yu, W., & Yan, J. (2008). Footstep planning for biped robot based on fuzzy Q-Learning approach. In *ICINCO-RA (1)* (pp. 183–188).

- Sedighi, K. H., Ashenayi, K., Manikas, T. W., Wainwright, R. L., & Tai, H. M. (2004). Autonomous local path planning for a mobile robot using a genetic algorithm. In *Congress on Evolutionary Computation CEC2004* (pp. 1338–1345).
- Seungsuk, H., Han, Y., & Hahn, H. (2007). Adaptive gait pattern generation of biped robot based on human's gait pattern analysis. *International Journal of Mechanical Systems Science and Engineering*, 1(2), 80–85.

Web Based Simulation and Remote Triggered Laboratory for Robots

A.T. Navaraja, Neha Jain, Debashree Sengupta and C.S. Kumar

Abstract This paper describes a web based virtual laboratory developed to facilitate learning robot kinematics and control through simulation and online control of some well-known robots in real-time with vision feedback system. The web based self-learning content and tools can be used in engineering education for both graduates and research scholars. Using Java Server Pages (JSPs), WAMP and Python, we provide a standard and robust platform for client environment. The website primarily addresses the delivery of basic concepts in robot kinematics.

Keywords Web based technologies · Kinematic simulation · Control of robots · Matlab builder JA

1 Introduction

Laboratories play a vital role in engineering and science program educational systems. Web based online methods not only demonstrate the laboratories, but also bring the theory to life. So, the client/students can see how the event occur and get affected by real world measurements. The experiments are designed to enhance the learning methodologies by bringing things into a virtual environment. However, these laboratories require expensive equipments to perform the experiments and are difficult to maintain. The web based online system developed at IIT Kharagpur can not only be used by the students within the institute, but can also be accessed by other institutions (<http://nptel.iitm.ac.in/courses.php>; <http://ocw.mit.edu/>).

In literature, there are many remotely triggered and virtual laboratories having applications in robotics and control systems (Tzafestas et al. 2006; Yeung and Huang 2003). Some remote triggered laboratories have been developed by using LabVIEW. For example, Stanford University established their Cyberlab for mea-

A.T. Navaraja (✉) · N. Jain · D. Sengupta · C.S. Kumar
Department of Mechanical Engineering, IIT Kharagpur, Kharagpur, India
e-mail: navarajacse@mech.iitkgp.ernet.in; navarajacse@gmail.com

asuring the physical properties of laser diode, using LabVIEW internet toolkit and vision feedback by NI-IMAQ software tools ([Stanford university-cyberlab](#)). A vision based tele-robotic control over internet for an industrial robot was developed and implemented using LabVIEW for image processing and was controlled using a Java servlet program (Pretty et al. 2008). IIT Kharagpur has used LabVIEW to set up experiments on analog signals and systems and access it via web (Deb and Dam 2013).

Most of the web based applications are developed using software like Java, C#, LabVIEW which require client side downloading and installation of runtime programs. Using these causes several drawbacks such as slow response time and version control based problems. Alternatively, using server technology provides an easy web experience to the client without any hassle of program installations. In this paper, a kinematic simulator has been designed for educational purposes, using web technologies. Matlab based web technology is widely adopted in most web-based robot kinematic/engineering applications and educational learning platforms (Bayilmis 2010; Rosello et al. 2007; Petropoulakis and Stephen 2005). Specifically, Matlab Builder JA has been used earlier for online tool development. The Matlab Builder JA is used in developing the web based environment for analysis of load flow studies and power systems (Malarvizhi and Veena 2011). In a similar approach, the Matlab Java builder is used in developing an online method to analyze pathology images (Markiewicz 2011). On a similar approach, a web-based ECG simulator was developed using MATLAB Web Figure and MATLAB Builder NE (Guney et al. 2012). Therefore, in the design of web simulator for robot kinematics, we have adopted Matlab Builder JA and MATLAB Web Figure (Guney et al. 2012; [MATLAB Builder JA 2 User's Guide, The Mathworks Inc.](#)). With the use of this simulator, kinematics of various manipulators can be projected on to the webpage, data like the transformation matrices can be fetched, stored at the server and retrieved for a smooth web experience of the robot application. For the remote triggered virtual lab, industrial robots like Puma 560 and Movemaster RM-501 available at CAD/CAM laboratory, IIT-KGP, were used. Web applications for the remote triggered lab were developed using LabVIEW as well as open source software such as Python, pySerial and JavaScript.

The main purpose of this stated work is to provide an easy web based environment for understanding the concepts of robotics and control systems. The web application for the concepts of robotics and control is made available through the virtual labs website. The website is aimed at providing online education in a simple and lucid manner along with easy accessibility to promote self-learning. In this paper, the development of kinematics simulator for Robotics and online control of Robots is emphasized, which can be effectively used for education through internet.

The rest of the paper is organized as follows. In Sect. 2, the software tools used for the design of web application are described. In Sect. 3, the requirements of an e-learning website for a typical robotics course are described. In Sect. 4, the design and architecture of the web based simulator and remote triggered lab is illustrated. In Sect. 4, the implementation of the online simulator and remote triggered Lab is

discussed. Finally, the paper is concluded in Sect. 5 with discussion on the effectiveness of the simulator.

2 Software Tools Used

2.1 Back End Tools Used at Server Side

A vast number of software tools are being used for developing simulations in various disciplines of engineering. The softwares used in developing the virtual lab on robot kinematics and online control systems are Solidworks, Matlab/Matlab Builder JA, WAMP and LAMP, python, pyserial, JSP, servlets, zone minder and JavaScript.

MATLAB is known as matrix laboratory because it works by the linear matrix computational technique. Matlab allows manipulation of matrix, plotting data and graph, interfacing other languages that have been written in C, C++, Java (MATLAB Tools, <http://in.mathworks.com/help/matlab/>). In order to show kinematics of robots in 3D simulation, the robot models are developed in Solidworks and imported into Matlab. In Matlab, the simulation of the model is developed in the form of functions. The Matlab Java Builder JA helps in packaging these functions as jar files. The Matlab functions are developed in such a way that the functions return output in the form of images and text. Java programming and J2EE architecture has been used in the web interface to the robotic applications. J2EE is known for its robustness and security and hence, suits large scale applications (Chunlin 1999). Also, J2EE has less memory utilization and quick access time (Hamed and Kafri 2009). Python is adopted here because of its effective approach to object oriented programming and efficient high level data structures. Python is popular for its interpreted nature, dynamic typing and elegant syntax. This makes it appropriate for rapid application development and scripting on most platforms. Python has an extensive standard library and interpreter which are open for all major platforms. Therefore, embedding the python interpreter into PHP becomes easy due to this extension, allowing instantiation and manipulation of Python instances from within PHP. Python also provides an API module for serial port communication called pySerial to access the serial port. ZoneMinder is intended for video surveillance applications. It allows capture, recording, analysis and monitoring of video data coming from one or more IP cameras through network attached to a Linux system. It requires PHP and MySQL, and is enhanced by a web server like Apache. Zone minder is used to generate vision feedback system to the client and starts recording robot motion in the local zone minder webserver when the robots are under action.

2.2 Front End Tools Used at Client Side

To avoid version control problem and network bandwidth consumption at client side, we opted light weight programming languages like JS, Ajax & PHP to ensure the execution of program at client side. JavaScript is a dynamic programming language used as a part of web browsers. The implementation of JavaScript allows client-side scripting to interact with user, communicate asynchronously, control the browser and manipulate the document content that is displayed ([JavaScript Wikipedia https://en.wikipedia.org/wiki/JavaScript](https://en.wikipedia.org/wiki/JavaScript)). Ajax (short for asynchronous JavaScript and XML) is a client-side development technique to create asynchronous Web applications. These web applications can send data to and retrieve from a server asynchronously without interfering with the behavior and display of the existing page using Ajax. These requests do not need to be asynchronous ([AJAX Wikipedia https://en.wikipedia.org/wiki/Ajax_\(programming\)](https://en.wikipedia.org/wiki/Ajax_(programming))). PHP (Hypertext Preprocessor) is a server scripting language. It is a powerful tool for making more interactive and dynamic Web pages. PHP is a widely-used open-source language for efficient server-side programming in web applications. PHP can be easily embedded into HTML code and python scripts. The PHP interpreter is generally implemented as a Common Gateway Interface (CGI) executable or a web server's native module. This interpreter handles the PHP code. Once the PHP code is executed, the resulting output is sent to its client by the web server. This output is usually in the form of a part of the generated web page, for example, a web page's HTML code, an image, video, embedded flash files and some encrypted data for secured communication.

3 Requirements for a Typical Robotics Course

3.1 Puma 560 & Movemaster RM-501

The Puma 560 is a robot manipulator with six degree of freedom. The end-effector of the robot arm can reach a point within its workspace from any direction. Each joint are controlled by individual brushed DC servo motors. The feedback from servos is collected from 500 to 1000 count 3-channel encoder and a potentiometer which has been mounted at the back of every motor. The global position of the robot end-effector can be determined from the given feedback information. The Mitsubishi Movemaster RM-501 robot is a robotic arm with five rotational joints. These are actuated with DC motors to each of which two encoders are associated which allow differential directional information to be read for each joint. The controller of RM501 and Puma 560 has been modified to control robot locally and remotely through www. The website shows the concept of kinematics through both the software simulators as well as the actual robot manipulator triggered and controlled remotely.

3.2 Forward Kinematics of a 6R Robot Manipulator

In Forward Kinematics, the position of the end-effector is computed using kinematic equations with given values of the joint parameters. A 6R robot manipulator is said to have 6 degrees of freedom. The 6R indicates that each joint of the manipulator is of the type revolute. There are various 6R robot manipulators that exist. We have developed the CAD model for Puma 560 as it is the one present at our CAD/CAM Lab, IIT Kharagpur. For the simulation, the model is provided an initial position, known as the base position. The user can select any joint angle and specify the angular value to perform simulation. With respect to angular value, the transformation matrix will be generated and posted in the webpage. Meanwhile, the change in manipulator end effector position according to the transformation matrix is also displayed on the client screen. The forward kinematics of a typical Puma 560 robot manipulator is shown in Fig. 1.

3.3 Forward Kinematics of a 4R Robot Manipulator

This web application simulator for the 5R robot manipulator also follows the same mechanism as the above stated 6R robot manipulator. All the joint angles of the manipulator are revolute in nature so only the angular values have to be changed in the DH parameters to invoke forward kinematics. Figure 2 shows a typical 5R robot manipulator with forward kinematics.

Fig. 1 Puma 560 robot simulator

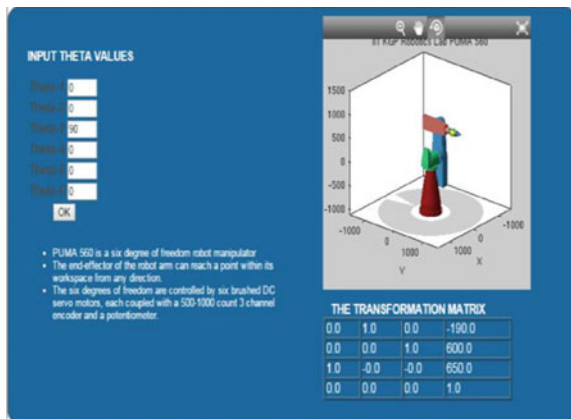
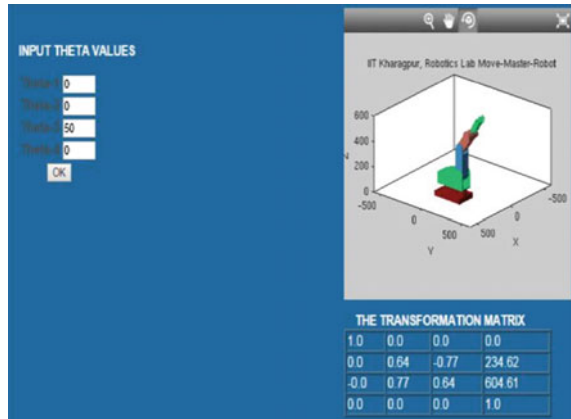


Fig. 2 Simulator for the 4R robot manipulator



3.4 Multi DOF Customized Manipulator

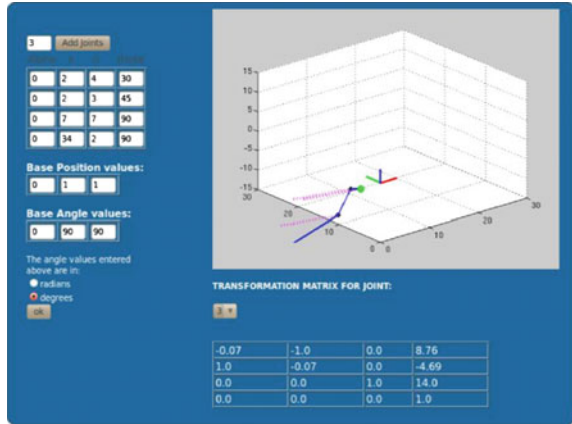
In order to understand the above mentioned serial-chain manipulator, a generic simulator was created. It was created with the aim of comparing different serial chain manipulators and studying the robot in different position and orientation (Sengupta et al. 2013). The generic multi-DOF manipulator can be created with any number of links, as per user requirements. The experiment is performed by following certain number of steps:

1. The base location of the manipulator is specified with the x-y-z coordinates and orientation i.e., the coordinate frame with respect to the origin by α, β, γ .
2. Each link can be added by clicking the button “add joint”.
3. The link and twist parameters of the manipulator are added for each joint. In addition, each joint can be chosen as prismatic or revolute by the customized input. The DH parameters, α , a , d , Θ are then specified for each joint accordingly.
4. The position kinematics is calculated. The Forward kinematics of the manipulator is found in the form of Homogeneous Transformation Matrix. The computation provides the overall transformation from base to the end-effector position as well as the link by link transformation.

The Fig. 3 displays the multilink manipulator simulator at the virtual lab website. An example is provided for a 4-link manipulator. The DH parameters for the manipulator are displayed in table form in webpage and the base frame position and orientation is provided as $x = 0$; $y = 0$; $z = 0$; $\alpha = 0$; $\beta = 0$; $\gamma = 90$.

The angles can be chosen in radians or degrees for each manipulator. The simulation provides the transformation matrix from the base frame to the end-effector frame.

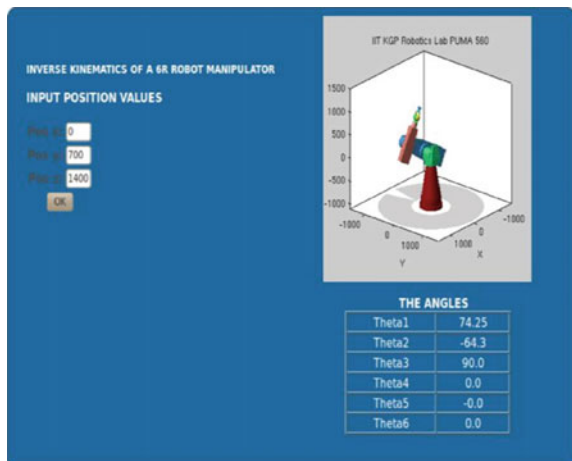
Fig. 3 The graph for a multilink manipulator when the angles are represented in degrees



3.5 Inverse Kinematics

In inverse kinematics, the joint parameters of the robot are calculated using kinematics equations to determine the end-effector desired position. An application illustrating the concept of inverse kinematics of a manipulator is developed for simulation. The web application is set to have an initial position of the manipulator and then the user provides the final position of the end-effector by the x, y, z co-ordinates. Figure 4 illustrates the inverse kinematics for Puma 560.

Fig. 4 Inverse kinematics simulator for Puma



4 System Architecture of Online Simulator and Remote Triggered Lab

System architecture of the web simulator for robots is composed of server and client layers as shown in Fig. 5. The server accepts request through internet from clients and process the request according to the client's demands and display the output. Matlab Builder JA and J2EE technology (Guney et al. 2012) are used at server side to perform all processes. Client can connect to the server and select the desired web application to visualize a concept of robot kinematics. Users can access the web simulator without installing any client side program. Therefore, users only need devices such as Laptop, smartphones, PC connected to the internet. The proposed system architecture is described in flowchart shown in Fig. 6. The software web simulator has been developed using *MATLAB Builder JA*, *MATLAB Web Figure* (Guney et al. 2012; Hamed and Kafri 2009) and J2EE technology (Fig. 7).

The software architecture of the remote triggered lab as shown in Fig. 8 is based on server and client method using Hypertext Transfer Protocol (HTTP). HTTP works as a request-response protocol between a client and server. The server returns response to the client, only when client submits request to the server. The server machines are operated using windows and Linux platform. We had created different servers for controlling the robot and vision feedback system by adopting divide and conquer method to reduce the overhead work at the server. The Robot control

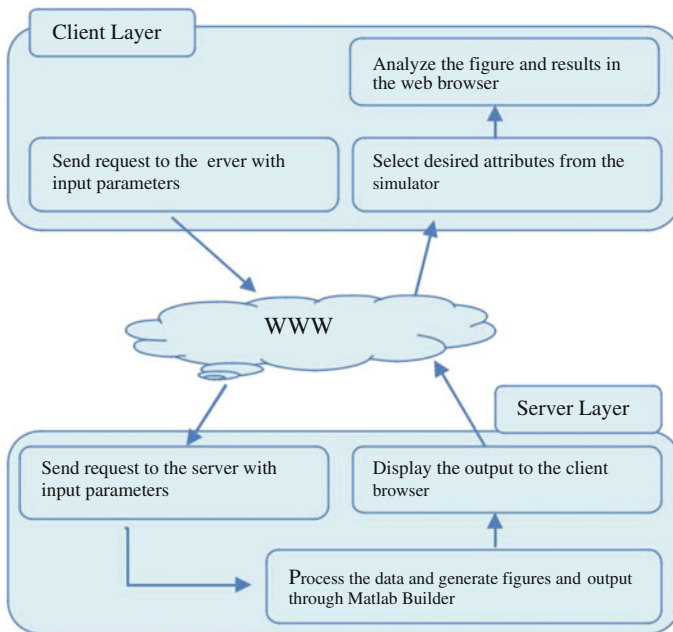
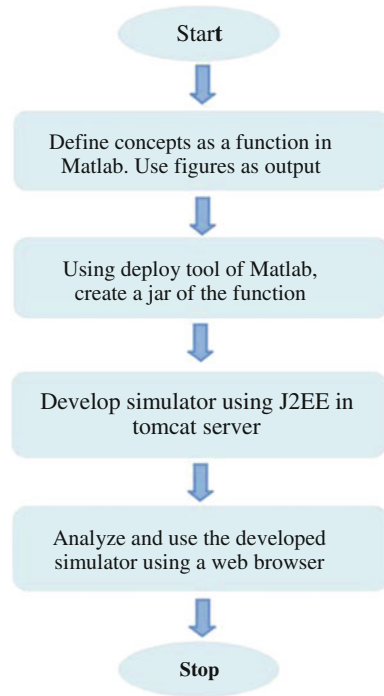


Fig. 5 The client-server architecture for the software

Fig. 6 Flowchart of the simulator design



system has been made on WAMP platform and vision system on LAMP platform both these server are bypassed through common gateway virtual lab sever using the reverse proxy method. In order to provide an easier client side experience, the web application has been developed using open source software. The system architecture diagram is shown in Fig. 7. Immediately after connecting to the global virtual lab server [vlabs.itkgp.ernet.in/mvl1/], the authentication is processed at the server and the remote triggered lab is available to client. The authentication is used to prevent accidents during robot in action and to avoid miscommunication. In any point of time only one client will be allowed to access the remote triggered lab to avoid traffic in the network or malfunctioning of the robot.

5 Implementation of Online Simulator and Remote Triggered Lab

In this section, the implementation of the stated architecture is presented. MATLAB Builder JA enables data conversion, sorting data and array shape using MWArray classes defined in the *javabuilder.jar* file (Malarvizhi and Veena 2011; Bayilmis 2010). The basic concepts of robotics are programmed in MATLAB and saved as functions. Since MATLAB Web Figure technology (Guney et al. 2012) is aimed to

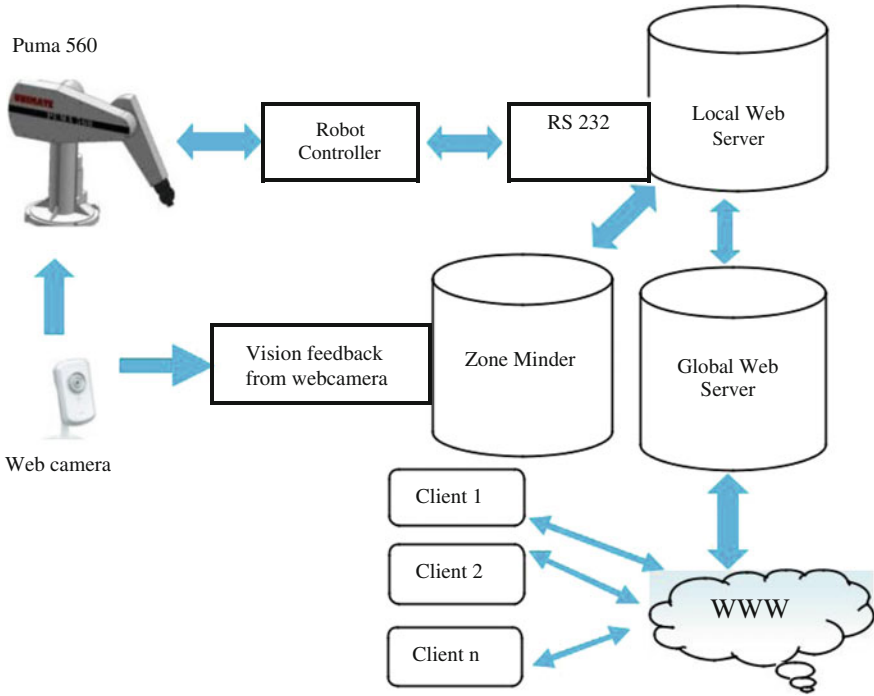
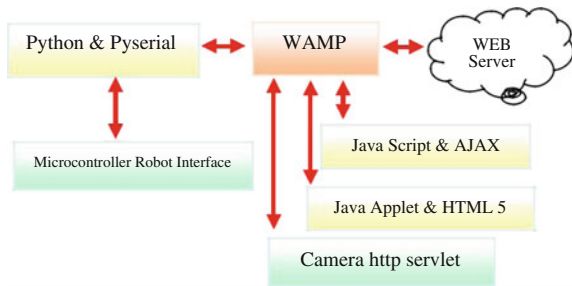


Fig. 7 System architecture context diagram

Fig. 8 Remote triggered lab software architecture



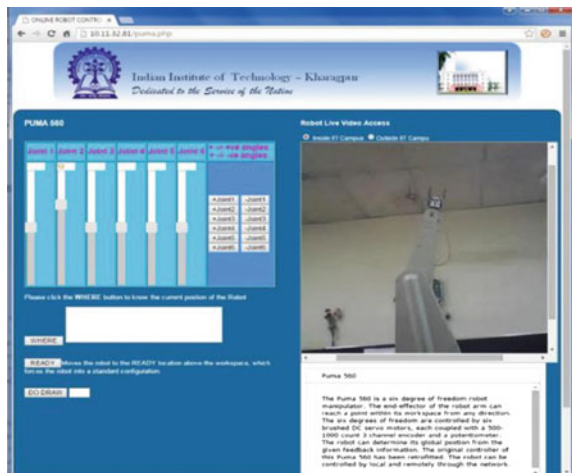
be used in these applications, a figure along with some arrays as text is returned through the Matlab function definition.

The MATLAB functions are packaged in the form of a jar using the MATLAB utility tool, MATLAB Builder JA. The package is created by the deployment tool of MATLAB by adding the necessary .m files to the project. After compilation, a jar is created which can be used in the Java web environment. At the server side, the classes in the jar are used by the servlet. A typical client request is initiated with a set of input parameters and submits from JSP which calls the servlet. The request is processed through the servlet by calling the MATLAB function packaged in the jar.

Fig. 9 Online robot control panel for Movemaster at client side with vision feedback system



Fig. 10 Online robot control panel for Puma 560 at client side with vision feedback system



This invokes MATLAB runtime. The function returns output in the form of text or a static image. The servlet displays the output back using AJAX. The figure is displayed as a Web Figure. This whole system is developed in a Linux environment.

The industrial robots MOVEMASTER and Puma 560 are used in this remote triggered lab Figs. 9 and 10. It has been controlled through WAMP, PYTHON & JS software. To control/actuate the robot, hardware connection should be established between the server and robot controller using serial port RS232. The serial port settings are made according to the robot microcontroller kit. The robot controller kits are modified accordingly to perform web based interaction. Also, python scripts are developed using *pyserial* for serial read and serial write operation on robot

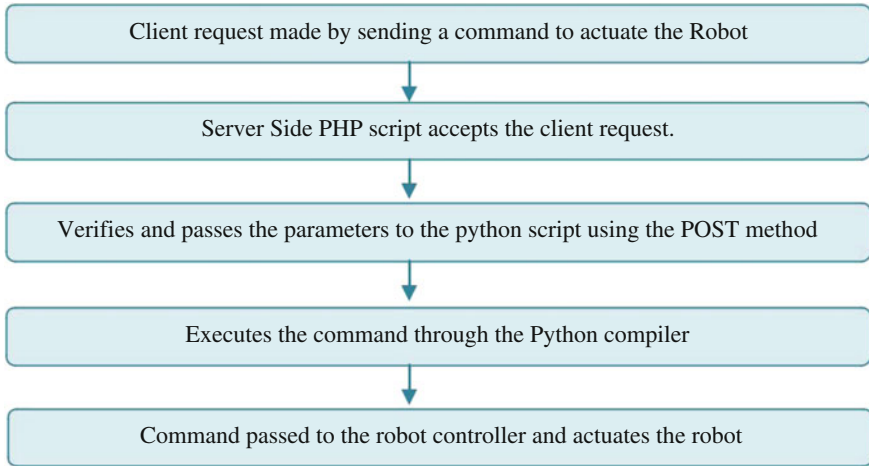


Fig. 11 Logic followed in remote triggered lab

controller. PHP, Ajax and Java scripts are embedded in HTML to provide user-interface for client activities. When clients request for an execution of their commands through a button click or text commands typed by client at text box, the respective *python* script file at server is invoked by passing the parameters to the server using POST method. POST method requests are never cached and have no restrictions on data length. The steps are illustrated in Fig. 11. In Puma 560, the client can view the end effectors' position with respect to robot workspace co-ordinate by pressing the *where* button. Both robots are executed using VAL Commands.

6 Conclusion

The paper presents a virtual laboratory of a real time software simulator and remote triggered robot control. The software simulator is developed using MATLAB Builder JA and J2EE technology. The laboratory enables easy analysis on robotics and control concepts by providing a dynamic simulator and then by providing online control to a live robot. Hence, the developed Web Based simulators require only a web browser at client side to perform simulation without needing any other plug-in. The Java web simulator developed using MATLAB builder JA provides a more comprehensible, adaptive and illustrative way of learning robotics concepts like kinematics. In addition, the hardware control gives a view of the real-life robot control. This provides users, the flexibility and space to compare and analyze the concepts with the learning material provided. The website is accessible 24 h and can be accessed through the link: <http://vlabs.iitkgp.ernet.in/mv11/>.

References

- AJAX Wikipedia [https://en.wikipedia.org/wiki/Ajax_\(programming\)](https://en.wikipedia.org/wiki/Ajax_(programming)).
- Bayilmis, C. (2010). Development of a web based educational interface using MATLAB builder NE with Web Figure for digital modulation techniques. *Computer Applications in Engineering Education*.
- Chunlin, L. (1999, October). A Java-based method for developing Web application system. In *APCC/OECC '99 Fifth Asia-Pacific Conference on Communications and Fourth Optoelectronics and Communications Conference* (Vol. 2, pp. 1079–1082).
- Deb, A. K., & Dam, T. (2013). A web based analog signals, network and measurement laboratory. In *International Conference on Soft Computing, Artificial Intelligence, Pattern Recognition, Biomedical Engineering and Associated Technologies* (pp. 58–63).
- E-learning courses from the IITs and IISc <http://nptel.iitm.ac.in/courses.php>.
- Guney, Esra, Ziya, E., & Cakiroglu, Murat. (2012). WebECG: A novel ECG simulator based on MATLAB Web Figure. *Advances in Engineering Software*, 45(1), 167–174.
- Hamed, O., Kafri, N. (2009). Performance testing for web based application architectures (.NET vs. Java EE). In *First International Conference on Networked Digital Technologies, 2009, NDT '09* (pp.218–224). Retrieved July 28–31, 2009.
- JavaScript Wikipedia <https://en.wikipedia.org/wiki/JavaScript>.
- Malarvizhi, R., & Veena, S. T. (2011). Web-based power flow analysis using Matlab Builder JA. In *2011 International Conference on Recent Advancements in Electrical, Electronics and Control Engineering(ICONRAEECE)* (pp. 156–159). IEEE.
- Markiewicz, Tomasz. (2011). Using MATLAB software with Tomcat server and Java platform for remote image analysis in pathology. *Diagnostic Pathology*, 6(Suppl 1), S18.
- MATLAB Builder JA 2 User's Guide, The Mathworks Inc.
- MATLAB Tools <http://in.mathworks.com/help/matlab/>.
- MIT Open Course ware <http://ocw.mit.edu/>.
- Petropoulakis, L., & Stephen, B. (2005). WebClass: Software to web-enable MATLAB for collaborative use. *Advances in Engineering Software*, 36, 497–503.
- Pretty, K., Parida, S. K., Navaraja, A. T., Kumar, J., Kumar, C. S. (2008). Framework and Implementation of a Vision Based Tele-robotic Control over Internet for an Industrial Robot AIMTDR-2008.
- Rosello, E. G., et al. (2007). A component framework for reusing a proprietary computer-aided engineering environment. *Advanced Engineering Software*, 38, 256–266.
- Sengupta, D., Jain, N., & Kumar, C. S. (2013, December). An educational website on kinematics of robots. In *2013 IEEE Fifth International Conference on Technology for Education (T4E)* (pp. 24–27). IEEE.
- Stanford university-cyberlab.
- Tzafestas, C. S., Palaiologou, N., & Alifragis, M. (2006). Virtual and remote robotic laboratory: Comparative experimental evaluation. *IEEE Transactions on Education*, 49(3), 360–369.
- Yeung, Kin, & Huang, Jie. (2003). Development of a remote-access laboratory: A dc motor control experiment. *Computers in Industry*, 52(3), 305–311.

Modular Robotic Assistance in Cluttered Environments: A Broad-Spectrum of Industrial Applications

Satwinder Singh, Akshit Kaplish and Ekta Singla

Abstract A broad perspective is presented for the utilization of modular robotic arms in various industrial tasks, particularly for cluttered environments. Parameters-based modules are proposed to develop reconfigurable manipulators according to the robotic parameters, resulting out of the design procedure. A brief description of the modules divisions and the optimal assembly planning is presented. Focus of the paper is the multi-layered approach for modules inventory, which can be referred as base for the further additions in the types of modules required in the library. A case study on a realistic problem of challenging welding sites is presented as one example of the upper layer of multi-layered spectrum. The results present the designed configurations and corresponding modular assembly.

Keywords Modular robots · Serial manipulators · Cluttered environments · Reconfigurable architecture

1 Introduction and Background

Primary advantage of modularity in serial link manipulators include *re-configurability* which signifies the possibility of on-site variation of the configuration of a modular manipulator for different task-based requirements. The related advantages are *availability of modules/links and reduction in repair time* during maintenance. This is one of the prime factors in industry and is directly affected by modularity in a way that if any module of manipulator fails, it can be replaced quickly. *Quick prototype development* to represent the realization of task-based designs, which normally result into unusual parameter values, is another advantage of modular architecture.

S. Singh (✉) · E. Singla
Indian Institute of Technology Ropar, Rupnagar, India
e-mail: anti.mid@gmail.com; satwindersn@iitpr.ac.in

A. Kaplish
Maharaja Agrasen Institute of Technology, New Delhi, India

In past, several works on modularity have been done and few of them are focused upon industrial serial manipulators. These efforts can be seen in Acaccia et al. (2008) in which modularity is applied to industrial robots like SCARA for pick and place operation and in the work presented by Chen (2015) representing the development of a work-cell environment for milling operations. A three-leveled approach on modular architecture is discussed in Song and Yang (2011) while showcasing the application of assembly automation. Modularity induces the characteristics of re-configurability, as presented in Aghili and Parsa (2007). Many of the works are related to self-reconfiguration, which is not applicable for industrial serial robotics arms. Modularity and Re-configurability's role can be clearly shown in many scientific facilities such as plants where complicated environments are present. An effort in this direction is presented by Pagala et al. (2014) for maintenance in highly ionizing environment like CERN. In this work, features like self-detachment and attachment using 3 degrees of freedom joints are discussed. In all these attempts, normally the system model of the reconfigured manipulator is worked upon after the change in the configuration. This can be avoided by developing a design strategy, a priori, which is with respect to the modular architecture. This will provide robotic parameters, which can be adapted by the modules for the required assembly.

This work presents the modularity for task-based synthesis of reconfigurable robots for cluttered environments which can result into unusual configurations. The proposed modular architecture and design methodology is such that it can be perceived in more general way which can encapsulate industry based tasks and complicated tasks involved in scientific facilities. The main focus of the paper is the broad perspective of types of applications which can be catered to through the proposed modules. The design of the modular manipulator and the architecture, divisions and assembly planning of the modules are briefed.

2 Modular-Design and Planning

2.1 Parameters Based Modular Architecture

The complete architecture is based on DH-parameters, which are pre-defined. Modularity in this architecture is so applied that the link-modules which act as units for constituting the complete serial-manipulator can broadly be divided into 3 different classes based on weight, size and motor used. The description about the division selection is given in Table 1.

Table 1 Module specifications

	Heavy	Medium	Light
Basic length (mm)	300	150	100
ξ	3	4	5
Weight (kg)	8.1	1.907	1.09

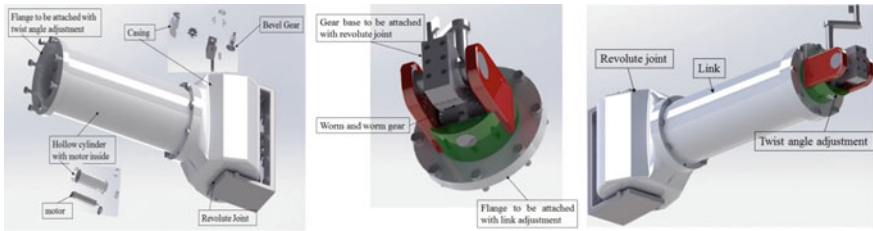


Fig. 1 Basic-length module, alpha module, complete link

Metric ξ defines the ability of motor to carry similar links based upon its capacity. Three different types of motors had been selected based upon a trade-off analysis between a motor’s weight and max torque capacity. Each link module has 3 components, as shown in Fig. 1.

1. *Basic-length link module*: This consists of a cylindrical casing with motor, internal gear box and encoder inside it, it’s length being the minimum length in a serial link chain for one type and an external gear-box with its casing. In this gear-box, 2 bevel gears are present one of them being fixed and another one coupled with motor’s shaft thus defining z-axis’ position. This casing is directly attached to alpha-module.
2. *Adaptive twist module*: This is a small part between a basic length link module and next link, for the twist angle adjustment. It comprises of a worm gear and a half cut worm wheel and is attached to the gear box casing. By rotating worm or changing the gear-set’s orientation about flange, alpha angle increments can be changed.
3. *Extended link length module*: It’s a 50 mm long link with 2 flanges at both ends and with no actuator inside it. It’s used for changing the value of the link lengths which is optional.

2.2 Design Strategy and Assembly Planning

Number of degree of freedoms (dof) can vary from 3 to 12 for this work. The number and the locations of TSLs are obtained. Number of dof are decided through an optimization problem solving exercise taking error between desired position of TSLs and actual position as the *objective function*. The problem is solved using augmented Lagrangian method keeping DH parameters as design variables. The obstacle collision avoidance (which is obtained using Proximity Query Package, PQP) and the bounds for DH parameters are taken as constraints. These bounds are decided based upon the modular architecture. Singla et al. (2010) presents the details of task-based synthesis of robotic manipulators.

Based upon the modular divisions, for n dof, certain conditions are presented to get possible assembly combinations with n modules.

- i. First link is fixed as Heavy and last as Light.
- ii. After Heavy, a Heavy or a medium must come.
- iii. After Medium, a Medium or a light must come.
- iv. After Light only Light can come.

Then for each combination, reachability is checked below a threshold value and certain limits on design variables which are DH parameters are taken as constraints and then first maximum gravitational joint torque on each joint is calculated using nested simulated annealing technique. This torque is divided by the maximum torque that the corresponding joint's motor can give. These normalized torques of all joints are added and $\sum \text{normalized torque-sum}$ is taken as the objective function. Thus minimum $\sum \text{normalized torque}$ is obtained for all the combinations and the method of Simulated Annealing is used for solving. The assembly with minimum torque-sum is selected for the given workspace.

3 Multi Layer Approach to Modularity

The applications of our modular manipulator design can be divided into a two-layer hierarchy. Different fields of science and industry wherever robotics and automation is applicable, form the upper layer. Lower layer consists of different environments in each field of the upper layer.

Our single modular library can be used for very different applications like *Assembly-Automation, repair and maintenance welding*, etc. at separate times. For each particular application, the *entire set of operations* that are supposed to be carried out by the manipulator is unique. For instance, in *repair and maintenance welding* end-effector will be a MIG welding gun or a grinding wheel or so used according to the steps required exclusively for welding only where as for *Nuclear plant maintenance* it can be for welding, cleaning, inspection of parts, etc. or in case of *Assembly automation*, a gripper for pick and place operation. Along with the difference in end-effectors, processes and the maximum payload may also vary with each of these applications. These sets divide modular library and show the application of modularity in a much broad manner i.e. the *upper layer*. It signifies the application of this modular library single handedly on a very large spectrum of applications. Eventually, special modules for each application can also be developed to increase the usefulness even further. However, the proposed set of the modules division do not cater to these variations. The concept can be expanded in the proposed multi-layer fashion.

On further dissection, the next layer of classification i.e. *lower layer* divides the modular library in its corresponding set broadly, on the basis of different *environments* and *arrays of manipulator-morphologies* used for each of these environments. Each of these environments, along with its *procedural-operations* and

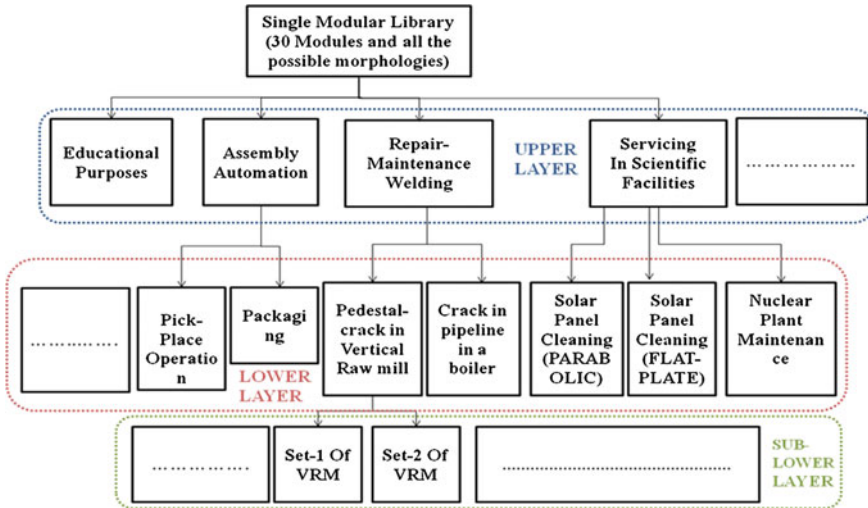


Fig. 2 A multi-layer approach to showcase the spectrum of possible service applications of modular robotic manipulators

array of morphologies required to implement them in different workspaces constitute a Single Job which is implemented at one time. These arrays vary depending upon how cluttered a particular environment is. For example, in one particular application like *Repair and Maintenance Welding*, multiple environments such as *Pedestal-crack in Vertical Raw mill*, *crack in a tyre of rotary kiln shell*, etc. are present. Here, in the first environment more redundancy is required than in latter as it is more cluttered as well as welding procedure can be different in both. This shows contrast between the two jobs and justifies the classification of lower-layer. Similarly, in case of *Servicing in scientific facilities*, different environments can be solar plant and nuclear plant, which may have same field of upper layer—say welding, but these are different from environment perspective.

The concept of modularity can be even further extended by introducing a *sub-lower layer* which shows that different assembly combination of modules with different base points can be used for different *work-spaces* inside the same environment of a particular application. All these assembly combinations form the array presented in Fig. 2.

4 Results and Discussion

A detailed case study on a repairing and welding pedestal cracks in Vertical Raw Mills (VRM) in a cement plant is presented, as shown in Fig. 3a, to represent the application of a task-based modular manipulator. This field of challenging welding

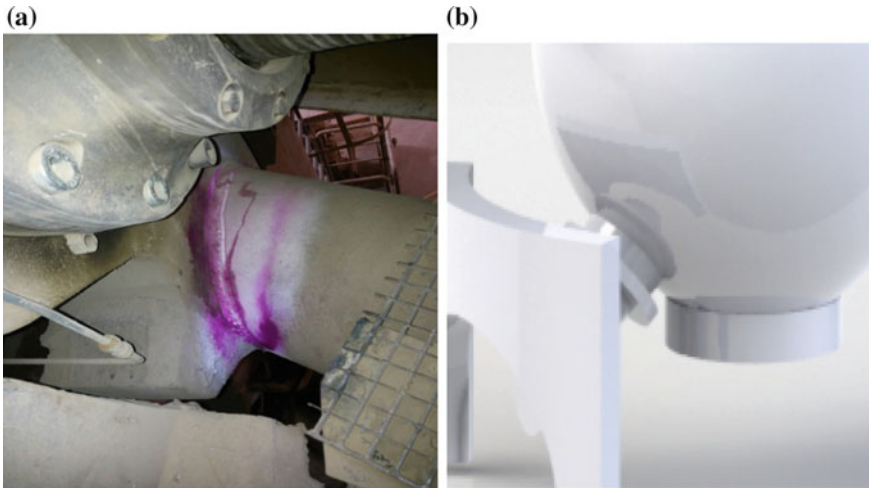


Fig. 3 a Photograph of an original crack in pedestal highlighted through chemical test. (*courtesy: Ador fontech Ltd.*) b 3-D Model of the environment of VRM

applications presents one of the member of the upper layer. With the crack-details given by the welder (*courtesy: Ador Infotech Ltd.*), a 3-Dimensional simulation of the fracture along with its location and environment is developed, as shown in Fig. 3b. Crack is analyzed and divided into equal number of TSLs at a certain resolution. All those TSLs which can be approximately approached by the same assembly of manipulator and are considered to constitute a single set. Each set of TSLs is given as input for a configuration planning and corresponding modular assembly is developed. This feasibility can be increased using hydraulic lift and rails to give a vertical and horizontal position flexibility respectively.

Eventually, high speed interfaces can be developed which takes fracture-details and environment as input, directly gives TSL-sets, their respective assembly configurations and base point locations as result and then pre-programs the control units accordingly. This can reduce the ease of welding to a very large extent as well as make process much efficient and faster. At the end-effector, *special vision-based* crack-following mechanisms can be made to give some autonomous assistance while welding the following crack.

The design process results into a 7-dof and a 6-dof manipulator for two workspaces. The resulting parameters through the optimal design process are given in Table 2 for the first case. Corresponding robotic configurations are shown with the cluttered workspaces, in Fig. 4.

Two different sets of 5 TSLs each, can be welded with *same or different modular assemblies*, as shown in Fig. 4. A 7 DOF configuration is resulted for the first set, as shown in Fig. 5a and a 6 DOF configuration is designed for the second set. The flexibility in the architecture is effective to deal with the requirements of change in

Table 2 TSLs and DH parameter values for 7-link manipulator used for Set-1

Link number # in serial link chain	DH parameter values with base point location = (320, 320, 230)							
	α_{i-1} (rad)	a_{i-1} (cm)	d_i (cm)	θ_i (rad)				
				TSL-1 (274, 385, 290)	TSL-2 (280, 385, 300)	TSL-3 (270, 385, 270)	TSL-4 (270, 388, 330)	TSL-5 (270, 390, 327)
1.	0	0	0.99	1.18	1.21	1.14	1.76	1.21
2.	0.69	34.94	0.9	1.13	1.10	1.19	0.93	1.10
3.	0.42	24.99	0.9	0.63	0.64	0.58	0.42	0.58
4.	1.21	14.9	0.9	0.13	0.28	-0.13	0.50	-0.13
5.	1.56	14.99	0.11	0.30	0.33	0.25	0.28	0.77
6.	1.35	14.99	0.599	0.68	0.54	0.91	0.03	1.76
7.	1.00	14.99	-0.627	0.65	0.56	0.77	0.19	0.28

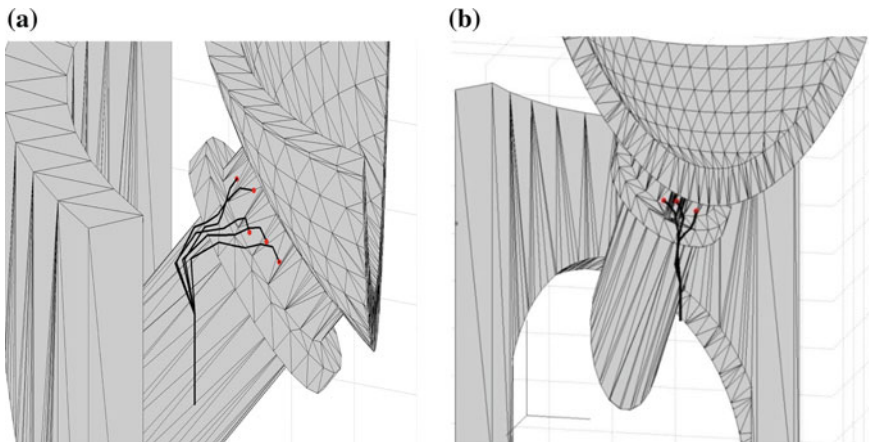


Fig. 4 Two different sets of TSLs (portions of crack) welded at separate times: Set-1 and Set-2, with different even in the number of modules assembled for the tasks

workspaces, with *same or different base points* at two different times, to cater to two different portions of crack. One of these sets is a bit interrupted with two supporting beams in its vicinity. This example, with two sets of *sub-lower layer*, shows the reliability and importance of the task-based modular robotics approach towards repair and maintenance welding at challenging situations.

The way this pedestal crack in the environment of VRM represents an example of an *upper layer* to be repaired using few different configurations, similarly another environment of a *tyre of rotary kiln shell* can be worked upon, where the cracks can be welded. That provides the example of *lower layer*, where the process is same but the environment parameters are different.

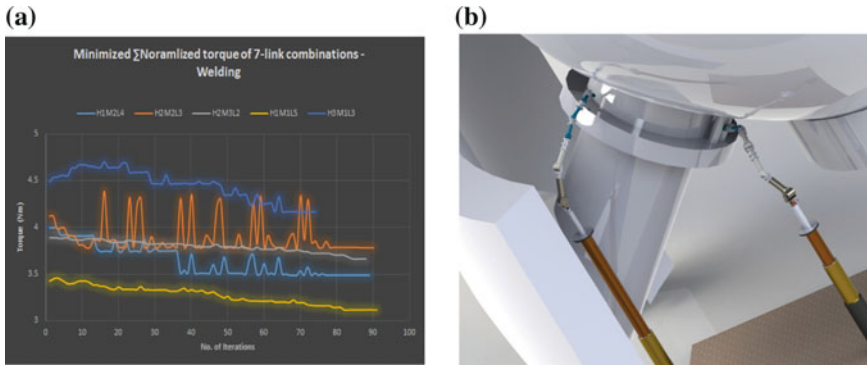


Fig. 5 **a** The torque analysis plots are shown for 5 different assemblies possible with 7-dof (for set-1 workspace). **b** The optimal assembly with minimum torque-sum of all the joints is shown

5 Conclusion

Parameters based modular architecture is presented for modular development of robotic arms for given tasks. The two-phase strategy of the design of the robotic parameters for given locations and the modular assembly of the corresponding manipulator for minimum torque-sum of joints is briefed. The methodology is implemented for a realistic environment depicting complicated tasks of welding for cracks in Vertical Raw Mills. The case study is presented as one of the fields in the upper layer of the multi-layered spectrum of the Modularity applications. This spectrum is another contribution of this paper which provides a consolidated pattern for further developments in modular architectures.

Acknowledgements Authors gratefully acknowledge the financial support of Department of Science and Technology (DST), Govt. of India, for this work. Authors are also thankful to *Ador fotech Ltd.* for sharing their information for the challenging aspects of welding applications.

References

- Acaccia, G., Bruzzone, L., & Razzoli, R. (2008). A modular robotic system for industrial applications. *Assembly Automation*, 28(2), 151–162.
- Aghili, F., & Parsa, K. (2007, August). A robot with adjustable dh parameters. In *International Conference on Mechatronics and Automation, ICMA 2007* (pp. 13–19). IEEE.
- Chen, I. M. (2015). Modular robots. In *Handbook of manufacturing engineering and technology* (pp. 2129–2168). London: Springer.
- Pagala, P., Ferre, M., & Armada, M. (2014, January). Design of modular robot system for maintenance tasks in hazardous facilities and environments. In *First Iberian Robotics Conference on ROBOT2013* (pp. 185–197). Springer International Publishing.

- Singla, E., Tripathi S., Rakesh, V., & Dasgupta, B. (2010), Dimensional Synthesis of kinematically redundant serial manipulators for cluttered environments. *Robotics and Autonomous Systems*.
- Song, L., & Yang, S. (2011). Research on modular design of perpendicular jointed industrial robots. In *Intelligent Robotics and Applications* (pp. 63–72). Berlin: Springer.

A Benchmarking Model for Indian Service Industries

Bhupender Singh, Sandeep Grover and Vikram Singh

Abstract Benchmarking is the most important tool for improvement which is proficient over comparison through other organizations known as the best within precise extent. This study marines the service industries to focus its modest edge such as customer service, function ability, policy, adequacy and many more though conveying other processes through opposition and highlights different types of Benchmarking process used in industries, that gives effective used of factors for their implementation. Thus, an attempt is made by authors to give a model for the evaluation of Benchmarking by using MADM (ANP) approach. A benchmarking model is proposed which can be implemented in service industries of developing countries like India as the industries are showing huge interest for improving their competitiveness in global scenario.

Keywords Benchmarking · Critical success factors (CSFs) · Analytical network process (ANP) · Service industries

1 Introduction

Benchmarking can be defined as the exploration towards industry best practices which lead to higher performance but can also observed as the constant search for reference themes due to the rapid change on all fronts. Benchmarking is recognized as an important tool aimed at incessant improvement of quality and an important business practice priority (Dattakumar and Jagadeesh 2003). This is a well-defined tool for improving the faintness concluded an improved process which measures its recital in contradiction of market leaders and inventions the market leaders attained their performance levels. The Benchmarking process consists of investigating

B. Singh (✉) · S. Grover · V. Singh
Department of Mechanical Engineering, YMCA University of Science and Technology,
Faridabad, India
e-mail: bhupee_28@yahoo.co.in

practices and establishing metrics where practices are interpreted as the processes that are employed and metrics are the quantified result of instituting practices. The decision to begin Benchmarking is valuable to companies by opening up many different ideas to processes, approaches and concerns. The purpose of Benchmarking is to systematically identify the processes and performance outcomes of an outstanding organization with those of its competitors processes and outcomes within the organization itself in the constantly changing business environment. This paper highlights seven different types of Benchmarking techniques, which gives effective use of factors for their implementation to authenticate the ranking of Benchmarking technique ANP approach has been applied through Super decision software 2.0.8. Experts were asked to give rating of the pair wise comparison of the factors on 1–9 scale. On this basis, Super decision software generated unweighted, Weighted Super matrix and Limit matrix. Factors priorities are directly occupied from Limiting matrix. As result, this research converts the subjective decision into objective process. Consequence of the ANP are weighted evaluation of the critical success factors which can be rank easily accordingly to their weightage.

These weights can be utilized in first phase of proposed model (as shown in Fig. 1) where different phases are completed on the basis of these CSFs. The further procedure of benchmarking model is discussed in implementation section of the paper. It stretches industries an outside focus and militaries them to aspect towards the competitors are adopting. Wide-ranging literature accessible on Benchmarking reveals the numerous surfaces of Benchmarking techniques by many scholars globally.

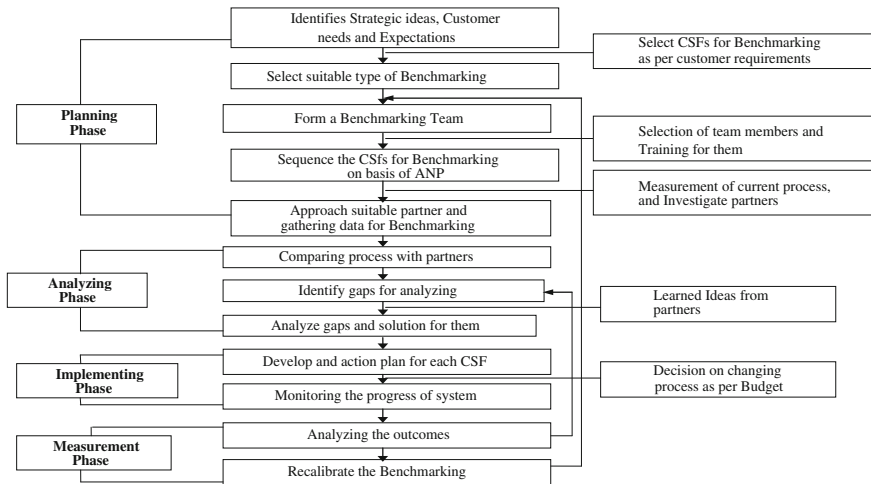


Fig. 1 Benchmarking model

2 Literature

Benchmarking was firstly applied in the 1970's for production industry to compare different parameters. Dattakumar and Jagadeesh (2003) suggested that it is an important tool which forces the industries to focus on improvements. Many researchers have done abundant literature survey on benchmarking in various fields like service and manufacturing industries such as Dattakumar and Jagadeesh (2003). Benchmarking can also be used in small and medium enterprises, traditional manufacturing industry, large environmental areas and various area of supply chain etc. Providing good Service is the main factor of benchmarking (Singh et al. 2015b). The requirement of benchmarking as a tool in any sector is very important (Singh et al. 2015b). Various tools and techniques are used to find intensity of benchmarking and maintain business in globally market. Multitude of researchers appeared in the literature applied various techniques as a trendy benchmarking tool over the past few years. Flexibility, cost and time demonstrated the development of the analytic network process (ANP) for the selection of material handling systems (MHS) in the design of FMS for a hypothetical case organization. Saaty (2009), established the real submission in various entertainment business of ANP. Singh et al. (2015a) have derived Fuzzy TOPSIS method for identification of ranking of internal department for improvement in industry.

3 Benchmarking Classification

- (a) Performance benchmarking: This is the assessment of performance procedures for the resolution of decisive in what way decent our industry is associated to others.
- (b) Internal benchmarking: A judgment among comparable operations inside own association.
- (c) Strategic benchmarking: This study is assumed when an attempt is made to disparity the strategic direction of the industries and the judgment with one's opposition in relations towards strategy.
- (d) External benchmarking: This type of benchmarking is used by corporations to pursue benefit of administrations that prospered on account of their practices.
- (e) Competitive benchmarking: A comparison with the best of the direct competitors. Benchmarking against other companies in the same industry, whether they are direct competitors or not.
- (f) Functional benchmarking: A judgment of methods with those of corporations with comparable processes in the similar function by one's industry.
- (g) Generic benchmarking: An assessment of work procedures with others who have advanced and paradigm work procedures Singh et al. (2013).

The critical success factors of Benchmarking implementation have been taken from literature and as per expert's decision few of them are used in this paper.

4 Analytical Network Process (ANP)

ANP is the general form of AHP that was proposed by Saaty in 1980. Through seeing qualitative and quantitative facets of a decision and over a pair wise comparison, it allows to set priorities amongst the elements and made the best decision. ANP (1996), instantaneously takes into account both feedback and dependence. ANP allows the best decision by permitting feedback within elements of a cluster (inner dependence) or between clusters (outer dependence). A brief description is given here because of space limitation. The ANP includes of the following foremost steps:

Step 1: Model construction through networks

Decision problem should be structured into networks by using appropriate methods or through brainstorming. Goal, clusters, elements and alternatives are identified for the decision problem to grow the ANP model. The main objective is identifying appropriate Benchmarking for the industry. As per ANP terminology the core factors and sub factors will be clusters and the elements. The model figure shows relationships between goal, clusters, elements and alternatives.

Step 2: Pairwise comparison and precedence vectors

In this step, Decision makers were asked to compare clusters over a sequence of questions for inner and outer dependence to attain the goal. The relative prominence values are resolute on the scale of 1–9. Wherever the score of 1 signifies the corresponding reputation among the elements and the score of 9 signifies the extreme prominence of one element completed the other. Pairwise comparison is accepted with admiration to goal. New matrix is designed and in each cluster the relatives weights are formed as eigenvector using formula. This comparison of pairwise at cluster level and at the level of element also. The pairwise comparison matrix is established to regulate the status of elements within each cluster. The e cluster will be found out. However, the matrices of other pairwise comparison are not shown due to space limitations. $b_{ij} = 1/b_{ji}$ is assigned to the inverse comparison. This step is completed to derive the eigen vectors and to form a supermatrix.

Step 3: Supermatrix formation

The outcome of step 2 is unweighted supermatrix. Supermatrix is actually a partitioned matrix. There are different forms that will be in this stage: Firstly unweighted super matrix and then e vectors found in the former steps through pairwise judgments are the entries for each column. Its columns represent priorities derived from the pairwise comparison of the elements. To obtain a convergence on the importance of weights, the supermatrix is raised to large powers and the resulted matrix is known as limit matrix.

In the weighted super matrix, where weights are multiplied by each submatrix for making the matrix column stochastic, and the sum of values in each column is equal to 1. It is necessary to check column entries of the unweighted supermatrix. If the unweighted supermatrix is not column stochastic then unweighted supermatrix is converted into weighted supermatrix by multiplying each submatrix by its weight

to make it column stochastic. This will produce a square matrix contingent upon the relationships that exist between numerous elements. Subsequently, these matrixes can't be signified in a single table nor it can be lodged in a single page thus these are not exposed in this paper.

5 Intensity of Critical Success Factors

To find the intensity of critical factors ANP approach has been applied through Superdecision software 2.0.8. As shown in Fig. 2, there are seven clusters having several factors. A questionnaire has been prepared to rate each factor of cluster with respect to the other factors. Experts were asked to give rating of the pairwise comparison of the factors on 1–9 scale. On this basis, Superdecision software generated unweighted matrix, Weighted Supermatrix and Limit matrix. Priorities of the factors can be directly taken from the Limit matrix. The top factors are availability, zero defects mentality, customer service, function ability, policy, adequacy and service level etc.

To find the intensity of critical factors ANP approach has been applied through Superdecision software 2.0.8. A questionnaire has been prepared to rate each factor of cluster with respect to the other factors. Experts were asked to give rating of the pairwise comparison of the factors on 1–9 scale. On this basis, Superdecision software generated unweighted matrix, Weighted Supermatrix and Limit matrix. Priorities of the factors can be directly taken from the Limit matrix (Singh et al. 2013). The priorities of the factors are shown in Table 1. The top factors are availability, zero defects mentality, customer service, function ability, policy, adequacy and service level etc. Level 1 exposes the overall goal, level 2 involves of the main objectives, and level 3 comprises the related attributes.

The entire problem of modeling the elements into network entering the pairwise comparison values and synthesizing the results were carried out using a test version of software package called superdecisions. Utilising the software may prevent a

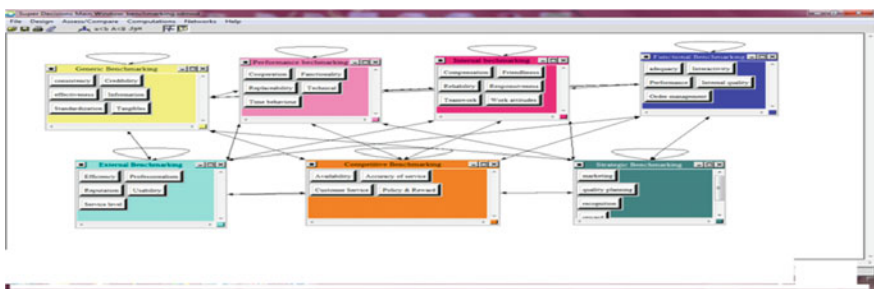


Fig. 2 Network representation of the ANP model

Table 1 Intensity of critical factors

S. no.	Name	Normalized by cluster	Limiting	S. no.	Name	Normalized by cluster	Limiting
1	Accuracy of service	0.19778	0.02999	19	Standardization	0.15739	0.02137
2	Availability	0.28348	0.04299	20	Tangibles	0.20767	0.0282
3	Customer service	0.26789	0.04062	21	Compensation	0.26829	0.03851
4	Policy and reward	0.25086	0.03804	22	Friendliness	0.16005	0.02297
5	Efficiency	0.25468	0.03503	23	Reliability	0.13223	0.01898
6	Professionalism	0.21525	0.0296	24	Responsiveness	0.12187	0.01749
7	Reputation	0.14254	0.0196	25	Teamwork	0.12229	0.01755
8	Service level	0.22357	0.03075	26	Work attitudes	0.19527	0.02803
9	Usability	0.16397	0.02255	27	Cooperation	0.21933	0.03072
10	Adequacy	0.24073	0.03679	28	Functionality	0.29918	0.0419
11	Interactivity	0.15095	0.02307	29	Replaceability	0.14265	0.01998
12	Internal quality	0.25126	0.0384	30	Technical	0.11441	0.01603
13	Order management	0.13418	0.02051	31	Time behavior	0.22442	0.03143
14	Performance	0.22288	0.03407	32	Marketing	0.14795	0.02051
15	Consistency	0.24389	0.03312	33	Quality planning	0.18606	0.02579
16	Credibility	0.10774	0.01463	34	Recognition	0.1812	0.02512
17	Effectiveness	0.13838	0.01879	35	Reward	0.1803	0.02499
18	Information	0.14493	0.01968	36	Zero defects	0.30449	0.04221

user from consideration the step by step method of ANP presented a generalized algorithm for ANP to include inter dependencies and response for decision making.

6 Implementation of Benchmarking Model

In India there is extreme competition for service industries as of same manufacturing industries hire different—2 service provider thus there is close competition which causes for improvement at various levels. So the industries want to adopt benchmark model for achieving best in their field. Therefore, it is suggested that service industry should adopt a benchmarking approach to continuously assess and improve the performance. Benchmarking in services enables the company to constantly monitor and assess its performance for operating techniques against other best of class industries. The process is important to continuous improvement in an industry's service and expense levels, where some of benefits from benchmarking for Service industries include:

- Development in market circumstances of the service provider
- Upgrading in level of customer contentment
- Recognize information that will improve throughput and lower expenses
- Expansion of information among all the departments
- Perfection in customer service and quality control
- Upgrading team spirit and self-confidence

Referring to the result of ANP, the aim is the selection of upgrading alternative for service industries to considerate, the Tangibles values. To improve Tangibles, industries had identified those good practices that can be knowledgeable from the market leader. However, it designates the assessment standard of rating for the development in alternatives as per descending order in the protest only. Subsequently dissimilar alternatives have their dissimilar evaluation standards, so there is requirement of defining their evaluations standard before selection of improved alternatives. Through incoming the ratings of sub-criteria for each altering incident into the step 3 of ANP methodology, the best practice is found. Reorganizing service capability with maximum is the best practice that industries should implement to improve its on-time delivery and also to evaluate the improved alternatives from the market leader, thus the best practice can be implemented. In fact, this is a continuous improvement process because the industries may improve its weaknesses one by one which completes the planning phase. The analyzing phase includes of three main steps (6th step), gap analysis (7th step) and crucial a set point for finest gap bargain (8th step). 6th step pledges with the identification of crucial performance pointers for individually CSFs by the benchmarking team. The seventh step consists of gap analysis. It completes the analysing phase. The implementing phase contains of two steps (i.e. 9th and 10th steps). The 9th step begins with emerging and applying an action plan for respectively CSFs where it must be supervised for proper implementation and to distinguish their progress on timely (i.e. 10th step). In last, measuring phase which consists of last 2 steps. 11th step begins with analyzing the results and compared with the conforming targeted optimal lessening in the gaps in the 8th step. In 12th step the benchmarking team will be recalibrated. The planned benchmarking approach is extensive and may be useful to other industries once their organizational CSFs are found.

7 Results and Conclusions

Since customer satisfaction is the main aim of service industries, so the derivation of the ANP should be done by customer's view, hence the benchmarking process may be customer concerned. However, for continuous improvement, selection of upgrading achievement and the relative weights should be completed by top management of any industries. This Study has identified CSFs and six categories are classified in an Indian service background with managerial feedback. For this, ANP methodology is used to grow the structural model relationships amid the

CSFs. In direction for applying the ANP methodology, Indian Service industries are considered to be benchmarked. This study identified five CSFs as a part of Benchmarking process to increase service industries chance of success in the market. These factors are the availability, zero defects, customer service, function ability, policy; adequacy. These factors are somewhat similar to those identified by various researchers all over world. Still, factors like service level and internal quality for organizations. The findings of the proposed structural framework and benchmarking model for service will serve as a guideline for successful adoption in the market. The proposed benchmarking model can be useful to different environments seizing their exclusive atmosphere which imitate their own preference deliberations. Analysis of the findings shows that these are the most important factors among all these factors and very needful requirement for industries developing country like India.

References

- Dattakumar, R., & Jagadeesh, R. (2003). A review of literature on benchmarking. *Benchmarking: An International Journal*, 10(3), 176–209.
- Saaty, T. L. (2009). Applications of analytic network process in entertainment. *Iranian Journal of Operations Research*, 1(2), 41–55.
- Singh, B., Grover, S., & Singh, V. (2013). An overview of Benchmarking process: The Continuous Improvement Tool. *International Journal of YMCAUST.*, 1(2), 80–83.
- Singh, B., Grover, S., & Singh, V. (2015a). A Benchmark model for internal assessment of industry using fuzzy Topsis approach. *International Journal of recent advancement in Mechanical Engineering*, 4(1), 93–105.
- Singh, B., Grover, S., & Singh, V. (2015b). An analytic hierarchy process for benchmarking of automobile car service industry in indian context. *Management Science Letters*, 5, 543–554.

Optimal Design of a Production System

P.K. Arora, Abid Haleem, M.K. Singh, Harish Kumar and D.P. Singh

Abstract The main objective of the manufacturing is to find a compromise between productivity and high efficiency. To achieve the goal, Industry have to solve many number of problems at the manufacturing floor. The author has conducted number of experiments on different manufacturing industries and collected processing time of each part in the cell and total time of completion and weekly production of the Firms and the same are considered by author for this research work to establish the objectivity of this work Three objectives function namely, minimizing the mean flow time; maximization of throughput; Combination of minimization of mean flow time and maximization of throughput has been developed. Mean flow time and throughput were calculated from conventional techniques as well as optimization techniques namely Genetic Algorithm and simulating annealing techniques. Results from both the optimization techniques were compared. From the results obtained by the execution of all the primitive and deterministic approaches on the sample problems with varying complexities.

Keywords Cellular manufacturing system · Genetic algorithm · Simulating annealing · Mean flow time · Throughput

P.K. Arora (✉)

Galgotias College of Engineering & Technology, Greater Noida, India
e-mail: pawanar@rediffmail.com

A. Haleem

Faculty of Engineering & Technology, Jamia Millia Islamia, New Delhi, India

M.K. Singh

Institute of Technology & Management, Aligarh, India

H. Kumar

CSIR–National Physical Laboratory, New Delhi, India

D.P. Singh

Mewar University, Chittaurgarh, India

© Springer India 2016

D.K. Mandal and C.S. Syan (eds.), *CAD/CAM, Robotics and Factories of the Future*, Lecture Notes in Mechanical Engineering,

DOI 10.1007/978-81-322-2740-3_67

1 Introduction

Cellular manufacturing involves the formation of part families based upon their similar processing requirements and grouping of machines into cells to produce the formed part families. Burbidge (1977) described the techniques of Production Flow Analysis (PFA), which are used to find the families of components, and associated groups of machines for group layout. PFA is an analytical technique, which finds the groups and families by a progressive analysis of the information contained in the component route cards. McAuley (1972) was the first to propose single linkage clustering to cluster machines. Cluster-analyze is the part-machine matrix. Guna Singh and Lashkari (1989) proposed a methodology to group the machines in cellular manufacturing system based on the tooling requirement of the parts, toolings available on the machines and the processing times.

2 Optimization Techniques Used

A number of researchers have worked for various developments in CMS in past using different tool. They have discussed and applied different techniques to optimize CMS for various applications. The paper has attempted to design the optimize the production system with Genetic algorithm and Simulated Annealing Techniques.

2.1 Genetic Algorithm

Initialization Initially many random individuals are generated to form an initial population. The number of individuals forms population size which completely depends on the nature of problem. Sometimes the population size may go up to hundreds and thousands. For initialization it's a matter of consideration that the generated population ideally covers the entire range of possible solution (the search space).

Selection Select two parent chromosomes from a population according to their fitness (the better fitness, the bigger chance to be selected).

Reproduction The next step is to generate the second generation from the current one. For this purpose, genetic operator crossover and mutation are used.

Termination-This generational process is repeated until reach the following conditions;

2.2 Simulated Annealing

Simulated annealing (SA) is technique used for solving optimization problems and the search for a minimum in a more general system. The algorithm employs a random search which accepts changes that decrease the objective function f (assuming a minimization problem).

$$\text{Probability } p = \exp(-\Delta f/T) \tag{1}$$

where Δf is the increase in f and T is a control parameter.

3 Model Formulation

Cellular manufacturing is the formation of part families based upon their similar processing requirements and grouping of machines into machine cells to produce the formed part families. A part family is a of parts which are similar either collection because of geometric shape and size or similar processing steps required in their manufacture. For the production system we have taken mean flow time and throughput into consideration.

3.1 Minimize the Mean Flow Time

Mean flow time is defined as the Average Completion time of the job. Mathematically it can be written as $\text{=(Total processing time + total waiting time)/}$ Number of jobs. For optimization we take mean flow time as minimum.

$$\begin{aligned} \text{Minimize, } MF &= \frac{\sum_{i \in SF} f_i}{SF} \text{ or} \\ \text{Maximize } F_1 &= 1 - \frac{MF_{seq}}{MF_{max}} \end{aligned} \tag{2}$$

where

MF_{seq} mean flow time related to some part sequence,

MF_{max} maximum mean flow time

f_i flow time of part i .

3.2 Maximize Throughput

It is defined as the productivity of a machine, procedure, process, or system over a unit period, expressed in a figure-of-merit or a term meaningful in the given context.

$$\begin{aligned} \text{TH} &= \sum_{i \in SF} \varepsilon_i \text{ or} \\ \text{Maximize } F_2 &= \frac{\sum_{i \in SF} \varepsilon_i}{\sum_{i=1}^I \varepsilon_i} \text{ or} \quad \text{Maximize } F_2 = \frac{TH_{seq}}{TH_{max}} \end{aligned} \quad (3)$$

where

- ε_i Contribution of part i in overall production
- TH_{seq} Throughput value in some sequence
- TH_{max} Maximum Throughput

3.3 Combination of Minimization of Mean Flow Time & Maximization of Throughput

To get the benefit of both the objective function, the combined objective function may be taken as the combination of both.

$$\begin{aligned} \text{Maximize } F_3 &= \frac{(W_1 \times F_1) + (W_2 \times F_2)}{(W_1 + W_2)} \\ &= \frac{\left(W_1 \times \left(1 - \frac{MF_{seq}}{MF_{max}} \right) \right) + \left(W_2 \times \left(\frac{TH_{seq}}{TH_{max}} \right) \right)}{(W_1 + W_2)} \end{aligned} \quad (4)$$

4 Result and Discussion

The data regarding mean flow time and throughput values of the plant using conventional configuration has been collected and same has been used for the model using GA and SA techniques. In this paper, initially GA has been used as a random search technique to determine an optimal sequence of part type in the cell sequence for any given problem. All the ten problems are tested using GA and the combined objective function (F_3) is used which incorporates both the maximization of throughput and minimization of the mean-flow time to evaluate the fitness of a candidate solution string. The working principle of this algorithm is assessed at each iteration according to the objective function F_3 , which is a logical combination

of minimization of mean-flow time and maximization of throughput. In order to ensure that the results did not have extraordinary variance, each problem was allowed to run ten times and the mean of the performance criteria has been calculated. The literature survey shows that a lot of researchers used simulated annealing to solve various combinatorial problems. This motivated the author to use the same concept in CMS and exhaustively test the technique with ten problems.

The data obtained from all techniques has been compared. It is found that SA and GA provide the better output than conventional technique in respect to the Mean flow time and throughput. The data obtained from ten different industry problems are compared in Figs. 1 and 2.

It is clear from the Figs. 1 and 2 that the GA based technique gives the good performance. However, the GA based technique gives optimal results for both the performance measures.

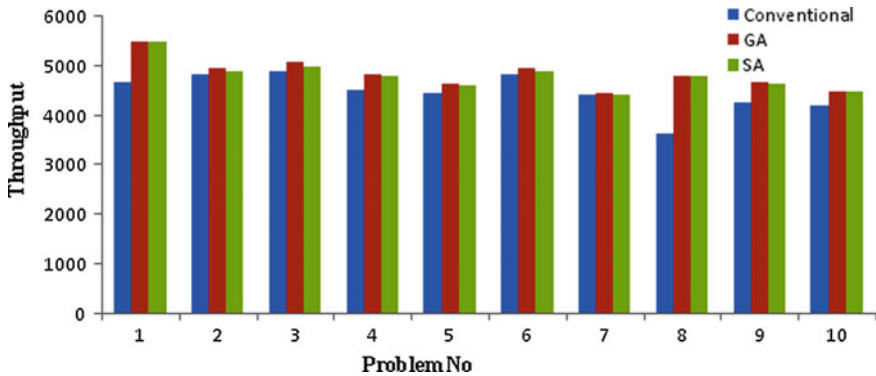


Fig. 1 Comparison of throughput

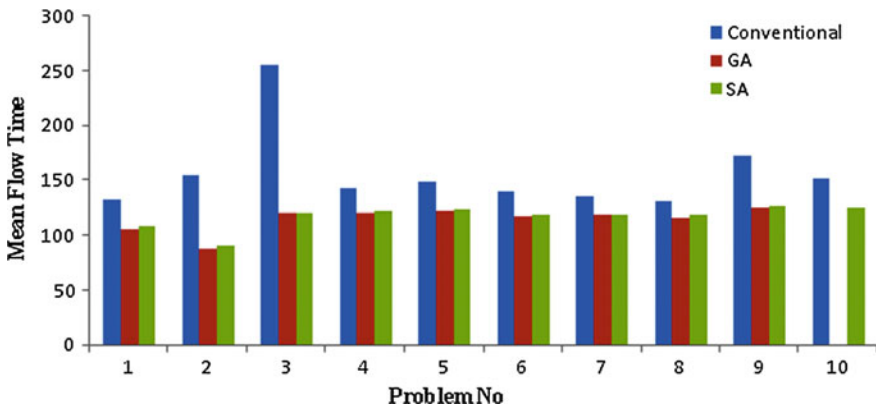


Fig. 2 Comparison of mean flow time

4.1 Comparison Between Genetic Algorithm and Simulating Annealing

Comparison in GA and SA are also done in objective function and mean flow times of the parts and throughput in Figs. 3, 4 and 5 with respect to objective function F1. Genetic Algorithm technique seemed to perform better than the primitive part type in the cell based measures.

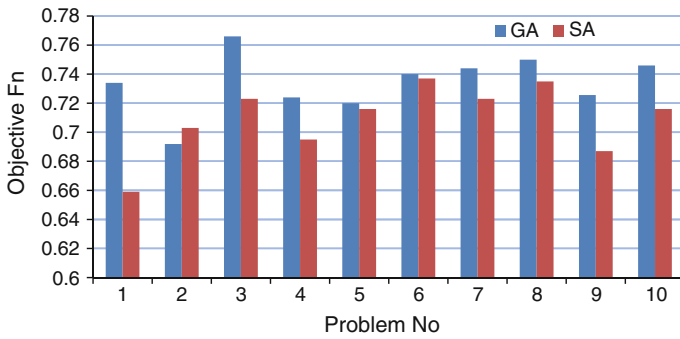


Fig. 3 Comparison of objective function Fn F1 in GA and SA techniques

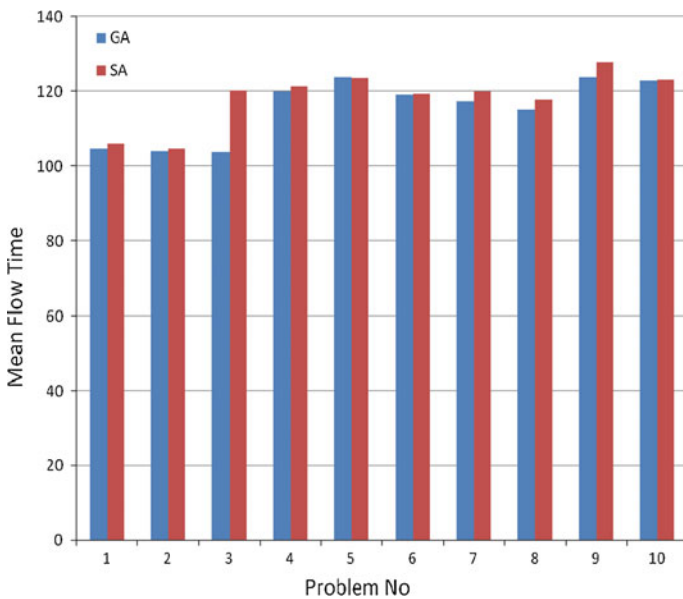


Fig. 4 Comparison of mean flow time with respect to objective function F1 in GA and SA

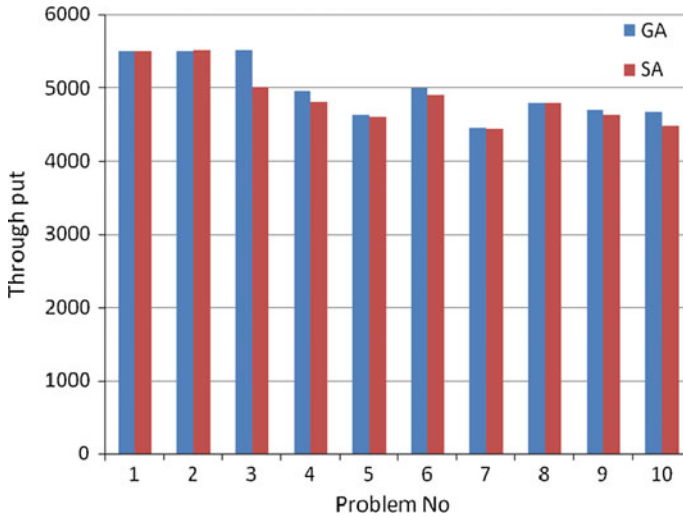


Fig. 5 Comparison of throughput with respect to objective function F1 in GA and SA techniques

5 Conclusions

It has found that both GA and SA techniques are giving better result than Conventional Techniques. Genetic algorithm and simulating techniques were employed to the same production problem. It has been found that there is reasonable amount of difference in the performance of production system with these two techniques. GA gives better result as compared to SA. The work was done for minimizing the mean flow time and maximizing the throughput under different conditions. The objective of this research was to develop a methodology that can be employing to production system.

References

Burbidge, J. L. (1977). A manual method for Production flow analysis. *Production Engineer*, 56(10), 34–38.

Gunasingh, K. R., & Lashkari, R. S. (1989). Machine grouping problem in cellular manufacturing systems—an integer programming approach. *International Journal of Production Research*, 27(9), 1465–1473.

McAuley, J. (1972). Machine grouping for efficient production. *The Production Engineer*, 51, 53–57.

Modelling and Analysis of a Novel Ancillary Braking System for All Terrain Vehicle

Amitansu Pattanaik and Nirbhay Jain

Abstract A concept of ancillary braking system was incorporated in vehicle to enhance performance parameters such as yaw moment control and off road abilities. In this additional braking system, we have controlled these parameters by applying brakes at the time of requirement. Computer Aided Engineering (CAE) analysis were performed on the ancillary braking system. Real world tests were done on vehicle to calibrate the improvements. It includes graphical representation of various design parameters. Area of improvement includes better off road abilities and yaw movement control which helps vehicle maneuverability and reduction of turning radius.

Keywords Secondary braking • Yaw movement control • Brake control • Off road control • Ansys

List of Symbols

Variables

A	Deceleration of the vehicle (m/s^2)
A_d	Disc surface swept by a brake pad (m^2)
g	Acceleration of gravity ($9.81 m/s^2$)
q_0	Heat flux entering the disc (W)
v	Initial speed of the vehicle (m/s)
X	Relative centre of gravity height
M	Total vehicle Mass (kg)
M_{fydn}	Dynamic front axle load (kg)

A. Pattanaik (✉)

Defence Terrain Research Laboratory, DRDO, Ministry of Defence,
Metcalfe House, Delhi, India
e-mail: amitansu@yahoo.com

N. Jain

Department of Mechanical Engineering, Northern India Engineering College,
GGSIU, Delhi, India
e-mail: nirbhayjain8@gmail.com

© Springer India 2016

D.K. Mandal and C.S. Syan (eds.), *CAD/CAM, Robotics and Factories of the Future*, Lecture Notes in Mechanical Engineering,
DOI 10.1007/978-81-322-2740-3_68

Greek Symbols

- ε_p Factor load distribution on the disc surface
 \emptyset Rate distribution of the braking forces
 φ Static axle load distribution

1 Introduction

In this competitive world there have been perpetual efforts to increase the performance of vehicle without compromising the safety of passengers (Fildes et al. 2015). One the most intense working environment is faced by all-terrain vehicles which are capable of tackling every terrain ranging from rocky to plain surfaces (Shrivastava 2014). Turning radius of ATV vehicles is more as compared to the other vehicles. To reduce the difference it can be incorporated in ATV vehicles due to its light weight with efficient results in low cost. Hence a system is incorporated into the vehicle which can effectively overcome the above mentioned situations which provides braking efforts to control yaw movement and convert open differential into close differential at the time of requirement. It helps vehicle to convert into close differential specification as soon as one wheel of ATV gets stuck and other rotate freely. Also the yaw movement controls turning radius and offering a stable in line condition controlling any lateral movement.

Several research have been done in this aspect but they don't provide such a conjoint effect of controlling various aspects at the same time (Singh et al. 2010). Whole idea is conceptualized to control the performance parameter of vehicle and our research focuses on controlling steering and transmission characteristic of vehicle. Light armoured vehicles which are mobile and adaptable are frequently required for defense applications (Eliyas and Hima Kiran Vithal 2014).

2 Theoretical Consideration

The initial heat flux q_0 entering the disc is calculated by the following formula (Belhocine and Bouchetara 2011):

$$q_0 = \frac{(1 - \emptyset) mgvz}{2 \cdot 2A_d \varepsilon_p} \quad (1)$$

The changes in axle loads during braking have no relationship to which axles are braked. They only depend on the static laden conditions and the deceleration (Limpert 2011).

$$\{(1 - \varphi) + (Xa)\} \cdot M = M_{fdyn} \tag{2}$$

3 Experimental

3.1 Rotor Modeling and Manufacturing

EN42 is widely used in commercial all-terrain vehicles. It was chosen for manufacturing of rotor because of its superior bending resistance, less wear rate and tangential load handling characteristic (Findik 2014). An original equipment manufacturer (OEM) type of brake rotor was selected according to design constraints of vehicle (shown in Fig. 2) and subsequent analysis were performed using CAE tools on the CAD model (shown in Fig. 1). An additional electrode zinc coating of 15 μm was done over rotor to improve the anti-rust properties.

3.2 Brake System Fabrication

An OEM master cylinder and caliper were selected according to the requirements. A hand actuating mechanism to actuate the brake system was fabricated and analysis were done to check for any discrepancy.

Fig. 1 The brake rotor CAD model **a** front view **b** side view

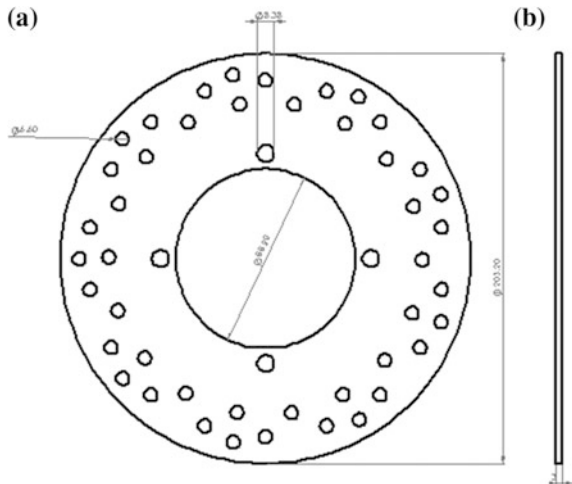
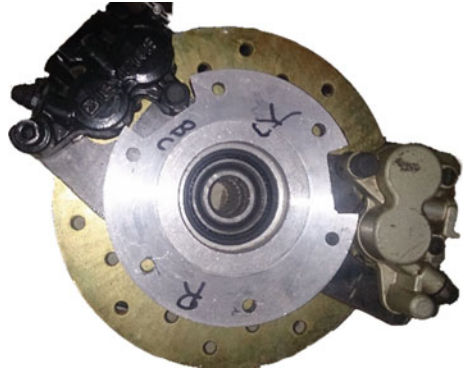


Fig. 2 Prototype

3.3 Testing

Brake calipers with a dual piston design were chosen because of their superior braking ability, compared to single piston calipers. Tandem master cylinder with a split type configuration was used. The total weight of the vehicle was 240 kg. The weight distribution for the car was estimated to be approximately 63:37 from the rear to the front calculated from Eq. (2). Static weight distribution of vehicle was 144 kg at the rear and 96 kg at the front. The torque output of the engine was 19.5 Nm. Appropriate testing environment was created and vehicle went through intensive testing.

Brake actuation set-up consisted of floor mounted assembly and lever arrangement which was easily actuated by the driver. Analyses were done on the actuation setup to ensure fail proof safety. Turning radius of car was measured at low speeds in accordance with Automotive Research Association of India (ARAI) standards to prevent analogues results and repeated values were taken for both turning radius and brake test to ensure accuracy and precision.

4 Results and Discussion

4.1 Brake Rotor Analysis

Several analysis are done on rotor namely thermal and force analysis to ensure failure proof function of rotor during entire period of test (COMSOL 2012).

Transient and single stop temperature rise analysis were conducted. The initial heat flux q_0 entering the disc is calculated by the Eq. (1). Temperature rise was calculated and similarly a distribution of temperature was obtain through analysis on ANSYS© Software. The energy dissipated in the form of heat can generate rises in temperature ranging from 300 to 800 °C (Belhocine and Bouchetara 2011).

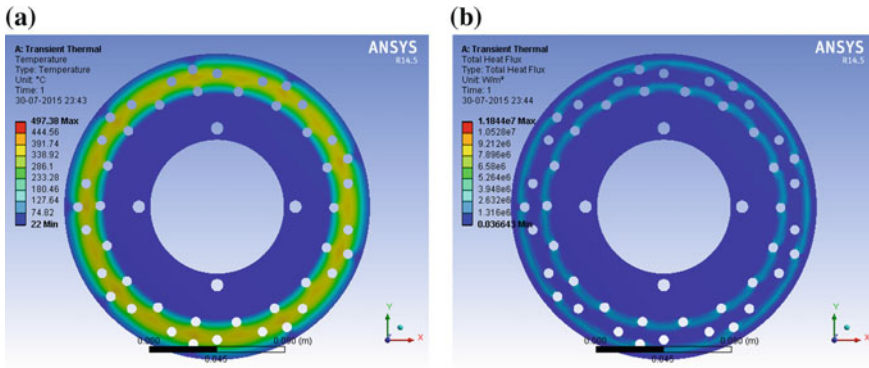


Fig. 3 The thermal analysis of a temperature rise b total heat flux

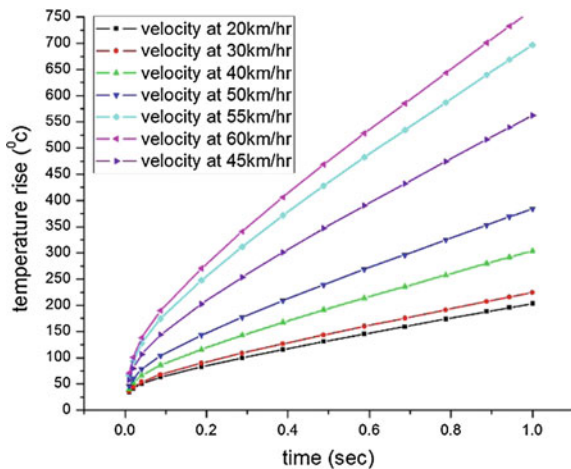
Figure 3a, b show that rotor temperature rise is within the temperature limit and free from commonly thermal distortions such as thermal cracking and rotor wrapping.

During the operation of rotor which was constantly spinning and making contact with the brake pad transient structural analysis were carried out and no point of objection was found.

Figures 4 and 5 shows that variation of temperature rise for different velocities are within the safe limits. Similarly the heat flux traveling through the rotor is tested for certain set of speeds and found to be within safe limits for every set of value.

Mechanical strength of rotor is another important factor to be considered (Naresh Babu and Siva Krishna 2013). Brake rotor was subjected to axial bending load and tangential load when it was subjected to force applied by brake pads on it. To ensure fail proof rotor both analyses (shown in Fig. 6a, b) were conducted on it. Force of 3096 N was applied to disc and subsequent distortions were examined.

Fig. 4 Variation of temperature rise for different velocities for a disc in transient case



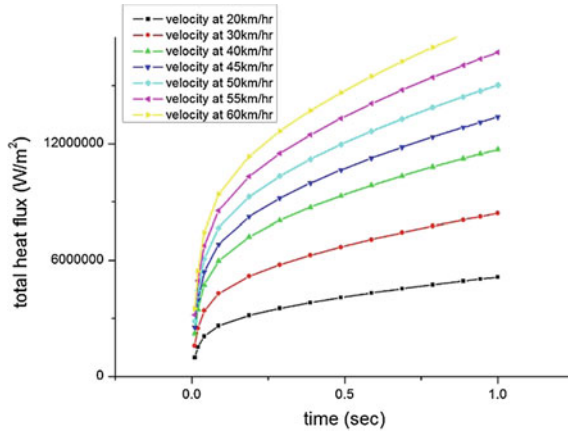


Fig. 5 Variation of total heat flux for different velocities for a disc in transient case

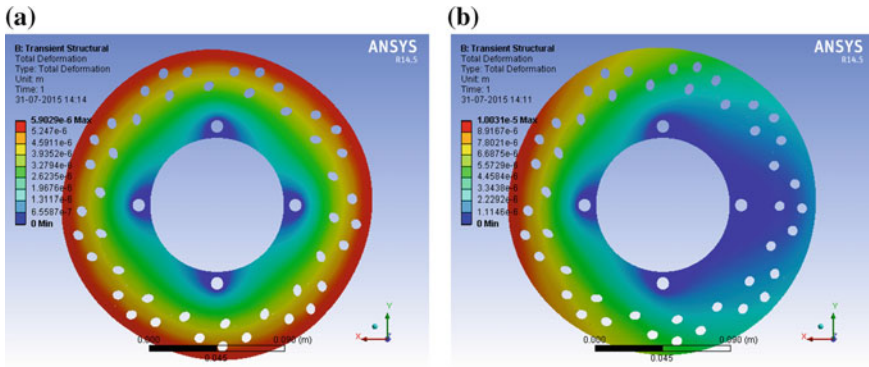


Fig. 6 Total deformation during structural analysis a axial loading b tangential loading

During analysis brake rotor showed high bending strength and it had good factor of safety.

Stress analyses were done to test the effect of cyclic loads of rotor under multiple stops conditions. Figure 7 shows that the brake rotor can withstand high cyclic loads up to 20,000 cycles which confirmed the use of material as bending strength plays a vital role in the functioning of rotor under unfavorable conditions. This rotor can be used for severe testing conditions, regularly faced by all-terrain vehicles under rough terrain and hence justifying the use of rotor.

Under low cycle operations high bending strength was possessed by rotor and under increased number of cycles bending strength reduces but was within the safe limits (Fig. 10).

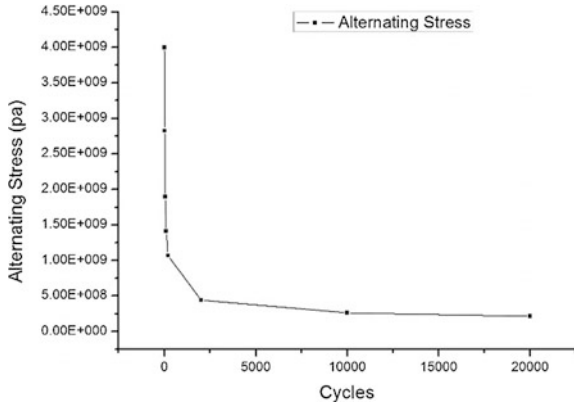


Fig. 7 Plot between alternating stress and load cycles

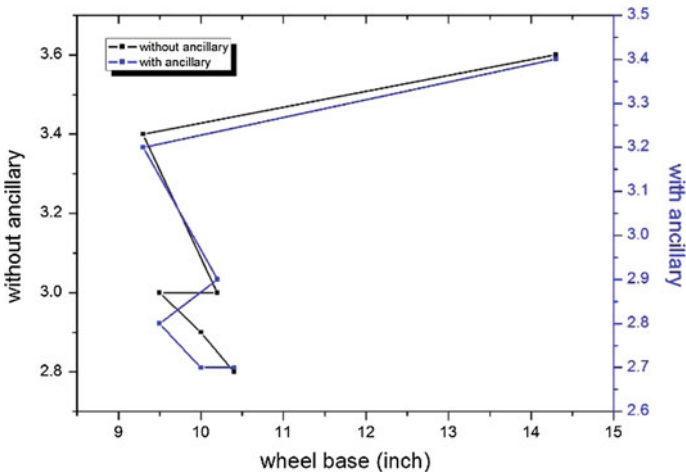


Fig. 8 Plot between the turning radius w.r.t to wheel base and track width

4.2 Brake Actuation Mechanism Analysis

Components of brake system were tested in solid works (shown in Fig. 9) to ensure fail proof operation. Bending strength was analyzed for actuation of the designed system and found to be within safe limits.

Fig. 9 CAD model of brake actuation system

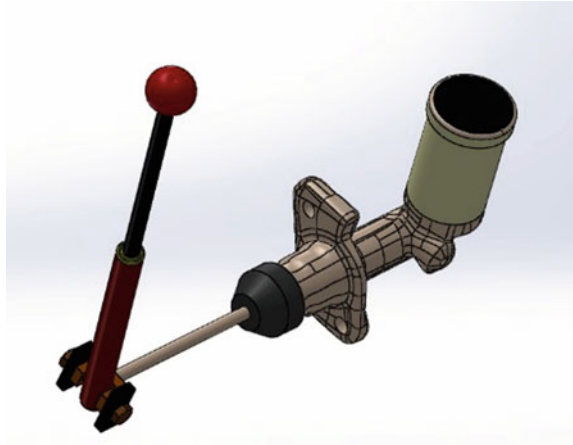


Fig. 10 ATV on which experiments were performed



4.3 Brake Performance Analysis

The purpose of entire ancillary system is to test and analyse the benefits possessed by it in an all-terrain vehicle. The primary use of system is to improve the maneuverability of vehicle (Jo et al. 2008). This includes yaw movement control and provides exceptional off road riding capability.

Improvements in off road capabilities are done by allowing the brake system to convert open differential system into closed differential system at the time of need (Canale and Fagiano 2010). Whenever one wheel faces slightly less coefficient of friction with road, it tends to lose traction and entire power is transferred to wheel with less traction. As a result one wheel spins continuously and other wheel remains at its position and all torque is transferred to free spinning wheel. Thus to overcome

this problem ancillary system applies braking force to the free spinning wheel, transferring torque to the stuck wheel enabling the vehicle to overcome obstacle. Figure 8 shows comparison of turning radius of vehicle without ancillary and with ancillary.

Whenever a wheel hits an obstacle while other wheel is stable, there is a yaw movement generated which is due to spinning of vehicle about y axis. This yaw movement can be controlled easily by application ancillary braking system. There are two basic steering conditions over steering and under steering.

Over Steering

In this case the wheel steers more than the path of turning. If this situation occurs then braking force is applied to the outer most wheel creating an anti-clockwise movement which brings back vehicle to its actual path.

Under Steering

In this case the wheel steers less than the path of turning. If this situation occurs then braking force is applied to the inner most wheel creating a clockwise movement which brings back vehicle to in vehicle with variable to its actual path (Khaknejad et al. 2013).

Apart from yaw movement ancillary brakes can help to reduce turning radius of vehicle. If we apply the brake to inner wheel (rear) then the vehicle can turn more than the desired value and make way through tightest space. Table 1 shows the comparison of turning radius for different angles chassis design.

Table 1 Table showing the comparison between the turning radius with and without ancillary system

Wheel base (inch)	Track width (inch)	Outer angle	Inner angle	Angle difference	Turning radius (m)	
					Without ancillary	With ancillary
51	51	21.5°	31.9°	10.4°	2.8	2.7
51	52	20.1°	30.1°	10.0°	2.9	2.7
53	51	20.2°	29.7°	9.5°	3	2.8
53	52	20.7°	30.9°	10.2°	3	2.9
55	51	19.5°	28.8°	9.3°	3.4	3.2
55	55	23.7°	37.5°	14.3°	3.6	3.4

5 Conclusion

We can conclude that off road ability and yaw movement can be controlled by ancillary braking system. Analysis were done on braking system to test discrepancies and no flaws were detected from design point of view. Ancillary system was tested on an ATV vehicle to measure improvements. Primary areas of improvements include better off road abilities in remote locations and yaw movement control to provide better straight line stability of vehicle, preventing any deviation from intended path as well as small turning radius, improving maneuverability.

Acknowledgments Author (Dr. Amitansu Pattanaik) would like to thank Dr. M.R. Bhutiyani, Director, DTRL for his constant encouragement. Author (Mr. Nirbhay Jain) would like to acknowledge team ‘Thunderbolt’, Mr. Sarthak Sethi & Mr. Sahban Usman Khan from Northern India Engineering College for their technical support.

References

- Belhocine, A., & Bouchetara, M. (2011). Thermal analysis of a solid brake disc. *Applied Thermal Engineering*, 32(2012), 59–67.
- Canale, M., & Fagiano, L. (2010). Comparing rear wheel steering and rear active differential approaches to vehicle yaw control. *Vehicle System Dynamics*, 48(5), 529–546.
- Eliyas, M., & Hima Kiran Vithal, V. (2014). Concept design of special vehicle for Indian military. *Sastech Journal*, 13(1).
- Findik, F. (2014). Latest progress on tribological properties of industrial materials. *Materials and Design*, 57(2014), 218–244.
- Fildes, B., Keall, M., Bos, N., Lie, A., Page, Y., Pastor, C., et al. (2015). Accident analysis and prevention. *Accident Analysis and Prevention*, 81(2015), 24–29.
- Heat Generation in a Disc Brake, Solved with COMSOL Multiphysics 4.3a. (2012).
- Jo, J.-S., You, S.-H., Joeng, J. Y., Lee, K. I., & Yi, K. (2008). Vehicle stability control system for enhancing stability, lateral stability and roll stability. *International Journal of Automotive Technology*, 9(5), 571–576.
- Khaknejad, B., Khalaj, A., Keshavarz, A., & Mirabdollahi, A. (2013). Improving understeering behaviour of a passenger car via rear axle bushing optimisation. SAE International.
- Limpert, R. (2011). Brake design and safety. Society of automotive engineers Inc, (3rd ed).
- Naresh Babu, K., & Siva Krishna, V. (2013). Structural design and thermal analysis of car disc brake rotor.
- Shrivastava, D. (2014). Designing of all terrain vehicle (ATV). *International Journal of Scientific and Research Publications*, 4(12), ISSN 2250-3153.
- Singh, O. P., Mohan, S., Venkata Mangaraju, K., Jayamathy, M., & Babu, R. (2010). Engineering failure analysis. *Engineering Failure Analysis*, 17(2010), 1155–1172.

Nonlinear Tracking Control of Parallel Manipulator Dynamics with Intelligent Gain Tuning Scheme

K.V. Varalakshmi and J. Srinivas

Abstract This paper presents modelling and control of highly nonlinear dynamics parallel manipulator system using neural network-based gain tuning technique in a model-based feedback linearization controller. Adaptive gain tuning approach is implemented for conventional computed torque control scheme. The proposed controller has very simple structure and takes little computational time while tracking a trajectory. A feed forward model is implemented to achieve the gains corresponding to the errors and their derivatives. The results are illustrated for a circular trajectory. Simulation results for a 3-RRR planar parallel manipulator show that the intelligent gain tuning technique has better performance than conventional computed torque control in terms of controllability and stability. An experimental analysis is presented for straight line trajectory.

Keywords Computed torque control · Lyapunov stability · Online gain tuning · Planar parallel manipulator · Sliding mode control

1 Introduction

Parallel manipulators are dynamically coupled, time-varying and highly nonlinear systems that are extensively used in high speed, high accuracy operations for various industrial tasks (Jun et al. 2011; Patel and George 2012). With these requirements, the accurate position control of the manipulator end-effector is a challenging task and also it is difficult to make use of parallel manipulators in real time tasks (Zubizarreta et al. 2013; Xue et al. 2013). Model based controllers designed with known

K.V. Varalakshmi (✉) · J. Srinivas
Department of Mechanical Engineering, National Institute of Technology,
Rourkela, Odisha, India
e-mail: kv.varalakshmi@gmail.com; 511me130@nitrrkl.ac.in

J. Srinivas
e-mail: srin07@yahoo.co.in

dynamics of parallel manipulators and it is a difficult task to design with an acceptable performance index (e.g., minimum error, better tracking capability and external disturbance rejection). Most popular approaches of model based controller are the augmented PD (APD) (Wei and Shuang 2014) and compute-torque control (CTC) (Amin et al. 2012; Li and Wu 2004), which are appropriate for trajectory tracking control with external disturbance rejection and system uncertainties. Many researchers combined robust classical techniques (e.g. Computed torque control) with non-classical methods (e.g. fuzzy and neural networks (NN)). Some other works proposed different online self-gain tuning approaches using hybrid techniques with function approximation capabilities using some advanced robust control techniques to achieve good tracking performance and stability of the system (Amin and Musa 2012; Tien et al. 2013a, b). Zuoshi et al. (2005) developed a combined computed torque and fuzzy control. Likewise a nonlinear PD control was proposed by (Francisco et al. 2014), where the gains are auto tuned using fuzzy controller. Lyapunov theorem is used for stability analysis to get guaranteed asymptotic convergence to zero for both tracking error and error rate. Muller and Hufnagel ((2012) proposed a CTC and augmented PD technique in redundant coordinates as an alternative to coordinate switching method. Many recent works also employed sliding mode control approach (Farzin and Nasri 2012; Wen and Chien 2014) due to its robustness in the adjustment of instabilities. Adaptive, Hybrid PID and PD SMCs were proposed for robotic manipulators (Acob et al. 2013; Ouyang et al. 2014) to estimate error uncertainties, here the decentralized PID controller acts as a feedback system to enhance the stability of the close-loop mechanism. Artificial Neural Networks are progressively identified as a successful tools for controlling nonlinear dynamic systems because of their advantages such as the ability to approximate arbitrary linear or nonlinear mapping through learning, less formal statistical training and ability to identify complex nonlinear relationships between dependent and independent variables and strong interaction between predicted variables. In this regard, self gain tuning techniques have been proposed to enhance the execution of such controllers. (Tien et al. 2013a, b) proposed an online self gain tuning method using neural networks with nonlinear PD-CTC that achieves good tracking performance in 5-bar parallel manipulator. But in this approach, they did not consider the external disturbances or un-modelled dynamics. An indirect disturbance observer was implemented by (Vinoth et al. 2014) to compensate the external disturbances prior to the controller design. Very few works applied the gain tuning approaches to higher degree of freedom parallel manipulators, due to its complex nonlinear dynamics. Present work proposes a neural network based auto-tuned PD-CTC for the 3-RRR planar manipulator. Here, the nonlinear PD-CTC is achieved by combining a conventional CTC and an intelligent gain tuning method using a two layer neural network in presence of model uncertainties and external disturbances. The advantages of the proposed controller over the conventional controllers have been illustrated.

2 Dynamics of Planar Parallel Manipulator

As shown in Fig. 1, a three degree of freedom 3-RRR planar parallel mechanism has three active and six passive joints connecting a mobile platform with fixed base using three limbs. The fixed frame XOY is attached to the base frame and moving frame X'PY' is considered on the mobile platform.

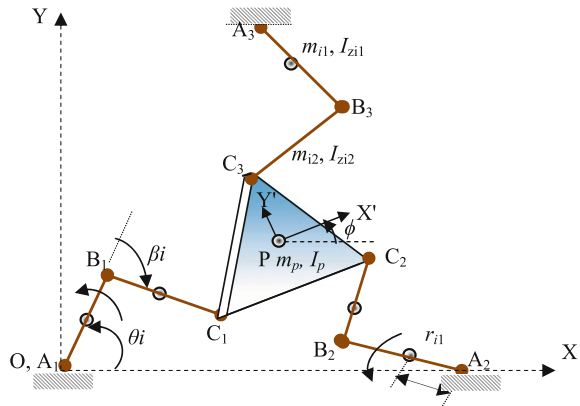
Two translations x_p, y_p and one rotation ϕ about Z axis constitute the end-effector (platform center P) coordinates. The active and passive joint vectors are respectively denoted by $q_a = [\theta_1, \theta_2, \theta_3]^T$, $q_p = [\beta_1, \beta_2, \beta_3]^T$ and l_{i1} and l_{i2} are the active and distal link lengths. The mass of the links m_{i1} and m_{i2} are concentrated at the centroid of each link about the axis normal to the XOY-reference plane. Also, their moments of inertia are considered as I_{zi1} and I_{zi2} . m_p is the mass of the mobile platform located at the centroid of the equilateral triangle P, and I_p is the moment of inertia about an axis equally oriented.

The dynamic model of open-loop system of the 3-RRR mechanism can be expressed as:

$$M(q)\ddot{q} + C(q, \dot{q})\dot{q} + N(q) = \tau_t \tag{1}$$

where $q = (q_a, q_p, X_p)^T \in \mathbb{R}^{9 \times 1}$ is the joint vector, $X_{mp} = (x_p, y_p, \phi)$ $\tau_t = (\tau_a, \tau_p, F_p)^T \in \mathbb{R}^{9 \times 1}$ is the torque vector $\tau_a = (\tau_{a1}, \tau_{a2}, \tau_{a3})^T$ is the input joint torque vector of active joints, $\tau_p = (\tau_{p1}, \tau_{p2}, \tau_{p3})^T = (0, 0, 0)^T$ is the input torque vector of passive joints and $F_{mp} = (f_x, f_y, \tau_{mp})^T$ is the applied wrench vector of the end-effector. $M(q)$ and $C(q, \dot{q}) \in \mathbb{R}^{9 \times 9}$ are the inertial and Coriolis matrices respectively, which are given in the matrix form below and $N(q) \in \mathbb{R}^{9 \times 1}$ is the vector of actuated torque. The above dynamic model can be simplified by considering external disturbances at the active joints. The loop closure constraints are considered using a Jacobian matrix. From D'Alembert's principle and the principle

Fig. 1 Kinematic structure of 3-RRR planar parallel manipulator



of virtual work, the configuration space can be smoothly parameterized by the actuator joint vector q_a .

$$\tau_a = W^T \tau_t \quad (2)$$

where

$$W = \begin{bmatrix} I \\ \frac{\partial q_p}{\partial q_a} \end{bmatrix} \quad (3)$$

W is the Jacobian matrix. By using the matrix W from the Eq. (3) the dynamic model of Eq. (1) can be transformed into the closed-loop kinematic structure as:

$$W^T M(q) \ddot{q} + C(q, \dot{q}) \dot{q} + N(q) = \tau_a \quad (4)$$

Thus, they are expressed in terms of active joint coordinates. The complete dynamics of the closed-loop mechanism can be written as:

$$\widehat{M}(q_a) \ddot{q}_a + \widehat{C}(q_a, \dot{q}_a) \dot{q}_a + \widehat{N}(q_a) = \tau_a \quad (5)$$

where

$$\widehat{M} = W^T M W, \widehat{C} = W^T M \dot{W} + W^T C W, \widehat{N} = W^T N$$

Accordingly the active joint torques can be computed. The dynamic model of Eq. (5) should have the following properties:

Property 1: \widehat{M} is positive definite and symmetric.

Property 2: $\widehat{M} - 2\widehat{C}$ is a skew-symmetric.

The exact dynamic model of the parallel manipulator will be never known due to nonlinear uncertainties in the system. If the modelling errors caused by these uncertainties are bounded, the actual dynamics can be expressed by combining the modelling errors and estimated dynamics in the following equation:

$$\widehat{M}_a(q_a) \ddot{q}_a + \widehat{C}_a(q_a, \dot{q}_a) \dot{q}_a + \widehat{N}(q_a) = \tau_a \quad (6)$$

where $\widehat{M}_a = \widehat{M} + \Delta \widehat{M}_a$ and $\widehat{C}_a = \widehat{C} + \Delta \widehat{C}_a$ are the actual dynamic parameters of the parallel manipulators; and $\Delta \widehat{M}_a$ and $\Delta \widehat{C}_a$ are the bounded modelling errors.

The vector of unknown external disturbances and uncertainties at the active joints can be expressed as follows:

$$\Delta\tau_a = \Delta\widehat{M}_a(q_a)\ddot{q}_a + \Delta\widehat{C}_a(q_a, \dot{q}_a)\dot{q}_a + \widehat{N}(q_a) + D(t) \tag{7}$$

where $D(t) \in \mathfrak{R}^{3 \times 1}$ is the vector of the external disturbances.

From Eqs. (6) and (7), the actual dynamic equation of the planar parallel manipulator in the active joint space as:

$$\widehat{M}(q_a)\ddot{q}_a + \widehat{C}(q_a, \dot{q}_a)\dot{q}_a + \Delta\tau_a = \tau_a \tag{8}$$

The dynamic model of Eq. (8) of the manipulator in the active joint space, which is similar as serial manipulator. But, the presences of uncertainties $\Delta\tau_a$ are enormous and highly nonlinear because of closed-loop constraints and the variation of the parameters.

3 Design of Controllers

Dynamic Eq. (6) of the manipulator is highly nonlinear due to the dynamic coupling between the kinematic links. In order to achieve a good performance of parallel manipulators in trajectory tracking problems different control techniques from nonlinear control theory are required.

3.1 Computed Torque Control

In computed torque control, the nonlinear dynamic equations of motion are reduced to linear form in terms of dynamic errors. Utilizing the computed torque control approach with a proportional-derivative (PD) outer control loop, the applied actuator torques are calculated at each time step using the following computed torque law as given in (Zuoshi et al. 2005).

$$\tau_c = \widehat{M}(q_a)(\ddot{q}_d + K_p e + K_v \dot{e}) + \widehat{C}(q_a, \dot{q}_a)\dot{q}_a \tag{9}$$

where τ_a is the computed torque applied to input links, K_p and K_v are the diagonal matrices of the proportional and derivative gains, and e and \dot{e} are the array of the position and velocity errors of the input links, $e = q_d - q_a$ and $\dot{e} = \dot{q}_d - \dot{q}_a$. Figure 2 shows the complete CTC approach.

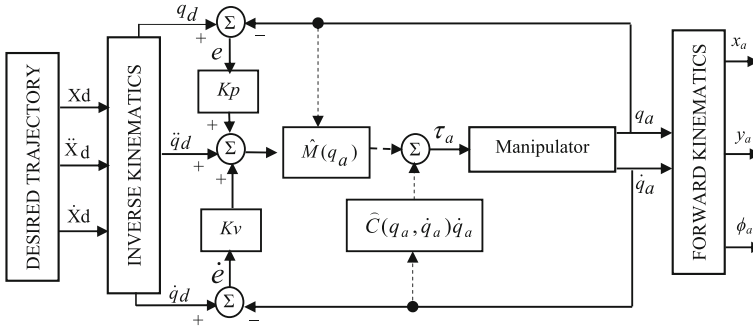


Fig. 2 Schematic diagram of the general CTC scheme

3.2 Design of Hybrid Sliding Mode Control

The first step in the design of the SMC is the design of sliding surface function of the system (9) as:

$$s = \dot{e} + \lambda e = \dot{q}_a - (\dot{q}_d - \lambda e) = \dot{q}_a - \dot{q}_d \tag{10}$$

where $\lambda = \text{diag}[\lambda_1, \lambda_2, \lambda_3]$ with $\lambda_i (i = 1, 2, 3)$ are the positive constants, which determines the motion feature in the sliding surface; and using dynamics written in terms of the new parameter of sliding surface as follows:

$$\tau_c = \hat{M}(q_a)\ddot{q}_d + \hat{C}(q_a, \dot{q}_a)\dot{q}_a + \hat{M}(q_a)(K_p e + K_v \dot{e} + K_s \text{sat}(s, \psi)) \tag{11}$$

where $K_s = \text{diag}[K_{s1}, K_{s2}, K_{s3}]$ is positive definite and represents the SMC gain. Also the saturation (Ouyang et al. 2014):

$$\text{sat}(s, \psi) = \begin{cases} \text{sign}(s) & \text{if } |s| > \psi \\ s/\psi & \text{if } |s| \leq \psi \end{cases} \tag{12}$$

In the above equation ψ is a diagonal matrix that determines the boundary layer of the sliding surfaces and $\text{sign}()$ is the signum function.

This control law replaces the model-dependent part of the SMC law with the linear feedback of the computed torque control law and retains the switching term of the SMC law. Because this control law only contains feedback control, it is more robust and less sensitive to changes in the dynamics of the system than pure SMC. With this, a model-free law is obtained with nonlinear feedback control for rigid robotic manipulators.

3.3 Design of Intelligent Gain Tuning Technique

The conventional control techniques which mentioned in literature achieve rarely the required performance in trajectory tracking with the presence of modeling errors and external disturbances with constant gain matrices K_p and K_v . In order to improve the performance of conventional control schemes, different nonlinear control techniques are employed. In present paper, the nonlinear PD-CTC is considered, which has the similar structure of CTC. The control law for the proposed scheme as follows:

$$\tau_c = \widehat{M}(q_a)(\ddot{q}_d + K_p e + K_v \dot{e}) + \widehat{C}(q_a, \dot{q}_a)\dot{q}_a = \widehat{M}(q_a)q'' + \widehat{C}(q_a, \dot{q}_a)\dot{q}_a \quad (13)$$

where $q'' = \ddot{q}_d + K_p e + K_v \dot{e}$; and K_p and K_v are time-varying gain matrices. $K_p = \text{diag}[K_{p1}, K_{p2}, K_{p3}]$; $K_v = \text{diag}[K_{v1}, K_{v2}, K_{v3}]$. For tuning the gain matrices K_p and K_v in nonlinear CTC controller Eq. (13), an intelligent tuning system proposed by Tien et al. (2013a, b) is applied. Here, the output of the NN is the input to the nonlinear PD-CTC:

$$q''_i = f(x_i), \quad i = 1, 2, 3. \quad (14)$$

in which x_i is the input of sigmoid function, $f(x_i)$ is defined in the following equation:

$$f(x_i) = \Psi \times \frac{(1 - e^{-Z})}{(1 + e^{-Z})} \quad i = 1, 2, 3. \quad (15)$$

where $\Psi = 2/Y_g$, $Z = 2x_i Y_g$, Y_g represents the sigmoid function's shape. Here the sigmoid function is the dependent of parameter Y_g (Tu and Kyoung 2006). Figure 3 shows the block diagram of NN model which is used in the intelligent gain tuning. In this, the NN has a single neuron, which is used to update the gains. Here, the input of the sigmoid function is considered as the output of the NN, which can be formulated as follows:

$$x_i(t) = \ddot{q}_d(t) + K_{pi}e_i(t) + K_{vi}\dot{e}_i(t), \quad i = 1, 2, 3. \quad (16)$$

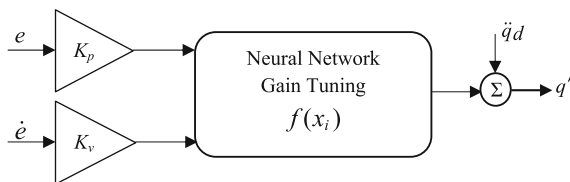


Fig. 3 Intelligent gain tuning using neural network

The gains K_{pi} and K_{vi} in Eq. (16) are automatically updated by NN in order to minimize the error which is defined as:

$$E_i = \frac{1}{2}(q_{di} - q_{ai})^2 \quad (17)$$

The following equations are updated gains:

$$K_{pi}(t+1) = K_{pi}(t) + \Delta K_{pi}(t) \quad (18)$$

$$K_{vi}(t+1) = K_{vi}(t) + \Delta K_{vi}(t) \quad (19)$$

In which the change of gains $\Delta K_{pi}(t)$ and $\Delta K_{vi}(t)$ can be computed by the steepest descent method (Tien et al. 2013a, b):

$$\Delta K_{pi}(t) = \mu_p e_i^2 \frac{4e^{-Z}}{(1+e^{-Z})^2}, \Delta K_{vi}(t) = \mu_v e_i \dot{e}_i \frac{4e^{-Z}}{(1+e^{-Z})^2} \quad (20)$$

The online self gain tuning technique should satisfy the conditions which were presented in (Tu and Kyoung 2006). The proof of the exponential stability of the parallel manipulator system controlled by the proposed controller (13) with intelligent gain tuning technique (19), (20) is described.

3.4 Stability Analysis

To show that the computed torque control technique linearizes the controlled system, the torques computed by (9) are substituted into in (5), yielding

$$\widehat{M}(q_a)\ddot{q}_a = \widehat{M}(q_a)(\ddot{q}_d + K_p e + K_v \dot{e}) \quad (21)$$

Premultiplying each term of the Eq. (21) by \widehat{M}^{-1} , and substituting the relationship, $\ddot{e} = \ddot{q}_d - \ddot{q}$. Provides the following linear relationship for the error:

$$K_p e + K_v \dot{e} + \ddot{e} = 0 \quad (22)$$

The above relation can be used for selecting the gains to get the desired nature of the closed-loop error response. Since the error Eq. (22) is linear, it is easy to select K_p and K_v so that the overall system is stable and $e \rightarrow 0$ exponentially as $t \rightarrow \infty$. Generally, if let $K_v = k_v I$, $K_p = k_p I$ with $s^2 + k_v s + k_p$ Hurwitz polynomial, then the control law (13) implemented to the system (21) results in exponential trajectory tracking. The system is parameterized by the end-effector coordinates in the control law (21).

4 Simulations

In order to demonstrate the effectiveness and robustness of the proposed control law, simulation results are presented in this section. To demonstrate robustness, several different cases are considered and the tracking performances of CTC, Hybrid SMC and proposed intelligent gain tuning technique are compared. The properties used for the manipulator are listed in Table 1.

A circular trajectory in XY plane is tracked using different controller schemes. The desired trajectory is defined as follows:

Circular Trajectory:

$$\{x_d = x_p - r \times \cos(t), y_d = y_p + r \times \sin(t)\} \tag{23}$$

where $r = 0.01$ m is the radius, $(x_p, y_p)^T = (0.21, 0.21)^T$ is the center of the circle and $t \in [0, 6.3]$. The orientation of the mobile platform is maintained constant throughout the trajectory ($\phi = 0^\circ$). In simulations, the control gains for CTC: $K_p = 1000$, $K_v = 63.25$, Hybrid SMC: $\lambda = 10$, $K_s = \text{diag}(100, 50, 25)$, $\psi = \text{diag}(0.08, 0.06, 0.02)$ are selected. The proposed controller parameters are set as the tuning speed parameters $\mu_p = 50000$, $\mu_v = 100$, sigmoid function's shape identifier, i.e., $Y_g = 0.01$, initial control gains for without external disturbance: $K_p = 800$; $K_v = 50$, and with external disturbance: $K_p = 500$; $K_v = 50$ are considered.

4.1 Tracking Control Without External Disturbances

First of all, the proposed intelligent gain tuning technique is applied for the tracking control for a prescribed trajectory, and the comparisons with conventional CTC and Hybrid SMC are presented in Fig. 4.

Figure 5 shows the tracking errors at the active joints of the mechanism and it is found that in all the joints on average the percentage error is less than one for the proposed control scheme. Figure 6 shows the corresponding updating gains. Figure 7 shows the required control torques for the manipulator to follow the trajectory with CTC and Hybrid SMC schemes.

Table 1 Geometric parameters of the 3-RRR planar manipulator

S. no.	Parameter	Length (m)	Mass (kg)	Inertia (kg m ²)
1	Active link (l_{11})	0.2500	0.4680	2.4380×10^{-3}
2	Passive link (l_{12})	0.1667	0.3120	0.7220×10^{-3}
3	Mobile platform (m_p)	0.1250	0.2340	1.8281×10^{-3}
4	Base platform	0.5000	–	–

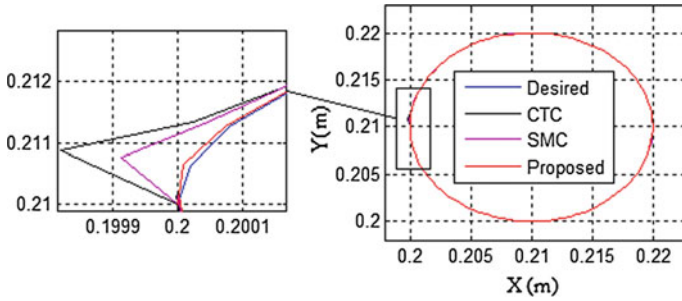


Fig. 4 Trajectory tracking of the end-effector without external disturbances

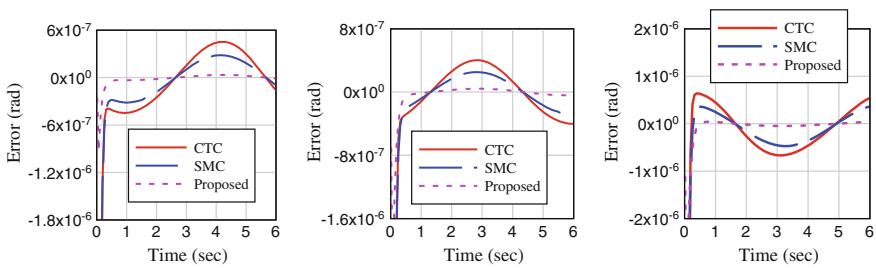


Fig. 5 Tracking errors at the actuated joints

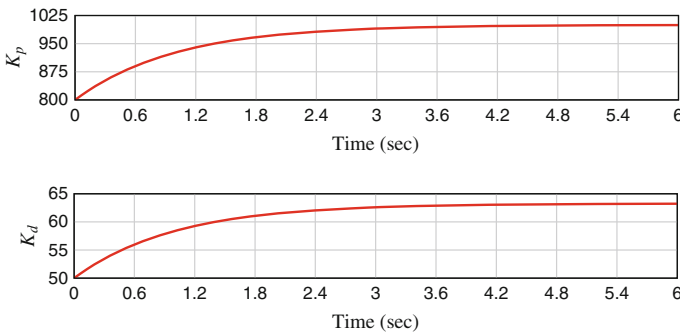


Fig. 6 Intelligent tuning method gains

4.2 Tracking Control with External Disturbances

In this simulation the external disturbances at the actuated joints are introduced randomly as a time-domain Gaussian noise signals (i.e., $\Delta\tau_a \leq 1$). All other parameters remain same as in the normal tracking conditions. The results of the simulation for all three controllers are shown in Fig. 8. Here, the proposed

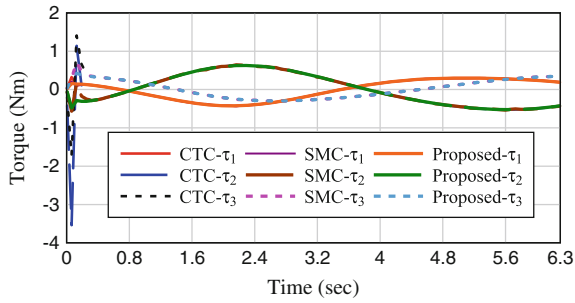


Fig. 7 Control torques at the actuated joints

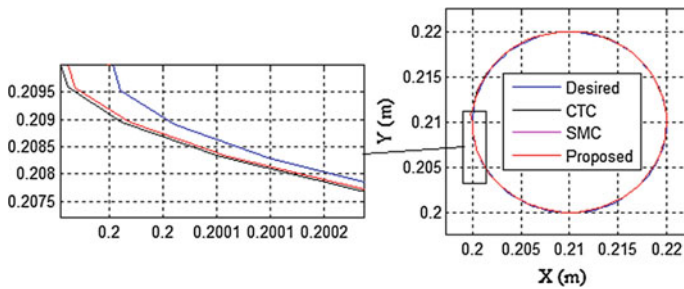


Fig. 8 Trajectory tracking of the end-effector with external disturbances

intelligent gain tuning technique has better computational time than conventional CTC and Hybrid SMC controllers. This shows that the proposed controller has a fast response time on X86-based PC with 4 GB RAM and 3.10 GHz dual core Intel processor and demonstrates its effectiveness in compensating for external disturbances. The tracking errors of the three actuated joints are shown in Fig. 9. From these figures, it is clear that the error of each actuated joint (in radian) is rapidly converging to zero and the proposed controller convergence rate is more compared with conventional CTC and Hybrid SMC.

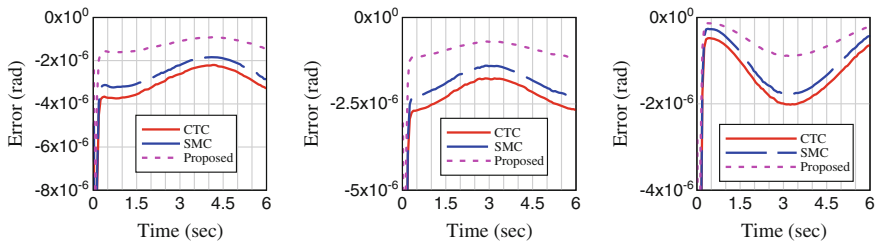


Fig. 9 Tracking errors at the actuated joints

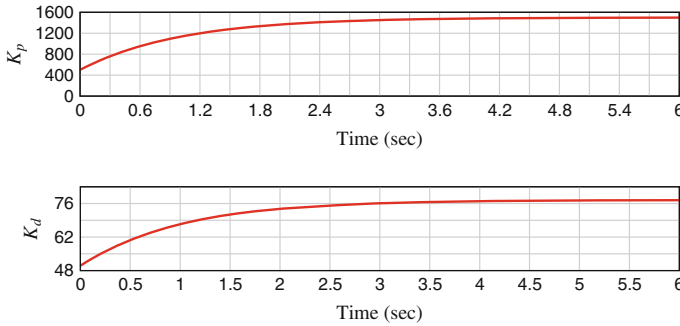


Fig. 10 Intelligent tuning method gains

Fig. 11 Control torques at the actuated joints

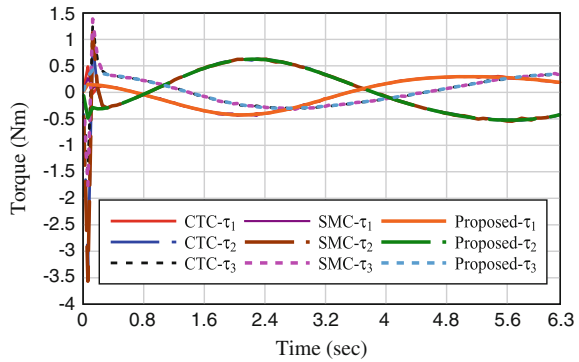
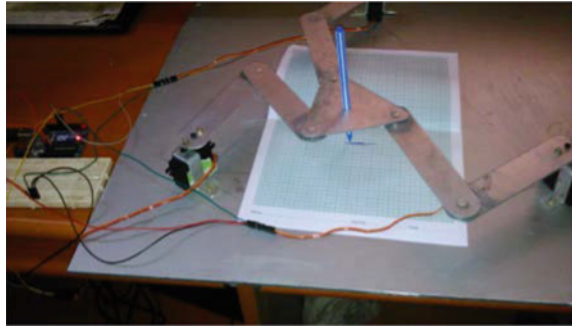


Figure 10 shows the updated gain history. In Fig. 11 the required torques for each actuated joint by the three controllers, i.e. conventional CTC, Hybrid SMC and intelligent gain tuning are illustrated and compared in the presence of external disturbances. From these, it can be concluded that the torques applied to each actuator by the conventional CTC and Hybrid SMC to reject disturbances are initially higher in magnitude than in the intelligent gain tuning technique, and may cause saturation in the actuators. Therefore, it is obvious that intelligent gain tuning technique performance is same as conventional control schemes under the same conditions, without increasing the maximum torques of the actuated joints.

4.3 Experimental Results

The experimental results for without disturbance is carried out for a scaled prototype having three servos as shown in Fig. 12. A straight-line trajectory between points $P_1(17.5,10.10)$ cm and $P_2(21.5,10.10)$ cm has been considered for the

Fig. 12 Scaled prototype



simulation. The prototype is connected to the Arduino UNO board and the desired joint angles are supplied to the prototype through Arduino program at a constant speed of 10 rpm for each servo. The results of the simulations are presented in Fig. 13 and the corresponding joint angles and the desired joint angles are shown in Fig. 14. Obviously, this controller in open-loop mode has a very rough trajectory in the Cartesian space. By using updated joint angles and their velocities, a computed torque will be supplied in every step of the trajectory. The work is under progress.

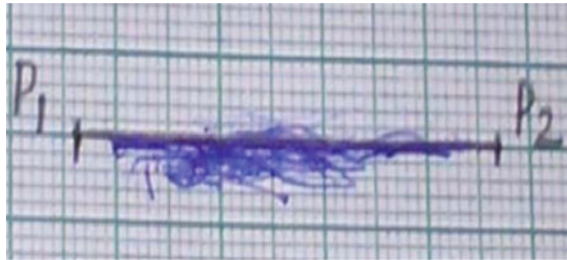


Fig. 13 Simulation results

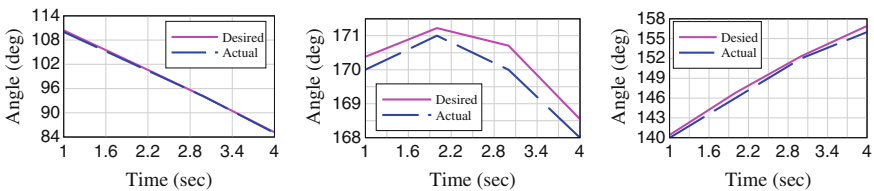


Fig. 14 Experimental and theoretical actuated joint angles

5 Conclusions

This paper presented trajectory tracking performance improvements of planar parallel manipulators with an intelligent gain-tuning approach based on a single layer neural network model. Based on CTC as a nominal controller, an intelligent gain tuning technique using neural network was proposed. Simulation results for a 3-RRR planar parallel manipulator show the effectiveness of the proposed controller for a given trajectory. It has been shown that the proposed controller with online gain tuning using neural network brings about the smallest tracking error and quicker convergence rate compared with conventional CTC and hybrid SMC controllers. The stability of the proposed controller was verified with Lyapunov stability theorem to guarantee the tracking performance of the manipulator. Main advantages of the proposed controller in comparison with the existing conventional CTC and Hybrid SMC methods are: (1) It can compensate the huge amount non-linear uncertainties and external disturbances as seen from error histories (2) The proposed controller does not require the upper limits of uncertainties and approximation errors. Future work could include implementation of proposed gain tuning for control of scaled model and design of disturbance rejection observer to the model operating in highly disturbed environments.

References

- Acob, J. M., Pano, V., & Ouyang, P. R. (2013). Hybrid PD sliding mode control of a two degree of-freedom parallel robotic manipulator. In *10th IEEE International Conference on Control and Automation (ICCA)*, Hangzhou, China.
- Amin, N., & Musa, M. (2012). Active disturbance rejection control of a parallel manipulator with self learning algorithm for a pulsating trajectory tracking task. *Scientia Iranica*, *19*(1), 132–141.
- Amin, N., Ali, Z., & Musa, M. (2012). Performance analysis of the computed torque based active force control for a planar parallel manipulator. *Applied Mechanics and Materials*, *110*, 4932–4940.
- Farzin, P., & Nasri, B. S. (2012). Review of sliding mode control of robotic manipulator. *World Applied Sciences Journal*, *18*(12), 1855–1869.
- Francisco, G. S., Victor, S., & Miguel, A. L. (2014). Fuzzy-tuned PD tracking control of a 3-RRR parallel manipulator: Stability analysis and simulations. *Intelligent Automation & Soft Computing*, *20*(2), 159–182.
- Jun, W., Jinsong, W., & Zheng, Y. (2011). A comparison study on the dynamics of planar 3-DOF 4-RRR, 3-RRR and 2-RRR parallel manipulators. *Robotics and Computer-Integrated Manufacturing*, *27*(1), 150–156.
- Li, Q., & Wu, F. X. (2004). Control performance improvement of a parallel robot via the design for control approach. *Mechatronics*, *14*(8), 947–964.
- Muller, A., & Hufnagel, T. (2012). Model-based control of redundantly actuated parallel manipulators in redundant coordinates. *Robotics and Autonomous Systems*, *60*(4), 563–571.
- Ouyang, P. R., Acob, J. M., & Pano, V. (2014). PD with sliding mode control for trajectory tracking of robotic system. *Robotics and Computer-Integrated Manufacturing*, *30*(2), 189–200.
- Patel, Y. D., & George, P. M. (2012). Parallel manipulators applications—A survey. *Modern Mechanical Engineering*, *2*, 57–64.

- Tien, D. L., Hee, J. K., & Young, S. S. (2013a). Chattering-free neuro-sliding mode control of 2-DOF Planar parallel manipulators. *International Journal of Advanced Robotic Systems*, 10(22), 1–15.
- Tien, D. L., Hee, J. K., Young, S. S., & Young, S. R. (2013b). An online self-gain tuning method using neural networks for nonlinear PD computed torque controller of a 2-dof parallel manipulator. *Neurocomputing*, 116(20), 53–61.
- Tu, D. C. T., & Kyoung, K. A. (2006). Nonlinear PID control to improve the control performance of 2 axes pneumatic artificial muscle manipulator using neural network. *Mechatronics*, 16(9), 577–587.
- Vinoth, V., Yogesh, S., & Santhakumar, M. (2014). Indirect disturbance compensation control of a planar parallel (2-PRP and 1-PPR) robotic manipulator. *Robotics and Computer-Integrated Manufacturing*, 30(5), 556–564.
- Wei, S., & Shuang, C. (2014). Robust nonlinear control of a planar 2-DOF parallel manipulator with redundant actuation. *Robotics and Computer-Integrated Manufacturing*, 30(6), 597–604.
- Wen, S. Y., & Chien, C. W. (2014). H^∞ tracking adaptive fuzzy integral sliding mode control for parallel manipulators. *Fuzzy Sets and Systems*, 248, 1–38.
- Xue, M. N., Guo, Q. G., Xin, J. L., & Zhi, D. B. (2013). Dynamics and control of a novel 3-DOF parallel manipulator with actuation redundancy. *International Journal of Automation and Computing*, 10(6), 552–562.
- Zubizarreta, A., Portillo, E., Cabanes, I., Orive, D., Marcos, M., & Pinto, Ch. (2013). Real-time environment design for testing advanced control approaches in parallel robots Application to the 5R parallel robot prototype. *International Journal of Advanced Manufacturing Technology*, 67(5–8), 1459–1475.
- Zuoshi, S., Jianqiang, Yi, Dongbin, Z., & Xinchun, Li. (2005). A computed torque controller for uncertain robotic manipulator systems: Fuzzy approach. *Fuzzy Sets and Systems*, 154(1), 208–226.

Study of Joining Different Types of Polymers by Friction Stir Welding

Nitin Panaskar and Ravi Terkar

Abstract Friction stir welding has been successfully employed for various types of polymers. The application of external heat source is beneficial in joining different types of polymers and fiber reinforced polymers by FSW. External heating elements such as heated shoe, viblade, hot air gun have been used to assist the Friction Stir Welding Process. Polymers with low melting point temperatures were easily joined while those with higher melting point temperatures either formed weaker joints or posed difficulty while welding. The Friction stir welding process also applies well to reinforced plastics. Joints of good tensile strength quality factor, flexural strength and shear strength are obtained. This paper reviews the work done with respect to joining of different types of polymers and fiber reinforced polymers and concludes by suggesting further scope for research in friction stir welding of polymers and polymer-hybrid composite materials.

Keywords Friction stir welding · Polymer · Fiber reinforced plastic · External heating

1 Introduction

Light weight materials such as thermoplastics and fiber-reinforced plastics find extensive application in aerospace, automobile, medical, electronic and construction industry (Wambua et al. 2003). Plastics have various advantages over metals. They possess higher strength to weight ratio compared to metals, good toughness and viscoelasticity, good environment resistance and excellent electrical resistance. Plastics can be processed easily by extrusion, compression moulding and injection moulding at low cost. The cost can be further reduced by recycling the scrap generated during the production process. However, larger and complex parts need

N. Panaskar (✉) · R. Terkar
Mukesh Patel School of Technology Management and Engineering, Mumbai, India
e-mail: njpanaskar@gmail.com

to be joined by welding (Marczis and Czigány 2002). Friction Stir Welding (FSW) is a comparatively newer welding process invented in 1991 by Thomas et al. (1995) and was initially developed for aluminium and Al alloys (Thomas and Nicholas 1997). Over the last two decades, FSW has shown potential to join copper (Lee and Jung 2004) and copper alloys (Park et al. 2004), magnesium alloy (Park et al. 2003), steel (Reynolds et al. 2003), titanium (Lee et al. 2005), metal matrix composites (Prado et al. 2003) and also to join dissimilar metals such as magnesium alloy to aluminium alloy (Yan et al. 2010), mild steel to aluminium alloy (Watanabe et al. 2006), aluminium to copper (Ouyang et al. 2006), Al alloy to titanium alloy (Chen and Nakata 2009). FSW has also recently been studied for thermoplastics (Bagheri et al. 2013; Squeo et al. 2009; Panneerselvam et al. 2004; Nelson et al. 2004; Kiss and Czigány 2012b).

Several studies have demonstrated that plastics such polyethylene, polypropylene, polyvinyl chloride, polyvinylidene fluoride, acrylonitrile butadiene styrene, nylon and polymethylmethacrylate have potential to be joined using FSW (Bagheri et al. 2013; Squeo et al. 2009; Panneerselvam et al. 2004; Nelson et al. 2004; Kiss and Czigány 2012b). FSW of plastics is different from FSW of metals because of the difference in the structure and morphology. Unlike metallic materials, polymers have low thermal conductivity, low melting temperature, low hardness, relatively poor impact resistance and short solidification time (Nelson et al. 2004; Troughton 2009). The heat generated during FSW is insufficient to soften the material in case of plastics. This signifies the necessity of using an external heat source to assist the conventional FSW process. This combination of using FSW and an external heat source is referred to as heat-assisted FSW in some studies (Mostafapour and Azarsa 2012). The conventional input parameters, namely, (a) Tool rotation speed, (b) Tool traverse speed, (c) Tool tilt/attack angle, studied for FSW of metals also apply for plastics. Conventionally, a conical threaded tool is used for performing FSW. A typical FSW tool is shown in Fig. 1.

Fig. 1 Conical threaded tool



Fig. 2 Heating arrangement on CNC vertical milling machine using hot air gun



Few studies have made use of external heat source with FSW and have succeeded to an acceptable level (Mostafapour and Azarsa 2012; Aydin 2010; Bagheri et al. 2013; Squeo et al. 2009; Kiss and Czigány 2012a; Nelson et al. 2004; Czigány and Kiss 2011). A typical heating arrangement using FSW tool and hot air gun is shown in Fig. 2. Heat-assisted FSW has been studied on all the above mentioned thermoplastics (Bagheri et al. 2013; Squeo et al. 2009; Panneerselvam et al. 2004; Nelson et al. 2004; Kiss and Czigány 2012b).

Alternatively, heating can also be achieved by using a novel technique such as Viblade instead of using an external heating source (Scialpi et al. 2009). Various techniques of external heating have been used as shown in Table 1. Currently, there is widespread use of composite structures which make it necessary to develop

Table 1 Heating methods in FSW of plastics

S. no.	Heated element/technique	Heating arrangement
1	Tool pin	Hot air gun
2	Work piece	Heater plate
		Heating through constraining shoe placed above the work piece
3	Using tool vibration	Viblade

reinforced plastics for applications such as turbine engine components (Nelson et al. 2004). The study has been performed on heat-assisted FSW of reinforced plastics. The reinforcements used in these studies are carbon fibers and glass fibers. Such reinforcements can be used to decrease the weight of the structures used in aerospace applications. An even greater decrease in weight can be achieved by using fiber-reinforcements at nano scale such as carbon nano tubes (CNT) or by using nano-sized powders. Nano-sized powders such as Al_2O_3 (Alumina), SiC and SiO_2 have been used as reinforcements to perform FSW and Friction Stir Processing (FSP) of metals (Lee et al. 2006; Mishra et al. 2003; Shafiei-Zarghani et al. 2009; Shamsipur et al. 2011). Nano-sized powders can also help to reduce the density of the composite material which makes them more suitable for aerospace applications (Guo et al. 2007). However, the feasibility of using such nano-sized powders in the case of FSW of polymeric materials has not yet been investigated extensively.

2 Literature Review

2.1 *Methods of Polymer Welding*

Plastics can be joined done by fastening, solvent bonding, adhesive bonding and by using welding methods such as dielectric, electric fusion, electromagnetic, extrusion, heat fusion, heat roll, hot gas, hot tool, induction, infrared, laser, linear vibration, microwave, orbital, resistive implant, solvent, spin, ultrasonic and FSW (Mistry 1997; Strand 2003; Takasu 2003; Yousefpour et al. 2004). FSW was first demonstrated on plastics in 1997 (Mistry 1997). Advantages of using FSW for plastics over other welding methods are as follows: higher joint efficiency, high repeatability, ease of use for both continuous and discrete joining, higher speed of operation and low cost tooling and machinery respectively.

2.2 *FSW of Polymer Materials*

Polyethylene (PE)

FSW has been studied on different types of polyethylene (PE) such as low density polyethylene (LDPE), medium density polyethylene (MDPE), high density polyethylene (HDPE), and ultra high molecular weight polyethylene (UHMWPE). Tensile strength of the joints obtained was up to 95 % of the base material while the lowest strength achieved was 46.2 %. Mostafapour and Azarsa (2012) used a heating shoe and reported 95 % tensile strength quality factor (TSQF) for HDPE while Nelson et al. (2004) also used a heating shoe and reported 91.5 % TSQF for HDPE. Aydin (2010) preheated the samples from bottom and reported 89 % TSQF

for UHMWPE. Squeo et al. (2009) used a combination of heating arrangements and reported 95 % TSQF in case of HDPE. Arici and Sinmazçelýk (2005) performed two pass FSW on MDPE and reported the tensile strength of the FSWed samples to be approximately the same as the base material. The reason for the higher amount of tensile strength achieved is that the root defect, which generally leads to failure in the weld zone, was eliminated in the second pass of FSW. In a similar experiment performed by Arici and Selale (2007), they reported up to 87 % TSQF and the lowest TSQF obtained was 59 %. Bozkurt (2012) optimized the FSW parameters for HDPE and reported 95 % TSQF.

Polypropylene (PP)

Polypropylene sheets of thicknesses varying from 0.9 mm to 10 mm have been successfully joined using FSW. Tensile strength of the joints achieved is in the range of 25–90 % with respect to the base material. Kiss and Czigány (2012a) performed FSW on polypropylene (PP) and reported 90 % TSQF with respect to the base material, by using an ancillary heating shoe. Nelson et al. (2004) also used a similar heating shoe arrangement and reported 86 % TSQF while Kiss and Czigány (2012b) reported 86 ± 2.6 % TSQF without external heating.

Kiss (2011) and Payganeh et al. (2011) were the first to perform FSW on glass fiber reinforced sheets (GFRS) of PP. Kiss (2011) reported 90 % TSQF for PP and 65 % for GRFS of PP. Czigány and Kiss (2011) reported 64 % flexural strength as compared to the base material. They observed that by using GFRS, the flexural strength of the seams produced on GFRS exceeded those of the seam produced on non-reinforced sheets by 27 %. Payganeh et al. (2011) performed FSW using different tools and reported 25 % TSQF by using GRFS. Ratanathavorn (2012) demonstrated lap welding of aluminium to PP by FSW and reported lap shear strengths up to 846 N with a joint width of 40 mm.

Acrylonitrile Butadiene Styrene (ABS)

FSW was first studied on ABS by Nelson et al. (2004). They used a heated shoe for FSW and reported 76.5 % TSQF. In a recent study, Bagheri et al. (2013) also used a heating shoe. They reported a maximum TSQF of 88.76 % while the minimum TSQF observed was 5.4 %. ABS is an amorphous substance and does not have a true melting point but it has a glass-liquid transition temperature of approximately 105 °C. In this context, it would be interesting to study the optimum process parameters for FSW of ABS since it can be readily joined by every common joining process (Bagheri et al. 2013).

Polyvinylidene fluoride (PVDF)

FSW of PVDF has only been studied by Nelson et al. (2004) using a heated shoe. They observed 75 % TSQF with respect to the base material.

Polyethylene Terephthalate Glycol (PETG)

Kiss and Czigány (2012a) performed FSW on PETG and PP and reported 90 % tensile strength quality factor (TSQF) for both the materials with respect to the base material. It was observed that the optimal TSQF for PETG is achieved at 1800 rpm while the same is achieved in PP at approximately 3000 rpm.

Nylon (Polyamide)

FSW of nylon has been studied by Nelson et al. (2004) using a heated shoe. They observed only 40 % TSQF in case of nylon 6 which is the most common commercial grade of moulded nylon. Unlike most thermoplastics, nylon requires a high amount of heat to bring it to a semisolid state so that proper stirring of the material can occur to generate a good weld. This occurs because nylon 6 has high melting point of 220 °C.

Teflon (PTFE)

FSW was first studied on ABS by Nelson et al. (2004) by using a heated shoe and observed that it is difficult to process Teflon. The tool just chopped off the material. Since Teflon has a high melting point of 327 °C, it does not easily melt and flow, thereby leading to a low strength weld. The tensile strength quality factor (TSQF) of joint as compared to base material is shown in Table 2.

Table 2 Tensile strength quality factor of joint with respect to base material

S. no.	Material	Type of joint	Tensile strength quality factor with respect to base material (%)
1	PE (HDPE)	Butt	91.5
2	PE (UHMW)	Butt	89
3	PP	Butt	86
4	ABS	Butt	76.5
5	PVDF	Butt	75
6	PETG	Butt	90
7	Nylon	Butt	40
8	Teflon (PTFE)	Butt	Difficult to Process

2.3 FSW of Polymers with Aluminium

Recently, FSW has also been studied by Ratanathavorn (2012) to produce lap joints by joining Aluminium alloys; namely AA5000 and AA6000, and polypropylene, PA12 and polyethylene teraphthalate. Joints were created by generating a stir zone of aluminum chips which was filled with melted thermoplastic. An evaluation of the joint strength was benchmarked with the relevant literatures on hybrid joining. The results of proposed technique showed that the maximum tensile shear strength of friction stir welded joints had the same order of magnitude as the joints welded by laser welding. Friction lap welding (FLW) is a new conception of joining method developed in Joining and Welding Institute (JWRI). The efficiency of joining metal and plastic using FLW was demonstrated by Liu et al. (2014) through a case study on aluminium alloy AA6061 and MC Nylon-6. The lap joints with high shear strength were obtained over a wide range of welding parameters.

3 Conclusion

Friction Stir Welding has been successfully employed to join various different similar as well as dissimilar metals. Polymers and fiber reinforced polymers having low melting point are welded by employing an external heat source. Joints of high efficiencies of at least 75 % tensile strength quality factor are obtained by employing low cost tooling and conventional machinery. A suitable heating arrangement is necessary to assist the softening of the polymer during FSW process. By employing two pass FSW, the root defect is eliminated, resulting in even higher tensile strength. Polymers with high melting point temperatures such as Nylon and Teflon posed difficulties in joining in spite of using FSW with external heat source. The joints produced had low tensile strength. Sintering of such high temperature melting materials before FSW and/or during FSW can make the joining process more feasible. FSW has also been successfully employed to produce butt and lap joints between aluminium alloys and polymers. Joints with good tensile and shear strengths were obtained for the hybrid joint. Though the exact potential of the FSW process is yet to be revealed, FSW holds great promise in joining thermoplastics, fiber reinforced polymers, polymer nanocomposites and other polymer-hybrid materials. FSW can further be applied to nano-particle reinforced polymers, nano-particle and fiber reinforced polymers and nanocomposite polymers.

References

- Arici, A., & Selale, S. (2007). Effects of tool tilt angle on tensile strength and fracture locations of friction stir welding of polyethylene. *Science and Technology of Welding and Joining*, *12*, 536–539.
- Arici, A., & Sinmazçelýk, T. (2005). Effects of double passes of the tool on friction stir welding of polyethylene. *Journal of Materials Science*, *40*, 3313–3316.
- Aydin, M. (2010). Effects of welding parameters and pre-heating on the friction stir welding of UHMW-polyethylene. *Polymer-Plastics Technology and Engineering*, *49*, 595–601.
- Bagheri, A., Azdast, T., & Doniavi, A. (2013). An experimental study on mechanical properties of friction stir welded ABS sheets. *Materials and Design*, *43*, 402–409.
- Bozkurt, Y. (2012). The optimization of friction stir welding process parameters to achieve maximum tensile strength in polyethylene sheets. *Materials and Design*, *35*, 440–445.
- Chen, Y. C., & Nakata, K. (2009). Microstructural characterization and mechanical properties in friction stir welding of aluminum and titanium dissimilar alloys. *Materials and Design*, *30*, 469–474.
- Czigány, T., & Kiss, Z. (2011). Friction stir welding of fiber reinforced polymer composites. In *Presented at the 18th International Conference on Composite Materials, ICCM*, Jeju, Korea.
- Guo, G., Wang, K. H., Park, C. B., Kim, Y. S., & Li, G. (2007). Effects of nanoparticles on the density reduction and cell morphology of extruded metallocene polyethylene/wood fiber nanocomposites. *Journal of Applied Polymer Science*, *104*, 1058–1063.
- Kiss, Z. (2011). *Friction stir welding of polymers*. Budapest University of Technology and Economics.
- Kiss, Z., & Czigány, T. (2012a). Effect of welding parameters on the heat affected zone and the mechanical properties of friction stir welded poly(ethylene-terephthalate-glycol). *Journal of Applied Polymer Science*, *125*, 2231–2238.
- Kiss, Z., & Czigány, T. (2012b). *Microscopic analysis of the morphology of seams in friction stir welded polypropylene*, *6*, 54–62.
- Lee, C. J., Huang, J. C., & Hsieh, P. J. (2006). Mg based nano-composites fabricated by friction stir processing. *Scripta Materialia*, *54*, 1415–1420.
- Lee, W. B., & Jung, S. B. (2004). The joint properties of copper by friction stir welding. *Materials Letters*, *58*, 1041–1046.
- Lee, W. B., Lee, C. Y., Chang, W. S., Yeon, Y. M., & Jung, S. B. (2005). Microstructural investigation of friction stir welded pure titanium. *Materials Letters*, *59*, 3315–3318.
- Liu, F. C., Liao, J., & Nakata, K. (2014). Joining of metal to plastic using friction lap welding. *Materials and Design*, *54*, 236–244.
- Marczisz, B., & Czigány, T. (2002). Polymer joints. *Periodica Polytechnica-Mechanical Engineering*, 117–126.
- Mishra, R., Ma, Z., & Charit, I. (2003). Friction stir processing: A novel technique for fabrication of surface composite. *Materials Science and Engineering A*, *341*, 307–310.
- Mistry, K. (1997). Tutorial plastics welding technology for industry. *Assembly Automation*, *17*, 196–200.
- Mostafapour, A., & Azarsa, E. (2012). A study on the role of processing parameters in joining polyethylene sheets via heat assisted friction stir welding: Investigating microstructure, tensile and flexural properties. *International Journal of Physical Sciences*.
- Nelson, T. W., Sorenson, C. D., & Johns, C. J. (2004). *Friction stir welding of polymeric materials*. U.S. Patent No. 6,811,632. Washington, DC: U.S. Patent and Trademark Office.
- Ouyang, J., Yarrapareddy, E., & Kovacevic, R. (2006). Microstructural evolution in the friction stir welded 6061 aluminum alloy (T6-temper condition) to copper. *Journal of Materials Processing Technology*, *172*, 110–122.
- Panneerselvam, K., Aravindan, S., Haq, A. N. (2004). Joining of plastics by frictional vibration. In *Presented at the International Symposium of Research Students on Materials Science and Engineering*, Chennai, India.

- Park, H. S., Kimura, T., Murakami, T., Nagano, Y., Nakata, K., & Ushio, M. (2004). Microstructures and mechanical properties of friction stir welds of 60% Cu–40% Zn copper alloy. *Materials Science and Engineering A*, 371, 160–169.
- Park, S. H. C., Sato, Y. S., & Kokawa, H. (2003). Effect of micro-texture on fracture location in friction stir weld of Mg alloy AZ61 during tensile test. *Scripta Materialia*, 49, 161–166.
- Payganeh, G. H., Mostafa Arab, N. B., Dadgar Asl, Y., Ghasemi, F. A., & Saeidi Boroujeni, M. (2011). Effects of friction stir welding process parameters on polypropylene composite welds. *International Journal of the Physical Sciences*, 6(19), 4595–4601.
- Prado, R. A., Murr, L. E., Soto, K. F., & McClure, J. C. (2003). Self-optimization in tool wear for friction-stir welding of Al 6061+20% Al₂O₃ MMC. *Materials Science and Engineering A*, 349, 156–165.
- Ratanathavorn, W. (2012). *Hybrid joining of aluminum to thermoplastics with friction stir welding*.
- Reynolds, A., Tang, W., Gnaupel-Herold, T., & Prask, H. (2003). Structure, properties, and residual stress of 304L stainless steel friction stir welds. *Scripta Materialia*, 48, 1289–1294.
- Scialpi, A., Troughton, M., Andrews, S., & De Filippis, L. A. C. (2009). VibladeTM: Friction stir welding for plastics. *Welding International*, 23, 846–855.
- Shafiei-Zarghani, A., Kashani-Bozorg, S. F., & Zarei-Hanzaki, A. (2009). Microstructures and mechanical properties of Al/Al₂O₃ surface nano-composite layer produced by friction stir processing. *Materials Science and Engineering A*, 500, 84–91.
- Shamsipur, A., Kashani-Bozorg, S. F., & Zarei-Hanzaki, A. (2011). The effects of friction-stir process parameters on the fabrication of Ti/SiC nano-composite surface layer. *Surface & Coatings Technology*, 206, 1372–1381.
- Squeo, E. A., Bruno, G., Guglielmotti, A., & Quadrini, F. (2009). Friction stir welding of polyethylene sheets. *The Annals of Dunarea de Jos University of Galati, Technologies in Machine Building*, 5, 241–246.
- Strand, S. (2003). Joining plastics—Can friction stir welding compete? In *Proceedings of the Electrical Insulation Conference and Electrical Manufacturing Coil Winding Technology Conference* (pp. 321–326).
- Takasu, N. (2003). Friction welding of plastics. *Welding International*, 17, 856–859.
- Thomas, W. M., & Nicholas, E. D. (1997). Friction stir welding for the transportation industries. *Materials and Design*, 18, 269–273.
- Thomas, W. M., Nicholas, E. D., Needham, J. C., Murch, M. G., Temple-Smith, P., & Dawes, C. J. (1995). *Friction welding*. US Patent Application, 54603176.
- Troughton, M. J. (2009) Introduction. In *Handbook of plastics joining* (2nd ed., pp. xxi–xxii). Boston: William Andrew Publishing.
- Wambua, P., Ivens, J., & Verpoest, I. (2003). Natural fibres: Can they replace glass in fibre reinforced plastics? *Composites Science and Technology*, 63, 1259–1264.
- Watanabe, T., Takayama, H., & Yanagisawa, A. (2006). Joining of aluminum alloy to steel by friction stir welding. *Journal of Materials Processing Technology*, 178, 342–349.
- Yan, Y., Zhang, D., Qiu, C., & Zhang, W. (2010). Dissimilar friction stir welding between 5052 aluminum alloy and AZ31 magnesium alloy. *Transactions of Nonferrous Metals Society of China* 20, Supplement 2, s619–s623.
- Yousefpour, A., Hojjati, M., & Immarigeon, J. P. (2004). Fusion bonding/welding of thermoplastic composites. *Journal of Thermoplastic Composite Materials*, 17, 303–341.

Single Point Incremental Forming Using Flexible Die

Deepesh Panjwani, Prashant K. Jain, M.K. Samal, J.J. Roy,
Debanik Roy and Puneet Tandon

Abstract Incremental sheet forming is an innovative process having ability to fulfill demands for customized sheet metal parts without using costly dies unlike traditional forming processes. However, shape deviation of formed parts is one of the drawbacks which need technological developments to use ISF on shop floor. Backdrawing, use of half dies and customized toolpaths are some of the techniques being worked out for reducing shape deviation but have some limitations. The present work investigates the flexible die developed to reduce shape deviation of the non-axisymmetric parts formed through SPIF. Experiments were carried out with different geometries to check the effectiveness of flexible die. Results show a significant improvement in the parts formed using flexible die over those formed without using it. This work gives another method for forming components with reduced bending. Also it proposes a new method of using bolts as flexible die which doesn't need to be changed with the part geometry.

Keywords Single point incremental forming (SPIF) · Two point incremental forming (TPIF) · Flexible supports · Duplex forming

1 Introduction

This section is divided in two parts, one of which deals with the process of ISF while other deals with the problem investigated in this work, i.e., shape deviation in parts and some of solutions proposed for it.

D. Panjwani (✉) · P.K. Jain · P. Tandon
PDPM Indian Institute of Information Technology, Design and Manufacturing, Jabalpur
482005, M.P., India
e-mail: panjwanideepesh7@gmail.com

M.K. Samal · J.J. Roy · D. Roy
Bhabha Atomic Research Centre, Trombay, Mumbai 400085, India

1.1 Incremental Sheet Forming

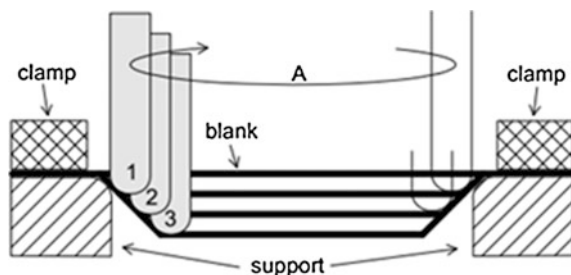
Rapid prototyping techniques like layered manufacturing (Taufik and Jain 2014) and ISF are being used for manufacturing customized parts which are the need of market today. The origin of ISF owes back to conventional sheet metal forming process of spinning where axisymmetric parts are formed by pressing of sheet with a rotating mandrel and force is applied with the help of roller ended tool. The process of ISF differs from spinning because of its capability of forming non-axisymmetric parts whereby spinning can only form axisymmetric components. A metallic sheet clamped around the edges is suppressed by a tool which can be ball nosed or hemi spherically ended. Tool moves in X and Y direction causing localized plastic deformation of sheet. The trajectory followed by the tool is same as geometry required while with each contour tool descends down by small distance known as stepdown. Figure 1 explains the process of ISF.

Solid models of the part to be formed are designed using CAD/CAM software which are also useful for generating toolpath according to the geometry designed (Gabriel and Adrian 2014). Some of the advantages of ISF include its flexibility of using same machine and tool facilities for manufacturing wide range of products. For small batch manufacturing, cost of product is reduced as dies are omitted in this process (Dai et al. 2000). Forming forces applied for localized deformation are not so high unlike conventional process of deep drawing (Bramley et al. 2005). Higher formability limits can be achieved because of localized deformation yielding higher amount of material (Jackson and Allwood 2009). Some limitations of this process are forming forces may have to be assessed for forming complex parts to ensure safety of tooling and equipment's used (Priyadarshi et al. 2015), achieving vertical walls, uneven thinning of sheet material and geometric accuracy of parts etc. (Pohlak et al. 2007).

1.2 Geometric Accuracy of Parts

Any sheet metal part formed is useful when it's manufactured within the tolerances limits. Some of the defects causing shape deviation of parts include bending of

Fig. 1 SPIF as conceived by (Emmens et al. 2010)



sheet near the clamped periphery, springback, pillow effect etc. (Micari et al. 2007). A study of FEM for geometric accuracy of parts in ISF was presented considering various shell element formulations (Sahu et al. 2015). Some of the earlier works done in this direction are mentioned in the following lines.

In majority of works backing plate is used to support the unclamped region of sheet. An elastic rubber tool was used by Tanakka et al. for supporting sheet. Back drawing is another good approach in which sheet once formed is flipped around its axis and the same tool path is used to suppress back the region of the sheet undergone bending. An important application of this technique can be seen in case where any kind of supports cannot be used below the sheet (Micari et al. 2007). One of the commonly used techniques is using a half die which is the replica of shape or geometry to be formed. Besides supporting the sheet it also guides the deformation of sheet eliminating chances of undesired bending (Attanasio et al. 2008). Duplex forming is also used to form complex geometries without shape deviation. In this two tools are used in which one above the sheet deforms it, while the one below the sheet acts as dynamic die supporting it (Malhotra et al. 2011). A different method proposed by Franzen et al. was using a Dyna-Die which minimizes shape deviation but can only form axisymmetric parts (Franzen et al. 2008).

The solutions mentioned above have some or the other limitation as process like backing plate and half die are not flexible because of their dependency on shape formed. Backdrawing is a good approach but is a post processing operation as it allows the sheet to bend and then rectify it which increases processing time. Limitation with TPIF is requirement of specially designed machines and it cannot be used with normal CNC machines. Therefore, a solution is required which has following features:

1. It is flexible enough to accommodate the changes in shape of part.
2. It should be a preprocessing operation which will save time unlike backdrawing.
3. It can be used with normal CNC machines which are easily available instead of designing especially dedicated machines like one used in TPIF.

The present research work deals with reduction of bending of sheet in SPIF process which enables us to form complex parts with near to desired geometric accuracy.

2 Methodology

Flexible die attached to fixture and the setup fabricated is developed (as shown in Fig. 2). Bolts can be rearranged repeatedly in up and down direction to support various geometries. To avoid any chances of bolt penetrating sheet or causing dents on sheet surface the tip of bolt were fitted with rubber caps which increase the supporting area. It also acts as a cushioning.

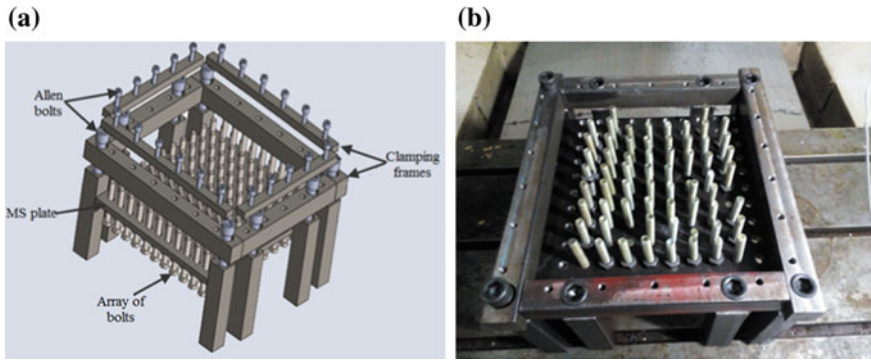


Fig. 2 a CAD model of proposed setup. b Developed experimental setup

3 Experiments Conducted

Two non-axisymmetric shaped geometries were selected for investigation. Figure 3 shows 3D CAD model of L and M shape geometries made by using SolidWorks 12.0. Toolpath was generated using CAM software DELCAM PowerMILL. Two forming tools of diameter 8 and 10 mm were used for L and M shape respectively. A11050, i.e., aluminium alloy was used as sheet material having thickness of 0.95 mm. For reducing the friction between sheet and tool hydraulic oil grade 68 was used. Table 1 shows the specification of parts formed.

OKUMA 3-axis CNC milling machine was used for conducting experiments. Figure 4 shows the CAD model of pattern in which bolt supports were arranged for conducting experiments on L and M shape. Bolts present under the area of sheet where forming takes place are lowered while other bolts act as support for the sheet.

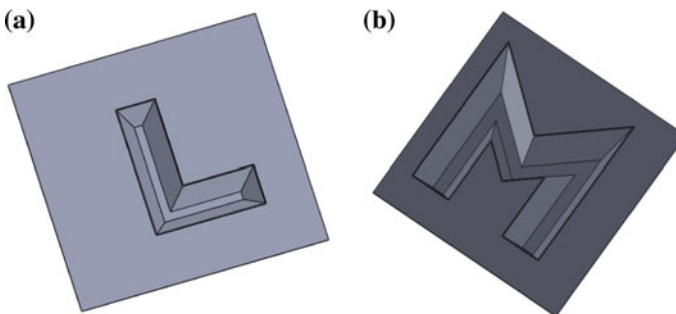


Fig. 3 CAD model of a L shape. b M shape

Table 1 Specifications of geometries

Geometry	L shape	M shape
Depth (mm)	30	30
Wall angle (°)	60	60

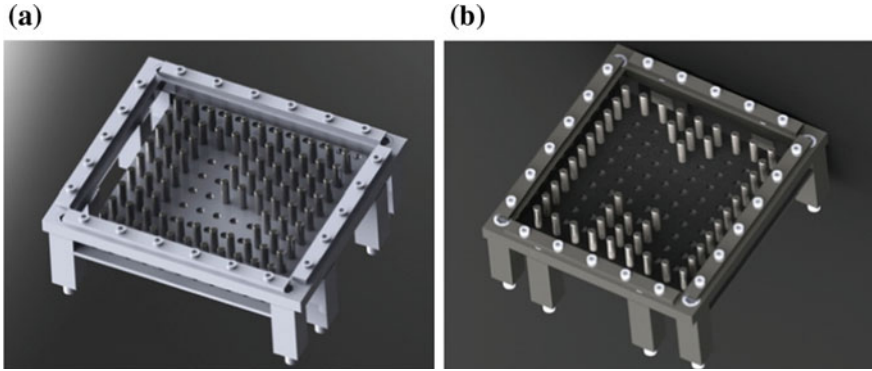


Fig. 4 CAD model of bolt supports arrangement. **a** L shape. **b** M shape

4 Results and Discussions

Analysis of bending of parts was done by forming L and M shape geometries initially using SPIF and then with SPIF using bolt supports. All parts were laser scanned to acquire point cloud data. Comparison of cross section for parts formed by SPIF and that formed by SPIF with bolt supports has been done to check the effectiveness of bolt supports technique. Formed parts were scanned using a laser scanner with a pitch of 1 mm. A reverse engineering software package Geomagic Control 2014 has been used to obtain cross section of parts at the region where bending is high. Figures 5, 6, 7 and 8 show the position of sectioning plane and cross section of the parts obtained for M and L shape.

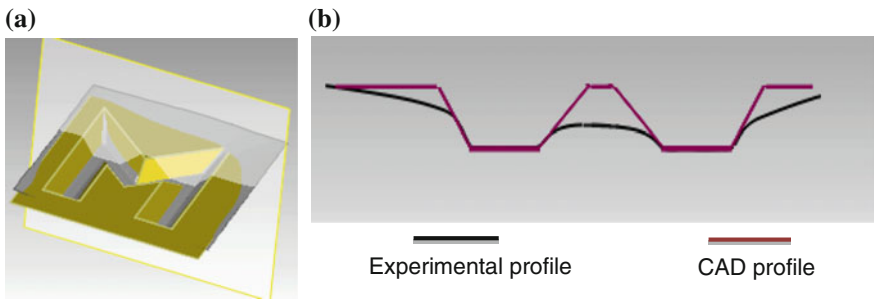


Fig. 5 Comparison of CAD model with formed M shape without bolt supports. **a** Section plane. **b** Cross section

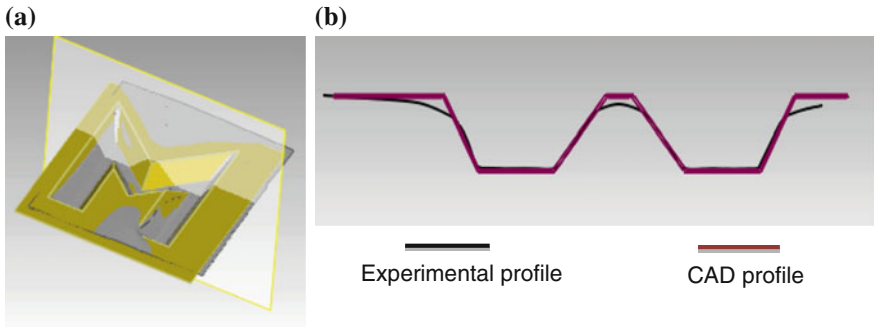


Fig. 6 Comparison of CAD model with formed M shape with support. **a** Section plane. **b** Cross section

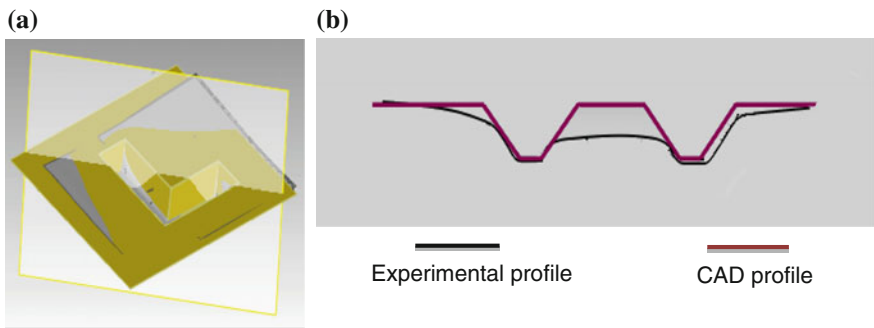


Fig. 7 Comparison of CAD model with formed L shape without support. **a** Section plane. **b** Cross section

Deviation between profile of CAD part and experimental part justify the effectiveness of bolt support for both the shapes. Bending of sheet in parts made by SPIF using bolt supports show a significant improvement over parts made without bolt supports. The decrease in bending of parts can be attributed to minimization of overhang between the outermost edge of geometry and clamping frame due to presence of bolt support. Figures 9 and 10 show images of formed parts.

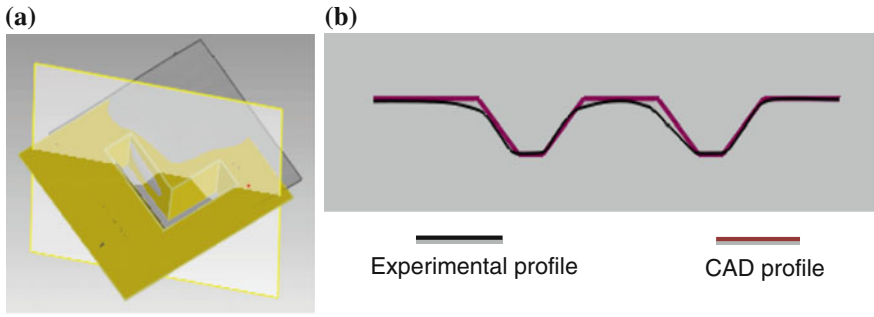


Fig. 8 Comparison of CAD model with formed L shape with support. **a** Section plane. **b** Cross section

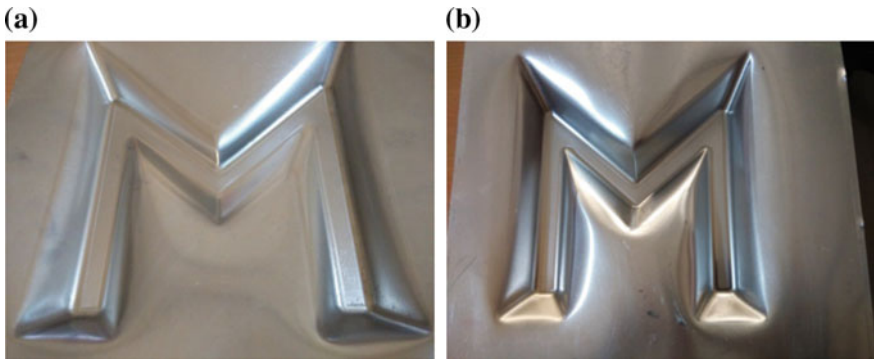


Fig. 9 Images of formed parts of M shape. **a** Without supports. **b** With supports

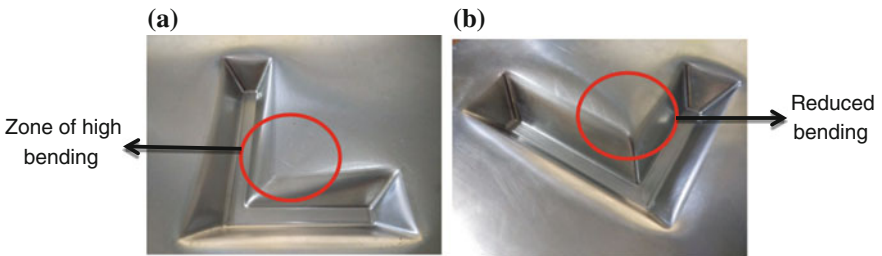


Fig. 10 Images of formed parts of L shape. **a** Without supports. **b** With supports

5 Conclusions

A fixture was developed incorporating the mechanism for holding bolts which supported the sheet while forming is carried out. The parts formed using the proposed mechanism show betterment over the parts made by SPISF. Shape deviation analysis for L and M shape shows reduction of bending of sheet near to the point where tool takes sharp turns.

Forming non-axisymmetric parts through SPIF is tedious because of the tools used like backing plate, clamping near to the boundary of the geometry etc. These tools have to be changed with the geometries and are not flexible. Thus, negating the advantages of ISF over conventional methods using dies and reducing the utility of ISF. The methodology mentioned in this work provides an important solution to the problem cited above and can be used as a reconfigurable die which works with different geometries.

Acknowledgments The authors would like to acknowledge Board of Research in Nuclear Sciences (BRNS), DAE, India for their financial and technical support.

References

- Attanasio, A., et al. (2008). Asymmetric two points incremental forming: Improving surface quality and geometric accuracy by tool path optimization. *Journal of Materials Processing Technology*, 197, 1–3.
- Bramley, A. N., et al. (2005). Asymmetric single point incremental forming of sheet metal. *Annals of CIRP*, 1(1).
- Dai, K., et al. (2000). CNC incremental sheet forming of an axially symmetric specimen and the locus of optimization. *Journal of Materials Processing Technology*, 102(1), 164–167.
- Emmens, W. C., et al. (2010). The technology of incremental sheet forming—A brief review of the history. *Journal of Materials Processing Technology*, 210(8), 981–997. doi:10.1007/s00170-014-6777-4.
- Franzen, V., et al. (2008). Dyna-Die: Towards full kinematic incremental forming. *International Journal of Material Forming*, 1(1), 1163–1166.
- Gabriel, P., & Adrian, B. (2014). Developing an experimental case in aluminium foils 1100 to determine the maximum angle of formability in a piece by Dieless-SPIF process. *IOP Conference Series: Materials Science and Engineering*, 65, 012027.
- Jackson, K., & Allwood, J. (2009). The mechanics of incremental sheet forming. *Journal of Materials Processing Technology*, 209(3), 1158–1174.
- Malhotra, R., et al. (2011). Improvement of geometric accuracy in incremental forming by using a squeezing toolpath strategy with two forming tools. *Journal of Manufacturing Science Engineering*, 133(6), 061019.
- Micari, F., et al. (2007). Shape and dimensional accuracy in single point incremental forming: state of the art and future trends. *Journal of Materials Processing Technology*, 191(1–3), 390–395.
- Pohlak, M., et al. (2007). Manufacturability and limitations in incremental sheet forming. *Proceedings of the Estonian Academy of Sciences (Engineering)*, 13(2), 129–138.
- Priyadarshi, S., et al. (2015). Feature based assessment of forming force behavior in incremental sheet forming. In *23rd International Conference on Computer Graphics, Visualization and Computer Vision (WSCG 2015)*. Plzen, Czech Republic, June 8–12, 2015 (pp. 95–104).

- Sahu, G., et al. (2015). *Shell element formulation based finite element modelling, analysis and experimental validation of incremental sheet forming process*.
- Taufik, M., & Jain, P. K. (2014). Volumetric error control in layered manufacturing, In *ASME 2014 International Design Engineering Technical Conferences and Computers and Information in Engineering Conference (IDETC/CIE)*, New York, USA, 2014.

Hilbert Curve Based Toolpath for FDM Process

Saquib Shaikh, Narendra Kumar, Prashant K. Jain
and Puneet Tandon

Abstract Fused Deposition Modelling (FDM) is one of the most widespread additive manufacturing technique used for fabricating 3D objects without any design constraints. It is a solid-based process in which polymers material in the form of semi molten state is extruded from the nozzle to fabricate the 3D objects. In the present work, a new tool path strategy for FDM process has been developed based on Hilbert curve. Hilbert curve is a space filling fractal curve and its hausdorff dimension is two. This curve is surjective and continuous in nature. The proposed tool path from developed program are validated though simulation and experimental results. The new approach has been simulated using MATLAB computing platform. Boolean operators like intersection and subtraction are utilized for finding the intersection points for the tool path generation. A self-developed extruder system based on screw extrusion is used for the real time application of the algorithm developed. The extruder head is reconfigured to an existing CNC milling machine for printing and production purpose. Case study for different types of prototypes are also presented to demonstrate the capabilities of developed tool path algorithm.

Keywords Hilbert curve · Fused deposition modelling · CNC milling machine · Fractal curves · Boolean operators · Toolpath algorithm

1 Introduction

Additive Manufacturing (AM) has gained significant importance in the last decade. This is because of complex shapes and geometries manufactured by additive manufacturing processes erstwhile impossible with conventional manufacturing

S. Shaikh (✉) · N. Kumar · P.K. Jain · P. Tandon
Mechanical Engineering Discipline, PDPM Indian Institute of Information Technology,
Design and Manufacturing, Jabalpur, India
e-mail: saquib.spce@gmail.com

technologies (Taufik and Jain 2013). 3D printing the other name of additive manufacturing processes is quite ubiquitous. Fused Deposition Modelling is one of the most popular AM process. FDM builds complex 3D parts layer-by-layer from a thermoplastic material. In this process, thermoplastic material in the form of filament is fed from a spool. The filament passes through rollers to the extruder head where it is heated to semi-molten state. Semi-molten filament is deposited through nozzle on a static worktable layer by layer to form 3D part (Taufik and Jain 2014). Toolpath strategies like raster patterns significantly affect the properties of printed objects (Senthilkumaran et al. 2009). Some of the properties are shrinkage, warpage, compressive and tensile strength of the part (Jain et al. 2010). There are different raster patterns which can be used such as short raster, long raster, alternate raster, spiral and contour patterns (Jain et al. 2008). McIntosh et al. (1997) studied shrinkage and deformation characteristics in fused deposition of ceramics. They found the effect of raster fill patterns on the shrinkage of components. Nickel et al. (2001) studied the residual stresses and deflections with respect to deposition patterns in Laser sintering process. Ma and Bin (2007) developed a Finite element model for Selective laser Sintering process. Asymmetrical temperature distribution and higher distortions were observed in 'S' scanning pattern compared to fractal scanning pattern. Chen et al. (2002) developed fractal toolpath for irregular shapes like parallelogram, octagon etc. and combination of such shapes. They verified the feasibility of fractal toolpaths for finishing process using an electric spark erosion mounted on an existing CNC machine. Griffith (1994) developed Hilbert curve based toolpath for milling machine i.e. for machining operations. Bertoldi et al. (1998) used the approach of domain decomposition in toolpath strategy and space-filling curves were used for toolpath generation for FDM process. Fractal based toolpath reduces distortion in the parts and improves mechanical properties. It is a good candidate for improved toolpath strategies (Kumar et al. 2009). Fractal based toolpath has not been extensively used in FDM process and this can be explored. Therefore a study of fractal based toolpath and part fabrication can be done. In this paper an algorithm based on Hilbert curve is developed for toolpath. The process used is screw extrusion based FDM process in which raw material in the form of pellets is used. The algorithm is validated using an extruder which is retrofitted to an existing CNC milling machine.

2 Methodology

A general overview of the part fabrication using Hilbert curve based toolpath process is shown in Fig. 1. The process consists of three stages namely CAD Model preparation, algorithm for Hilbert Curve generation, and Part fabrication.

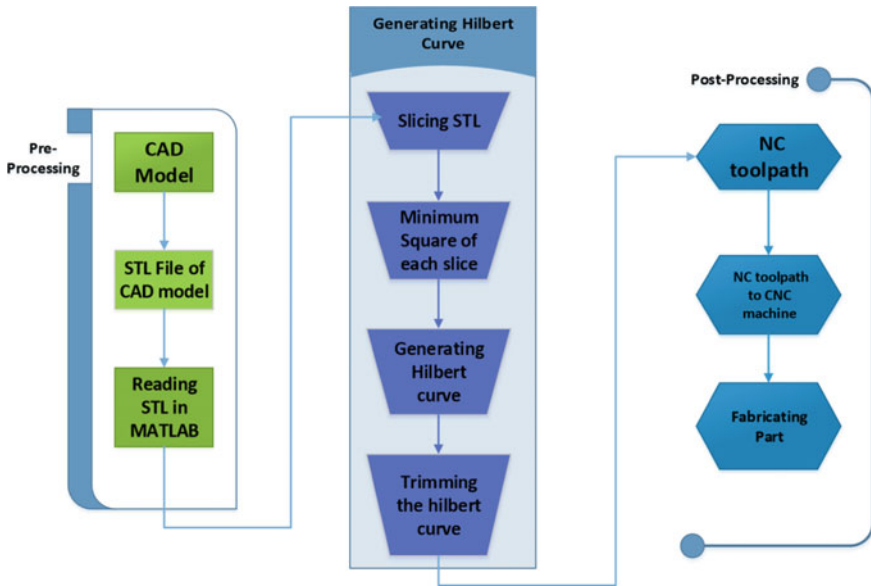


Fig. 1 Process overview of part fabrication

2.1 CAD Model Preparation

CAD Model: The object to be fabricated can be modelled using any CAD software like SolidWorks, CATIA, Creo etc.

STL File of CAD Model: CAD model of object is converted to STL file format which is the de facto standard for additive manufacturing.

Reading STL file in MATLAB: STL file of object is then fed into MATLAB computing platform and is read to extract the relevant information about the contour of the object.

2.2 Hilbert Curve Generation

Slicing STL: STL file read in MATLAB is sliced into layers using appropriate slicing algorithms. The whole object is divided into specified no. of layers which is required to be additively manufactured.

Minimum Square of each Slice: A bounding box for each slice is calculated and higher dimension side of bounding box is taken as the side of minimum square for which Hilbert curve is to be generated.

Generating Hilbert curve: Based on minimum square a Hilbert curve of specified order is generated using Lindermyer system.

Trimming the Hilbert Curves: As the Hilbert curve is outside the contour dimensions, it has to be trimmed to get it fit on the contour. Now the trimmed Hilbert curve co-ordinates are stored in matrix.

2.3 Part Fabrication

NC toolpath: The co-ordinates of trimmed Hilbert curve are outputted as NC code into a text file with appropriate machine controls and parameters like feed, spindle speed.

NC toolpath to CNC machine: The NC code generated is fed into three axis CNC milling center on which extruder head setup is mounted.

Fabricating Part: The NC code is executed to print the objects using different materials and parameters.

2.4 Implementation of Hilbert Curve on Object

This is the next step after slicing of STL file of the CAD model. In this step for every layer or slice a Hilbert curve is generated according to appropriate process parameters. Let $P = [0, 1]$ represent a closed unit interval on real number field and $S = [0, 1]^2$ represent a closed unit square on the same real number field. Now partition the interval P into four equal subintervals and S into four equal subsquares. Each Subinterval can be mapped onto each subsquares. The next step is to divide each subinterval into four equal subintervals and each subsquare is divided into four equal subsquare and the process is repeated. Continuing the process till infinity we divide P and S into 4^n subintervals and subsquares. According to Hilbert, the subintervals and subsquares can be mapped in such a manner that we get a space filling curve. Such a mapping is shown in the Fig. 2 which shows first three iterations of the Hilbert curve.

A MATLAB code has been developed considering the mathematical construction of Hilbert curve based on Lindermayer system for sliced model of STL file (Lindermayer 1992). A recursive function has been developed for generating Hilbert curve for different slices of object considering order of the curve as user control. Contour data obtained for different slices of the STL file is stored in a matrix. For each slice a bounding box is calculated considering the maximum and minimum co-ordinates of the contour points. Now the greater dimension of the bounding box is considered as the side of the minimum square in which Hilbert curve is to be mapped. After determining the minimum square for a slice and taking the order of the curve as user input, Hilbert curve is constructed based on Lindermayer system $L \rightarrow +RF-LFL-FR+$, $R \rightarrow -LF+RFR+FL-$. Hilbert curve for various different geometries like freeform geometry, geometry with holes are shown in the Fig. 3.

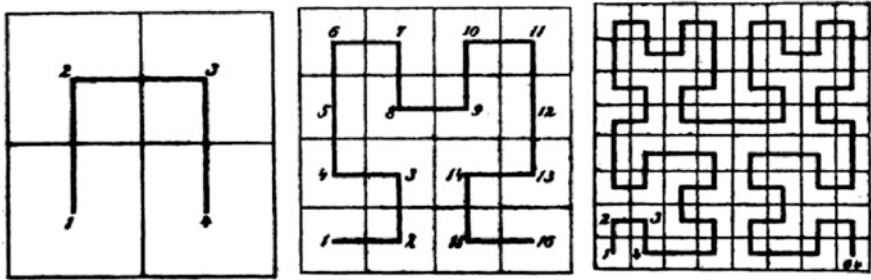


Fig. 2 First three iterations of Hilbert curve (Sagan 1994)

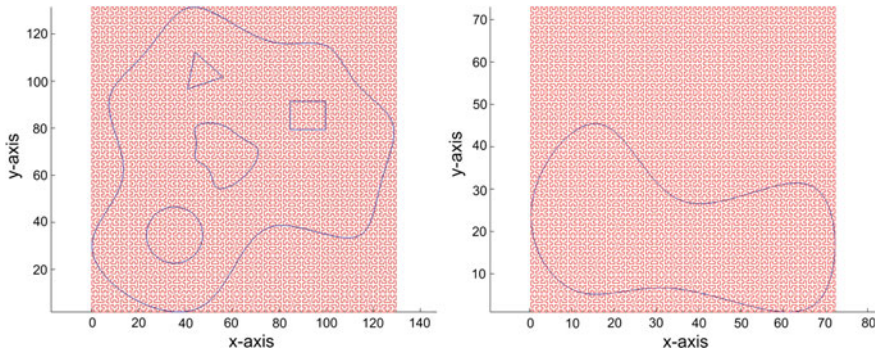


Fig. 3 Hilbert curve for slices of different objects

Different test cases shown above validate that the Hilbert curve generation works very well for a variety of different object geometry with complex features. Now after generating Hilbert curve for complete sliced model of CAD file all the data is stored appropriately. Contour data of each slice including holes is stored in matrices. The co-ordinates of Hilbert curve generated for each slice is also stored in matrices. This data is used further for computations like finding intersection points and trimming the Hilbert curve.

2.5 Trimming the Hilbert Curve

This is the next step after generating Hilbert curves for each slices of the object. The process of trimming the Hilbert curve is accomplished with the help of boolean operations like intersection and subtraction applied between Hilbert curve and contour data. In view of application of Boolean operators to geometric objects trimming of Hilbert curve is performed.

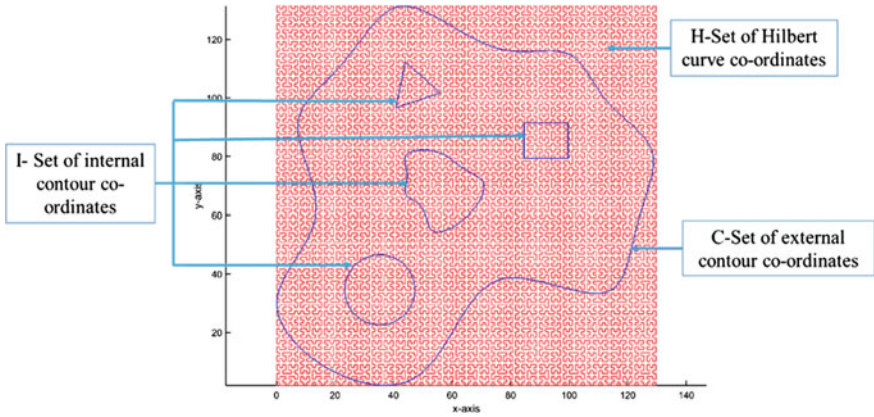


Fig. 4 Sets of different data

Let

H = Co-ordinates matrix of Hilbert curve (Fig. 4)

C = Co-ordinates Matrix of external contour data

I = Co-ordinates matrix of internal contour data (holes)

First, the subtraction operation on C and I is performed. This operation gives the set of data of the external contour excluding the internal contour. This data is stored in the new set T (Fig. 5). On this set T and H an intersection operation is done which finally result in trimming the Hilbert curve. Trimmed Hilbert curve is stored in a set Q (Fig. 6).

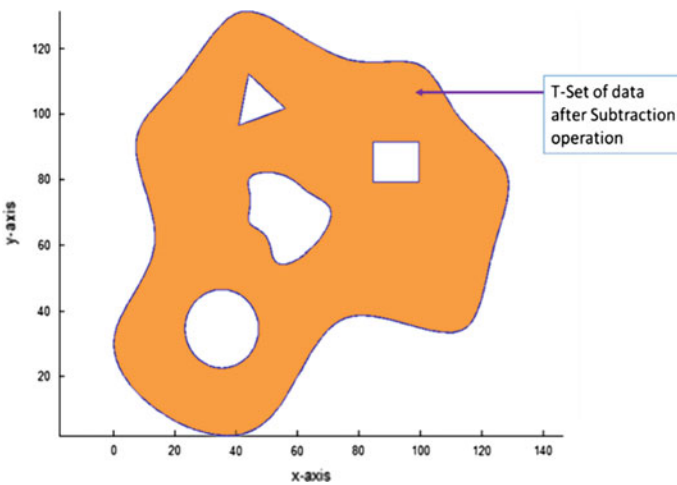


Fig. 5 Subtraction operation

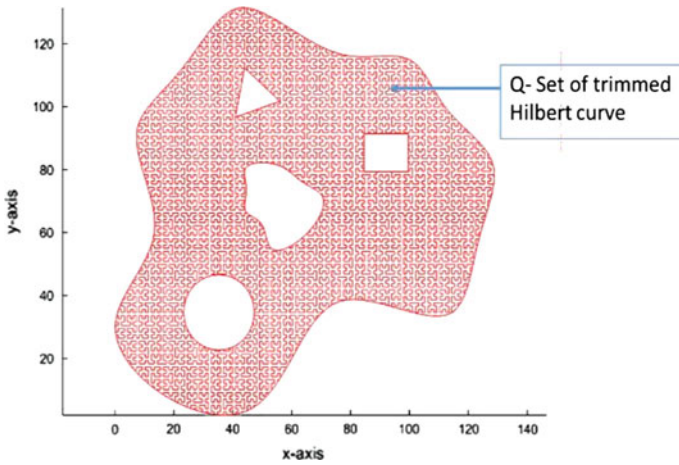


Fig. 6 Intersection operation

$$T = C - I \quad Q = H \cap T$$

The co-ordinates of the trimmed Hilbert curve are then transferred to a text file in appropriate NC programming format (G and M codes). This toolpath is verified and simulated in CNC Simulator Software for possible errors. After verifying and simulating the toolpath is transferred it to CNC milling centre for part fabrication. Parameters set for printing an object are checked with a dry run of single layer before actual printing starts.

After finding the intersection points, all the point for toolpaths are stored in matrix which follows the Hilbert curve property.

2.6 CNC-Milling Assisted Fused Deposition System

A system based on screw extrusion based FDM is used for implementing the developed algorithm and investigating the Hilbert based toolpath for improved mechanical properties over raster (linear) toolpaths. For this an extruder head which can be used as a tool in existing three axes vertical milling centre is utilized. OKUMA MB-46VAE-R Vertical Machining centre is used for mounting the extruder head. The extruder is designed in such a way that it can be used as a tool on milling centre. This facilitates in programming the toolpath using existing G and M codes. Instead of filament pellets of polymeric material is used as raw material. This system is part of DST sponsored project titled “Development of Additive-Subtractive Integrated RP System for Improved Part Quality”.

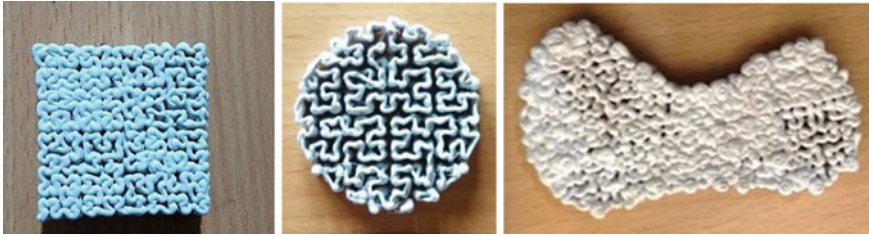


Fig. 7 Parts fabricated using toolpath based on Hilbert curve

3 Results and Discussions

The developed algorithms and setup was used to successfully implement the Hilbert curve based toolpath. The algorithm works for different geometry and gives a toolpath in the form of CNC code which can be used on existing CNC milling machine.

3.1 Validation

Different objects like square plate, porous cylinder and freeform geometry was printed using the developed algorithm (Fig. 7). The polymeric material used is Recycled Acrylonitrile Butadiene Styrene (ABS M204) in the form of pellets. Flow rate of the extruded material depends on the spindle speed or the rotation of screw. Deposition of material on the bed also depends on the feed of the extruder head. A series of experiments with different spindle rpm and feed rate were performed. Finally spindle speed of 150 rpm and feed rate between the range of 750 and 1000 mm/min were found suitable for printing. The parts fabricated using the developed system show a wide variety of products with different geometrical features can be made. Also it shows the successful implementation of the developed Hilbert curve based toolpath for Fused Deposition process.

4 Conclusion

An algorithm based on Boolean operators for determining intersection points between arbitrary geometries and Hilbert curve is used for toolpath strategy. Toolpaths generated is verified and validated using a retrofitted extruder head used on an existing CNC milling machine. Different parts are fabricated using Hilbert curve based toolpath and feasibility is verified. Future work will be to investigate effect of Hilbert curve based toolpath on mechanical properties of parts.

Acknowledgments The authors would like to thank Department of Science and Technology for sponsoring the project and allowing to use the setup developed at IIITDM Jabalpur for algorithm implementation.

References

- Bertoldi, M. et al. (1998). Domain decomposition and space filling curves in toolpath planning and generation. In *Proceeding of the 1998 Solid Fabrication Symposium* (pp. 267–276).
- Chen, C. C. A., Juang, Y. S., & Lin, W. Z. (2002). Generation of fractal toolpaths for irregular shapes of surface finishing areas. *Journal of Materials Processing Technology* 146–150.
- Griffiths, J. G. (1994). Toolpath based on Hilbert's curve. *Computer-Aided Design*, 26(11), 839–844.
- Jain, P. K., Pandey, P. M., & Rao, P. V. M. (2008). Effect of delay time on part strength in selective laser sintering. *The International Journal of Advanced Manufacturing Technology*, 43 (1–2), 117–126.
- Jain, P. K., Pandey, P. M., & Rao, P. V. M. (2010). Tailoring material properties in layered manufacturing. *Materials and Design*, 31(7), 3490–3498.
- Kumar, G. S., Pandithevan, P., & Ambatti, A. R. (2009). Fractal raster tool paths for layered manufacturing of porous objects. *Virtual and Physical Prototyping*, 4(2), 91–104.
- Lindermayer, A., & Holland, J. H. (1992). Lindenmayer Systems. In G. Rozenberg & A. Salomaa (Eds.), Berlin, Heidelberg: Springer.
- Ma, L., & Bin, H. (2007). Temperature and stress analysis and simulation in fractal scanning-based laser sintering. *The International Journal of Advanced Manufacturing Technology*, 34(9–10), 898–903.
- McIntosh, J. J., Danforth, S. C., & Jamalabad, V. R. (1997). Shrinkage and deformation in components manufactured by fused deposition of ceramics. In *Solid Freeform Fabrication Proceedings* (pp. 159–166).
- Nickel, A. H., Barnett, D. M., & Prinz, F. B. (2001). *Thermal stresses and deposition patterns in layered manufacturing.*, 317, 59–64.
- Sagan, H. (1994). *Space-filling curves*. New York: Springer.
- Senthilkumaran, K., Pandey, P. M., & Rao, P. V. M. (2009). Influence of building strategies on the accuracy of parts in selective laser sintering. *Materials and Design*, 30(8), 2946–2954.
- Taufik, M., & Jain, P. K. (2013). Role of build orientation in layered manufacturing: A review. *International Journal of Manufacturing Technology and Management*, 27(1/2/3), 47.
- Taufik, M., & Jain, P. K. (2014). Volumetric error control in layered manufacturing. In *19th Design for Manufacturing and the Life Cycle Conference; 8th International Conference on Micro- and Nanosystems* (vol. 4, p. V004T06A017). ASME.

Development of Edge Processing and Drawing Algorithms for a 6 Axis Industrial Robot

G. Kalaiarasan, A. Tony Thomas, C. Kirubha and B. Saravanan

Abstract The development of edge processing algorithm and drawing algorithm of an industrial robot is presented in this paper. This programming was developed with an industrial robot (ABB IRB 1410) using RAPID programming language and Robot studio simulator. Drawing is considered as task of skilled humans for obtaining precise layout. Almost all draftsmen use their hands and fingers to draw that are replaced by manipulator and gripper in case of the robot. It is tedious to transform the Images to Car Bodies, Glasses; this process of capturing the image and reproducing it by programming the ABB Industrial robot will provide a solution.

Keywords Industrial robot · End effector · Edge processing · RAPID GUI programming language · Lab VIEW

1 Introduction

Mechatronics is a blend of mechanical, electrical and electronics engineering. Mechatronics is a synergetic integration of control system, computer sciences with precise control of sensors and actuators to improve production system, which

G. Kalaiarasan (✉)

Department of Mechatronics Engineering, VIT University, Vellore, India

e-mail: gk.arasan@gmail.com; acramcket29@gmail.com

A. Tony Thomas · C. Kirubha · B. Saravanan

Department of Mechatronics Engineering, Kongu Engineering College, Perundurai, Erode, India

e-mail: dec84tony@gmail.com

C. Kirubha

e-mail: kirubhasekar4@gmail.com

B. Saravanan

e-mail: saravananbhaskar94@gmail.com

© Springer India 2016

D.K. Mandal and C.S. Syan (eds.), *CAD/CAM, Robotics and Factories of the Future*, Lecture Notes in Mechanical Engineering,

DOI 10.1007/978-81-322-2740-3_73

replaces humans in assembly lines. A computer or a controlling device is used to control the robot. A robotics system incorporates not only robot but also the other parallel systems and devices that are incorporated together for better performance. The computer acts as the supervisor that controls the motion of the system with the logic developed by programming. Based on the logic of the program the motion of the robot is altered or modified by the computer system. Thus the robot is designed in a way it is adaptable to the task by reprogramming it (within its limit and work envelope).

2 Literature Survey

Abigo et al. (2012) in this paper programming of ABB robot to recreate different characters with modified end effector incorporated to the ABB robot is discussed. The modified end effector discussed in this paper is also attached with a cleaning accessory. With this modified tool accessory the end effector resolves two applications of writing and cleaning at different Tool Center Point (TCP) orientation. The RAPID program is uploaded to the system as a backup into the flex pendant of the robot. By this improvement in the system, the project was able to reproduce all the characters at maximum accuracy over the system. Thus, in one step it enables a commercial industrial robot on performing some of human tasks and operations.

Ravi Kumar et al. (2011) aims to detect edge of an image by computer system is one of the most fundamental and significant operation in image processing. Edge detection is always one of the fundamental studies of computer vision and image processing. This paper firstly describes the characteristics of edges, the properties of traditional edge detection methodology and then analyzing the results obtained in MATLAB, which is commonly used to realize the hybrid programming that in order to expand the scientific computing ability of LabVIEW simulation software. In addition to that combining the results from images to preserve the class consistency of edge detection.

Pedro et al. (2008) in this paper presents a robotic system where the user can instruct and program a robot by showing what it should do, and with a high-degree of understanding from the robot's programming language. By code generation technique and force control system the programming is done to the robot or by natural human interfaces like speech and gesture. The performance of this system is compared with a similar system that uses manual guidance system based on a force control strategy instead of gesture control.



Fig. 1 CAD model and prototype

2.1 System Design

The entire experimental setup of the system is shown in the Fig. 1 which constitutes of the robot manipulator with an end effector, which is controlled by the IRC 5 controller by using the flex pendant.

Robot Manipulator

The manipulator is the device, which is used for the axial control of the system. IRB 1410 is a industrial robot that can be mounted on a floor with 6-axis, used in industrial manufacturing application. It is the manipulator, which operates with 200–600 V supplies by using 50 or 60 Hz frequency. 5 kg of payload and reach of 1.44 m is achieved by the external axis of the robot. The maximum speed of 7000 mm/s is attained during the full automation mode of the robot.

Flex Pendant

The flex pendant is the teach pendant unit, which is a hand held operator unit used for operating the robot system to perform specific task. It is used to modifying the work object, jogging the robot manipulator, and also in modifying the RAPID program that runs the current system of the robot. Teaching the machine for jogging and adapting is done with the help of the flex pendant.

IRC 5 Controller

All the motion and controls of the robot manipulator is controlled and supervised by the IRC-5 controller. Driver module and the control module combining together to form a controller unit. The control module contains computer Input and Output

ports and internal flash memory, which runs all data's and variables for proper operation of the robot system. The drive module consists of all the power electronics devices that supply the robot motors to control its actuation based on the program developed.

End Effectors

The end effector is the main part which directly in contact with the real time system. The end effector was designed with 100 mm × 70 mm × 70 mm size with a internal extruded hole of 10 ± 5 mm diameter for the pen holder. For combining the end effectors to the robot manipulator, an extruded circle of diameter 60 mm with an extrusion of about 8 mm is done. The end effector is replaced based on the application it is being used.

2.2 System Implementation

System Description

Problem Definition

1. Development of an edge processing algorithm for converting 3D image into contrast 2D image using Lab VIEW.
2. Development of drawing algorithm for the conversion of contrast into movement coordinates of the robot.
 1. Drawing Table
 2. IRB 1410 Robot Manipulator
 3. Camera
 4. IRC 5 Controller
 5. Computer with Lab VIEW software
 6. Flex pendent
 7. Object to capture

Lab VIEW

LabVIEW is a graphical programming language with user-integrated system. Integrated development environment and human machine interface is designed and developed by using the front panel of the simulator. HMI screen development is the most time consuming operation for better human interaction. The logic of

programming is done at the back panel of the LabVIEW with proper data flow of variable and data's.

Computer Imaging

Acquisition and processing of images to the digitized from is known as the computer imaging. The visual information is converted into data form. Computer representation of an image requires the equivalent of many thousands of processed data and information, so the massive amount of data required for image digitizing is a primary reason for the development of many sub areas with field of computer imaging, such as image compression and segmentation. Computer imaging is categorized by two primary techniques:

1. Computer Vision.
2. Image Processing.

Direct Acquisition Method

Direct acquisition method is accomplished by direct capturing from camera. The camera and lighting condition must be in good. It will detect the edges and display it. Vision acquisition block is used to implement the direct acquisition method and it will result in a test function. In this we can test the camera and image quality before capturing the image. Figure 2 represents the acquired image by using the vision acquisition block in LabVIEW.

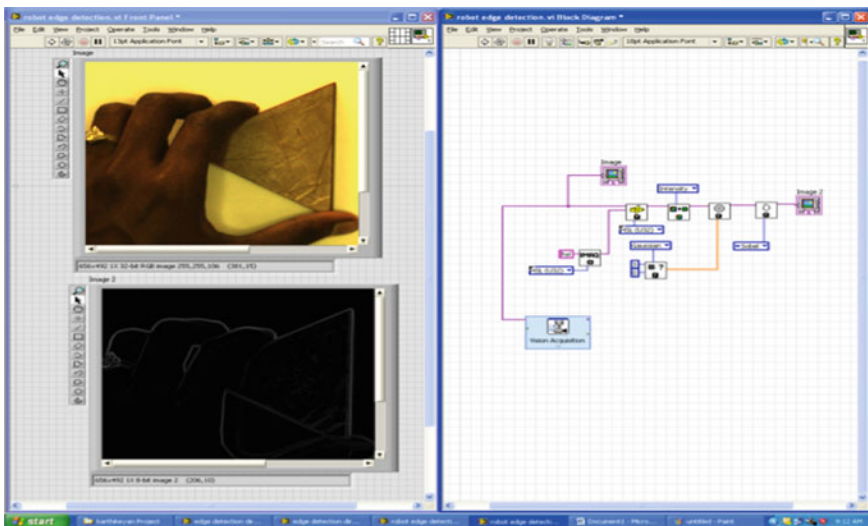


Fig. 2 Direct acquisition front panel and block diagram

3 Results and Discussions

3.1 Edge Detection

For the process of Edge detection file path method is being implemented. This method is being accomplished by specifying the file path of the image. The image file path should be stored in the directory. The Algorithm is developed in the manner that it reads only the images of JPEG and bmp formats. Once the images being identified then it is being converted into gray image of 32bit and 8bit for the purpose of preprocessing in LabView. In order to obtain the image for the processing in Lab view, threshold value is varied in order to obtain the image over the front panel of the system. By varying the threshold value the image shown in Fig. 3 is obtained in LabVIEW.

3.2 Coordinates Transformation Algorithm

Once the image is being captured and tuned for the processing by varying the threshold value by the front panel of Lab View, it is necessary to convert the detected edge of the image into x and y coordinates for delivering it to the

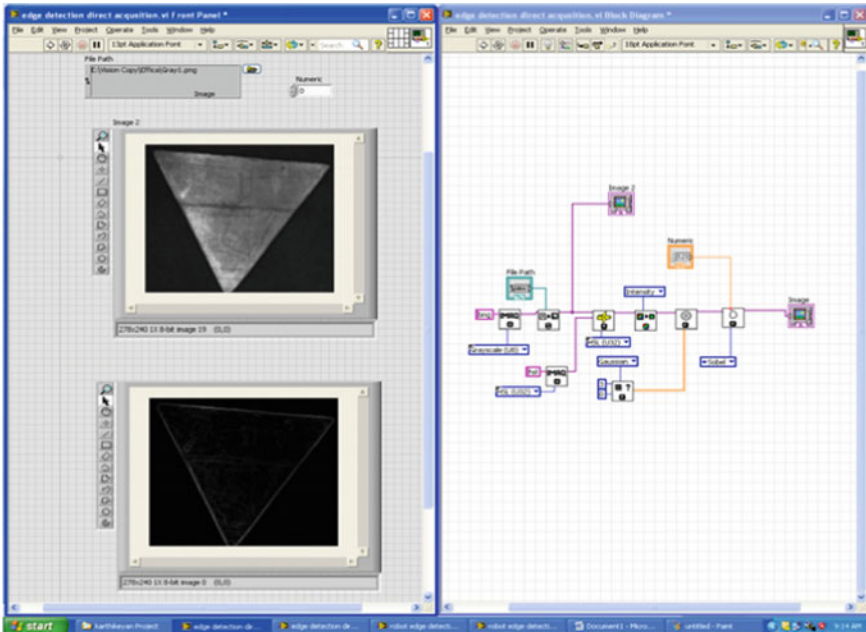


Fig. 3 File path method front panel and block diagram

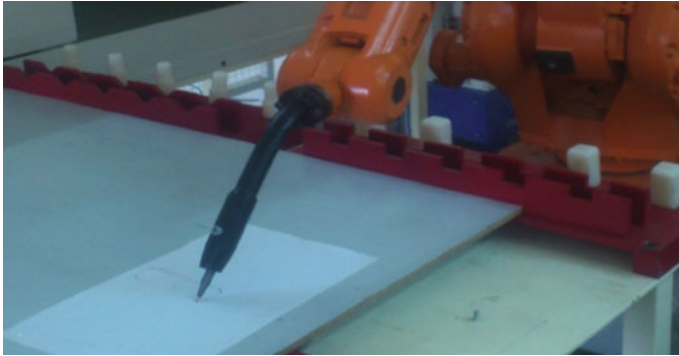


Fig. 4 Robot drawing in sheet

movement of the robotic manipulator. Based on the origin point which is being predefined the system develops the coordinates of edge of the image. The developed data is being communicated to the robotic manipulator with the help of RS232 communication hub. In order to establish the communication VISA architecture is employed. As in the Fig. 5 shows how the coordinate value is transferred to the manipulator in definite interval of time in order to achieve point-to-point movement of the manipulator; by transferring the data continuously the continuous movement is achieved. The final movement of the manipulator is posturized in the Fig. 4.

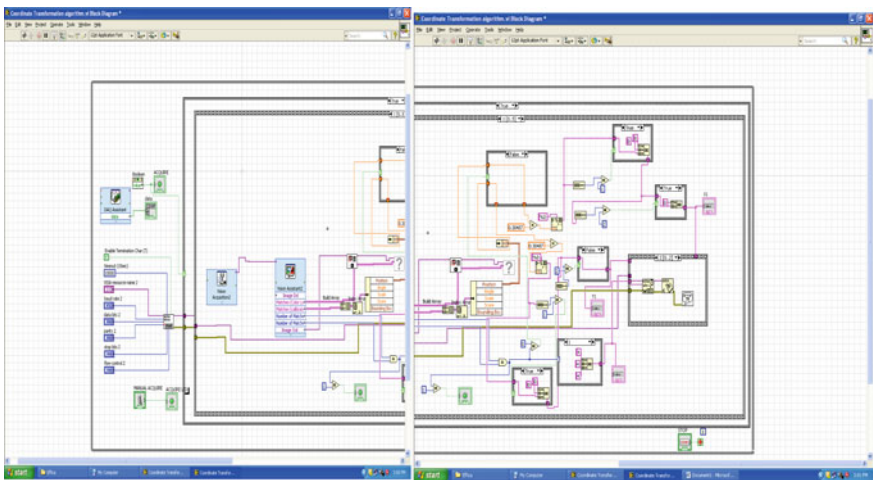


Fig. 5 Graphical programming Coordinates transformation algorithm

3.3 Conclusion and Future Enhancement

The experimental work infers the development of an edge-processing algorithm for converting 3D image into contrast 2D image using Lab VIEW and developing the drawing algorithm for the conversion of contrast into movement coordinates of the robot. The Robot can draw with the high speed, accuracy and repeatability for every pixel detected in edge processing algorithm and the robot was also able to reproduce in multiple copies.

References

- ABB IRB 1410 Product Manual.
- Abigo, I., & Tarig, F. (2012). IEEE 'programming ABB industrial robot for an accurate drawing. *IEEE Transactions on Applied Su* 21(3).
- Pedro, N., & Norberto Pires, J. (2008) High level programming for industrial Robotics using gestures, force and control. *IEEE Transactions on Robotics*, 14(4).
- Rapid Programming Manual - IEETA.
- Ravi Kumar, A. V., & Nataraj, K. R., PhD. Asst. Professor ECE Department, SJBIT (2011) Result analysis of LabVIEW and MatLab in application of image edge detection. *International Journal of Computer Applications* (0975-888), 48(9).

Experimental Investigation and Fuzzy Modelling of Flatness and Surface Roughness for WCB Material Using Face Milling Operation

Saurin Sheth and P.M. George

Abstract Optimum selection of process parameters may help to achieve the best dimensional and geometric tolerances during machining. This can be achieved by developing a model using the experimental data, which in turn helps in prediction of the responses in context of input variables. The present paper deals with the investigation of WCB material, a base material for valve. 2^3 full factorial design with four centre points is selected to perform the reliable experiments. Here the input variables are spindle speed, feed rate and depth of cut. While the output parameters are surface roughness and flatness. The soft computing technique Fuzzy Logic is applied to predict the responses. The values predicted from the model and experimental values are very close, with more than 95 % accuracy. Further four more experiments are performed at various combinations for validation of developed model. The error in the predicted and measured values are less than 8 %, shows the validity of model for further use.

Keywords Fuzzy · Speed · Feed · Depth of cut · Flatness · Surface roughness · Face milling · Modelling

1 Introduction

There are natural limits and capabilities of the machine tool to generate certain quality of work piece. To achieve the higher production rate along with quality in terms of the tolerances, both geometrical and dimensional, need analysis and prior

S. Sheth (✉)

Mechatronics Engineering Department,
G.H. Patel College of Engineering & Tech, VV Nagar, Gujarat, India
e-mail: shethsaurin81@gmail.com

P.M. George

Mechanical Engineering Department,
B V M Engineering College, VV Nagar, Gujarat, India
e-mail: pmgeorge02@yahoo.com

© Springer India 2016

D.K. Mandal and C.S. Syan (eds.), *CAD/CAM, Robotics and Factories of the Future*, Lecture Notes in Mechanical Engineering,
DOI 10.1007/978-81-322-2740-3_74

769

experimentation. Machine tool manufacturers are not providing the capabilities of machine tool in terms of the tolerances, which leads to model it in context of various parameters. Geometric Dimensioning & Tolerancing (GD & T) is a method for stating and interpreting design requirements. With GD & T, variations of a part from its specified size and form are controlled to ensure part functionality and interchangeability (Drake 2009). Various review works carried out in the direction of form and orientation control. The controls considered are Flatness, Straightness and Parallelism (Vora et al. 2011). Taguchi method and Response surface methodology for optimization of surface roughness in machining of Gun metal with a HSS tool is carried out. The cutting parameters used are spindle speed, feed and depth of cut (Francis et al. 2013). Taguchi methodology is used to investigate the effects of various parameters of end milling process like spindle speed, depth of cut, feed rate on surface finish (Joshi et al. 2012). The effect of machining parameters were analyzed in context of MRR and Spread for flashing operation of precision steel ball manufacturing (Patel et al. 2014). They have performed ANOVA and regression analysis for the same (Patel and Sheth 2013). A fuzzy logic based model is being developed for predicting kerf width during laser machining (Patel et al. 2015).

2 Experimentation

2.1 Work Piece Material

The test work piece material is WCB, wrought cast steel with grade B. It has excellent strength properties at high temperature and corrosion resistance. In general it is used in manufacturing of valves, flanges, fittings, or other pressure-containing parts for high-temperature service. Both valve body and door are shown in Fig. 1, where two matting planar surfaces together create metal to metal seal, for a dual plate check valve. A perfect metal to metal seal without

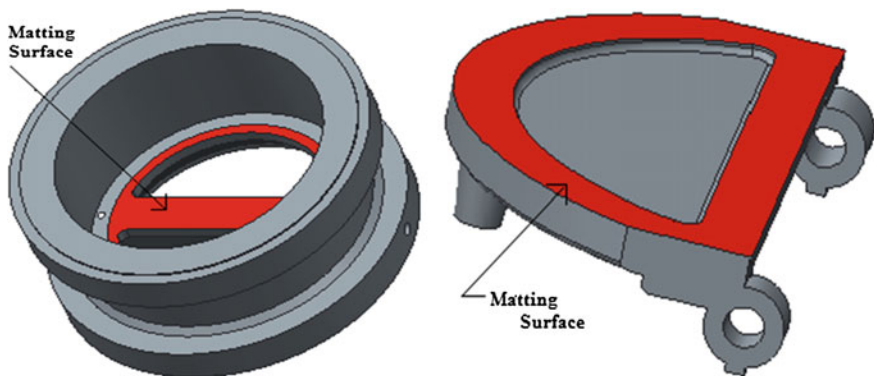


Fig. 1 Model of valve body and door

significant rocking can be achieved by desired flatness and proper surface roughness. So deviation in flatness and surface roughness is one of the dominant reasons for leakage (Mistry et al. 2013). Flatness control, as a geometrical tolerance, is commonly used on planar surface capable of resting on mating planar surface without any significant rocking. The mechanism behind the formation of flatness as geometric tolerance is very dynamic, complicated, and process dependent (Modi et al. 2013). So, the investigation of flatness and surface roughness of WCB material creates new scientific domain in the machining.

2.2 Machine Tool and Cutting Tool

Machinability tests were carried out on the 3-axis CHIRON FZ 16 L/CNC Milling having spindle motor power of 5.7 kW. Miracle coated VP15TF insert, which is having excellent heat resistance, oxidation resistance and high tool life during machining of harder work piece, is used for face milling operation.

2.3 Experimental Procedure

Experiments are carried out on blocks having size of 60 mm × 60 mm × 50 mm of WCB material. Spindle speed, Feed and Depth of cut are selected as input variables to perform experiments according to 2³ full factorial with four center points experimental design. The levels of input variables are shown in Table 1. Block is clamped by using hydraulic vice as shown in Fig. 2. All six sides of the block is

Table 1 Factors and levels

Factors	Coded factors	Low level (-)	High level (+)	Center points
Spindle speed (rpm)	A	500	1200	850
Feed (mm/min)	B	150	300	225
Depth of cut (mm)	C	0.1	0.5	0.3

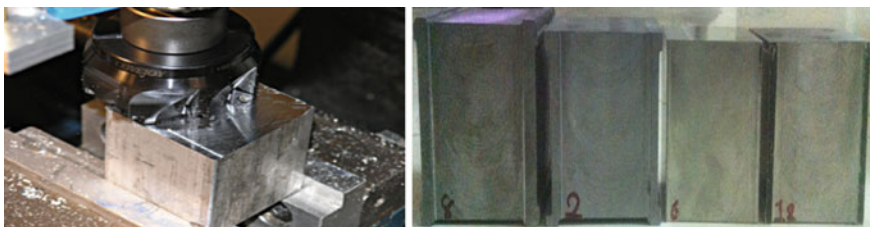


Fig. 2 Machining of work-piece and machined work-piece

initially machined and then after face milling process is carried out on each face of block to create 50 mm wide slot throughout length. Here no. of passes and coolant flow rate are constant. The machined work pieces are shown in Fig. 2 (Modi 2014).

2.4 Measuring Techniques

Flatness Measurement is carried out using hexagon make Co-Ordinate Measuring Machine (CMM), having servo controlled axes with resolution of 0.1 μm . It has Motorized Index able probe head with Touch trigger probing system. Here for measuring flatness, rectangle grid extraction strategy is used to extract points from the surfaces. Points are extracted from the all surfaces having 35 mm \times 35 mm cross section with 5 mm grid size. Surface roughness measurement is carried out on Surf test SV-2100 with condition for measuring surface roughness is Meas. Length (X) = 4.8000 mm, Meas. Pitch = 0.0005 mm, Measuring Speed = 0.50 mm/s etc. Surface roughness of each sides of the blocks is measured. Table 2 shows the responses according to coded factors and treatment combinations using 2^3 full factorial with the four center point experimental design (Montgomery 2009).

3 Development of Fuzzy Logic Model to Predict Flatness and Surface Roughness

Fuzzy logic (FL) is an Expert System widely used due to its successful applications in many control and prediction systems. It suits very well in defining the relationship between inputs and desired outputs of a system. A predictive response for

Table 2 Measurement of flatness and surface roughness

Treatment combination	Coded factors			Responses	
	A	B	C	Flatness (mm)	Surface roughness (μm)
1	–	–	–	0.027	2.1195
a	+	–	–	0.019	2.1035
b	–	+	–	0.038	5.7466
ab	+	+	–	0.028	4.4532
c	–	–	+	0.026	2.5713
ac	+	–	+	0.023	1.7697
bc	–	+	+	0.040	6.5157
abc	+	+	+	0.028	2.0633
Center points	0	0	0	0.021	2.8351
	0	0	0	0.018	2.8004
	0	0	0	0.020	3.0775
	0	0	0	0.018	2.4305

weld width has been developed using fuzzy logic for MIG welding (Patel et al. 2015). An acceleration is predicted in context of speed, feed and depth of cut for lathe machine using fuzzy logic (Sheth et al. 2015). MATLAB Fuzzy Logic Tool Box helps to develop the fuzzy model (Sheth et al. 2014b).

3.1 Membership Functions of Inputs and Outputs Fuzzy Variables

Triangular shape of membership function is employed to describe the fuzzy sets for input variables as shown in Fig. 3. Even triangular shape of membership functions is used to describe the fuzzy sets for output variable. Eight membership functions are defined for surface roughness and flatness as shown in Fig. 4 (Majumdar 2010).

3.2 Fuzzy Rules

A set of 8 rules have been constructed based on the actual measured results of Flatness and Surface roughness in face milling operation of WCB material. It shown in Fig. 5.

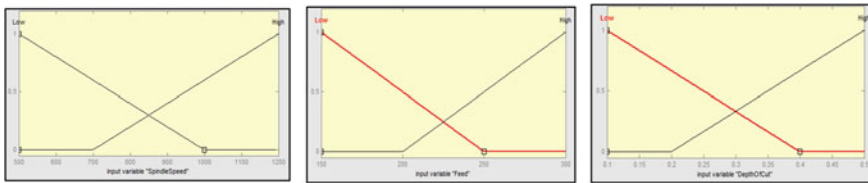


Fig. 3 Membership function for spindle speed, feed and depth of cut

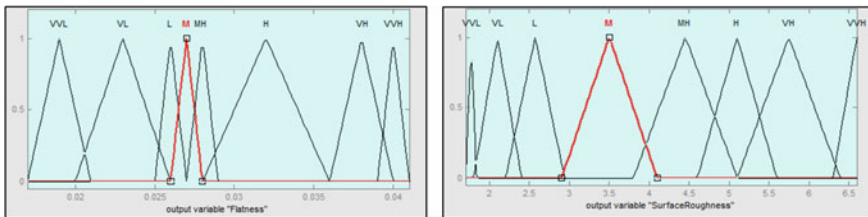


Fig. 4 Membership Function for flatness and surface roughness

```
1. (SpindleSpeed==Low) & (Feed==Low) & (DepthofCut==Low) => (Flatness=M)(SurfaceRoughness=V/L) (1)
2. (SpindleSpeed==High) & (Feed==Low) & (DepthofCut==Low) => (Flatness=V/L)(SurfaceRoughness=V/L) (1)
3. (SpindleSpeed==Low) & (Feed==High) & (DepthofCut==Low) => (Flatness=V/H)(SurfaceRoughness=V/H) (1)
4. (SpindleSpeed==High) & (Feed==High) & (DepthofCut==Low) => (Flatness=M/H)(SurfaceRoughness=M/H) (1)
5. (SpindleSpeed==Low) & (Feed==Low) & (DepthofCut==High) => (Flatness=L)(SurfaceRoughness=L) (1)
6. (SpindleSpeed==High) & (Feed==Low) & (DepthofCut==High) => (Flatness=V/L)(SurfaceRoughness=V/L) (1)
7. (SpindleSpeed==Low) & (Feed==High) & (DepthofCut==High) => (Flatness=V/H)(SurfaceRoughness=V/H) (1)
8. (SpindleSpeed==High) & (Feed==High) & (DepthofCut==High) => (Flatness=M/H)(SurfaceRoughness=V/L) (1)
```

Fig. 5 Fuzzy rules

3.3 Defuzzification

Defuzzification is the conversion of the fuzzy quantity to real value. The present model uses centroid of area (COA) defuzzification method, due to its wide acceptance and capability in giving more accurate result compared to other methods. Figure 6 shows the various fuzzy surfaces related to Spindle speed, Feed, Depth of cut in context of flatness and surface roughness (Sheth et al. 2014a).

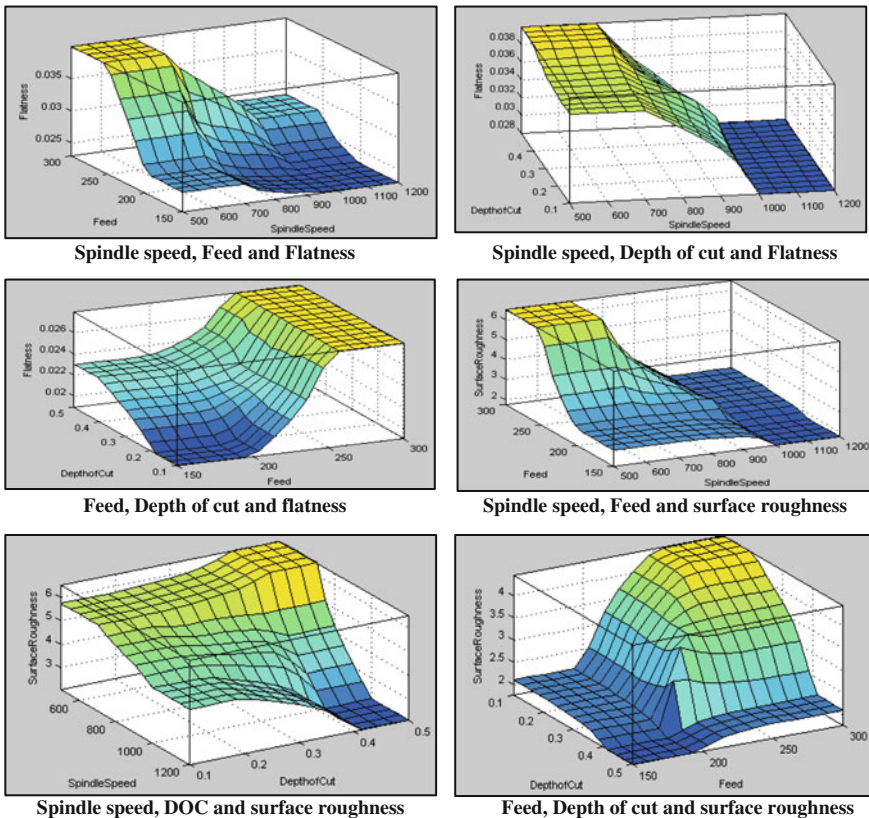


Fig. 6 Fuzzy surfaces for flatness and surface roughness

3.4 Prediction of Flatness and Surface Roughness for WCB Material

The developed fuzzy model is used to predict the Flatness and Surface roughness. A sample prediction is shown in Fig. 7. Here Spindle speed = 500 rpm, Feed = 225 mm/min and Depth of cut = 0.5 mm is considered as input variables. The predicted Flatness = 0.033 and Surface roughness = 3.76 while the measured flatness = 0.032 and surface roughness = 4.112 respectively. The individual percentage error is obtained by dividing the absolute difference of the predicted and measured values by the measured value.

4 Validation of Developed Fuzzy Logic Model

Fuzzy logic model have been develop to predict Flatness and Surface roughness of the valve material WCB. In order to validate this models, experiments needs to be conducted at different levels with different combinations other than that used to develop the model. Four new experiments are conducted to check the accuracy and error of the model to predict Flatness and Surface roughness for WCB material. Table 3 shows the measured values, predicted values and error while predicting using developed model.

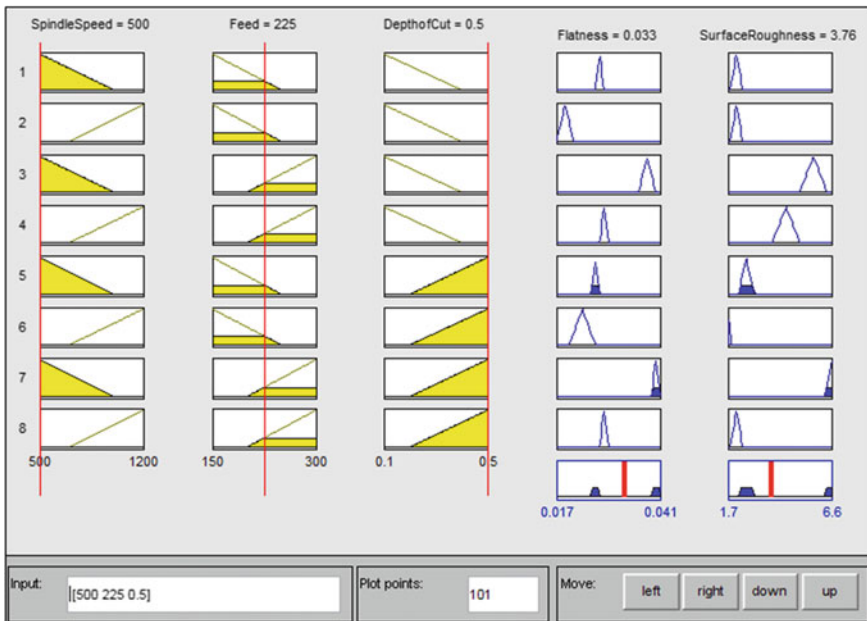


Fig. 7 Prediction of flatness and surface roughness

Table 3 Error of flatness and surface roughness

No. of experiment	Parameters (Inputs)			Measured flatness	Measured surface roughness	Fuzzy flatness	Fuzzy surface roughness	Fuzzy error flatness	Fuzzy error surface roughness
	A	B	C						
1	-1	0	1	0.032	4.112	0.033	3.76	3.12	8.56
2	1	0	-1	0.022	3.683	0.022	3.72	0	1
3	0	-1	0	0.023	2.296	0.0226	2.32	1.73	1.04
4	0	1	0	0.036	4.271	0.0357	4.71	0.83	0.23

5 Conclusion and Future Scope

A fuzzy logic based model to predict flatness and surface roughness is developed in context of input parameters speed, feed and depth of cut for WCB material. Table 3 shows the prediction error associated with the validation experiments. It shows that the max error by fuzzy logic is 3.12, 8.56 % and average error is 1.42, 2.70 % while predicting the flatness and surface roughness respectively. Since the minimum accuracy is 91.54 % the model can be improved by performing more experiments at more levels. From the fuzzy surfaces it seems that to achieve good surface roughness high spindle speed, high depth of cut and lower feed rate is desirable. While for reducing the flatness error high spindle speed, lower depth of cut and lower feed rate is desirable. The controversy in depth of cut leads to multi objective optimization. But the influence of Depth of Cut is very less on both the responses. So, to achieve the desire quality more focus should be made in the right selection of spindle speed and feed. The developed predictive model is very useful to the practicing engineers to reduce the scrape and rework. Even it may be helpful in optimizing the machining parameters to obtain the desire value of surface roughness and flatness. Thus it leads to the productivity enhancement. Such kind of modelling can be done for various other materials as well as other geometrical errors also.

References

- Drake, P. J. (2009). Dimensioning and tolerancing handbook. New York: McGraw-Hill.
- Francis, V., & Dubey, A. (2013). Application of Taguchi and response surface methodologies for surface roughness in face milling operation. *International Journal of Mechanical and Production Engineering Research and Development*, 3(2), 213–220.
- Joshi, A., & Kothiyal, P. (2012). Investigating effect of machining parameters of CNC milling on surface finish by Taguchi method. *International Journal on Theoretical and Applied Research in Mechanical Engineering*, 1(2), 60–65.
- Majumder, A. (2010). Comparison of ANN with RSM in predicting surface roughness with respect to process parameters in Nd: YAG laser drilling. *International Journal of Engineering Science and Technology*, 2(10), 5175–5186.

- Montgomery, D. C. (2009). *Design and Analysis of Experiments* (7th ed.). New York: Wiley.
- Mistry, B., George, P. M., & Sheth, S. (2013). Study and scope of DFMA and GD&T in manufacturing process: A case study on dual plate check valve. In *Proceeding of 7th International Conference on Advanced Computing and Communication Technologies (ICACCT™-2013)*. doi:10.13140/2.1.2294.8642.
- Modi, B. S., George, P. M., & Sheth, S. (2013). Study and investigate effect of cutting parameters on flatness for dual plate check valve. In *Proceeding of 7th International Conference on Advanced Computing and Communication Technologies (ICACCT™-2013)*. doi:10.13140/2.1.3867.7286.
- Modi, B. (2014). *Effect of cutting parameters on flatness of dual plate check valve* PG Thesis, BVM Engineering College, Gujarat, India.
- Patel, P. J., & Sheth, S. (2013). Effect of various parameters on material removal rate in flashing operation of precision steel ball manufacturing process. In *1st International and 16th National Conference on Machines and Mechanisms (iNaCoMM2013)*, pp. 332–338.
- Patel, P. J., Sheth, S., & Chauhan, P. (2014). Effect of various parameters on spread in flashing operation of precision steel ball manufacturing process. *Procedia Materials Science*, 5, 2224–2232.
- Patel, T., Sheth, S., Modi, B. S., & Patel, P. (2015). Experimental investigation and forecast of weld penetration in MIG welding process on WCB Material. In *Proceeding of the International Conference on Advances in Production and Industrial Engineering* (pp. 186–191). doi:10.13140/RG.2.1.3550.4163.
- Patel, P., Modi, B. S., Sheth, S., & Patel, T. (2015b). Experimental investigation, modelling and comparison of kerf width in laser cutting of GFRP. *Bonfring International Journal of Industrial Engineering and Management Science*, 5(2), 55–62.
- Sheth, S., Modi, B. S., George, P. M., & Patel, P. (2014a). A fuzzy logic based model to predict MRR in flashing operation of precision steel ball manufacturing process. *Procedia Materials Science*, 5, 1837–1845.
- Sheth, S., Modi, B. S., Patel, T., & George, P. M. (2014b). A fuzzy logic based model to predict weld width—A case study of hard facing process using MIG welding on dual plate check valve. *Applied Mechanics and Materials*, 592–594, 8–12. doi:10.4028/www.scientific.net/AMM.592-594.8.
- Sheth, S., Modi, B. S., Patel, D., & Chaudhari, A. B. (2015). Modeling and prediction using regression, ANN and fuzzy logic of real time vibration monitoring on lathe machine in context of machining parameters. *Bonfring International Journal of man machine interface*, 3(3), 30–35.
- Vora, N. A., George, P. M., & Joshi, S. P. (2011). Effect of machining parameters on geometric form control and orientation control—A review. In *Proceeding of National Conference on Recent Trends in Engineering & Technology*.

A Retrospective Investigation of Different Uncertainty of Measurement Estimation Approaches

Harish Kumar, P.K. Arora, Girija Moona, D.P. Singh, Jasveer Singh and Anil Kumar

Abstract The general method which has been widely used for computation of Uncertainty of measurement is law of propagation of uncertainty (LPU) method as discussed in Guide for Uncertainty of Measurement (GUM). Numbers of other new methods, with the time, have been evolved for the assessment of Uncertainty of measurement in metrological and measurement related applications. Monte Carlo Method (MCM), has been given the most emphasis and has been recommended by JCGM wide its supplement for Uncertainty of measurement vide JCGM supplement 101: 2008. This paper is an attempt to discuss briefly, the procedure and role of Monte Carlo Method technique in Uncertainty of measurement.

Keywords Monte Carlo simulation · Uncertainty · Vickers hardness · Law of propagation

1 Introduction

A measurement process is drafted with the aim of determining the value of the measurand or the objective or the value of the output quantity to be measured. A measurement therefore proceeds with an appropriate specification of the output quantity, the method of measurement adopted, and the measurement procedure in accordance to standards. The concept of uncertainty is very vital in the history of measurement, since inception. Error and analysis of error is significant while analysis the outcome of any measurement procedure, it can be understood that

H. Kumar (✉) · G. Moona · J. Singh · A. Kumar
CSIR – National Physical Laboratory, New Delhi, India
e-mail: kumarh@nplindia.org

P.K. Arora
Galgotias College of Engineering and Technology, Greater Noida, India

D.P. Singh
Mewar University, Chittaurgarh, India

despite of evaluating factors affecting the measurement process and their implication, there is considerable scope for uncertainty and the correctness of the stated result, doubt about the result of the measurement.

2 Uncertainty of Measurement

Uncertainty of measurement may be considered as the degree of doubt that exists about the result of any measurement procedure and its outcome. Each measurement carries some degree of doubt with it despite of careful measurement. Each standard procedure attempts to discuss salient features of any measurement procedure and role of different factors involved. The uncertainty of measurement result implies that there are shortcomings of the measurand or its magnitude, which is very difficult to predict. After making suitable corrections for the investigated effects, the outcome of measurement is indicative only. Influence of random as well as systematic factors make the measurement process outcome an approximation. The factors are enlisted by certain statistical features like mean, median, distribution etc. Possible sources of uncertainty for a measurement process as given <http://www.bipm.org/en/publications/guides/vim.html>:

- (a) Measurand is not defined suitably;
- (b) Sample do not define population properly;
- (c) Influence of environment not defined for the measurement procedure or measurand;
- (d) Resolution of measuring instrument is limited;
- (e) Reference value of measurement standards or reference materials are is not defined suitably;
- (f) A number of assumptions and approximations taken into account for the measurement method and procedure adopted;
- (g) Significant variation in the outcome of measurement process during measurement;
- (h) Different kind of bias in instruments;

Depending upon the nature of factors mentioned above, their implications over the measurement procedure and measurand differently.

3 LPU Method for Uncertainty Evaluation

The evaluation of uncertainty is most significant part of any measurement process. Evaluation of uncertainty of measurement for the given measurement procedure depends on knowledge of the nature of the measurand quantity as well as the measurement process. Significance of the uncertainty of measurement evaluated

depends over the understanding, critical analysis, and integrity of different components contributing in assigning of the value.

A measurand, Y represents the outcome of the measurement procedure and depends upon several input parameters X_1, X_2, \dots, X_N , Y is the function of these input factors or quantity (Fig. 1).

Different input quantities like X_1, X_2, \dots, X_N , defines the nature of the output quantity, Y and their individual behaviour keeps on influencing the output. The uncertainty of measurement associated with these input parameters will affect the uncertainty of measurement with the output quantity along with the uncertainty due to the measurement procedure itself. These values and uncertainties can be obtained from different series of observations as well as reference values or the judgment of the operator. An approximate of the measurand Y , symbolized by y , is evaluated from Eq. (1) using input approximates x_1, x_2, \dots, x_N for the X_1, X_2, \dots, X_N . Thus the output approximate y is given by (Fig. 2).

The GUM uncertainty of measurement framework is based on LPU. This is derived from a set of estimates to make the calculations simple depending upon the available different models. In accordance to different models available and the nature of parameter, uncertainties are propagated by Taylor series. To make the calculation simpler, only first order is taken into account. Higher order will tend to improve the accuracy of procure adopted, but due to complexity of model, only first order is taken into account. By doing so, the model is defined where y is a function of variables x_1, \dots, x_N (ISO 1995).

$$y = f(x_1, x_2, \dots, x_N) \tag{1}$$

Simplifying leads to the general expression, which has been mentioned below for propagation of uncertainty for LPU,

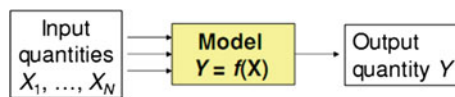
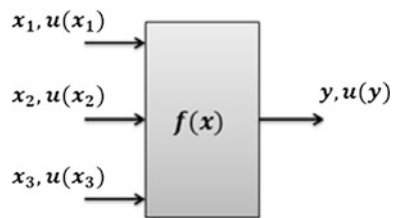


Fig. 1 Output as a function of input variables (Couto et al. 2013)

Fig. 2 Propagation of uncertainty (Couto et al. 2013)



$$u_y^2 = \sum_{i=1}^N \left(\frac{\partial f}{\partial x_i} \right)^2 u_{x_i}^2 + 2 \sum_{i=1}^{N-1} \sum_{j=i+1}^N \left(\frac{\partial f}{\partial x_i} \right) \left(\frac{\partial f}{\partial x_j} \right) \text{cov}(x_i, x_j) \quad (2)$$

u_y combined standard uncertainty y,

u_{x_i} uncertainty for the i th input quantity, x

Equation is further simplified as:

$$u_y^2 = \sum_{i=1}^N \left(\frac{\partial f}{\partial x_i} \right)^2 u_{x_i}^2 \quad (3)$$

The steps iterated for evaluation and expressing the uncertainty of the result of a measurement as may be as follows:

- (a) Define relationship between Y and X_i , where, $Y = f(X_1, X_2, \dots, X_N)$.
- (b) Determine x_i .
- (c) Calculate the standard uncertainty $U(x_i)$.
- (d) Calculate the covariance associated.
- (e) Calculate output value Y, for the input quantities X_i .
- (f) Calculate the combined standard uncertainty $U_c(y)$.
- (g) Calculate expanded uncertainty $U = k \cdot U_c(y)$, define k on the basis of the level of confidence.
- (h) Summarize the result in terms of y with $U_c(y)$ or expanded uncertainty U.

4 Limitations of LPU Approach

- (a) Taylor series model adopted should have insignificant non-linearity, which has not been discussed in GUM approach.
- (b) Another limitation of GUM approach is the validity of the theorem of central limit.
- (c) GUM approach may not be valid in the following cases:

Either, one or more input factor or their magnitude is larger than the others, or distributions of the input parameter not symmetric (Couto et al. 2013).

5 Monte Carlo Method

The term Monte Carlo method was used in 1940s by physicists, who were working on nuclear weapon project. Monte Carlo method is an iterative algorithm that is based on repeated random sampling to calculate its results. Because repeated computation and random numbers, Monte Carlo methods are suited to computer.

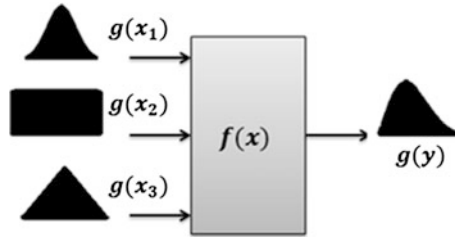


Fig. 3 Propagation of uncertainty distributions (Couto et al. 2013)

The MCM has been discussed by the GUM Supplement 1. It includes the propagation of defined model distributions for input factor to define the distribution of the output, whereas according to GUM, the uncertainties are to be propagated according to their distributions (Lee et al. 2014; Wubbeleer et al. 2008; Rocha et al. 2012).

Figure 3 describes the basis of MCM.

The GUM Supplement defines a series of steps to implement MCM:

- (i) Define input and output parameters;
- (ii) modelling;
- (iii) Approximation of the probability density functions (PDFs) for the input parameters;
- (iv) Setup Monte Carlo simulation;
- (v) Run Monte Carlo simulation;
- (vi) Summary and representation of the results.

The steps 1 and 2 are same as in GUM approach and provides foundation to the methodology of MCM. Step 3 includes the selection of the suitable PDFs for the input parameter to calculate the output. Step 4 involves determining the number of Monte Carlo trials. It is worthy to mention here that the Supplement also recommends number M of trials (Cox et al. 2003; Couto et al. 2013; JCGM 2008):

$$M > \frac{10^4}{1 - p} \tag{4}$$

where p is coverage probability.

The numerical tolerance of the uncertainty of the output, or standard deviation, can be obtained is defined by $c \times 10^1$. The numerical tolerance δ is:

$$\delta = \frac{1}{2} 10^1 \tag{5}$$

Now run the MCM simulation and report the results as follows:

- (a) Approximation of output quantity;
- (b) Standard deviation or uncertainty;

- (c) Coverage probability;
- (d) Lower and upper Limits of the output.

6 Conclusions

- (a) The paper discusses different approaches widely used for evaluation of uncertainty of measurement.
- (b) LPU and MCM are most widely accepted approaches.
- (c) MCM offers advantages of propagation of distribution of uncertainty rather than propagation of uncertainty as in case of LPU.
- (d) JCGM supplements stress upon the evaluation of uncertainty of measurement using MCM.

References

- Couto, P. R. G., Damascena, J. C., & Oliverira, S. P. (2013). *Monte Carlo method applied to uncertainty in measurement*. INTECH.
- Cox, M., Harris, P., & Siebert, B. R.-L. (2003). Evaluation of measurement uncertainty based on the propagation of distributions using Monte Carlo method. *Measurement Techniques*, 46, 824–833.
- ISO GUM (1995). *Guide of the expression of uncertainty in measurement*.
- JCGM 101:2008 (2008). *Evaluation of measurement data—supplement 1 to the guide to the expression of uncertainty in measurement—propagation of distributions using a Monte Carlo method*.
- Lee, S. W., Chung, B. D., Bang, Y. S., & Sung, W. B. (2014). Analysis of uncertainty quantification method by comparing monte-carlo method and Wilks' formula. *Nuclear Engineering and Technology*, 46, 481–488.
- Rocha, W. F. C., & Nogueira, R. (2012). Monte Carlo method for the evaluation of measurement uncertainty of pharmaceutical certified reference materials. *Journal of Brazilian Chemical Society*, 23, 385–391.
- Wubbeler, G., Krystek, M., & Elster, C. (2008). Evaluation of measurement uncertainty and its numerical calculation by a Monte Carlo method. *Measurement Science Technology*, 19, 084009.

Design of Automatic Fuel Filling System Using a Mechatronics Approach

Saurin Sheth, Kavita H. Patel and Harsh Patel

Abstract With the rapid growth of life, usage of automobile is increasing day by day, leading to an increase of fuel filling stations. In the present scenario, these filling stations are totally manually operated which consumes time & requires man power. Wherein sparsely populated areas, the labour cost is more, due to less population density. Due to less availability of labour, and climatic conditions some of these filling stations wouldn't be open for 24*7. Keeping these factors in mind, a mechatronics approach is made to design an automatic fuel filling system, which would be cost effective, open 24*7, minimum labour required and optimum time taken to fill fuel. The car has to be parked in a specific region, wherein using image processing a close loop system will be generated which guides the robotic arm to align itself to the fuel tank. Once the arm has aligned itself, the consumer has to enter the amount for the quantity of petrol to be filled in the car by swiping his card in the machine. The pump gets actuated and the tank starts getting filled with fuel. Once the entered volume of fuel had been filled in the car, the pump stops the supply of fuel and the arm returns to its initial position. Using this approach even the owner could monitor the pump online from any corner of the world and also overcome the idea of petrol theft.

Keywords Image processing · Robotic arm · Petrol theft · Cost effective · Automation · Design

S. Sheth (✉) · K.H. Patel · H. Patel
Mechatronics Engineering Department, GCET, Vallabh Vidyanagar, Anand, India
e-mail: saurinsheth@gcet.ac.in; skywater1994@gmail.com

K.H. Patel
e-mail: kavita_12mc@gcet.ac.in

1 Introduction

Looking at the present factors of petrol theft, climatic conditions and money crisis, an approach in optimizing the fuel filling system has been designed. The above idea of fuel filling automatically has been previously put into force but, due to some reasons it hasn't been successful (Corfitsen and Radlursvagen 1997). In our proposed system a vehicle has to proceed for fill up following the color signals or markers into the bay, as soon as it is parked the sensors and camera capture the car fuel tank details and send them to the controller. The controller obtains the coordinates using an algorithm. The robot is aligned to the coordinates as driven by the controller, so the robotic arm can do its alignment with the fuel tank. In this project the payment has to be made using mobile app, or through ATM. The payment of the fuel in our project has been assumed to be entered by the user itself. The robotic arm proceeds into the fuel cap which starts filling fuel, with the commands of the controller. As soon as it finishes the process it is ready for the next vehicle. The above design is comfortable, easy to operate, safe, clean and environment friendly.

1.1 Literature Review

The first design was put up by Rotec engineering, Netherlands (Rotec, Web). The vehicles working in stone crushing, construction sites, building roads and much more consume a lot of fuel as all tasks are done by the fuel combustion, so the Rotec engineering designed the machine or station for filling such giant vehicles. The drawback of their design is that it is limited only to the giant vehicles and the speed for filling the fuel is higher and difficult to control. It can't even be made smaller in size so that it can fill the small vehicles, but it occupies a lot of space, so the setup for fuel filling by Rotec engineering is too bulky and constrained to only high fuel capacity vehicles. Then the husky and Fuelmatics jointly designed an approach in which a pneumatic hand and a vacuum is used to open the lid and the pneumatic hand to fill the petrol (Husky, Web). Looking at the procedure working it is consuming a lot of time, in opening the lid, filling and retraction, which is a drawback and cannot be implemented in the real life problem (Husky-Automatic Refueling System, YouTube). A project has been made by a student in University of Hong Kong in 2002 on this ideology, but the speed and detection of the car has not been discussed to the point (Shiu et al. 2002). Only the filling process has been automated, due to which it doesn't count the time for the other activities, so which is not preferred to be put into force.

1.2 Need

According to our design, we can specify the flow rate of fuel for different range of vehicles as per their fuel tank capacity, so the process can be speeded up and the frequency of vehicles filled can be increased. The above mentioned point can be done through coding of the controller so that it drives the motor driver with a specific voltage that is required to drive the pump. As voltage varies the total amount of flow also varies as per the pump specifications. As the process is fully automated no need of labour except for maintenance and inspection. We can also setup the system at any place on highways, sparsely populated areas and can be controlled from a station away from it. It is 24*7 open and easy to operate. The setup can be situated in any place as the weather doesn't affect the machine unless it is a natural hazard. The present scams of providing lesser fuel to the customers can be overcome by this approach as the exact fuel specified by the controller is filled into the automobile or vehicle. The petrol stations have started cheating their customers by stealing so of the amount of fuel from each delivery, which is finally made lump sum and amounts to a ransom of theft, so keeping these factors in mind we ideated this design. Special security for the machine is also kept that when the machine is tempered with, a security alarm is rung and a notification to the nearest police station is sent. Other security issues can be taken care of accordingly.

2 Design Proposals

2.1 Assumptions in the Design

- The lid of the car is kept open always as shown in Fig. 1.
- All cars entering into the bay are of mono fuel, either petrol, or diesel.
- The payment will be paid directly to the controller.

Fig. 1 Fuel box



2.2 Proposed Designs

Figure 2 shows the flow chart of the system. It is having various logical and decision making things. It is giving the clear idea of the system, how it works. It shows the steps from entering of the car till the filling gets over.

Proposed Design 1

A microchip is inserted into the fuel cap, so that the exact location of the fuel filling port is recognized by sensor. But the above mentioned idea is not feasible to all cars, as we have to fit all cars with microchips, which is both expensive and next to impossible. The limitation is that the new cars can be manufactured in such a way that the chip is inserted but the question arises for the old cars? So the above ideology was rejected.

Proposed Design 2

A delta bot with 3 links can be manufactured as shown in Fig. 3, so that it can plot the maximum points in the 2d plane of the fuel tank. It is totally controlled with

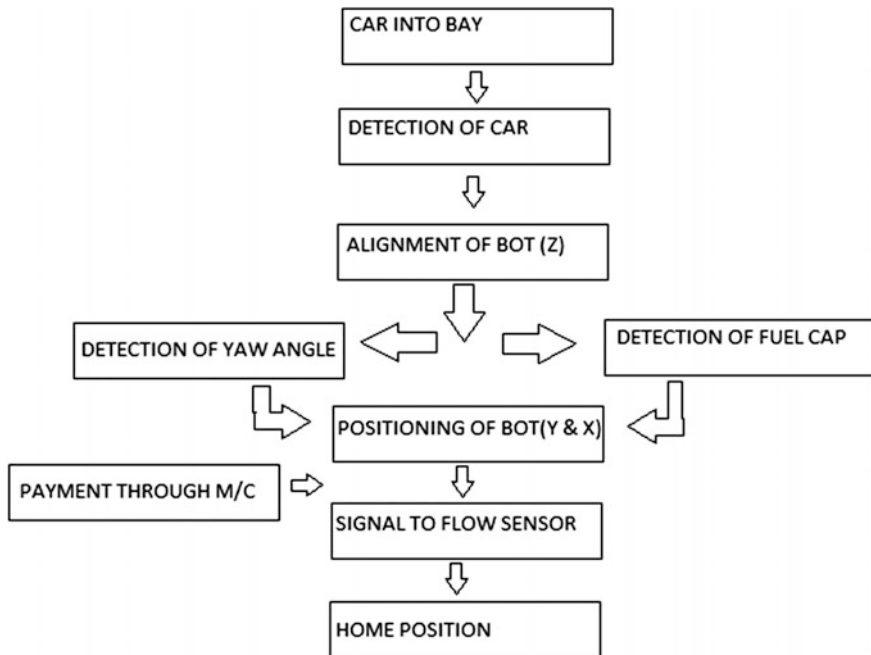


Fig. 2 Flowchart of setup

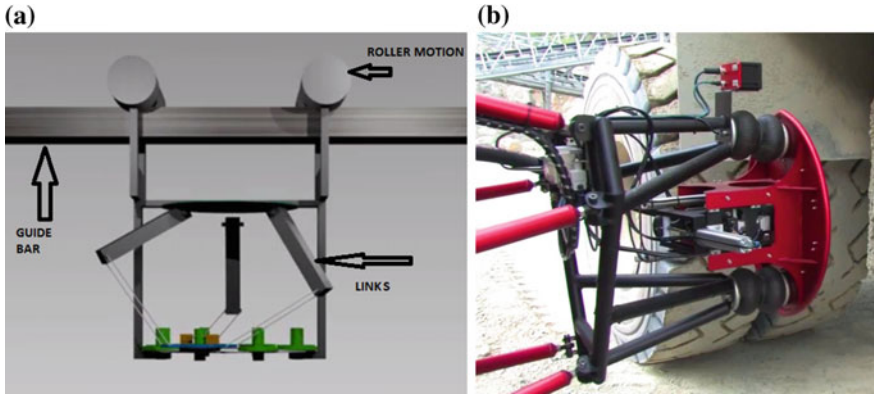


Fig. 3 a Top view of delta bot. b Proposed mounting on arm

sensors and a controller (Andre 2009). The limitations of these design are that the code program for bot is complex and difficult to debug (Ecorchard and Maurine 2005). The manufacturing of the delta bot is also very difficult. The delta bot occupies a large volume parameter, which is a constraint to smaller pumps (Rotec, Web).

Proposed Design 3

The structure is set to be as that of a gantry style robot but the sensors used in it are IR sensors. The sensors are used as a feedback, they contribute in completing the closed loop (John 1986). This design with respect to the sensors has the constraint of long time response to the system, which makes the system slow. The validity of the IR sensors is also limited, as weather and prolonged usage damages it. Due to slowness, it can cause traffic which is not likely in our system.

Proposed Design 4

The design has a gantry style, with cameras used for image processing and getting the actual data. The selection of car is done by RFID, which is used in electronic toll communication (Lung-Chang 2008). The RFID is used to know, the car details, car fuel type etc. From the car details as shown in Fig. 4 already fed data from the controller compare and give the output of the fuel tank dimensions from standard levels (Richardo et al. 2009). Then the coordinates are rectified according to the angle that is found out in the camera. Then the controller has the exact coordinates so it can give it to the gantry robot for alignment (Gajjar and Sheth 2014a, b).

The limitations of the above ideology is that the car without the RFID tag cannot be filled with petrol. The company provides RFID only to the newly manufactured

Fig. 4 Tag Id (RFID)



cars in India. And once the front glass is broken or the RFID is damaged anyhow, it takes a period of 4–6 months to update with a new RFID. Once the RFID is updated, you have to even update all the details with the RTO (Road and Transport Organisation) department.

Proposed Design 5

In this design the detection of the fuel tank is done using 4 point locator or signal mark. The marks are spotted on the fuel tank in such a manner that its coincidence will become the centre of the fuel tank, which is shown in Fig. 5 using image processing (Sheth et al. 2010). As viewed from an angle, the centre will always remain the same and even homography can be used. So the controller easily captures the four points and finds out the centre using algorithms (Chauhan et al. 2011).

Fig. 5 Sticker method



3 Measurement of Car and Fuel Box Dimensions

At present few cars are measured to decide the range and work volume of the mechanism. Figure 6 shows the terminologies associated with the car for measurement. Table 1 shows the sample data collected by measuring various category of cars.

4 Conceptual Mechanism and Working

The conceptual sketch has been shown in Fig. 7, along with the components required and methodology of automation. Various components used here are (a) Camera A for top view of car, (b) Camera B for fuel fill side view of car, (c) Arduino Uno, Microcontroller, (d) Fuel cap, (e) 2 servo motors for z axis control



Fig. 6 Car details

Table 1 Measurements of fuel box with respect to car (all dimensions in mm)

Car	Length	Width	Height	Min cap	Max cap	Cap OD	Cap ID	Fuel box (H)	Fuel box (W)
Toyota, Innova	4585	1760	1760	1005	1030	60	40	166	205
Suzuki, Wagon-R	3600	1475	1670	875	900	58	46	166	160
Tata, Bolt	3825	1695	1562	910	925	58	46	166	180

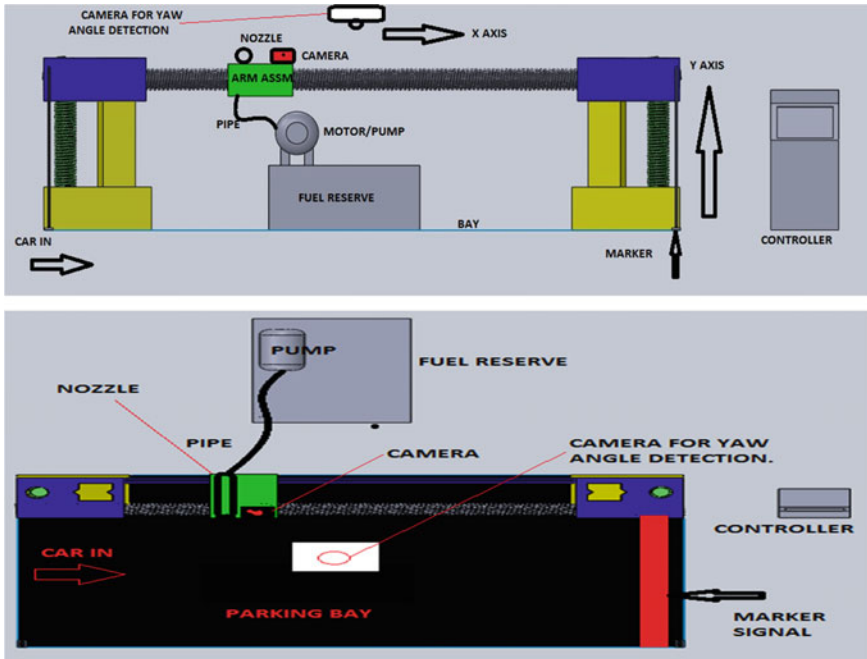


Fig. 7 Conceptual sketch of automatic fuel station

with 1500 rpm, (f) 1 servo motor for x axis control with 2000 rpm, (g) motor for y-axis control, (h) motor for yaw angle control, (i) Flow sensor, (j) Pump for fuel filling, (k) Pipe and Nozzle. The components are shown in Fig. 8.

4.1 Mounting of Components and Its Function in the System

- (a) The camera on ceiling, to capture the picture of the car when parked in a bay within the specific region.
- (b) The camera on the robotic arm setup, to capture the four points of the car. Here the color stickers are pasted.
- (c) The controller is Arduino UNO, which is an open source platform. It sends the signals to the drives.
- (d) Fuel cap is mounted in the fuel box by replacing the existing one. Here a special type of cap, make of Fuelmatics, is to be mounted as it has an advantage that it works like a non-return valve. So there is no need of closing it. Whenever required to fill in fuel, just pierce the fuel cap and fuel can be

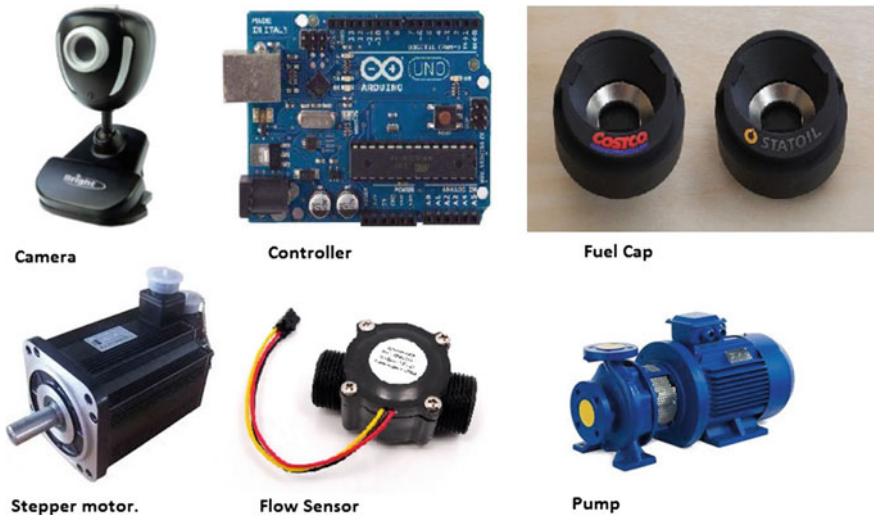


Fig. 8 Components required for proposed system

inserted (Fuelmatics, Web). This will save the time for opening and closing of fuel cap.

- (e) The stepper motors of various power ratings are used to actuate the mechanisms as per the requirement of fuel box dimensions. The use of stepper motor ensures the fast response (Virani et al. 2013).
- (f) The flow sensor is used to measure the amount of fuel that is filled into the fuel tank from the fuel reserve. The flow sensor is fitted between the pump and the nozzle. One of its wires is connected to the controller for continuous readings.
- (g) The pump can be used with varying discharge and head as per the reservoir design.

4.2 Working Methodology of Automatic System

When a car is entered into the parking/bay, the car as to be parked according to the marker signals. Camera A captures the top view of the car position in the bay. Simultaneously camera B captures the fuel filling side of the car by capturing four points on the fuel box. Both the images will go to the controller for further processing. The image sent by camera A will be processed to obtain a line of fuel filling side (Parikh et al. 2013). This line along with the robot reference will decide the yaw angle. If a car is parked at an angle then this yaw angle will ensure the no spill of fuel. Meanwhile image sent by camera B will be processed to obtain the center point of fuel cap (Gajjar et al. 2014). This will give the X, Y and Z coordinates of the fuel cap, which is fed to the controller. According to this the drives of the

mechanism will align the robotic arm to the center of the fuel cap. The x axis varies from 3200 mm till the maximum length of the car. The y axis motion varies from a range of 900–1100 mm. At present home position is decided with $x = 3500$ mm, $y = 1000$ mm and $z = 0$ mm. As per the customers requirement a payment is made, which decides the quantity of fuel to be filled, which can be done using PLC (Patel et al. 2015). Now the arm moves in the Z direction so that it pierces the fuel cap. Once it is ensured that the arm is pierced then the pump will be actuated to deliver the fuel. When the flow sensor reading matches with the calculated value of controller the pump stops. Then retraction of z axis takes place and robot returns to the home position.

5 Conclusion and Future Scope

The present work describes the methodology and mechatronics design approach of automatic fuel filling station. The proposed filling station is having various advantages:

- a. It can work for 24×7 in all the environments.
- b. It may reduce the man power.
- c. Fuel theft and wastage is almost negligible.
- d. Fatigueless and safe operation during filling.

The time study of all the operation can be done to find out cost effectiveness of the proposed system. Automatic payment method can be developed for ease of operation. Lead screw may be replaced by ball screw for fast responses in the highly populated areas.

References

- Andre, O. (2009). Modelling and control of a delta –3 robot.
- Chauhan, V., Sheth, S., Hindocha, B. R., Shah, R., Dudhat, P., & Jani, P. (2011). Design and development of a machine vision system for part color detection and sorting. In *Proceedings of Second International Conference on Signals, Systems & Automation (ICSSA)* (pp. 90–93). doi:10.13140/2.1.1628.7526.
- Corfitsen, S., & Radlursvagen. (1997). Patent US5638875-Apparatus for automatic Refuelling of Vehicles.
- Ecorchard, G., & Maurine, P. (2005). Self-calibration of delta parallel robots with elastic deformation compensation. *Intelligent Robots and Systems*, pp. 462–467.
- Fuelmatics systems AB, Box 24137, se-104 51 Stockholm, Sweden, Web: www.fuelmatics.com.
- Gajjar, B. R., & Sheth, S. (2014a). Design and automation in back plug press fitting process of ball pen assembly. *Applied Mechanics and Materials*, 592, 2596–2600.
- Gajjar, B. R., & Sheth, S. (2014b). Investigation of automation strategy and its effect on assembly cost: a case study on ball pen assembly line. *International Journal of Current Engineering and Technology*, 3, 89–92.

- Husky and Fuelmatics: automatic refuelling system, Web: www.youtube.com/watch?v=0bz2u5unapa.
- Husky corporation, 2325 Husky Way Pacific, MO 63069, Web: www.husky.com.
- John, C. J. (1986). Introduction to robotics mechanics & control. Addison-Wesley Publishing Company Inc.
- Lung-Chuang, W. (2008). Enhancing construction quality inspection and management using RFID technology. *Automation in Construction*, 17, 467–479.
- Parikh, P. A., Joshi, K. D., & Sheth, S. (2013). Color guided vehicle—an intelligent material handling mechatronic system. In *Proceedings of the 1st International and 16th National Conference on Machines and Mechanisms (iNaCoMM2013)*, IIT Roorkee, India, pp. 628–635.
- Patel, T., Sheth, S., & Patel, P. (2015). Design of semi-automatic hydraulic blanking machine using PLC. In *National Conference on Innovative & Emerging Technologies (NCIET-2015)*, pp. 410–412. doi: 10.13140/RG.2.1.4529.6803.
- Rotec Engineering B.V, Verlengde Gliderweg 30, 8304 BK Emmeloord, Netherlands, Web: www.rotec-engineering.nl.
- Sheth, S., Kher, R., Shah, R., Dudhat, P., & Jani, P. (2010). Automatic sorting system using machine vision. *Multi-Disciplinary International Symposium on Control, Automation & Robotics*,. doi:10.13140/2.1.1432.1448.
- Shiu, K. T., Ka, L. F., Zhang, Y., & Chan, C. M. (2002). An automated gas station attendant. *IEEE Intelligent Systems*.
- Tesoriero, R., Gallud, J. A., Lozano, M. D., & Penichet, M. R. (2009). Tracking autonomous entities using RFID technology. *IEEE Transactions on Consumer Electronics*, 55, 650–655.
- Virani, M., Vekariya, J., Sheth, S., & Tamboli, K. (2013). Design and development of automatic stirrup bending mechanism. In *Proceedings of the 1st International and 16th National Conference on Machines and Mechanisms (iNaCoMM2013)* (pp. 598–606). IIT Roorkee, India.
- William Pong, Edward Fredkin, Patent US6237647-Automatic Refuelling Station, 29 May 2001.

A Framework for Evaluation of Environmental Sustainability in Pharmaceutical Industry

Geo Raju, Harpreet Singh, Prabir Sarkar and Ekta Singla

Abstract The term sustainability is generating much interest both among organizations and as a research topic. This article focuses on the environmental aspect of sustainability in pharmaceutical industry. The main objective of this paper is to present a framework for evaluation of environmental sustainability of formulated products (dosage forms) in pharmaceutical industry. Indicators used in pharmaceutical industry to evaluate environmental sustainability are also presented. Life cycle assessment (LCA) studies undertaken in pharmaceutical sector are explored and a list of these studies is presented in this paper. As part of framework building, each phase of LCA viz. goal and scope definition, inventory analysis, impact assessment, and interpretation was taken into account. For each of the above-mentioned phases, methods that may be undertaken to quantify the environmental burden caused by formulated pharmaceutical products were prepared based on literature review.

Keywords Life cycle assessment · Pharmaceuticals · Sustainability · Indicators · Inventory analysis · Impact assessment

1 Introduction

The term sustainability is generating much interest both among organizations and as a research topic. Various stakeholders, especially government regulators, community activists, non-governmental organizations (NGOs), and global competitors, are exerting pressure on companies to commit to the cause of resource optimization and pollution reduction. Earlier companies used to implement sustainability practices on the grounds of regulatory requirements (Melacini et al. 2010) but recently companies started undertaking sustainable initiatives as a possible alternative for gaining or maintaining a competitive advantage (Sarkis 2003). This induced the

G. Raju (✉) · H. Singh · P. Sarkar · E. Singla
Indian Institute of Technology Ropar, Rupnagar, India
e-mail: connectjiyo@gmail.com

need for evaluating the environmental initiatives and quantifying the sustainable performance of a company.

Sustainability metrics are one of the widely used tools for measuring the sustainability performance of an organization (Veleva et al. 2003). The boundary condition to be considered, i.e. whole supply chain analysis or analysis within a company premise, while evaluating the sustainability performance is a major issue (Finkbeiner 2009). Life cycle assessment (LCA) method would be helpful in this regard as it is extensively used to estimate the potential environmental impacts of a product, service, or activity across all its life cycle stages, from raw material extraction to disposal.

This article focuses on the environmental aspect of sustainability in pharmaceutical industry. The main objective of this paper is to present a framework for evaluation of environmental sustainability of formulated products (dosage forms) in pharmaceutical industry. Indicators used in pharmaceutical industry to evaluate environmental sustainability are also presented. LCA studies undertaken in pharmaceutical sector are explored and a list of these studies is presented in this paper.

2 Methodology

In order to achieve the objectives of this paper, a literature survey on the topic, 'indicators for measuring environmental sustainability', was initially performed. The literature review was focused on the identification of suitable metrics that can be used in pharmaceutical sector for evaluating and benchmarking progress towards sustainability. An in-depth review of literature on LCA studies in pharmaceutical sector was also performed with a view to develop a framework for evaluating and quantifying the sustainable performance of pharmaceutical formulation industry. As part of framework building, each phase of LCA viz. goal and scope definition, inventory analysis, impact assessment, and interpretation was taken into account. For each of the above-mentioned phases, methods that may be undertaken to quantify the environmental burden caused by formulated pharmaceutical products were prepared based on literature review.

3 Results and Discussion

3.1 *Environmental Metrics in Pharmaceutical Industry*

Environmental metrics act as a means to gauge the activities that have been undertaken to move towards a broader goal of environmental sustainability. Metrics are easy to use and can easily be used for modeling and what-if analysis of scenarios involving different processes or reaction pathways. Initially the focus was on

Table 1 Environmental metrics for sustainability evaluations in the pharmaceutical industry

Metrics	Description
E-factor (Sheldon 1992)	Mass ratio of waste to desired product
Atom economy (Trost 1991)	Ratio of molecular mass of desired product to that of all reactants
Effective mass yield (Frey et al. 1999)	Mass ratio of desired product to non-benign reactants
C-factor (Voss et al. 2009)	Mass ratio of the CO ₂ to product mass
Process mass intensity	Total mass of materials used to produce a specified mass of product

identifying environmental metrics that can be used for quantifying process waste (Sheldon 1992) but Jiménez-González et al. (2012) pointed out the need to identify metrics that could incorporate resource efficiency; portrait environmental health and safety compliance of the materials and processes by taking into consideration the overall life cycle of a product or service. Some of the commonly used environmental metrics in pharmaceutical sector are listed in Table 1.

GlaxoSmithKline (GSK) has developed its own metrics such as carbon efficiency and reaction mass efficiency (Curzons et al. 2001). Carbon efficiency is the ratio of amount of carbon in the product to that in the reactants. Reaction mass efficiency account for reactant mass and therefore includes yield and atom economy.

Tufvesson et al. (2013) pointed out that a metric may not take into consideration the multi faceted nature of the environmental problems, may focus only on a single environmental impact category, e.g. carbon dioxide emission, which may result in sub-optimization of problem, i.e. minimization in waste generation may be traded for CO₂ emission etc. Another serious concern with use of metrics is that the same weight is assigned to all variants of waste engendered.

3.2 LCA of Pharmaceutical Products

LCA methodology provides a framework of directly applicable environmental metrics to evaluate and quantify the sustainability of a product or process across its life cycle. LCA is a methodology used for quantifying the energy and materials used, the wastes released to the environment, and assessing the environmental impacts of those energy, materials and wastes, of a product system, process or activity by taking into consideration the whole life cycle, i.e. from raw material extraction and conversion, manufacturing, transportation, sales, distribution, use, till final disposal (SETAC 1993). The LCA methodology is defined by the ISO 14040 standard (ISO 2006) and consists of four complementary components: goal and scope definition, inventory analysis, impact assessment, and interpretation. The purpose of the study along with definition of system under study is described in the goal and scope definition. The goal and scope of the study must be clearly defined and also must be

consistent with the intended application (ISO 2006). The backbone of an LCA is the life cycle inventory (LCI). All data needed to model the product or activity under study is collected in inventory analysis phase. The collected data is processed in the next stage, viz. Life Cycle Impact Assessment (LCIA) phase in order to identify the potential environmental impacts based on some metrics or indexes such as eco-indicator 99. In the interpretation phase the results from inventory analysis and impact assessment phase are summarized.

The use of LCA to analyze pharmaceutical products or processes is still limited. Only a few studies are published, most of them undertaken to get a better grasp of the wider environmental impacts of various processes, contrast various chemical routes, and different unit operations based on their environmental implications (Jiménez-González et al. 2012). The reason for the publication of only a limited number of LCA studies in pharmaceuticals can be attributed to the confidentiality nature of data involved in the process. Moreover pharmaceuticals are among the most complex chemicals produced, and the available data on fine chemical production are very scarce in general. Pharmaceuticals are generally produced in multi-purpose plants (Sziijarto et al. 2008), with equipments and utilities shared between the production lines. Consumption of utilities such as steam and electricity are determined on a plant level as it is a tough task to get data on energy consumption n a process level or product level.

Most of the published LCA studies of pharmaceuticals provide comparative data rather than absolute data. Some pharmaceutical companies have developed their own streamlined LCA tool to gain insights about the environmental impacts of chemical processing activities within reasonable timelines. For example, GSK has developed a streamlined LCA tool called FLASC (Fast Life cycle Assessment of Synthetic Chemistry) to systematically evaluate synthetic organic reactions and processes (Curzons et al. 2007). Some illustrative examples of the application of LCA in pharmaceutical industry are presented in Table 2.

3.3 Framework to Evaluate Sustainability of Formulated Pharmaceutical Products

A life cycle approach was proposed in order to assess the burdens related to environmental sustainability of formulated pharmaceutical products. The study of literature on application of LCA in pharmaceutical sector revealed that most of these studies are concentrated on production of Active Pharmaceutical Ingredients (API). The reason for this trend can be attributed to high cost and intellectual property value of API. The study of API has helped to accrue some knowledge on typical hotspots and to identify the relation between cost and environmental implications as well as the environmental implications of various dosage forms such as tablets, liquids, ointments, etc. (Jiménez-González and Overcash 2014). Several pharmaceutical companies have undertaken LCA of formulated

Table 2 Examples of the application of LCA in pharmaceutical industry

Reference	Pharmaceutical product/process	Description	Boundary condition
Wernet et al. (2010)	API	Environmental profile of API and comparison with that of basic chemicals	Cradle-to-gate
Ponder and Overcash (2010)	Vancomycin hydrochloride	Identify the hotspots in the supply chain with respect to material and energy consumption, and emission	Cradle-to-gate
Bruggink and Nossin (2006)	Cephalexin	Assessment of bio-based routes to the product	Cradle-to-gate
Jiménez-González (2000)	Sertraline	Environmental profile of chemical synthesis of product	Cradle-to-gate
Kim et al. (2009)	Enzymes	Estimate the life cycle impacts of three enzymes and identify the suitability of modular life cycle inventory estimation techniques	Cradle-to-gate
Cespi et al. (2015)	Viagra	Comparison of optimized medicinal route vs commercial route	Cradle-to-gate
Jödicke et al. (1999)	Enantioselective reduction	Comparison of metal catalyst and biocatalyst for enantioselective reduction of ketoesters	Cradle-to-gate

pharmaceutical products but they are not publicly reported. Therefore there is a lack of benchmark for LCA of formulated pharmaceutical products. Each phase of LCA is considered in the framework building.

1. Goal: The goal of the study is to identify and analyze the gate-to-gate environmental impacts in the production and packaging of a formulated pharmaceutical product. Another goal is to identify the hotspots in the production process of a tablet, syrup or an ointment. There could be other goals such as comparison of continuous and batch manufacturing, comparison between different dosage forms, state-of-art vs emerging technology, resource consumption and waste generation when different binders are used etc.
2. Scope: The scope encompasses the potential impact of production and packaging process of dosage forms using a gate-to-gate approach. The upstream life cycle phases which include extraction of raw materials, API and excipient production and its transportation are excluded. Usage phase is also not included. The study should include all onsite utilities such as AHU, water treatment units, boiler etc. and waste treatment plant. The gate-to-gate boundary condition for the study is presented in Fig. 1.

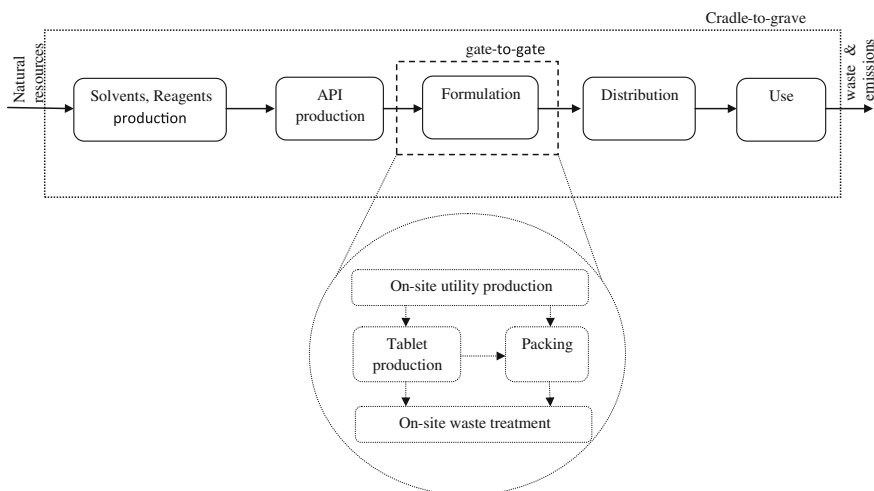


Fig. 1 Life cycle of pharmaceuticals within the boundaries of cradle-to-grave and formulation gate-to-gate

3. Functional unit: Functional unit must be defined correctly; quantitatively, qualitatively and in time. If the goal of the study is to compare two products, then the selection of functional unit is very crucial (Baumann and Tillman 2004). For the study of formulated products, functional unit of one tablet (e.g. one paracetamol tablet of 500 mg), one bottle of syrup, or one vial of medication can be used depending on the dosage form.
4. Reference system: A reference system is needed so that a process or product can be compared in relation that. It is quiet difficult to choose a good reference system for pharmaceuticals to compare two products or processes due to difference in quality, efficacy and optimization (Tufvesson et al. 2013).
5. Life cycle inventory: Developing an inventory for LCA of a product or process is a big challenge. A large number of data is needed from a variety of sources accompanied with the absence of data for many of the raw material required for production of pharmaceuticals makes development of LCI a hard endeavor. LCI creation is done in a modular manner, incorporating material requirements, energy modules, and waste generation from the production process, waste treatment modules, AHU systems, water treatment plants, steam generation units and cleaning and maintenance.

Material inventory for the production process of formulated product can be generated from the study of batch process reports (BPR). Energy modules for production process can be calculated using the power rating of equipments and the time taken for each process step. Waste is mainly generated from the cleaning of the equipments. It can be quantified only on daily basis. Energy modules for steam generation, Air and water treatment, cooling using cooling towers can be obtained from commercial LCI

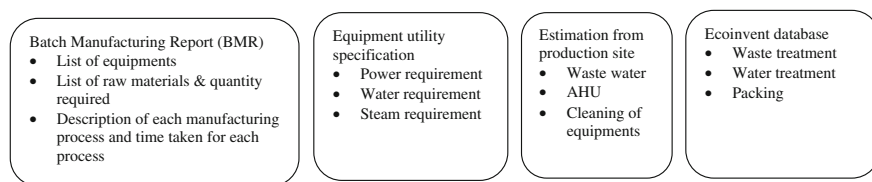


Fig. 2 Approach to develop data inventory for gate-to-gate LCA of formulated pharmaceutical products

databases such as ecoinvent and GaBi. Figure 2 presents the data inventory development approach for gate-to-gate LCA of pharmaceuticals.

6. Allocation method: When a specific process produces more than one product of commercial value, the raw material and energy requirement, the form of waste treatment and the emissions generated, need to be properly allocated to each product. In formulation industry, different dosage forms are manufactured simultaneously. So there is a need to allocate material outputs, energy requirements and waste generation between these dosage forms. But allocation cannot be done on the basis of mass content of the product as it is not proportionate. Best possible way is to avoid allocation and to depend on estimation.
7. Life cycle impact assessment (LCIA): The results of LCIA can be represented in different forms. Direct inventory data gives the energy consumption, material consumption and emissions throughout the life cycle of the product. Individual potential impacts give measures such as global warming potential, eutrophication etc. Indexes like eco-indicator 99 and Tool for the Reduction and Assessment of Chemical Impacts (TRACI) incorporate a wider range of impact categories, pollutants, sources, and life cycle stages (Jiménez-González and Woodley 2010).

Case study: This framework was analysed by conducting LCA of Paracetamol (acetaminophen) 500 mg tablet. A functional unit of one paracetamol 500 mg tablet was used. The scope of the study was to identify the hotspots in the production process. The boundary of the LCA covered production and packing activities including onsite utilities such as AHU, water treatment units, boiler and waste treatment plant. LCI of the study was generated in a modular manner as discussed in the framework. LCI was created with the help of data from a formulation plant. Material inventory was generated from batch process report and energy modules were created using information from equipment utility requirement. A summary of inputs for the production of paracetamol tablet is given in Table 3. The detailed life cycle inventory and analysis will be discussed in future publications.

Table 3 Summary of inputs for the production of paracetamol tablet

Item Name	Quantity/Tablet
Paracetamol API (mg)	500.00
Dicalcium Phosphate (mg)	60.00
Starch (mg)	134.80
Sodium starch glycollate (mg)	10.00
PVPK-30 (mg)	15.00
Methyl paraben sodium (mg)	0.80
Propyl paraben sodium (mg)	0.20
Cross carmellose sodium (mg)	5.00
Aerosil (mg)	3.00
Purified talcum (mg)	15.00
Magnesium stearate (mg)	6.20
DM Water (mg)	150.00
Electricity (kWh)	2.64×10^{-5}

4 Conclusion

A framework for evaluation of environmental sustainability of formulated products (dosage forms) in pharmaceutical industry was presented based on literature review. Literature review of LCA of pharmaceuticals revealed that the use of LCA to analyze pharmaceutical products or processes is still limited. Additionally, most of the available literature studies concentrated on the production of Active Pharmaceutical Ingredients (API), since, expenses and Intellectual property Rights (IPR)s resides on APIs. Even though LCA of formulated pharmaceutical products have been undertaken they are not published in any journals. The LCA of pharmaceuticals give comparative data rather than absolute data. Developing data inventory for LCA of pharmaceuticals is not an easy endeavor. The framework presented in this paper need to be tested using more detailed case studies.

References

- Baumann, H., & Tillman, A. M. (2004). The Hitch Hiker's guide to LCA. An orientation in life cycle assessment methodology and application, External organization.
- Bruggink, A., & Nossin, P. (2006). Assessment of bio-based pharmaceuticals: The Cephalixin case. In *Renewables-Based technology* (pp. 315–329). Hoboken: Wiley.
- Cespi, D., Beach, E. S., Swarr, T. E., Passarini, F., Vassura, I., Dunn, P. J., & Anastas, P. T. (2015). Life cycle inventory improvement in the pharmaceutical sector: assessment of the sustainability combining PMI and LCA tools. *Green Chemistry*, *17*, 3390–3400. doi:10.1039/C5GC00424A.
- Curzons, A. D., Jiménez-González, C., Duncan, A. L., Constable, D. J. C., & Cunningham, V. L. (2007). Fast life cycle assessment of synthetic chemistry (FLASC™) tool. *International Journal of Life Cycle Assessment*, *12*, 272–280. doi:10.1065/lca2007.03.315.

- Curzons, A. D., Mortimer, D. N., Constable, D. J. C., & Cunningham, V. L. (2001). So you think your process is green, how do you know?—Using principles of sustainability to determine what is green—a corporate perspective. *Green Chemistry*, *3*, 1–6. doi:10.1039/b007871i.
- Fava, J., Consoli, F., Dennison, R., Dickson, K., Mohin, T., & Vigon, B. (Eds.). (1993). *A conceptual framework for life-cycle impact assessment*. Pensacola: SETAC and SETAC Foundation for Environmental Education.
- Finkbeiner, M. (2009). Carbon footprinting—opportunities and threats. *The International Journal of Life Cycle Assessment*, *14*(2), 91–94.
- Frey, D., Claeboe, C., Brammer, L., Jr, et al. (1999). Toward a “reagent-free” synthesis. *Green Chemistry*, *1*, 57–59.
- ISO (2006). SS-EN ISO 14044, Environmental management—life cycle assessment—requirements and guidelines. ISO.
- Jiménez-González, C. (2000). Life cycle assessment in pharmaceutical applications. Ph.D. Thesis, North Carolina State University, Raleigh, NC.
- Jiménez-González, C., Constable, D. J. C., & Ponder, C. S. (2012). Evaluating the “Greenness” of chemical processes and products in the pharmaceutical industry—a green metrics primer. *Chemical Society Reviews*, *41*, 1485–1498. doi:10.1039/C1CS15215G.
- Jiménez-González, C., & Overcash, M. R. (2014). The evolution of life cycle assessment in pharmaceutical and chemical applications—a perspective. *Green Chemistry*, *16*, 3392. doi:10.1039/c4gc00790e.
- Jiménez-González, C., & Woodley, J. M. (2010). Bioprocesses: Modeling needs for process evaluation and sustainability assessment. *Computers & Chemical Engineering*, *34*, 1009–1017. doi:10.1016/j.compchemeng.2010.03.010.
- Jödicke, G., Zenklusen, O., Weidenhaupt, A., & Hungerbühler, K. (1999). Developing environmentally-sound processes in the chemical industry: A case study on pharmaceutical intermediates. *Journal of Cleaner Production*, *7*, 159–166. doi:10.1016/S0959-6526(98)00075-4.
- Kim, S., Jiménez-González, C., & Dale, B. E. (2009). Enzymes for pharmaceutical applications—a cradle-to-gate life cycle assessment. *International Journal of Life Cycle Assessment*, *14*, 392–400. doi:10.1007/s11367-009-0081-9.
- Melacini, M., Salgaro, A., & Brugnoli, D. (2010). A model for the management of WEEE reverse logistics. *International Journal of Logistics Systems and Management*, *7*(1), 1–18.
- Ponder, C., & Overcash, M. (2010). Cradle-to-gate life cycle inventory of vancomycin hydrochloride. *Science of the Total Environment*, *408*, 1331–1337.
- Sarkis, J. (2003). A strategic decision framework for green supply chain management. *Journal of Cleaner Production*, *11*(4), 397.
- Sheldon, R. A. (1992). *Organic synthesis—past, present and future, chemistry and industry*. London: Ten Alps Publishing.
- Szűjarto, A., Papadokostantakis, S., Fischer, U., & Hungerbühler, K. (2008). Bottom-up modeling of the steam consumption in multipurpose chemical batch plants focusing on identification of the optimization potential. *Industrial and Engineering Chemistry Research*, *47*, 7323–7334. doi:10.1021/ie071291o.
- Trost, B. (1991). The atom economy—a search for synthetic efficiency. *Science*, *254*, 1471–1477. doi:10.1126/science.1962206.
- Tufvesson, L. M., Tufvesson, P., Woodley, J. M., & Börjesson, P. (2013). Life cycle assessment in green chemistry: overview of key parameters and methodological concerns. *International Journal of Life Cycle Assessment*, *18*, 431–444. doi:10.1007/s11367-012-0500-1.
- Veleva, V., Hart, M., Greiner, T., & Crumbley, C. (2003). Indicators for measuring environmental sustainability: A case study of the pharmaceutical industry. *Benchmarking International Journal*, *10*, 107–119. doi:10.1108/14635770310469644.

- Voss, B., Andersen, S. I., Taarning, E., & Christensen, C. H. (2009). C Factors pinpoint resource utilization in chemical industrial processes. *ChemSusChem*, 2, 1152–1162. doi:[10.1002/cssc.200900215](https://doi.org/10.1002/cssc.200900215).
- Wernet, G., Conradt, S., Isenring, H. P., Jiménez-González, C., & Hungerbühler, K. (2010). Life cycle assessment of fine chemical production: a case study of pharmaceutical synthesis. *International Journal of Life Cycle Assessment*, 15, 294–303. doi:[10.1007/s11367-010-0151-z](https://doi.org/10.1007/s11367-010-0151-z).

Aero-Structure Interaction for Mechanical Integration of HP Compressor Blades in a Gas Engine Rotor

N. Vinayaka, Nilotpal Banerjee, B.S. Ajay Kumar
and Kumar K. Gowda

Abstract Aero-structure interaction during turbomachinery blade design has become an important area of research due to its critical applications in aero engines, land based gas turbines. Studies reveal that a small mistuning leads to stress build up through mode localization under operating conditions. This paper deals with a case study of Aero-structure interaction for a free standing HP blade of a gas turbine. Assuming 100 % fixity at blade root, the study involves critical parametric evaluations involved in achieving Mechanical Integrity in airfoil design and blade platform design. Mechanical Integrity involves stress checks, frequency margins, Campbell diagram, gross yield stress and so on, for design and off-design conditions for a given stage efficiency of 72 % in an Ideal HP compressor of a gas turbine engine.

Keywords Blade airfoil · Stress stiffening · Spin softening · Campbell diagram · Excitor box · Separation margins · Aero-structure interaction · Gross yield stress

1 Introduction

Mechanical Integrity of blades to the rotor is the fundamental and most important criteria for all Turbo engines. The blade offers stiffness against the external steady and alternating loads and contributes to the Mechanical Integrity. The most difficult

N. Vinayaka · N. Banerjee
National Institute of Technology, Durgapur, India

N. Vinayaka (✉)
Nitte Meenakshi Institute of Technology, Bangalore, India
e-mail: vn23design.engg@gmail.com

B.S. Ajay Kumar
Bangalore Institute of Technology, Bangalore, India

K.K. Gowda
Vivekananda Institute of Technology, Bangalore, India

task in rotating machines, such as turbo machinery is to overcome the effects due to centrifugal load and gas bending loads and provide suitable blade stiffness (Ewins 2010; Huang 1981).

Since decades, rotary engines find its applications to produce power with various working fluid mediums like wind, water, steam and gas. There has been tremendous advancements in the Gas turbine technology to improve overall efficiency by optimizing stage performance parameters, weight reduction by using suitable composite materials, usage of desired super alloys for the targeted thrust force, to reduce numbers of blades per stage, providing suitable thermal barrier coatings on blade surface for high temperature operating conditions, introducing blade cooling holes for enhancing the stage thermal efficiencies and more number of research laboratories are set up, wherein the engines are tested for actual working conditions at a suitable altitude and results are tracked and monitored for analyzing performance maps and then finally the gas engine is assembled to the commercial aircraft.

Gas Engines are rotary complex machines, wherein Aero-structure interaction for airfoil design and Mechanical Integration is a real challenge. The interaction is very important because it is a win-win situation to both structural engineer as well as fluid flow path designer. Achieving thermal efficiency becomes more important to the flow path designer which results in blades as thin as possible. Whereas for achieving Mechanical Integration obtaining uniform gross yield strength throughout blade length becomes a challenging task and low peak stress at transition radius around the hub of the airfoil is the design objective.

During high speed operating conditions, the Aero-structures are subjected to Elasto-Plastic yielding. The Centrifugal force induced due to rotation acts along blade length from its root hub to blade tip and accounts for an approximately 70–75 % frequency increase associated with blade bending modes of vibration, whereas the Coriolis coupling effects leads to other modes of blade vibration. Compressor blades are modeled as rotating cantilever beams with airfoil cross section to study the vibration characteristics related to their dynamic behavior. Due to rotation two counteracting effects, Spin-Softening (or centrifugal softening) and Stress-Stiffening are observed in blades.

2 Problem Definition, Objectives and Design Considerations

2.1 Problem Definition

The Mechanical Integrity in bladed disc has two steps, one is to achieve the best airfoil. Secondly, to achieve the best root fixation in bladed disc assembly. The present work main focus is to achieve the best airfoil through Aero-structure interaction. Customized methodology is ensured to achieve the stress checks and

separation margin through frequency evaluation for centrifugal load and gas bending forces in a HP compressor stage of a gas turbine engine.

2.2 Objectives

- a. Achieve Mechanical Integration in airfoil design in gas turbines with smooth transition radius to minimize localized stresses.
- b. Achieve safe gross yield strength from hub to tip as per design consideration.
- c. Analyze the blades for separation margins along with Excitor box using Campbell diagrams.
- d. Study the role of Spin Softening and Stress Stiffening on the blade frequency evaluation.
- e. Achieve customized methodology for aero-structure interaction in free standing blades.

2.3 Design Considerations

The Normal Operating speed of the machine chosen is 8000 rpm. The Blade material chosen is Titanium alloy (Ti 6Al 4V) whose properties are as follows— Density, Young's Modulus, Poisson's ratio, Yield Strength and Thermal Co-efficient of expansion are $4.43\text{E-}9$ Tones/mm³, $1.138\text{E}5$ MPa, 0.342, 880 MPa, $9.7\text{e-}6$ /°C (At operating temperature 410 °C) (Lebele-Alawa et al. 2008). Blade height is 40 mm, Shroud thickness is 2 mm, hub thickness is 5 mm. Blade transition radius is 3 mm. Factor of safety assumed is 1.65 for allowable design stress of 522.6537 MPa. Separation margins assumed is left margin 5 % and right margin 5 % for the chosen operating speeds, top 5 % and bottom 5 % in the Excitor box. The Peak Stress to achieve for 1e^6 cycles is 1065 MPa. Mean Diameter of rotor is 584 mm, No of blades is 65, Pitch of blades in the rotor is 28.53 mm, Stage efficiency is 72 %, Blade axial chord is 36 mm (Bazhenov et al. 2013).

The blade model shown in Fig. 3 is discretized into hexahedral elements using 'h' type higher order elements and the resulting discretized model is as shown in Fig. 4. The number of elements count is 10,729 and the number of nodes count is 17,373.

3 Descriptions of Vibration Characteristics in Rotating Machines

Rotary blades are subjected to high centrifugal stresses and vibratory stresses in a Gas Engine HP Rotor apart from gas bending forces. In the design of rotating machines the determination of blade natural frequencies is an important criteria since blade fatigue failure occurs at or near resonant frequencies. Hence, study of vibration characteristics plays an important role in designing rotating machines. The excitations arise from each obstructing component in the flow path of gas stream from HP stator blades to HP rotor blades per stage like nozzles, Coupling Bolts, Spline Joints, Coupling Misalignment loads, Contact surface between joints, Coupling sliding velocity and the geometry and positioning of blade Interconnecting elements. Studies reveal that in few cases blades are subjected to resonance due to start up and shut down cycle time variations and at speeds very close to operational speed. These blades are susceptible for failures, unless very close grid frequency control is maintained (Ewins 2010; Huang 1981). Therefore, designers have to provide sufficient blade damping to get the desired blade life.

3.1 Stress Stiffening

Stress Stiffening is the effect caused due to Centrifugal force and tends to increase the blade stiffness. Hence, there is an increase in resonant frequencies. It is usually considered for thin structures whose bending stiffness is very small compared to axial stiffness and it couples the in-plane and transverse displacements (Madhavan et al. 2014). Therefore, Centrifugal force increases with the radial displacement acting away from the rotary axis and decreases when the motion is towards the axis.

3.2 Spin Softening

Spin Softening is the effect caused due to Centrifugal force by spinning action of rotor, which results in blade softening to take place at high temperature and high speed operating conditions causing relative circumferential motions and decreases the blade natural frequencies due to decrease in blade stiffness, leading to a distorted structure. As small deflection analysis cannot directly account for changes in geometry, the effect can be accounted for by an adjustment of the stiffness matrix called Spin Softening (Madhavan et al. 2014).

3.3 Mechanical Efficiency

The Fig. 1 shows the airfoil geometry of the designed blade of 40 mm height, number of blades in rotor is 65, pitch is 28.53 mm, stage efficiency is 72 % with an axial chord of 36 mm. The U/C_0 ratio achieved through CFD program is about 0.5 and its impulse load diagram is as shown in Fig. 2.

3.4 Blade Geometry

Importance of Blade Parameters in Achieving the Maximum Thermal Efficiency for a Given Airfoil

The critical parameters considered are leading edge, trailing edge, chord length, angle of attack, blade height, taper, twist and so on (Shankar et al. 2010). In the present study for a mean diameter of 584 mm of 1st stage HP rotor, the number of blades were fixed with a chord length of 36 mm for a free standing blade shown in Fig. 3. The Fig. 4 shows the corresponding blade meshed model. The thermal efficiency achieved per stage is 72 %.

Importing the airfoil for structural evaluation assuming 100 % fixity at root (Tulsidas and Shantharaja 2015) with a blade platform thickness of 5 mm, the blade is subjected to gas bending load at 8000 rpm. As per design considerations the

Fig. 1 Airfoil geometry

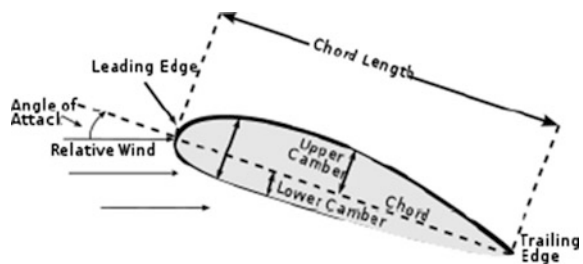
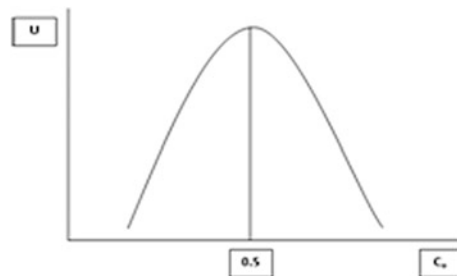


Fig. 2 Impulse load diagram



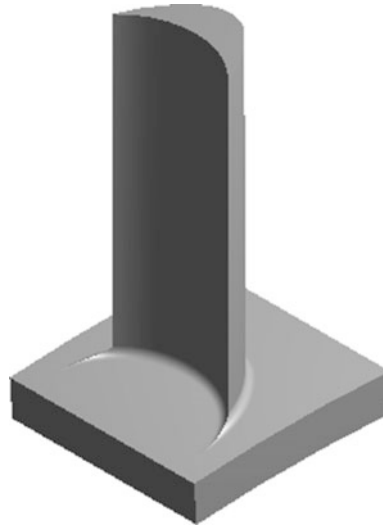


Fig. 3 Free standing blade model

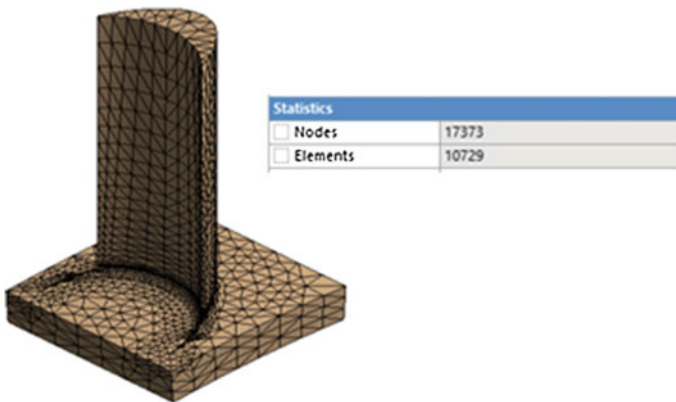


Fig. 4 Free standing blade meshed model

average sectional stress obtained at each section is 501.19 MPa and is as shown in Fig. 6. The variation of section stress shows the average stress from hub to tip is well within allowable gross stress of 522.6537 MPa. The peak stress at transition happens to be 1260 MPa for a fillet transition radius of 2 mm. One more iteration is carried out keeping transition radius as critical parameter. The next trial peak stress result is 1065 MPa for transition radius of 3 mm which is good enough to achieve $1e6$ fatigue cycles as per the design considerations and its stress distribution is as shown in Fig. 5. These two checks namely the gross yield section stress and peak

Fig. 5 Stress distribution near transition radius

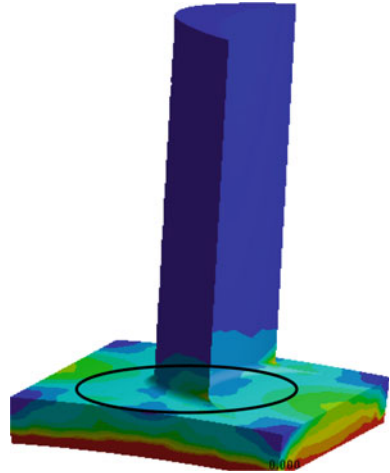
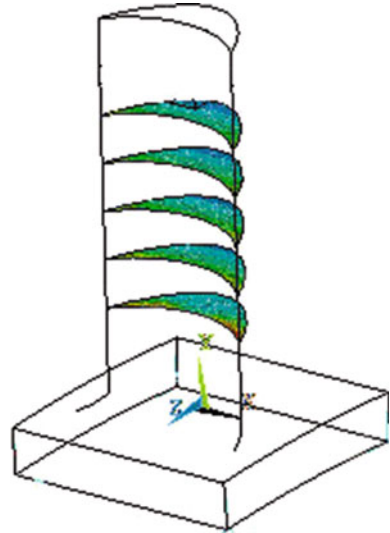


Fig. 6 Section stress distribution (Gross yield)



stress at blade hub are the two stress checks which is critical from stress point of view (Kyungkook Kim and Young Shin Lee 2014).

Mode Shape Identification and Separation Margin Evaluation

The free standing blade behaves like a cantilever beam fixed at one end and free at the other end. The first 5 modes namely bending, 1st Flip, 2nd Flip, Torsion and in plane modes are considered as critical modes for evaluation. The running speed harmonics i.e. $(X = \frac{N}{60})$, were N rated rpm excitations up to 10X is considered as critical for the wake forces leaving the airfoil for the analysis.

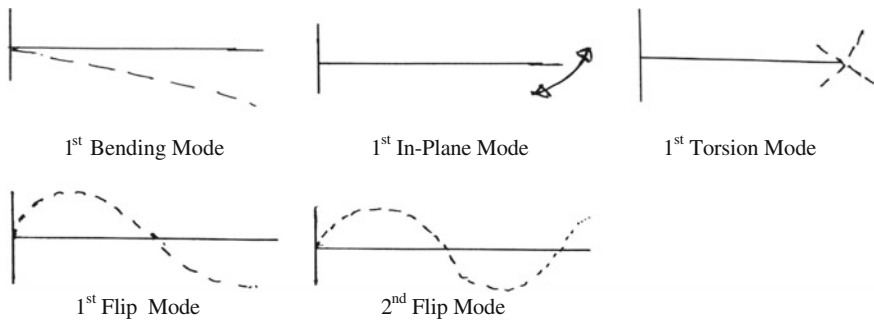


Fig. 7 First 5 modes of cantilever blade vibration (Yuan et al. 2015)

The Fig. 7 shows the mode shapes of a free standing blade. Here, the disk mode participation is not considered for the present study. However the Campbell diagram is drawn at rated rpm. Importance is given for the 1st Mode of blade vibration due to powerful excitations come out for the first 8 engine orders. If sufficient separation margins are not achieved the blade undergoes resonance and subjected to high cycle fatigue. Hence, tuning of the initial modes with high margin of safety becomes important. The stiffening of the blades due to centrifugal forces will increase the frequency, however, at hot condition the blade achieves saturation temperature during softening of blade takes place, leading to dip in frequency levels. The interaction of these two significant parameters are predominant in frequency evaluation of free standing blades. In order to understand the effect on natural frequencies of blade for free standing, stress stiffening and spin softening cases separately, the Campbell diagram is plotted. The Campbell diagram for first mode frequency (Ewins 2010; Bhat et al. 1996) lies between 20X and 25X as shown in Fig. 8 for natural frequency with zero load condition. The Excitor box indicates the separation margins as shown in Fig. 10.

With the stress stiffening effect considered the 1st mode frequency shifts with marginal increase in frequency by 2 %. Considering the gas load with thermal gradient the blade softening effect without stress stiffening calls for 1 % drop in frequency margins. Under Ideal condition the combined effect of stress stiffening and spin softening has to be considered. With both the effects being considered the Campbell diagram shown in Fig. 8 clearly indicates a margin of 5 % to left and 7 % to right and 20 % to top and 20 % to bottom margins.

Test Cases Performed Are

- a. Frequency evaluation for free standing blades with Stress Stiffening, Spin Softening, Combined Stress Stiffening and Spin Softening and without Stress Stiffening and Spin Softening effects for the first 3 modes.
- b. Campbell diagram for free standing blades with Stress Stiffening, Spin Softening, Combined Stress Stiffening and Spin Softening and without Stress Stiffening and Spin Softening effects.

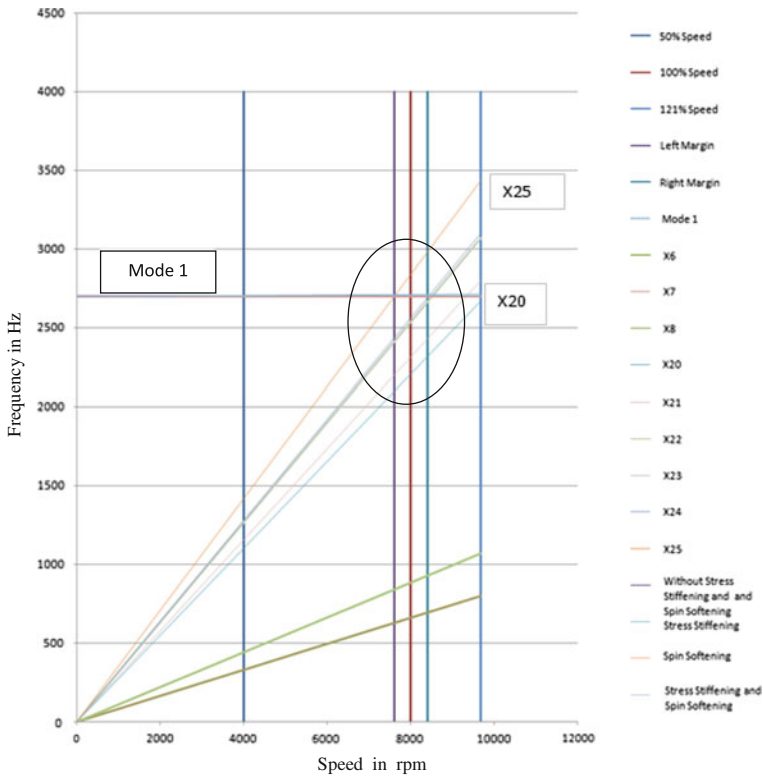


Fig. 8 Campbell diagram for free standing blade with stress stiffening, spin softening, combined stress stiffening and without stress stiffening and spin softening

- c. Frequency versus Speed analysis for Mode 1 for free standing blade with Stress Stiffening, Spin Softening, Combined Stress Stiffening and Spin Softening and without Stress Stiffening and Spin softening for zero speed, 50 % speed, 100 % speed and 121 % over-speed loads.
- d. Analysis of frequency separation margins in the Excitor box.

4 Results and Discussion

a. Modal Frequencies of Free Standing Blade for the Considered Test Cases Are

The Table 1 shows the results obtained after performing modal analysis for all the 4 test cases considered at various operating speeds for the first 3 modes and their frequency variations is analyzed in detail by plotting Campbell diagram as shown in Fig. 8.

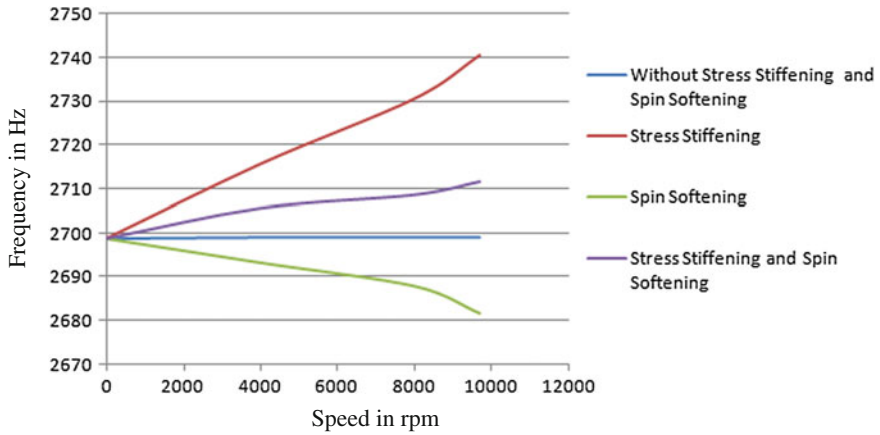


Fig. 9 Plot of mode 1 frequency variations for free standing blade with stress stiffening, spin softening, combined stress stiffening and spin softening and without stress stiffening and spin softening

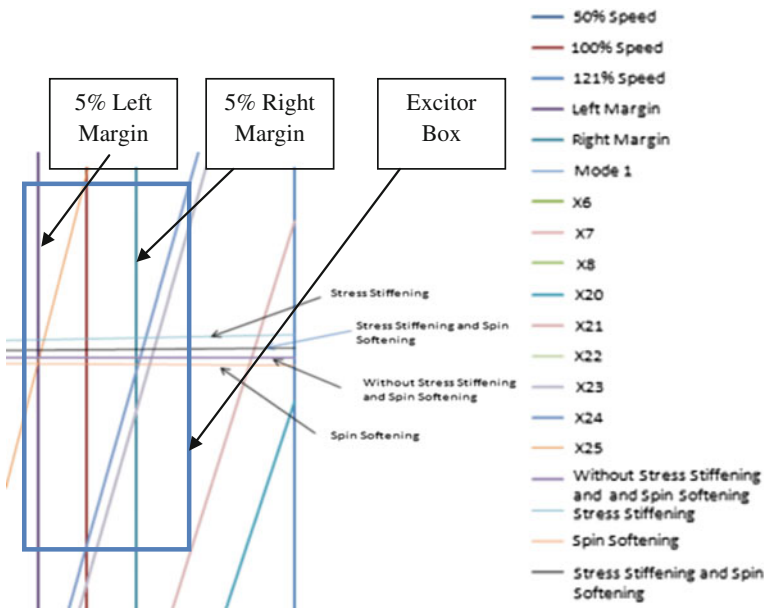


Fig. 10 Excitor box for free standing blade with stress stiffening, spin softening, combined stress stiffening and spin softening

Table 1 List of Modal frequencies for zero, 50, 100 and 121 % load conditions for first 3 Modes

Sl. no	Test case	Mode No	Operating speeds			
			0 rpm	4000 rpm	8000 rpm	9680 rpm
1	Free standing blade without stress stiffening and spin softening	Mode 1	2698.7	2699.1	2699.2	2699.3
		Mode 2	5049.8	5050.1	5050.2	5050.4
		Mode 3	9985.7	9985.8	9986.1	9986.3
2	Free standing blades with stress stiffening	Mode 1	2698.7	2715.7	2730.7	2740.6
		Mode 2	5049.8	5066.8	5081.6	5106.5
		Mode 3	9985.7	10002.7	10017.6	10042.2
3	Free standing blade with spin softening	Mode 1	2698.7	2693.2	2687.8	2681.6
		Mode 2	5049.8	5044.4	5039.1	5032.9
		Mode 3	9985.7	9980.4	9974.8	9968.7
4	Free standing blade with stress stiffening and spin softening	Mode 1	2698.7	2705.7	2708.7	2711.7
		Mode 2	5049.8	5056.8	5059.8	5062.8
		Mode 3	9985.7	9992.7	9996.2	9999.7

b. Campbell Diagram for Free Standing Blade

The Campbell diagram shown in Fig. 8 inference that the Mode 1 frequency lies between X20 and X25 excitations for all the cases taking separation margins as 5 % to left and 5 % to right of operating speed 8000 rpm. The highlighted area is the Excitor box which is the area of prime importance which shows the frequency separation margins and mode excitations passing through it, which is analyzed in detail in Fig. 10. The above Campbell diagram shows that up to X24 excitations from initial X1 excitation, the blade is not subjected to any resonance. In practice usually up to X8 excitations, the blades are checked for resonance which has been well achieved in this case and hence the blade is safe.

c. Frequency Versus Speed Analysis for Mode 1

Since from the above Campbell diagram we see that almost all the excitations up to X24 pass within the 1st Mode for the assumed operating speed of 8000 rpm, it calls for in depth analysis of the frequency variations for the test cases considered. Hence, to identify these modal frequency variations between the test cases of Stress Stiffening, Spin Softening, Combined Stress Stiffening and Spin Softening and without Stress Stiffening and Spin Softening test cases, the analyzed Modal frequencies for all load cases for Mode 1 are tabulated below in Table 2 for the better understanding and the frequency variations are as shown in Fig. 9.

The above plot shows that there is a minimum difference of 5 % between the frequencies of stress stiffening and spin softening for Mode 1 and how they vary with respect to the case when they both are applied together and are compared to the case for without Stress Stiffening and Spin Softening. The Fig. 9 shows that stress stiffening increases the frequency with increase in speed and spin softening decreases the frequency with increase in speed accounting to the case for without

Table 2 List of modal frequencies for zero, 50, 100 and 121 % load conditions for 1st Mode

Speed in rpm	Frequencies in Hz			
	Without stress stiffening and spin softening	Stress stiffening	Spin softening	Stress stiffening and spin softening
0	2698.7	2698.7	2698.7	2698.7
4000	2699	2715.7	2693.2	2705.7
8000	2699	2730.7	2687.8	2708.7
9680	2699	2740.6	2681.6	2711.7

stress stiffening and spin softening passing in between these two. Whereas the combined effect of Stress Stiffening and Spin Softening which is the ideal case in practical, passes in between the cases of Stress Stiffening and without Stress Stiffening and Spin Softening.

d. Analysis of Frequency Separation Margins in the Excitor Box

The Excitor box shown in Fig. 10 is a detailed representation of the frequency excitations passing over the modal frequencies in the considered operating speed range i.e. from 95 % speed to 105 % speed and is derived from Campbell diagram. From the above figure we see that there is an increase in the operating margin to 7 % at right, 20 % at top, 20 % to bottom and 5 % to left as seen in the Excitor box upon subjecting the blade to stress stiffening and spin softening, as it would cause increase in the frequency for stress stiffening case and decrease in frequency for spin softening case respectively.

5 Conclusion

- Mechanical Integration in airfoil design in gas turbines was achieved with a smooth transition radius of 3 mm to minimize localized stresses to 310.12 MPa which is well within the gross yield strength.
- Safe gross yield strength of 522.6537 MPa was achieved from hub to tip as per design considerations.
- The blade was analyzed for separation margins along with Excitor box using Campbell diagram which shows a minimum separation margin of 5 % to left, 7 % right, 20 % to top and 20 % to bottom of operating speed range for mode 1 frequency was achieved.
- The role of Spin Softening and Stress Stiffening on the blade frequency evaluation was studied and results show that there is 1–3 % decrease or increase in frequency as seen from the Excitor box which is less in magnitude as this is the case study for a HP small blade whereas in LP Compressor as the blade length is longer than HP there is a significant increase in % variations for the above cases.
- A customized methodology for aero-structure interaction in free standing blades was achieved.

- f. From Excitor box it concludes that the % variations of frequencies for the considered test cases are less than 1 % for zero speed, less than 2 % for 50 % load (4000 rpm), less than 2.5 % for 100 % load (8000 rpm) and less than 3 % for 121 % load (9680 rpm) for a HP compressor stage blade.
- g. Using the other parameters like chord length, Leading edge and thickness of airfoil the frequency variations can be obtained for a maximum percentage of 1–5 %.

References

- Bhat, M. M., Ramamurti, V., & Sujatha, C. (1996). Studies on the determination of natural frequencies of industrial turbine blades. *Journal of Sound and Vibration*, 196(5), 681–703.
- Bazhenov, V. A., Gulyar, A. I., Piskunov, S. O., & Andrievskii, V. P. (2013). Design life assessment of the blade root of a gas turbine unit under thermo mechanical loading. *Journal of Strength of Materials*, 45(3), 329–339.
- Ewins, D. J. (2010). Control of vibration and resonance in Aero engines and rotating machinery—An overview. *International Journal of Pressure Vessels and Piping*, 87, 504–510.
- Huang, W. (1981). Free and forced vibration of closely coupled turbomachinery blades. *AIAA Journal*, 19(7), 918–924.
- Kim, K., & Lee, Y. S. (2014). Model characteristics and fatigue strength of compressor blades. *Journal of Mechanical Science and Technology*, 28(4), 1421–1429.
- Lebele- Alawa, B. T., Hart, H. I., Ogaji, S. O. T., & Probert, S. D. (2008). Rotor Blades profile influence on a gas turbine's compressor effectiveness. *Journal of Applied Energy*, 85, 494–505.
- Madhavan, S., Jain, R., Sujatha, C., & Sekhar, A. S. (2014). Vibration based damage detection of rotor blades in a gas turbine engine. *Journal of Engineering Failure Analysis*, 46, 26–39.
- Shankar, M., Kumar, K., & Ajit Prasad, S. L. (2010). T-root blades in a steam turbine rotor: A case study. *Journal of Engineering Failure Analysis*, 17, 1205–1212.
- Tulsidas, D., & Shantharaja, M. (2015). Effect of taper and twisted blade in steam turbines. *International Journal of Science Technology and Management*, 4(1), 1537–2394.
- Yuan, J., Allegri, G., Scarpa, F., Rajasekaran, R., & Patsias, S. (2015). Novel parametric reduced order model for aeroengine blade dynamics. *Journal of Mechanical Systems and Signal Processing*, 62–63, 235–253.

Appraisalment of Mass Customization Capability Level Using Multi-grade Fuzzy Approach

Jayant K. Purohit, M.L. Mittal, Milind Kumar Sharma
and Sameer Mittal

Abstract The manufacturing organizations around the globe have been observing a paradigm shifting from mass production to mass customization (MC). Mass customization capability (MCC) is the ability of a firm to produce varieties of customized products quickly, on a large scale and at a cost comparable to mass-production through flexible production processes and responsive supply chain. The goal of this paper to report a existing mass customization capability level (MCCL) appraisalment of Indian bicycle manufacturing firm using multi-grade fuzzy approach. Through this study, a MCCL measurement model integrated with multi-grade fuzzy approach was designed. After the computation of MCCL index, the areas for improvement have been identified to adopt and implement mass customization strategy in the case firm. The approach contributed in this paper could be employed as appraisalment equipment for estimating an organization's capability to turn out to be a mass customizer.

Keywords Mass customization · Fuzzy approach · Mass customization capability level index

J.K. Purohit (✉) · M.L. Mittal
Department of Mechanical Engineering, Malaviya National
Institute of Technology, Jaipur, India
e-mail: Jkpurohit17@gmail.com

M.K. Sharma
Department of Production and Industrial Engineering,
MBM Engineering College, Jodhpur, India

M.K. Sharma
Faculty of Engineering and Architecture, JNV University,
Jodhpur, India

S. Mittal
Department of Industrial Engineering & Management System
Engineering, West Virginia University, West Virginia, USA

1 Introduction

In this vibrant trade situation with escalating speed of globalization, Indian manufacturing industries have to battle with robust international competition, varying customer demands and varying conditions related to adoption of novel manufacturing practices and information technologies. Globalization has converted the aspect of the competition among many industries dynamically moving ahead from upholding steady pace, unchanging oligopoly market era to hyperactive competitive environments. The mass customization strategy has been adopted by an increasing number of manufacturing firms to strengthen their operational capabilities to attain competitive advantages through product differentiation and cost advantages. Mass Customisation is a suitable approach to link the gap in the midst of mass production and personalized customer requirements (Schuh et al. 2007). According to Chen et al. (2006), the modern manufacturing industries have been observing a change in the manufacturing pattern, from craft production to mass production and mass production to mass customization (MC). By and large MC concept has been associated to the capacity of the manufacturer to propose high volume of tailored products using floppy processes, with manufacturing costs comparable to those of mass production produce (Duray 2002; DaSilveira et al. 2001; Tu et al. 2004; Kaplan et al. 2006) where Piller (2004) define MC as Customer co-design process of products and services, which meet the needs of each individual customer within a fixed solution space, characterized by established but still flexible and responsive processes. According to Tu et al. (2004) mass customization capability is a firm's ability to make products that meet diverse customer requirements speedily at a price that is parallel to bulk-produced goods. The measurement of mass customization capability level achieves significance as it is a gauge of firm's likeliness to adopt MC strategy. A theoretical model for MCCL measurement has been developed from the literature review. The ratings of the experts have been gathered for performing the MCCL measurement. Multi-grade fuzzy approach has been employed for calculation of MCCL followed by detection of areas of improvement.

The succeeding sections are formed as follows. The Sect. 2 presents a review of relevant organization of literature on firms' mass customization capability level appraisal and fuzzy logic. Then the Sect. 3 proposes a conceptual framework development and case study. Managerial implications, discussion and conclusions are drawn in the Sect. 5 of the paper.

2 Literature Review

The literature has been reviewed from the perspective of mass customization capability and its appraisal and fuzzy logic.

2.1 Literature Review on Mass Customization Capability and Its Appraisalment

MCC relates to the ability of a firm to reliably put forward a eminent quantity of diverse product varieties in a fairly immense market that demands tailor-made products without compromising in terms of cost, delivery and quality (Liu et al. 2006; Tu et al. 2001). Several researchers have dug into the consequences of assorted enablers of mass customization practices on MCC of the firm through empirical observation. For instance, Duray (2002) classified manufacturer on the basis of customer participation in design process to set degree/level of mass customization and application of modularity in product design used to explore economies and responsiveness in production. Prasad (2000) Describes intelligent information system framework for incorporated product development can offer a configuration potential to customize sales orders based on choices. Tu et al. (2004) build a framework to relate customer closeness; modularity based manufacturing practices and mass customization capability. They found statistically noteworthy and encouraging relationships between customer closeness, modularity-based manufacturing practices, and mass customization capability. Huang et al. (2008) empirically investigate the relationship between internal and external learning, effective process implementation and mass customization capability. Kristal et al. (2010) suggest quality management practices as one of the prospective factors affecting MC capability. Liu et al. (2010) notice influential relationship between firms mass customization capability and managerial practices to reduce ambiguity in demand forecasting and delivery of product where disclose that new product development information technology (NPDIT) and supplier collaboration IT are related to MCC, either directly or indirectly through modular product design. Lai et al. (2012) establish that supply chain integration straight forwardly progress MCC, and that in-house integration too has an encouraging indirect effect on MCC through customer incorporation. Observational studies have ascertained noteworthy direct effects of product modularity (Duray 2002; Liu et al. 2010; Tu et al. 2004) and supply chain integration (Huang et al. 2008; Kristal et al. 2010; Lai et al. 2012) on MCC. Kumar (2004) intend a metrics for mass customization to determine modularity in product design and degree of Customization. Aigbedo (2007) offers a framework for estimating the appropriate level of mass customization that is worthy to meet customers' necessities in a cost effective approach. Li et al. (2010) analyze empirically the relationship among six production-related affecting factors and level of mass customization. Bruun et al. (2014) presents a visual design tool—the Interface diagram—which aims to support the engineering process of developing modularity in complex product systems in mass customization environment. Daaboul et al. (2015) advocates that the positions of product differentiation points and customer order decoupling points are to be defined simultaneously as MC levers.

Lampel et al. (1996) use a gamut from pure customization to pure standardization, where pure customization draws the condition when customization is present in all parts of the value chain including design, fabrication, assembly, and so forth. Tailored customization pertains to the state when an existing design is modified to certain customers' desires, after which the product is gathered and in some cases parts are manufactured to customers' stipulation. The case when standard modules are assembled to customers' orders is denoted customized standardization in Lampel's framework. Finally, segmented standardization pertains to distinguished ways of packaging; distributing and exposing standard products to customers, without customer participation in either engineering or production.

2.2 Literature Review on Fuzzy Logic

The fuzzy logic approach is established on human logic and takes benefit of conceptual Know-how without limits. Some of the concepts of fuzzy logic include fuzzy set, lingual variables, probability distribution and fuzzy if then rules. The proper choice of linguistic variables is more important (Vinodh and Chintha 2011; Mishra et al. 2013). The perspective of the experts needs to be ascertained using fuzzy numbers and membership functions. The membership functions are used for translating the linguistic variables into fuzzy numbers (Singh et al. 2006). Azadeh et al. (2012) employs fuzzy simulation and conventional simulation to model and show perceived improvement in a manufacturing system.

3 Development of Conceptual Model

For an enterprise having marginally mass customization practice, it should acquire a number of eminent mass customization enablers. It is, consequently, a vital issue for appraising organizations mass customization capability level of and to establish whether an organization is ready for adopting MC strategy in turbulent market condition fruitfully. So organizations have to look for approaches to adopt MC practices and establish the extent of MCC they can achieve. For MCC appraisal, in order to settle on MCC prospectives, some measurement index or scale is in fact necessary.

The MC practices and concepts are basic elements to the MC measurement index. Broad literature analysis on diverse MC models and related appraisal policy; an incorporated model for MCC appraisal system has been planned and adopted in the current lesson which consists of three level MC indices as provided in Table 1. The model contains three levels of MCC. Level 1 consists of Three MC enablers; Level 2 consists of ten MC attributes and Level 3 consists of a twenty eight MC criterions.

Table 1 Conceptual model for Appraisalment of mass customization capability level

S.no.	Enabler	Criteria	Attributes
1	Supply chain integration	Supplier integration	Supplier lead time reduction
			Collaborative product design with supplier
		Customer integration	Customer learning
			Customer knowledge acquisition
			Collaborative product design with customer
		Internal integration	Data integration
			Integrative inventory management
			Cross functional teams for process improvement
			Cross functional teams for product development
		Information integration	Enterprise resource planning
			Web based interactive system
			Integrated logistics information system
		2	Manufacturing Methodology
Process modularity			
Dynamic teaming			
Postponement	Form postponement		
Time based Manufacturing technologies	Just in time supply chain		
	Cellular manufacturing		
	Preventive maintenance		
3	Digital Manufacturing	Advanced Manufacturing technology	CNC machines
			Automated inspection and testing
			Automated material handling
			Automated storage and retrieval system
			Flexible manufacturing system
		IT-enabled manufacturing process technology	Computer aided manufacturing
			Computer integrated manufacturing
		IT-enabled product development technology	Computer aided design
			Computer aided engineering

The aforementioned model has been case studied in an Indian Bicycle manufacturing firm (XYZ) at northern India. Mass customization capability of the said industry has been analyzed and interpreted from managerial viewpoint.

Appraisalment of mass customization capability level using multi-grade fuzzy approach has been illustrated in later sections.

4 Appraisalment of MCC Using Fuzzy Logic

Organization's MC applications are the main achievement gauges that guarantee essential prospective power and competitiveness to counter suitably towards numerous business modifications in harmony with consumer's necessity. Therefore, MC practices have to offer ways for MCC measurement for a particular organization. The MCC index can be defined as amalgamation of MC practices strength levels. This means to what amount assorted MC enablers are being executed properly. The fuzzy MCC index appraisal system is a stepladder structural framework; it includes various fuzzy broad appraisal techniques to be employed. The calculation is to be launched from subordinate layer (MC criteria) to the center layer (MC attributes); then lastly to apex layer (MC enablers) to attain requisite MCC index. The thought of stepladder structure study with two diverse stages has been espoused in the current study. The initial component is to develop an MCC model; lastly, to calculate the MCC index in vague perspective.

- Step 1 By employing the information obtained from literature examination, a MCC index appraisal framework has been created by investigating business environment, competitive bazaar situation, consumers' restriction and professional's outlook by a survey. It has been premeditated as a three-level structure. The main intention i.e. MCC, inclined by a number of MC enablers/providers, that have been positioned at the uppermost level of the ladder. The foremost goal has been separated into three scopes: Supply chain integration, manufacturing methodology and digital manufacturing.
- Step 2 A working group of decision-makers is to be created. There is a working group of four decision-makers who are accountable for appraising the MCC index under three MC enablers for a particular manufacturing industry.
- Step 3 professional's outlook are to be strained from the decision-makers for suitable ratings and significance weights of diverse MC metrics. The appraisalment group has to calculate combined fuzzy weight W_{ij} and W_i . Here W_{ij} is the combined fuzzy priority weight of j th MC criteria (which is under i th attribute); W_i be the weight of i th MC attribute.
- Step 4 The MCC index of the company is characterized by I . It is the multiplication of the overall appraisal element (R) and the overall weight (W). The relation for MCC index is shown as follows:

$$I = W \times R$$

The MCC index appraisal is done at three steps: as primary appraisal, secondary and tertiary appraisal. The computation is executed in a structural order from last level to middle level and finally at top level i.e. to attain overall MCC index. The appraisalment has been divided into five levels of mass customization as provided by Lampel et al. because all MC factor involves fuzzy fortitude. $I = \{10, 8, 6, 4, 2\}$ (8–10 correspond to ‘Pure Customization’, 6–8 correspond to ‘Tailored Customization’, 4–6 correspond to ‘Customized Standardization’, 2–4 correspond to ‘Segmented Standardization’ and less than 2 correspond to ‘Pure Standardization’). Four professionals joined in a conversation meeting for MCC appraisal. Table 2 shows the single factor appraisal and weights granted by professionals.

Table 2 Single factor appraisalment and weights provided by experts

I_i	I_{ij}	I_{ijk}	E1	E2	E3	E4	W_{ij}	W_i	W		
I_1	I_{11}	I_{111}	6	5	5	6	0.4	0.2	0.3		
		I_{112}	6	4	6	5	0.6				
	I_{12}	I_{121}	5	6	7	5	0.3	0.2			
		I_{122}	5	6	5	7	0.3				
		I_{123}	4	3	4	5	0.4				
	I_{13}	I_{131}	6	6	6	5	0.3	0.25			
		I_{132}	4	5	7	6	0.2				
		I_{133}	5	7	6	6	0.25				
		I_{134}	7	6	6	7	0.25				
	I_{14}	I_{141}	7	8	6	7	0.35	0.35			
		I_{142}	5	3	4	3	0.4				
		I_{143}	6	7	6	5	0.25				
	I_2	I_{21}	I_{211}	7	8	7	6	0.4		0.5	0.3
			I_{212}	6	5	7	5	0.4			
I_{213}			6	6	5	7	0.2				
I_{22}		I_{221}	6	5	6	7	1	0.15			
I_{23}		I_{231}	8	7	7	7	0.3	0.35			
		I_{232}	4	5	5	5	0.4				
		I_{233}	7	7	8	7	0.3				
I_3	I_{31}	I_{311}	8	7	9	7	0.3	0.4	0.4		
		I_{312}	6	7	7	7	0.1				
		I_{313}	6	6	5	6	0.1				
		I_{314}	5	5	6	6	0.1				
		I_{315}	6	6	4	6	0.4				
	I_{32}	I_{321}	5	6	6	7	0.4	0.3			
		I_{322}	5	7	5	6	0.6				
	I_{33}	I_{331}	5	6	5	7	0.5	0.3			
		I_{332}	7	5	6	6	0.5				

4.1 Primary Appraisalment Calculation

The computation concerning to 'Supplier Integration' criterion is revealed as follows:
 Weights concerning to 'Supplier Integration' criterion $W_{11} = (0.4, 0.6)$
 Appraisalment vector pertaining to 'Supplier Integration' criterion is specified by R_{11}
 Index pertaining to 'Supplier Integration' criterion is specified by

$$I_{11} = W_{11} \times R_{11}$$

$$R_{11} = \begin{pmatrix} 6 & 5 & 5 & 6 \\ 6 & 4 & 6 & 5 \end{pmatrix}$$

$$I_{11} = (6, 4.4, 5.6, 5.4)$$

Using the same principle, the index pertaining to various MC criteria have been derived $I_{12} = (4.6, 4.8, 5.2, 5.6)$; $I_{13} = (5.6, 6.05, 6.2, 5.95)$; $I_{14} = (5.95, 5.75, 5.2, 4.9)$; $I_{21} = (6.4, 6.4, 6.6, 5.8)$; $I_{22} = (6, 5, 6, 7)$; $I_{23} = (6.1, 6.2, 6.5, 6.2)$; $I_{31} = (6.5, 6.3, 6.1, 6.4)$; $I_{32} = (5, 6.6, 5.4, 6.4)$; $I_{33} = (6, 5.5, 5.5, 6.5)$.

4.2 Secondary Appraisalment Calculation

The computation concerning to 'Supply Chain Integration' enabler is given by:
 $I_1 = W_1 \times R_1$
 Weight concerning to 'Supply Chain Integration' enabler is given by: $W_1 = (0.2, 0.2, 0.25, 0.35)$
 Appraisalment vector pertaining to 'Supply Chain Integration' enabler is specified by: R_1
 Index pertaining to 'Supply Chain Integration' enabler is specified by: $I_1 = (5.6025, 5.365, 5.53, 5.4025)$

Using the similar rule, the subsequent indices have been resulting for left over Mass customization enablers.

$$I_2 = (6.235, 6.12, 6.475, 6.12); I_3 = (5.9, 6.15, 5.71, 6.43)$$

$$R_1 = \begin{pmatrix} 5.6025 & 5.365 & 5.53 & 5.4025 \\ 6.235 & 6.12 & 6.475 & 6.12 \\ 5.9 & 6.15 & 5.71 & 6.43 \end{pmatrix}$$

$$R = \begin{pmatrix} 6 & 4.4 & 5.6 & 5.4 \\ 4.6 & 4.8 & 5.2 & 5.6 \\ 5.6 & 6.05 & 6.2 & 5.95 \\ 5.95 & 5.75 & 5.2 & 4.9 \end{pmatrix}$$

4.3 Tertiary Appraisalment Calculation

The significance of MCC index of XYZ has been computed as follows:

On the whole weight $W = (0.3, 0.3, 0.4)$.

Overall appraisalment vector given by R .

4.4 Mass Customization Capability Index $I = W \times R$

$$I = (5.91125, 5.9055, 5.8855, 6.02875)$$

$$I = 1/4(5.91125 + 5.9055 + 5.8855 + 6.02875) = 5.93275 \in (4, 6)$$

5 Results and Discussions

Supported on the appraisalment of MCC, MCC index calculated by means of multi-grade fuzzy approach for XYZ by-cycle manufacturing company is found to be 5.93. This indicates that XYZ having the capabilities to adopt strategies of mass customization with customized standardization. The index close to 6 advocates that firm could attain tailored customization level if it works on few areas of mass customization attributes. Some of the areas identified for MCC improvement.viz Web based Interactive System, Collaborative product design with customer and supplier, Application of Cellular Manufacturing system and Flexible Manufacturing system and automated storage and retrieval system.

References

- Aigbedo, H. (2007). An assessment of the effect of mass customization on suppliers, inventory levels in a JIT supply chain. *European Journal of Operational Research*, 181(2), 704–715.
- Azadeh, A., Raofi, Z., Haghnevis, M., & Madadi, M. (2012). A unique fuzzy simulation approach for concurrent improvement of customer satisfaction in integrated information and production processes with ambiguity. *Concurrent Engineering*, 20(4), 287–299.
- Bruun, H. P. L., Mortensen, N. H., & Harlou, U. (2014). Interface diagram: Design tool for supporting the development of modularity in complex product systems. *Concurrent Engineering*, 22(1), 62–76.
- Chen, J. C. H., Parker, L. J., & Lin, B. (2006). Technopreneurship in Native American businesses: current issues and future trends with a case study. *International Journal of Management and Enterprise Development*, 3(1/2), 70–84.
- Daaboul, J., Da Cunha, C., Le Duigou, J., Novak, B., & Bernard, A. (2015). Differentiation and customer decoupling points: An integrated design approach for mass customization. *Concurrent Engineering*, 1063293X15589767.

- DaSilveira, G., Borenstein, D., & Fogliatto, F. S. (2001). Mass customization: Literature review and research directions. *International Journal of Production Economics*, 72(1), 1–13.
- Duray, R. (2002). Mass customization origins: mass or custom manufacturing? *International Journal of Operations & Production Management*, 22(3), 28–314.
- Huang, X., Kristal, M. M., & Schroeder, R. G. (2008). Linking learning and effective process implementation to mass customization capability. *Journal of Operations Management*, 26(6), 714–729.
- Kaplan, A. M., & Haenlein, M. (2006). Toward a parsimonious definition of traditional and electronic mass customization. *Journal of Product Innovation Management*, 23(2), 168–182.
- Kristal, M. M., Huang, X., & Schroeder, R. G. (2010). The effect of quality management on mass customization capability. *International Journal of Operations & Production Management*, 30(9), 900–922.
- Kumar, A. (2004). Mass customization: metrics and modularity. *International Journal of Flexible Manufacturing Systems*, 16(4), 287–311.
- Lai, F., Zhang, M., Lee, D., & Zhao, X. (2012). The impact of supply chain integration on mass customization capability: An extended resource-based view. *IEEE Transactions on Engineering Management*, 59(3), 443–456.
- Lampel, J., Mintzberg, H. (1996). Customizing customization. *Sloan Management Review Fall*, 38, 21–30.
- Liu, G., Shah, R., & Schroeder, R. G. (2010). Managing demand and supply uncertainties to achieve mass customization ability. *Journal of Manufacturing Technology Management*, 21(8), 990–2010.
- Liu, G. J., Shah, R., & Schroeder, R. G. (2006). Linking work design to mass customization: A sociotechnical systems perspective. *Decision Sciences*, 37(4), 519–545.
- Mishra, S., Datta, S., & Mahapatra, S. S. (2013). Grey-based and fuzzy TOPSIS decision-making approach for agility evaluation of mass customization systems. *Benchmarking: An International Journal*, 20(4), 440–462.
- Piller, F. T., Moeslein, K., & Stotko, C. M. (2004). Does mass customization pay? An economic approach to evaluate customer integration. *Production Planning & Control*, 15(4), 435–444.
- Prasad, B. (2000). Converting computer-integrated manufacturing into an intelligent information system by combining CIM with concurrent engineering and knowledge management. *Industrial Management & Data Systems*, 100(7), 301–316.
- Schuh, G., Baessler, E., & Meier, J. (2007). An evaluation method for the identification of flexible production technologies for Mass Customisation in the automotive industry. *International Journal of Manufacturing Technology and Management*, 10(4), 347–359.
- Singh, R. K., et al. (2006). Lean tool selection in a die casting unit: A fuzzy-based decision support heuristic. *International Journal of Production Research*, 44(7), 1399–1429.
- Tu, Q., Vonderembse, M. A., & Ragu-Nathan, T. S. (2001). The impact of time-based manufacturing practices on mass customization and value to customer. *Journal of Operations Management*, 19(2), 201–217.
- Tu, Q., Vonderembse, M. A., Ragu-Nathan, T. S., & Ragu-Nathan, B. (2004). Measuring modularity-based manufacturing practices and their impact on mass customization capability: A customer-driven perspective. *Decision Sciences*, 35(2), 147–168.
- Vinodh, S., & Chinthia, S. K. (2011). Leanness assessment using multi-grade fuzzy approach. *International Journal of Production Research*, 49(2), 431–445.

Analysis of Solar Ejector–Jet Refrigeration System Using Eco-Friendly Material R1234yf

Gaurav and Raj Kumar

Abstract Air-conditioning of living spaces is indispensable for human beings in the modern life. Ejector cycles are very reliable and simple but their energy efficiency is very low and, therefore, its affect after combining with solar energy can facilitate better system performance. Currently, the vapor compression air-conditioning system uses R134a in the air-conditioning system that is one of the cause of the global warming. In present work, a low global warming potential (GWP) refrigerant material R1234yf is used in the solar ejector-jet refrigeration cycle instead of R134a and its affect on coefficient of performance, refrigerating effect is investigated. Refrigerant R1234yf working fluids provides good energy efficiency and environmental option for solar ejector-jet compression systems and its cycle simulation showed that the proposed ejector-jet cycle can provide energy savings if it is supplied with solar energy.

Keywords Global warming potential · R1234yf · Energy efficiency · Ejector-jet cycle

1 Introduction

The ejector-jet refrigeration is similar to conventional refrigeration cycles, with an evaporator, a compressor device, a condenser and refrigerant as basic system components. Instead of mechanical compression device, the system characteristically employs an ejector and pump to compress the refrigerant to the condenser pressure level. One of the simplest approaches for using thermal energy in cooling is by the use of ejector cycles (Eames et al. 1995). Ejector cycles are very reliable, low maintenance, freedom from vibration, simple, and have limited applications in

Gaurav (✉) · R. Kumar

Department of Mechanical Engineering, YMCA University of Science & Technology,
Faridabad 121006, Haryana, India
e-mail: gaurav.citm@gmail.com

© Springer India 2016

D.K. Mandal and C.S. Syan (eds.), *CAD/CAM, Robotics and Factories of the Future*, Lecture Notes in Mechanical Engineering,
DOI 10.1007/978-81-322-2740-3_80

831

the field of air-conditioning. However, their energy efficiency is about 0.2 or less. It is expected that combining the ejector cycle with solar energy can facilitate higher energy efficiency. At present, the vapor compression system is mainly used in the air-conditioning and refrigeration and it is desirable to combine the solar energy-driven system with the vapor compression system for energy saving as well as to provide a comfortable environment. Environmental sustainability concerns such as global warming and the depletion of fossil fuels have led to shift the focus on the use of renewable energy, which has a very little impact on environment. Cizungu et al. (2001) theoretically compared the performance of a jet compression refrigeration system using R123, R717, R152a, and R134a and established that R134a refrigerant is the most suitable refrigerant for vapor compression refrigeration system not only from better thermodynamic properties consideration but also from environmental consideration. Vidal and Colle (2010) theoretically evaluated a solar driven jet-compression refrigeration system and showed the effects of the collector area and the storage tank using R141b as refrigerant for obtaining a thermal capacity of 10.5 kW. Yu et al. (2007) conducted a theoretical study using R142b refrigerant with the refrigerant sub cooling after the expansion valve, by another liquid-gas ejector. The study established that the performance may be improved up to 10 % as compared to simple jet compression refrigeration cycles. Sankarlal and Mani (2007) carried out an experimental investigation of a jet-compression refrigeration system using refrigerant R717 as working fluid. The influence of the various parameters such as area, compression and expansion ratio on the performance of the system was studied for an air conditioning application with a cooling load of less than 1.0 kW. Boumaraf and Lallemand (2009) worked out a software for the simulation and evaluated the performance of a jet-compression refrigeration system using refrigerant R142b and R600a. It was found that R142b had better thermodynamic performance than R600a mainly due to the molecular weight of the former being higher than the latter. Although the single jet-compression refrigeration system has an interesting range of applications, but its compression ratios is limited to 4.0, reducing its application limited to air conditioning only. At the same time, the COP values vary from theoretical value of 0.11 to 0.6 for the parameters range of temperature between 70 °C and 90 °C in the generator, 20 °C–50 °C in the condenser and 5 °C in the evaporator. Arsie et al. (2007) proposed to combine the ejector cycle with the vapor compression cycle by using the cascade cycle with an ejector cycle working at high temperature and a vapor compression cycle working at low temperature. Yu and Du (2010) worked for a single jet compression cycle behavior with R143a as refrigerant under designed conditions and a comparison was made of the proposed system with a subcritical condition, one under the similar operating conditions with R134a refrigerant.

Combining an ejector thermal compressor that operates best at steady state with a variable solar heat source as the generator poses difficulties. Rare studies were found that considered the dynamics of this coupling. Most of researchers worked on steady state analysis under various design conditions. Through a lot of work had already been done on thermo economic analysis of ejector—jet refrigeration system

(Nguyen et al. 2001; Sun 1997, 1999) but only few researchers worked using refrigerant R1234yf in vapor jet refrigeration system. The ejector cycle water as working fluid requires a large specific volume and consequently a large piping volume which is not desirable in many applications in air-conditioning. In this work, a solar ejector-jet refrigeration system is investigated for providing higher energy efficiency using low GWP refrigerant R1234yf.

2 Materials and Methods

As far as combined solar ejector–jet vapor compression refrigeration system is concerned, the most suitable application is in air conditioning because of the relatively higher evaporator temperatures required than for refrigeration applications. The search of new working fluids with negligible impact on environment has not ended and, therefore, hydrocarbons working fluids R1234yf provides good energy efficiency and environmental option for ejector- jet compression systems although they will require carefully developed security protocols due to their flammability.

An ejector is a device in which a higher pressure fluid (called primary fluid) is used to induce a lower pressure fluid (called secondary fluid) into the ejector for mixing. Fluids from these two streams mix together and discharge to a pressure that lies in between the pressures of primary fluid and secondary fluid (Fig. 1). In an ejector refrigeration cycle, the compressor used in a vapour compression system is replaced by ejector and a pump. The refrigerant R1234yf is cooled down in the condenser and separated into two parts. One stream goes into the evaporator through the expansion valve and the other is pumped back to the generator. Ejector refrigeration system has inherent advantage of no moving parts and hence less maintenance needed in operation. The suffix g, e, c refers to generator, evaporator and condenser respectively (Fig. 2).

Fig. 1 Solar ejector-jet refrigeration system

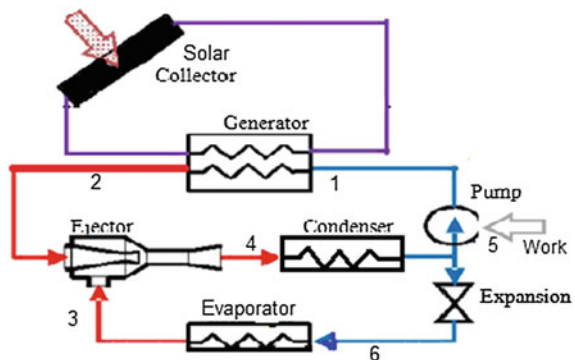
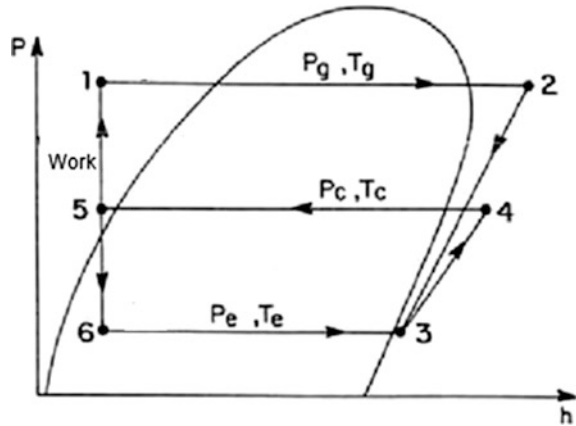


Fig. 2 P-h diagram of solar ejector-jet refrigeration system



3 Analysis

Few factors have been selected same as that of available for R134a for the analysis of refrigerant R1234yf. The analysis of the solar-driven ejector refrigeration system was performed with the following conditions for simulation:

- [1]. The incident solar radiation is 600 W/m^2 , and a double-glazed flat-plate solar collector is used with an area of 4.2 m^2 , Collector heat removal factor = 0.8 and heat loss coefficient = $3.5 \text{ W/m}^2 \text{ K}^1$. The maximum midsummer solar output of 6.5 kWh was obtained.
- [2]. Pump work input is negligible in comparison to energy supplied in generator.
- [3]. The exit temperature of the solar collector is assumed to be $5 \text{ }^\circ\text{C}$ above the generating temperature.
- [4]. The cooling capacity required for air-conditioning is 1.5 kW.
- [5]. Compression efficiency = 0.7.
- [6]. Water is circulated between the solar collector and the generator for heat transfer.
- [7]. Temperature of $24 \text{ }^\circ\text{C}$ is required to be maintained in the air-conditioned space.
- [8]. Ambient air temperature is $32 \text{ }^\circ\text{C}$ which also is used as the reference temperature for the analysis.
- [9]. Mass flow rate of R1234yf through evaporator is 0.0136 kg/s and generator is 0.0389 kg/s at $15 \text{ }^\circ\text{C}$ evaporator temperature and $80 \text{ }^\circ\text{C}$ generator temperature. Mass flow rate in evaporator varies with generator temperature (Dai et al. 2012).
- [10]. Agrawal et al. 2012 presented property table for the refrigerant R1234yf at varying temperature and pressure. The generating temperature, condenser temperature, evaporator temperature and corresponding saturation pressure were selected (Table 1).

Table 1 Design condition of the refrigeration system

	Temperature (°C)	Saturation pressure of R1234yf (MPa)
Generator	80	2.51
Condenser	45	1.158
Evaporator	15	0.51

It may be noted that the refrigerant coming out from the nozzle at very high velocity and it has to entertain refrigerant vapour from evaporator at very low velocity. Giving the required momentum to the refrigerant is called entrainment of the vapour and the motive refrigerant will lose some energy. To reduce the losses better design of ejector is required. Frictional losses of the flow inside the ejector through the converging diverging nozzle are the main cause for the exergy loss in the ejector. However the performance of the ejector increases hugely at increased evaporator temperatures. A higher mass flow rate requires a higher energy supply to the generator. A key performance parameter of the ejector is the entrainment ratio. This is a ratio of the entrained flow in evaporator to the generator flow:

$$\omega = \frac{m_{ev}}{m_{gen}}$$

A high entrainment ratio is therefore desirable because it means that a higher amount of evaporation/cooling is achieved with a smaller amount of thermal energy.

Input energy from sun to the solar collector (E_s) is given by following relation

$$E_s = f\sigma T^4 + (1 - f)\sigma T_{planet}^4 - \sigma T_{sc}^4$$

where f is the sunlight dilution factor and it is 2.16×10^{-5} on the earth.

σ Stefan-Boltzmann constant

T_{sc} Average temperature of the solar collector

T_{planet} Temperature of planet

The absorbed solar radiation is converted into available heat (Q_{ava}) as follows:

$$E_s = Q_{ava} \left[1 - \left(\frac{T_{ref}}{T_{sc}} \right) \right]$$

T_{ref} reference temperature for the analysis

W_p Work input by the pump

4 Results and Discussion

The COP of any refrigeration cycle is defined as the ratio between the heat removal in the evaporator and the energy input into the cycle and is a measure of the performance of the system. The overall COP of the ejector cycle is defined as:

$$\text{COP} = \frac{Q_e}{Q_g}$$

Simulation results for various system performance parameters are shown in Table 2. Solar energy supplied in generator decreases with decrease in generator temperature. Air-conditioning of building is carried out at 22–24 °C, therefore, 15 °C is essential for the evaporator coil for effective heat transfer. It may be noted that the refrigerant coming out from the nozzle at very high velocity and it has to entertain refrigerant vapour from evaporator at very low velocity. However the performance of the ejector increases hugely at increased evaporator temperatures. Higher evaporator temperature (18 °C) will result in more mass flow rate through evaporator and hence, increase in entrainment efficiency but the heat transfer through heat exchanger will be difficult and it results in decreasing the refrigerating effect (Table 3). Therefore, it may not be appropriate to use 9–12 °C temperature in the evaporator coil as it will reduce mass flow rate, entrainment efficiency and refrigerating effect.

Table 2 COP of solar ejector-jet refrigeration system at different generator temperature

S. N.	Generator temperature (°C)	Solar energy supplied in generator Q_g (kW)	Refrigerating effect (kW) at Evaporator temperature, 15°C	COP
1	80	5.45	1.66	0.305
2	79	5.38	1.66	0.309
3	78	5.31	1.65	0.311
4	77	5.24	1.64	0.313
5	76	5.17	1.61	0.312

Table 3 COP of solar ejector-jet refrigeration system at different evaporator temperature

S. N.	Evaporator coil temperature (°C)	Refrigerating effect Q_e (kW)	Solar energy supplied in generator Q_g (kW) at generator temperature, 80 °C	COP
1	9	1.50	5.45	0.275
2	12	1.58	5.45	0.29
3	15	1.66	5.45	0.305
4	18	1.62	5.45	0.297

5 Conclusion

A solar ejector-jet vapor compression cooling cycle is proposed using R1234yf for the utilization of solar energy in air-conditioning of building instead of R134a. The main findings of this study are summarized as follows:

1. It is not necessary that increase in evaporator temperature will result in increase in refrigerating effect and COP. An optimum evaporator temperature exists at which refrigerating effect and entrainment efficiency provides best COP.
2. Solar energy requirement decreases with decrease in generator temperature in solar ejector-jet refrigeration system.
3. Refrigerant R1234yf working fluids provides good energy efficiency and environmental option for solar ejector-jet compression systems and its cycle simulation demonstrated that the proposed ejector-jet cycle can provide energy savings if solar energy is supplied.
4. When the generator temperature decreases, the COP of solar ejector-jet refrigeration system increases.

References

- Agrawal, A, Cornelio, A. A., & Limperich, D. (2012). Investigation of cubic EOS models for HFO-1234yf refrigerant used in automotive application, Purdue University. In *International Conference on Refrigeration and Air-Conditioning* (Vol. 2253, pp. 1–10).
- Arsie, I., Rizzo, G., & Sorrentino, M. (2007). Optimal design and dynamic simulation of a hybrid solar vehicle. *SAE Transactions - Journal of Engines*. doi:10.4271/2006-01-2997.
- Boumaraf, L., & Lallemand, A. (2009). Modeling of an ejector refrigerating system operating in dimensioning and of dimensioning conditions with the working fluid R142b and R600a. *Applied Thermal Engineering*, 29, 265–274.
- Cizungu, K., Mani, A., & Groll, M. (2001). Performance comparison of vapour jet refrigeration system with environment friendly working fluids. *Applied Thermal Engineering*, 21, 585–598.
- Dai, Z., Huang, Y., Tang, L., & Chen, G. (2012). Ejector performance of a pump-less ejector refrigeration system driven by solar thermal energy, Purdue University. In *International Conference on Refrigeration and Air-Conditioning* (Vol. 2412, pp. 1–9).
- Eames, I. W., Aphornaratana, S., & Haider, H. (1995). A theoretical and experimental study of a small-scale steam jet refrigerator. *International Journal Refrigeration*, 18(6), 378–386.
- Nguyen, V., Riffat, S., & Doherty, P. (2001). Development of a solar powered passive ejector cooling system. *Applied Thermal Engineering*, 21(2), 157–168.
- Sankarlal, T., & Mani, A. (2007). Experimental investigations on ejector refrigeration system with ammonia. *Renewable Energy*, 32(8), 1403–1413.
- Sun, D.-W. (1997). Solar powered combined ejector-vapour compression cycle for air conditioning and refrigeration. *Energy Conversion and Management*, 38(5), 479–491.
- Sun, D.-W. (1999). Comparative study of the performance of an ejector refrigeration cycle operating with various refrigerants. *Energy Conversion and Management*, 40(8), 873–884.
- Vidal, H., & Colle, S. (2010). Simulation and economic optimization of a solar assisted combined ejector vapor. *Applied Thermal Engineering*, 30(5), 478–486.

- Yu, J., Ren, Y., Chen, H., & Li, Y. (2007). Applying mechanical subcooling to ejector refrigeration cycle for improving the coefficient of performance. *Energy Conversion and Management*, 48(4), 1193–1199.
- Yu, J., & Du, Z. (2010). Theoretical study of a transcritical ejector refrigeration cycle with refrigerant R143a. *Renewable Energy*, 35(9), 2034–2039.

Numerical Investigation of Thermohydraulics Performance in Elliptical Twisted Duct Heat Exchanger

Suvanjan Bhattacharyya, Himadri Chattopadhyay, Tarun Kanti Pal
and Anirban Roy

Abstract Heat transfer behaviour in twisted elliptical duct swirl generator is investigated numerically. Twisted geometry is a widely used technique for heat transfer enhancement. This work presents the investigation of a elliptical twisted duct (ETD) for turbulent heat transfer in air using computational fluid dynamics (CFD) modelling. In the present paper, transition—SST model which can predict the change of flow regime from laminar through intermittent to turbulent has been used for numerical simulations. While the aspect ratio of major and minor axes of the elliptical duct is 0.5, the pitch length (Y) is varied between 0.5 and 1.0. The results indicate that the smaller pitch length yields a higher heat transfer value with relatively lower performance penalty. The transition from laminar to turbulent regime is observed between Reynolds numbers of 1000–3500 for all cases. For all investigated cases, heat transfer enhancement (η) tends to increase with the increase of Reynolds number. This result is useful for the design of solar thermal heaters and heat exchangers.

Keywords Heat transfer enhancement · Elliptical duct · Twisted duct · Heat exchanger · Numerical simulation

1 Introduction

An increased demand by industry has led to a significant gain in momentum of research interests in heat transfer for efficient heat exchange equipment. Heat transfer enhancement process in tubes is very important to design new generation heat

S. Bhattacharyya (✉) · A. Roy
Mechanical Engineering Department, MCKV Institute of Engineering, Liluah,
Howrah 711 204, West Bengal, India
e-mail: suvanjanr@gmail.com

H. Chattopadhyay
Jadavpur University, Kolkata 700 032, West Bengal, India

T.K. Pal
College of Engineering & Management, Kolaghat 721 171, West Bengal, India

exchangers with better efficiency. Twisted pipe is a very promising efficient heat exchange pipe which was developed in last century. Generally, enhancement techniques in convective heat transfer are of two types—active and passive techniques. The active processes require external forces like an acoustic or surface vibration; on the other hand passive process requires typical geometries such as a roughness on the surface, some geometry acting as a turbulator, etc. Both active and passive processes are being used by researchers since nearly a century to increase the rate of heat transfer in heat exchangers (Bejan and Kraus 2003; Webb 1994; Bergles 2002).

Heat transfer characteristics under transitional flow conditions in most of thermal problems are of considerable interest. Predicting transition of laminar regime to turbulent in heat transfer augmentation techniques will be highly useful to design any heat transfer equipment. Abraham et al. (2009), states the theory which provides quantitative results for the heat transfer coefficients in round pipes for the three possible flow regimes: laminar, transitional, and turbulent. This unique model that is based on a laminar-to-turbulent transition can also correctly predict flow natures for purely laminar or purely turbulent flows.

The thermo-hydraulic performance is influenced by the twisted-duct generated swirl flow and the boundary layer separation-reattachment. Heat transfer and flow resistance characteristics of different twisted tubes have been investigated extensively. Ievlev et al. (1982) and Dzyubenko (2005, 2006) studied numerically by using CFD model or experimentally on heat transfer and fluid flow characteristics of the duct side or shell.

The theory is based on a model of laminar-to-turbulent transition which is also viable for purely laminar and purely turbulent flow. Al-Fahed and Chakroun (1996) found that there is an optimum tape width, depending on the pitch, hydraulic diameter and Reynolds number, for the best heat transfer characteristics and also reports that tight-fit tape giving more promising results over the loose-fit one. Suresh et al. (2004) studied numerically on thermo-hydraulic performance of twisted-tape inserts in a large hydraulic diameter annulus. Manglik et al. (1994) investigated numerically the laminar convection heat transfer in circular-segment, uniform wall temperature ducts with a straight tape insert. Bhattacharyya and Saha (2012), Bhattacharyya et al. (2013) and Saha et al. (2012) have observed that the centre-cleared twisted tapes in combination with rib roughness perform significantly better than the individual enhancement technique acting alone for laminar flow through a circular duct up to a certain amount of twisted-tape centre-clearance.

In this work, ETD (when the duct is elliptical and is twisted in axial axis) is a pumping method of heat transfer augmentation as reported in Zhang et al. (2012), it has been observed from the literature review that the twisted-tape inserts, ribs inserts with different angle have been reported earlier but no researcher have not reported in details yet over computational work on elliptical twisted duct with different pitch. The fluid flow due to elliptical twisted duct generated swirl flow is likely reported into provide greater mixing in the flow resulting in increased heat and momentum diffusion. This may increase heat transfer associated with increased pressure drop. In this paper, therefore, the turbulent flow numerical heat transfer and pressure drop results of elliptical twisted duct are presented.

2 Model and Governing Equations

A three-dimensional geometry in Fig. 1a of the elliptical twisted duct was used as computational model. Twisted elliptical duct is, therefore, used to mix the gross flow effectively in turbulent to reduce the thermal resistance in the core flow through the channel. Uniform velocity profile was used at the inlet of the duct. Uniform wall temperature boundary condition is considered with no slip. The range of Reynolds number employed is 200–10,000. Table 1 shows the range of geometrical parameters.

The governing equations are discretized on a non-uniform structured grid using finite volume method and transition—SST model has been used from Menter et al. (2002), which predicts the change of flow regime from laminar through intermittent

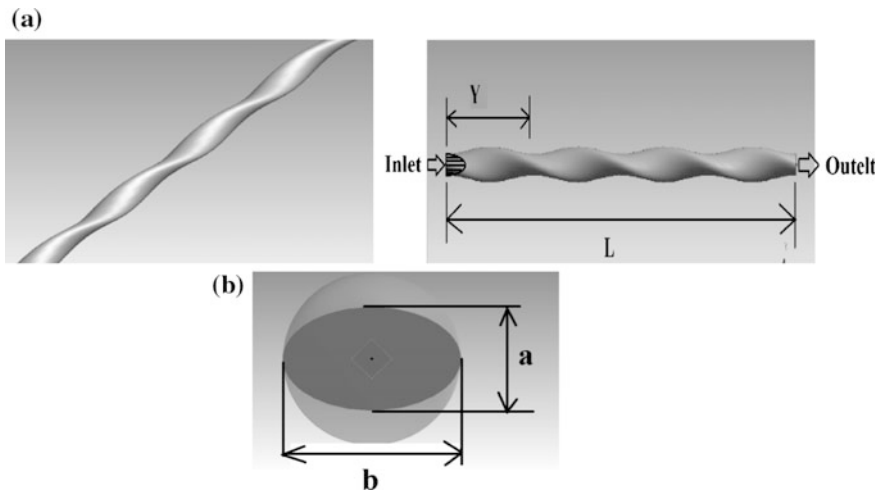


Fig. 1 a Elliptical twisted duct section, b major and minor axis of elliptical twisted-duct

Table 1 Specifications of various duct used

Sl. no.	Tube number	Twist pitch, y in (m)
1	ETD 1	0.50
2	ETD 2	0.62
3	ETD 3	0.75
4	ETD 4	0.87
5	ETD 5	1.00
6	No turn elliptical duct (NTET)	–
7	Circular smooth duct (SCT)	–

to turbulent. The velocities and pressures were predicted using semi implicit pressure linked equations (SIMPLE) scheme. The interpolation of the gradients of velocities and temperature used the third-order accurate scheme. While the gradients for intermittency, turbulent kinetic energy, specific dissipation rate, and momentum thickness used second order accurate upwind scheme. The discretized equations are then linearized using an implicit scheme and solved iteratively using Ansys Fluent 15, 3d double precision solver. The convergence criteria for continuity, momentum and energy are 10^{-4} , 10^{-5} , and 10^{-7} respectively.

The three dimensional governing equations of continuity, momentum and energy equations are solved using Transient SST model. Ansys Fluent 15 is used to solve the following governing equations.

$$\frac{\partial u_i}{\partial x_i} = 0 \quad (1)$$

$$\rho \left(u_i \frac{\partial u_j}{\partial x_i} \right) = - \frac{\partial p}{\partial x_i} + \frac{\partial}{\partial x_i} \left((\mu + \mu_{turb}) \frac{\partial u_i}{\partial x_i} \right) \quad j = 1, 2, 3 \quad (2)$$

$$\left(u_i \frac{\partial \Theta}{\partial x_i} \right) = \frac{\partial}{\partial x_i} \left(\left(\alpha + \frac{\nu_{turb}}{\text{Pr}_{turb}} \right) \frac{\partial \Theta}{\partial x_i} \right) \quad (3)$$

$$\frac{\partial(\rho u_i \kappa)}{\partial x_i} = \gamma \cdot P_\kappa - \beta_1 \rho \kappa \omega + \frac{\partial}{\partial x_i} \left(\left(\mu + \frac{\mu_{turb}}{\sigma_\kappa} \right) \frac{\partial \kappa}{\partial x_i} \right) \quad (4)$$

$$\frac{\partial(\rho u_i \omega)}{\partial x_i} = A \rho S^2 - \beta_2 \rho \omega^2 + \frac{\partial}{\partial x_i} \left(\left(\mu + \frac{\mu_{turb}}{\sigma_\omega} \right) \frac{\partial \omega}{\partial x_i} \right) + 2(1 - F_1) \rho \frac{1}{\sigma_{\omega 2}} \omega \frac{\partial \kappa}{\partial x_i} \frac{\partial \omega}{\partial x_i} \quad (5)$$

where,

$$\mu_{turb} = \frac{a \rho \kappa}{\max(a \omega, SF_2)} \quad (6)$$

$$\frac{\partial(\rho \gamma)}{\partial t} + \frac{\partial(\rho u_i \gamma)}{\partial x_i} = P_{\gamma,1} - E_{\gamma,1} + P_{\gamma,2} - E_{\gamma,2} + \frac{\partial}{\partial x_i} \left(\left(\mu + \frac{\mu_{turb}}{\sigma_\gamma} \right) \frac{\partial \gamma}{\partial x_i} \right) \quad (7)$$

$$\frac{\partial(\rho \Pi)}{\partial t} + \frac{\partial(\rho u_i \Pi)}{\partial x_i} = P_{\Pi,t} + \frac{\partial}{\partial x_i} \left(\sigma_{\Pi,t} (\mu + \mu_{turb}) \frac{\partial \Pi}{\partial x_i} \right) \quad (8)$$

The Eqs. (4), (5), (7) and (8) are the additional equations which are solved along with regular equations of continuity (1), momentum (2) and energy (3) for calculating velocities, pressure, temperature, turbulent kinetic energy, specific turbulent dissipation and intermittency (γ). The state of transition will depend on γ which varies from 0 to 1. Near 0 value of γ determines the state as laminar, while the value near 1 determines the flow as turbulent.

3 Numerical Solution and Boundary Conditions

All physical properties of air have been assumed to be constant. The inlet velocity has been defined as a fully developed flow having a parabolic profile through a circular pipe. It is also assumed that the inlet temperature of the fluid is 300 K. Turbulent intensity of 10 % is prescribed at the inlet. The temperature of the wall of the pipe is considered to be at constant temperature of 500 K and there is no-slip boundary condition between the wall and flow volume interface.

Figure 1b shows the entrance geometry of the problem consists of ETD of 0.02 m diameter of five different pitches. Different grid sizes were tested as part of grid independence study. After a rigorous grid independence check, a mesh consisting of 405,293 cells were used for the present computation. The meshing of the tube is showing in the Fig. 2.

In this present study the following parameters are of interest.

Reynolds Number,

$$Re = \frac{\rho U D_h}{\mu} \tag{9}$$

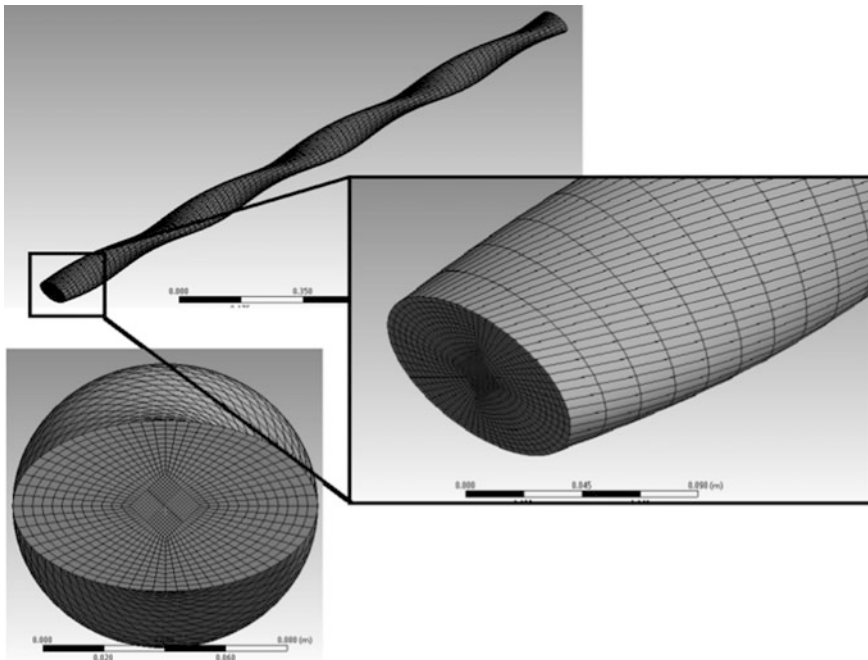


Fig. 2 Structured mesh generation of elliptical twisted duct

The friction factor f is computed by

$$f = \frac{(\Delta P/L)D_h}{\frac{1}{2}(\rho U^2)}. \quad (10)$$

The local Nusselt's number,

$$Nu = \frac{hD_h}{k}. \quad (11)$$

The average Nusselt's is obtained by the area-weight average method,

$$Nu_{avg} = \frac{\int Nu \cdot dA}{\int dA} \quad (12)$$

The thermal effectiveness η is measured as ratio of the heat transfer coefficient of the augmented surface to the heat transfer coefficient of a smooth pipe used by Yang et al. (2011).

$$\eta = \frac{(Nu/Nu_o)}{(f/f_o)^{0.33}} \quad (13)$$

where, Nu_o and f_o stand for Nusselt's number and friction factor for smooth duct, respectively.

4 Result and Discussion

The results of heat transfer, friction factor, turbulent intensity, intermittency and thermal performance factor characteristics in the ETD under the turbulent flow regime are described in the present section. The effect of twisted pitch (γ) performance is presented.

Q-criterion is given by

$$Q = \frac{1}{2} \left(\Omega_{ij}^2 - S_{ij}^2 \right) \quad (14)$$

where,

$$\Omega_{ij} = \frac{1}{2} \left(\frac{\partial u_i}{\partial x_j} - \frac{\partial u_j}{\partial x_i} \right) \quad (15)$$

$$S_{ij} = \frac{1}{2} \left(\frac{\partial u_i}{\partial x_j} + \frac{\partial u_j}{\partial x_i} \right) \quad (16)$$

The Reynolds number used in this computational study are from $Re = 500$ (fully laminar) to $Re = 6000$ (fully turbulent) with the transition in between. The turbulent intensity at the inlet of the jet is given as 10 %, this intensity decreases for laminar conditions where as it increases in turbulent conditions. Iso-surface Q-criterion for different pitches at $Re = 5000$ is presented in Fig. 3. There is a secondary flow vortex formation in the tube, which may help in increasing the heat transfer rate. There is a clear view where the vortices are developing inside the tube. More eddies start appearing with increase in Reynolds number and completely became turbulent at $Re = 5000$. It is seen from the above figure that at small pitch ($y = 0.5$) the vortices are more than the higher pitches.

The heat transfer performance of ETDs is presented in the form of Nusselt number. Variation of Nusselt numbers with Reynolds numbers for the ETDs with different pitch and the SCT are given in Fig. 4a. Reynolds numbers is varied from 200 to 10,000. In Fig. 4a, it can be observed that the Nusselt numbers for all the ducts increase with Reynolds numbers. This increase in Nusselt number indicates an enhancement in heat transfer coefficient. It is also seen from the Fig. 4a that all the tested ETDs have a better heat transfer performance than the other no turn elliptical duct (NTET) and circular smooth duct (SCT). It is also seen from the Fig. 4a that twisted pitch $y = 0.5$ has the best heat transfer performance amongst the other ducts twisted pitch, while smooth circular duct (SCT) is lower. This implies that the heat transfer rate increases with decreasing twisted pitch. Also it should be noted that the Nusselt number for NTET is slightly higher than that of SCT within the entire spectrum of presented Reynolds numbers.

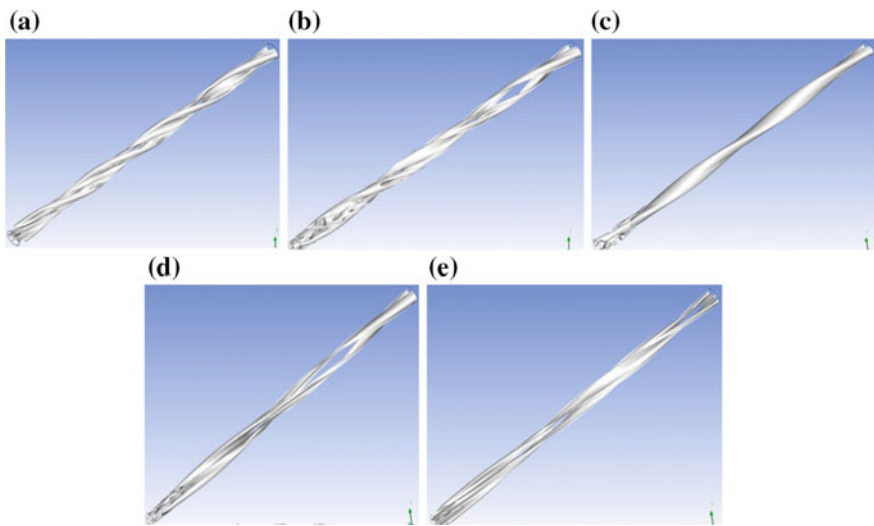


Fig. 3 Iso surfaces of Q-criterion for different pitches. **a** $y = 0.5$, **b** $y = 0.62$, **c** $y = 0.75$, **d** $y = 0.87$, and **e** $y = 1.0$ at $Re = 5000$

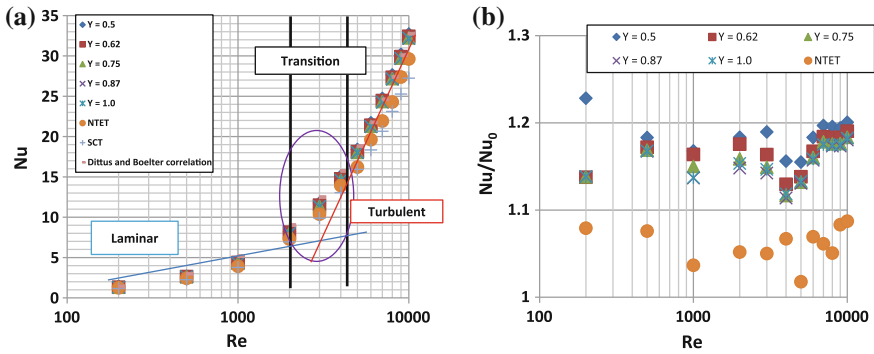


Fig. 4 a Nusselt number versus Reynolds number for different ducts, b Nusselt number ratio (Nu/Nu_0) versus Reynolds number for different ducts

The effectiveness of heat transfer enhancement for all the elliptical duct relative to the smooth circular duct (SCT) was compared in Fig. 4b. The Nusselt number ratio for all the tested ETDs slowly increases in the turbulent region after Reynolds number of 6000 is reached. This indicates that the heat transfer enhancement of the ETDs is significant at both laminar and turbulent flow regions when compared to the transition flow regime. The Nusselt number ratios for twisted ratio $\gamma = 0.5$ that has the best heat transfer performance while NTET has the base one. It can be also noted that after Reynolds number 6000 all the ETDs are increase steadily and one can assume that it gives promising results at turbulent zone.

Friction factor results are presented in Fig. 5. It is seen from Fig. 5a that as the Reynolds number is increased, with the decrease of friction factor. The friction factor values for all the ETDs have higher value than the base case and NTET. Friction factors are higher at lower Reynolds number and then decreases slowly at

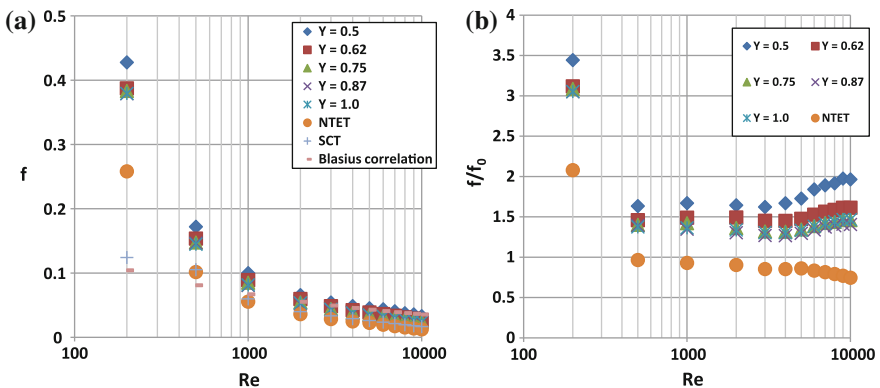


Fig. 5 a Friction factor versus Reynolds number for different ducts, b friction factor ratio (f/f_0) versus Reynolds number for different ducts

higher Reynolds numbers. This is because the attributed to the use of twisted duct with a smaller twist ratio which led to a higher viscous loss near the duct wall regions caused by a stronger swirl flow or turbulence flow and long residence time in the duct.

Figure 5b shows that the ratio of friction factor of twisted elliptical duct to circular smooth duct. From the figure it can be seen that (f/f_0) decreases with Reynolds numbers from 200 to 2000. After Reynolds number of 2000 is reached the graph depicts flat-lined values for f/f_0 throughout the transition region. Then it again slides up with the increase of Reynolds number. The values of f/f_0 is greater than unity for all twisted elliptical ducts except NTET which shows a steady decline throughout the entire range of Reynolds number; this indicates that the pressure drop in all twisted elliptical ducts is more than the base case.

Figure 6 shows the trends of variation in turbulent intensity (TI) with increasing Reynolds number for all the ducts. At the entry of the tube the turbulent intensity is given 10 %. Turbulent intensity increases with increase of Reynolds number. From the Fig. 6, it can be seen that the highest level of turbulent intensity is about 80 % at Reynolds number of 9000–10,000. Twisted pitch $y = 0.5$ has the highest TI, whereas SCT has the lowest TI. Twist ratio ($y = 0.62, 0.75, 0.87$ and 1.0) is also giving some promising TI values at higher Reynolds number.

The ETDs’ overall performance is evaluated using the heat transfer performance evaluation criteria factor (performance factor) η . This is defined as the ratio of the tube side Nusselt number, Nu , for the ETD to that of the SCT, Nu_0 , for equal pumping power. This is shown in Eq. (13).

In Fig. 7 shows the efficiency over the presented Reynolds number range. In most of the cases the ducts provide an enhancement index value greater than unity. For values of twist ratio greater than $y = 0.5$, yields promising values of enhancement index. At high Reynolds number the performance of NTET is comparable to the

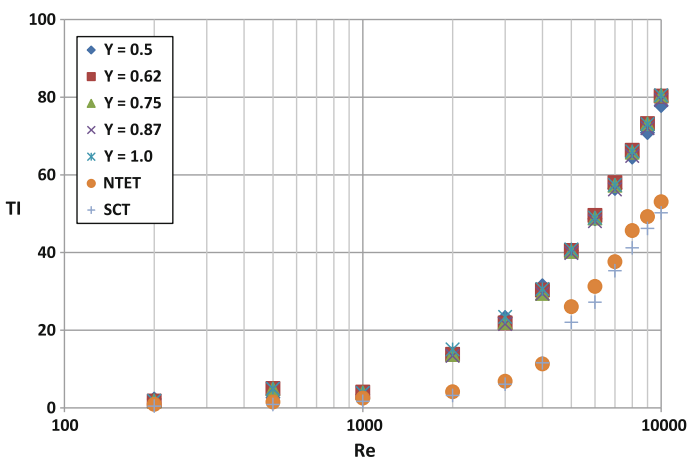


Fig. 6 Turbulence intensity (TI) versus Reynolds number for different ducts

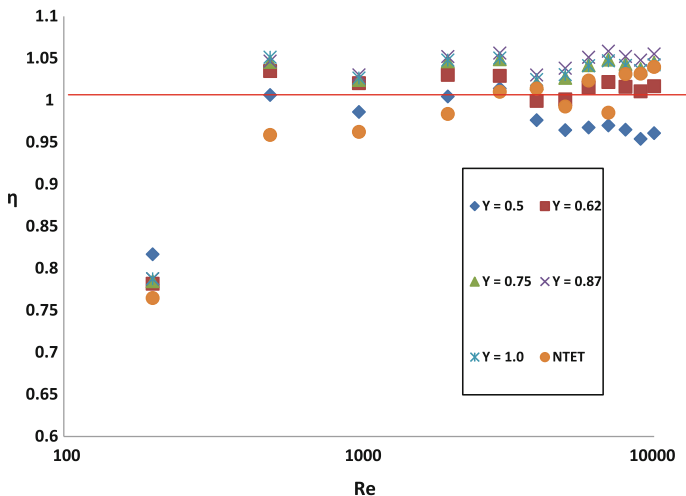


Fig. 7 Enhancement efficiency versus Reynolds number for different ducts

enhancement indices of the other ducts. For Twist ratio of $\gamma = 0.5$ it is noticed that the enhancement index falls at higher turbulent region. Also one can see from the Fig. 7 that $Y = 0.87$ has the highest efficiency.

5 Conclusion

In the present work an experimental and analytical work has been done to investigate the influence of elliptical twisted duct for several twisted pitches ($\gamma = 0.5, 0.62, 0.75, 0.87$ and 1.0) on the heat transfer with the changes of Nusselt Number (Nu), friction factor (f), turbulent intensity (TI). It has been also investigated over the efficiency enhancement. The computational results exhibit that the Nusselt Number is higher than that of the smooth circular tube in the elliptical duct. This proves that it has a good effect on heat transfer enhancement. In the ETD, the axial variation of friction factor value decreased exponentially. The local friction factor decreased with the increment of Reynolds Number. The heat transfer efficiency is higher than unity for most of the ducts over entire Reynolds Number ranges. The numerical investigation shows that the lower twisted pitch can increase the heat transfer rate. But due to increment of turbulence intensity, flow resistance is also increased. The computational results exhibit that a twist ratio in between 0.87 and 1.0 would show the significantly large efficiencies. The easy fabrication of elliptical twisted duct makes it a promising heat transfer enhancer.

References

- Abraham, J. P., Sparrow, E. M., & Tong, J. C. K. (2009). Heat transfer in all pipe flow regimes: Laminar, transitional/intermittent, and turbulent. *International Journal of Heat and Mass Transfer*, 52, 557–563.
- AI-Fahed, S., & Chakroun, W. (1996). Effect of tube tape clearance on heat transfer for fully developed turbulent flow in a horizontal isothermal tube. *International Journal Heat and Fluid Flow*, 17(2), 173–178.
- Bejan, A., & Kraus, A. D. (2003). *Heat transfer handbook* (pp. 1029–1130). New Jersey: Wiley.
- Bergles, A. E. (2002). EXHFT for fourth generation heat transfer technology. *Experimental Thermal and Fluid Science*, 26, 335–344.
- Bhattacharyya, S., & Saha, S. K. (2012). Thermohydraulics of laminar flow through a circular tube having integral helical rib roughness and fitted with centre cleared twisted-tape. *Experimental Thermal and Fluid Science*, 42, 154–162.
- Bhattacharyya, S., Saha, S., & Saha, S. K. (2013). Laminar flow heat transfer enhancement in a circular tube having integral spiral rib roughness and fitted with centre cleared twisted-tape. *Experimental Thermal and Fluid Science*, 44, 727–735.
- Dzyubenko, B. V. (2005). Influence of flow twisting on convective heat transfer in banks of twisted tubes. *Heat Transfer Research*, 36(6), 449–459.
- Dzyubenko, B. V. (2006). Estimation of the thermohydraulic efficiency of heat exchanging apparatuses with twisted tubes. *Heat Transfer Research*, 37(4), 349–363.
- Ievlev, V. M., Dzyubenko, B. V., Dreitser, G. A., & Vilemas, Y. V. (1982). In-line and cross-flow helical tube heat exchangers. *International Journal of Heat and Mass Transfer*, 25(3), 317–323.
- Manglik, R. M., & Bergles, A. E. (1994). Fully developed laminar heat transfer in circular-segment ducts with uniform wall temperature. *Numerical Heat Transfer Part A, Applications*, 26, 499–519.
- Menter, F., Esch, T., & Kubacki, S. (2002). Transition modelling based on local variables. In *Fifth International Symposium on Engineering Turbulence Modeling and Measurements*, Mallorca, Spain.
- Saha, S. K., Bhattacharyya, S., & Pal, P. K. (2012). Thermohydraulics of laminar flow of viscous oil through a circular tube having integral spiral rib roughness and fitted with centre-cleared twisted tape. *Experimental Thermal and Fluid Science*, 41, 121–129.
- Suresh, K. P., Mahanta, P., & Dewan, A. (2004). Study of heat transfer and pressure drop in a large hydraulic diameter annulus. In *The 17th National Heat and Mass Transfer Conference and 6th ISHMT/ASME, Heat and Mass Transfer Conference* (pp. 62–66), Indira Gandhi Centre for Atomic Research, Kalpakkam, India.
- Webb, R. L. (1994). *Principles of enhanced heat transfer*. New York: Wiley.
- Yang, S., Zhang, L., & Xu, X. (2011). Experimental study on convective heat transfer and flow resistance characteristics of water flow in twisted elliptical tubes. *Applied Thermal Engineering*, 31, 2981–2991.
- Zhang, L., Yang, S., & Xu, X. (2012). Experimental study on condensation heat transfer characteristics of steam on horizontal twisted elliptical tubes. *Applied Energy*, 97, 881–887.

Erratum to: TiC, W₂C Reinforced Ti-W MMC Coating Developed on Ti-6Al-4V Substrate Through Laser Cladding

Parth Gattani, Barun Halder, Adil Azeem and Partha Saha

Erratum to:

Chapter 25 in: D.K. Mandal and C.S. Syan (eds.),
CAD/CAM, Robotics and Factories of the Future,
Lecture Notes in Mechanical Engineering,
DOI [10.1007/978-81-322-2740-3_25](https://doi.org/10.1007/978-81-322-2740-3_25)

In the original version, the corresponding author's name, affiliation and email id were missing in the chapter TiC, W₂C Reinforced Ti-W MMC Coating Developed on Ti-6Al-4V Substrate Through Laser Cladding.

The online version of the original chapter can be found under
DOI [10.1007/978-81-322-2740-3_25](https://doi.org/10.1007/978-81-322-2740-3_25)

P. Gattani · B. Halder · A. Azeem · P. Saha
Department of ME, IIT Kharagpur, Kharagpur 721302, West Bengal, India

B. Halder (✉)
Department of ME, BIET, Suri, India
e-mail: b4barun@gmail.com

© Springer India
D.K. Mandal and C.S. Syan (eds.), *CAD/CAM, Robotics and Factories of the Future*, Lecture Notes in Mechanical Engineering,
DOI [10.1007/978-81-322-2740-3_82](https://doi.org/10.1007/978-81-322-2740-3_82)

Author Index

A

Acherjee, Bappa, 23
Ahirwar, Arvind, 535
Ahmad, Faraz, 159, 173
Ajay Kumar, B.S., 807
Alakshendra, Veer, 263, 275
Anjaneyulu, J., 183
Arora, P.K., 697, 779
Azeem, Adil, 253
Azhmyakov, V., 299

B

Bahendwar, Yogesh S., 417
Bahubalendruni, M.V.A. Raju, 397
Bandyopadhyay, Asish, 345
Banerjee, Krishnendu, 243
Banerjee, Nilotpall, 807
Banerjee, Tapas, 345
Banerjee, Jeet, 69
Banerji, Soma, 69
Bepari, Bikash, 481
Bernard, Bonny, 217
Bhattacharyya, Suvanjan, 839
Bhaumik, Adrish, 97
Biswal, Bibhuti Bhusan, 397
Biswas, D., 33
Bright, Glen, 137, 207
Britto, Preethika Immaculate, 217

C

Carvajal Rojas, J.H., 299
Chatterjee, Debabrata, 97
Chattopadhyay, Himadri, 839
Chaudhary, Himanshu, 287, 387
Chaudhury, Arkadeep Narayan, 243
Chauhan, Purvi, 523
Chiddarwar, Shital S., 263, 275
Chittawadigi, Rajeevlochana G., 59

D

Dangayach, G.S., 77, 379
Das, Abhijit, 357
Das, Debasish, 579
Das, Riddhi, 589
Das, Santanu, 33, 345
Datta, Debasis, 243
Deb, A.K., 313
Deb, Sankha, 313, 323, 357
Deepak, B.B.V.L., 397, 405
Desai, Saamil, 523
Dewanjee, D., 33

G

Garg, Harry, 461
Gaurav, 831
Gattani, Parth, 253
George, P.M., 769
Ghosh, Arnab, 243
Gorana, V.K., 13
Gowda, Kumar K., 807
Grover, Sandeep, 689
Guha, Spandan, 345
Gupta, Sumit, 379

H

Haleem, Abid, 697
Harnarinesingh, Randy E.S., 51
Hayat, Abdullah Aamir, 115
Hota, Roshan Kumar, 535, 543

J

Jain, Neha, 665
Jain, Nirbhay, 705
Jain, Prashant K., 741, 751
Jain, Rahul, 13, 77, 553
Jaju, Abhishek, 553
Jha, Abhishek, 263, 275

Jogal, Swapnil, 563
 Joshi, Ravi Prakash, 59
 Joy, M.L., 509

K

Kakandikar, G.M., 455
 Kalaiarasan, G., 761
 Kalsi, Nirmal S., 499
 Kanwar, Karuna, 159
 Kaplish, Akshit, 679
 Karar, Vinod, 461
 Kasie, Fentahun Moges, 137
 Khandelwal, Rishika, 471
 Kiran Kumar, K., 103
 Kirthana, S., 367
 Kirubha, C., 761
 Kolay, Tanumoy, 481
 Krishna Mohana Rao, G., 183
 Kuar, Arunanshu S., 23
 Kulkarni, Ninad, 455
 Kulkarni, Omkar, 455
 Kumani, Devi Singh, 287
 Kumar, Anil, 779
 Kumar, Arvind, 615
 Kumar, Ashwani, 159, 173
 Kumar, C.S., 665
 Kumar, Cheruvu Shiv, 535, 543
 Kumar, Harish, 697, 779
 Kumar, Manish, 397
 Kumar, Narendra, 751
 Kumar, Raj, 831
 Kundra, T.K., 195, 229
 Kundu, P., 33

L

Lewis, Winston G., 425
 Lewis, Winston G., 435

M

Madhu Babu, V., 543
 Mahapatra, Abhijit, 85
 Mahata, D., 445
 Maheshwari, Sachin, 195, 229
 Majumder, Somajyoti, 589
 Mandal, Bijoy, 33
 Mandal, Dipak Kumar, 1
 Manjunatha, B., 491
 Manna, Soumya Kanti, 1
 Meena, M.L., 77
 Mekonnen, Bewketu Gizachew, 207
 Mishra, A., 491
 Mishra, Atul, 323
 Mishra, Subham, 481

Mishra, Vinaytosh, 491
 Misra, Dipten, 23
 Mitra, Souren, 23
 Mittal, M.L., 821
 Mittal, Sameer, 821
 Mondal, Abhijit, 243
 Moona, Girija, 779
 Mundada, Ankit Omprakash, 149

N

Naik, Sawankumar, 625
 Nandedkar, V.M., 455
 Navaraja, A.T., 665
 Nayan, Kamal, 481

P

Pal, Abhishek Rudra, 149
 Pal, Prabir K., 553
 Pal, Raj Kumar, 461
 Pal, Tarun Kanti, 839
 Panaskar, Nitin, 731
 Panjwani, Deepesh, 741
 Parikh, Priyam Anilkumar, 637
 Patel, Harsh, 785
 Patel, Kavita H., 785
 Patel, Trupal, 637
 Pathak, Vimal Kumar, 335
 Patil, P.P., 159, 173
 Pattanaik, Amitansu, 705
 Pradhan, Saibal Kumar, 1
 Prasanth, Hari, 651
 Pratihari, Dilip Kumar, 85, 149, 579
 Pungotra, Harish, 499
 Purohit, Jayant K., 821

R

Raju, B.M.V.A., 405
 Raju, Geo, 797
 Raju, N.V.S., 127
 Ramamohan Rao, T., 367
 Ramsobag, Geeta G., 43
 Rao, C.A., 405
 Rao, P.N., 379
 Rathee, Sandeep, 195, 229
 Rathore, J.K., 13
 Rautela, Anubha, 491
 Ray, D.D., 569
 Ray, Dip N., 569
 Ray, Ranjit, 69, 445
 Rodriguez, Ricardo, 435, 425
 Roy, Anirban, 839
 Roy, Biplob, 589
 Roy, Debanik, 741

Roy, Gour Gopal, 579
 Roy, J.J., 741
 Roy, Shibendu Shekhar, 85

S

Sabharwal, Kamal, 603
 Sadanand, Ratan, 59
 Saha, Partha, 253
 Saha, Subir Kumar, 59, 115
 Sainul, I.A., 313
 Samal, M.K., 741
 Sameer, S.K., 543
 Samuel, Cherian, 491
 Sangle, Akshata, 455
 Saravanan, B., 761
 Sarkar, Prabir, 797
 Sastry, G.V.K.R., 103
 Sebastian, Bijo, 589
 Sengupta, Debashree, 665
 Shaikh, Saquib, 751
 Sharma, Kamal, 563
 Sharma, Milind Kumar, 821
 Sharma, S.K., 491
 Sharma, Sanjeev, 553
 Shendkar, Sumit, 455
 Sheth, Saurin, 523, 637, 769, 785
 Shinde, Harshal, 455
 Shome, Sankar Nath, 69, 445
 Shruthi, C.M., 509
 Sikder, B., 33
 Singh, Amit Kumar, 335, 379, 387
 Singh, Bhupender, 689
 Singh, D.P., 697, 779
 Singh, Harpreet, 797
 Singh, Jasveer, 779
 Singh, M.K., 697

Singh, Namita, 553
 Singh, Paramjit, 499, 603
 Singh, Ramanpreet, 387
 Singh, Satwinder, 679
 Singh, Vikram, 689
 Singla, Ekta, 679, 797
 Sinha, G.R., 417
 Srinivas, J., 715
 Srivastava, Manu, 195, 229
 Subhashini, P.V.S., 127
 Sudheer, A.P., 509, 651
 Surya Kiran, G.V.V., 543
 Syan, Chanan S., 43, 51

T

Tabassum, Meher, 569
 Tandon, Puneet, 741, 751
 Terkar, Ravi, 625, 731
 Thondiyath, Asokan, 471
 Tomer, Vipul, 173
 Tony Thomas, A., 761

U

Udai, Arun Dayal, 115

V

Varalakshmi, K.V., 715
 Venkata Rao, G., 127
 Vinayaka, N., 807

W

Walker, Anthony, 137, 207

Y

Yashaswi, Ramkrishna, 195, 229